A. V. Narlikar (Ed.)

Frontiers in Magnetic Materials

A.V. Narlikar

Frontiers in Magnetic Materials

A.V. Narlikar (Ed.)

Frontiers in Magnetic Materials

With 491 Figures and 22 Tables

Springer

Prof. Dr. Anant V. Narlikar
UGC-DAE Consortium for Scientific Research
University Campus
Khandwa Road
Indore-452017, MP
India

ISBN-10 3-540-24512-X **Springer Berlin Heidelberg New York**
ISBN-13 978-3-540-24512-4 **Springer Berlin Heidelberg New York**

Library of Congress Control Number: 2005923313

Springer is a part of Springer Science+Business Media

springeronline.com

Printed in Germany

Typesetting: Data conversion by the author.
Final processing by PTP-Berlin Protago-TEX-Production GmbH, Germany
Cover-Design: medionet AG, Berlin
Printed on acid-free paper 62/3141/Yu - 5 4 3 2 1 0

CONTRIBUTORS

AKIMITSU, *J.*
Department of Physics and Mathematics
Aoyama-Gakuin University
5-10-1 Fuchinobe
Sagamihara
Kanagawa 229-8558
JAPAN

ANDO, *Yoichi*
Central Research Institute of Electric Power Industry
Komae
Tokyo 201-8511
JAPAN

ASAKA, *T.*
High Voltage Electron Microscopy Station (HVEMS)
National Institute for Materials Science (NIMS)
Tsukuba 305-0044
JAPAN

AWANA, *V.P.S.*
National Physical Laboratory,
Dr K.S. Krishnan Road,
New Delhi-110012,
INDIA

BAJPAI, *A.*
UGC-DAE Consortium for Scientific Research
University Campus
Khandwa Road
Indore 452017
INDIA
Formerly : Inter University Consortium for DAE Facilities
Present address: Tata Institute of Fundamental Research, Homi Bhabha Road,
Mumbai 400 005, INDIA

BANERJEE, *A.*
UGC-DAE Consortium for Scientific Research
University Campus
Khandwa Road
Indore 452017,
INDIA
Formerly : Inter University Consortium for DAE Facilities

BENNEMANN, *K. H.*
Institut für Theoretische Physik
Freie Universität Berlin
Arnimallee 14
D-14195 Berlin
GERMANY

BERTSCHAT, *H. H.*
Bereich Strukturforschung
Hahn-Meitner-Institut Berlin GmbH,
D-14109 Berlin
GERMANY

BLUMBERG, *G.*
Bell Laboratories
Lucent Technologies
Murray Hill
NJ 07974
USA

BOECHAT, *B.*
Instituto de Física
Universidade Federal Fluminense
Av. Litorânea
s/n, Campus da Praia Vermelha
Niteroi, 24.210-340, RJ
BRAZIL

BOOTHROYD, *A.T.*
Clarendon Laboratory
Department of Physics
University of Oxford
Parks Road
Oxford OX1 3PU,
UK.

BREWER, *William D.*
Fachbereich Physik
Freie Universität Berlin
14195 Berlin
GERMANY

BÜNEMANN, *Jörg*
Fachbereich Physik and Material Sciences Center
Philipps-Universität Marburg
D-35032 Marburg
GERMANY

CHOUTEAU, *G.*
Grenoble High Magnetic Field Laboratory,
MPI-FKF and CNRS,
B.P. 166,
38042 Grenoble cedex 9,
FRANCE

CHOVAN, *J.*
Department of Physics
University of Crete and Research Centre of Crete
Heraklion
GREECE

CONTINENTINO, *M.A.*
Instituto de Física
Universidade Federal Fluminense
Av. Litorânea,
s/n, Campus da Praia Vermelha
Niteroi, 24.210-340, RJ
BRAZIL

de BRION, ***S.***
Grenoble High Magnetic Field Laboratory,
MPI-FKF and CNRS,
B.P. 166,
38042 Grenoble cedex 9,
FRANCE

DOWBEN, *P.A.*
Department of Physics and Astronomy, and
The Center for Materials Research and Analysis (CMRA)
255 Behlen Laboratory of Physics
University of Nebraska
P.O. Box 880111
Lincoln
Nebraska 68588-0111
USA

EISAKI, *H.*
Nanoelectronic Research Institute
AIST
Tsukuba
Ibaraki 305-8568
JAPAN

FERNANDES, *J.C.*
Instituto de Física
Universidade Federal Fluminense
Av. Litorânea
s/n, Campus da Praia Vermelha
Niteroi, 24.210-340, RJ
BRAZIL

GEBHAARD*, Florian*
Fachbereich Physik and Material Sciences Center
Philipps-Universität Marburg
D-35032 Marburg
GERMANY

GOZAR, *A.*
Bell Laboratories, Lucent Technologies
Murray Hill,
NJ 07974
USA
and
University of Illinois at Urbana-Champaign
Urbana, IL 61801
USA

GUIMARÃES, *R.B.*
Instituto de Física
Universidade Federal Fluminense
Av. Litorânea
s/n, Campus da Praia Vermelha
Niteroi, 24.210-340, RJ
BRAZIL

JENKINS, *S.J.*
Department of Chemistry
University of Cambridge
Lensfield Road,
Cambridge CB2 1EW
U.K.

JENSEN, *P. J.*
Institut für Theoretische Physik
Freie Universität Berlin
Arnimallee 14
D-14195 Berlin
GERMANY

JUNGWIRTH, *Tomas*
School of Physics and Astronomy
University of Nottingham
Nottingham NG7 2RD
U.K.
and
Institute of Physics ASCR
Cukrovarnicka 10
162 53 Praha 6
CZECH REPUBLIC

KAGEYAMA, *Hiroshi*
Department of Chemistry
Graduate School of Science
Kyoto University
Kyoto 606-8502
JAPAN

KARPPINEN*, M.*
Materials and Structures Laboratory
Tokyo Institute of Technology
Yokohama 226-8503
JAPAN

KIMOTO, *K.*
High Voltage Electron Microscopy Station (HVEMS)
National Institute for Materials Science (NIMS)
Tsukuba 305-0044
JAPAN
and
Advanced Materials Laboratory (AML)
National Institute for Materials Science (NIMS)
Tsukuba 305-0044
JAPAN

KOMIYA, *Seiki*
Central Research Institute of Electric Power Industry
Komae
Tokyo 201-8511
JAPAN

MAKAROVA, *Tatiana*
Umeå University
90187 Umeå
SWEDEN

MATSUDA, *M.*
Advanced Science Research Center
Japan Atomic Energy Research Institute
Tokai
Ibaraki 319-1195
JAPAN

MATSUI, *Y.*
High Voltage Electron Microscopy Station (HVEMS)
National Institute for Materials Science (NIMS)
Tsukuba 305-0044
JAPAN
and
Advanced Materials Laboratory (AML)
National Institute for Materials Science (NIMS)
Tsukuba 305-0044
JAPAN

MOSHNYAGA, *V.*
I Physikalisches Institut
Universität Göttingen
Friedrich-Hund-Platz 1
D-37077 Göttingen
GERMANY

MOTOYAMA, *N.*
Department of Physics and Mathematics
Aoyama-Gakuin University
5-10-1 Fuchinobe
Sagamihara
Kanagawa 229-8558
JAPAN

NAGAI, *T.*
High Voltage Electron Microscopy Station (HVEMS)
National Institute for Materials Science (NIMS)
Tsukuba 305-0044,
JAPAN

NAIR, *Sunil*
UGC-DAE Consortium for Scientific Research
University Campus
Khandwa Road
Indore 452017
INDIA
Formerly : Inter University Consortium for DAE Facilities
Present address: Tata Institute of Fundamental Research, Homi Bhabha Road,
Mumbai 400 005, INDIA

NAKAJIMA, *T.*
Materials Design and Characterization Laboratory,
Institute for Solid State Physics,
University of Tokyo,
5-1-5 Kashiwanoha,
Kashiwa,
JAPAN

NÚÑEZ-REGUEIRO, *M.D.*
Laboratoire de Physique des Solides,
Bâtiment 510,
Université Paris-Sud,
91405 Orsay,
FRANCE

OHM, *Torsten*
Institut für Physik
Universitat Dortmund
D-44221 Dortmund
GERMANY

PAPANICOLAOU, *N.*
Department of Physics
University of Crete and Research Centre of Crete
Heraklion
GREECE

PRABHAKARAN, *D.*
Clarendon Laboratory,
Department of Physics
University of Oxford
Parks Road
Oxford OX1 3PU
U.K.

SAGUIA, *A.*
Instituto de Física
Universidade Federal Fluminense
Av. Litorânea
s/n, Campus da Praia Vermelha
Niteroi, 24.210-340, RJ
BRAZIL

SINOVA, *Jairo*
Physics Department
Texas A&M University
College Station
Texas 77843-4242
USA

TERASAKI, *Ichiro*
Department of Applied Physics,
Waseda University,
Tokyo 169-8555,
JAPAN

UEDA, *Y.*
Materials Design and Characterization Laboratory,
Institute for Solid State Physics,
University of Tokyo,
5-1-5 Kashiwanoha,
Kashiwa,
JAPAN

UEHARA, *M.*
Yokohama National University
Faculty of Engineering
Division of Intelligent Systems Engineering
79-1 Tokiwadai
Hodogaya-ku
Yokohama
Kanagawa 240-8501
JAPAN

WEBER, *Werner*
Institut für Physik
Universitat Dortmund
D-44221 Dortmund
GERMANY

WEISER, *Stefan*
Institut für Physik
Universitat Dortmund
D-44221 Dortmund
GERMANY

YAMAUCHI, *H.*
Materials and Structures Laboratory
Tokyo Institute of Technology
Yokohama 226-8503
JAPAN

PREFACE

The field of Magnetism, perhaps the oldest branch of physics, today provides the world's second largest industry, with magnetic materials claiming a market next only to semiconductor industry. In the current scenario the demand for magnetic materials is fast rising and Magnetism has taken central stage in science and technology. Even more excitingly, several exotic magnetic phenomena and novel materials have recently been discovered, many of which seem to hold the vital keys to unlocking new technology as well as challenging physics. This edited book, *Frontiers in Magnetic Materials*, focuses on the current achievements and state of art advancements in the frontal magnetic materials.

The phenomenal success of magnetic materials may be ascribed to four relevant happenings in the last 10-15 years; (1) A dramatic refinement and development of new methods and probes for magnetic materials characterization, (2) overall improvements in general expertise and techniques in sample synthesis, (3) discovery of high Tc superconductivity phenomenon in rare-earth based cuprate and related systems, and (4) the global realization of importance of nano-science and –technology.

During mid-80s, the traditional characterization techniques like magnetic susceptibility, magnetometry, magnetic resonance, neutron scattering, heat capacity etc., got a tremendous impetus through the use of microprocessors and commercial SQUIDS. As a consequence, the measurement capabilities for bulk magnetic properties got vastly refined. Interestingly, the same materials, which had already been exhaustively studied 40-50 years ago, now began yielding exciting new findings and deeper insights, which had hitherto not been possible. Likewise, the atomic level sensing capability of the microscopic nuclear probes, like Mössbauer and perturbed angular correlation spectroscopies also got enhanced. The sample processing too became more reliable to successfully synthesize reproduceable good quality single crystals and epitaxial films of complex materials in varied structures like, ultra-thin monolayers, multilayers, sandwiches, etc., with intriguing magnetic properties.

The remarkable discovery of high temperature superconductivity in La-based cuprate in 1986 triggered a renewed interest in RE-based perovskite manganites and related magnetic systems that had already been exhaustively studied many years earlier. But now with improved sample processing and characterization, the studies led to the exciting discovery of the CMR and charge/orbital ordering effects and the start of a gigantic activity in fundamental research and technology. Some of these along with a few double perovskites and other magnetic systems have interestingly been found half-metallic ferromagnets possessing a pronounced spin polarization at very low temperatures. This makes them strong candidates for the prospective 'spintronic' and tunneling magneto-resistance (TMR) devices. Similarly, several other fascinating magnetic systems, such as spin ladders and chain materials, presenting interesting situations of qunatum magnetism, have really been the off-shoots of high Tc cuprates.

This edited book takes stock of the above developments and many more. For instance, it presents detailed coverages of magnetism of two dimensional borates, and a host of highly

anisotropic oxy-borates, field induced transitions from incommensurate magnetism to commensurate magnetism in layered antiferromagnets, curious differences in orbital and spin states of two apparently similar nickel oxides, detailed ac susceptibility studies probing, spin glass, superparamagnetic and long range ordered systems, site-dependent order/disorder effects in perovskite manganite, and growth and properties of bi-layer manganite single crystals.

The success in sample processing and characterization during the last decade has led to the synthesis of unusual magnetic systems showing dual properties. The examples of these are ferromagnetic semiconductors, magneto-superconductors and magneto-thermoelectrics. Furthermore unconventional magnetism has been discovered in various forms of carbon, such as graphite, fullerenes, nanotubes etc.,where processing the materials differently seem to change them from ferromagnetic to superconducting !

Mounting importance of nano-level studies has led to the ingenious ways of producing nanoparticle samples and the advent of powerful new techniques for element specific studies, layer-by-layer and even leading to atomic resolution, suitable for investigating magnetism of nanoclusters, bi- and trilayer systems and even single atoms at surfaces and interfaces. The book carries an interesting overview of these modern methods of characterising magnetic materials. The success at the nano-level has opened-up new frontiers, namely magnetism of nanoclusters, surface and interface magnetism, low dimensional magnetism, interacting nanostructure magnetism etc., all holding an intense technological prospects, are covered in this edited book. The potential of high resolution TEM and the Lorentz TEM for observational studies of magnetic materials has been convincingly demonstrated. Finally, turning from these exotic new materials to the perennial problem of magnetism of nickel, this edited book presents an interesting approach that applies the original Gutzwiller variational scheme to multiband problem.

Frontiers in Magnetic Materials comprises 24 chapters on the mentioned topical areas, written by noted international experts in the field and should be of central interest to researchers and specialists in physics and materials science faculties of academic institutes as well as relevant industries. At the same time, the book is also likely to be of relevance for final year undergraduates reading physics and materials science.

I would like to thank all the contributors for their splendid and timely cooperation. I am grateful to William Brewer for his help and suggestions in planning the book and to Alok Banerjee for useful comments. Thanks are further extended to the IUC, Indore and UGC-DAE Consortium for Scienific Research, Indore for providing the necessary infrastructure facilities.

November, 2004 Anant V. Narlikar

CONTENTS

SINGLE CRYSTALS OF BILAYER MANGANITES

D. Prabhakaran and A.T. Boothroyd

GUTZWILLER-CORRELATED WAVE FUNCTIONS: APPLICATION TO FERROMAGNETIC NICKEL

Jörg Bünemann, Florian Gebhard, Torsten Ohm, StefanWeiser, and Werner Weber

CHEMISTRY OF HALF-METALLIC AND RELATED CATION ORDERED DOUBLE PEROVSKITES

M. Karppinen and H. Yamauchi

DILUTE MAGNETIC SEMICONDUCTORS

Jairo Sinova and Tomas Jungwirth

UNCONVENTIONAL MAGNETISM IN CARBON BASED MATERIALS

Tatiana Makarova

ORBITAL AND SPIN ORDER IN THE TRIANGULAR S=1/2 LAYERED COMPOUND (Li,Na)NiO_2

S. de Brion, M.D. Núñez-Regueiro, and G. Chouteau

STRUCTURES AND ELECTROMAGNETIC PROPERTIES OF THE A-SITE ORDERED PEROVSKITE MANGANITE

Y. Ueda and T. Nakajima

THE LIMITS TO SPIN-POLARIZATION IN FINITE-TEMPERATURE HALF-METALLIC FERROMAGNETS

P.A. Dowben and S.J. Jenkins

LAYERED COBALT OXIDES AS A THERMOELECRIC MATERIAL

Ichiro Terasaki

COMMENSURATE AND INCOMMENSURATE MAGNETISM IN LAYERED ANTIFERROMAGNETS

J. Chovan and N. Papanicolaou

MAGNETISM IN HIGHLY ANISOTROPIC BORATES: EXPERIMENT AND THEORY

M.A. Continentino, J.C. Fernandes, R.B. Guimarães, B. Boechat, and A. Saguia

METAL-INSULATOR TRANSITION AND MAGNETORESISTANCE IN MANGANITE THIN FILMS: LATTICE STRAIN AND DISORDER EFFECTS

V. Moshnyaga

MAGNETISM OF INTERACTING TWO-DIMENSIONAL NANOSTRUCTURES

P. J. Jensen and K. H. Bennemann

SURFACE AND INTERFACE MAGNETISM ON THE ATOMIC SCALE

H. H. Bertschat

MAGNETO–SUPERCONDUCTIVITY OF RUTHENO-CUPRATES

V.P.S. Awana

SUPERCONDUCTIVITY AND MAGNETISM IN LADDER AND CHAIN COMPOUNDS-PHYSICS OF $(Sr,Ca)_{14}Cu_{24}O_{41}$

M. Uehara, N. Motoyama, M. Matsuda, H. Eisaki, and J. Akimitsu

AN EXPERIMENTAL REALIZATION OF THE SHASTRY-SUTHERLAND MODEL

Hiroshi Kageyama

COLLECTIVE SPIN AND CHARGE EXCITATIONS IN $(Sr,La)_{14-x}Ca_xCu_{24}O_{41}$ QUANTUM SPIN LADDERS

A. Gozar and G. Blumberg

ELECTRONIC PROPERTIES OF α' – NaV_2O_5

A. Gozar and G. Blumberg

COLLECTIVE MAGNETIC EXCITATIONS IN $SrCu_2(BO_3)_2$

A. Gozar and G. Blumberg

MAGNETIC AND CHARGE CORRELATIONS IN $La_{2-x-y}Nd_ySr_xCuO_4$: RAMAN SCATTERING STUDY

A.Gozar, Seiki Komiya, Yoichi Ando, and G. Blumberg

MODERN METHODS FOR INVESTIGATING MAGNETISM

William D. Brewer

Fachbereich Physik. Freie Universität Berlin, 14195 Berlin, Germany

1. INTRODUCTION

The study of magnetism is one of the oldest fields of physics and was the subject of a major treatise (Gilbert's *de magnete*) over 400 years ago. The basic principles and mech-anisms responsible for the existence of magnetic fields and moments and the coupling of the latter within magnetic materials were elucidated in the first half of the 20th century. Nevertheless, there remain a number of open questions and puzzles, particularly relating to magnetism in certain classes of materials and in certain geometries (e.g. thin films, interfaces, small clusters). An especially interesting field is the origin and details of magnetic anisotropy in thin films and at interfaces, relevant to phenomena such as perpendicular magnetisation and exchange bias, that in turn may prove to provide the keys to new technologies for high-density data storage and switching elements.

These and other properties of magnetic systems can be studied by the long-established methods of magnetometry and susceptometry, neutron scattering and magnetic resonance, as well as by magneto-optical techniques. All of these have been improved and refined in the past 20 years and have enormously increased sensitivity (e.g. through the use of SQUID detection) as well as flexibility (*in situ* studies of surfaces and thin films in ultrahigh vacuum or UHV). Moreover, they have been complemented in the past decades by a number of less conventional techniques which offer even higher sensitivity, spectral and spatial resolution, atomic selectivity, and the ability to separate orbital and spin contributions to magnetic moments. During the same time period, the rapid development of theoretical methods based on the density functional approach has allowed the calculation of ever-finer details of the formation and interactions of magnetic moments and has permitted a refined interpretation of the experimental data.

It is the goal of this chapter to provide a brief survey of some of these new experimental methods and to show examples of their application to the study of magnetism, especially in thin films and at interfaces. There will be no attempt to provide an exhaustive summary of all these new developments or of all the groups who have contributed to them worldwide; instead, a few representative examples more familiar to the author will be cited with a moderate degree of detail. Still more detailed information on a few particular techniques can be found in some of the other chapters in this book.

2. TOPICS TREATED

We mention the following areas of novel experimental techniques as applied to the magnetism of thin films and interfaces:

(1) Reflectometry with polarised neutrons
(2) Excited-nuclear methods
(3) X-Ray spectroscopies and microscopy
(4) Spectroscopy and microscopy with spin-polarised electrons
(5) Magnetic scanning microscopy

Of these, the X-ray and excited-nuclear methods are the oldest. The former developed over most of the 20th century, while the latter came into use in the 1960's. However, their application to the study of magnetic systems, particularly nanoscale systems such as thin films, small clusters, and interfaces, is relatively recent. In the case of the X-ray methods, this application awaited the development of intense sources of monochromatic, polarised X-radiation from electron storage rings (synchrotron sources), while in the case of the excited-nuclear methods, it resulted from the availability of well-characterised samples (UHV technology) and of soft-landing and implantation methods for introducing the probe atoms. The other methods have been developed or have become practical only in the past two decades and were quickly applied to interesting magnetic systems. We will discuss each of these topics separately, giving a brief history of its development and application, and then concentrate on a few representative experiments performed in recent years in our own group. The last two topics will be discussed only summarily, without, as mentioned above, making any attempt to give a complete survey of groups working in the field. For the latter, we refer where appropriate to review articles in the literature.

3. MODERN METHODS

(1) Polarised-Neutron Reflectometry (PNR)

Magnetic investigations using polarised neutrons are not new, having been developed in the 1950's for bulk systems. They played an important role in the elucidation of many magnetic structures, especially those of antiferromagnetic materials. However, neutrons, due to their weak interactions with matter, are not inherently surface-sensitive and require relatively large amounts of sample material, so these methods were for many years applied only to studies of bulk properties. The development of reflectometers which allow scattering of polarised

neutrons at grazing angles and therefore give good sensitivity for multilayers or in favourable cases for thin films took place in the 1980's and the method is now standard for the investigation of thin magnetic films and interfaces [1]. It has been treated in numerous reviews and books [2-5], and there is an extensive literature on its application to magnetic studies.

It is important to note that neutron reflectometry by thin bi-, tri- or multilayers is distinctly different from conventional neutron diffraction by bulk crystal lattices. In the latter, the primary scatterers are the atoms themselves: their atomic nuclei, which are essentially pointlike, and their electronic shells (which on the scale of neutron wavelengths are also localised and can be described by an atomic form factor). The scattering process can be treated by a straightforward kinematic theory and the resulting diffraction pattern directly reflects the lattice structure, with fixed Bragg peaks corresponding to the lattice spacings in different directions. In reflectometry from multilayers, scattering from individual atoms can be neglected within a continuum model, and instead whole layers (within the coherence length of the neutron beam) can be treated as scattering elements. The scattering process is described by dynamical scattering theory, and the important quantity determining the diffraction pattern is the effective index of refraction of the various layers as well as layer spacings and thicknesses. This is illustrated in the figure below:

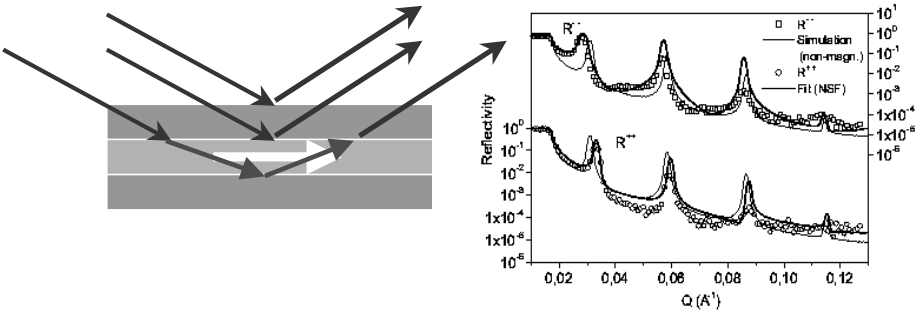

Fig. 1. *Left:* a schematic representation of neutron reflectometry from a magnetic trilayer. The grey layers are nonmagnetic and have a different index of refraction for polarised neutrons from the blue (magnetised) layer; in the latter, depending on whether the neutron spin is parallel or antiparallel to the layer magnetisation, the index of refraction will vary. The result is a shift in the Bragg peaks (*right*, data from Ref. [6]). The thin solid lines represent the case where all layers are nonmagnetic; the Bragg peaks then reflect only the superlattice spacing. With a magnetised layer, the peaks are shifted to higher or lower Q values, depending on the relative orientation of neutron spins and magnetisation (here along the 'specular ridge').

We give an example from the recent literature [6,7]. It involves the study of a typical exchange-bias system, Co/CoO, using PNR to investigate the mechanisms of magnetisation reversal and domain formation. 'Exchange bias' (EB) is an induced shift and broadening of the hysteresis curve of a ferromagnet when it is in intimate contact with an antiferromagnet. EB has important potential applications but is still not understood in detail, although it was discovered nearly 50 years ago [8]. Co/CoO is the archetype exchange-bias system, and was indeed the first one to be discovered. It can be prepared in the form of ultrathin films by e.g.

evaporation of Co in UHV and *in situ* oxidation [9]. The role of a nonmagnetic 'spacer' layer between the ferromagnetic Co and antiferromagnetic CoO layers is also of interest for understanding the microscopic interactions at the metal-oxide interface [10]. This system has recently been studied using PNR by several groups [7,11,12]. By applying PNR at various points along the hysteresis curve of the magnetic Co layers (Fig. 2), one can obtain information about the details of the magnetisation reversal processes which are important for understanding exchange bias in detail and for potential applications in fast magnetic switching devices.

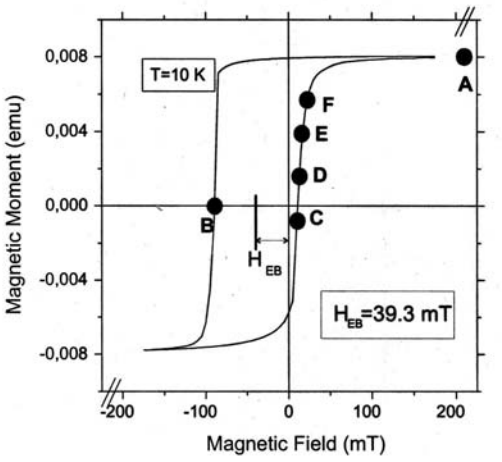

Fig. 2. The [Co(16.4 nm)/CoO(2.0 nm)/Au(3.4 nm)]$_{20}$ multilayer sample used in [6] shows a large exchange-bias effect (shift of the centre of the loop to negative applied fields by an amount given by the exchange-bias field H_{EB} as well as an asymmetric hysteresis loop). Neutron studies were carried out at the marked points on the hysteresis curve (measured here by SQUID magnetometry, figure adapted from Refs. [6] and [7]).

Results of neutron reflectometry measurements are shown in Fig. 3 for a Co/CoO multilayer sample (required for sensitivity reasons; the technique would work in principle on a single bilayer, but the signal/noise ratio is poor). Reflection coefficients are given for three cases: the open and filled square data points (R^{++} and R^{--}) represent non-spinflip reflections, in which the neutron polariser and analyser are parallel to each other and no change in the neutron spin occurs on scattering from the sample. This is the case when the neutron spins are parallel or antiparallel to the magnetisation of the magnetic domains in the magnetic (Co) layers, as at point A on the hysteresis loop in Fig. 2 (magnetic saturation). A corresponding shift of the Bragg peaks (only the first peak near Q = 0.03 Å^{-1} is shown here) to higher or lower scattering vectors Q for parallel (R^{++}) or antiparallel (R^{--}) magnetisation is observed, and little intensity is seen at the nonmagnetic Q-value, indicating that all the domains point along the same axis. The triangular data points (R^{+-}) represent spinflip scattering, which occurs when significant magnetisation components perpendicular to the neutron spins are present. This is not the case at point A, where the spinflip signal is at the noise level, 3 to 4 orders of magnitude weaker than the non-spinflip signals.

At point B, where the overall magnetisation of the sample is zero during the magnetisation reversal with decreasing (negative) applied field, i.e. at the negative coercive field, a different picture emerges: the two spin orientations give nearly identical reflections, indicating an equal number of domains magnetised parallel or antiparallel to the neutron spin direction. The spinflip signal is clearly stronger, but still more than an order of magnitude below the non-spinflip data. At point D, on the other side of the loop at increasing applied field, i.e. at the positive coercive field, still another distribution of magnetic domains is observed: here, the shifts in the Bragg peak have vanished and the data points resemble the simulation for scattering from nonmagnetic layers. The spinflip signal now has the same

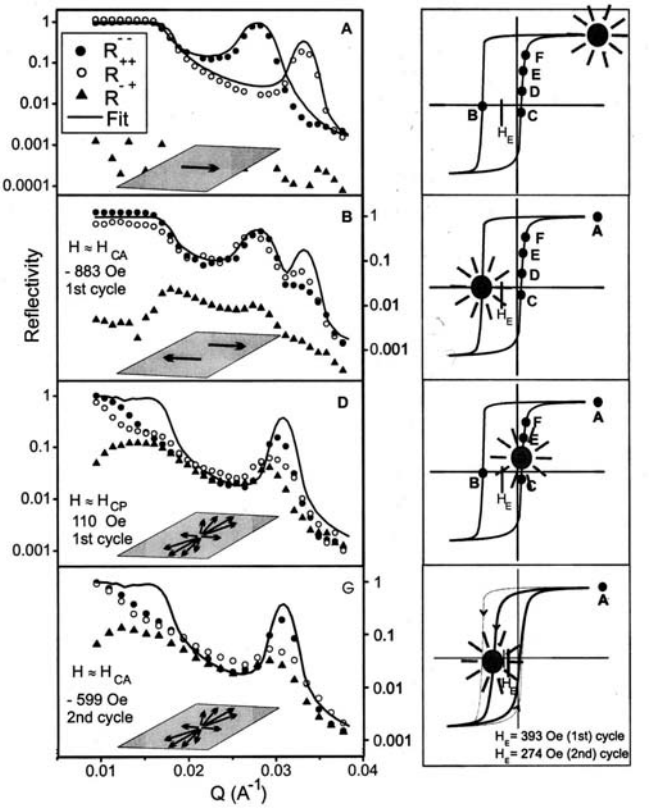

Fig. 3. PNR signals at four different points along the hysteresis curve of a Co/CoO multilayer sample. The spectra at left show the reflectometry data for the first Bragg peak, the magnetisation curves at the right illustrate the magnetic state of the sample at the same applied fields. The narrower loop in the bottom plot on the right is observed after a second magnetisation cycle and shows the 'training' effect of repeated magnetic cycling. Figure modified from Refs. [6] and [7].

strength as the non-spinflip data, indicating that domains lie in all directions within the layer plane. The conclusion is that the magnetisation reversal on the negative side of the loop takes place primarily by domain growth in the new direction, while the reversal on the positive side occurs by domain rotation. After a second magnetic-field cycle (point G, 'training' effect), both reversals proceed by domain rotation.

The temperature dependence of the PNR signals is indicated in Fig. 4, where the reflections at the first Bragg peak are shown at room temperature, well above the blocking temperature of the sample (ca. 200 K, below which the exchange bias effect sets in), and at 10 K, well below the blocking temperature.

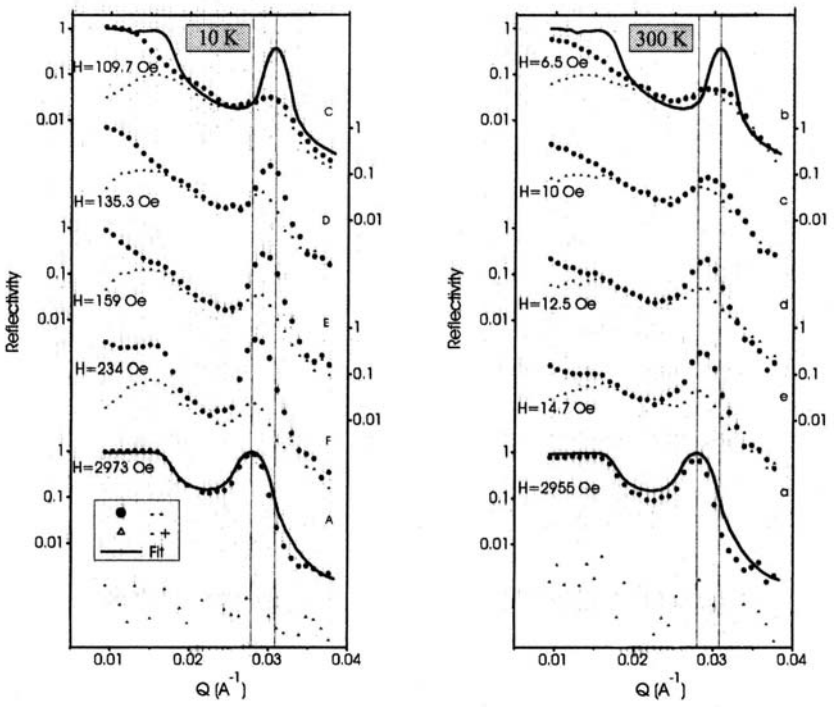

Fig. 4. PNR signals (circles = non-spinflip, small triangles = spinflip data) near the first Bragg peak from the Co/CoO multilayer at two measuring temperatures, below (*left*, 10 K) and above (*right*, 300 K) the blocking temperature, below which exchange bias sets in. The bottom curve is for magnetic saturation (point A in Fig. 2), while the upper curves are taken at applied fields near the positive coercive field at the given temperature. The solid curve at the top of the figure is a simulation for non-magnetic layers, the curves at the bottom are for magnetic saturation. From Refs. [6,7].

A gradual shift of the position of the Bragg peak towards the saturation value can be seen in the figure at both temperatures. Spinflip and non-spinflip intensities are comparable just below the coercive field value at both temperatures, but the spinflip intensity decreases

rapidly as the applied field passes above the coercive field. In the unbiased state at 300 K, the hysteresis loop is very narrow and magnetisation reversal occurs at both coercive fields by domain rotation. In the exchange-biased state at 10 K, the reversal is similar at the positive coercive field, where the hysteresis loop is rounded (Figs.2 and 3), but it exhibits a different mechanism at the sharp corner of the loop near the negative coercive field.

Careful comparison of the signal intensities in Figs.3 and 4 indicates some 'missing' intensity near the magnetisation reversals. This is due to off-specular scattering which scatters intensity out of the specular ridge. Off-specular scattering can be caused by chemical roughness of the interfaces in the multilayer sample, or to 'magnetic roughness' as a result of the domain structure in the magnetic layers [13-16]. The latter is dependent on the applied magnetic field, while the former is not. In [6], the off-specular or diffuse scattering was

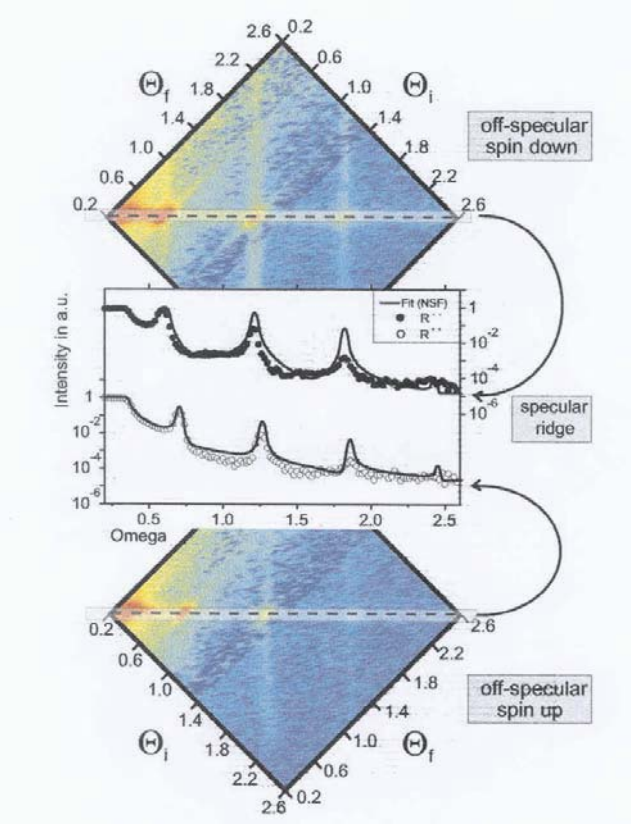

Fig. 5. (Θ_i, Θ_f) intensity maps for the two neutron spin directions scattered from a Co/CoO multilayer at magnetic saturation. The scattered intensity as a function of the two angles is shown as a false-colour map (above and below); red corresponds to the highest scattering intensity. The corresponding data along the specular ridge are given as an inset between the intensity maps. From Ref. [6].

studied by using a position-sensitive neutron detector to measure the scattered intensity away from the Bragg angles, yielding a two-dimensional map on which the specular ridge appears as a high-intensity line on which the initial and scattering angles, Θ_i and Θ_f, meet the specular reflection condition (shown by dashed lines in Fig.5). Scattered intensity outside this line is off-specular. The streaks perpendicular to the specular ridge at the positions of the Bragg peaks indicate correlated roughness, which persists over several bilayers within the multilayer. The intensity of off-specular scattering is related to the size of the magnetic domains; compare the scattering from a magnetically-saturated multilayer in Fig.5 and Fig.6 (*left*) with that near the coercive field in Fig.6 (*right*).

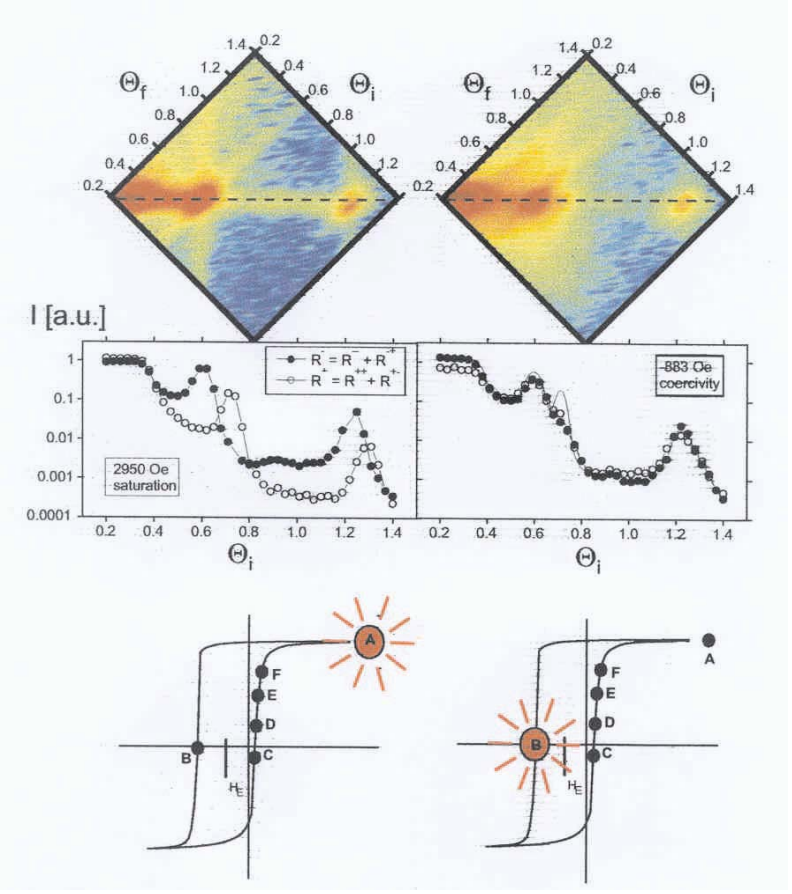

Fig. 6. Intensity maps as in Fig.5, for magnetic saturation (*left*) and near the negative coercive field in the exchange-biased state (*right*). The magnetisation curves in the lower part show the corresponding points on the hysteresis loop. Note the clear increase in off-specular scattering near the coercive field. From Ref. [6].

It can be concluded from the comparison of the off-specular scattering at different applied fields that the domains which rotate at points D (and G) in the hysteresis loop (Figs. 2 and 3) are generally smaller than those which grow by domain-wall movement at point B. Additional information abut vertical correlations in roughness can in principle also be obtained by a quantitative analysis of the off-specular scattering.

Similar conclusions were reached in Refs. [11] and [12] using samples of the same exchange-bias system grown by different methods. PNR thus represents a powerful method to obtain detailed information about the magnetisation of ultrathin layers and multilayers which is not otherwise available, and it complements conventional methods for studying magnetisation and domain formation.

(2) Excited-Nuclear Methods

These techniques involve the use of probe atoms containing excited atomic nuclei, i.e. radioactive nuclei. As initially developed in the early 1960's, they employed the *ex situ* production of atoms in an excited nuclear state in a cyclotron or reactor, which were then introduced into the sample thermally (by melting or diffusion) or later by implantation from an isotope separator or through recoil from a target in a cyclotron. In some cases, *in situ* neutron activation could also be used. These methods all involve generating a non-isotropic distribution of the nuclear substates by angular momentum transfer, selection of an anisotropic subpopulation, thermal equilibrium at very low temperatures, or resonant absorption or scattering of nuclear radiation from a fixed direction. This anisotropic distribution then precesses in space due to its interaction with the local magnetic field, and the resulting variations in the pattern of radiations emitted from the excited nuclei can be observed either with time resolution (PAD, PAC, resonance scattering), integrally (LTNO), or with energy resolution (ME). The abbreviations stand for the "in-beam perturbed angular distribution" method (PAD) [17-20], in which the excited nuclear state is produced and aligned by a nuclear reaction on-line in a cyclotron and then recoil-implants from the reaction target into the sample, where its precession in the local magnetic field at the implantation site can be detected as a time-dependent modulation of the emitted radiation intensity; or the "perturbed angular correlation" (PAC) method [21,22], in which a cascade of two subsequent gamma rays from the excited probe nuclei is observed in coincidence, whereby the observation of the first radiation selects an anisotropic subensemble of the nuclei, whose precession can then be observed via the second gamma ray in the time domain as in PAD; or the "low-temperature nuclear orientation" (LTNO) method [23,24], where the excited nuclei are brought into thermal equilibrium at very low temperatures and the resulting anisotropic Boltzmann distribution is observed integrally as a function of temperature and applied magnetic field; or the "Mössbauer Effect" (ME), where recoil-free resonant absorption or scattering of gamma radiation generates an anisotropic excited nuclear ensemble which can be studied either with energy resolution (using a Doppler-modulated radioactive source outside the sample), or in the time domain (using the pulsed, monochromatised radiation from a synchrotron source) [25]. In each case, the quantity measured is the hyperfine magnetic field acting at the probe site (and in some cases additionally the electric quadrupole field gradient at the site), giving information about the magnetic state of the probe atom and its environment.

A common feature of these methods is their extreme sensitivity, due to the sensitive detection of the emitted gamma radiations. Adequate signals can be obtained from a fraction of a monolayer of probe atoms, in some cases much less (down to 10^6 atoms). The methods are also element-specific and can be site-specific (through implantation onto specific lattice sites which can be identified from their isomer shifts, quadrupole interactions, or concentration dependence). These techniques are thus ideally suited for investigating magnetism in structures on the nanometre or even the atomic scale. Studies as a function of sample temperature and applied magnetic field can give information about hysteresis curves, changes in magnetic ansiotropy such as spin reorientation transitions, and changes in site occupation by the probe atoms. Indirect information about the relative contributions of spin and orbital magnetism can be obtained from the signs and magnitudes of observed magnetic hyperfine fields combined with *ab initio* calculations. We present in this section an example of each of these techniques.

a) PAD in-beam

This method was developed at Stony Brook and elsewhere in the 1970's [18,19] and has been extensively applied in the past 20 years to the study of dilute alloys by several groups [26-29]; see the reviews [30,31] for the history and details of the method.

It employs the production of excited, aligned nuclear states by a nuclear reaction, usually induced by a heavy-ion beam striking a thin target foil. The excited atoms recoil with energies of several MeV and implant deeply into the sample which is placed behind the target foil. A static magnetic field applied perpendicular to the beam direction adds vectorially to the hyperfine field present at the implantation site, and the aligned probe nuclei precess in this overall or "local" field, emitting gamma rays which are detected by two or more detectors placed in the reaction plane. The counting rates in these two detectors, measured as a function of time following a beam pulse which gives a "start" signal, typically have the form of a damped oscillation, whose frequency reflects the precession rate in the local magnetic field at the probe site. The amplitude of a particular oscillation signal is a measure of the population of the corresponding site, while its damping time gives information about magnetic nuclear relaxation and other damping mechanisms (electric quadrupole interactions, inhomogeneous broadening due to long-range magnetic interactions, variations in hyperfine fields at different sites). The Fourier transform of these oscillations to the frequency domain is equivalent to the NMR signal (which would be observed if NMR could be carried out with sufficient sensitivity to detect the extremely dilute probe atoms). A schematic of the principle of the method is shown in Fig. 7.

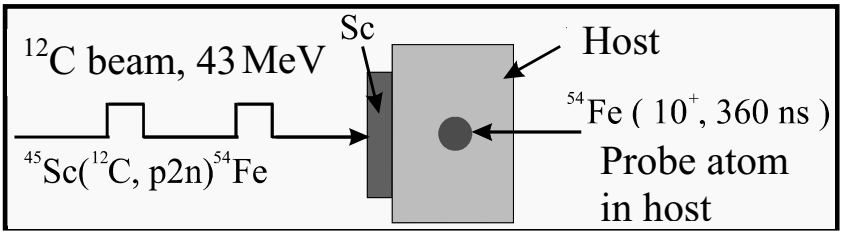

Fig. 7. Schematic representation of an In-Beam TDPAD experiment.

In recent years, PAD has been applied to the study of what might best be called “local clusters”, i.e. groups of interacting atoms within a solid host, which can exhibit changes in magnetic properties of constituent atoms due to exchange coupling and hybridisation, i.e. to variations in the local density of states (LDOS). It has thus contributed to the study of magnetism on the atomic scale.

We mention two examples illustrating the use of the ^{54}Fe probe, produced in an excited nuclear state by the nuclear reaction ^{12}C [^{45}Sc, p2n] ^{54}Fe, which is itself induced by a 43 MeV carbon beam impinging on a natural Sc target foil (cf. Fig. 7). For the experiments on “local cluster” formation, Au-based alloys were used as host materials. The gold was alloyed with either nonmagnetic constituents such as Cu, Ag, or Pd, forming a nonmagnetic host metal in which changes in the LDOS at the Fe site due to different near-neighbour configurations could be observed to change the magnetic character of the Fe atoms, or else with magnetic constituents such as Cr or Co, forming a spin-glass host alloy in which the implanted Fe was observed to form strongly-coupled local magnetic clusters with neighbouring magnetic atoms by exchange coupling. In all cases of Au-based host alloys, the Fe ions were found to implant almost exclusively onto substitutional sites in the host lattice.

Figure 8 shows some representative examples of “spin-rotation” spectra or time spectra obtained in TDPAD experiments using the ^{54}Fe probe in Au_xAg_{1-x} alloys. These spectra, denoted as *R(t)*, give the time dependence of the counting rates in two detectors, plotted as the difference of the two counting rates normalised by their sum *vs.* time following a beam pulse, thereby eliminating the trivial time dependence due to the nuclear decay lifetime (360 ns for ^{54}Fe). As mentioned above, they resemble damped oscillation curves and contain essentially three items of information: an amplitude, an oscillation frequency ω, and a damping time. When more than one magnetically distinct implantation site is occupied, the observed *R(t)* is a superposition of curves from each site, giving rise to a beat pattern due to the different precession frequencies. The amplitude of each component is a measure of the occupation of the corresponding site, while its precession frequency gives information about the local field acting on the probe nuclei there.

In general, the implanted magnetic probe atoms form a paramagnetic moment system, whose electronic magnetic moments are aligned in the applied magnetic field at the measurement temperature. Their macroscopic magnetic susceptibility then obeys a Curie or Curie-Weiss law and is a measure of the degree of alignment of the moments, i.e. the paramagentic magnetisation, under the given *B/T* conditions. This alignment is transferred to the probe nuclei via the magnetic hyperfine field B_{hf}, which depends on the particular host/probe combination studied. It is e.g. ca. -20 T in the case of dilute Fe in a pure Au host. In a host where the implanted probe atoms are nonmagnetic (e.g. Fe in Sc), the corresponding precession frequency ω_o is due only to the applied field *B* (with a small correction for the Knight shift), and this frequency thus can serve as a precise, readily measured internal standard. In a magnetic system, the observed frequency ω differs from ω_o, and the normalised frequency $\beta = \omega/\omega_o$ can be regarded as a measure of the alignment of the paramagnetic moments at the given value of *B/T* (it can be considered to be a “local permeability”). Alternatively, the quantity $\beta' = \beta - 1$ is termed the “local susceptibility” and usually obeys a Curie law, $\beta' = C/T$. The temperature dependence of β or β' is characteristic of the paramagnetic susceptibility of the system, but the Curie constant *C* also contains the hyperfine

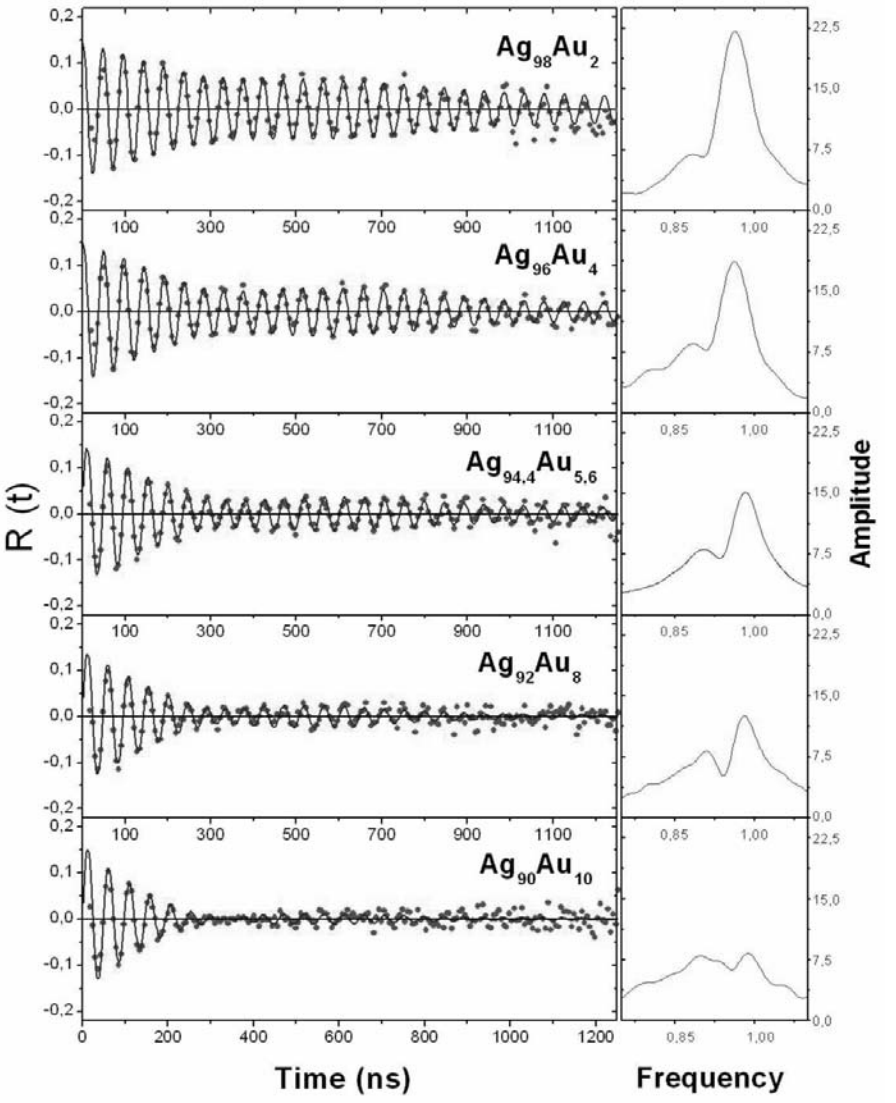

Fig. 8. Spin-rotation or "Spiro" spectra from ^{54}Fe implanted into $Ag_{1-x}Au_x$ alloys as shown. These spectra were recorded at T = 300 K in an applied field B = 2 T. At the right, the corresponding transforms to the frequency domain (maximum-entropy plots) are given. Beats can be clearly seen and are reflected in the frequency spectra as a double peak structure. Figure adapted from Refs. [33] and [39].

field B_{hf} which transfers the information about the alignment of the atomic, paramagnetic moments to the probe nuclei. The Curie constant is given by the relation

$$C = g_J \mu_B (J+1) B_{hf} / 3 k_B,$$

where the electronic moment is assumed to be described by a g-factor g_J, J is the total electronic angular momentum quantum number, and k_B is the Boltzmann constant. When an additional interaction of the electronic moments with their surroundings is present, e.g. in the case of the Kondo effect, a Curie-Weiss law results: $\beta' = C/[T+T_W]$, where the Weiss temperature T_W is a characteristic temperature of the interaction (e.g. the Kondo temperature).

Plotting the measured normalised frequencies β or local susceptibilities β' *vs.* inverse temperature then allows the evaluation of the Curie constants *C*, as shown in Fig. 9.

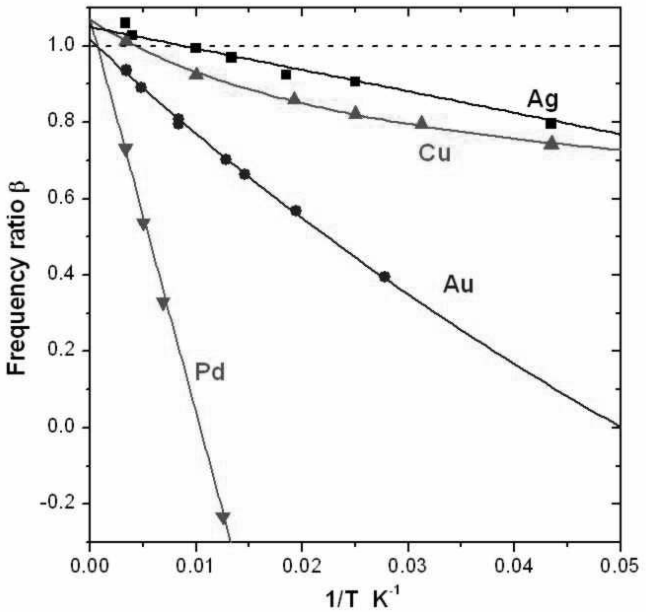

Fig. 9. The frequency ratio β as a function of inverse temperature for ^{54}Fe implanted into pure host metals as shown, measured in the high-temperature region ($T > 20$ K). The slope of the fitted line gives the Curie constant *C*. The dashed horizontal line at β = 1.00 represents a nonmagnetic case, and the extrapolation to $1/T = 0$ gives the Knight shift. In some temperature range, deviations from the straight Curie line due to the finite Kondo temperature are to be expected (cf. the curvature for Cu and Au hosts). From Ref. [39].

Since the Curie constant *C* as determined in a PAD experiment (cf. Fig.9) contains two factors (the paramagnetic moment of the probe atom in the given host environment, and the hyperfine field acting at its nucleus), the influence of these two quantities cannot be experimentally separated. Here, comparison with *ab initio* density functional theories, which

can calculate the moments reliably and the hyperfine fields with an accuracy of order 10%, may indicate which of these quantities is responsible for observed behaviour of the probe atoms on different sites or in different hosts. In Fig.9, only a single site is present and analysis of the fitted curve permits, in principle, evaluation of the Curie constant C, the Kondo temperature T_K and the Knight shift K for dilute Fe in various noble-metal hosts. The hyperfine field for e.g. Fe in Au is known from Mössbauer experiments [32], so that the magnetic moment on Fe in Au can be derived from the experiments. Note that the case of Fe in pure Ag is practically impossible to study by methods requiring a macroscopic concentration of Fe, such as conventional magnetometry or neutron scattering, due to the very limited solubility of Fe in Ag (the maximum concentration reached in the TDPAD experiments is less than 10^{-9} at%).

A more interesting case is shown in Fig.10 for the alloy hosts $Ag_{1-x}Au_x$, where magnetically distinct sites for Fe probe atoms are observed depending on their local environment (number of Ag nearest neighbours, NN, of the Fe atom). By comparing the amplitudes of each signal with the probability of a particular site occupation in a random alloy as a function of concentration x, the sites can be identified in terms of different NN configurations.

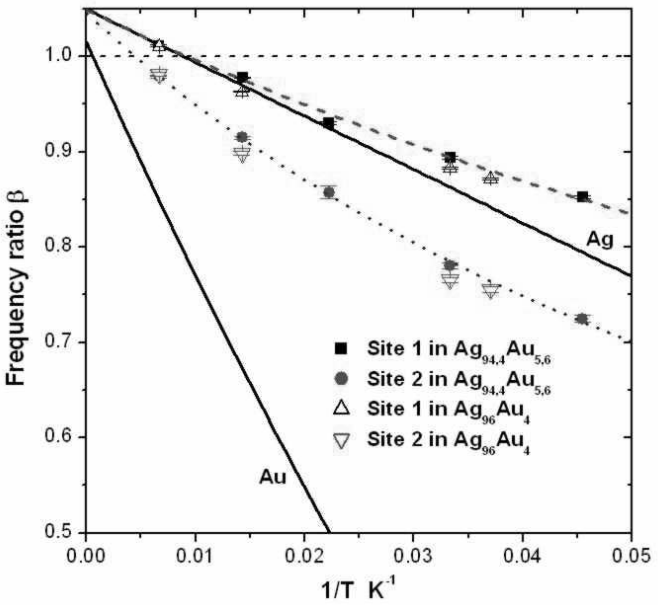

Fig. 10. The frequency ratio β *vs.* inverse temperature for ^{54}Fe implanted into $Ag_{1-x}Au_x$ alloy hosts. The solid lines represent the fits for pure Ag and Au hosts as determined e.g. in Ref. [27] and shown in Fig.9. The upper curve with data points is for Site 1, similar to the results for pure Ag, from alloy hosts with $x = 0.056$ and 0.04; the data points from Site 1 in the alloys closely follow the line for pure Ag host at high temperatures. A new site, Site 2, is observed in the alloys and can be identified as Fe atoms having a single Au nearest neighbour. Its Curie constant lies between those found for Fe in pure Ag and in pure Au. From Refs.[33] and [39].

The first notable feature seen in Figs.9 and 10 is the great difference in Curie constants found for Fe in pure Ag and pure Au hosts. It corresponds to the large difference in hyperfine fields for Fe in Ag and Fe in Au, observed already in Mössbauer source experiments on highly dilute samples in the 1970's [32]. A detailed explanation of this difference awaited the development of *ab initio* thories which can reliably calculate the hyperfine fields and electronic moments on the Fe impurity atoms [34-37]. Some results for Fe in AuAg alloys are collected in Table 1.

Table 1. Calculated spin and orbital moments and hyperfine fields for Fe in AuAg alloys

Host	Theor. Method[1]	Spin moment	Orbital moment	Total moment	B_{hf} (theory)	B_{hf} (expt.)[2]
Ag	I	3.073	0.134	3.207	-6.67	-3.4(1) T
	II	3.020	0.110	3.130	-7.08	
	III	3.046	0.692	3.712	-2.81	
Au	I	3.149	0.022	3.171	-17.86	-20.6(4)T
	II	3.002	0.009	3.011	-16.53	
	III	3.075	0.080	3.082	-22.25	
11Ag+ 1Au	I	3.075	0.126	3.201	-7.60	-8.7(8) T
	II	3.020	0.088	3.108	-8.50	
	III	3.047	0.270	3.290	-6.61	

1. Method I: Spin-polarised KKR method [34]; method II: Real-space ASA-LMTO method [35]; method III: spin moments average from I and II, orbital moments method II but with orbital polarisation correction [38]. See Ref. [33].
2. From Refs. [32,33].

The second striking feature seen in Fig.10 is the new site, labelled Site 2, seen in the alloys. It can be identified with the help of the statistical model as arising from Fe with one Au and 11 Ag NN (cf. lower rows in Table 1). This can be seen particularly clearly in the frequency domain (right panels of Fig.8), where a shoulder (due to Site 2) is seen to occur at frequencies below the main peak (Site 1). Its intensity increases with increasing Au concentration. As seen in Fig. 10, the corresponding Curie line lies between those for pure Ag host and pure Au host. Site 1, in contrast, gives a Curie curve essentially identical to the data for pure Ag host at high temperatures; its curvature at lower temperatures is due to the Kondo effect as mentioned above. It can be concluded that Site 1 corresponds to Fe atoms with 12 Ag NN which behave as in pure Ag host (but with a higher Kondo temperature), while Site 2 corresponds to Fe atoms with 11 Ag and one Au neighbour. The *ab initio* calculations show that the total Fe magnetic moment is not very different in Ag, Au, or alloy hosts (compare Table 1; maximum variation of *ca*. 20%). The large, discrete change seen on introducing a single Au neighbour atom into the NN shell of Fe in Ag is mainly due to the suppression of orbital magnetism by hybridisation and exchange with the Au neighbour. The moderate orbital moment present on Fe in Ag is almost completely quenched in Au host and already strongly reduced in the alloy by a single Au NN. This causes only a minor change in the total moments, since the dominant spin moment does not change, but it gives rise to a considerable change in the hyperfine field B_{hf} at the Fe nucleus because of the large, positive hyperfine

field constant for orbital moments as mentioned above: even a small orbital moment causes a noticeable difference in B_{hf}. The change in the measured Curie constant C is thus mainly due to the *hyperfine fields* and their sensitivity to orbital magnetism in this case of non-magnetic alloy hosts.

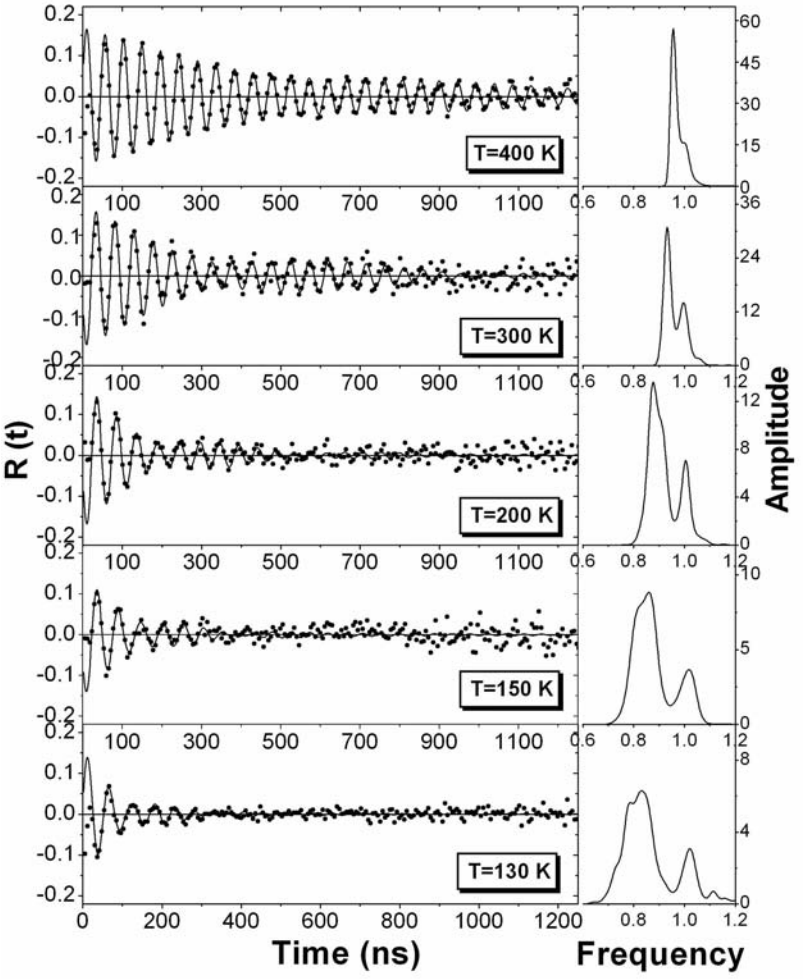

Fig. 11. Spin-rotation spectra of Fe in $Au_{1-x}Cr_x$ host alloys as a function of temperature, taken at an applied field of B = 2.0 T; here, for a sample with x = 0.023. From Ref. [39].

A completely different situation is represented by Au alloy hosts with magnetic alloying partners such as 3*d* metals. These form spin glasses at higher concentrations of the magnetic component and have been the subject of much study in the past. Fig.11 shows spin-rotation spectra from ^{54}Fe in the host alloy $Au_{0.977}Cr_{0.023}$ as a function of temperature. Again, beats are seen in the time spectra, corresponding to a second site, as clearly seen in the frequency spectra at the right in the figure (from Ref. [39]).

We note that the TDPAD method is limited in its temperature range by two effects: at high temperatures, the frequency shifts $\omega = \omega - \omega_o$ become very small owing to the Curie-law temperature dependence, and are no longer observable above a certain temperature, typically a few hundred K (cf. Fig.11). At low temperatures, the nuclear relaxation times become increasingly short (longer electronic fluctuation times lead to short nuclear relaxation times in the Abragam-Pound regime, above a few K). This can be seen in Fig.11, where the damping time is seen to become very short below 150 K, and the lines in the frequency spectra are correspondingly broadened. The precise range in which measurements can be carried out depends on the system studied, but is typically limited to 500 K ≥ T ≥ 15 K. In the magnetic alloy hosts discussed here, the lower limit is nearer to 100 K due to long-range magnetic interactions which shorten the effective damping time still more. At very low temperatures, below about 1 K (Korringa regime), the nuclear relaxation times would again become long and TDPAD measurements could be carried out if other damping sources are not too strong, but this has not yet been done in practice due to technical reasons (heating by the ion beam).

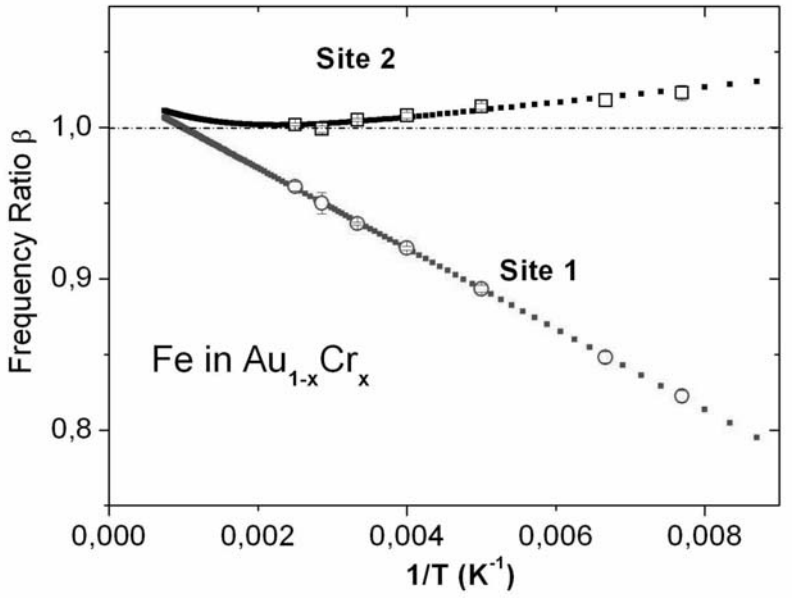

Fig. 12. Frequency ratios β for the two sites observed from Fe in a $Au_{1-x}Cr_x$ host alloy with x = 2.3 at.% *vs.* inverse temperature in the range T > 120 K and for B = 2 T (data points). The dotted curves are fits to the pairing model (see text). Adapted from Ref. [40].

The analysis of the spin-rotation spectra for Fe in $Au_{1-x}Cr_x$ host alloys leads to the Curie-Weiss curves shown in Fig.12 (for the example of x = 0.023). The points denoted as "Site 1" correspond to the stronger peak in the frequency spectra of Fig.11 and are identical to the Curie curve observed for Fe in pure Au host (cf. Fig.9; the curvature seen there due to the finite Kondo temperature is not visible here in these higher-temperature data). This signal is attributable to Fe atoms implanted onto sites with no Cr NN, as shown by the statistical model (points on curve "0 Cr NN" in Fig.13). The other curve and data points labelled "Site 2" corresponds to the weaker peak in Fig.11 and has a much smaller positive Curie constant, notably different from Site 1. Comparison to the site occupation probability statistics shows this site to be associated with Fe implanted into locations with one –and only one-- Cr NN ("1 Cr NN" in Fig.13).

This drastic change in Curie constant on adding a single Cr neighbour was at first surprising, since a change of a factor of five in magnitude and a sign reversal of the hyperfine field are not to be expected on substituting one neighbour. The explanation proved to be a strong exchange coupling of the Fe and Cr atoms when they are nearest neighbours. The coupled entity, which might be termed a *magnetic nanocluster*, has a net magnetic moment opposite to that of the Fe alone and a factor of *ca*. 5 smaller, since Fe and Cr couple anti-ferromagnetically and the Cr moment is somewhat larger in magnitude. First-principles calculations of the moments, hyperfine fields and coupling constants [41,42] combined with a thermodynamic model for the temperature dependence of the paramagnetic susceptibility of

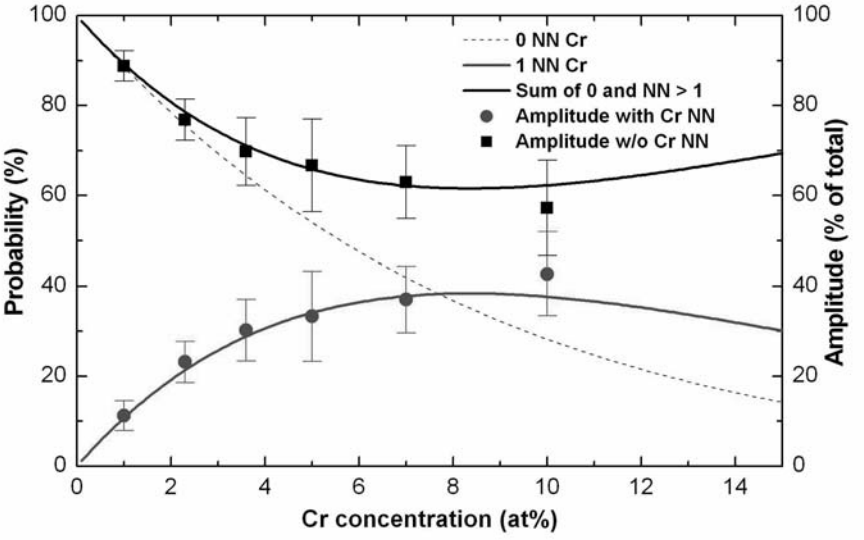

Fig. 13. The calculated probability of occurrence in a random alloy of various near-neighbour configurations as a function of the concentration of the minor alloying partner (here Cr in a cubic Au matrix). The left-hand scale shows calculated probabilities, the right-hand scale the relative amplitudes of the signals observed from different implantation sites (squares: Site 1, circles: Site 2) at the given host alloy concentration. Adapted from Refs. [39,40].

the resulting system of coupled moments leads to the dotted curve in Fig.12, which fits the data points very well. The only fit parameter is the strength J_{eff} of the exchange coupling; the best fit was obtained for J_{eff} = 5.25 mRy, about 25% larger than calculated in Ref. [41]. This represents a remarkable agreement considering the difficulty of calculating the small coupling energies. The fitted Curie constant, C = +4.38 K, is in excellent agreement with the calculated value of +4.43 K using the most recent *ab initio* values of the moments in the coupled pair (μ_{Fe} = 3.01 μ_B, μ_{Cr} = 3.59 μ_B) and the hyperfine field at the Fe nucleus in the pair, B_{hf} = -19.2 T [42].

The question arises as to why larger clusters, e.g. Fe-Cr-Cr triplets, are not observed as separate sites, although their statistical probability is not negligible in the observed concentration range (cf. Fig.13). The calculated coupling constants J_{eff} for Cr-Cr and Cr-Fe couplings indicate that the Cr-Cr pairing is about three times stronger than the Fe-Cr pairing. The model leads in this case to a Curie constant for the Fe-Cr-Cr triplets of about C = -18.8 K, less than 30% smaller than that for Fe at pure Au sites (Fig.14). This small shift is not detectable within the line-width of the Site 1 signal, which thus includes both Fe with no Cr NN and Fe with two Cr NN. The signal amplitude indeed agrees with this hypothesis, as can be seen in Fig. 13 (curve "Sum of 0 and > 1 Cr NN"). At the highest Cr concentrations studied, there is in fact some indication of a shoulder on the Site 1 line, but the sensitivity and resolution of the measure-ments do not allow its quantitative evaluation.

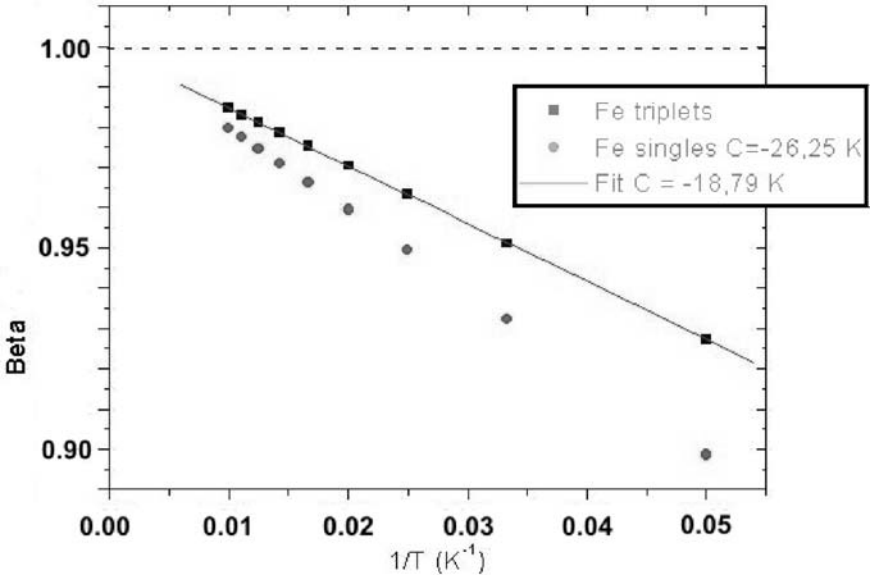

Fig. 14. Plot of the frequency ratio β vs. inverse temperature for Fe with only Au neighbours in a AuCr matrix (circles) and Fe in Fe-Cr-Cr triplets (model calculation, squares). The line is a fit to the triplet points, giving the Curie constant C = -18.79 K, about 30% less than that for Fe with no Cr neighbours. The model calculation is due to P.J. Jensen (see Ref. [40]).

The situation in the magnetically frustrated triplets can be understood inruitively as follows: in the limit of very strong Cr-Cr coupling, the Cr moments would simply couple antiferromagnetically to give a net zero moment, leaving the Fe free, i.e. nearly identical to Fe on a site with no Cr NN. The same argument applied to quartets of type Fe-Cr-Cr-Cr would lead to a signal similar to that from the pairs, but these larger clusters are not statistically significant within the observed concentration range.

This coupling is not specific to the Fe-Cr system, but can be observed also for Fe-V, which according to calculations and experiments [41,43] also couples antiferromagnetically, however with a different coupling strength J_{eff} from that in Fe-Cr. The other cases within the Fe-3*d* series (Fe-Mn, Fe-Fe, Fe-Co) are difficult to observe, either because the coupling is very weak (Fe-Mn), or because it is *ferromagnetic*, leading to a less drastic change in total moment in going from free Fe to the coupled pair. In the case of Fe-Fe coupling, line broadening due to long-range interactions in the alloy additionally makes the observation of "magnetic nanoclusters" difficult [27].

b) PAC after "soft landing" of radioactive probe atoms

This technique is described in some detail in the chapter "Surface and Interface Magnetism on an Atomic Scale" by H. Bertschat in this book. A number of examples are given there, and we refer the reader to that chapter for more details and references. This technique for surface studies was pioneered by the group of G. Schatz at the University of Konstanz [44, 45]. In various forms it has also been developed by B. Niessen and coworkers in Groningen [46], by G. Catchen *et al.* at the Pennsylvania State University [47], and by M. Rots *et al.* in Leuven, Belgium [48].

c) Low temperature nuclear orientation of ultrathin layers

In the low temperature nuclear orientation (LTNO) method, probe atoms in an excited nuclear state are introduced into the sample prior to the experiment by neutron irradiation or implantation (on-line implantation has also been applied extensively, but as yet has been used mostly for nuclear-physics studies). The sample is cooled in a cryostat to very low temperatures, in the mK range, at which the thermal energy is comparable with the splitting of the nuclear sublevels in the local magnetic field at the site of the probe atoms. The resulting Boltzmann distribution is characterised by unequal populations of the nuclear sublevels, corresponding to a spatial orientation of the excited nuclei. The radiations which they emit are thus anisotropic in space, and this anisotropy can be detected, e.g. by gamma-ray detectors located outside the cryostat, and can serve as an indicator of the local magnetic fields acting on the probe nuclei. Reviews of the technique were given in e.g. [49,50].

The method is particularly sensitive to the angular distribution of local fields and can thus be used to study non-colinear induced magnetic moments in thin films and at interfaces. It is also element-specific and can detect signals simultaneously and separately from different layers in a multilayered structure. Its first application to magnetism in thin films was carried out by the Leuven (Belgium) nuclear orientation group in collaboration with the Prague and

Berlin groups [51-54]. Ag/Fe multilayers were studied extensively, and a canting of the induced magnetic moments in the Ag spacers was found [55].

We give here as an example of this technique its application to the study of interfaces between ferromagnetic (FM) and antiferromagnetic (AF) materials with nonmagnetic spacer layers [6,56]. In this case, it can be used to study the origin of the exchange bias (EB) effect [see Section (1)] which arises at FM/AF interfaces. As mentioned in Section (1), the role of a nonmagnetic spacer layer between the FM and AF layers in exchange-bias systems is of interest for clarifying the mechanism of EB [10]. It has been shown by a number of experiments and calculations that magnetic moments are induced via exchange coupling on nonmagnetic atoms in a spacer layer adjacent to a magnetic layer [55, 57]. The range of such couplings is very short, and detectable induced moments are found only on atoms directly adjacent to the interface. This effect is not to be confused with the long-range polarisation of conduction electrons in nonmagnetic spacers (RKKY interaction), which is responsible for the coupling of entire magnetic layers across the spacer. Since LTNO requires local fields of the order of 2 T to give a detectable signal, and thus induced moments of at least 0.05 μ_B, it will be sensitive only to those nonmagnetic spacer atoms directly within the interface layer and is thus very specific to interface effects in bi- and multilayers. Moreover, it is the only technique which is both sensitive and specific enough to study the induced magnetism in 'nonmagnetic' spacers in such magnetic layered systems.

The samples used in Ref. [56] were prepared by MBE of Co onto passivated Si or Al_2O_3 substrates, with selective oxidation to produce well-defined CoO layers [9]. They consisted of Co/Au/CoO trilayers exhibiting the exchange-bias effect at low temperatures, and for comparison, of similar Co/Au/Co and CoO/Au/CoO trilayers, i.e. FM/NM/FM or AF/NM/AF systems (NM = nonmagnetic). The radioactive atoms required for the LTNO measurements were introduced by irradiation with thermal neutrons, producing ^{60}Co in the Co and CoO layers and ^{198}Au in the Au spacers. It has been demonstrated [58] that neutron irradiation causes minimal damage to the interface if fast neutrons are carefully avoided. These isotopes are both well suited for LTNO measurements, having simple nuclear decay schemes and large, well-known nuclear magnetic moments as well as significant anisotropy parameters for the emitted gamma rays [59]. In this work, the Co layers had a typical thickness of 16.4 nm, CoO of 2.0 nm, and the Au spacers ranged from 0.5 to 1.25 nm in thickness.

Figure 15 gives an overview of the results of LTNO investigations of magnetic trilayers from Ref. [56]. The figure shows original data (counting rates W(θ) at a particular angle θ with respect to the applied magnetic field $\boldsymbol{B}$, normalised by the counting rate at a high temperature, where the gamma rays are emitted isotropically) for three trilayers, each with a 0.5 nm thick Au spacer between two magnetic layers. In the upper part a) of the figure, data from a FM/NM/FM trilayer (Co/Au/Co), represented at the left, are shown. On cooling to 8.2 mK, the counting rates in detector D1 (parallel to $\boldsymbol{B}$) decrease strongly for both isotopes (^{60}Co in the FM Co layers, ^{198}Au in the spacer). At the same time, the corresponding counting rates in detector D2 (perpendicular to $\boldsymbol{B}$) increase, but less strongly (red data points). The explanation is given on the right, where schematic polar diagrammes of W(θ) at T = 1 K [W(θ) = 1.00] and at low temperatures (W(θ) shows strong angular dependence as indicated) are shown. In this sample, which is magnetically saturated by the applied field, all the magnetic moments are parallel to $\boldsymbol{B}$ and the local fields acting at the Co and Au nuclei are

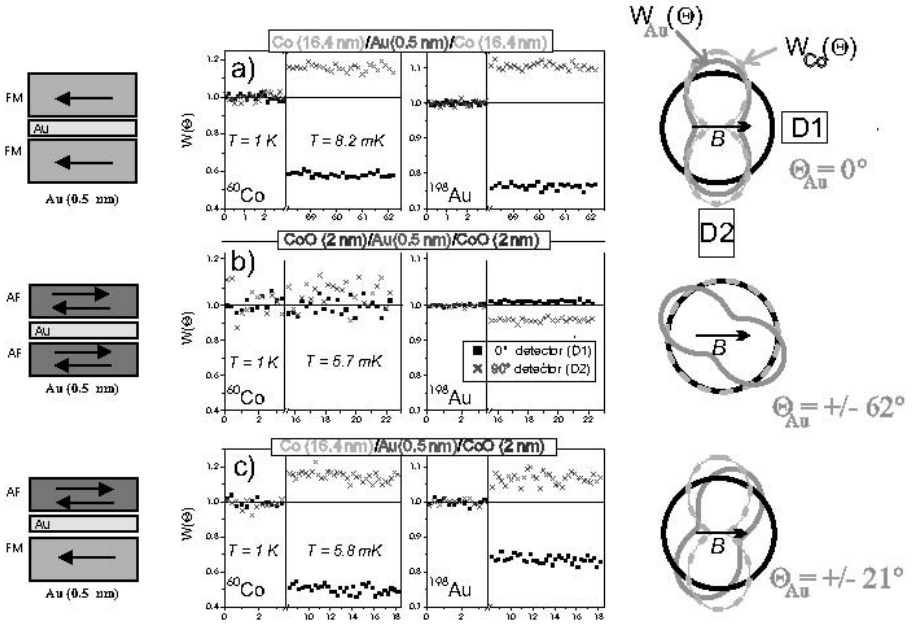

Fig. 15. The left-hand column shows schematically the structure of the trilayer samples studied; the intermediate or 'spacer' layer is gold of 0.5 nm thickness. The upper and lower layers are FM Co [a), above], AF CoO [b), centre], or both, giving an exchange-bias structure [c), below]. Arrows indicate the orientations of magnetic moments. In the middle column, data are shown for the two isotopes studied, ^{60}Co and ^{198}Au, at a 'high' temperature (1 K), where the nuclei are not oriented and their gamma rays are emitted isotropically, and for a low temperature as indicated, where appreciable nuclear orientation and gamma-ray anisotropy are observed. The right-hand column shows a schematic representation of the gamma-ray distribution as observed by two detectors (D1, D2) in the sample plane, parallel and perpendicular to the applied magnetic field $\boldsymbol{B}$. The polar diagrammes indicate the anisotropy (normalised counting-rate W(θ) at a particular angle θ relative to the quantisation axis defined by $\boldsymbol{B}$). The heavy black circles represent the isotropic distribution at T = 1 K, the light curves show the anisotropic distributions from the two isotopes at low temperatures. These data were collected at an applied field of B = 500 mT (saturation of the Co layers). Figure adapted from Refs. [6] and [56].

also parallel to $\boldsymbol{B}$. The values of W(θ) at a particular angle as functions of B and T give the values of the hyperfine fields and the magnetisation curve of the sample, independently for the two nuclei. The field acting at the Co nuclei has the well-known value for bulk Co metal, while the field acting at the Au nuclei reflects the induced magnetic moments on Au atoms at the Co/Au interfaces. With a Au thickness of only 0.5 nm, essentially all Au atoms are at the

interface and all thus experience the same induced moments and resulting magnetic hyperfine fields. The 'canting angle' Θ_{Au} for the induced moments and fields at the Au nuclei is thus 0^o. In the middle part b) of the figure, data are shown for an AF/NM/AF trilayer, with a 0.5 nm Au spacer between two 2.0 nm CoO layers. Thermal contact to the sample was maintained through a Ag capping layer which made metallic contact to the sample holder. In this case, the ^{198}Au shows a smaller effect in the reversed sense to that of Co/Au/Co, i.e. the counting rate in detector D1 increases somewhat at low temperatures (T = 5.7 mK). The ^{60}Co, in contrast, shows no detectable gamma-ray anisotropy even at this low temperature. This could have several causes: the magnetic hyperfine field at Co on CoO might be too small to give a detectable nuclear orientation (this is however not the case; it has been determined by NMR to be +49.5 T [60], quite sufficient to give a large gamma-ray anisotropy at 5.7 mK). Secondly, there could be a domain structure in the AF CoO layers which by its symmetry averages the observable nuclear orientation to zero. We cannot rule this out, but hold it to be unlikely, since an induced orientation was observed in the adjacent Au layer. Thirdly, the nuclear spin-lattice relaxation (SLR) time may be so long in this insulating material that the Co nuclei never approach thermal equilibrium at low temperatures. This is the most likely explanation, since nuclear SLR times are known to become very long in insulators at low temperatures; estimates based on the Neèl temperature of CoO lead to SLR times of years, so that the experimental measuring times of a few days are not sufficient to obtain detectable nuclear orientation of Co in CoO. Improper cooling of the samples can be ruled out by the effect seen in the Au spacer and by the observed cooling of the external ^{54}Mn*Ag* nuclear thermometer. The small, reversed gamma-ray anisotropy effect seen from ^{198}Au can be attributed to a smaller induced moment in Au adjacent to a CoO layer as compared to metallic Co, and to a canting of the induced Au moments by an angle $\Theta_{Au} = 62^o$ as shown on the right; rotation of the angular distribution by this amount reproduces the ratio of counting rates in detectors D1 and D2 precisely. This analysis assumes cylindrical symmetry of the angular distribution, as shown in the figure. This assumption can be tested by using a third gamma-ray detector perpendicular to the plane of the sample, which was done in some cases (see below).

The existence of induced moments and a net nuclear orientation in the Au layer adjacent to AF CoO demonstrates clearly that there is a preferred axis of magnetisation at the CoO/Au interface, which probably arises from uncompensated Co moments in the interface region. It also practically rules out the possibility of a domain symmetry of the CoO that averages the observable nuclear orientation to zero, since this would apply to the induced moments in the Au spacer as well. This is an interesting finding in terms of the origin of the exchange-bias effect, as it clearly demonstrates a preferred axis in this nominally magnetically compensated AF material, at least at the interface to another material, and shows that this axis can be aligned by a magnetic field. The large canting of the induced Au moments relative to the field direction may indicate a complex magnetic structure in the CoO interface layer or may be intrinsic to the coupling between Co moments in CoO and adjacent Au atoms.

The lower part of Fig.15, labelled c), shows results for an exchange-bias trilayer, FM/NM/AF, with a relatively thick (16.5 nm) Co layer separated by a 0.5 nm Au spacer from the 2.0 nm thick CoO AF layer. A Ag capping layer served as before to protect the thin trilayers and make thermal contact to the sample holder. Here, the data from ^{60}Co, mostly originating in the thicker FM Co layer, are similar to those obtained for sample a), as would be expected. The induced moments in the Au spacer, however, give rise to different values of the counting rates in D1 and D2 and to a different D1/D2 ratio, indicating both a different

value of the average hyperfine field at the Au nuclei and a canting of the gamma-ray distribution from ^{198}Au. The derived canting angle is $\Theta_{Au} = 21^{o}$, less than in the case of two Au/CoO interfaces but not negligible. Here, the canting can be attributed only to those Au atoms adjacent to the CoO interface, while the Au atoms at the Au/Co interface can be presumed to have their induced moments aligned parallel to ***B***, as for sample a). The superposition of the two types of interface atoms gives rise to the apparent reduction in the average canting angle as compared to sample b).

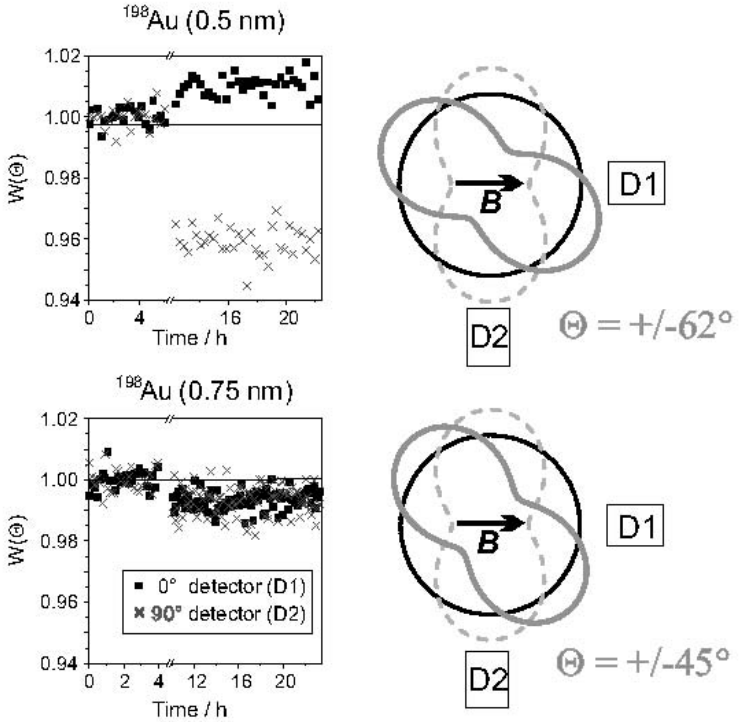

Fig. 16. Thickness dependence of the nuclear orientation of ^{198}Au in a CoO/Au/CoO trilayer. At the left are counting-rate data from two detectors (D1, D2) at the normalisation temperature T = 1 K (up to 4 hrs.) and at low temperatures near 6 mK, above for a Au spacer thickness of 0.5 nm as in Fig.15, below for a thickness of 0.75 nm. Both the values and the ratio of counting rates in D1 and D2 are quite different in the two cases. The different ratio indicates a reduced canting angle as shown at the right. The different values indicate a smaller average hyperfine field at the ^{198}Au nuclei in the thicker Au spacer layer. Figure adapted from [6,56].

To study the range of the exchange coupling which induces magnetic moments on Au atoms in the nonmagnetic spacer layer, experiments were performed on trilayers with different spacer thicknesses, as summarised in Fig.16. The upper part shows the same data as

Fig.15, part b), indicating a canting angle of $\Theta_{Au} = 62^{o}$ in the thin Au spacer where essentially all the atoms are at a Au/CoO interface. In the thicker Au layer, both the average canting angle ($\Theta_{Au} = 45^{o}$) and the average hyperfine field are smaller. This can be understood by considering that in the thicker layer, a considerable fraction of Au atoms are not directly at an interface. If, as suggested, the exchange coupling is effective only to adjacent atoms, these 'bulk' Au atoms will experience no (or very small) induced moments and hyperfine fields and will contribute only an isotropic background to the measured counting rates, reducing the

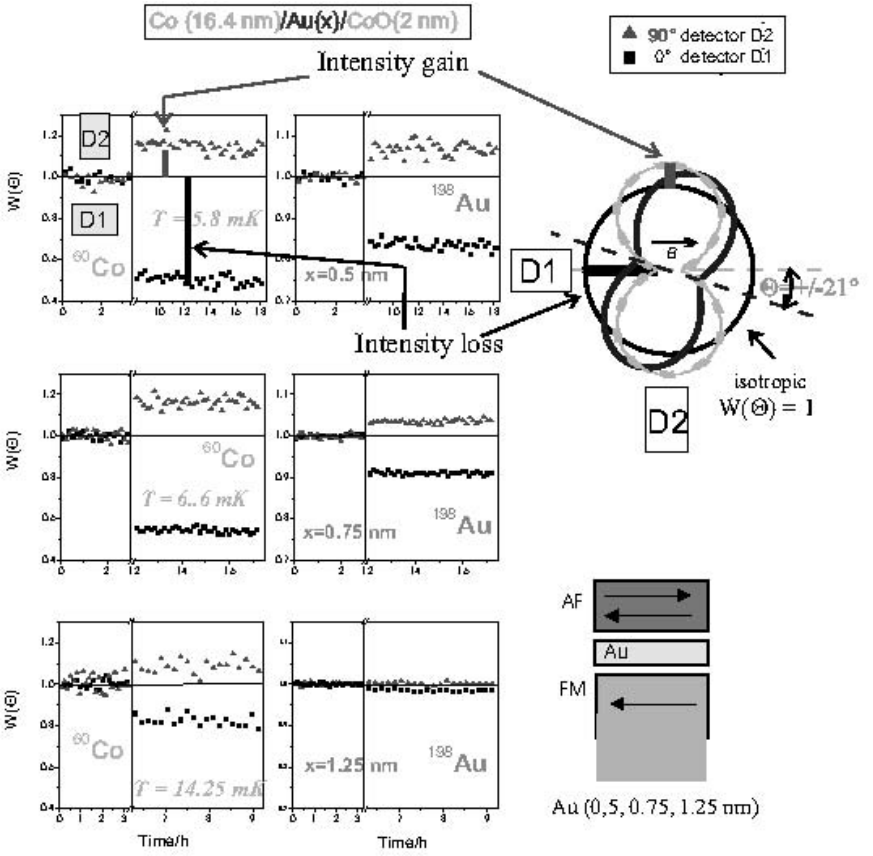

Fig. 17. Results of LTNO measurements on exchange-bias samples $Co/Au_x/CoO$ with increasing Au thickness x. The data in the upper graphs show counting rates from a sample with $x = 0.5$ nm as in Fig.15. The middle data are for $x = 0.75$ nm, the bottom graphs for $x = 1.25$ nm. In each case, the counting rates at high (normalisation) temperature and at a low temperature as indicated are shown for ^{60}Co (left) and ^{198}Au (right). The applied magnetic field was 500 mT in all cases, magnetically saturating the FM Co layers. Figure after Ref. [6].

observed average values of Θ_{Au} and B_{hf}. Applying a 'two-site model', in which Au atoms at the Au/CoO interface are assumed to contribute the full nuclear orientation effect while those one or more atomic layers away contribute only an isotropic signal, the hyperfine fields at the interface atoms are found to agree for the two Au spacer thicknesses (24(2) T for the 0.5 nm spacer, 21(2) T for the 0.75 nm spacer). This provides convincing evidence for the short range of the interaction which induces magnetic moments on the Au spacer atoms. In these experiments, a third detector placed perpendicular to the sample plane was used to verify that the canting of the induced moments occurs only within the sample plane.

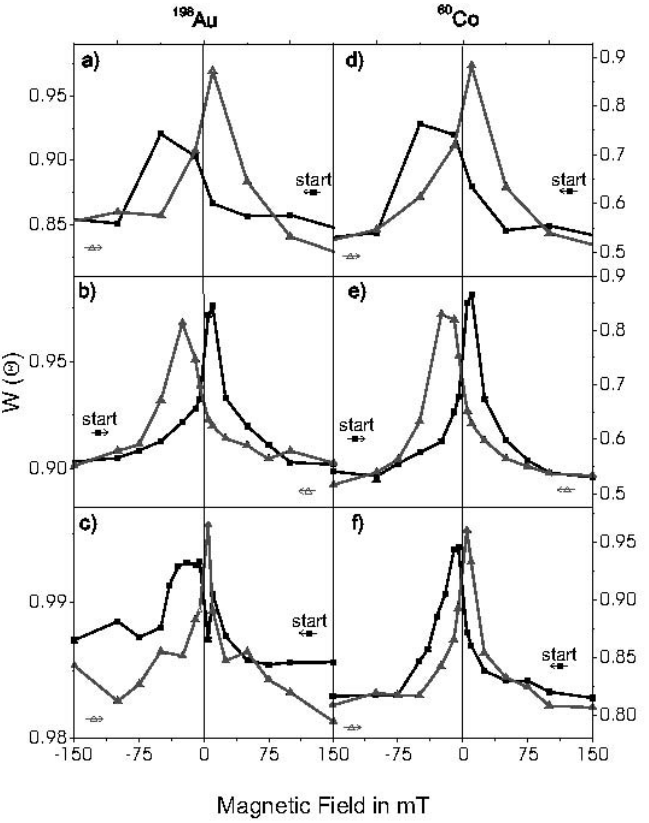

Fig. 18. Magnetic hysteresis curves determined via nuclear orientation in the FM (Co) and NM (Au) layers of FM/NM/AF trilayers as described in the text. The left panels show the results for ^{198}Au in the Au spacers, the right-hand panels show ^{60}Co results (due only to Co in the FM Co layers, since no nuclear orientation of Co in the CoO layers was observed; see above). The three rows correspond to the three samples as shown in Fig.17: a) and d) are for a Au spacer thickness x = 0.5 nm, b) and e) for x = 0.75 nm, and c) and f) for x = 1.25 nm. Figure adapted from Refs. [6] and [56].

The spacer-thickness dependence for exchange-bias (EB) samples, with trilayers consisting of Co(16.4 nm)/Au(x)/CoO(2.0 nm), was also studied and is summarised in Fig. 17. Again, counting rates at high and at low temperatures are shown for the Co and Au isotopes for two gamma-ray detector positions. The upper panel in Fig.17 shows the same data as Fig.15 c), for a Au thickness of x = 0.5 nm. The angular distribution from Co, dominated by Co atoms in the thick FM layer, is aligned along the applied field $\boldsymbol{B}$, while the Au induced moments show a canting angle of 21° as shown at the right of the figure. With increasing spacer thickness, the Co gamma-ray anisotropies remain unchanged (the smaller effect seen in the bottom panel is due to the higher measurement temperature of 14.25 mK in this case). The Au anisotropies decrease drastically with increasing Au thickness, however. This is again due to the short range of the exchange coupling which induces magnetic moments on Au; in the thicker layers, many Au atoms are located away from the interfaces with the magnetic layers and contribute essentially an isotropic signal, reducing the observed gamma-ray anisotropy. The observed values are consistent with an average hyperfine field of B_{hf} = 48(4) T on Au atoms adjacent to the interfaces with Co and CoO. This value is in turn equal to the average of the hyperfine fields observed for Au adjacent to Co in the Co/Au/Co trilayers, 78(3) T, and for Au adjacent to CoO in the CoO/Au/CoO trilayers, 22.5(2) T.

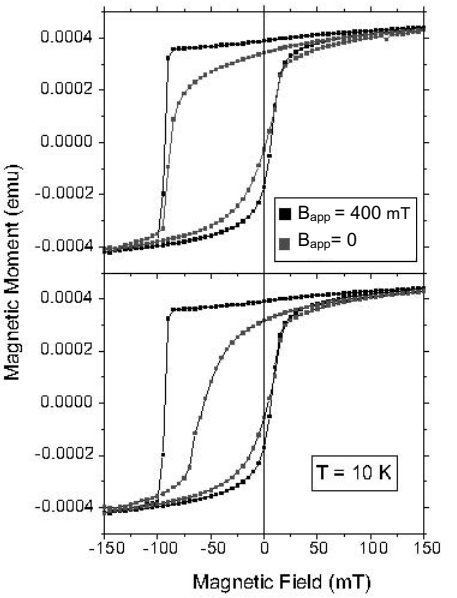

Fig. 19. Magnetic hysteresis curves measured by SQUID magnetometry on EB samples similar to those used for the nuclear orientation measurements, showing the effect of zero-field cooling from the remanent state (coloured curves) as compared to field cooling in an applied field of 400 mT (black curves). Measurements at T = 10 K. The upper zero-field-cooled curve was registered starting with the applied field parallel to the remanent magnetisation, the lower curve with the applied field opposite to the remanence direction. After Ref. [6].

The reduced canting angle, which was found to be approximately constant at a value near 22^o, results from the superposition of signals from Au atoms at the Au/Co interface, where no canting is observed, and at the Au/CoO interface, with canting angles in the region of 60^o.

To obtain more information, in particular about exchange bias, magnetic hysteresis curves were measured using the nuclear orientation effect from Co and Au as an indicator of magnetic alignment in the EB samples consisting of Co/Au/CoO trilayers. Results are shown in Fig.18. Beginning at the cooling field of 500 mT, the field was reduced in steps and the nuclear orientation measured at each field value; at zero field, the field sweep was continued with the field reversed relative to the original cooling field, and its magnitude was increased up to a saturation value of -500 mT. The procedure was then reversed to arrive back at the starting value. Fig.18 shows data for the two isotopes (^{198}Au in the Au spacers, ^{60}Co in the FM Co layers) and for the three samples as shown in Fig.17, with varying Au thickness *x*. The maxima at $W(\theta)$ values near 1.00 correspond to a complete lack of nuclear orientation, i.e. zero magnetisation of the sample layers. Note the asymmetry and shift in the maxima for decreasing and increasing applied fields. This corresponds to the asymmetry and shift in the hysteresis curves measured by conventional magnetometry on e.g. the Co in Co/CoO exchange-bias samples (Fig.19). A striking feature is the similarity of the curves seen for the Co and the Au layers. This is the first observation of exchange bias within the nominally nonmagnetic spacer layer of an FM/NM/AF trilayer.

d) Resonant nuclear scattering

This technique involves nuclear excitation, but as practised today and with reference to magnetism at interfaces and in thin films, the excitation is often carried out using resonant synchrotron radiation, so that it could equally well be treated in Section (3). The use of conversion-electron detection (CEMS) increases the surface sensitivity of conventional Mössbauer spectroscopy and there exists a considerable literature regarding this technique [61], which we will however not treat further here.

The currently very active field of resonance scattering using synchrotron radiation [62] also has an extensive literature. We mention as examples the study of ^{57}Fe probe layers in thin-film systems as well as a recent measurement on Fe/Cr multilayers [63].

(3) X-Ray spectroscopies and microscopy

These methods, both for magnetic studies and for obtaining structural information, have been recently reviewed by H. Wende [64]. They are based upon the fact that absorption of a polarised X-ray photon by an inner atomic shell results in the excitation or emission of a spin-polarised electron. In magnetic materials, the possible final states for the electron are inequivalent for the two spin directions (majority and minority directions), leading to a difference in absorption cross-sections for different photon polarisations (or magnetisation directions). The spectral energy region immediately above an absorption edge gives information about the electronic structure and magnetism of the absorbing atom and its immediate surroundings, and is usually referred to as XMCD (for “X-ray magnetic circular dichroism”; experiments with linearly-polarised X-ray photons are also possible). Studies of

the spectral region further from the edge are termed MEXAFS (for "magnetic extended X-ray absorption fine structure") and give information about the neighbouring atoms, their positions, vibrations, and magnetism, and, in favourable cases, about the bonding electrons between them ("Atomic EXAFS"). Applying X-ray imaging techniques allows these methods to be performed with spatial resolution, i.e. magnetic microscopy [65]. Variation of the angle of incidence of the X-rays can also provide sensitivity to certain sites or to surfaces and thin films. Due to the selectivity of the absorption edges, the methods are atom- and X-ray edge-selective, and, with modern undulator sources on third-generation storage rings, they can attain sensitivities equivalent to a fraction of a monolayer of absorbing atoms [66].

The XMCD effect was predicted theoretically in the mid-1970's [67]. Its observation awaited the availability of suitable sources of polarised X-rays and was realised 10 years later using second-generation synchrotron sources by G. Schütz *et al*. [68]. About the same time, X-ray linear dichroism and resonant magnetic scattering were also observed [69]. XMCD and MEXAFS have in the intervening two decades become standard techniques for investigating magnetic materials, and with the advent of greatly increased sensitivity using third-generation synchrotron sources, they are now applicable to thin films and interfaces. We give below an example of recent work in this area, illustrating the power of the techniques, which can directly distinguish between spin and orbital contributions to magnetic moments.

a) Orbital contributions to local magnetic moments in dilute alloys [70,71]

In this work, the high sensitivity of XMCD performed at modern undulator X-ray sources together with its atomic selectivity and ability to separate spin and orbital contri-butions to magnetic moments were employed to study the orbital moments on impurities from the 3*d* series in Au host. The 3*dAu* alloys are a classical system for studying the formation of local moments in metals and were investigated in detail theoretically and experimentally [72,73] over 40 years ago. They played an important role in the elucidation of the Kondo effect [74] and, at higher impurity concentrations, of spin-glass behaviour [75]. However, although there were indications of the importance of orbital effects in early studies [76,77], no direct observations could be made and the evidence was derived indirectly, e.g. from the values of observed magnetic hyperfine fields (cf. Section (2) above).

The samples used for these XMCD studies [70,71] were alloys of V, Cr, Mn, Fe, and Co in the range of 1 at.% concentration in pure Au host, as well as Mn in Cu host. They were made by electron-beam or induction-levitation melting in UHV or inert-gas atmosphere and were rapidly cooled after homogenisation to prevent cluster formation. In the form of small discs, these samples were mounted in the UHV cryostat of the ID08 beamline at ESRF [78] where they could be cooled to about 5 K and above at applied magnetic fields of up to 7 T. Surface contamination was removed by sputtering with Ar ions until no evidence of oxygen or compound formation was observable in the XMCD spectra at the $L_{II,III}$ edges of the 3*d* impurity and at the oxygen K edge.

The ID08 beamline has been described in detail [78]. Circularly polarised X-radiation from the *Apple II* undulators is monochromatised by the *Dragon* monochromator and focus-sed onto the sample, passing a Au grid whose photocurrent serves as a monitor of beam intensity. Absorption spectra were registered in the region of the $L_{II,III}$ edges of the 3*d* impurities by stepping the monochromator through the spectral range of interest and meas-uring total electron yield via the current drain on the sample holder. The relative sign of the

applied magnetic field and the X-ray polarisation could be reversed both by changing the phase of the undulator and thus the sign of circular polarisation of the X-ray beam, or by reversing the magnetic field from the superconducting solenoid in the cryostat. The spectra showed clear absorption features at the $L_{II,III}$ edges, superimposed on a strong but featureless background due to the Au alloy host. The latter was measured in separate experiments under identical conditions with pure Au and subtracted from the spectra, which were normalised by the beam-intensity monitor signal. Figures 20 and 21 show the absorption spectra obtained from the impurities Mn and Co for different relative orientations of field and polarisation.

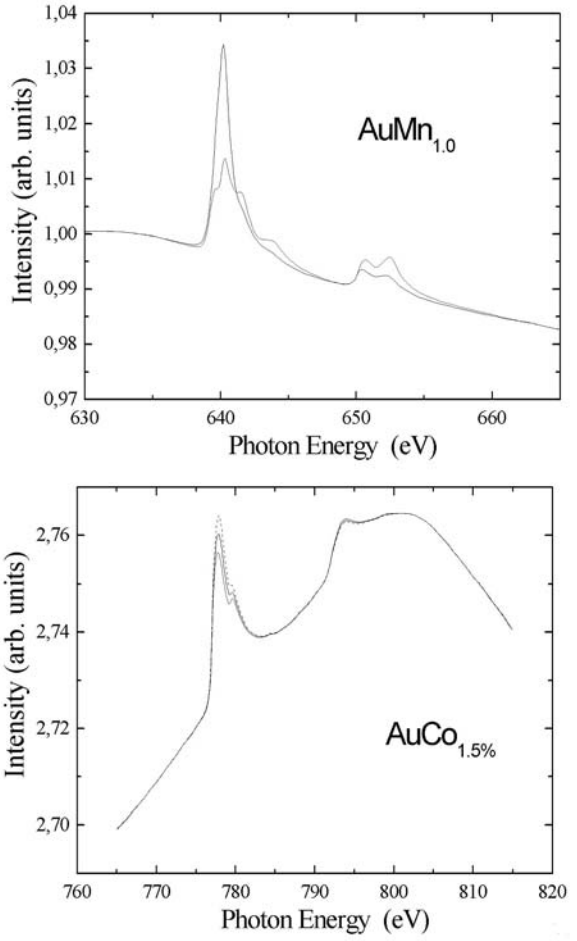

Figs. 20 and 21. X-ray absorption spectra of Mn (1 at.%) in Au (Fig. 20, above) and Co (1.5 at.%) in Au at their $L_{II,III}$ edges. The two curves represent (++) and (+-) orientations of applied field and circular polarisation of the X-rays. In Fig. 21, the average absorption spectrum is also shown.

Absorption of circularly-polarised X-ray photon near an edge corresponding to an inner electronic shell of the absorbing atom results in emission of a spin-polarised electron from the shell. The spin polarisation is due to angular-momentum conservation in the photo-emission process. The emitted electron can be reabsorbed into an empty state at higher energy. In the $L_{II,III}$-edge absorption studied here, the emitting states are the $2p_{1/2,3/2}$ levels and the electrons are excited into the hole states in the 3*d* shells. Since, in a magnetic atom, the latter are magnetically polarised, i.e. different magnetic substates are unequally populated, the overall probability of excitation depends on the spin polarisation of the photoelectrons and on the magnetic moments (spin and orbital) residing on the 3*d* orbitals. Thus the total X-ray absorption probability is different for different relative orientations of the applied field (which aligns the paramagnetic local moments) and the circular polarisation of the X-rays (which determines the spin polarisation of the photoelectrons). The difference of absorption spectra with field and polarisation parallel (++, --) and antiparallel (+-, -+) is a measure of the magnetic moments and is termed the XMCD spectrum. By comparing the XMCD effect at the two edges, the spin and orbital moments can be determined independently. The straight-forward way of doing this is to apply the "sum rules" obtained by Thole *et al.* [79]. These are, however, based on an atomic description of the absorbing atom which may not be valid for impurities in a metal host. The latter have properties between those of free atoms and those of bulk solids or compounds.

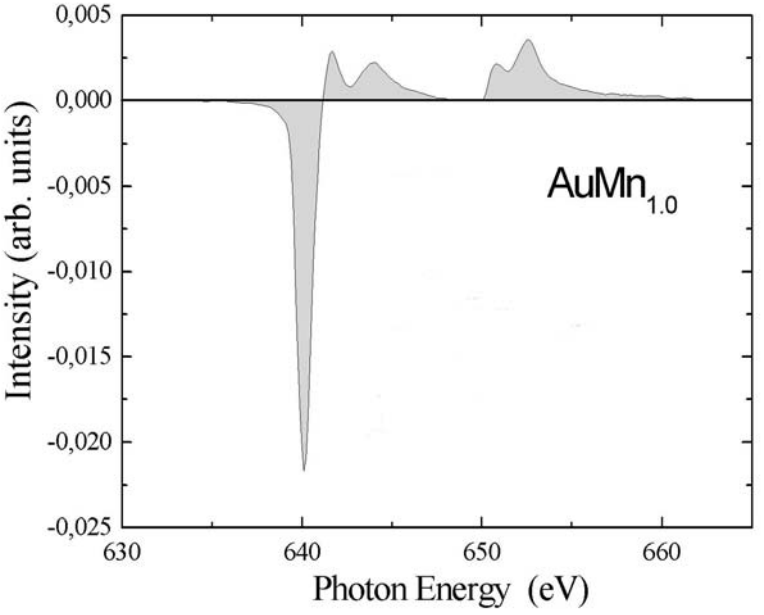

Fig. 22. The XMCD or difference spectrum obtained from the absorption spectra in Fig. 20 by subtraction of the (+-) from the (++) spectrum. The large dichroitic effect is typical of Mn in a magnetic state and in a metallic environment. The peak areas can be related to the spin and orbital magnetic moments. Figure adapted from Ref. [70].

Figure 22 ilustrates the XMCD spectrum obtained in the case of *Mn*Au. Despite the relatively low concentration of the Mn impurities, an excellent signal/noise ratio could be achieved in scans lasting less than 30 min. The XMCD spectra were collected at constant temperature for different combinations of field and polarisation directions and as a function of applied field magnitude, giving magnetisation curves as shown below in Fig. 24.

Rather than using the complete sum rules, a simpler analysis can be made in terms of the *ratio* of orbital to spin moments, which forgoes the detailed sum-rule analysis and makes use only of the ratio R of the total areas of the absorption peaks at the L_{II} and L_{III} edges:

$$\mu_l/\mu_s^{eff} = (2/3)(1+R)/(1-2R) .$$

The effective spin moment μ_s^{eff} includes the spin-dipolar contribution which cannot be separated without studying the angular dependence of the XMCD [80].

Figure 23 summarises the X-ray absorption spectra of the impurities Cr—Co in Au host, corrected for the host absorption background, and the difference (XMCD) spectra obtained from them.

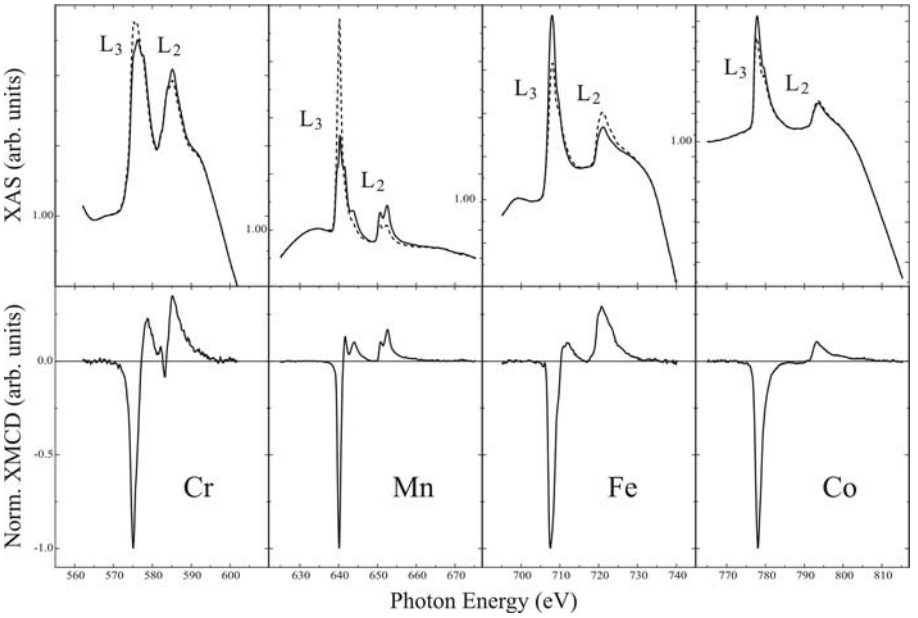

Fig. 23. X-ray absorption spectra near the $L_{II,III}$ edges of Cr, Mn, Fe, and Co as dilute impurities in Au host (upper panel), and the derived difference or XMCD spectra (lower panel). The full and dashed curves in the upper spectra represent the case of applied field and X-ray circular polarisation parallel and antiparallel, respectively. Their difference gives the XMCD signals shown below. Adapted from Refs. [70,71].

Figure 24 shows the magnetisation curve obtained for Mn in Au by varying the applied field and acquiring XMCD spectra at each field value. Comparison with the absolute magnitudes of the moments measured with the same samples in a SQUID magnetometer permits the "calibration" of the moments derived from the sum rules.

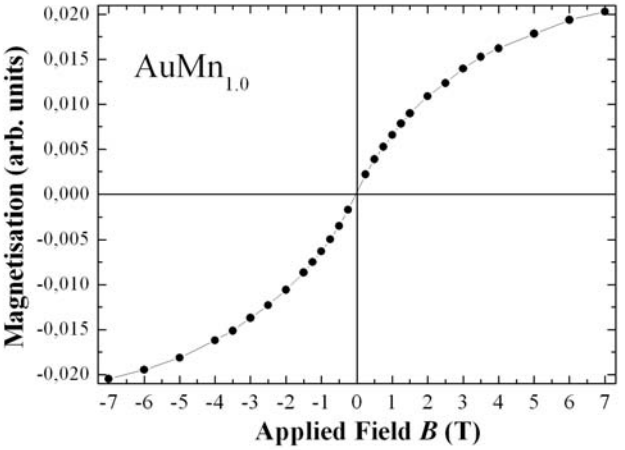

Fig. 24. Magnetisation curve obtained from XMCD measurements on Mn*Au* (1 at.%) as a function of applied field. The area of the L_{III} XMCD signal was used as a measure of the relative magnetisation of the paramagnetic Mn moments. From Ref. [71].

We note that the interpretation of the magnetic moment ratios obtained from the area ratios *R* of the XMCD spectra in these experiments is still not straightforward. The impurities are subject to the Kondo effect [73,74] due to magnetic scattering of the host conduction electrons off the local impurity moments. This effect will be different for spin and orbital contributions to the local moments. (What is referred to in the literature as the "orbital Kondo effect" is the scattering of conduction electrons with nonzero orbital angular momenta, e.g. *p*- and *d*-like conduction electrons, from a pure spin local moment. The case of scattering from a local orbital moment has, to our knowledge, not been treated theoretically.) The Kondo effect leads to a screening of the local moment below the characteristic temperature T_K, so that the susceptibility becomes constant at low temperatures and the paramagnetic character of the local moment system is suppressed. This is a single-impurity effect which would be present even in infinitely dilute samples. In addition, at the finite concentrations used here, the samples are spin glasses due to magnetic interactions of the impurity moments, and their magnetic structure will "freeze" into a disordered state below the characteristic glass temperature T_G. The samples were all investigated by SQUID susceptometry and their glass temperatures determined before the XMCD experiments were performed; care was taken to carry out the experiments at temperatures in the paramagnetic regime above T_G. The Kondo temperatures cited in the literature vary somewhat with experimental method and sample preparation, but they lie in the range of 1 K for Cr*Au* and Fe*Au*, in the mK range for Mn*Au*,

and in the range of 150-300 K for V*Au* and Co*Au* [73]. Thus the measurement temperatures in the XMCD experiments were well above the Kondo temperature for all the impurities studied except for V and Co. In these cases, the large applied magnetic field partially suppresses the Kondo effect, effectively restoring the magnetic moment. If the moment consists of both spin and orbital components, this restoration may occur to a different degree for the two types of moment, so that the observed ratio is not necessarily identical to the free-moment (high-temperature) limit. In addition, the spin contribution detected by XMCD consists of both a pure spin moment and a spin-dipolar or tensor contribution, which has been calculated for free atoms but was not included in the *ab initio* calculations [35] for impurities. The observed orbital/spin moment ratios are therefore lower limits, and allowing for the spin-dipolar term would increase the value of the moment ratio.

Keeping all these limitations in mind, one can derive the moment ratios shown in Figure 25 (from Ref. [70]).

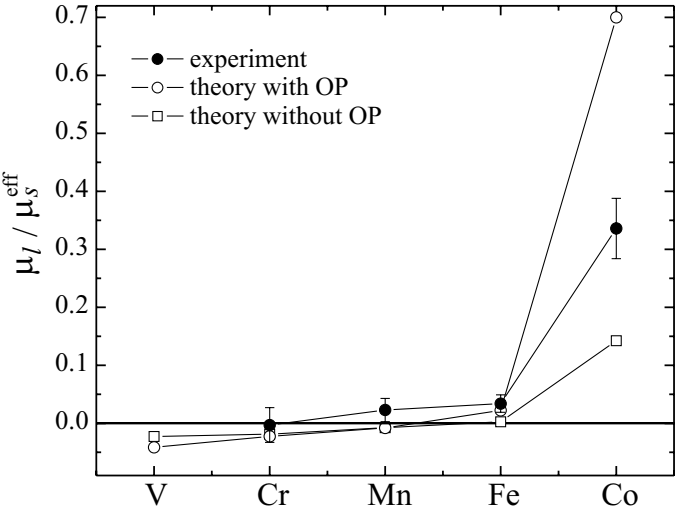

Fig. 25. Orbital-to-spin moment ratios derived from the peak-area ratios in the $L_{II,III}$ XMCD spectra of 3*d* impurities in Au, compared to the calculated ratios [35]. OP refers to the "orbital polarisation" or self-consistency correction applied to the calculation of the orbital magnetic moment [38], which may overestimate its magnitude, while the calculation without OP certainly underestimates it; compare Ref. [35]. Figure after Ref. [70].

The experimental trends are in good agreement with the *ab initio* theory. The orbital moment is small in most cases (we note that the XMCD effect observed from V*Au* was very small and there was some indication of internal oxidation in those samples, so the results are not included in Fig. 25).

The large orbital moment seen for CoAu is as predicted by theory and is a result of the details of the host band structure and its hybridisation with the local 3*d* states of the

impurities; the minority bands in the local density of states essentially determine the magnitude of the orbital moment which will form in a particular case, accounting for the difference between Fe*Ag*, with a relatively large orbital moment (Section (2)), and Fe*Au*, with a small orbital moment as verified here. Co forms large orbital moments in both Ag and Au hosts, but not in Cu host. Mn, in the centre of the 3*d* series, has only a very small orbital moment in all three hosts (in a purely atomic picture, its orbital moment would vanish, but this is not the case for impurities in a metallic environment). However, its orbital magnetism is somewhat stronger in the large-volume Au host than in the small Cu lattice. This theoretical prediction is borne out by these XMCD experiments on Mn*Au* and Mn*Cu* (not shown). The XMCD technique thus permits studies of magnetic moment formation on an atomic scale and can also be applied to small clusters in a nonmagnetic host or on a surface [66].

(4) Spectroscopy and microscopy with spin-polarised electrons

These methods are closely related to the X-ray techniques, and are based upon the emission of spin-polarised electrons due to a combination of excitation by polarised photons and the different occupations of majority and minority electronic subbands in magnetic materials; however, in this case the spin polarisation of the emitted electrons is detected directly, in contrast to the X-ray methods where the photon absorption coefficient is the experimentally observed quantity. These methods were pioneered by Siegmann and co-workers in the 1960's and 70's [81], and their flexibility has been enormously expanded in recent years with the development of improved sources and detectors of polarised electrons. Spin-polarised electrons can also be emitted by nonmagnetic materials irradiated with polar-ised photons, and serve as sources of polarised electrons for a variety of applications. A recent review of applications to magnetic imaging was given by W. Kuch [82]. We list a few applications from the literature of recent years in Ref. [83--85], as a sample of the considerable literature in this field.

(5) Magnetic scanning microscopy

Scanning-probe microscopy methods (SPM) were introduced by G. Binnig and H. Rohrer at IBM Zurich in 1981 in the form of the scanning tunneling microscope (STM). (A useful collection of Internet links to information on SPM topics, of which some have however unfortunately changed their URL's, can be found in Ref. [86]).

Since then, a number of refinements using different tip materials and geometries have been introduced. The goal of *magnetic* scanning microscopy is to employ a spin-sensitive tip which selectively emits or absorbs spin-polarised electrons and thus provides sensitivity to the local magnetic state of the surface over which it is scanned. These methods are under development, and offer great promise for the imaging of magnetic structures of surfaces and thin films which could, in principle, achieve atomic resolution and quantitative moment determination. We give a few references to this rapidly-developing field, again as examples of the types of investigations which are possible [87--89].

4. CONCLUSIONS

We have attempted to give a brief overview of a variety of modern methods which complement the traditional techniques of magnetometry, susceptibility, transport properties, ferromagnetic resonance and specific heat measurements used for studying magnetic systems in the past. While these older methods have been enormously improved in sensitivity, enabling the study of very small samples and even of ultrathin films and multilayers, they remain essentially “bulk” methods which measure properties averaged over the whole sample. The newer techniques mentioned here often permit element-specific studies and layer-by-layer or even atomic resolution, allowing the study of nanoclusters, bi- and trilayer systems with atomic monolayer thickness, and even single atoms on surfaces and at interfaces. The literature of these interesting techniques is vast and growing, and the reader is encouraged to examine the Internet sites quoted for links to the latest developments.

REFERENCES

[1] see e.g. C. F. Majkrzak, Physica **B 173**, 375 (1991); H. Zabel, Applied Physics **A 58**, 159 (1994).

[2] A. van der Graaf, *Polarized Neutron Reflectometry on Thin Magnetic Films* (Delft University Press, 1997; ISBN: 90-407-1526-2).

[3] H. Zabel, "Future trends in heterostructure research with neutron scattering" in *Frontiers of Neutron Scattering*, ed. Albert Furrer (World Scientific, 2000), p.210.

[4] C. F. Majkrzak, Physica **B 221**, 342 (1996).

[5] H. Zabel, R. Siebrecht, and A. Schreyer, Physica **B 276**, 17 (2000).

[6] M. Gierlings, Dissertation: "Magnetic Properties of Exchange-coupled Antiferro-magnetic/ferromagnetic Multilayers Studied by Polarized Neutron Reflectometry and Low Temperature Nuclear Orientation", Freie Universität Berlin (2002); see *http://www.diss.fu-berlin.de/2003/33/*.

[7] M. Gierlings, M. Prandolini, H. Fritzsche, M. Gruyters, and D. Riegel, „Change and Asymmetry of Magnetization Reversal for a Co/CoO Exchange-bias System", Phys. Rev. **B 65**, 092407 (2002).

[8] W. H. Meiklejohn and C. B. Bean, Phys. Rev. **105**, 904 (1957).

[9] M. Gruyters and D. Riegel, J. App. Phys. **88**, 6610 (2000); M. Gruyters, M. Gierlings, and D. Riegel, Phys. Rev. **B 64**, 132401 (2001).

[10] N.J. G.okemeijer, T. Ambrose, and C.L. Chien, Phys. Rev. Lett.**79**, 4270 (1997).

[11] R. Radu, M. Etzkorn, V. Leiner, T. Schmitte, A. Schreyer, K. Westerholt, and H. Zabel, "Polarized Neutron Reflectomerty Studies on Co/CoO Exchange Biased Multilayers", Appl. Phys. **A 74**,1570 (2002) [Suppl 1].

[12] W.-T. Lee, S. G. E. te Velthuis, G. P. Felcher, F. Klose, T. Gredig, and E. D. Dahlberg, „Ferromagnetic Domain Distribution in Thin Films During Magnetization Reversal", Phys. Rev. **B 65**, 224417, (2002).

[13] J.A. Borchers, J.A. Dura, J. Unguris, D. Tulchinsky, M.H. Kelley, C.F. Majkrzak, S.Y. Hsu, R. Loloee, W.P. Pratt, Jr., and J. Bass, "Observation of Antiparallel Magnetic Order in Weakly Coupled Co/Cu Multilayers", Phys. Rev. Lett. **82**, 2796 (1999).

[14] S. Langridge, J. Schmalian, C.H. Marrows, D.T. Dekadjevi, and B.J. Hickey, "Quantification of Magnetic Domain Disorder and Correlations in Antiferromagnetically Coupled Multilayers by Neutron Reflectometry", Phys. Rev. Lett. **85**, 4964 (2000).

[15] B. Nickel, A. Rühm, W. Donner, J. Major, H. Dosch, A. Schreyer, H. Zabel, and H. Humblot, "Spin-resolved off-specular neutron scattering maps from magnetic multilayers using a polarized ^{3}He gas spin filter", Rev. Sci. Instrum **72**, 163 (2001).

[16] B. Toperverg, O. Nikonov, V. Lauter-Pasyuk and H.J. Lauter, „Towards 3D polarization analysis in neutron reflectometry", Physica **B 297**, 169 (2001).

[17] Rafailovich, M.H., Dafni, E., Mahnke, H.-E-, Sprouse, G.D., "Observation of a Positive Hyperfine Field for Dilute Fe Impurities in Ca", Phys. Rev. Lett. **50**, 1001 (1983).

[18] Th. Kornrumpf, K. Nishiyama, and D. Riegel, "Anomalously Small Knight Shift and Relaxation Rate in the Nonalloying System: Isolated Yttrium Ions in Liquid Rubidium", Phys. Rev. Lett. **49**, 1274 (1982).

[19] Rafailovich, M.H., Dafni, E., Mahnke, H.E., Sprouse, G.D., and Vapirev, E., "The paramagnetism of dilute Fe impurities in Pt", Hyperfine Interactions **10**, 821 (1981).

[20] Dafni, E., Rafailovich, M.H., Little, W.A., and Sprouse, G.D., "Influence of Radiation Damage on Perturbed Angular Distributions: the Po*Pb* System", Phys. Rev. **C23**, 90 (1981).

[21] Frauenfelder, H., and Steffen, R.M., "Angular Correlations" in *Alpha-, Beta- and Gamma-Ray Spectroscopy*, ed. K. Siegbahn (North-Holland, Amsterdam 1965).

[22] Karlsson, E., Matthias, E., and Siegbahn, K., Editors, *Perturbed Angular Correlations* (North-Holland, Amsterdam 1964).

[23] De Groot, S.R., Tolhoek, H.A., and Huiskamp, W.J., "Orientation of Nuclei at Low Temperatures", in *Alpha-, Beta- and Gamma-Ray Spectroscopy*, ed. K. Siegbahn (North-Holland, Amsterdam 1965).

[24] Stone, N.J., Chap. 8 in: *Low-Temperature Nuclear Orientation* eds. N.J. Stone and H. Postma (North-Holland, Amsterdam 1986).

[25] E. Gerdau, U. van Bürck and R. Rüffer in *Nuclear Resonant Scattering of Synchrotron Radiation*, Eds. E. Gerdau and H. de Waard, Hyperfine Interactions **123-125**, 3 (2000).

[26] A. Metz, S. Frota- Pessôa, J. Kapoor, D. Riegel, W.D. Brewer, and R. Zeller, "Substitutional and Interstitial Fe in *hcp*-Ti, Zr, and Hf: Theory and Experiments", Phys. Rev. Lett. **71**, 3525 (1993).

[27] A. Metz, J. Kapoor, D. Riegel, and W.D. Brewer, „Local Observation of the Impurity-Impurity Interactions in Paramagnetic *Au*Fe Alloys", Phys. Rev. Lett. **73**, 3161 (1994).

[28] J. Kapoor, D. Riegel, Yi Li, C. Polaczyk, J. Andres, F. Mezei, R. Sielemann, Y. Yoshida, W.D. Brewer, L.A. de Mello, and S. Frota-Pessôa, "Observation of Magnetism in Fe at an Interstitial Site in a Metal Host", Phys. Rev. Lett. **78**, 1279 (1997).

[29] A A Tulapurkar, S N Mishra, R G Pillay, H Salunke and G P Das, "Local magnetism of isolated Mo atoms at substitutional and interstitial sites in Yb metal: Experiment and Theory", Phys. Rev. Lett, **85**, 1978 (2000).

[30] Riegel, D. and Gross, K.-D., in *Nuclear Physics Applications on Materials Science*, Eds. E. Recknagel and J. C. Soares, NATO ASI Proc. Series E, Vol. **144** (Kluwer Academic, Dordrecht 1988), p. 327.

[31] D. Riegel and W.D. Brewer, "Magnetic Behavior of Implanted Transition-Metal Probes at Different Lattice Sites in Metals", Australian. J. Phys. **51**, 157 (1998).

[32] T.A. Kitchens and R.D. Taylor, "Summary of Mössbauer evidence associated with the Kondo effect", Phys. Rev. **B9**, 344 (1974); P. Steiner and S. Hüfner, „Local magnetization of Fe in Ag",Phys. Rev. **B12**, 842 (1975).

[33] R. Kirsch, M. J. Prandolini, O. Beutler, W. D. Brewer, M. Gruyters, J. Kapoor, D. Riegel, H. Ebert and S. Frota-Pessôa, "The formation of orbital moments on iron impurities in $Ag_{1-x}Au_x$ alloys", Europhys. Lett. **59** (2002), 430.

[34] H.Ebert, in *Electronic Structure and Physical Properties of Solids'*, ed.H.Dreyssé (Lecture Notes in Physics, Vol. **535**: Springer, Berlin 2000), p.191.

[35] S.Frota-Pessôa, Phys.Rev. **B46**, 14570 (1992); S.B. Legoas, A.A.Araujo, B.Laks, A.B. Klautau and S. Frota-Pessôa, Phys. Rev. **B61**, 10417 (2000); S.Frota-Pessôa, "Magnetic behavior of 3*d* impurities in Cu, Ag, and Au:First-principles calculations of orbital moments", Phys.Rev. **B69**, 104401 (2004).

[36] P. Blaha, K. Schwarz, P. Sorantin and S.B. Trickey, Comput. Phys. Commun. **59**, 399 (1990).

[37] S. Blügel, H. Akai, R. Zeller and P.H. Dederichs, Phys. Rev. **B35**, 3271 (1987); H. Ebert, P. Strange and B.L. Gyorffy, Z. Phys. **B73**, 77 (1988).
[38] O. Eriksson, B. Johansson, R.C. Albers, A.M. Boring, and M.S.S. Brooks, Phys. Rev. **B42**, 2707 (1990).
[39] O. Beutler, Dissertation, Freie Universität Berlin, 1998, unpublished.
[40] O. Beutler, R. Kirsch, P.J. Jensen, W.D. Brewer, J. Kapoor, D. Riegel, and S. Frota-Pessôa, „Exchange-coupled magnetic pairs: Fe-Cr in a Au host matrix“, submitted to Europhys. Lett. (2004).
[41] S.Frota-Pessôa, J. Mag. Magn. Mat. **226-230**, 1021 (2001).
[42] S.Frota-Pessôa: see Ref. [35], and to be published.
[43] R. Kirsch, Dissertation, Freie Universität Berlin, 2001, unpublished.
[44] G. Schatz: "Surface Studies with Hyperfine Probes", in *Proc. of the Nato Advanced Study Institute on Nuclear Physics Applications in Materials Science*, eds. E. Recknagel and J.C. Soares, Portugal 1987, p. 29.
[45] J. Voigt, R. Fink, G. Krausch, B. Luckscheiter, R. Platzer, U. Wöhrmann, X.L. Ding and G. Schatz: "Magnetic Hyperfine Field at ^{111}In Probes in the Topmost Atomic Layer of Ni(111) Surfaces", Phys. Rev. Lett. **64** (1990) 2202; J. Voigt, X.L. Ding, R. Fink, G. Krausch, B. Luckscheiter, R. Platzer, U. Wöhrmann and G. Schatz, "Monolayer-Resolved Detection of Magnetic Hyperfine Fields at Cu/Ni(111) Interfaces", Phys. Rev. Lett. **66** (1991) 3199; B.-U. Runge, M. Dippel, G. Filleböck, K. Jacobs, U. Kohl, G. Schatz: "Induced Magnetic Field at Ag Sites near an Fe(100)/Ag(100) Interface", Phys. Rev. Lett. **79** (1997), 3054; U. Kohl, M. Dippel, G. Filleböck, K. Jacobs, B.-U. Runge, G. Schatz: "Local magnetism of ultrathin fcc-Co Films on Cu(100) investigated by ^{111}In probes", Surface Science **407** (1998), 104.
[46] C. Laurens, M.F. Rosu, F. Pleiter, and L. Niesen „Low-energy deposition of ^{111}In on Cu(17 1 1) surfaces”, NATO ASI Series B: Physics Vol. **360**, Surf. Diff.: Atom. and Coll. Proc., ed. M.C. Tringides (Plenum, New York, 1997), 679; C.R. Laurens, M.F. Rosu, F. Pleiter, and L. Niesen,“Soft-landing deposition of radioactive probe atoms on surfaces”, Hyp. Int. **120/121** (1999), 59; C.R. Laurens, M.F. Rosu, F. Pleiter, and L. Niesen, “Soft-landing ion deposition of isolated radioactive probe atoms on surfaces: a novel method”, Phys. Rev. Lett. **78,** 4075 (1997).
[47] G. Catchen, D. Loubychev, and R. Platzer, “Electric-field gradients at group-III sites on GaAs and InAs (111)B surfaces”, Hyperfine Interactions **136**, 633 (2001).
[48] Vantomme A., Degroote B., Degroote S., Vanormelingen K., Meersschaut J., Croonenborghs B., Van Eek S.M., Pattyn H., Rots M., Langouche G., “Hyperfine interaction studies with monolayer depth resolution using ultra-low energy radioactive ion beams”, Nuclear Instruments and Methods **B 190**, 840 (2002); Wilgocka-Slezak D., Slezak T., Croonenborghs B., Rots M., Karas W., Krop K., Spiridis N., Korecki J., “Experimental studies of the non-collinear magnetic states in epitaxial FeAu multilayers”, Journal of Magnetism and Magnetic Materials **240**, 536 (2002) .
[49] *Low Temperature Nuclear Orientation*, eds. N.J. Stone and H. Postma (North- Holland, Amsterdam 1986).
[50] W D Brewer, “Recent developments in low-temperature nuclear orientation”, Rep. Prog. Phys. **53**, 483 (1990).

[51] L. Vanneste, W.D. Brewer, J. Camps, J. Dekoster, P. De Moor, T. Phalet, M. Trhlík, P. Schuurmans, N. Severijns, A. Van Geert, and Y. Vanhellemont, "Study of MBE Fe/Ag Multilayer Systems with Nuclear Orientation", Hyp. Int. **C1**, 303 (1996).

[52] M. Trhlík, E. Beck, W.D.Brewer, J. Dekoster, H. Stèpánková, J. Kohout, and G. Langouche, "Nuclear Spin-Lattice Relaxation of Co Nuclei in an Fe/Co Multilayer at Low Temperatures", Czech. J. Phys. **46**, 2181 (1996).

[53] M. Trhlík, M. Rotter, N. Severijns and L.Vanneste, „Nuclear Orientation as a Tool for Investigation of Magnetic Multilayers", Australian J. Phys. **51** 255 (1998).

[54] Trhlík M ., De Moor P ., Pari P ., Rotter M ., Severijus N ., Van Geert A ., Vanneste L. "Low-temperature nuclear orientation of ^{160}Tb in Tb/Fe multilayers", Czechoslovak J. of Phys. **46**, 2207 (1996); M. Trhlík, K. Mibu, P. De Moor, P. Pari, M. Rotter, N. Severijns, T. Shinjo, A. Van Geert, L. Vanneste, "Evidence for perpendicular magnetic anisotropy of Tb in Tb/Fe multilayers", Journal of Physics: Condensed Mattter **8**, 8907 (1996).

[55] Phalet, T.; Prandolini, M.J.; Brewer, W.D.; De Moor, P.D.; N.; Schuurmans, P.; Severijns, N.; Turrell, B.G.; Van Geert, A.; Vereecke, B.; and Versyck, S.: 'Non-collinear magnetic hyperfine fields on the Ag spacers in Fe/Ag multilayers', Phys. Rev. Lett. **86**, 902 (2001).

[56] M. Gierlings, M.J. Prandolini, M. Gruyters, W.D. Brewer, and D. Riegel, "On the possibility of detecting asymmetric magnetization reversal processes in exchange bias systems by low temperature nuclear orientation', J. Magn. Magn. Mat. **240**, 280 (2002); M. Gierlings, M. Gruyters, and D. Riegel, M.J. Prandolini,T. Funk and W. D. Brewer, "A study of the induced magnetism in the Au spacer layer of Co/Au/CoO Exchange Bias trilayers and related systems", submitted to Phys. Rev. **B** (2004).

[57] F. Wilhelm, P. Poulopoulos, G. Ceballos, P. Srivastava, H. Wende, K. Baberschke, D. Benea, H. Ebert, M. Angelakeris, N.K. Flevaris, D. Niarchos, A. Rogalev and N.B. Brookes; "Layer-resolved magnetic moments in Ni/Pt multilayers", Phys. Rev. Lett.**85**, 413 (2000); Y. Kobayashi,. S. Nasu, T. Emoto, and T. Shinjo, Hyp. Int. **94**, 2273 (1994); B.U. Runge, M. Dippel, F. Filleböck, K. Jacobs, U. Kohl, and G. Schatz, Phys. Rev. Lett. **79**, 3054 (1997).

[58] Phalet, T., Prandolini, M.J., Brewer, W.D., Dekoster, J., De Moor, P., Severijns, N., Schuurmans, P., Turrell, B.G., Van Geert, A., Vanneste, L., Vereecke, B, Versyck, S., "A Study of the Induced Magnetic Hyperfine Fields in Fe/Ag Multilayers", Hyp. Int. **120/121**, 209 (1999); Prandolini, M.J. *et al.*, "Nuclear Orientation Studies of Ag Hyperfine Fields in Fe/Ag Multilayers", J. Magn. Magn. Mat. **198-199**, 291 (1999).

[59] P. Raghavan, At. Data Nucl. Data Tables **42**, 189 (1989); see also Ref. [49].

[60] K. Okada and H. Yasuoka, J. Phys. Soc. Japan **43**, 34 (1977).

[61] See e.g. *Material Research in Atomic Scale by Mössbauer Spectroscopy* (NATO Science Series II: Mathematics, Physics and Chemistry, Vol. **94**) , eds. Miroslav Mashlan, Marcel Miglierini and Peter Schaaf (Kluwer Academic Publishers, Dordrecht 2003).

[62] E. Gerdau, R. Rüffer, H. Winkler, W. Tolksdorf, C.P. Klages, and J.P. Hannon, "Nuclear Bragg Diffraction of Synchrotron Radiation in Yttrium Iron Garnet", Phys. Rev. Lett. **54**, 835 (1985); G.V. Smirnov, Hyp.Int. **97/98**, 551 (1996); E. Gerdau E. and U. v. Bürck, in *Resonant Anomalous X-Ray Scattering Theory and Applications* , eds. G. Materlik, C.J. Sparks, K. Fischer (Elsevier Science B.V., Amsterdam 1994). For useful links, see also *http://www.ipc.uni-stuttgart.de/~tanja/links.html*

[63] A.I. Chumakov, L. Niesen, D.L. Nagy, and E.E. Alp, "Nuclear resonant scattering of synchrotron radiation by multilayer structures", Hyp. Int. **123/124**, 427 (2000); L.Niesen *et al.*, "Magnetic behavior of probe layers of ^{57}Fe in thin Fe films observed by means of nuclear resonant scattering of synchrotron radiation", Phys. Rev. **B58**, 8590 (1998); A. Nefedov, J. Grabis, A. Bergmann, F. Radu and H. Zabel, " X-ray resonant magnetic scattering of Fe/Cr superlattices", submitted to Phys. Rev. **B** (2004).
[64] H. Wende, "Recent advances in the X-ray absorption spectroscopy", Rep. Progr. Phys. (in press, online publication Sept. 2004).
[65] P. Fischer, G. Schütz, G. Schmahl, P. Guttmann, and D. Raasch, Z. Phys. **B**: Condens. Matter **101**, 313 (1996); P. Fischer, T. Eimüller, G. Schütz, P. Guttmann, G. Schmahl, K. Prögl, and G. Bayreuther, J. Phys. **D31**, 649 (1998); P. Fischer, T. Eimüller, G. Schütz, M. Köhler, G. Bayreuther, G. Denbeaux, and D. Attwood, "Study of in-plane magnetic domains with magnetic transmission X-ray Microscopy", J. Appl. Phys. **89**, 7159 (2001).
[66] P. Gambardella *et al.*, Phys. Rev. Lett. **88**, 047202 (2002); P. Gambardella *et al.*, Science **300**, 1130 (2003).
[67] J.L. Erskine and E.A. Stern, Phys. Rev. **B12**, 5016 (1975).
[68] G. Schütz, W. Wagner, W. Wilhelm, and P. Kienle, Phys. Rev. Lett. **58**, 737 (1987).
[69] K. Namikawa, M. Ando, T. Nakajima, and H. Kawata, J. Phys. Soc. Japan **54**, 4099 (1985); G. Van der Laan, B.T. Thole, G.A. Sawatzky, J.B. Goedkoop, J.C. Fuggle, J.-M. Esteva, R. Karnatak, J.P. Remeika, and H.A. Dabkowska, Phys. Rev. **B34**, 6529 (1986).
[70] W.D. Brewer, A. Scherz, C. Sorg, H. Wende, K. Baberschke, P. Bencok, and S. Frota-Pessôa, „Direct observation of orbital magnetism in cubic solids", Phys. Rev. Lett. **93**, 077205 (2004).
[71] A. Scherz, Dissertation: "Spin-dependent X-ray Absorption Spectroscopy of 3*d* Transition Metals" (Freie Universität Berlin, 2004, ISBN 3-89825-779-7); see *http://www.dissertation.de.*
[72] J. Friedel, Adv. Phys. **3**, 446 (1954); Nuovo Cimento Suppl. **7**, 287 (1958); P.W. Anderson, Phys. Rev. 124, 41 (1961); Comments on solid State Phys. **3**, 153 (1971).
[73] C. Rizzuto, "Formation of localized moments in metals: experimental bulk properties", Rep. Prog. Phys. **37**, 147 (1974).
[74] J. Kondo, Progr. Theor. Phys. **32**, 37 (1964); Solid State Phys. **23**, 183 (1969).
[75] J. A. Mydosh, *Spin Glasses* (Taylor & Francis, London 1995); P. Nordblad, L. Lundgren and L. Sandlund, J. Mag. Magn. Mater. **54**, 185 (1986).
[76] A. Narath and D. C. Barham, Phys. Rev. **B7**, 2195 (1973); J. Boysen, W. D. Brewer, and J. Flouquet, Solid State Comm. **12**, 1095 (1973).
[77] L. Dwörin and A. Narath, Phys. Rev. Lett. **25**, 1287 (1970).
[78] See *http://www.esrf.fr/UsersAndScience/Experiments/XASMS/ID08/UsersGuide*
[79] B.T. Thole, P. Carra, F. Sette, and G. Van der Laan, Phys. Rev. Lett. **68**, 1943 (1992); P. Carra, B.T. Thole, M. Altarelli, and X. Wang, Phys. Rev. Lett. **70**, 694 (1993). See also H. Ebert, "Spin-orbit –influenced spectroscopies of magnetic solids", *Lecture Notes in Physics*, eds. H. Ebert and G. Schütz (Springer, Berlin 1996), 159-177.
[80] J. Stöhr and H. König, Phys. Rev. Lett. **75**, 3748 (1995).

[81] G. Busch, M. Campagna, P. Cotti and H.C. Siegmann, "Observation of Electron Polarization in Photoemission", Phys. Rev. Lett. **22**, 597 (1969); G. Busch, M. Campagna and H.C. Siegmann, "Polarized Photoelectrons from the Europium-Chalcogenides", Solid State Comm. **7**, 775 (1969); G. Busch, M. Campagna and H.C. Siegmann, "Photoemission of Spin-Polarized Electrons from Ferromagnets", J. Appl. Phys. **41**, 1044 (1970); U. Bänninger, G. Busch, M. Campagna and H.C. Siegmann, "Photoelectron Spin Polarization and Ferromagnetism of Crystalline and Amorphous Nickel", Phys. Rev. Lett. **25**, 585 (1970); U. Bänninger, G. Busch, M. Campagna and H.C. Siegmann, "Electron Spin Polarization in Photoemission from Dy and Gd and the Role of Electron-Magnon Scattering", J. de Physique **32**, 290 (1970). See also the review "Emission of Polarized Electrons from Solids" by M. Campagna, D.T. Pierce, F. Meier, K. Sattler, H.C. Siegmann, in: *Advances in Electronics and Electron Physics* **41**, 113 (1976).

[82] W. Kuch, "Imaging Magnetic Microspectroscopy", in: H. Hopster and H. P. Oepen, eds., *Magnetic Microscopy of Nanostructures* (Springer, Berlin 2004).

[83] Uzdin, V. M., Knabben, D., Hillebrecht, F. U., and Kisker, E., "Magnetic Dichroism and Spin-Resolved Photoemission From Rough Interfaces", Phys. Rev. **B59**, 1214 (1999).

[84] LH. Tjeng, B. Sinkovic, N. B. Brookes, J. B. Goedkoop, R. Hesper, E. Pellegrin, F. M. F. de Groot, S. Altieri, S. L. Hulbert, E. Shekel, and G. A. Sawatzky, "*Spin*-Resolved Photoemission on *Anti*-Ferromagnets: Direct Observation of Zhang-Rice Singlets in CuO", Phys. Rev. Lett. **78**, 1126 (1997)

[85] K. Starke, A.P. Kaduwela, Y. Liu, P.D. Johnson, M.A. Van Hove, C.S. Fadley, V. Chakarian, E.E. Chaban, G. Meigs, and C.T. Chen, "Spin-polarized photoelectrons excited by circularly polarized radiation from a nonmagnetic solid", Phys. Rev. **B53**, R10 544 (1996).

[86] See *http://www.embl-heidelberg.de/~altmann/*

[87] U. Schlickum, W. Wulfhekel, and J. Kirschner, "Spin-polarized scanning tunneling microscope for imaging the in-plane magnetization", Appl. Phys. Lett. **83**, 2016 (2003).

[88] Friedrich, J., Rozhko, I., Voss, J., Hillebrecht, F. U., Kisker, E., and Wedemeier, V., "Scanning Microscopy of Magnetic Domains Using the Fe 3*p* Core Level Transverse Magneto-Optical Kerr Effect", J. Appl. Phys. **85**, 4610 (1999).

[89] R. Wiesendanger, M.Bode, M. Kleiber, M. Löhndorf, R. Pascal, A. Wadas and D. Weiss, „Magnetic nanostructures studied by scanning probe microscopy and spectroscopy", J. Vac. Sci. Technol. **B15**, 1330 (1997).

PROBING MAGNETIC PHASES IN DIFFERENT SYSTEMS USING LINEAR AND NON LINEAR SUSCEPTIBILITY

A. Banerjee, A. Bajpai[*], and Sunil Nair[*]

UGC-DAE Consortium for Scientific Research[†], University Campus, Khandwa Road, Indore 452017, India

1. INTRODUCTION

Study of the magnetic phases in various systems is an important activity of condensed matter physics and materials science research. Variety of phases found in magnetic systems are probed by many different measurement techniques depending on the nature of the magnetism as well as on the associated magnetic transitions. A system is explored from the response it gives to the excitations induced by the probes. Depending on the technique used, the magnetic system is explored in different length and time scales. When the response is collected directly from atoms or their electrons then it is broadly called a microscopic probe like neutron scattering, Mössbauer effect, Magnetic Circular Dichroism etc. On the contrary, in conventional dc-magnetization or ac-susceptibility measurements the response is collected from the magnetic induction or force exerted by the bulk of the sample that defines the length scale of the measurement as macroscopic. In between, there is the mesoscopic length scale when the primary response originates from the collections of atoms whose dimensions are much smaller than the bulk of the sample like magnetic domains or magnetic clusters. The measurement techniques such as small-angle neutron scattering, neutron de-polarization and magnetic force microscopy belongs to this category because for them the response originates from the magnetic clusters or magnetic domains present in the sample. However, these length scales of the probes are neither directly related to the intrinsic length scales of magnetic order

[*] Present address: Tata Institute of Fundamental Research, Homi Bhabha Road, Mumbai 400 005, India.
[†] Formerly: Inter University Consortium for DAE Facilities.

of the system nor with the penetration depth of the probe. For example, neutron scattering, Mössbauer effect or ac-susceptibility measurements contain signatures of both magnetic long-range and short-range orders. Likewise, magnetic circular dichroism and magneto-optic Kerr effect are efficient tools to probe the surface magnetism having penetration depths restricted to only a few tens of nanometers. Nevertheless, the former is a microscopic probe where the response depends on the absorption of x-rays by individual atoms whereas response for the latter depends on the total magnetization of the surface produced by a large collection of atoms. Similarly, the time scales involved in various measurement techniques varies from about 10^{-12} second for neutron spin-echo measurement to 1 second or more for dc-magnetization measurement. The importance of the time scale of the measurement arises mainly to probe the magnetic relaxation or the spin dynamics. The measurement techniques like Mössbauer effect, muon depolarization, nuclear magnetic resonance (NMR) and electron spin resonance (ESR) probe the local spin dynamics in time scale $< 10^{-5}$ seconds. Whereas, global dynamics or long wavelength relaxation processes of metastable magnetic systems are probed by techniques like dc-magnetization or ac-susceptibility measurements. Thus different measurement techniques probe the magnetic systems with different approaches and very often one needs to use a combination of them to develop reasonable understanding about any system. However, it is also possible to do in-depth study of magnetic systems by exhaustively utilizing the potential of a particular technique. In this article, an attempt is made to exemplify how ac-susceptibility (ac-χ) can be used to unravel the magnetism of interesting metastable magnetic systems and the associated short-range order as well as to effectively probe the critical behaviour of systems with long-range magnetic order.

1.1. LINEAR AND NON LINEAR AC-χ AS A PROBE FOR MAGNETIC SYSTEMS

A magnetic specimen, when placed in an alternating magnetic field ($H = H_0 \sin 2\pi ft$) results in a time varying magnetization (M), which is measured by using a simple set-up consisting of a primary and two oppositely wound secondary coils. In general M can be written in terms of H as

$$M = M_0 + \chi_1 H + \chi_2 H^2 + \chi_3 H^3 + \ldots. \quad (1)$$

Where M_0 is the magnetization created by the internal field and χ_1, χ_2, χ_3 are the first-, second- and third-order susceptibilities respectively, which can be directly measured using a mutual inductance bridge in ac-susceptibility measurement [1]. The magnetization M has an inversion symmetry with respect to the sign of H in the absence of any superimposed dc-magnetic field or a symmetry-breaking internal field as a consequence of which the even order susceptibilities $\chi_2, \chi_4 \ldots$.remain absent.

The small amplitude of the ac field (H) allows one to accurately measure the true initial susceptibility (χ) which otherwise has to be estimated from the extrapolation of high field data. The added advantage of measuring χ as a function of the probe frequency ($f \sim 1/\tau_{probe}$) of the applied field is that it provides useful information of the various time constants intrinsic to the magnetic system (τ_{system}) . In fact, the use of linear and non linear ac-χ as a probe for characterizing a magnetic materials initially gained popularity, due to the easy manifestation of metastability through the frequency dependence of χ_1 in a variety of canonical spin glasses (SG) and an assembly of small magnetic particle termed as superparamagnets (SPM).

Consequently, a frequency dependence in ac-χ (χ_1) together with a bifurcation of field-cooled (FC) and zero-field-cooled (ZFC) magnetization (i.e. history dependent magnetization) were considered sufficient to assign a spin-glass phase in many systems. However, a cursory glance at literature over the last 3 decades show that many long-range order systems like ferromagnets (FM) antiferromagnets (AFM) show typical time and history dependence in bulk susceptibility (both ac and dc) similar to what one observes in a conventional spin glass (SG) or superpramagnets (SPM) [1]. However, it is to be noted that the physical origin and the underlying physics behind this qualitatively similar time and history effect in first order susceptibility may have completely different physical origins. For instance, the origin of metastability in a spin-glass like system is the 'frustration effect' arising from random competing interactions leading to a co-operative *freezing* of the spin system on a broad timescale. Superparamagnets consisting of small magnetic particles or clusters give rise to metastability purely because of dynamic phenomenon called *blocking* arising out of competition between thermal and anisotropy energies of the individual magnetic entities [1,2]. However, in conventional ferro/antiferromagnets the time and history effects can arise from domain wall dynamics/pinning and issues related with anisotropy [3].

It is thus clear that the mere observation of frequency dependence in ac-χ, particularly in the first-order susceptibility or history dependence in dc-magnetization is not conclusive enough for exact determination of the magnetic ground state. This is especially true for those samples which are neither tailor made small particle systems nor from the family of canonical spin glasses. *It is here that the measurement and analysis of the higher order susceptibility becomes crucial.* As it will become clear in the later part of this article, at times the higher order susceptibility can provide much needed information to differentiate among a variety of magnetic orders such as FM, AFM, Ferrimagnet, SG, SPM etc., hidden in the magnetic specimen. For instance, non-linear susceptibility was introduced as a direct probe for the divergence of Edwards-Anderson order parameter, signifying the onset of spin-glass transition [2]. Though in the past, there have been efforts to discern a spin glass phase from a superparamagnetic phase in conventional small particle systems using higher order susceptibility [4], there have been little effort for in-depth study in a vast variety of bulk magnetic materials including transition metal oxides, magnetic ceramics, metals etc., exhibiting signatures of metastability in bulk magnetization studies, the origin of which remains ambiguous.

The endeavor of this article is to bring out the subtle features exhibited by higher order magnetic susceptibility in a variety of systems and to emphasize the role which it can play in the determination of magnetic phase. We have broadly divided our study in three parts. Section 2 deals with studies on SPM and SG phases and Section 3 is devoted to the conventional long range magnetic orders like FM and AFM. We have elaborated more on our experimental results in a series of a *diluted antiferromagnets* and in a series of *amorphous ferromagnets*. This is to lay emphasis on the subtle experimental observations and the robustness of the underlying theoretical predictions related to higher order susceptibility, even in such unconventional magnetic specimens. Apart from this, it is experimentally shown that *all the critical exponents* required to characterize a FM phase transition can be determined using linear and non-linear low-field susceptibility alone in conjunction with the relevant scaling equations. Finally, a brief account of a study on a weakened *charge-ordered* system and *electronic phase separation* using linear as well as non-linear ac-susceptibility is given in

the Section 4 of this article to elucidate the relevance of this technique in investigating systems of current interest.

2. PROBING SPIN GLASS AND SUPERPARAMAGNETIC SYSTEMS

Both SG and SPM systems exhibit qualitatively similar features in the first order susceptibility, i.e., a sharp peak in χ_1 which is frequency dependent[5]. Added to this, the third order susceptibility χ_3 is theoretically expected to show a negative peak as a function of temperature in both the systems. In a situation like this, when both χ_1 and χ_3 show exactly similar temperature dependence around T_G or T_B for a SG and SPM phase respectively, a detailed study of their corresponding field and frequency dependence of χ_1 and χ_3 can provide the missing link as guided by theories and earlier experiments [2,6-12]. A pioneering work addressing this issue has been taken up for $Au_{96}Fe_4$ system known to be a spin glass and $Cu_{97}Co_3$, which is a conventional SPM. This work explores the subtle differences in the nature of χ_3 to differentiate SPM from the SG phase, the details of which can be found in Ref.[4] and also in references therein.

Here we elaborate on this issue using some experimental results obtained on a series of polycrystalline AFM sample, which, on dilution has shown typical signatures of metastability in bulk magnetization. The samples in this particular series of compounds are neither from a family of a canonical spin glass nor a tailor made SPM and hence our purpose is to illustrate that how χ_3 can be effectively used to identify the underlying magnetic phase in this series of compounds, $Li_xNi_{1-x}O$.

2.1. METASTABLE MAGNETISM IN Li-Ni-O

Pure NiO is a well known antiferromagnetic insulator and Li was substituted to tune the band gap accordingly to change the conductivity properties. This substitution not only generated a series of compounds with interesting physical properties but also generated a technologically important material for use as an insertion electrode in Li batteries. The systematic study of the structure and the magnetic phases of $Li_xNi_{1-x}O$ over the whole composition range was initiated many decades ago by Goodenough et.al. [13]. Since then a variety of magnetic orders have been proposed for different composition ranges of this series [14-18] and various aspects related to the origin of the magnetic ordering of this system is being debated even in the recent times [19,20]. In this section a systematic study of the magnetic phases around two important compositions i.e. x = 0.35 and 0.5 is presented to demonstrate how the long standing controversies related to the magnetic phases are resolved through the measurement of low-field linear (χ_1) and non-linear (χ_n) ac-susceptibilities [21-23]. The details about sample preparation and structural characterization can be found in reference [21]. Since high magnetic fields can smear the transition and mask the intrinsic signatures of the magnetic system, only low field dc-magnetization and ac-susceptibility measurements were performed to characterize this magnetic system using home made set-ups [24,25].

Figure 1 shows the real part of first-order ac-susceptibility (χ_1^r) for x = 0.35 sample of the $Li_xNi_{1-x}O$ series as measured at different frequencies of the exciting ac-field depicting the probe time effect on the magnetic transition. Inset of the same figure shows the bifurcation of zero-field-cooled (ZFC) and field-cooled (FC) dc-susceptibilities below the transition for this sample indicating the dependence on the field history of the measurement.

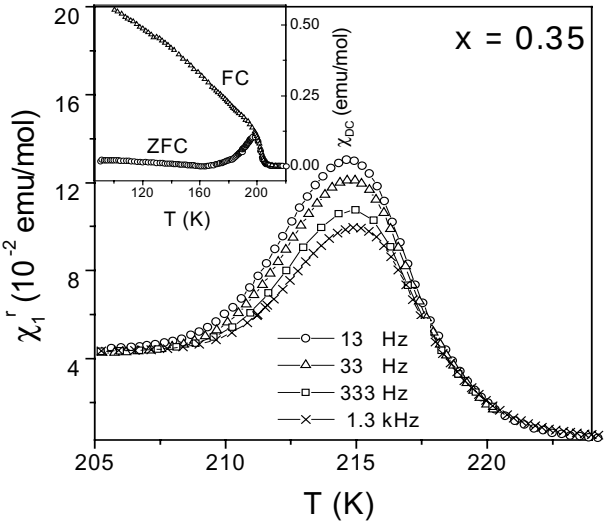

Fig 1. Temperature dependence of χ_1^r for the $Li_xNi_{1-x}O$ sample with x = 0.35 at the Field 1 Oe and in different frequencies. Inset shows FC and ZFC dc-susceptibility for x = 0.35 measured at 20 Oe

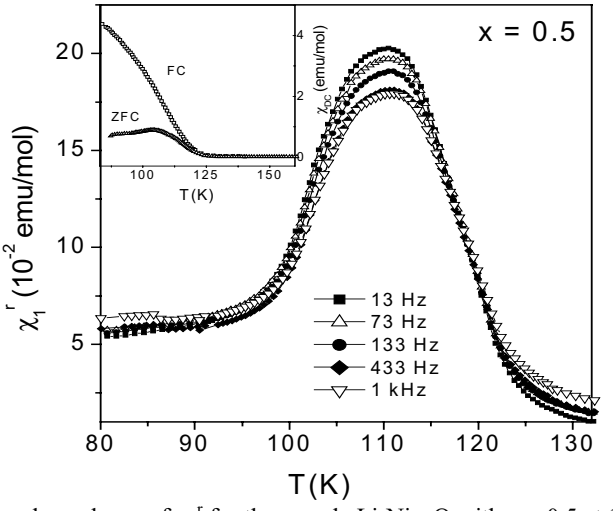

Fig 2. Frequency dependence of χ_1^r for the sample $Li_xNi_{1-x}O$ with x = 0.5 at 1 Oe. Inset shows FC and ZFC dc-susceptibility for x = 0.5 measured at 20 Oe

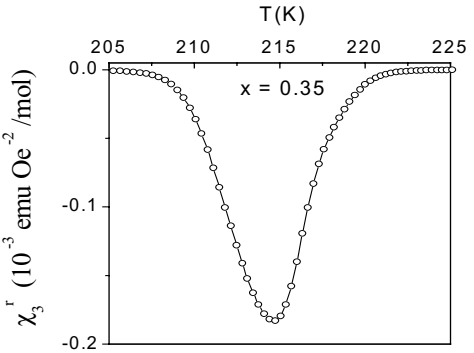

Fig 3. The negative peak in the real part of the χ_3^r as a function of temperature for the sample with x = 0.35.

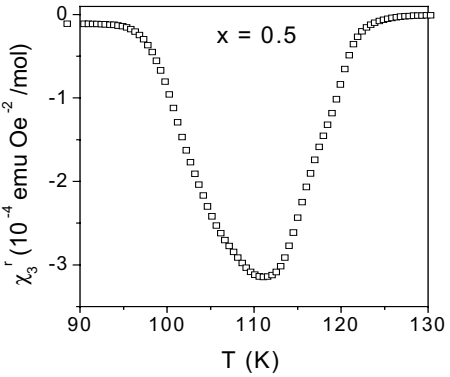

Fig 4. The negative peak in the real part of the χ_3^r as a function of temperature with x = 0.5

The frequency dependence of ac-χ for x = 0.5 sample is shown in Figure 2 and the inset of this figure shows the history dependence of dc-susceptibility for the same sample. Thus samples of both the compositions have shown time and history dependent magnetization which are generic features of magnetically disordered systems showing metastable magnetism like SG, cluster-glasses, SPM and even inhomogeneous ferromagnets [2,5]. We show that in such cases, the third order susceptibility χ_3 can be used as a probe to discern the cause of metastability, guided by theories and earlier experiments [2, 6-12].

The third-order ac-susceptibility (χ_3) for the x = 0.35 and 0.5 samples are shown in figures 3 and 4. Both of them show qualitatively similar pronounced negative peaks at temperatures where χ_1 has shown peak for the respective samples (figures 1-2). Since both systems like SG or SPM are expected to show negative peak in χ_3 around the transition, it becomes non-trivial to identify the exact nature of magnetic transitions in these two samples only on the basis of qualitative features of χ_3.

However, a detailed analysis of χ_3 can unambiguously indicate the true nature of these transitions. It is well known theoretically, that for SG systems, χ_3 is expected to have a negative divergence at the glass transition temperature (T_G) as the amplitude of the measuring ac-field (H) and the frequency of the ac-field (f) tend to zero [6]. Further, it is also shown that the divergence of χ_3 as the spin-glass transition is approached from the high temperature is given by $\chi_3 = \tau\varepsilon^{\gamma_3}$, where ε is the reduced temperature $(T-T_G)/T_G$, γ_3 is the critical exponent and τ is the related critical amplitude. This behavior have been observed experimentally for many SGs; for instance, see reference [8]. Here it should be borne in mind that the f- and H-dependent peak in χ_1 is non-critical for a SG transition.

Contrary to this, since the SPM is understood as a progressive blocking of moments of the magnetic particles or clusters in the experimental timescales it neither shows criticality in χ_1 nor in χ_3 with H, f or T. The linear as well as higher order susceptibility has normal field and temperature dependence for SPM above the Blocking temperature (T_B), that is the temperature at which the peak in susceptibility occurs and Wohlfarth's model can be used to calculate the temperature dependence of χ_1 and χ_3 [4,5, 8]. The total magnetization (M) of a system of non-interacting SPM particles can be given as $M = n\langle\mu\rangle L(\langle\mu\rangle H/k_BT)$, where n is the number of particles per unit volume, $\langle\mu\rangle$ is the average magnetic moment of a single entity (magnetic particle), k_B is the Boltzman constant and L(x) is the Langevin function. The linear and non-linear susceptibilities above T_B can thus be calculated to be $\chi_1 = n\langle\mu\rangle/3k_BT$ and $\chi_3 = -(n\langle\mu\rangle/45)(\langle\mu\rangle/3k_BT)^3$. Thus χ_1 shows a 1/T dependence and χ_3 shows a $-1/T^3$ dependence.

Figure 5 and 6 show the results of the H and f dependence of the peak value of χ_3 for samples with x = 0.35. The measured $|\chi_3^{max}|$ for sample with x = 0.35 clearly indicates a diverging behaviour of χ_3 in the limit $H\rightarrow 0$, $f \rightarrow 0$ at $T = T_G$.

It is to be noted that χ_1 does not show such diverging behavior with H as is shown in ref. [21] The diverging behaviour of χ_3 is further substantiated in the figures 7 and 8 where the log-log plots of $|\chi_3^{max}|$ against H or f follows straight lines.

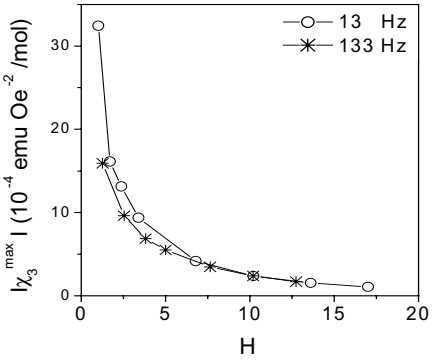

Fig 5. $|\chi_3(r)^{max}|$ Vs. applied ac field for the sample x = 0.35 measured at frequency 13 and 133 Hz.

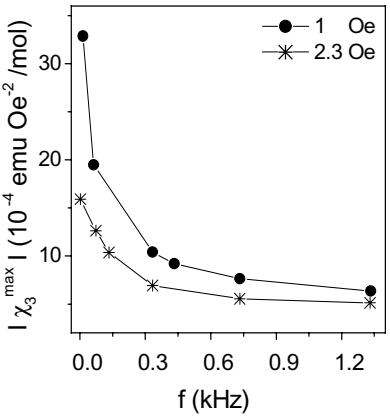

Fig 6. $|\chi_3(r)^{max}|$ Vs. frequency for the sample x = 0.35 measured at ac field of 1 and2.3 Oe.

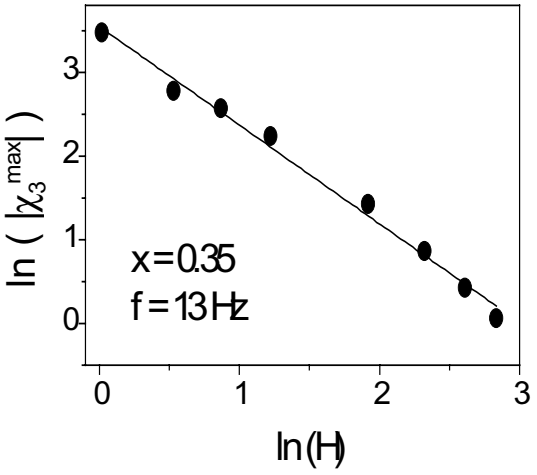

Fig 7. A log-log plot of $|\chi_3^{max}|$ against ac field for the sample x = 0.35

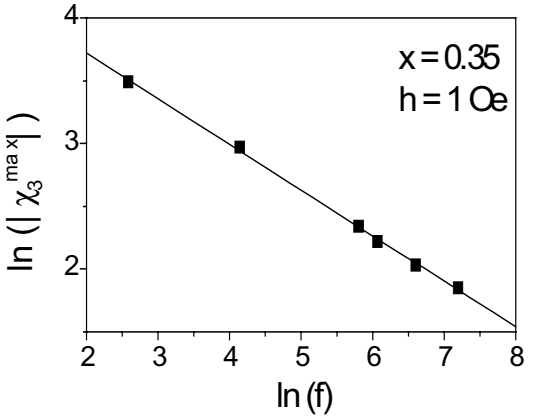

Fig 8. A log-log plot of $|\chi_3^{max}|$ against frequency for the sample x = 0.35

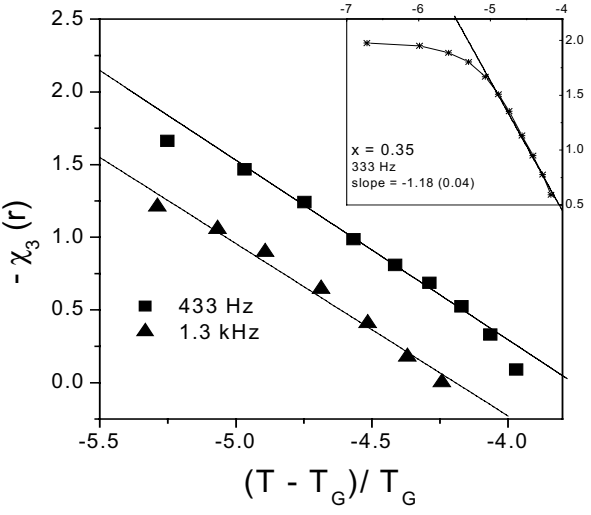

Fig 9. Log-Log plot of χ_3 against reduced temperature $\varepsilon = (T-T_G)/T_G$ for x = 0.35 sample at frequency 433 Hz and 1.3 kHz. Inset shows the same at 333 Hz

Finally, the criticality of χ_3 as a function of temperature is illustrated in the figure 9, where a log-log plot for χ_3 against the reduced temperature $(T-T_G)/T_G$ is shown. From this plot, it is found that the critical exponent associated with χ_3 is close to that of the random-bond Ising spin-glass ($\gamma_3 = 1.18 \pm 0.04$). This analysis of the χ_3 data shows that the low temperature magnetic phase of the x = 0.35 sample can be unambiguously concluded to be a spin-glass like.

In a complete contrast to this, when similar measurements were repeated for the x = 0.5 sample no such criticality in χ_3 could be found as is shown in figures 10 and 11.

Moreover, the variation of $|\chi_3^{max}|$ with H or f is much smaller than what is found for the sample with x = 0.35 in figures 5 and 6. Thus χ_3 does not become critical in the limit $H \rightarrow 0$, $f \rightarrow 0$ for x = 0.5 sample. More significantly, it is shown in figure 12 that χ_3 has a T^{-3} dependence as predicted by the Wohlfarth's model for superparamagnetic particles. It needs to be mentioned here that χ_1 follows a 1/T dependence as described earlier.

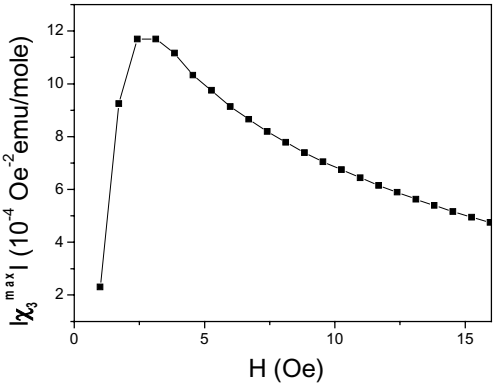

Fig 10. $|\chi_3(r)^{max}|$ Vs. ac field for the sample x = 0.5.

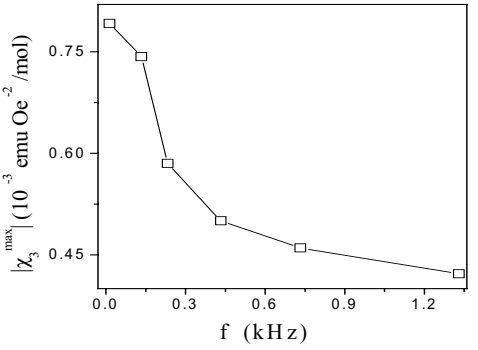

Fig 11. $|\chi_3(r)^{max}|$ Vs. frequency for the sample x = 0.5 measured at ac field of 2.26 Oe.

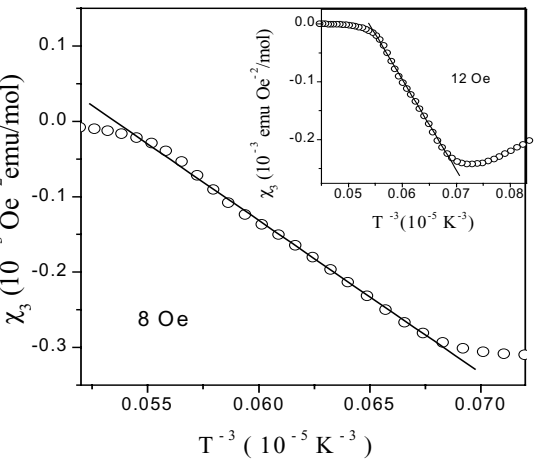

Fig 12. T^{-3} dependence of of χ_3 above the blocking temperature for the sample x = 0.5 measured at 8 Oe. Inset shows the same for 12 Oe field.

Hence, it can be concluded from the preceding analysis that the magnetic transition observed for the sample with x = 0.5 arises from the thermal blocking of the superparamagnetic particles contrary to the spin-glass like freezing observed in the sample with x = 0.35 [21-23].

3. PROBING LONG RANGE ORDERING

A universality class based on the dimensionality of the magnetic lattice and the order-parameter is assigned to a system depending on the values of the critical exponents which characterize the phase transition [26,27]. Hence, to develop a proper understanding about the long-range ordered state it is essential that the critical exponents associated with the phase transition are precisely determined. Conventionally, exhaustive measurements of both low-field ac-susceptibility and high field dc-magnetization are needed to obtain the relevant critical exponents required for the complete characterization of the paramagnetic to ferromagnetic phase transition [27,28]. Considering the fact that ideal second-order paramagnetic to ferromagnetic phase transition is defined in the zero external field, a large applied field is likely to smear the true critical behaviours apart from introducing field-induced effects in many systems thus making low field susceptibility measurements advantageous. Moreover, the Kouvel-Fisher (K-F) analysis of the ac-susceptibility data is a well established method to independently determine both the transition temperature (T_C) as well as the susceptibility exponent γ [29]. Thus, it is not surprising that the conventional second-order paramagnetic to ferromagnetic phase transition has been extensively studied

using linear susceptibility measurements to characterize the nature of the transition for a variety of systems [27,28].

In spite of the fact that non-linear effects become more pronounced in the vicinity of a phase transition the behaviour of the higher-order susceptibilities across conventional phase transitions has remained relatively less explored. This is primarily because of the fact that the non-linear susceptibilities are usually a couple of orders smaller in magnitude than their linear counterparts, thus making it more difficult to measure. Apart from this, the theoretical understanding about the non-linear susceptibilities is far from being satisfactory as far as these magnetic systems are concerned, though treatments of the critical regimes based on the simple mean field models [30] as well as more complicated Sherrington-Kirkpatric [31], Bethe approximation models [32] exist. However, there are a few experimental studies of the third ordered susceptibility (χ_3) on ferromagnetic systems [30,33,34] which though predominantly qualitative in nature have included attempts on characterizing these transitions by the determination of the critical exponents. Recently, a study has been made to understand the hysteresis effect in ferromagnet through the measurement of non-linear susceptibilities [35].

Measurements of the non linear susceptibility in antiferromagnetically ordered systems are even rarer as compared to that reported in ferromagnets and these investigations have relied on indirect measurement techniques like the magneto-optical Faraday Rotation to characterize the magnetic phase transition [36,37]. Besides these conventional long range order spin transitions, χ_3 has also been used in studying quadrapolar interactions in some rare earth intermetallic compounds [38] and to probe the presence [39] or absence [40] of these multispin correlation functions in some heavy Fermion systems. The ferromagnetic order is accompanied with internal field which acts like a symmetry-breaking field and gives rise to the second-order susceptibility (χ_2). This aspect has been exploited to investigate the coexistence of ferromagnetic order and spin-glass phase in the system $(NiFe)_{25}Au_{75}$ [41]. Though underutilized till date, χ_2 is a promising tool for discerning the presence and dynamics of mixed phase systems, like transition metal oxides, where such a mixed phase can arise due to electronic phase separation.

In this section, a calculation based on the molecular-field approach [30] is presented to show the true nature of criticality of χ_3 across a paramagnet to ferromagnetic phase transition. This is substantiated by the detailed measurement of linear as well as nonlinear susceptibilities on a series of amorphous ferromagnetic samples [42].

3.1 THEORY

When an external field H is applied to a collection of 'n' particles, the net magnetic moment is given by

$$m = n\mu\tanh\left[\frac{\mu H}{kT}\right] \tag{2}$$

where μ is the Bohr's Magneton and k is the Boltzmann constant. The total magnetic field which the dipoles experience is given by $H = H + \lambda M$. Where λ is the molecular-field constant and the magnetization (M) can now be written as

$$M = N\mu\tanh\frac{\mu}{kT}(H + \lambda M) \tag{3}$$

where N is the particle density (N = n/V).

Now, for temperature above the ferromagnetic transition temperature (T_C) i.e. in the paramagnetic region M has inversion symmetry with respect to the applied field H, hence the magnetization can be written as

$$M = \chi_1 H + \chi_3 H^3 + \chi_5 H^5 + \ldots. \tag{4}$$

Substituting this in equation (3),

$$\chi_1 H + \chi_3 H^3 = N\mu \tanh \frac{\mu}{kT}(H + \lambda[\chi_1 H + \chi_3 H^3 + \ldots\ldots]) \tag{5}$$

Using the expansion $\tanh(x) = x - \frac{1}{3}x^2$ and using the expression for T_C from the mean-field theory i.e. $kT_C = N\mu^2\lambda$; and comparing the coefficients of H, H^3 etc.

$$\chi_1 = \frac{N\mu^2}{kT_c} \frac{1}{\left(\frac{T}{T_c} - 1\right)} \tag{6}$$

$$\chi_3 = -\frac{N\mu^4}{3k^3T^3} \frac{T}{T_c} \frac{1}{\left(\frac{T}{T_c} - 1\right)^4} \tag{7}$$

It is clear from equations (6) and (7) that as the T_C is approached from the high temperature side, that is in the limit of $T \rightarrow T_C^+$, χ_1 has a positive divergence, whereas χ_3 is expected to show a negative divergence.

Now, for temperature below the ferromagnetic transition temperature (T_C) i.e. for $T < T_C$, because of the presence of spontaneous magnetization, M does not have the inversion symmetry with respect to the applied field H, hence the magnetization can be written as

$$M = M_0 + \chi_1 H + \chi_2 H^2 + \chi_3 H^3 + \ldots. \tag{8}$$

where M_0 is the spontaneous magnetization. Substituting equation (8) in the equation (3),

$$M = N\mu \tanh\{\frac{\mu}{kT}[\lambda M_o + (\lambda\chi_1 + 1)H + \lambda\chi_2 H^2 + \lambda\chi_3 H^3]\} \tag{9}$$

Expanding tanh(x) and comparing the coefficients of different powers of H, we get

$$M_0 = N\mu\left[\frac{\mu\lambda M_0}{kT} - \frac{1}{3}\frac{\mu^3\lambda^3 M_0^3}{k^3T^3}\right] \tag{10}$$

$$\chi_1 = \frac{N\mu^2}{kT_c} \frac{\left[1 - \left(\frac{T_c}{T}\right)^2\left(\frac{M_0}{N\mu}\right)^2\right]}{\left[\frac{T}{T_c} - \left(1 - \left(\frac{T_c}{T}\right)^2\left(\frac{M_0}{N\mu}\right)^2\right)\right]} \tag{11}$$

$$\chi_2 = - \frac{kT_c M_0 \chi_1^3}{N^3 \mu^4} \frac{1}{\left[1-\left(\frac{T_c}{T}\right)^2\left(\frac{M_0}{N\mu}\right)^2\right]^3} \tag{12}$$

$$\chi_3 = \frac{\chi_1^4}{\left[1-\left(\frac{T}{T_c}\right)^2\left(\frac{M_0}{N\mu}\right)^2\right]^4}\left(\frac{\lambda}{(N^2\mu^2)}\right)\left[2\frac{\lambda T_c}{T}\frac{M_0^2}{(N\mu^2)}\frac{\chi_1}{\left[1-\left(\frac{T_c}{T}\right)^2\left(\frac{M_0}{N\mu}\right)^2\right]} - \frac{1}{3}\frac{T}{T_c}\right] \tag{13}$$

Equation (10) is solved for the spontaneous magnetization and yield for $T < T_C$

$$\left(\frac{M_0}{N\mu}\right)^2 = 3\left(\frac{T}{T_c}\right)^2\left(1-\frac{T}{T_c}\right) \tag{14}$$

Substituting this value of $(M_0/N\mu)^2$ in the value of χ_1 and simplifying,

$$\chi_1 = \frac{N\mu^2}{2kT_c}\frac{\left[3\frac{T}{T_c}-2\right]}{\left[1-\frac{T}{T_c}\right]} \tag{15}$$

Hence it is clear that χ_1 diverges in the positive side as T_C is approached from the low temperature side, that is in the limit of $T \rightarrow T_C^-$.

Now substituting equations (14) and (15) in the equation (13) and simplifying,

$$\chi_3 = \frac{8}{3}\frac{\left(\frac{N\mu^2}{2kT_c}\right)^4}{\left(1-\frac{T}{T_c}\right)^4}\frac{\lambda T}{(N\mu)^2 T_c} \tag{16}$$

where it is obvious that χ_3 also has a positive divergence in the limit $T \rightarrow T_C^-$.

Hence it is clear from the above that for a paramagnetic to ferromagnetic transition χ_3 shows divergence in the negative side in the limit of $T \rightarrow T_C^+$ whereas it shows a divergence in the positive direction in the limit of $T \rightarrow T_C^-$. Thus at T_C, χ_3 would be expected to cross the temperature axis.

3.2 EXPERIMENTS

To experimentally verify the true critical behavior χ_3 as suggested by these calculations, an extensive study of linear and non-linear ac-susceptibility measurements were performed on a well characterized ferromagnetic system so that the advantages of the present study become

obvious. The samples chosen for the present study is from a series of amorphous ferromagnetic metallic glass $Fe_5Co_{50}Ni_{17-X}Cr_XB_{16}Si_{12}$ with x = 5, 10 and 15 referred as A2, A3 and A4 respectively. This series was extensively studied in the past, details of which can be found in the references [43-45].

Figures 13(a), 13(b) and 13(c) show the Kouvel-Fisher plots i.e. $1/\chi_1\ d/dT(\chi_1^{-1})$ versus T for the A2, A3 and A4 samples respectively. The inverse of the slope directly gives the value of the susceptibility exponent γ and the intercept of the straight line on the temperature axis gives the value of T_C. The values of T_C and γ found form this measurement are in reasonable agreement with the values reported earlier as is shown in the Table 1.

Table 1. Values of the susceptibility exponent γ and the transition temperature T_C as determined from the Kouvel-Fisher analysis of the first-order susceptibility. The values determined by the earlier workers are given for comparison.

	A2	A3	A4
T_C (K)	267.44 267 [A]	222.76 222.2 [A]	174.37 174 [B]
γ	1.16±0.0008 1.19 [A]	1.388±0.01 1.38 [A]	1.41±0.01 1.73 [B]

[A] Values determined in the reference [43] using ac-susceptibility measurements.

[B] Values determined in the reference [43] using high field dc-magnetization.

It is clear from the mean field calculation given earlier that χ_3 is expected to diverge on both sides of phase transition and change sign at T_C. However, this critical behavior is not easy to observe primarily because the expansion of M in terms of higher powers of H, which was used for the calculation is strictly valid for small values of H. Hence, to observe true critical behavior, measurements have to be done at very low fields, and higher fields tend to smear the transition . It is difficult to predict a priori the fields at which this critical behavior will be seen, as it depends on the extent of non-linearity in the system and thus varies from sample to sample. It is also to be noted that at higher measuring fields, the contributions from domains can become dominant and mask the true critical behavior of the spin system.

Careful low-field measurements have shown the predicted critical behaviour in χ_3 for this series of amorphous ferromagnets. Figures 14(a), 14(b) and 14(c) show the critical behaviour for the A2, A3 and A4 samples respectively. It can be clearly seen from the figure 14 that χ_3 changes sign across T_C and the exact T_C can be directly determined from the crossover of χ_3 on the temperature axis. These experimental T_C values are given in Table 2. It is to be noted that T_C determined from the crossover of χ_3 matches well with those determined from the Kouvel-Fischer analysis (Table 1). This matching of T_C from two different measurements not only substantiates the fact that the measured χ_3 is a genuine response of the spin system but also the crossover of χ_3 can be used as a direct method to determine T_C .

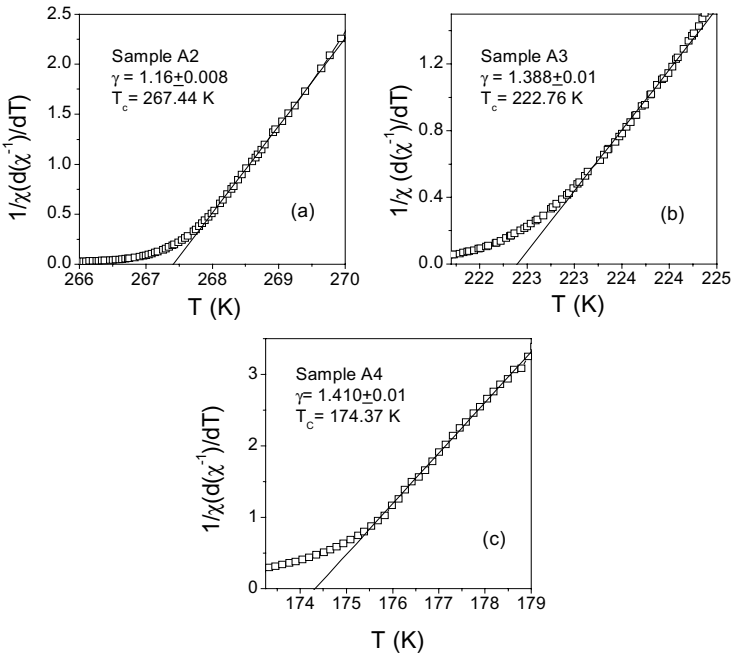

Fig. 13. Kouvel-Fisher plots of the first order susceptibility for the samples A2, A3 and A4. The value of the γ and T_C as determined from the plots are given in the respective graphs.

It can be seen in Figure 14(a) that the A2 sample shows a double transition accompanied by two crossovers. This sample has gives an uncharacteristically low value for susceptibility exponent γ, a fact observed by earlier workers as well. Considering the fact that this sample has the largest percentage of Ni and is close to the critical concentration, this double transition could be arising from the clusters with a distribution of T_Cs, which is common for this class of materials. However, it is interesting to note that no direct evidence of such a distribution is evident from the linear susceptibility measurements. This only goes on to show that low-field nonlinear susceptibility is more sensitive tool than the linear susceptibility, as far as studies of spin systems near the transition is concerned.

As mentioned earlier, the field in which the measurement is performed is an important consideration in the study of criticality in χ_3. This can be clearly seen in figure 15, which shows the field dependence of χ_3 for the A3 sample at measuring frequency of 133.33 Hz. It is clear that the critical feature is sharpest at the lowest measuring field and increasing the measuring field tend to wipes off this critical behavior indicating that larger applied fields destabilizes the system from its equilibrium ground state.

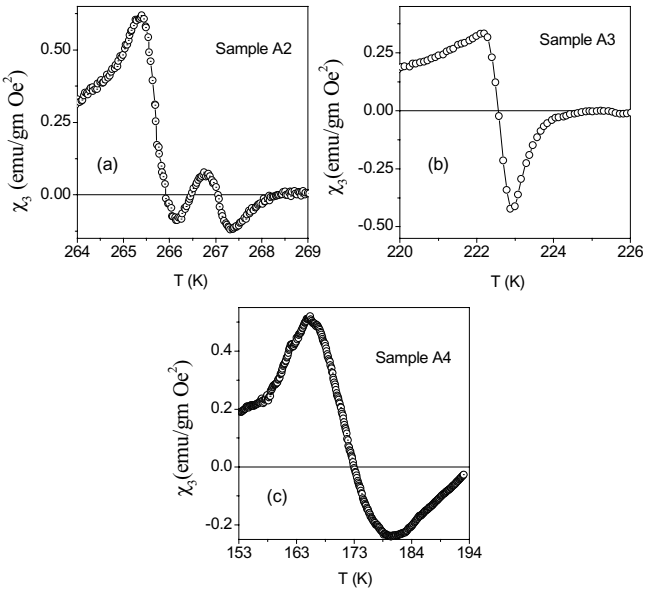

Fig. 14. The critical feature of χ_3 as observed in the third-order ac-susceptibility for A2, A3 and A4 samples. The measurements were done at frequency 133.33 Hz and exciting field of 200 mOe.

Accurate determination of the transition temperature (T_C) is an important consideration in the study of critical behavior across the ferromagnetic phase transition. The most popular techniques used for this purpose are Kouvel-Fischer plot or Arrot's plot [46]. However, in both these techniques the T_C is determined from the fitted data. Apart from this, the Arrot's plot is made from the high field measurements which is associated with the complications related to high field measurements used to probe the critical regime as mentioned earlier [47].

An attempt is made here to show how the crossover in χ_3 on the temperature axis can be used to directly as well as accurately determine the T_C in the limit of $H \rightarrow 0$. Figure 16 shows the variation of the crossover temperature of the χ_3 with the applied field.

The critical exponent associated with the third-order susceptibility, γ_3, is determined from the slope of the straight line in the double-logarithmic plot of $(-3/4)\chi_3 H^2$ versus ε, where $\varepsilon = [(T-T_C)/T_C]$ and the value of T_C is taken from crossover point χ_3 on the temperature axis as mentioned earlier. Figures 17(a), 17(b) and 17(c) show these plots for A2, A3 and A4 samples respectively as $T \rightarrow T_C^+$. The exponents γ_3 determined from these plots for A2, A3 and A4 samples turns out to be 4.57, 4.80 and 5.04 respectively which match well with the 3D Heisenberg value of 4.88. A deviation from the straight-line can be seen as T approaches T_C.

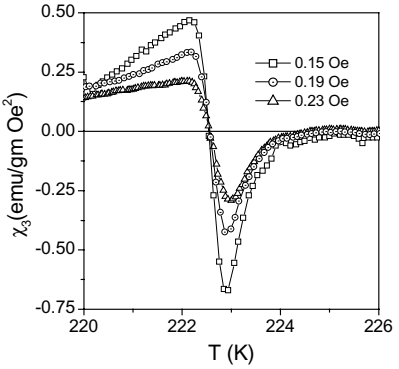

Fig. 15. The field dependence of χ_3 for the A3 sample measured at frequency of 133.33 Hz. It is clear that the critical behaviour is suppressed with applied field.

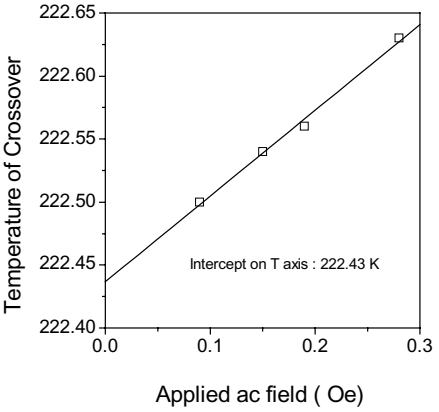

Fig. 16. The temperature of the crossover T_C as a function of measuring ac-field for the A3 sample. A linear behaviour is observed and the interpolation to zero field provides the unique way to determine the true transition temperature.

These curvatures in the plots close to T_C arise mainly due to the dominating presence of higher-order terms close to the transition temperature apart from the inhomogeneities present in the samples.

Thus from the measurements of low-field linear and non-linear ac-susceptibilities the exponents γ and γ_3 for this series of samples are determined. The other critical exponents α, β, δ and Δ associated with specific heat, spontaneous magnetization, field dependence of magnetization at T_C and gap exponent respectively needed for the complete characterization of the phase transition can be calculated using the following scaling relations

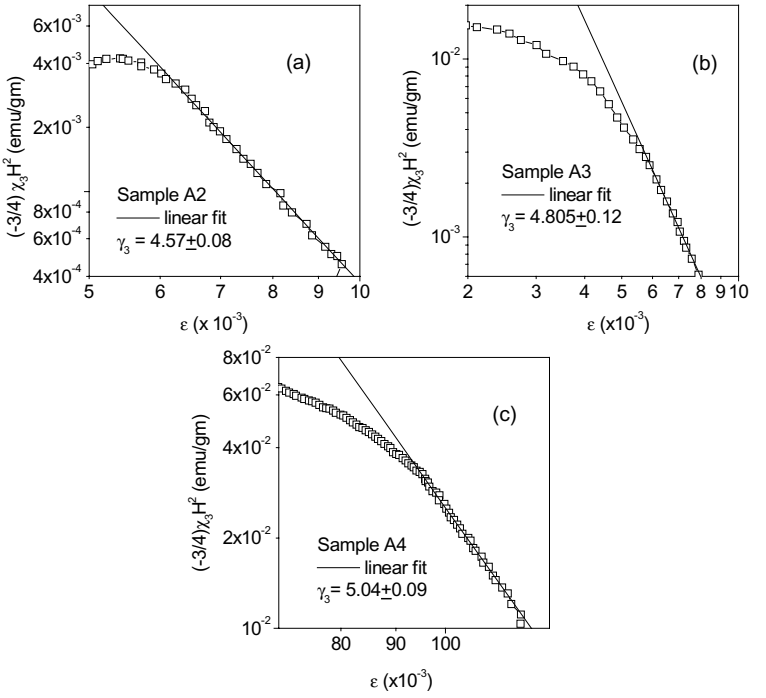

Fig. 17. Double-logarithmic plots of χ_3 versus reduced temperature (ε) for the A2, A3 and A4 samples. The slopes of the straight lines give the value of the exponent γ_3 for the respective samples.

$$\gamma_3^{+} = \gamma + 2\Delta,$$

$$\Delta = \gamma + \beta,$$

$$\delta = 1 + \gamma/\beta,$$

$$\text{and } \alpha + 2\beta + \gamma = 2 .$$

All the exponents required for a complete characterization of this series is calculated and given in Table 2.

It can be clearly seen that the values determined in the present study mach reasonably well with those given in reference [43]. The only exponent in which a large difference is seen is α which is calculated by using Rushbrooke equality $\alpha + 2\beta + \gamma = 2$. The ambiguity in the value of this exponent is probably because the values determined in the reference [43] from the combination of both low ac-field and high dc-field measurements, as is the general practice. Whereas in the present case they are all determined from the low-field measurements alone.

Table 2. Values of all the critical exponents as determined from the linear and non-linear ac-susceptibility measurements and calculated using scaling relations. T_C (χ_3) are the value of transition temperatures determined from the crossover of χ_3 in the temperature axis. The values quoted from the previous work for comparison.

	A2	A3	A4
γ	1.16±0.0008 1.19 [A]	1.388±0.01 1.38 [A]	1.41±0.01
γ_3	4.57 ± 0.08	4.805 ± 0.12	5.04 ± 0.09
Δ	1.705	1.708	1.815
β	0.545 0.35[A]	0.32 0.41[A]	0.405 0.52[A]
α	-0.25 0.2[A]	0.03 -0.2[A]	-0.22 -0.7[A]
δ	3.12 4.42[A]	5.33 4.49[A]	4.48 4.32[A]
T_C (χ_3)	267.05	222.55	173.45

[A] Values determined in the reference [43] .

Hence, the following advantages of the low-field linear and non-linear susceptibilities as an effective probe to study the paramagnetic to ferromagnetic phase transition is unambiguously demonstrated :

(i) Determination all the relevant critical exponents needed to characterize the magnetic phase transition only from the low-field linear and non linear susceptibility measurements.

(ii) Directly ascertain the T_C and accurately determine the zero-field T_C, which otherwise has to be estimated from extrapolation of high field data.

(iii) Detecting subtle features not seen in the linear susceptibility measurements.

4. INVESTIGATING WEAKENED CHARGE ORDERED STATE AND ELECTRONIC PHASE SEPARATION

A study on the so called 'glassy' behaviour in weakened *charge-ordered* state and the phenomenon of *electronic phase separation* is presented in this section to show how low-field linear as well as non-linear susceptibility measurements culminate as valuable probe for interesting magnetic systems. Hole doped manganites systems have attracted enormous attention in the recent time because they have displayed many interesting phenomenon like *colossal-magnetoresistance*, *charge-ordering*, *electronic phase separation* etc [48-50]. Manganites with hole concentration close to 50% have an important role and are being extensively studied since the Coulombic repulsive forces are known to stabilize the formation of charge and orbital ordered antiferromagnetic ground state in these systems. A variety of relaxation effects possibly arising out of phase competition are observed around this compositions, but whether these 'glassy' phases mimic the canonical spin-glasses or whether electronic phase separation leads to a new form of '*glassiness*' remains to be understood.

In order to understand these, a half doped charge-ordered system, $Pr_{05}Ca_{0.5}MnO_3$ which is known to be a narrow bandwidth system with robust charge-ordering is selected for this study. Mn site substitution in the half doped charge ordered manganites has emerged as a popular means to comprehend the charge ordering and the concomitant antiferromagnetism. It is now well known that Mn site substitution affects the magnetism by tailoring the strength of the magnetic exchange and also induces various interesting phases in this class of materials [51-55]. Though many magnetically metastable phases are observed at low temperatures in the Mn site substituted weakened charge ordered state, the exact nature of the ground state remains to be properly understood. It is important that the Mn site substitution should not lead to the significant change in the structure or add any magnetic interaction to the parent compound. Hence, non-magnetic Al is chosen for Mn site substitution since its ionic radius match very well with that of Mn^{4+} present in the system. It has been shown from the detailed analysis of the structure that Al substitution in $Pr_{0.5}Ca_{0.5}MnO_3$ up to 10% of Al does not have any significant effect on the structure [56]. Further, it is shown that in $Pr_{0.5}Ca_{0.5}Mn_{1-X}Al_XO_3$ the strength of charge ordering progressively decrease with the increase in Al. In an attempt to understand the evolution of magnetic phases in weakened charge ordered system with quenched non-magnetic impurities, a detailed study is made on the $Pr_{0.5}Ca_{0.5}Mn_{0.975}Al_{0.025}O_3$ compound using linear as well as nonlinear susceptibilities and dc-magnetization. Since large fields can mask the intrinsic signatures of inhomogeneously magnetized systems, the low-field measurements are made to discern the magnetic ground state as shown in the figure 18. The inset of Figure 18 shows the weakening of charge ordering on Al substitution in $Pr_{0.5}Ca_{0.5}MnO_3$ which otherwise shows a sharp peak around 240K arising from the charge ordering. On 2.5% Al substitution this peak gets broadened and shifts to lower temperature indicating the weakening of charge ordering. It is known that the parent $Pr_{0.5}Ca_{0.5}MnO_3$ has an antiferromagetic order below about 175K. Though the signature of this antiferromagnetic transition is not seen in the inset of figure 18, it is detected from the magnetocaloric effect determined from the dc-magnetization measurement [56]. Figure 18 shows that the dilution of magnetic lattice by 2.5% Al substitution causes the long-range antiferromagnetic transition temperature (T_N) to drop to about 50K. Interestingly, an additional feature is observed at lower temperature as evident by a cusp in the zero field cooled (ZFC) dc-magnetization at

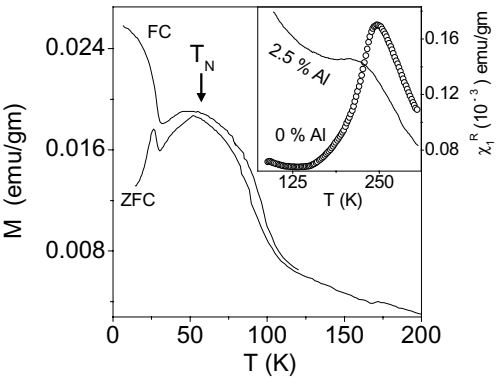

Fig. 18. ZFC and FC dc-magnetization of the $Pr_{0.5}Ca_{0.5}Mn_{0.975}Al_{0.025}O_3$ at a measuring field of 100 Oe. The inset shows the first-order ac-susceptibility at measuring field of 12.5 Oe and frequency of 133 Hz for $Pr_{0.5}Ca_{0.5}MnO_3$ and $Pr_{0.5}Ca_{0.5}Mn_{0.975}Al_{0.025}O_3$ samples.

26K. Moreover, a strong irreversibility or history dependence is observed as indicated by the large bifurcation in the ZFC and field cooled (FC) magnetization measurement. Ac-susceptibility measurement has also shown this sharp feature at 26K which was accompanied with signatures of metastable magnetization. In the absence of any observable χ_2 arising from the internal fields of the system, this low temperature metastable magnetic phase can be attributed to either spin-glass/cluster-glass or superparamagnetic phases present in the system. However, as mentioned in the section 2, the physical processes which give rise to such cusp in susceptibility and metastable magnetization for these diverse classes of systems is entirely different.

As mentioned in the preceding parts of this article, for the spin-glasses or cluster-glasses, it is the co-operative *freezing* of the 'frustrated' spins or clusters of spins, arising from the competing ferromagnetic and antiferromagnetic interactions, which give rise to the history and time dependent metastable magnetism in the systems. Whereas, in superparamagnets, it is a purely a dynamic phenomenon arising from the *thermal blocking* of the magnetization of the individual spin clusters in their easy directions decided by the anisotropies of the respective clusters/entity, which is responsible for the cusp in ZFC dc-magnetizaion or in ac-susceptibility.

To identify the origin of the cusp observed at 26 K and to ascertain the nature of the magnetic ground state of the $Pr_{0.5}Ca_{0.5}Mn_{0.975}Al_{0.025}O_3$ sample, a detailed study of the non-linear ac-susceptibility was undertaken. The χ_3 shows a negative peak at the same temperature (T_P) where a cusp is seen in χ_1 (not shown here). Hence it needs to be verified whether this peak is critical in the limits of $H \rightarrow 0$ and $T \rightarrow T_P$ indicating the divergence of the Edwards-Anderson order-parameter which in turn signify the *freezing* of spins or spin-clusters leading to a spin-glass like transition or it is non-critical as a function of H and T indicating

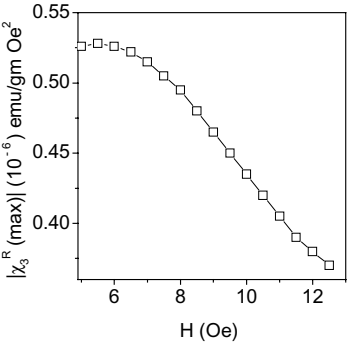

Fig. 19. The peak value of χ_3 plotted as a function of applied ac field H for $Pr_{0.5}Ca_{0.5}Mn_{0.975}Al_{0.025}O_3$ sample, clearly indicate that χ_3 is not critical with H.

superparamagnet like *blocking* of clusters of spins. This is vividly demonstrated by plotting the peak value of χ_3 as a function of H. This is shown in figure 19, where the value of the real part of χ_3 at the negative peak denoted by $|\chi_3^{R(max)}|$ is plotted as a function of H for $Pr_{0.5}Ca_{0.5}Mn_{0.975}Al_{0.025}O_3$ sample. Here, χ_3 is clearly seen to saturate in the limit $H \rightarrow 0$, indicating that the low temperature phase occurs due to the thermal blocking of magnetic entities and is not a co-operative freezing phenomenon. To reconfirm this, the temperature dependence of χ_3 above T_P is analyzed in the similar fashion as it is done in section 2 for $Li_XNi_{1-X}O$ series of samples.

Figure 20 shows that the real part of χ_3 has a T^{-3} dependence indicated by the straight line fit above T_P similar to what is observed for superparamagnets. This further substantiates the fact that the low temperature phase observed in $Pr_{0.5}Ca_{0.5}Mn_{0.975}Al_{0.025}O_3$ sample is superparamagnetic in nature contrary to the earlier findings where spin-glass like phase was attributed to analogous systems from the linear susceptibility measurements alone.

Thus it becomes evident that such low temperature metastable magnetic features in the similar systems need to be properly identified through comparative rigorous measurements. Further, it has been shown that it is possible to estimate the average moment associated with the spin clusters or roughly determine their size from the ratio of χ_3/χ_1 using the respective equations for superparamagnetic clusters as given in section 2.

Finally, an exciting aspect of ac-susceptibility measurements and its merits are presented through a straightforward and simple study to detect the occurrence of *electronic phase separation* in $Pr_{0.5}Ca_{0.5}Mn_{0.975}Al_{0.025}O_3$ from the *thermal hysteresis* as shown in figure 21. It is to be noted that ac-susceptibility captures only the dynamic or the reversible part of magnetization unlike the dc-magnetization measurements which measures the total magnetization. Hence no system with static disorder which even exhibit metastable magnetism like spin-glass, cluster-glass or superparamagnets will show the effect of thermal hysteresis in ac susceptibility. The thermal hysteresis in ac-susceptibility can take place only

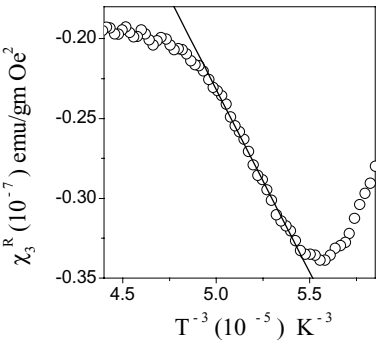

Fig. 20. Temperature variation of χ_3 above T_P for $Pr_{0.5}Ca_{0.5}Mn_{0.975}Al_{0.025}O_3$ sample. The straight line is a T^{-3} fit to χ_3 measured at 12.5 Oe and frequency 133 Hz.

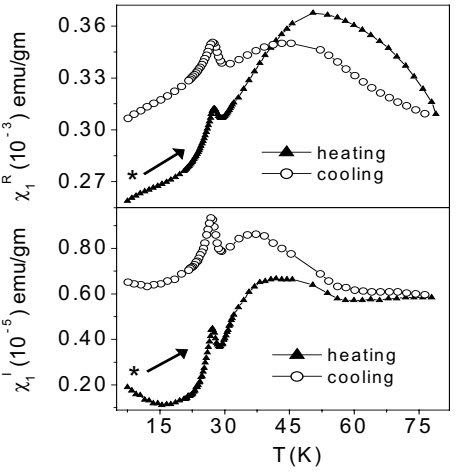

Fig. 21. The upper panel shows the real part of first-order ac-susceptibility as measured at a field of 2.5 Oe and a frequency of 733 Hz for the $Pr_{0.5}Ca_{0.5}Mn_{0.975}Al_{0.025}O_3$ sample in heating and cooling cycles. The lower panel shows the imaginary of the first-order ac-susceptibility part as measured during the same run. The asterisk indicate the beginning of the thermal cycle with the arrow indicating the direction.

when the system changes dynamically with respect to the temperature cycle. In the present case it happens because of electronic phase separation. The upper panel of figure 21 shows the real part of first-order ac-susceptibility (χ_1^R) as measured at a field of 2.5 Oe and a frequency of 733 Hz for the $Pr_{0.5}Ca_{0.5}Mn_{0.975}Al_{0.025}O_3$ sample showing large hysteresis behaviour as a function of thermal cycling. It also shows that there is no observable change in the temperature where the cusp in susceptibility is observed (T_P) which is identified as the blocking temperature of the superparamagnetic clusters indicating that the cluster volume does not change. However, there is significant change in the temperature of the broad feature observed around 50K. This broad feature is also observed in dc-magnetization measurement (figure 18) and is related to the antiferromagetic order of the weakened charge ordered state.

The reduction in the temperature of the peak of this feature in the cooling run indicate that the electronic phase separation reduces the hole concentration from the bulk of the clusters, correspondingly reducing the antiferromagetic transition temperature (T_N). This reduction in the hole concentration of the bulk would enhance its concentration at the respective domain walls without any observable change in the size of the clusters. This is evident from the lower panel of the figure 21 which shows that the imaginary part of the first-order ac-susceptibility (χ_1^I) is consistently higher in the cooling run. Here, it is to be noted that χ_1^I arises from the magnetic loss in the system and an enhanced χ_1^I in the cooling run is presumably arising as a consequence of larger inter-cluster interactions across the hole enriched domain walls. It is important to mention here that there is no observable χ_2 in the system, thus ruling out the presence of any ferromagnetic phase in this state.

Thus a unique scenario of electronic phase separation is presented by probing a system with linear and non-linear susceptibilities alone, where it is shown that in a weakened charge ordered state the electronic phase separation changes the hole concentration of the bulk of the clusters with respect to the domain walls without invoking any ferromagnetic phase which is shown to be invariably present in all other phase separated manganites studied earlier. A detailed quantitative study on the above mentioned system and the related electronic phase separation using linear as well as non-linear susceptibilities is presented in a recent publication [57].

REFERENCES

[1] *Magnetic Susceptibility of Superconductor and Other Spin Systems* (Eds. R. A. Hein, T. L. Francavilla and D. H. Liebenberd) Plenum, New York, (1991); and references therein.

[2] K. Binder and A. P. Young, Rev. Mod. Phys. 58 (1986) 803.

[3] P. A. Joy and S. K. Date, J. Magn. Magn. Mater. 218 (2000) 229.

[4] T. Bitoh, K. Ohba, M. Takamatsu, T.Shirane and S. Chikazawa, J. Phys. Soc. Jpn. 62 (1993) 2583.

[5] J. –L Tholence, *Magnetic Susceptibility of Superconductor and Other Spin Systems* (Eds. R. A. Hein, T. L. Francavilla and D. H. Liebenberd) Plenum, New York, (1991), p. 503.

[6] S. Katsura, Prog. Theor. Phys. 55 (1976) 10049.

[7] E. P. Wohlfarth, Phys. Lett. A 70 (1979) 489.

[8] T. Bitoh, K. Ohba, M. Takamatsu, T. Shirane, and S. Chikazawa, J. Magn. Magn. Mater. 154 (1996) 59.

[9] S. Chikazawa, C. J. Sandberg, and Y. Miyako, J. Phys. Soc. Jpn. 50 (1981) 2884.

[10] T. Bitoh, K. Ohba, M. Takamatsu, T. Shirane and S. Chikazawa, J. Phys. Soc. Jpn. 64 (1995) 1311.

[11] Q. Y. Chen, *Magnetic Susceptibility of Superconductor and Other Spin Systems* (Eds. R. A. Hein, T. L. Francavilla and D. H. Liebenberd) Plenum, New York, (1991), p. 81.

[12] M. Suzuki, Prog. Theor. Phys. 58 (1977) 1151.

[13] J. B. Goodenough, D. G. Wickam, and W. J. Croft, J. Phys. Chem. Solids 5 (1958) 107.

[14] Jan N. Reimers, J. R. Dahn, J. E. Greedan, C. V. Stager, G. Liu, I. Davidson, and U. Von Sacken, J. Solid State Chem. 102 (1993) 8486.

[15] P. Ganguly, V. Ramaswamy, I. S. Mulla, R. F. Shinde, P. P. Bakare, S. Ganpathy, P. R. Rajmohanan, and N. V. K. Prakash, Phys. Rev. B 46 (1992) 11595.

[16] K. Hirakwa, H. Kadowaki, and K. Ubukoshi, J. Phys. Soc. Jpn. 55 (1985) 323.

[17] J. P. Kemp, P. A. Cox, and J. W. Hodby, J. Phys. Condens. Matter 2 (1990) 6699.

[18] P. Kuper, G. Kruizinag, J. Ghijsen, and G. A. Sawatzky, Phys. Rev. Lett. 62 (1989) 221.

[19] F. Reynaud, D. Mertz, F. Celestini, J. –M. Debierre, A. M. Ghorayeb, P. Simon, A. Stepanov, J. Voiron, and C. Delmas, Phys. Rev. Lett. 86 (2001) 3638.

[20] F. Vernay, K. Penc, P. Fazekas, and F. Mila, Phys. Rev. B 70 (2004) 014428.

[21] A. Bajpai and A. Banerjee, Phys. Rev. B 55 (1997) 12439.

[22] A. Bajpai and A. Banerjee, Phys. Rev. B 62 (2000) 8996.

[23] A. Bajpai and A. Banerjee, J. Phys.: Condens. Matter 13 (2001) 637.

[24] A. Bajpai and A. Banerjee, Rev. Sci. Instrum. 68 (1997) 4075.

[25] R. V. Krishnan and A. Banerjee, Rev. Sci. Instrum. 70 (1999) 85.

[26] H. Eugene Stanley, *Introduction to Phase Transitions and Critical Phenomena,* Oxford Science Publication, Oxford, (1971).

[27] S. N. Kaul, J. Magn. Magn. Mater. 53 (1985) 5.
S. N. Kaul, A. Hofmann, and H. Kronmuller, J. Phys. F: Met. Phys. 16 (1986) 365.

[28] Sunil Nair, A. Banerjee, A. V. Narlikar, D. Prabhakaran, and A. T. Boothroyd, Phys. Rev. B 68 (2003) 132404.

[29] J. S. Kouvel and M. Fisher, Phys. Rev. 136 (1964) A1626.
[30] T. Sato and Y. Miyako, J. Phys. Soc. Jpn. 51 (1981) 1394.
[31] K. Wada and H. Takayama, Prog. Theor. Phys. 64 (1980) 327.
[32] S. Fujiki and S. Katsura, Prog. Theor. Phys. 65 (1981) 1130.
[33] T. Bitoh, T. Shirane, and S. Chikazawa, J. Phys. Soc. Jpn. 62 (1993) 2837.
[34] T. Shirane, T. Moriya, T. Bitoh, A. Sawada, H. Aida and S. Chikazawa, J. Phys. Soc. Jpn. 64 (1995) 951.
[35] C. Rüdt, P. J. Jensen, A. Scherz, J. Lindner, P. Poulopoulos, and K. Baberschke, Phys. Rev. B 69 (2004) 014419
[36] U. A. Leitao and W. Kleemann, Europhys. Lett. 5 (1998) 529.
[37] J. Kushhauer and W. Kleemann, J. Phys.: Cond. Matter. 7 (1995) L1.
[38] P. Morin and D. Schmitt, Phys. Rev. B 23 (1981) 5936.
[39] A. P. Ramirez, P. Coleman, P. Chandra, E. Bruck, A. A. Menovsky, Z. Fisk and E. Bucher, Phys. Rev. Lett. 68 (1992) 2680.
[40] A. P. Ramirez, P. Chandra, P. Coleman, Z. Fisk, J. L. Smith and H. R. Ott, Phys. Rev. Lett. 73 (1994) 3018.
[41] A. Chakravarti and R. Ranganathan, Solid State Commun. 82 (1992) 591.
[42] Sunil Nair and A. Banerjee, Phys. Rev. B 68 (2003) 094408.
[43] A. Das and A. K. Majumdar, Phys. Rev. B 47 (1993) 5828.
[44] A. Das and A. K. Majumdar, J. Magn. Magn. Mater. 128 (1993) 47.
[45] A. Das and A. K. Majumdar, Phys. Rev. B 43 (1991) 6042.
[46] Anthony Arrot, Phys. Rev. 108 (1957) 1394.
[47] Amikam Aharony, *Introduction to the Theory of Ferromagnetism,* Clarendon Press, Oxford (1996).
[48] *Colossal Magnetoresistance, Charge Ordering and Related Properties of Manganese Oxides,* edited by C. N. R. Rao and B. Raveau, World Scientific, Singapore (1998).
[49] Y. Tokura, *Colossal Magnetoresistive Oxides*, Gordon and Breach Science Publisher, Singapore (2000).
[50] E. Dagotto, *Nanoscale Phase Separation and Colossal Magnetoresistance*, Springer-Verlag, Berlin (2003).
[51] V. Hardy, A. Maignan, S. Hebert, and C. Martin, Phys. Rev. B 67 (2003) 024401.
A. Maignan, V. Hardy, C. Martin, S. Hebert, and B. Raveau, J. Appl. Phys. 93 (2003) 7361.
[52] T. Kimura, R. Kumai, Y. Okimoto, and Y. Tokura, Phys. Rev. B 62 (2000) 15021.
[53] Joonghoe Dho, W. S. Kim, and N. H. Hur, Phys. Rev. Lett. 89 (2002) 027202.
[54] T. Kimura, Y. Tomioka, R. Kumai, Y. Okimoto, Y. Tokura, Phys. Rev. Lett. 83 (1999) 3940.
[55] R. Mahendiran, A. Maignan, S. Hebert, C. Martin, M. Hervieu, J. F. Mitchell and P. Schiffer, Phys. Rev. Lett. 89 (2002) 2866021.
[56] Sunil Nair and A. Banerjee, cond-mat 039406.
[57] Sunil Nair and A. Banerjee, Phys. Rev. Lett. 93 (2004) 117204.

TRANSMISSION ELECTRON MICROSCOPY STUDY ON MANGANESE OXIDES

T. Asaka[1], T. Nagai[1], K. Kimoto[1,2], and Y. Matsui[1,2]

[1]High Voltage Electron Microscopy Station (HVEMS), National Institute for Materials Science (NIMS), Tsukuba 305-0044, Japan

[2] Advanced Materials Laboratory (AML), National Institute for Materials Science (NIMS), Tsukuba 305-0044, Japan

1. INTRODUCTION

Manganese oxides with perovskite-related structures have been attracting a lot of attention because of their unusual charge-transport and magnetic properties, such as colossal magnetoresistance (CMR) effect [1-4] and charge-ordering phenomena [5-12]. Recent extensive studies have revealed that these features can result not only from the double-exchange (DE) interaction [13,14] but also from other instabilities competitive with the DE interaction, such as the antiferromagnetic (AF) superexchange, Jahn-Teller (JT), charge-orbital ordering interactions, etc. These interactions often strongly couple with the lattice-system through the orbital degree of freedom of the e_g electrons on Mn^{3+} ions in MnO_6 oxtahedra.

A number of studies related to the charge ordering have been performed so far. The charge ordering, in which Mn^{3+} and Mn^{4+} are arranged alternatively, occurs in manganese oxides with a small one-electron bandwidth [5-12]. For example, in $Pr_{1-x}Ca_xMnO_3$, the charge-ordering phase has been observed for a wide range of x ($0.3 \leq x \leq 0.75$) [15,16]. It has been reported that the charge ordering in the system can be melted by the application of magnetic [17-19] or electric fields [20], or by x-ray [21], visible-IR light [22-24], or electron [25] irradiation. Based on the x-dependence of the magnetic field necessary to melt the charge ordering for $x < 1/2$ compounds, Tomioka *et al*. reported that deviation of x from 1/2 changes

the robustness of the charge-ordering state [17,18]. The charge ordering is accompanied by an ordering of e_g orbitals of the $d_{3x^2-r^2}/d_{3y^2-r^2}$ type and the cooperative Jahn-Teller distortion [5-8,26-28]. Here, the *x*, *y*, and *z*-axes were nearly parallel to [110], [$\bar{1}$10], and [001], respectively, in the *P*bnm orthorhombically distorted perovskite. Superlattice reflections found in the diffraction patterns were evidence of orbital ordering.

It is known that the CMR effect and melting transitions in the charge-ordering phase are closely related to the appearance of a ferromagnetic metallic state. Usually, the ferromagnetic metallic state in manganese oxides is described in terms of the double-exchange (DE) mechanism. On the other hand, magnetic domains and domain walls in manganese oxides in the ferromagnetic phase may strongly affect not only the magnetic properties but also the electron-transport properties of these oxides. Recently, Mathur *et al*. reported that the measured resistivity of a magnetic domain wall is considerably higher, by several orders of magnitude, than that expected due to the simple DE mechanism [29]. The scattering of charge carriers by domain walls may be a possible cause of low-temperature magnetoresistance [30-32].

The layerization of the perovskite structure (the so-called Ruddlesden-Popper structure) is very important in terms of control of dimensionality of electronic structure in transition-metal oxides. Figure 1 shows the schematic crystal structures of Ruddlesden-Popper series $(R,A)_{n+1}Mn_nO_{3n+1}$, where *R* and *A* are the trivalent rare-earth and divalent alkaline-earth ions, respectively. The structure of this homologous series is based on alternate stacking of rock-salt-type block layers $(R,A)_2O_2$ and *n*-MnO_2 sheets along the *c* axis. In this paper, we present the results of a study on $(R,A)MnO_3$ ($n = \infty$: perovskite-type structure) and $(R,A)_2MnO_4$ ($n = 1$: K_2NiF_4-type structure).

Concerning the charge-orbital ordering structure in manganese oxides, there are two significant issues. One is an existence of the charge-orbital ordering without correspondence to the hole concentration for hole-doping level of $x < 1/2$, and the other is striking discrepancy between "Wigner-crystal" [9] and "bi-stripe" [11] models for hole-doping level of $x < 1/2$. The modulation wave vector of the charge-orbital ordering for the compounds with $x \geq 1/2$ corresponds to the hole-doping level. For example, the modulation wave vectors for the compounds with $x = 1/2$ and 2/3 are (0,1/2,0) [7,8,16] and (0,1/3,0) [9,10,12], respectively. In contrast, the (0,1/2,0) superlattice reflection is always observed for $Pr_{1-x}Ca_xMnO_3$ with $0.3 \leq x \leq 0.5$ [16,33], which indicates orbital ordering with the same periodicity as $x = 1/2$. Jirak *et al.* [16] interpreted this phenomenon as demonstrating that an e_g orbital with occupancy of less than one existed on the Mn^{4+} sites based on the results from their powder neutron diffraction experiments. For the charge-ordering phase with $x \geq 1/2$, on the other hand, while longitudinal displacement of atoms was suggested in the "bi-stripe" model, Radaelli *et al*. [34] and Wang *et al*. [35] proposed the "Wigner-crystal" charge-orbital arrangement in which the displacement of atoms is transverse to the modulation wave vector. However it was difficult to directly observe the transverse modulation in real space mainly because the atomic displacement is very small [35]. In this paper, we mention our views on these issues, based on our transmission electron microscopy (TEM) studies.

Magnetic domains in perovskite-type manganese oxides and their related materials have been directly observed by using various techniques, such as magnetic force microscopy [36,37], scanning Hall probe microscopy [38], and Kerr microscopy [39]. Recently, Lloyd *et al.* have investigated magnetic domain walls in ferromagnetic $La_{0.7}Ca_{0.3}MnO_3$ films by using the Fresnel method in Lorentz transmission electron microscopy (TEM) [40]. There are two

commonly used imaging methods, called the Fresnel and the Foucault methods, in Lorentz TEM [41,42]. The Fresnel method enables observing domain walls rather than domains. In this study, we mainly used the Fresnel method. Lorentz TEM is characterized by high resolution on the nanometer scale and high sensitivity even to small variations in magnetization. Using the Fresnel method of Lorentz TEM, we can directly observe the interaction between domain walls and lattice defects and the dynamic behavior of domain walls in real time.

In this paper, we report on our low-temperature electron diffraction and electron microscopy studies of manganese oxides. Our analyses have revealed a new form of structural modulation for perovskite-type $Pr_{1-x}Ca_xMnO_3$ [43,44] and a sinusoidal transverse modulation for single-layered $Nd_{1-x}Sr_{1+x}MnO_4$ [45] and $Nd_{1-x}Ca_{1+x}MnO_4$ [46]. We discuss their origins in terms of the ordering of extra e_g electrons for the former and the existence of a charge-density wave (CDW) and an orbital-density wave (ODW) for the latter. In Lorentz TEM study, the behavior of magnetic domain structures and the relationship between crystal structures and the magnetic domain structures are discussed [47].

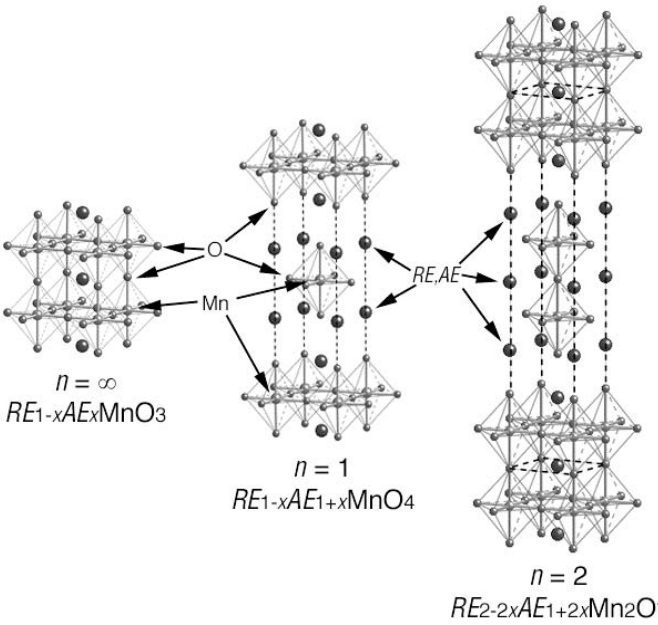

Fig. 1. Schematic illustrations of crystal structures of perovskite-type $RE_{1-x}AE_xMnO_3$, single-layered $RE_{1-x}AE_{1+x}MnO_4$, and double-layered $RE_{2-2x}AE_{1+2x}Mn_2O_7$.

2. EXPERIMENTS

We examined single crystalline samples and polycrystalline ones of the manganese oxides. The single crystalline samples were grown by a floating-zone method, and the polycrystalline ones were synthesized by conventional solid-state reaction in air.

TEM specimens were prepared with two procedures. Some samples were ground under CCl_4 then dispersed on Cu grids coated with holy-carbon support films, and the others were thinned with Ar^+ ion sputtering.

The specimens were examined with a Hitachi H-1500 high-voltage transmission electron microscope operating at 800 kV and with Hitachi HF-3000S analytical transmission electron microscope operating at 300 kV and with Hitachi HF-3000L Lorentz transmission electron microscope operating at 300 kV. In the high-voltage electron microscope and analytical one, the specimens are put in the objective lens. Therefore the samples are exposed to magnetic fields about 2 to 3 Tesra yielded by the objective lens. On the other hand, in the Lorentz microscope, the specimens are not exposed to magnetic fields because the samples are put out of the objective lens. Thus, we can observe the magnetic domain structures without magnetic fields. The specimens were cooled from room temperature to 80 K on an Oxford liquid-nitrogen cooling holder. Simulations of electron diffraction patterns and high resolution TEM images based on dynamical diffraction theory were carried out with MacTempas software.

Bright/dark field imaging and high-resolution imaging were carried out with the well-known conventional methods. However, imaging of Lorentz TEM is not familiar to many researchers. Here we briefly describe the principle of imaging in the Fresnel method of Lorentz TEM (Fig. 2) [41,42].

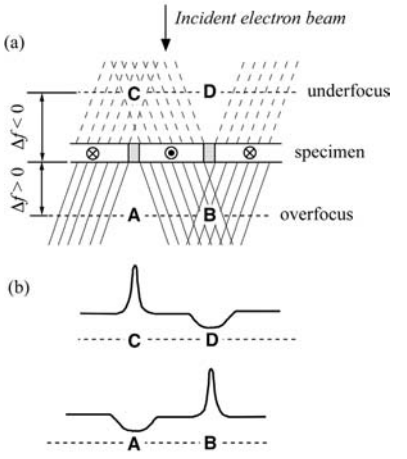

Fig. 2. Schematic description of principle of Fresnel imaging in Lorentz microscopy. (**a**) Tracks of electron beam, and (**b**) the distribution of intensity of electron on the image plane [Ref. 42].

When the incident electron beam penetrates a specimen with a magnetic domain structure, the electrons are deflected by the Lorentz force. If the objective lens of the Lorentz electron microscope is underfocused or overfocused, electrons coming through different domains will produce images in which the walls appear as bright (white) and dark (black) lines. These lines reverse their contrast between the underfocused and overfocused images. The bright (white) and dark (black) lines corresponding to the domain walls are called convergent images and divergent images, respectively. These images disappeared under in-focus conditions.

3. RESULTS AND DISCUSION

Charge-Orbital Ordering Structure

Perovskite-type $Pr_{1-x}Ca_xMnO_3$

First, we show the TEM study for $Pr_{5/8}Ca_{3/8}MnO_3$. The electron diffraction patterns obtained from $Pr_{5/8}Ca_{3/8}MnO_3$ at room temperature indicate a *P*bnm orthorhombic structure with lattice parameters $a \approx b \approx \sqrt{2}a_P$ and $c \approx 2a_P$ (a_P: the lattice constant of the simple cubic perovskite cell). The typical [001]-zone electron-diffraction pattern at room temperature is shown in Fig. 3(a). Here, the $h00$, $0k0$, and $00l$ reflections with h, k, and $l = 2n+1$ (n: integer), respectively, are caused by double diffraction.

Here we focus on our low-temperature investigation of the charge-ordering transition in $Pr_{5/8}Ca_{3/8}MnO_3$. The samples were cooled down from room temperature and observed traces of diffuse scattering that was slightly extent in the b^* direction below 260 K, and then became superlattice reflection spots below 230 K. Figure 3(b) shows the [001]-zone electron-diffraction pattern at 92 K. As compared with the pattern at room temperature, additional superlattice reflections with a modulation wave vector $\boldsymbol{q}_1 = (0,1/2,0)$ appeared. We carried out the same electron diffraction experiments on $Pr_{1-x}Ca_xMnO_3$ with $x = 0.3$, 0.35, 0.4, 0.45, and 0.5, and all samples had the same superstructure with $\boldsymbol{q}_1$ at 92 K. This feature is in stark contrast to the abovementioned case of $x \geq 1/2$. Furthermore, the temperature dependence of the $\boldsymbol{q}_1$ superlattice reflections for the $x < 1/2$ compounds differed from that for the $x \geq 1/2$ compounds. While incommensurate superlattice reflections were observed for the compounds with $x \geq 1/2$ above the antiferromagnetic spin-ordering temperature T_N [7,8,11,48], the superlattice reflections for the present compounds with $x < 1/2$ were always observed at the commensurate positions and only changed in intensity at $T_N < T < T_{CO}$. The $\boldsymbol{q}_1$ superstructure reflections in the $x = 1/2$ compounds are ascribed to the $d_{3x^2-r^2}/d_{3y^2-r^2}$-type of orbital ordering. The same type of charge-orbital ordering occurs in $Pr_{5/8}Ca_{3/8}MnO_3$ at low temperatures.

At lower temperatures, superstructure reflections with another modulation wave vector from $\boldsymbol{q}_1$ were found. Figure 3(d) shows the [$\bar{1}$10]-zone electron-diffraction pattern of $Pr_{5/8}Ca_{3/8}MnO_3$ at 92 K. Sharp superstructure reflections, which were not observed at room temperature (Fig. 3(c)), can be seen. The modulation wave vector is commensurate and can be denoted as $\boldsymbol{q}_2 = (1/4,1/4,1/2)$. The superstructure reflections with $\boldsymbol{q}_2$ appear as very weak diffuse scattering below 150 K. As the temperature decreased, the intensities of the superlattice reflections increased. However, while the diffuse scattering became sharp superlattice spots below 100 K, the wave vector $\boldsymbol{q}_2$ did not change throughout the cooling.

Upon warming from 92 K, the $\boldsymbol{q}_2$ superlattice reflections remained as sharp spots with decreasing intensity up to 200 K. They subsequently became diffuse scattering, and then completely disappeared at ~ 250 K. The temperature dependence of the $\boldsymbol{q}_1$ superlattice reflections was qualitatively the same as the behavior of the $\boldsymbol{q}_2$ superlattice reflections described above. The $\boldsymbol{q}_1$ superlattice reflections changed into diffuse scattering at about 200 K and disappeared at about 270 K. The intensities of both the $\boldsymbol{q}_1$ and $\boldsymbol{q}_2$ superlattice reflections show large hystereses between cooling and warming.

Here we discuss the origin of the $\boldsymbol{q}_2$ reflections. As shown in Fig. 3(d), the intensities of the first-order superlattice reflections near fundamental spots are stronger than for second-order ones. This indicates that the fundamental structure is modulated by periodic atomic displacement. The $\boldsymbol{q}_2$ superlattice reflections should not be ascribed to a twin structure of two domains in the direction of the [001] and [$\bar{1}$10] zone-axis, taking account of the features in the electron-diffraction pattern and the subsequent lattice image. The [$\bar{1}$10]-zone lattice image shown in Fig. 4 obviously indicates that this material has a modulation structure at 80 K. The 7.6-Å periodic contrasts, corresponding to the lattice constant c, are overlaid obliquely with the 10.9-Å modulation contrasts, corresponding to the magnitude of $\boldsymbol{q}_2$. Furthermore, the $\boldsymbol{q}_1$ and $\boldsymbol{q}_2$ superlattice spots began to appear at different temperatures, as mentioned above. Therefore, the $\boldsymbol{q}_2$ modulation structure does not originate from twin variants.

We prove that the $\boldsymbol{q}_1$ and $\boldsymbol{q}_2$ modulation structures exist in the single domain and are not caused by any other phases that result from phase separation or imhomogeneity of the chemical composition. Figure 5(a) shows the dark field image formed by a $\boldsymbol{q}_2$ superlattice spot at 80 K. The bright parts are domains with the $\boldsymbol{q}_2$ modulation structure and the dark lines show antiphase boundaries. Rotating the specimen around the c-axis by 45° causes the $\tilde{1}$1] (or $\tilde{1}$1]) zone-axis pattern shown in the inset of Fig. 5(b) to appear in the same part of the crystal. In this diffraction pattern, superstructure spots caused by the $\boldsymbol{q}_1$ modulation appeared. The dark field image formed by these spots is shown in Fig. 3(b). The bright parts caused by the $\boldsymbol{q}_1$ modulation structure approximately coincided with the $\boldsymbol{q}_2$ modulated domain shown in Fig. 5(a). [Note that the lines on the left in Fig. 5(b) show the twin boundaries. These boundaries did not appear in Fig. 5(a) because the crystal orientation is undesirable for the observation of this type of twin boundary, which is the twin boundary between the *ac* and the *bc* domains.] Therefore, this compound had $\boldsymbol{q}_1$ and $\boldsymbol{q}_2$ modulation structures in the same spatial distribution. Furthermore, when we examined the temperature dependence of the [100]-zone electron-diffraction pattern during the cooling stage, we observed a typical change in the $\boldsymbol{q}_1$ superlattice reflection spots. The electron diffraction patterns in the cooling stage at 297, 110, and 92 K are shown in Figs. 5(c), (d), and (e), respectively. Only the second-order reflections of the $\boldsymbol{q}_1$ modulation structure are discernible down to 110 K. We inferred from our analysis of the diffraction patterns that the space group is $P2_1/m$. All the expected superlattice reflection spots caused by the $\boldsymbol{q}_1$ modulation structure appear at 92 K. This indicates that the symmetry probably becomes lower when both $\boldsymbol{q}_2$ and $\boldsymbol{q}_1$ modulation structures are formed simultaneously.

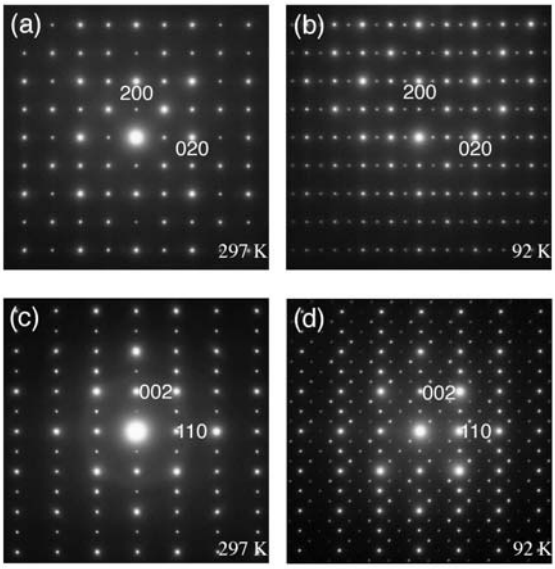

Fig. 3. [001]-zone electron-diffraction patterns of $Pr_{5/8}Ca_{3/8}MnO_3$ obtained at (**a**) room temperature and (**b**) 92 K, respectively. The presence of superlattice reflections with a modulation wave vector (0,1/2,0) is evident. [$\bar{1}$10]-zone electron-diffraction patterns obtained at (**c**) room temperature and (**d**) 92 K, respectively. The presence of superlattice reflections along the [112] direction is evident.

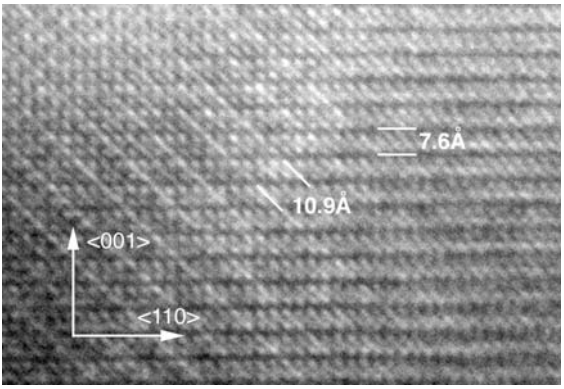

Fig. 4. [$\bar{1}$10]-zone lattice image obtained at 80 K. In addition to the contrast of the lattice constant c (~ 7.6 Å), the contrast of the $\boldsymbol{q}_2$ superlattice is shown obliquely.

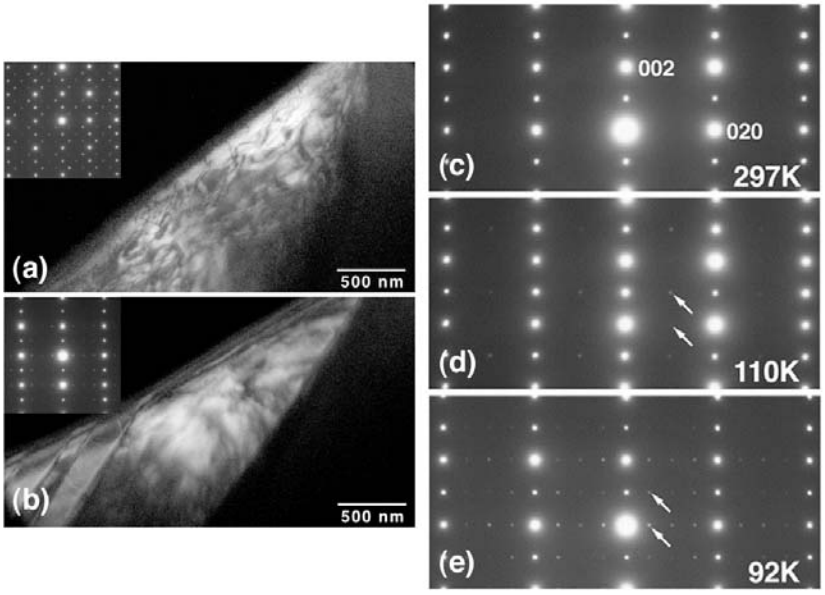

Fig. 5. Dark field images obtained from the superlattice reflections. (**a**) [$\bar{1}$10] and (**b**) [100] zone-axis images from the same part of the crystal. The insets are the corresponding electron diffraction patterns. The image shown in (b) was obtained after 45° rotation of the sample around the *c*-axis. The [100]-zone electron-diffraction patterns were obtained at (**c**) room temperature, (**d**) 110 K, and (**e**) 92 K. Arrows correspond to superlattice reflections with a modulation wave vector $\boldsymbol{q}_1$.

We interpret the cause of the $\boldsymbol{q}_2$ modulation structure in terms of the ordering of extra e_g electrons along the *c*-axis. Here, we propose a possible model of a structure in charge-orbital ordered state for $Pr_{5/8}Ca_{3/8}MnO_3$. First, the $\boldsymbol{q}_1$ modulation structure, which is similar to the charge-orbital ordering in $La_{1/2}Ca_{1/2}MnO_3$ and $Pr_{1/2}Ca_{1/2}MnO_3$, must remain essentially. Second, Mn^{3+} ions must be substituted partially on the Mn^{4+} sublattice in the $x = 1/2$-type of charge ordering. In our model, charge ordering on this sublattice is very important. From the chemical composition, the ratio of Mn^{3+} to Mn^{4+} in this sublattice should be 1 : 3. The extra e_g electrons occupy $3d_{3z^2-r^2}$ orbitals on the Mn^{4+} sublattice, as in the model by Jirak *et al* [16]. $Mn^{3+}O_6$ octahedra would accompany the Jahn-Teller distortion. Taking the direction of the $\boldsymbol{q}_2$ vector into consideration also, the proposed model is as shown in Fig. 6. The extra e_g electrons are shown as dark gray symbols of Mn^{3+} in the shadowed areas of Fig. 6. This model is consistent with the findings of previous optical [49] and thermopower [50] studies. A computer simulation based on this model also agrees fairly well with the obtained patterns, as shown in Fig. 7.

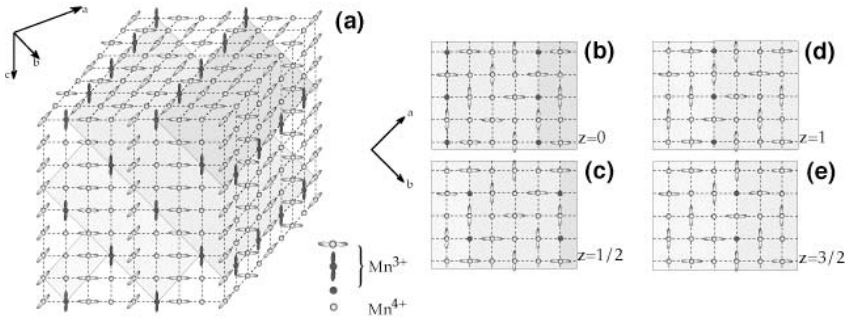

Fig. 6. (**a**) Proposed model of the charge/orbital ordering structure for $Pr_{5/8}Ca_{3/8}MnO_3$. In this illustration, all ions except Mn are omitted. (**b**)-(**e**) the *ab* planes in the proposedmodel.

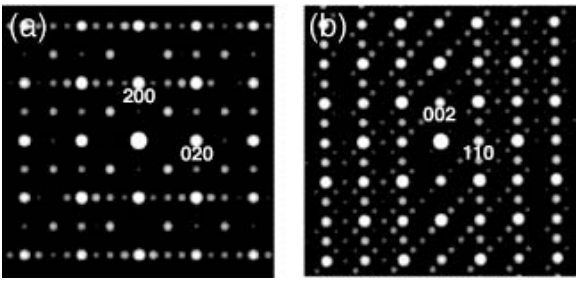

Fig. 7. Simulated (**a**) [001]-zone and (**b**) [$\bar{1}$10]-zone axes electron diffraction patterns using the proposed structure model .

In our model, the temperature dependence of the nucleation and growth of the $\boldsymbol{q}_2$ modulation structure can be interpreted as follows. During the first stage of cooling, it is conceivable that nucleation of the $\boldsymbol{q}_1$ superstructure occurs as short-range ordering that includes disordered planes with random occupation of e_g orbitals, perpendicular to the *b*-axis, judging from the trace of diffuse scattering extent in the b^* direction in the [001]-zone diffraction patterns. If the orbital disordering planes are laid in the $\boldsymbol{q}_1$ orbital ordered phase, the $\boldsymbol{q}_2$ modulation structure will not be formed. The extra e_g electrons occupy the $d_{3z^2-r^2}$ orbital in the long-range orbital ordered state, as described above. In the short-range orbital ordering state, however, there is a possibility that the orbital disordering planes cause random occupation of extra e_g orbitals. Therefore, long-range orbital ordering of the $\boldsymbol{q}_1$ superstructure is necessary for nucleation and growth of the $\boldsymbol{q}_2$ modulation structure. In fact, when long-range orbital ordering of $\boldsymbol{q}_1$ was observed in the electron diffraction patterns and the dark field images of the $\boldsymbol{q}_1$ superstructure spots at lower temperatures, the $\boldsymbol{q}_2$ modulation structure was identified. This model also explains the lower $\boldsymbol{q}_2$ transition temperature. Moreover, it is worth mentioning that the onset temperature of the $\boldsymbol{q}_2$ modulation structure is close to the antiferromagnetic spin-ordering temperature T_N, ~ 160 K [50].

By investigation for the compounds with other chemical composition, we found that the $\boldsymbol{q}_2$ modulation structure appears only in a range of $0.36 \leq x \leq 0.4$. However, even in the compounds with the deviation of x from 3/8, the superlattice reflections with the wave vector $\boldsymbol{q}_2$ = (1/4,1/4,1/2) were observed. In other words, the periodic lattice distortion caused by charge-orbital ordering is not corresponding to hole-doping level. In order to understand this behavior, we performed the observations of dark field TEM images formed by the $\boldsymbol{q}_2$ superlattice spots. The dark field images formed by the superlattice spots for x = 0.36, 0.375 and 0.4 compounds at 80 K are shown in Fig. 8 (a), (b), (c), respectively. Bright parts indicate the domains with the $\boldsymbol{q}_2$ modulation structure in these images. In the image of the x = 0.375 compound, shown in Fig. 8(b), it is considered that the sharp black lines are corresponding to the antiphase boundaries and the dark regions indicate the phase not formed $\boldsymbol{q}_2$ modulation structure ($\boldsymbol{q}_2$ charge-disordering phase). In the image of the x = 0.36 compound, the bright areas are very small and scattered with diameter of several 10 to 100 nm, as shown in Fig. 8(a), compared with ones in the image of the x = 0.375 compound. This indicates the short-range charge-orbital ordering within $\boldsymbol{q}_2$ charge-disordering matrix. The intensity of $\boldsymbol{q}_2$ superlattice reflection is very week in the corresponding electron diffraction pattern. In the image of the x = 0.4 compound, many broad dark lines are observed in the bright areas indicating charge-orbital ordering domains, as shown in Fig. 8(c). The dark lines are nearly perpendicular to <112>, that is, the direction of wave vector of $\boldsymbol{q}_2$ superlattice. We considered that the dark lines indicate the charge-disordering domain boundaries between $\boldsymbol{q}_2$ charge-ordering phases. Because the superlattice reflections with the commensurate wave vector (1/4,1/4,1/2) were observed in spite of the hole-concentration with the deviation from x = 3/8, we considered that the charge-orbital ordering $\boldsymbol{q}_2$ modulation structures with hole-concentration x = 3/8 are formed in the parts of the bright areas, and the dark areas indicating $\boldsymbol{q}_2$ charge-disordering phase have a part to adjust the hole- (electron-) concentration for x = 0.36 and 0.4 compound. It would be necessary to investigate the interface of the charge-orbital ordering and disordering phase by means of high-resolution TEM etc.

We found another modulation structure in x = 0.36 compound. HRTEM image and corresponding electron diffraction pattern of x = 0.36 compound at 80 K is shown in Fig. 9(a). This modulation structure is observed at local areas. The wave vector is incommensurate, and can be denoted as (1/3-δ, 1/3-δ, 2/3-δ) (δ ~ 0.03). In Fig. 9(a), the linear contrasts with the space of $3d_{112}$ are observed clearly, perpendicular to <112> direction. Moreover, antiphase boundaries are also found. The antiphase boundaries can be regarded as 4 times periodicity of d_{112}, (namely, the space of $4d_{112}$). We considered that the incommensurate-superlattice reflections are excited from both the 3 times period phase and antiphase boundaries with 4 times periodicity. We show the proposal model about the charge-orbital ordering structure of the 3 times period phase including the antiphase boundaries with $4d_{112}$ in Fig. 9(b). According to this model, the 3 times period phase has a low hole-concentration corresponding to x = 1/3, in spite of hole-doping level x = 0.36. However we considered that the hole-concentration is adjusted by the presence of antiphase boundaries with 4 times periodicity. Therefore, it is considered possible that commensurate charge-orbital ordering structure with wave vector (1/3,1/3,2/3) exists in x = 1/3 compound. The low-temperature TEM experiments for the x = 1/3 compound are in progress.

Recently, this charge-orbital ordering structure attracts considerable attention as one kind of CDW state [51-53]. This charge-orbital ordering can be viewed as a qusei-one-dimensional electronic structure with a reduced dimensionality compared to the x = 0.5-type

of charge-orbital ordering. Wahl *et al*. have been interpreted the nonlinear electrical response observed in their dielectric measurements as a CDW state which is led by the qusei-one-dimensional electronic structure in this compound [53].

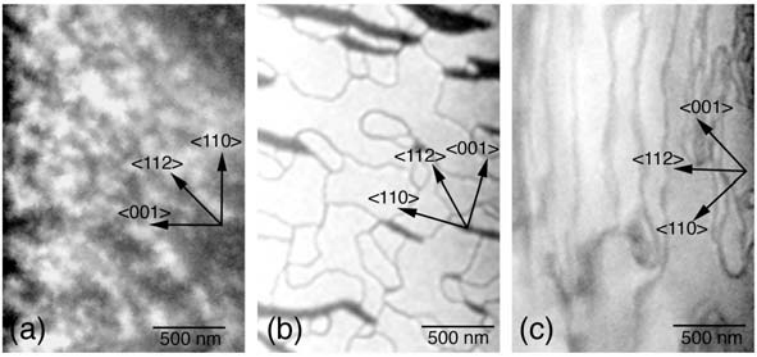

Fig. 8. The dark filed images of the (**a**) $x = 0.36$, (**b**) $x = 0.375$, and (**c**) $x = 0.4$ compounds, obtained from $\boldsymbol{q}_2$ superlattice reflections at 80 K.

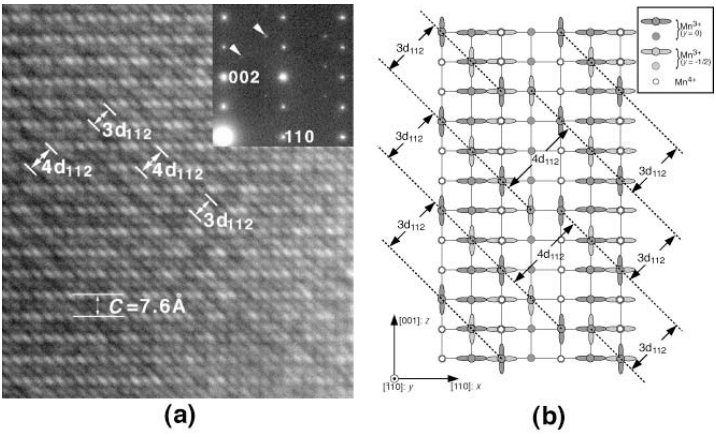

Fig. 9. (**a**) [$\bar{1}$10]-zone axis lattice image of the $x = 0.36$ compound obtained at 80 K. The inset is the corresponding electron diffraction pattern. Arrows indicate the superlattice spots. (**b**) The proposed model of charge-orbital ordering structure for this phase.

Single-layered $Nd_{1-x}Sr_{1+x}MnO_4$ and $Nd_{1-x}Ca_{1+x}MnO_4$

Next, we show the TEM study for the single-layered $Nd_{1-x}Sr_{1+x}MnO_4$ and $Nd_{1-x}Ca_{1+x}MnO_4$. The electron diffraction patterns obtained from $Nd_{1-x}Sr_{1+x}MnO_4$ at room temperature (300 K) indicate $I4/mmm$ tetragonal structure (K_2NiF_4 type structure) with lattice parameters a = 0.3832 nm, c = 1.2368 nm (x = 2/3), a = 0.3821 nm, c = 1.2380 nm (x = 3/4). The typical [001]-zone electron diffraction pattern at room temperature is shown in Fig. 10(a).

For $Nd_{1-x}Ca_{1+x}MnO_4$, the electron diffraction patterns obtained at room temperature indicate that the fundamental structures consisted of two distorted types corresponding to the chemical composition. One is the *B*mab orthorhombic structure (ortho I) in $0.55 \leq x < 0.73$ and the other is the *A*cam orthorhombic one (ortho II) in $0.73 \leq x \leq 0.75$. Such distorted structures can be derived from rotations of MnO_6 octahedra around the $[110]^t$ axis (ortho I) or the $[001]^t$ axis (ortho II) in a tetragonal $I4/mmm$ K_2NiF_4-type structure, respectively, (The superscipt '*t*' indicates that the index is written in a pseudo-tetragonal setting.) as shown in Figs. 11(a) and 11(b).

We focus here on our low-temperature investigation of the charge-ordering transitions in $Nd_{1-x}Sr_{1+x}MnO_4$ and $Nd_{1-x}Ca_{1+x}MnO_4$. For $Nd_{1-x}Sr_{1+x}MnO_4$, we cooled the samples from room temperature and observed weak satellite reflections around the fundamental Bragg reflections below ~ 270 K, as shown in Figs. 10(b) and 10 (c). On the other hand, weak satellite reflections can be observed at relatively higher temperatures (e.g. ~ 330 K for the x = 2/3 compound) in $Nd_{1-x}Ca_{1+x}MnO_4$, as shown in Fig. 12(b). These appearances of weak satellite reflections indicate the onset of charge ordering (T_{CO}). Here the higher T_{CO} suggests that the charge ordered state are quite stabilized in this system. In single-layered manganese oxides, the rocksalt-type blocks obstruct the transfer of e_g electrons vertical to the MnO_2 network. Moreover, in $Nd_{1-x}Ca_{1+x}MnO_4$, the MnO_6 octahedra networks have some distortions such as tilt and buckling. Such structural distortions reduce the transfer of e_g electrons with in the network, which further enhances the stability of charge ordering. In both systems, intensities of the satellite reflections increased progressively with decreasing temperature [We show the behavior for $Nd_{1-x}Ca_{1+x}MnO_4$ (x = 2/3) in Fig. 13].

In $Nd_{1-x}Ca_{1+x}MnO_4$, the superlattice reflections appear for all hole-doping levels of $0.55 \leq x \leq 0.75$, that is, commensurate and incommensurate e_g electron concentration of $0.25 \leq n_e \leq 0.45$. We show the relationship between the propagation vector of the superstructure $\boldsymbol{k}_s$ and the composition x in Fig. 14. On the other hand, in $Nd_{1-x}Sr_{1+x}MnO_4$, the superlattice reflections can be observed for only commensurate doping levels (e.g. x = 2/3 and 3/4, n_e = 1/3 and 1/4). The modulation wave vector can be denoted as $\boldsymbol{k}_s = (1-x)\boldsymbol{a}^*_{rect}$. Here $\boldsymbol{a}^*_{rect}$ indicates $\boldsymbol{a}^*$ for $Nd_{1-x}Ca_{1+x}MnO_4$ and $\boldsymbol{k}_{110}/2$ for $Nd_{1-x}Sr_{1+x}MnO_4$, respectively. The equivalent relationships between the wave vector and doping level have been observed for other manganese oxide with $x \geq 1/2$, such as $La_{1-x}Ca_xMnO_3$ and $Pr_{1-x}Ca_xMnO_3$. In addition, note that the $m\boldsymbol{a}^*_{rect} \pm n\boldsymbol{k}_s$ superlattice reflections are kinematically forbidden but the multiple scattering of electron beams in the [001]-zone electron diffraction patterns. This feature suggests that atomic displacements in the present systems indicate transverse type to the a axis, and is inconsistent with the longitudinal displacement proposed in the "bistripe" model.

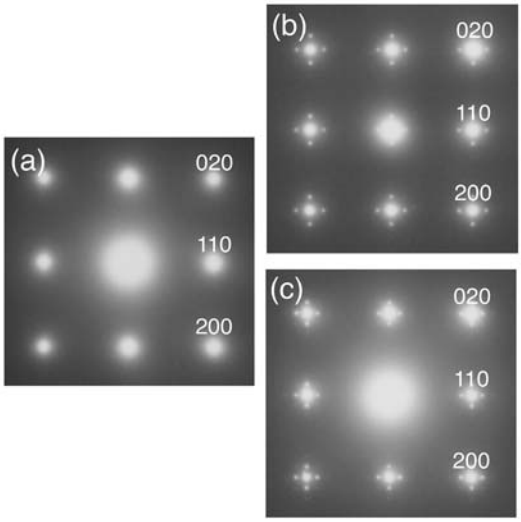

Fig. 10. [001] zone-axis electron diffraction patterns of $Nd_{1-x}Sr_{1+x}MnO_4$ (**a**) at 300 K for x = 2/3, (**b**) at 80 K for x = 2/3, and (c) at 80 K for x = 3/4. [The pattern at 300 K for x = 3/4 is almost identical to (**a**).] The presence of superlattice reflections at low temperature is evident.

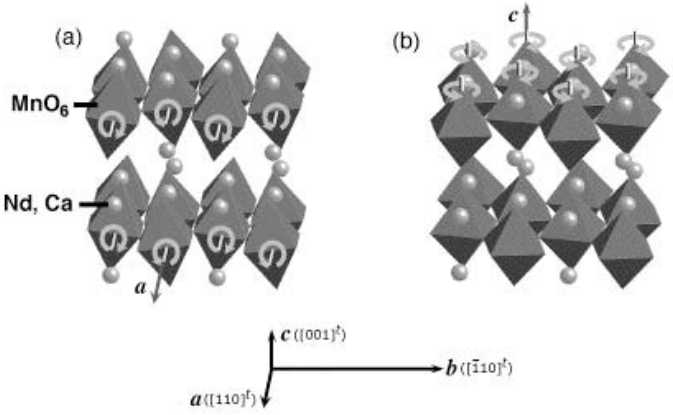

Fig. 11. Schematic illustrations of fundamental crystal structures of $Nd_{1-x}Ca_{1+x}MnO_4$ ($0.55 \leq x \leq 0.75$). (**a**) The *B*mab orthorhombic phase (ortho I) in $0.55 \leq x < 0.73$. (**b**) *A*cam orthorhombic phase (ortho II) in $0.73 \leq x \leq 0.75$.

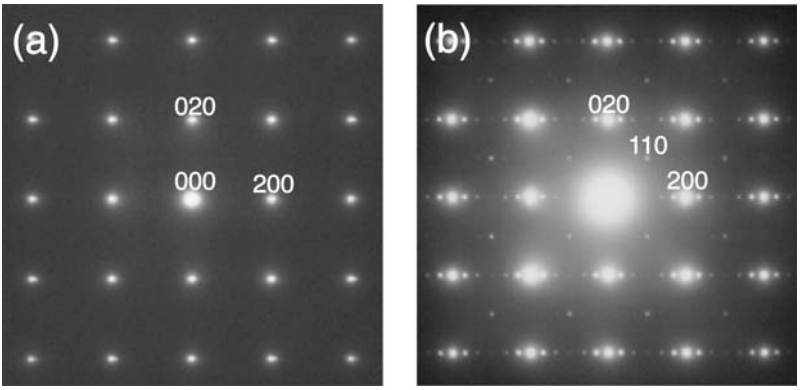

Fig. 12. [001]-zone electron-diffraction patterns of $Nd_{1-x}Ca_{1+x}MnO_4$ (x = 0.69) obtained at (**a**) 340 K and (**b**) 80 K, respectively.

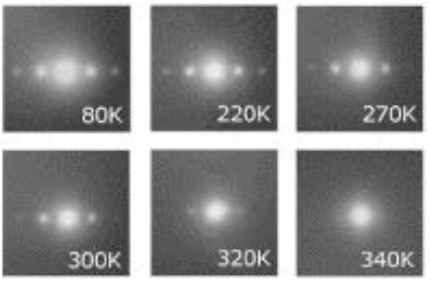

Fig. 13. Temperature dependence of the superlattice reflection intensity for $Nd_{1-x}Ca_{1+x}MnO_4$ (x = 2/3).

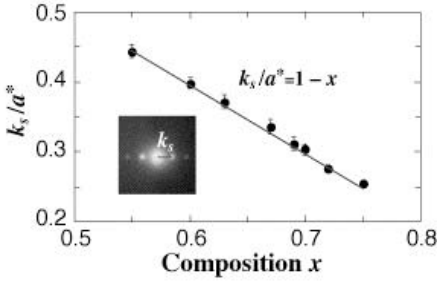

Fig. 14. The relation ship between the propagation vector of the superstructure $\boldsymbol{k}_s$ and the composition x.

In order to clarify the modulation structure, high-resolution images were investigated. In $Nd_{1-x}Sr_{1+x}MnO_4$, normal K_2NiF_4 structure is shown in the image taken at temperatures above T_{CO}. Figure 15 show the high-resolution images taken along the [001] direction (a) at 300 K for $Nd_{1-x}Sr_{1+x}MnO_4$ (x = 2/3), (b)-(b') at 80 K for x = 2/3, and (c)-(c') at 80 K for x = 3/4. [(b') and (c') are diagonally stretched images.] The images at 80 K (< T_{CO}) show clearly superlattice fringes and "transverse modulation" of the crystal structure, with the same periods of $6d_{110}$ (x = 2/3) or $8d_{110}$ (x = 3/4). In addition, it can be seen in Fig. 16 that the charge-orbital ordered crystals consist of domains with one-dimensional modulation along the [110] or [1 $\bar{1}$0] direction, and that the superlattice reflections showing "two-dimensional" modulation in the electron diffraction patterns come from the superlattice twin variants. The observed sinusoidal transverse modulation is in good agreement with invisibility of higher-order superlattice reflections in the diffraction patterns (Fig. 10).

The modulation structures of $Nd_{1-x}Ca_{1+x}MnO_4$, are quite similar to those of $Nd_{1-x}Sr_{1+x}MnO_4$. However, the incommensurate-modulation structures even appear in $Nd_{1-x}Ca_{1+x}MnO_4$, while only above-mentioned commensurate-modulations can be observed in $Nd_{1-x}Sr_{1+x}MnO_4$. Figures 17(a) and 17(b) show the high-resolution images taken along the [001] direction at 80 K (< T_{CO}) for the sample with a commensurate doping level of x = 2/3 and for the sample with a incommensurate doping level of x = 0.7, respectively. As shown in the high-resolution images of charge-orbital ordered $Nd_{1-x}Sr_{1+x}MnO_4$, the both images of Figs. 17(a) and 17(b) exhibit superlattice fringes and nearly sinusoidal transverse modulation of the crystal structure along the a axis ($[110]^t$) with the same commensurate and incommensurate periods of $3a$ ($6d_{110}{}^t$) and ~$3.3a$ (~$6.7d_{110}{}^t$), respectively. Here note that the shapes of the octahedra shown in Fig. 17(b) cannot be classified because of the incommensurate periodicity.

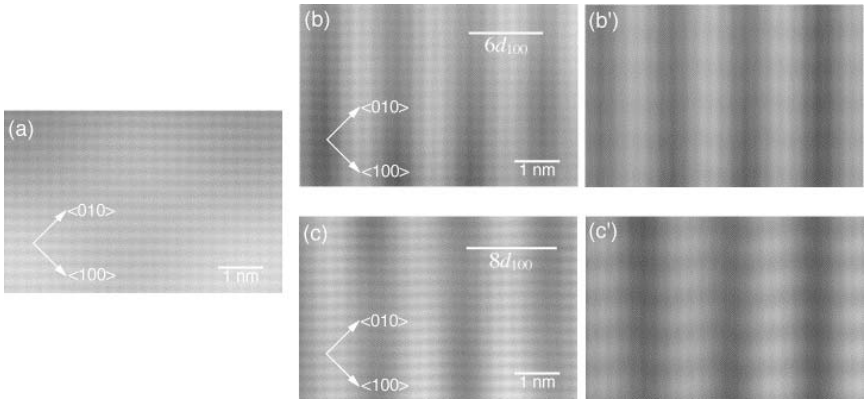

Fig. 15. High-resolution images of $Nd_{1-x}Sr_{1+x}MnO_4$, taken along the [001] direction (**a**) at 300 K for x = 2/3, (**b**)-(**b'**) at 80 K for x = 2/3, and (**c**)-(**c'**) at 80 K for x = 3/4. (**b'**) and (**c'**) are diagonally (along the [$\bar{1}$10] direction) stretched images. Superlattice fringes and "sinusoidal transverse modulation" of the crystal structure at low temperature are clearly shown.

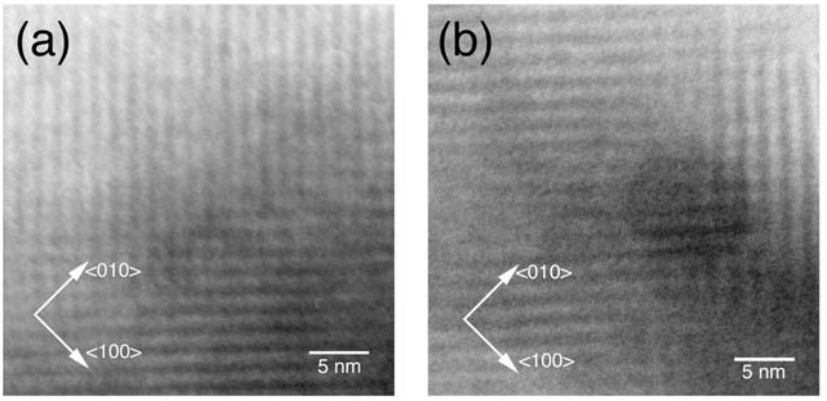

Fig. 16. Lattice images of $Nd_{1-x}Sr_{1+x}MnO_4$, taken at 80 K along the [001] direction for (**a**) x = 2/3 and (**b**) x = 3/4, showing the superlattice fringes with the period of $6d_{110}$ (x = 2/3) or $8d_{110}$ (x = 3/4).

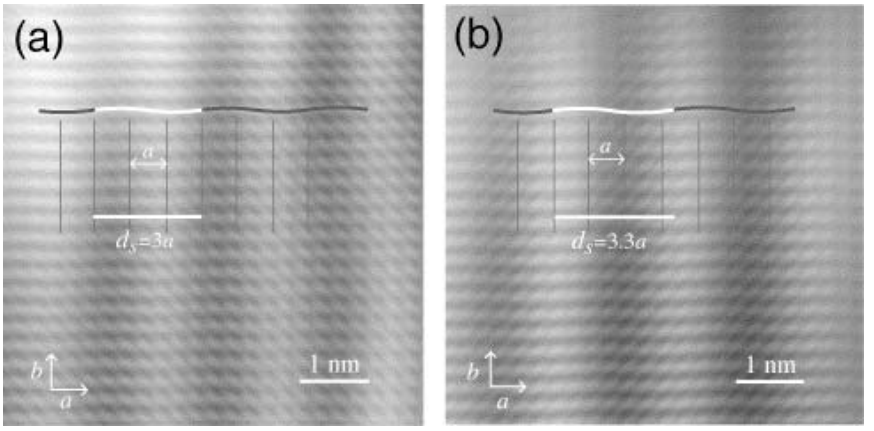

Fig. 17. High-resolution images of $Nd_{1-x}Ca_{1+x}MnO_4$, taken along the [001] direction at 80 K (**a**) for x = 2/3 and (**b**) for x = 0.7, respectively.

We proposed the structure model given by a sinusoidal transverse modulation on the basis of the high-resolution images, and show them in Fig. 18. If we select a position of the Mn atom for the origin of the atomic position parameter along $[110]^t$ (x), and the transverse displacement is described as $\Delta y = b_{max}\sin(2\pi x_s)$ (b_{max}: maximum displacement, x_s: fractional coordinates along the direction of modulation). According to undermentioned simulations of electron diffraction patterns, b_{max} is estimated as less than ~0.33. It can be seen that MnO_6 octahedra are most distorted where the central Mn atom is located at the coordinates of $x_s = 0$, or $x_s = 1/2$ in the proposed models, and that the direction of the Jahn-Teller distortion is different between $x_s = 0$ and $x_s = 1/2$ MnO_6 octahedra; the one direction is at nearly right angles to the other. This significant feature concerning MnO_6 distortion leads to a basic agreement with the "Wigner-crystal" model, where Jahn-Teller-distorted $Mn^{3+}O_6$ stripes are arranged as far apart as possible to minimize the Coulomb repulsion energy. The phase setting of structural modulation in our model coincides with that in a representative "Wigner-crystal" model based on synchrotron x-ray and neutron powder-diffraction analyses by Radaelli *et al*., although they do not use the transverse sinusoidal wave, but a transverse rectangle one as the atomic displacement. Moreover the successive change in the amplitude of MnO_6 distortion with the position x_s, that is, "sinusoidal wave", suggests that the modulation of the manganese valence – a CDW of e_g electrons – or the fluctuation of e_g electrons around the position of $x_s = 0$ and $x_s = 1/2$.

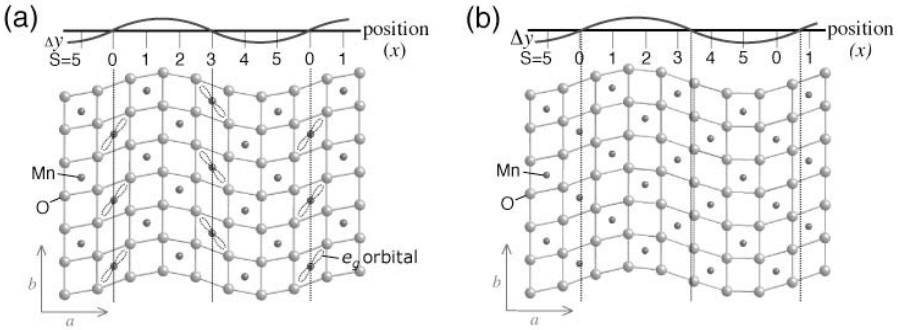

Fig. 18. Proposed superstructure model (**a**) for $x = 2/3$ and (**b**) for $x = 0.7$, respectively.

We performed simulations of electron diffraction patterns and high-resolution electron microscopy images for using the proposed modulation model shown in Figure 18. The simulated electron diffraction patterns are fairly good agreement with the experimentally observed ones. Here the simulations show that the intensities of the superlattice reflections increase as the atomic displacements increase. Further, the crystal tilt leads to the reproduction of $m\boldsymbol{a}^*_{rect} \pm n\boldsymbol{k}_s$ superlattice reflections excited by multiple scattering [Figs. 19(a) and 19(b)]. This simulation result also indicates that local crystal areas have slight deviations from the exact [001] zone-axis orientation in the practical situation when the patterns shown in Figs. 10 and 12 are observed. The high-resolution electron microscopy image simulation under the condition reproduced well the experimentally observed images [Figs. 15 and 17].

We also carried out the simulations using a transverse rectangle structural modulation, which is exactly consistent with "Wigner-crystal" model. The simulated electron diffraction patterns are roughly good agreement with the experimental ones, but some weak higher order superlattice reflections not observed in experiments appear in the simulated patterns. These results support the proposed modulation structure model – transverse "sinusoidal" modulation –.

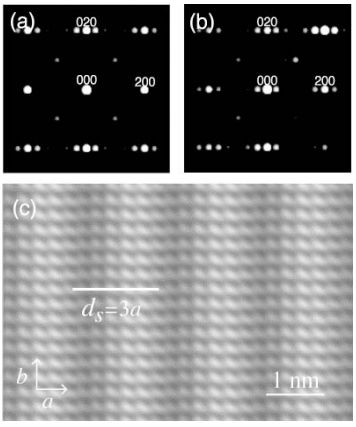

Fig. 19. (**a**) and (**b**) Simulated electron diffraction patterns using the proposed superstructure model shown in Fig. 18. The simulations were conducted for the cases of (**a**) crystal tilt: $h = k = 0$ mrad and (**b**) h = 30 mrad, k = -30mrad (crystal thickness: t = 16 nm). (**c**) Simulated HREM image using the proposed model. The simulation was carried out under the conditions of crystal tilt: h = 30 mrad, k = -30 mrad; crystal thickness: t = 12 nm; and defocus: Δf = -480 nm.

Here we discuss the modulation of charge and orbital states in the present systems, based on the observed transverse and sinusoidal structural distortion in both the commensurate and incommensurate carrier concentrations. As mentioned above, a possible CDW in overdoped single-layered manganites has been proposed [54], where the successive change in the amplitude of the Jahn-Teller distortion in MnO_6 octahedra with the position has been interpreted as the modulation of the manganese valence, that is, the density of e_g electrons. We demonstrate such a CDW state in Figure 20. Fig. 20(a) shows the illustration of the orbital state by the pseudospin space [55,56]. It is assumed that a motion of the pseudospin is confined in the xz plane, and θ_i describes the orbital state at the i site as follows:

$$|\theta_i\rangle = \cos(\theta_i/2)|x^2\text{-}y^2\rangle + \sin(\theta_i/2)|3x^2\text{-}r^2\rangle.$$

In the case of the pure CDW state, the orbital state toward the direction perpendicular to the stripe varies as indicated alternately by the two straight arrows (I) in Fig. 20(a). The variations of both Mn valence and θ are plotted as a function of position in the left panels of Fig. 20(b). Although the Mn valence (or density of e_g electrons) successively varies with the position, the

change in θ is "discrete" between $\pm\pi/3$. Here we propose the possibility of an orbital-density wave state, which was recently discussed by Koizumi *et al*. We can also regard the observed modulated structure as the ODW state. In the case of the pure ODW state, the density of e_g electrons should be constant. However, the orbital state varies on the curved arrows (II) in Fig. 20(a), that is, it oscillates successively $\theta = \pm\pi/3$, as shown in the right panels of Fig. 20(b). We consider that the real charge-orbital state in the single-layered manganites takes a mean position between the above two extreme situations.

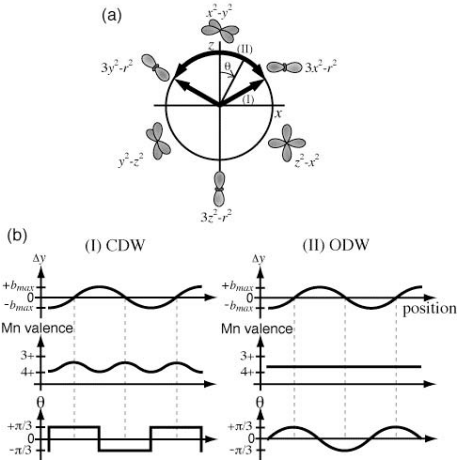

Fig. 20. Schematic picture of the e_g orbital state by the peudospin space. $\theta = -\pi/3$, 0, and $\pi/3$ correspond to $3y^2$-r^2, x^2-y^2, and $3x^2$-r^2 orbital states, respectively. (**b**) Mn valence (or electron density) and θ as a function of position (along the direction vertical to the stripe) in the charge-density wave state (left) and the orbital-density wave state (right).

Ferromagnetic Domain Structure

We focused on $Nd_{1/2}Sr_{1/2}MnO_3$ with orthorhombically distorted perovskite structure. This compound exhibits phase transitions at low temperatures. On cooling, $Nd_{1/2}Sr_{1/2}MnO_3$ undergoes the following transitions [57]: from the paramagnetic insulator state to the ferromagnetic metal state at the Curie temperature, $T_C \sim 250$ K, and then to the charge-ordered CE-type antiferromagnetic state at the charge-ordering temperature, $T_{CO} \sim 150$ K. It is known that the ferromagnetic (FM) metal – charge-ordered (CO) antiferromagnetic insulator phase transition is a first-order one [57], accompanying with the *I*bmm orthorhombic (FM) – $P2_1/m$ monoclinic (CO) structural phase transition [58,59].

First, we show the images of magnetic domain walls of $Nd_{1/2}Sr_{1/2}MnO_3$ in the ferromagnetic state. Figure 23(a) to (c) show the typical Lorentz TEM images of the present compound observed at ~ 225 K, taken with the underfocus of –500 μm, in-focus condition and the overfocus of +500 μm, respectively. Characteristic straight black and white lines can

be seen in Figs. 23(a) and (c), but they almost disappear in Fig 23(b). The black and white lines in Fig. 23 (a) reverse their contrast in Fig. 23 (c). We concluded from such observation that the straight black and white lines represent, respectively, divergent and convergent images of the magnetic domain walls. We found that the manganese oxides had a magnetic domain structure, similar to the one of typical ferromagnetic metal materials, such as Fe and Co [41,42]. The curved lines in each image, on the other hand, show bend-contours and thickness fringes, which are not due to the magnetism. The straight lines indicated by the arrows in the center of Fig. 23(b) are due to twin boundaries between which micro twins formed with crystallographic axes rotated 90° on the c axis. We can see convergent and divergent images at the twin boundaries in Figs. 23(a) and (c). Therefore, we can conclude that the twin boundaries play the role of magnetic domain walls at temperatures between 150 and 245 K. This indicates that magnetic domain wall is pinned strongly at the structural twin boundaries.

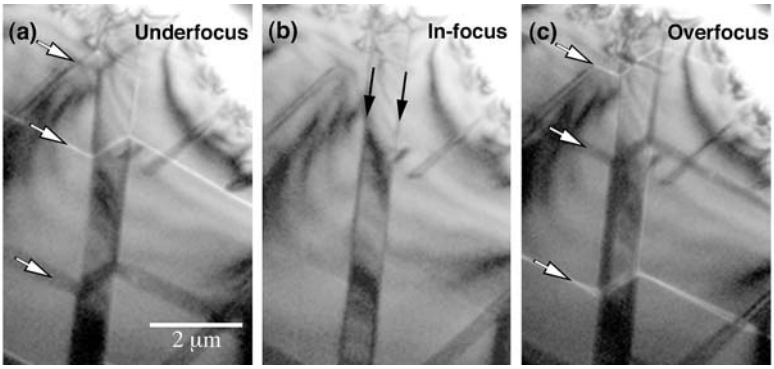

Fig. 21. Lorentz TEM images of $Nd_{1/2}Sr_{1/2}MnO_3$ at ~ 225 K: (**a**) underfocused, (**b**) in-focus, and (**c**) overfocused. Straight black and white lines indicated by white arrows in (**a**) and (**c**) represent, respectively, divergent and convergent images of domain walls. Arrows in (**b**) show the twin boundaries.

Figure 24 shows a Lorentz TEM image of the *ab* plane in $Nd_{1/2}Sr_{1/2}MnO_3$ at 180 K. The domain walls were oriented along the [100] direction in the main part, and along the [110] direction in the micro twins. We examined the domains by electron diffraction and found from the magnetic splitting of the central spot in the diffraction pattern that the direction of magnetization in each domain was along the long sides of the domain, as indicated by the white arrows in Fig. 24. This suggests that the compound has a magnetocrystalline anisotropy. We consider that the easy directions of magnetization are the [100] and [110] directions.

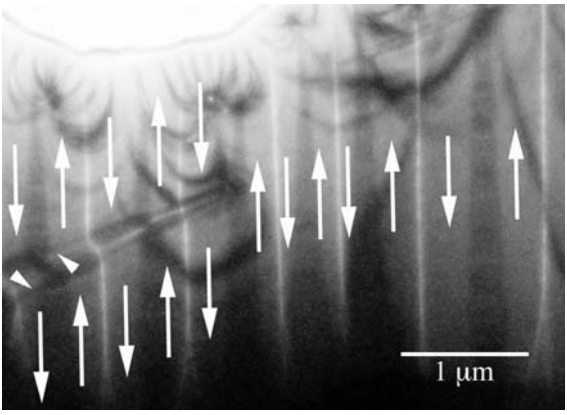

Fig. 22. A [001]-zone Lorentz TEM image obtained at 180 K. Magnetic domain walls are oriented along the [100] and [110] directions. White arrows indicate the direction of magnetization within each domain.

Figure 25 shows the dynamic behavior of magnetic domain walls on the changing in temperature. On cooling, magnetic domain walls started to appear at 245 K (near T_C). They were first observed inside the micro twins as shown in Fig. 25(b). As the temperature decreased, while the bulk magnetization in the present compound increased according to the measurements of magnetic susceptibility, the volume of ferromagnetic phase increased gradually, as shown in Figs. 25(b)-(d). The movements of the domain walls can be characterized as discontinuous domain-wall jumps. This suggests that the domain walls got released from the pinning sites as a result of thermal excitation, and then jumped to new stable positions [60,61]. Such discontinuous domain-wall jumps activated by thermal excitation and the ac field in the manganese oxides, which were observed by means of ac susceptibility measurements, have already been reported [62,63]. Here, some of the domain walls were always located at the twin boundaries, as mentioned above. Therefore the twin boundaries can be regarded as a strong pinning site. When the temperature decreased below 150 K, the ferromagnetic phase characterized by the presence of domain walls gradually disappeared (near T_{CO}) due to the growth of the antiferromagnetic charge-ordering phase, as shown in Figs. 25(e) and 25(f).

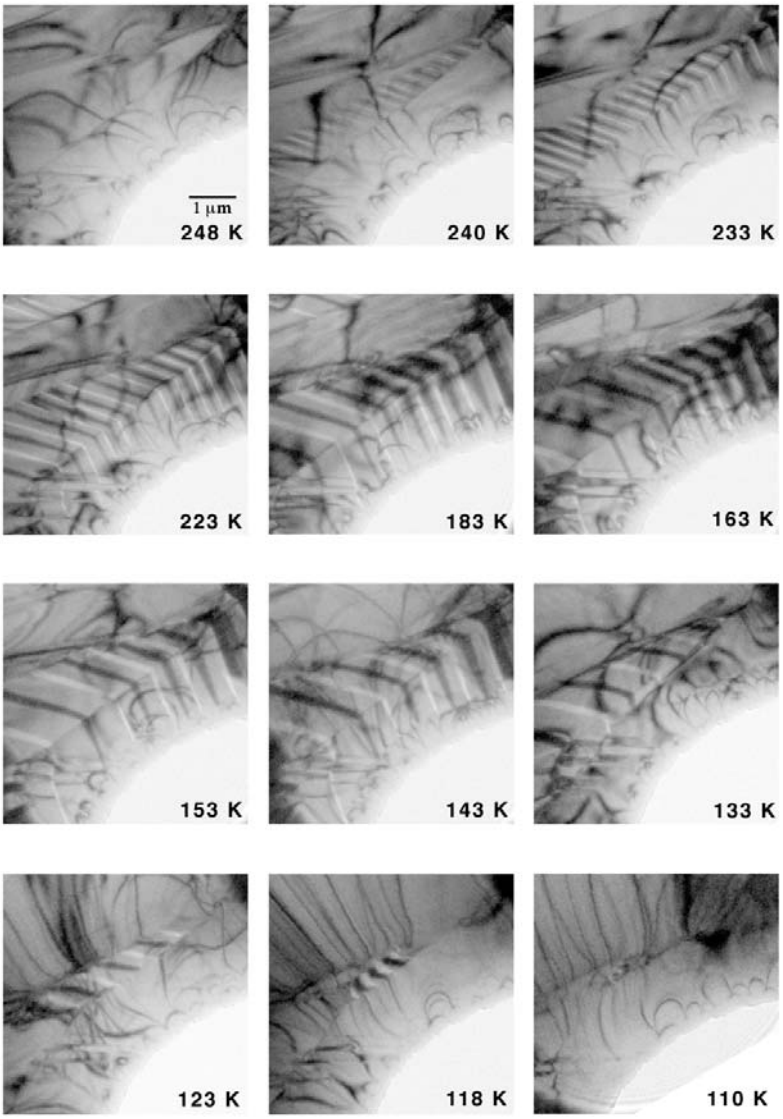

Fig. 23. Temperature variations of magnetic domain walls in Lorentz TEM images of $Nd_{1/2}Sr_{1/2}MnO_3$.

4. CONCLUSION

Charge-orbital ordering structure

Perovskite-type $Pr_{1-x}Ca_xMnO_3$

We have investigated the crystal structure of $Pr_{1-x}Ca_xMnO_3$ (x =3/8) in the charge-orbital ordering state by means of low-temperature TEM. Superlattice reflection spots with a modulation wave vector $\boldsymbol{q}_1$ = (0,1/2,0) appeared below 230 K. With a further decrease in temperature, an additional modulation structure was generated. This modulation structure first appeared as diffuse scattering below 150 K, and then as sharp spots with a modulation wave vector $\boldsymbol{q}_2$ = (1/4,1/4,1/2) below 100 K. We interpreted this modulation structure in terms of the charge-orbital ordering of extra Mn^{3+} ions. We also examined compounds with x = 0.3 to 0.5, and confirmed the appearances of $\boldsymbol{q}_2$ superstructure spots in the compounds with x = 0.36 to 0.4.

Single-layered $Nd_{1-x}Sr_{1+x}MnO_4$ and $Nd_{1-x}Ca_{1+x}MnO_4$

We have presented direct observation of the transverse and sinusoidal structural modulations in single-layered manganites, $Nd_{1-x}Sr_{1+x}MnO_4$ and $Nd_{1-x}Ca_{1+x}MnO_4$, by high-resolution electron microscopy. The observations and simulation studies support that the charge-orbital ordered states in the single-layered manganites are explained with a Wigner-crystal-type model, which is accompanied by a charge-orbital-density wave of e_g electrons.

Ferromagnetic Domain Structure

Magnetic domain structures of $Nd_{1/2}Sr_{1/2}MnO_3$ were investigated by means of low-temperature Lorentz electron microscopy. On cooling, magnetic domain walls started to appear at 250 K, and they were oriented straight along the [100] and [110] directions. With a further decrease in temperature, the volume of each magnetic domain increased with discontinuous domain-wall jumps.

Acknowledgement

The authors thank C. Tsuruta, Y. Tokura, T. Arima, T. Kimura, Y. Tomioka, H. Kuwahara, S. Yamada, Y. Anan, S. Tsutsumi, and A. Yamazaki for valuable discussions and collaborations. This work was supported by the MultiCore Project and the ‘Ultra High-Voltage TEM Analysis Support’ in Nanotechnology Researchers Network Project from the Ministry of Education, Science, and Culture, Japan.

REFERENCES

[1] K. Chahara, T. Ohno, M. Kasai, and Y. Kozono, Appl. Phys. Lett. 63 (1993) 1990.
[2] R. von Helmolt, J. Wecker, B. Holzapfel, L. Shultz, and K. Samwer, Phys. Rev. Lett. 71 (1993) 2331.
[3] S. Jin, T. H. Tiefel, M. McCormack, R. A. Fastnacht, R. Ramesh, and L. H. Chen, Science 264 (1994) 413.
[4] Y. Tokura, A. Urushibara, Y. Moritomo, T. Arima, A. Asamitsu, and G. Kido, J. Phys. Soc. Jpn. 63 (1994) 3931.
[5] E. O. Wollan and W. C. Koehler, Phys. Rev. 100 (1955) 545.
[6] J. B. Goodenough, Phys. Rev. 100 (1955) 564.
[7] C. H. Chen and S-W. Cheong, Phys. Rev. Lett. 76 (1996) 4042.
[8] P. G. Radaelli, D. E. Cox, M. Marezio, and S-W. Cheong, Phys. Rev. B 55 (1997) 3015.
[9] C. H. Chen, S-W. Cheong, and H. Y. Hwang, J. Appl. Phys. 81 (1997) 4326.
[10] A. P. Ramirez, P. Shiffer, S-W. Cheong, C. H. Chen, W. Bao, T. T. M. Palstra, P. L. Gammel, D. J. Bishop, and B. Zegarski, Phys. Rev. Lett. 76 (1996) 3188.
[11] S. Mori, C. H. Chen, and S-W. Cheong, Nature (London) 392 (1998) 473.
[12] M. T. Fernandez-Diaz, J. L. Martinez, J. M. Alonso, and E. Herrero, Phys. Rev. B 59 (1999) 1277.
[13] C. Zener, Phys. Rev. 82 (1951) 403.
[14] P. W. Anderson and H. Hasegawa, Phys. Rev. 100 (1955) 675.
[15] E. Pollert, S. Krupicka, and E. Kuzmicova, J. Phys. Chem. Solids 43 (1982) 1137.
[16] Z. Jirak, S. Krupicka, Z. Simsa, M. Dlouha, and S. Vratislav, J. Magn. Magn. Mater. 53 (1985) 153.
[17] Y. Tomioka, A. Asamitsu, Y. Moritomo, and Y. Tokura, J. Phys. Soc. Jpn. 64 (1995) 3626.
[18] Y. Tomioka, A. Asamitsu, H. Kuwahara, Y. Moritomo, and Y. Tokura, Phys. Rev. B 53 (1996) 1689.
[19] H. Yoshizawa, H. Kawano, Y. Tomioka, and Y. Tokura, Phys. Rev. B 52 (1995) 13145.
[20] A. Asamitsu, Y. Tomioka, H. Kuwahara, and Y. Tokura, Nature (London) 388 (1997) 50.
[21] V. Kiryukhin, D. Casa, J. P. Hill, B. Keimer, A. Vigliante, Y. Tomioka, and Y. Tokura, Nature (London) 386 (1997) 813.
[22] K. Miyano, T. Tanaka, Y. Tomioka, and Y. Tokura, Phys. Rev. Lett. 78 (1997) 4257.
[23] M. Fiebig, K. Miyano, Y. Tomioka, and Y. Tokura, Appl. Phys. Lett. 74 (1999) 2310.
[24] K. Ogawa, W. Wei, K. Miyano, Y. Yomioka, and Y. Tokura, Phys. Rev. B 57 (1998) 15033.
[25] M. Hervieu, A. Barnabe, C. Martin, A. Maignan, and B. Raveau, Phys. Rev. B 60 (1999) 726.
[26] H. Kawano, R. Kajimoto, H. Yoshizawa, Y. Tomioka, H. Kuwahara, and Y. Tokura, Phys. Rev. Lett. 78 (1997) 4253.
[27] K. Nakamura, T. Arima, A. Nakazawa, Y. Wakabayashi, and Y. Murakami, Phys. Rev. B 60 (1999) 2425.
[28] M. v. Zimmermann, J. P. Hill, D. Gibbs, M. Blume, D. Casa, B. Keimer, Y. Murakami, Y. Tomioka, and Y. Tokura, Phys. Rev. Lett. 83 (1999) 4872.

[29] N. D. Mathur, P. B. Littlewood, N. K. Todd, S. P. Isaac, B.-S. Teo, D.-J. Kang, E. J. Tarte, Z. H. Barber, J. E. Evetts, and M. G. Blamire, J. Appl. Phys. 86 (1999) 6287.
[30] P. Schiffer, A.P. Ramirez, W. Bao, and S.-W. Cheong, Phys. Rev. Lett. 75 (1995) 3336.
[31] M. Yamanaka and N. Nagaosa, J. Phys. Soc. Jpn. 65 (1996) 3088.
[32] G. Tatara and H. Fukuyama, Phys. Rev. Lett. 78 (1997) 3773.
[33] D. E. Cox, P. G. Radaelli, M. Marezio, and S-W. Cheong, Phys. Rev. B 57 (1998) 3305.
[34] P. G. Radaelli, D. E. Cox, L. Capogna, S.-W. Cheong, and M. Marezio, Rhys. Rev. B 59 (1999) 14440.
[35] R. Wang, J. Gui, Y. Zhu, and A. R. Moodenbaugh, Phys. Rev. B 61 (2000) 11946.
[36] Q. Lu, C.C. Chen, and A. Lozanne, Science 276 (1997) 2006.
[37] Y. Wu, Y. Suzuki, U. Rudiger, J. Yu, A. D. Kent, T. K. Nath, and C. B. Eom, J. Appl. Phys. 75 (1999) 2295.
[38] T. Fukumura, H. Sugawara, T. Hasegawa, K. Tanaka, H. Sasaki, T. Kimura, and Y. Tokura, Science 284 (1999) 1969.
[39] A. Gupta, G. Q. Gong, G. Xiao, P. R. Duncombe, P. Lecoeur, P. Trouilloud, Y. Y.Wang, and J. Z. Sun, Phys. Rev. B 54 (1996) 15629.
[40] S. J. Lloyd, N. D. Mathur, J. C. Loudon, and P. A. Midgley, Phys. Rev. B 64 (2001) 172407.
[41] P. J. Grundy and R. S. Tebble, Adv. Phys. 17 (1968) 153.
[42] P. B. Hirsh, A. Howie, P. B. Nicholson, D. W. Pashley, and M. J. Whelan, *Electron Microscopy of Thin Crystals*, Krieger, Florida (1977), pp 388.
[43] T. Asaka, S. Yamada, S. Tsutsumi, C. Tsuruta, K. Kimoto, T. Arima, and Y. Matsui, Phys. Rev. Lett. 88 (2002) 097201.
[44] T. Asaka, S. Tsutsumi, S. Yamada, T. Arima, C. Tsuruta, K. Kimoto, and Y. Matsui, Physica C 357-360 (2001) 313.
[45] T. Nagai, T. Kimura, A. Yamazaki, T. Asaka, K. Kimoto, Y. Tokura, and Y. Matsui, Phys. Rev. B 65 (2002) 060405.
[46] T. Nagai, T. Kimura, A. Yamazaki, Y. Tomioka, K. Kimoto, Y. Tokura, and Y. Matsui, Phys. Rev. B 68 (2003) 092405.
[47] T. Asaka, Y. Anan, T. Nagai, S. Tsutsumi, H. Kuwahara, K. Kimoto, Y. Tokura, and Y. Matsui, Phys. Rev. Lett. 89 (2002) 207203.
[48] S. Mori, C. H. Chen, and S.-W. Cheong, Phys. Rev. Lett. 81 (1998) 3972.
[49] Y. Okimoto, Y. Tomioka, Y. Onose, Y. Otsuka, and Y. Tokura, Phys. Rev. B 59 (1999) 7401.
[50] S. Yamada, T. Arima, H. Ikeda, and K. Takita, J. Phys. Soc. Jpn. 69 (2000) 1278.
[51] N. Kida and M. Tonouchi, Phy. Rev. B 66 (2002) 024401.
[52] A. Wahl, S. Mercone, A. Pautrat, M. Pollet, and C. Simon, and D. Sedmidubsky, Phys. Rev. B 68 (2003) 094429.
[53] S. Mercone, A. Wahl, A. Pautrat, M. Pollet, and C. Simon, J. Mag. Mag. Mat. 272-276 (2004) 388.
[54] S. Larochelle, A. Mehta, N. Kaneko, P. K. Mang, A. F. Panchula, L. Zhou, J. Arthur, and M. Greven, Phys. Rev. Lett., 87 (2001) 095502.
[55] J. Kanamori, J. Appl. Phys. 31 (1960) 14S.
[56] K. I. Kugel and D. I. Khomskii, Zh. Eksp. Teor. Fiz. 64 (1973) 1429 [Sov. Phys. JETP 37 (1973) 725].

[57] H. Kuwahara, Y. Tomioka, A. Asamitsu, Y. Moritomo, and Y. Tokura, Science 270 (1995) 961.
[58] V. Caignaert, F. Millange, M. Hervieu, E. Suard, and B. Raveau, Solid State Commun. 99 (1996) 173.
[59] C. Ritter, R. Mahendiran, M. R. Ibarra, L. Morellon, A. Maignan, B. Raveau, and C.N.R. Rao, Phys. Rev. B 61 (2000) R9229.
[60] D.C. Jiles and D.L. Atherton, J. Magn. Magn. Mater. 61 (1986) 48.
[61] J. Horvat, E. Babic, Z. Marohnic, and H. H. Liebermann, J. Magn. Magn. Mater. 87 (1990) 339.
[62] X.L. Wang, J. Horvat, H. K. Liu, and S. X. Dou, Phys. Rev. B 58 (1998) 2434.
[63] M. Muroi, R. Street, J. W. Cochrane, and G. J. Russell, Phys. Rev. B 64 (2001) 024423.

SINGLE CRYSTALS OF BILAYER MANGANITES

D. Prabhakaran and A.T. Boothroyd

Clarendon Laboratory, Department of Physics,
University of Oxford, Parks Road, Oxford OX1 3PU, UK.

1. INTRODUCTION

Transition-metal oxides are of growing interest owing to the tremendous variation in their electrical and magnetic properties [1-5]. They exhibit spectacular electronic phenomena, such as colossal magnetoresistance (CMR), metal-insulator transitions, and superconductivity [1, 6]. Extensive investigations of doped transition metal oxides with different chemical substitutions, especially involving alkaline elements, have uncovered rich phase diagrams, and have provided detailed insight into the interplay between spin, charge, orbital and lattice degrees of freedom which is behind much of the physics of these materials. This effort has had important returns from a technological point of view, such as in the areas of magnetic sensors, ferroelectric memories, and superconducting devices [2].

The most widely studied manganites are those based on the perovskite structure with the general formula $(R,A)_{n+1}Mn_nO_{3n+1}$ (R: rare earth element, A: alkaline element), often called Ruddlesden-Popper (RP) phases. In the RP compounds, 'n' represents the number of layers of vertex-shared MnO_6 octahedra stacked along the [001] direction as shown in Fig. 1. The $n = \infty$ layer $(R,A)MnO_3$ compounds have a three-dimensional perovskite-type structure. These exhibit strong CMR effects. The single layer $n = 1$ $(R,A)_2MnO_4$ compounds have the two-dimensional K_2NiF_4 type structure composed of one layer of MnO_6 octahedra separated by a layer of (R/A, O). These compounds are insulating, with antiferromagnetic, charge ordered, spin glass or mixed-phase ground states. Finally, the n = 2 bilayered $(R,A)_2Mn_2O_7$ compounds have two layers of MnO_6 octahedra separated by a layer of (R,A) cations and O anions which adopt a tetragonal crystal structure.

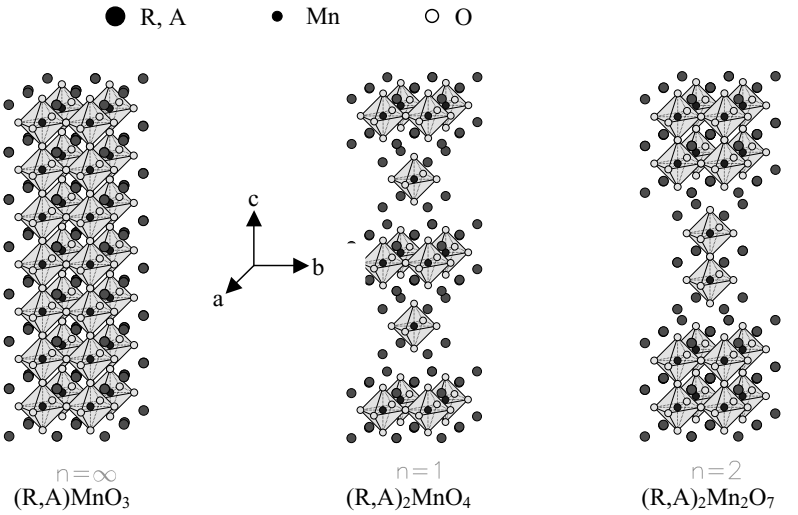

Fig.1. Schematic structures of the Ruddlesden-Popper series (layered perovskite structures) $(R,A)_{n+1}Mn_nO_{3n+1}$ (n = ∞, 1 and 2), where R and A are the trivalent rate-earth and divalent alkaline-earth ions, respectively.

This review is concerned primarily with the bilayer manganites of the form $La_{2-2x}Sr_{1+2x}Mn_2O_{7+\delta}$. For certain levels of doping (x) the application of a magnetic field to these materials causes a large reduction resistivity, a behaviour which parallels and in some cases exceeds the CMR effect observed previously in the perovskite $R_{1-x}A_xMnO_3$ phases [2]. High quality single crystal samples are indispensable for experimental investigations of the mechanisms behind CMR. Because of their high melting point, single crystals of the RP manganites have been grown either by flux [7, 8] or floating-zone [1, 9-15, 24-26, 33, 35, 38–42] techniques.

The quasi- two-dimensional structure of the bilayer manganites means they have highly anisotropic physical properties, and makes them of interest in studies of the effect of reduced dimensionality on the CMR effect. Recent interest in the doped bilayer manganite series (n = 2) stems from the observation of ferromagnetic order at temperature T_c ~100 K with an accompanying metal-insulator transition [1]. The n = 2 series exhibits a transition from a ferromagnetic (FM) metal to an antiferromagnetic insulator (AFI) with doping of alkaline metal elements on the rare earth sites [16]. Another interesting phenomena is the charge ordering (CO) which occurs for $0.4 \le x \le 0.75$ (A = Sr) [17]. Electrical and magnetic properties of the bilayer manganites have been investigated over a range of doping level ($0.3 \le x \le 0.75$) and its magnetic phase diagram have been mapped out [18]. The CMR effect is observed most clearly in the doping level $0.3 \le x \le 0.5$ [19, 20].

One of the most challenging problems in the preparation of the n = 2 compounds part is the elimination of high temperature ferromagnetic phases, generally referred to as intergrowths or extrinsic phases [21]. These are usually associated with terrace-like features in the magnetization at temperatures above 200 K. These terraces were first observed in data

from polycrystalline $La_{2-2x}Sr_{1+2x}Mn_2O_{7+\delta}$ with $x = 0.33$ by MacChesney et al. [22], who suggested they might result from the existence of long-range two-dimensional spin correlations in the paramagnetic state. Similar suggestions have been made by other authors more recently [1, 23, 24]. This idea is supported by the observation of ferromagnetic spin correlations above T_C by neutron scattering in a sample of $La_{1.2}Sr_{1.8}Mn_2O_7$ [25, 26], and by evidence for ferromagnetic clusters above T_C in $La_{1.35}Sr_{1.65}Mn_2O_7$ from electron-spin resonance [27]. On the other hand, Heffner et al. did not detect the expected in-plane spin correlations in a crystal of $La_{1.4}Sr_{1.6}Mn_2O_7$ by muon-spin rotation [28].

The principal magnetic features are illustrated in Figs. 2(a) and 2(b), which show the magnetization of a single crystal of $La_{1.3}S_{1.7}Mn_2O_{7+\delta}$ measured with a field of 5 Oe applied parallel ($H \parallel ab$) and perpendicular ($H \parallel c$) to the layers. The sharp rise in magnetization below T_C = 130 K is the bulk ferromagnetic ordering transition. Above 130 K the magnetization has a broad terrace sloping down towards 250 K. On the high temperature edge of the terrace a number of small steps can be seen extending up to 360 K as shown in in the inserts to Figs. 2(a) and 2(b).

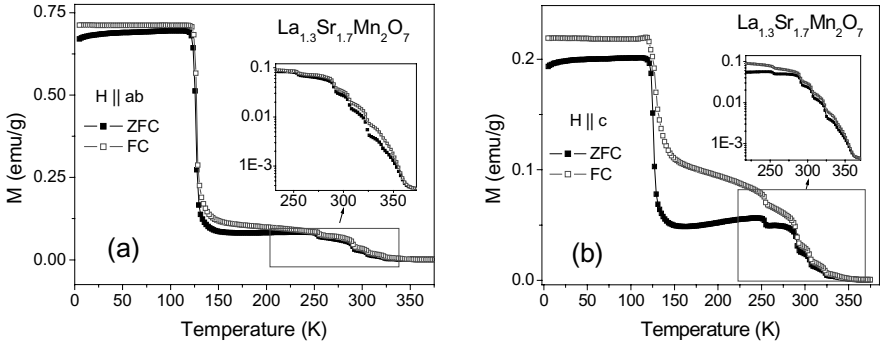

Fig. 2. Magnetization of a $La_{1.3}Sr_{1.7}Mn_2O_7$ single crystal as a function of temperature, measured with an applied field of 5 Oe aligned with (a) $H \parallel ab$ and (b) $H \parallel c$. The inserts show the detail of the step-like features on a log scale.

Notice that the value of the magnetization in the high temperature region (220 K – 360 K) is nearly the same for both $H \parallel ab$ and $H \parallel c$. Below the ferromagnetic transition temperature, T_C = 130 K, however, there is a very strong anisotropy.

An entirely different explanation for magnetization terrace observed above T_C was proposed by the Argonne group [29-31]. Following the earlier observations [32] of intergrowths of $(La,Sr)_{n+1}Mn_nO_{3n+1}$ phases with $n > 2$, Potter et al. [30] suggested that the high-temperature magnetization terrace arises not only from short-range ferromagnetic spin order intrinsic to the $n = 2$ host material, but instead from an extrinsic ferromagnetic contribution associated with $n > 2$ intergrowth layers. The existence of intergrowths with several different 'n' values in the same sample could then also explain the step-like fine structure observed at temperatures above 200 K. This suggestion was also supported by Moreno et al. [33] who observed new ferromagnetic resonances in the electron paramagnetic

resonance (EPR) signal above T_C. On the other hand, a different proposal for an intrinsic origin of the steps was put forward by Wu et al. [34] who argued that it arose from charge ordering and a series of Mn spin reorientation transitions in the Mn–O layers.

The potential of $La_{2-2x}Sr_{1+2x}Mn_2O_{7+\delta}$ compounds in technological applications makes it important to correlate the extrinsic intergrowth phases with the physical properties of these materials, and to learn how to control the microstructure. A number of such studies have been published. Moreno et al. [33] reported that the amount of extrinsic phases in single crystals grown by the floating-zone method increased as the growth rate increased. Floating-zone crystal growth parameters were also studied by Velazquez et al, [35, 36] who in addition investigated the effect of partial substitution of Ca for Sr. It is observed that excess oxygen in the system can change the resistivity and CO transition temperature [37, 38], and so very controlled conditions are needed to prepare good quality samples.

Growth of single crystals by the floating-zone method has reported by several groups [1, 24-26, 33, 35, 38–42], but in most of the cases crystal growth has been performed in flowing gas at ambient pressure. Since the manganites have a high melting point special attention is needed to overcome the problem of evaporation during crystal growth. The Mn evaporation during crystal growth in the perovskite structure manganite was compensated by adding excess amount of Mn and by growing under several atmospheres pressure [12]. Good quality crystals have been grown this way. Evaporation during crystal growth of the two-layered (n = 2) manganite has not been discussed so far, and little effort has been made to grow single crystals of free of the extrinsic phase.

Here we report crystal growth and magnetization measurements on crystals of $La_{2-2x}Sr_{1+2x}Mn_2O_{7+\delta}$, in particular x = 0.35, grown under different conditions by the floating-zone method. The composition x = 0.35 was chosen as a focus because it has almost the highest ferromagnetic ordering transition temperature T_C of the series [43]. We also pay attention to the composition x = 0.45, which shows both ferromagnetic (FM) and charge ordering (CO) under different growth conditions. Crystals with $0.5 \leq x \leq 0.6$ have also been grown under oxygen pressure and we examine some of their properties, especially the CO temperature. Our aim was to study what effect different preparation conditions have on the magnetic features describes above. This work differs from previous single crystal studies in that crystal growth was carried out in a high pressure atmosphere as well as under ambient conditions. We were encouraged to experiment with high pressure after work on the $La_{1-x}Sr_xMnO_3$ system had shown that high pressure growth could improve the quality of the crystals [12]. Here we describe investigations on the effects of varying the atmospheric composition during crystal growth, and of post-annealing the crystals. For reference, we also performed annealing studies on polycrystalline (crystal powder) sample to study how the physical properties change with oxygen content [37, 44]. A number of other experimental studies performed on the crystals are reported elsewhere [45-49].

2. EXPERIMENTAL DETAILS

Polycrystalline samples of nominal composition $La_{2-2x}Sr_{1+2x}Mn_2O_7$ (x = 0.3–0.6) were prepared by the conventional solid state reaction technique using high purity (>99.99%) powders of La_2O_3, $SrCO_3$ and MnO_2. Pre-heating of La_2O_3 at 1100^{o}C for 12h and drying of the other chemicals before weighing is necessary to achieve good stochiometry. The mixed

powders were sintered at three different temperatures 1300^{o}C, 1400^{o}C and 1500^{o}C respectively for 48h with intermediate grinding. After confirming the single phase purity, cylindrical rods of size 10–12 mm diameter and 120 mm length were prepared using a cold hydraulic press, and subsequently sintered at 1550^{o}C for 6 h in a vertical sintering furnace.

Crystals were grown in a controlled atmosphere using an optical floating-zone furnace (Crystal Systems Inc.,). The growth rate was between 5 mm/h and 7 mm/h with 40 rpm counter rotation of the seed and feed rods. The grown crystals were analysed using powder and Laue X-ray diffraction (XRD) patterns and magnetic measurements were performed on rectangular-shaped crystals of approximate size 3x4x2 mm^3 with a SQUID magnetometer (Quantum Design). A small measuring field (H = 5 Oe) was applied either parallel to the *ab* plane ($H \parallel ab$) or parallel to the *c* axis ($H \parallel c$). DC magnetization was collected both while cooling in the measuring field (FC) and while heating after cooling in zero field (ZFC). Scans of the magnetization as a function of applied field were performed at a number of fixed temperatures, and AC susceptibility measurements were carried out with 999.7 Hz frequency in a static field of strength 3 Oe.

To illustrate the effects of using different atmospheres in the crystal growth process we report results for the $La_{1.3}Sr_{1.7}Mn_2O_{7+\delta}$ (x = 0.35) composition in detail. For the remaining compositions we report results only from crystals grown under optimum conditions. Crystals of x = 0.35 were melt-grown either (A) in a flow of air at ambient pressure, (B) in an oxygen-rich (O_2:Ar = 3:1) pressurized atmosphere (~8 atm), or (C) in an argon-rich (O_2:Ar = 1:30) pressurized atmosphere. We denote crystals grown under these three conditions by A, B and C respectively. The phase purity of the crystals was checked by powder x-ray diffraction (XRD) and electron probe micro-analysis (EPMA). After growth, crystals A and C were subject to annealing at 1000^{o}C for 15 h in a flow of argon (20 cc/min.) and oxygen (20 cc/min.) respectively. In addition, parts of the as-grown crystals were ground and subject to the same annealing treatment, and likewise for a batch of the polycrystalline starting powder.

3. RESULTS AND DISCUSSION

3.1 x = 0.35

We begin by describing our experiments on crystal growth of $La_{1.3}Sr_{1.7}Mn_2O_7$ under different atmospheric conditions. First we tried with ambient pressure and a flow of different gases (air, argon and oxygen) at the rate of 200 ml/min. With air, we were able to get many platelets of very shiny crystals grown parallel to the growth axis of the rod, but formation of a single grain was very difficult even after 70 mm length of growth. The same result was found when oxygen flow was used, except that we observed a noticeable change in between the grain boundaries with the appearance of a dull gray film coating. This coating separates the gains and it leads to macro-crack formation when the growing crystal was cooled from high temperature. We have observed some changes in the physical properties of the grown crystal, especially magnetic properties, and these will be explained in the later.

Following these studies, we experimented with a flowing mixture of Ar and O_2 (30%). In order to control and to have uniform oxygen content in the growing crystal we opted for a slow growth rate (3-4 mm/h). Even though we were able to get strain-free, good-quality single crystals, evaporation from the melt caused the inside of the quartz tube to be covered with a

thin coating which blocked the passage of light and prevented us from scanning more than a few centimetre length.

Later we used a high pressure (up to 8 atm) atmosphere comprising either pure Ar or mixed gases (Ar+O_2), and grew the crystals at a speed of 5–6 mm/h. One such grown boule is shown in Fig. 3(a). With these conditions we were able to run the experiment for longer period without any evaporation problem, and were also able to obtain single crystals of size up to 60 mm length and 9 mm diameter. We have observed two facets after a few centimetre length of growth from the polycrystalline seed rod. The growth direction of the crystal rods was found to be parallel to the *ab* plane. One of the crystals was examined by neutron Laue diffraction (Fig. 3(b)) and the sharp diffraction spots indicated good crystalline quality. Another noticeable observation we made was that the feed material started reacting with the atmosphere for the higher Sr content materials. To overcome this problem we changed the proportions of Ar and O_2 (O_2 rich atmosphere up to 97% with increase of Sr doping) and growth was then found to be stable. A single crystal seed was also used for the crystal growth. Seeding improved the single crystal size, but due to the appearance of micro-cracks in the seed during heating macro cracks appeared in the grown crystal. These caused the grown crystal to cleave. The feed rod was pre-densified by an initial at a faster growth rate ~12–20 mm/h. This pre-densification was necessary for the higher Sr doped ($x > 0.45$) bilayer manganites, as well as one-layer manganites.

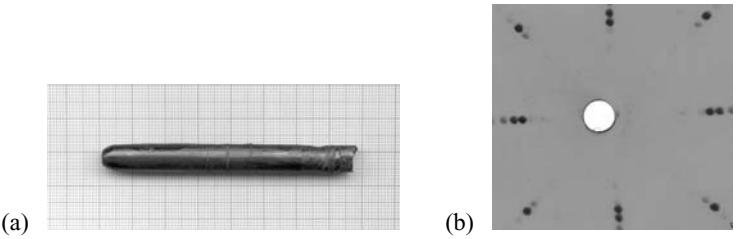

Fig. 3. (**a**) As grown $La_{1.4}Sr_{1.6}Mn_2O_7$ crystal rod (**b**) Neutron Laue pattern of $La_{1.3}Sr_{1.85}Mn_2O_7$ crystal.

X-ray diffraction (XRD) characterization on powdered crystals confirmed that the crystals were single phase, without any traceable impurity. The crystals were found to be tetragonal, and the XRD lattice parameters are listed in Table 1. The values for the starting powder are consistent with those in the literature [37, 50] but, the *a* parameter value of the crystals are systematically smaller (by 0.003–0.006 Å) than the value for the polycrystalline sample. Among the crystals, the *a* parameter value increases systematically with increasing proportion of oxygen in the growth atmosphere, while the *c* parameter decreases. This variation is consistent with that observed for polycrystalline $La_{1.4}Sr_{1.6}Mn_2O_{7+\delta}$ annealed under different conditions [50], but is opposite to what is observed for polycrystalline $La_{1.2}Sr_{1.8}Mn_2O_{7+\delta}$ [37]. If we assume that the cell parameters of $La_{1.3}Sr_{1.7}Mn_2O_{7+\delta}$ have the same dependence on oxygen content as $La_{1.4}Sr_{1.6}Mn_2O_{7+\delta}$ and that the polycrystalline sample is stoichiometric in oxygen ($\delta = 0$), then this indicates that all our crystals are slightly oxygen-deficient with 'δ' in the range –0.02 to –0.04. The structure will change from tetragonal to orthorhombic by decreasing δ= –0.27 [37]. The value of the *c* axis decreases systematically with increasing proportion of Sr content in the crystal and are shown in Fig.3(c).

Table 1. Lattice parameter values of polycrystalline and single crystal samples.

Sample	Lattice parameters (Å)		c/a
	a	c	ratio
Starting powder (Polycrystalline)	3.8696	20.2434	5.2314
Crystal A (Air flow)	3.8630	20.2255	5.2357
Crystal B (O_2 rich pressure)	3.8659	20.2185	5.3000
Crystal C (Ar rich pressure)	3.8622	20.2507	5.2433

The chemical composition of some crystals was checked by EPMA and found to be constant within a single grain (Sr content variation - ±0.02), but varied between crystals grown under similar conditions (maximum Sr content variation - ±0.04).

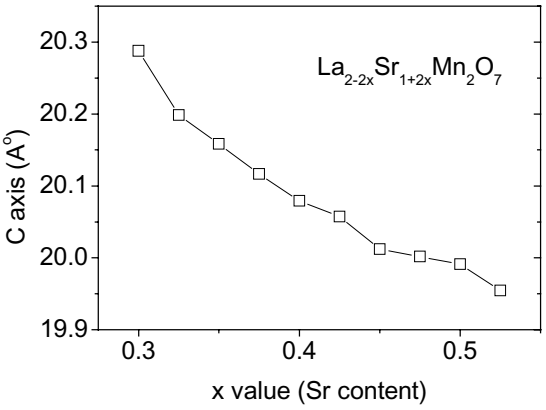

Fig. 3.(c). Variation of the *c* axis lattice parameter with Sr content *x* in $La_{2-2x}Sr_{1+2x}Mn_2O_7$.

The magnetization M of the bilayer manganites is very sensitive to the magnitude of the applied *dc* field *H* [30, 33]. This property is illustrated in Fig. 4, which shows the ratio *M*/*H* measured on crystal A at four different applied fields over the temperature range 220 K to 350 K. At an applied field of 5 Oe one can clearly see the sequence of steps on the downslope of the terrace, but as H increases *M*/*H* is strongly reduced and the steps become smeared out. Therefore, in order to study the high temperature magnetization most of our measurements were made in low field (<10 Oe).

Figs. 5(a) and (b) show the temperature dependence of the magnetization of crystals A, B and C measured over the temperature range 2 K to 375 K in a field of 5 Oe applied parallel and perpendicular to the layers, respectively. For $H \parallel ab$, crystals A and B show very sharp ferromagnetic transitions at $T_C = 130 \pm 2$ K with virtually no difference between FC and ZFC measurements over the whole temperature range. The value of T_C found here is in agreement with previous single crystal data [43], but is ~5 K higher than the values reported for a single crystal grown under oxygen flow [51] as well as polycrystalline samples [50]. At higher temperatures crystals A and B both show an extended terrace with six discrete steps at 253 K, 290 K, 306 K, 320 K, 340 K and 360 K (the same for both A and B).

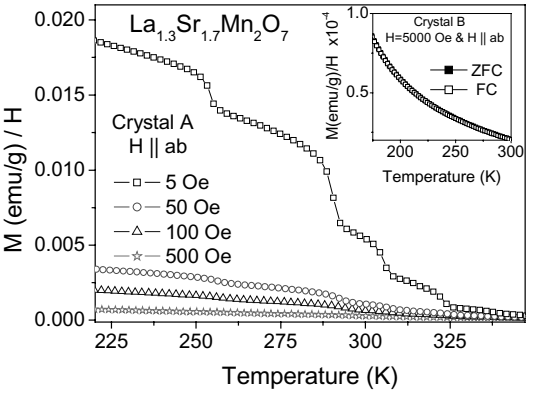

Fig. 4. Temperature variation of M/H for $La_{1.3}Sr_{1.7}Mn_2O_{7+\delta}$ ($H \parallel ab$) single crystal A under different applied fields. The insert shows M/H for crystal B in high field (H = 5000 Oe)

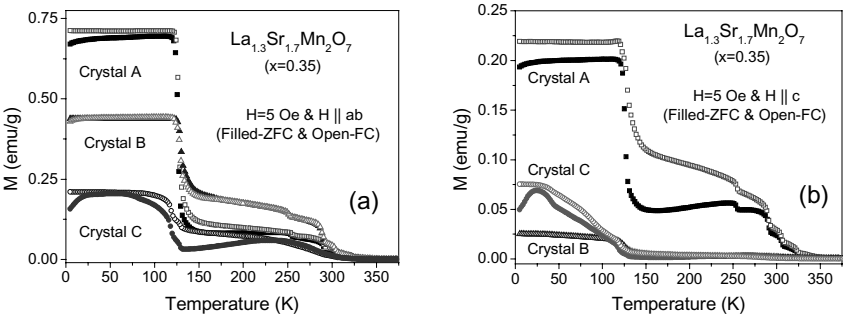

Fig. 5. Temperature dependence of magnetization for $La_{1.3}Sr_{1.7}Mn_2O_7$ single crystal with an applied field of H = 5 Oe along (**a**) $H \parallel ab$ and (**b**) $H \parallel c$.

The 360 K step marks the onset of the terrace. Crystal C exhibits a broader ferromagnetic transition, and a clear difference between FC and ZFC runs is observed below ~ 250 K. Over the whole temperature range the magnetization of C is smaller than that of A and B, and the steps are almost entirely smeared out. Below T_C the magnetization becomes nearly constant for $H \parallel ab$ (Fig. 5(a)), with M(A) > M(B) > M(C). Below ~20 K there is a small drop in the ZFC M data for all three crystals.

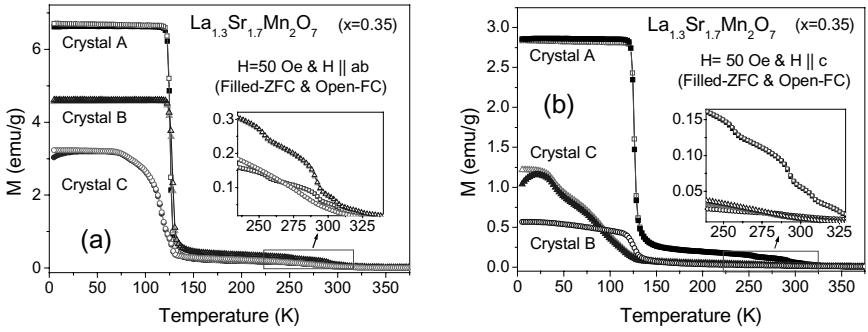

Fig. 6. Temperature dependence of the magnetization of the $La_{1.3}Sr_{1.7}Mn_2O_7$ single crystals with a field of $H = 50$ Oe applied (**a**) $H \parallel ab$ and (**b**) $H \parallel c$.

For the data taken with $H \parallel c$ (Fig. 5(b)) the terrace region is very prominent relative to the ferromagnetic signal for crystal A, but much less prominent for crystals B and C. The ferromagnetic transition is now extremely broad in crystal C, and the magnitude of M below T_C appears in the order $M(A) > M(C) > M(B)$. In the terrace region M is much larger for A (by an order of magnitude) than for B or C. All the crystals exhibit a magnetization that is larger for $H \parallel ab$ than $H \parallel c$, confirming the easy-plane anisotropy of the Mn spins. As just mentioned, crystal C does not exhibit a sharp transition at T_C in Figs. 5(a) & 5(b). Indeed, the data show anomalies at 40 K, 75 K and 120 K, as well as 130 K. The latter two are suggestive of two ferromagnetic transitions. To demonstrate the field dependence of the high temperature steps all three crystals were studied under a 50 Oe applied field and the magnetization versus temperature curve for both $H \parallel ab$ and $H \parallel c$ are shown in Figs. 6(a) & 6(b) respectively. Notice that crystal A has a very sharp ferromagnetic transition, and that the high temperature magnetization terrace/steps has been suppressed relative to the ferromagnetic signal with only a small increase in applied field. The difference between ZFC and FC anomaly for all the crystals has almost disappeared under the 50 Oe applied field.

Ac susceptibility studies have been used to investigate the competition between different kinds of magnetic interactions using the frequency dependence [32]. We next present more detailed investigations into the terrace steps region. Figs. 7(a) and 7(b) show the in-phase component of the *ac* susceptibility of the three crystals measured with $H_{ac} \parallel ab$ and $H_{ac} \parallel c$ respectively. For these measurements there was no DC field, and the steps are now very clear in both orientations, but particularly with $H_{ac} \parallel c$ where they appear as peaks. Interestingly, the signal is nearly two orders of magnitude smaller when $H_{ac} \parallel c$ than when $H_{ac} \parallel ab$. These data confirm that the steps occur at the same temperatures for A and B, but reveal in addition broad and weak steps in the data for C approximately coincident with those of A and B.

In order to study the effect of annealing, the crystals were heated under different atmospheres at 1000°C for 15 h. Crystal A (grown in air flow) was annealed under Ar flow, and crystal C (grown in Ar-rich atmosphere) was annealed under O_2 flow. The temperature dependence of the magnetization for the annealed crystals is shown in Fig 8(a). The magnetization of Ar-annealed crystal A decreased slightly after annealing, but the

magnetization steps remained. On the other hand, magnetization steps appeared after annealing crystal C in oxygen, even though they were not initially present. This observation suggests that oxygen plays a role in the formation of the magnetization steps, although annealing in Ar does not remove the steps.

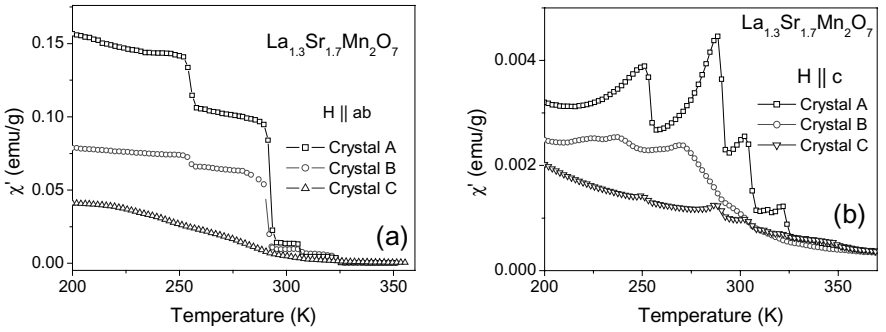

Fig. 7. Temperature dependence of the in-phase component of the *ac* susceptibility of $La_{1.3}Sr_{1.7}Mn_2O_7$ measured in zero static field, with (**a**) $H_{ac} \parallel ab$ and (**b**) $H_{ac} \parallel c$.

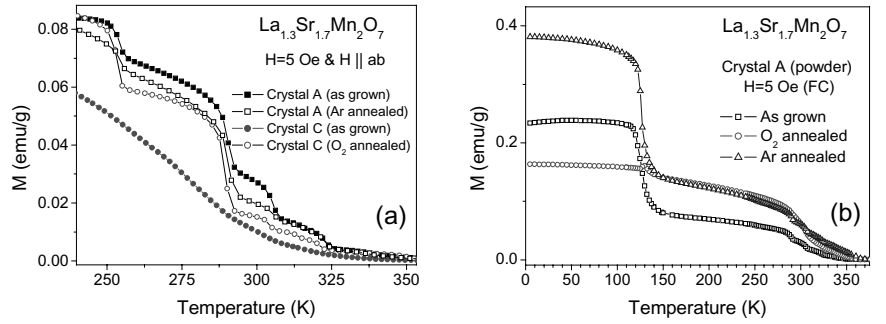

Fig. 8. Temperature dependent magnetisation of $La_{1.3}Sr_{1.7}Mn_2O_7$ measured with an applied field of 5 Oe. (**a**) annealed crystals A and C, (**b**) annealed crystal A powdered.

Annealing single crystals does not always guarantee a uniform change in oxygen content because of the small surface area to volume ratio of crystals. To study the behaviour of the crystals grown under difference atmosphere and with different heat treatments we powdered all the three crystals and annealed at 1000^{o}C for 15 h under both oxygen and argon flow. Magnetisation measurements for all the powdered crystals were carried out in the FC mode under 5 Oe applied field. In the case of crystal A (powder), annealed under Ar the magnetisation value increased nearly 25% as that of as grown as shown in Fig 8(b). The rapid change in the magnetization may be due to the removal of oxygen from the large surface area of the powder particles. The oxygen-annealed crystal A powder showed a very weak

ferromagnetic transition at 130 K which indicates that over doping with oxygen may destroy the ferromagnetic effect. This effect may be similar to the hole doping. However, the extrinsic phase magnetization steps were found to be the same for the O_2 and Ar annealed crystal A powders. The temperature dependence of powdered samples of crystals B and C are shown in Figs. 9(a) and (b), respectively. After annealing in Ar, the magnetization of powdered crystal B increased by about ~25% consistent with crystal A. Unlike crystal A, however, the ferromagnetic transition of powdered crystal B does not change much after annealing in oxygen. In contrast to samples A and B, sample C (Fig. 9(b)) annealed under both oxygen and Ar shows huge increases in the magnetization above T_C, and a smaller increase in magnetization below T_C. Notice that terrace steps are evident in the magnetization of the unannealed powdered crystal C (Fig. 9(b)), but were not present in the data for the original crystal (Fig. 5(a)). This indicates that the surface area of the sample may also have a strong influence on the formation of the extrinsic phase.

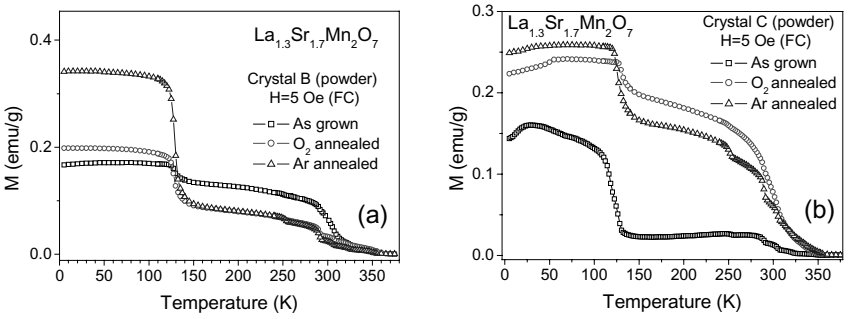

Fig. 9. Temperature dependent magnetization of $La_{1.3}Sr_{1.7}Mn_2O_7$ measured in an applied field of 5 Oe for the (**a**) annealed crystal B powder and (**b**) annealed crystal C powder.

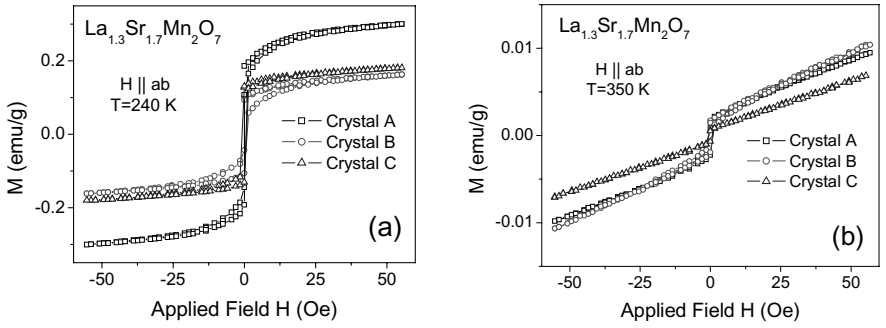

Figs. 10. Magnetic hysteresis curves of $La_{1.3}Sr_{1.7}Mn_2O_7$ crystals measured with $H \parallel ab$ at (**a**) 240 K and (**b**) 350 K, respectively.

To learn more about the field dependence in the terrace region we measured $M(H)$ loops at two different temperatures, 240 K and 350 K, for both field directions, $H \parallel ab$ and $H \parallel c$. The results are shown in Figs. 10 and 11. In all cases there is a jump on crossing $H = 0$ indicating a ferromagnetic reversal. At 240 K the *ab* plane magnetization saturates on application of relatively small fields ~10 Oe. The *c* axis magnetization is an order of magnitude smaller and does not saturate in the measured field range. All the curves exhibit a degree of hysteresis, but the effect is most pronounced for crystal A. Crystal C exhibits very little hysteresis. At 350 K the magnetization is of similar magnitude for $H \parallel ab$ and $H \parallel c$, and is almost linear in field apart from the jump at $H = 0$.

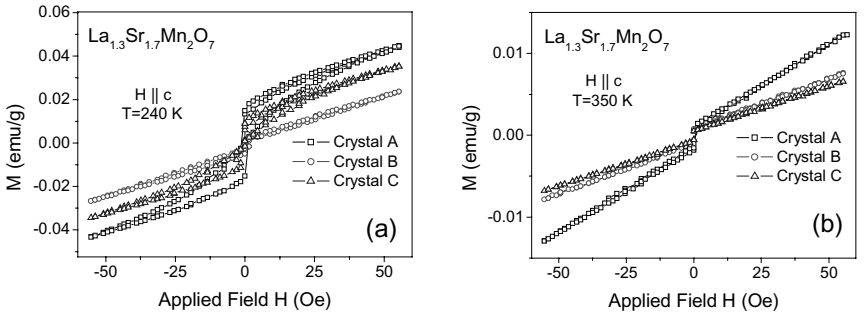

Figs. 11. Magnetic hysteresis curves of $La_{1.3}Sr_{1.7}Mn_2O_7$ crystals measured with $H \parallel c$ at (**a**) 240 K and (**b**) 350 K, respectively.

3.2 $x = 0.45$

We will now discuss some results obtained on crystals with higher Sr doping. For doping levels above $x \sim 0.4$ the planar FM-I structure begins to be affected by an intra-bilayer AFM coupling. For $x \geq 0.39$ two magnetic phases have been observed. On cooling below room temperature a transition is first observed to the AFM-I structure, and then at a lower temperature second magnetic transition is observed to a canted magnetic structure [52]. However, there is very little experimental data available in the crossover region between FM and AFM behaviour.

In order to study this composition region we prepared crystals with $x = 0.45$. We grew crystals under 6 atm pressure in two different growth atmospheres, argon (Ar) and 15% oxygen mixed with Ar (Ar/O_2). The grown crystals were a few millimetres in length, and the molten zone was unstable for lower pulling rates (< 6 mm/h). To improve the size of the crystal, pre-densified feed rods (12–20 mm/h) were employed. The powder XRD shows that the *c* axis value of the Ar crystal (c = 19.9893 Å) was slightly high compared to the Ar/O_2 (c = 19.9713 Å) crystal.

The magnetization of the $x = 0.45$ crystals exhibits strong differences compared with the $x = 0.35$ crystals. Figure 12(a) shows the temperature dependence of the *ac* susceptibility of both the Ar and the Ar/O_2 crystals of $La_{1.1}Sr_{1.9}Mn_2O_7$ ($x = 0.45$) measured with $H \parallel ab$ and $H \parallel c$ (shown in the insert). For the Ar/O_2 crystal the data indicate successive AFM (T_N = 230 K) and canted FM (T_C ~110 K) transitions. The magnetization is one order of magnitude

larger for $H \parallel ab$ compared with $H \parallel c$, consistent with the ordered moments lying in the *ab* plane. Notice that the extrinsic phase terrace is present for both field orientations of the Ar/O_2 crystal starting at around 330 K, but there is not the succession of steps at around room temperature that were seen in the $x = 0.35$ crystal (Fig 5(a)). The susceptibility of the Ar-grown crystal is considerably smaller than that of the Ar/O_2 crystal. This may be a result of the lower oxygen content in the Ar crystal. Another difference is that the FM transition temperature has moved to a lower temperature (T_C ~75 K). At higher temperatures there are several features, which might indicate more than one AFM transition.

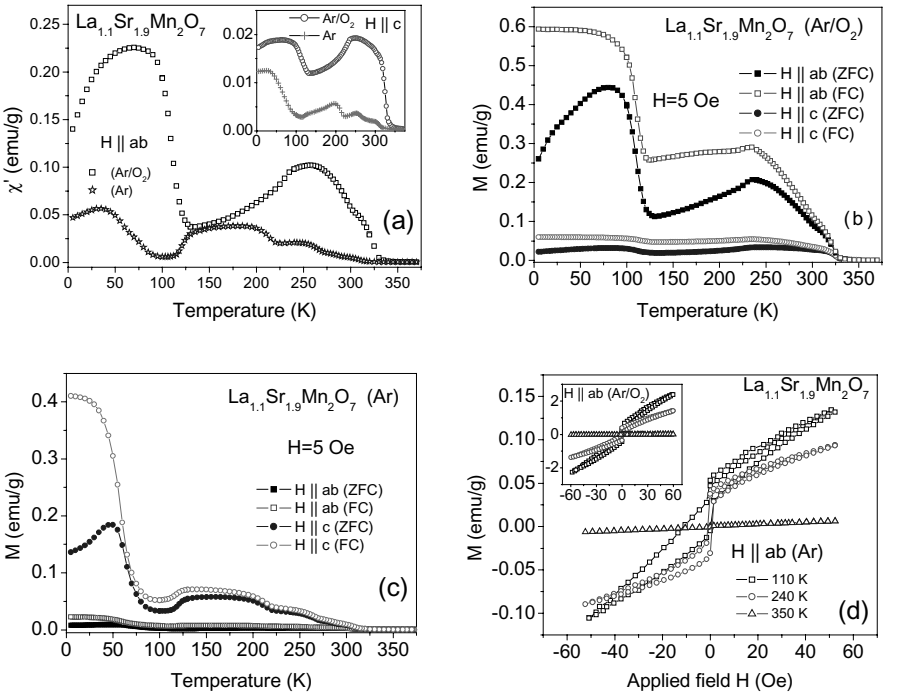

Fig. 12. (**a**) Temperature dependence of the *ac* susceptibility of $La_{1.1}Sr_{1.9}Mn_2O_7$ crystals grown in Ar and Ar/O_2 high pressure atmospheres. Main frame $H_{ac} \parallel ab$, insert $H_{ac} \parallel c$. *Dc* magnetization of the Ar/O_2 crystal. (**c**) *dc* magnetization of the Ar crystal and (**d**) *Dc* magnetization as a function of field ($H \| ab$) for the Ar crystal (main frame) and for the Ar/O_2 crystal (insert).

The temperature dependence of the *dc* magnetisation (ZFC and FC) of $La_{1.1}Sr_{1.9}Mn_2O_7$ with $H \parallel ab$ and $H \parallel c$ is shown in Fig. 12(b) for the Ar/O_2 grown crystal, and in Fig. 12(c) for the Ar grown crystal. For both crystals there is a large difference between the FC and ZFC magnetization. This difference could be the result of disorder in the stacking as the AFM order as it propagates along the *c* axis, due to competition between FM and AFM interactions between the Mn–O sheets [54]. For the Ar crystal, the FC–ZFC difference is

larger in the canted FM phase, but smaller in the AFM-I phase, relative to the Ar/O_2 crystal. This observation suggests that oxygen deficiency tends to stabilize the AFM phase, which could account for the lower FM transition temperature of the Ar crystal relative to the Ar/O_2 crystal. Figure 12(d) shows *M*/*H* loops for the two crystals measured at 110 K, 240 K, and 350 K. At 350 K the magnetization is linear with field, but at the lower temperatures the curves show hysteresis and a jump in *M* at *H* = 0 indicative of FM behaviour. Since there is no bulk FM at 240 K we associate the weak FM behaviour at this temperature with the same extrinsic phases that produced the magnetization terrace/steps in the $x = 0.35$ crystal.

3.3 $x = 0.5 – 0.6$

Due to the low viscosity of the molten zone, it has only been possible to grow small platelet crystals with $x \geq 0.5$. Crystals of a few mm in size can be cleaved easily from the grown boule. Charge ordering (CO) and orbital ordering (OO) are characteristic futures for $x \geq 0.5$. Generally, charge ordering is defined as the ordering of the metal ions in different oxidation states in specific lattice sties of a mixed valent materials, in this case Mn^{3+}/Mn^{4+}. FM behaviour has completely disappeared in this more highly doped range.

The temperature dependence of the *ac* susceptibility of $La_{2-2x}Sr_{1+2x}Mn_2O_7$ ($0.5 \leq x \leq 0.6$) in zero static field is given in Figs. 13(a) and 13(b) for $H \parallel ab$ and $H \parallel c$, respectively. From synchrotron x-ray studies [53] it has been established that the $x = 0.5$ crystals exhibits mixed CO/OO below ~230 K, and A-type AFM ordering below T_N ~200 K [19]. Direct evidence of the CO state has also been reported using low temperature transmission electron microscopy (TEM) [17]. Therefore, we associate the CO/OO transition with the steep rise in magnetization around 230 K and the antiferromagnetic transition with the sharp drop in magnetization around 200 K. We find that the CO/OO transition temperature reaches a maximum of ~250 K for $x = 0.55$, and decreases to ~225 K for x=0.6. On the other hand, the AFM transition becomes difficult to locate in the susceptibility for $x \geq 0.55$. Broad transition have seen for the x=0.525 crystal in H $\parallel$ *c* axis but, the magnitude was one order less compared to H $\parallel$ *ab* plane.

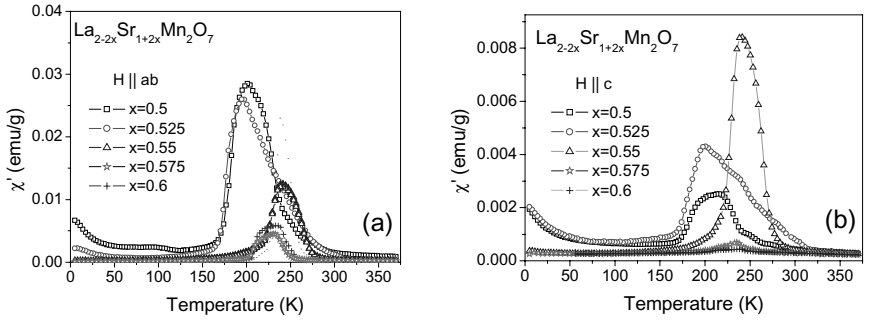

Fig. 13. Temperature dependence of the *ac* susceptibility of $La_{2-2x}Sr_{1+2x}Mn_2O_7$ ($0.5 \leq x \leq 0.6$) measured in a field of 3 Oe with (**a**) $H \parallel ab$ and (**b**) $H \parallel c$.

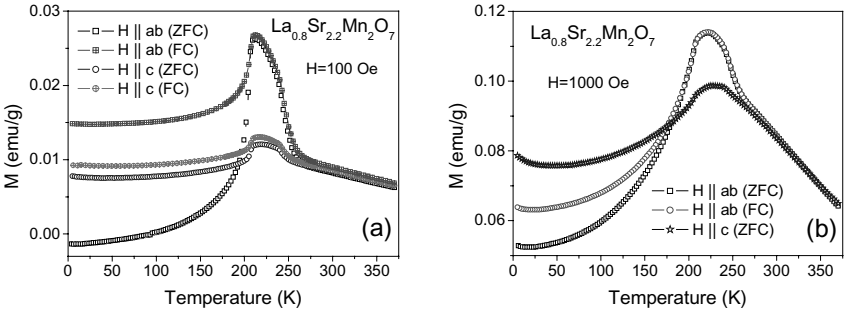

Fig. 14. Temperature dependence of magnetisation of $La_{0.8}Sr_{2.2}Mn_2O_7$ measured along $H \parallel ab$ and $H \parallel c$ in an applied fields of (**a**) 100 Oe and (**b**) 1000 Oe respectively.

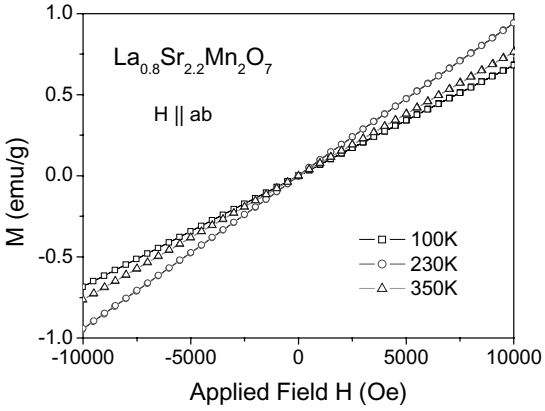

Fig. 15. Magnetisation versus applied field for $La_{0.8}Sr_{2.2.}Mn_2O_7$ with $H \parallel ab$ and $H \parallel c$ measured at different temperatures.

Figure 14 shows magnetization data for the crystal with $x = 0.6$. In Fig. 14(a) a large difference between ZFC and FC is observed below 200 K for $H \parallel ab$. This suggests the system enters a glassy magnetic state. The effect is reduced in larger fields, as shown in Fig. 14(b).

Figure 15 shows the magnetization as a function of applied field ($H \parallel ab$) for the crystal with $x = 0.6$. In contrast with the behaviour at $x = 0.45$ (Fig. 12(d)) and below (Figs. 10 and 11) we see that this crystal does not exhibit any FM behaviour, even at 100 K. This is expected since at $x = 0.6$ there is no canted FM phase, but it also shows that the weak FM signal from the extrinsic phase is now entirely absent.

4. CONCLUSIONS

Single crystals of $La_{2-2x}Sr_{1+2x}Mn_2O_7$ have been successfully grown under different controlled atmospheres. Ar rich atmosphere during growth have found to be an advantage to reduce the extrinsic phase. The use of a high pressure oxygen growth atmosphere helps to grow higher Sr ($x > 0.5$) doped crystal. The magnetic properties of the crystals were carefully studied under very low applied magnetic field, which brings out some subtle effects. Crystals that exhibit bulk ferromagnetism, or canted ferromagnetism also exhibit a magnetization terrace above T_C with discrete steps on the high temperature side. We have found weak ferromagnetic behaviour over the whole magnetization terrace up to 350 K. The origin of the steps is still not clear, but we have found that their appearance changes markedly with the crystal growth conditions. We do not observe this terrace/step feature for crystals with $x > 0.5$, so their existence seems to correlate with the presence of the ferromagnetic/canted ferromagnetic phase.

Magnetic measurements on crystals grown in different atmospheres, as well as on post-annealed crystals and powdered crystals, indicate that the ferromagnetic properties of $La_{2-2x}Sr_{1+2x}Mn_2O_7$ are sensitive to oxygen content, both in the bulk ferromagnetic phase below T_C and at temperatures above T_C where the magnetization terrace and steps are observed. A quantitative analysis of the oxygen content of annealed samples would be very useful to correlate the change in behaviour with oxygen content. Crystals have been prepared so far up to doping levels of $x = 0.6$. It will be interesting to continue to higher doping levels, where measurements on polycrystalline samples indicate a region of the phase diagram lacking in long range charge and magnetic order.

ACKNOWLEDGMENT

We would like to thank Fred Wondre, Norman Charnley and Shamima Chaudhury for help with the crystal characterization. We are grateful to the Engineering and Physical Sciences Research Council of Great Britain for financial support.

REFERENCES

[1] Y. Moritomo, A. Asamitsu, H. Kuwahara and Y. Tokura, Nature 380 (1996) 141.
[2] C.N.R. Rao, A.K. Cheetham and R. Mahesh, Chem. Mater. 8 (1996) 2421.
[3] C.H. Chen, S.-W. Cheong and A. S. Cooper, Phys. Rev. Lett. 71 (1993) 2461.
[4] K. Asai, O. Yokokura, N. Nishimori, H. Chou, J.M. Tranquada, G. Shirane, S. Higuchi, Y. Okajima and K. Kohn, Phys. Rev. B 50 (1994) 3025.
[5] K. Takada, H. Sakurai, E.T. Muromachi, F. Izumi, R.A. Dilanian, and T. Sasaki, Nature 422 (2003) 53.
[6] M.A. Senaris-Rodriguez and J.B. Goodenough, J. Solid State Chem. 118 (1995) 323.
[7] B. M. Wanklyn J. Mater. Sci. 7 (1972) 813.
[8] B.X. Gu, S.Y. Zhang, H.C. Zhang and B.G. Shen, J. Magn. Magn. Mater. 204 (1999) 45.
[9] T. Hashimoto, N. Ishizawa, N. Mizutani and M. Kato, J. Crystal Growth 84 (1987) 207.
[10] A. Urushibara, Y. Moritomo, T. Arima, A. Asamitsu, G. Kido and Y. Tokura, Phys. Rev. B 51 (1995) 14103.
[11] D. Shulyatev, S. Karabashev, A. Arsenov and Ya. Mukovskii, J. Crystal Growth 198/199 (1999) 511.
[12] D. Prabhakaran, A.I. Coldea, A.T. Boothroyd and S.J. Blundell, J. Crystal Growth 237-239 (2002) 806.
[13] Y. Moritomo, Y. Tomioka, A. Asamitsu, Y. Tokura and Y. Matsui, Phys. Rev. B 51 (1995) 3297.
[14] P. Reutler, O. Friedt, B. Buchner, M. Braden and A. Revcolevschi, J. Crystal Growth 249 (2003) 222.
[15] T. Kimura, K. Hatsuda, Y. Ueno, R. Kajimoto, H. Mochizuki, H. Yoshizawa, T.Nagai, Y. Matsui, A. Yamazaki and Y. Tokura, Phys. Rev. B 65 (2001) 20407.
[16] J.F. Mitchell, D.N. Argyriou, A. Berger, K.E. Gray, R. Osborn and U. Welp, J. Phys. Chem. 105 (2001) 10731.
[17] J.Q. Li, C. Dong, L.H. Liu and Y.M. Ni, Phys. Rev. B 64 (2001) 174413.
[18] J. Dho, W.S. Kim, H.S. Choi, E.O. Chi and N.H. Hur, J. Phys.: Condens. Matter 13 (2001) 3655.
[19] C.D. Ling, J.E. Millburn, J.F. Mitchell. D.N. Argyriou, J. Linton and H.N. Bordallo, Phys. Rev. B 62 (2000) 15096.
[20] N.H. Hur, J.T. Kim, K.H. Yoo, Y.K. Park, J.C. Park, E.O. Chi and Y.U. Kwon, Phys. Rev. B 57 (1998) 10740.
[21] W.S. Kim, H.S. Choi, B.C. Nam, E.O.Chi, K.W. Lee and N.H. Hur, Phys. Stat. Sol. (a) 185 (2001) 401.
[22] J.B. MacChesney, J.F. Potter and R.C. Sherwood, J. Appl. Phys. 40 (1969) 1243.
[23] T. Kimura, Y. Tomioka, H. Kuwahara, A. Asamitsu, M. Tamura, and Y. Tokura, Science 274 (1996) 1698.
[24] T. Kimura, A. Asamitsu, Y. Tomioka, and Y. Tokura, Phys. Rev. Lett.79 (1997) 3720.
[25] T.G. Perring, G. Aeppli, Y. Moritomo and Y. Tokura, Phys. Rev. Lett. 78 (1997) 3197.
[26] J.F. Mitchell, D.N. Argyriou, J.D. Jorgensen, D.G. Hinks, C.D. Potter and S.D. Bader, 55 (1997) 63.

[27] O. Chauvet, G. Goglio, P. Molinie, B. Corraze and L. Brohan, Phys. Rev. Lett. 81 (1998) 1102.
[28] R.H. Heffner, D.E. MacLaughlin, G.J. Nieuwenhuys, T. Kimura, G.M. Luke, Y.Tokura and Y.J. Uemura, Phys. Rev. Lett. 81 (1998) 1706.
[29] R.P. Sharma, P. Fournier, R.L. Greene, T. Venkatesan, J.F. Mitchell and D. Miller, J. Appl. Phys. 83 (1998) 7351.
[30] C.D. Potter, M. Swiatek, S.D. Bader, D.N. Argyriou, J.F. Mitchell, D.J. Miller, D.G. Hinks, and J.D. Jorgensen, Phys. Rev. B 57 (1998) 72.
[31] S.D. Bader, R.M. Osgood III, D.J. Miller, J.F. Mitchell and J.S. Jiang, J. Appl. Phys. 83 (1998) 6385.
[32] R. Seshadri, A. Maignan, M. Hervieu, N. Nguyen and B. Raveau, Solid State Comm. 101 (1997) 453.
[33] N.O. Moreno, P.G. Pagliuso, C. Rettori, J.S. Gardner, J.L. Sarrao, J.D. Thompson, D.L. Huber, A. Garcia-Flores and S.B. Oseroff, Physica B 292 (2000) 1.
[34] S.Y. Wu, W.-H. Li, K.C. Lee, and H.D. Yang, Physica B 259-261 (1999) 839.
[35] M. Velazquez, C. Haut, B.Hennion and A. Revcolevschi, J. Crystal Growth 220 (2000) 480.
[36] M. Velazquez, A. Revcolevschi, J.P. Renard, and C. Dupas, Eur. Phys. J. B 23 (2001) 307.
[37] K. Ruck, M. Sgraja, G. Krabbes, K. Dorr, K.-H. Muller and M. Khristov, J. Alloys and Compounds, 306 (2000) 151.
[38] Y. Kodama, Y. Nakanishi, N. Yoshimoto and M. Yoshizawa, Solid State Comm. 128 (2003) 335.
[39] G. Balakrishnan, M.R. Lees and D.M.K. Paul, J. Phys: Condens. Matter 9 (1997) L471.
[40] A. Imaduddin, H. Kanazawa, N. Yoshimoto, M. Matsukawa and M. Yoshizawa, Physica B 281&282 (2000) 502.
[41] D. Prabhakaran and A.T. Boothroyd J. Mater. Sci.: Materials in Electronics **14** (2003) 587.
[42] B.J. Campbell, D.N. Argyriou, J.F. Mitchell, R. Osborn, B. ouladdiah and C.D. Ling, Phys. Rev. B 69 (2004) 104403.
[43] M. Medarde, J.F. Mitchell, J.E. Millburn, S. Short and J.D. Jorgensen, Phys. Rev. Lett. 83 (1999) 1223.
[44] C.-J. Liu, C.-S. Sheu and M.-S. Huang, Phys. Rev. B 61 (2000) 14323.
[45] A.I. Coldea, S.J. Blundell, C.A. Steer, F.L. Pratt, D. Prabhakaran and J.F. Mitchell, Physica B 326 (2003) 500.
[46] S. Nair, A. Banerjee, A.V. Narlikar, D. Prabhakaran and A.T. Boothroyd, Phys. Rev. B 68 (2003) 132404.
[47] A. Oleaga, A. Salazar, D. Prabhakaran and A.T. Boothroyd, J. Appl. Phys. 95 (2004) 7366.
[48] S.B. Wilkins, P.D. Spencer, P.D. Hatton, S.P. Collins, M.D. Roper, D. Prabhakaran and A.T. Boothroyd. Phys. Rev. Lett. 91 (2003) 167205.
[49] S. B. Wilkins, P.D. Hatton, M.D. Roper, D. Prabhakaran and A. T. Boothroyd, Phys. Rev. Lett. 90 (2003) 187201.
[50] Y.-H. Choi, E.-O. Chi, Y.-U. Kwon, H.C. Kim, H.-C. Ri, C.-H. Lee, J.-S. Lee and H.S. Shim, Phys. Rev. B 63 (2001) 054437.

[51] T. Okuda, T. Kimura, and Y. Tokura, Phys. Rev. B 60 (1999) 3370.
[52] M. Kubota, H. Fujioka, K. Hirota, K. Ohoyama, Y. Moritomo, H. Yoshizawa and Y. Endoh, J. Phys. Soc. Jpn. 69 (2000) 1606.
[53] S.B. Wilkins, P.D. Spencer, T.A.W. Beale, P.D. Hatton, M.V. Zimmermann, S.D. Brown, D. Prabhakaran and A.T. Boothroyd, Phys. Rev. B 67 (2003) 205110.
[54] X.J. Chen, C.L. Zhang, J.S. Gardner, J.L. Sarrao and C. C. Almasan, Phys. Rev. B 68 (2003) 64405.

GUTZWILLER-CORRELATED WAVE FUNCTIONS: APPLICATION TO FERROMAGNETIC NICKEL

Jörg Bünemann[1], Florian Gebhard[1], Torsten Ohm[2], Stefan Weiser[2], and Werner Weber[2]

[1] Fachbereich Physik and Material Sciences Center,
Philipps-Universität Marburg, D-35032 Marburg, Germany

[2] Institut für Physik,
Universität Dortmund, D-44221 Dortmund, Germany

1 Introduction

1.1 Ferromagnetism: whither theory?

Metallic ferromagnetism has since long been a controversial subject in solid-state theory. From early on, two schools of thought have been competing. The first, based on ideas of Slater, Stoner, and Wohlfarth, turns to the band aspects of metallic ferromagnets such as iron, cobalt, and nickel [1]. The itineracy of the conduction electrons, including those of the open $3d$ shell, is considered to dominate the electron-electron interaction. The second school, going back to van-Vleck [2] and Gutzwiller [3], stresses the localized character of the $3d$ electrons in transition metals and their compounds; local magnetic moments are indeed manifest in magnetic insulators which are often oxides and halides of transition metals. In the van-Vleck–Gutzwiller school, local moments are seen as an important source of magnetism, common to both ferromagnetic transition metals and their insulating compounds. Therefore, the van-Vleck–Gutzwiller school emphasizes the importance of correlations as a consequence of the electron-electron interactions.

As the Slater–Stoner–Wohlfarth school considers electronic correlations to be of minor importance, it treats the electron-electron interaction in simple approximations such as Hartree–Fock theory, see [1]. Later, the density-functional theory (DFT) in its spin-dependent versions (SDFT) took over the role of Hartree–Fock or x_α schemes of the Slater school. For more than two decades, SDFT energy-band calculations by various groups have provided reasonably accurate results for quite a number of properties of metallic ferromagnets, e.g., magnetic moments and the overall shape of the Fermi surface. An early problem was the observation that SDFT in standard local-density approximation (LDA) does not give the bcc lattice as the most stable crystal structure for iron, instead fcc Fe is found to be stable. This problem was overcome by the introduction of generalized gradient expansions (GGA) of the density [4].

Until recently the van-Vleck–Gutzwiller school could not provide much more than intuitive arguments for its case because ferromagnetism is seen as a genuine, difficult many-body problem. For decades, only simplistic models could be treated with some reliability, e.g., the one-band Hubbard model, which, however, exhibits ferromagnetism only for an extremely large Hubbard interaction or a pathological density of state [5]. In the past, despite some partial successes [6], correlated-electron theory could not describe real materials in much detail. Over the last decade new theoretical tools have been developed which try to combine the merits of density-functional theory with those of advanced many-body approaches, e.g., the LDA-*GW* approximation [7]. A general problem of correlated-electron theories is the construction of suitable model Hamiltonians. Progress in this direction has been made recently, e.g., the 'down-folding' scheme permits a systematic construction of Hamiltonians in a reduced Hilbert space [8]. The one-particle dynamics of models for correlated lattice electrons can be determined, in principle, within the dynamical mean-field theory (DMFT) [9, 10, 11] which becomes exact in the limit of an infinite number of nearest neighbors (coordination number $Z \to \infty$). The 'static approximation' to DMFT is the 'LDA+U' scheme which has been applied to a variety of correlated-electron systems [12, 13, 14]. Moreover, DMFT has been extended in various ways, e.g., a combination of the LDA-*GW* approximation and the DMFT has been put forward [15]. Therefore, correlated-electron theories seem to approach a level of quality where a faithful comparison with experiments becomes possible.

In our group, we have extended the original Gutzwiller variational scheme to the full multi-band problem. Our theory provides total energies and magnetic moments of competing magnetic and non-magnetic phases and the single-particle excitation energies within Fermi-liquid theory. Thereby, our theory describes the dispersion of the conduction and valence bands and the Fermi surface as accessible, e.g., by angle-resolved photoemission spectroscopy (ARPES), and the predictions of our Gutzwiller correlated-electron theory can be tested against experiments on transition metals and its compounds.

1.2 The nickel problem

In this article we address ferromagnetic nickel as the prototype of band ferromagnetic materials. On the experimental side, one of the reasons why nickel has been in the focus of interest, much more than iron or cobalt, is the relative ease to grow large single crystals.

Consequently, a lot of experimental investigations have been carried out on nickel in order to determine its magnetic properties and electronic structure. For a review, we refer to the articles [1, 16, 17, 18].

On the theoretical side, of all the iron group magnetic metals nickel is the most celebrated case of discrepancies between SDFT predictions and experimental results. Early on, de-Haas–van-Alphen data indicated the presence of only one hole ellipsoid in the Fermi surface of the minority spin bands, located around the X-point of the Brillouin zone [19]. In contrast, energy band calculations using SDFT predict two hole ellipsoids around the X-point, the X_5-state of pure $d(t_{2g})$ orbital character, and the X_2-state of pure $d(e_g)$ orbital character. Concomitantly, neutron scattering experiments [20] revealed that the orbital character of the nickel magnetic moment exhibits less e_g admixture than predicted by energy band calculations.

ARPES measurements confirmed the de-Haas–van-Alphen results: the minority X_2-state of pure $d(e_g)$ orbital character was found to lie slightly below the Fermi level. Furthermore, the photoemission data differ considerably from SDFT over the whole range of occupied $3d$ bands. Most importantly, the width of the occupied part of the $3d$ bands is approximately $W = 3.3\,\mathrm{eV}$ [21, 22], whereas SDFT gives $W_{\mathrm{SDFT}} = 4.5\,\mathrm{eV}$, or larger [23]. ARPES studies also reveal big discrepancies between SDFT and experiment in the exchange splittings of majority and minority spin bands near the Fermi energy. The SDFT results give a rather isotropic exchange splitting of about 650 meV to 750 meV. whereas photoemission data show small and highly anisotropic exchange splittings between 160 meV for pure $3d(e_g)$-states such as X_2 and 330 meV for pure $3d(t_{2g})$-states such as S_3 near the X-point.

Another discrepancy concerns the position of the $L_{2'}$-state. Experimentally, it is found approximately 1 eV below the Fermi energy E_{F} whereas the SDFT puts it to about 0.3 eV below E_{F}. This state is special as it represents the most binding, pure $4p$-state [24]. An incorrect $4p$-level implies that DFT slightly underestimates the partial density of the $4p$ electrons and, thus, the $3d$-hole density.

Lastly, the size and the direction of the magnetic moment pose a big problem to SDFT. Early experiments using ferromagnetic electron resonance and the Einstein–de-Haas effect have produced the values $g = 2.183$ and $g' = 1.835$ which result in an orbital moment of $\mu_{\mathrm{orb}} = 0.0507\mu_{\mathrm{B}}$ per atom for nickel [1]. In general, the values of the orbital part of the magnetic moments in band ferromagnets are not very well reproduced in SDFT. Iron and cobalt show large deviations [25], even in relativistic SDFT calculations [26]. Moreover, the magneto-crystalline anisotropy energies are not correct, i.e., they come with the wrong sign in SDFT. As shown by Aubert and Gersdorf [27, 28], the value of the dominant anisotropy constant is $K_1 = -8.8\,\mu\mathrm{eV}$, i.e., the (111) direction is the easy axis in nickel. For a (001) magnetic moment, the energy is higher with an energy difference $E_{\mathrm{aniso}} \equiv E_{111} - E_{001} \approx -3\,\mu\mathrm{eV}$ per atom. In contrast, it is $E_{\mathrm{aniso}} > 0$ in SDFT calculations, e.g., by Daalderoop [26] so that $K_1 > 0$. The SDFT results for cobalt and iron are equally disappointing. At low temperatures, the complex behavior of the magnetic anisotropy as a function of temperature and the magnetic field was interpreted by Gersdorf [27] to be caused by a shift of the electronic state (001) $X_{2\downarrow}$ to about 3 meV *above* the Fermi energy. The famous second hole ellipsoid around the $X_{2\downarrow}$ indeed exists [27] as long as the

magnetic moment has an angle of less than 18 degrees with the (001) direction. However, the states (100) $X_{2\downarrow}$ and (010) $X_{2\downarrow}$ remain below E_{F}, about 33 meV [27].

All these discrepancies could not be overcome by SDFT modifications such as the GGA variants [4]. Apparently, a substantial improvement of SDFT results for nickel along these lines is presently not within reach. Recent correlated-electron theories remove the SDFT shortcomings only partially. For example, with LDA+U-type calculations it seems to be possible to adjust to experiment the orbital moment, the magnetic anisotropy, and the Fermi surface topology [13, 14]; however, other quantities, especially the entire quasi-particle band structure, remain elusive within these correlated-electron theories.

1.3 Scope of this work

In this article we show that our Gutzwiller theory resolves all of the discrepancies described in Section 1.2. Gutzwiller theory reproduces the experimental Fermi surface topology, the quasi-particle band structure with the correct width and the anisotropic exchange splittings, and the magnetic anisotropy. This success for nickel corroborates the early views by van-Vleck and Gutzwiller: the inclusion of the electron-electron interaction on a many-body level is essential for a proper understanding of itinerant ferromagnetism.

We structure our article as follows. In Section 2 we introduce our general Gutzwiller-correlated wave functions for multi-band Hubbard models. In Section 3 we present analytical results in the limit of infinite coordination number which we apply to nickel. The remaining Sections 4–7 are devoted to an improved, concise derivation of our theory. A short outlook closes our presentation.

The class of variational wave functions for which our formulae apply goes much beyond our previous investigations [29, 30, 31]. First, the Gutzwiller correlator now employs projections onto eigenstates of an effective atomic Hamiltonian which makes the variational Hilbert space much more flexible with respect to local correlations. Second, our variational states cover the case of superconductivity in correlated multi-band lattice systems. For ferromagnetic nickel, it does not seem to be necessary to exploit fully these new flexibilities. Therefore, we restrain ourselves to the normal-conducting state.

2 Gutzwiller variational theory

In this section we first define Gutzwiller variational wave functions for multi-band Hubbard models. In the limit of infinite coordination number, $Z \to \infty$, the expectation value of the Hamiltonian can be written in terms of an effective single-particle Hamiltonian. We use this expression as an approximation in our numerical studies on fcc nickel ($Z = 12$).

2.1 Definitions

2.1.1 Gutzwiller-correlated wave functions

We consider the Gutzwiller-correlated wave functions

$$|\Psi_{\mathrm{G}}\rangle \equiv \hat{P}_{\mathrm{G}}|\Psi_0\rangle \,. \tag{1}$$

Here, $|\Psi_0\rangle$ is a normalized quasi-particle vacuum so that we may later apply Wick's theorem. Expectation values in $|\Psi_0\rangle$ are denoted by

$$\langle \hat{A} \rangle_0 \equiv \langle \Psi_0 | \hat{A} | \Psi_0 \rangle \ . \tag{2}$$

Expectation values in $|\Psi_{\rm G}\rangle$ are denoted by

$$\langle \hat{A} \rangle_{\rm G} \equiv \frac{\langle \Psi_{\rm G} | \hat{A} | \Psi_{\rm G} \rangle}{\langle \Psi_{\rm G} | \Psi_{\rm G} \rangle} \ . \tag{3}$$

The Gutzwiller correlator is a product of local correlators,

$$\hat{P}_{\rm G} \equiv \prod_{\mathbf{m}} \hat{P}_{{\rm G}|\mathbf{m}} \ , \tag{4}$$

which induce transitions between atomic configurations on lattice site $\mathbf{m}$,

$$\hat{P}_{{\rm G}|\mathbf{m}} \equiv \sum_{I_1, I_2} \lambda_{I_1, I_2|\mathbf{m}} |I_1\rangle_{\mathbf{m}\mathbf{m}} \langle I_2| \ . \tag{5}$$

Atomic configurations with at least one electron are defined by

$$|I\rangle_{\mathbf{m}} \equiv \prod_{\sigma \in I} \hat{c}^{+}_{\mathbf{m},\sigma} |{\rm vacuum}\rangle_{\mathbf{m}} \ . \tag{6}$$

The operator $\hat{c}^{+}_{\mathbf{m},\sigma}$ ($\hat{c}_{\mathbf{m},\sigma}$) creates (annihilates) an electron on lattice site $\mathbf{m}$ in the local spin-orbitals $\sigma = 1, 2, \ldots, (2N_{\rm o})$ ($N_{\rm o} = 1, 3, 5$ for s, p, d electrons). The sets I comprise all possible atomic occupancies with $|I| = 1, 2, \ldots, (2N_{\rm o})$ electrons. $I = (\emptyset), (\sigma_1), (\sigma_1, \sigma_2), \ldots,$ $(\sigma_1, \ldots, \sigma_{2N_{\rm o}})$ denotes configurations with no, one, two, ..., $2N_{\rm o}$ electrons. A fixed order among the orbitals is assumed, i.e., we have $\sigma_1 < \sigma_2 < \ldots < \sigma_{2N_{\rm o}}$ in the definition of the sets I. For example, there is only one configuration $(2N_{\rm o}) \equiv (\sigma_1, \ldots, \sigma_{2N_{\rm o}}) = (1, \ldots, 2N_{\rm o})$ which represents a fully occupied atom. All standard set operations are defined for the sets I, e.g., $I = I_1 \cup I_2$ is the set union, and $I = I_1 \setminus I_2$ denotes the set of elements in I_1 which are not in I_2. We define the complement of I as $\bar{I} \equiv (2N_{\rm o}) \setminus I$. Altogether there are $D_{\rm at} = 2^{2N_{\rm o}}$ atomic configurations, $D_{\rm at} = 4, 64, 1024$ for s, p, d electrons.

We demand that $|I_1| + |I_2|$ is even in (5). This restriction permits pairing correlations with an even number of Fermions as in BCS theory. Furthermore, we address only Hermitian Gutzwiller correlators, $\hat{P}_{{\rm G}|\mathbf{m}} = \hat{P}^{+}_{{\rm G}|\mathbf{m}}$. Consequently, we demand

$$\lambda_{I_1, I_2|\mathbf{m}} = \lambda^{*}_{I_2, I_1|\mathbf{m}} \ . \tag{7}$$

Therefore, we can find atomic states $|\Gamma\rangle_{\mathbf{m}}$ such that

$$\hat{P}_{{\rm G}|\mathbf{m}} = \sum_{\Gamma} \lambda_{\Gamma|\mathbf{m}} \hat{m}_{\Gamma|\mathbf{m}} \tag{8}$$

with real parameters $\lambda_{\Gamma|\mathbf{m}}$. Here,

$$\hat{m}_{\Gamma|\mathbf{m}} = |\Gamma\rangle_{\mathbf{m}\mathbf{m}} \langle \Gamma| \tag{9}$$

is the projection operator onto the state $|\Gamma\rangle_{\mathbf{m}}$. In terms of atomic configurations we have

$$|\Gamma\rangle_{\mathbf{m}} = \sum_I A_{I,\Gamma|\mathbf{m}} |I\rangle_{\mathbf{m}} \quad , \quad |I\rangle_{\mathbf{m}} = \sum_\Gamma A^*_{I,\Gamma|\mathbf{m}} |\Gamma\rangle_{\mathbf{m}} \tag{10}$$

where the unitary matrix $\tilde{A}_{\mathbf{m}}$ diagonalizes the matrix $\tilde{\lambda}_{\mathbf{m}}$,

$$\lambda_{\Gamma_1|\mathbf{m}} \delta_{\Gamma_1,\Gamma_2} = \sum_{I_1,I_2} A^*_{I_1,\Gamma_1|\mathbf{m}} \lambda_{I_1,I_2|\mathbf{m}} A_{I_2,\Gamma_2|\mathbf{m}} \; . \tag{11}$$

In general, the state $|\Gamma\rangle_{\mathbf{m}}$ can be chosen as the eigenstates of some *effective* local atomic Hamiltonian $\hat{H}^{\rm eff}_{\rm at}$.

2.1.2 Multi-band Hubbard models

In this work we focus on ferromagnetism of transition metals. Therefore, we study the multi-band Hubbard model for N electrons on L lattice sites,

$$\hat{H} = \hat{T} + \hat{H}_{\rm at} \tag{12}$$

with

$$\hat{T} = \sum_{\mathbf{i},\mathbf{j},\sigma\sigma'} t^{\sigma\sigma'}_{\mathbf{i},\mathbf{j}} \hat{c}^+_{\mathbf{i},\sigma} \hat{c}_{\mathbf{j},\sigma'} = \sum_{\mathbf{k};\sigma\sigma'} \epsilon^0_{\sigma\sigma'}(\mathbf{k}) \hat{c}^+_{\mathbf{k},\sigma} \hat{c}_{\mathbf{k},\sigma'} \; , \tag{13}$$

$$\epsilon^0_{\sigma\sigma'}(\mathbf{k}) \equiv \frac{1}{L} \sum_{\mathbf{i},\mathbf{j}} e^{-{\rm i}\mathbf{k}(\mathbf{j}-\mathbf{i})} t^{\sigma\sigma'}_{\mathbf{i},\mathbf{j}} \; , \tag{14}$$

where we used translational invariance, $t^{\sigma\sigma'}_{\mathbf{i},\mathbf{j}} \equiv t^{\sigma\sigma'}(\mathbf{i}-\mathbf{j})$ to introduce the bare energy-band matrix elements $\epsilon^0_{\sigma\sigma'}(\mathbf{k})$. Note that we set $t^{\sigma\sigma'}_{\mathbf{i},\mathbf{i}} = 0$, i.e., the kinetic energy operator does not include the local potential terms $\epsilon_{\mathbf{i},\sigma\sigma'} \equiv \epsilon_{\sigma\sigma'}$ (e.g., exchange splittings, spin-orbit interaction) which are contained in the general, purely local Hamiltonian

$$\hat{H}_{\rm at} = \sum_{\mathbf{m}} \sum_{I_1,I_2} U_{I_1,I_2|\mathbf{m}} |I_1\rangle_{\mathbf{m}\mathbf{m}} \langle I_2| = \sum_{\mathbf{m}} \sum_{\overline{\Gamma}} E_{\overline{\Gamma}|\mathbf{m}} \hat{m}_{\overline{\Gamma}|\mathbf{m}} \; . \tag{15}$$

The projector onto the atomic eigenstate $|\overline{\Gamma}\rangle_{\mathbf{m}}$ on site $\mathbf{m}$ is denoted $\hat{m}_{\overline{\Gamma}|\mathbf{m}}$. The unitary matrix $\tilde{B}_{\mathbf{m}}$ diagonalizes the matrix $\tilde{U}_{\mathbf{m}}$,

$$E_{\overline{\Gamma}_1|\mathbf{m}} \delta_{\overline{\Gamma}_1,\overline{\Gamma}_2} = \sum_{I_1,I_2} B^*_{I_1,\overline{\Gamma}_1|\mathbf{m}} U_{I_1,I_2|\mathbf{m}} B_{I_2,\overline{\Gamma}_2|\mathbf{m}} \; . \tag{16}$$

For translation invariance, we have $E_{\overline{\Gamma}|\mathbf{m}} \equiv E_{\overline{\Gamma}}$, $U_{I_1,I_2|\mathbf{m}} \equiv U_{I_1,I_2}$, $\lambda_{I_1,I_2|\mathbf{m}} \equiv \lambda_{I_1,I_2}$, and $\lambda_{\Gamma|\mathbf{m}} \equiv \lambda_\Gamma$. Note that the eigenstates $|\overline{\Gamma}\rangle_{\mathbf{m}}$ of $\hat{H}_{\rm at}$ need not be identical to $|\Gamma\rangle_{\mathbf{m}}$. Therefore, the number of parameters λ_{I_1,I_2} in our general definition of the Gutzwiller correlator (5) is of the order of $D^2_{\rm at}$ [$= \mathcal{O}(10^6)$ for d electrons]. In most practical applications, it is impossible to scan such a large variational space numerically. Therefore, one has to work with eigenstates $|\Gamma\rangle_{\mathbf{m}}$ of some *effective* atomic Hamiltonian $\hat{H}^{\rm eff}_{\rm at}$ which is characterized by a few physically motivated parameters. In this way, the numerical problem basically

reduces to the minimization of the ground-state energy with respect to the real variational parameters λ_Γ. This minimization problem is numerically tractable because the number of variational parameters is now reduced to the dimension of the atomic Hilbert space, $D_{\rm at} = \mathcal{O}(10^3)$ for d electrons.

The values for the electron-transfer parameters $t_{\mathbf{i},\mathbf{j}}^{\sigma\sigma'}$ and the correlation parameters U_{I_1,I_2} (or, equivalently, for $\epsilon^0_{\sigma\sigma'}(\mathbf{k})$ and $E_{\overline{\Gamma}}$) depend on the specific material under investigation. We shall specify them for nickel in Section 3.

2.2 Effective single-particle Hamiltonian for nickel

For our studies on nickel we simplify the calculations by working with the correlator

$$\hat{P}_{\mathrm{G}|\mathbf{m}} = \sum_\Gamma \lambda_\Gamma \hat{m}_{\Gamma|\mathbf{m}} \tag{17}$$

in which we choose the states $|\Gamma\rangle_\mathbf{m}$ to be identical to the eigenstates of the atomic Hamiltonian in (15), $|\Gamma\rangle_\mathbf{m} \equiv |\overline{\Gamma}\rangle_\mathbf{m}$. Therefore, our main numerical problem is the minimization of the variational energy with respect to the parameters λ_Γ.

In order to determine the variational ground state of $\hat{H}$ one first needs to calculate the expectation value

$$\langle \hat{H} \rangle_{\mathrm{G}} = E^{\rm var}(\{\lambda_\Gamma\}, \{|\Psi_0\rangle\}) \tag{18}$$

of the Hamiltonian $\hat{H}$ as a function of the variational parameters λ_Γ and the one-particle wave-function $|\Psi_0\rangle$. In the limit of infinite spatial dimensions the expectation value of the local Hamiltonian (15) becomes

$$E^{\rm at}(\{m_\Gamma\}) = L \sum_\Gamma E_\Gamma m_\Gamma \ . \tag{19}$$

The probability for finding the atomic state $|\Gamma\rangle_\mathbf{m}$,

$$m_\Gamma \equiv \langle \hat{m}_{\Gamma|\mathbf{m}} \rangle_{\mathrm{G}} = \lambda_\Gamma^2 \langle \hat{m}_{\Gamma|\mathbf{m}} \rangle_0 \ , \tag{20}$$

may be used to replace the original variational parameters λ_Γ because $\langle \hat{m}_{\Gamma|\mathbf{m}} \rangle_0$ is a simple function of the local density-matrix for the non-interacting system,

$$C_{\sigma\sigma'} = \langle \hat{c}^+_{\mathbf{m},\sigma} \hat{c}_{\mathbf{m},\sigma'} \rangle_0 \ . \tag{21}$$

The one-particle product state $|\Psi_0\rangle$ is the ground state of the effective single-particle Hamiltonian

$$\hat{T}^{\rm eff} = \sum_{\mathbf{k};\sigma\sigma'} \epsilon_{\sigma\sigma'}(\mathbf{k}) \hat{c}^+_{\mathbf{k},\sigma} \hat{c}_{\mathbf{k},\sigma'} \ , \tag{22}$$

$$\epsilon_{\sigma\sigma'}(\mathbf{k}) \equiv \sum_{\gamma\gamma'} Q^{\sigma\sigma'}_{\gamma\gamma'} \epsilon^0_{\gamma\gamma'}(\mathbf{k}) + \eta_{\sigma\sigma'} \ , \tag{23}$$

where the tensor elements $Q^{\sigma\sigma'}_{\gamma\gamma'}$ are known functions of the parameters m_Γ and the density matrix $C_{\sigma\sigma'}$, and $\eta_{\sigma\sigma'}$ are Lagrange parameters which act as effective on-site energies, see

Sections 6 and 7. The one-particle eigenvalues ($\equiv E_{\mathbf{k},\tau}$) of $\hat{T}^{\mathrm{eff}}$ can be interpreted as quasi-particle energies within a Landau–Gutzwiller Fermi-liquid theory, see [31] and Section 7. As we will see in the case of nickel, these eigenvalues are in very good agreement with the band energies as found in ARPES experiments. For the kinetic energy we find

$$E^{\mathrm{kin}}(\{m_\Gamma\},\{C_{\sigma\sigma'}\},\{\eta_{\sigma\sigma'}\}) = \sum_{\sigma\sigma',\gamma\gamma'} Q^{\sigma\sigma'}_{\gamma\gamma'}(\{m_\Gamma\},\{C_{\sigma\sigma'}\}) \sum_{\mathbf{k}} \epsilon^0_{\gamma\gamma'}(\mathbf{k}) \langle\Psi_0|\hat{c}^+_{\mathbf{k},\sigma}\hat{c}_{\mathbf{k},\sigma'}|\Psi_0\rangle \ , \tag{24}$$

The local density matrix $C_{\sigma\sigma'}$, via eq. (21), and, therefore, the variational energy E^{var} may be considered as functions of m_Γ and $\eta_{\sigma\sigma'}$. The remaining numerical task is then to minimize E^{var} with respect to these parameters. There are, however, still up to $(2N_{\mathrm{o}})^2+1$ constraints which have to be respect during the minimization, see (47)–(50). For example, the completeness of the states $|\Gamma\rangle_{\mathbf{m}}$ apparently leads to the constraint $\sum_\Gamma m_\Gamma = 1$. There is no simple recipe for the most efficient way to implement these constraints in the numerical minimization procedure. In previous works [29, 30] we have proposed the following strategy: We perform a transformation of the local orbital basis onto a new one in which the local density matrix is diagonal. In this new basis, the main $(2N_{\mathrm{o}})^2$ constraints could then be implemented by the diagonalization of a $2N_{\mathrm{o}}$-dimensional matrix which we called the 'Z-matrix'. In the following section we present results using this strategy. The final numerical results should not be affected by the way the constraints are implemented.

3 Results for ferromagnetic nickel

In this section we first specify our model parameters. Then we give some details of our variational calculations. Finally, we discuss our results for the quasi-particle band structure and the magnetic anisotropy.

3.1 Model specifications

The multi-band Gutzwiller theory is not an ab-initio theory. It is based on a multi-band Hubbard Hamiltonian whose parameters need to be specified. For metallic systems, the use of a Hubbard model is well justified: screening is very efficient so that the effects of the Coulomb interaction between electrons at distances larger than the inverse Fermi wave number k_{F}^{-1} can be incorporated in the 'bare' band structure, and only the local, effective Coulomb matrix elements need to be taken into account explicitly.

3.1.1 Electron-transfer amplitudes and local potential terms

For nickel, we consider a minimal model which includes only those bands which are partly filled within a paramagnetic LDA calculation. Therefore, our multi-band Hubbard Hamiltonian $\hat{H}$ comprises of 18 spin orbitals, namely $3d$, $4s$, and $4p$. The non-magnetic local-density approximation to DFT provides the LDA band structure $\epsilon^{\mathrm{LDA}}_\tau(\mathbf{k})$. We represent the bare energy-band matrix elements $\epsilon^0_{\sigma\sigma'}(\mathbf{k})$ in the kinetic energy operator $\hat{T}$ in terms of real electron-transfer integrals $t^{\sigma\sigma'}(\mathbf{r})$ in the two-center approximation [32] which range up

to third nearest neighbors, $N_{\mathbf{r}} \leq 3$. We choose these parameters and the local potential terms $\epsilon_{\sigma\sigma'}$ in such a way that our tight-binding fit reproduces the LDA band structure. In this fit we include information on the symmetry of the single-particle states [33].

Table 1: Electron-transfer parameters $t_{\sigma\sigma'}(\mathbf{r})$ to $N_{\mathbf{r}}$-th neighbors (all energies in eV).

$N_{\mathbf{r}}$	$ss\sigma$	$sp\sigma$	$sd\sigma$	$pp\sigma$	$pp\pi$
1	−1.0292	1.2047	−0.5933	1.2144	−0.5284
2	−0.1039	0.2234	−0.1089	0.5989	−0.2205
3	−0.0050	−0.0223	−0.0223	0.0137	0.0076
	$pd\sigma$	$pd\pi$	$dd\sigma$	$dd\pi$	$dd\delta$
1	−0.6960	0.2300	−0.4780	0.3150	−0.0481
2	−0.2092	0.0524	−0.0848	0.0336	−0.0007
3	−0.0439	−0.0023	−0.0245	−0.0011	0.0024

For the optimal choice, the **k**-averaged root-mean-square deviation between our tight-binding fit and the LDA band structure up to 2 eV above the Fermi energy is 15 meV for the $3d$ bands and for the $4sp$ bands. Our values of the electron-transfer parameters are summarized in Table 1. These model parameters have already been used for the calculations reported in Refs. [30, 34].

For the on-site parameters we find for both spin species

$$\begin{aligned}
\epsilon_{4s,4s} &\equiv \epsilon_s &&= 5.6022\,\text{eV}\,, \\
\epsilon^{\text{LDA}}_{4p,4p} &\equiv \epsilon^{\text{LDA}}_p &&= 8.5335\,\text{eV}\,, \\
\epsilon_{4p,4p} &\equiv \epsilon^{\text{shift}}_p &&= 7.7835\,\text{eV}\,, \\
\epsilon_{3d(t_{2g}),3d(t_{2g})} &\equiv \epsilon_{t_{2g}} &&= -0.0290\,\text{eV}\,, \\
\epsilon_{3d(e_g),3d(e_g)} &\equiv \epsilon_{e_g} &&= 0.0436\,\text{eV}\,.
\end{aligned} \tag{25}$$

where ϵ^{LDA}_p is the result from the fit to LDA and $\epsilon^{\text{shift}}_p$ is used in practical calculations for a better agreement between our Gutzwiller theory and ARPES experiments for nickel, see below. For the total crystal-field splitting we find $\epsilon_{\text{cf}} = \epsilon_{t_{2g}} - \epsilon_{e_g} = -0.0726\,\text{eV}$.

The energetically highest-lying state of pure d character is X_5 (purely t_{2g}), 0.18 eV above the Fermi energy. The state X_2 (purely e_g) lies 0.025 eV above E_{F}. The width of the $3d$ bands can be estimated from $E(X_5) - E(X_1) = 4.45\,\text{eV}$ (X_1 is predominantly of $d(e_g)$ character), or from $E(X_5) - E(L_1) = 4.63\,\text{eV}$ (L_1 is predominantly $d(t_{2g})$).

Next, we address the $L_{2'}$-state. Experiment locates this state at about 1.0 eV below E_{F}. The SDFT calculations for ferromagnetic nickel as well as our Gutzwiller theory find the $L_{2'}$-state about 0.3 eV below the Fermi energy when we use the LDA $4p$ orbital energy $\epsilon^{\text{LDA}}_p = 8.5335\,\text{eV}$. Therefore, we shift the $4p$ orbital energy by 0.75 eV to $\epsilon^{\text{shift}}_p = 7.7835\,\text{eV}$, and find the $L_{2'}$-state 0.97 eV below E_{F}. In the following we present results which use $\epsilon^{\text{shift}}_p = 7.7835\,\text{eV}$. This choice enhances the $4p$ partial density by approximately 0.1 electron and, correspondingly, enhances the $3d$ hole charge by the same amount so that we work with $n_d = 8.78$ [24]. The remaining 1.22 valence electrons are about evenly split between the $4s$ level and the three $4p$ levels.

3.1.2 Atomic interactions

As described above, the paramagnetic LDA calculation provides a first single-particle contribution to the local Hamiltonian,

$$\hat{H}_{\rm at}^{(1a)} = \sum_{\mathbf{m},\sigma} \epsilon_{\sigma\sigma} \hat{c}^{+}_{\mathbf{m},\sigma} \hat{c}_{\mathbf{m},\sigma} \tag{26}$$

with $|\sigma\rangle = |4s, 4p, 3d\rangle \otimes |\uparrow,\downarrow\rangle$. In addition to these single-particle contributions, we include the spin-orbit interaction for the $3d$ electrons only, $|\sigma\rangle = |3d\rangle \otimes |\uparrow,\downarrow\rangle$. Hereby we restrict ourselves to the dominant, purely atomic contributions of the form

$$\hat{H}_{\rm at}^{(1b)} = \sum_{\mathbf{m},\sigma\sigma'} \frac{\zeta}{2} \langle \sigma | \hat{l}_x \tilde{\sigma}_x + \hat{l}_y \tilde{\sigma}_y + \hat{l}_z \tilde{\sigma}_z | \sigma' \rangle \hat{c}^{+}_{\mathbf{m},\sigma} \hat{c}_{\mathbf{m},\sigma'} \; . \tag{27}$$

Here, ζ is the strength of the spin-orbit coupling, $\tilde{\sigma}_{x,y,z}$ are the three Pauli matrices, and $\hat{l}_{x,y,z}$ are the Cartesian components of the vector operator for the angular momentum. For the spin-orbit coupling constant we choose $\zeta = 0.080\,\mathrm{eV}$ as in Refs. [35, 36].

The second part of the local interaction is the two-particle Coulomb interaction,

$$\hat{H}_{\rm at}^{(2)} = \sum_{\mathbf{m}} \sum_{\sigma_1,\sigma_2,\sigma_3,\sigma_4} \mathcal{U}(\sigma_1,\sigma_2;\sigma_3,\sigma_4) \hat{c}^{+}_{\mathbf{m},\sigma_1} \hat{c}^{+}_{\mathbf{m},\sigma_2} \hat{c}_{\mathbf{m},\sigma_3} \hat{c}_{\mathbf{m},\sigma_4} \; . \tag{28}$$

The intra-atomic interactions in the $4s$ and $4p$ shell are rather weak when compared to the broad $4sp$ energy bands. Thus, we expect only small correlation effects in these bands. We also neglect correlations between $4sp$ electrons and $3d$ electrons beyond those contained in the LDA band structure. This is a more serious approximation as we neglect magnetic polarization effects on the $4sp$ bands and thus may underestimate the $4sp$ contribution to the magnetic moment. Under these assumptions, the spin-orbit sum in (28) runs over the $3d$ orbitals only. The Hamiltonian of the full atomic problem, $\hat{H}_{\rm at} = \hat{H}_{\rm at}^{(1a)} + \hat{H}_{\rm at}^{(1b)} + \hat{H}_{\rm at}^{(2)}$, provides the matrix elements between two atomic configurations I_1 and I_2 in (15),

$$U_{I_1,I_2} = {}_{\mathbf{m}}\langle I_1 | \hat{H}_{\rm at}^{(1a)} + \hat{H}_{\rm at}^{(1b)} + \hat{H}_{\rm at}^{(2)} | I_2 \rangle_{\mathbf{m}} \; . \tag{29}$$

The atomic eigenstates $|\Gamma\rangle_{\mathbf{m}}$ can be written as product states,

$$|\Gamma\rangle_{\mathbf{m}} = |\Gamma_{3d}\rangle_{\mathbf{m}} |\Gamma_{4s}\rangle_{\mathbf{m}} |\Gamma_{4p}\rangle_{\mathbf{m}} \; . \tag{30}$$

In our Gutzwiller theory we correlate the $3d$ states $|\Gamma_{3d}\rangle_{\mathbf{m}}$ only, i.e., the variational parameter λ_Γ is independent of the $4sp$ configuration $|\Gamma_{4s}\rangle_{\mathbf{m}} |\Gamma_{4p}\rangle_{\mathbf{m}}$. This leads to a numerically tractable problem with $\mathcal{O}(10^3)$ variational parameters for the atomic $3d$ states.

Naturally, we must not completely ignore the Coulomb interaction of the $4sp$ electrons. In this case a big charge flow from the $3d$ to the $4sp$ bands and unphysically small occupations of the $3d$ shell would result. One way to overcome the charge flow problem is to introduce a chemical potential which keeps the $3d$ partial charge fixed during the calculations, $n_d = 8.78$; see [34] for an alternate method which gives essentially the same results.

Gutzwiller theory produces an optimum magnetic (spin-only) moment which is too large by about 10%. It should be mentioned that the SDFT results show a similarly large overshooting of the magnetic moment. To best compare with experiment, we thus carry out calculations at fixed magnetic moment for the total energy, with either the spin-only moment fixed to the (spin-only) experimental value of $\mu_{\rm spin} = 0.55\mu_{\rm B}$ [30] or with the total magnetic moment fixed to the full experimental moment of $\mu = 0.606\mu_{\rm B}$ when the spin-orbit coupling is included [37].

3.1.3 Parameters for the Coulomb interaction

It remains to determine the Coulomb interaction parameters $\mathcal{U}(\sigma_1, \sigma_2; \sigma_3, \sigma_4)$ in (28). In the spherical-atom approximation, there are only three independent interaction parameters, namely the Slater–Condon integrals F_0, F_2, and F_4, from which all Coulomb interaction parameters can be determined. We prefer the Racah definition, see [38], where the parameters A, B, and C are used which are linear combinations of the Slater–Condon integrals.

The spherical-atom approximation is excellent in cubic systems. In principle, the Coulomb interaction among $3d(t_{2g})$ electrons may differ from the Coulomb interaction among $3d(e_g)$ electrons because the radial parts of their orbital wave functions can be different. Measurements of d-d transitions of magnetic impurities with cubic site symmetry in non-magnetic oxide hosts show that these differences are marginal. The d^3 multiplets ^3H and ^3P, which are accidentally degenerate in spherical-atom approximation, split by cubic two-particle corrections but not by the crystal field. However, they are found to be degenerate within the experimental resolution of some meV [38]. In test calculations we have used different A parameters for $d(t_{2g})$ electrons and $d(e_g)$ electrons but we have not found any features in our quasi-particle energies which would indicate a failure of the spherical-atom approximation.

The Racah parameters B and C are related to the Slater integrals F_2 and F_4. They determine the splitting of the multiplets of a specific $3d^n$ configuration. They can be determined experimentally from d-d transition spectra for magnetic impurity ions in non-magnetic insulating hosts. Typical values for all kinds of transition metal ions are tabulated in [38]. It is found experimentally that the ratio C/B varies smoothly between 4 and 5; $C/B = 4$ is obtained theoretically when hydrogen $3d$ wave functions are used. Experimentally, the values for B and C for Ni^{2+} and Ni^{3+} ions are known [38]. When we linearly extrapolate these values to a neutral atom we find our values for nickel as $B = 0.09\,\text{eV}$ and $C = 0.40\,\text{eV}$ so that we employ a ratio $C/B = 4.4$. The values for B and C are close to the 'bare' atomic values, i.e., the screening appears to be of little importance to B and C. For a fixed ratio C/B, we may replace the two interaction parameters B and C by a single effective parameter J, as is quite often done in the LDA+U literature. This exchange coupling J is related to B and C by

$$\frac{B}{2} + \frac{C}{5} = \frac{J}{7}\,. \tag{31}$$

For our nickel values for B and C we find $J = 0.88\,\text{eV}$, a value very similar to the ones used by Anisimov et al. [12] and others.

The Racah parameter A (basically the U parameter of the Hubbard model) determines the separation of the various d^n multiplets. The 'bare' values, as calculated, e.g., from atomic wave-functions are of the order of 25 eV, as discussed already in Herring's book on magnetism [39] and confirmed recently in [40]. There is a technique to extract U parameters using 'constraint' density-functional theory and supercell geometries. It has been found that for minimum-basis models the U-values are smallest. For example, in the case of the cuprates, values $U \leq 2\,\mathrm{eV}$ were found for a single-band Hubbard model whereas a three-band model including the oxygen $2p$ states employs $U_{dd} \approx 8\,\mathrm{eV}$ [41]. Similar results have been found in the case of $BaBiO_3$ [42]. For $3d$ band models, values of $U = 4 \ldots 6\,\mathrm{eV}$ have been reported [43]. For the $4s$-$4p$-$3d$ multi-band case of nickel, no such calculations are available but values $U \approx 10\,\mathrm{eV}$ appear to be reasonable. We choose A in such a way that our Gutzwiller theory reproduces the experimental $3d$ band width. For our 18 orbital basis we find $A = 9\,\mathrm{eV}$ to reproduce best the quasi-particle $3d$ band width $W = 3.3\,\mathrm{eV}$; a value of $A = 12\,\mathrm{eV}$ leads to $W = 3.0\,\mathrm{eV}$. If we worked with a model of only ten $3d$ spin orbitals, the corresponding band-width reduction is achieved for $A \approx 4\,\mathrm{eV}$.

3.2 Details of the calculations

The minimization problem consists of two parts. We have to optimize the Hubbard interaction through the variational parameters m_Γ ('internal' variation) and the kinetic energy through the one-particle product state $|\Psi_0\rangle$ and its quasi-particle excitation spectrum ('external' variation). During the variations we keep the partial densities fixed through a 'chemical potential' and work for fixed magnetization (spin-only in the absence of spin-orbit coupling). These two minimization steps are done recursively. The separation of 'internal' and 'external' minimization offers the advantage that computer time-consuming integrations in momentum space are reduced to a minimum.

Experimentally, the anisotropy energy is $E_{\mathrm{aniso}} \approx -3\,\mu\mathrm{eV}$ per atom. Therefore, our total-energy calculations must reach an accuracy of $\mathcal{O}(0.1\,\mu\mathrm{eV})$ per atom.

3.2.1 Band calculations

The calculation of the kinetic energy contribution to the variational ground-state energy requires the sum over quasi-particle energies up to the Fermi energy E_F. In the absence of the spin-orbit coupling we use the point-group symmetry of the fcc lattice and calculate all quantities in the irreducible part of the Brillouin zone. This amounts to a reduction of the zone volume by a factor of 48. In order to generate our mesh in momentum space, we divide the distance between the Γ and the X point by 20. This is the standard $\mathbf{k}$-mesh used in all our calculations. For the calculations with cubic symmetry this results in 916 points and $4.0 \cdot 10^3$ tetrahedra for the mapping of the Fermi surface in the irreducible part of the Brillouin zone. For the calculations including spin-orbit coupling, we use the same mesh. Now that the $\mathbf{k}$-summation runs over the full Brillouin zone, we sample over $3.4 \cdot 10^4$ $\mathbf{k}$-points and $1.6 \cdot 10^5$ tetrahedra.

For the numerical integrations required for the calculation of the kinetic energy, we use the tetrahedron method as described in [44]. Additionally, in all calculations we

employ a refinement of the numerical integration near E_{F} whereby we check whether or not a tetrahedron contains states within a certain energy shell around E_{F}. If so, we divide the tetrahedron into eight smaller ones and repeat the integration using the smaller tetrahedra. For the spin-only (full moment) nickel calculations our integration refinement near E_{F} results in $4.0 \cdot 10^4$ ($1.7 \cdot 10^6$) additional tetrahedra in momentum space close to E_{F}.

In order to achieve an accuracy of 10^{-7} eV for the ground-state energy, we need to suppress numerical noise. For example, a numerical integration yields the elements of the single-particle on-site density matrix $\tilde{C}$ (21). For cubic symmetry, some diagonal elements should be identical but they show some scattering. Even worse, off-diagonal elements which should be zero by symmetry are finite, of the order $\mathcal{O}(10^{-6})$, albeit we perform our calculations in double precision. The main reason for the numerical noise is the limited accuracy of the tetrahedral method and of the integration refinement. In principle, numerical noise can be reduced by choosing a finer **k**-mesh; finite computational resources bar this route to higher accuracy. Instead, we take advantage of all symmetries of the problem, e.g., in a system with cubic symmetry the on-site density matrix $\tilde{C}$ becomes diagonal. Therefore, off-diagonal matrix elements can be set to zero, and diagonal elements are replaced by their average.

3.2.2 Variational procedure

The variational energy has to be minimized with respect to the internal variational parameters m_Γ and the external parameters $\eta_{\sigma\sigma'}$. The latter can be interpreted as the effective on-site energies, crystal-field splittings, exchange splittings, and spin-orbit couplings. As shown in Section 3.1 for cubic nickel, symmetry allows three external variational parameters for the $3d$ electrons: the effective crystal-field splitting $\epsilon_{\mathrm{cf}}^{\mathrm{eff}}$ and the effective exchange splittings $\Delta^{\mathrm{eff}}(t_{2\mathrm{g}})$ and $\Delta^{\mathrm{eff}}(e_{\mathrm{g}})$, which are different for $3d(t_{2g})$ and $3d(e_g)$ electrons. Symmetry also allows exchange splittings for the $4sp$ orbitals but these turn out to be of very minor importance, as long as we do not include the atomic electron-electron interaction between $3d$ electrons and $4sp$ electrons, see Section 3.1. When we include the spin-orbit coupling (27) there is another external variational parameter, ζ^{eff}, the magnitude of the spin-orbit coupling for our quasi-particle description.

The optimization of the external parameters for a given tensor $\tilde{Q}$ is analogous to the Hartree–Fock variational theory, i.e., it is a familiar self-consistent band-structure problem. We would reproduce the results of a pure mean-field LDA+U approach if we set $Q^{\sigma\sigma'}_{\gamma\gamma'} = \delta_{\gamma,\sigma}\delta_{\gamma',\sigma'}$. In the case of nickel, however, we found that $\tilde{Q}$ deviates significantly from this simple diagonal form. This explains why mean-field theories fail to describe the electronic properties of nickel correctly.

The variation of the internal variational parameters m_Γ was the centerpiece of our programming efforts. All our schemes use random number generators for the starting values of the variational parameters so that we can easily test the stability of our results. We repeat the runs for different seeds and study the scatter of the results, not only in the total energy, but also in the values of the individual variational parameters.

For fixed external variational parameters, the kinetic energy (24) changes only due to the internal variational parameters m_Γ. The tensor $\tilde{Q}$ in (24) is a product of matrices $\tilde{q}$

whose entries can be written in the form

$$q_{\sigma_1,\sigma_2} = \sum_{\Gamma_1,\Gamma_2} \Sigma(\sigma_1,\sigma_2;\Gamma_1,\Gamma_2)\sqrt{m_{\Gamma_1}}\sqrt{m_{\Gamma_2}} \; . \tag{32}$$

Most of the elements of the tensor $\widetilde{\Sigma}$ can be prepared before we start the variation of the internal variational parameters, i.e., they do not change during the optimization of the parameters m_Γ. Note that the eigenvalues and eigenvectors of the matrix $\widetilde{Z}$ feed into the tensor $\widetilde{\Sigma}$. The matrix $\widetilde{Z}$ of size 10×10 has to be recalculated and diagonalized at each internal variation step as it ensures fulfillment of the conditions (47) and (48), see Section 4.1. However, only a few of the elements in $\widetilde{\Sigma}$ are affected by these recalculations.

The present code simply varies each m_Γ one by one, calculates the matrix $\widetilde{Z}$ and the corrections to the matrix $\widetilde{q}$ in each step, computes the matrices $\widetilde{q}$ and $\widetilde{C}$, and carries out the total-energy summations both for the interaction energy and the kinetic energy. The use of the matrix $\widetilde{q}$ considerably speeds up the calculation and variation of $\widetilde{Q}$ and thus of the kinetic energy.

A large number of variational parameters is very small, e.g., the probability m_Γ for a local configuration Ni^{7+} is tiny. We use a cut-off below which such variational parameters are set to zero and are no longer varied. In general, big variational parameters influence the energy more strongly than small ones so that we vary big variational parameters more often. Typically, we perform $1.0 \cdot 10^5$ to $5.0 \cdot 10^5$ variations to reach convergence. Hereby, the energy reduction in the last $2.0 \cdot 10^4$ variations is less than $0.1\,\mu$eV. When we repeat the run for different seeds, the total energy scatters by less than $1\,\mu$eV. The individual scatter of band and interaction energies is of the order $\mathcal{O}(\mu\text{eV})$. The scatter in the most significant m_Γ values is of the order $\mathcal{O}(10^{-4})$, the same holds true for the diagonal elements of the matrix $\widetilde{q}$.

3.3 Quasi-particle band structure without spin-orbit coupling

First we address the case where we set the spin-orbit coupling to zero and work with a fixed spin-only moment of $\mu_{\text{spin}} = 0.55$. Figure 1 and table 2 summarize our results which are in very good agreement with ARPES experiments.

Our calculations show the expected dependence of the $3d$ band width on the magnitude of the Racah parameter A via the hopping reduction tensor $\widetilde{Q}$. As can be seen from table 2, the $3d$ band width agrees very well with experiment for $A = 9\,\text{eV}$. The Racah parameters only indirectly influence the quasi-particle bands through the matrix $\widetilde{Q}$ whose elements determine the reduction of the electron-transfer amplitudes. Modifications of the values for A, B, and C cause overall energy shifts but they only weakly influence specific band states. Now that the value of A is so much bigger than B and C, there is very little dependence of the $3d$ band width on the value of the Racah parameters B and C.

A central result of our Gutzwiller theory is the anisotropic exchange splitting. The magnetization of our sample leads to the effective exchange splittings for $3d(e_g)$ states and $3d(t_{2g})$ states, $\Delta^{\text{eff}}(t_{2g}) = 0.25\,\text{eV}$, and $\Delta^{\text{eff}}(e_g) = 0.11\,\text{eV}$ which differ by more than a factor of two. Correspondingly, in the quasi-particle band structure near E_{F}, states of pure t_{2g} character (e.g., X_5, $W_{1'}$) exhibit a large splitting of majority and minority spin

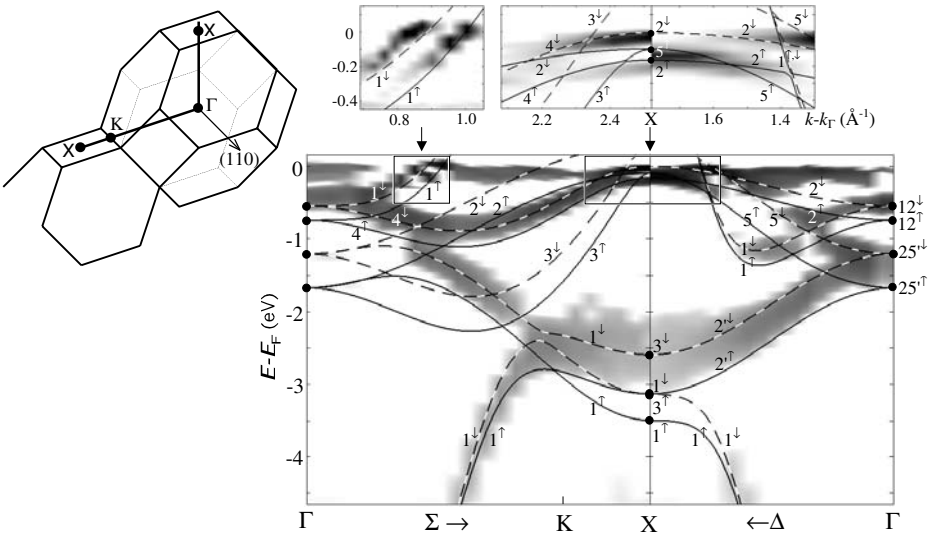

Figure 1: Grey-scale plot of the negative second derivative of the ARPES intensity for nickel with respect to energy, $-d^2I/dE^2$, on a logarithmic scale (insets: linear scale) for the ΓKX and ΓX directions of the Brillouin zone. The dispersionless structure at E_F is due to a residual Fermi edge resulting from indirect transitions. Some bands (Δ_2, X_1, Σ_2, Σ_3, Σ_1 towards Γ) are not seen due to unfavorable matrix elements, depending on geometry and chosen final state [30]. Theoretical curves are G-DFT, see table 2.

states of about 400 meV whereas the states with pure e_g character (e.g., X_2) exhibit small splittings of about 150 meV to 200 meV, see table 2. An important consequence of this anisotropy is the result that the state $X_{2\downarrow}$ lies slightly below the Fermi energy. This result is robust in all our calculations with Gutzwiller theory, e.g, it also applies for $A = 12$ eV.

The large anisotropy of the exchange splitting has been found experimentally by spin-polarized ARPES studies along the Λ-line of the Brillouin zone [45], and is well reproduced by our Gutzwiller theory, see table 2. In contrast, the SDFT energy bands show a much larger but rather isotropic exchange splitting because the exchange-correlation potential is constructed both from superposed $3d(t_{2g})$ and $3d(e_g)$ charge densities, i.e., the exchange-correlation potential is independent of the orbitals. In our Gutzwiller theory the two values for the exchange splittings result from two independent variational parameters.

It is relatively easy to understand the reason for the large anisotropy of the exchange splittings. The width of the $3d(t_{2g})$ bands is mainly determined by the first-neighbor electron-transfer integral $(dd\sigma)_1$, the largest $3d$-$3d$ matrix element, see table 1. The width of the $3d(e_g)$ bands does not depend on the $(dd\sigma)_1$ integral, but only on the much smaller $(dd\sigma)_2$ integral to second nearest neighbors. In addition there is some first-neighbor $3d(e_g)$-$3d(t_{2g})$ hybridization via the large $(dd\pi)_1$ integral. Thus, the most strongly anti-

bonding bands are the $3d(t_{2g})$ bands which form the top of the $3d$ bands. Electron-electron interaction enforces the exchange splitting of the bands up to the point where the limit of strong ferromagnetism is reached and the majority spin bands are completely filled. In the minority spin bands, some energy can be gained when the occupation of the anti-bonding $3d(t_{2g})$ bands is reduced, at the expense of the occupation of the top of the $3d(e_g)$ bands, i.e., of the occupation of the $X_{2\downarrow}$ state.

Table 2: Binding energies in eV with respect to the Fermi energy $E_{\rm F}$ (> 0 for occupied states). $\langle \ldots \rangle$ indicates the spin average, error bars in the experiments without spin resolution are given as $\pm$. Theoretical data show the spin average and the exchange splittings in square brackets. The second column denote the orbital character of the states, $t \equiv t_{2g}$, $e \equiv e_g$, capital letters: dominant character. The spin-polarized data $\langle \Lambda_{3;f} \rangle$ were taken at fractions f of the ΓL distance, with the emphasis on the analysis of the exchange splittings. G-DFT and SDFT calculations are without spin-orbit coupling and a fixed spin-only moment of $\mu_{\rm spin} = 0.55\mu_{\rm B}$.

Symmetry	Character	Experiment	Reference	G-DFT	SDFT
$\langle \Gamma_1 \rangle$	S	8.90±0.30	[30]	8.86	8.96[−0.11]
$\langle \Gamma_{25'} \rangle$	T	1.30±0.06	[30]	1.44[0.46]	1.99[0.43]
$\langle \Gamma_{12} \rangle$	E	0.48±0.08	[30]	0.65[0.195]	0.86[0.41]
$\langle X_1 \rangle$	sE	3.30±0.20	[22]	3.31[0.36]	4.37[0.20]
$\langle X_3 \rangle$	T	2.63±0.10	[30]	2.86[0.54]	3.82[0.37]
$X_{2\uparrow}$	E	0.21±0.03	[30]	0.165	0.35
$X_{2\downarrow}$	E	0.04±0.03	[30]	0.01	−0.09
$X_{5\uparrow}$	T	0.15±0.03	[30]	0.10	0.23
$\Delta_{e_g}(X_2)$	E	0.17±0.05	[30]	0.155	0.44
$\Delta_{t_{2g}}(X_5)$	T	0.33±0.04	[21]	0.38	0.56
$\langle K_1 \rangle$	sptE	3.10±0.20	[22]	2.76[0.33]	3.66[0.26]
$\langle K_2 \rangle$	spTe	2.48±0.06	[22]	2.59[0.50]	3.37[0.32]
$\langle K_3 \rangle$	pT	0.90±0.20	[22]	1.36[0.41]	1.73[0.37]
$\langle K_4 \rangle$	pE	0.47±0.03	[30]	0.51[0.185]	0.70[0.41]
$\langle L_1 \rangle$	sT	3.66±0.10	[30]	3.51[0.515]	4.56[0.23]
$\langle L_3 \rangle$	tE	1.43±0.07	[30]	1.51[0.34]	2.02[0.40]
$L_{3\uparrow}$	Te	0.18±0.03	[30]	0.22	0.38[0.50]
$\langle L_{2'} \rangle$	P	1.00±0.20	[22]	0.97[0.0]	0.24[−0.12]
$\langle W_{2'} \rangle$	pE	2.60±0.20	[22]	2.66[0.31]	3.46[0.24]
$\langle W_3 \rangle$	pT	1.70±0.20	[22]	2.04[0.47]	2.69[0.36]
$\langle W_1 \rangle$	sE	0.65±0.10	[22]	0.69[0.20]	0.94[0.39]
$W_{1'\uparrow}$	T	0.15±0.10	[22]	0.11	0.23[0.56]
$\langle \Lambda_{3;1/3} \rangle$	ptE	0.57[0.16±0.02]	[45]	0.67[0.22]	0.90[0.42]
$\langle \Lambda_{3;1/2} \rangle$	ptE	0.50[0.21±0.02]	[45]	0.55[0.26]	0.76[0.44]
$\langle \Lambda_{3;2/3} \rangle$	pTE	0.35[0.25±0.02]	[45]	0.33[0.29]	0.49[0.48]

3.4 Magnetic anisotropy

We now turn on the spin-orbit coupling. Again, we perform fixed-moment calculations, now with the full magnetic moment $\mu = 0.606\,\mu_{\rm B}$. Our total-energy calculations including spin-orbit coupling are two to three orders of magnitude more time consuming than the calculations discussed in Section 3.3 because our **k**-sums run over the full Brillouin zone, all hundred elements of the matrix $\tilde{q}$ must be calculated and all thousand internal variational parameters must be optimized, and additional external variational parameters appear, e.g., the effective spin-orbit coupling $\zeta^{\rm eff}$.

Table 3: Theoretical binding energies in eV with respect to the Fermi energy $E_{\rm F}$ (> 0 for occupied states) with and without spin-orbit coupling. The second column denote the orbital character of the states, $t \equiv t_{2g}$, $e \equiv e_g$, capital letters: dominant character. For the calculations without spin-orbit coupling, G-DFT, we used a spin-only moment of $\mu_{\rm spin} = 0.55\,\mu_{\rm B}$. In the spin-orbit calculation, G-DFT(SO), we worked with a fixed moment of $0.606\,\mu_{\rm B}$ along the (111)-direction. The directions Λ and the L-points in the Brillouin zone are not equivalent: the first and the second energy belong to the directions parallel and perpendicular to (111), respectively.

Symm.	Char.	G-DFT	G-DFT(SO)
$\Gamma_{25'\uparrow}$	T	1.67	1.74 1.67 1.17
$\Gamma_{25'\downarrow}$	T	1.21	1.25 1.21 1.17
$X_{2\uparrow}$	E	0.17	0.19
$X_{2\downarrow}$	E	0.01	0.02
$X_{5\uparrow}$	T	0.10	0.13 0.11
$X_{5\downarrow}$	T	-0.28	-0.27 -0.32
$L_{3\uparrow}$	Te	0.22	0.26 ; 0.24 0.20 ; 0.22

Symm.	Char.	G-DFT	G-DFT(SO)
$\Lambda_{3;1/3\uparrow}$	ptE	0.78	0.81 ; 0.80 0.76 ; 0.78
$\Lambda_{3;1/3\downarrow}$	ptE	0.57	0.61 ; 0.59 0.56 ; 0.57
$\Lambda_{3;1/2\uparrow}$	ptE	0.68	0.72 ; 0.70 0.66 ; 0.69
$\Lambda_{3;1/2\downarrow}$	ptE	0.42	0.47 ; 0.44 0.39 ; 0.41
$\Lambda_{3;2/3\uparrow}$	pTE	0.47	0.52 ; 0.50 0.45 ; 0.48
$\Lambda_{3;2/3\downarrow}$	pTE	0.19	0.22 ; 0.20 0.16 ; 0.18

Our optimal ground state displays an orbital moment of $\mu_{\rm orb} = 0.052\,\mu_{\rm B}$ which agrees very well with the experimental value of $\mu_{\rm orb} = 0.0507\,\mu_{\rm B}$ [1]. In the Hartree–Fock limit of our method, $\lambda_\Gamma \equiv 1$, we obtain $\mu_{\rm orb,\,HF} = 0.032\,\mu_{\rm B}$. Obviously, the orbital-moment contribution to the total moment almost doubles when we apply our Gutzwiller theory. This is due to the fact that correlations induce non-diagonal elements in the matrix $\tilde{q}$; they

become nonzero because the spin-orbit coupling lifts the cubic symmetry. An analysis of the quasi-particle bands shows that the non-diagonal elements of the matrix $\tilde{q}$ induce electron transfers with spin flips in the effective single-particle Hamiltonian. These processes give an additional contribution to the orbital moment. The effective value for the spin-orbit coupling becomes smaller, $\zeta^{\text{eff}} = 0.070\,\text{eV}$ for the optimum ground-state energy. This is a 12% reduction compared to the bare spin-orbit coupling constant $\zeta = 0.080\,\text{eV}$. Calculations with a fixed $\zeta^{\text{eff}} = \zeta$ yield higher ground-state energies and an approximately 10% larger orbital moment.

The central external variational parameters, the effective exchange splittings $\Delta^{\text{eff}}(t_{2g})$ and $\Delta^{\text{eff}}(e_g)$ as well as the effective crystal-field $\epsilon_{\text{cf}}^{\text{eff}}$, are very similar to the spin-only calculations. Consequently, the quasi-particle bands do not change very much from the quasi-particle bands as described in Section 3.3. However, degeneracies at high-symmetry points and lines are lifted. In table 3, we give some of the energies at high-symmetry points and lines, taken from a calculation where the magnetic moment lies parallel to the (111)-direction, the easy axis of nickel. Near the Fermi energy the splittings should be detectable by high resolution ARPES. Note that the state which derives from the $X_{2\downarrow}$-state still lies slightly below the Fermi energy.

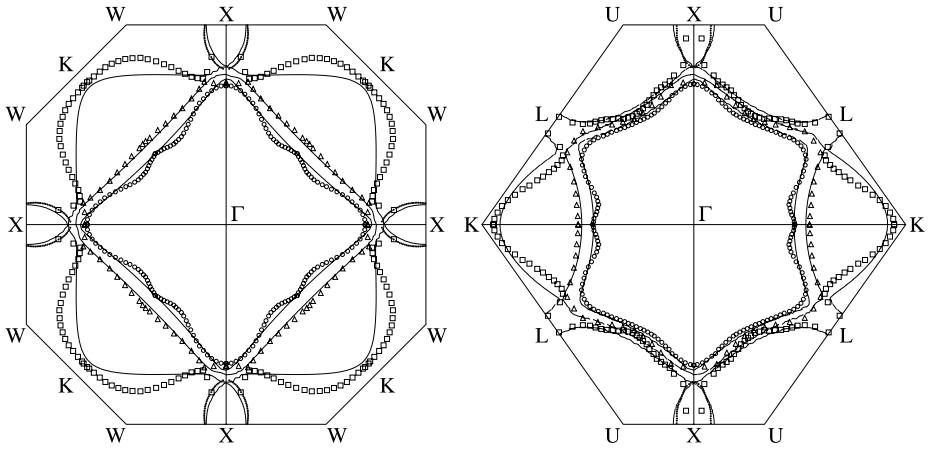

Figure 2: Cut of the Fermi surface with the plane ΓXK and the plane ΓXL in the Brillouin zone. Open symbols are data of Stark, communicated in [46], filled dots are de-Haas–van-Alphen data from [19], and lines are the results from Gutzwiller theory.

The spin-orbit coupling causes the former majority and minority spin bands to couple so that band crossings of spin-up bands and spin-down bands are avoided. As a consequence, the topology of the Fermi surface changes slightly. These changes affect only a few areas on the Fermi surface. In figure 2, we show a cut of the Fermi surface in the ΓKX plane and in the ΓXL plane, respectively.

The theoretical Fermi surface agrees very well with the de-Haas–van-Alphen data of Stark, which have been communicated through the paper of Callaway and Wang [46].

However, the experimental data exhibit oscillations in these cuts which are not reproduced by our Gutzwiller theory. In fact, no band calculation whatsoever has produced these wiggles. We suspect that these wiggles are artifacts of the reconstruction procedure from the raw data: in a magnetic field of several Tesla, the Fermi surface topology itself can change, as we now discuss.

When we align the magnetic moment along the (001)-direction, the quasi-particle energy of the X-states at (100) and at (010) differ from the energy of the (001) X-state; the three states are degenerate when the moment is along the (111) direction. The spin-orbit coupling induces a splitting of the formerly degenerate $X_{2\downarrow}$ state by 30 meV, and the energy of the (001) $X_{2\downarrow}$-state in the presence of the spin-orbit coupling lies approximately 6 meV *above* the Fermi energy whereas the other two state lie 25 meV below E_{F}. Thereby our Gutzwiller theory confirms the scenario put forward by Gersdorf [27].

The differences in ground-energies of the states with the magnetic moment aligned in the (111) direction and with the magnetic moment aligned in the (001) direction, $E_{\mathrm{aniso}} \equiv E_{111} - E_{001}$, is $E_{\mathrm{aniso,\,Gutz}} \approx -10\,\mu$eV per atom. Thus we get the correct sign and order of magnitude of the experimental energy difference, $E_{\mathrm{aniso}} = -3\,\mu$eV per atom. In order to improve the confidence in our results, we have repeated our numerical integrations over the Brillouin zone with a denser mesh but for fixed external variational parameters. Our calculations using a denser mesh with up to $2.5 \cdot 10^5$ $\mathbf{k}$-points in the Brillouin zone confirm the result of a (111) easy axis in nickel. Therefore, we are confident that Gutzwiller theory calculations produce reliable results for the magnetic anisotropy energies. Further studies with even larger $\mathbf{k}$-meshes are in progress.

4 Diagrammatic approach

In this section we develop a general scheme to evaluate expectation values for single-site and two-site operators using the variational analog of Feynman diagrams.

4.1 Conditions

We need to evaluate expectation values of operators $\hat{O}_{\mathbf{i}}$ and $\hat{O}_{\mathbf{i},\mathbf{j}} = \hat{c}^{(+)}_{\mathbf{i},\sigma}\hat{c}^{(+)}_{\mathbf{j},\sigma}$ for $\mathbf{i} \neq \mathbf{j}$ with the wave function (1),

$$\langle \hat{O}_{\mathbf{i}} \rangle_{\mathrm{G}} = \frac{\langle \Psi_0 | \left[\prod_{\mathbf{m} \neq \mathbf{i}} \hat{P}^2_{\mathrm{G}|\mathbf{m}} \right] \hat{P}_{\mathrm{G}|\mathbf{i}} \hat{O}_{\mathbf{i}} \hat{P}_{\mathrm{G}|\mathbf{i}} | \Psi_0 \rangle}{\langle \Psi_0 | \prod_{\mathbf{m}} \hat{P}^2_{\mathrm{G}|\mathbf{m}} | \Psi_0 \rangle} , \tag{33}$$

$$\langle \hat{O}_{\mathbf{i},\mathbf{j}} \rangle_{\mathrm{G}} = \frac{\langle \Psi_0 | \left[\prod_{\mathbf{m} \neq \mathbf{i},\mathbf{j}} \hat{P}^2_{\mathrm{G}|\mathbf{m}} \right] \hat{P}_{\mathrm{G}|\mathbf{i}} \hat{P}_{\mathrm{G}|\mathbf{j}} \hat{O}_{\mathbf{i},\mathbf{j}} \hat{P}_{\mathrm{G}|\mathbf{i}} \hat{P}_{\mathrm{G}|\mathbf{j}} | \Psi_0 \rangle}{\langle \Psi_0 | \prod_{\mathbf{m}} \hat{P}^2_{\mathrm{G}|\mathbf{m}} | \Psi_0 \rangle} . \tag{34}$$

The square of the local Gutzwiller correlator can be reduced to

$$\hat{P}^2_{\mathrm{G}|\mathbf{m}} = \sum_{I_1, I_2} \overline{\lambda}_{I_1, I_2|\mathbf{m}} |I_1\rangle_{\mathbf{m}\mathbf{m}} \langle I_2| \tag{35}$$

with

$$\overline{\lambda}_{I_1,I_2|\mathbf{m}} = \sum_{I'} \lambda_{I_1,I'|\mathbf{m}} \lambda_{I',I_2|\mathbf{m}} \,. \tag{36}$$

We aim at a diagrammatic calculation of $\langle \hat{O}_{\mathbf{i}} \rangle_{\mathrm{G}}$ and $\langle \hat{O}_{\mathbf{i},\mathbf{j}} \rangle_{\mathrm{G}}$. In such an approach, the sites $\mathbf{m} \neq \mathbf{i}, \mathbf{j}$ in (33) and (34) will play the role of inner vertices.

In a first step, we eliminate all local contributions at the inner vertices which arise after the application of Wick's theorem to the numerators in (33) and (34). As in a previous work [29], we expand $\hat{P}^2_{\mathrm{G}|\mathbf{m}}$ in terms of new local operators,

$$\begin{aligned} \hat{P}^2_{\mathrm{G}|\mathbf{m}} &= 1 + \left[\hat{P}^2_{\mathrm{G}|\mathbf{m}}\right]^{\mathrm{HF}} \,, \\ \left[\hat{P}^2_{\mathrm{G}|\mathbf{m}}\right]^{\mathrm{HF}} &= \sum_{I_1,I_2;|I_1|+|I_2|\geq 2} x_{I_1,I_2|\mathbf{m}} \left(\hat{n}_{I_1,I_2,\mathbf{m}} - \left[\hat{n}_{I_1,I_2,\mathbf{m}}\right]^{\mathrm{HF}} \right) \,, \end{aligned} \tag{37}$$

where

$$\hat{n}_{I_1,I_2,\mathbf{m}} \equiv \prod_{\sigma_1 \in I_1} \hat{c}^+_{\mathbf{m},\sigma_1} \prod_{\sigma_2 \in I_2} \hat{c}_{\mathbf{m},\sigma_2} \,. \tag{38}$$

The Hartree–Fock operator for an even number $n \geq 4$ of Fermion operators is defined recursively,

$$\begin{aligned} [\hat{a}_1 \ldots \hat{a}_n]^{\mathrm{HF}} &\equiv \langle \hat{a}_1 \ldots \hat{a}_n \rangle_0 \\ &+ {\sum_{\{\gamma_1,\ldots,\gamma_n\}=0}^{1}}' (-1)^{f_{\mathrm{s}}(\{\gamma_i\})} \left\{ \left(\prod_{\ell=1}^{n} \hat{a}_\ell^{\gamma_\ell} \right) - \left[\prod_{\ell=1}^{n} \hat{a}_\ell^{\gamma_\ell} \right]^{\mathrm{HF}} \right\} \left\langle \prod_{\ell=1}^{n} \hat{a}_\ell^{1-\gamma_\ell} \right\rangle_0 \end{aligned} \tag{39}$$

with

$$f_{\mathrm{s}}(\{\gamma_i\}) \equiv \sum_{\ell=1}^{n} (\ell - \frac{1}{2}) \gamma_\ell \,. \tag{40}$$

The prime in (39) indicates that $2 \leq \sum_{\ell=1}^{n} \gamma_\ell \leq n-2$ is even. For $n = 2$ we have

$$[\hat{a}_1 \hat{a}_2]^{\mathrm{HF}} = \langle \hat{a}_1 \hat{a}_2 \rangle_0 \,. \tag{41}$$

By construction, the operator in (37) generates diagrams with exactly $|I_1|$ ($|I_2|$) non-local lines that enter (leave) the lattice site $\mathbf{m}$. All diagrams with trivial local Hartree–Fock bubbles are automatically excluded.

For our diagrammatic evaluation we demand that at least four lines meet at every inner vertex,

$$x_{I_1,I_2|\mathbf{m}} = 0 \quad \text{for} \quad |I_1| + |I_2| = 2 \,. \tag{42}$$

We can fulfill these conditions by restricting our parameters $\lambda_{I_1,I_2|\mathbf{m}}$. Using the form (37) together with (42) one easily sees that

$$\langle \hat{P}^2_{\mathrm{G}|\mathbf{m}} \rangle_0 = 1 \,, \tag{43}$$

$$\langle \hat{c}^+_{\mathbf{m},\sigma} \hat{P}^2_{\mathrm{G}|\mathbf{m}} \hat{c}_{\mathbf{m},\sigma'} \rangle_0 = \langle \hat{c}^+_{\mathbf{m},\sigma} \hat{c}_{\mathbf{m},\sigma'} \rangle_0 \,, \tag{44}$$

$$\langle \hat{c}^+_{\mathbf{m},\sigma} \hat{P}^2_{\mathrm{G}|\mathbf{m}} \hat{c}^+_{\mathbf{m},\sigma'} \rangle_0 = \langle \hat{c}^+_{\mathbf{m},\sigma} \hat{c}^+_{\mathbf{m},\sigma'} \rangle_0 \,, \tag{45}$$

$$\langle \hat{c}_{\mathbf{m},\sigma} \hat{P}^2_{\mathrm{G}|\mathbf{m}} \hat{c}_{\mathbf{m},\sigma'} \rangle_0 = \langle \hat{c}_{\mathbf{m},\sigma} \hat{c}_{\mathbf{m},\sigma'} \rangle_0 \tag{46}$$

must be fulfilled. This follows from the fact that, apart from the trivial term in (37), at least four lines meet at every vertex; a contraction with two 'external' fermionic operators leaves at least one uncontracted pair whose local contraction, however, vanishes by construction of new local operators (37). Explicitly,

$$\sum_{I_1,I_2} \overline{\lambda}_{I_1,I_2|\mathbf{m}} m^0_{I_1,I_2|\mathbf{m}} = 1 \,, \tag{47}$$

$$\sum_{I_1(\sigma\in I_1)} \sum_{I_2(\sigma'\in I_2)} \overline{\lambda}_{I_1\setminus\sigma,I_2\setminus\sigma'|\mathbf{m}} m^0_{I_1,I_2|\mathbf{m}} = \langle \hat{c}^+_{\mathbf{m},\sigma}\hat{c}_{\mathbf{m},\sigma'}\rangle_0 \,, \tag{48}$$

$$\sum_{I_1(\sigma\in I_1)} \sum_{I_2(\sigma'\in I_2)} \overline{\lambda}_{I_1\setminus\sigma,I_2|\mathbf{m}} m^0_{I_1,I_2\setminus\sigma'|\mathbf{m}} = \langle \hat{c}^+_{\mathbf{m},\sigma}\hat{c}^+_{\mathbf{m},\sigma'}\rangle_0 \,, \tag{49}$$

$$\sum_{I_1(\sigma\in I_1)} \sum_{I_2(\sigma'\in I_2)} \overline{\lambda}_{I_1,I_2\setminus\sigma'|\mathbf{m}} m^0_{I_1\setminus\sigma,I_2|\mathbf{m}} = \langle \hat{c}_{\mathbf{m},\sigma}\hat{c}_{\mathbf{m},\sigma'}\rangle_0 \,. \tag{50}$$

Here, we introduced the expectation value

$$\begin{aligned} m^0_{I_1,I_2|\mathbf{m}} &= \langle\Psi_0|I_1\rangle_{\mathbf{m}\,\mathbf{m}}\langle I_2|\Psi_0\rangle \\ &= \langle\Psi_0|\hat{n}_{I_1,I_2|\mathbf{m}}\hat{n}^{\mathrm{h}}_{I_1\cup I_2|\mathbf{m}}|\Psi_0\rangle \,, \end{aligned} \tag{51}$$

with

$$\hat{n}^{\mathrm{h}}_{I|\mathbf{m}} \equiv \prod_{\sigma\in\overline{I}} (1-\hat{n}_{\mathbf{m},\sigma}) \tag{52}$$

and

$$\hat{n}_{\mathbf{m},\sigma} \equiv \hat{c}^+_{\mathbf{m},\sigma}\hat{c}_{\mathbf{m},\sigma} \,. \tag{53}$$

Equations (47)–(50) can be used to fix some of the variational parameters $\lambda_{I_1,I_2|\mathbf{m}}$, for example those with $|I_1|+|I_2|\leq 1$.

4.2 Diagrammatics

With the help of (37) we expand the product over the squares of local Gutzwiller correlators in (33) [and in (34)] in the form

$$\prod_{\mathbf{m}\neq\mathbf{i},\mathbf{j}} \hat{P}^2_{\mathrm{G};\mathbf{m}} = 1 + \sum_{\mathbf{m}}{}' \left[\hat{P}^2_{\mathrm{G};\mathbf{m}}\right]^{\mathrm{HF}} + \frac{1}{2}\sum_{\mathbf{m}_1,\mathbf{m}_2}{}' \left[\hat{P}^2_{\mathrm{G};\mathbf{m}_1}\right]^{\mathrm{HF}} \left[\hat{P}^2_{\mathrm{G};\mathbf{m}_2}\right]^{\mathrm{HF}} + \dots \,, \tag{54}$$

where the prime on the sums indicates that all lattice sites are different from each other and from $\mathbf{i}$ [and $\mathbf{j}$]. When Wick's theorem is applied to the numerators in (33) and in (34) we can introduce *new contractions* between two Fermi operators $\hat{a}_{\mathbf{m},\sigma}$ and $\hat{a}_{\mathbf{n},\sigma}$ ($\hat{a}=\hat{c}$ or $\hat{a}=\hat{c}^+$)

$$K^0_{\mathbf{m},\sigma;\mathbf{n},\sigma'} = \langle \hat{a}_{\mathbf{n},\sigma}\hat{a}_{\mathbf{m},\sigma'}\rangle_0 - \delta_{\mathbf{n},\mathbf{m}}\langle \hat{a}_{\mathbf{n},\sigma}\hat{a}_{\mathbf{n},\sigma'}\rangle_0 \,. \tag{55}$$

In most cases, $\mathbf{n}\neq\mathbf{m}$ holds and the new definition of a contraction reduces to the usual one because the extra term proportional to $\delta_{\mathbf{n},\mathbf{m}}$ vanishes. In those cases where Fermi operators on the same site are contracted the contribution must vanish because

we subtracted all local Hartree contributions in $\left[\hat{P}^2_{\mathrm{G};\mathbf{m}}\right]^{\mathrm{HF}}$. The new contraction in (55) fulfills this condition.

The application of Wick's theorem thus gives a result which we would have obtained if we had worked with Grassmann operators instead of Fermion operators in the definition of the expectation values; all Grassmann operators $\hat{a}^g_{\mathbf{i},\sigma}$ anti-commute with each other

$$\left[\hat{a}^g_{\mathbf{i},\sigma}, \hat{a}^g_{\mathbf{j},\sigma'}\right]_+ = 0 \,, \tag{56}$$

so that local contractions always vanish,

$$\langle \hat{a}^g_{\mathbf{i},\sigma} \hat{a}^g_{\mathbf{i},\sigma'} \rangle_0 = 0 \,. \tag{57}$$

The use of Grassmann operators instead of Fermi operators also shows that we may now drop the restrictions on the lattice sums because all contributions with two lattice sites put equal vanish due to the anti-commutation relation between the corresponding Grassmann operators. In this way we have generated a diagrammatic theory in which lines between two vertices $\mathbf{n}$ and $\mathbf{m}$ are given by the one-particle density matrices $K^0_{\mathbf{m},\sigma;\mathbf{n},\sigma'}$ defined in (55), and $x_{I_1,I_2|\mathbf{m}}$ gives the strength of a vertex $(I_1, I_2|\mathbf{m})$ with $|I_1|$ in-going lines and $|I_2|$ out-going lines.

Now we are in the position to apply the linked-cluster theorem so that all disconnected diagrams in the numerator in (33) [and in (34)] cancel the corresponding denominator. Then, the calculation of the expectation values (33) and (34) is reduced to the sum over all connected diagrams according to the Feynman rules with lines and vertices as defined above.

5 Exact results for infinite coordination number

By construction, at least four lines meet at every inner vertex. Due to the absence of local Hartree–Fock contributions two inner vertices are always connected by at least three independent paths of lines (there is no diagram with a single inner vertex). For lattices with Z nearest neighbors,

$$K^0_{\mathbf{m},\sigma|\mathbf{n},\sigma'} \sim \mathcal{O}\left(Z^{-|\mathbf{n}-\mathbf{m}|/2}\right) \,; \tag{58}$$

for a simple cubic lattice in d dimensions, $Z = 2d$. Therefore, the contribution of all diagrams with inner vertices vanishes at least proportional to $1/\sqrt{d}$ in the limit of infinite dimensions. Thus, not a single diagram needs to be calculated in infinite dimensions, i.e., we arrive at the result

$$\langle \hat{O}_{\mathbf{i}} \rangle_{\mathrm{G}} = \langle \Psi_0 | \hat{P}_{\mathrm{G}|\mathbf{i}} \hat{O}_{\mathbf{i}} \hat{P}_{\mathrm{G}|\mathbf{i}} | \Psi_0 \rangle \,, \tag{59}$$

$$\langle \hat{O}_{\mathbf{i},\mathbf{j}} \rangle_{\mathrm{G}} = \langle \Psi_0 | \hat{P}_{\mathrm{G}|\mathbf{i}} \hat{P}_{\mathrm{G}|\mathbf{j}} \hat{O}_{\mathbf{i},\mathbf{j}} \hat{P}_{\mathrm{G}|\mathbf{i}} \hat{P}_{\mathrm{G}|\mathbf{j}} | \Psi_0 \rangle \tag{60}$$

in $d = \infty$ dimensions. The result (60) can be further simplified because in $d = \infty$ dimensions there can be only a single line connecting the two external vertices $\mathbf{i}$ and $\mathbf{j}$.

5.1 Local quantities

Now we address the local operators for the particle densities,

$$\hat{n}_{\mathbf{i},\sigma\sigma'} \equiv \hat{c}^{+}_{\mathbf{i},\sigma}\hat{c}_{\mathbf{i},\sigma'} \ , \tag{61}$$

the pairing densities,

$$\hat{s}_{\mathbf{i},\sigma\sigma'} \equiv \hat{c}_{\mathbf{i},\sigma}\hat{c}_{\mathbf{i},\sigma'} \ , \tag{62}$$

and the local interaction

$$\hat{H}_{\rm at} \equiv \sum_{\mathbf{m}} \sum_{J_1,J_2} U_{J_1,J_2|\mathbf{m}} |J_1\rangle_{\mathbf{m}\mathbf{m}}\langle J_2| \ . \tag{63}$$

In infinite dimensions we have

$$\begin{aligned} n_{\mathbf{i},\sigma\sigma'} &= \langle \hat{n}_{\mathbf{i},\sigma\sigma'}\rangle_{\rm G} = \langle \hat{P}_{{\rm G}|\mathbf{i}}\hat{c}^{+}_{\mathbf{i},\sigma}\hat{c}_{\mathbf{i},\sigma'}\hat{P}_{{\rm G}|\mathbf{i}}\rangle_0 \\ &= \sum_{I_1,I_4} N^{\sigma\sigma'}_{I_1,I_4|\mathbf{i}} m^0_{I_1,I_4|\mathbf{i}} \ . \end{aligned} \tag{64}$$

Here we defined the matrix elements for the local densities as

$$\begin{aligned} N^{\sigma\sigma'}_{I_1,I_4|\mathbf{i}} &\equiv \sum_{I_2,I_3} \lambda_{I_1,I_2|\mathbf{i}}\lambda_{I_3,I_4|\mathbf{i}}\, {}_{\mathbf{i}}\langle I_2|\hat{c}^{+}_{\mathbf{i},\sigma}\hat{c}_{\mathbf{i},\sigma'}|I_3\rangle_{\mathbf{i}} \\ &= \sum_{I(\sigma\sigma'\notin I)} \lambda_{I_1,I\cup\sigma|\mathbf{i}}\lambda_{I\cup\sigma',I_4|\mathbf{i}} {\rm fsgn}(\sigma,I){\rm fsgn}(\sigma',I) \end{aligned} \tag{65}$$

where

$${\rm fsgn}(\sigma,I) \equiv \langle I\cup\sigma|\hat{c}^{+}_{\sigma}|I\rangle \tag{66}$$

is ± 1 if it takes an odd/even number of anti-commutations to shift the state σ to its proper place in the ordered sequence I. Correspondingly, we find

$$\begin{aligned} s_{\mathbf{i},\sigma\sigma'} &= \langle \hat{s}_{\mathbf{i},\sigma\sigma'}\rangle_{\rm G} = \langle \hat{P}_{{\rm G}|\mathbf{i}}\hat{c}_{\mathbf{i},\sigma}\hat{c}_{\mathbf{i},\sigma'}\hat{P}_{{\rm G}|\mathbf{i}}\rangle_0 \\ &= \sum_{I_1,I_4} S^{\sigma\sigma'}_{I_1,I_4|\mathbf{i}} m^0_{I_1,I_4|\mathbf{i}} \ . \end{aligned} \tag{67}$$

Here we defined the matrix elements for the local pairing amplitudes as

$$\begin{aligned} S^{\sigma\sigma'}_{I_1,I_4|\mathbf{i}} &\equiv \sum_{I_2,I_3} \lambda_{I_1,I_2|\mathbf{i}}\lambda_{I_3,I_4|\mathbf{i}}\, {}_{\mathbf{i}}\langle I_2|\hat{c}_{\mathbf{i},\sigma}\hat{c}_{\mathbf{i},\sigma'}|I_3\rangle_{\mathbf{i}} \\ &= \sum_{I(\sigma\sigma'\notin I)} \lambda_{I_1,I|\mathbf{i}}\lambda_{I\cup(\sigma\sigma'),I_4|\mathbf{i}} {\rm fsgn}(\sigma,I){\rm fsgn}(\sigma',I){\rm fsgn}(\sigma,\sigma') \ . \end{aligned} \tag{68}$$

Lastly, along the same lines we find

$$\begin{aligned} E^{\rm at} &= \langle \hat{H}_{\rm at}\rangle_{\rm G} \\ &= \sum_{\mathbf{i}} \langle \hat{P}_{{\rm G}|\mathbf{i}} \sum_{J_1,J_2} U_{J_1,J_2|\mathbf{i}} |J_1\rangle_{\mathbf{i}\mathbf{i}}\langle J_2|\hat{P}_{{\rm G}|\mathbf{i}}\rangle_0 \\ &= \sum_{\mathbf{i}} \sum_{I_1,I_4} \overline{U}_{I_1,I_4|\mathbf{i}} m^0_{I_1,I_4|\mathbf{i}} \ , \end{aligned} \tag{69}$$

where

$$\overline{U}_{I_1,I_4|\mathbf{i}} \equiv \sum_{I_2,I_3} \lambda_{I_1,I_2|\mathbf{i}}\lambda_{I_3,I_4|\mathbf{i}} U_{I_2,I_3|\mathbf{i}} \ . \tag{70}$$

5.2 Single-particle density matrices

Now we evaluate the single-particle density matrix

$$P_{\mathbf{i},\sigma;\mathbf{j}\sigma'} \equiv \langle \hat{c}^{+}_{\mathbf{i},\sigma} \hat{c}_{\mathbf{j},\sigma'} \rangle_{\mathrm{G}} \tag{71}$$

and the one-particle pairing matrix

$$S_{\mathbf{i},\sigma;\mathbf{j}\sigma'} \equiv \langle \hat{c}_{\mathbf{i},\sigma} \hat{c}_{\mathbf{j},\sigma'} \rangle_{\mathrm{G}} \tag{72}$$

for $\mathbf{i} \neq \mathbf{j}$.

We start with $\hat{O}_{\mathbf{ij}} = \hat{c}^{+}_{\mathbf{i},\sigma} \hat{c}_{\mathbf{j},\sigma'}$ in (34) and evaluate

$$\hat{P}_{\mathrm{G}|\mathbf{i}} \hat{c}^{+}_{\mathbf{i},\sigma} \hat{P}_{\mathrm{G}|\mathbf{i}} = \sum_{I_1, I_4} c^{*}_{I_1,I_4|\mathbf{i},\sigma} |I_1\rangle_{\mathbf{ii}} \langle I_4| \tag{73}$$

with

$$\begin{aligned} c^{*}_{I_1,I_4|\mathbf{i},\sigma} &\equiv \sum_{I_2,I_3} \lambda_{I_1,I_2|\mathbf{i}} \lambda_{I_3,I_4|\mathbf{i}\,\mathbf{i}} \langle I_2 | \hat{c}^{+}_{\mathbf{i},\sigma} | I_3 \rangle_{\mathbf{i}} \\ &= \sum_{I(\sigma \notin I)} \mathrm{fsgn}(\sigma, I) \lambda_{I_1,I\cup\sigma|\mathbf{i}} \lambda_{I,I_4|\mathbf{i}} \,. \end{aligned} \tag{74}$$

In $d = \infty$ dimensions only a single line can join the two external vertices $\mathbf{i} \neq \mathbf{j}$ in (60). In the first case, the contraction at $\mathbf{i}$ is done with a creation operator $\hat{c}^{+}_{\mathbf{i},\gamma}$. There are two possibilities, it can either be $\gamma \in I_1$, with

$$|I_1\rangle_{\mathbf{ii}} \langle I_4| = \left(\mathrm{fsgn}(\gamma, I_1 \setminus \gamma)\, \hat{n}_{I_1\setminus\gamma,I_4|\mathbf{i}}\, \hat{n}^{\mathrm{h}}_{I_1\cup I_4|\mathbf{i}} \right) \hat{c}^{+}_{\mathbf{i},\gamma} \,, \tag{75}$$

or $\gamma \in \overline{I_1 \cup I_4}$, with

$$|I_1\rangle_{\mathbf{ii}} \langle I_4| = -\left(\mathrm{fsgn}(\gamma, I_4)\, \hat{n}_{I_1,I_4\cup\gamma|\mathbf{i}}\, \hat{n}^{\mathrm{h}}_{I_1\cup I_4\cup\gamma|\mathbf{i}} \right) \hat{c}^{+}_{\mathbf{i},\gamma} \,. \tag{76}$$

Altogether, the amplitude for such a process is given by

$$q^{*}_{\mathbf{i},\sigma\gamma} \equiv \sum_{I(\gamma\notin I)} \sum_{I'} \mathrm{fsgn}(\gamma, I) (m^{0(\gamma)}_{I,I'|\mathbf{i}} c^{*}_{I\cup\gamma,I'|\mathbf{i},\sigma} - m^{0}_{I',I\cup\gamma|\mathbf{i}} c^{*}_{I',I|\mathbf{i},\sigma}) \,. \tag{77}$$

Here, we introduced the expectation value

$$m^{0(\gamma)}_{I,I'|\mathbf{i}} \equiv \langle \hat{n}_{I,I'|\mathbf{i}}\, \hat{n}^{\mathrm{h}}_{I\cup I'\cup\gamma|\mathbf{i}} \rangle_0 \,. \tag{78}$$

In previous works [29, 30], the factors $q^{*}_{\mathbf{i},\sigma\gamma}$ were denoted by $\sqrt{q_{\mathbf{i},\sigma\gamma}}$. In general, however, $q^{*}_{\mathbf{i},\sigma\gamma}$ is not a positive real number.

The second case is only possible if there are superconducting pairing correlations in $|\Psi_0\rangle$. Then, the line between $\mathbf{i}$ and $\mathbf{j}$ can also be an anomalous propagator, i.e., the contraction at $\mathbf{i}$ can be done with an annihilation operator $\hat{c}_{\mathbf{i},\gamma}$. Again, we obtain two contributions, $\gamma \in I_4$, which gives

$$|I_1\rangle_{\mathbf{ii}} \langle I_4| = \hat{c}_{\mathbf{i},\gamma} \left(\mathrm{fsgn}(\gamma, I_2 \setminus \gamma)\, \hat{n}_{I_1,I_4\setminus\gamma|\mathbf{i}}\, \hat{n}^{\mathrm{h}}_{I_1\cup I_4|\mathbf{i}} \right) \,, \tag{79}$$

and $\gamma \in \overline{I_1 \cup I_4}$, which contributes

$$|I_1\rangle_{\mathbf{i}\mathbf{i}}\langle I_4| = \hat{c}_{\mathbf{i},\gamma}\left(\mathrm{fsgn}(\gamma, I_1)\,\hat{n}_{I_1\cup\gamma,I_4|\mathbf{i}}\,\hat{n}^{\mathrm{h}}_{I_1\cup I_4\cup\gamma|\mathbf{i}}\right) . \tag{80}$$

Therefore, the amplitude for the anomalous process can be written as

$$\bar{q}_{\mathbf{i},\sigma\gamma} \equiv \sum_{I(\gamma\notin I)}\sum_{I'} \mathrm{fsgn}(\gamma, I)(m^{0(\gamma)}_{I',I|\mathbf{i}}c^*_{I',I\cup\gamma|\mathbf{i},\sigma} + m^0_{I\cup\gamma,I'|\mathbf{i}}c^*_{I,I'|\mathbf{i},\sigma}) . \tag{81}$$

With these definitions we find for the one-particle density matrix

$$\begin{aligned} P_{\mathbf{i},\sigma;\mathbf{j}\sigma'} &= \sum_{\gamma\gamma'}\Big[q^*_{\mathbf{i},\sigma\gamma}q_{\mathbf{j},\sigma'\gamma'}\langle\hat{c}^+_{\mathbf{i},\gamma}\hat{c}_{\mathbf{j},\gamma'}\rangle_0 + \bar{q}_{\mathbf{i},\sigma\gamma}\bar{q}^*_{\mathbf{j},\sigma'\gamma'}\langle\hat{c}_{\mathbf{i},\gamma}\hat{c}^+_{\mathbf{j},\gamma'}\rangle_0 \\ &\qquad q^*_{\mathbf{i},\sigma\gamma}\bar{q}^*_{\mathbf{j},\sigma'\gamma'}\langle\hat{c}^+_{\mathbf{i},\gamma}\hat{c}^+_{\mathbf{j},\gamma'}\rangle_0 + \bar{q}_{\mathbf{i},\sigma\gamma}q_{\mathbf{j},\sigma'\gamma'}\langle\hat{c}_{\mathbf{i},\gamma}\hat{c}_{\mathbf{j},\gamma'}\rangle_0\Big] \end{aligned} \tag{82}$$

in the limit of infinite dimensions.

Analogously, for the one-particle pairing matrix we find

$$\begin{aligned} S_{\mathbf{i},\sigma;\mathbf{j}\sigma'} &= \sum_{\gamma\gamma'}\Big[q_{\mathbf{i},\sigma\gamma}q_{\mathbf{j},\sigma'\gamma'}\langle\hat{c}_{\mathbf{i},\gamma}\hat{c}_{\mathbf{j},\gamma'}\rangle_0 + \bar{q}^*_{\mathbf{i},\sigma\gamma}\bar{q}^*_{\mathbf{j},\sigma'\gamma'}\langle\hat{c}^+_{\mathbf{i},\gamma}\hat{c}^+_{\mathbf{j},\gamma'}\rangle_0 \\ &\qquad q_{\mathbf{i},\sigma\gamma}\bar{q}^*_{\mathbf{j},\sigma'\gamma'}\langle\hat{c}_{\mathbf{i},\gamma}\hat{c}^+_{\mathbf{j},\gamma'}\rangle_0 + \bar{q}^*_{\mathbf{i},\sigma\gamma}q_{\mathbf{j},\sigma'\gamma'}\langle\hat{c}^+_{\mathbf{i},\gamma}\hat{c}_{\mathbf{j},\gamma'}\rangle_0\Big] \end{aligned} \tag{83}$$

in the limit of infinite dimensions.

6 Variational ground-state energy

In this section we specify the variational problem in the limit of high dimensions. We use translational invariance to render the problem numerically tractable.

6.1 Variational problem

The variational ground-state energy for the multi-band Hamiltonian (12) is given by

$$E^{\mathrm{var}}(\{\lambda_{I_1,I_2|\mathbf{i}}\},\{|\Psi_0\rangle\}) = \langle\hat{H}\rangle_{\mathrm{G}} . \tag{84}$$

With the help of the results of Section 5, this expectation value is readily evaluated in infinite dimensions. We find

$$E^{\mathrm{var}}(\{\lambda_{I_1,I_2|\mathbf{i}}\},\{|\Psi_0\rangle\}) = E^{\mathrm{kin}}(\{\lambda_{I_1,I_2|\mathbf{i}}\},\{|\Psi_0\rangle\}) + E^{\mathrm{at}}(\{\lambda_{I_1,I_2|\mathbf{i}}\},\{|\Psi_0\rangle\}) , \tag{85}$$

$$E^{\mathrm{kin}}(\{\lambda_{I_1,I_2|\mathbf{i}}\},\{|\Psi_0\rangle\}) = \sum_{\mathbf{i},\mathbf{j};\sigma\sigma'}\sum_{\alpha,\alpha'=+,-} t^{\alpha\alpha';\sigma\sigma'}_{\mathbf{i},\mathbf{j}}\langle\Psi_0|\hat{c}^{\alpha}_{\mathbf{i},\sigma}\hat{c}^{\alpha'}_{\mathbf{j},\sigma'}|\Psi_0\rangle , \tag{86}$$

$$E^{\mathrm{at}}(\{\lambda_{I_1,I_2|\mathbf{i}}\},\{|\Psi_0\rangle\}) = \sum_{\mathbf{i}}\sum_{I_1,I_4}\overline{U}_{I_1,I_4|\mathbf{i}}m^0_{I_1,I_4|\mathbf{i}} . \tag{87}$$

where $\overline{U}_{I_1,I_4|\mathbf{i}}$ is given in (70). The superscripts $\alpha, \alpha' = +/-$ were introduced in order to distinguish creation and annihilation operators ($\hat{c}^- \equiv \hat{c}$). Mathematically, these superscripts are interpreted as real numbers, e.g., $\hat{c}^{(-\alpha)}$ is equal to $\hat{c}^+$ or $\hat{c}$ when $\alpha = -$ or $\alpha = +$, respectively. For the hopping amplitudes in (86) we find

$$t^{+-;\sigma\sigma'}_{\mathbf{i},\mathbf{j}} = \frac{1}{2}\sum_{\tau\tau'}\left(q^*_{\mathbf{i},\tau\sigma}q_{\mathbf{j},\tau'\sigma'}t^{\tau\tau'}_{\mathbf{i},\mathbf{j}} - \bar{q}^*_{\mathbf{i},\tau\sigma}\bar{q}_{\mathbf{j},\tau'\sigma'}t^{\tau',\tau}_{\mathbf{j},\mathbf{i}}\right) \ , \ t^{-+;\sigma\sigma'}_{\mathbf{i},\mathbf{j}} = -\left(t^{+-;\sigma\sigma'}_{\mathbf{i},\mathbf{j}}\right)^* \ , \tag{88}$$

$$t^{++;\sigma\sigma'}_{\mathbf{i},\mathbf{j}} = \frac{1}{2}\sum_{\tau\tau'}\left(q^*_{\mathbf{i},\tau\sigma}\bar{q}^*_{\mathbf{j},\tau'\sigma'}t^{\tau\tau'}_{\mathbf{i},\mathbf{j}} - \bar{q}^*_{\mathbf{i},\tau\sigma}q^*_{\mathbf{j},\tau'\sigma'}t^{\tau',\tau}_{\mathbf{j},\mathbf{i}}\right) \ , \ t^{--;\sigma\sigma'}_{\mathbf{i},\mathbf{j}} = -\left(t^{++;\sigma\sigma'}_{\mathbf{i},\mathbf{j}}\right)^* \ . \tag{89}$$

The interaction energy is given in terms of the variational parameters $\lambda_{I_1,I_2|\mathbf{i}}$ and purely local expectation values in $|\Psi_0\rangle$. With the help of Wick's theorem these expectation values can be expressed solely in terms of the local single-particle density matrix $\widetilde{C}_{\mathbf{m}}$ with entries

$$C^{\alpha\alpha'}_{\mathbf{m},\sigma\sigma'} = \langle \hat{c}^{\alpha}_{\mathbf{m},\sigma}\hat{c}^{\alpha'}_{\mathbf{m},\sigma'}\rangle_0 \ . \tag{90}$$

6.2 Minimization

6.2.1 Effective single-particle Schrödinger equation

We have to optimize the variational ground-state energy (85) with respect to all parameters $\{\lambda_{I_1,I_2|\mathbf{i}}\}$ and the set of all one-particle quasi-particle vacua $\{|\Psi_0\rangle\}$, whereby the equations (47)–(50) have to be obeyed. The latter may be fulfilled by fixing the parameters $\{\lambda_{I_1,I_2|\mathbf{i}}\}$ for $|I_1|, |I_2| \leq 1$, which are then functions of $\widetilde{C}_{\mathbf{i}}$ and $\{\widetilde{\lambda}_{\mathbf{i}}\} \equiv \{\lambda_{I_1,I_2|\mathbf{i}}\}$ with $|I_1|, |I_2| \geq 2$. We introduce the tensors $\widetilde{\eta}_{\mathbf{i}}$ of Lagrange multipliers with entries $\eta^{\alpha,\alpha'}_{\mathbf{i},\sigma\sigma'}$ and the multiplier E^{SP} in order to fulfill equation (90) and to ensure the normalization of $|\Psi_0\rangle$. In addition, we fix the average number of particles $N = nL$ in $|\Psi_{\mathrm{G}}\rangle$ with the help of the Lagrange multiplier Λ. Then, the variational ground-state energy E_0^{var} is given by

$$E_0^{\mathrm{var}} = \underset{\{\widetilde{\lambda}_{\mathbf{i}}\},\{\widetilde{C}_{\mathbf{i}}\},\{\widetilde{\eta}_{\mathbf{i}}\},\Lambda,\{|\Psi_0\rangle\},E^{\mathrm{SP}}}{\mathrm{Minimum}} E_{\mathrm{c}}\left(\{\widetilde{\lambda}_{\mathbf{i}}\},\{\widetilde{C}_{\mathbf{i}}\},\{\widetilde{\eta}_{\mathbf{i}}\},\Lambda,\{|\Psi_0\rangle\},E^{\mathrm{SP}}\right) \tag{91}$$

$$\begin{aligned} E_{\mathrm{c}}(\ldots) = {} & E^{\mathrm{var}}\left(\{\widetilde{\lambda}_{\mathbf{i}}\},\{\widetilde{C}_{\mathbf{i}}\}\{|\Psi_0\rangle\}\right) - E^{\mathrm{SP}}\left(\langle\Psi_0|\Psi_0\rangle - 1\right) \\ & - \sum_{\mathbf{i},\sigma\sigma'}\sum_{\alpha,\alpha'}\left[\eta^{\alpha\alpha'}_{\mathbf{i},\sigma\sigma'}\left(C^{\alpha\alpha'}_{\mathbf{i},\sigma\sigma'} - \langle\Psi_0|\hat{c}^{\alpha}_{\mathbf{i},\sigma}\hat{c}^{\alpha'}_{\mathbf{i},\sigma'}|\Psi_0\rangle\right) + \mathrm{c.c.}\right] \\ & + \Lambda\left(\sum_{\mathbf{i},\sigma} n_{\mathbf{i},\sigma\sigma}\left(\{\widetilde{\lambda}_{\mathbf{i}}\},\{\widetilde{C}_{\mathbf{i}}\}\right) - N\right) . \end{aligned} \tag{92}$$

The minimization with respect to $|\Psi_0\rangle$ can be carried out explicitly and leads to the effective one-particle Schrödinger equation

$$\hat{T}^{\mathrm{eff}}|\Psi_0\rangle = E^{\mathrm{SP}}\left(\{\widetilde{\lambda}_{\mathbf{i}}\},\{\widetilde{C}_{\mathbf{i}}\},\{\widetilde{\eta}_{\mathbf{i}}\}\right)|\Psi_0\rangle \ , \tag{93}$$

$$\begin{aligned} \hat{T}^{\mathrm{eff}} &\equiv \frac{1}{2}\sum_{\mathbf{i},\sigma;\mathbf{j},\sigma'}\sum_{\alpha\alpha'}\left[\left(t^{\alpha\alpha';\sigma\sigma'}_{\mathbf{i},\mathbf{j}} + 2\delta_{\mathbf{i},\mathbf{j}}\eta^{\alpha\alpha'}_{\mathbf{i},\sigma\sigma'}\right)\hat{c}^{\alpha}_{\mathbf{i},\sigma}\hat{c}^{\alpha'}_{\mathbf{j},\sigma'} + \mathrm{h.c.}\right] \\ &= T_0 + \frac{1}{2}\sum_{\mathbf{i},\sigma\mathbf{j},\sigma'}\sum_{\alpha\alpha'}\left[\left[t^{\alpha\alpha';\sigma\sigma'}_{\mathbf{i},\mathbf{j}} + \delta_{\mathbf{i},\mathbf{j}}\left(\eta^{\alpha\alpha'}_{\mathbf{i},\sigma\sigma'} - \eta^{\alpha'\alpha}_{\mathbf{i},\sigma'\sigma}\right)\right]\hat{c}^{\alpha}_{\mathbf{i},\sigma}\hat{c}^{\alpha'}_{\mathbf{j},\sigma'} + \mathrm{h.c.}\right] \ , \end{aligned} \tag{94}$$

where

$$T_0 = \sum_{\mathbf{i},\sigma} \left[\left(\eta^{+-}_{\mathbf{i},\sigma\sigma} + \eta^{-+}_{\mathbf{i},\sigma\sigma} \right) + \text{c.c.} \right] \ . \tag{95}$$

We assume that the optimum wave-function $|\Psi_0\rangle$ is the ground-state of the Hamiltonian (94). In this way, $|\Psi_0\rangle$ becomes a function of $\{\widetilde{\lambda}_\mathbf{i}\}, \{\widetilde{C}_\mathbf{i}\}, \{\widetilde{\eta}_\mathbf{i}\}$, and the remaining task is to find the minimum

$$E_0^{\text{var}} = \underset{\{\widetilde{\lambda}_\mathbf{i}\},\{\widetilde{C}_\mathbf{i}\},\{\widetilde{\eta}_\mathbf{i}\},\Lambda}{\text{Minimum}} E_\text{c}(\{\widetilde{\lambda}_\mathbf{i}\}, \{\widetilde{C}_\mathbf{i}\}, \{\widetilde{\eta}_\mathbf{i}\}, \Lambda) \ , \tag{96}$$

$$\begin{aligned} E_\text{c}(\ldots) &= E^{\text{SP}}\left(\{\widetilde{\lambda}_\mathbf{i}\}, \{\widetilde{C}_\mathbf{i}\}, \{\widetilde{\eta}_\mathbf{i}\}\right) + E^{\text{at}}\left(\{\widetilde{\lambda}_\mathbf{i}\}, \{\widetilde{C}_\mathbf{i}\}\right) \\ &\quad - \sum_{\mathbf{i},\sigma\sigma'} \left[\sum_{\alpha\alpha'} \left(\eta^{\alpha\alpha'}_{\mathbf{i},\sigma\sigma'} C^{\alpha\alpha'}_{\mathbf{i},\sigma\sigma'} + \text{c.c.} \right) - \delta_{\sigma\sigma'} \Lambda \left(n_{\mathbf{i},\sigma\sigma}\left(\{\widetilde{\lambda}_\mathbf{i}\}, \{\widetilde{C}_\mathbf{i}\}\right) - n \right) \right] \ . \end{aligned} \tag{97}$$

6.2.2 Translational invariance

To make further progress we assume translational invariance. Then, the single-particle Hamiltonian in the Bloch basis with wave vectors $\mathbf{k}$ has the form

$$\hat{T}^{\text{eff}} = T_0 + \sum_{\mathbf{k};\sigma\sigma'} \sum_{\alpha\alpha'} \epsilon^{\alpha\alpha'}_{\sigma\sigma'}(\mathbf{k}) \hat{c}^{\alpha}_{(\alpha\mathbf{k}),\sigma} \hat{c}^{\alpha'}_{(-\alpha'\mathbf{k}),\sigma'} \ , \tag{98}$$

where the coefficients

$$\begin{aligned} \epsilon^{\alpha\alpha'}_{\sigma\sigma'}(\mathbf{k}) &= \frac{1}{L} \sum_{\mathbf{i},\mathbf{j}} e^{-\text{i}\mathbf{k}(\mathbf{j}-\mathbf{i})} \left(t^{\alpha\alpha';\sigma\sigma'}_{\mathbf{i},\mathbf{j}} + \frac{1}{2}\delta_{\mathbf{i},\mathbf{j}} \left(\eta^{\alpha\alpha'}_{\sigma\sigma'} - \eta^{\alpha'\alpha}_{\sigma'\sigma} + \left[\eta^{(-\alpha')(-\alpha)}_{\sigma'\sigma}\right]^* - \left[\eta^{(-\alpha)(-\alpha')}_{\sigma\sigma'}\right]^* \right) \right) \\ &= \frac{1}{2} \sum_{\tau\tau'} Q^{\alpha\alpha';\sigma\sigma'}_{\tau\tau'} \epsilon^0_{\tau\tau'}(\mathbf{k}) + \frac{1}{2} \left(\eta^{\alpha\alpha'}_{\sigma\sigma'} - \eta^{\alpha'\alpha}_{\sigma'\sigma} + \left[\eta^{(-\alpha')(-\alpha)}_{\sigma'\sigma}\right]^* - \left[\eta^{(-\alpha)(-\alpha')}_{\sigma\sigma'}\right]^* \right) \end{aligned} \tag{99}$$

are the elements of the matrices $\widetilde{\epsilon}^{\alpha\alpha'}_\mathbf{k}$. In (99) we used the bare energy-band matrix (14) and introduced the coefficients

$$Q^{+-;\sigma\sigma'}_{\tau\tau'} = q^*_{\tau\sigma} q_{\tau'\sigma'} - \bar{q}^*_{\tau\sigma} \bar{q}_{\tau'\sigma'} \ , \ Q^{-+;\sigma\sigma'}_{\tau\tau'} = -\left(Q^{+-;\sigma\sigma'}_{\tau\tau'} \right)^* \tag{100}$$

$$Q^{++;\sigma\sigma'}_{\tau\tau'} = q^*_{\tau\sigma} \bar{q}^*_{\tau'\sigma'} - \bar{q}^*_{\tau\sigma} q^*_{\tau'\sigma'} \ , \ Q^{--;\sigma\sigma'}_{\tau\tau'} = -\left(Q^{++;\sigma\sigma'}_{\tau\tau'} \right)^* \ . \tag{101}$$

Let us regard the operators $\hat{c}^\alpha_{\mathbf{k},\sigma}$ as elements of vectors $\hat{\mathbf{c}}^\alpha_\mathbf{k}$. Then, the effective Hamiltonian $\hat{T}^{\text{eff}}$ can be written in terms of matrix products,

$$\hat{T}^{\text{eff}} = T_0 + \sum_\mathbf{k} \begin{pmatrix} \hat{\mathbf{c}}^+_\mathbf{k} \\ \hat{\mathbf{c}}^-_{-\mathbf{k}} \end{pmatrix}^{\text{T}} \begin{pmatrix} \widetilde{\epsilon}^{+-}_\mathbf{k} & \widetilde{\epsilon}^{++}_\mathbf{k} \\ \widetilde{\epsilon}^{--}_\mathbf{k} & \widetilde{\epsilon}^{-+}_\mathbf{k} \end{pmatrix} \begin{pmatrix} \hat{\mathbf{c}}^-_\mathbf{k} \\ \hat{\mathbf{c}}^+_{-\mathbf{k}} \end{pmatrix} \ . \tag{102}$$

The matrix in (102) may be diagonalized by means of a Bogoliubov transformation

$$\begin{pmatrix} \hat{\mathbf{c}}^-_\mathbf{k} \\ \hat{\mathbf{c}}^+_{-\mathbf{k}} \end{pmatrix} = \begin{pmatrix} \widetilde{u}^{--}_\mathbf{k} & \widetilde{u}^{-+}_\mathbf{k} \\ \widetilde{u}^{+-}_\mathbf{k} & \widetilde{u}^{++}_\mathbf{k} \end{pmatrix} \begin{pmatrix} \hat{\mathbf{h}}^-_\mathbf{k} \\ \hat{\mathbf{h}}^+_{-\mathbf{k}} \end{pmatrix} \ , \tag{103}$$

where we introduced new fermionic operators $\widehat{\mathbf{h}}^{\alpha}_{\mathbf{k}}$ and matrices $\widetilde{u}^{\alpha\alpha'}_{\mathbf{k}}$ with elements $\widehat{h}^{\alpha}_{\mathbf{k},\gamma}$ and $u^{\alpha\alpha'}_{\sigma\gamma}(\mathbf{k})$, respectively. For reasons of consistency the matrices $\widetilde{u}^{\alpha\alpha'}_{\mathbf{k}}$ obey the symmetries

$$\widetilde{u}^{++}_{-\mathbf{k}} = \left(\widetilde{u}^{--}_{\mathbf{k}}\right)^{*} \quad , \quad \widetilde{u}^{+-}_{-\mathbf{k}} = \left(\widetilde{u}^{-+}_{\mathbf{k}}\right)^{*} \; . \tag{104}$$

The fermionic commutation rules of the new operators $\widehat{\mathbf{h}}^{\alpha}_{\mathbf{k}}$ are ensured when the matrix in (103) is unitary. In (102)–(104) we have used the standard notations for the transposition $\widetilde{M}^{\mathrm{T}}$, the complex conjugate $\widetilde{M}^{*}$, and the Hermitian conjugate $\widetilde{M}^{\dagger}$ of a matrix $\widetilde{M}$.

After the diagonalization $\hat{T}^{\mathrm{eff}}$ becomes

$$\begin{aligned} \hat{T}^{\mathrm{eff}} &= T_0 + \frac{1}{2}\sum_{\mathbf{k}} \left(E_{\mathbf{k},\gamma}\widehat{h}^{+}_{\mathbf{k},\gamma}\widehat{h}_{\mathbf{k},\gamma} - E_{\mathbf{k},\gamma}\widehat{h}_{\mathbf{k},\gamma}\widehat{h}^{+}_{\mathbf{k},\gamma} \right) \\ &= T_0 + E_0 + \sum_{\mathbf{k}} E_{\mathbf{k},\gamma}\widehat{h}^{+}_{\mathbf{k},\gamma}\widehat{h}_{\mathbf{k},\gamma} \; , \end{aligned} \tag{105}$$

where the real quantities $E_{\mathbf{k},\gamma} = \delta_{\gamma\gamma'}E_{\gamma\gamma'}(\mathbf{k})$ are the elements of the diagonal matrix

$$\widetilde{E}_{\mathbf{k}} = 2\sum_{\alpha\alpha'} \left(\widetilde{u}^{(-\alpha)-}_{\mathbf{k}}\right)^{\dagger} \widetilde{\epsilon}^{\alpha\alpha'}_{\mathbf{k}} \widetilde{u}^{\alpha'-}_{\mathbf{k}} \; , \tag{106}$$

and

$$E_0 = -\frac{1}{2}\sum_{\mathbf{k}} \mathrm{Tr}\left(\widetilde{E}_{\mathbf{k}}\right) \; . \tag{107}$$

For the derivation of (105)–(106) we have used the following symmetries of the matrices $\widetilde{\epsilon}^{\alpha\alpha'}_{\mathbf{k}}$,

$$\widetilde{\epsilon}^{\alpha\alpha'}_{-\mathbf{k}} = -\left(\widetilde{\epsilon}^{\alpha',\alpha}_{\mathbf{k}}\right)^{\mathrm{T}} = -\left(\widetilde{\epsilon}^{\alpha',\alpha}_{\mathbf{k}}\right)^{*} \qquad (\alpha \neq \alpha') \; , \tag{108}$$

$$\widetilde{\epsilon}^{\alpha,\alpha}_{-\mathbf{k}} = -\left(\widetilde{\epsilon}^{\alpha,\alpha}_{\mathbf{k}}\right)^{\mathrm{T}} = -\left(\widetilde{\epsilon}^{\alpha',\alpha'}_{\mathbf{k}}\right)^{*} \qquad (\alpha \neq \alpha') \tag{109}$$

which follow from (99) and

$$\epsilon^{0}_{\gamma',\gamma}(\mathbf{k}) = \left(\epsilon^{0}_{\gamma,\gamma'}(\mathbf{k})\right)^{*} = \epsilon^{0}_{\gamma,\gamma'}(-\mathbf{k}) \tag{110}$$

which result from hermiticity of $\hat{T}$ and the fact that our electron-transfer amplitudes are real. Note that the matrices $\widetilde{u}^{\alpha,\alpha'}_{\mathbf{k}}$, $\widetilde{\epsilon}^{\alpha\alpha'}_{\mathbf{k}}$, the operators $\widehat{h}^{\alpha}_{\mathbf{k},\gamma}$, and the energies $E_{\mathbf{k},\gamma}$ still depend on the parameters $\widetilde{\lambda}, \widetilde{\eta}, \widetilde{C}$. The Fermi-gas ground state of (105) is given as

$$|\Psi_0\left(\widetilde{\lambda}, \widetilde{\eta}, \widetilde{C}\right)\rangle = {\sum_{\mathbf{k},\gamma}}' \hat{h}^{+}_{\mathbf{k},\gamma}|\mathrm{vacuum}\rangle \; . \tag{111}$$

Here, the prime on the sum indicates that only those single-particle states with

$$E_{\mathbf{k},\gamma}\left(\widetilde{\lambda}, \widetilde{\eta}, \widetilde{C}\right) \leq E_{\mathrm{F}} \equiv 0 \tag{112}$$

are filled and

$$E^{\mathrm{SP}}\left(\widetilde{\lambda}, \widetilde{\eta}, \widetilde{C}\right) = T_0\left(\widetilde{\eta}\right) + E_0\left(\widetilde{\lambda}, \widetilde{\eta}, \widetilde{C}\right) + {\sum_{\mathbf{k},\gamma}}' E_{\mathbf{k},\gamma}\left(\widetilde{\lambda}, \widetilde{\eta}, \widetilde{C}\right) \tag{113}$$

is the energy of the 'Fermi-gas' ground state. In principle, the variational ground-state energy can now be calculated by a minimization of the energy-functional

$$\begin{aligned} E_{\rm c}(\tilde{\lambda},\tilde{C},\tilde{\eta},\Lambda) &= E^{\rm SP}\left(\tilde{\lambda},\tilde{C},\tilde{\eta}\right) + E^{\rm at}\left(\tilde{\lambda},\tilde{C}\right) - L\sum_{\sigma\sigma'}\sum_{\alpha\alpha'}\left(\eta^{\alpha\alpha'}_{\sigma\sigma'}C^{\alpha\alpha'}_{\sigma\sigma'} + \text{c.c.}\right) \\ &\quad + L\Lambda\left(\sum_{\sigma} n_{\sigma\sigma}\left(\tilde{\lambda},\tilde{C}\right) - n\right) \end{aligned} \tag{114}$$

with respect to all parameters x_i in $\tilde{\lambda},\tilde{C},\tilde{\eta},\Lambda$, i.e.,

$$E_0^{\rm var} = E_{\rm c}(\tilde{\lambda}^0,\tilde{C}^0,\tilde{\eta}^0,\Lambda^0) \tag{115}$$

where

$$\left.\frac{\partial}{\partial x_i}E_{\rm c}\right|_{\{x_i\}=\{x_i^0\}} = 0\,. \tag{116}$$

Minimizing $E_{\rm c}$ in this straightforward way requires rather time-consuming calculations of expectation values in $|\Psi_0\rangle$ for every single variation of our parameters. Such a strategy is prohibitive, in particular due to the large number of variational parameters $\tilde{\lambda}$. Therefore, one needs to develop more sophisticated numerical strategies when our general theory is to be applied to realistic model system.

7 Landau–Gutzwiller quasi-particles

The Gutzwiller theory, as described in the previous section, is a variational approach and by itself a method to examine ground-state properties only. As shown in Refs. [31, 47], it is possible to use the approximate Gutzwiller-correlated ground state for the calculation of elementary excitations. In particular, the 'band structure' $E_{\mathbf{k},\gamma}$ derived in the previous section gives the variational excitation energies of Landau–Gutzwiller quasi-particles.

7.1 Definition of single-particle excitations

Originally, Gutzwiller-correlated wave functions were introduced as Fermi-liquid ground states for ordinary metals [3]. More generally, they are Fermi-liquid ground states in the sense of an adiabatic continuity to some non-interacting reference system which can be a Fermi gas, a BCS superconductor, or a band insulator. For all such cases, quasi-particle and quasi-hole states are readily identified. To this end, we define quasi-particle and quasi-hole creation operators as

$$\hat{e}^{+}_{\mathbf{p},\tau} := \hat{P}_{\rm G}\hat{h}^{+}_{\mathbf{p},\tau}(\hat{P}_{\rm G})^{-1}\,, \tag{117}$$

$$\hat{v}_{\mathbf{p},\tau} := \hat{P}_{\rm G}\hat{h}_{\mathbf{p},\tau}(\hat{P}_{\rm G})^{-1}\,. \tag{118}$$

These operators obey usual Fermi anti-commutation relations,

$$[\hat{e}^{+}_{\mathbf{p},\tau},\hat{v}_{\mathbf{p}',\tau'}]_{+} = \delta_{\mathbf{p},\mathbf{p}'}\delta_{\tau\tau'}\,, \tag{119}$$

$$[\hat{e}^{+}_{\mathbf{p},\tau},\hat{e}^{+}_{\mathbf{p}',\tau'}]_{+} = [\hat{v}_{\mathbf{p},\tau},\hat{v}_{\mathbf{p}',\tau'}]_{+} = 0\,, \tag{120}$$

and they create quasi-particles/quasi-holes in the variational Gutzwiller ground-state, as can be seen from

$$\widehat{e}^{+}_{\mathbf{p},\tau}\widehat{v}_{\mathbf{p},\tau}|\Psi_{\mathrm{G}}\rangle = \Theta(E_{\mathrm{F}}-E_{\mathbf{p},\tau})|\Psi_{\mathrm{G}}\rangle \;, \tag{121}$$

$$\widehat{v}_{\mathbf{p},\tau}\widehat{e}^{+}_{\mathbf{p},\tau}|\Psi_{\mathrm{G}}\rangle = \Theta(E_{\mathbf{p},\tau}-E_{\mathrm{F}})|\Psi_{\mathrm{G}}\rangle \;. \tag{122}$$

We define the quasi-particle or quasi-hole excitation energy as

$$E_{\pm}(\mathbf{p},\tau) \equiv \pm\left(E^{\mathrm{var}}_{\pm}(\mathbf{p},\tau)-E^{\mathrm{var}}_{0}\right)-\mu^{\pm}\left(N^{\mathrm{var}}_{\pm}(\mathbf{p},\tau)-N\right) \;, \tag{123}$$

where the upper and lower sign corresponds to quasi-particles and quasi-holes, respectively. Here,

$$E^{\mathrm{var}}_{\pm}(\mathbf{p},\tau)=\frac{\langle\Psi^{(\mathbf{p},\tau)}_{\mathrm{G},\pm}|\hat{H}|\Psi^{(\mathbf{p},\tau)}_{\mathrm{G},\pm}\rangle}{\langle\Psi^{(\mathbf{p},\tau)}_{\mathrm{G},\pm}|\Psi^{(\mathbf{p},\tau)}_{\mathrm{G},\pm}\rangle} \quad , \quad N^{\mathrm{var}}_{\pm}(\mathbf{p},\tau)=\frac{\langle\Psi^{(\mathbf{p},\tau)}_{\mathrm{G},\pm}|\hat{N}|\Psi^{(\mathbf{p},\tau)}_{\mathrm{G},\pm}\rangle}{\langle\Psi^{(\mathbf{p},\tau)}_{\mathrm{G},\pm}|\Psi^{(\mathbf{p},\tau)}_{\mathrm{G},\pm}\rangle} \tag{124}$$

are the expectation values of the energy and the average particle number in the quasi-particle/quasi-hole states

$$|\Psi^{(\mathbf{p},\tau)}_{\mathrm{G},+}\rangle \equiv \widehat{e}^{+}_{\mathbf{p},\tau}|\Psi_{\mathrm{G}}\rangle=\hat{P}_{\mathrm{G}}\widehat{h}^{+}_{\mathbf{p},\tau}|\Psi_0\rangle\equiv\hat{P}_{\mathrm{G}}|\Psi^{(\mathbf{p},\tau)}_{0,+}\rangle \;, \tag{125}$$

$$|\Psi^{(\mathbf{p},\tau)}_{\mathrm{G},-}\rangle \equiv \widehat{v}_{\mathbf{p},\tau}|\Psi_{\mathrm{G}}\rangle=\hat{P}_{\mathrm{G}}\widehat{h}_{\mathbf{p},\tau}|\Psi_0\rangle\equiv\hat{P}_{\mathrm{G}}|\Psi^{(\mathbf{p},\gamma)}_{0,-}\rangle \;. \tag{126}$$

The one-particle state $|\Psi_0\rangle$ is defined according to (111) in terms of the operators $\widehat{h}^{+}_{\mathbf{k},\gamma}$. Note that $|\Psi_0\rangle$ and $\widehat{h}^{+}_{\mathbf{k},\gamma}$ have to be used with their optimum values, given by the parameters $\tilde{\lambda}^0,\tilde{\eta}^0,\tilde{C}^0,\Lambda^0$. The quasi-particle excitation energy (123) is measured from the (variational) chemical potential $\mu^{\pm}$ which describes the energy for adding a particle to the system or subtracting it, respectively,

$$\mu^{\pm}=\pm(E^{\mathrm{var}}_{0}(N\pm1)-E^{\mathrm{var}}_{0}(N)) \;. \tag{127}$$

$E^{\mathrm{var}}_{0}(N)$ is the (variational) ground-state energy for a system with N electrons. For a metallic or superconducting system, $\mu^{+}=\mu^{-}=\mu$. For an insulating system, $\Delta^{\mathrm{var}}=\mu^{+}-\mu^{-}$ defines the gap in our variational theory. The variational ground-state energy (115) depends on the particle density $n=N/L$ implicitly, due to the n-dependence of all parameters x^0_i in $\tilde{\lambda}^0,\tilde{C}^0,\tilde{\eta}^0,\Lambda^0$, and, explicitly, through the term $-\Lambda n$ in (114). Therefore, $\mu_{\pm}$ is given by

$$\mu_{\pm}=\frac{1}{L}\frac{d}{dn}E_{\mathrm{c}}(\{x^0_i(n)\},n)=\frac{1}{L}\sum_{\{x_i\}}\left.\frac{\partial E_{\mathrm{c}}}{\partial x_i}\right|_{x_i=x^0_i}\frac{dx^0_i}{dn}-\Lambda^0_{\pm}=-\Lambda^0_{\pm} \;, \tag{128}$$

where we used (116) and the fact that, in an insulating system, both $\mu_{\pm}$ and Λ^0 are discontinuous as a function of n.

7.2 Quasi-particle dispersion

We write the energies $E_0^{\rm var}$ and $E_\pm^{\rm var}(\mathbf{p},\gamma)$ in (123) as

$$\begin{aligned} E_0^{\rm var} &= \frac{1}{2}\sum_{\sigma\sigma',\gamma\gamma',\alpha\alpha'} Q^{\alpha\alpha';\gamma\gamma'}_{\sigma\sigma'}(\tilde\lambda^0,\tilde C^0)\,K^{\alpha\alpha';\gamma\gamma'}_{\sigma\sigma'}(\tilde\lambda^0,\tilde C^0,\tilde\eta^0) + E^{\rm at}(\tilde\lambda^0,\tilde C^0)\;, \\ E_\pm^{\rm var}(\mathbf{p},\tau) &= \frac{1}{2}\sum_{\sigma\sigma',\gamma\gamma',\alpha\alpha'} Q^{\alpha\alpha';\gamma\gamma'}_{\sigma\sigma'}(\tilde\lambda^0,\tilde C^0+\tilde\Delta_\pm^{\mathbf{p},\tau})\sum_{\mathbf{k}}\epsilon^0_{\sigma\sigma'}(\mathbf{k})\langle\Psi^{(\mathbf{p},\tau)}_{0,\pm}|\hat c^\alpha_{(\alpha\mathbf{k}),\gamma}\hat c^{\alpha'}_{(-\alpha'\mathbf{k}),\gamma'}|\Psi^{(\mathbf{p},\tau)}_{0,\pm}\rangle \\ &\quad + E^{\rm at}(\tilde\lambda^0,\tilde C^0+\tilde\Delta_\pm^{\mathbf{p},\tau})\;, \end{aligned} \tag{129}$$

where

$$K^{\alpha\alpha';\gamma\gamma'}_{\sigma\sigma'}(\tilde\lambda,\tilde C,\tilde\eta) = \sum_{\mathbf{k}}\epsilon^0_{\sigma\sigma'}(\mathbf{k})\langle\hat c^\alpha_{(\alpha\mathbf{k}),\gamma}\hat c^{\alpha'}_{-(\alpha'\mathbf{k}),\gamma'}\rangle_0\;. \tag{130}$$

The tensor $\tilde\Delta_\pm^{\mathbf{p},\tau}$ gives the change of $\tilde C$ due to the creation of a quasi-particle or a quasi-hole,

$$\tilde\Delta^{\alpha\alpha'}_{\pm;\gamma\gamma'}(\mathbf{p},\tau) = \pm\left(V^{\alpha\alpha'}_{\gamma\gamma'}(\mathbf{p},\tau) - V^{\alpha'\alpha}_{\gamma'\gamma}(\mathbf{p},\tau)\right)\;, \tag{131}$$

where we introduced

$$V^{\alpha\alpha'}_{\gamma\gamma'}(\mathbf{p},\tau) = \left(u^{(-\alpha)-}_{\gamma\tau}(\mathbf{p})\right)^* u^{\alpha'-}_{\gamma'\tau}(\mathbf{p}). \tag{132}$$

The sum over $\mathbf{k}$ in (129) is readily evaluated,

$$\begin{aligned} \sum_{\mathbf{k}}\epsilon^0_{\sigma\sigma'}(\mathbf{k})\langle\Psi^{(\mathbf{p},\tau)}_{0,\pm}|\hat c^\alpha_{(\alpha\mathbf{k}),\gamma}\hat c^{\alpha'}_{-(\alpha'\mathbf{k}),\gamma'}|\Psi^{(\mathbf{p},\tau)}_{0,\pm}\rangle &= K^{\alpha\alpha';\gamma\gamma'}_{\sigma\sigma'}(\tilde\lambda^0,\tilde C^0,\tilde\eta^0) \\ &\quad \pm\left(V^{\alpha\alpha'}_{\gamma\gamma'}(\mathbf{p},\tau)\epsilon^0_{\sigma\sigma'}(\mathbf{p}) - V^{\alpha'\alpha}_{\gamma'\gamma}(\mathbf{p},\tau)\epsilon^0_{\sigma'\sigma}(\mathbf{p})\right)\;. \end{aligned} \tag{133}$$

To order $(1/L)^0$ the expansion of $\delta E^\pm_{\mathbf{p},\tau}\equiv 2(E^{\rm var}_\pm(\mathbf{p},\tau)-E^{\rm var}_0)$ with respect to $\tilde\Delta^{\mathbf{p},\tau}_\pm$ yields

$$\begin{aligned} \delta E^\pm_{\mathbf{p},\tau} &= \pm\sum_{\sigma\sigma',\gamma\gamma'}\sum_{\alpha\alpha'} Q^{\alpha\alpha';\gamma\gamma'}_{\sigma\sigma'}\left(V^{\alpha\alpha'}_{\gamma\gamma'}(\mathbf{p},\tau)\epsilon^0_{\sigma\sigma'}(\mathbf{p}) - V^{\alpha'\alpha}_{\gamma'\gamma}(\mathbf{p},\tau)\epsilon^0_{\sigma'\sigma}(\mathbf{p})\right) \\ &\quad + \sum_{\rho\rho',\alpha\alpha'}\left[\sum_{\sigma\sigma',\gamma\gamma'} K^{\alpha\alpha';\gamma\gamma'}_{\sigma\sigma'}\left.\frac{\partial Q^{\gamma\gamma'}_{\sigma\sigma'}}{\partial C^{\alpha\alpha'}_{\rho\rho'}}\right|_{\tilde C=\tilde C^0} + \left.\frac{\partial E^{\rm at}}{\partial C^{\alpha\alpha'}_{\rho\rho'}}\right|_{\tilde C=\tilde C^0}\right]\Delta^{\alpha\alpha'}_{\pm;\rho\rho'}(\mathbf{p},\tau) \\ &\quad + \sum_{\rho\rho',\alpha\alpha'}\left[\sum_{\sigma\sigma',\gamma\gamma'} K^{\alpha\alpha';\gamma\gamma'}_{\sigma\sigma'}\left.\frac{\partial Q^{\gamma\gamma'}_{\sigma\sigma'}}{\partial\left(C^{\alpha\alpha'}_{\rho\rho'}\right)^*}\right|_{\tilde C=\tilde C^0} + \left.\frac{\partial E^{\rm at}}{\partial\left(C^{\alpha\alpha'}_{\rho\rho'}\right)^*}\right|_{\tilde C=\tilde C^0}\right]\left(\Delta^{\alpha\alpha'}_{\pm;\rho\rho'}(\mathbf{p},\tau)\right)^*\;. \end{aligned} \tag{134}$$

We use

$$\begin{aligned} \pm E_{\mathbf{p},\tau} &= \pm\frac{1}{2}\sum_{\sigma\sigma',\gamma\gamma'}\sum_{\alpha\alpha'} Q^{\alpha\alpha';\gamma\gamma'}_{\sigma\sigma'}\left(V^{\alpha\alpha'}_{\gamma\gamma'}(\mathbf{p},\tau)\epsilon^0_{\sigma\sigma'}(\mathbf{p}) - V^{\alpha'\alpha}_{\gamma'\gamma}(\mathbf{p},\tau)\epsilon^0_{\sigma'\sigma}(\mathbf{p})\right) \\ &\quad + \frac{1}{2}\sum_{\gamma\gamma',\alpha\alpha'}\left[\left(\left(\eta^{\alpha\alpha'}_{\gamma\gamma'}\right)^0 - \left(\eta^{\alpha'\alpha}_{\gamma'\gamma}\right)^0\right)\Delta^{\alpha\alpha'}_{\pm;\gamma\gamma'}(\mathbf{p},\tau) + \text{c.c.}\right]\;. \end{aligned} \tag{135}$$

to evaluate the first line in (134). For the second and the third line we employ

$$\sum_{\sigma\sigma',\gamma\gamma'} K^{\alpha\alpha';\gamma\gamma'}_{\sigma\sigma'}\left.\frac{\partial Q^{\alpha\alpha';\gamma\gamma'}_{\sigma\sigma'}}{\partial C^{\alpha\alpha'}_{\rho\rho'}}\right|_{\tilde C=\tilde C^0} = \left\langle\frac{\partial}{\partial C^{\alpha\alpha'}_{\rho\rho'}}\hat T^{\rm eff}\right\rangle_0 = \left.\frac{\partial E^{\rm SP}}{\partial C^{\alpha\alpha'}_{\rho\rho'}}\right|_{\tilde C=\tilde C^0} \tag{136}$$

and the corresponding equation where $C^{\alpha\alpha'}_{\rho\rho'}$ is replaced by $\left(C^{\alpha\alpha'}_{\rho\rho'}\right)^*$. In (136) we have used the fact that the dependence of $K^{\alpha\alpha';\gamma\gamma'}_{\sigma\sigma'}$ on $\tilde{C}$ can be ignored in the derivative of E^{SP} with respect to $\tilde{C}$ because $|\Psi_0\rangle$ is an exact eigenstate of $\hat{T}^{\mathrm{eff}}$ and E^{SP} is its eigenvalue. Using (114) and (116) we can rewrite this expression as

$$\left.\frac{\partial E^{\mathrm{SP}}}{\partial C^{\alpha\alpha'}_{\rho\rho'}}\right|_{\widetilde{C}=\widetilde{C}^0} = -\left.\frac{\partial E^{\mathrm{at}}}{\partial C^{\alpha\alpha'}_{\rho\rho'}}\right|_{\widetilde{C}=\widetilde{C}^0} + \frac{1}{2}\left(\left(\eta^{\alpha\alpha'}_{\rho\rho'}\right)^0 - \left(\eta^{\alpha'\alpha}_{\rho'\rho}\right)^0\right) - \delta_{\rho\rho'}\Lambda^0_{\pm}\sum_{\sigma}\left.\frac{\partial n_{\sigma\sigma}}{\partial C^{\alpha\alpha'}_{\rho\rho'}}\right|_{\widetilde{C}=\widetilde{C}^0}, \quad (137)$$

where, again, the same equations hold with $\tilde{C}$ and $\tilde{\eta}$ replaced by $\tilde{C}^*$ and $\tilde{\eta}^*$, respectively. With these results and

$$N^{\mathrm{var}}_{\pm}(\mathbf{p},\tau) - N = \sum_{\sigma}\left[\left.\frac{\partial n_{\sigma\sigma}}{\partial C^{\alpha\alpha'}_{\rho\rho'}}\right|_{\widetilde{C}=\widetilde{C}^0}\Delta^{\alpha\alpha'}_{\pm;\rho\rho'} + \mathrm{c.c.}\right] \quad (138)$$

we find $E_{\pm}(\mathbf{p},\gamma) = E_{\mathbf{p},\gamma}$ for the quasi-particle and quasi-hole excitation energy. This relations shows that the 'band structure' $E_{\mathbf{p},\tau}$ describes meaningful quasi-particle bands.

8 Outlook

Our Gutzwiller theory provides a very good description of the quasi-particle band structure of ferromagnetic nickel. We obtain the correct exchange splittings and, in particular, we reproduce the experimental Fermi-surface topology. We find the correct (111)-direction of the magnetic easy axis and the right order of magnitude of the magnetic anisotropy. Our theory even reproduces the experimentally observed change of the Fermi-surface topology when the magnetic moment is oriented along the (001) axis.

Our investigations show that SDFT should be improved along the following lines. First, it needs to incorporate an orbital dependence of the exchange-correlation potential in order to reproduce the anisotropy of the exchange splittings. It may also be used to correct the partial densities of the $3d$ and $4sp$ electrons. Second, it should allow an effective spin-orbit coupling.

Thus far, our calculations have focused on the quasi-particle band structure at zero temperature. Several extensions of the Gutzwiller theory are possible. First, as shown in [47], we can also address magnetic excitations. Therefore, Gutzwiller theory should reproduce the spin-wave spectrum of nickel. Second, we can generalize the idea of elementary excitations to transitions between atomic states which are induced by photoemission. In this way we should also be able to make contact with the experimentally observed '6 eV-peak' [48].

We emphasize that our Gutzwiller theory as presented here is not limited to nickel. We may apply it equally to other transition metals and their compounds, for example NiO [49]. Our theory also covers superconducting pairing which we may apply to superconductivity in multi-band systems. The Gutzwiller approach can and will be applied to many interesting correlated-electron problems in the future.

References

[1] E.P. Wohlfarth in *Handbook of Magnetic Materials* **1**, ed. by E.P. Wohlfarth (North Holland, Amsterdam, 1980), p. 1.

[2] J.H. van Vleck, Rev. Mod. Phys. **25**, 220 (1953).

[3] M.C. Gutzwiller, Phys. Rev. Lett. **10**, 159 (1963).

[4] J.P. Perdew and Y. Wang, Phys. Rev. B **33**, 8800 (1986); A.D. Becke, Phys. Rev. A **38**, 3098 (1988).

[5] M. Ulmke, Eur. Phys. J. B **1**, 301 (1998); J. Wahle, N. Blümer, J. Schlipf, K. Held, and D. Vollhardt, Phys. Rev. B **58**, 12749 (1998).

[6] W. Nolting, W. Borgieł, V. Dose, and Th. Fauster, Phys. Rev. B **40**, 5015 (1989).

[7] L. Hedin, Phys. Rev. **139**, A796 (1965); F. Aryasetiawan, Phys. Rev. B **46**, 13051 (1992).

[8] O.K. Andersen, O. Jepsen, and D. Glötzel in *Highlights of Condensed-Matter Theory*, ed. by F. Bassani, F. Fumi, and M. Tosi (North-Holland, Amsterdam, 1985), p. 59; W.R.L. Lambrecht and O.K. Andersen, Phys. Rev. B **34**, 2439 (1986); O. K. Andersen and T. Saha-Dasgupta, Phys. Rev. B **62**, R16219 (2000).

[9] For an introduction to dynamical mean-field theory and its applications to real materials, see, for example, K. Held, I.A. Nekrasov, G. Keller, V. Eyert, N. Blümer, A.K. McMahan, R.T. Scalettar, T. Pruschke, V.I. Anisimov, and D. Vollhardt in *Quantum Simulations of Complex Many-Body Systems: From Theory to Algorithms*, ed. by J. Grotendorst, D. Marks, and A. Muramatsu (NIC Series Vol. **10**, 2002), p. 175.

[10] M.B. Zölfl, Th. Pruschke, J. Keller, A.I. Poteryaev, I.A. Nekrasov, and V.I. Anisimov, Phys. Rev. B **61**, 12810 (2000).

[11] A.I. Lichtenstein, M.I. Katsnelson, and G. Kotliar, Phys. Rev. Lett. **87**, 067205 (2001).

[12] V.I. Anisimov, J. Zaanen, and O.K. Andersen, Phys. Rev. B **44**, 943 (1991).

[13] I. Yang, S.Y. Savrasov, and G. Kotliar, Phys. Rev. Lett. **87**, 216405 (2001).

[14] Y. Xie and J.A. Blackman, Phys. Rev. B **69**, 172407 (2004).

[15] S. Biermann, F. Aryasetiawan, and A. Georges, Phys. Rev. Lett. **90**, 086402 (2003).

[16] M. Donath, Surf. Sci. Rep. **20**, 251 (1994).

[17] M.B. Stearns in *Landolt–Börnstein New Series Group III*, Vol. 19A, ed. by H.P.J. Wijn (Springer, Berlin, 1986), p. 24.

[18] A. Goldmann, W. Gudat, and O. Rader in *Landolt–Börnstein New Series Group III*, Vol. 23C2, ed. by A. Goldmann (Springer, Berlin, 1994).

[19] D.C. Tsui, Phys. Rev. **164**, 669 (1967).

[20] H.A. Mook, Phys. Rev. **148**, 495 (1966).

[21] D.E. Eastman, F.J. Himpsel, and J.A. Knapp, Phys. Rev. Lett. **40**, 1514 (1978).

[22] W. Eberhardt and E.W. Plummer, Phys. Rev. B **21**, 3245 (1980).

[23] V.L. Moruzzi, J.F. Janak, and A.R. Williams, *Calculated Electronic Properties of Metals* (Pergamon Press, New York, 1978).

[24] This appears to be a general problem of the underlying DFT calculation. The same problem appears for 4*d* transition metals of bcc structure: the position of the purely 5*p*-state $N_{2'}$ also appears shifted by about 0.7 eV to lower energies as compared to the DFT results, see G.W. Crabtree, D.H. Dye, D.P. Karim, D.D. Koelling, and J.B. Ketterson, Phys. Rev. Lett. **42**, 390 (1977).

[25] M.J. Singh, J. Callaway, and C.S. Wang, Phys. Rev. B **14**, 1214 (1976).

[26] G.H.O. Daalderop, P.J. Kelly, and M.F.H. Schuursmans, Phys. Rev. B **41**, 11919 (1990).

[27] R. Gersdorf and G. Aubert, Physica B **95**, 135 (1978).

[28] R. Gersdorf, Phys. Rev. Lett. **40**, 344 (1978).

[29] J. Bünemann, W. Weber, and F. Gebhard, Phys. Rev. B **57**, 6896 (1998).

[30] J. Bünemann, F. Gebhard, T. Ohm, R. Umstätter, S. Weiser, W. Weber, R. Claessen, D. Ehm, A. Harasawa, A. Kakizaki, A. Kimura, G. Nicolay, S. Shin, and V.N. Strocov, Europhys. Lett. **61**, 667 (2003).

[31] J. Bünemann, F. Gebhard, and R. Thul, Phys. Rev. B **67**, 075103 (2003).

[32] J.C. Slater and G.F. Koster, Phys. Rev. **94**, 1498 (1954).

[33] W. Weber and L.F. Mattheiss, Phys. Rev. B **25**, 2270 (1982).

[34] T. Ohm, S. Weiser, R. Umstätter, W. Weber, J. Bünemann, J. Low Temp. Phys. **126**, 1081 (2002).

[35] A. Abragam and B. Bleaney, *Electron paramagnetic resonance of transition ions* (Clarendon Press, Oxford, 1970).

[36] P. Bruno in *Magnetismus von Festkörpern und Grenzflächen* (24. IFF-Ferienkurs, Forschungszentrum Jülich GmbH, 1993), p. 24-1; P. Escudier, Ann. Phys. (Paris) **9**, 125 (1975).

[37] W. Weber et al., in preparation.

[38] S. Sugano, Y. Tanabe, and H. Kamimura, *Multiplets of Transition-Metal Ions in Crystals* (Pure and Applied Physics **33**, Academic Press, New York, 1970).

[39] C. Herring in *Magnetism, Vol. IV*, ed. by G. T. Rado and H. Suhl (Academic Press, New York, 1966), p. 1.

[40] I. Schnell, G. Czycholl, and R.C. Albers, Phys. Rev. B **68**, 245102 (2003).

[41] M.S. Hybertson, M. Schlüter, and N.E. Christensen, Phys. Rev. B **39**, 9028 (1989).

[42] G. Vielsack and W. Weber, Phys. Rev. B **54**, 6614 (1996).

[43] V.I. Anisimov and O. Gunnarsson, Phys. Rev. B **43**, 7570 (1991).

[44] J. Rath and A.J. Freeman, Phys. Rev. B **11**, 2109 (1975).

[45] K.-P. Kämper, W. Schmitt, and G. Güntherodt, Phys. Rev. B **42**, 10696 (1990).

[46] C.S. Wang and J. Callaway, Phys. Rev. B. **15**, 298 (1977); J. Callaway in *Physics of Transition Metals 1980*, ed. by P. Rhodes (Conf. Ser. Notes **55**, Inst. of Physics, Bristol, 1981), p. 1.

[47] J. Bünemann, J. Phys. Cond. Matt. **13**, 5327 (2001).

[48] S. Hüfner, *Photoelectron spectroscopy*, 2nd edition (Solid-State Sciences **82**, Springer, Berlin, 1995).

[49] S. Weiser, PhD thesis (Universität Dortmund, 2005), unpublished.

CHEMISTRY OF HALFMETALLIC AND RELATED CATION-ORDERED DOUBLE PEROVSKITES

M. Karppinen and H. Yamauchi

Materials and Structures Laboratory, Tokyo Institute of Technology,
Yokohama 226-8503, Japan

1. INTRODUCTION

Ferromagnetic halfmetals (HMs) have - since their discovery in 1983 [1] - been in the focus of increasing interest, as application of such materials is expected to revolutionize near-future "spintronics" [2]. In a HM carriers are characteristically 100 % spin polarized. This allows HMs to be utilized in tunneling-type magnetoresistance (TMR) devices in which the spin-dependent electron transfer across the intrinsic or extrinsic barrier is sensitively controlled by external magnetic fields. A normal ferromagnetic metal - even though showing an imbalance in the number of the spin-up and spin-down conduction electrons - is not a HM. In an ideal HM, only one of the two spin bands is partially occupied at the Fermi level, while the other has zero density of states across the Fermi level, see Fig. 1 for a schematic illustration. As a consequence, the electrical conduction is due to carriers of one spin direction only. In the strictest sense, perfect halfmetallicity is limited to perfect crystals at zero temperature; real HMs typically exhibit dramatic decreases in spin polarization due to thermal effects and intrinsic crystal and surface imperfections [3].

Theoretical predictions have yielded a number of HM candidates, but only a handful has been experimentally uncovered to date. Among them, transition metal oxides with "strongly-correlated" *d* electrons have taken a majority [4]. In Table 1, prototype HM compounds are listed.

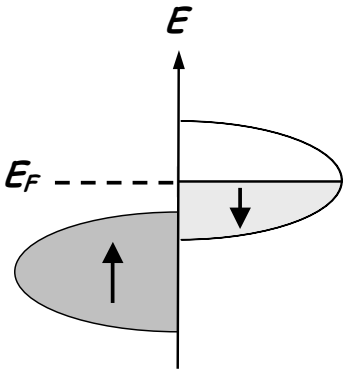

Fig. 1. Schematic illustration of the band structure of a halfmetal.

Among the few kinds of oxide HMs discovered so far, Sr_2FeMoO_6 is one of the most promising candidates for room-temperature low-field TMR applications [5]: the first Sr_2FeMoO_6-based devices have already been built up, *e.g.* magnetic tunnel junctions [6]. In comparison to the colossal magnetoresistance (CMR) manganites, Sr_2FeMoO_6 has a higher T_C (Curie temperature), see Table 1. Another interesting characteristics of Sr_2FeMoO_6 is that, unlike the $(La,Sr)MnO_3$ magnetoresistors, it is stoichiometric or "self-doped". In fact, Sr_2FeMoO_6 is just an example of the larger family of ferro- or ferrimagnetic iron-oxide magnetoresistors, $A_2FeB''O_6$ [A = Ca, Sr, Ba, rare-earth element (*RE*); B'' = Mo, Re] [7] of the same basic *B*-site ordered double-perovskite (DP) structure.

Table 1. Prototype HM compounds and their crystal structures and Curie temperatures.

Compound	**Structure**	T_C **[K]**
NiMnSb	Half Heusler "alloy"	730
Ni_2MnGa	Heusler "alloy"	340
CrO_2	Rutile	390
$Tl_2Mn_2O_7$	Pyrochlore	160
Fe_3O_4	Inverse spinel	860
$(La,Sr)MnO_3$	Perovskite	370
Sr_2FeMoO_6	Double perovskite	420
CrAs	Zinc blende	> RT

Besides the *B*-site ordered DPs, another category of phases is also yielded upon cation ordering within the basic ABO_3 perovskite structure, that is, the *A*-site ordered $A'A''B_2O_{5+\delta}$ (A' = Ba; A'' = *RE*; B = Mn, Fe, Co) DPs [8]. None of these compounds has so far been verified as a HM. Nevertheless, they host related and exciting phenomena and functions. In

the present short review, we discuss the material variety of cation-ordered perovskite oxides putting emphasis on the chemical aspects characteristic to these materials, such as oxygen (non)stoichiometry [9], redox chemistry and cation ordering [10,11]. These characteristics are important not only from the scientific point of view but also in terms of potential applications, as they are likely to affect the desired functions.

2. CATION ORDERING IN THE PEROVSKITE STRUCTURE

Starting from the single-perovskite (SP) structure of ABO_3, new compounds are derived upon co-occupation of one or both of the two cation sites, *A* or *B*, with multiple cation species. The cation substituent may occupy the original SP cation site either randomly or in an ordered manner. In the case of an ordered arrangement not only the symmetry but also the size of the unit cell changes. The double perovskites are the most common examples of ordered lattices, obtained with one-to-one stoichiometry of the two *A*-site (*A*' and *A*'') or *B*-site (*B*' and *B*'') constituents, see Fig. 2.

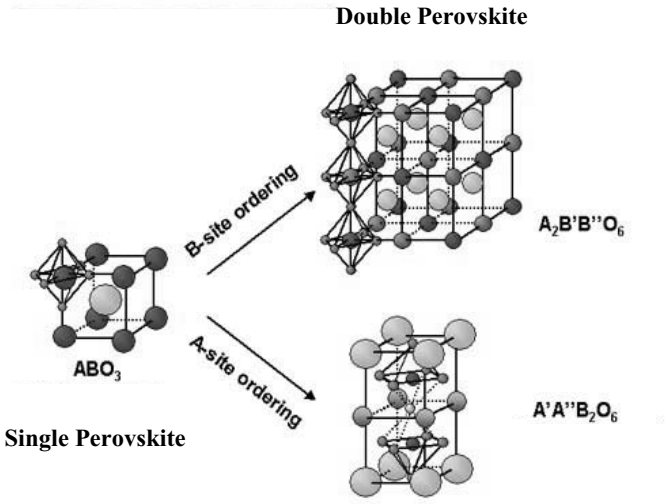

Fig. 2. Derivation of the *A*-site ordered ($A'A''B_2O_6$) and the *B*-site ordered ($A_2B'B''O_6$) douple-perovskite structures from the single-perovskite (ABO_3) structure. Note that for the sake of clarity, not all oxygen atoms are shown.

In a perfectly *B*-site ordered DP, $A_2B'B''O_6$, the octahedral *B*-cation site is alternatively occupied with two cations, *B*' and *B*'', of different charges, such that each $B'O_6$ octahedron is surrounded by six corner-sharing $B''O_6$ octahedra, and *vice versa*. The ideal face-centered cubic unit cell of a *B*-site ordered DP is $2 \times 2 \times 2 = 8$ times larger than the primitive cubic cell of the SP that corresponds to the disordered case, see Fig. 2. As a rule of thumb, the larger the

difference between the charges of the two *B*-site cations is, the higher is the equilibrium degree of order at the *B* site. If the charge difference between the *B*' and *B*'' cations is larger than two, *i.e.* $A^{II}{}_2B^{I}B^{VII}O_6$ or $A^{II}{}_2B^{II}B^{VI}O_6$, complete ordering is commonly achieved, whereas for the $A^{II}{}_2B^{III}B^{V}O_6$ perovskites various degrees of order are observed depending on the synthesis conditions [11]. The actual degree of order depends also on the particular *A*, *B*' and *B*'' cations. Empirically it has been observed that for a fixed *B*'-*B*'' combination the degree of order increases as the size of the *A* cation decreases [11].

Ordering about the *A* site is typically achieved with divalent Ba (*A*' cation) and trivalent *RE* (*A*'' cation) [8]. Around the smaller *A*'' cation, oxygen deficiency is common. By varying the *A*':*A*'' ratio, it is possible to build up layered perovskite structures consisting of *A*'O, *A*''O_δ and BO_2 layers, *i.e.* the double perovskite $A'A''B_2O_{5+\delta}$ for the 1:1 ratio, the triple perovskite $A'_2A''B_3O_{8+\delta}$ for the 2:1 ratio, *etc*. The basic SP unit cell is doubled, tripled, *etc*., respectively. The *A*-site ordered double-perovskite structure forms for several *B*-site constituent elements, as discussed in detail in Chapter 4. The triple-perovskite structure is known for *B* = Cu and Fe, *i.e.* the prototype high-T_c superconductor $Ba_2RECu_3O_{7-\delta}$ ($CuBa_2RECu_2O_{7-\delta}$ or Cu-1212) [12] and $Ba_2REFe_3O_{8\pm\delta}$ [13-16]. Quadruple and quintuple perovskites have been stabilized for *B* = Cu only, *i.e.* the ultra-high-pressure-synthesized $Ba_2Ca_2Cu_4O_{8+\delta}$ ($CuBa_2Ca_2Cu_3O_{8+\delta}$ or Cu-1223) and $Ba_2Ca_3Cu_5O_{10+\delta}$ ($CuBa_2Ca_3Cu_4O_{8+\delta}$ or Cu-1234) high-T_c superconductors with divalent Ca rather than trivalent *RE* as the *A*''-site cation [17-21]. Here it should be noted that the "higher-ordered" perovskites are heavily oxygen deficient. They also exhibit various oxygen-coordination polyhedra for the *B* cation even at $\delta = 0$ (Fig. 3). For example, in the quadruple-perovskite structure of $Ba_2Ca_2Cu_4O_8$ or $CuBa_2Ca_2Cu_3O_8$ with the layer sequence of BaO-Cu-BaO-CuO_2-Ca-CuO_2-Ca-CuO_2 the coordination number (CN) of copper is 2, 5, 4 and 5, respectively.

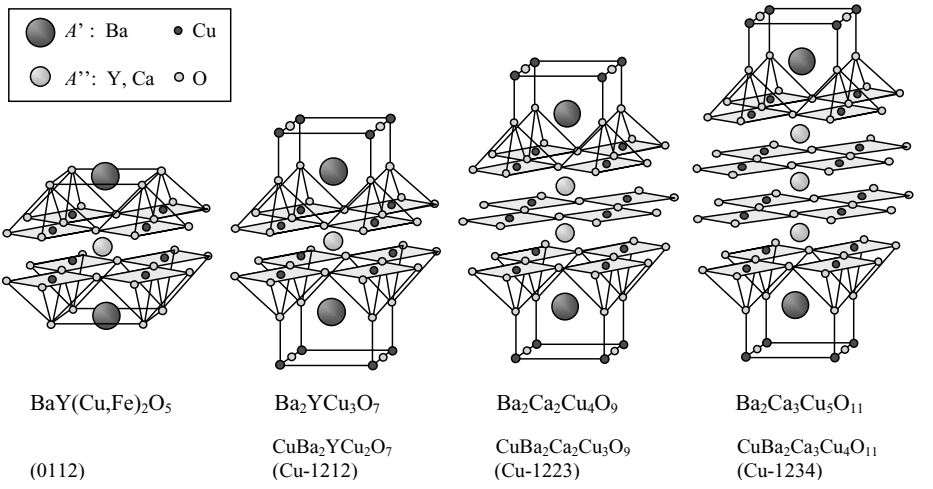

Fig. 3. Crystal structures of the double, triple, quadruple and quintuple perovskites of copper.

3. *B*-SITE ORDERED DOUBLE PEROVSKITES

The Sr_2FeMoO_6 phase was synthesized for the first time in 1963 and found to be a ferri/ferromagnetic conductor with a magnetic transition temperature as high as ~420 K [22-24]. By now the halfmetallicity and the TMR phenomenon are well established not only for Sr_2FeMoO_6 [5] but for many other related *B*-site ordered DPs, $A_2B'B''O_6$ [7]. Efforts to enhance the room-temperature TMR effect have typically been directed towards cation substitutions and methods for controlling the long-range ordering of the Fe and Mo atoms. Here we first (Sections 3.1 - 3.5) discuss various synthesis, chemical, structural and magnetic-property aspects of these phases using Sr_2FeMoO_6 as an example, and then in Sections 3.6 and 3.7 shortly summarize the most interesting cation substitution/replacement schemes employed.

3.1. Synthesis Techniques

The Sr_2FeMoO_6 phase forms best under strongly reduced oxygen partial pressures [25]. This is understood by the fact that either one (or both) of its *B*-site cation constituents possesses a relatively low valence value, *i.e.* lower than III for Fe and/or VI for Mo. If the oxygen partial pressure is not low enough, more oxidized phases such as $SrMoO_4$ and/or $SrFeO_{3-\delta}$ appear as impurity phases. The most commonly employed synthesis route involves firing of mechanically mixed, commercially available precursor powders ($SrCO_3$, Fe_2O_3 and MoO_3) in flowing H_2-containing gas (H_2/CO_2, Ar, N_2) at relatively high temperatures (~1200 ^oC) [5,25]. The drawback of this method is that once one aims at samples with a high degree of Fe/Mo order long heating periods are required to complete the cation diffusion (see Section 3.4), but at the same time such a long firing in flowing gas at a high temperature is likely to yield cation-nonstoichiometric samples due to partial evaporation of the constituent metals (here particularly Mo). Samples synthesized through the solid-state synthesis route in H_2-containing gas flow have a high probability to contain metallic Fe as an impurity that often escapes the detection in an ordinary x-ray diffraction measurement. Moreover, application of an H_2-containg gas flow brings about the need to pay extra attention to experimental safety.

Closing the precursor powder into an ampoule (sealed fused-quartz tube) for "encapsulation synthesis" efficiently prevents undesired evaporation. To minimize the possible evaporation of the reactant(s), the empty volume left inside the ampoule after sample loading could be filled with additional fused-quartz rods (Fig. 4). In a completely closed system, generation of gaseous decomposition products from the synthesis precursors is harmful. Therefore carbonates and nitrates can not be used as the precursor: it should be in an oxide or metallic form. For controlling the partial pressure of oxygen [$p(O_2)$], two different approaches have been employed. In the early works, SrO, Fe_2O_3, Mo and MoO_3 were used as constituents of the precursor and the amount of oxygen introduced into the ampoule in the form of the precursor was controlled by varying the ratio, Mo:MoO_3 [22-24]. (The same would be achieved by using mixtures of Fe, FeO and/or Fe_2O_3 instead.) In an alternative (and more precise) approach, an "external getter" for oxygen is used to adjust the $p(O_2)$. For the synthesis of Sr_2FeMoO_6, metallic iron was revealed to work best [26,27]: within the typical temperature range of 800 - 1150 ^oC used for synthesis, Fe equilibrates with FeO and O_2 such that $p(O_2)$ ranges from $10^{-19.5}$ - $10^{-12.6}$ atm accordingly (Fig. 4) [28]. Note that for the Fe/FeO "redox couple" the precise value of $p(O_2)$ is defined not by the amount of Fe grains (if in

excess) but by the temperature only. To prevent the reactant mixture from excess-iron contamination, the Fe grains are placed in a separate crucible inside the ampoule. An example of packing of the ampoule for the oxygen-getter-controlled low-O_2-pressure encapsulation (OGC-LOPE) synthesis is shown in Fig. 4.

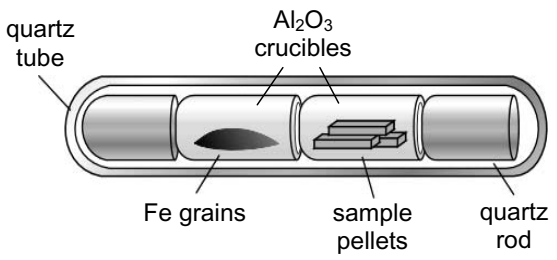

T [°C]	log $p(O_2)$
800	-19.5
850	-17.5
900	-16.5
950	-15.5
1000	-14.7
1050	-14.1
1100	-13.1
1150	-12.6

Fig. 4. Packing of the fused-quartz ampoule for oxygen-getter-controlled low-O_2-pressure encapsulation (OGC-LOPE) synthesis of Sr_2FeMoO_6. In the presence of Fe (Fe/FeO redox couple) as an oxygen getter, $p(O_2)$ is controlled by the synthesis temperature [26,28].

The time required for successful synthesis can be shortened if the metal constituents, Sr, Fe and Mo, are mixed in atomic scale *prior* the synthesis employing an appropriate wet-chemistry route [29-32]. To use solution-homogenized precursor powders is highly beneficial since it facilitates the phase-formation and cation-ordering processes even at low temperatures within reasonable time periods. Employment of a wet-chemical route furthermore enables a precise control of the particle size that is important in terms of the intergrain TMR characteristics [29,31,33]. High-quality precursor powders are readily obtained by *e.g.* complexing the dissolved cations from the solution by EDTA (ethylenediaminetetraacetic acid) [32]. Using such highly homogeneous powder as a precursor, single-phase samples are obtained even when the synthesis is performed at a temperature as low as 900 ºC. Especially advantageous is to combine the wet-chemistry precursor-preparation route to the encapsulation sample-synthesis technique described above: with such a combination, Sr_2FeMoO_6 samples with almost complete Fe/Mo ordering were successfully synthesized [32]. The saturation magnetization of such samples reached a value of 3.96 μ_B that is very close to the theoretical value of 4 μ_B, see Section 3.5.

The first single-crystal [34,35] and thin-film [36,37] syntheses of Sr_2FeMoO_6 were reported soon after the phase was recognized as a HM. The former was accomplished by the floating-zone technique, whereas for the latter the pulsed-laser deposition technique was used.

3.2. Oxygen Stoichiometry

Oxygen nonstoichiometry is usually considered as one of the common characteristics of perovskite-derived structures. Nevertheless, attempts to experimentally verify or deny the presence of oxygen vacancies/excess in *B*-site ordered DP samples have been rare. This is not

due to the lack of a proper oxygen-content determination technique. In Ref. [26], a straightforward wet-chemical redox analysis method is presented that can be used for precise oxygen-content determination of Sr_2FeMoO_6 and other related perovskite-oxide samples containing cation species at reduced oxidation states. The sample is dissolved in oxygen-freed acidic solution from which the total amount of the thus formed reduced species, Fe^{II} and/or Mo^{V}, is determined by subsequent constant-current anodic oxidation, *i.e.* coulometric titration. Both Fe^{II} and Mo^{V}, if present, are oxidized quantitatively. From the time required for complete oxidation the number of electrons produced and thereby the total amount of reduced species is obtained. This tells us unambiguously the oxygen content of the sample. Figure 5 shows a schematic illustration of a coulometric titration cell.

Anodic-oxidation reactions

$Fe^{2+} \rightarrow Fe^{3+} + e^-$

$Mo^{5+} \rightarrow Mo^{6+} + e^-$

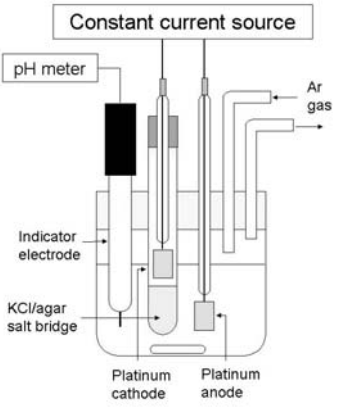

Fig. 5. Coulometric titration cell used for oxygen-content analysis of Sr_2FeMoO_6 samples.

From coulometric titration experiments it has been confirmed that Sr_2FeMoO_6 samples synthesized by means of the OGC-LOPE technique possess the stoichiometric oxygen content (within the experimental accuracy of ±0.03) independent of the synthesis temperature even though $p(O_2)$ considerably varies when the synthesis temperature is varied (refer to Fig. 4 in Section 3.1) [27]. Similarly, isovalent *A*-site cation substitutions and also aliovalent *B*''-site substitutions were found not to affect the oxygen content: the oxygen content *per* formula unit was determined at 6.00 ± 0.03 for all the three A_2FeMoO_6 phases with A = Ba, Sr and Ca [38], and for various samples in the $Sr_2Fe(Mo,W/Ta)O_6$ system [39,40]. In line with this, no indication of five-coordinated Fe species has been seen in any of the published ^{57}Fe Mössbauer spectra of Sr_2FeMoO_6 samples (within the detection limit of ~2 % of Mössbauer spectroscopy), but the spectra are always well fitted with six-coordinated Fe components only (see Section 3.4 for details) [32,38,39,41,42]. Experimental data thus support the "self-doping" concept of the *B*-site ordered $A_2FeB''O_6$ DPs, as these compounds seem to be stoichiometric not only for the cation composition but also in terms of the oxygen content.

3.3. Cation Valences

Actual valence states of the *B*-site cations in $A_2Fe(Mo,Re)O_6$-type DPs were discussed for the first time in 1970's [43]. Debate on the topic was renewed when these materials were highlighted as HMs [44]. From band structure calculation for Sr_2FeMoO_6 [5,45-48], strong mixing of the itinerant *d* electron from formally pentavalent Mo ($4d^1$; t_{2g}^1; $S = 1/2$) and the minority spin t_{2g} band of formally trivalent, high-spin Fe ($3d^5$; $t_{2g}^3 e_g^2$; $S = 5/2$) is revealed (see Fig. 6). In other words, the itinerant electron of Mo^V is likely to transfer part of its charge and spin density to Fe^{III}, and accordingly mixed-valence or "valence-fluctuation" states of II/III and V/VI are expected for Fe and Mo, respectively.

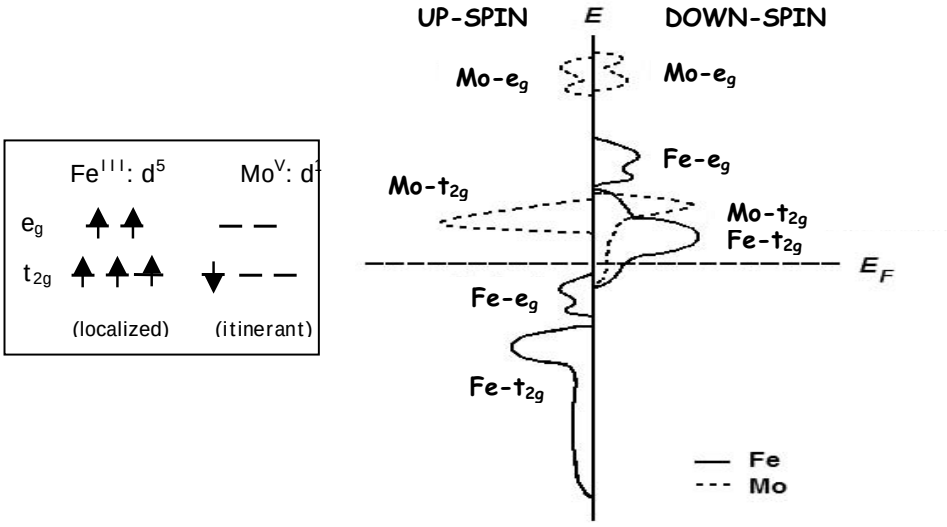

Fig. 6. Schematic illustration of the electronic structure of Sr_2FeMoO_6 [49].

The mixed-valence state of II/III for Fe was first experimentally diagnosed on the basis of ^{57}Fe Mössbauer spectroscopy data [41]. The hyperfine parameters revealed from Mössbauer spectra for Fe in Sr_2FeMoO_6 are intermediate of those typically obtained for high-spin Fe^{III} and high-spin Fe^{II} [38,39,41,42,50,51]. Among the various hyperfine parameters, isomer shift (*IS*) measures most straightforwardly the valence state of iron. For the (majority) Fe atoms in Sr_2FeMoO_6, the 77-K *IS* value is ~0.7 mm/s, whereas values around 0.3 mm/s and 1.0 mm/s, respectively, are expected for high-spin Fe^{III} and Fe^{II} in an oxide of a perovskite-like structure. Internal field (*B*) is another hyperfine parameter that reflects the Fe valence. High-spin Fe^{III} ($S = 5/2$) in five- or six-fold coordination usually has a saturation internal field higher than 50 T. For Fe in Sr_2FeMoO_6 somewhat decreased *B* values around 45 T are observed in accordance with the II/III mixed-valence state and thus a reduced number of unpaired electrons.

X-ray absorption near-edge structure (XANES) spectroscopy is another powerful tool to probe the valence state of iron in Sr_2FeMoO_6: both *K*- and *L*-edge data give strong evidence for the mixed-valence state [40]. For reliable interpretation of the spectral features the key is to find proper reference compounds in which Fe atoms exist in an oxide environment as akin as possible to that in Sr_2FeMoO_6. Accordingly, the two solid-solution series, $Sr_2Fe(Mo,W)O_6$ and $Sr_2Fe(Mo,Ta)O_6$, together provide us with an ideal reference system. The end-members, Sr_2FeWO_6 [52] and Sr_2FeTaO_6 [53], contain octahedrally-coordinated Fe^{II} and Fe^{III}, respectively. Both compounds are antiferromagnetic (AFM) owing to the d^0 ($S = 0$) configuration of W^{VI} and Ta^{V}. Increasing the amount of W^{VI} in $Sr_2Fe(Mo,W)O_6$ makes the valence of Fe gradually approach the II state, whereas an increase in the Ta^{V} content in $Sr_2Fe(Mo,Ta)O_6$ causes the Fe valence to shift towards III.

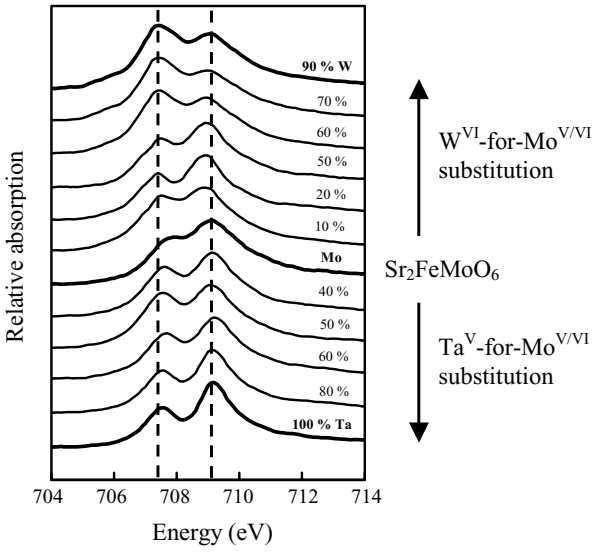

Fig. 7. Fe L_3-edge XANES spectra for a series of $Sr_2Fe(Mo,W)O_6$ and $Sr_2Fe(Mo,Ta)O_6$ samples [40].

In the Fe *L*-edge XANES spectrum the main spectral features originate from dipole transitions from the core Fe 2*p* level to the empty Fe 3*d* states [54,55]. (Transitions $2p \rightarrow 4s$ are also allowed but much weaker, contributing only to the smooth background at higher energies.) The spectra are separated into two regions due to core-hole spin-orbit interaction: Fe $2p_{3/2}$ (L_3 edge: 705 ~ 715 eV) and Fe $2p_{1/2}$ (L_2 edge: 715 ~ 730 eV). In Fig. 7, shown are the L_3 portions of the spectra for various samples of $Sr_2Fe(Mo,W/Ta)O_6$ [40] Each L_3 spectrum is divided into two peaks: the splitting and the intensity ratio between the two peaks are determined by the interplay of crystal-field effects and electronic interactions. For Fe^{II} species in an octahedral crystal field typically seen is that the lower energy peak (~707 eV) is stronger than the higher energy peak (~709 eV) [54,55]. For Fe^{III} species the order of the peaks is reversed. This is what is precisely seen for the $Sr_2Fe(Mo,W/Ta)O_6$ sample series: the lower-

energy peak is stronger than the higher-energy peak for heavily W^{VI}-substituted samples and weaker for the heavily Ta^{V}-substituted ones. The Sr_2FeMoO_6 sample possesses intermediate spectral features as compared with those for the strongly W- and Ta-substituted samples, as a manifestation of the $Fe^{II/III}$ mixed-valence state in it [40].

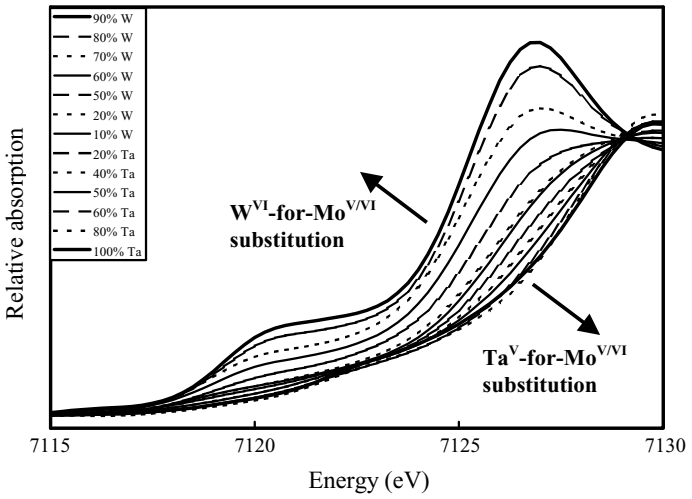

Fig. 8. Fe *K*-edge XANES spectra for a series of $Sr_2Fe(Mo,W)O_6$ and $Sr_2Fe(Mo,Ta)O_6$ samples [40].

Figure 8 displays the narrow spectral range (due to transitions $1s \rightarrow 4p$) from 7115 to 7130 eV of the Fe *K*-edge XANES spectra for a series of $Sr_2Fe(Mo,W/Ta)O_6$ samples [41]. An increase in the valence state of iron is expected to shift this main absorption edge to the higher energy. The spectra of the $Sr_2Fe(Mo,W/Ta)O_6$ samples are located roughly between those for $Fe^{II}O$ and α-$Fe^{III}_2O_3$ (not shown in Fig. 8). More importantly, the absorption edge monotonously shifts to the higher energy first with decreasing amount of W^{VI} that replaces $Mo^{V/VI}$ in $Sr_2Fe(Mo,W)O_6$ and then with increasing amount of Ta^{V} to replace $Mo^{V/VI}$ in $Sr_2Fe(Mo,Ta)O_6$, *i.e.* with the expected valence of Fe increasing from II to III. Here it should be emphasized that details of the spectral features of the $Sr_2Fe(Mo,W/Ta)O_6$ samples are somewhat different from those of the simple reference oxides, $Fe^{II}O$ and α-$Fe^{III}_2O_3$, whereas within the $Sr_2Fe(Mo,W/Ta)O_6$ double-perovskite series, the spectral features evolve smoothly. This underlines the fact that the sample series itself provides us with the best reference system.

From Fig. 8, even though the absorption energy values for the Mo-rich compositions are intermediate between those for strongly W^{VI}- or Ta^{V}-substituted samples (as a manifestation of the intermediate valence state of iron in these samples) the shift of the *K*-edge absorption energy is larger for the W^{VI}-substituted samples as compared with those substituted with Ta^{V} [40]. This behaviour might indicate that the actual valence of Fe in Sr_2FeMoO_6 is not precisely 2.5 but somewhat higher than that value.

The mixed-valence state of iron as confirmed for Sr_2FeMoO_6 by means of the two spectroscopy probes, Mössbauer and XANES, is in line with neutron diffraction [30,35,50,56-58] and x-ray magnetic circular dichroism [59] data showing reduced magnetic moment values at both the Fe and the Mo sites from the values expected for high-spin Fe^{III} ($t_{2g}^3 e_g^2$; S = 5/2) and Mo^{V} (t_{2g}^1; S = 1/2). For Mo, the mixed-valence state, $Mo^{V/VI}$, has been confirmed from an NMR study as well [60]. Since Fe was shown to exist in a mixed-valence state (besides Sr_2FeMoO_6) in Sr_2FeReO_6 too [61], it seems that mixed valency is inherent to the *B*-site ordered DP HMs.

3.4. *B*-site Cation Ordering

Incomplete ordering of the *B*-site cations is characteristic to many of the *B*-site ordered DPs. This has particularly been observed for the $A_2Fe(Mo,Re)O_6$ phases, in which rather equally-sized Fe and Mo/Re atoms tend to exchange their crystallographic positions to some extend [5,62]. Thermodynamics tells us that samples with the highest degree of (*B*-site cation) order are obtained using low synthesis temperatures. However, at low temperatures cation diffusion becomes slow and the degree of order is rather kinetically controlled. Thus, in practice to obtain highly ordered samples of the Sr_2FeMoO_6 phase or related DPs, long synthesis periods at moderate temperatures are required.

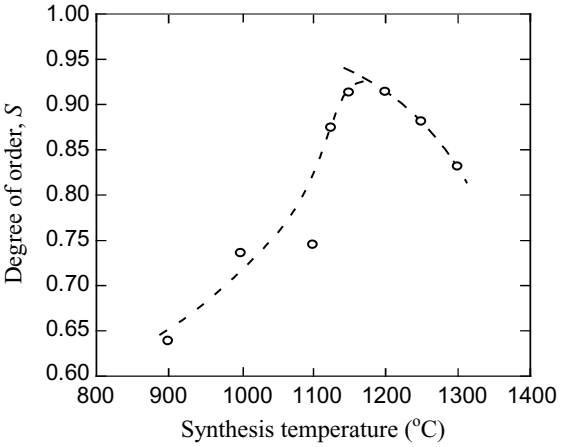

Fig. 9. Long-range order parameter (S) for Sr_2FeMoO_6 samples synthesized at various temperatures by the OGC-LOPE technique described in Section 3.1 (synthesis time: 50 hours) [27].

The ampoule synthesis technique described in Section 3.1 is highly beneficial as sample encapsulation prevents the undesired evaporation of constituent metal(s) during the long periods of heat treatment needed for completion of the ordering process. In Fig. 9, the long-range order parameter ($S \equiv 2\omega_{Fe} - 1$, where ω_{Fe} is the occupancy of Fe at the "right" Fe site refined from x-ray diffraction data) is plotted against the synthesis temperature for samples

fired for 50 hours at various temperatures ranging from 900 to 1300 °C [27]. A maximum in *S* is seen about 1150 °C, indicating that thermodynamic equilibrium is reached in the vicinity of that temperature. The data points above 1150 °C thus present the thermal equilibrium values of *S* at respective temperatures, whereas for the temperature range lower than 1150 °C (in which *S* increases as the synthesis temperature increases) the ordering is apparently controlled by kinetics.

From Fig. 9, the optimum temperature range to obtain high-*S* samples is found to be about 1150 °C: lowering the synthesis temperature below ~1150 °C would not considerably enhance the equilibrium value of *S* but would make the sintering time required to achieve the anticipated equilibrium value markedly longer. At 1150 °C, the Sr_2FeMoO_6 phase forms quite rapidly; even for samples fired at this temperature for 4 hours only, all the x-ray diffraction peaks are for the DP phase, though the ordering is not yet complete. To decrease the concentration of misplaced or "antisite" (AS) Fe/Mo atoms, *i.e.* to increase the value of *S*, longer synthesis/heating periods are required. Here it should be noted that the highest value of $S \approx 0.96$ (at 1150 °C) is reached much faster for samples prepared from a wet-chemically-mixed precursor powder [32] than for those from a mechanically mixed powder [27] (Fig. 10). In solution the starting metal ions are mixed in an atomic scale, which enables us to achieve a homogeneous reaction system and efficiently obtain samples with a high degree of cation order at the *B* site.

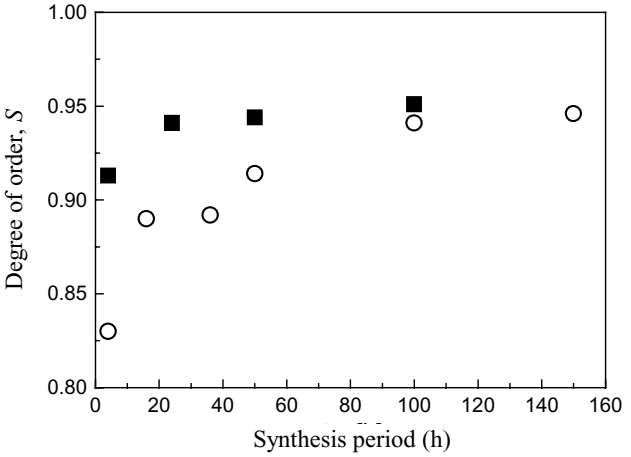

Fig. 10. Long-range order parameter (*S*) for Sr_2FeMoO_6 samples synthesized at 1150 °C for various periods by the OGC-LOPE technique (Section 3.1) from wet-chemically prepared (solid squares) [32] and mechanically mixed (open circles) [27] precursors.

Not only AS point defects as discussed above, but also more extended defects, *i.e.* "antiphase boundaries" (APB), are common to ordered structures consisting of regularly repeated distinct structural units (here $SrFeO_3$ and $SrMoO_3$ units), see Fig. 11. Such defects are formed at the interface of two perfectly ordered regions that are (crystallographically

identical but) in different phases in terms of the alternating stacking of the Fe and Mo atoms. This offset by half a unit cell creates a plane of 180° Fe-O-Fe (or Mo-O-Mo) bonds that were initially assumed to be strongly antiferromagnetic [44,63], in contrast to the ferromagnetic Fe-Fe (or Mo-Mo) interaction within the ideally ordered lattice. The first direct experimental evidence for APBs in Sr_2FeMoO_6 came from high-resolution electron microscopy images for samples synthesized at lower temperatures [64].

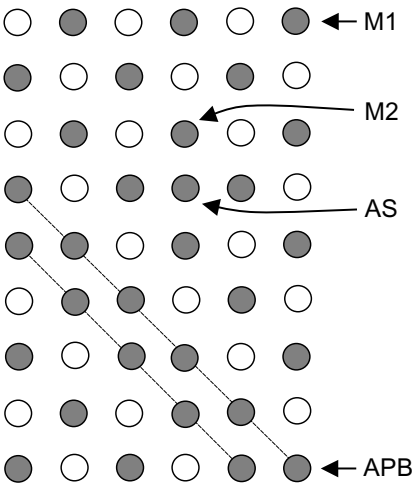

Fig. 11. Schematic illustration of the different environments of Fe atoms in Sr_2FeMoO_6: the filled/ empty spheres are for Fe/Mo atoms. Note that the O atoms are omitted.

Mössbauer spectroscopy provides us with a uniquely powerful tool to detect the different Fe species and to determine their concentrations in the various Sr_2FeMoO_6 samples. A typical 77-K ^{57}Fe Mössbauer spectrum for Sr_2FeMoO_6 - readily fitted with four (sextet or magnetic) subspectra - is shown in Fig. 12. The relative intensity of each subspectrum is a one-to-one measure of the concentration of the corresponding Fe species, whereas the refined hyperfine parameters, *IS* and *B*, reveal information related to the valence and spin state and the magnetic and crystal-field effects about the Fe atom concerned. The AS Fe atoms are clearly visible in most of the spectra collected for Sr_2FeMoO_6 [32,38,39,41,42,51,65]: the obtained hyperfine parameters are typical of high-spin trivalent Fe in an oxide environment. The most intense subspectrum (denoted M1) is naturally due to Fe atoms in an ideally ordered lattice. As discussed in Section 3.3, these atoms adopt the II/III mixed valence state with hyperfine parameters approximately intermediate between those for Fe^{II} and Fe^{III}. Quite interestingly, Mössbauer spectroscopy further distinguishes these ideally ordered Fe atoms with six Mo neighbours from those Fe atoms (denoted M2) occupying the right Fe site but being located adjacent to an AS Fe atom (refer to Fig. 11). Hyperfine parameters for these M2 Fe atoms are slightly different from those describing an M1 Fe atom, indicating a valence state somewhat

closer to III. The relative intensities of the two subspectra, AS and M2, should both reflect the concentration of AS defects: in the case of random distribution of the AS atoms an intensity ratio of 1:6 is expected. This is what is typically seen for samples with relatively small AS concentrations, whereas the larger ratio than 1:6 seen for samples with the higher AS concentrations indicates clustering of the AS atoms.

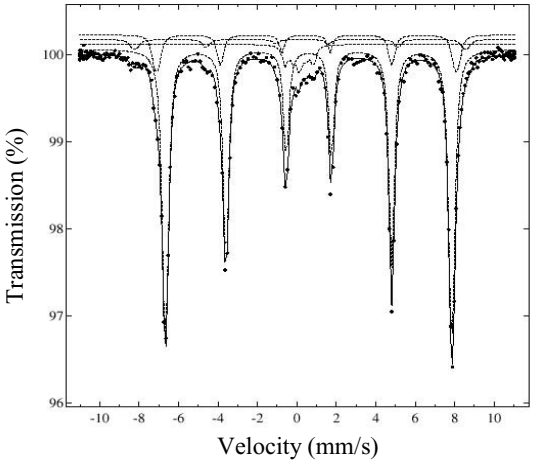

Fig. 12. Typical 77-K ^{57}Fe Mössbauer spectrum for A_2FeMoO_6-type samples [38]. The subspectra used in the fitting are displayed above the spectrum in the order of M2, AS, APB and M1 from the top.

Iron atoms sitting at APBs should also be visible in the ^{57}Fe Mössbauer spectra, if existing [51]. Among the subspectra detected for Sr_2FeMoO_6, the one (denoted APB) with the smallest B value most likely has its origin in Fe atoms at the APBs [65]. If so, unlike the predicted strong AFM nature the APBs would be magnetically strongly frustrated. The ways to control the concentration of APB defects and the impacts of the APBs on the MR and other physical-property characteristics remain to be clarified yet.

The AS defects are known to substantially influence the properties of the DP phase, reducing the average saturation magnetization [62,66] (see Section 3.5) and eventually also the magnetic transition temperature, T_C [27,32,67]. For large AS concentrations a change from a ferri/ferromagnetic state into a spin-glass-type behaviour was reported [58,68]. Moreover, the AFM islands formed at the ASs may create pinning centers for the domain walls. Increase in the AS defect concentration apparently depresses the halfmetallic character (or the degree of spin polarization). In line with this, it has been reported that the presence of AS atoms has a significant effect on the low-field TMR characteristics [69,70], such that for samples with a higher degree of order the MR values are higher. On the other hand, moderate levels of ASs might be beneficial as well, due to the fact that application of an external magnetic field suppresses the spin disorder in the magnetically frustrated areas about the AS defects [64,70,71].

3.5. Magnetic Properties

The magnetism of Sr_2FeMoO_6 and related DPs arises from the localized $S = 5/2$ core spin of the formally trivalent Fe atoms. The conduction band has one delocalized electron *per* formula unit that tends to align antiparallel to the Fe spin. It is believed that the ferromagnetic (FM) interaction between Fe atoms is transmitted by the itinerant t_{2g}-spin down electrons of both Mo(4*d*) and Fe(3*d*) character [72,73]. A saturation magnetization (M_S) of 4 μ_B *per* formula unit is expected on the basis of antiferromagnetic coupling between high-spin $Fe^{2.5}$ ($3d^{5.5}$, $S = 2.25$) and $Mo^{5.5}$ ($4d^{0.5}$, $S = 0.25$). Note that the same value is obtained if one assumes Fe^{III} ($3d^5$, $S = 2.5$) and Mo^{V} ($4d^1$, $S = 0.5$) or Fe^{II} ($3d^6$, $S = 2$) and Mo^{VI} ($4d^0$, $S = 0$). In other words, the magnitude of M_S is not dependent on the degree of valence mixing.

As mentioned in the previous section, AS defects are believed to suppress the magnitude of M_S. Experimentally a linear dependence is commonly observed between M_S and the degree of order, S [27,32], that follows well the "theoretical" line of $M_S = 4S$ [51,66]. This relation is derived based on a simple model that assumes ferrimagnetic arrangement among all the *B*-cation neighbours.

3.6. *A*-site Substitutions

The divalent *A*-site Sr in Sr_2FeMoO_6 can be substituted completely by the other "isovalent" alkaline earth cations, Ca^{II} and Ba^{II}, and partially by the largest trivalent *RE* cations, *e.g.* La^{III}. The latter is considered to result in "electron doping" of the *B* cation lattice.

3.6.1. Isovalent Substitution

The valence state of the mixed-valent $Fe^{II/III}$ species is not necessarily fixed at a certain precise number but it is likely to be controlled by the size of the *A* cation, *i.e.* the "isovalent substitution" or "chemical pressure" effect. As the very first approach it is interesting to consider the average ionic radius of the *B*-site cations (r_B) for the two limit cases of Fe^{III}-Mo^{V} and Fe^{II}-Mo^{VI}: r_B is ~0.63 Å (0.645-0.61 Å) for the former case and ~0.69 Å (0.78-0.59 Å) for the latter [74]. We thus expect that an increase in the (average) size of the *A*-site cation would result in a shift of positive charge from Fe to Mo, and *vice versa*. In fact, this is the trend experimentally observed for a series of $(Sr,Ca,Ba)_2FeMoO_6$ samples [38].

In Fig. 13, the *IS* value refined from ^{57}Fe Mössbauer data is plotted for the $(Sr,Ca,Ba)_2FeMoO_6$ system against the average ionic radius of the *A*-site cations (r_A) [38]. The straightforward interpretation is that the higher the *IS* value is, the lower is the valence value of the mixed-valence Fe in the sample, *i.e.* closer to II. For all the compositions from *A* = Ca to Ba not only the *IS* value but also the other hyperfine parameters obtained from the Mössbauer spectra confirm that Fe remains in the mixed-valence state. However, there is a systematic shift towards divalency with increasing r_A, especially within the *A* = (Sr,Ba) range upon increasing the Ba content [38,51,75]. Interestingly, as the valence of Fe approaches II, the difference in charges between Fe and Mo increases, and parallel with this the degree of Fe/Mo order increases [38,76].

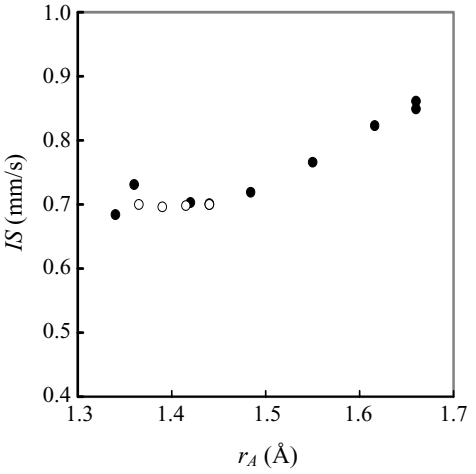

Fig. 13. Isomer shift (*IS*) value as refined from 77-K ^{57}Fe Mössbauer spectra (main subspectra) plotted against the average ionic radius of the *A*-site cations (r_A) for a series of A_2FeMoO_6 samples synthesized by two different techniques [38]: encapsulation technique (•) and H_2/Ar gas-flow technique (o) (see Section 3.1).

With decreasing r_A the crystal symmetry is lowered, being cubic for A = Ba (*Fm*3*m* [57]), tetragonal for A = Sr (*I*4/*m* [50]) and monoclinic for A = Ca ($P2_1/n$ [30]). On the other hand, T_C has a maximum that exceeds 410 K around A = Sr (for A = Ca and Ba, T_C is *ca*. 320 and 330 K, respectively) [77,78]. In the most straightforward way, T_C could be assumed to increase with decreasing distance and buckling angle of the Fe-O-Mo bonding. Thus when going from Ba to Sr, T_C increases as a consequence of the decreasing bonding distance, whereas from Sr to Ca the effect of the shrinkage in the bonding distance is less pronounced and more than compensated by the increase in the Fe-O-Mo buckling.

Owing to its low T_C value in comparison with that of the prototype Sr_2FeMoO_6, it was the Ba_2FeMoO_6 compound for which intragrain MR was observed for the first time [78] to coexist together with that of the tunneling-type intergrain MR. The former is seen only in the very vicinity about T_C and is explained by a double-exhange-like mechanism (refer to the CMR manganites), whereas the latter has its origin in the halfmetallicity of the compound and is most pronounced at low temperatures [78].

3.6.2. Electron Doping

Carrier doping through aliovalent cation substitution is a commonly employed approach to tune the properties of strongly-correlated-electron oxides. For Sr_2FeMoO_6 this is achieved by means of aliovalent RE^{III}-for-Sr^{II} substitution [79]. Only the largest *RE*s have been found to enter the phase. For *RE* = La, essentially single-phase $(Sr_{1-x}RE_x)_2FeMoO_6$ samples have been reported up to $x \approx 0.5$, but the crystal symmetry is lowered upon heavy substitution [80]. From

the smaller size of La^{III} than that of Sr^{II} one would expect that the unit cell volume decreases with increasing x in $(Sr_{1-x}La_x)_2FeMoO_6$. Nevertheless, the observed outcome is opposite indicating that the size is controlled by the electron-doping effect on the (Fe/Mo)-O bond (that is lengthened when the valence of Fe/Mo decreases) rather than by purely steric effects [80-82]. The most remarkable effect of the RE^{III}-for-Sr^{II} substitution on the physical properties is a significant increase in the value of T_C, from ~420 K even up to ~490 K [80]. At the same time the degree of order markedly decreases [42,81,82].

Ideally, the number of electrons within the *B*'-*B*'' (= Fe-Mo) sublattice should increase upon the RE^{III}-for-Sr^{II} substitution. Photoemission spectroscopy (PES) studies have confirmed that electron density indeed increases at the Fermi level (composed of the Fe t_{2g} and the Mo t_{2g} states) [83]. In chemistry terminology, either Fe or Mo (or both) should get reduced. It has been shown by means of various independent probes that the bulk of electron doping is received by the Mo atoms rather than the Fe atoms. From ^{57}Fe Mössbauer data [42] a small though visible increase in the isomer shift is seen for the mixed-valent $Fe^{II/III}$ atoms occupying the right site, indicating a slight movement towards divalency of these atoms. This is, however, over-counterbalanced by the increase in the fraction of antisite Fe atoms with the III valence state. Thus, in overall the average valence of Fe increases. At the same time, both neutron diffraction [79] and NMR spectroscopy [84] provide evidence that the magnetic moment of Mo is significantly affected (increased due to electron doping), while that of Fe remains unaffected. As the final evidence, PES data (collected by changing the incoming photon energy) conclude that the increased density of states at E_F is predominantly of the Mo t_{2g} character [83].

3.7. *B*-site Substitutions

Among the $A_2FeB''O_6$ phases other than the Mo-based HMs, those with *B*'' = Re are probably the most interesting ones. This is because Sr_2FeReO_6 and Ba_2FeReO_6 have turned out to be HM magnetoresistors, too [7,85]. The Ca-variant, Ca_2FeReO_6, is rather unique: it has been known as a ferromagnet with a very high T_C value (see Table 2), but showing an insulating behaviour in terms of the transport property [86,87]. Within $(Sr_{1-x}Ca_x)_2FeReO_6$, the metal-insulator (MI) transition occurs about x = 0.4 [88]. As revealed from ^{57}Fe Mössbauer spectroscopy data, among the three A_2FeReO_6 phases with *A* = Ca, Sr, Ba the first one contains Fe atoms at the highest valence state, *i.e*. the closest to the III state [87]. In fact, the pure Ca_2FeReO_6 phase shows another MI transition related with a structural transition upon cooling below ~150 K [88]. This temperature-controlled MI transition promotes a further valence shift of the Fe atoms towards the III state [89].

The two solid-solution systems, $Sr_2Fe(Mo,W)O_6$ and $Sr_2Fe(Mo,Ta)O_6$, are other examples of the *B*-site ordered DP systems showing a composition-controlled MI transition [39,90-93]. As already mentioned in Section 3.3, the end compounds, Sr_2FeWO_6 and Sr_2FeTaO_6, are AFM insulators owing to the stability of Fe^{II}-W^{VI} and Fe^{III}-Ta^{V} configurations. Note that both W^{VI} and Ta^{V} have the d^0 electron configuration that lacks the itinerant electron responsible for metallic conductivity and mediation of the ferromagnetic coupling among the Fe atoms in Sr_2FeMoO_6 and related DP HMs. Quite interestingly, for a certain rather heavy substitution ranges the $Sr_2Fe(Mo,W/Ta)O_6$ systems show strongly enhanced low-temperature MR characteristics [39,90,92]. This was initially explained on the basis of a percolation model

[90] but later an alternative/additional explanation was suggested in which the enhancement in the low-temperature MR was attributed to an additional intragrain MR effect originating from the AFM nature of the areas rich in W or Ta embedded in the halfmetallic Sr_2FeMoO_6 matrix (that naturally is responsible for the tunneling-type intergrain MR effect) [39].

As for the single-perovskite structure, there exists a large variety of different cation compositions for the *B*-site ordered DP structure, too [94-96], though the actual degree of *B*-site cation order also varies widely [11]. Among them, some of the *B*' = Cr compounds exhibit pronouncedly high T_C values, *i.e.* ~460 K for halfmetallic Sr_2CrWO_6 [95,97] and the record-high (among the *B*-site ordered DPs) value of 635 K for Sr_2CrReO_6 [98]. In Table 2, listed are T_C values reported for representative ferri/ferromagnetic *B*-site ordered DPs, $A_2B'B''O_6$, together with space groups for these compounds. Two general trends are recognized: for the same *B*'-*B*'' combination (*i*) the crystal symmetry becomes lower in the order of Ba > Sr > Ca for the *A*-site cation, whereas (*ii*) for T_C a maximum is seen at *A* = Sr. In regards to (*ii*), the Ca_2FeReO_6 compound is an evident exception.

Finally we like to point out that the *B*-site ordered DP structure has also been considered as a potential host for such an *oxymoron* [101] as an "antiferromagnetic halfmetal". The AFM-HM is a nonmagnetic metal with perfectly spin-polarized conduction electrons [102]. Theoretical electronic structure calculations have predicted some candidate DPs, such as La_2MnVO_6 [101] and La*A*VRuO$_6$ (*A* = Ca, Sr, Ba) [103], but experimentally these candidate phases or any other phases with confirmed AFM-HM characteristics have not been realized yet. However, the success in synthesizing ordered samples of the $La_2Cr^{III}Fe^{III}O_6$ phase (with two isovalent *B*-site cations) as an artificial superlattice of $LaCrO_3$ and $LaFeO_3$ by means of laser ablation [104] is a promising first step in the desired future efforts in stabilizing novel *B*-site ordered DP compounds with exotic functions.

Table 2. Examples of *B*-site ordered DP oxides, $A_2B'B''O_6$, and their space groups and Curie temperatures.

***A* cation**	***B*' cation**	***B*'' cation**	**Space Group**	**T_C [K]**	**Refs.**
Ca	Fe	Mo	$P2_1/n$	320	30
Sr	Fe	Mo	$I4/m$	420	50
Ba	Fe	Mo	$Fm3m$	330	57
Ca	Fe	Re	$P2_1/n$	540	86,87,99,100
Sr	Fe	Re	$I4/m$	405	99,100
Ba	Fe	Re	$Fm3m$	300	100
Ca	Cr	W	$P2_1/n$	160	95
Sr	Cr	W	$Fm3m$	460	95
Ba	Cr	W	$P62c$	145	95
Ca	Cr	Re	$P2_1/n$	360	98
Sr	Cr	Re	$I4/mmm$*	635	98

*as reported

4. *A*-SITE ORDERED DOUBLE PEROVSKITES

The *A*-site ordered DP structure was first established for Ba*RE*$(Cu_{0.5}Fe_{0.5})_2O_5$ with *RE* = Y in 1988 [8]. Later the same structure has been observed for compounds with various *RE*s and *B*-site constituents. The DP structure with the *B* site that is occupied only by a single element, is known for *B* = Co [105], Mn [106] and Fe [107]. For copper, the maximum *B*-site occupation so far reached is $x = 0.7$ in samples of (Ba,La)Y$(Cu_xFe_{1-x})_2O_{5+\delta}$ obtained through an ultra-high-pressure high-temperature treatment [108]. Of the exciting phenomena revealed for the *A*-site ordered DPs we should mention (*i*) the relatively large MR effect in Ba*RE*$Co_2O_{5+\delta}$ [109], (*ii*) the metal-insulator transition in Ba*RE*$Co_2O_{5.5}$ [110], (*iii*) the charge-ordering/spin-state transition in Ba*RE*$Co_2O_{5.0}$ [111], and (*iv*) the two-step valence-separation and charge-ordering transition in Ba*RE*$Fe_2O_{5.0}$ [112,113].

4.1. Synthesis

Within the three Ba*REB*$_2O_{5+\delta}$ systems of *B* = Co, Mn and Fe, the phases with *B* = Co are the easiest to be synthesized: they form in air, O_2 and N_2 atmospheres with most of the *RE*s (Y, Nd ~ Ho). The *B* = Mn (*RE* = *e.g.* Y, La) and the *B* = Fe (*RE* = Y, Nd ~ Ho) phases require strongly reduced oxygen partial pressures to form. For both the systems, an oxygen-getter-controlled low-O_2-pressure encapsulation synthesis technique (parallel to that presented in Section 3.1 for Sr_2FeMoO_6) has proven to work well [114,115].

For Ba*RE*$Fe_2O_{5+\delta}$, the same redox couple of Fe/FeO as employed in the OGC-LOPE synthesis of Sr_2FeMoO_6 may be used [114,116,117]. This is natural, since in these two systems Fe possesses an essentially equivalent mixed valence state of II/III. At the synthesis temperature of 985 °C as optimized for the Ba*RE*$Fe_2O_{5+\delta}$ phases, the partial pressure of oxygen equilibrates at ~10^{-15} atm. For Ba*RE*$Mn_2O_{5+\delta}$ (*RE* = Y [115]), a somewhat weaker reductant than Fe, *i.e.* FeO for the formation of a redox couple FeO/Fe_3O_4, should be used. Accordingly, the $p(O_2)$ range covered is lower; at the temperature of 1100 °C used for the synthesis, $p(O_2) \approx 10^{-10}$ atm. Among the Ba*RE*$Mn_2O_{5+\delta}$ phases, the OGC-LOPE technique has so far been employed only for *RE* = Y, to yield essentially single-phase DP samples. This has not necessarily been the case for the other synthesis approaches. For example, firing in pure argon easily ends up with mixtures of the two simpler oxides, $BaMnO_{3-\delta}$ and *RE*$MnO_{3-\delta}$ [106,118,119]. The OGC-LOPE synthesis of Ba*RE*$Mn_2O_{5+\delta}$ with FeO as the oxygen getter results in samples with no excess oxygen, *i.e.* $\delta \approx 0$ [115]. In order to achieve changes in oxygen content, a post-annealing treatment is required, see Section 4.2.

In the case of the Fe-based phase, single-phase samples are readily obtained through the OGC-LOPE synthesis [114,116,117], but again the disadvantage is that the technique does not allow precise oxygen-content control. An elegant way for perfect *in-situ* oxygen-content control was presented in the original paper on the Ba*RE*$Fe_2O_{5+\delta}$ phase [107] and successfully employed in the later works on the same phase [112,113,120-124]. In this technique a vertical tube furnace is used that allows efficient sample quenching. The precise value of $p(O_2)$ inside the furnace is controlled by mixing Ar, H_2 and H_2O (water vapour) gases in appropriate ratios. Using this technique, highly homogeneous Ba*RE*$Fe_2O_{5+\delta}$ samples are obtained in which δ may vary in the range from 0 to ~0.8 (for Nd) [112,113,120,121,124].

4.2. Oxygen Nonstoichiometry

In the *A*-site ordered DP structure, *i.e.* Ba*REB*$_2$O$_{5+\delta}$ with the layer sequence of BaO-*B*O$_2$-*RE*O$_\delta$-*B*O$_2$, the changes in the oxygen content occur solely in the *RE*O$_\delta$ layer. The completely oxygen-depleted composition of $\delta \approx 0$ is achieved for all the *B*-site constituents, Co, Mn and Fe. On the other hand, in terms of the *RE* constituent, a general trend is seen that the larger the *RE* constituent is, the larger is the maximum δ value, and thus the wider is the oxygen-content variation range [124-127]. In Fig. 14, this is demonstrated with the data for three Ba*RE*Co$_2$O$_{5+\delta}$ phases with *RE* = Nd, Eu and Ho [127].

Techniques for precise oxygen-content analysis are available for all the Ba*REB*$_2$O$_{5+\delta}$ phases: cerimetric titration for the *B* = Fe oxides [112,113,120-124] and iodometric titration for the *B* = Mn oxides [115]. For the *B* = Co oxides the number of available techniques is the largest: cerimetric, iodometric and coulometric titrations (with two variants in terms of the reductant) are all relevant possibilities [9,128].

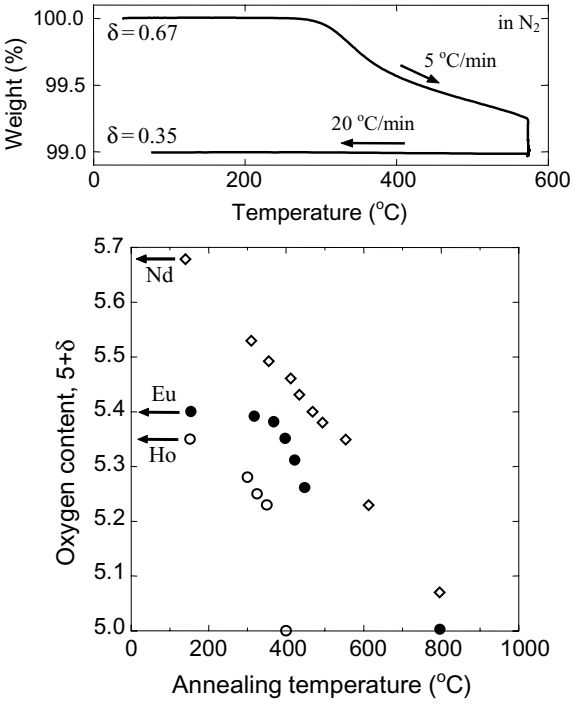

Fig. 14. Upper figure: TG curve for a TCOD annealing of BaNdCo$_2$O$_{5+\delta}$ to obtain a partly deoxygenated sample of $\delta = 0.35$ from that with $\delta = 0.67$ (the given oxygen-content values are from cerimetric titration). Lower figure: Dependence of $5+\delta$ on the TCOD-annealing temperature for the Ba*RE*Co$_2$O$_{5+\delta}$ phases with *RE* = Nd (◇), Eu (●) and Ho (○) [127]. Oxygen contents of the corresponding as-air-synthesized samples are marked with arrows.

Like the B = Fe counterparts (discussed in Section 4.1), the A-site ordered DP phases with B = Co exhibit wide variation ranges for the oxygen content with a possibility for continuous tuning (up to $\Delta\delta \approx 0.7$ for RE = Nd, see Fig. 14) [126-128]. To obtain samples with an intermediate oxygen-content value, the "temperature-controlled oxygen-depletion" or TCOD [9] technique has proven to be advantageous. A TCOD annealing is carried out for an oxygen-rich starting composition in a thermobalance in an inert atmosphere (N_2 or Ar) at a prefixed temperature. From a thermogravimetric (TG) monitoring of the corresponding weight loss an *in-situ* estimate is obtained for the amount of oxygen depleted from the original sample upon the post-annealing. For a more precise value of oxygen content in the oxygen-depleted sample, wet-chemical redox analysis is needed [128]. In Fig. 14, shown is a TCOD-TG curve that demonstrates the preparation of a $BaNdCo_2O_{5+\delta}$ sample with $\delta = 0.35$ from one with an oxygen-richer composition of $\delta = 0.67$ (as determined by cerimetric titration).

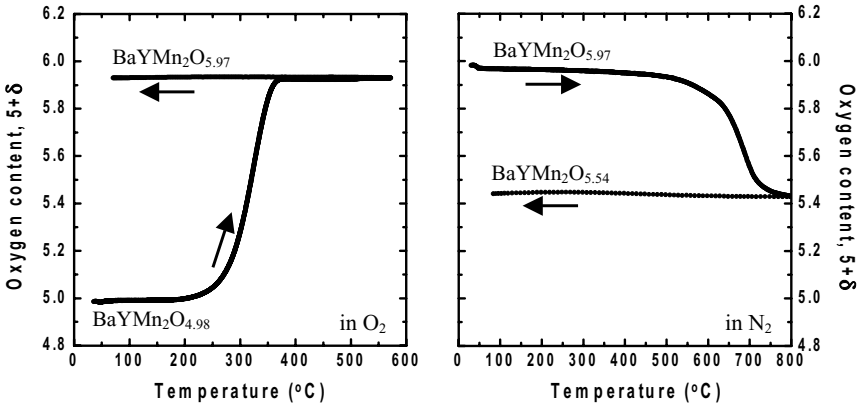

Fig. 15. TG curves for oxygenation of as-synthesized $BaYMn_2O_{4.98}$ in O_2 (left) and deoxygenation of oxygenated $BaYMn_2O_{5.97}$ in N_2 (right) [115]. The precise oxygen contents given are from iodometric titration. Heating and cooling rates: 1 °C/min.

The situation for the Mn-based DPs is completely different from those for the Fe- and Co-based phases: BaREMn$_2$O$_{5+\delta}$ may be oxygenated even up to $\delta = 1$, but at the same time continuous tuning of oxygen content within $0 < \delta < 1$ is not possible [115,129]. Once the oxygen-deficient ($\delta \approx 0$) A-site ordered DP framework of BaREMn$_2$O$_{5+\delta}$ is formed through a low-p(O_2) synthesis, the phase tolerates lower-temperature oxygenation in 1 atm O_2 gas without decomposing. This results in the fully-oxygenated BaREMn$_2$O$_{6.0}$ composition [115,126,130-132]. In Fig. 15, shown is a TG curve for such a process when RE = Y [115]: incorporation of oxygen occurs up to $\delta = 1.0$ in a single step in the temperature range of 250 ~ 400 °C. When the thus-obtained fully-oxygenated $BaYMn_2O_{6.0}$ phase is subsequently deoxygenated by means of post-annealing in N_2, oxygen is lost to the level of $\delta = 0.5$ only. From the TG curve for the N_2 annealing (Fig. 15) it is seen that oxygen depletion occurs in a single sharp step within 550 ~ 650 °C. Attempts to obtain samples with $0.5 < \delta < 1$ by means of

N_2 annealing at temperatures between 550 and 650 ^oC were not successful. It thus seems that only three distinct phases exist in the $BaYMn_2O_{5+\delta}$ system: $BaYMn_2O_{5.0}$, $BaYMn_2O_{5.5}$ and $BaYMn_2O_{6.0}$, see Fig. 16 for their crystal structures [115]. A very similar conclusion has also been made for the *RE* = La system, $BaLaMn_2O_{5+\delta}$ [129,130]. From the synthesis point of view, the situation may be summarized as follows: the $\delta = 0.5$ and 1.0 phases of Ba*RE*$Mn_2O_{5+\delta}$ can not be prepared directly but only through a three-step synthesis route, *i.e.* (*i*) low-O_2-pressure synthesis of the Ba*RE*$Mn_2O_{5+\delta}$ DP framework itself, (*ii*) low-temperature oxygenation in O_2 to obtain the fully-oxygenated $\delta \approx 1.0$ phase, and (*iii*) reduction (in N_2 at intermediate temperatures [115] or in an evacuated ampoule in the presence of Ti metal as a reductant [129]) to finally reach the $\delta \approx 0.5$ stoichiometry. The latter two steps are topotactic redox reactions in which the cation arrangement remains unchanged.

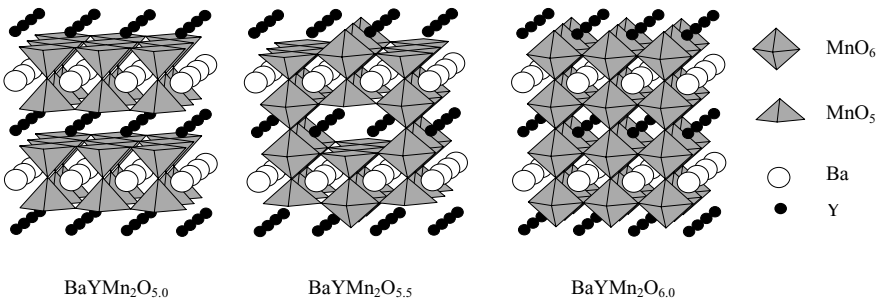

Fig. 16. Crystal structures of $BaYMn_2O_{5.0}$, $BaYMn_2O_{5.5}$ and $BaYMn_2O_{6.0}$ [115].

The excess oxygen atoms in the *RE*O_δ layer serve as extra apical oxygen atoms for the MnO_5 pyramids comprising the MnO_2 layers. Accordingly, some of the pyramids are transformed into MnO_6 octahedra (Fig. 16). For the intermediate-oxygen-content composition, Ba*RE*$Mn_2O_{5.5}$, it has been revealed that the excess-oxygen atoms and oxygen vacancies in the *RE*$O_{0.5}$ layer are ordered [115,129], see Section 4.3. In such a case the unit cell is expanded and the chemical formula should be written as $Ba_2RE_2Mn_4O_{11}$, *i.e.* with integers only. This furthermore means that the Ba*RE*$Mn_2O_{5+\delta}$ system does not exhibit oxygen nonstoichiometry, even though the "$\delta = 0.5$" phases at first glance might look like as being nonstoichiometric.

4.3. Oxygen Ordering in Ba*REB*$_2$O$_{5+\delta}$ at $\delta = 0.5$

Compounds with the two end oxygen stoichiometries of $\delta = 0$ and 1 in the Ba*RE*$Mn_2O_{5+\delta}$ system are tetragonal in crystal symmetry (space group *P*4/*nmm* for $BaYMn_2O_{5.0}$ [131] and *P*2 for $BaYMn_2O_{5.0}$ [115,133,134]), whereas the structure for the intermediate-oxygen-content compounds is orthorhombic (*Ammm* [115,129]). This has been considered as an indication of oxygen-vacancy ordering in the $\delta = 0.5$ compounds [110,115].

The precise pattern of excess-oxygen/vacancy (or MnO_6 octahedron/MnO_5 pyramid) ordering in Ba*RE*$Mn_2O_{5.5}$ was revealed from careful structural characterizations [115,129]. The crystal structure consists of rows of MnO_5 pyramids and MnO_6 octahedra running along one of the two *ab*-plane axes. Along the *c* axis the sequence of the octahedral and pyramidal units is: MnO_6-MnO_6-MnO_5-MnO_5 (refer to Fig. 16). Manganese atoms in the two different types of Mn-O polyhedra are perfectly isovalent (trivalent): bond-valence-sum calculation reveals an exactly same valence value of 3.31 for the octahedral and pyramidal Mn sites in $BaYMn_2O_{5.5}$ [115]. Both the sites are furthermore strongly distorted with four shorter in-plane Mn-O bonds and one (pyramidal) or two (octahedral) longer bonds from Mn to the apical oxygen atom(s). This is in agreement with a d^4 Jahn-Teller state of high-spin Mn^{III}.

The Co-based DPs, Ba*RE*$Co_2O_{5.5}$, show oxygen ordering as well [126,135]. However, the ordering pattern is not completely identical to that in Ba*RE*$Mn_2O_{5.5}$: within the *ab* plane the pattern is equivalent to that in the Mn counterpart, but along the *c* axis each CoO_6 octahedron/CoO_5 pyramid is sandwiched by equal species from both sides.

4.4. Charge Ordering in Ba*REB*$_2$O$_{5+\delta}$ at $\delta = 0$

In the case of the *A*-site ordered DP oxides of iron, no studies yet have been devoted to the possible existence of oxygen ordering about $\delta = 0.5$. On the other hand, the excess-oxygen-free composition of Ba*RE*Fe_2O_5 has been studied thoroughly [112,113,116,117,120-124,136]. From ^{57}Fe Mössbauer spectroscopy [112] and careful crystal structure analysis based on both synchrotron x-ray and neutron diffraction data [113], a valence separation and charge-ordering transition akin to the Verwey transition in Fe_3O_4 [137,138] has been verified. Above the transition temperature, T_V, both the Mössbauer and the structure-analysis probes detect a single Fe site only. From the given cation and oxygen stoichiometry, a mixed-valence 2.5 state is straightforwardly concluded for this Fe site and also clearly evidenced from the hyperfine parameters refined from the Mössbauer data [112] and from bond-valence-sum calculation based on the crystal-structure data [113]. At T_V the mixed-valent $Fe^{2.5+}$ species then separate into equal amounts of divalent and trivalent Fe atoms. More detailed studies have shown that the valence separation occurs in two distinct steps: upon cooling through T_V, first a premonitory transition occurs into $Fe^{2.5+\varepsilon}$ and $Fe^{2.5-\varepsilon}$ species (distinguishable by Mössbauer spectroscopy) at temperatures some tens of degrees above T_V, where the final separation into Fe^{II} and Fe^{III} species and their three-dimensional ordering take place [113,121,123].

The long-range charge ordering (CO) in Ba*RE*Fe_2O_5 is accompanied with an abrupt increase in the subtle orthorhombic distortion seen above T_V [113]. The charge-ordering pattern is of a chain-type, *i.e.* isovalent Fe atoms are ordered into chains along the shorter of the two *ab*-plane axes, presumably as an indication of ordering of the doubly occupied d_{xz} orbitals of Fe^{II} [122,123]. Without such orbital ordering, a checker-board-type pattern in which all Fe atoms are surrounded by aliovalent Fe neighbours would be expected [139,140]. In fact, this is what is seen for the Mn analog, $BaYMn_2O_5$ [131]. On the other hand, the Co-based DPs, Ba*RE*Co_2O_5, exhibit the same chain-type charge-order pattern as the Fe-based ones [111,141]. A plausible excuse for the fact that the long-range charge ordering was not detected for Ba*RE*Co_2O_5 with *RE* = Nd [142] might be that the samples studied may not have been precisely stoichiometric in terms of the oxygen content [128]. From the studies on the

Ba*RE*$Fe_2O_{5+\delta}$ system it has been learned that the CO superstructure is highly sensitive to very small oxygen nonstoichiometry, δ [121]. In the case of Ba*RE*Co_2O_5 (*RE* = Y, Ho), the charge-ordered state persists up to the transition temperature (T_{CO}) of 210 ~ 220 K [111,141]. On the other hand, $BaYMn_2O_5$ has been found charge ordered at all temperatures investigated so far.

From isovalent "smaller-for-larger" cation substitution studies for Ba*RE*Fe_2O_5, it has been revealed that decreasing the size of the *RE* constituent increases the transition temperature T_V (230 ~ 310 K) [124], whereas gradual substitution of Ba by Sr decreases it [143]. These seemingly opposite trends are reasonable, however, since the two substitution schemes have opposite effects on the magnitude of the RT ($> T_V$) orthorhombic distortion ($s \equiv a - b$). It appears that T_V indeed correlates with s such that an increase in the distortion increases T_V, as it makes it easier for the Fe^{II}-d_{xz} orbital ordering to occur below T_V [143]. A similar relation is concluded from physical-pressure experiments for $BaSmFe_2O_5$ [136]. It furthermore seems that a scaling relation of the same kind (with s) may apply to the T_{CO} value of Ba*RE*Co_2O_5 too: in Ref. [144] results from physical-pressure experiments are presented for the *RE* = Y compound.

4.5. Physical Properties

The crystal and redox chemical discussions of the previous sections may be summarized by the recognition that in the spin-charge-orbital-coupled DP systems of Ba*REB*$_2O_{5+\delta}$, upon increasing the excess-oxygen content δ interesting situations are seen in terms of coordination number and valence state of the active *B*-site 3*d* cations. (*i*) At $\delta = 0$ all the *B* cations have the same CN of 5 but two valence states (II and III). (*ii*) At $\delta = 0.5$ the situation is just opposite, *i.e.* all the Fe atoms are trivalent, but half of them are pyramidally (CN = 5) and another half octahedrally (CN = 6) coordinated. (*iii*) Finally at $\delta = 1$, we return to the situation of a single CN (= 6) but two valence states (III and IV). The large spectrum of the exciting functional and other physical properties arises from this complexity of chemistry. Iron and manganese are believed to possess a high-spin electron configuration in these DP oxides, but for cobalt various spin-state transitions are common. Accordingly, the Co-based DPs exhibit the richest variety of potentially useful functions. Here only a handful of representative/most interesting physical characteristics of the three systems, Ba*RE*$Co_2O_{5+\delta}$, Ba*RE*$Mn_2O_{5+\delta}$ and Ba*RE*$Fe_2O_{5+\delta}$, are highlighted.

Since the discovery of the considerably large MR effect in Ba*REB*$_2O_{5+\delta}$ [109,126], the Co-based *A*-site ordered DPs have been a subject of intensive research. The orthorhombic oxygen-ordered Ba*RE*$Co_2O_{5.5}$ phases [110,135,141,142,145-148] are metallic at high temperatures, but upon cooling they experience a metal-insulator transition with a transition temperature (T_{MI} = 280 ~ 400 K) that increases with the size of the *RE* constituent. Coinciding with this transition, a structural transition has been detected that is furthermore believed to be related with a spin-state transition. In the narrow temperature window, $T_M \le T \le T_C$ ($T_C < T_{MI}$), these phases are ferromagnetic, but below a metamagnetic transition temperature (T_M), they turn into antiferromagnets. The oxygen-depleted Ba*RE*$Co_2O_{5.0}$ phases [111,127,141,149] are AFM up to temperatures above RT. The Co^{II}/Co^{III} charge ordering transition appears at $T_{CO} < T_N$ (see Fig. 17 for *RE* = Y [127]).

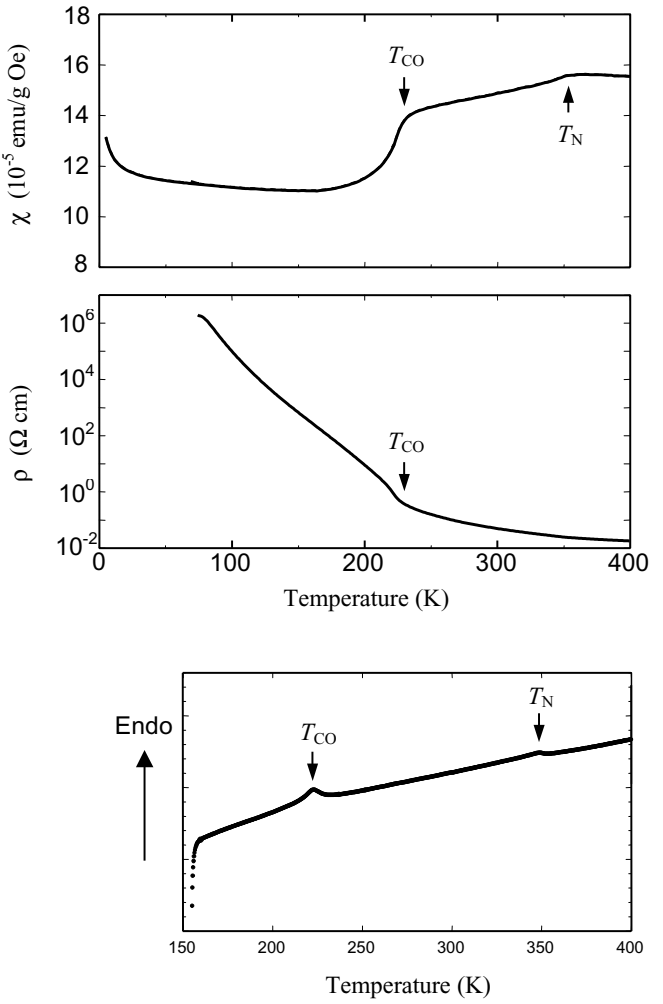

Fig. 17. Magnetic susceptibility (χ; FC curve), electrical resistivity (ρ) and DSC data (heating rate: 20 K/min) for $BaYCo_2O_{5.0}$ [127].

Among the Ba*RE*$Mn_2O_{5+\delta}$ systems that with *RE* = Y is best characterized so far. At RT the three $BaYMn_2O_{5+\delta}$ phases (δ = 0, 0.5 and 1) are all insulators; attempts to introduce carriers through Ca^{II}-for-RE^{III} substitution have not been successful in terms of enhancing the electrical conductivity [150]. However, the fully-oxygenated $BaYMn_2O_{6.0}$ phase undergoes several successive phase transitions, and the higher-temperature phases are metallic; the MI transition is seen at ~480 K [151]. Upon further cooling the phase undergoes a paramagnetic

to AFM transition at 180 ~ 200 K [115,132,151]. The oxygen-free $BaYMn_2O_{5.0}$ phase is ferrimagnetic below ~166 K [106,115,131]. For $BaYMn_2O_{5.5}$ the magnetization curve indicates a weak ferro/ferrimagnetic type transition about 130 K [115].

The $BaREFe_2O_{5+\delta}$ phases are AFM ($T_N \approx 430$ K [124]) and show semiconductive-type transport behaviour. The valence-separation/charge-ordering transition described in Section 4.4 is manifested by changes in volume, entropy, electrical conductivity and magnetic susceptibility and also by a small negative MR effect [113,116,120].

Acknowledgement

We acknowledge with the most sincere gratitude the indispensable contributions of our many co-authors and colleagues: our present and former students of Tokyo Institute of Technology and Helsinki University of Technology, Drs. T. Motohashi and Y.H. Huang (Tokyo Tech.), Dr. J. Lindén (Åbo Akademi), Profs. H. Fjellvåg and P. Karen (Univ. Oslo), Prof. R.S. Liu and Dr. J.M. Chen and their students (National Taiwan Univ. & NSRRC), Prof. Y. Moritomo (Nagoya Univ.), Dr. Y. Matsui and his group members (NIMS) and Prof. N. Hamada (Tokyo Science Univ.): Kiitos, Tack, Xie-Xie, Arigatou gozaimashita !

This work was supported by Grants-in-aid for Scientific Research (Nos. 15206002 and 15206071) from the Japan Society for the Promotion of Science.

REFERENCES

[1] R.A. de Groot, F.M. Mueller, P.G. van Engen and K.H.J. Buschow, Phys. Rev. Lett. 50 (1983) 2024.

[2] G.A. Prinz, Science 282 (1998) 1660; S.A. Wolf, D.D. Awschalom, R.A. Buhrman, J.M. Daughton, S. von Molnár, M.L. Roukes, A.Y. Chtchelkanova and D.M. Treger, Science 294 (2001) 1488; S.A. Chambers and Y.K. Yoo, MRS Bull. 28 (2003) 706.

[3] P.A. Dowben and R. Skomski, J. Appl. Phys. 95 (2004) 7453.

[4] J.M.D. Coey and C.L. Chien, MRS Bull. 28 (2003) 720.

[5] K.-I. Kobayashi, T. Kimura, H. Sawada, K. Terakura and Y. Tokura, Nature 395 (1998) 677.

[6] M. Bibes, K. Bouzehouane, A. Barthélémy, M. Besse, S. Fusil, M. Bowen, P. Seneor, J. Carrey, V. Cros, A. Vaurès, J.-P. Contour and A. Fert, Appl. Phys. Lett. 83 (2003) 2629.

[7] K.-I. Kobayashi, T. Kimura, Y. Tomioka, H. Sawada, K. Terakura and Y. Tokura, Phys. Rev. B 59 (1999) 11159.

[8] L. Er-Rakho, C. Michel, Ph. Lacorre and B. Raveau, J. Solid State Chem. 73 (1988) 531.

[9] M. Karppinen and H. Yamauchi, Oxygen Engineering for Functional Oxide Materials, *International Book Series: Studies of High Temperature Superconductors*, Vol. 37, (Ed. A.V. Narlikar), Nova Science Publishers, New York (2001), pp. 109-143.

[10] F. Galasso, *Structure, Properties and Preparation of Perovskite-Type Compounds*, Pergamon, Oxford (1969).

[11] P. Woodward, R.-D. Hoffmann and A.W. Sleight, J. Mater. Res. 9 (1994) 2118.

[12] M.K. Wu, J.R. Ashburn, C.J. Torng, P.H. Hor, R.L. Meng, L. Gao, Z.J. Huang, Y.Q. Wang and C.W. Chu, Phys. Rev. Lett. 58 (1987) 908.

[13] S.H. Lee, W.T. Kim and J.D. Jung, Sae Mulli 29 (1989) 614; Y. Matsumoto and J. Hombo, J. Solid State Chem. 93 (1991) 395; M. ElMassalami, A. Elzubair, H.M. Ibrahim and M.A. Rizgalla, Physica C 183 (1991) 143.

[14] Q. Huang, P. Karen, V.L. Karen, A. Kjekshus, J.W. Lynn, A.D. Mighell, N. Rosov and A. Santoro, Phys. Rev. B 45 (1992) 9611.

[15] P. Karen, A. Kjekshus, Q. Huang, J.W. Lynn, N. Rosov, I. Natali Sora, V.L. Karen, A.D. Mighell and A. Santoro, J. Solid State Chem. 136 (1998) 21.

[16] J. Lindén, M. Lippmaa, P. Karen, A. Kjekshus and M. Karppinen, J. Solid State Chem. 138 (1998) 87; J. Lindén, A. Kjekshus, P. Karen, J. Miettinen and M. Karppinen, J. Solid State Chem. 139 (1998) 168; J. Lindén, P. Karen, A. Kjekshus, J. Miettinen and M. Karppinen, J. Solid State Chem. 144 (1999) 398.

[17] M.A. Alario-Franco, C. Chaillout, J.J. Capponi, J.L. Tholence and B. Souleite, Physica C 222 (1994) 52.

[18] C.-Q. Jin, S. Adachi, X.-J. Wu, H. Yamauchi and S. Tanaka, Physica C 223 (1994) 238; X.-J. Wu, S. Adachi, C.-Q. Jin, H. Yamauchi and S. Tanaka, Physica C 223 (1994) 243.

[19] T. Ito, H. Suematsu, K. Isawa, M. Karppinen and H. Yamauchi, Physica C 308 (1998) 9.

[20] T. Ito, H. Suematsu, M. Karppinen and H. Yamauchi, Physica C 308 (1998) 198.

[21] M. Karppinen, H. Yamauchi, Y. Morita, M. Kitabatake, T. Motohashi, R.S. Liu, J.M. Lee and J.M. Chen, J. Solid State Chem. 177 (2004) 1037.
[22] F.K. Pattersson, C.W. Moeller and R. Ward, Inorg. Chem. 2 (1963) 196.
[23] F.S. Galasso, F.C. Douglas and R.J. Kasper, J. Chem. Phys. 44 (1966) 1672.
[24] T. Nakagawa, J. Phys. Soc. Jpn. 24 (1968) 806.
[25] T. Nakamura, K. Kunihara and Y. Hirose, Mater. Res. Bull. 16 (1981) 321.
[26] T. Yamamoto, J. Liimatainen, J. Lindén, M. Karppinen and H. Yamauchi, J. Mater. Chem. 10 (2000) 2342.
[27] T. Shimada, J. Nakamura, T. Motohashi, H. Yamauchi and M. Karppinen, Chem. Mater. 15 (2003) 4494.
[28] F.D. Richardson and J.H.E. Jeffes, J. Iron Steel Inst. 160 (1948) 261.
[29] C.L. Yuan, S.G. Wang, W.H. Song, T. Yu, J.M. Dai, S.L.Ye and Y.P. Sun, Appl. Phys. Lett. 75 (1999) 3853.
[30] J.A. Alonso, M.T. Casais, M.J. Martínez-Lope, J.L. Martínez, P. Velasco, A. Munõz and M.T. Fernández-Díaz, Chem. Mater. 12 (2000) 161.
[31] W.H. Song, J.M. Dai, S.L. Ye, K.Y. Wang, J.J. Du and Y.P. Sun, J. Appl. Phys. 89 (2001) 7678.
[32] Y.H. Huang, J. Lindén, H. Yamauchi and M. Karppinen, Chem. Mater. (2004) in press.
[33] H. Han, B.J. Han, J.S. Park, B.W. Lee, S.J. Kim and C.S. Kim, J. Appl. Phys. 89 (2001) 7687.
[34] Y. Tomioka, T. Okuda, Y. Okimoto, R. Kumai, K.-I. Kobayashi and Y. Tokura, Phys. Rev. B 61 (2000) 422.
[35] Y. Moritomo, S. Xu, A. Machida, T. Akimoto, E. Nishibori, M. Takata, M. Sakata and K. Ohoyama, J. Phys. Soc. Jpn. 69 (2000) 1723.
[36] T. Manako, M. Izumi, Y. Konishi, K.-I. Kobayashi, M. Kawasaki and Y. Tokura, Appl. Phys. Lett. 74 (1999) 2215.
[37] H. Asano, S.B. Ogale, J. Garrison, A. Orozco, Y.H. Li, E. Li, V. Smolyaninova, C. Galley, M. Downes, M. Rajeswari, R. Ramesh and T. Venkatesan, Appl. Phys. Lett. 74 (1999) 3696.
[38] Y. Yasukawa, J. Lindén, T.S. Chan, R.S. Liu, H. Yamauchi and M. Karppinen, J. Solid State Chem. 177 (2004) 2655.
[39] J. Lindén, T. Yamamoto, J. Nakamura, H. Yamauchi and M. Karppinen, Phys. Rev. B 66 (2002) 184408.
[40] M. Karppinen, H. Yamauchi, Y. Yasukawa, J. Lindén, T.S. Chan, R.S. Liu and J.M. Chen, Chem. Mater. 15 (2003) 4118.
[41] J. Lindén, T. Yamamoto, M. Karppinen, H. Yamauchi and T. Pietari, Appl. Phys. Lett. 76 (2000) 2925.
[42] J. Lindén, T. Shimada, T. Motohashi, H. Yamauchi and M. Karppinen, Solid State Commun. 129 (2003) 129.
[43] A.W. Sleight and J.F. Weiher, J. Phys. Chem. Solids 33 (1972) 679.
[44] J.B. Goodenough and R.I. Dass, Int. J. Inorg. Mater. 2 (2000) 3.
[45] D.D. Sarma, P. Mahadevan, T. Saha-Dasgupta, S. Ray and A. Kumar, Phys. Rev. Lett. 85 (2000) 2549.
[46] Z. Fang, K. Terakura and J. Kanamori, Phys. Rev. B 63 (2001) 180407.
[47] H. Wu, Phys. Rev. B 64 (2001) 125126.

[48] Z. Szotek, W.M. Temmerman, A. Svane, L. Petit and H. Winter, Phys. Rev. B 68 (2003) 104411.
[49] E. Rautama, N. Hamada, H. Yamauchi and M. Karppinen, unpublished.
[50] O. Chmaissem, R. Kruk, B. Dabrowski, D.E. Brown, X. Xiong, S. Kolesnik, J.D. Jorgensen and C.W. Kimball, Phys. Rev. B 62 (2000) 14197.
[51] J.M. Grenèche, M. Venkatesan, R. Suryanarayanan and J.M.D. Coey, Phys. Rev. B 63 (2001) 174403.
[52] G.J. Blasse, Inorg. Nucl. Chem. 27 (1965) 993; T. Nakagawa, K. Yoshikawa and S.J. Nomura, Phys. Soc. Jpn. 27 (1969) 880; H. Kawanaka, I. Hase, S. Toyama and Y.J. Nishihara, Phys. Soc. Jpn. 68 (1999) 2890.
[53] F. Galasso, L. Katz and R. Ward, J. Am. Chem. Soc. 81 (1959) 820.
[54] J.P. Crocombette, M. Pollak, F. Jollet, N. Thromat and M. Gautier-Soyer, Phys. Rev. B 52 (1995) 3143.
[55] M. Gautier-Soyer, J. Eur. Cer. Soc. 18 (1998) 2253.
[56] B. García-Landa, C. Ritter, M.R. Ibarra, J. Blasco, P.A. Algarabel, R. Mahendiran and J. García, Solid State Commun. 110 (1999) 435.
[57] C. Ritter, M.R. Ibarra, L. Morellon, J. Blasco, J. García and J.M. De Teresa, J. Phys.: Condens. Matter 12 (2000) 8295.
[58] D. Sánchez, J.A. Alonso, M. García-Hernández, M.J. Martínez-Lope, J.L. Martínez and A. Mellergård, Phys. Rev. B 65 (2002) 104426.
[59] M. Besse, V. Gros, A. Barthélémy, H. Jaffrès, J. Vogel, F. Petroff, A. Mirone, A. Tagliaferri, P. Bencok, P. Decorse, P. Berthet, Z. Szotek, W.M. Temmerman, S.S. Dhesi, N.B. Brookes, A. Rogalev and A. Fert, Europhys. Lett. 60 (2002) 608.
[60] Cz. Kapusta, P.C. Riedi, D. Zajac, M. Sikora, J.M. De Teresa, L. Morellon and M.R. Ibarra, J. Magn. Magn. Mater. 242-245 (2002) 701.
[61] J. Gopalakrishnan, A. Chattopadhyay, S.B. Ogale, T. Venkatesan, R.L. Greene, A.J. Millis, K. Ramesha, B. Hannoyer and G. Marest, Phys. Rev. B 62 (2000) 9538.
[62] A.S. Ogale, S.B. Ogale, R. Ramesh and T. Venkatesan, Appl. Phys. Lett. 75 (1999) 537.
[63] H.Q. Yin, J.-S. Zhou, R. Dass, J.-P. Zhou, J.T. McDevitt and J.B. Goodenough, J. Appl. Phys. 87 (2000) 6761.
[64] J. Navarro, Ll. Balcells, F. Sandiumenge, M. Bibes, A. Roig, B. Martínez and J. Fontcuberta, J. Phys. Condens. Matter 13 (2001) 8481.
[65] J. Lindén, M. Karppinen, T. Shimada, Y. Yasukawa and H. Yamauchi, Phys. Rev. B 68 (2003) 174415.
[66] Ll. Balcells, J. Navarro, M. Bibes, A. Roig, B. Martínez and J. Fontcuberta, Appl. Phys. Lett. 78 (2001) 781.
[67] J. Navarro, J. Nogués, J.S. Munõz and J. Fontcuberta, Phys. Rev. B 67 (2003) 174416.
[68] D. Sánchez, J.A. Alonso, M. García-Hernández, M.J. Martínez-Lope, M.T. Casais and J.L. Martínez, J. Mater. Chem. 13 (2003) 1771.
[69] D.D. Sarma, E.V. Sampathkumaran, S. Ray, R. Nagarajan, S. Majumbar, A. Kumar, G. Nalini and T.N. Guru Row, Solid State Commun. 114 (2000) 465.
[70] M. García-Hernández, J.L. Martínez, M.J. Martínez-Lope, M.T. Casais and J.A. Alonso, Phys. Rev. Lett. 86 (2001) 2443.
[71] D. Sánchez, M. García-Hernández, N. Auth and G. Jakob, J. Appl. Phys. 96 (2004) 2736.

[72] M. Tovar, M. Causa, A. Butera, J. Navarro, B. Martínez, J. Fontcuberta and M. Passeggi, Phys. Rev. B 66 (2002) 24409.
[73] C. Frontera and J. Fontcuberta, Phys. Rev. B 69 (2004) 14406.
[74] R.D. Shannon, Acta Cryst. A 32 (1976) 751.
[75] N. Nguyen, F. Sriti, C. Martin, F. Bourée, J.M. Grenèche, A. Ducouret, F. Studer and B. Raveau, J. Phys.: Condens. Matter 14 (2002) 12629.
[76] R.C. Yu, P. Zhao, F.Y. Li, Z.X. Liu and C.Q. Jin, Phys. Rev. B 69 (2004) 214405.
[77] B.-G. Kim, Y.-S. Hor and S.-W. Cheong, Appl. Phys. Lett. 79 (2001) 388.
[78] A. Maignan, B. Raveau, C. Martin and M. Hervieu, J. Solid State Chem. 144 (1999) 224.
[79] Y. Moritomo, Sh. Xu, T. Akimoto, A. Machida, N. Hamada, K. Ohoyama, E. Nishibori, M. Takata and M. Sakata, Phys. Rev. B 62 (2000) 14224.
[80] J. Navarro, C. Frontera, Ll. Balcells, B. Martínez and J. Fontcuberta, Phys. Rev. B 64 (2001) 92411.
[81] C. Frontera, D. Rubi, J. Navarro, J.L. García- Munõz, J. Fontcuberta and C. Ritter, Phys. Rev. B 68 (2003) 12412.
[82] D. Rubi, C. Frontera, G. Herranz, J.L. García- Munõz, J. Fontcuberta and C. Ritter, J. Appl. Phys. 95 (2004) 7082.
[83] J. Navarro, J. Fontcuberta, M. Izquierdo, J. Avila and M.C. Asensio, Phys. Rev. B 69 (2004) 115101.
[84] M. Wojcik, E. Jedryka, S. Nadolski, J. Navarro, D. Rubi and J. Fontcuberta, Phys. Rev. B 69 (2004) R100407.
[85] T.H. Kim, M. Uehara, S.-W. Cheong and S. Lee, Appl. Phys. Lett. 74 (1999) 1737.
[86] W. Prellier, V. Smolyaninova, A. Biswas, C. Galley, R.L. Greene, K. Ramesha and J. Gopalakrishnan, J. Phys.: Condens. Matter 12 (2000) 965.
[87] J. Gopalakrishnan, A. Chattopadhyay, S.B. Ogale, T. Venkatesan, R.L. Greene, A.J. Millis, K. Ramesha, B. Hannoyer and G. Marest, Phys. Rev. B 62 (2000) 9538.
[88] H. Kato, T. Okuda, Y. Okimoto, Y. Tomioka, K. Oikawa, T. Kamiyama and Y. Tokura, Phys. Rev. B 65 (2002) 144404.
[89] S. Nakamura, M. Tanaka, H. Kato and Y. Tokura, J. Phys. Soc. Jpn. 72 (2003) 424.
[90] K.-I. Kobayashi, T. Okuda, Y. Tomioka, T. Kimura and Y. Tokura, J. Magn. Magn. Mater. 218 (2000) 17.
[91] R.I. Dass and J.B. Goodenough, Phys. Rev. B 63 (2001) 64417.
[92] J. Lindén, T. Yamamoto, J. Nakamura, M. Karppinen and H. Yamauchi, Appl. Phys. Lett. 78 (2001) 2736.
[93] T. Okuda, K.-I. Kobayashi, Y. Tomioka and Y. Tokura, Phys. Rev. B 68 (2003) 144407.
[94] M.T. Anderson, K.B. Greenwood, G.A. Taylor and K.R. Poeppelmeier, Prog. Solid State Chem. 22 (1993) 197.
[95] J.B. Philipp, P. Majewski, L. Alff, A. Erb, R. Gross, T. Graf, M.S. Brandt, J. Simon, T. Walther, W. Mader, D. Topwal and D.D. Sarma, Phys. Rev. B 68 (2003) 144431.
[96] H. Kato, T. Okuda, Y. Okimoto, Y. Tomioka, K. Oikawa, T. Kamiyama and Y. Tokura, Phys. Rev. B 69 (2004) 184412.
[97] J.B. Philipp, D. Reisinger, M. Schonecke, A. Marx, A. Erb, L. Alff, R. Gross and J. Klein, Appl. Phys. Lett. 79 (2002) 3654.

[98] H. Kato, T. Okuda, Y. Okimoto, Y. Tomioka, Y. Takenoya, A. Ohkubo, M. Kawasaki and Y. Tokura, Appl. Phys. Lett. 81 (2002) 328.
[99] T. Alamelu, U.V. Varadaraju, M. Venkatesan, A.P. Douvalis and J.M.D. Coey, J. Appl. Phys. 91 (2002) 8909.
[100] J.M. De Teresa, D. Serrate, J. Blasco, M.R. Ibarra and L. Morellon, Phys. Rev. B 69 (2004) 144401.
[101] W.E. Pickett, Phys. Rev. B 57 (1998) 10613.
[102] H. Van Leuken and R.A. de Groot, Phys. Rev. Lett. 74 (1995) 1171.
[103] J.H. Park, S.K. Kwon and B.I. Min, Phys. Rev. B 65 (2002) 174401.
[104] K. Ueda, H. Tabata and T. Kawai, Science 280 (1998) 1064.
[105] W. Zhou, C.T. Lin and W.Y. Liang, Adv. Mater. 5 (1993) 735; W. Zhou, Chem. Mater. 6 (1994) 441.
[106] J.P. Chapman, J.P. Attfield, M. Molgg, C.M. Friend and T.P. Beales, Angew. Chem. Int. Ed. Engl. 35 (1996) 2482.
[107] P. Karen and P.M. Woodward, J. Mater. Chem. 9 (1999) 789.
[108] M. Nagase, J. Lindén, H. Suematsu, M. Karppinen and H. Yamauchi, Phys. Rev. B 59 (1999) 1377.
[109] C. Martin, A. Maignan, D. Pelloquin, N. Nguyen and B. Raveau, Appl. Phys. Lett. 71 (1997) 1421.
[110] D. Akahoshi and Y. Ueda, J. Phys. Soc. Jpn. 68 (1999) 736.
[111] T. Vogt, P.M. Woodward, P. Karen, B.A. Hunter, P. Henning and A.R. Moodenbaugh, Phys. Rev. Lett. 84 (2000) 2969.
[112] J. Lindén, P. Karen, A. Kjekshus, J. Miettinen, T. Pietari and M. Karppinen, Phys. Rev. B. 60 (1999) 15251.
[113] P. Karen, P.M. Woodward, J. Lindén, T. Vogt, A. Studer and P. Fischer, Phys. Rev. B 64 (2001) 214405.
[114] J. Nakamura, J. Lindén, H. Suematsu, M. Karppinen and H. Yamauchi, Physica C 338 (2000) 121.
[115] M. Karppinen, H. Okamoto, H. Fjellvåg, T. Motohashi and H. Yamauchi, J. Solid State Chem. 177 (2004) 2122.
[116] J. Nakamura, J. Lindén, M. Karppinen and H. Yamauchi, Appl. Phys. Lett. 77 (2000) 1683.
[117] J. Nakamura, J. Lindén, H. Yamauchi and M. Karppinen, Solid State Commun. 121 (2002) 269.
[118] T.P. Beales, M. Mölgg, J. Jutson and C.M. Friend, Phys. Stat. Sol. A 161 (1997) 271.
[119] J.M. McAllister and J.P. Attfield, J. Mater. Chem. 8 (1998) 1291.
[120] P. Karen, P.M. Woodward, P.N. Santosh, T. Vogt, P.W. Stephens and S. Pagola, J. Solid State Chem. 167 (2002) 480.
[121] P. Karen, J. Solid State Chem. 170 (2003) 9.
[122] P.M. Woodward and P. Karen, Inorg. Chem. 42 (2003) 1121.
[123] P.M. Woodward, E. Suard and P. Karen, J. Am. Chem. Soc. 125 (2003) 8889.
[124] P. Karen, J. Solid State Chem. 177 (2004) 281.
[125] K. Lehmus, M. Kochi, M. Karppinen, H. Yamauchi and L. Niinistö, Int. J. Inorg. Mater. 2 (2000) 203.
[126] A. Maignan, C. Martin, D. Pelloquin, N. Nguyen and B. Raveau, J. Solid State Chem. 142 (1999) 247.

[127] M. Karppinen, T. Motohashi and H. Yamauchi, unpublished.
[128] M. Karppinen, M. Matvejeff, K. Salomäki and H. Yamauchi, J. Mater. Chem. 12 (2002) 1761.
[129] V. Caignaert, F. Millange, B. Domengès, B. Raveau and E. Suard, Chem. Mater. 11 (1999) 930.
[130] F. Millange, V. Gaignaert, B. Domengès, B. Raveau and E. Suard, Chem. Mater. 10 (1998) 1974.
[131] F. Millange, E. Suard, V. Caignaert, B. Raveau, Mater. Res. Bull. 34 (1999) 1.
[132] T. Nakajima, H. Kageyama and Y. Ueda, J. Phys. Chem. Solids 63 (2002) 913.
[133] H. Kageyama, T. Nakajima, M. Ichihara, Y. Ueda, H. Yoshizawa and K. Ohoyama, J. Phys. Soc. Jpn. 72 (2003) 241.
[134] T. Nakajima, H. Kageyama, M. Ichihara, K. Ohoyama, H. Yoshizawa and Y. Ueda, J. Solid State Chem. 177 (2004) 987.
[135] Y. Moritomo, T. Akimoto, M. Takeo, A. Machida, E. Nishibori, M. Takata, M. Sakata, K. Ohoyama and A. Nakamura, Phys. Rev. B 61 (2000) R13325.
[136] Y. Moritomo, M. Hanawa, Y. Ohishi, K. Kato, J. Nakamura, M. Karppinen and H. Yamauchi, Phys. Rev. B 68 (2003) R60101.
[137] E.J.W. Verwey, Nature 144 (1939) 327.
[138] J.P. Wright, J.P. Attfield and P.G. Radaelli, Phys. Rev. Lett. 87 (2001) 266401.
[139] P.W. Anderson, Phys. Rev. 102 (1956) 1008.
[140] J. Wang, W. Zhang and D.Y. Xing, Phys. Rev. B 66 (2002) 52410.
[141] E. Suard, F. Fauth, V. Caignaert, I. Mirebeau and G. Baldinozzi, Phys. Rev. B 61 (2000) R11871.
[142] J.C. Burley, J.F. Mitchell, S. Short, D. Miller and Y. Tang, J. Solid State Chem. 170 (2003) 339.
[143] J. Nakamura, M. Karppinen, P. Karen, J. Lindén and H. Yamauchi, Phys. Rev. B (2004) in press.
[144] Y. Moritomo, M. Hanawa, S. Xu, H. Ishikawa, Y. Ohishi, K. Kato, T. Honma, P. Karen, M. Karppinen and H. Yamauchi, Phys. Rev. B 69 (2004) 134118.
[145] C. Frontera, J.L. García- Munõz, A. Llobet and M.A.G. Aranda, Phys. Rev. B 65 (2002) R180405.
[146] F. Fauth, E. Suard, V. Caignaert and I. Mirebeau, Phys. Rev. B 66 (2002) 184421.
[147] A. Maignan, V. Gaignaert, B. Raveau, D. Khomskii and G. Sawatzky, Phys. Rev. Lett. 93 (2004) 26401.
[148] H.D. Zhou and J.B. Goodenough, J. Solid State Chem. 177 (2004) 3339.
[149] F. Fauth, E. Suard, V. Caignaert, B. Domengès, I. Mirebeau and L. Keller, Eur. Phys. J B 21 (2001) 163.
[150] H. Okamoto, M. Karppinen and H. Yamauchi, unpublished.
[151] T. Nakajima, H. Kageyama, M. Ichihara, K. Ohoyama, Y. Yoshizawa and Y. Ueda, J. Solid State Chem. 177 (2004) 987.

DILUTE MAGNETIC SEMICONDUCTORS

Jairo Sinova[1] and Tomas Jungwirth[2,3]

[1] Physics Department, Texas A&M University, College Station, Texas 77843-4242, USA
[2] School of Physics and Astronomy, University of Nottingham, Nottingham NG7 2RD, United Kingdom
[3] Institute of Physics ASCR, Cukrovarnicka 10, 162 53 Praha 6, Czech Republic

1. INTRODUCTION

Ferromagnetic semiconducting materials are obtained by doping (III,V) semiconductors with magnetic transition metal ions such as Mn and Cr. The chemical affinity of these ions induces charge carriers which in turn mediate an effective ferromagnetic coupling between the magnetic ions, creating a ferromagnetic ordered state below the Curie temperature. These materials exhibit a large array of collective phenomena and their tunability and broad phase space has attracted a lot of attention. Part of the strong interest in diluted magnetic semiconductors (DMS) has been fueled by the possibility of integrating the functionalities of semiconductors and magnetic materials to create new types of devices which coalesce storage and processing capabilities in a fully semiconducting environment. The seemingly endless demand for technological advances in our society, whose global interdependence in communications and technology is evident throughout our daily activities, motivates part of the thrust in this area. Moore's law, predicting an exponential growth of computational ability, is now believed to be in peril and there is a need for a new technological revolution if the fast pace of technology is to be maintained.

Such a technological revolution will take place if three major goals can be achieved in the development of ferromagnetic (III,Mn)V materials: i) room temperature carrier mediated ferromagnetism, ii) dependence of transport and optical properties on the magnetic state, and iii) that the materials properties remain sensitive to doping, external fields, and light. Since the first observation of ferromagnetism at low temperatures in (III,Mn)V semiconductors in

the early nineties [1], steady progress has taken place in each of these major fronts. More importantly, over the last six years, jumpstarted by the discovery of ferromagnetism in (Ga,Mn)As with ferromagnetic temperatures in excess of 100 K due to post-growth annealing [2], the efforts in this field have increased dramatically in several coordinated fronts, both experimental and theoretical. This strong research effort has yielded many rapid advances, prompting the need for an overall review of at least several fast evolving parts of this scientific quest. In this chapter we give an overview of current topics which are now well understood, current theoretical approaches, and review in detail the transport properties of these materials on the metallic regime using the effective Hamiltonian model which have favored in our research and has proven very successful in obtaining qualitative and quantitative understanding. Other important areas, such as the insulating low-doping regime have been covered by other reviews [3,4]. Furthermore, we will narrow our focus on the most widely studied and well understood material, (Ga,Mn)As.

As in any review, a preference must be given to the more relevant publications containing the most recent developments and the ones which have had the largest impact in understanding these complex materials. We refer to a more extended and precise database of published and pre-print works maintained within the "Ferromagnetic Semiconductors Web Project" at http://unix12.fzu.cz/ms. This web-site contains a large body of theoretical and experimental results (that can be obtained in several formats), as well as the most extended bibliography database linked to diluted magnetic (III,V) semiconductors that we are aware of.

We also note that a few review articles on other aspects of the physics of DMS, which we will only touch upon briefly, have appeared over the past few years and may help the reader who wants to extend the narrow scope of this chapter. Given however the rapid developments over the past two years alone, the reader should be warned that these reviews, although excellent, may not suffice to give the most current experimental developments and theoretical understanding and justifications. Several extended papers on the physics of ferromagnetism and proposed mechanisms are shown in Refs. [2,5,6,7]. A theoretical review of the widely used phenomenological Zener mean field model, highly succesful in (Ga,Mn)As and (In,Mn)As studies, is presented in Ref. [8] and [9]. A large body of work up to 2001 in density functional first principles calculations in (III,V) DMS is also available in Ref. [10]. Another theoretical approach based on lattice models and dynamical mean field treatment of disorder, most successful in the low-doping regime, is reviewed in Ref. [3]. The ever important effects of disorder, omnipresent in these materials, is reviewed in Ref. [4]. A general discussion behind the technological motivation for DMS has been presented in [11, 12, 13, 14], where optical insulators and magneto-resistance elements are explored. A large part of this review is based on a manuscript written by the authors which, in addition to the transport properties, also reviews the magneto-optical properties of these materials within the infrared regime [15].

We organize the rest of this chapter as follows: In Sec. 2 we present a short general overview of DMS from the experimental facts point of view. In Sec. 3 we briefly discuss the theoretical model used and its experimental basis to describe the metallic regime. Sec. 4 reviews the transport properties of DMS such as diagonal resistivity, magneto-resistance anisotropy, and anomalous-Hall effect. A short summary and outlook with different open questions is given in section V.

2. The Basic Picture of DMS

The basic idea behind creating these novel ferromagnetic materials is simple: based on the lower valence of Mn, substituting Mn in a (III,V) semiconductor for the cations (the III elements) can dope the system with holes; beyond a concentration of 1% there are enough induced holes to mediate a ferromagnetic coupling between the local S=5/2 magnetic moments provided by the strongly localized $3d^5$ electrons of Mn and a ferromagnetic ordered state can ensue. This rudimentary but generally correct picture of ferromagnetism in many (III,Mn)V materials is of course acquired by putting together the different experimental results obtained through different characterization techniques of the materials. The simplicity of the model hides within it a plethora of physical effects present in these materials such as metal-insulator transitions, carrier mediated ferromagnetism, disorder physics, magneto-resistance effects, magneto-optical effects, quantum critical behavior, post-growth dependent properties, etc.

In any doped semiconductor, an understanding of its properties must be preceded by a study of the doping impurities. Since, in this case, the Mn impurity dopants provide the local magnetic moments responsible for ferromagnetism and, at the same time, provide the hole carriers which mediate the exchange coupling between the impurities themselves, understanding the nature of the impurities and the different states that they induce is fundamental to establish a relevant theoretical model.

2.1 Impurities in DMS

Under equilibrium growth conditions, the solubility of Mn in III-V semiconductor crystals has an upper limit of 0.1%. Phase separation and surface segregation takes place above this concentration. To circumvent this problem, low-temperature molecular beam epitaxy (LT-MBE) technique was applied leading to the first successful growth of InAs and GaAs based DMS [1]. The most common and stable position of Mn in the host semiconductor lattice is on the Ga site [16,17,18,19,20].

An important initial question is ‘what is the neutral state of the Ga-substitutional Mn impurity?’. Experimentally, through electron paramagnetic resonance (EPR) and optical measurements [17,21,22], for even very few percentage of Mn (lower by an order of magnitude than the concentration marking the metal-insulator transition) the only impurity level observed is the d5-Mn^{2+} ionized state, indicating that indeed the strong localized $3d^5$ electrons with total spin S=5/2 are a good starting point for theoretical models. The corresponding $3d^5$ plus a weakly bound hole neutral state is observed experimentally only within a narrow range of Mn concentrations due to a complete compensation in the low Mn doping regime and due to the Mott insulator-to-metal transition at high doping. Other candidates for the Mn neutral impurity such as $3d^4$ states, important for double-exchange models to be applicable, are not observed experimentally [17].

Furthermore, the itinerant holes originating from the Mn acceptor level have also been observed through photoemission experiments [23,24] to be associated with the ones of the host semiconductor valence band, i.e. they have As 4p-character, which provides further evidence for the shallow acceptor nature of the substitutional Mn impurity in GaAs and InAs.

Other impurities present because of the non-equilibrium growth process (As-antisites and Mn-interstitials) compensate the induced holes and therefore reduce the free carrier concentration with respect to the substitutional-Mn density. Annealing procedures, at temperatures slightly lower than growth temperature, have shown a reduction of the amount of compensation [5,25,26,27,28,29,30]. The initial procedure [5] has now been modified by different groups [25,26,27,30] and the carrier concentration can actually be tuned precisely through resistance-monitored annealing [25]. Two possible mechanisms for the reduction of compensation have been considered: either the number of As-antisites is reduced through migration of As atoms to their correct sites, or the Mn-interstitials migrate to the surface or to the substitutional sites. Early theoretical models assumed the former scenario, however, a recent key Rutherford backscattering experiment [26] has shown that it is the reduction of Mn-interstitials and their out-diffusion to the surface [29] which is responsible for lowering the amount of compensation.

2.2. Other experimental observations in DMS

Besides the experimental results revealing what is happening in the complicated annealing process and the nature of the impurities, there are other experimental observations that provide key clues for understanding the origins and fundamental properties of (Ga,Mn)As and (In,Mn)As DMS [8]:

a) The ferromagnetic behavior of DMS materials is only observed above a critical doping level of about 1% [5]. At lower doping the compensation is almost complete and the mediating carriers needed to exchange-couple the localized Mn moments are not present and no clear ferromagnetic ordering occurs.

b) The carrier-induced ferromagnetic nature of the ordered state has been demonstrated by field-effect (In,Mn)As experiments [31] where the carrier concentration was tuned by a gate and the corresponding critical temperature was modified accordingly.

c) Strain effects, due to the lattice mismatch between the DMS layer and the substrate, influence the magnetic anisotropy of the ferromagnetic state. It has been shown that the ferromagnetic easy axis can be along the growth direction or in the plane depending on whether the strain is tensile or compressive [5,9]. Such phenomena are interpreted in terms of well known strain effects in the spin-orbit coupled valence bands of the host semiconductor.

c) Both magneto-optical effects, e.g. magnetic circular dichroism (MCD) [32], and resistivity measurements above the critical temperature [33], indicate an anti-ferromagnetic coupling between the local $3d^5$ electrons and the valence holes. This so-called kinetic-exchange interactions originates from the hybridization between the Mn 3d-orbitals and the neighboring As 4p-orbitals and is much larger than the pure Coulomb exchange interaction [34].

e) In transport measurements, a large anomalous-Hall effect (AHE) completely dominates the low-field off-diagonal resistance coefficient. The strong intrinsic spin-orbit coupling present

in the host semiconductor valence band can account for the measured magnitude and sign of the AHE.

There are of course many other relevant experiments which are not highlighted above which must be taken into account. However the interpretation of some or most of them are still being debated, since they seem to depend critically on the annealing procedures and can be interpreted in several ways. The above results are considered to be general and well established and will likely not change in newly grown samples as the materials development progresses.

3. Theoretical Models of DMS

The modeling of collective behavior of interacting electrons is a complicated task and, in many instances, must be guided by experimental evidence of the low energy degrees of freedom in order to obtain a correct minimal model which will capture the observed effects and will make useful predictions. With this in mind, there are typically three approaches, somewhat complementary, used to describe DMS systems: (1) first principles density-functional theory (DFT) and microscopic tight-binding models, (2) effective Hamiltonian models, and (3) lattice models.

DFT is an important tool for studying microscopic origins of ferromagnetism through calculations of electronic, magnetic, and structural ground-state properties [10]. A local-density-approximation (LDA) of the DFT, combined with disorder-averaging coherent-potential approximation (CPA) or supercell approach, has been used successfully to address physical parameters of (III,Mn)V DMS that are derived from total-energy calculations, such as the lattice constants [35], and formation and binding energies of various defects [19,20]. However, in Mn-doped DMS, LDA fails to account for strong correlations that suppress fluctuations in the number of electrons in the d-shell. As a result, the energy splitting between the occupied and empty d-states is underestimated which leads to an unrealistically large d-state local DOS near the top of the valence band and to an overestimate of the strength of the sp-d hybridization [10,36]. This shortcomings have been corrected recently by LDA+U and self-interaction corrected LDA schemes, which account for correlations among Mn 3d electrons, and have been used to obtain more realistic energy spectra and show agreement with the experimental observation that the valence holes have mostly As 4p-character [37].

A practical approach that circumvents some of the complexities of this strongly-correlated many-body problem is the microscopic tight-binding (TB) band-structure theory. Within the model, local changes of the crystal potential at Mn and other impurities are represented by shifted atomic levels. A proper parameterization of these shifts, of the Hubbard correlation potential that favors single occupancy of the localized d-orbitals, the Hund potential forcing the five d-orbital spins to align, and of the hopping amplitudes between neighboring atoms provides correct band gap for the host III-V semiconductor and an appropriate exchange splitting of the Mn d-levels. Even though the TB model is a semi-phenomenological theory, it shares the virtue of first principles approaches of treating disorder microscopically. The decoherence of Bloch quasiparticle states or effects of doping and disorder on the strength of the sp-d exchange coupling and effective Mn-Mn interaction are among the problems that have been analyzed using this tool [38,39,40].

In the metallic regime, where the largest critical ferromagnetic temperatures are achieved (for doping levels above 1.5% [41]), semi-phenomenological models that are built on Bloch states of the host semiconductor band quasiparticles, rather than localized basis states appropriate for the localized regime [42], provide the natural starting point for a model Hamiltonian which reproduces many of the observed experimental effects. Recognizing that the length scales associated with holes in the DMS compounds are still long enough, a **k·p** envelope function description of the semiconductor valence bands is appropriate. Since for many properties, e.g. anomalous Hall effect and magnetic anisotropy, it is necessary to incorporate intrinsic spin-orbit coupling in a realistic way, the six-band (or multiple-band, in general) Kohn-Luttinger (KL) **k·p** Hamiltonian that includes the spin-orbit split-off bands is desirable [43,9]. The approximation of using the KL Hamiltonian to describe the free holes is based primarily in the shallow acceptor picture demonstrated by the experiments [16,17,18] in (Ga,Mn)As and (In,Mn)As and must be re-examined for any other DMS materials that this model is applied to.

Besides the KL Hamiltonian parameters of the host III-V compound which have long been established [44], the phenomenological part of the strategy follows from asserting, rather than deriving, the localized nature of the Mn d-orbital moments and from parameterizing the sp-d hybridization by an effective exchange constant J_{pd}. The localization assumption is again verified by electron resonance experiments [16,17,18] and the value of J_{pd} is obtained from resistivity measurements in the paramagnetic regime [33] and MCD measurements [32]. Hence, the effective Hamiltonian considered within this model is

$$H = H_{KL} + J_{pd} \sum_I \vec{S}_I \cdot \vec{s}(\vec{r})\, \delta(\vec{r} - \vec{R}_I) + H_{dis}\,, \tag{1}$$

where H_{KL} is the six-band (multiple-band) Kohn-Luttinger (KL) **k·p** Hamiltonian [8,9], the second term is the short-range antiferromagnetic kinetic-exchange interaction between local spin $\vec{S}_I$ at site $\vec{R}_I$ and the itinerant hole spin (a finite range can be incorporated in more realistic models), and H_{dis} is the scalar scattering potential representing the difference between a valence band electron on a host site and a valence band electron on a Mn site and the screened Coulomb interaction of the itinerant electrons with the ionized impurities.

Several approximations can be used to vastly simplify the above model, namely, the virtual crystal approximation (replacing the spatial dependence of the local Mn moments by a constant average) and the mean field theory description [8,9]. In the metallic regime, the disorder can be treated by a Born approximation or by more sophisticated, exact-diagonalization or Monte-Carlo methods [45,46,47,48,49]. The effective Hamiltonian in Eq. (1) allows us to use standard electron-gas theory tools to account for hole-hole Coulomb interactions. This envelope function approximation model is also suitable for studying magnetic semiconductor heterostructures, like superlattices, quantum wells and digitally doped layers [50]. The validity of such semi-phenomenological Hamiltonian, which does not contain any free parameters, must be confirmed ultimately by experiments. Its accurate description of many thermodynamic and transport properties of metallic (Ga,Mn)As samples, such as the measured transition temperature [51,52], the anomalous Hall effect [53,54], the anisotropic magneto-resistance [45,53], the magneto-crystalline anisotropy [43,55], the spin-stiffness [55], the ferromagnetic domain wall widths [56], the magnetic dynamic damping

coefficients [57], and the magneto-optical properties [9,46,58], has proven the merit of this effective Hamiltonian approach.

One has to keep in mind, however, that as any semi-phenomenological model it may fail to capture the correct physics that leads to the ferromagnetic phase in some materials or in a certain range of parameter values. Such models can only be verified by careful comparison with experiments and tested through their predictions and agreement with experiments. For example, Mn-doped nitride and phosphate compounds or insulating DMS samples with low concentration of Mn ions require a theoretical description that goes beyond the picture of the host band quasiparticles that are weakly hybridized with the localized Mn d-electrons. Particularly nitrates are not believed to be well modeled by this semi-phenomenological Hamiltonian since Mn is a deep acceptors in this case and and charge fluctuations on the Mn d-levels may play an important role.

There has also been theoretical work on (III,Mn)V DMS materials based on a still simpler model where holes are assumed to hop only between Mn acceptor sites, where they interact with the Mn moments via phenomenological exchange interactions [3,59]. These models have the advantage of approaching the physics of the insulating dilute Mn limit, and can also be adapted to include the holes that are localized on other ionized defects besides the Mn acceptors through dynamical mean field (or CPA) techniques. However, the free-parameter nature of this phenomenological approach and their oversimplified electronic structure allows to make only qualitative predictions, and the models are also not appropriate for studying the high T_c metallic samples.

4. Transport properties of DMS systems

The different transport coefficients of DMS and their magnetic, temperature, and material composition dependence have been the most important and widely used characterization tools of DMS. Besides the diagonal resistivity which indicates metal-insulator transitions and possible critical behavior at the ferromagnetic transition temperature, other material transport properties such as anisotropic magneto-resistance, anomalous and ordinary Hall effect, and giant magneto-resistance have been used to both characterize and test the different theoretical models of DMS materials. In this section we consider the general features of the diagonal conductivity, how the exchange coupling between the localized moments and free carriers is extracted within the paramagnetic regime, doping and carrier concentration conductivity dependence at low temperatures, the anisotropic magneto-resistance, and the anomalous-Hall effect. Throughout, we will focus on the comparison of theoretical models (mainly the semi-phenomenological effective Hamiltonian model relevant to the metallic regime) to the different experimental observations.

4.1 General features of resistivity in DMS

DMS materials can exhibit insulating or metallic behavior (defined by the resistivity in the limit of zero temperature) depending on its doping level and post-growth annealing procedures. In as-grown samples, metallic behavior is typically observed for a range of 2-5%

Mn doping and an insulating behavior for higher and lower doping than this range [60]. In addition to this metal-insulator quantum transition, the resistivity as a function of temperature typically exhibits a peak or shoulder near the ferromagnetic transition temperature for both insulating (peak) and metallic (shoulder) samples [60,61,62,63]. The non-monotonic behavior near T_c is typically associated with critical-scattering but so far no theory has been developed which explains such behavior in a qualitative or quantitative way. Typically the Fisher-Langer theory of correlated fluctuations is invoked. However, this theory predicts an infinite derivative of the resistivity at T_c , which is clearly not the case in any studied (Ga,Mn)As DMS sample. There exists also a drastic reduction of the resistivity upon annealing, associated with the increase of the carrier concentration and to a lesser extent a reduction of the disorder scatterers [25,60,61,62,63]. The on-set of the metal-insulator transition at 1.5% Mn doping is close to the Mott insulator limit of a doped semiconductor similar to Si:P and the optimally annealed samples remain metallic throughout the whole range of Mn concentrations above 1.5% [41].

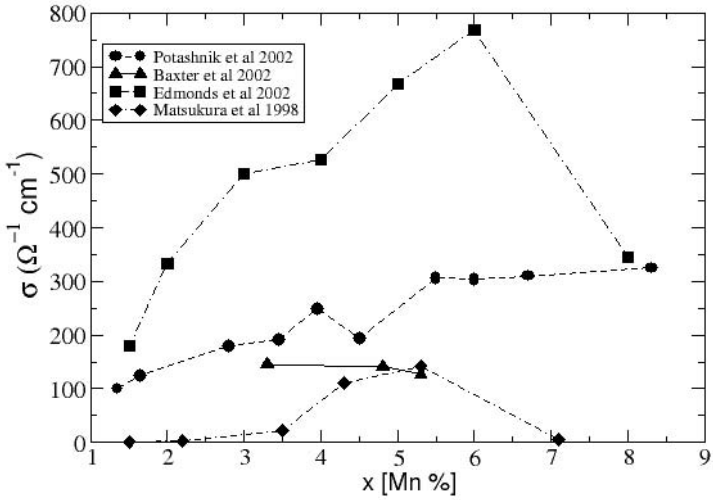

Fig. 1 Conductivity σ measured at 4 K or lower vs. Mn percentage concentration for (Ga,Mn)As. The symbols correspond to: squares to Ref. 25, circles to Ref. 61, triangles to Ref. 66, and diamonds to Ref. 60.

The number of research groups involved in the materials growth process, each trying a slightly different annealing process, has increased over the past few years and with it a dramatic increase of carrier concentration and conductivity has taken place, as shown in Fig. 1. At the same time the T_c has also increased in accordance with the mean field theory prediction that $T_c \sim p^{1/3}$, where x is the Mn concentration and p is the carrier concentration. The shoulder in ρ observed in the most recent optimally annealed samples near T_c has been partially explained theoretically in terms of the variation of the Fermi surface and the transport scattering time associated with the ferromagnetic to paramagnetic phase

transition [64]. However, there is no model at present that reproduces fully the behavior observed in ρ as a function of temperature near T_c in the metallic regime for most samples. There has also been theoretical progress in understanding the low temperature regime [45] (Sec. 4.3) and the role of scattering off magnetic impurities in the high temperature paramagnetic regime [33,60].

4.2 Scattering off the kinetic-exchange potential in the paramagnetic regime

The contribution from magnetic impurities to the resistivity behavior observed above T_c can be understood assuming scattering from the kinetic-exchange term in the Hamiltonian

$$H_{k-e} = J_{pd} \sum_I \vec{S}_I \cdot \vec{s}(\vec{r})\, \delta(\vec{r} - \vec{R}_I)\,. \tag{2}$$

The corresponding contribution to the resistivity is given by [33,34]

$$\rho_s = 2\pi^2 \frac{k_F}{pe^2} \frac{m^{*2} J_{pd}^2}{h^3} N_{Mn} \left[2\chi_\perp(T,B) + \chi_\parallel(T,B) \right], \tag{3}$$

where k_F is the carrier Fermi wave vector, h is the Planck constant, N_{Mn} the density of substitutional Mn, m^* is the effective mass of the carrier, and e is the electron charge. $\chi_\perp = M/B$ and $\chi_\parallel = \partial M/\partial B$ are the transverse and longitudinal magnetic susceptibilities. Using transport data, the susceptibility can be determined from the Hall resistivity due to the dominant contribution from the anomalous Hall effect which is proportional to the magnetization [33]. The analysis of magneto-resistance data above T_c gives a value for J_{pd}=55 ± 10 meV nm^3. This result is in agreement with optical MCD data.

We note that the initial expression used to analyze the magneto-resistance data which replaces the susceptibility factor by [S(S+1)- $\langle \mathbf{S} \rangle^2$], neglected the correlations between neighboring Mn spins and overestimated J_{pd} by a factor of 3 in disagreement then with the MCD measurement of J_{pd} [60].

4.3 Boltzman transport theory of DMS

The zero temperature conductivity of metallic DMS samples can be obtained from the effective Hamiltonian (Eq. (1)) and by treating disorder scattering perturbatively. The valence band holes interact with randomly located spins of substitutional Mn impurities via the kinetic-exchange interaction, and with randomly located ionized defects and each other via Coulomb interactions. At zeroth order, the interactions are replaced by their spatial averages, so that the Coulomb interaction vanishes and hole quasiparticles interact with a spatially constant kinetic-exchange field. The corresponding mean-field Hamiltonian for the itinerant holes reads

$$H_0 = H_{KL} + J_{pd} N_{Mn} S\hat{\Omega} \cdot \vec{s}\,, \tag{4}$$

where $\hat{\Omega}$ is the orientation of fully polarized substitutional Mn local moments and $\vec{s}$ is the envelope-function hole spin operator [43]. Using the eigenstates of the Hamiltonian in Eq. (4), the first order Born approximation of the elastic scattering rate, and the relaxation-time-approximation solution to the semiclassical Boltzmann equation, the diagonal dc conductivity tensor along one of the cube edges of the host lattice can be written as [45]:

$$\sigma_{\alpha\alpha} = \frac{e^2}{V} \sum_{n\vec{k}} \frac{1}{\hbar \Gamma_{n,\vec{k}}} \left(\frac{\partial E_{n\vec{k}}}{\partial k_\alpha} \right)^2 \delta(E_F - E_{n\vec{k}})\,, \tag{5}$$

where $\Gamma_{n,\vec{k}}$ is the quasiparticle elastic scattering rate, n and $\vec{k}$ are the band and wavevector indices, $E_{n\vec{k}}$ are the eigenstates of the Hamiltonian (4) and E_F is the Fermi energy.

The Born approximation estimate of the transport weighted scattering rate from substitutional Mn impurities is given by:

$$\Gamma^{Mn}_{n\vec{k}} = \frac{2\pi}{\hbar} N_{Mn} \sum_{n'} \int \frac{d\vec{k}'}{(2\pi)^3} \left| M^{\vec{k},\vec{k}'}_{n,n'} \right|^2 \delta(E_{n\vec{k}} - E_{n'\vec{k}'})(1 - \cos\theta_{\vec{k},\vec{k}'})\,, \tag{6}$$

with the scattering matrix element,

$$M^{\vec{k},\vec{k}'}_{n,n'} = J_{pd} S \left\langle z_{n\vec{k}} \left| \hat{\Omega} \cdot \vec{s} \right| z_{n'\vec{k}'} \right\rangle - \frac{e^2}{\varepsilon_{host}\varepsilon_0 (|\vec{k} - \vec{k}'|^2 + q^2_{TF})} \left\langle z_{n\vec{k}} \middle| z_{n'\vec{k}'} \right\rangle, \tag{7}$$

Here ε_{host} is the host semiconductor dielectric constant, $z_{n\vec{k}}$ is the six-component (multi-component) envelope-function eigenspinor of the unperturbed Hamiltonian (4), and the Thomas-Fermi screening wavevector

$$q_{TF} = \sqrt{\frac{e^2 DOS(E_F)}{\varepsilon_{host}\varepsilon_0}}\,,$$

where *DOS(E_F)* is the density of states at the Fermi energy [45]. This model incorporates the fact that the transport properties of these materials are not solely determined by the scattering from substitutional Mn impurities and allows explicitly for scattering from compensating defects, which have been seen to play a key role in the resistivity through the post-growth annealing as discussed earlier [5,25,26,27,28,29,30]. As-antisite defects are non-magnetic double-donors and contribute to scattering through a screened charge Z=2 Coulomb potential. The double-donor Mn interstitials [25,28] are unlikely to be magnetically ordered and can also be modeled as a Z=2 screened Coulomb potential [20].

Assuming a parabolic-band dispersion for majority heavy-hole states the kinetic-exchange scattering contribution to the scattering rate can be estimated by,

$$\Gamma_{pd} = \frac{N_{Mn} J_{pd}^2 S^2 m^* \sqrt{2m^* E_F}}{4\pi\hbar^4}.$$

The Mn and As-antisite Coulomb scattering leads to scattering rate Γ_C given by the Brooks-Herring formula [45]. For (Ga,Mn)As, taking a heavy-hole effective mass $m^*=0.5m_e$, p=0.4 nm^{-3} and Mn doping x=5%, these estimates give $\hbar\Gamma_{pd}$ ~ 20 meV and $\hbar\Gamma_C$ ~ 150 meV. A full numerical six-band calculation is consistent with these estimates, and predicts that the Coulomb contribution to the elastic scattering rate is several times larger than the kinetic-exchange contribution for typical chemical compositions. Note that these estimates give an immediate check on the assumption of the theory itself, since even in the heavily doped and compensated (Ga,Mn)As DMS, the lifetime broadening of the quasiparticle ($\hbar\Gamma$) is smaller than the valence band spin-orbit coupling strength (Δ_{so}=341 meV) and the typical Fermi energy.

Fig. 2 shows σ_{xx}, calculated numerically using the six-band Kohn-Luttinger model and Eqs. (5) and (6), for a fully strained $Ga_{0.94}Mn_{0.06}As$ sample. The substrate-DMS lattice mismatch, $e_0 \equiv (a_{sub} - a_{DMS})/a_{DMS}$, is between -0.002 and -0.003 in this case [2,65,66]. The absolute conductivities predicted by this model are reasonably consistent with experiment [25,66,67]. The disagreement for lower Mn concentrations (x<4%) of the theoretical conductivities is most likely due to some combination of inaccuracy in the scattering amplitude estimates, unaccounted sources of scattering, and, especially at small x, coherent scattering effects that eventually lead to localization observed as an upturn in ρ at the lowest temperatures.

In addition to the AHE (Sec. 4.4), strong spin-orbit coupling in the semiconductor valence band leads to anisotropies in the longitudinal transport coefficients. In particular, when the magnetization **M** is rotated by applying an external magnetic field stronger than the magneto-crystalline anisotropy field the in-plane conductivity changes [66,68]. Fig. 3 shows the theoretical and experimental AMR coefficients,

$$AMR_{op} = [\sigma_{xx}(M \parallel \hat{z}) - \sigma_{xx}(M \parallel \hat{x})]/\sigma_{xx}(M \parallel \hat{x})$$

and

$$AMR_{ip} = [\sigma_{xx}(M \parallel \hat{y}) - \sigma_{xx}(M \parallel \hat{x})]/\sigma_{xx}(M \parallel \hat{x}),$$

for seven (Ga,Mn)As samples [53,25,66]. Here $\hat{z}$ is the growth direction. Results of the two disordered system models, one assuming As-antisite and the other one Mn-interstitial compensation, are plotted in Fig. 3. As in the AHE case, the theoretical results are able to account semi-quantitatively for the AMR effects in the (Ga,Mn)As DMS, with somewhat better agreement obtained for the model that assumes Mn-interstitial compensation, which confirms indirectly the experimental finding that the compensating defects are dominated by Mn-interstitials [28]. Note that although the magnitude of the conductivities tends to be overestimated, the magneto-transport effects are relatively insensitive to scattering strength, reflecting instead the strong spin-orbit coupling in the valence band of the host semiconductor as compared to the Fermi energy [53].

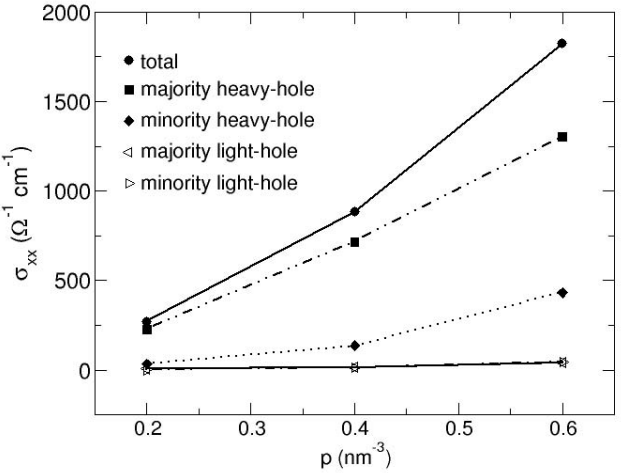

Fig. 2 Conductivity of the (Ga,Mn)As film as a function of the total hole density. These results were obtained for a GaAs semiconductor host doped with 6% Mn. For typical hole densities the current is carried mostly by the majority heavy-holes.

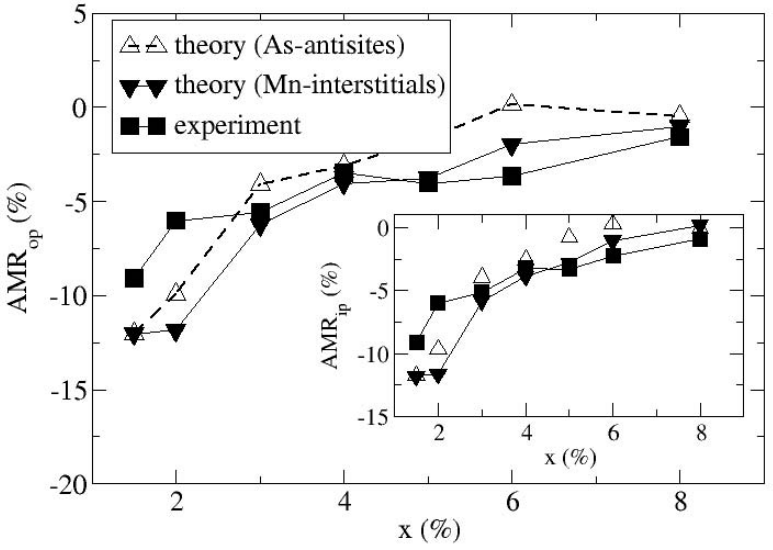

Fig. 3 Experimental AMR coefficients and theoretical data obtained assuming As-antisite compensation and Mn-interstitial compensation of AMR_{op} and AMR_{ip}. After Ref. 53.

A large anisotropic magneto-resistance effect is observed experimentally also in the off-diagonal symmetric conductivity component ($\sigma_{xy} = +\sigma_{yx}$) when magnetization direction changes from parallel to $\hat{x}$- or $\hat{y}$-axis, where $\sigma_{xy} = \sigma_{yx} = 0$, to a general orientation in the x-y plane tilted from the two transport measurement axes, where $\sigma_{xy} = \sigma_{yx} \neq 0$ [69]. The effect is called sometimes a 'planar Hall effect' but we emphasize that the true Hall response requires the symmetry $\sigma_{xy} = -\sigma_{yx}$. The anomalous contribution to this asymmetric off-diagonal transport coefficient is discussed in the following section.

4.4 Hall resistivity and the Anomlaous Hall effect

One of the most important characterization tools of magnetic materials is the anomalous Hall effect. The Hall resistance $R_{Hall} \equiv \rho_{xy} / d$ of a magnetic thin film is empirically observed to contain two distinct contributions. The first is proportional to the applied magnetic field, **B,** and arises from the normal Hall effect contribution, and the second, called the anomalous Hall contribution, is observed to be proportional to the magnetization [70]:

$$R_{Hall}=R_0 B+R_S M, \tag{8}$$

where M is the magnetization perpendicular to the thin film surface, and R_0 and R_S are the ordinary and anomalous Hall coefficients respectively. The ordinary Hall effect is due to the Lorenz force on the carriers and is used to measure the concentration and nature of the free carriers since R_0 is linearly proportional to the free carrier density and its sign determines whether they are electrons or holes. On the other hand, the anomalous Hall effect is a direct consequence of the presence of spin-orbit coupling in the system. In many instances, such as the DMS for example, the anomalous contribution is much greater than the ordinary Hall effect, making the carrier density hard to measure since large magnetic fields must be used to extract the linearity in the field of the Hall resistance. However, the overwhelming of the Hall coefficient by R_S allows one to utilize the anomalous Hall effect as an indirect measure of the magnetization. Empirically R_S is observed to depend quadratically or linearly on the diagonal resistivity, ρ, depending on the material. For example, for the case of Fe [70] and GaMnAs [65] the dependence on the resistivity is quadratic. These two resistivity dependencies of R_S correspond to different possible origins of the anomalous Hall effect which we discuss below. However, in spite of its wide use, it is surprising how much confusion has surrounded the understanding of this effect over the past six decades. Although much progress has taken place over the past few years with the creation and study of new materials, no single theory has been able to systematically and convincingly explain the constant puzzle of side-jump vs. intrinsic mechanisms although it is at present a feasible but challenging undertaking.

4.5 The embroiled history of the anomalous Hall effect

Before discussing the theoretical description of the anomalous Hall effect in DMS, it is appropriate to make an excursion to the history of the field in order to understand clearly the

origin of the controversies and the strengths and weaknesses of the different arguments put forth by different researchers. Often such summaries are done in two or three sentences giving an oversimplified view of the controversy and the different points of view, some of which have been challenged in later literature but still remain in the general folklore.

The first detailed theoretical consideration of the anomalous Hall effect was given by Karplus and Luttinger [71], where they considered the problem from a perturvative point of view (with respect to an applied electric field) and obtained a contribution to the Hall conductivity in systems with spin-orbit coupled Bloch states given by the expression (Eq. 2.16 and 2.17 in Ref. [71])

$$\sigma_{xy} = -\frac{2e^2}{V}\sum_{n\vec{k}} n_F(E_{n\vec{k}})\,\mathrm{Im}\left\langle \frac{\partial u_{n\vec{k}}}{\partial k_y}\middle|\frac{\partial u_{n\vec{k}}}{\partial k_x}\right\rangle \tag{9}$$

where n_F is the Fermi occupation number of the Bloch state $\left|u_{n\vec{k}}\right\rangle$. This expression is obtained by ignoring impurity scattering (i.e. clean limit) and can also be obtained from the Kubo linear response theory in this clean limit (see below). One of its immediate successes was the prediction that R_S is proportional to ρ^2 in agreement with many materials, Fe being the primary example. Immediately after Karplus and Luttinger's pioneering work, Smit [72] considered the problem of impurity scattering within a Boltzman formalism using a model Hamiltonian of an electron gas, i.e. plain waves, without intrinsic spin-orbit coupling and a scattering potential containing both direct and spin-orbit coupled terms:

$$H = \frac{\hat{p}}{2m} + V(r) + \frac{1}{2m^2c^2r}\frac{\partial V(r)}{\partial r}\hat{S}_z\hat{L}_z\,, \tag{10}$$

where the impurity potential is $V(r)=0$ for $r>R$ and $V(r)=V_0$ for $r<R$. Within the Boltzman formalism, he obtained a second type of contribution to the Hall conductivity due to the asymmetric scattering from impurities originating from the spin-orbit coupling term. This so called skew-scattering mechanism predicts, in contrast to the intrinsic effect found by Karplus and Luttinger, that $R_S \propto \rho$ (i.e. density of scatterers) and depends on the type and range of the scattering potential. It was also noted that the magnitude of the effect within such simplified model was many orders of magnitude lower than the observed magnitude of the AHE but, as it was shown later, the origin of this deficiency is the lack of intrinsic spin-orbit coupling present in the crystal Bloch states. However, Smit also criticized Karplus and Luttinger's result claiming the intrinsic contribution vanishes. Such claim (see below) is now understood to be unjustified but has remained lingering in the AHE literature, generating much confusion.

Karplus and Luttinger [71] did not consider impurity scattering, hence omitted the skew-scattering contribution in their calculation. To remedy this, Kohn and Luttinger [73] developed a consistent (and somewhat cumbersome) treatment to obtain the transport coefficients in the presence of spin-orbit coupling and disorder scattering based on a density matrix expansion. Such approach is equivalent to the Kubo linear response formalism but technically more difficult when applied to real physical systems. Within this formalism the expansion is done to first order in spin-orbit coupling and impurity scattering strengths. They

obtained, besides the previous Karplus and Luttinger result (Eq. 135 in Ref. [73], however note that it has the wrong sign later corrected in Ref. [74], formal expressions for additional contributions due to impurity scattering. Applying this formalism to a model with uncorrelated impurity potential and small scattering strength [74], Luttinger obtained, besides the Smit's skew-scattering term, the same final expression as Karplus and Luttinger *but* with the opposite sign (Eq. 3.26 in Ref. [74]). Somehow, in addition to the intrinsic Karplus and Luttinger term, there seemed to be an additional contribution from scattering *in the high mobility limit* giving a contribution identical to the intrinsic one but with a factor of -2 in front of it, hence the flip of sign of the final expression. No explanation was given of why such a scattering contribution *does not* depend in any way on the scattering potential but simply on the electronic structure of the system. However, Luttinger showed inequivaquely that the cancellation argued by Smit does not take place [74]. In a slightly different formalism Adams and Blouht [75] agreed with Luttinger's results and pointed out that Smit's error occurs from an inconsistency involving a change of representation of his density matrix when calculating the current.

A few years later Berger [76] made his first contribution to the problem introducing the idea (contained within Luttinger's formalism) of the side-jump scattering mechanism. He considered the problem of wave-packet scattering off an impurity potential as in Eq. (10), showing that in addition to skew scattering there exists a side-step type of scattering. This so called side-jump, as in the Luttinger formalism, was independent of the scattering potential, leaving one with the strange notion that an extrinsic scattering mechanism resulted in an intrinsic property. After putting this contribution in a Boltzman type of formalism he obtained a result which was four orders of magnitude lower than the Karplus and Luttinger intrinsic result. He then argued that the intrinsic spin-orbit coupling of the system increases this side-jump scattering by such factor. In his case the sign of the effect is not directly considered and his result, as already mentioned, is independent of the scattering potential itself. A similar type of formalism was put forth by Lyo and Holstein [77] claiming similar results but ignoring, for some unknown reason, the intrinsic non-vanishing contributions of Karplus and Luttinger.

It is then that Leroux-Hugon and Ghazali [78] pointed out the resolution of the missing order of magnitude of the skew-scattering. By looking simply at scattering of Bloch electrons from ionized impurities $V_{ion(r)}$ alone and going to second order in the Born approximation within the collision term of the Boltzman transport theory, they obtained a skew-scattering contribution with a much higher magnitude than the one coming from the spin-orbit coupling of the impurities themselves. Hence, it became evident that it is the presence of *intrinsic* spin-orbit coupling through the crystal potential which is ultimately responsible for the magnitude of all the anomalous Hall effect contributions observed and a system with weak or no intrinsic spin-orbit coupling will not exhibit a detectable contribution to the R_{Hall}.

To elucidate this confusing and farraginous atmosphere, Nozieres and Lewiner [79], following the formalism introduced by Fivaz [80] in terms of effective Hamiltonians of semiconductors, developed a theory applicable to narrow gap semiconductors equivalent to Luttinger's [74] but with the final result being more physically transparent. Going to linear order in impurity scattering and spin-orbit coupling and combining them with a Boltzamn type of approach, they obtained different contributions to the Hall current and different behavior when considering opposite orders of limits of $\omega \to 0$ and $\tau \to \infty$, where ω is the

frequency of the applied electric field and τ is the quasiparticle lifetime (see Table I and Eqs. 59, 60a, and 60b in Ref. [79]). Besides the skew-scattering contribution which depends on the type of scattering potential, in the limit $\omega\tau >> 1$ (with $\tau \to \infty$ first), considered by some authors to be the weak scattering limit (see Refs. [81] and [95]), the result is that of Karplus and Luttinger [71]. On the other hand, for $\omega\tau << 1$, the opposite sign expression of Luttinger [74] is recovered. One must note however that this result seems to be very specific to the model (single band) and to the meaning of the limit $\tau \to \infty$ as admitted by the authors themselves [74,79].

After this, Berger and Smit exchanged salvos in a series of confusing comments [82,83,84,85] in which Smit's old argument, that there is no such a thing as side-jump or intrinsic contribution, seems to have been finally put to rest. It was after this that Chazalviel [81], using Nozieres-Lewier-Luttinger [74,79] and Leroux-Hugon and Ghazalis [78] results, attempted to compare phenomenologically the AHE theory to n-InSb and n-Ge experimental data with some success. Within such models, the relative importance of the side-jump/intrinsic contribution $\sigma_{AH}^{sj/\mathrm{int}}$ (which are the same magnitude but of opposite sign depending on the limits [79,81,95]) to the skew-scattering contribution σ_{AH}^{sk} depends on the nature of the scatterers (only through the skew-scattering dependence). For scattering from ionized impurities one has [78,81]

$$\left|\frac{\sigma_{AH}^{sj/\mathrm{int}}}{\sigma_{AH}^{sk}}\right| = \frac{cN}{pr_s k_F l}, \tag{11}$$

with N/p being the ratio of the total number of ionized impurities and carrier density, r_s is the average distance between carriers in units of Bohr radious, l is the mean free path, and c~10, varying slightly with scattering length. For short range scattering potential considered by Luttinger [74] and Nozieres and Lewiner [79], $V(\vec{r}) = V_0 \delta(\vec{r} - \vec{r}_i)$:

$$\left|\frac{\sigma_{AH}^{sj/\mathrm{int}}}{\sigma_{AH}^{sk}}\right| = \frac{3}{\pi |V_0| DOS(E_F) k_F l}, \tag{12}$$

where $DOS(E_F)$ is the density of states at the Fermi energy and k_F is the Fermi wave-vector. These estimates can be a useful first guess at which mechanism dominates in different materials but one must keep in mind the simplicity of the models used to estimate such ratio.

In spite of the theory being incomplete, and in some cases self-contradictory and puzzling, the theoretical developments remained somewhat dormant until recent interest in new ferromagnetic and spintronic materials have rekindled these ideas. This emerging field has demonstrated the need for a better theoretical understanding of the AHE which has constantly been used to characterize ferromagnetic materials.

We emphasize that there is, at this stage, no controversy regarding the skew-scattering contribution. In most materials such contribution, although present, is minor and in most ferromagnetic materials the quadractic dependence of R_S is observed even at the lowest temperatures. However, if somehow, one could artificially turn down ρ one would eventually reach a regime where such contribution is dominant, a fact which very few people dispute

since the origin of such contribution is rather transparent and reassuringly extrinsic in nature. However, the flip of sign of the expressions derived by Luttinger [74] and Nozieres and Leweir [79] within the simple one band model in the different order of limits of $\omega\tau$, remains quite disturbing and a source of continuous debate. After all, these results are only obtained in a limit where, supposedly, the skew scattering would always dominate. As we will see below, it seems that in many materials experimental comparisons, the ultimate test of validity of any theory, are more consistent with the intrinsic Karplus and Luttinger [71] contribution than the reversed sign one of Luttinger [74]; the sign of the effect being a simple thing to check.

A possible resolution to the problem would be to perform the Hall conductivity calculation within the Kubo linear response formalism, treating disorder and spin-orbit coupling on an equal footing. This can be achieved by starting from the Dirac representation and taking the weak relativistic limit after treating disorder in the usual fashion. In this way, any spin-orbit coupling contribution comes naturally from the Dirac representation and therefore is automatically taken into account. On the other hand, if one starts from the Pauli Hamiltonian, an immediate question arises: which vertex corrections capture the different contributions to the anomalous Hall effect? Such an approach was taken recently by Crepieux, Dugaev, and Bruno [86,87,88]. The work considers, however, a free electron gas model rather than a crystalline environment, hence ignoring the intrinsic spin-orbit coupling effects. In spite of this simplification, the authors obtained many useful findings. They where able to pinpoint which diagrams correspond to the skew and the side-jump scattering in the Pauli Hamiltonian by identifying them from the corresponding ones arising naturally from the Dirac formalism. Notably, these diagrams within the Pauli Hamiltonian, are not the standard ones that one would take into account naturally. Their main result, Eq. 50 and 51 in Ref. [86], is in reasonable agreement with Berger's simpler treatment of this free electron gas problem.

Taking into consideration the confusion generated by the possible relevance of the side-jump scattering mechanism, several researchers have chosen to focus instead on the original intrinsic contribution to the AHE proposed by Karplus and Luttinger and ignore impurity scattering all together or simply include its effects through the Born approximation which introduces a finite quasiparticle lifetime. In DMS, e.g., this approach is partly motivated by the strong intrinsic spin-orbit coupling in the host valence bands that makes much of the above theoretical discussions inapplicable since they relied on the perturbation treatment of the spin-orbit coupling. One of the main attractions of the intrinsic AHE theory is the ability to do calculations in models with realistic electronic band-structures. This approach has been used, for example, to analyze the AHE in layered 2D ferromagnets such as $SrRuO_3$, in pyrochlore ferromagnets [89,90,91,92], in the colossal magneto-resistance manganites [93], in Fe [94], in DMS [53,54], and as a natural starting point to address infrared magneto-optical effects such as the Kerr and Faraday effects [58]. The application of this approach to these different materials and their successful comparison to experiments is perhaps the most poignant criticism to the old theories regarding the side-jump scattering as the fundamental origin of the effect.

4.6 Anomalous Hall effect in DMS

The original discovery of ferromagnetism in (III,Mn)V semiconductors was established by measuring the AHE in both the high and low temperature regimes [1]. The comparison with

remnant magnetization measurements using a SQUID magnetometer confirmed that AHE measurement can be used to determine ferromagnetic critical temperature [1].

Recently Jungwirth, Niu, and MacDonald [54] reintroduced the original Karplus and Luttinger, pointing out that the intrinsic contribution to the AHE is proportional to the Berry phase acquired by a quasiparticle wave function upon traversing closed path on the spin-split Fermi surface. They applied the theory to metallic (III,Mn)V materials using both the 4-band and 6-band **k·p** description of the valence band electronic structure [43] and obtained results in a quantitative agreement with the experimental data in (Ga,Mn)As and (In,Mn)As DMS. In DMS systems, the estimate given in Eq. (11) gives a ratio of intrinsic to skew scattering contribution of the order of 50, hence the intrinsic contribution in these systems is likely to dominate [95]. Edmonds *et al*. [96] found that in metallic DMS systems $R_S \propto \rho^2$. In a follow up work [53] a more careful comparison of the theory, reformulated within the Kubo formalism, was done in order to account for finite quasiparticle lifetime effects important only for quantitative comparison with the experimental data. Within the Kubo formalism the dc Hall conductivity for non-interacting quasiparticles is given by

$$\sigma_{xy} = \frac{ie^2\hbar}{m^2}\int\frac{d\vec{k}}{(2\pi)^3}\sum_{n\neq n'}\frac{f_{n'\vec{k}}-f_{n\vec{k}}}{E_{n\vec{k}}-E_{n'\vec{k}}}\frac{\left\langle n\vec{k}\right|\hat{p}_x\left|n'\vec{k}\right\rangle\left\langle n'\vec{k}\right|\hat{p}_y\left|n\vec{k}\right\rangle}{E_{n'\vec{k}}-E_{n\vec{k}}+i\hbar\Gamma}. \qquad (13)$$

Looking at the real part of the dc Hall conductivity in the clean limit ($\hbar\Gamma \to 0$), the delta-function contribution from the denominator vanishes due to the Fermi factor differences and we obtain

$$\sigma_{xy} = \frac{e^2\hbar}{m^2}\int\frac{d\vec{k}}{(2\pi)^3}\sum_{n\neq n'}(f_{n'\vec{k}}-f_{n\vec{k}})\frac{\mathrm{Im}[\left\langle n'\vec{k}\right|\hat{p}_x\left|n\vec{k}\right\rangle\left\langle n\vec{k}\right|\hat{p}_y\left|n'\vec{k}\right\rangle]}{(E_{n'\vec{k}}-E_{n\vec{k}})^2}. \qquad (14)$$

Realizing that the dipole matrix elements considered above can be written as $\left\langle n'\vec{k}\right|\hat{p}_\alpha\left|n\vec{k}\right\rangle = \frac{m}{\hbar}\left\langle n'\vec{k}\right|\frac{\partial H(\vec{k})}{\partial k_\alpha}\left|n\vec{k}\right\rangle$, Eq. (14) can be shown to be equivalent to Eq. (9). However, within the Kubo formalism, it is straightforward to account for the finite lifetime broadening of the quasiparticles within the simple Born approximation by allowing Γ above to be finite. The effective lifetime for transitions between bands *n* and *n*', $\tau_{n,n'} \equiv 1/\Gamma_{n,n'}$, can be calculated by averaging quasiparticle scattering rates calculated from Fermi's golden rule including both screened Coulomb and exchange potentials of randomly distributed substitutional Mn and compensating defects as done in the dc Boltzman transport studies [45,46]. In Fig. 4 the compensation is assumed to be due entirely to As-antisite defects. The valence band hole eigenenergies $E_{n\vec{k}}$ and eigenvectors $\left|n\vec{k}\right\rangle$ in Eqs. (13) and (14) are obtained by solving the six-band Kohn-Luttinger Hamiltonian in the presence of the exchange field, $\vec{h} = N_{Mn}SJ_{pd}\hat{z}$ [43]. Here $N_{Mn}=4x/a_{DMS}^2$ is the Mn density in the $Ga_{1-x}Mn_xAs$ epilayer with a lattice constant a_{DMS}, the local Mn spin S=5/2, and the exchange coupling constant *Jpd*=55 meV nm^{-3}.

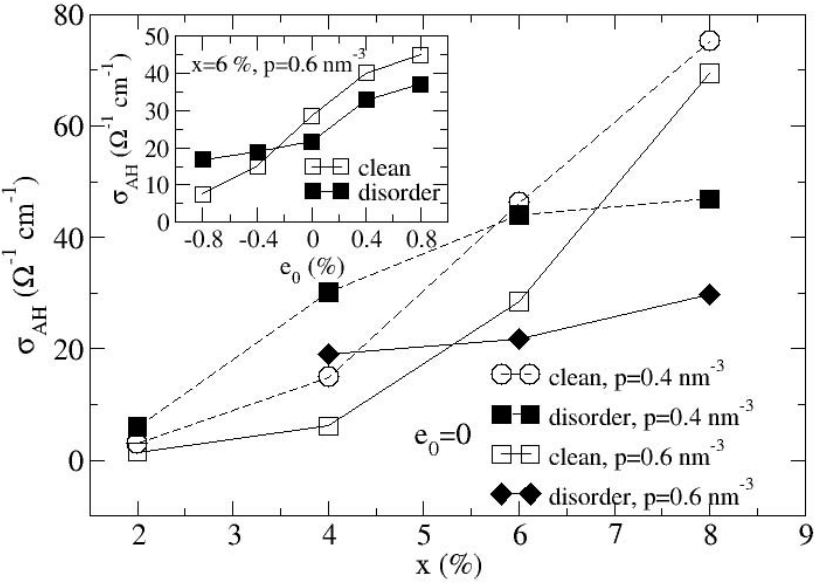

Fig. 4 Theoretical anomalous Hall conductivity of $Mn_xGa_{1-x}As$ DMS calculated in the clean limit (open symbols) and accounting for the random distribution of Mn and As-antisite impuriries (filled symbols), after Ref. 53.

Fig. 4 demonstrates that whether or not disorder is included, the theoretical anomalous Hall conductivities are of order 10 $\Omega^{-1}cm^{-1}$ in the (Ga,Mn)As DMS with typical hole densities, p~0.5$ nm^{-1}, and Mn concentrations of several per cent. On a quantitative level, disorder tends to enhance σ_{AH} at low Mn doping and suppresses AHE at high Mn concentrations where the quasiparticle broadening due to disorder becomes comparable to the strength of the exchange field. The inset in Fig. 4 also indicates that the magnitude of the AHE in both models is sensitive not only to hole and Mn densities but also to the lattice-matching strains between substrate and the magnetic layer, $e_0 \equiv (a_{sub} - a_{DMS})/a_{DMS}$.

A systematic comparison between theoretical and experimental AHE data is shown in Fig. 5 [53]. The results are plotted vs. nominal Mn concentration x while other parameters of the seven samples studied are listed in the figure legend. The measured σ_{AH} values are indicated by filled squares; triangles are theoretical results obtained in the clean limit or for a disordered system assuming either the As-antisite or Mn-interstitial compensation scenario. In general, when disorder is accounted for, the theory is in a good agreement with experimental data over the full range of studied Mn densities from x=1.5% to x=8%. The effect of disorder, especially when assuming Mn-interstitial compensation, is particularly strong in the x=8% sample shifting the theoretical σ_{AH} much closer to experiment compared to the clean limit theory. The remaining quantitative discrepancies between theory and experiment have been attributed to the resolution in measuring experimental hole and Mn densities [53].

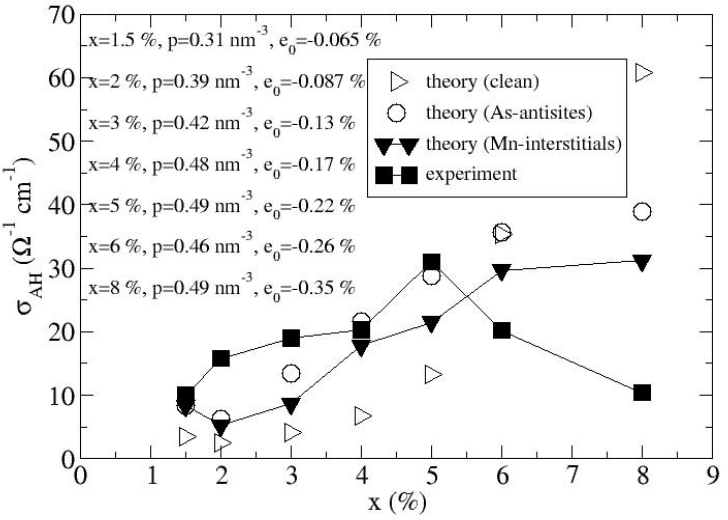

Fig. 5 Comparison between experimental and theoretical anomalous Hall conductivities, after Ref. 53.

We conclude this section by mentioning other studies of the anomalous Hall effect in regimes and geometries which we have not focused on here. A study within the non-metallic regime or hopping transport regime, not covered in any detailed within this review, has been done by Burkov *et al.* [97] following the ideas utilized in the mettalic Berry's phase approach but generalized to hopping transport regime. Their results are in good agreement with experimental data in this regime which encompass samples with less than 1% doping. At temperatures above T_c, a theory based on semiclassical Boltzman transport has suggested the presence of anomalous Hall voltage noise within this regime which could be a further test of the intrinsic AHE model [98].

A recent theoretical study by Bruno *et al*. [99] has suggested an alternative experimental system to test the topological Hall effect arising from the Berry phase similar to Eq. (9). Here the difference is that the system has a spatially varying magnetization. Upon a local gauge transformation which makes the quantization axis oriented along the local magnetization direction, the problem becomes that of a gauge vector potential corresponding to monopole fields. Such a system can be created by sandwiching a thin film (II,Mn)VI semiconductor and a lattice of iron nano-rods oriented perpendicular to the doped semiconductor epilayer. Future experiments might show whether such a device can be grown efficiently and the theory tested.

5. Summary

This review has focused on highliting the rapid developments in material research of metallic ferromagnetic (III,Mn)V semiconductors over the past few years. Although the successes have been extensive in the understanding and development of the bulk properties of the (Ga,Mn)As and (In,Mn)As systems within the metallic regime, many challenges remain both in other (III,Mn)V based semiconductors and lower dimensionalities such as digitally doped heterostructures. Both transport and magneto-optical effects will remain a very fruitfuil ground to make progress in these materials. At the time of writing, there is still a lot of work being done trying to sort out the more complicated physics of (Ga,Mn)N and several reports of high T_c measurements in the digitally doped materials. We simply keep watching in fascination the rapid developments and challenges posed by new experiments which will undoubtedly generate interesting physics and new understandings of these fascinating materials.

REFERENCES

[1] H. Ohno, H. Munekata, T. Penney, S. von Moln, and L.L. Chang, Phys. Rev. Lett. 68, (1992) 2664.
[2] H. Ohno, Science 281, 951 (1998).
[3] S.D. Sarma, E.H. Hwang, and A. Kaminski (2003), Solid State Comm. 127, 99 (2003).
[4] C. Timm, J. Phys.: Condensed Matter 15, R1865 (2003).
[5] H. Ohno, J. Magn. Magn. Mater. 200, 110 (1999).
[6] T. Dietl, Semicond. Sci. Technol. 17, 377 (2002).
[7] F. Matsukura, H. Ohno, and T. Dietl, Handbook of Magnetic Materials 14, 1 (2002).
[8] J. Konig, J. Schliemann, T. Jungwirth, and A. H. MacDonald, in *Electronic Structure and Magnetism of Complex Materials*, edited by D.Singh and D.Papaconstantopoulos (Springer Verlag Berlin, 2003).
[9] T. Dietl, H. Ohno, and F.Matsukura, Phys. Rev. B 63, 195205 (2001).
[10] S.Sanvito, G.Theurich, and N.Hill, Journal of Superconductivity 15, 85 (2002).
[11] S.A. Wolf, D.D. Awschalom, R.A. Buhrman, J.M. Daughton, S.von Molnar, M.L. Roukes, A.Y. Chtchelkanova, and D.M. Treger, Science 294, 1488 (2001).
[12] T. Dietl, Acta Phys. Polon. A 100, 139 (2001).
[13] J.F. Gregg, I.Petej, E.Jouguelet, and C.Dennis, J. Phys. D: Appl. Phys. 35, R121 (2002).
[14] H. Ohno, F. Matsukura, and Y. Ohno, JSAP International 5, 4 (2002).
[15] J. Sinova, T. Jungwirth, and J. Cerne, Int. Journ. of Modern Phys. B 18, 1083 (2004).
[16] A.K. Bhattacharjee and C.B. ala Guillaume, Sol. State Comm. 113, 17 (2000).
[17] M. Linnarsson, E. Janzn, B. Monemar, M. Kleverman, and A. Thilderkvist, Phys. Rev. B 55, 6938 (1997).

[18] J. Schneider, U. Kaufmann, W. Wilkening, M. Baeumler, and F. Kohl, Phys. Rev. Lett. 59, 240 (1987).
[19] S.C. Erwin and A. Petukhov, Phys. Rev. Lett. 89, 227201 (2002).
[20] J. Masek and F. Maca, Acta Phys. Polon. A 100, 319 (2001).
[21] J. Szczytko, A. Twardowski, M.Palczewska, R. Jablonski, J. Furdyna, and H. Munekata, Phys. Rev. B 63, 085315 (2001).
[22] J. Szczytko, A. Twardowski, K. Swiatek, M. Palczewska, and K.A. M. Tanaka, T. Hayash, Phys. Rev. B 60, 8304 (1999).
[23] J. Okabayashi, A. Kimura, T. Mizokawa, A. Fujimori, T. Hayashi, and M. Tanaka, Phys. Rev. B 59, R2486 (1999).
[24] J. Okabayashi, A. Kimura, O. Rader, T. Mizokawa, A. Fujimori, T. Hayashi, and M. Tanaka, Phys. Rev. B 64, 125304 (2001).
[25] K. Edmonds, K. Wang, R. Campion, A. Neumann, N. Farley, B. Gallagher, and C. T. Foxon, Appl. Phys. Lett. 81, 4991 (2002).
[26] K.C. Ku, S.J. Potashnik, R.F. Wang, M.J. Seong, E.Johnston-Halperin, R.C. Meyers, S.H. Chun, A.Mascarenhas, A.C. Gossard, D.D. Awschalom, etal., Appl. Phys. Lett. 82, 2302 (2003).
[27] R. Mathieu, B.S. Sorensen, J. Sadowski, J. Kanski, P. Svedlindh, and P.E. Lindelof, Phys. Rev. B 68, 184421 (2003).
[28] K.M. Yu, W. Walukiewicz, T. Wojtowicz, I. Kuryliszyn, X. Liu, Y. Sasaki, , and J.K. Furdyna, Phys. Rev. B 65, 201303 (2002).
[29] K. Edmonds, P. Boguslawski, K. Wang, R. Campion, N. Farley, B. Gallagher, C. Foxon, M. Sawicki, T. Dietl, M. Nardelli, Phys. Rev. Lett. 92, 037201 (2004).
[30] I. Kuryliszyn-Kudelska, T. Wojtowicz, X. Liu, J.K. Furdyna, W. Dobrowolski, J.Z. Domagala, E. Lusakowska, M. Goiran, E. Haanappel, and O.Portugall (2003).
[31] H. Ohno, D. Chiba, F. Matsukura, T. Omiya, E. Abe, T. Dietl, Y. Ohno, and K. Ohtani, Nature 408, 944 (2000).
[32] J. Szczytko, W. Mac, A. Twardowski, F. Matsukura, and H. Ohno, Phys. Rev. B 59, 12935 (1999).
[33] T. Omiya, F. Matsukura, T. Dietl, Y. Ohno, T. Sakon, M. Motokawa, and H. Ohno, Physica E 7, 976 (2000).
[34] T. Dietl, Handbook of Semiconductors Vol. 3 B (1994).
[35] J. Masek, J. Kudrnovsky, and F. Maca, Phys. Rev. B 67, 153203 (2003).
[36] H. Akai, Phys. Rev. Lett. 81, 3002 (1998).
[37] J. Park, S. Kwon, and B. Min, Physica B 281, 703 (2000).
[38] J. Masek and F. Maca, Acta Phys. Polon. A 102, 667 (2002).
[39] J. Blinowski and P. Kacman, Phys. Rev. B 67, 121204 (2003).
[40] T. Jungwirth, J. Masek, J. Sinova, and A. H. MacDonald, Phys. Rev. B 68, 161202(R) (2003).
[41] R. Campion, K. Edmonds, L. Zhao, K. Wang, C. Foxon, B. Gallagher, and C. Staddon, J. Cryst. Growth 251, 311 (2003).
[42] R.N. Bhatt, M.Berciu, M.P. Kennett, and X. Wan, Journal of Superconductivity 15, 71 (2002).
[43] M. Abolfath, T. Jungwirth, J. Brum, and A. H. MacDonald, Phys. Rev. B 63, 054418 (2001).

[44] I. Vurgaftman, J. Meyer, and L. Ram-Mohan, J. Appl. Phys 89, 5815 (2001).
[45] T. Jungwirth, M. Abolfath, J. Sinova, J. Kucera, and A. H. MacDonald, Appl. Phys. Lett. 81, 4029 (2002).
[46] J. Sinova, T. Jungwirth, S.-R.E. Yang, J. Kucera, and A. H. MacDonald, Phys. Rev. B 66, 041202 (2002).
[47] S.-R.E. Yang, J. Sinova, T. Jungwirth, Y. Shim, and A. H. MacDonald, Phys. Rev. B 67, 045205 (2003).
[48] J. Schliemann, Phys. Rev. B 67, 045202 (2002).
[49] J. Schliemann and A. H. MacDonald, Phys. Rev. Lett. 88, 137201 (2002).
[50] B. Lee, T. Jungwirth, and A. H. MacDonald, Semicond. Sci. Technol.17, 393 (2002).
[51] T. Dietl, H. Ohno, F. Matsukura, J. Cibert, and D. Ferrand, Science 287, 1019 (2000).
[52] T. Jungwirth, J. Konig, J. Sinova, J. Kucera, and A. H. MacDonald, Phys. Rev. B 66, 012402 (2002).
[53] T. Jungwirth, J. Sinova, K. Wang, K.W. Edmonds, R. Campion, B. Gallagher, C. T. Foxon, Q. Niu, and A. H. MacDonald, Appl. Phys. Lett. 83, 320 (2003).
[54] T. Jungwirth, Q. Niu, and A. H. MacDonald, Phys. Rev. Lett. 88, 207208 (2002).
[55] J. Konig, T. Jungwirth, and A. MacDonald, Phys. Rev. B 64, 184423 (2001).
[56] T. Dietl, J. Konig, and A.H. MacDonald, Phys. Rev. B 64, 241201 (2001).
[57] J. Sinova, T. Jungwirth, Y.S. X.Liu, J. Furdyna, W.A. Atkinson, and A. H. MacDonald , Phys. Rev. B 69, 085209 (2004).
[58] J. Sinova, T. Jungwirth, J. Kucera, and A. H. MacDonald, Phys. Rev. B 67, 235203 (2003).
[59] A.Chattopadhyay, S.D. Sarma, and A.J. Millis, Phys. Rev. Lett. 87, 227202 (2001).
[60] F. Matsukura, H. Ohno, A. Shen, and Y. Sugawara, Phys. Rev. B 57, R2037 (1998).
[61] S.J. Potashnik, K.C. Ku, S.H. Chun, R.F. Wang, M.B. Stone, N. Samarth, and P. Schiffer (2002), cond-mat /0212260.
[62] A.V. Esch, L.V. Bockstal, J.D. Boeck, G. Verbanck, A.S. van Steenbergen, P.J. Wellmann, B. Grietens, R.B.F. Herlach, and G. Borghs, Phys. Rev. B 56, 13103 (1997).
[63] T. Hayashi, M.Tanaka, K.Seto, T.Nishinaga, and K.Ando, Appl. Phys. Lett. 71, 1825 (1997).
[64] M. Lopez-Sancho and L.Brey, Phys. Rev. B 68, 113201 (2003).
[65] K.W. Edmonds, R.P. Campion, K.-Y. Wang, A.C. Neumann, B.L. Gallagher, and P.C.M. C. Foxon, J. Appl. Phys. 93, 6787 (2002).
[66] D.V. Baxter, D.Ruzmetov, J.Scherschligt, Y.Sasaki, X.Liu, J.K. Furdyna, and C.H. Mielke, Phys. Rev. B 65, 212407 (2002).
[67] S.J. Potashnik, K.C. Ku, R.Mahendiran, S.H. Chun, R.F. Wang, N.Samarth, and P. Schiffer, Phys. Rev. B 66, 012408 (2002).
[68] K. Wang, K.Edmonds, R.Campion, L.Zhao, A.Neumann, C.Foxon, B.Gallagher, and P.Main (2002), cond-mat/0211697.
[69] H. Tang, R.Kawakami, D.Awschalom, and M.Roukes, Phys. Rev. Lett. 90, 107201 (2003).

[70] L. Chien and C.R. Westgate, *The Hall Effect and Its Applications* (Plenum, New York, 1980).
[71] R. Karplus and J.Luttinger, Phys. Rev. 95, 1154 (1954).
[72] J. Smit, Physica 21, 877 (1955).
[73] W. Kohn and J.Luttinger, Phys. Rev. 108, 590 (1957).
[74] J. Luttinger, Phys. Rev. 112, 739 (1958).
[75] E. Adams and E.Blount, J. Phys. Chem. Solids 10, 286 (1959).
[76] L. Berger, Phys. Rev. B 2, 4559 (1970).
[77] S. Lyo and T.Holstein, Phys. Rev. Lett. 29, 423 (1972).
[78] P. Leroux-Hugon and A.Ghazali, J. Phs. C 5, 1072 (1972).
[79] P. Nozieres and C.Lewiner, Le Journal de Physique 34, 901 (1973).
[80] R. Fivaz, Phys. Rev. 183, 586 (1969).
[81] J. Chazalviel, Phys. Rev. B 11, 3918 (1975).
[82] J. Smit, Phys. Rev. B 8, 2349 (1973).
[83] L. Berger, Phys. Rev. B 8, 2351 (1973).
[84] J. Smit, Phys. Rev. B 17, 1450 (1978).
[85] L. Berger, Phys. Rev. B 17, 1453 (1978).
[86] A. Crepieux and P. Bruno, Phys. Rev. B 64, 014416 (2001).
[87] A. Crepieux and P. Bruno, Phys. Rev. B 64, 094434 (2001).
[88] V.K. Dugaev, A. Crepieux, and P. Bruno, Phys. Rev. B 64, 104411 (2001).
[89] M. Onoda and N. Nagaosa, J. Phys. Soc. Jap. 71, 19 (2001).
[90] Z. Fang, N. Nagaosa, K.S. Takahashi, A. Asamitsu, R. Mathieu, T.Ogasawara, H. Yamada, M. Kawasako, Y. Tokura, and K. Terakura, Science 302, 92 (2003).
[91] Y. Taguchi, Y. Oohara, H. Yoshizawa, N. Nagaosa, and Y. Tokura, Science 291, 2573 (2001).
[92] R. Shindou and N. Nagaosa, Phys. Rev. Lett. 87, 116801 (2001).
[93] J. Ye, Y.b.Kim, A.J. Millis, B.I. Shraiman, P. Majumdar, and Z. Tesanovic, Phys. Rev. Lett. 83, 3737 (1999).
[94] Y. Yao, L. Kleinman, A.H. MacDonald, J. Sinova, T. Jungwirth, D. sheng Wang, Wang, and Q. Niu, Phys. Rev. Lett. 86, 037204 (2004).
[95] T. Dietl, F. Matsukura, H. Ohno, J. Cibert, and D. Ferrand , NATO Advanced Research Workshop "Recent Trends on Physical Phenomena in High Magnetic Fields", Les Houches, February 2002.
[96] K.W. Edmonds, K.Y. Wang, R.P. Campion, A.C. Neumann, C.T. Foxon, B.L. Gallagher, and P.C. Main, Appl. Phys. Lett 81, 3010 (2002).
[97] A. Burkov and L. Balents, Phys. Rev. Lett. 91, 057202 (2003).
[98] C. Timm, F.von Oppen, and F. Holfing, Phys. Rev. B 69, 115202 (2004).
[99] P. Bruno, V.K. Dugaev, and M. Taillefumier (2003), cont-mat/0310522.

UNCONVENTIONAL MAGNETISM IN CARBON BASED MATERIALS

Tatiana Makarova

Umeå University, 90187 Umeå, Sweden

1. INTRODUCTION

Recently, a number of publications appeared in which reproducible observations of the room-temperature ferromagnetic behavior of various carbon allotropes, such as graphite, fullerenes, microporous carbon and nanofoam were reported. Theoretical studies have shown that specific features of the electronic structure of carbon could give rise to ferromagnetic or superconducting correlations retained at high temperatures. This review collects the experimental studies of the carbon-based magnets and describes the current status of the theoretical work.

2. MAGNETIC PROPERTIES OF DIAMOND AND GRAPHITE

Diamond

Diamond and graphite are the carbon allotropes formed with the sp^3 and sp^2 bond networks, respectively. Bonding determines the difference in the band structure: diamond is an insulator with an energy gap of 5.3 eV between σ and σ^* bands, while the π and π^* bands in graphite slightly overlap making graphite semimetallic. Magnetism of diamond conforms to the same rules as magnetism of tetrahedral semiconductors [1]. According to the van Vleck formula, the magnetic susceptibility of diamond includes two diamagnetic contributions (from the core

electrons and from valent electrons) and the paramagnetic term, which originates from virtual magnetic dipole transitions between the valence and conduction bands. The total molar susceptibility of diamond under the assumption that the unit cell consists of two atoms is $\chi = 11.8 \cdot 10^{6}$ cm^3/mol, and the specific susceptibility equals to about 0.5 10^{-6} emu/g.

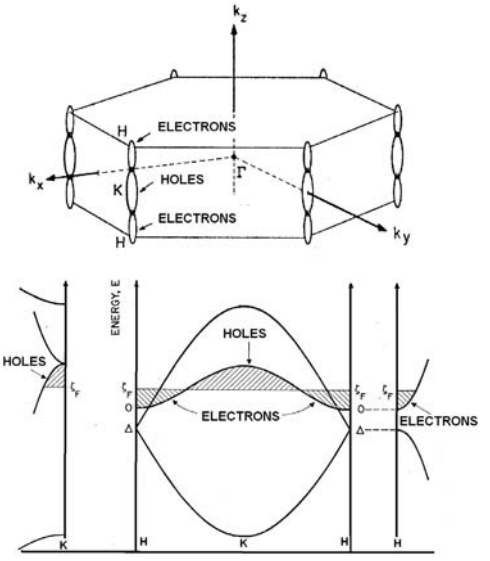

Fig. 1. Upper panel: Brillouin zone of graphite. Lower panel: Energy bands of graphite near the vertical zone edge HKH as given by the Slonczewski-Weiss model. Adapted from [2]

Graphite

Graphite is the equilibrium phase of carbon under the ambient conditions. The understanding of magnetic behavior of graphite was obtained on the basis of its band structure (Fig. 1). The band structure of graphite is described in the region of the Fermi surfaces by the Slonczewski-Weiss-McClure model [2, 3]. Magnetic susceptibility of graphite was calculated using the band parameters of this model [4]. The only important effect not included in the Slonczewski-Weiss-McClure model is the correlation of electron motion due to the Coulomb interaction, though this effect is expected to be important.

One of the characteristic physical properties of graphite is large anisotropic diamagnetic susceptibility [6]. The room-temperature values of the susceptibility are reported to be in the range $\chi_{\perp} = -(20 - 50) * 10^{-6}$ emu/g with the magnetic field applied along the c-axis and $\chi_{\parallel} = -(0.4 - 0.5) * 10^{-6}$ emu/g with the field parallel to the carbon layers. In addition to diamagnetism, graphite exhibits a Pauli-type paramagnetism due to the charge carriers, but its contribution is

several orders of magnitude less $\chi_P \sim 10^{-8}$ emu/g [7]. Fig. 2 shows the summary of the temperature dependencies of magnetic susceptibilities for different carbon allotropes: graphite, diamond, nanotubes and fullerene C_{60}.[8].

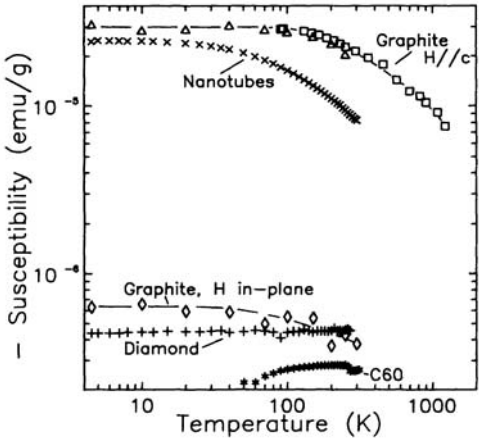

Fig. 2. Summary of the temperature dependencies of the susceptibility of various carbon materials identified in the picture. Note that the ordinate is negative [8].

Careful measurements show that experimental values of $\chi_{\|}$ inevitably include a diamagnetic contribution from $\chi_{\perp}$, which is caused not only by incorrect alignment of the sample but mainly by the natural corrugation of graphene planes even in highly oriented graphite. Thus, it is possible that the true value of $\chi_{\|}$ is several orders of magnitude smaller or even has the opposite sign [9].

Some of the authors point to the nonlinear, field-dependent magnetic susceptibilities in a range of carbon-based materials such as C_{60}, carbon nanotubes, diamond and graphite This nonlinear behaviour is prominent at low fields and it vanishes at relatively high fields [8, 10, 11]. The low-field dependence of the moment is paramagnetic, as shown in the Fig. 3. The origin of the low-field paramagnetic contribution is still unknown, and it cannot be due to the misalignment, since the c-axis susceptibility is strongly diamagnetic.. This behavior was attributed to the field dependence of the spectral energy separations of the van Vleck paramagnetic term of the susceptibility [10], to the Aharonov-Bohm effect (in the case of nanotubes) [11] or to the presence of impurities [8] In view of recent findings [9], we consider this behaviour as the intrinsic property of this class of materials. Understanding of the non-linear behaviour in low magnetic fields should have significant bearing on the interpretation of the magnetic properties of this class of materials.

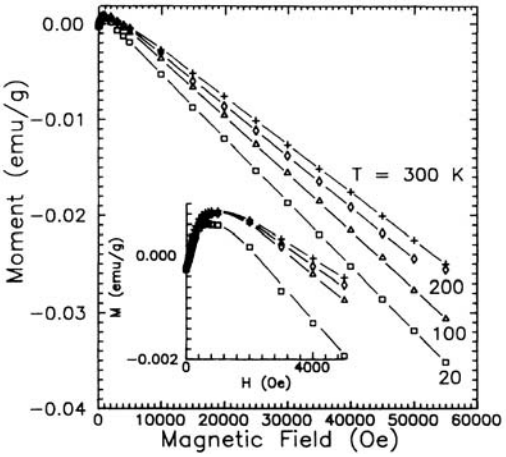

Fig. 3. Field dependence of the magnetic moment of HOPG, with the field aligned perpendicularly to the c axis, taken at the temperatures shown. The inset shows the low-field behavior magnified [8].

Intermediate graphite-diamond structure

A hypothetical crystal has been proposed that contains equal numbers of sp^2 and sp^3 hybridized carbon atoms and the presence of three-dimensional ferromagnetic ordering at room temperature is predicted. The ferrocarbon crystal appears to have a rhombohedral lattice. Quasi-graphite layers contain six-membered rings arranged in the "sofa" form. Calculated spontaneous magnetic moment is equal to 230 emu/g [12].

3. GRAPHITE WITH STRUCTURAL DEFECTS

Bulk graphite with a perfect structure is a diamagnetic material whose magnetic susceptibility is second only to that of superconductors. Graphite containing certain defects can exhibit spontaneous magnetization. This behavior is caused not only by carbon atoms but mainly by its “honeycomb” structure. Certain defects in this structure give rise to a sharp asymmetric peak in the density of states at the Fermi level. In order for ferromagnetism to arise in a system of itinerant electrons, it is necessary that the density of states at the Fermi level be fairly high. Graphite can become magnetic as a result of Lieb ferrimagnetism [13], which is a modification of antiferromagnetism in a bipartite system with a disbalance of sites in sublattices. Another possibility is the ferromagnetism of flat bands according to the Mielke–Tasaki mechanism [14]. Flat band ferromagnetism is often discussed in the context of possible organic magnetism, because it is organic substances that can form the required energy-band pattern, which will be illustrated below by considering various types of defects in graphite.

The effects of the electron-electron interactions in a graphene layer are predicted to lead to the occurrence of ferromagnetic, antiferromagnetic and superconducting instabilities [15]. Superconducting-like behavior was found in highly oriented pyrolytic graphite [16] and in carbon films formed by sputtering of spectroscopically pure graphite in an electrical arc discharge [17].

Finite size of graphene layers

Three types of defects in graphite can be recognized provisionally: porosity, edges of the planes, and so-called topological defects.

The electronic properties of graphene planes of finite size differ radically from those of bulk graphite. In order to describe the magnetic susceptibility of quasi-2D graphites, one has to take into account the contributions of the atomic-core diamagnetism, the Pauli paramagnetism and Landau diamagnetism of conduction electrons, the orbital diamagnetism, the Curie paramagnetism, and the orbital paramagnetic van Vleck contribution. The diamagnetic susceptibility of graphene planes of a finite size is primarily controlled by the charge-carrier concentration related to structural defects.

If graphite has a steplike surface, localized states appear at the Fermi level, caused by the cut of a graphite sheet and localized near the step (Fig. 4) [18].

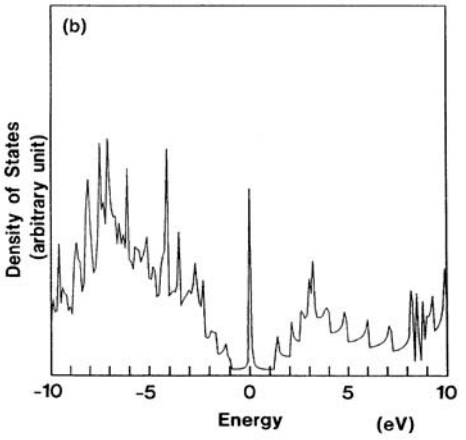

Fig. 4. Calculated density of states of the stepped graphite surface [18].

Porous Graphite

The “honeycomb” structure, i.e., an ideal infinite network of hexagons composed of light-element atoms, has the energy-band structure of a semimetal. The same plane, but porous and studded with hexagonal holes (Fig. 5), becomes semiconductive, semimetallic, or metallic, depending on the size and arrangement of the holes, and flat bands appear systematically in the

electronic structure. In some of the classes the symmetry enforces dispersionless bands to exist, which implies the occurrence of spin ferromagnetism when the electron correlation is turned on. These provide a unique opportunity for band structure engineering. [19]. On the basis of the Lieb theorem, it is predicted that organic ferromagnetism can appear in a "superhoneycomb" bipartite structure. Another porous-graphite model that takes into account the ordered structure of the plane edges also reveals the presence of flat bands in the electronic structure [20]. The energy-band pattern of porous graphite is governed not only by the shape of voids but mainly by the symmetry; in some cases, the energy gap is a periodic function of the distance between voids. It is shown theoretically that the energy-band structure of porous graphite allows for the separation of spin and charge [21].

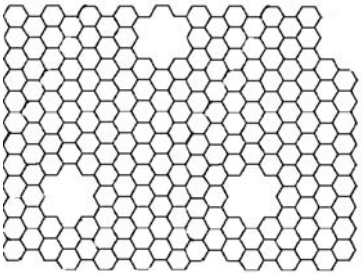

Fig. 5. An example of a porous graphite plane.

Edges of the Planes

Finite graphite structures have specific boundary states. Two types of edges of a graphene plane are recognized when considering the electronic structure of micrographite: a phenanthrene (or "armchair") edge and an acene (or "zigzag") edge (Fig. 6). Unsaturated valence bonds at the boundaries of graphene flakes are filled with stabilizing elements; these stabilizers are theoretically considered to be hydrogen atoms. It is typically assumed that a zigzag-type edge is stabilized by a single hydrogen atom. A "bearded" edge (considered by Klein and Bytautas [22] and referred to as the Klein edge) differs from a zigzag-type edge in that, in the former, each edge carbon atom is bonded to two hydrogen atoms. Peculiar electronic properties of the zigzag edges were first investigated by the late M. Fujita, and this egde is referred to as Fujita's edge.

There is a sharp distinction between the electronic states with different shapes of edges. Narrow and long graphene ribbons with zigzag edges feature a sharp peak in the density of states at the Fermi energy; such a peak is not observed in the case of bulk graphite. The edge states are of primary importance in the case of nanosized graphite [23]. Graphite ribbons have an extremely high density of states at the Fermi level, which leads to paramagnetism and (for a certain packing) to antiferromagnetism. A nanographite ribbon can be characterized by the type of the long edge and by the number of cells N between the edges (Fig. 7). Zigzag-type ribbons are always metallic, whereas the armchair ribbons are metallic only if $N = 3m - 1$, where m is an

integer. A specific feature of the zigzag ribbons is the appearance of a pair of almost flat bands on the Fermi energy (Fig. 7).These bands create a sharp peak in the density of states at the Fermi level in the region where the π and π* bands of 2D graphite contact each other. The charge density in the flat band state is strongly localized on the zigzag edge sites [24].

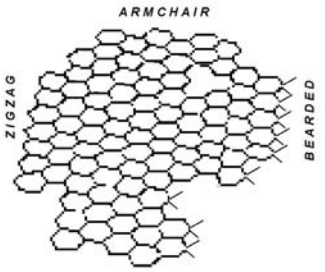

Fig. 6. Types of graphene plane edges.

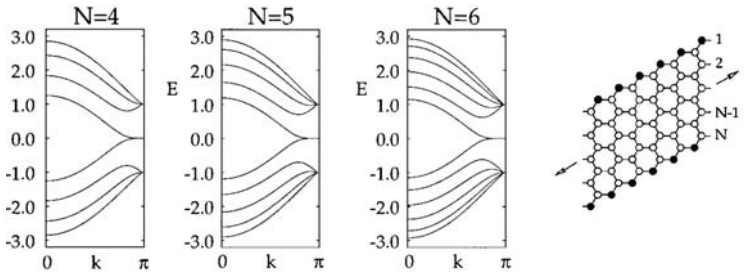

Fig. 7. Calculated band structures $E(k)$ of zigzag ribbons with various width (N= 3; 4; 5). Right panel: The network skeleton of a zigzag ribbon of the width N. The edge sites are indicated by solid circles on each side [24].

Since the edge states give rise to a peak in the density of states at the Fermi level, these states contribute to the Pauli susceptibility that balances the orbital diamagnetism. The response of the strips with zigzag edges remains diamagnetic at high temperatures. As temperature decreases, this response is replaced by the temperature (T) dependence of magnetic susceptibility in the form $\chi_C = C/T$, where C is the Curie constant [25].

This type of χ (T) dependence was observed experimentally for graphitized diamond [26] and activated carbon fibres; in the latter case, the dangling bonds were localized in 10-Å-sized microvoids [27].

The presence of flat energy bands near the Fermi level has a considerable influence on the graphite electronic structure with zigzag edges. A consideration of the effects of electron–electron interactions in the frame of the Hubbard model shows that there can be a spontaneous magnetic ordering in nanographite. In the case of the zigzag-type strips, a ferrimagnetic structure is possible; the appearance of magnetic ordering controlled by the magnitude of the surface deformation caused by the electron–phonon interaction [28]

The corresponding energy bands exhibit almost no dispersion at the Fermi level. The wave functions are mainly localized at the zigzag edge. Fujita *et al.* [29] used the Hubbard model in the mean-field approximation and assumed that the π electrons at a zigzag-type edge could give rise to a ferrimagnetic system of spins. Localized states do not appear in graphite structures with an armchair-type edge. The graphene perimeter of an arbitrary shape can be described as a combination of zigzag- and armchair-type edges. The boundary states, which cannot be disregarded, appear even in grapheme planes with a poorly pronounced zigzag structure: three to four jags in the edge are sufficient to cause appreciable changes in the electronic structure.

If both edges of the graphene tape are of the zigzag or bearded type, the total spin moment is equal to zero, since a π-electron system forms a bipartite structure with an equal number of sites in the sublattices.

Local magnetic moments tend to interact antiferromagnetically at the edges. The spin-wave mode of this magnetic state was studied in the random-phase approximation using the Hubbard model. When the spin polarization is taken into account in the Heisenberg model, an energy gap is formed. However, analysis shows that the gap is narrow and the tendency towards ferrimagnetic correlations at the edges is pronounced [30]. The use of the Möbius boundary conditions for a graphene ribbon with zigzag-type edges leads to destruction of the bipartite system and suppresses the spin polarization, which gives rise to a magnetic domain wall. The magnetic domain width is governed by the Coulomb interaction [31].

Magnetic nanographite

The entrapment of hydrogen by dangling bonds at the nanographite perimeter can induce a finite magnetization. A theoretical study of a graphene ribbon in which each carbon atom is bonded to two hydrogen atoms at one edge (the Klein edge) and to a single hydrogen atom at the other edge (the zigzag-type edge) shows that the structure has a finite total magnetic moment: bipartite structure with a different number of sites in each sublattice is formed. The bipartite system is stable and features a spin-polarized flat band. The magnetism obtained using the local spin density approximation (LSDA) calculations is interpreted as an appearance of ferrimagnetism in the Hubbard model with flat bands [32]. The same mechanism occurs in the case of hypergraphites, i.e., structures with edges where completely degenerate states appear [33]. Combination of the magnetic and non-magnetic edge structures (by means of hydrogenation, fluorination or oxidation) is proposed as a guiding principle to design magnetic nanographite: a magnetic material made only from light elements [34].

Packing of the Planes

Unusual magnetism was predicted theoretically and observed experimentally in nanocrystals of carbon material that were formed as stacks of graphene layers. There is a sharp dependence of the magnetic behaviour of nanographite systems on the order of alternation of graphene planes. The Hubbard model was used by Harigaya [35] to consider the simplest packing *A–A* (where the sites of carbon atoms were identical for all layers) and the packing *A–B* (where every other layer was shifted by half the cell width, so that the layers alternated as in hexagonal graphite) (Fig. 8). Harigaya considered the situation where the number of atomic sites and the number of electrons is the same for all grapheme planes. The matrix element for hopping between the layers is larger in the case of the *A–B* sequence, which gives rise to a finite magnetization of the structure. For an ideal *A–B* packing and also for a structure with smaller values of interplanar spacing due to a slight shift of the *B* layers with respect to the *A* layers [36], an antiferromagnetic solution was obtained. The *A–B* packing is characteristic of the most abundant hexagonal graphite modification and is apparently typical of nanographite systems, since nontrivial magnetic properties (spin glass state) [37, 38] and the variation in the ESR line as a result of adsorption of gases [39]) were discovered experimentally.

Packing of the planes has a great influence on the magnetic properties of bulk graphite: the properties of hexagonal and rhombohedral graphite are different [40].

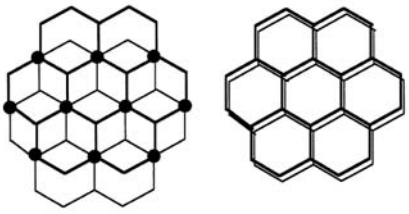

Fig. 8. Stacked nanographite with zigzag edges. The bold and thin lines show the first and second level, respectively. The stacking is the A-B type (left) and A-B type (right) [35].

An Open Electron Shell

A model of a closed electron shell cannot account for the experimental fact that the magnetic moment decreases as the interplanar spacing decreases as a result of adsorption of water molecules [41]. Calculations for systems with an open electron shell in an isolated nanographite layer were performed [42]. An open electron shell can be formed either by changing the geometric parameters or by adding active side groups that supply nanographite with electrons or holes. Effective potential was used to simulate the charge that comes from the side functional groups [43, 44]; it was shown that absolute values of the total magnetic moment in nanographite with an open electron shell decreased with decreasing interplanar spacing, which was completely consistent with experimental data. Ferromagnetism is stable in the regions with an intense interlayer hopping interaction and a strong Coulomb repulsion of electrons at the lattice sites.

The Curvature of the Graphene Plane

The magnetic properties of bulk graphite can be changed radically owing to the Stone–Wales rearrangement [45]: the rotation of two neighboring carbon bonds by an angle $\pi/2$ transforms four hexagons into two pentagons and two hexagons (Fig. 9). As a result, flat bands appear in the energy band structure. Variations in the curvature due to the appearance of hexagons and pentagons instead of hexagons are referred to as topological defects, Stone–Wales defects, or 5/7 defects. The periodic system of these defects completely changes the energy-band structure of graphite; a nondispersive band is formed along one of the directions, while the peak in the density of states caused by defects is located near the Fermi level [46].

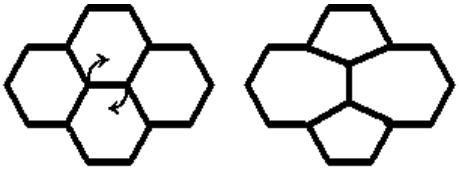

Fig. 9. Formation of a Stone-Wales defect in a honeycomb lattice.

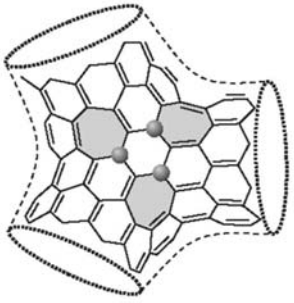

Fig. 10. Introduction of trivalent carbon radicals, emphasized by the gray spheres, in the aromatic system of the otherwise tetravalent carbon atoms in the tetrapod core. The radicals are associated with heptagons,indicated by gray shading [47].

Investigation of a nanotube junction (Fig. 10). which contains a region of a negatibe Gaussian curvature, has shown that this structure has a negative ground state. The origin of magnetism is different from magnetism discussed in the previous sections: the spin polarization at a graphite edge due to the presence of undercoordinated carbon atoms. Here, unpaired spins may be introduced by carbon radicals, not only by undercoordinated carbon atoms. This magnetic behavior originates in the presence of trivalent carbon radicals, which are introduced and sterically stabilized within the aromatic system of the otherwise tetravalent carbon atoms in the

core of the tetrapod structure. Spin density functional calculations for the graphitic pattern containing negatively curved graphitic surfaces indicate the presence of four unpaired spins in the electronic ground state. This magnetic behavior originates in the presence of trivalent carbon radicals, which are introduced and sterically stabilized within the aromatic system. Similar type of magnetism is expected to occur in other graphitic structures with a negative Gaussian curvature [47]. The magnetism is caused by the nanometer-sized conducting segments of sp^2 carbon. It could also occur in other nanostructured solids, which may be different from the tetrapod structure. If it is a general phenomenon, this discovery may strongly influence the emerging field of spintronics.

A Defect Consisting of a Carbon Atom and a Carbon Vacancy

The energies of adsorption and diffusion of carbon adatoms on the graphene plane were calculated from first principles. These calculations show that a defect consisting of a carbon vacancy and a carbon adatom features both high mobility and magnetism [48]. In equilibrium state, the carbon adatom forms a bridge between two carbon atoms at the surface. Calculations performed using the density-functional method show that this carbon adatom should have magnetic moment equal to $0.45\mu_B$. The magnetism the adatom is explained by the fact that the atoms of substrate and the adatom are hybridized differently. The surface atoms are transformed into sp^3 hybridization, whereas the adsorbed atoms remain in the sp^2 state. The adatom electrons are distributed in the following way: two electrons are involved in the covalence bonding with the atoms of the graphene plane. One of remaining electrons forms the dangling sp^2 bond, whereas the second electron is distributed between sp^2 bond and the p_z orbital. This p_z orbital is (according to the symmetry) orthogonal to the surface π-orbitals and cannot form a band if it remains localized and, consequently, spin-polarized. Apparently, the dangling sp^2 bond is partially spin-polarized; however, this effect is negligible.

A carbon atom diffuses mainly over the plane (the barrier for diffusion between the planes is four times higher). In the course of diffusion, the magnetic moment decreases and vanishes at a quarter of the diffusion path. Why does the magnetic moment vanish? At the transitional point during the diffusion, the atom has only a single bond with the surface, so the hybridization changes to the *sp* type. Thus, two free *p* orbitals appear and accept an excess electron; these orbitals can be found at the same level as the π orbitals at the surface and, thus, form bands. The spin density becomes delocalized, and the magnetism first vanishes and then reappears when the atom approaches the next stable state.

Consequently, the atoms diffuse as nonmagnetic particles and become magnetic at equilibrium sites. Their high mobility leads to frequent collisions of adatoms and to their annihilation as a result of recombination. However, the pinning and combination of adatoms into clusters should be expected; the aforementioned clusters have remanent magnetization even at high temperatures. The Curie temperature was estimated to be 100–200 K using the difference between the energies of the paramagnetic ($S = 0$) and ferromagnetic states.

Structures with Elements from the First Row of the Periodic Table

The ability to form flat bands is not only a property of carbon atoms; this property is inherent to planes that are composed of atoms bonded hexagonally to each other and feature zigzag-type edges or zigzag-type boundaries between chemically different elements. The origination of magnetic ordering is caused by the edge or interface states that are characteristic of tubular structures and hexagonally bonded structures. Heteronanotubes and heteroplanes composed of boron and nitrogen (like those composed of carbon) are nanodimensional ferromagnets [49]. The presence of two factors is sufficient to attain ferromagnetic or ferromagnetic states: a zigzag-type boundary between the chemically differing elements and a disbalance between the number of carbon atoms in each sublattice. The electronic structure of the planes composed of hexagonally coordinated B, N, and C atoms was calculated from first principles; the calculations show that the ground state of BNC planes with a certain stoichiometry is ferromagnetic. Magnetic and nonmagnetic solutions were derived for two types of lattices (BNC 1 and BNC 2, Fig. 11); in both cases, the ferromagnetic ground state was found to be lower in terms of energy. As the level of doping becomes higher, the ferromagnetic correlations are reduced; however, calculations by the LSDA method show quite clearly that ferromagnetic solutions are stable with respect to the doping level. The transition from ferromagnetic to nonmagnetic states occurs when we have from 0.02 to 0.05 electrons per unit cell for two different lattice types [50].

A possibility the ferromagnetic ordering in some isoelectron-substituted ferrocarbon [12] modifications has been investigated. The results prove the presence of the ferromagnetic ordering in the C_3H_6, $C_2BH_6^-$, $C_2NH_6^+$ [51].

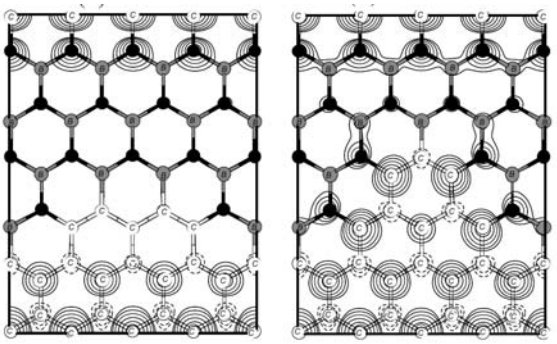

Fig. 11. Contour plot of spin density on the BNC heterosheet. (**a**) BNC-I and (**b**) BNC-II. Positive and negative values of the spin density are shown by solid and dashed lines, respectively. White, shaded, and black circles denote positions of C, B, and N atoms, respectively. Each contour represents twice (or half) the density of its neighboring contour lines [49].

4. EXPERIMENTAL DATA ON HIGH-TEMPERATURE MAGNETISM IN GRAPHITIC CARBONS

The reasons why one cannot expect high-temperature ferromagnetism in carbon are well known [52]:
(i) the singlet state leading to antiferromagnetism energetically more favorable for organic pairs of radicals;
(ii) unpaired spins in organic substances practically do not interact with each other, since these spins are separated by large spin-free fragments; and (iii) an attempt to bring together the spins of radicals ultimately results in a chemical reaction.

Nevertheless, about 100 papers and 30 patents have been published in which methods for obtaining structures that either consisted only of carbon or included elements of the first row of the periodic table and had nonlinear magnetization at room temperature are described; these were ferromagnetic *in sensu maiore*. Reproducible results obtained recently for polymerized fullerenes and proton-irradiated graphite suggest that specific ordering of carbon atoms, which is favourable for spontaneous magnetization, arises under various critical conditions, such as high temperatures and pressures or irradiation. Both small values of total magnetization of the sample and microscopy studies indicate that the ferromagnetic phase originates in the form magnetic islands in a nonmagnetic matrix.

Ferromagnetic- and superconducting-like behavior of graphite

Y. Kopelevich et al. identified both ferromagnetic and superconducting-like magnetization hysteresis loops in HOPG samples below and above room temperature [16].

This is the first experimental work, clearly showing high-temperature ferromagnetic-like behavior and possible "hot" superconductivity in graphite. When the field is applied parallel to basal planes, the M (H) hysteresis loops are ferromagnetic-like, and m (H) = M(H) $\times$V is proportional to the sample volume V, demonstrating that the ferromagnetic behavior is a bulk property of the sample. Heat treatment at 800 K in the He gas atmosphere strongly enhances the magnetic signal. For fields applied parallel to the basal planes, the main contribution is diamagnetic, but subtraction of a linear diamagnetic background reveals superconducting-like hysteresis loops. A thorough study has shown absence of correlation between the magnetic properties and impurity content and proved the intrinsic origin for the ferromagnetism found in graphite [9].

Hydrogen-treated graphite

Irradiation with protons can be used to produce ferromagnetic spots on samples of highly oriented pyrolytic graphite (Fig. 12) [53]. Magnetic force microscope studies showed that a magnetic signal appeared in an irradiated region; this signal varied in an applied external field. The extremely high reproducibility of the results obtained for special impurity-free samples indicate that the origin of the above signal is related to carbon. The strength of the magnetic signal is only a factor of similar to 10 smaller than that obtained on Fe particles [54]. Presumably, this effect is caused by induced disorder with a partial change of hybridization from the sp^2 type

to the sp^3 type. In addition, it is suggested that the presence of hydrogen is important for the inducement of ferromagnetism as similar experiments with irradiation with helium ions do not yield a magnetic contrast. The explanations of the effects are based on the formation of di-hydrogenated and mono-hydrogenated edges [32] or on the absorption of hydrogen atoms on irradiation induced vacancies [55].

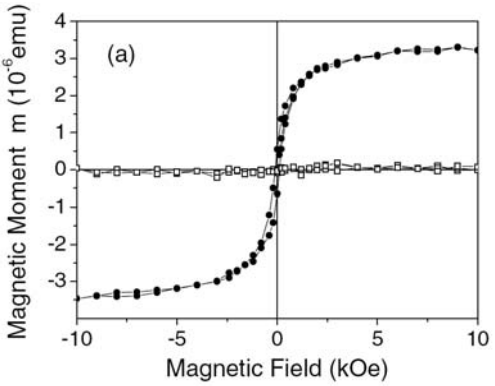

Fig. 12. Magnetic moment (in units of 10^{-6} emu) measured at T = 300 K as a function of the magnetic field, for the graphite sample before (open squares) and after (full circles) proton irradiation [53].

Microporous carbon

The occurrence of high-temperature ferromagnetism has been found in microporous carbon with a three-dimensional nanoarray (zeolite) structure. The results provide evidence that the ferromagnetic behavior of MC is governed by isolated clusters. Ferromagnetism in microporous carbon can be associated with the fragments with positive and/or negative curvature. [56].

Carbon nanofoam

The carbon nanofoam produced by bombarding carbon with a high frequency pulsed laser an inert gas displays strong paramagnetic behaviour, that is very unusual for the carbon allotropies [57]. The material contains both sp^2 and sp^3 bonded carbon atoms and exhibits ferromagnetic-like behaviour with a narrow hysteresis curve and a high saturation magnetization. Strong magnetic properties fade within hours at room temperature; however, at 90 K the foam's magnetism persists for up to 12 months and ranges from 0.36 to 0.8 emu/g. The localized unpaired spins are believed to occur because of topological and bonding defects associated with the sheet curvature [58].

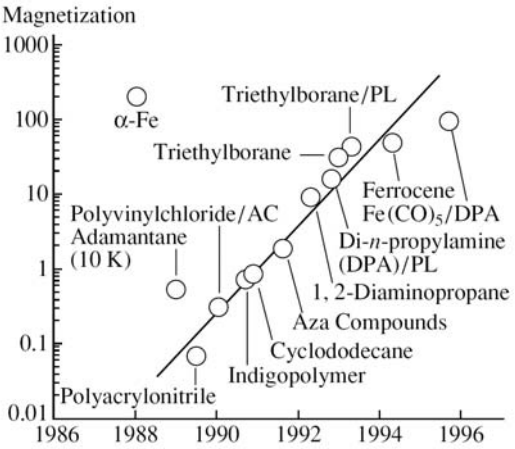

Fig. 13. Values of magnetization of magnetic carbon obtained from various starting materials in the National Institute for Materials Science and Chemical Reactions (Japan). The data for iron and iron-containing carbon are also shown for comparison [59].

Carbonaceous ferromagnetics from organic compounds

Contrary to the previous sections, the results discussed in this section, are poorly reproducible. However, large amount of the publications and similar regularities allow one to state that creation a room-temperature carbon magnet by pyrolysis of organic materials is only a question of technology. Fig. 13 shows the room-temperature magnetization values for carbonaceous materials obtained by pyrolysis of various organic substances. For comparison, the values of magnetization for α-Fe and magnetic carbon synthesized from iron-containing organic substances are also given.

Chain of interacting radicals

Some of the examples of chains of interacting radicals are BIPO and indigo polymers (Fig. 14) [60, 61]. Poly-BIPO featured spontaneous magnetization M = 0.02 emu/g that vanished at a temperature of 420–460 K. In subsequent publications [62, 63], a higher magnetization after phase separation was reported: M = 0.5 emu/g; however, no differences in structural units and chemical properties were detected. The absence of transition-metal impurities was ensured to within 10^{-5} wt % according to the data of inductively coupled plasma (ICP) emission spectroscopy.

A linear polymer based on indigo is magnetic at temperatures as high as 200°C [64]. If the content of iron is 26–28 ppm and of cobalt and nickel is less than 1 ppm, the substance

features saturation magnetization, remanent magnetization, and coercivity equal to $M_s = 0.7$ emu · G/g, $M_r = 0.08$ emu · G/g, and $H_c = 120$ Oe, respectively. If it is assumed that the effect is related to impurities and the organic matrix is nonmagnetic, an amount of 3200 ppm of Fe should be introduced in order to attain the above values of magnetization. The ESR spectrum includes a narrow line with parameters $g = 2.0048$ and $H_{pp} = 7$ G and also a broad band in the high-spin region.

Torrance *et al.* [65] used the reaction of *s*-triaminobenzene with iodine to obtain a black insoluble polymer with ferromagnetic properties that were retained up to a temperature of 700 K but did not recover when cooled owing to thermal decomposition of the sample.

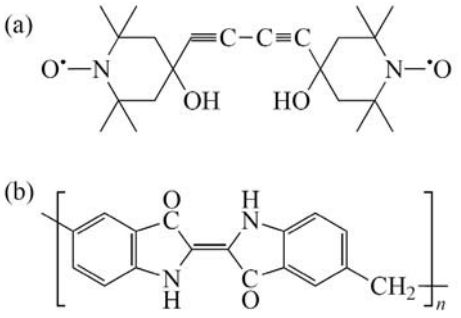

Fig. 14. (a) A BIPO monomer and (b) a unit of indigo polymer.

Structures composed of sp^2 - and sp3-coordinated carbon atoms

The magnetic properties of pyrolytic carbon are of particular interest. Pyrolytic carbon prepared at relatively moderate temperatures (900–1500 K) has a highly oriented structure and contains a large number of unpaired spins in the graphite skeleton, which interact with each other [66]. The material is a 3D structure that is composed of an approximately equal number of sp^2 and sp^3 hybridized carbon atoms.

Pyrolysis of organic compounds at relatively low temperatures yields a highly oriented graphite-like material with a high concentration of unpaired spins. Exchange interaction between spins was observed in some cases.

Using pyrolysis of adamantane (a tricyclo bridged hydrocarbon) at 1000°C in an argon atmosphere, one can obtain a substance that exhibits a pronounced ferromagnetic hysteresis. The parameters $M_s = 0.5$ emu · G/g, $M_r = 0.35$ emu · G/g, and $H_c = 600$ Oe are the results of measurements at 10 K; however, the values of magnetization at 400 K are approximately 1/3 of those given above [67]. According to the ESR data, the concentration of spins amounts to about 10^{21} spin/g at room temperature and with a content of transition metals no higher than 25 ppm. Ferromagnetic carbon based on adamantane was reproducibly obtained by several research

teams. However, the following general rule for unidentified ferromagnetic compounds was confirmed: if two samples are prepared under identical conditions, one of them is found to be ferromagnetic and the other is not [68].

Studies of the structure show that two special features are characteristic of samples with nonlinear magnetization: a highly oriented structure of the material and a high concentration of unpaired electrons: small disorder is introduced in an ideal structure. The diffraction pattern includes peaks at 2Θ= 9°, 17.5°, and 25.5°, which corresponds to an interplanar spacing of 3.49 Å [69].

Pyrolysis at 1000°C was used to obtain magnetic structures from other starting materials as well, i.e., polyvinyl chloride, phenol resins, and a pyren-benzaldehyde polymer [70]. Pronounced magnetic properties (M_s = 1.07 emu/g, M_r = 0.21 emu/g, and H_c = 163 Oe at 4 K) were observed in pyrolytic carbon obtained by heating cyclodecane to 950°C [71]. The above values of magnetization can be interpreted in two ways: either 0.2% of carbon atoms have unpaired interacting spins or the material contains 4800 ppm of iron. ICP emission and the X-ray characteristic radiation indicate that there is no more than 50 ppm of iron in the material and the amount of other metals is below the sensitivity of the methods. The values of magnetization and coercivity at room temperature amounted to 80% of those at 4 K; the material completely lost its magnetic properties after exposure to air for about one month. The ESR spectra of this material were typical of a carbon magnetic structure: a broad line located at about 2940 G and a narrow line with g = 2.0014 and H_{pp} = 6.3 G. The relative contribution of the paramagnetic signal increases with decreasing temperature, and the intensity of the broad-line signal is almost directly proportional to the saturation magnetization.

Carbon structures containing trivalent elements.

Good results are obtained using pyrolysis of nitrogen- containing compounds. The latter exhibit a clearly pronounced isomeric effect: stronger magnets are obtained from branched starting components. In other words, the geometric arrangement of radicals is important for attaining an ordered spin structure. Ferromagnetic molecules $(–CH_2–CH–CN–)_n$ were obtained by pyrolysis of polyacrylonitrile [72]. The triarylmethane resin is a diamagnetic material. However, when this material is synthesized in a magnetic field, a ferromagnet is obtained; this apparently happens owing to radicals that are formed in the course of dehydrogenation [73].

A 3D PIRO-pan structure was obtained by pyrolytic decomposition of polyacrylonitrile [74]. The material was distinguished by a high concentration of spins (10^{23} cm^{-3}), and various samples had a saturation magnetization of 6–15 emu · G/g; the separated magnetic phase was more crystalline than the nonmagnetic phase. Analysis of the impurities using laser-assisted mass microanalysis (LAMMA), secondary-ion mass spectroscopy (SIMS), and electron-emission spectroscopy showed that there were no correlations between the impurity content and magnetization. The majority impurities in ferromagnetic carbon are nitrogen (2.3 at %) and oxygen (4.7 at %).

The magnetic properties of substances obtained by decomposition of a mixture of phenyldiamine and melamine are very sensitive to the decomposition temperature; the best

results obtained as a result of decomposition at 600°C are M_s = 0.624 emu/g, $M_r = 6.65 \cdot 10^{-2}$ emu/g, and H_c = 125 Oe[75]. A substance obtained by pyrolysis of guanine (one of the amino acids of DNA) has similar properties [76]. A dark-red substance with an unusually high saturation magnetization M_s = 10.4 emu/g can be obtained by treating a mixture of triphenoxytriazine TPTA and melamine at 950°C in an argon atmosphere with a certain amount of dry air [77]. The ESR spectrum consists of a very broad line and indicates that the spin concentration amounts to $4.7 \cdot 10^{23}$ spin/g. The intensity of peaks decreases with temperature; however, the integrated intensity remains unchanged owing to an increase in the line breadth H_{pp}. Temperature dependences of the *g*-factor and H_{pp} are nontrivial. Both parameters decrease with temperature, whereas H_{pp} increases with temperature and the *g*-factor is temperature-independent in conventional 3D ferromagnets. The temperature dependence of magnetic susceptibility determined from the ESR data is also unconventional. The temperature dependences of saturation magnetization in magnetic carbon deserve attention: the magnetic properties are temperature-independent up to temperatures that are much higher than 295 K.

The technological conditions and starting organic compounds are extremely important for preparation of ferromagnetic carbon from nitrogen-containing organic compounds. The ratio between the concentrations of hydrogen and carbon [H] and [C] in the starting material is particularly critical [78]. As soon as this ratio exceeds 1.5, a sharp increase in the saturation magnetization of the reaction product is observed. Several dozens of substances were studied; it is believed that atomic hydrogen generated during thermal decomposition is very important from the structural standpoint, since this hydrogen prevents graphitization of the material.

Diaminopropane has the largest value [H]/[C] = 3.3 of all the starting materials studied; the product of pyrolysis features a saturation magnetization of 10.5 emu/g or 0.022 μ_B per carbon atom. The temperature dependence of magnetization does not obey the Curie–Weiss law (Fig. 15). The Curie point is at a temperature higher than 500 K; however, it is impossible to determine this temperature owing to thermal decomposition of the material [79]. Analysis by powder X-ray diffraction, electron diffraction, and transmission electron microscopy have shown that the material is amorphous. Some structural information of the material can be obtained from the FTIR ATR measurements, which prove that the material comprises a mixture of the sp^2 and sp^3 carbons. Other evidence of the mixed structure is: (1) the presence of the aromatic nitrile and heterocyclic compounds, indicating that aromatization and /or heterocyclization occurs in the process; (2) the values of electrical conductivity are much lower than for graphite or sp^2 carbon; (3) STM and AFM observations demonstrate an irregular array of carbon atoms of benzenoid rings.

Studies of a large number of ferromagnetic materials obtained from various nitrogen-containing substances showed that the structure of these materials is most often amorphous and disordered. In order to reveal the structural–magnetic correlations, samples of ferromagnetic carbon were subjected to various doses of plasma treatment, after which the percentage of amorphous carbon and the value of magnetization were measured. A one-to-one correspondence between the above two parameters was observed: the higher the content of amorphous carbon, the higher the spontaneous magnetization [80]. A second tendency was observed in studying ferromagnetic carbon obtained by pyrolysis of polyacrylonitrile: the magnetic properties are

closely related to the presence of various radicals, which are mainly nitroxides that exist at the edges of graphite-like structures [81]. Apparently, a pure ferromagnetic carbon substance has been never separated, but a ferromagnetic phase is typically present in the form of inclusions in the nonmagnetic matrix.

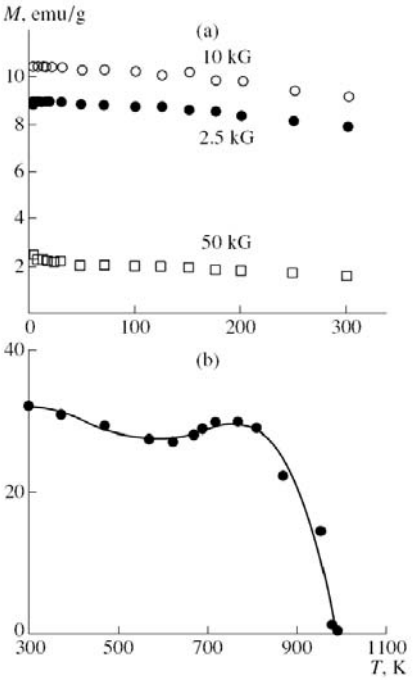

Fig. 15. Temperature dependences of magnetization in magnetic carbon obtained by pyrolysis of (**a**) diaminopropane ($C_3H_{10}N_2$ at 950°C [79] and (**b**) triethylborane ($C_6H_{15}B$) at 810°C [59].

There is a general difficulty in producing organic magnetic materials: complex chemical processes involve a large number of reactions, and the results are hard to reproduce. Despite the fact that the mechanism of origination of ferromagnetism in carbon structures that do not contain metal atoms remains unclear, several dozens of patents for methods of producing these structures have been granted [82. The common feature of these patents is the recommendation to heat organic substances in a complex (steplike) way, sometimes in the presence of a magnetic field, and to stop the processes halfway to graphitization. Another group of patents describes the carbon structures that contain nitrogen, boron, or phosphorus and feature values of magnetization as large as 60 emu/g.

Thus, there are publications that describe technological processes that make it possible to obtain magnetic carbon structures where the ferromagnetic ordering is attained at the π-delocalized spins caused by the presence of a trivalent element in the carbon skeleton. In addition, structures in which alternating sp^2- and sp^3-hybridized carbon atoms that act as elements of different valence can be obtained.

Iron-containing graphite

Studies of meteorite graphite [83] that contained iron-containing minerals showed that the total experimental magnetization exceeded the calculated magnetization by a factor of 1.5 even if overestimated values of the iron contribution were used. The above effect is attributed to ferromagnetic graphite, which constitutes more than half the material of the meteorite and has an average magnetic moment equal to $0.05\mu_B$ per carbon atom. The temperature dependence of saturation magnetization indicates that there are several phase transitions related to iron and iron oxides; however, the phase transition at 570 K is interpreted as corresponding to the Curie temperature of extraterrestrial graphite. It is believed that the most plausible version of magnetic ordering is the inducement of a magnetic moment by ferromagnetic inclusions.

5. NANOTUBES

It has been shown both experimentally and theoretically that the model in [84], which was originally suggested for quasi-2D graphites is applicable to the case of multiple- wall carbon nanotubes [85]. The magnetic properties of single-wall nanotubes are mainly governed by the spin polarization and ring currents that surround a nanotube if the field is directed along the nanotube axis [86]. The experimental value of diamagnetic susceptibility for multiple-wall nanotubes is close to that for misoriented graphite [87]; reliable data for single-wall nanotubes are so far lacking because of the inevitable presence of the catalyst's ferromagnetic particles.

Okada and Oshiyama have reported that ferromagnetic spin alignment was theoretically obtained in some finite zigzag nanotubes. The authors interpreted the result as a consequence of larger exchange splitting than energy loss due to breaking bonding states in some nanotubes. Magnetism strongly depends on the diameter and the chirality of the tube [88, 89].

Nanohorns

Nanohorns are the short single-wall nanotubes closed on one side. The diamagnetic susceptibility for single wall nanohorns indicated a value smaller than that of randomly oriented graphite by an order of magnitude, but showing a magnitude comparable to those of fullerenes. It is suggested that the large diamagnetism expecting for sp^2 networked carbon materials is canceled by the Van Vleck constant paramagnetism [90].

Nanotori

A theoretical study revealed an unusually high paramagnetism of nanotubes that are closed upon themselves to form toroids if the radius of the toroid is equal to a certain "magic" number. The

large paramagnetic moment is due to the interplay between the toroidal geometry and the ballistic motion of the π electrons in the metallic nanotube. [91].

6. FULLERENES

Even in the first publication dedicated to the discovery of fullerenes, it was mentioned that spheroidal clusters should have unusual magnetic properties due to the cyclic delocalization of electrons. However, calculations using the London method showed that the addition to the magnetic susceptibility due to π-electron circular currents was unusually small [92] and was controlled by the relative strength of two non-equivalent molecular bonds.

In subsequent publications, the question of the negligible contribution of the π-electron currents to the magnetic susceptibility of fullerene C_{60} was considered again. It turned out the fact that the π-electron system does not contribute to dielectric susceptibility cannot be used as an indicator of the absence of ring currents [93].

The paramagnetic currents flowing in pentagonal fullerene rings are nearly equal to currents in the benzene ring. However, the paramagnetic contribution of currents in pentagons is completely compensated by the diamagnetic contribution of hexagons [94]. It has been shown that paramagnetic currents in five-membered rings are generated by active motion electrons around double bonds that are adjacent to the vertices of pentagons. [95]. Calculations of chemical shifts at the centres of faces for the series of fullerenes $C_{32} - C_{180}$ confirmed that the regions of aromaticity and antiaromaticity in fullerenes are in fact related to hexagons and pentagons, respectively [96].

Once the hexagons are responsible for the diamagnetic contribution to susceptibility and pentagons are responsible for the paramagnetic contribution, it is reasonable to assume that, as the fullerene size increases (i.e., as the number of hexagons increases and the number of pentagons remains unchanged), the compensating paramagnetic contribution decreases. This means that diamagnetic susceptibility should increase steadily with cluster size and ultimately approach that of graphite.

However, this tendency is observed only for giant fullerenes; as expected, the fullerene C_{5000} has susceptibility equal to that of graphite [97]. The diamagnetic susceptibility of clusters with a number of atoms less than 100 varies randomly, which is attributed to the dependence of the characteristics of bonds in pentagons and hexagons on the structure [98]. It is interesting that electric polarizability increases steadily in the sequence C_{60}-C_{70}-C_{84}, whereas the magnetic susceptibility increases drastically when C_{60} is replaced by C_{70} and then decreases with a further increase in the fullerene size [99].

Experiments (Fig. 16) confirmed both the small value of magnetic susceptibility of C_{60} and the much larger value for C_{60}; these values are $\chi = - 0.35 \cdot 10^{-6}$ and $- 0.59 \cdot 10^{-6}$ emu/g for C_{60} and C_{70}, respectively. The temperature dependences of magnetic susceptibility are typically expressed as the sum of diamagnetic and paramagnetic terms; the paramagnetism is related to intercalated oxygen. There is no paramagnetic contribution to susceptibility in single crystals that were grown under special conditions and were never in contact with oxygen [100]. At the same

time, there is evidence that paramagnetism is related not only to oxygen but also to intrinsic defects, for example, ions. A drastic change (jump) in susceptibility is observed at the point of orientational phase transition. This jump is attributed to a change in the shape of the molecule, which is caused by intermolecular collective interaction. It was also reported that high-resolution measurements of magnetization in C_{60} and C_{70} powders revealed additional phase transitions interpreted as transitions to the spin glass state [101].

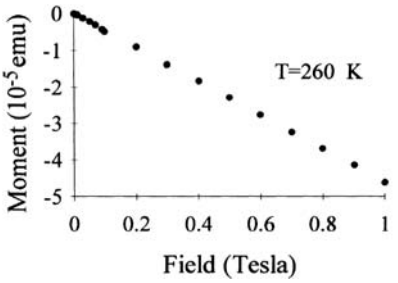

Fig. 16. Total magnetic moment, m, of the single crystal C_{60} as a function of applied field. The susceptibility, from the slope of the straight line, is $\chi = -4.6 \cdot 10^{-9}$ in the cgs units [100].

Fullerenes Polymerized by irradiation

The ferromagnetism of polymerized fullerenes was reported for the first time in 1996. The exposure of C_{60} crystals to high-intensity light from a xenon lamp in the presence oxygen gives rise to a nonlinear field dependence of magnetization with a pronounced hysteresis [102]. A similar result was obtained in a repeat experiment: the samples were exposed to radiation from a xenon lamp with intensity I = 10 mW/cm2 for 30 days. The control powder was irradiated in a sealed evacuated cell; changes in the magnetic properties were not detected to within the measurement accuracy [103].

A starting van der Waals fullerene crystal is diamagnetic. The susceptibility is almost temperature-independent, except at low temperatures, where the paramagnetic term $\chi_p \sim 1/T$ becomes important. The exposure of fullerene to oxygen in the dark increases the magnitude of the Curie paramagnetism, which is most likely caused by intercalated oxygen; a certain paramagnetic contribution can be made by defects in fullerene. The temperature dependence of magnetic susceptibility is changed radically if the crystals under investigation are exposed to visible light in the presence of oxygen. In this case, magnetic susceptibility changes its sign and becomes positive in the entire temperature range. The susceptibility increases with the exposure time.

Fullerenes irradiated in the presence of oxygen feature a nonlinear magnetization curve. The saturation magnetization increases with the irradiation time (see Fig. 17).

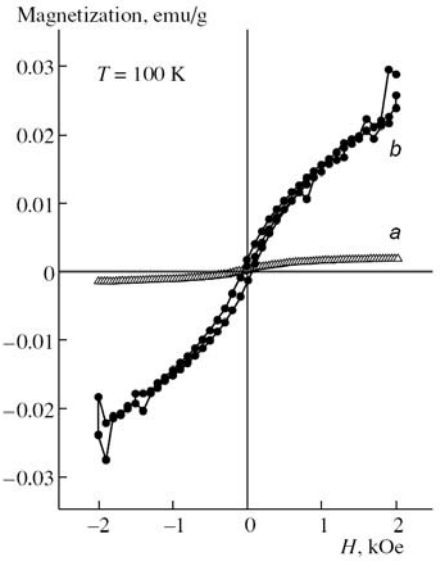

Fig. 17. Magnetic properties of phototransformed fullerenes. Magnetization loops for the C_{60} powder exposed to light in the presence of oxygen for (a) 48 and (b) 720 h [103].

Plots of magnetization as a function of magnetic field are almost identical at 5 K and at room temperature. At still higher temperatures, magnetization begins to decrease but remains finite at temperatures as high as 500 K.

The amount of polymerized material that can be obtained by photopolymerization is inevitably small. Photons with energies in the range of band-to-band transitions are required for polymerization. A strong absorption corresponds to band-to-band transitions; as a result, the penetration depth of radiation is very small and amounts to 100–500 fullerene layers for different wavelengths. If C_{60} powder with a grain size of ~10 μm is irradiated, phototransformation affects only 1% of the fullerene volume. The values of the magnetic moment reported are very small and are no larger than 0.001 μ_B per fullerene. One can enhance the magnetization by dissolving the crystal in toluene. As a result, an unreacted part of the fullerenes is removed and the value of magnetization is increased by two orders of magnitude (to 0.1 μ_B per fullerene molecule). X-ray and Raman studies show that the concentrated ferromagnetic phase is the mainly the orthorhombic phase of polymerized C_{60}.

Studies aimed at visualizing the magnetic response have been carried out. C_{60} films were subjected to radiation from an argon laser with photon energy $h\nu$= 2.4 eV and a power density of I = 1 W/cm2; the radiation dose amounted to 10^5 photons per C_{60} molecule.

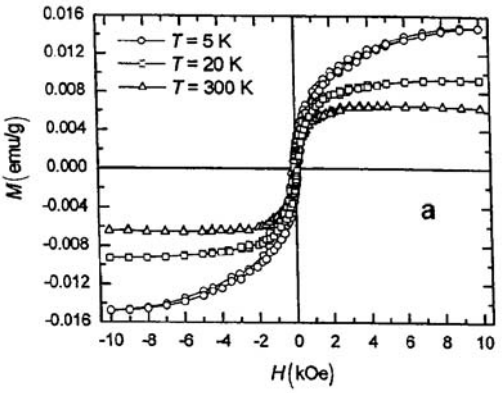

Fig. 18.. Magnetization of C_{60} powder subjected 254 nm ultraviolet radiation for 4 h. in flowing oxygen to as a function of dc magnetic field at 5, 20, and 300 K measured using a SQUID magnetometer [104].

There were no magnetic domains in the starting C_{60} films. Several topographic inhomogeneities were detected within the unexposed area. However, these inhomogeneities did not produce any signal in the magnetic microscopy. In contrast, a weak (but nontrivial) magnetic signal from the laser-irradiated area was detected.

The largest magnetic-field gradient is attained at the grain centre and at the grain boundary; evidently, magnetism of the layers is caused by some of the structural changes described above. The grain boundaries are imperfect regions that contain dangling interfullerene bonds. It cannot be excluded that damaged molecules or even fragments of a destroyed fullerene cage are present at the grain boundaries; however, the number of the above fragments is evidently small since they are not detected by spectroscopic methods.

The electron paramagnetic resonance spectrum of C_{60} photolyzed in the presence of a low pressure of oxygen or in air shows a very broad, asymmetric derivative signal at room temperature and at a magnetic field position well removed from g=2.000. With decreasing temperature, the broad line shifts to lower magnetic fields and increases further in linewidth, as expected for a ferromagnetic resonance signal. A low-field nonresonant derivative signal is also observed, consistent with the existence of ferromagnetism. Ferromagnetism up to room temperature in photolyzed C_{60} is confirmed unequivocally by superconducting quantum interference device measurements of the dc magnetization as a function of magnetic field (Fig. 18) [104].

Fullerenes Polymerized Under Pressure

A magnetically ordered phase is also formed in the case of polymers obtained under pressure. This phase was observed for the first time in rhombohedral C_{60} (*Rh*-C_{60}) prepared under a pressure of 6 GPa in a very narrow temperature range (slightly higher than 1000 K). The highest

magnetization was obtained for the sample prepared at 1075 K [105]. The magnetization curves measured in the magnetic-field range –2 kOe < H < 2 kOe were practically identical at temperatures of 10 and 300 K, the Curie temperature was 500 K. The remanent magnetization in both cases was equal to M_r = 0.015 emu/g, and the coercivity was H_c = 300 Oe. Saturation of magnetization is observed in the fields with a strength of ~$2 \cdot 10^4$ Oe. If the experimental value of the spin concentration $n = 5 \cdot 10^{18}$ cm^{-3} is used, the magnetic moment can be estimated as 0.4 μ_B per electron.

The results of this study were verified and confirmed by Narozhnyi *et al.* [106]. A series of samples were produced under a pressure of 6 GPa and at temperatures of 925–1125 K. Nonlinear magnetization was observed only in five out of eight samples that were prepared in the very narrow temperature range 1000 K < T < 1065 K. One of the samples prepared at 1055 K featured magnetization that exceeded the value given above by a factor of 4; the Curie temperature was T_C = 820 K.

Experiments on the polymerization of fullerenes were also carried out at other pressures. A paramagnetic polymerized fullerene phase is formed at a pressure of 2.5 GPa, which is favorable for the origination of the tetragonal phase (often not alone but mixed with the rhombohedral phase). Evidence of magnetic ordering was observed in the sample prepared in the temperature range 1000 K < T < 1075 K [106]. The largest magnetic signal was obtained in the sample polymerized at 1025 K. The samples prepared at temperatures higher than 1100 K were diamagnetic, much like graphite or nonpolymerized fullerene

It was found that the duration of polymerization considerably affects the possibility of obtaining samples with evidence of ferromagnetism. The number of unpaired spins increases in the course of the first several minutes of treatment under pressure, then attains a maximum, and finally starts to decrease. Consequently, the magnetic properties are very sensitive to the duration of preparing the samples, so that optimal conditions for obtaining the ferromagnetic phase should be sought in the 3D p–T–t space [108].

An increase in the pressure to 9 GPa leads to similar results. The samples are diamagnetic if the polymerization temperature is below 800 K; however, if the temperature exceeds 800 K, a pronounced magnetic hysteresis is superimposed on the paramagnetic signal. If the polymerization temperature is too high, a sharp transition to diamagnetism is observed; a poorly pronounced hysteresis loop can be recognized against the background of this transition [109]. A sharp decrease in the ferromagnetic contribution to the magnetic response and the transition to diamagnetic behavior are observed when studies of the structure indicate the onset of destruction of fullerene cages.

The pressure and temperature conditions at which ferromagnetic fullerenes were synthesized, are collected in Fig. 19. These points were obtained in several different groups and by different methods: Toroid-type or piston-cylinder apparatus. In each case the results were obtained only around the “magic line” of the diagram.

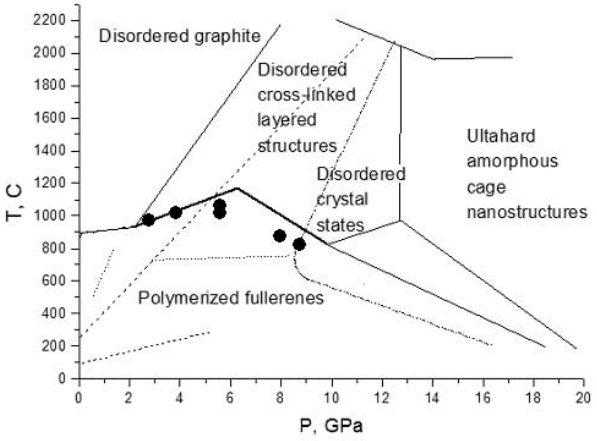

Fig. 19. Map of pressures and temperatures required for preparation of various carbon phases from C_{60} fullerenes [Adapted from 118]. Large closed circles indicate the conditions under which the phases exhibiting spontaneous magnetization were obtained.

Magnetic Domains in Polymerized Fullerenes

Magnetic-force microscopy (MFM) was used to identify three types of regions in the ferromagnetic fullerene samples; these regions differ in magnetic properties [110].

In region *A* (Fig. 20, a), the amplitude of surface roughness does not exceed 60 nm and the presence of domains does not correlate with the topography in any respect. The direction of magnetization is inclined to the surface. The domain walls are almost parallel to each other. There are two types of domains: wide (~2 μm) and narrow (~0.6 μm); however, the length of domains is always ~20 μm. Region *B* (Fig. 20,, b) contains undulatory domains.

Here, one can detect a certain correlation between the topology and the magnetism: the main peaks in the topographic and magnetic images coincide with each other. A comparison of the AFM and MFM results shows that the largest gradient of magnetic forces is observed at the crystallite boundaries, where the magnetization direction is nearly perpendicular to the surface. Region *C* occupies 70% of the area; none of the magnetic domains are observed in this region.

If an external magnetic field **B** is applied parallel to the surface in a situation where the direction of domains is inclined or perpendicular to the sample surface, the magnetization direction will change. This behavior is further proof that the origin of the signal is intrinsic.

Indeed, an application of a field of 0.01 T radically affects the image in regions *A* and *B*; however, the image contrast is not affected by the field in any way. The images in the regions *A* and *B* are also affected if the magnetic-field direction is changed to the opposite direction.

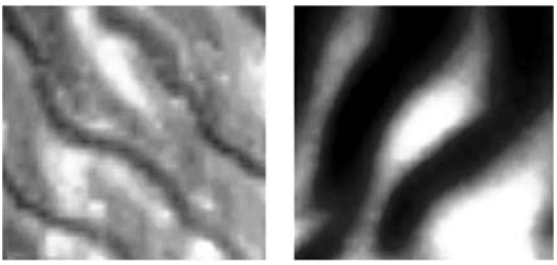

Fig. 20. Images of the magnetic-field gradient in an impurity-free polymerized fullerene. Region *A* (10×10 μm^2) includes parallel magnetic domains on the smooth crystallite surface. Region *B* (2.5×2.5 μm^2) m2) includes the domains at the boundaries of crystallites.

The area occupied by domains of types *A* and *B* amounts to 30% of the total area of the impurity-free zone studied. Thus, polymerized C_{60} constitutes a mixture of magnetic and nonmagnetic portions, so only a part of the sample makes a contribution to the total magnetization.

Ferromagnetism in Other Fullerene Structures

The characteristic features of ferromagnetic behaviour at room temperature have been observed not only in polymerized fullerenes but also in other fullerene-based structures. The report on a solution of organic polymers into which fullerene was introduced by ultrasonic dispersion was one of the first [111]. After condensation of the solution, there remained a film of a fullerene-containing polymer with ferromagnetic properties that were attributed to the adduct radicals $C_{60}R_n$ (R = H, F, CF_3).

The hybrid fullerenes $C_{60}H_{36}$ obtained by transfer hydrogenation had saturation magnetization M_s = 0.04 emu/g at room temperature; it is noteworthy that all the other compositions were found to be diamagnetic [112]. Ferromagnetism was also observed in the $C_{60}H_{24}$ structure [113]. Twelve samples of $C_{60}H_x$ ($24 \leq x \leq 32$) were prepared under pressure with an excess of hydrogen; each sample exhibited a nonlinear magnetization curve and a coercivity of about 100 Oe. The saturation magnetization was typically very small; however, three samples exhibited saturation magnetization that was much higher than that in the remaining samples of the batch: 0.046, 0.054, and 0.16 μ_B /C_{60}.

These samples were synthesized under identical conditions and had the same composition $C_{60}H_{24}$ and an *fcc* crystal structure. The ferromagnetic properties of hydrogenated fullerenes become less pronounced with time. The samples are found to be diamagnetic over a period of a year, and analysis of the samples detects no changes either in the composition or in the crystal structure. The curves $M(H)$ are identical in the range 80–300 K, and the Curie point is much higher than room temperature; this behavior (as in the case of polymerized fullerenes) is inconsistent with small values of magnetization.

To explain this fact, one could consider various models based on ferrimagnetism, the canting of magnetic moments, or weak ferromagnetism. However, the evolution to the diamagnetic (rather than the antiferromagnetic) state and the appreciable spread in the values of magnetization from sample to sample count in favour of magnetic islands in a nonmagnetic matrix.

7. THE ROLE OF IMPURITIES IN THE MAGNETISM OF CARBON STRUCTURES

The main question arising in studies of magnetism in carbon structures is related to the role of metallic impurities. *Caveat emptor* [114] (caution against error) was first expressed at the early stages of research on organic magnetic materials and retains its validity to the present day. Iron makes up 5% of the earth's crust, whereas carbon less than 0.01%. Any household organic material contains several tenths of one percent of iron, although this circumstance does not transform the organic substance into a ferromagnetic material. All the publications cited here include an analysis of impurities and the following basic arguments. If the iron impurity atoms, whose content typically amounts to 20–100 ppm, are distributed uniformly in the material, they cannot make a contribution to the magnetization owing to the large interatomic distances and the resulting impossibility of exchange interactions. If it is assumed that ferromagnetic properties are caused by the clusterization of iron atoms under specific experimental conditions, the calculated resulting magnetic moment (taking into account all metal atoms) is always found to be smaller than the experimental value by one to three orders of magnitude.

An impurity-based model cannot explain the dependences of magnetic properties on technology, the concentrations of hydrogen or oxygen, the isomeric composition, crystallinity, and the hybridization of carbon atoms.

In order to maintain objectivity, we note immediately that magnetic properties can be greatly affected by a mechanical effect without any changes in the elemental composition. Effects such as pressure, grinding, and pulverization generate radicals and are conducive to a more uniform distribution of impurity iron clusters. A specially prepared ultradisperse powder will be attracted to a magnet; we verified this effect in coal, glass, aluminium, grass, and peat.

Special additives of iron to activated carbon showed that the effect of iron did not manifest itself if the iron content is lower than 6–8% [115]. Decomposition of a PDA organic substance with various values of iron content (from 3.5 to 2200 ppm) was also studied; magnetic properties of the reaction products were analyzed. A sharp transition from the diamagnetic to paramagnetic states and a nonlinear magnetization curve were observed when the content of iron in the starting material was changed from 2000 to 2100 ppm [116].

The report on ferromagnetism in fragments of the Canyon Diablo giant meteorite [83] makes one reconsider the problem of carbon magnetism. In that study, magnetic properties of graphite with inclusions of magnetite were considered. Graphite is a semimetal, whereas magnetite is a half-metal; equalization of the chemical potential for electrons with differing spin orientations at the interface leads to the complete spin polarization of neighbouring carbon atoms. If the spin-related splitting of graphite energy bands amounts to several electronvolts, the Fermi level shifts to the region with a higher density of states and sustains the spin polarization. Thus,

the magnetite inclusions are found to be surrounded by a region of spin polarization. The idea of induced magnetism in graphite is very attractive from both the theoretical and the practical standpoints. If the model is correct, one can obtain lightweight, inexpensive, and biocompatible magnetic materials by introducing a small amount of iron into carbon structures.

It is difficult to apply the model under consideration to polymerized fullerenes. Ferromagnetic domains were observed in regions with linear dimensions of about 250 μm, where only carbon atoms were detected to within the measurement accuracy of 1 ppm. The question arises as to whether the source of magnetic contrast in "impurity-free" regions can still be related to impurities. One cannot expect the fields to extend for hundreds of micrometers from iron grains if there are no external fields (the above grains are no more than a micrometer in size). Let us still assume that the distant iron-impurity atoms can give rise to an external field (hypothesis *1*). It is noteworthy that magnetic domains can appear only in a magnetic material; however, elemental analysis shows that the material consists only of carbon to within an accuracy of 1 μg/g. Let us then accept another hypothesis: iron acts as a trigger that transforms carbon into a magnetic material (hypothesis *2*). The effect of magnetic proximity can be observed at distances as large as 100 nm from inclusions of magnetic material. The distance to the nearest impurity cluster exceeds 0.1 mm in the regions occupied by magnetic domains. In the direction perpendicular to the plane, impurities were not detected within the characteristic depth available for analysis by particle-induced X-ray emission (PIXE); this depth is approximately equal to 35 μm. Another hypothesis is based on the assumption that macroscopic magnetism in polymerized C_{60} is ensured by impurities whose amount is smaller than 1 μg/g; if this hypothesis (hypothesis *3*) is not accepted, one then has to state that pure carbon is a magnetic material [110].

Models of magnetism in fullerenes

As shown above, the models of magnetism in carbon structures are diverse. These models range from those based on calculations of an ideal graphite–diamond structure with ferromagnetic interaction or on ferromagnetism due to topological defects in the graphite structure to those based on the magnetic-proximity effects induced by metallic impurities. Nevertheless, it cannot be stated with confidence which of the models can be applied to the experimental facts described above. Polymerized C_{60} is a comparatively simple structure; it is conceivable that investigation of this structure can furnish insight into the mechanisms of origination of magnetic ordering in carbon.

The first attribute of fullerene polymerization consists in the transformation of sp^2 hybridized fullerenes into a structure that contains alternating sp^2 and sp^3 hybridized atoms.

The second special feature of polymerization consists in the specific orientation of molecules. It has been shown repeatedly that it is the orientation of C_{60} that plays the most important role in the origination of exchange interaction.

The third special feature is not a characteristic of polymerization but rather is typical of specific processes that occur during experiments. These processes include the formation of a ferromagnetic phase under conditions that are very close to those of the destruction of fullerenes. Two types of defects may be considered: defects of the molecule itself and defects formed as a result of the disruption of interfullerene bonds. Both types of defects are characteristic of both

fullerenes polymerized under pressure and the phototransformed phase; therefore, one should not disregard either of these possibilities.

The hypothesis about undamaged fullerenes is supported by the following facts. In the case of fullerenes polymerized under a high pressure, the temperature of formation of the ferromagnetic phase is approximately 100 K lower than that of the collapse of the fullerene cage. Bonds connecting molecules in the polymer phase are much weaker than those of the cage itself. These bonds are considered diamond-like, although they are much weaker than those in diamond, are directed at right angles to each other rather than at 109.45° (as in diamond), and are destroyed as a result of heating to 560 K. It is quite possible that it is these bonds that constitute the weak point in the polymerized structure and can be a source of unpaired spins.

Ferromagnetism was observed not only in fullerenes on the verge of collapse but also in structures where the integrity of the cage was unquestionable: in hydrated fullerenes, compounds containing palladium, and disperse C_{60} in the polymer matrix.

The situation where some of the molecules are destroyed or damaged should be also considered.

It was initially stated [105] that magnetism ceases to exist completely as a result of depolarization; however, this statement was later corrected [117]. Magnetization decreases irreversibly after annealing; however, this decrease is specific for each sample. One of the samples lost only 2% of magnetization, and the X-ray diffraction patterns remained unchanged after annealing and corresponded as before to the rhombohedral phase of polymerized C_{60}. This result is nontrivial since the rhombohedral phase is typically depolymerized at 560 K. It is likely that the phase formed under critical conditions features enhanced structural stability accompanied by magnetic stability.

It seems that the irradiation of fullerenes with visible and ultraviolet light should not affect the integrity of the molecules themselves. However, it has been repeatedly reported that photoexcitation of a $C_{60} - O_2$ system leads to the formation of carbonyl structures and, if the light intensity is high, to the dissociation of carbon molecules and formation of amorphous carbon. If it is assumed that the change in magnetic properties of fullerene films is caused by defects, the parallel between the magnetism of fullerenes polymerized by exposure to light and pressure then becomes clear. Let us consider a diagram of the pressures and temperatures required to produce polymerized fullerenes [118]. In this diagram, one can find regions that correspond to the formation of orthorhombic, tetragonal, and hexagonal polymerized phases. It is also possible to determine the conditions under which the fullerene cage is broken with the formation of several postfullerene phases. The closed circles indicating the conditions for observing the ferromagnetic behavior of fullerene materials are located in the critical region (see Fig. 19). The arrangement of these circles follows the run of the line that separates polymerized fullerenes from destroyed fullerenes.

In the models of ferromagnetic fullerenes, the following possibilities are considered: (i) a fraction of the fullerene cages are broken, and, thus, unpaired electrons appear at the dangling bonds; (ii) the shape of the fullerene cage changes as a result of Stone–Wales transformations; and (iii) fullerenes remain intact, but unpaired electrons are formed at interfullerene links. In an alternative approach, a high-spin ground state of charged fullerene polymer is considered; this state arises owing to the contribution of electron correlation to the total energy [119].

Structural defects in fullerene cages

In a theoretical paper [120], Andriotis *et al.* suggested a scenario in which structural defects (vacancies) and sp^3 -hybridized atoms interact (Fig. 21). A correlation should exist between spin moments for magnetic ordering to appear. Since the defects are widely spaced, interaction between them is indirect and needs a mediator. The dipole moment induced by a vacancy can play the role of such a mediator. The Coulomb interaction between localized excess charges and electric dipoles ensures a means for the exchange interaction between magnetic moments.

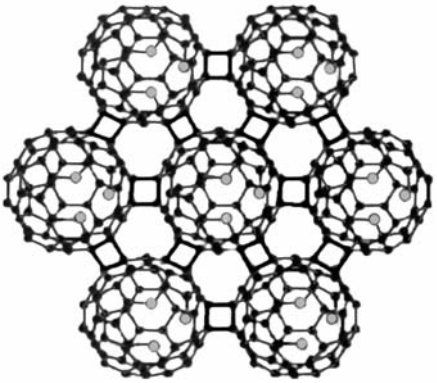

Fig. 21. Model of interaction between defects in rhombohedral C_{60}. The atoms surrounding the defect (a carbon vacancy) are shown as large gray circles.

The cage of a C_{60} fullerene can be made open by a sequence of Stones–Wales transformations that require lower energies than the breakage of the bonds. As illustrated in Fig. 22, a sequence of five transformations converts fullerene to a fragment of a nanotube. Of the first three intermediate states, referred to as *SW*-I, *SW*-II, and *SW*-III, the first is antiferromagnetic and the second is ferromagnetic. In order to verify this identification, the distribution of spins was considered for various configurations. The spin density is highest at the sites where a zigzag-type edge with dangling bonds is formed. The degree of overlap of electron clouds in the *SW*-II structure is lower than in the *SW*-I structure, so the ferromagnetic ordering in *SW*-II is stabilized.

The result of calculations is consistent with previous concepts about the formation of a partially filled flat band that gives rise to magnetic instability. The difference between this and graphite ribbons consists in the fact that the total moment does not attenuate in this structure. It is predicted that, in the case of open nanotubes with a specific configuration, the effect should be much more pronounced than in the case of fullerenes [121].

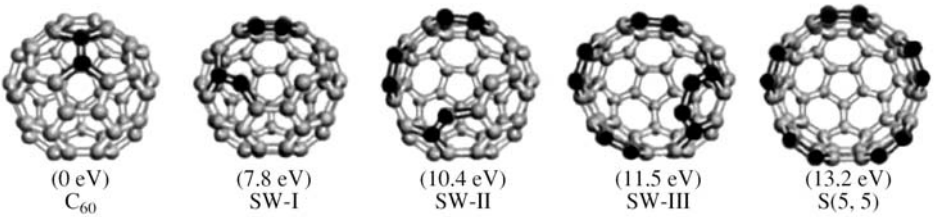

Fig. 22. Models of intermediate metastable structures formed as a result of the transformation of C_{60} into a segment of an open (5, 5) nanotubes according to the Stone–Wales reactions. The atoms involved in the reactions are depicted by closed circles. The initial fullerene and the final *SW*-III structure are nonmagnetic; the structure *SW*-I is antiferromagnetic and the structure *SW*-II is ferromagnetic [121].

C_{60} as a magnetic coupling unit

Several studies have indicated that ferromagnetism can be an intrinsic property of polymerized C_{60} provided that it is polymerized under special conditions. Usual C_{60} polymers do not exhibit peculiar magnetic properties [122]. Okada and Oshiyama have checked the possibility of different bonding (single or double) between the C_{60} molecules in a polymeric network and shown that that polymerized structures attained at the double bonds are semiconducting whereas polymerized structures attained at single bonds are metallic. In the latter case a substantial density of states at Fermi level is formed, nevertheless, the C_{60} polymers do not exhibit any magnetic ordering [123].

However, the situation can be changed if the polymers are synthesized under special conditions. Theoretical *ab initio* computations on C_{60}–C_{60} dimers have shown that under the influence of an external pressure the C–C bonds become shorter. After some distance the triplet state which becomes more stable than the singlet state [124]. The triplet state is preserved after releasing the pressure.

The ability of C_{60}-fullerene to act as a magnetic coupling unit between radical centers has been evaluated using *ab initio* method. The results indicate that functionalized C_{60}-fullerenes have a very good potential to couple radical centers. Depending on the relative position of the two radical centers, the resulting interaction is ferro- or antiferromagnetic [125].

The phenomenon of fullerene ferromagnetism can be understood within the model of charged fullerene dimers. The charge sources could be broken interfullerene bonds, partially destructed fullerene cages or various defects and impurities. It is important that the impurities do not have to be magnetic: even carbon impurity in the all-carbon network can act as a magnetic trigger. Singlet state is energetically preferable for a neutral dimmer. However, the charged dimer in the triplet state has lower energy compared to the singlet state, and, therefore, the ground state of a charged dimer is triplet. Finally, the stable charged fullerene dimer $(C_{60})_2^{-1}$ does exist and has a reasonable bond length. On the basis of these numerical findings, the authors suggest the following physical mechanism of ferromagnetism in fullerene polymers: The high-spin ground state of fullerene units is stabilized by the presence of by donor impurities, or any other mechanisms of microscopic electric charge inhomogeneities. The fullerene clusters, dimer being

the simplest possibility, turn out to be charged and their ground state is magnetic. According to the experimental results, we deal with the elemental carbon impurity appeared due to (i) exceeded temperatures for the pressure polymerization; (ii) presence of oxygen under phototransformation [126].

8. POSSIBLE APPLICATIONS OF MAGNETIC CARBON

Two main reasons advance further studies of magnetic carbon. The first one is scientific curiosity: what cases magnetic behavior in a structure made of atoms that have no magnetic moment. Electronic instabilities in pure carbon are predicted to lead to various types of ordering, from ferromagnetic to superconducting, and carbon structures promise many surprises yet to come. Second, new materials have always been a dominant factor in driving advances in material usage.

Several scenarios that account for (or predict) the magnetism of carbon have been suggested: volume magnetism of an ideal structure that contains alternating sp^2- and sp^3-hybridized atoms, induced magnetism, and atomic-scale magnetism caused by structural imperfection.

If it is technologically feasible to produce a bulk carbon magnetic material in a macroscopic amount, one can then expect applications of this material in engineering, as well as in medicine and biology as a unique biocompatible magnetic material. An ideal structure containing alternating sp^2 and sp^3 hybridized carbon atoms theoretically exceeds the specific magnetization of α-Fe, making the system potentially attractive. Magnetic carbon materials are suitable as toner for copiers and other business machines; they are welcome in medicine, for example, in drug delivery systems: it is a biocompatible magnet. Possible high-tech applications include computer memory devices or spintronic devices, taking into account their semiconducting properties. Magnetic fullerenes together with carbon nanotubes can be used as building blocks in the all-carbon integrated circuits.

If the phenomenon of carbon magnetism is basically related to the boundary states, then further development of this effect can be expected in the field of nanotechnology; specifically, it was suggested that open nanotubes be used as nanodimensional magnets. The experimentally observed possibility of changing the magnetic properties of fullerenes and graphite by irradiating these materials can be used to produce magnetic patterns by nanolithography.

Since the industrial revolution, manufacturing has been creating wasteful by-products, usually harmful to life and expensive to disarm. Carbon is a material that meets the demands for environmental protection, public health and safety. New materials have always been a decisive factor the development of new technologies. The publications cited in this review show that the properties of carbon, which is the main element in all creatures, are far from fully understood.

REFERENCES

[1] S. Hudgens, M. Kastner, and H. Fritzsche, Phys. Rev.Lett. 33, 1552 (1974).
[2] J. C. Slonczewski and P. R. Weiss, Phys. Rev. 109 (1958) 272.
[3] J. W. McClure, Phys. Rev. 108 (1957) 612.
[4] M. P. Sharma, L. G. Johnson, and J. W. McClure, Phys. Rev. B 9 (1974) 2467.
[5] S. J. Williamson, S. Foner, and M. S. Dresselhaus. Phys. Rev. 140 (1965) A1429.
[6] N. Ganguli, K. S. Krishanan, Proc. R. Soc. London 177 (1941) 168.
[7] G. Wagoner, Phys. Rev. 118 (1960) 647.
[8] J. Heremans, D. Olk, and T. Morell, Phys. Rev. B 49 (1994) 15122.
[9] P. Esquinazi, A. Setzer, R. Hohne, C. Semmelhack, Y. Kopelevich, D. Spemann, T. Butz, B. Kohlstrunk, M. Losche, Phys. Rev. B 66, (2002) 024429.
[10] M. F. Ling, T. R. Finlayson, and G. L. Raston, Aust. J. Phys. 52 (1999) 913.
[11] V. Likodimos, S. Glenis, N. Guskos, and C.L. Lin, Phys. Rev. B 68 (2003) 045417.
[12] A. A. Ovchinnikov and L. I. Shamovsky, J. Mol. Struct.:THEOCHEM 251 (1991) 133 .
[13] E. H. Lieb, Phys. Rev. Lett. 62 (1989) 1201.
[14] A. Mielke and H. Tasaki, Commun. Math. Phys. 158 (1993) 341.
[15] S. G. Lebedev. Nucl. Instr. Meth. A 521 (2004) 22.
[16] Y. Kopelevich, P. Esquinazi, J.H.S. Torres, and S. Moehlecke, J. Low Temp. Phys. 119 (2000) 691.
[17] J. Gonzalez, F. Guinea, and M. Vozmediano, Phys. Rev.B 63, 134 421 (2001).
[18] K. Kobayashi, Phys. Rev. B 48 (1993) 1757.
[19] N. Shima and H. Aoki, Phys. Rev. Lett. 71 (1993) 4389.
[20] H. Kajii, K. Yoshino, T. Sato, and T. Yamabe, J. Phys. D: Appl. Phys. 33 (2000) 3146.
[21] H. Takeda, H. Kajii, and K. Yoshino, Jpn. J. Appl. Phys., Part 1, 41 (2002) 3782.
[22] D. J. Klein and L. Bytautas, J. Phys. Chem. A 103 (1999) 5196.
[23] K. Yoshizawa, K. Okahara, T. Sato, et al., Carbon 32 (1994)1517.
[24] K. Nakada, M. Fujita,G. Dresselhaus, M. S.. Dresselhaus. Phys. Rev. B 54 (1996) 17954-17961.
[25] K. Wakabayashi, M. Fujita, H. Ajiki, and M. Sigrist, Physica B 280 (2000) 388.
[26] O. E. Andersson, B. L. V. Prasad, H. Sato, T.Enoki, Y. Hishiyama, Y. Kaburagi, M. Yoshikawa, and S. Bandow, Phys. Rev. B 58, 16 387 (1998).
[27] A. Nakayama, K. Suzuki, T. Enoki, S. L. Divittorio, M. S. Dresselhaus, K. Koga, M. Endo, N. Shindo. Synth. Met. 57, 3736 (1993).
[28] K. Wakabayashi, M. Fujita, K. Kusakabe, and K. Nakada, Czech. J. Phys. 46, 1865 (1996).
[29] M. Fujita, K. Wakabayashi, K. Nakada, and K. Kusakabe, J. Phys. Soc. Jpn. 65, 1920 (1996).
[30] K. Wakabayashi, M. Sigrist, and M. Fujita, J. Phys. Soc. Jpn. 67, 2089 (1998).
[31] K. Wakabayashi and K. Harigaya, J. Phys. Soc. Jpn. 72, 998 (2003).
[32] K. Kusakabe and M. Maruyama, Phys. Rev. B 67, 092 406 (2003).
[33] K. Kusakabe and Y. Takagi, Mol. Cryst. Liq. Cryst. 387, 231 (2002).

[34] M. Maruyama, and K. Kusakabe,J. Phys. Soc. Jpn. 73 (2004) 656.
[35] K. Harigaya, J. Phys.: Condens. Matter 13, 1295 (2001).
[36] K. Harigaya, Chem. Phys. Lett. 340, 123 (2001).
[37] Y. Shibayama, H. Sato, T. Enoki, and M. Endo, Phys.Rev. Lett. 84, 1744 (2000).
[38] T. Enoki, N. Kawatsu, Y. Shibayama, H.Sato, R. Kobori, S. Maruyama, and K. Kaneko, Polyhedron 20, 1311 (2001).
[39] N. Kobayashi, T. Enoki, C. Ishii, K.Kaneko, and M. Endo, J. Chem. Phys. 109, 1983 (1998).
[40] S. Chehab, K.Guerin, J. Amiell, and S. Flandrois, Eur. Phys. J. B13 (2000) 235.
[41] H. Sato, N. Kawatsu, T. Enoki, M.Endo, R. Kobori, S. Maruyama, and K. Kaneko, Solid State Commun. 125, 641 (2003).
[42] K.Harigaya, A. Yamashiro, Y. Shimoi, K. Wakabayashi, Y. Kobayashi, N. Kawatsu, K. Takai, H. Sato, J. Ravier, T. Enoki, and M. Endo. J. Phys. Chem. Solids 65 (2004) 123.
[43] K. Harigaya, Chem. Phys. Lett. 339, 23 (2001).
[44] K. Harigaya and T. Enoki, Chem. Phys. Lett. 351, 128 (2002).
[45] A. J. Stone and D. J. Wales, Chem. Phys. Lett. 128, 501 (1986).
[46] M. Igami, K. Nakada, M. Fujita, and K. Kusakabe, Czech. J. Phys. 46, 2715 (1996).
[47] N. Park, M. Yoon, S. Berber, J. Ihm, E. Osawa, and D. Tomanek. Phys. Rev. Lett. 91 (2003) 237204.
[48] P. O. Lehtinen, A. S. Foster, A. Ayuela, A. Krasheninnikov, K. Nordlund, R. M. . Nieminen, Phys. Rev.Lett. 91, 017 202 (2003).
[49] A. Oshiyama, S. Okada, and S. Saito, Physica B (Amsterdam) 323, 21 (2002).
[50] S. Okada and A. Oshiyama, Phys. Rev. Lett. 87, 146803 (2001).
[51] K. V. Bozhenko and A. A. Ovchinnikov, Synth. Metals 71 (1995) 1803.
[52] Magnetism: Molecules to Materials, Ed. by J. S. Miller and M. Drillon (Weinheim, New York, 2002), Vols. 1–4.
[53] P. Esquinazi, D. Spemann, R. Hohne, A. Setzer, K. H. Han, and Butz T. Phys. Rev. Lett. 91 (2003) 227201.
[54] K. H. Han, D.Spemann, P. Esquinazi, R. Hohne, V. Riede, and T. Butz. Adv. Mater. 15 (2003) 1719.
[55] P. O. Lehtinen, A. S. Foster, Yuchen Ma, A. V. Krasheninnikov, R. M. Nieminen, Phys. Rev. Lett (2004), in press.
[56] Y. Kopelevich, R. R. da Silva, J. H. S.Torres, A. Penicaud, T. Kyotani. Phys. Rev. B 68 (2003) 092408.
[57] A.V. Rode, R. G. Elliman, E.G. Gamaly, R.G. Veinger, A.G. Christy, S.T. Hyde, and B. Luther-Davies. Appl. Surf. Sci. 197 (2002) 644.
[58] A. V. Rode, E. G. Gamaly, A. G. Christy, J. G. FitzGerald, S. T. Hyde, R. G. Elliman,B. Luther-Davies, A. I. Veinger, J. Androulakis, J. Giapintzakis, cond-mat/0310751 (2003)
[59] K. Murata and H. Ushijima, J. Natl. Inst. Mater. Chem. Res. 4, 1 (1996).
[60] Yu. V. Korshak, A. A. Ovchinnikov, and A. M. Shapiro, JETP Lett. 43, 399 (1986).
[61] Yu. V. Korshak, T. V. Medvedeva, A. A. Ovchinnikov, and V. N. Spektor, Nature 326, 370 (1987)

[62] Y. Cao, P. Wang, and Z. Hu, Synth. Met. 27, B625(1988).
[63] Y. Cao, P. Wang, Z. Hu, Solid State Commun. 68, 817 (1988).
[64] H. Tanaka, K. Tokuyama, T. Sato, and T. Ota, Chem. Lett. 10, 1813 (1990).
[65] J. B. Torrance, S. Oostra, and A. Nazzal, Synth. Met. 19, 70 (1987)..
[66] K. Murata, H. Ushijima, and H. J. Ueda, J. Chem. Soc. Chem. Commun. 7, 567 (1992)
[67] K. Kawabata, M. Mizutani, M. Fukuda, and S. Mizogami, Synth. Met. 33, 399 (1989).
[68] K. Tanaka, M. Kobashi, and H. Sanekata, J. Appl. Phys. 71, 836 (1992).
[69] S. Mizogami, M. Mizutani, M. Fukuda, and K. Kawabata, Synth. Met. 43, 3271 (1991).
[70] K. Murata, T. Masuda, and H. Ueda, Chem. Express 5, 597 (1990).
[71] K. Murata, H. Ueda, and K. Kawaguchi, Synth. Met. 44, 357 (1991).
[72] Yu. A. Katulevskii, M. A. Magrupov, and A. A. Muminov, Phys. Status Solidi A 127, 223 (1991).
[73] M. Ota, M. Otani, and M. Igarashi, Chem. Lett. 7, 1179 (1989).
[74] Y. M. Shulga, A. I. Boldyrev, and A. A. Ovchinnikov, Chem. Phys. Lett. 189, 577 (1992).
[75] H. Araki, R. Matsuoka, and K. Yoshino, Solid State Commun. 79, 443 (1991).
[76] H. Araki and K. Yoshino, Jpn. J. Appl. Phys., Part 2 31, L130 (1992).
[77] H. Araki, Y. B. Roh, N. Kuwamura, and K. Yoshino, Jpn. J. Appl. Phys., Part 2 31, L337 (1992).
[78] K. Murata, H. Ushijima, H. Ueda, and K. Kawaguchi, J. Chem. Soc. Chem. Commun. 18, 1265 (1991).
[79] K. Murata, H. Ushijima, and H. J. Ueda, J. Chem. Soc. Chem. Commun. 7, 567 (1992).
[80] H. Ushijima, K. Murata, H. Ueda, and K. Kawaguchi, Mol. Cryst. Liq. Cryst. 233, 351 (1993).
[81] R. Setnescu, S. Jipa, T. Setnescu, et al., Carbon 37, 1 (1999).
[82] T. L. Makarova, Studies of High-Tc Superconductivity, Ed. by A. Narlikar (Nova Sci., Huntington, 2003), Vol. 45, p. 107.
[83] J. M. D. Coey, M. Venkatesan, C. B. Fitzgerald, A. P. Douvalis, and I. S. Sanders., Nature 420, 156 (2002).
[84] A. S. Kotosonov, JETP Lett. 43, 37 (1986).
[85] A. S. Kotosonov and S. V. Kuvshinnikov, Phys. Lett. A 230, 377 (1997).
[86] M. F. Lin and K. W. K. Shung, Phys. Rev. B 52, 8423 (1995).
[87] S. Bandow, J. Appl. Phys. 80, 1020 (1996).
[88] A. Oshiyama, S. Okada and S. Saito: Physica B 323 (2002) 21.
[89] S. Okada and A. Oshiyama: J. Phys. Soc. Jpn. 72 (2003) 1510.
[90] S. Bandow, F. Kokai, K. Takahashi, M. Yudasaka, and S. Iijima, Appl. Phys. A 73, 281 (2001).
[91] L. Liu, G. Y. Guo, C. S. Jayanthi, and S. Y. Wu, Phys. Rev. Lett. 88, 217 206 (2002).
[92] V. Elser and R. C. Haddon, Nature 325, 792 (1987).
[93] A. Pasquarello, M. Schlüter, and R. C. Haddon, Science 257, 1660 (1992).
[94] R. C. Haddon, Science 261, 1545 (1993).
[95] R. Zanasi and P. Fowler, Chem. Phys. Lett. 238, 270 (1995)
[96] M. Buhl, Chem. Eur. J. 4, 734 (1998).

[97] R. C. Haddon and A. Pasquarello, Phys. Rev. B 50, 16 459 (1994).
[98] M. Saunders, A. Jimenez-Vazquez, R. J. Cross, W. E. Billups, C. Gesenberg, A. Gonzalez, W. Luo, R. C. Haddon, F. Diederichm A. Herrmann. Am. Chem. Soc. 117, 9305 (1995).
[99] D. Jonsson, P. Norman, K. Ruud, H. Agren, and T. Helgaker, J. Chem. Phys. 109, 572 (1998).
[100] W. L. Luo, H. Wang, R. S. Ruoff, J. Cioslowski, and S, Phelps, Phys. Rev. Lett. 73, 186 (1994).
[101] V. Buntar, H. W. Weber, and M. Ricco, Solid State Commun. 98, 175 (1996
[102] Y. Murakami and H. Suematsu, Pure Appl. Chem. 68, 1463 (1996).
[103] T. L. Makarova, K.-H. Han, P. Esquinazi, R. R. da Silva, Y.Kopelevich, I. B. Zakharova, and B. Sundqvist, Carbon 41, 1575 (2003).
[104] F. J.Owens, Z.Iqbal, L. Belova, and K. V. Rao. Phys. Rev. B 69 (2004) 033403.
[105] T. L. Makarova, B. Sundqvist, P. Esquinazi, R. Höhne, Y. Kopelevich, P. Scharff, V. A Davydov, L. S. Kashevarova, A. V. Rakhmanina. Nature 413, 718 (2001).
[106] V. N. Narozhnyi, K.-H. Müller, D. Eckert, A. Teresiak, L. Dunsch, V. A. Davydov, L. S. Kashevarova, A. V. Rakhmanina. Physica B, 329, 537 (2003).
[107] T. L. Makarova, B. Sundqvist, and Y. Kopelevich, Synth. Met. 137, 1335 (2003).
[108] T. L. Makarova and B. Sundqvist, High Press. Res. 23, 135 (2003)
[109] R. A. Wood, M. H Lewis, M. R. Lees, S. M. Bennington, M. G. Cain, Kitamura N. J. Phys., Condens. Matter, 14, L385 (2002).
[110] K. H Han. D. Spemann, R. Höhne, A. Setzer, T. Makarova, P. Esquinazi, Butz T. Carbon, 41 (2003) 785.
[111] M. Ata, M. Machida, H. Watanabe, and J. Seto, Jpn. J. Appl. Phys., Part 1 33, 1865 (1994).
[112] A. S. Lobach, Y. M. Shul'ga, O. S. Roshchupkina, A. I. Rebrov, A. A. Perov, Y. G, Morozov, V. N. Spector, A. A. Ovchinnikov, Fullerene Sci. Technol., 6, 375 (1998).
[113] V. E. Antonov, I.O. Bashkin. , S. S. Khasanov, A. P. Moravsky, Yu. G. Morozov, Yu. M Shulga, Yu. A Ossipyan, E.G. Ponyatovsky. J. Alloys and Comp., 330, 365 (2002).
[114] J. S. Miller, Adv. Mater. 4, 298 (1992).
[115] H. Ueda and K. Murata, Nippon Kagaku Kaishi, No. 12855 (1992).
[116] A. Ouchi, K. Saito, and Y. Koga, Chem. Lett., No. 12, 1083 (1995).
[117] R. Höhne and P. Esquinazi, Adv. Mater. 14, 753 (2002).
[118] V. D. Blank, S. G. Buga, G. A. Dubitsky, N. R. Serebryanaya, M. Y. Popov, B. Sundqvist. Carbon, 36, 319 (1998).
[119] O. E. Kvyatkovskii, M. G. Shelyapina, B. F. Shchegolev, I. B. Zakharova, T. L. Makarova, in Abstracts of IWFAC'2003 (St. Petersburg, Russia, 2003), p. 270
[120] A. N. Andriotis, M. Menon, R. M. Sheetz, and L. Chernozatonskii, Phys. Rev. Lett. 90, 026 801 (2003).
[121] Y.-H. Kim, J. Choi, K. J. Chang, and D. Tomanek, Phys. Rev. B 68, 125 240 (2003)

[122] D. W. Boukhvalov, P. F.Karimov, E. Z. Kurmaev, T.Hamilton, A. Moewes, L. D. Finkelstein, M. I.Katsnelson, V. A.Davydov, A. V. Rakhmanina, T. L.Makarova, Y. Kopelevich, S. Chiuzbaian, M. Neumann. Phys. Rev. B 69 (2004) 115425.
[123] S. Okada, and A.Oshiyama. Phys. Rev. B 68 (2003) 235402.
[124] J. Ribas-Ariño, and J. J. Novoa, Angew. Chem. 43 (2004) 577.
[125] J. Ribas-Ariño, and J. J. Novoa, J. Phys. Chem. Sol. 65 (2004) 787.
[126] O.E. Kvyatkovskii, I.B. Zakharova, A.L. Shelankov, T. L. Makarova. AIP conference proceedings, in press.

ORBITAL AND SPIN ORDER IN THE TRIANGULAR S=1/2 LAYERED COMPOUND (LI,NA)NIO_2

S. de Brion[1], M.D. Núñez-Regueiro[2], and G. Chouteau[1]

[1] Grenoble High Magnetic Field Laboratory, MPI-FKF and CNRS,
B.P. 166, 38042 Grenoble cedex 9, France

[2] Laboratoire de Physique des Solides, Bâtiment 510, Université Paris-Sud,
91405 Orsay, France

1. INTRODUCTION

In the field of strongly correlated electron systems, noticeable interest has emerged recently on the physics induced by orbitals [1]. The prototype compounds are oxides built up with transition metal ions (TM) which present an orbital degeneracy. Figure 1 gives a sketch of the five *d* orbitals with their peculiar spatial distribution of the electronic density. The strength and shape of the exchange and super-exchange paths, that is, the magnetic structure of the system are determined by the orbital geometry and occupancy. The fivefold degeneracy is partially lifted by the crystal field of the surrounding oxygen ions depending on the symmetry. An example is given in Figure 2 for Ni^{2+} in an octahedral environment, where, in the low spin state (S=1/2), the two fold degeneracy of the e_g orbitals is lifted by a tetragonal distortion. This is the so called Jahn-Teller effect [2].

At the same time, these transition metal ions most often carry a spin. The interplay between the orbital and spin degrees of freedom can lead to very rich phase diagrams [1]. Spectacular examples can be found in the manganese perovskites $L_{1-x}M_xMnO_3$ [3] where L=La, Nd, Pr, etc, and M=Ca, Sr, Ba, etc. These compounds are well known for their colossal magnetoresitance which occurs close to a magnetic transition. Depending on the orbital occupancy of the manganese ions and the associated orbital order, different magnetic phases are observed: insulating antiferromagnetic phases with several orbital orders, or a ferromagnetic, metallic, orbitally disordered phase. In these compounds, spins and orbitals are

strongly coupled leading to ordering temperatures of similar magnitude for both degrees of freedom. The main spin exchange paths take place via nearly 180° TM-O-TM bounds in a three dimensional lattice.

On the other hand, considering only spins, low dimensionality, magnetic frustration, and quantum effects can also lead very peculiar phase diagrams with or, more surprisingly, without magnetic long range order [4]. In fact, in frustrated lattices the degeneracy of the magnetic ground state can be frequently lifted by quantum fluctuations or a second order energy scale [5].

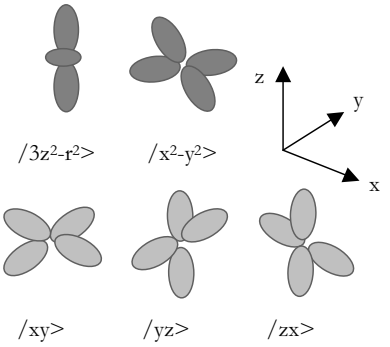

Fig. 1. 3d transition metal electronic orbitals as seen by the spatial distribution of their electronic density.

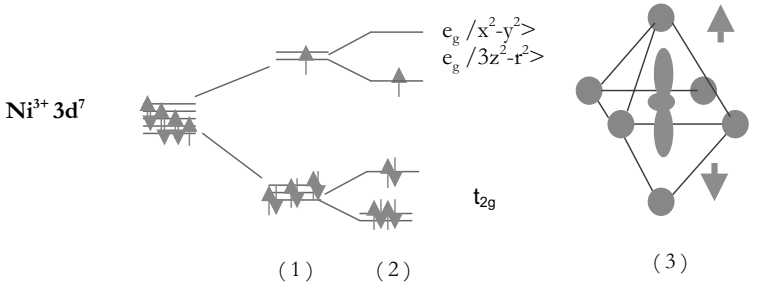

Fig. 2. Ni^{3+} 3d electronic level in an octahedral crystal field (1) and with the Jahn-Teller deformation (2) corresponding to an elongated octahedron (3).

More recently, the new physics emerging from the non-trivial coupling between orbitals and spins has been largely studied theoretically while the experimental realisations are still very rare. $LiNiO_2$ is one particularly interesting example.

Since its synthesis in 1958 by Goodenough et al. [6], $LiNiO_2$ is a subject of continuous debate. Its ideal structure can be described as a packing of Li and NiO_2 slabs built up of edge sharing NiO_6 octahedra (Figure 3). Therefore, magnetic Ni^{3+} and nonmagnetic Li hexagonal planes alternate along the <111> direction, giving rise to a quasi-two-dimensional triangular magnetic lattice. This compound belongs to the family of lamellar compounds of general formula $LiAO_2$ (A=Ni, Co, Mn, Fe) where Li^+ ions can easily be removed and reinserted into the structure under the application of an electric field, making them very interesting materials for potential battery applications. On the other hand, since A^{3+} ions are magnetic, $LiAO_2$ systems are good models for 2D magnetism. The case of $LiNiO_2$ is very peculiar. Indeed the pure compound $LiNiO_2$ does not exist. Additional Ni^{2+} ions are always present in the Li layers, leading to the average formula $Li_{1-x}Ni_{1+x}O_2$ and strongly influencing the magnetic properties. The x parameter is very dependent on the sample preparation method. Detailed chemistry and magnetic analysis of this compound as a function of x has definitely allowed to overcome the initial disagreement between results from different groups (see [7] and references therein). On the other hand, theoretical interest in this system comes from the interplay between different degrees of freedom: twofold orbital degeneracy of the Ni^{3+} (t_{2g}^6 e_g^1) ions and their eventual coupling to the S=1/2 spins, the effect of frustration in the triangular Ni lattice, and the elusive nature of the magnetic interactions.

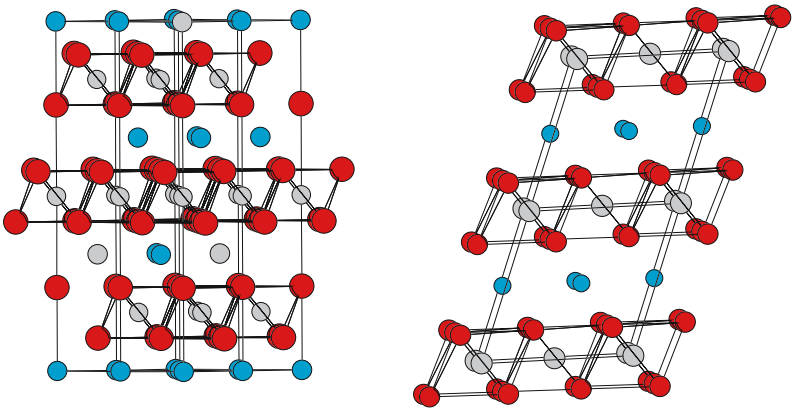

Fig. 3. Lamellar structure of $LiNiO_2$ (left) and $NaNiO_2$ (right) at room temperature showing the Li layers (in blue), the Ni layers (in grey) where the Ni atoms are surrounded by O atoms (in red) in an octahedral environment. This octahedron is elongated in $NaNiO_2$. Note also that some Ni atoms replace Li atoms in $LiNiO_2$ so that the exact formula is $Li_{1-x}Ni_{1+x}O_2$.

Several experimental studies have been performed on the fundamental properties of $LiNiO_2$ [6-21] as well as the isomorphic and isoelectronic compound $NaNiO_2$ [22-24]. In fact, as expected, $NaNiO_2$ undergoes a collective Jahn-Teller distortion reducing its symmetry from rhombohedral to monoclinic below 480K (Figure 1). It shows a long range antiferromagnetic order below 20K. On the other hand, $LiNiO_2$ exhibits several puzzling properties when

compared to $NaNiO_2$: i) its remains rhombohedral down to 2 K with no cooperative Jahn-Teller deformation, ii) no long range magnetic order has been detected either by specific heat down to 200mK [17], susceptibility [19] or neutron diffraction experiments [9,11]. This behaviour remains a mystery and has given rise to blossoming theories. In particular, $LiNiO_2$ has been recently considered as the first experimental realization of a quantum spin orbital liquid [5,25,26,28]. We will review here our main experimental results on its orbital and magnetic properties. $NaNiO_2$ is better understood and will be used as the model system for $LiNiO_2$. We shall focus on Electron Spin Resonance (ESR) since this technique is sensitive to the local symmetry as well as the local magnetic field at the Ni ions. Relevance of the different theoretical models will be also discussed.

2. ORBITAL PROPERTIES OF $NANIO_2$

The orbital order in $NaNiO_2$ [24] has been studied by neutron diffraction (Figure 4) together with high frequency, high magnetic field Electron Spin Resonance (Figure 5) [20,23]. The monoclinic C2/m structure at room temperature (Figure 3, right) is characterised by a ferrodistorsive orbital ordering: the NiO_6 octahedra become elongated, with four short Ni-O distances (d_{Ni-O}=1.91Å) and two long Ni-O distances (d_{Ni-O}=2.14Å) and are all distorted in the same direction giving rise to a cooperative crystallographic distortion. The electronic configuration of Ni^{3+} in an octahedral crystal field is given in Figure 2. The five electronic levels of the 3d orbitals are lifted by the octahedral crystal field into lower t_{2g} levels and higher e_g levels. For Ni^{3+} ($3d^5$), in the low spin state, that leaves a twofold degeneracy on the e_g levels. This degeneracy is further reduced by a Jahn-Teller deformation: the observed distortion of the oxygen octahedra indicates that it is the $|3z^2\text{-}r^2\rangle$ orbital occupation which is favoured, the elongation taking place along the z direction.

This has been confirmed by high frequency Electron Spin Resonance. The ESR spectrum at 285GHz is clearly anisotropic (Figure 5) showing two characteristic features. Due to their different line shape, they can be assign unambiguously to the parallel ($g_{//}$) and perpendicular ($g_{\perp}$) components of the g factor. A study at different frequencies shows that the splitting between the two features is proportional to the resonance magnetic field: this is a confirmation that it arises from g factor anisotropy and allows its precise determination. At 200K, these values are: $g_{//}$ =2.03 and $g_{\perp}$=2.28. The deviation of the g factor from the free electron value arises from spin-orbit coupling with the excited orbital states. Although this mechanism cannot remove the orbital degeneracy, it affects the g tensor differently depending on the orbital occupancy. The fact that $g_{//}<g_{\perp}$ implies that it is the $|3z^2\text{-}r^2\rangle$ orbital which is active. More details can be found in [23]. The oxygen octahedra should then be elongated, which is exactly what is experimentally observed: the crystallographic data show the cooperative elongation of these octahedra.

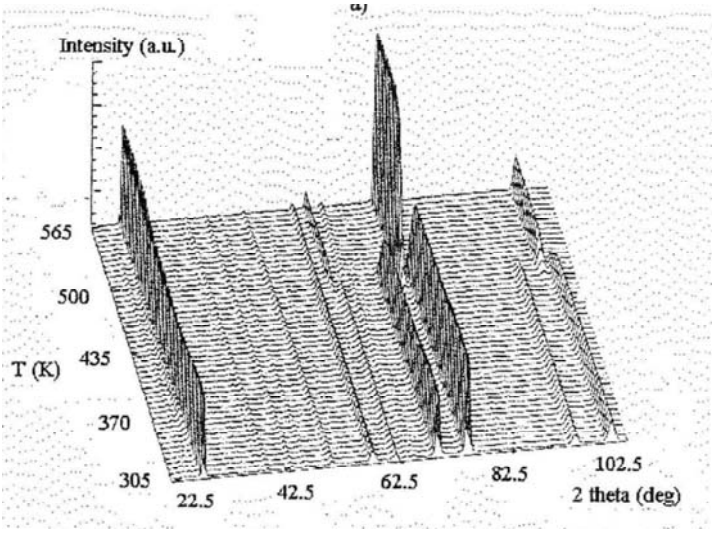

Fig. 4. Temperature dependence of neutron powder diffraction patterns in $NaNiO_2$ close to the Jahn-Teller transition, from reference [24].

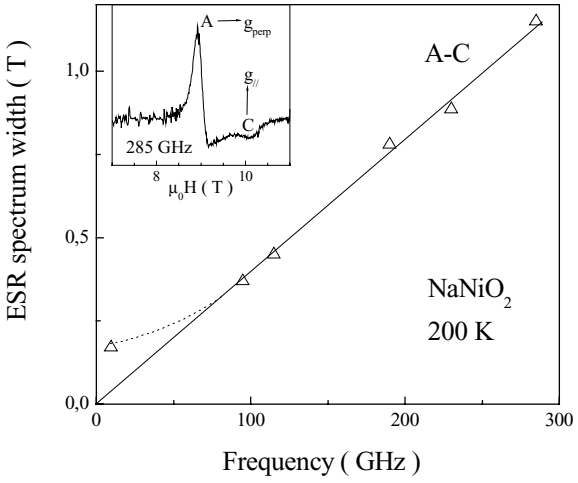

Fig. 5. Frequency dependence of the ESR spectrum width at 200K for $NaNiO_2$ with, in insert, a typical spectrum, showing the g factor anisotropy with $g_{//} > g_{\perp}$, from reference [20].

Note that the use of high frequency combined with high magnetic field allowed the determination of the g anisotropy in $NaNiO_2$: the splitting of the spectrum is not large enough compared to the initial line width to be detectable by X band measurements.

This Jahn-Teller deformation disappears at high temperature: around 480K, the neutron diffraction pattern becomes simpler (Figure 4) showing en enhanced symmetry of the crystal. The monoclinic C2/m structure of $NaNiO_2$ at room temperature disappears and a rhombohedral structure α-$NaFeO_2$ prevails (R-3m space group). In this high temperature phase, there is neither orbital ordering nor deformation of the oxygen octahedra. This is typical of a Jahn-Teller transition: at high enough temperature, thermal energy overcomes the energy barrier between one direction for the elastic deformation (elongation in the z direction for instance) and the others (x and y directions); at low enough temperature, the crystal deformation allows the system to lower its energy. This corresponds to a cooperative ferro-orbital distortion in $NaNiO_2$ with all octahedra elongated along the same direction.

This structural transition is first order: thermal hysteresis is observed in the neutron diffraction pattern whether the data are collected upon warming or cooling. This transition is also visible in the magnetic susceptibility [22,24]: there is an anomaly around 480K which also shows thermal hysteresis (see Insert in Figure 8).

3. ORBITAL PROPERTIES OF $LINIO_2$

As mentioned above, $LiNiO_2$ samples are never stoichiometric. Additional Ni^{2+} ions substitute Li^+ ions in the Li layers, leading to the average formula $Li_{1-x}Ni_{1+x}O_2$, or more precisely $[Li_{1-x}{}^{1+}Ni_x{}^{2+}][Ni_x{}^{2+}Ni_{1-x}{}^{3+}]O_2$. It is now well established [7,13,14,18] that the off stoichiometry parameter x strongly depends on the preparation conditions. Since it induces the coexistence of Ni^{3+} and Ni^{2+} ions in non equivalent sites it also strongly influence the magnetic properties of the materials. We will discuss later how the magnetic properties are dependent on this parameter and allow the precise determination of the off stoichiometry as well as the sample homogeneity.

$Li_{1-x}Ni_{1+x}O_2$ never present a collective Jahn-Teller distortion as $NaNiO_2$: all samples remain in the R-3m α-$NaFeO_2$ at room temperature [18,29], which is the crystallographic structure observed in $NaNiO_2$ above its Jahn-Teller transition. The most diluted sample (x=0.004) was studied also at 4K: the crystallographic data confirm that no change of symmetry occurs [20]. The absence of a collective Jahn-Teller distortion is particularly puzzling. For the electronic configuration of the Ni^{3+} ions as shown in Figure 2, one expects that the orbital degeneracy of the e_g electron will be lifted by a Jahn-Teller distortion unless quantum effects combined with strong coupling with spin degrees of freedom will lead to a quantum liquid state as proposed in [5,25,26,28]. $LiNiO_2$ would then be the first experimental realisation of such a state.

Complementary experimental techniques are necessary to sort out the true orbital state of $LiNiO_2$. One of them is ESR. It has been used successfully to investigate the orbital and spin state of Ni^{3+} in perovskite-type rare-earth-nickel oxides [30]. In these compounds, Ni^{3+} is in its low spin state (as usually observed). A static or dynamical Jahn-Teller effect occurs depending on the rare earth. The static Jahn-Teller distortion is evidenced by g factor

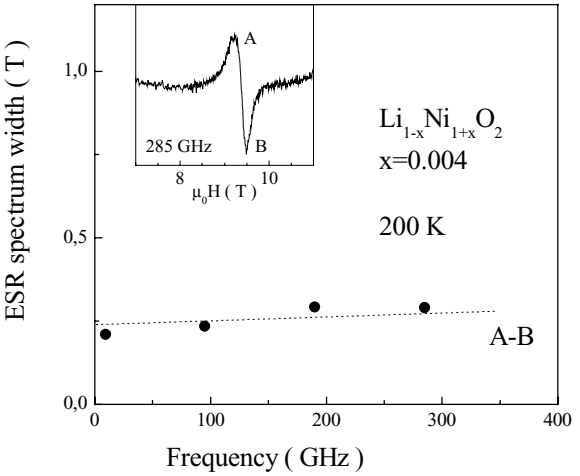

Fig. 6. Frequency dependence of the ESR spectrum width at 200K for $LiNiO_2$ together with a typical ESR spectrum, which illustrates the absence of g factor anisotropy, from reference [20].

anisotropy with $g_{//}<g_{\perp}$, as observed in $NaNiO_2$. When the effect is dynamical, the ESR spectrum becomes isotropic and recovers its static character at low enough temperature.

$Li_{1-x}Ni_{1+x}O_2$ was also studied by ESR for different off-stoichiometries: x=0.12, 0.06 [7] and 0.004 [20]. For the most diluted sample, a study at different frequencies at 200K clearly shows that the ESR spectrum is single line with a linewidth independent of the resonance magnetic field as can be seen in Figure 6 where the same scale of Figure 5 is used: the g factor is isotropic in contrast to the case of $NaNiO_2$. At lower temperature, the spectrum becomes anisotropic (Figure 18). The same behaviour is observed in less diluted samples (Figure 7). The temperature at which the anisotropy occurs as well as the amplitude of the anisotropy are stoichiometry dependent. This anisotropy was first interpreted as a Jahn-Teller effect which would become dynamical at high temperature. However the line shape is reversed compared to what is observed in $NaNiO_2$ (Figure 4) and other Ni^{3+} compounds [30]. This would mean that the Jahn-Teller effect favours the $|x^2-y^2>$ orbital instead of the $|3z^2-r^2>$ orbital. This is very unlikely. EXAFS measurements on $Li_{0.92}Ni_{1.08}O_2$ [31] show that, even at room temperature, the oxygen octahedra are elongated with four short Ni-O distances (d_{Ni-O}=1.91Å) and two long Ni-O distances (d_{Ni-O}=2.09Å) as in $NaNiO_2$. Moreover, the observed ESR anisotropic spectrum clearly resembles the one obtained on $NaNiO_2$ at temperatures close to the magnetic ordering temperature (Figure 18) and should then be interpreted similarly.

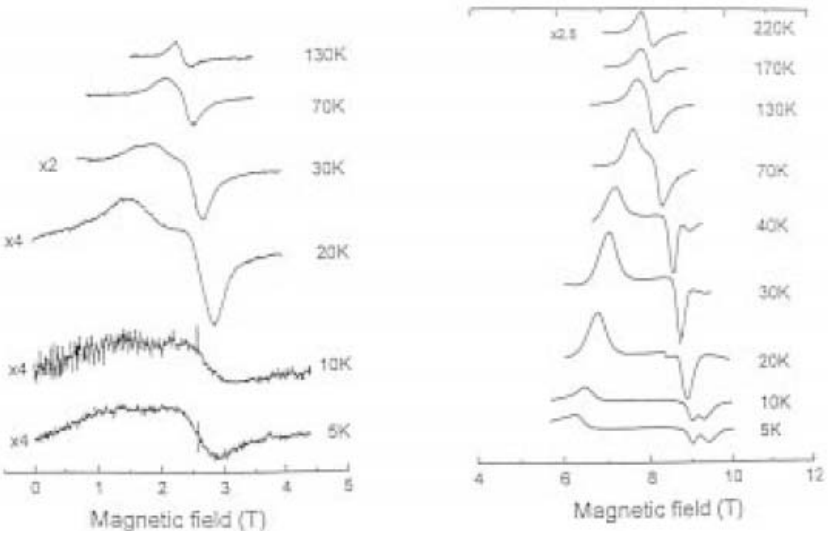

Fig. 7. ESR spectra at different temperatures for the $Li_{0.98}Ni_{1.02}O_2$ compound. Left: 73GHz, right: 246GHz, from reference [7]. At high temperature, the ESR signal is isotropic.

Coming back to the ESR results on the most diluted sample (Figure 6), it is clear that the g factor is isotropic at 200K. This behaviour should be compared with the observed Jahn-Teller distortion in EXAFS at room temperature, which is similar in shape and magnitude to the Jahn-Teller deformation in $NaNiO_2$ at the same temperature. If one would invoke a dynamical effect, one should compare the time scale of the EXAFS experiment (10^{-9}s) with the relevant time scale in ESR. We take the highest frequency measurement (285GHz), and a Jahn-Teller deformation identical to the one in $NaNiO_2$, which gives rise to a shift of 1.14T for $g_{\perp}$-$g_{//}$, and obtain the corresponding time scale of 10^{-14}s: this is shorter than for EXAFS where a local, static deformation is observed! Even if we take the ESR measurements at the lowest frequency (9GHz), the time scale is reduced by a factor 10, and is still much shorter than for the EXAFS measurements. This is then inconsistent with a dynamical Jahn-Teller effect. No clear explanation has been proposed yet to reconcile both experimental results.

In a recent paper, Reynaud et al. [17] have interpreted their magnetic susceptibility and ESR data as evidences of an orbitally frustrated state below $T_{of}\approx$400K. This interpretation is based on the observation that anomalous magnetic behaviour occurs in two different temperature ranges: the first one (at tenth of Kelvin) is unambiguously present and will be discussed in detail in the section on magnetic properties of $LiNiO_2$. The second one, at $T_{of}\approx$400K is much less convincing. This very small magnetic anomaly is certainly within the experimental error and it cannot be excluded that the high temperature data suffered from oxygen loss.

There is yet no clear experimental evidence of what is the true orbital ground state of $LiNiO_2$.

4. MAGNETIC PROPERTIES OF $NANIO_2$

The magnetic properties of $NaNiO_2$ were first measured by Bongers et al. in1966 on a single crystal [22]. More detailed measurements with, in particular, an extended magnetic field range, were obtained on a powdered sample by Chappel et al. [21,24].

The magnetic susceptibility of $NaNiO_2$ is plotted in Figure 8. The compound becomes antiferromagnetic below 20K and presents Curie-Weiss behaviour above 100K with a positive Curie-Weiss temperature: θ=+36K [21-24]. The positive sign of θ indicates the predominance of ferromagnetic interactions and the effective moment ($1.85\mu_B$) corresponds unambiguously to the low-spin state ($t_{2g}^6 e_g^1$) of Ni^{3+} with S=1/2.

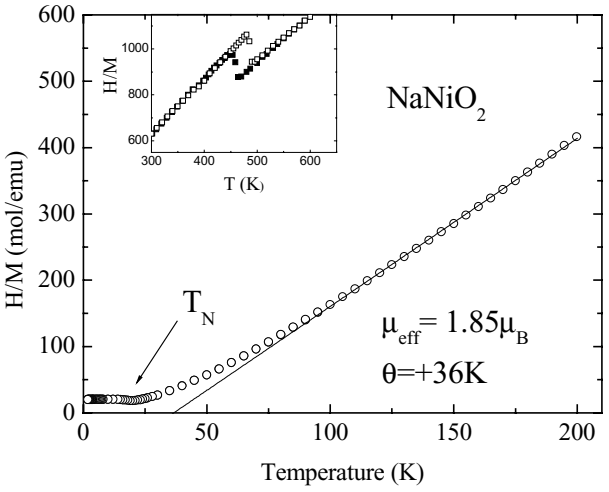

Fig. 8. Inverse of the magnetic susceptibility as a function of temperature showing the Curie-Weiss behavior and the ordering temperature. Insert: idem close to the Jahn-Teller transition where a change in the susceptibility occurs. From references [21,24].

At higher temperature, at the Jahn-Teller transition (Insert of Figure 8), a change in the susceptibility is clearly observed, which reflects an enhancement of the effective moment and probably also some reduction of the Curie-Weiss temperature, although the experimental data do not cover a sufficient temperature range to give a definitive answer.

The magnetization curve obtained in the ordered phase at 4K (Figure 9) shows saturation around 12T and a moment $1\mu_B$/Ni which agrees again with the low spin state of Ni^{3+}. A spin flop field is observed at 1.8T. This kind of features is typical of an A type antiferromagnet: the triangular Ni planes are all ferromagnetic and alternate thanks to an antiferromagnetic coupling between the planes. The spin flop field and the saturation field characterize this antiferromagnetic coupling.

For this simplest magnetic structure, a mean field calculation leads to a weak antiferromagnetic interaction between the Ni planes (J_{AF}=-1.3K) and a ferromagnetic interaction in the planes (J_F=+13K). These results are in agreement with Goodenough-Kanamori rules for magnetic exchange via oxygen orbitals: the 180° bonds between Ni^{3+} from adjacent layers lead to an antiferromagnetic coupling, while the 90° bonds between Ni^{3+} in the triangles of each planes lead to a ferromagnetic coupling [32]. The true magnetic structure is probably more complex [21].

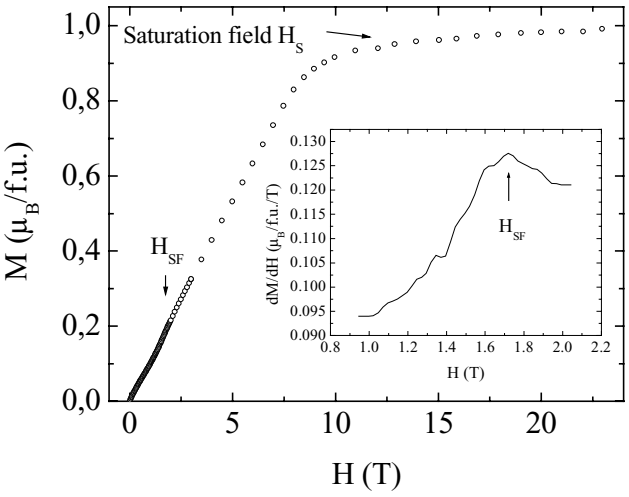

Fig. 9. Magnetization curve at 4K in the ordered phase of $NaNiO_2$. Insert: derivative of the magnetization curve showing the spin flop field at 1.8T. From reference [21].

5. MAGNETIC PROPERITIES $LINIO_2$

In the literature, many different magnetic ground states have been proposed for $LiNiO_2$: the system has been considered as a possible quantum spin liquid [8], a 2D frustrated antiferromagnet [11], a weakly coupled 2D Ising ferromagnet [9], a 2D Heisenberg ferromagnet [12], a spin glass [13,15], and more recently, as the physical realisation of a quantum spin-orbital liquid [5,16,17,25,26,28]. It is now clear that some of these interpretations have been motivated by different samples, as the magnetic properties of $Li_{1-x}Ni_{1+x}O_2$ are extremely sensitive to the preparation conditions [7,13,14,18]. Since this is also crucial for battery capacity, a great effort has been devoted to the synthesis and characterisation of the samples these last years.

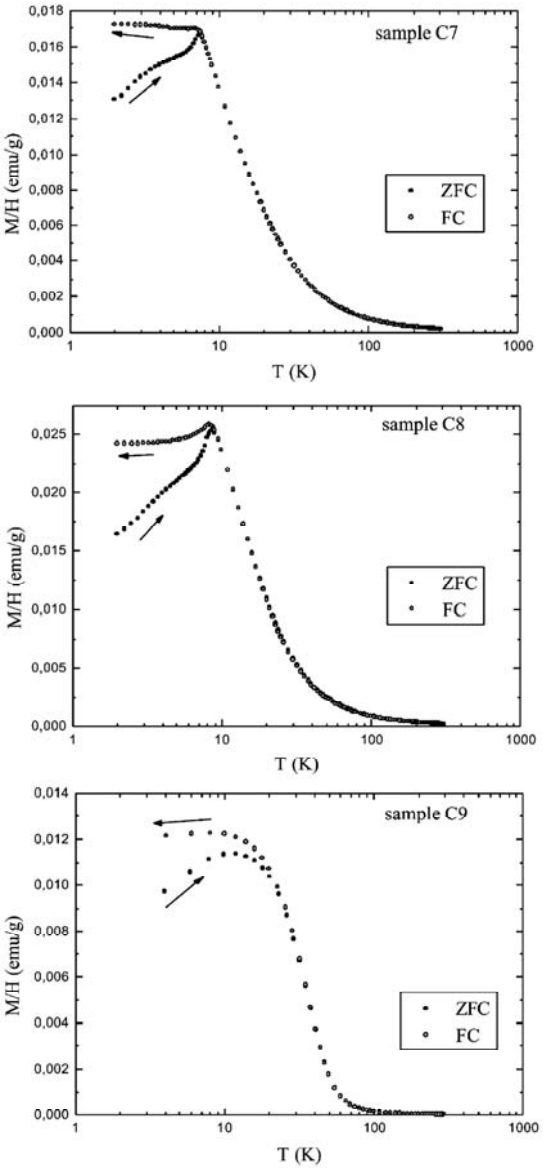

Fig. 10. Temperature dependence of the DC susceptibility in 1-mT for the $Li_{1-x}Ni_{1+x}O_2$ samples C7 (x=0.004), C8 (x=0.015) and C9 (x=0.062). Open and closed marks correspond to measurements on field cooling and on heating after zero field cooling, respectively. From reference [18].

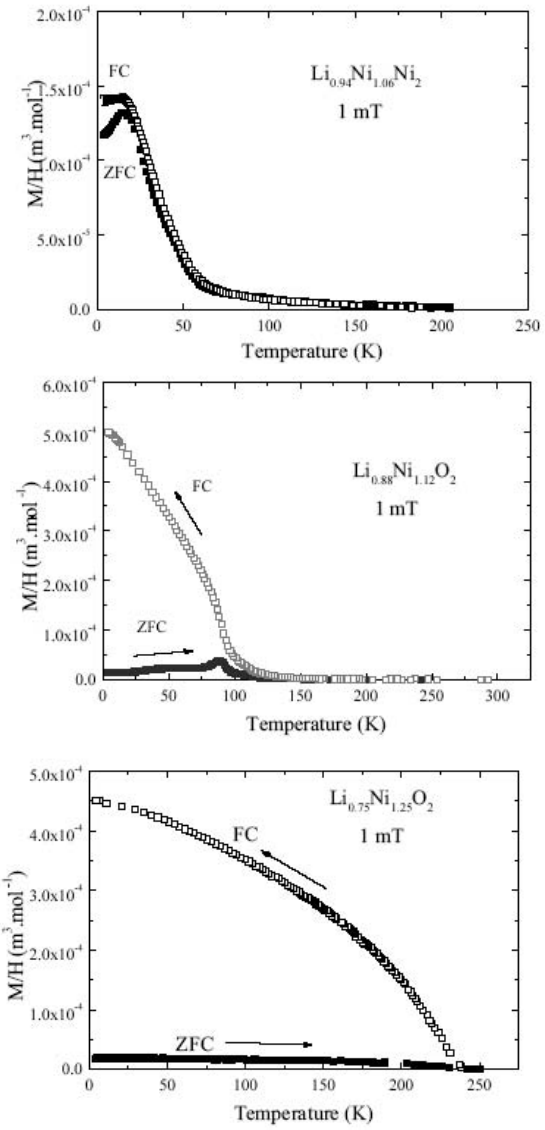

Fig. 11. Temperature dependence of the DC susceptibility in 1mT for $Li_{1-x}Ni_{1+x}O_2$ samples with x=0.06, 0.12 and 0.25. Open and closed marks correspond to measurements on field cooling and zero field cooling, respectively. From reference [7].

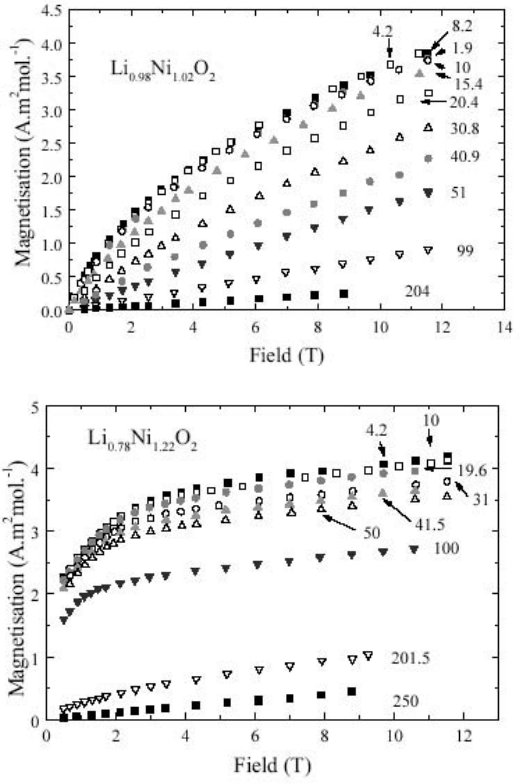

Fig. 12. Magnetic field dependence of the magnetization at different temperatures for $Li_{1-x}Ni_{1+x}O_2$ samples in the diluted regime (x=0.02) and in the cluster regime (x=0.22). From reference [7].

It has been shown that small amounts of Ni^{2+} (S=1) ions substitute to Li^+ ones in the Li layers (Figure 2 left). This substitution is accompanied by a valence change of the Ni ions in the Ni planes from +3 (S=1/2) to +2 (S=1), so that the exact formula is $[Li_{1-x}^{1+}Ni_x^{2+}][Ni_x^{2+}Ni_{1-x}^{3+}]O_2$. The amount of Ni^{2+} strongly depends on the preparation conditions. The knowledge of the Ni^{2+}/Ni^{3+} ratio is the key to understand the magnetic properties. This is particularly obvious on DC susceptibility measurements as a function of temperature as given in Figure 10 for the most diluted samples ($x \leq 0.06$) and in Figure 11 for the most concentrated ones ($0.06 \leq x \leq 0.25$). Typical magnetization curves are also reported in Figure 12. As x is increased, the compound evolves smoothly from a spin glass (diluted samples), to a cluster regime and finally to a three dimensional ferrimagnet. We will now detail the different regimes.

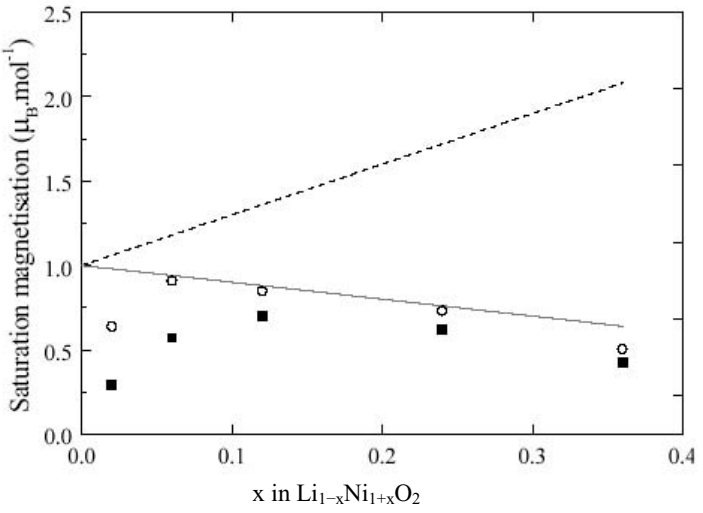

Fig. 13. Saturation magnetization of the $Li_{1-x}Ni_{1+x}O_2$ family deduced from the high field part of the magnetization curves. The straight lines are fits (see text). From reference [7].

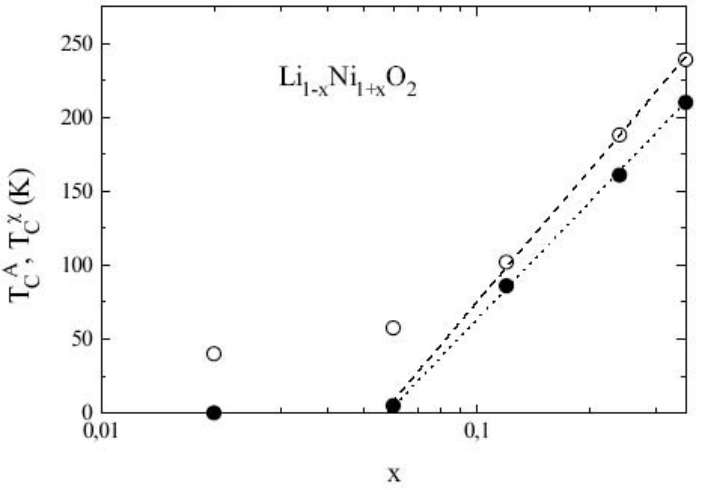

Fig. 14. Ordering temperatures obtained using different criteria (Arrot plot for T_C^A, inflexion point in the susceptibility for T_C^X), showing the existence of a critical concentration at $x_C \approx 0.06$, from reference [7].

In the cluster regime, as in $Li_{0.78}Ni_{1.22}O_2$ (Figure 12), a clear saturation of the magnetization appears at moderate magnetic fields (2 to 3 T), although a high field susceptibility remains. In Figure 13 these saturated magnetisation values M_S are plotted as a function of the off stoichiometry x. In a simplified model, M_S can be written as follows: $M_S = x\,\mu(Ni^{2+}) + (1-x)\,\mu(Ni^{3+})$ where x is the off stoichiometry and μ the magnetic moment carried by the particular Ni ion. This equation assumes that Ni^{2+} and Ni^{3+} moments align independently under a magnetic field. However Ni^{2+} ions in the lithium layers are linked to the Ni^{3+} slabs through a very strong 180° Ni-O-Ni antiferromagnetic super-exchange bound which is about the same as in NiO. They cannot saturate in a 12 T field: their contribution to M_S is negligible but it is visible in the high field susceptibility. Only the second term of the equation should then be taken into account. This gives the straight line in Figure 13. Taking also into account the Ni^{2+} contribution gives the dashed line. Clearly, our model based on the magnetization from $(1-x)$ Ni^{3+} ions fits well the data above a threshold concentration $x_c \approx 0.6$. This is the cluster regime.

The ordering temperature varies significantly with x as can be seen in Figure 11. Since the system is rather inhomogeneous in this concentration range, different criteria can be taken to determine this temperature, but the tendency is the same (Figure 14): an increase of the ordering temperature with the off stoichiometry and the same lower cut-off at $x_c \approx 0.6$. The highest critical temperature observed is around 240K: this is the 3D ferromagnetic phase sometimes present in lower concentrated samples which are not chemically homogeneous.

In the diluted regime, for $x \leq x_c$, no saturation of the magnetization is observed even below the critical temperature. Two examples are given in Figure 12 with $Li_{0.98}Ni_{1.02}O_2$ and in Figure 17 with $Li_{0.996}Ni_{1.004}O_2$. The susceptibility as a function of temperature shows hysteresis between the field cooled and zero field cooled data below the critical temperature; there is a cusp at the critical temperature in the zero-field cooled curve while the field cooled one exhibits a plateau. All this is typical of the spin glass behaviour with also the dependence of the critical temperature on frequency in ac-susceptibility. This critical temperature decreases as the off stoichiometry is reduced. The smallest value reported in the literature ($T_g \approx 7.5$K) has been obtained for $x \approx 0.004$ [18].

Above T_g, the compounds exhibit a Curie-Weiss behaviour as seen in Figure 15 where the inverse of the susceptibility is plotted as a function of temperature together with the linear fit from the Curie-Weiss law. There also the magnetic behaviour depends on the stoichiometry: while the effective moment in the Curie-Weiss law does not change significantly, the Curie-Weiss temperature decreases when x is decreased (Figure 16). It is important to point out that, when plotted as a function of $x < 0.06$, the Curie-Weiss temperature, θ has a linear behaviour (Figure 16), which does not extrapolate to zero for $x = 0$ but to $\theta_c = +24$K.

The positive sign of θ shows the predominance of ferromagnetic interactions as in $NaNiO_2$. This indicates that, in the ideal $LiNiO_2$, ferromagnetic intralayer interactions remain, as in $NaNiO_2$ and are dominant. This seems to rule out theoretical interpretations based on magnetic frustration in the Ni triangular lattice. In addition the knowledge of θ allows a precise determination of x.

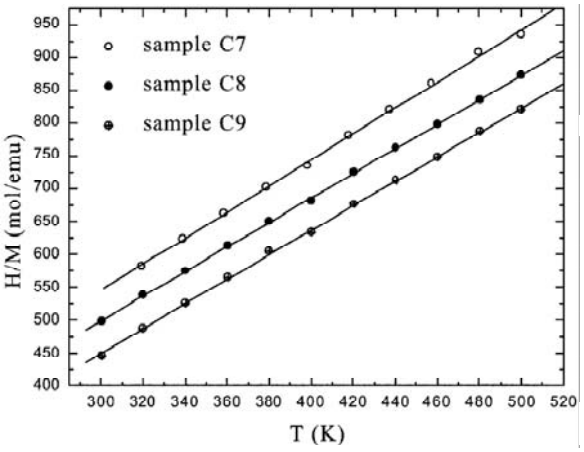

Fig. 15. Inverse of the magnetic susceptibility as a function of temperature for several samples showing the Curie-Weiss behaviour. From reference [18].

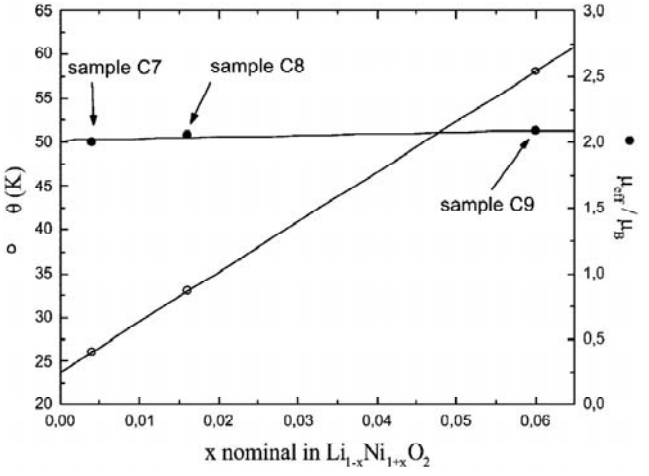

Fig. 16. Sample dependence of the Curie-Weiss temperature θ and the effective moment from the data shown in Fig. 11. From reference [18].

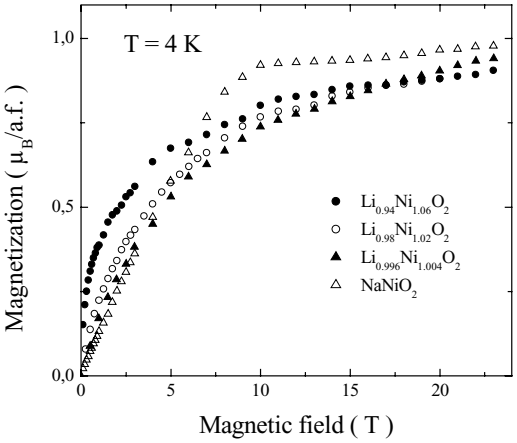

Fig. 17. Magnetization up to 23 T of $NaNiO_2$ and various quasi-stoichiometric $Li_{1-x}Ni_{1-x}O_2$ samples at 4 K. From reference [20].

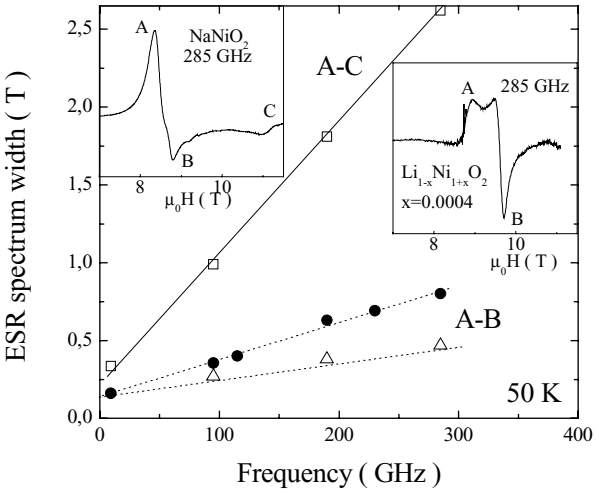

Fig. 18. Low-temperature frequency dependence of the ESR spectrum width for $NaNiO_2$ (triangles) and $Li_{1-x}Ni_{1-x}O_2$, $x \approx 0.004$, corresponding to the features *A-B* and *A-C*. Insert: typical spectra. From reference [20].

Figure 17 reports magnetization curves as a function of magnetic field at 4K for $Li_{1-x}Ni_{1-x}O_2$ samples with x=0.06, 0.02 and 0.04. The magnetization curve of $NaNiO_2$ at the same temperature (in the antiferromagnetic phase) is also given as a comparison. We note that both the low field and high field magnetization tends towards the one of $NaNiO_2$ as x is reduced. The initial susceptibility decreases: the low-field curvature, the signature of ferrimagnetic clusters, vanishes when $x \approx 0$, approaching the linear behaviour observed for the antiferromagnet $NaNiO_2$. At the same time, the high field magnetization increases, approaching $1\mu_B$, the value extrapolated when no more ferrimagnetic clusters are present and complete saturation occurs as in $NaNiO_2$. All this is an indication that pure $LiNiO_2$ would have the same magnetic behaviour of $NaNiO_2$.

The same tendency is seen in Electron Spin Resonance measurements at 50K, for the most diluted sample (x=0.004) as shown in Figure 18. In $NaNiO_2$, as the magnetic transition is approached, the ESR spectrum becomes wider. The feature associated with g// at 200K (Figure 5) shifts to higher field values while the feature associated with $g_\perp$ at 200K splits into line A and B and is shifted towards a lower field. The same tendency is observed in $Li_{0.096}Ni_{1.004}O_2$ except that the g value is isotropic so that only features A and C are present.

The magnetization, susceptibility, and ESR measurements clearly show that the magnetic properties of very diluted $Li_{1-x}Ni_{1+x}O_2$ approach those of $NaNiO_2$ [20]. We have interpreted this as due to the presence of ferrimagnetic clusters formed around the extra Ni ions. The pure compound $LiNiO_2$ would have the magnetic structure of $NaNiO_2$ despite their different orbital states. At low temperature, the weak antiferromagnetic interplane interaction of the $NaNiO_2$ should leads to an antiferromagnetic macroscopic order. However, the smaller size of the Li ions does not allow perfect stacking of the Na-Ni layers and some Ni^{2+} ions always go into the Li layers. The 180° superexchange path between this extra Ni ion in the Li in plane and the Ni ion above in the Ni plane induces an antiferromagnetic coupling [32] as well as the superexchange path with the Ni ion below. This double mechanism induces an effective interplane Ni-Ni local ferromagnetic coupling, while the direct superexchange path between Ni plane is antiferromagnetic. Such competition of interactions leads to local magnetic frustration. Figure 19 shows a sketch of this frustration mechanism.

Assuming that spins around a cluster turn progressively like a magnetic wall, to finally adopt the AF stacking of $NaNiO_2$, an estimation of the number of perturbed spins by each additional Ni ion can be made. To simplify, in the case of an uniaxial crystal, the characteristic wall length is written $\delta = a\sqrt{\frac{8H_E}{3H_A}}$ where a is the cell parameter, and H_E and H_A are the exchange and anisotropic fields, respectively. Taking the characteristic field values obtained for $NaNiO_2$ yields $\delta \approx 6a$. In our hexagonal symmetry, up to sixth-neighbour spins are perturbed, i.e., 60 spins per cluster. Therefore, less than1% of excess Ni in the Li planes can induce complete magnetic disorder in $Li_{1-x}Ni_{1+x}O_2$ [20]. At the critical threshold $x_C \approx 0.6$, percolation occurs and a long range ferromagnetic order is established. This frustration mechanism prevents the stabilization of long range ordering, and explains the spin-glass behaviour observed in quasi-stoechiometric $Li_{1-x}Ni_{1+x}O_2$ at low temperature, without the necessity of evoking a spin-liquid state as proposed by other authors [5, 16, 25, 26, 28].

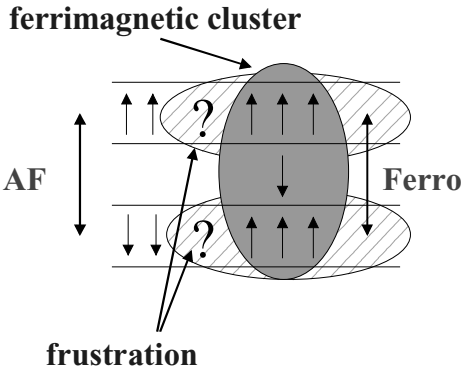

Fig. 19. Sketch of the magnetic frustration mechanism proposed for quasi-stoichiometric $Li_{1-x}Ni_{1+x}O_2$. From reference [20].

6. THE SOLID SOLUTION $LI_{1-X}NA_XNIO_2$

Recently, the solid solution $Li_{1-x}Na_xNiO_2$ has been synthesized and characterized both cristallographically and magnetically. It is not possible to synthesize single phase samples for arbitrary Li/Na ratio. As shown in Fig.20 and reported by Matsumura et al. [33], the $LiNiO_2/NaNiO_2$ phase diagram contains three different single phase solid solution regions, in between which, two phase mixtures are observed. For $x \leq 0.3$, the R-3m α-$NaFeO_2$ structure type of $LiNiO_2$ is found (RII phase). For $x \geq 0.9$, the monoclinic C2/m phase of $NaNiO_2$ is observed, with substitution of Li^+ for Na^+ ions. In a small concentration range about $x \approx 0.8$, a new rhombohedral phase (RI phase) is obtained, which has the same structural arrangement as $LiNiO_2$, but quite different cell parameters: the c/a ratio is 5.24 instead of 4.94 for $LiNiO_2$. The exact cationic composition of this phase found both by Rietveld refinement of the x-ray data and atomic absorption is $Li_{0.30(1)}Na_{0.70(1)}$. No structural phase transition could be detected by neutron powder diffraction for $Li_{0.3}Na_{0.7}NiO_2$ down to 1.5K. Therefore, this phase remains rhombohedral in this temperature range and does not undergo a cooperative JT ordering. In this respect, it behaves like $LiNiO_2$ and not like $NaNiO_2$.

The magnetic properties of these different phases present some similarities. As an illustration, Figure 21 represents the temperature dependence of the magnetic susceptibility and its inverse for the three compounds. They all show a maximum in the susceptibility at low temperature: 20K for $NaNiO_2$, 25K for $Li_{0.3}Na_{0.7}NiO_2$ and 9K for $LiNiO_2$.

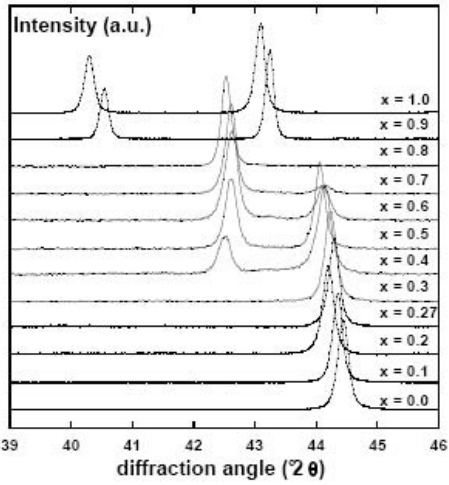

Fig. 20. X-ray diffractograms as a function of the nominal composition $Li_{1-x}Na_xNiO_2$ [21].

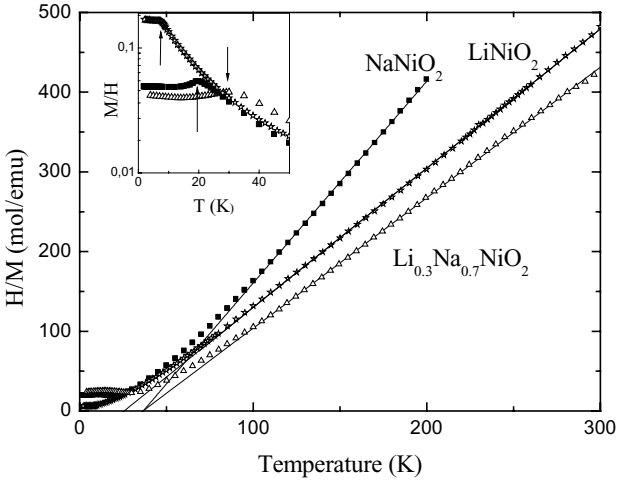

Fig. 21. Reciprocal susceptibility versus temperature, showing the Curie-Weiss behaviour for the three compounds $Li_{1-x}Na_xNiO_2$, x=0, 0.7 and 1. Insert: Susceptibility around the magnetic transitions. From reference [21].

However, in $LiNiO_2$, as it was discussed previously, there is no long range magnetic order, and we attribute this fact to the presence of extra Ni ions in the Li plane. $NaNiO_2$ and $Li_{0.3}Na_{0.7}NiO_2$ are stoichiometric (no extra Ni^{2+} ions are present in the Na/Li planes within the accuracy of the Rietveld refinement of the neutron and X ray diffractograms). The field dependence of the magnetization at 4K for both compounds is quite different from the one of $LiNiO_2$ as can be seen in Figure 22: while for the latter a smooth increase is observed, two spin flop fields are observed for $NaNiO_2$ and $Li_{0.3}Na_{0.7}NiO_2$ (H_{c0}≈1.8T and 0.05T, H_{c1}≈7T and 5T respectively) preceding the saturation field (H_{sat}≈13T and 19T respectively). Such behaviour indicates that long range magnetic order exists for these two Na compounds, with a similar magnetic structure. As for $NaNiO_2$, neutron diffraction measurements failed to detect magnetic Bragg peaks in $Li_{0.3}Na_{0.7}NiO_2$ probably because of their weaknesses and/or the complexity of the magnetic phase. In particular the presence of two spin flop fields cannot be explain with just two magnetic sublattices as for a simple A type antiferromagnet as proposed in [22,23].

All three compounds present Curie-Weiss behaviour with positive Curie-Weiss constant (+26K for $LiNiO_2$, +40K for $Li_{0.3}Na_{0.7}NiO_2$ and +36K for $NaNiO_2$). For all them, ferromagnetic interactions prevail. For the two magnetically ordered compounds $NaNiO_2$ and $Li_{0.3}Na_{0.7}NiO_2$, in a first approach, their magnetic structure can be described as an antiferromagnetic stacking of ferromagnetic planes [22,23]. Then only H_{sat} and H_{c0} are relevant. We derive then the corresponding antiferromagnetic interaction J_{AF} (in between the Ni planes) as well as the anisotropy field H_A which align the magnetic moments in a given direction: J_{AF}=-1.3K and -1.9K, H_A=250mT and 0.2mT for $NaNiO_2$ and $Li_{0.3}Na_{0.7}NiO_2$ respectively. From the Curie-Weiss constant, we get the average ferromagnetic interaction in the Ni planes: J_F=+13.3K and +15.2K respectively. A slight increase in all these interactions is observed in the non Jahn-Teller compound $Li_{0.3}Na_{0.7}NiO_2$ compared to the Jahn-Teller compound $NaNiO_2$. A drastic decrease of the anisotropy field is observed. Note also the slight change in the slope of the inverse susceptibility as a function of temperature: the effective magnetic moment is increased (from 1.85μ_B to 2.1 μ_B). These effects are related to the different orbital configuration for the Ni ions.

To summarize, $Li_{0.3}Na_{0.7}NiO_2$ exhibits no Jahn-Teller transition contrary to $NaNiO_2$. This proves their very different orbital ground state. On the other hand, they present a similar magnetic structure with similar exchange energies. Therefore we conclude that in these systems, orbital and spin degrees of freedom are decoupled. The orbital contribution can only be seen in the value of the magnetic moment and the anisotropy field associated with Ni^{3+} ions. Although we cannot conclude about the orbital occupation in the Li containing compounds, $NaNiO_2$ can most probably be the spin model for the magnetic ground state of pure $LiNiO_2$. The exact magnetic structure of $NaNiO_2$, most likely a modulated one derived from the A-type antiferromagnet, remains to be determined.

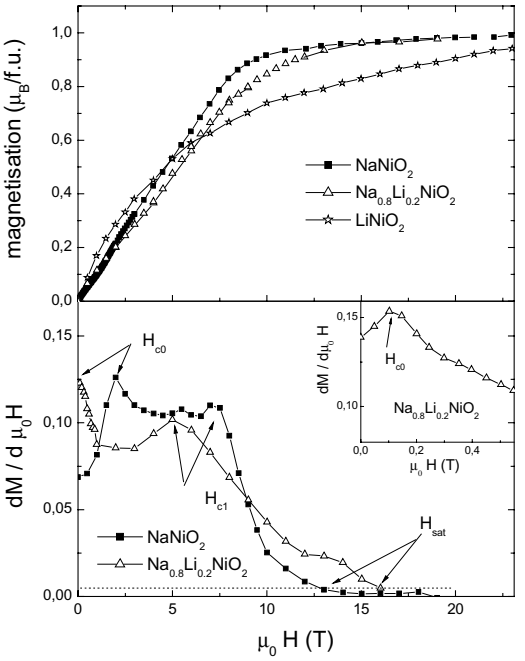

Fig. 22. Field dependence (top) and field derivative of the magnetization (bottom) at 4K, showing the 3 characteristic fields. Inset: blow up of the low field results for $Li_{0.3}Na_{0.7}NiO_2$. From reference [21]

7. CONCLUSION

This work intends to describe the experimental status of the controversy about the orbital and spin states in the quantum triangular layer $NaNiO_2$ and $LiNiO_2$ compounds. It is puzzling that $NaNiO_2$ undergoes a cooperative Jahn–Teller transition, and at a much lower temperature to long range magnetic ordering, but $LiNiO_2$ does not. This completely different behavior for these two S=1/2 twofold orbital degenerate oxides has therefore suggested several theoretical interpretations. Although new experimental data have been available recently, the discussion on the different proposed models is still open and the situation is unsettled.

The first point to clarify is whether the orbital and magnetic behavior observed for $LiNiO_2$ is intrinsic or not. In fact, while $NaNiO_2$ compounds show a perfect stacking of Ni and Na planes to observe the long range orbital and magnetic ordering, the smaller size of the Li

ions leads necessarily to the presence of Ni ions in the Li planes of $LiNiO_2$. Furthermore, its magnetic properties are strongly dependent of these always present impurities. It has been shown that they induce some magnetic frustration, which is enough to prevent the establishment of any long range magnetic order. Indeed in $NaNiO_2$ and $Li_{0.3}Na_{0.7}NiO_2$, which do not present extra Ni ions in the Li plane, a long range magnetic order is established and both compounds have similar magnetic properties despite different orbital states. This common magnetic behaviour would certainly persist in the ideally pure compound $LiNiO_2$.

For the different orbital states observed in these triangular layer compounds, two different theoretical views have been proposed depending on the interplay between orbital and spin degrees of freedom. While previous analysis [32] and recent theoretical calculations by Mostovoy and Khomskii [27] suggest that in these nearly 90° TM-O-TM bond systems orbitals and spins are essentially decoupled, other authors [5,16,25,26,28] considered that the spin ordering in $NaNiO_2$ not observed in $LiNiO_2$ is a consequence of the different orbital configurations.

The interesting calculation of Daré et al.[34] suggests that a large enough trigonal distortion can generate antiferromagnetic interactions in the Ni planes in addition to the ferromagnetic interactions derived from the Goodenough-Kanamori-Anderson rules. This could be important since the coexistence of ferromagnetic and antiferromagnetic interactions could explain the lack of magnetic ordering in $LiNiO_2$. But this parameter has been quantified in our structural analysis and $LiNiO_2$ has the lowest trigonal distortion compared to the Na containing compounds. Therefore this mechanism should lead to a stronger antiferromagnetic contribution in $NaNiO_2$ and $Li_{0.3}Na_{0.7}NiO_2$ than in $LiNiO_2$, while the opposite occurs according to the measured Curie-Weiss temperatures. This last experimental result also confirms our analysis that in these layered compounds with ~90° super-exchange bonds, orbitals and spins are essentially decoupled.

Finally, the calculations by Vernay et al. [28] for a spin-orbital model on the triangular lattice with in-plane antiferromagnetic interactions show a very rich phase diagram. The authors argue that it could explain the general behaviour of these oxides but, even considering all their arguments, these new experimental results make difficult to justify the orbital-spin coupling model, since in its present form, their different magnetic states come from different orbital occupations.

To conclude, we reported the strong x-dependence of the magnetic properties of $Li_{1-x}Ni_{1+x}O_2$ samples. We have also studied the ferrodistortive transition in $NaNiO_2$: ESR results show that below the transition temperature the $|3z^2\text{-}r^2>$ orbital occupation is favoured, leading to FM in-plane interactions. Then, considering that, in a first approach, the magnetic structure of $NaNiO_2$ corresponds to an antiferromagnetic stacking of ferromagnetic planes and that this is also the case for pure $LiNiO_2$, we have proposed a model showing how the frustration induced by off-stoichiometric effects, always present in real $LiNiO_2$ samples, can inhibit the 3D magnetic ordering observed for $NaNiO_2$.

Furthermore, we have proved the decoupling between the orbital and spin degrees of freedom in $(Na,Li)NiO_2$ compounds: the orbital occupation can change without significantly modify the magnetic properties. However, no definite experimental proof and theoretical explanation has emerged yet on the orbital ground state of $LiNiO_2$. More work is required to

achieve a clear complete description of the orbital and magnetic states in these triangular S=1/2 layered compounds, which represent an important chapter of quantum frustrated magnetism.

ACKNOWLEDGMENTS

We would like to thank S. Bach, N. Baffier, A.-L. Barra, C. Belhomme, V. Bianchi, P. Bordet, D. Caurant, E. Chappel, C. Darie, C. Delmas, F. Dupont, M. Holzapfel, O. Isnard, J. P. Pereira-Ramos, A. Rougier, A. Stepanov, P. Strobel, A. Sulpice, and P. Wilmann for their participation in the reported results. We also acknowledge useful discussions with A.-M. Daré, A. M. Gorayeb, D. I. Khomskii, J. E. Lorenzo, F. Mila, M. V. Mostovoy, A. M. Ole , and F. Vernay.

The Grenoble High Magnetic Field Laboratory is ‘‘laboratoire associé à l’Université Joseph Fourier-Grenoble.’’

REFERENCES

[1] Y. Tokura and N. Nagaosa, Science **288** (2000) 462.
[2] H. A. Jahn and E. Teller, Proc. Roy. Soc. **A116** (1937) 220.
[3] See for instance: *Colossal magnetoresistance, charge ordering and related properties of manganese oxides,* Ed. C. N. R. Rao and B. Raveau, World Scientific (1998).
[4] A. P. Ramirez, *Handbook of magnetic materials,* Ed. K. H. J. Buschow, Elsevier, Amsterdam **13** (2001) 423.
[5] L. F. Feiner, A. M. Ole , and J. Zaanen, Phys. Rev. Lett. **78** (1997) 2799; A. M. Ole , L. F. Feiner, and J. Zaanen, Phys. Rev. B **61** (2000) 6257.
[6] J. B. Goodenough, D. G. Wickham, and W. J. Croft, J. Phys. Chem. Solids **5** (1958).
[7] A.-L. Barra, G. Chouteau, A. Stepanov, A. Rougier, and C. Delmas, Eur. Phys. J. B **7** (1999) 551.
[8] H. Hirakawa, H. Kadowaki, and K. Ubukoshi, J. Phys. Soc. Jpn. **54** (1985) 3526.
[9] J. P. Kemp, P. A. Cox, and J. Hodby, J. Phys. Cond. Matter **2** (1990) 6699.
[10] K. Hirakawa, R. Osborn, A. D. Taylor, and K. Takeda, J. Phys. Soc. Jpn. **54** (1990) 3081.
[11] K. Hirota, Y. Nakazawa, and M. Ishikawa, J. Magn. Magn. Mater. **90-91** (1990) 279; H. Yoshizawa, H. Mori, K. Hirota, and M. Ishikawa, J. Phys. Soc. Jpn **59** (1990) 2631; K. Hirota, H. Yoshizawa, and M. Ishikawa, J. Phys. Cond. Matter **4** (1992) 6291.
[12] R. Stonayova, E. Zhecheva, and C. Friebel, J. Phys. Chem. Solids **54** (1993) 9.
[13] J. N. Reimers, J. R. Dahn, J. E. Greedan, C.V. Stager, G. Liu, I. Davidson, and U. von Sacken, J. Solid State Chem. **102** (1993) 542.
[14] K. Yamaura, M. Takano, A. Hirano, and R. Kanno, J. Solid State Chem **127** (1996) 109.
[15] A. Bajpai and A. Banerjee, Phys. Rev. B **55** (1997) 12439.
[16] Y. Kitaoka, T. Kobayashi, A. Koda, H. Wakabayashi, Y. Niino, H. Yamakage, S. Taguchi, K. Amaya, K. Yamaura, M. Takano, A. Hirano, and R. Kanno, J. Phys. Soc. Japan **67** (1998) 3703.
[17] F. Reynaud, D. Mertz, F. Celestini, J. M. Debierre, A. M. Gorayeb, P. Simon, A. Stepanov, J. Voiron, C. Delmas, Phys. Rev. Lett. **86** (2001) 3638.
[18] V. Bianchi, D. Caurant, N. Baffier, C. Belhomme, E. Chappel, G. Chouteau, S. Bach, J. P. Pereira-Ramos, A. Sulpice, and P. Wilmann, Solid State Ionics **140** (2001) 1.
[19] E. Chappel, M. D. Núñez-Regueiro, G. Chouteau, C. Darie, V. Bianchi, D. Caurant, and N. Baffier, Physica B **294-29** (2001) 124.
[20] E. Chappel, M. D. Núñez-Regueiro, S. de Brion, G. Chouteau, V. Bianchi, D. Caurant, and N. Baffier, Phys. Rev. B **66** (2002) 132412.
[21] M. Holzapfel, S. de Brion, C. Darie, P. Bordet, E. Chappel, G. Chouteau, P. Strobel, A. Sulpice and M. D. Núñez-Regueiro, cond-mat/ 040329 (2004).
[22] P. F. Bongers and U. Enz, Solid State Comm. **4** (1966) 153.
[23] E. Chappel, M. D. Núñez-Regueiro, F. Dupont, G. Chouteau, C. Darie, and A. Sulpice, Eur. Phys. J. B **17** (2000) 609.
[24] E. Chappel , M. D. Núñez-Regueiro, G. Chouteau, O. Isnard, and C. Darie, Eur. Phys. J. B **17** (2000) 615.
[25] Y. Q. Li , M. Ma, D. N. Shi, and F. C. Zhang , Phys. Rev. Lett. **81** (1998) 3527.
[26] M. van der Bossche, F.-C. Zhang, and F. Mila, Eur. Phys. J. B **17** (2000) 367; M. van der Bossche, P. Azaria, P. Lecheminant, and F. Mila, Phys. Rev. Lett. **86** (2001) 4124

[27] M. V. Mostovoy and D. I. Khomskii, Phys. Rev. Lett. **89** (2002) 227203.
[28] F. Vernay, K. Penc, P. Fazekas, F. Mila, Phys. Rev. B **70** (2004) 014428.
[29] A. Rougier, P. Gravereau, and C. Delmas, J. Electrochem. Soc **143** (1996) 1168.
[30] A. P. Ganguly, G. Demazeau, J. M. Dance, and P. Hagenmuller, Solid State Commun. **73** (1990) 617.
[31] A. Rougier, C. Delmas, and A.V. Chadwick, Solid State Commun. **94** (1995) 123.
[32] M. D. Núñez-Regueiro, E. Chappel, G. Chouteau, and C. Delmas, Eur. Phys. J. B **16** (2000) 37.
[33] T. Matsumura , R. Kanno, R. Gover, Y. Kawamoto, T. Kamiyama, and B. J. Mitchell, Solid State Ionics **152** (2002) 303.
[34] A.-M. Daré, R. Hayn, and J.-L. Richard, Europhys. Lett. **61** (2003) 803.

STRUCTURES AND ELECTROMAGNETIC PROPERTIES OF THE *A*-SITE ORDERED PEROVSKITE MANGANITE

Y. Ueda and T. Nakajima

Materials Design and Characterization Laboratory, Institute for Solid State Physics, University of Tokyo, 5-1-5 Kashiwanoha, Kashiwa, Japan

1. INTRODUCTION

Manganese perovskites with a formula $(R^{3+}_{1-x}A^{2+}_{x})MnO_3$ ($0 < x < 1$), where R^{3+} and A^{2+} represent in general rare-earth ions and alkaline-earth ions (Ca and Sr), respectively, have been extensively investigated for the past ten years [1]. The potential application to the industrial technology has apparently accelerated the research activity, and as a result deepened our comprehension of this system. Now, it is widely accepted that the dopant concentration x and the band width (or the tolerance factor) are dominant two parameters which enable us to systematically tune the magnetic and transport properties including the colossal magnetoresistance (CMR) and metal-insulator (MI) transition accompanied by the charge and orbital order (CO) [1].

The structure of perovskite RMnO$_3$ consists of a MnO$_2$ square sublattice and a RO rock-salt sublattice, as shown in Fig. 1. The mismatch between the larger MnO$_2$ and smaller RO sublattices is relaxed by tilting MnO$_6$ octahedra, leading to the lattice distortion from a cubic structure to, mostly, an orthorhombic GdFeO$_3$ type structure with a cell of $\sqrt{2}a_p \times \sqrt{2}b_p \times 2c_p$, where a_p, b_p and c_p denote the primitive cell for the simple cubic perovskite. In this lattice distortion, the bond angle $\angle$Mn-O-Mn deviates from 180°, resulting in a significant change in the effective one-electron bandwidth (W) or equivalent e_g-electron transfer interaction (t). In the substitution system of $(R^{3+}_{1-x}A^{2+}_{x})MnO_3$ with a fixed x and a random distribution of R^{3+} and A^{2+}, the structural and electromagnetic properties have been

explained well by the degree of mismatch, that is, the tolerance factor $f = (\langle r_A \rangle + r_O)/[\sqrt{2}\,(r_{Mn}+r_O)]$, where $\langle r_A \rangle$, r_{Mn} and r_O are (averaged) ionic radii for the respective elements, because W or t is changed by varying f.

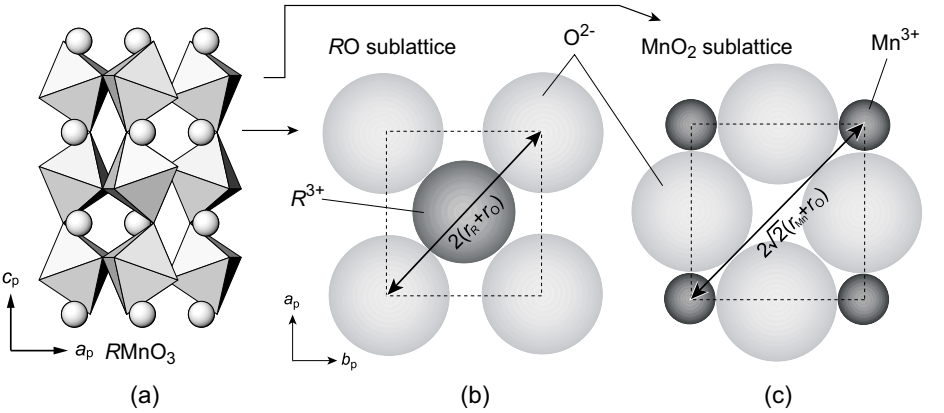

Fig. 1. Structural concept of perovskite manganite. The crystal structure of RMnO$_3$ (**a**) consists of RO rock-salt sublattice (**b**) and MnO$_2$ square sublattice (**c**). The mismatch between the larger MnO$_2$ and smaller RO sublattices is relaxed by tilting MnO$_6$ octahedra, leading to the lattice distortion from a cubic structure to an orthorhombic GdFeO$_3$-type structure (**a**).

Figure 2 shows the generalized phase diagram for $(R^{3+}_{0.5}A^{2+}_{0.5})MnO_3$ (A^{2+} = Ca and Sr) with a half doping level x = 0.5 [1], where the ferromagnetic metal (FM) generated by the double-exchange (DE) interaction is dominant near f = 1 (maximal W or t), while the CE-type CO insulator (COI(CE)) is most stabilized in the lower f region (f < 0.975). In the middle region (f ~ 0.975), the competition between the ferromagnetic DE and the antiferromagnetic CO interactions results in various phenomena including CMR.

However, probably underestimated to date or even neglected in many cases, has been the effect of randomness or compositional inhomogeneity in the crystal structure, which inevitably exists when we deal with solid solutions except the end members, x = 0 and 1. This effect may destroy some hidden phase which otherwise may be present at given x and W (f). Apart from such effect, it is very interesting how the A-site randomness affects the physical properties of $(R^{3+}_{1-x}A^{2+}_{x})MnO_3$. The phenomena such as CMR and the electronic phase separation [2] may be induced by the A-site randomness. Although the search for the compound without the A-site randomness had been motivated by its intriguing properties, almost all the works devoted to a series of perovskite manganites so far were on the disordered manganites with R^{3+} and A^{2+} ions being randomly distributed.

Very recently the A-site ordered manganites, RBaMn$_2$O$_6$ (R = Y and rare earth elements), have been successfully synthesized [3-12]. The discovery of novel structural and physical properties in the A-site ordered manganites RBaMn$_2$O$_6$ has demanded new

comprehension about perovskite manganese oxides [3-12]. In this chapter, the structures and electromagnetic properties of the *A*-site ordered manganites RBaMn$_2$O$_6$ are reviewed and discussed in terms of the structural characteristics. Furthermore the structures and electromagnetic properties of the *A*-site disordered Ba-based manganites $R_{0.5}$Ba$_{0.5}$MnO$_3$, including the systematic study of the *A*-site randomness effect in Pr-compounds (R = Pr), are reviewed in comparison with the ordered form RBaMn$_2$O$_6$.

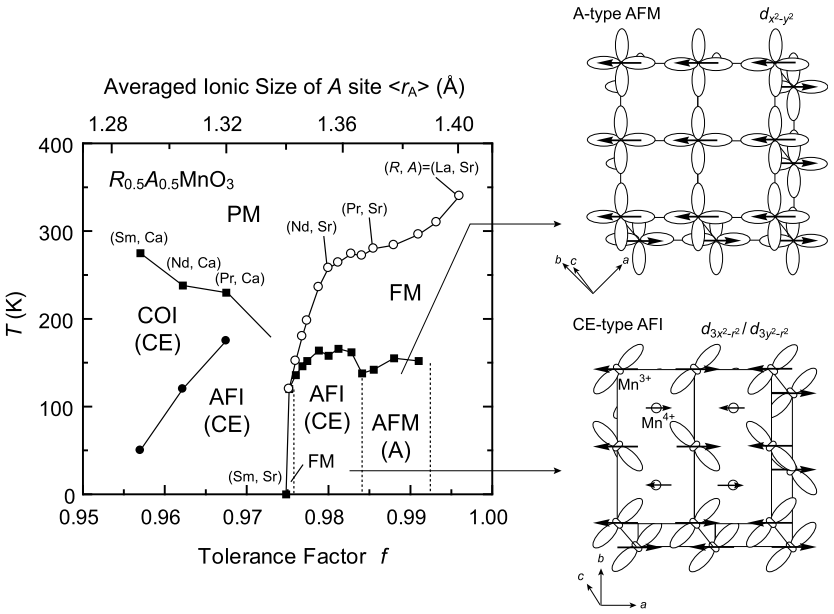

Fig. 2. Generalized phase diagram for ($R^{3+}_{0.5}A^{2+}_{0.5}$)MnO$_3$ [1]. FM: ferromagnetic metal, AFM(A): A-type antiferromagnetic metal, COI(CE): CE-type charge/orbital ordered insulator, AFI(CE): antiferromagnetic CE-type charge/orbital ordered insulator, PM: paramagnetic metal phases. The charge, orbital and spin alignments are shown for AFM(A) and AFI(CE) phases.

2. SAMPLE PREPARATION

The ordinary *A*-site disordered manganites ($R^{3+}_{0.5}A^{2+}_{0.5}$)MnO$_3$ (A^{2+} = Ca and Sr) have been prepared by a solid state reaction in the air, while the synthesis of the *A*-site ordered manganites RBaMn$_2$O$_6$ requires the following two procedures (see the flowchart in Fig. 3). Starting reagents R_2O_3, MnO$_2$, and BaCO$_3$ with 99.99 % purities were ground thoroughly, pressed into pellets and calcined in an Ar flow (6N) at 1573 K for 48 h. Such rather reductive atmosphere (6N-Ar; P_{O_2} <10^{-4} atm) provides oxygen-deficient perovskite RBaMn$_2$O$_5$ with a layer type ordering of R and Ba and the lack of oxygen in the RO layers. This is due to the general preference of the small R^{3+} ions to take eight-fold coordination in RBaMn$_2$O$_5$ rather

than twelve-fold coordination in $(R^{3+}_{0.5}A^{2+}_{0.5})MnO_3$. This preference has been seen in the Ba-based perovskite oxides with *A*-site cations whose ionic radii are very different from Ba^{2+}, for examples, $YBa_2Cu_3O_7$, $LaBa_2Cu_3O_7$ and $YBaCo_2O_5$ [13,14]. The second step is annealing the obtained specimen in flowing O_2 at 773 K for 48 h, which leads to the full oxidation ($R$$BaMn_2O_6$) of the specimen without any diffusion of the *A*-site cations. This reaction is reversible and indicates the topotactic nature of the transformation between $R$$BaMn_2O_5$ and $R$$BaMn_2O_6$. On the other hand, powder samples of the *A*-site disordered form $R_{0.5}Ba_{0.5}MnO_3$ were obtained by a solid state reaction of the same starting compounds at 1623 K in 1% O_2/Ar gas, followed by annealing at 1173 K in O_2 gas for 1 day (Path I in Fig. 3). Annealing of $R$$BaMn_2O_6$ under O_2 gas at high temperatures gave the insufficient *R*/Ba solid-solution (Path II in Fig. 3). The Pr-compounds; $[Pr_gBa_{1-g}]_P[Pr_{1-g}Ba_g]_BMn_2O_6$ ($0.5 \leq g \leq 1.0$) with S = 87(4)% (PB87), 70(4)% (PB70), 57(6)% (PB57), 32(2)% (PB32) and 25(6)% (PB25) were prepared from $PrBaMn_2O_6$ (PB96: S = 96(2)%) by controlling the annealing time and temperatures (1273~1623 K) in O_2 gas, where $[\ ]_P$ (or $[\ ]_B$) represents Pr-sites (or Ba-sites) in $PrBaMn_2O_6$ and the degree of *A*-site order (S) is defined as $S = (2g\text{-}1) \times 100$ %. The S was determined by the Rietveld analysis of powder X-ray and neutron diffractions.

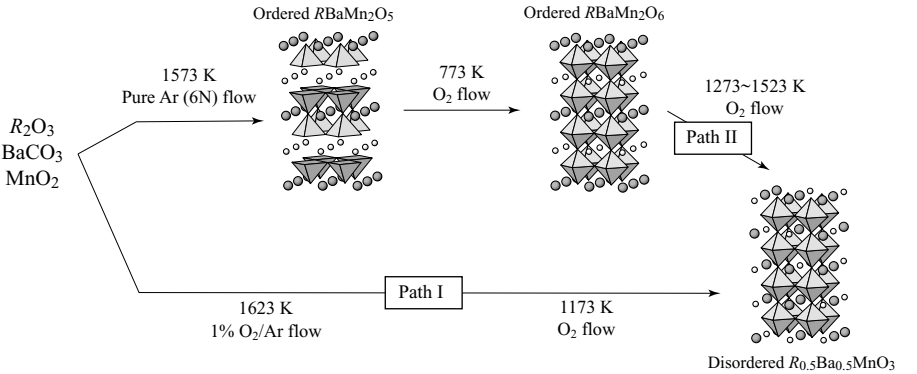

Fig. 3. Flowchart of sample preparation.

3. THE *A*-SITE ORDERED MANGANITES $R$$BaMn_2O_6$

3.1. General aspect of the crystal structure of $R$$BaMn_2O_6$

The *A*-site ordered manganites $R$$BaMn_2O_6$ have a remarkable structural feature in addition to the absence of the *A*-site randomness. The most significant structural feature of $R$$BaMn_2O_6$ is that the MnO_2 square sublattice is sandwiched by two types of rock-salt layers, *R*O and BaO with different lattice sizes, as schematically shown in Fig. 4. This means that the structural and physical properties of $R$$BaMn_2O_6$ can be no longer explained in terms of the basic structural distortion, that is *f*, as in $R_{0.5}A_{0.5}MnO_3$ (*A* = Ca and Sr). The lattice size of the *A*O layer is much smaller in *R*O layer and much larger in BaO layer than that of the MnO_2 layer.

The large mismatch between *R*O- and BaO-lattices introduces a strong frustration to the MnO_2 sublattice and as a result the MnO_6 octahedron itself is heavily distorted in a noncentrosymmetric manner that both Mn and oxygen atoms in the MnO_2 layer are displaced toward the *R*O layer (Fig. 4(c)), in contrast to the rigid MnO_6 octahedron in the *A*-site disordered manganites $(R_{1-x}A_x)MnO_3$ (*A* = Ca and Sr). Such deformation must give a new perturbation to the competition of multi-degrees of freedom among charge, orbital, spin and lattice. The novel structural and electromagnetic properties of $RBaMn_2O_6$ reviewed below could be closely related to such structural frustration or deformation.

From the structural and electromagnetic properties, $RBaMn_2O_6$ can be first classified into two groups, *R* = La, Pr and Nd (the first group) and *R* = Sm ~ Y, and the later group is separated into further two groups, *R* = Sm, Eu and Gd (the second group) and *R* = Tb, Dy, Ho and Y (the third group).

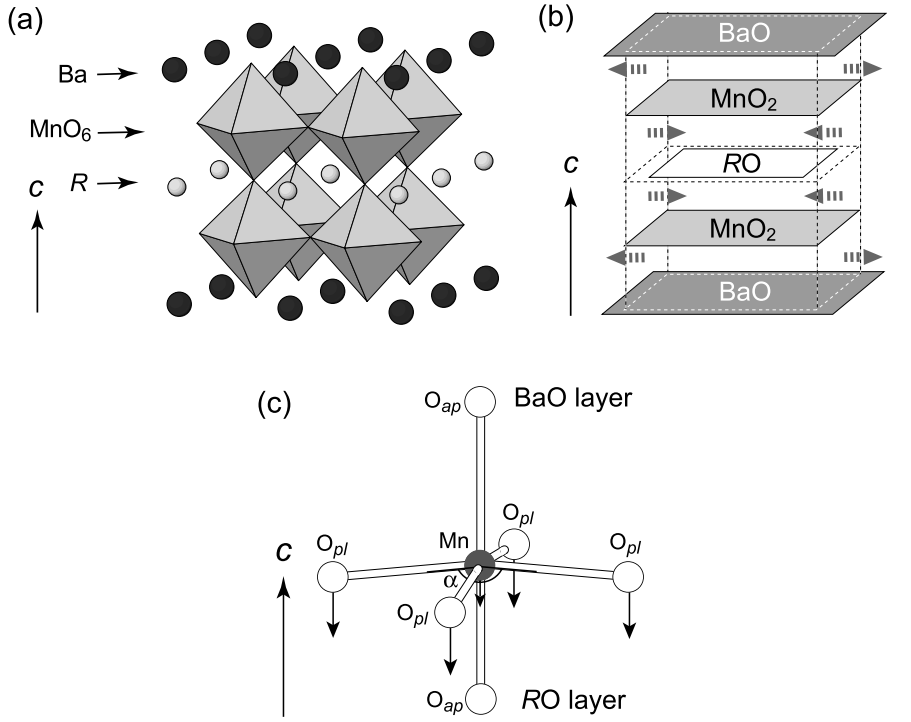

Fig. 4. Crystal structure (**a**), structural concept (**b**) and an illustration of the distorted MnO_6 octahedra (**c**) of the *A*-site ordered manganites $RBaMn_2O_6$.

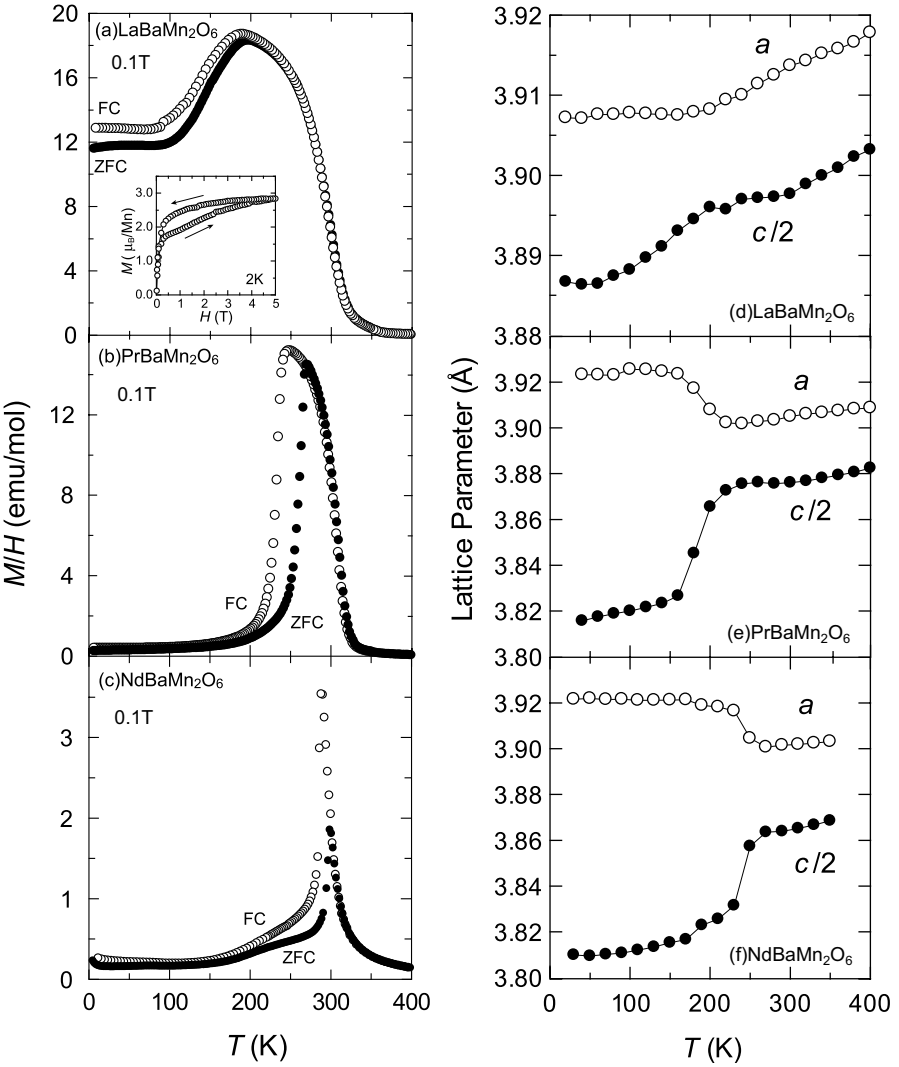

Fig. 5. Temperature dependences of magnetic susceptibility (*M*/*H*) (**a**)-(**c**) and lattice parameters (**d**)-(**f**); $LaBaMn_2O_6$: (**a**) and (**d**), $PrBaMn_2O_6$: (**b**) and (e), $NdBaMn_2O_6$: (**c**) and (**f**). The magnetization was measured under 0.1 T on zero-field cooled (ZFC) and field cooled (FC) processes. The inset in Fig. 5(**a**) shows the magnetization curves of $LaBaMn_2O_6$ at 2 K. The lattice parameter was determined on cooling process. The elongation of the *a*-axis and the contraction of the *c*-axis at FM-to-AFM(A) transition in $PrBaMn_2O_6$ and $NdBaMn_2O_6$ are compatible with the $d_{x^2-y^2}$ orbital ordering.

3.2. Structures and electromagnetic properties of *R*$BaMn_2O_6$ (*R* = La, Pr and Nd) [6]

The crystal structure of *R*$BaMn_2O_6$ (*R* = La, Pr and Nd) at 400 K (paramagnetic state) has a simple tetragonal a_p x a_p x $2c_p$ cell with a space group of *P*4/*mmm* and has no tilt of MnO_6 octahedra which is rare in manganese perovskites. On the other hand, the MnO_6 octahedron itself is distorted in a way as illustrated in Fig. 4(c): Both Mn and oxygen atoms (O_{pl}) in the MnO_2 plane are displaced toward the *R*O layer to a larger extent for O_{pl}. As a result, the angle of $\angle O_{pl}$-Mn-O_{pl} (=$\angle\alpha$, see Fig. 4(c)) deviates from 180° to 176.4° (La), 174.7° (Pr) and 173.7° (Nd), while that of $\angle O_{ap}$-Mn-O_{ap} (O_{ap}: apical oxygen atom) is 180° in all compounds. The distance of Mn-O_{ap} is shortened (1.913 Å for La, 1.902 Å for Pr and 1.894 Å for Nd) in the *R*O side, while that is elongated (1.989 Å for La, 1.979 Å for Pr and 1.978 Å for Nd) in the BaO side. Intermediate values are obtained for the distance of Mn-O_{pl} (1.960 Å for La, 1.956 Å for Pr and 1.955 Å for Nd).

The magnetic susceptibilities (*M*/*H*) and lattice parameters of *R*$BaMn_2O_6$ (*R* = La, Pr and Nd) are shown in Fig. 5 as a function of temperature. These compounds show the paramagnetic-metal (PM) to ferromagnetic-metal (FM) transition without any structural change at T_C = 330 K (La), 310 K (Pr) and 300 K (Nd), respectively. The neutron diffraction study reveals the coexistence of antiferromagnetic CE-type CO phase (AFI(CE)) with FM phase below 200 K in $LaBaMn_2O_6$ and the FM-to-AFM(A) (A-type antiferromagnetic metal) transition at T_N = 270 K in $PrBaMn_2O_6$ and T_N = 290 K in $NdBaMn_2O_6$. The AFI(CE) phase in $LaBaMn_2O_6$ is converted to the FM phase under external magnetic field, as shown in the inset of Fig. 5(a). The volume fraction of the AFI(CE) phase is estimated to be about 30 % from the difference of magnetization between 0.3 T and 5 T at 2 K. A slight amount of the AFI(CE) phase coexists with the AFM(A) phase in the ground state of $PrBaMn_2O_6$, while no trace of AFI(CE) phase is seen in $NdBaMn_2O_6$. The FM-to-AFM(A) transition associated with $d_{x^2-y^2}$ orbital order is consistent with the change of lattice parameters observed, namely the elongation of the *a*-axis and the contraction of the *c*-axis at T_N, as shown in Fig. 5.

3.3. Structures and electromagnetic properties of *R*$BaMn_2O_6$ (*R* = Sm ~ Ho and Y) [3-5,7,8]

The crystal structure of *R*$BaMn_2O_6$ (*R* = Sm ~ Ho and Y) at room temperature has a larger cell of $\sqrt{2}a_p \times \sqrt{2}b_p \times 2c_p$ with a tilt of MnO_6 octahedra. The unit cell for *R* = Sm, Eu and Gd is nearly tetragonal ($a_p = b_p$) but that for *R* = Tb, Dy, Ho and Y is distorted to a monoclinic one.

Figure 6 shows magnetic susceptibility (*M*/*H*), resistivity (□) measured using sintered pellet and differential scanning calorimetry (DSC) curves for $EuBaMn_2O_6$ as the typical example of the second group. The second group, *R*$BaMn_2O_6$ (*R* = Sm, Eu and Gd), shows the CO transition (MI transition) at T_{CO} = 375 K (Sm), 400 K (Eu) and 410 K (Gd), accompanied by the structural change from the high temperature orthorhombic structure to the low temperature tetragonal structure. The antiferromagnetic transition takes place at T_N = 250 K (Sm), 230 K (Eu) and 210 K (Gd) below T_{CO}. As described below, the CO pattern has an in-plane superstructure of $2\sqrt{2}a_p \times \sqrt{2}b_p$ characteristic of the CE-type CO and a new stacking variation with a four-fold periodicity along the *c*-axis.

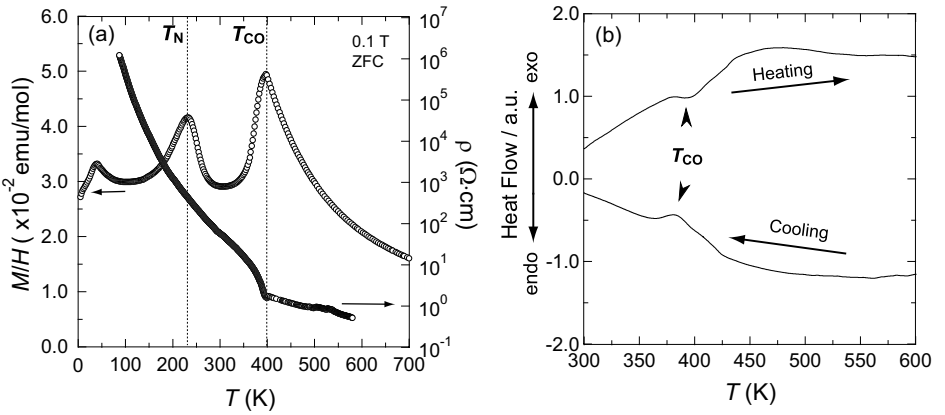

Fig. 6. Temperature dependences of magnetic susceptibility (M/H) and resistivity (□) (**a**), and DSC curves (**b**) for $EuBaMn_2O_6$.

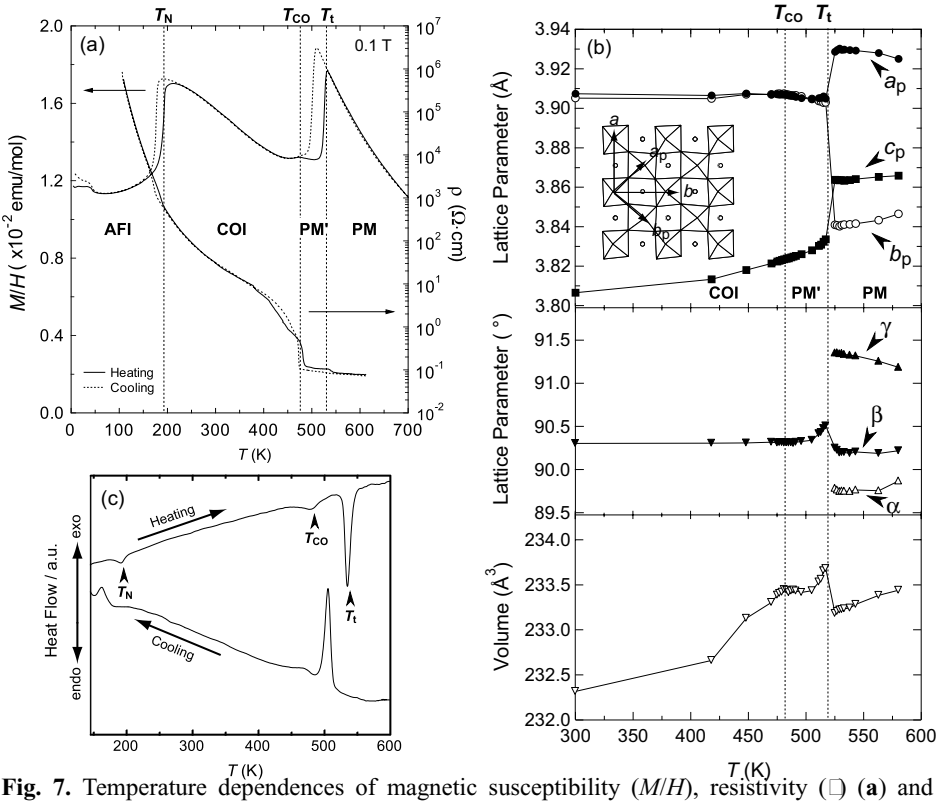

Fig. 7. Temperature dependences of magnetic susceptibility (M/H), resistivity (□) (**a**) and lattice parameters (**b**), and DSC curves (**c**) for $YBaMn_2O_6$.

The third group RBaMn$_2$O$_6$ (R = Tb, Dy, Ho and Y), on the other hand, shows the distinct three transitions; structural transition at T_t, CO transition (MI transition) at T_{CO} and antiferromagnetic transition at T_N on cooling [3,4,5,7,8]. Typical examples of magnetic susceptibility (M/H), resistivity (□) (using sintered pellet), lattice parameters and DSC curves for YBaMn$_2$O$_6$ are shown in Fig. 7. The transition at T_t is a first-order phase transition verified by the large DSC peak and the jump of lattice parameters, where the crystal structure changes from the high temperature triclinic $P\bar{1}$ structure to the low temperature monoclinic $P2$ structure [7]. The magnetic susceptibility sharply decreases and the conductivity remains metallic across T_t. Above T_t the magnetic interaction deduced from Curie-Weiss fitting of magnetic susceptibility is a ferromagnetic one (θ = 271 K) generated by the isotropic DE interaction, while below T_t it changes to an antiferromagnetic one. The CO transition (MI transition) occurs at T_{CO} below T_t, taking with a slight change of magnetic susceptibility, a weak DSC peak and no significant change of lattice parameters. This transition seems to be a second-order one because of no significant hysteresis behavior.

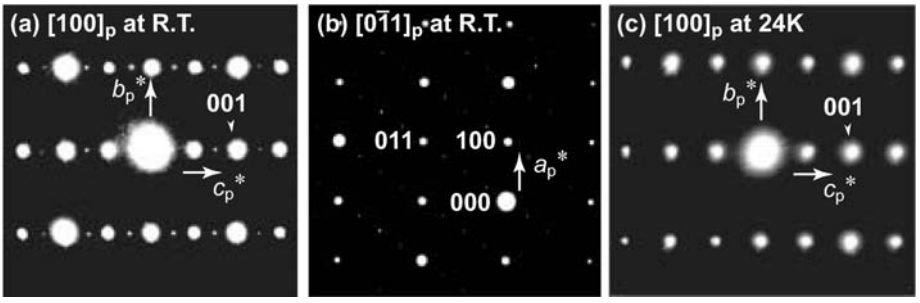

Fig. 8. The electron diffraction patterns of YBaMn$_2$O$_6$: the [100]$_p$-zone axis (**a**), the [0$\bar{1}$1]$_p$ zone axis (**b**) at room temperature and the [100]$_p$-zone axis (c) at 24 K.

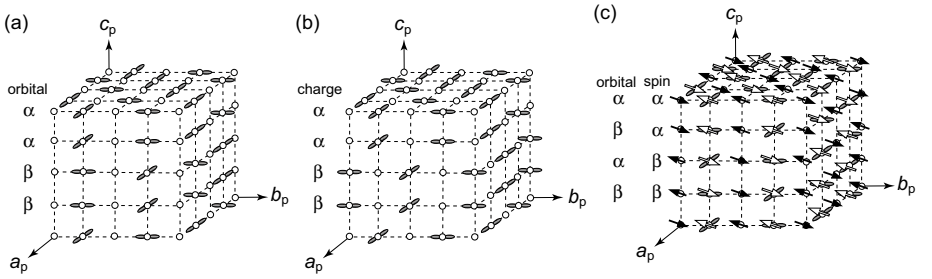

Fig. 9. (**a**) and (**b**) Modified CE-type CO patterns with a four-fold periodicity ($\alpha\alpha\beta\beta$) along the c-axis. The lobes indicate the $d_{3x^2-r^2}/d_{3y^2-r^2}$ type orbitals at Mn^{3+} sites, while the circles denote the Mn^{4+} sites. (**c**) A possible charge, orbital and spin ordering pattern in AFI(CE) phase.

The TEM (transmission electron microscopy) study reveals an inplane superstructure of $2\sqrt{2}a_P \times \sqrt{2}b_P$ characteristic of the CE-type CO and a new stacking variation with a four-fold periodicity along the *c*-axis, as shown in Figs. 8(a) and (b) [5,7,11,12]. There are various methods of piling up the CE-type layers along the *c*-axis so as to satisfy the unit cell $2\sqrt{2}a_P \times \sqrt{2}b_P \times 4c_P$. Figures 9(a) and (b) show two possible models, both of which have the stacking sequence along the *c*-axis described by ($\alpha\alpha\beta\beta$). The model shown in Fig. 9(a) has the uniform alignment of Mn^{3+}/Mn^{4+} and ($\alpha\alpha\beta\beta$)-type stacking of the $d_{3x^2-r^2}$- and $d_{3y^2-r^2}$-orbitals [7], while the model in Fig. 9(b) has the ($\alpha\alpha\beta\beta$)-type stacking of charges/orbitals [11].

The CO phase (COI(CE)) orders antiferromagnetically at T_N. The antiferromagnetic transition has a considerable thermal hysteresis, as clearly seen in the DSC curves (Fig. 7 (c)), indicating a first-order transition. The nature of the first-order transition is verified from the TEM study. As shown in Fig. 8(c), when the system enters into antiferromagnetic state (AFI(CE)), the four-fold periodicity along the *c*-axis in COI(CE) phase disappears, although the inplane superstructure of the CE-type CO is kept. Therefore the CO pattern in AFI(CE) phase can be considered to have a ($\alpha\alpha$)- or ($\alpha\beta$)-type stacking of the CE-type layers along the *c*-axis. On the other hand, neutron diffraction study reveals the CE-type spin-ordering pattern in the *a*-*b* plane and a four-fold periodicity along the *c*-axis [5,7,11,12]. One candidate of charge/orbital and spin ordering pattern in AFI(CE) phase is shown in Fig. 9(c).

3.4. Electronic phase diagram of *R*$BaMn_2O_6$

The results of structures and electromagnetic properties for *R*$BaMn_2O_6$ are summarized in Fig. 10 in a phase diagram [4,6,8]. Here the phase diagram is expressed as a function of the ratio of ionic radius, $r_I = r_{R^{3+}} / r_{Ba^{2+}}$, instead of *f*. The r_I is a measure of mismatch between *R*O- and BaO-lattices. It is natural that the FM state generated by the DE interaction is dominant in *R*$BaMn_2O_6$ (*R* = La, Pr and Nd) with no tilt of MnO_6 octahedra, while the CO state is stabilized in *R*$BaMn_2O_6$ (*R* = Sm ~ Ho and Y) with a tilt of MnO_6 octahedra. The layer type ordering of R^{3+} and Ba^{2+} makes stable the AFM(A) phase associated with the two-dimensional $d_{x^2-y^2}$ orbital ordering.

Compared with the *A*-site disordered $R_{0.5}A_{0.5}MnO_3$ (*A* = Sr, Ca), *R*$BaMn_2O_6$ displays remarkable features: (1) the CO transition at temperatures far above 300 K, (2) a new stacking variation of the CE-type CO with a four-fold periodicity along the *c*-axis (4CE-CO), (3) the absence of both lowering of T_C (or T_{CO}) and FM-to-AFI(CE) transition responsible for CMR in the phase boundary between FM and COI(CE), (4) the presence of structural transition at T_t above T_{CO}, and (5) the electronic phase segregation in the end member $LaBaMn_2O_6$. These novel properties are closely related to the characteristic structure. The relatively high T_{CO} can be understood as the effect of the absence of the *A*-site randomness. The 4CE-CO could be strongly correlated to the inherent structural alternation, i.e., the *R*/Ba order along the *c*-axis; the ($\alpha\alpha\beta\beta$)-type stacking is naturally explained if the sign of the interlayer charge/orbital interaction alternatively changes due to the *R*/Ba order. Lowering the transition temperatures (T_{CO} and T_C) and FM-to-AFI(CE) transition as observed around the critical region in $R_{0.5}A_{0.5}MnO_3$ (*A* = Sr, Ca) are not recognized in the phase diagram of *R*$BaMn_2O_6$. The absence of such behaviors in *R*$BaMn_2O_6$ is partly due to the absence of the *A*-site randomness.

In the critical region, the FM (or AFM) and CO interactions compete with each other and they are significantly affected by composition, coherent size of crystal, external field *etc*. The FM (or AFM) and CO interactions are spatially distributed in $R_{0.5}A_{0.5}MnO_3$ (A = Sr, Ca) with the A-site randomness. Such fluctuation of interactions enhances the criticality. On the other hand, it could be more definite which interaction becomes dominant in RBaMn$_2$O$_6$ without the A-site randomness. The features (4) and (5) are closely related to the inherent structural frustration. Considering the tolerance factors, f_1 = 1.2 for $Ba^{2+}/Mn^{+3.5}$ and f_2 = 0.8 for $Y^{3+}/Mn^{+3.5}$ [15], for example, each MnO_2 layer in YBaMn$_2$O$_6$ should feel strain forces with the opposite signs (or a structural frustration) from the adjacent YO and BaO layers, as shown in Fig. 4(b). With this frustration, one cannot achieve an adequate compensation for this structural mismatch only from the tilting of the rigid MnO_6 octahedra. As a consequence, the shape of the MnO_6 octahedron deviates heavily from the ideal (regular) octahedron in a way shown in Fig. 4(c); the MnO_2 planar oxygen ions (O_{pl}) are displaced largely from the ideal position z = 0.25 toward the RO layer, and the apical oxygen ions (O_{ap}) including the RO layer are shortened while those including the BaO layer are elongated.

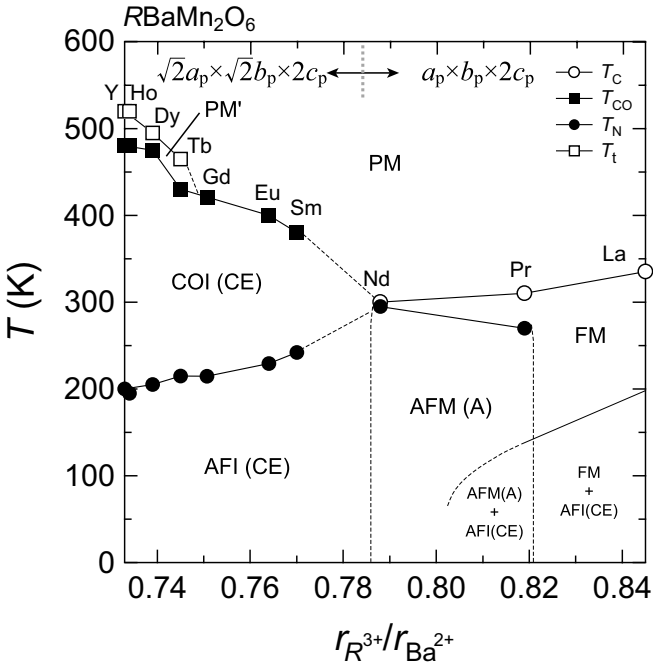

Fig. 10. Phase diagram of RBaMn$_2$O$_6$. The notation for each phase is the same as defined in Fig. 2. T_C: ferromagnetic transition temperature, T_N: antiferromagnetic transition temperature, T_{CO}: charge/orbital order transition temperature, T_t: structural transition temperature.

The structural transition at T_t is a remarkable feature observed in the third group with larger mismatch between RO and BaO lattices. The PM phase above T_t has a triclinic $P1$ symmetry with a $\sqrt{2}a_P \times \sqrt{2}b_P \times 2c_P$ unit cell, while the PM' phase below T_t has a monoclinic $P2$ symmetry with a $\sqrt{2}a_P \times \sqrt{2}b_P \times 2c_P$ unit cell. According to Glazer's notation [16-18], the octahedral tilting is approximately described as $a^-b^-c^-$ in the PM' phase, while it is $a^0b^-c^-$ in the PM phase. In the ordinary solid solution of $R_{0.5}A_{0.5}MnO_3$ (A = Ca and Sr), the MI transition to the CO state is always accompanied by a drastic first-order structural phase transition [1]. In RBaMn$_2$O$_6$ (R = Tb, Dy, Ho and Y), however, the metallic behavior is still retained in the PM' phase despite the drastic first-order structural phase transition at T_t, where the magnetic interactions abruptly change from ferromagnetic above T_t to antiferromagnetic below T_t [3,7]. Add to this, considering the unusual structural transition from the low-temperature higher symmetry to the high-temperature lower symmetry, a hidden parameter may play a role in compensating for the lattice entropy. The ab-plane orbital ordering has been proposed in the PM' phase [4,7,8], in which not the $d_{3x^2-r^2}/d_{3y^2-r^2}$ orbitals (responsible for the insulating CE structure below T_{CO}) but the $d_{x^2-y^2}$ orbitals are occupied. Actually, this orbital ordering is compatible with the increase of $(a_p + b_p) / 2$ and the decrease of c_p (see Fig. 7(b)), which would be induced so as to relax the peculiar lattice distortion arising from both the layered structure and octahedral tilting.

The last feature, the coexistence of the FM and AFI(CE) phases in LaBaMn$_2$O$_6$, is an unexpected phenomenon. A similar coexistence has been observed in $R_{1-x}A_xMnO_3$ (A = Ca and Sr) so far and attributed to the A-site randomness or fluctuation of composition [19]. In Fig. 2, there exists a critical region where the FM and CO interactions compete with each other and therefore the transition from FM to AFI(CE) as a function of temperature, which is responsible for CMR, is observable. Since the A-site ordered system does not have such randomness, the observed electronic phase segregation is an essential behavior caused by the interplay among spin, charge, orbital and lattice degrees of freedom. If the ratio $r_{R^{3+}}/r_{Ba^{2+}}$ were an appropriate measure of the bandwidth as is the case of f for $R_{0.5}A_{0.5}MnO_3$ (A = Ca and Sr), such a critical region would be located between SmBaMn$_2$O$_6$ and NdBaMn$_2$O$_6$, and a FM-to-AFI(CE) transition would be expected in NdBaMn$_2$O$_6$ adjacent to SmBaMn$_2$O$_6$. In reality, the ground state of NdBaMn$_2$O$_6$, however, is the A-type AFM and a fractional transition from FM to AFI(CE) is observed in LaBaMn$_2$O$_6$ far from SmBaMn$_2$O$_6$. This implies that LaBaMn$_2$O$_6$ might be located closer to the CO state and the bandwidth would become larger as LaBaMn$_2$O$_6$ < PrBaMn$_2$O$_6$ < NdBaMn$_2$O$_6$. Here it should be noticed again that RBaMn$_2$O$_6$ (R =La, Pr and Nd) has no tilt of MnO$_6$ octahedra. It is known that the tilt of MnO$_6$ octahedra in ordinary manganese perovskites occurs in order to fit the larger MnO$_2$ sublattice to the smaller AO sublattice (f < 1). No tilt of MnO$_6$ octahedra is expected to occur either when the MnO$_2$ lattice has the almost same size as the AO lattice ($f \approx 1$) or when the MnO$_2$ lattice is expanded by the AO lattice ($f > 1$). In RBaMn$_2$O$_6$ (R = La, Pr, Nd) with relatively larger R^{3+}, the expansion of the MnO$_2$ lattice by the much larger BaO lattice (f = 1.071) might overwhelm the contraction by the smaller RO lattice (f = 0.982 for LaO, f = 0.964 for PrO and f = 0.950 for NdO) [15], in contrast to the case of RBaMn$_2$O$_6$ with R = Sm and later rare earth elements. Actually, the Mn-O$_{pl}$ distance (~1.96 Å) is elongated compared with that (1.91~1.94 Å) for the regular $Mn^{3.5+}O_6$ [6]. The increase of Mn-O$_{pl}$ distance and the deviation of the angle ∠Mn-O$_{pl}$-Mn from 180° would result in the decrease of bandwidth. In addition, the alternate stacking of RO and BaO layers would provide two-dimensional

character in the structure, which would be preferable for the $d_{x^2-y^2}$ type orbital order (A-type AFM). These structural characteristics explain well the present results; No tilt structure stabilizes FM but the two-dimensional character in the structure leads to A-type AFM associated with $d_{x^2-y^2}$ type orbital order as the ground states of $NdBaMn_2O_6$ and $PrBaMn_2O_6$. The much elongation of Mn-O_{pl} distance in $LaBaMn_2O_6$ destabilizes FM to some extent as a result of the decrease of bandwidth and results in the fractional transition from FM to AFI(CE) (coexistence of FM and AFI(CE) phases as the ground state). The effect of Mn-O_{pl} distance on the bandwidth has never been seen nor discussed in the ordinal perovskite manganese oxides, because they have finite tilt of MnO_6 octahedra, by which the bandwidth is dominantly controlled.

4. THE *A*-SITE DISORDERED MANGANITES $R_{0.5}Ba_{0.5}MnO_3$

4.1. Structures and electromagnetic properties of $R_{0.5}Ba_{0.5}MnO_3$ [8,20-23]

All compounds of $R_{0.5}Ba_{0.5}MnO_3$ crystallize in a primitive cubic perovskite structure. The lattice parameters of $R_{0.5}Ba_{0.5}MnO_3$ at room temperature are shown in Fig. 11(a). The lattice parameter decreases with decreasing ionic radius of R^{3+}. The simple cubic cell means no tilt of MnO_6 octahedra in contrast to the orthorhombic $GdFeO_3$ type distortion of $R_{0.5}A_{0.5}MnO_3$ (*A* = Ca and Sr). In general, the mismatch between the larger MnO_2 and the smaller (*R*,*A*)O sublattices is relaxed by tilting MnO_6 octahedra, resulting in the lattice distortion from cubic to, mostly, the orthorhombic $GdFeO_3$-type structure. In $R_{0.5}Ba_{0.5}MnO_3$, the *f* is in the range from 1.026 (La/Ba) to 0.995 (Y/Ba), which are rather close to $f = 1$, comparing to the variation $0.955 < f < 1$ in $R_{0.5}A_{0.5}MnO_3$ (*A* = Ca and Sr). Therefore the simple cubic structures of $R_{0.5}Ba_{0.5}MnO_3$ can be partly understood from the *f*-values close to 1, that is relatively small mismatch between the MnO_2 and ($R_{0.5}Ba_{0.5}$)O lattices. Here, it should be noticed that the *f* is beyond 1 in $R_{0.5}Ba_{0.5}MnO_3$ (*R* = La, Pr and Nd). From the simple cubic structures of $R_{0.5}Ba_{0.5}MnO_3$, one may expect FM generated by the DE interaction as the stable electronic state. The ground state of $La_{0.5}Ba_{0.5}MnO_3$ is actually a pure FM and the ferromagnetic transition temperature T_C decreases by 50 K compared with $T_C = 330$ K in $LaBaMn_2O_6$, as shown in Fig. 12 (a). On the other hand, $Pr_{0.5}Ba_{0.5}MnO_3$ and $Nd_{0.5}Ba_{0.5}MnO_3$ show the increase of magnetic susceptibility (*M/H*) below about 150 K and then show glassy behaviors below about 50 K, evidenced by significant differences of *M/H-T* curves on zero-field cooled (ZFC) and field cooled (FC) processes. As an example, the *M/H-T* curve for $Pr_{0.5}Ba_{0.5}MnO_3$ is shown in Fig. 12(b). More typical spin-glass behaviors have been observed in $R_{0.5}Ba_{0.5}MnO_3$ with Sm^{3+} and smaller R^{3+}s. The typical *M/H-T* curves of $Sm_{0.5}Ba_{0.5}MnO_3$ and $Y_{0.5}Ba_{0.5}MnO_3$ are shown in Fig. 12(c) and 12(d), respectively. In $Y_{0.5}Ba_{0.5}MnO_3$, there is no trace of the three transitions observed in $YBaMn_2O_6$, except for the spin-glass (SG) transition at $T_G = 30$ K. The electrical resistivities of $R_{0.5}Ba_{0.5}MnO_3$ (*R* = Nd ~ Y) show semiconductive behaviors and the activation energy E_a decreases with decreasing the ionic radius of R^{3+} ion.

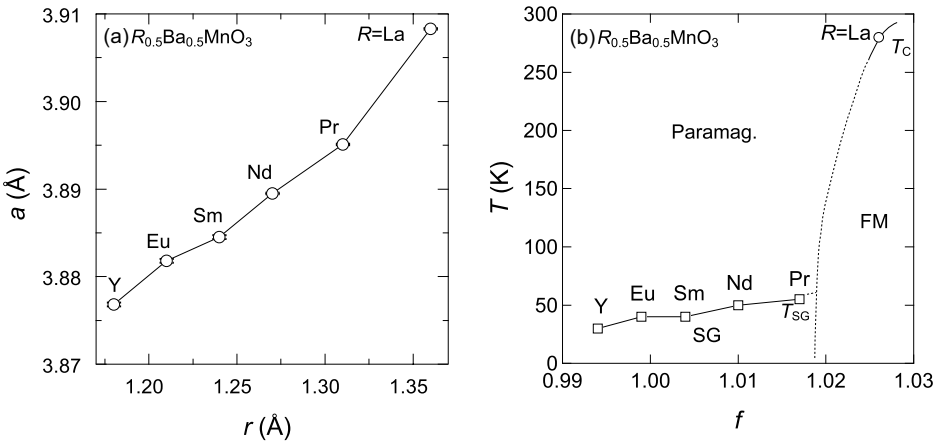

Fig. 11. Lattice parameters at room temperature (**a**) and phase diagram as a function of the tolerance factor *f* (**b**) for the *A*-site disordered $R_{0.5}Ba_{0.5}MnO_3$. SG: spin glass phase.

The results of magnetic properties of $R_{0.5}Ba_{0.5}MnO_3$ are summarized in Fig. 11(b) as the phase diagram. Here we compare the phase diagram among $RBaMn_2O_6$, $R_{0.5}Ba_{0.5}MnO_3$ and $R_{0.5}A_{0.5}MnO_3$ (A = Ca and Sr). The electronic states characteristic of perovskite manganites, for example AFM(A) and COI(CE) seen in $RBaMn_2O_6$ and $R_{0.5}A_{0.5}MnO_3$ (A = Ca and Sr), are absent in $R_{0.5}Ba_{0.5}MnO_3$. Instead of these states, magnetic glassy states govern the electronic state of $R_{0.5}Ba_{0.5}MnO_3$. The magnetic glassy state could be due to a disorder effect that hinders magnetic long-range ordering and it could occur as a result of the competition between randomly distributed ferromagnetic and antiferromagnetic interactions. Since the ionic radius of Ba^{2+} (= 1.61 Å) is much larger than that of Sr^{2+} (= 1.44 Å) and R^{3+} (≤1.36 Å) [15], $R_{0.5}Ba_{0.5}MnO_3$ could include any spatial heterogeneity in a nanometer scale, which results in magnetic nonhomogeneous states. Only the largest La^{3+} among R^{3+}s forms a homogeneous solid-solution at the *A*-sites with Ba^{2+} and the magnetic long-range ordering of FM is realized in $La_{0.5}Ba_{0.5}MnO_3$.

It has been suggested that the electromagnetic properties of perovskite manganites with *A*-site cations randomly distributed depend on not only *f* but also the variance of *A*-cation radius distribution σ^2 defined as $\sigma^2 = \sum y_i r_i^2 - r_A^2$, where r_i is the ionic radius of each *A*-site cation, y_i is the fractional occupancy of the *i* ion, r_A is the average ionic radius of *A*-site cations [24]. The value of σ^2 indicates the magnitude of potential disorder effect. Here, we discuss the ground states of the *A*-site disordered systems $R_{0.5}A_{0.5}MnO_3$ (A = Ca, Sr and Ba) in terms of σ^2. Figure 13 shows the mapping of $R_{0.5}A_{0.5}MnO_3$ (A = Ca, Sr and Ba) on a σ^2-$\langle r_A \rangle$ diagram. The data of $R_{0.5}A_{0.5}MnO_3$ (A = Sr and Ca) are quoted from the literatures [1,25]. The thick lines in Fig. 13 represent possible phase boundaries. The magnetic long-range orderings (AFI, AFM and FM) tend to be stabilized in the lower σ^2 region ($\sigma^2 < 10^{-2}$); otherwise, the magnetic glassy state is obviously dominant above $\sigma^2 = 10^{-2}$, except FM in $La_{0.5}Ba_{0.5}MnO_3$. Thus the difference of the ionic radius between *A*-site cations significantly influences magnetic long-range ordering in perovskite manganites.

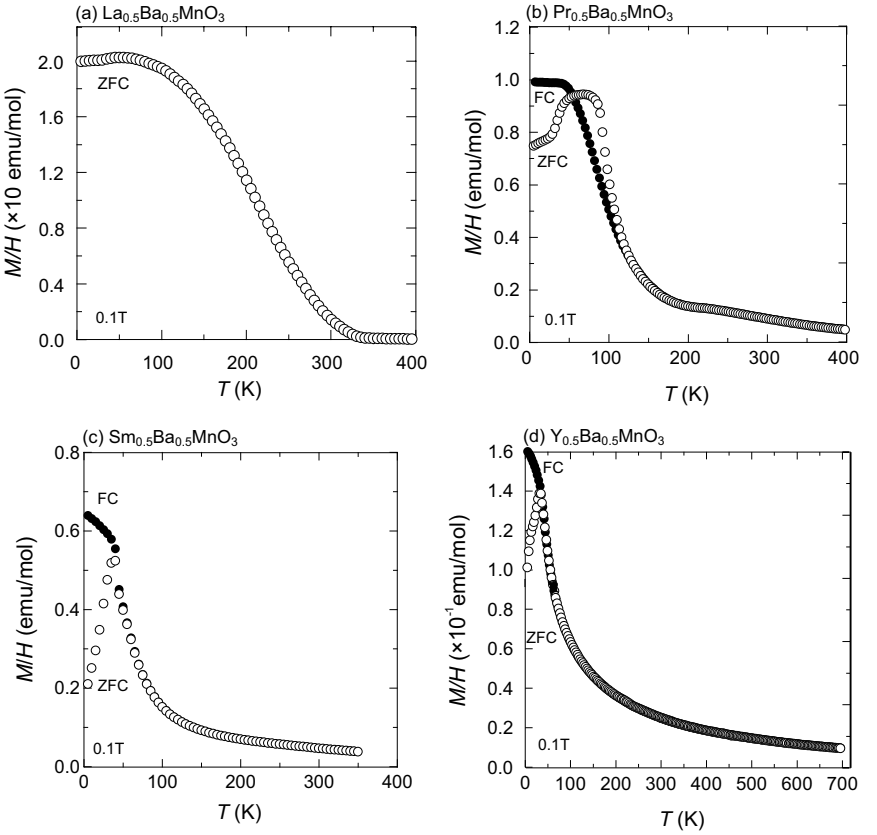

Fig. 12. Temperature dependence of magnetic susceptibility (M/H) for $La_{0.5}Ba_{0.5}MnO_3$ (**a**), $Pr_{0.5}Ba_{0.5}MnO_3$ (**b**), $Sm_{0.5}Ba_{0.5}MnO_3$ (**c**) and $Y_{0.5}Ba_{0.5}MnO_3$ (**d**).

4.2. The *A*-site randomness effect in Pr-compounds [22]

The structure and electromagnetic properties of perovskite manganites are significantly affected by the *A*-site disorder. In this section, the *A*-site randomness effect is demonstrated from the systematic study of the Pr-compounds (PB96 – PB00) with various degrees of the *A*-site randomness (see **2. SAMPLE PREPARATION**), where PB96 and PB00 are $PrBaMn_2O_6$ and $Pr_{0.5}Ba_{0.5}MnO_3$, respectively. The crystal structure is a simple tetragonal $P4/mmm$ for PB96 - PB25 and a simple cubic $Pm\bar{3}m$ for PB00. The lattice parameters, a and $c/2$, gradually approach each other with increasing the degree of the *A*-site disorder and terminate to the a-parameter of the cubic PB00. With increasing the *A*-site disorder, MnO_6 octahedra gradually approach to regular octahedra.

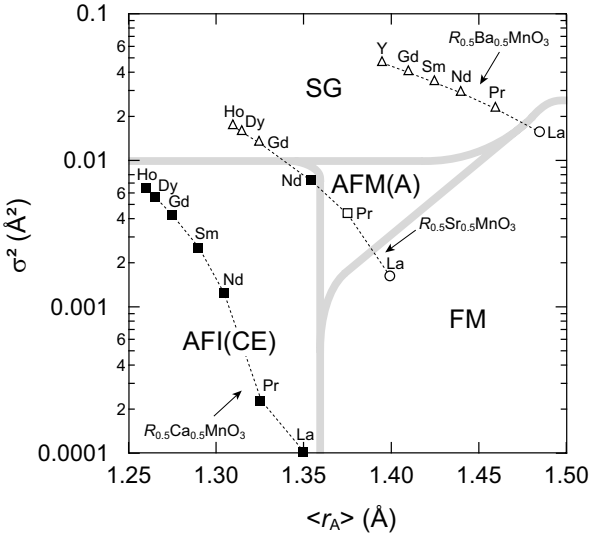

Fig. 13. The mapping of $R_{0.5}A_{0.5}MnO_3$ (A = Ca, Sr and Ba) on a σ^2 - $<r_A>$ diagram. (See the text). FM: ferromagnetic metal, AFM(A): A-type antiferromagnetic metal, AFI(CE): antiferromagnetic CE-type charge/orbital ordered insulator, SG: spin glass phases.

The magnetic susceptibilities (M/H) of Pr-compounds measured under 0.1 T are shown in Fig. 14(a). PB96 ($PrBaMn_2O_6$) shows FM transition at T_C = 303 K, followed by AFM(A) transition at T_N = 245 K. With increasing the A-site randomness, both T_C and T_N slightly decrease and AFM(A) transitions become broad. Furthermore some amount of FM state coexists with AFM(A) state below T_N in PB87 and PB70, which is evidenced by a considerable amount of temperature independent M/H below T_N. On the other hand, PB32 and PB25 with a considerable A-site disorder exhibit clear FM transitions at T_C = 158 K and 152 K, respectively. Since the saturated values of M/H of PB32 and PB25 are lower than that expected from full moment, any short-range magnetic ordered phase and/or AFM(A) phase coexist with FM phase. The rather low T_Cs for the second group (PB32 and PB25) compared with T_Cs for the first group (PB96-PB70) suggest two types of FM phase in Pr-compounds. This might be reflected in the M/H-T curve with two peaks around 200 K and 180 K for the intermediate compound PB57, namely PB57 includes two FM phases and each FM phase transforms to AFM(A) phase at independent temperatures (200 K and 180 K), showing peaks in M/H-T curve. Finally, the perfect disordered PB00 ($Pr_{0.5}Ba_{0.5}MnO_3$) has a much smaller M/H than that of other compounds and shows a spin-glass like transition at 50 K, as shown in the inset of Fig. 14(a). The presence of a small amount of AFM(A) phase at low temperature was confirmed by neutron diffraction measurements, as mentioned before, but any trace of long-range ordered phase FM was not observed.

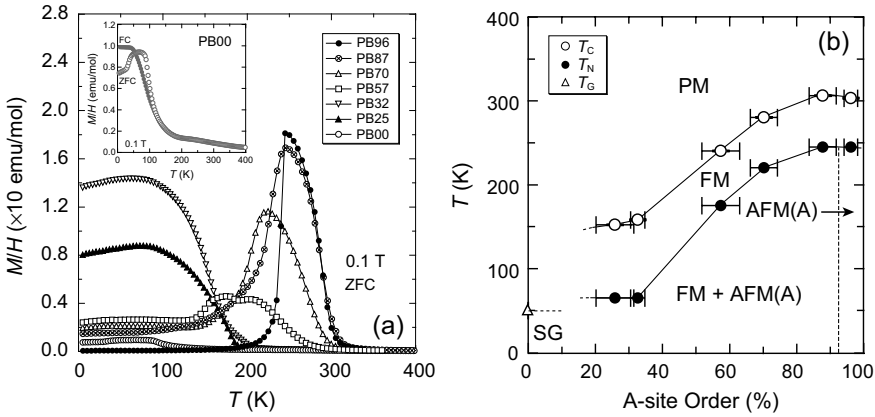

Fig. 14. (**a**) Temperature dependence of magnetic susceptibility (M/H) for Pr-compounds (PB96 ~ PB00) under 0.1 T. (**b**) Phase diagram for Pr-compounds as a function of the degree of the A-site order (see the text). PM: paramagnetic metal. FM: ferromagnetic metal, AFM(A): A-type antiferromagnetic metal, SG: spin glass phases.

The obtained results of Pr-compounds are summarized in Fig. 14(b). The A-site order stabilizes AFM(A) state associated with the $d_{x^2-y^2}$ orbital order (layer type), because the layer type order of R/Ba and the consequent distortion of MnO_6 octahedra introduce two-dimensionality in the crystal structure. The increase of the A-site disorder makes AFM(A) state unstable because of the decrease of structural anisotropy (two-dimensionality). On the other hand, it is advantageous to FM state generated by the isotropic DE interaction and leads to FM state for PB32 and PB25. However, the effect of σ^2 is simultaneously enhanced by the A-site disorder and finally results in magnetic glassy state in the disordered form PB00. The A-site randomness in Ba-based manganites clearly suppresses not only FM transition but also AFM(A) transition and ultimately leads the system to magnetic glassy state.

Figures 15(a)-(c) show the temperature variation of electrical resistivity (□) in PB96, PB32 and PB00 at 0 and 5 T. For PB96 in which AFM(A) state is stable, magnetic field dependence of resistivity is a little, although AFM(A) transition temperature is suppressed by 18 K at 5 T. On the other hand, magnetoresistance (MR) effect is observed below T_C (= 158 K) for ferromagnetic PB32 and below 120 K even for PB00 which has no long-range ferromagnetic order. The MR effects of these compounds at 5 T are summarized in Fig. 15(d), where MR(%) is given by $\mathrm{MR}(\%) = \{[\rho(0) - \rho(H)]/\rho(0)\} \times 100\%$ with □(H) in 5 T and □(0) in zero magnetic field. With increasing the A-site randomness, MR effect increases and the maximum MR effect reaches to 2360 % in PB00, although the temperature (T_{MR}) at the maximum MR effect decreases. It is obvious that the A-site randomness increases MR effect in Pr-compounds.

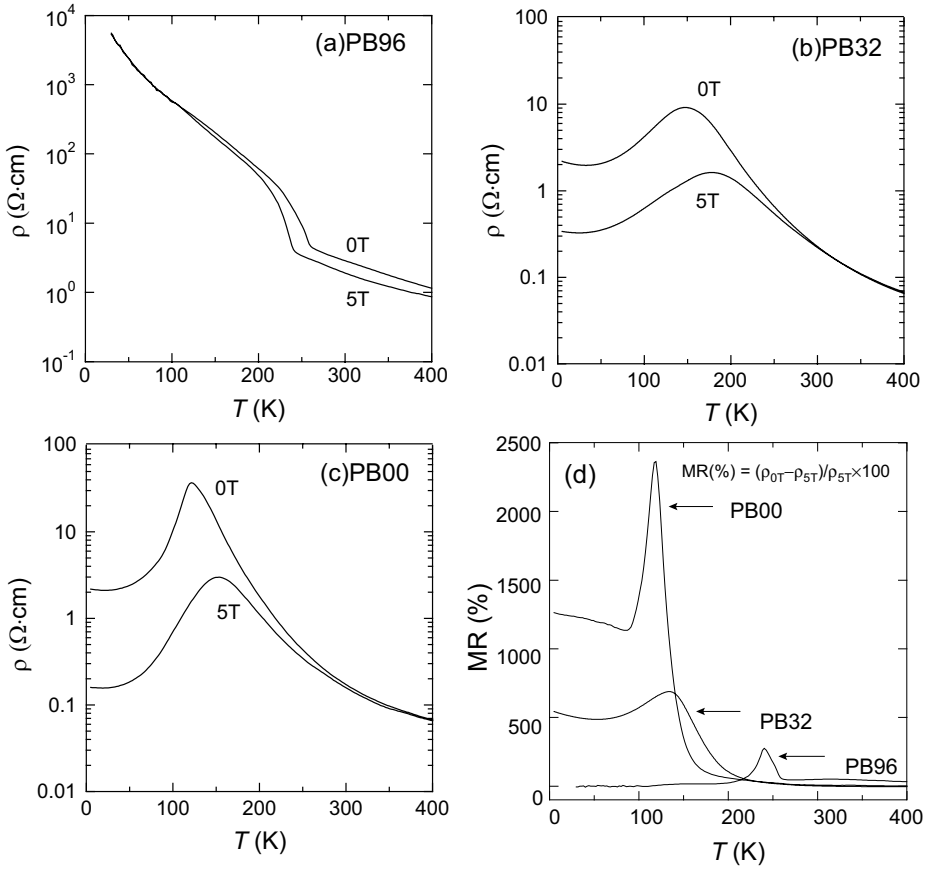

Fig. 15. Temperature dependence of electrical resistivity (□) at 0 and 5 T for PB96 (**a**), PB32 (**b**) and PB00 (**c**), and magnetoresistance (MR) vs. temperature plots (**d**) for PB96, PB32 and PB00. MR effect was measured between 0 and 5 T.

The decrease of resistivity below 150 K in PB32 is due to the development of FM state and the observed MR effect could be associated with the conversion of coexisted phases (AFM(A) phase or magnetic glassy phase) to FM phase by an external magnetic field. On the other hand, PB00 shows no long-range magnetic ordering; nevertheless it shows similar behaviors of resistivity and MR effect. Such behaviors would be due to the development of short-range magnetic ordering and the conversion of magnetic glassy phase to FM phase by an external magnetic field. At 2 K in PB00, a peculiar behavior, as shown in Fig. 16(a), has been observed. The resistivity decreases stepwise as the magnetic field increases, while the magnetization increases stepwise with the close relation to the resistivity behaviors. These behaviors are not reversible in the magnetic field but the same behaviors recover once the

sample is heated up to 150 K and then cooled down under no magnetic field. The stepwise behaviors in the magnetization and resistivity are observed up to 4.9 K but they vanish dramatically at 5.0 K, as shown in Fig. 16(b).

Similar behaviors were observed in $Pr_{0.5}Ca_{0.5}MnO_3$ doped with a few percent of other cations such as Sc, Ga or Co on the Mn site and were explained by an impurity induced-disorder, with the coexistence of several short-range AFI(CE) phases and small FM regions [26,27]. The present system has neither FM-to-AFI(CE) transition nor dopant in contrast to $Pr_{0.5}Ca_{0.5}MnO_3$. A model based on ordinal two-phase mixture cannot explain the behavior. For instance, AFI(CE) phase in the coexistence with FM phase is continuously converted to FM phase, as shown in the inset of Fig. 5(a). We have no explanation for such multi-step magnetization and resistivity change at present. However we would like to emphasize a close relation between the observed behavior and any spatial heterogeneity in a nanometer scale.

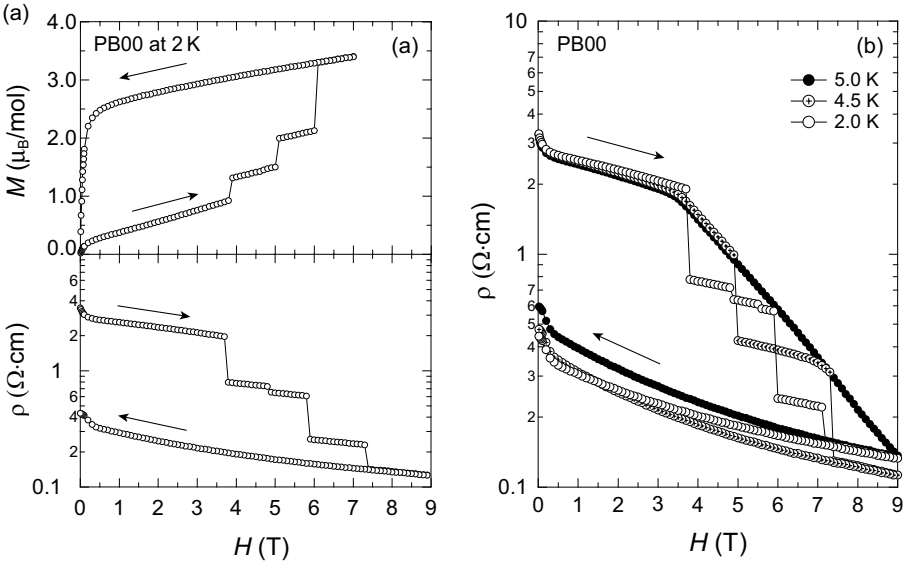

Fig. 16. (**a**) Magnetic field dependences of resistivity (□) and magnetization (*M*) at 2 K for $Pr_{0.5}Ba_{0.5}MnO_3$ (PB00). The resistivity decreases stepwise as the magnetic field increases, while the magnetization increases stepwise with the close relation to the resistivity behaviors. These behaviors are not reversible in the magnetic field but the same behaviors recover once the sample is heated up to 150 K and then cooled down under no magnetic field. (**b**) Magnetic field dependences of resistivity (□) at various temperatures in $Pr_{0.5}Ba_{0.5}MnO_3$ (PB00). The stepwise behaviors of resistivity abruptly vanish at 5.0 K.

5. SUMMARY

The *A*-site ordered manganite RBaMn$_2$O$_6$ has a remarkable structural feature that the MnO$_2$ square sublattice is sandwiched by two types of rock-salt layers, *R*O and BaO with different lattice sizes. This means that the structural and physical properties of RBaMn$_2$O$_6$ can be no longer explained in terms of the basic structural distortion, that is the tolerance factor, as in the *A*-site disordered manganite $R_{0.5}A_{0.5}$MnO$_3$ (*A* = Ca and Sr). In addition to the absence of the *A*-site randomness, the large mismatch between *R*O- and BaO-lattices introduces a strong frustration to the MnO$_2$ sublattice and as a result the MnO$_6$ octahedron itself is heavily distorted in a noncentrosymmetric manner that both Mn and oxygen atoms in the MnO$_2$ plane are displaced toward the *R*O layer, in contrast to the rigid MnO$_6$ octahedron in the *A*-site disordered manganite $(R_{1-x}A_x)$MnO$_3$ (*A* = Ca and Sr). Such deformation gives a new perturbation to the competition of multi-degrees of freedom among charge, orbital, spin and lattice and results in some novel structural and electromagnetic properties of RBaMn$_2$O$_6$ as follows:

(1) The charge and orbital ordered temperatures T_{CO} are relatively high, which could be due to the absence of *A*-site randomness.

(2) The charge/orbital ordered manner in the paramagnetic CE-type charge/orbital ordered insulating state COI(CE) has a new stacking variation of the in-plane CE-type charge/orbital order with a four-fold periodicity along the *c*-axis, which could be due to a layer type order of *R* and Ba. Furthermore the new charge/orbital ordered manner changes into a new type with a two or single periodicity along the *c*-axis in the antiferromagnetic CE-type charge/orbital ordered insulator state AFI(CE).

(3) The critical behaviors; the lowering of transition temperatures and the ferromagnetic metal to the antiferromagnetic charge/orbital ordered insulator transition responsible for CMR, are absent around the phase boundary between ferromagnetic metal and charge/orbital ordered insulator, which could be due to the absence of *A*-site randomness.

(4) There exists a structural transition at the temperature above T_{CO} in RBaMn$_2$O$_6$ (*R* = Tb, Dy, Ho and Y), which is possibly accompanied by the $d_{x^2-y^2}$ type orbital order. This suggests the separation of charge and orbital degrees of freedom. The transition would be induced so as to relax the peculiar lattice distortion arising from both the layered structure and octahedral tilting.

(5) LaBaMn$_2$O$_6$ shows a fractional transition from the ferromagnetic metal to the antiferromagnetic CE-type charge/orbital ordered insulator, which would be due to the decrease of bandwidth related to the increase of Mn-O distance.

On the other hand, the electronic states characteristic of perovskite manganites such as charge/orbital ordered state seen in RBaMn$_2$O$_6$ and $R_{0.5}A_{0.5}$MnO$_3$ (*A* = Ca and Sr) are absent in the *A*-site disordered Ba-based manganite $R_{0.5}$Ba$_{0.5}$MnO$_3$ with the simple cubic perovskite structure. Instead of these states, magnetic glassy states govern the electronic state of $R_{0.5}$Ba$_{0.5}$MnO$_3$. The magnetic glassy state could be due to a disorder effect that hinders magnetic long-range ordering and it could occur as a result of the competition between randomly distributed ferromagnetic and antiferromagnetic interactions. Since the ionic radius of Ba^{2+} is much larger than that of Sr^{2+} and R^{3+}, $R_{0.5}$Ba$_{0.5}$MnO$_3$ could include any spatial

heterogeneity in a nanometer scale, which results in magnetic nonhomogeneous states. The mapping of $R_{0.5}A_{0.5}MnO_3$ (A = Ca, Sr and Ba) on σ^2- $\langle r_A \rangle$ diagram, where σ^2 is the variance of A-cation radius distribution and $\langle r_A \rangle$ is the average ionic radius of A-site cations, says that the magnetic long-range orderings tend to be stabilized in the lower σ^2 region ($\sigma^2 < 10^{-2}$); otherwise, the magnetic glassy state is dominant above $\sigma^2 = 10^{-2}$. From the systematic study of the Pr-compounds with various degrees of the A-site randomness, it is obvious that the A-site randomness increases magnetoresistance (MR) effect. The peculiar behavior that the resistivity and magnetization change stepwise under external magnetic fields is observed in $Pr_{0.5}Ba_{0.5}MnO_3$. It would be also closely related to any spatial heterogeneity in a nanometer scale.

REFERENCES

[1] See for reviews: C. N. R. Rao and B. Raveau, *Colossal Magnetoresistance, Charge Ordering and Related Properties of Manganese Oxides*; World Scientific, Singapore (1998).

[2] S. Mori, C. H. Chen, and S-W. Cheong, Phys. Rev. Lett. **81** (1998) 3972.

[3] T. Nakajima, H. Kageyama and Y. Ueda, J. Phys. Chem. Solids **63** (2002) 913.

[4] T. Nakajima, H. Kageyama, H. Yoshizawa, and Y. Ueda, J. Phys. Soc. Jpn. **71** (2002) 2843.

[5] H. Kageyama, T. Nakajima, M. Ichihara, Y. Ueda, H. Yoshizawa, and K. Ohoyama, J. Phys. Soc. Jpn. **72** (2003) 241.

[6] T. Nakajima, H. Kageyama, K. Ohoyama, H. Yoshizawa, and Y. Ueda, J. Phys. Soc. Jpn. **72** (2003) 3237.

[7] T. Nakajima, H. Kageyama, K. Ohoyama, H. Yoshizawa, and Y. Ueda, J. Solid State Chem. **177** (2004) 987.

[8] Y. Ueda and T. Nakajima, J. Phys.:Condens. Matter **16** (2004) S573.

[9] F. Millange, V. Caignaert, B. Domengés, B. Raveau, and E. Suard, Chem. Mater. **10** (1998) 1974.

[10] S. V. Trukhanov, I. O. Troyanchuk, M. Hervieu, H. Szymczak and K. Barner, Phys. Rev. B **66** (2002) 184424.

[11] M. Uchida, D. Akahoshi, R. Kumai, Y. Tomioka, T. Arima, Y. Tokura, and Y. Matsui, J. Phys. Soc. Jpn. **71**, 2605 (2002).

[12] T. Arima, D. Akahoshi, K. Oikawa, T. Kamiyama, M. Uchida, Y. Matsui, and Y. Tokura, Phys. Rev. B **66** (2002) 140408.

[13] T. Wada et al., Phys. Rev. B **39** (1989) 9126; K. Otzschi et al., Physica C **235-240** (1994) 839.

[14] D. Akahoshi and Y. Ueda, J. Phys. Soc. Jpn. **68** (1999) 763; ibid., J. Solid State Chem. **156** (2001) 355.

[15] R. D. Shannon and C. T. Prewitt, Acta Cryst., B **25** (1969) 925.

[16] A.M. Glazer, *Acta Cryst*. B**28,** 3384 (1972).

[17] P. M. Woodward, *Acta Cryst.* B**53**, 32 (1997).

[18] P. M. Woodward, *Acta Cryst*. B**53**, 44(1997).

[19] H. Kawano, R. Kajimoto, H. Yoshizawa, Y. Tomioka, H. Kuwahara and Y. Tokura, cond-mat/9808286.
[20] T. Nakajima and Y. Ueda, J. Alloys and Compounds (2004) (in press).
[21] D. Akahoshi, M. Uchida, Y. Tomioka, T. Arima, Y. Matsui, Y. Tokura, Phys. Rev. Lett. **90** (2003) 177203.
[22] T. Nakajima, H. Yoshizawa and Y. Ueda, J. Phys. Soc. Jpn. **73** (2004) 2283.
[23] F. Millange, V. Caignaert, B. Domengés, B. Raveau, and E. Suard, Chem. Mater. **10** (1998) 1974.
[24] L.M. Rodriguez-Martinez and J. P. Attfield, Phys. Rev. B **54** (1996) 15622.
[25] T. Terai, T. Sasaki, T. Kakeshita, T. Fukuda, T. Saburi, H. Kitagawa, K. Kindo and M. Honda, Phys. Rev. B **61** (2000) 3488.
[26] S. Hébert, V. Hardy, A. Maignan, R. Mahendiran, M. Hervieu, C. Martin and B. Raveau, J. Solid State Chemistry **165** (2002) 6.
[27] R. Mahendiran, A. Maignan, S. Hébert, C. Martin, M. Hervieu, B. Raveau, J. F. Mitchell and P. Schiffer, Phys. Rev. Lett., **89** (2002) 286602.

THE LIMITS TO SPIN-POLARIZATION IN FINITE-TEMPERATURE HALF-METALLIC FERROMAGNETS

P.A. Dowben[1] and S.J. Jenkins[2]

[1] Department of Physics and Astronomy
and the Center for Materials Research and Analysis (CMRA)
255 Behlen Laboratory of Physics, University of Nebraska, P.O. Box 880111, Lincoln, Nebraska USA 68588-0111

[2] Dept. of Chemistry, University of Cambridge, Lensfield Road, Cambridge CB2 1EW, United Kingdom

1. INTRODUCTION

High electron spin polarization is regarded as an essential ingredient for spin-electronics applications. Several classes of materials are currently under investigation as potential high polarization components, including the growing family of predicted half-metallic compounds: ferromagnets possessing only one spin channel for conduction (usually, but not always, majority-spin). Because the resistance of the spin-down channel goes to infinity for $D_{\downarrow}(E_F) = 0$, the supposed half-metallic systems are, potentially, of considerable interest in the construction of spin electronic devices [1-3].

The proposal that there might exist such half-metallic ferromagnet materials with 100% zero-temperature spin polarization at the Fermi level has quite a long history [3-8] dating back to de Groot [5-8], with the semi Heusler alloys (NiMnSb) [5-17], the full Heusler alloys [5,17-28], the zinc-blende and Würtzite structure materials [29-51], the colossal magnetoresistance materials ($La_{1-x}Sr_xMnO_3$ [52-57], $La_{1-x}Ca_xMnO_3$ [56-58], $Pr_{1-x}Sr_xMnO_3$ [59], Sr_2FeMoO_6 [60], $LaSr_2Mn_2O_7$ [57,61-63]), and other magnetic metal oxides (CrO_2 [64-69] and Fe_3O_4 [70-72] being among the most cited candidates for 100 % spin polarization. Other materials have also been suggested to be half-metallic ferromagnets as well [4,57,73-75].

Practical electronic devices [76,77], including nonvolatile magnetic random-access memory elements [77,78], that exploit the spin as well as the charge of the electron, operate at temperatures somewhat above 0 K (ideally with an operational temperature range extending above room temperature). Finite temperature effects must therefore be considered, including magnon and phonon excitations. These are, however, not the only complications that must be contemplated. Indeed, if either spin-injection into a semiconductor, or spin polarized tunneling is the goal, then the interface electronic states have to be considered, as well as the effects of finite temperature on these electronic states at the interface and the quality of the interface itself. This means that the influence of the spin dependent bulk and surface Debye temperatures on the spin dependent electron-phonon scattering [79,80] and thermally activated interdiffusion and interface reactions cannot be ignored. These many complications cannot be discussed extensively here, but we do discuss the limitations to half-metallic behavior common to all potential half-metallic systems. We ask whether these materials are indeed "operationally" better spin injectors than Fe (40%), Co (34%) or even Ni (23%) at room temperature and whether interfaces, with high polarization, can be constructed more readily with these materials.

Defects and substitutional disorder [26,27,81-88], which are likely to increase with increasing temperature, also contribute to the spin-minority (↓) DOS. Note that structural disorder yields, via spin-orbit coupling, non-collinear spin structures [81-82,89-90], but an analog mechanism is operative in all imperfect and low-symmetry magnetic solids [90-93]. However, bulk structural disorder [26,27,81-88] (as opposed to interface disorder, as discussed in section 6) is essentially temperature independent in the region between 0 K and room temperature. Thus the observed strong temperature dependence of the spin polarization of half-metallic ferromagnets must be associated with other factors that we will explore herein.

2. THE PROBLEM WITH MAGNONS

Far below T_c, the densities of states (DOS) of *ordinary* ferromagnets are only weakly modified by thermal fluctuations, because k_BT is much smaller than the Fermi energy and band structure distortions are small. Essentially, low-temperature thermal disorder leads to slight modifications of the spin-dependent exchange potential and of the spin-up and spin-down densities of states [93-94]. However, as elaborated in [95-99], half-metallic ferromagnets are an exception, with qualitatively new low-temperature effects.

As discussed in [95-97], a simple tight-binding description of magnets with disordered moments is provided by

$$\mathcal{H}_{\mu vik\alpha\beta} = \mathcal{T}_{\mu vik}\,\delta_{\alpha\beta} - V_\mu\,\delta_{\mu\nu}\,\delta_{ik}\,\delta_{\alpha\beta} - I_o\,\delta_{\mu\nu}\,\delta_{ik}\,\mathbf{e}_i.\boldsymbol{\sigma}_{\alpha\beta} \qquad (1)$$

Here $\mathcal{T}_{\mu vik} = \langle\phi_\mu(\mathbf{r}-\mathbf{R}_i)|\mathcal{T}|\phi_\nu(\mathbf{r}-\mathbf{R}_k)\rangle$ is the hopping integral between a μ-type orbital at $\mathbf{R}_i$ and a ν-type orbital at $\mathbf{R}_k$, V_μ is the crystal-field energy for the μ-type orbital, I_o is the intra-atomic d-electron exchange, and $\mathbf{e}_i$ is the local magnetization direction. In terms of Eq. (1), ferromagnetism results from the I_o Stoner term, which reduces and enhances the energies of ↑ and ↓ electrons, respectively.

In the absence of spin disorder, that is at zero temperature, the spin structure of a ferromagnet can be described by the Pauli matrix:

$$\sigma_z = \begin{pmatrix} 1 & 0 \\ 0 & -1 \end{pmatrix} \tag{2}$$

The starting point for describing finite-temperature spin disorder is the standard spin-1/2 rotation matrix which rotates a ↑ spin by the angles θ and ϕ [95]:

$$\hat{U}(\phi,\theta) = \begin{pmatrix} \cos\left(\frac{\theta}{2}\right) e^{i\phi/2} & \sin\left(\frac{\theta}{2}\right) e^{-i\phi/2} \\ -\sin\left(\frac{\theta}{2}\right) e^{i\phi/2} & \cos\left(\frac{\theta}{2}\right) e^{-i\phi/2} \end{pmatrix} \tag{3}$$

The exchange term in Eq. (1) is diagonalized by a unitary matrix $\Pi_i \hat{U}^{+}(\phi_i,\theta_i)$ [95-97]. In the resulting expression:

$$\mathcal{H}^{t}{}_{\mu vik\alpha\beta} = \mathcal{T}_{\mu vik} \Sigma_\gamma U_{\alpha\gamma}(\phi_i,\theta_i) U^{+}{}_{\gamma\beta}(\phi_k,\theta_k) - (V_\mu \delta_{\alpha\beta} + I_o \sigma_{z\alpha\beta}) \delta_{\mu\nu} \delta_{ik} \tag{4}$$

the thermal spin disorder has been mapped onto random hopping integrals.

One (semi-classical) way of viewing the non-collinear excited states of the system is as a small-angle tilt in the local magnetisation axis. An alternative (fully quantum) way is to view the ground state of the system as characterised by a fixed global magnetisation axis, onto which is overlaid an ensemble of collective planewave-like fluctuations in the local value of the z-component of spin (i.e. magnons). The magnon picture, however, has a limited range of applicability. Single-particle approaches, such as density functional theory (DFT), are based on the idea that the electrons can be described wholly in terms of interactions with an effective potential due to the ground state system. Such approaches are only fully valid when electron scattering events that lead to fluctuations from the ground state are vanishingly rare, and hence these techniques are incapable of including electronic interactions with collective excitations such as magnons. At the other extreme, when scattering out of the ground state becomes the dominant feature of the system, the lifetime of a single-particle excitation would be so short as to render the electron-magnon scattering picture essentially meaningless as a tool for understanding the electronic structure. In such cases, a completely many-body picture of the system would be required. Between these two extremes, the quasiparticle regime implies the existence of relatively long-lived excitations beyond the ground state that can be treated in a single-particle-like manner, with appropriate perturbations. Both collective magnons and individual electrons can therefore be considered as meaningful entities, and many-body effects are reduced to the description of relatively infrequent scattering processes. In this regime, it is appropriate to ask how the influence of magnons changes the electron density of states as a function of temperature.

Figure 1 shows typical finite-temperature ↑ and ↓ densities of states. The effect of the spin mixing on the two subbands is indicated by the dark areas. This distortion of the ↑ DOS has the character of a quantitative correction (region I), but in the ↓ gap the DOS changes qualitatively, from zero to nonzero (region II). In other words, finite-temperature effects do

not reduce to a smearing of the Fermi level by a relative amount of the order of k_BT/E_F. As indicated in Fig. 1, the spin mixing yields small $D_\downarrow(E)$ values in the middle of the spin-down gap, well above the highest energy level occupied at zero temperature.

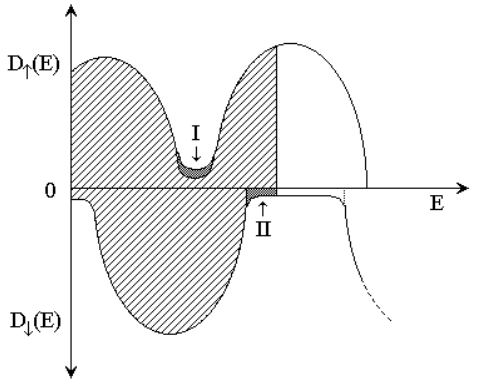

Fig. 1. Schematic ↑and ↓ densities of states (dark shadowing denotes regions occupied at finite temperature only). From [95-97].

As a consequence, the resistance of the ↓ channel changes from infinity to a finite value. A crude estimate for the magnitude of this spin-mixing contribution to the DOS is

$$D_\downarrow(E) \approx \frac{M_o - M_s(T)}{M_o + M_s(T)} D_\uparrow(E) \qquad (5)$$

where $M_s(T)$ is the spontaneous magnetization and $M_o = M_s(0)$ [95-97]. Here $M_s(T)$ reflects both Bloch-type spin-wave excitations and specific features such as many-sublattice effects. The appearance of the spin-down density (II) in Fig. 1 has a simple physical interpretation: a ↑ electron hops onto a neighboring atomic site characterized by a different axis of quantization. In the frame of the neighboring atom, the spin wave function has nonzero projections onto both ↑ and ↓ states. For random disorder, the spin mixing can be interpreted as an Anderson localization of spin-polarized 3d electrons in a thermally randomized atomic potential.

In considering a magnetic tunnel junction geometry (ferromagnet/insulator/ferromagnet) Itoh, Ohsawa and Inoue [98] have calculated the spin-polarization at interfaces (reproduced in Figure 2) with and without spin fluctuations considered. The effect of spin fluctuation is quite noticeable.

It is very difficult to see how magnons can be eliminated from potential half-metallic systems to provide true half-metallic behavior. While the long-wavelength (and hence low energy) magnons will be the modes with the most quanta (according to Bose-Einstein statistics), suppression of these long period magnons (those at the very lowest energy) cannot be easily achieved by keeping the crystallite size small, and this approach has its own complications as discussed below. In our opinion, half-metallic ferromagnetism is an idealized limit, realistic only in perfect crystals at zero temperature.

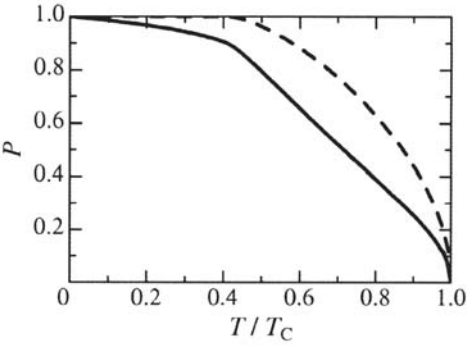

Fig. 2. The temperature dependence of the polarization P either with (solid) and without (dashed) spin fluctuations for a half-metallic. Adapted from reference [98] with permission.

3. THE PROBLEM WITH SPIN-POLARONIC NON-QUASIPARTICLE STATES

In addition to the issues relating to finite-temperature emission and absorption of real magnons described above, it has recently been pointed out that zero-temperature interactions with virtual magnons are also potentially of significance in the half-metal case [15]. As long ago as 1973, Edwards and Hertz [100] demonstrated that the Hubbard model for strong broad band ferromagnets supported spin polaron modes in which electrons or holes may become bound to a virtual magnon excitation. Since magnons are necessarily carriers of integral *minority* spin, the resulting composite quasiparticle carries half-integral minority spin and may only spontaneously arise from (or decay into) either a minority-spin *electron* or a majority-spin *hole*. In the case of a narrow band ferromagnet, more akin to the typical half-metal, Irkhin and Katsnelson [101] have demonstrated that these spin polarons take on a non-quasiparticle character, implying that their spectral functions are sufficiently broad as to prevent the construction of a meaningful dispersion relation. In either case, the significance of such states is that spin-flip processes link them to the regular electronic band structure, with (in principle) measurable consequences.

To give the simplest example, consider conducting spin-polarised photoemission and inverse photoemission experiments on a majority-metallic half-metal, at energies within the minority-spin band gap. Without the non-quasiparticle states, one would expect that majority-spin electrons could be injected into the sample at energies above the Fermi level, but that minority-spin electrons could not. In fact, however, the near-instantaneous decay of minority-spin electrons to form spin polarons means that a non-zero density of states will nonetheless be recorded. In photoemission, however, the inability of minority-spin holes to decay into spin polarons means that the expected result of zero minority-spin density of states will be obtained. This asymmetric contribution to the density of states is illustrated clearly in calculations by Katsnelson and co-workers [15] for NiMnSb. In minority-metallic half-metals, where the gap occurs in the majority-spin channel, these arguments are reversed, so that non-quasiparticle states contribute to the apparent majority-spin density of states in the energy range below the Fermi level, but not above.

The effect of these non-quasiparticle states on the transport properties of half-metals is, as yet, unclear. Irkhin and Katsnelson describe them as having low mobility [102], and the spin-selection rules mentioned above seem to preclude their having any significance in mediating spin-flip scattering of electrons or holes. That is to say, an electron or hole may become bound within a spin polaron, but upon decay of the non-quasiparticle excitation the released electron or hole will possess the same spin as the original. On the other hand, the fact that only *virtual* magnons are involved implies that whatever influence these states may produce will be apparent even down to vanishingly low temperatures. At finite temperatures, of course, interactions with the real magnon spectrum will become increasingly important, as outlined in the preceding section.

4. THE PROBLEM OF MAGNON PHONON COUPLING

As magnon excitations lead to only small decreases in polarization at low temperatures (near zero Kelvin), more or less proportional to the drop in magnetization (equation 5), the dramatic drop in polarization observed well below room temperature for many potential half metallic systems suggests that yet another temperature dependent mechanism for depolarization exists. The tunnel magnetoresistance of $La_{1-x}Sr_xMnO_3/SrTiO_3/La_{1-x}Sr_xMnO_3$ where x = 0.2 and x = 0.3 dramatically drops at about 27 K [103] and 130 K [104-108], respectively. Dramatic drops in the measured polarization have been seen for $La_{0.7}Ca_{0.3}MnO_3$ [109], CrO_2 [110-113], and NiMnSb [114-117]. These significant drops in band polarization with increasing temperature, often by more than 50%, are not reflected in the temperature dependent magnetization, taken in experimental conditions with an applied external magnetic field.

From all experimental indications, these dramatic drops in polarization may reflect a quasi phase transition in which magnetic ordering is preserved but the extent of magnetic ordering is dramatically perturbed [95,114,118]. For NiMnSb(100), indeed, the magnetic circular dichroism (MCD) data exhibits a huge decrease in the relative spin and orbital moment and the inferred band polarization as the temperature is increased above 80 K [114], shown in Fig. 3 and summarized in Fig. 4. This is accompanied by a decrease in the <200> neutron magnetic scattering factor with increasing temperature [114-115] (indicated as in the inset of Figure 4). For NiMnSb total 4.025 μ_B moment from high field magnetometry (at 10 K) is consistent with half-metallic character [114-115], local moment on the Mn at 15 K is 3.79 ± 0.02 μ_B and falls to 3.55 ± 0.02 μ_B at 260 K, while the local moment on the Ni sites changes little [114-115]. The observed decrease in the local moments with increasing temperature is consistent with the decrease in the $\frac{d(\Delta R/R)}{d(\mu_0 H)}$ magnetoresistance above 80 K (Figure 4a) [114,116,118] and is indicative of the onset of a large spin minority channel at temperatures above 80 to 100 K. The fact that the local moments change, even under high field conditions, suggests that there is a change in the moment coupling between Mn and Ni at about 80 K [114].

This cross-over from a high polarization ferromagnet to a ferromagnet with more conventional behavior is also manifest in the temperature dependent resistivities of many postulated half-metallics, though not with any clearly consistent changes in the power law dependence with temperature. The resistance of NiMnSb with temperature fits a $T^{1.65}$ power

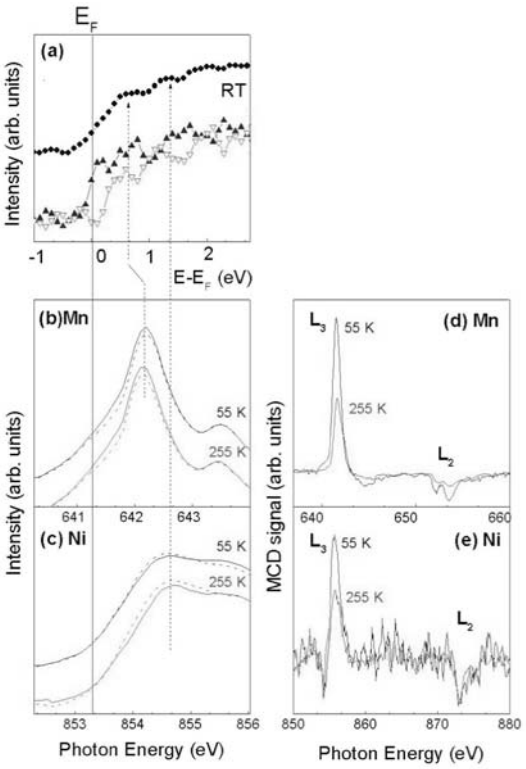

Fig. 3. The comparison of the SPIPES, MCD and XAS spectra for NiMnSb(100), taken from [114]. The spin-polarized inverse photoemission (SPIPES) (▲-spin up, ▽-spin down) and integrated (●) data for the stoichiometric NiMnSb(100) clean surface at 300K (a) are compared X-ray absorption results across Mn 2p (b) and Ni 2p (c) core levels, shifted by the core level binding energies. Spectra at two different temperatures are shown for the X-ray adsorption to illuminate the fact that the integrated unoccupied density of states is somewhat insensitive to the phase transition at 80 K. The magnetic circular dichroism signal across both the L_2 and L_3 edges of Mn (d) and Ni (e) are shown for two different temperatures to indicate the profound change that occurs between 80 to 100 K in the spin and orbital momentum. The dashed lines indicate the possible corresponding unoccupied states orbitals in SPIPES with the XAS.

law above 80 K (close to $T^{3/2}$) but follows a T^2 power law below 80 K, as shown in Figure 4b, and is also consistent with a cross-over in magnetic ordering at 80 to 100 K, though the material remains ferromagnetic [114,116-120]. There is evidence of a similar transition in the resistance data obtained from manganese perovskites $La_{1-x}Sr_xMnO_3$ [121,122], $La_{0.67}(Pb,Ca)_{0.33}MnO_3$ [122,123], and $La_{1-x}Ca_xMnO_3$ [123] where the resistance seems to follow a higher order power law with temperature, at low temperature, but follows a T^2 power

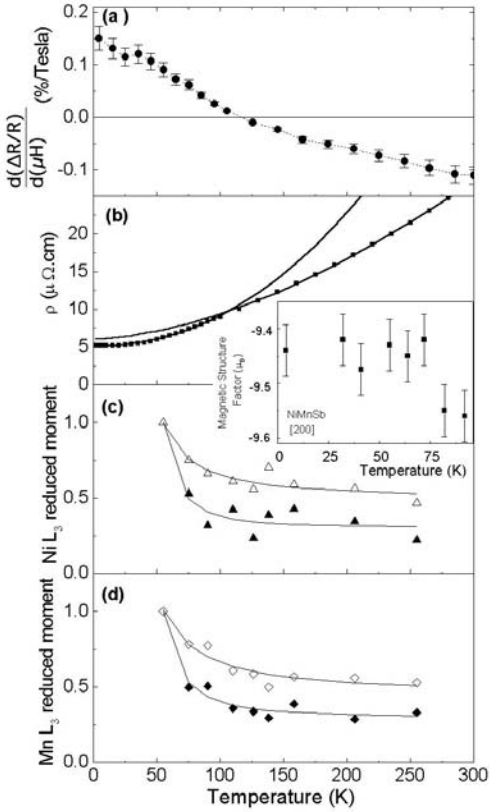

Fig. 4. Evidence of the meta-magnetic transition in NiMnSb, taken from [114], with permission. The magneto-resistance slope $\frac{d(\Delta R/R)}{d(\mu_0 H)}$ taken between 1 and 6 Tesla (a), compared to the resistance (b), the relative Ni moment derived from MCD (c) and relative Mn moment (d) derived from MCD. Note that the changes in the moment observed in MCD compare well with the onset of changes in the magneto-resistance and resistance in NiMnSb, as well as the change in the magnetic structure factor for the <200> peak in neutron scattering shown as an inset, as adapted from [115]. The T^2 and $T^{1.65}$ curves fitted to the resistance data.

law above the cross-over. Similar changes in the power law dependence have also been obtained for the full Heusler alloys [124-126] with increasing temperature. To show the deviation from the $\rho_0+\alpha(H)T^2$ dependence, Lin, Salamon and coworkers plotted $\alpha(H)^{-1}d\rho/d(T^2)$, as shown in Figure 5 for a variety of manganese perovskites [122-123]. While one-magnon scattering might result in a T^2 power law dependence in a weak ferromagnet [4,120,122,127-130], this does not appear to apply to the case of NiMnSb [116-120] or the

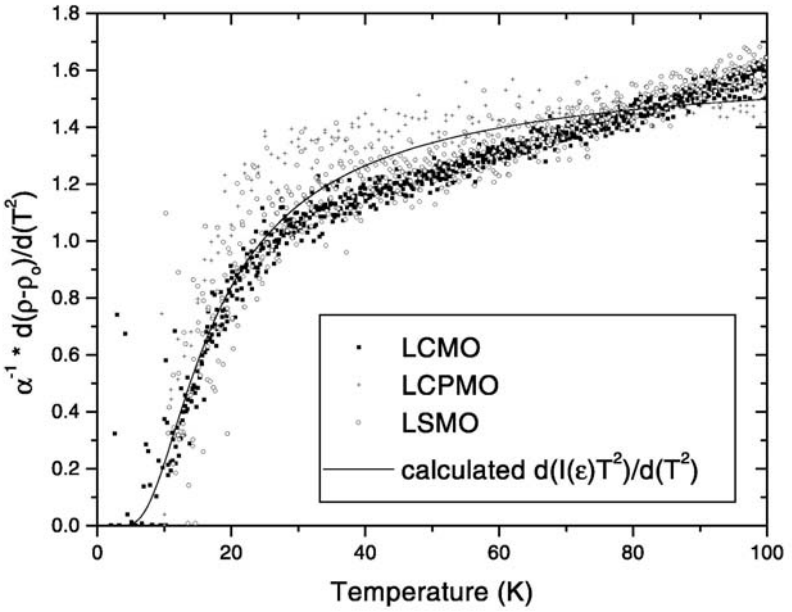

Fig. 5. The derivative of the experimental resistivity data $\alpha(H)^{-1}d\rho/d(T^2)$ for $La_{1-x}Sr_xMnO_3$, $La_{0.67}(Pb,Ca)_{0.33}MnO_3$ and $La_{1-x}Ca_xMnO_3$ [123]. The calculated curve shows the fit expected for a single magnon scattering model. With permission from Myron Salamon.

full Heusler alloys [124-126]. Other explanations must be sought that address this temperature dependent transition in magnetic moment, resistance behavior and field dependent resistance that is correlated to dramatic losses in band polarization for NiMnSb.

Gauging the magnitude of the spin polarization at the Fermi level and its pronounced drop well below room temperature, we must take into account the multi-sublattice character of potential half-metallic ferromagnets [95-97]. Sublattice effects associated with the compound structure of the half-metallics yield low-energy transverse optical modes which couple to spin waves and reduce the net magnetization. In real space, these spin-wave modes correspond to a tilting between neighboring atomic spins, the tilt angle depending on the k vector where the phonon and magnon bands cross. Generally, the closer to the Brillouin zone edge the magnons and transverse optical modes couple, the greater the tilt angle.

In the case of NiMnSb it is known [131] that a nearly dispersionless transverse optical mode occurs at about 28 meV, as shown by the phonon band structure reproduced in Figure 6. In terms of $3k_BT$, this corresponds to 103 K—very close to the temperature at which there is a dramatic loss in Ni and Mn magnetization in NiMnSb [114], as just discussed. In the semi-Heusler alloys, this corresponds to a tilting between neighboring Ni and Mn atoms. In real space, the mode means that the spins of Mn next nearest neighbors form an angle of the order of 60º, while all the Mn moments are misaligned with respect to the nickel moments [114].

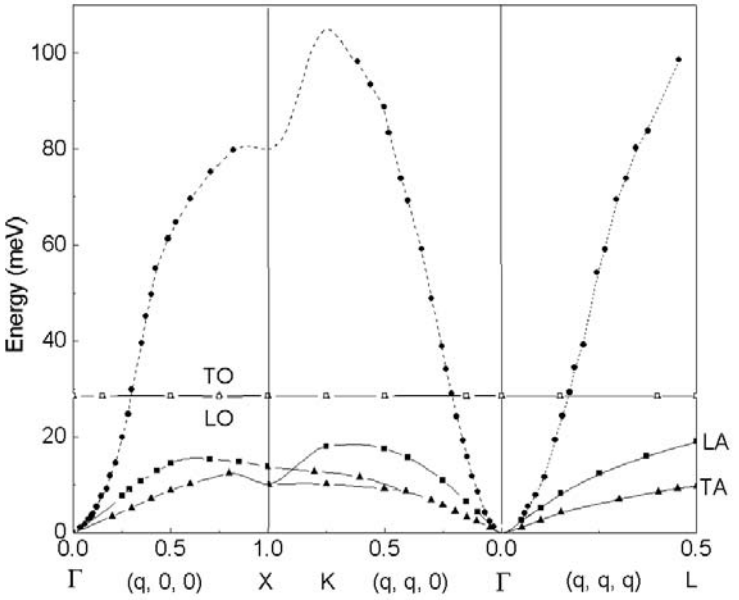

Fig. 6. The phonon and magnon band structure for NiMnSb taken from [131]. Dispersion curves for magnons (●) , longitudinal phonons (■), and transverse phonons (▲) at 300 K are shown. No magnetic field was applied.

Manganese perovskites exhibit a low-temperature spin-wave softening and broadening of magnetoelastic origin [132-137], closely related to the proximity of a charge-ordered insulating state [132]. The effect occurs where the magnon dispersion crosses the longitudinal optical branch of the phonons, at $ka/2\pi \approx 0.3$ [132-135]. The lowest transverse optical modes in these systems, about 23 meV for $La_{0.7}A_{0.3}MnO_3$ (A = Ca, Sr) [132-133], are consistent with the 'cross-over' behavior in the transport data. This magnon-phonon coupling, combined with the resistivity behavior, suggests the existence of meta-magnetic transitions, similar to those observed in NiMnSb [114], at about 80-100 K. Again, the presence of such magnon-phonon coupling should result in a loss of net spin polarization due to the attendant decrease in spin wave stiffness. Indeed there are indications this does occur in the manganese perovskites, as noted above, at about 100-130 K [104-109]. Indeed the magnon-phonon coupling is quite strong [136-137], so strong in fact that the magnons are completely damped from about $ka/2\pi \approx 0.3$ to the Brillouin zone boundary [132-135], as seen in Figure 7.

The specific situation encountered in half-metallic ferromagnets reflects the many-sublattice character of all of these compounds. Note that similar phonon modes exist in a variety of compounds, including materials such as CrO_2 and Fe_3O_4. The finite-k spin disorder is reminiscent of a meta-magnetic phase transition into a noncollinear state, and the states in the spin-down gap (region II in Fig. 1) reflect the presence of partly or completely reversed spins in the thermally excited state.

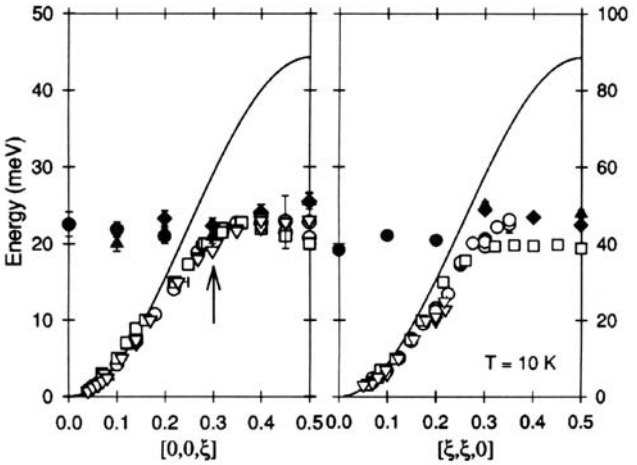

Fig. 7. The optical phonon modes (filled symbols) are plotted together with the magnon modes for $Pr_{1-x}Sr_xMnO_3$ (□), $Nd_{1-x}Sr_xMnO_3$ (∇), and $La_{1-x}Ca_xMnO_3$ (O) as a function of wave vector [132-135]. The expected magnon dispersion curve is indicated. Reproduced with permission of J. Zhang.

This problem with the coupling of the magnons to the transverse optical modes means that an elevated Curie temperature is NOT a good indicator of spin polarization at elevated temperatures. Thus the semi Heusler alloys ABC (A=Ni, Pd, Pt; B=Mn, C=P, As, Sb) with a T_c = 740 K have just as significant drops in polarization below room temperatures as the manganese perovskites: $La_{0.35}A_{0.65}MnO_3$ (A= Sr, Ba, Pb) with a T_c = 360 K or CrO_2 with a T_c = 397 K.

5. THE PROBLEM OF INTERFACES

One could consider suppressing the long period (and low energy) magnons by breaking up the half-metallic ferromagnetic crystal into small crystallites, but this approach does not provide any advantage. Yes, it is true that the long period magnons cannot be supported in an isolated small crystallite, but the long range magnetic ordering between crystallites will make long wavelength magnons difficult to suppress entirely. In addition, the creation of small crystallites necessarily creates interfaces. Furthermore, if such interfaces alter the net polarization, even if the microstructure is not an issue, this has consequences for almost any spintronics device application, as interfaces are key to all such devices.

Spin minority surface states in the half-metallic systems are well known [8,17,34,83,140-142] and can 'develop' into interface states in the presence of overlayers [83,141-142]. Thus the creation of more interfaces increases the spin minority population with the consequent loss of half-metallic character. This presents a considerable problem even near 0 K.

It might be argued that the influence of surface- or interface-localised minority-spin states on electronic transport properties would be minimal, because they do not extend into the bulk

of the half-metal and thus cannot support a current. Indeed, at precisely 0 K this objection might well be valid. Even at liquid He temperatures, however, it is evident that such localised states can, in fact, contribute significantly to the overall flow of current through a surface or interface. The classic example of such a situation is to be found in STM imaging of certain metals whose bulk band structures display a partial gap at the Fermi level when projected onto the surface Brillouin zone. Such a gap can support Shockley-type surface states, whose parabolic dispersion curves betray two-dimensional free-electron-like behaviour (see Figure 8). Clearly, these states are quite capable of supporting a current parallel to the surface, but not in the direction normal to the surface. Nevertheless, STM experiments on Cu(111) [143-150], Ag(111) [151-152], Au(111) [150,152-156] and a range of other surfaces [157-161] have revealed that the tunnelling current under certain tip and bias conditions may actually be entirely dominated by surface state effects. How can this apparent anomaly be explained?

The simple answer is that the surface states are not completely decoupled from the bulk of the semi-infinite crystal. Although the location of these 2 dimensional states in a bulk-forbidden gap suppresses hybridisation with 3 dimensional states, electrons and holes may nevertheless be transferred from one to the other through scattering processes, subject to the twin constraints of energy and crystal-momentum conservation. Although various such scattering processes might occur, let us concentrate first on the absorption and/or emission of phonons.

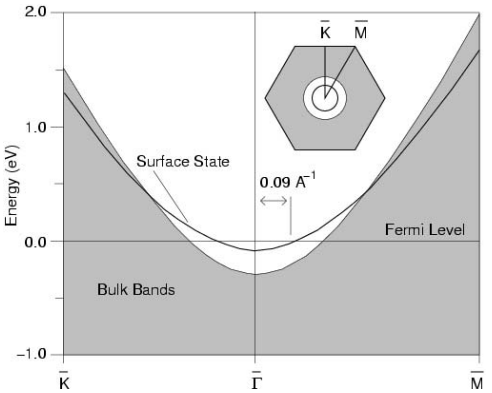

Fig. 8. Projected bulk band structure and surface state of Ag(111), with the surface Brillouin zone shown inset, from a DFT calculation by Jenkins [162].

Typical phonon energies are very small compared to the Fermi energy, but they do carry significant crystal-momentum. In consequence, their emission or absorption can allow scattering of electrons and holes between surface states near the zone center and bulk states nearer the zone edge. In this way, current may flow into or out of the surface by means of a two-step process: tunnelling between tip and surface state, plus scattering between surface state and bulk state. Since the surface state extends considerably further into the vacuum than typical bulk states, this scattering-assisted process can be competitive with direct tunnelling via bulk-like states, provided that the scattering rate is not too slow.

In addition to the phonon scattering mechanism described above, scattering by defects may also play a major role in linking bulk and surface states. In the absence of crystalline order, the conservation of crystal-momentum (as opposed to actual momentum) is no longer a requirement. The effect is familiar from the theory of photoemission, whereby electrons ejected from a well-ordered surface are subject to conservation of crystal-momentum in the dimensions parallel to the surface, but not in the dimension of broken symmetry normal to the surface. In the limit of a rough surface or interface, therefore, the picture of well-defined Bloch states provided by band theory disappears completely, and the wave vector is no-longer a good quantum number. When the defect concentration is relatively low, however, one may treat the system as if it were a perfect crystal, including scattering events merely as perturbations in which states of differing crystal-momenta may exchange particles. Thus, low-energy defect scattering can, just like phonon scattering, allow electrons and holes to be transferred between surface states at the zone center and bulk states at the zone edge. At the surface, however, the entire boundary may be considered as an extended "defect", so that scattering between surface and bulk states is likely to be rather facile. The consequences for the tunnelling current are analogous to the phonon case.

This rather extended discussion of non-magnetic surface states in STM is intended simply to underline the importance of scattering in allowing localised states to play a major role in mediating current flow across an interface. In the half-metallic case, of course, the inclusion of spin alters the situation slightly, but the basic story remains the same. For the sake of comparison, consider a conjectural STM experiment for the (001) surface of NiMnSb (Figure 9a). In this case, we ask whether tunnelling via the localised minority-spin surface states at the Fermi level can contribute to the overall current.

The first point to note is that no bulk-like minority-spin states exist near the Fermi level, even at the zone edge. Thus, scattering processes that provide *only* a large change in crystal-momentum are of no interest to us. We may also rule out high-energy scattering processes (i.e. of energy comparable with the minority-spin band gap). Clearly then, we explicitly require processes that change the spin of the scattered electron or hole. Once again, there are two main possibilities: scattering by magnons, and scattering by open-shell defects. These latter include not only impurity atoms, but also possibly self-interstitials, vacancies and the surface/interface itself.

The case of magnon scattering is rather analogous to phonon scattering, in that it produces a large change in crystal-momentum and a small change in energy, but with the added characteristic of reversing the electron spin. Similarly, the symmetry-breaking associated with defect scattering allows a relaxation of crystal-momentum conservation, just as in a non-magnetic system; now, however, the spin of the scattered electron or hole may be exchanged with that of an electron or hole localised in the incomplete shell of the defect site. Either way, electrons or holes in the minority-spin surface states may be transferred to majority-spin bulk states and vice versa. Since the surface states again extend into the vacuum rather further than do the bulk states, scattering-assisted transport across the boundary is likely to be competitive with direct tunnelling via majority-spin states.

Although the examples discussed above clearly relate to surface phenomena, the principles apply equally well to tunnelling across interfaces. The quality of a prospective spin-valve heterostructure therefore rests upon the nature of any interface states that may exist, and the likelihood of spin-flip scattering through either magnons or open-shell defects. In the case of magnons, the arguments rehearsed in the earlier sections of this article are worthy of recall,

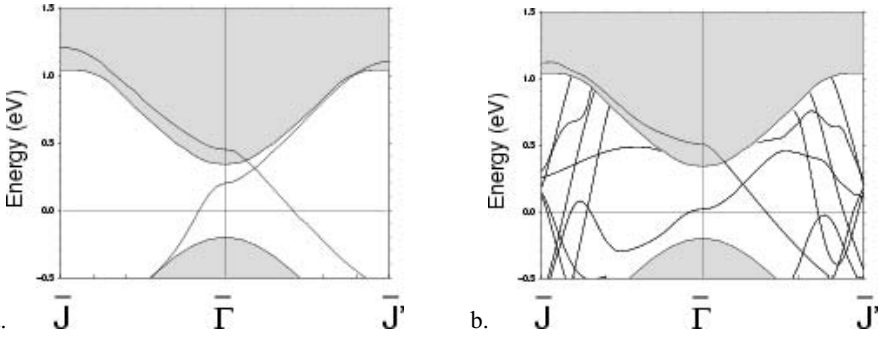

Fig. 9. Projected bulk minority-spin band structures of NiMnSb (shaded) showing (a) DFT-calculated surface states of NiMnSb(001), and (b) interface and overlayer states of NiMnSb(001)/Sb, adapted from [138,140]

while in the case of defects the ever-present spectre of interfacial segregation demands further pause for thought. Neither should one believe that these issues affect only tunnel junctions; even in the Ohmic geometry, a high local density of minority-spin interface states still provides ample opportunity for enhanced spin-flip scattering relative to the ideal case.

In principle, however, it may at least be possible to ameliorate some of the worst effects of the interface states by engineering the electronic structure of the interface. As stressed above, crystal-momentum is a conserved quantity in transport across an ideal boundary, so that a ballistic device, in which current flows primarily through states of zero parallel crystal-momentum, might not be too badly affected so long as the interface states are avoided at the zone center at the energy of choice. This raises the issue of control over detailed electronic structure through appropriate manipulation over atomic structure.

By way of example, let us consider a little more closely the case of NiMnSb, where segregation issues have seriously hampered experimental efforts to produce well-ordered and stoichiometric surfaces. Even concentrating on just the simplest (001) surface facet, we find ourselves faced with non-trivial questions of surface composition. The surface could conceivably possess two differing surface terminations, ending on either a Ni layer or on a MnSb layer. Which of these will be preferred? From an experimental perspective the preparation of *any* well-ordered surface of this type is fraught with difficulty, success being achieved through the use of a protective Sb capping-layer; this latter may be removed by flash annealing, and characterisation of the surface indicates a stoichiometric MnSb-termination [163,164]. Even so, the electronic structure of the surface region is not found to be half-metallic; minority-spin surface states encroach into the band gap region, crossing the Fermi level along an elliptical contour in reciprocal space [138].

The nature of these NiMnSb(001) surface states is, indeed, highly unusual, resembling neither Shockley nor Tamm typology: the dispersion curves are parabolic, but the effective mass suffers an apparent change in sign when the surface wave vector is rotated by 90° (see Figure 9a). The effect seems to be due to the interplay between the Sb p-orbital and Mn d-orbital contributions to the surface states, and the fact that these are clearly modulated by the arrangement of second-layer Ni atoms. The result is a (001) surface that has C_{2v} symmtry and

the allowed irreducible representations are A_1 (s, p_z, $d_{3z^2-r^2}$, $d_{x^2+y^2}$), A_2 (d_{xy}), B_1 (p_x, d_{xz}) and B_2 (p_y, d_{yz}).

In fact, the energy-wave vector surfaces mapped out by these states may be visualised as two sheets, touching at just two points (electronic conical intersections) in the Brillouin zone. The lower sheet displays A_1 symmetry character at the zone center, while the upper displays B_1 symmetry at the same point; the Fermi contour varies between A_1 symmetry at its greatest extent along the $\overline{\Gamma J}$ direction, and B_1 symmetry at its greatest extent along the $\overline{\Gamma J'}$ direction. The consequences of such unusual dispersion for spin-injection can, at present, only be guessed. What seems apparent is that minority-spin electrons injected into the upper surface state would be somewhat constrained (in the absence of spin-flip scattering and radiative transitions) to follow a very particular path through one or other of the two conical intersections. An electron may enter a surface state at the zone center, having A_1 symmetry, but eventually is likely to thermalise to the Fermi level with a finite wave vector in the $\overline{\Gamma J'}$ direction and in a state having B_1 symmetry! More usefully, perhaps, we might note that majority-spin electrons injected at the zone center *just above* the Fermi level (or majority-spin holes injected just below) would be almost immune to spin-flip scattering, due to the absence of minority-spin surface states from that region. A small window is thus apparent, within which spin-polarised conduction might occur, but only if devices can be designed specifically to exploit this loophole.

As already mentioned, however, the growth of metallic, semiconducting or insulating overlayers on half-metallic substrates (or vice versa) does not necessarily give grounds to hope for a general passivation of the minority-spin surface states. Although they may be altered by contact with the overlayer, it is entirely possible that they will eventually transform into interface states [83,139-142]. In the case of NiMnSb(001) discussed above, for example, the deposition of a half-monolayer of Sb has been shown to severely disrupt the DFT-calculated surface states, but the original eigenfunctions reassert themselves as interface states for coverages of a monolayer and above [140]. Furthermore, the A_1 symmetry state drops in energy at the zone center, closing the window previously described (see Figure 9b). Clearly, existing work has barely begun to elucidate the links between surface and interface electronic structure in the half-metallic materials.

6. THE PROBLEM OF INTERFACE COMPOSITION

Implicit in the existence of surface states is the free energy created by symmetry breaking at a surface. Indeed, there is a free enthalpy difference between the surface and bulk in both the Heusler alloys [164] and the manganese perovskites [165]. This energy difference, plotted for NiMnSb in Figure 10, is quite significant and will lead to surface states, as discussed above, as well as surface reconstructions, changes in chemical reactivity and segregation as indicated in Figure 11. While these surface and interface effects may share some similarities in origin let us now consider the problems of surface composition and surface segregation.

Surface and interface problems should not be a surprise. There is a strong chemical potential for surface segregation in the postulated half-metallic ferromagnetic materials [164,165] that results in equilibrium surfaces at elevated temperatures that are not the same stoichiometry as the bulk. Evidence of the resulting surface segregation has been found for

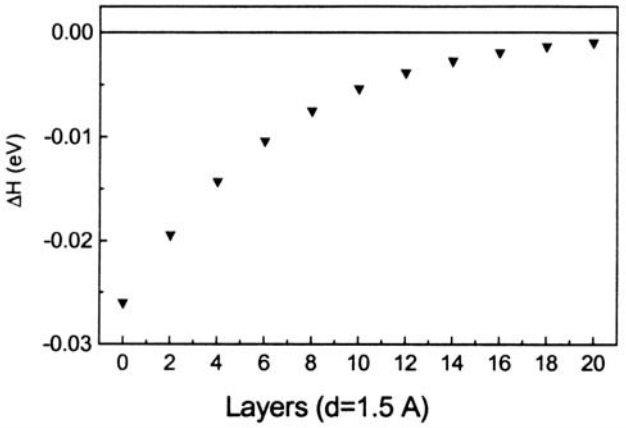

Fig. 10. The free energy difference between the surface and the bulk of stoichiometric NiMnSb, extrapolated from experimental data using simple statistical mechanics models [164].

NiMnSb(001) [163-164,166-168], TiCoSb [167-168] and the manganese perovskites $La_{1-x}A_xMnO_3$ (A=Ca, Sr, Pb) [165,169-177]. The extent of segregation can be considerable once equilibrium is established and extends from the surface well into the bulk; it need not be localized just to the surface layer. Indeed, in the half-metallic ferromagnetic systems, at least for those systems characterized in detail, surface segregation is rarely restricted to just the surface terminal layers. Variations in composition due to surface segregation can extend often 5 to 10 unit cells away from the surface, as is evident for NiMnSb (detailed in Figure 12) and the manganese perovskites. It is very clear that for the postulated half-metallic ferromagnets, the stoichiometric surface is rarely stable at finite (elevated) temperatures.

The dynamics of surface segregation that include the gradual concentration gradient of one species or another as one approaches the surface and the possible random arrangement of defect sites in the surface layers are far from completely understood. This theoretical problem poses a considerable challenge, but it is clear that as temperature increases, kinetic barriers to segregation are overcome, and are accompanied by a changing free enthalpy of segregation. Thus depolarization due to magnons, phonons, and the non-quasiparticle states that dominates at lower temperatures, is supplanted by even greater depolarization due to compositional changes in the surface region [163,166,172], as seen in Figure 13, and alluded to in the previous section.

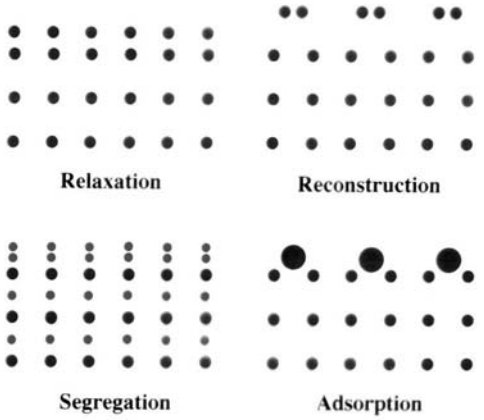

Fig. 11. Schematic representation of reconstructions, segregation and surface reactivity that can occur concomitantly with the presence of electronic surface states.

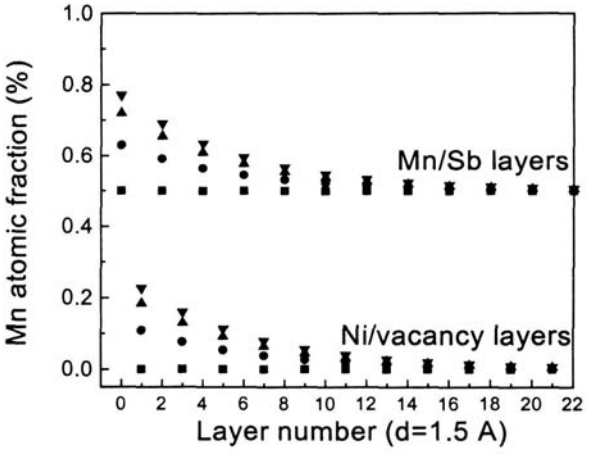

Fig. 12. The concentration of Mn in the near surface region obtained from fits from the angle resolved X-ray photoemission from [164]. The odd layers are Mn/Ni. The Mn concentration profiles denoted by the different symbols (● < ▲ < ▼) indicates increasing segregation and filling of vacancies in the near surface region with annealing at 700 K [164].

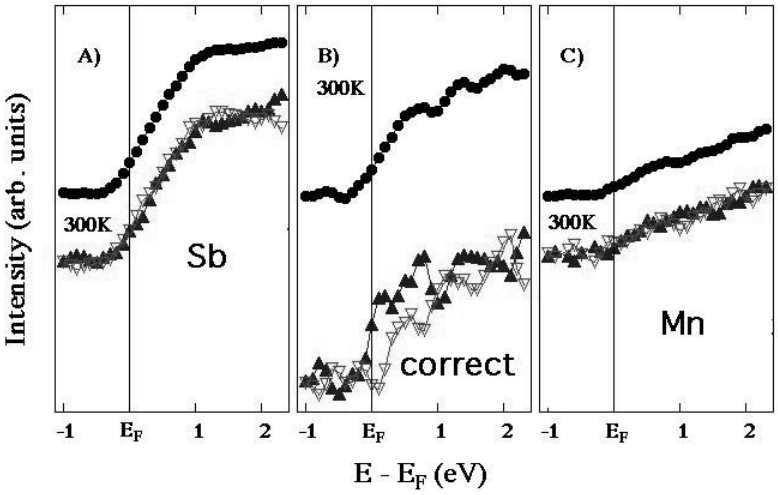

Fig. 13. Spin polarized inverse photoemission spectra at normal incidence to NiMnSb (001) with spin integrated inverse photoemission shown for comparison (●) probing the unoccupied states above the Fermi energy. (**a**) For an NiMnSb surface capped with an Sb overlayer (**b**) Following the removal of excess Sb to form the ordered and stoichiometric MnSb terminated (100) surface. (**c**) Following Mn segregation to the surface region after (**b**). ▲-spin up, ▽-spin down are both indicated. Adapted from [163].

Even for postulated half-metallic systems that preserve stoichiometry in the surface region, the resulting stable surface terminal layer, can affect polarization, as noted above. The surface terminal layer can depend not only upon composition of the bulk material, but also on the orientation of the surface layer, even in the absence of segregation. The termination layer of $La_{0.9}Ca_{0.1}MnO_3$ is a La-Ca-O layer [165,174] but the termination layer of $La_{0.65}A_{0.35}MnO_3$, with x=0.35, has been consistently determined to be an Mn-O layer [177-184], except in the case of $La_{0.65}Sr_{0.35}MnO_3$ [169,171] where the stable surface region is a different perovskite: a Ruddlesden-Popper phase. Because there are few experimental studies that compellingly identify the surface composition of manganese perovskite surface terminal layers in the absence of any surface segregation, and the stable surface of the CrO_2 surface is almost always Cr_2O_3 [185,186], we choose to illuminate the complex issue of the stability of postulated half-metallic surfaces (the surface terminal layer) in the absence of segregation by using the example of the semi-Heusler alloy NiMnSb.

The surface termination of the (111) face of NiMnSb is more complex than the (001) described in the previous section. The cleavage of a bulk crystal must create two inequivalent surfaces; the 'A' surface nominally terminates with a complete trilayer ending on a plane of Mn atoms, while the 'B' surface nominally terminates with a complete trilayer ending on a plane of Sb atoms. Indeed, these terminations were assumed to be the correct description of the surface in the first DFT calculations, carried out by de Wijs and de Groot [139]. It is clear, however, that other terminations are possible. The nominal 'A' surface (hereafter A_α) may lose its final layer of Mn atoms to create the A_β surface (ending with a bilayer terminating on

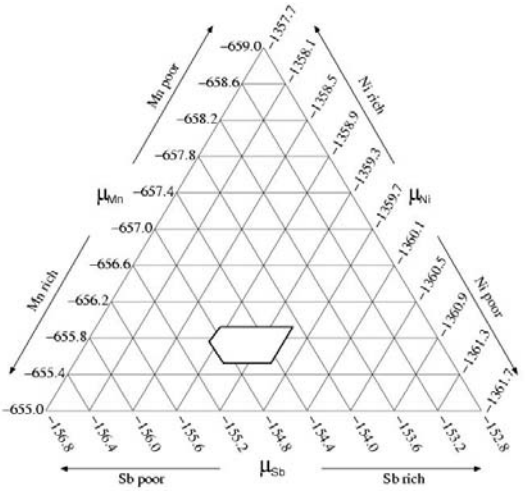

Fig. 14. The region of chemical potential space for which NiMnSb is thermodynamically stable against segregation [187].

a plane of Ni atoms) or be further depleted to create the Aγ surface (ending with a monolayer of Sb atoms). Similarly, the nominal 'B' surface (hereafter B_α) may lose its final layer of Sb atoms to create the B_β surface (ending with a bilayer terminating on a plane of Ni atoms) or be further depleted to create the Bγ surface (ending with a monolayer of Mn atoms). The stability of these different surface terminations can be analysed theoretically with reference to the calculated chemical potentials of the constituent elements Ni, Mn and Sb, and of their complementary binary compounds MnSb, NiSb and NiMn [187]. Thermodynamic considerations dictate that the surface chemical potentials of Ni, Mn and Sb must lie within the region highlighted in Figure 14.

Now, the free energies of the various surface structures may be determined according to the equation

$$F = E - \mu_{Ni} N_{Ni} - \mu_{Mn} N_{Mn} - \mu_{Sb} N_{Sb} \tag{6}$$

where μ_x is the chemical potential of species *x*, and N_x is the number of atoms of that species in the structure. The internal energy may readily be obtained through some appropriate DFT calculation, whereupon the free energy may be derived. It then becomes possible simply to read off which structure (or structures) will be favoured under all permissible conditions indicated by the region specified in Figure 15. In this case, it turns out that the only allowed A surface is the Aγ termination, and the only allowed B surface is the B_α termination. Both of these are Sb-terminated structures, but while the B_α surface ends in an apparently natural manner, with a complete trilayer, the Aγ surface ends with a single monolayer of Sb. Clearly the driving force to have Sb atoms at the surface is dominant over the natural tendency for the crystal structure to cleave along its least-dense plane. In fact, the tendency towards Sb

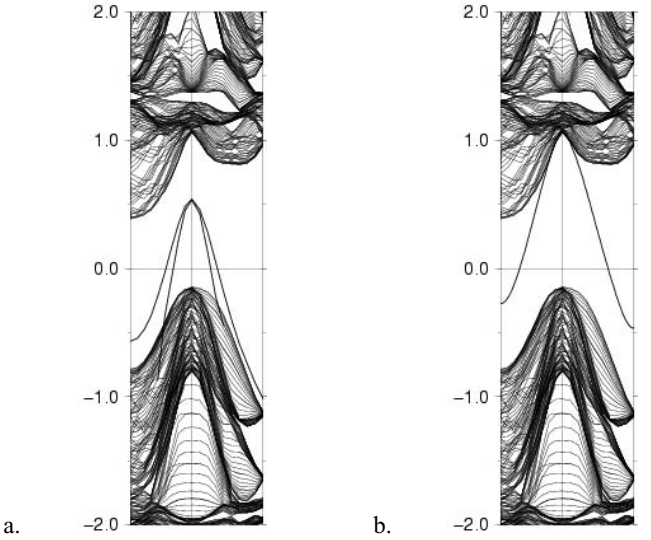

Fig. 15. Projected bulk minority-spin band structure (lines common to both panels) and surface states of NiMnSb(111) in (**a**) the Aγ termination and (**b**) the B_α termination [187].

termination seems to be a general feature of the materials considered, as not only the MnSb(0001) surface but also the NiSb(0001) surface display the same behaviour.

The surface composition is far from unimportant when considering the electronic structure of the surface, as an examination of the band structures of NiMnSb(111) will demonstrate: both the Aγ and B_α terminations feature inverted parabolic dispersion curves, whereas there are two nearly degenerate states in the Aγ case, for B_α there is only one (see Figure 15).

7. EXPERIMENTAL PROOF OF HALF-METALLIC CHARACTER ?

Perhaps you are indeed convinced that 98% spin polarization is not 100 % spin polarization, even at 1.6 K. Perhaps you are also convinced that magnons are difficult to suppress, in spite of a fond desire for 100% spin polarization at room temperature. What about those claims of 100% spin polarization at room temperature ?

There have been various experimental arguments in favor of true half-metallic ferromagnetism [1,3,104,110,188-196]. For example, even though tunnel junctions include contributions from the spin dependent Fermi velocity [197,198], which could effectively enhance the tunnel magneto-resistance, no tunnel magneto-resistive junctions measurement has provided a strong indication of half-metallic character. The highest tunnel-magnetoresistance values reached have been as high as 150 to 730% [103,105-106,109] to 1800% [104], and this only at very low temperatures (though very high values of magneto-resistance have been observed at 77 K [109], and room temperature [199]). Unfortunately,

Table 1. Experimental spin polarization determined by spin-polarized electron spectroscopies at elevated sample temperatures. With the exception of the spin-polarized *inverse* photoemission experiments in [114,163,172,192,209], all data were obtained by spin-polarized photoemission.

Potential Half-Metallic System	polarization claim	temperature
$La_{0.7}Sr_{0.3}MnO_3$	100±5% [188]	40 K
	100 % [192]	100 K
$La_{0.7}Pb_{0.3}MnO_3$	much less than 80% [172]	300 K
	13% [208]	10 K
CrO_2	95 % [189]	293 K
	95 % [190]	293 K
Fe_3O_4	-80±5% [191]	293 K
	-40 % [206]	130 K
NiMnSb	50 % [166]	300 K
	45 % [209]	300 K
	40 % [207]	300 K
	high but not near 100% [114,163]	300 K

interface and defect scattering contributions to the magneto-resistance are difficult to eliminate, making such measurements less than compelling. It is hard to see how magnon scattering can be eliminated from magneto-resistive junctions with small applied bias [200].

Transport spin-polarization measurements, using point-contact Andreev reflection, have generally provided the highest measured polarizations to date [194-195,201-205]. In spite of several claims of proof of half-metallic character for CrO_2, based on the very high polarizations derived from the point contact Andreev reflection [194-195], superconducting tunnel junctions [196], and magneto-resistive transport [110] measurements, these measured values of polarization (96±1% [194], 98.4% [195], 97% [82], 82% [196] respectively) generally miss the mark of 100% for the postulated half-metallic systems, even at temperatures of 1.6 K. The analysis of the data must be taken with considerable care [201,204] and cannot ignore Fermi velocity contributions. In the case of $La_{2/3}Sr_{1/3}MnO_3$, the appreciable spin minority population at 1.5 K is probably a band-structure effect [201].

In the very low temperature polarization measurements [194-196], there is really no compelling evidence that there are no magnon contributions at low temperatures, even at 1.6 K. Indirect proof of half-metallic character from the magnetic moment measured at high fields is likely to be very insensitive to a small spin minority density of states. In our opinion, half-metallic ferromagnetism is an idealized limit, realistic only in perfect crystals at zero temperature.

Apart from a somewhat ambiguous scanning tunneling microscopy spectroscopy study undertaken at 77 K [193], claims of 100% spin polarization at more elevated temperatures (>40 K) rest on evidence from spin-polarized photoemission [188-191] and spin polarized

inverse photoemission [192], as summarized in Table 1. Spin-resolved photoemission measurements [189-191] and spin polarized inverse photoemission [192] that claim to provide evidence of half-metallic behavior, in fact, do not. (Of course not all such measurements have led to such claims [163,166,172,206-209].) Finite temperature effects leading to the population of spin minority states near E_F, just described, would be most significant at wave vectors near band crossings of the Fermi level, which generally occurs away from $\bar{\Gamma}$, the surface Brillouin zone center. Finite temperature effects may not, therefore, be observed in these measurements at normal emission [188-189] (for spin-polarized photoemission) or normal incidence [192] (for spin-polarized inverse photoemission), even for stoichiometric surfaces. Similarly, spin minority surface states leading to a loss of half-metallic character, as noted above, would not generally be observed if measurements are only undertaken at the $\bar{\Gamma}$ $\underline{k}_{||}=0$ point.

While polarization at the Brillouin zone center ($\mathbf{k}_{\|}= 0$) does correspond to long range magnetic order, it is not clear that the polarization is, in fact, easily related to the magnetic moment for any given system. This is dramatically illustrated in Figure 3. The polarization of the NiMnSb(100) surface, determined by the difference of spin up and down in spin-polarized inverse photoemission (SPIPES) of NiMnSb [114,163], suggests a very high spin polarization near the Fermi level (nearly 100% above background for $\mathbf{k}_{\|}= 0$ and T=300 K in the spin-polarized inverse photoemission spectra [114,163]), as seen in Figures 3a and 13b. Subject to the necessary selection rules [210], X-ray adsorption spectra (XAS) reflect the joint density of states between the core level and the unoccupied states and both these core excitation spectra and magnetic circular dichroism (MCD) spectra (the difference between circular light XAS signals taken with opposite magnetization directions, indicated in Figure 1d and e) can be roughly compared to inverse photoemission. From this comparison in the region close to the Fermi level, the large polarization asymmetry in spin polarized inverse photoemission can be attributed to strong contribution from the Mn spin and orbital moments at remanence [114]. Yet, as the temperature is increased above 80 K, the MCD exhibits a huge decrease in the relative spin and orbital moment, as seen in Figure 3 and summarized in Figure 4 for NiMnSb. In XAS, however, the apparent density of states near the Fermi level (threshold) does not change significantly for Mn or Ni. Therefore, the polarization of NiMnSb(100) close to 100% at an elevated finite temperature (300 K here), at the Brillouin zone center ($\mathbf{k}_{\|}= 0$), is not a good indicator of the maximum possible remanent band moment or indeed the total 'integrated' band polarization in the NiMnSb system. The comparison of spin polarized inverse photoemission and MCD results [114] are clear proof that any angle-resolved spin-polarized photoemission or spin-polarized inverse photoemission measurements, with limited wave vector sampling, cannot be taken as sufficient evidence of half-metallic ferromagnetic character if the sample is crystalline or is polycrystalline with texture growth.

The negligible DOS at the Fermi level ($D(E_F) \sim 0$) in the spin-polarized photoemission spectra of $La_{2/3}Sr_{1/3}MnO_3$ [188] and CrO_2 [189] and in spin-polarized inverse photoemission for $La_{2/3}Pb_{1/3}MnO_3$ [172] suggests that either the surface is not the correct stoichiometry in those studies (see [169,171] for $La_{2/3}Sr_{1/3}MnO_3$, [163,164] for NiMnSb, and [185,186] for CrO_2) as discussed above in section 6 or that the Fermi level crossings are well away from $\bar{\Gamma}$ (or some combination of both effects). To a *small* extent final state effects in photoemission can contribute [211], but likely surface composition, surface electronic structure and choice of incidence (or emission) angle dominate. A band structure like that of gadolinium, with a

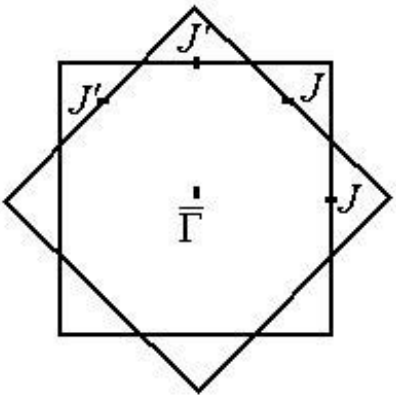

Fig. 16. A schematic C_{2v} surface Brillouin zone, applicable to the (001) surfaces of the perovskites and Heusler alloys and illustrating that crystalline texture may rotate the Brillouin zone but leaves the zone center unperturbed.

strong magnetic surface state near the Fermi energy at $\bar{\Gamma}$, might appear to be "half-metallic" (or at least a very high polarization ferromagnet) if such measurements are taken at only one wave vector near the surface Brillouin zone center [212-214]. No one would argue that gadolinium is a half-metallic system with this band structure. Crystalline disorder that might occur, but cannot be used as an argument for "complete" sampling of the Brillouin zone. In such strongly textured thin films, disorder would result in some cylindrical averaging of k-points away from $\bar{\Gamma}$ but leave the $\bar{\Gamma}$ point unperturbed, as indicated in Figure 16. So "proof" of half-metallic character must necessarily remain elusive.

8. SUMMARY

In conclusion, we have shown that finite-temperature spin disorder destroys the complete spin polarization characteristic of half-metallic ferromagnets. The present findings are relevant to the question of whether and under what circumstances there exists the 'ideal', that is a fully spin polarized half-metallic system with a single spin conduction channel. The many-sublattice structures of the half-metallic ferromagnets yield transverse optical phonon modes which couple to the magnons and tend to reduce the net magnetization and the Fermi-level spin polarization at comparatively low temperatures. In a strict sense, this thermally activated spin mixing means that half-metallic ferromagnetism is limited to perfect crystals at zero temperature. This mechanism is modified and, in general, enhanced by crystal imperfections, and by surface and interface effects, particularly if the interface Debye temperature is lower than the bulk as is so often the case.

At low temperatures (say below 20 K) we have limits to polarization due to magnons and non-quasiparticle states, at intermediate temperatures (in the region of 50 to 150 K), because

the postulated half metallic systems are all compound systems, we have further limits to polarization, indeed large polarization decreases due to magnon-phonon coupling. At higher temperatures, in the region of room temperature and above, we have compositional problems due to segregation to surface and interfaces, and these latter effects are irreversible. In addition, any real device involves interfaces, so even in the absence of segregation, the interfaces will also contribute to the spin minority density of states as a result of interface states, even at zero temperature.

Bearing in mind that magnetization is not the same as polarization, and that it is the interface electronic structure that dominates spin-injection in real systems, it may be that the elemental ferromagnets (Co, Fe, and Ni) are in fact better "spin injectors" than the half-metallic systems at elevated temperatures. While at low temperatures (in the region of zero Kelvin) the postulated half-metallic system may have high polarizations, indeed much higher than the elemental ferromagnets, the polarization falls rapidly with increasing temperature. Many of these materials will have bulk polarizations that are a small fraction of the polarization of the elemental ferromagnets by room temperature.

Acknowledgements

The support of the Office of Naval Research, NSF "QSPINS" MRSEC (DMR 0213808) and the Office of Naval Research are gratefully acknowledged. One of us (SJJ) is grateful to The Royal Society for a University Research Fellowship. The authors are grateful for the comments and contributions of Ralph Skomski, Leo Sandraskii, David Edwards, Anthony N. Caruso, Hae-Kyung Jeong, Takashi Komesu, Camelia Borca, Delia Ristoiu, Jiandi Zhang, Jean-Pierre Nozières, Myron Salamon, Gavin Bell, Chris McConville and David King.

REFERENCES

[1] W. E. Pickett and J. Moodera, Physics Today 54 (2001) 39
[2] M. Ziese, Rept. Prog. Phys. 65 (2002) 143-249
[3] J.M.D. Coey and C.L. Chien, MRS Bulletin 28 (2003) 724
[4] V. Yu. Irkhin and M.I. Katsnel'son, Physics Uspekhi 37 (1994) 659; Uspekhi Fizicheskikh Nauk. 164 (1994) 705-724
[5] C. Palmstrøm, MRS Bulletin 28 (2003) 725
[6] R.A. de Groot, F.M. Mueller, P.G. van Engen, and K.H.J. Buschow, Phys. Rev. Lett. 50 (1983) 2024
[7] R.A. de Groot, F.M. Mueller, P.G. van Engen, and K.H.J. Buschow, J. Appl. Phys. 55 (1984) 2151
[8] C.M. Fang, G.A. de Wijs, R.A. de Groot, J. Appl. Phys. 91 (2002) 8340
[9] J. Kübler, Physica B 127 (1984) 257
[10] K.E.H.M. Hanssen, an d P.E. Mijnarends, Phys. Rev. B 34 (1986) 5009
[11] I. Galanakis, S. Ostanin, M. Alouani, H. Dreysse, and J.M. Wills, Phys. Rev. B 61 (2000) 4093
[12] J.-S. Kang, J.-G. Park, C.G. Olson, S.J. Youn and B.I. Min, J. Phys.: Condens. Matter 7 (1995) 3789
[13] M. Zhang, X. Dai, H. Hu, G. Liu, Y. Cui, Z. Liu, J. Chen, J. Wang and G. Wu, J. Phys.: Condens. Matter 15 (2003) 7891
[14] M. Pugaczowa-Michalska, Acta Physica Polonica A 103 (2003) 393-402
[15] L. Chioncel, M.I. Katsnelson, R.A. de Groot RA, A.I. Lichtenstein, Phys. Rev. B 68 (2003) art. no. 144425
[16] K.E.H.M. Hanssen and P.E. Mijnarends, Phys. Rev. B 34 (1986) 5009
[17] I. Galanakis, J. Phys. Cond. Matter 14 (2002) 6329
[18] I. Galanakis, P.H. Dederichs, N. Papanikolaou, Phys. Rev. B 66 (2002) art. no. 174429
[19] I. Galanakis, P.H. Dederichs, N. Papanikolaou, Phys. Rev. B 66 (2002) art. no. 134428
[20] S. Ishida, T. Masaki, S. Fujii, S. Asano, Physica B-Condensed Matter 245 (1998) 1
[21] S. Ishida, S. Fujii, S. Kashiwagi, S. Asano, J. Physical Society Japan 64 (1995) 2152
[22] S. Ishida, S. Kashiwagi, S. Fujii, S. Asano, Physica B 210 (1995) 140
[23] S. Fujii, S. Ishida, S. Asano, J. Phys. Soc. Jpn. 64 (1995) 185
[24] S. Fujii, S. Sugimura, S. Ishida, S. Asano, J. Phys.: Condens. Matter 2 (1990) 8583
[25] S. Fujii, S. Ishida, and S. Asano, J. Phys. Soc. Jpn. 58 (1989) 3657
[26] S. Picozzi, A. Continenza, A.J. Freeman, Phys. Rev. B 66 (2002) art. no. 094421
[27] S. Picozzi, A. Continenza, A.J. Freeman, Phys. Rev. B 69 (2004) art. no. 094423
[28] R. Weht, W.E. Pickett, Phys. Rev. B 60 (1999) 13006
[29] B.G. Liu, Phys. Rev. B 67 (2003) art. no. 172411
[30] W.H. Xie, Y.Q. Xu, B.G. Liu, D.G. Pettifor, Phys. Rev. Lett. 91 (2003) art. no. 037204
[31] Y.Q. Xu, B.G. Liu, D.G. Pettifor, Physica B: Condens. Matter 329 (2003) 1117
[32] Y.Q. Xu, B.G. Liu, D.G. Pettifor, Phys. Rev. B 66 (2002) art. no. 184435
[33] W.H. Xie, B.G. Liu, D.G. Pettifor, Phys. Rev. B 68 (2003) art. no. 134407
[34] W.H. Xie, B.G. Liu, J. Phys.: Condens. Matter 15 (2003) 5085
[34] I. Galanakis, Phys. Rev. B 66 (2002) art. no. 012406
[36] I. Galanakis, P. Mavropoulos, Phys. Rev. B 67 (2003) art. no. 104417

[37] M.C. Qian, C.Y. Fong, W.E. Pickett and H.-Y Wang, J. Appl. Phys. 95 (2004) 7459
[38] H. Akinaga, T. Manago, M. Shirai, Japn. J. Appl. Phys. (Part 2) 39 (2000) L1118
[39] J.E. Pask, L.H. Yang, C.Y. Fong, W.E. Pickett, S. Dag, Phys. Rev. B 67 (2003) art. no. 224420
[40] C.Y. Fong, M.C. Qian, J.E. Pask, L.H. Yang, S. Dag, Appl. Phys. Lett. 84 (2004) 239
[41] J.C. Zheng, J.W. Davenport, Phys. Rev. B 69 (2004) art. no. 144415
[42] A. Continenza, S. Picozzi, W.T. Geng, A.J. Freeman, Phys. Rev. B 64 (2001) art. no. 085204
[43] S. Picozzi, T. Shishidou, A.J. Freeman, B. Delley, Phys. Rev. B 67 (2003) art. no. 165203
[44] Y.J. Zhao, W.T. Geng, A.J. Freeman, B. Delley, Phys. Rev. B 65 (2002) art. no. 113202
[45] M. Zhang, H. Hu, G. Liu, Z. Liu, Y. Cui, G. Wu, J. Low Temp. Phys. 135 (2004) 267
[46] M. Zhang, H.N. Hu, Z.H. Liu, G.D. Liu, Y.T. Cui, G.H. Wu, J. Magn. Magn. Mater. 270 (2004) 32
[47] M. Zhang, H.N. Hu, G.D. Liu, Y.T. Cui, Z.H. Liu, J.L. Wang, G.H. Wu, X.X. Zhang, L.Q. Yan, H.Y. Liu, F.B. Meng, J.P. Qu, Y.X, Li, J. Phys. Condens. Matter 15 (2003) 5017
[48] S. Sanvito, N.A. Hill, Phys. Rev. B 62 (2000) 15553
[49] B. Sanyal, L. Bergqvist, O. Eriksson, Phys. Rev. B 68 (2003) art. no. 054417
[50] R.A. Stern, T.M. Schuler, J.M. MacLaren, D.L. Ederer, V. Perez-Dieste and F.J. Himpsel, J. Appl. Phys. 95 (2004) 7468
[51] J. Kübler, Phys. Rev. B 67 (2003) art. no. 220403
[52] W.E. Pickett, D.J. Singh, Phys. Rev. B 53 (1996) 1146
[53] D.J. Singh and W.E. Pickett, Phys. Rev. B 57 (1998) 88
[54] H. Kino, F. Aryasetiawan, I. Solovyev, T. Miyake, T. Ohno, K. Terakura, Physica B: Cond. Matt. 329 (2003) 858
[55] W.E. Pickett, D.J. Singh, J. Magn. Magn. Mater. 172 (1997) 237
[56] P.K. de Boer and R.A. de Groot, Compt Mat. Res. 10 (1998) 240
[57] S.F. Matar, Prog. Solid State Chem. 31 (2003) 239
[58] P.K. de Boer, H. van Leuken, R.A. de Groot, T. Rojo, G.E. Barberis, Solid State Comm. 102 (1997) 621
[59] J.S. Kang, T.W. Noh, C.G. Olson, B.I. Min, J. Electron Spectrosc. Rel. Phenom. 114 (2001) 683
[60] K.-I. Kobayashi, T. Kimura, H. Sawada, K. Terakura, Y. Tokura, Nature (London) 395 (1998) 677
[61] J.E. Medvedeva, V.I. Anisimov, M.A. Korotin, O.N. Mryasov, A.J. Freeman, J. Magn. Magn. Materials 237 (2001) 47
[62] P.K. de Boer, R.A. de Groot, Phys. Rev. B 60 (1999) 10758
[63] W.E. Pickett, Phys. Rev. B 57 (1998) 10613
[64] K. Schwarz, J. Phys. F 16 (1986) L211
[65] H. van Lueken and R.A. de Groot, Phys. Rev. B 51 (1995) 7176
[66] M.A. Korotin, V.I. Anisimov, D.I. Khomskii and G.A. Sawatzky, Phys. Rev. Lett. 80 (1998) 4305
[67] S. P. Lewis, P.B. Allen, and T. Sasaki, Phys. Rev. B 55 (1997) 10253
[68] I.I. Mazin, D.J. Singh, C. Ambrosch-Draxl, Physical Review B 59 (1999) 411

[69] S. Matar, G. Demazeau, J. Sticht, V. Eyert, J. Kubler, J. de Physique I 2, (1992) 315; ibid, 4 (1994) 1259
[70] R.A. de Groot and K.H.J. Bischow, J. Magn. Magn. Mater. 54-57 (1986) 1377
[71] M. Penicaud, B. Silberchoit, C.B. Sommers, and J. Kübler, J. Magn. Magn. Mater. 103 (1992) 212
[72] H.T. Jeng, G.Y. Guo, Phys. Rev. B 65 (2002) art. no. 094429
[73] I.I. Mazin, Appl. Phys. Lett. 77 (2000) 3000
[74] T. Shishidou, A.J. Freeman, R. Asahi, Phys. Rev. B 64 (2001) art. no. 180401
[75] M. Lauer, R. Valenti, H.C. Kandpal, R. Seshadri, Phys. Rev. B 69 (2004) art. no. 075117
[76] G.A. Prinz, Science 282 (1998) 1660
[77] S.A. Wolf, D.D. Awschalom, R.A. Buhrman, J.M. Daughton, S. von Molnar, M.L. Roukes, A.Y. Chtchelkanova, D.M. Tregar, Science 294 (2001) 1488
[78] A. Cho, Science 296 (2002) 249
[79] D.J. Kim, Physics Reports 171 (1988) 129; D.J. Kim and S. Ukon, Prog. Theor. Phys. Suppl. 69 (1980) 281
[80] Hae-Kyung Jeong, R. Skomski, C. Waldfried, Takashi Komesu, P.A. Dowben, E. Vescovo, Phys. Lett. A 324 (2004) 242-246
[81] D. Orgassa, H. Fujiwara, T. C. Schulthess, and W. H. Butler, Phys. Rev. B 60 (1999) 13237
[82] D. Orgassa, H. Fujiwara, T. C. Schulthess, and W. H. Butler, J. Appl. Phys. 87 (2000) 5870
[83] S. Picozzi, A. Continenza, A.J. Freeman, J. Appl. Phys. 94 (2003) 4723
[84] S. Ishida, T. Masaki, S. Fujii, S. Asano, Physica B-Condensed Matter 239 (1997) 163
[85] Y. Miura, K. Nagao, M. Shirai, Phys. Rev. B 69 (2004) art. no. 144413
[86] M. Pugaczowa-Michalska, Acta Physica Polonica A 103 (2003) 393
[87] J. Tobola, L. Jodin, P. Pecheur, H. Scherrer, G. Venturini, B. Malaman, S. Kaprzyk, Phys. Rev. B 64 (2001) art. no. 155103
[88] M.P. Raphael, B. Ravel, Q. Huang, M.A. Willard, S.F. Cheng, B.N. Das, R.M. Stroud, K.M. Bussmann, J.H. Claassen, V.G. Harris, Phys. Rev. B 66 (2002) art. no. 104429
[89] I.V. Solovyev and K. Terakura, Phys. Rev. B 63 (2001) art. no. 174425
[90] J. König, H.-H. Lin and A.H. MacDonald, Phys. Rev. Lett. 84 (2000) 5628
[91] R. Skomski, J. Phys. Condens. Matter 15 (2003) R841
[92] L. M. Sandratskii, Phys. Rev. B 64 (2001) 134402
[93] L. M. Sandratskii, Adv. Phys. 47 (1998) 91
[94] L. M. Sandratskii and J. Kübler, *Magnetism and Electronic Correlations in Local Moment Systems*, Eds. M. Donath, P. A. Dowben, and W. Nolting, World Scientific, Singapore 1998, p. 271.
[95] R. Skomski and P. A. Dowben, Europhys. Lett. 58 (2002) 544
[96] P. A. Dowben and R. Skomski, J. Applied Physics 93 (2003) 7948
[97] P.A. Dowben and R. Skomski, J. Applied Physics 95 (2004) 7453
[98] H. Itoh, T. Ohsawa, and J. Inoue, Phys. Rev. Lett. 84 (2000) 2501
[99] A.H. MacDonald, T. Jungwirth and M. Kasner, Phys. Rev. Lett. 81 (1998) 705
[100] D.M. Edwards and J.A. Hertz, J. Phys. F: Metal Phys. 3 (1973) 2191
[101] V.Y. Irkhin and M.I. Katsnelson, J. Phys. C: Solid State Phys. 18 (1985) 4173
[102] V.Y. Irkhin, M.I Katsnelson, European Phys. J. B 30 (2002) 481

[103] T. Obata, T. Manako, Y. Shimakawa and Y. Kubo, Appl. Phys. Lett. 74 (1999) 290
[104] M. Bowen, M. Bibes, A. Barthélémy, J.-P. Contour, A. Anane, Y. Lemaître and A. Fert, Appl. Phys. Lett. 82 (2003) 233
[105] J.Z. Sun, W.J. Gallagher, P.R. Duncombe, L. Krusin-Elbaum, R.A. Altman, A. Gupta, Yu Lu, G.Q. Gong, and Gang Xiao, Appl. Phys. Lett. 69 (1996) 3266
[106] M. Viret, J. Nassar, M. Drouet, J. P. Contour, C. Fermon, and A. Fert, J. Magn. Magn. Mater. 198-199 (1999) 1
[107] J. Z. Sun, Phil. Trans. R. Soc. (London) A 356 (1998) 1693
[108] Yu Lu, X.W. Li, G.Q. Gong, Gang Xiao, A. Gupta, P. Lecoeur, J.Z. Sun, Y.Y. Wang and V.P. Dravid, Phys. Rev. B 54 (1996) R8357
[109] M.H. Jo, N.D. Mathur, N.K. Todd, and M.G. Blamire, Phys. Rev. B 61 (2000) 14905
[110] J.M.D. Coey, and M. Venkatesan, J. Appl. Phys. 91 (2002) 8345
[111] S.M. Watts, S. Wirth, S. von Molnár, A. Barry, and J.M.D. Coey, Phys. Rev. B **61** (2000) 9621
[112] J.M.D. Coey, A.E. Berkowitz, L. Balcells, F. Putris, and A. Barry, *Phys. Rev. Lett.* **80** (1998) 3815
[113] H.Y. Hwang, and S.W. Cheong, Science **278** (1997) 1607
[114] C.N. Borca, T. Komesu, H. Jeong, P. A. Dowben, D. Ristoiu, Ch. Hordequin, J. P. Nozières, J. Pierre, S. Stadler, and Y. U. Idzerda, Phys. Rev. B **64** (2001) art. no. 052409
[115] Ch. Hordequin, E. Lelievre-Berna, and J. Pierre, Physica B **234-236** (1997) 602
[116] Ch. Hordequin, D. Ristoiu, L. Ranno, and J. Pierre, Euro. Phys. J. B **16** (2000) 287
[117] C.T. Tanaka, J. Nowak and J.S. Moodera, J. Appl. Phys. **81** (1997) 5515
[118] L. Ritchie, G. Xiao, Y. Ji, T.Y. Chen, C.L. Chien, M. Zhang, J.L. Chen, Z.H. Liu, G.H. Wu, X.X. Zhang, Phys. Rev. B 68 (2003) art. no. 104430
[119] C. Hordequin, J. Pierre, R. Currat, J. Magn. Magn. Mater. 162 (1996) 75
[120] J.S. Moodera and D.M. Mootoo, J. Appl. Phys. 76 (1994) 6101
[121] N. Furukawa, J. Phys. Soc. Jpn. 69 (2000) 1954
[122] M. Jaime, P. Lin, M.B. Salamon and P.D. Han, Phys. Rev. B 58 (1998) R5901
[123] P. C. Lin, PhD. Dissertation, University of Illinois, 2001.
[124] M.S. Lund, J.W. Dong, J. Lu, X.Y. Dong, C.J. Palmstrøm and C. Leighton, Appl. Phys. Lett. 80 (2002) 4798
[125] L.J. Singh, Z.H. Barber, Y. Miyoshi, W.R. Branford and L.F. Cohen, J. Appl. Phys. 95 (2004) 7231
[126] L.J. Singh, Z.H. Barber, Y. Miyoshi, Y. Bugoslavsky, W.R. Branford and L.F. Cohen, Appl. Phys. Lett. 84 (2004) 2367
[127] T. Kasuya, Prog. Theor. Phys. 16 (1956) 58
[128] T. Kasuya, Prog. Theor. Phys. 22 (1959) 227
[129] I. Mannari, Prog. Theor. Phys. 22 (1959) 325
[130] G.K. White and S.B. Woods, Philos. Trans. R. Soc. London A 251 (1958) 273
[131] C.N. Borca, D. Ristoiu, Takashi Komesu, Hae-kyung Jeong, Ch. Hordequin, J. Pierre, J.P. Nozieres, and P.A. Dowben, Appl. Phys. Lett. 77 (2000) 88
[132] P. Dai, H. Y. Hwang, J. Zhang, A. Fernandez-Baca, S.-W. Cheong, C. Kloc, Y. Tomioka, and Y. Tokura, Phys. Rev. B 61 (2000) 9553
[133] J. Zhang, P. Dai, A. Fernandez-Baca, E.W. Plummer, Y. Tomioka, and Y. Tokura, Phys. Rev. Lett. 86 (2001) 3823

[134] H. Hwang, P. Dai, S.-W Cheong, G. Aeppli, D.A. Tennant, H.A. Mook, Phys. Rev. Lett 80 (1998) 1316
[135] N. Furukawa, and K. Hirota, Physica B 291 (2000) 324
[136] X.D. Wang, Phys. Rev. B 57 (1998) 7427
[137] L.M. Woods, Phys. Rev. B 65 (2000) 014409
[138] S.J. Jenkins and D.A. King, Surf, Sci. Lett. 494 (2001) L793
[139] G.A. de Wijs and R.A. de Groot, Phys. Rev. B 64 (2001) 020402
[140] S. J. Jenkins and D.A. King, Surf. Sci. Lett. 501 (2002) L185
[141] S. Picozzi, A. Continenza, A.J. Freeman, J. Phys. Chem. Solids 64 (2003) 1697
[142] V.K. Lazarov, Ph.D. Thesis, University of Wisconsin-Milwaukee, 2003
[143] M. F. Crommie, C. P. Lutz and D. M. Eigler, Science 262 (1993) 218
[144] M. F. Crommie, C. P. Lutz and D. M. Eigler, Nature 363 (1993) 524
[145] E.J. Heller, M. F. Crommie, C. P. Lutz and D. M. Eigler, Nature 369 (1994) 464
[146] M. F. Crommie, C. P. Lutz, D. M. Eigler and E.J. Heller, Physica D 83 (1995) 98
[147] M. F. Crommie, C. P. Lutz, D. M. Eigler and E.J. Heller, Surf. Rev. and Lett. 2 (1995) 127
[148] M. F. Crommie, C. P. Lutz, D. M. Eigler and E.J. Heller, Surf. Sci. 362 (1996) 864
[149] H. C. Manorahan, C. P. Lutz and D. M. Eigler, Nature 403 (2000) 512
[150] L. Petersen, P. Laitenberger, E. Laegsgaard and F. Besenbacher, Phys. Rev. B 58 (1998) 7361
[151] P. Avouris, I. W. Lyo and P. Molinasmata, Chem. Phys. Lett. 240 (1995) 423
[152] P. Avouris, I.W. Lyo, R. E. Walkup and Y. Hasegawa, J. Vac. Sci. Technol. B 12 (1994) 1447
[153] Y. Hasegawa and P. Avouris, Phys. Rev. Lett. 71 (1993) 1071
[154] P. Avouris and I. W. Lyo, Science 264 (1994) 942
[155] W. Chen, V. Madhavan, T. Jamneala and M. F. Crommie, Phys. Rev. Lett. 80 (1998) 1469
[156] M. F. Crommie, J. Electron Spect. Rel. Phenom. 109 (2000) 1
[157] P. T. Sprunger, L. Petersen, E. W. Plummer, E. Laegsgaard and F. Besenbacher, Science 275 (1997) 1764
[158] P. Hofmann, B. G. Briner, M. Doering, H. P. Rust, E.W. Plummer and A. M. Bradshaw, Phys. Rev. Lett. 79 (1997) 265
[159] B. G. Briner, P. Hofmann, M. Doering, H. P. Rust, E.W. Plummer and A. M. Bradshaw, Phys. Rev. B 58 (1998) 13931
[160] L. Petersen, B. Schaeffer, E. Laegsgaard, I. Stensgaard and F. Besenbacher, Surf. Sci. 457 (2000) 319
[161] K. H. Hansen, J. Gottschalck, L. Petersen, B. Hammer, E. Laegsgaard, F. Besenbacher and I. Stensgaard, Phys. Rev. B 63 (2001) 115421
[162] S. J. Jenkins, unpublished
[163] Delia Ristoiu, J.P Nozières, C.N. Borca, Takashi Komesu, Hae-kyung Jeong and P.A. Dowben, Europhys. Lett. 49 (2000) 624-630
[164] Delia Ristoiu, J.P Nozières, C.N. Borca, B. Borca and P.A. Dowben, Appl. Phys. Lett. 76 (2000) 2349
[165] Jaewu Choi, Jiandi Zhang, S.-H. Liou, P.A. Dowben and E.W. Plummer, Phys. Rev. B 59 (1999) 13453

[166] G.L. Bona, F. Meier, M. Taborelli, E. Bucher and P.H. Schmidt, Solid State Commun. 56 (1985) 391
[167] A.N. Caruso, C.N. Borca, D. Ristoiu, J.P. Nozières, P.A. Dowben, *Surface Science* 525 (2003) L109
[168] A.N. Caruso and C.N. Borca, *Recent Developments in Magnetism and Magnetic Materials* 1 (2003) 33-48
[169] Hani Dulli, P.A. Dowben, S.-H. Liou and E.W. Plummer, Phys. Rev. B 62 (2000) R14629
[170] C.N. Borca, Delia Ristoiu, Q.L. Xu, S.-H. Liou, S. Adenwalla, and P.A. Dowben, Journ. Appl. Phys. 87 (2000) 6104
[171] Hani Dulli, E.W. Plummer, P.A. Dowben, Jaewu Choi, and S.-H. Liou, Applied Phys. Lett. 77 (2000) 570
[172] C. N. Borca, Bo Xu, Takashi Komesu, Hae-Kyung Jeong, M.T. Liu, S.-H. Liou, S. Stadler, Y. Idzerda and P.A. Dowben, Europhysics Letters 56 (2001) 722
[173] C.N. Borca, Bo Xu, Takashi Komesu, Hae-Kyung Jeong, M.T. Liu, S.-H. Liou, and P.A. Dowben, Surface Science Letters 512 (2002) L346
[174] Jaewu Choi, C. Waldfried, S.-H. Liou, and P.A. Dowben, J. Vac. Sci. Technol. A16 (1998) 2950
[175] Wei Zhang, Xiaoru Wang and Ian Boyd, Appl. Phys. Lett. 73 (1998) 2745
[176] L.-C. Dufour and G.L. Bertrand, G. Caboche, P. Decorse, A. El Anssari, A. Poirson and M. Vareille, Solid State Ionics, 101-103 (1997) 661
[177] C.N. Borca, Delia Ristoiu, Q.L. Xu, S.-H. Liou, S. Adenwalla, and P.A. Dowben, Journ. Appl. Phys. 87 (2000) 6104
[178] Jaewu Choi, Hani Dulli, Yu Feng, S.-H. Liou, P.A. Dowben, and M.A. Langell, Physica Status Solidi (b) 214 (1999) 45
[179] Jiandi Zhang, D. N. McIlroy, P.A. Dowben, S.-H. Liou, R.F. Sabirianov and S.S. Jaswal, Sol. State Comm. 97 (1996) 39
[180] Carlo Waldfried, D.N. McIlroy, S.-H Liou, R. Sabiryanov, S.S. Jaswal, and P.A. Dowben, J. Phys. Cond. Matt. 9 (1997) 1031
[181] D.N. McIlroy, C. Waldfried, Jiandi Zhang, Jaewu Choi, F. Foong, S.-H. Liou, and P.A. Dowben, Phys. Rev. B54 (1996) 17438
[182] M. Yoshimoto, H. Maruta, T. Ohnishi, K. Sasaki, and H. Koinuma, Appl. Phys. Lett. 73 (1998) 187
[183] M. Izumi, Y. Konishi, T. Nishihara, S. Hayashi, M. Shinohara, M. Kawasaki and Y. Tokura, Appl. Phys. Lett. 73 (1998) 2497
[184] A. A. Zakharov, H. Nylén, M. Quavford, I. Lindau, M. Leandersson, M.B. Tsetlin and M.N. Mikheeva, Phys. Rev. B56 (1997) 9030
[185] J. Dai, J. Tang, H. Xu, L. Spinu, W. Wang, K.-Y. Wang, A. Kumbhar, M. Li and U. Diebold, Appl. Phys. Lett. 77 (2000) 2840
[186] Ruihua Cheng, B. Xu, C.N. Borca, A. Sokolov, C.-S. Yang, L. Yuan, S.-H. Liou, B. Doudin and P.A. Dowben, Appl. Phys. Lett. 79 (2001) 3122
[187] S. J. Jenkins, Phys. Rev. B, submitted
[188] J.-H. Park, E. Vescovo, H.-J. Kim, C. Kwon, R. Ramesh, and T. Venkatesan, Nature 392 (1998) 794
[189] K.P. Kämper, W. Schmitt, G. Güntherodt, R.J. Gambino, and R. Ruf, Phys. Rev. Lett. 59 (1987) 2788

[190] Y.S. Dedkov, M. Fonine, C. Konig, U. Rüdiger, G. Güntherodt, S. Senz, and D. Hesse, Appl. Phys. Lett. 80 (2002) 4181
[191] Y.S. Dedkov, U. Rüdiger, and G. Güntherodt, Phys. Rev. B 65 (2002) art. no. 064417
[192] R. Bertacco, M. Portalupi, M. Marcon, L. Duo, F. Ciccacci, M. Bowen, J.P. Contour and A. Barthélémy, J. Magn. Magn. Mater. 242-245 (2002) 710
[193] J.Y.T. Wei, N.C. Yeh , and R.P. Vasquez, Phys. Rev. Lett. 79 (1997) 5150
[194] Y. Ji, G.J. Strijkers, F.Y. Yang, C.L. Chien, J. M. Byers, A. Anguelouch, G. Xiao, and A. Gupta, Phys. Rev. Lett. 86 (2001) 5585
[195] A. Anguelouch, A. Gupta, Gang Xiao, G.X. Miao, D.W. Abraham, S. Ingvarsson, Y. Ji, and C.L. Chien, J. Appl. Phys. 91 (2002) 7140
[196] J.S. Parker, S.M. Watts, P.G. Ivanov and P. Xiong, Phys. Rev. Lett. 88 (2002) art. no. 196601
[197] I.I. Mazin, Phys. Rev. Lett. 83 (1999) 1427
[198] I.I. Mazin, Europhys. Lett. 55 (2001) 404
[199] J.J. Versluijs, M.A. Bari, and J.M.D. Coey, Phys. Rev. Lett. 87, 6601 (2001)
[200] A.M. Bratkovsky, Appl. Phys. Lett. 72, 2334 (1998)
[201] B. Nadgorny, I. I. Mazin, M. Osofsky, R.J. Soulen, P. Broussard, R.M. Stroud, D.J. Singh, V.G. Harris, A. Arsenov, and Ya. Mukovskii, Phys. Rev. B 63 (2001) 184433
[202] R.J. Soulen, J.M. Byers, M.S. Osofsky, B. Nadgorny, T. Ambrose, S.F. Cheng , P. R. Broussard, C. T. Tanaka, J. Nowak , J. S. Moodera, A. Barry, and J. M. D. Coey, Science 282 (1998) 85
[203] W.J. DeSisto, P.R. Broussard, T.F. Ambrose , B.E. Nadgorny, and M.S. Osofsky, Appl. Phys. Lett. 76 (2000) 3789
[204] I.I. Mazin, A.A. Golubov and B. Nagorny, J. Appl. Phys. 89 (2001) 7576
[205] Y. Ji, G.J. Strijkers, R.Y. Yang, and C.L. Chien, Phys. Rev. B 64 (2001) art. no. 224425
[206] S.A. Morton, G.D. Waddill, S. Kim, I.K. Schuller, S.A. Chambers, J.G. Tobin, Surf. Science 513 (2002) L451
[207] W. Zhu, B. Sincovic, E. Vescovo, C. Tanaka and J.S. Moodera, Phys. Rev. B 64 (2001) art. no. 060403(R)
[208] S.F. Alvarado, W. Eib, P. Mutz, H.C. Sigmann, M. Capagna and J.P. Remeika, Phys. Rev. B 13 (1976) 4918
[209] Wolfgang Gretz, Doctoral Thesis: "*Spin- und winkelauflösende Inverse Photoemission an NiMnSb*", Fachbereich Physik, Free University of Berlin (1991)
[210] C.N. Borca, Takashi Komesu and P.A. Dowben, J. Electron Spectrosc. Rel. Phenom. 122 (2002) 259
[211] R. Joynt, Science 284 (1999) 777
[212] I.N. Yakovkin, T. Komesu, and P. A. Dowben, Phys. Rev. B 66 (2002) art. no. 035406
[213] R.q. Wu and A.J. Freeman, J. Magn. Magn. Mater. 99 (1991) 81
[214] K. Maiti, M.C. Malagoli, A. Dallmeyer and C. Carbone, Phys. Rev. Lett. 88 (2002) art. no. 167205

LAYERED COBALT OXIDES AS A THERMOELECRIC MATERIAL

Ichiro Terasaki

Department of Applied Physics, Waseda University, Tokyo 169-8555, Japan

1. INTRODUCTION

A thermoelectric material is a material that converts heat into electric power (and electric power into heat) through the thermoelectric phenomena in solids. Figure 1 shows a schematic picture of thermoelectric power generation. In the presence of temperature gradient, the thermoelectric material works as a kind of battery. Such an energy conversion is called thermoelectrics [1], which has attracted a renewed interest in recent years.

Since this energy conversion is done by electrons in solids, we can make full use of solids. First, the thermoelectric device has no moving parts, and is operated without maintenance. Secondly, it produces no waste matter through conversion process. Thirdly, it can be processed at a micro/nano size, and can be implemented into electronic devices.

For more than 50 years, degenerate semiconductors have been used for thermoelectrics, and oxides have been regarded as unsuitable. Most unexpectedly, however, we have discovered that the layered cobalt oxides exhibit good thermoelectricity comparable to that of the conventional thermoelectric materials [2-10], and oxide thermoelectrics is not a mere dream any longer [11].

In this article, we will begin with basic introduction of thermoelectric power generation, and briefly review the crystal structures and the thermoelectric properties of newly found layered cobalt oxides. Then we will discuss an origin of the unusually large thermopower in terms of the spin (and orbital) degrees of freedom on the Co ion. We will further introduce some anomalous properties associated with spin degrees of freedom, and finally mention future prospects.

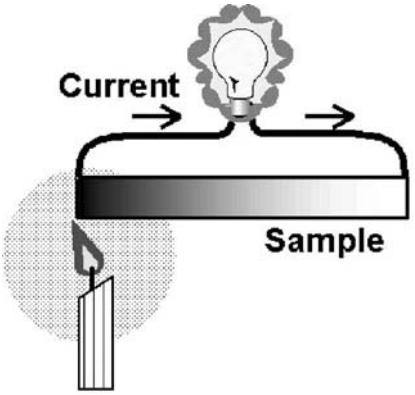

Fig. 1. Schematic picture of thermoelectric power generation.

2. BRIEF SUMMARY OF THERMOELECTRICS

An electron in solids is an elementary particle with a negative charge of e, and carries electric current. Since an enormous number of electrons are at thermal equilibrium in solids, they also carry heat and entropy. Thus in the presence of temperature gradient, they can flow from a hot side to a cold side to cause an electric current. This implies a coupling between thermal and electrical phenomena, which is called thermoelectric effects.

The Seebeck effect and the Peltier effect are predominant thermoelectric effects. The Seebeck effect is a phenomenon that voltage (V) is induced in proportion to applied temperature gradient (ΔT), written by

$$V = S\Delta T, \tag{1}$$

where S is called the Seebeck coefficient (thermoelectric power, or thermopower). The Peltier effect is a phenomenon that the heat absorption/emission (Q) is induced at the junctions to the leads by the applied current (I), written by

$$Q = \Pi I, \tag{2}$$

where Π is the Peltier coefficient. This is the reverse process to the Seebeck effect. According to the Onsagar relation, S and Π satisfy the relation

$$\Pi = ST. \tag{3}$$

Quite generally, the electric current density $\mathbf{j}$ (particle flow) and the thermal current density $\mathbf{q}$ are written as functions of electric field $\mathbf{E}$ and temperature gradient $\nabla(-T)$

$$\mathbf{j} = \sigma\mathbf{E} + S\sigma\nabla(-T), \tag{4}$$

$$\mathbf{q} = \Pi\sigma\mathbf{E} + \kappa'\nabla(-T), \tag{5}$$

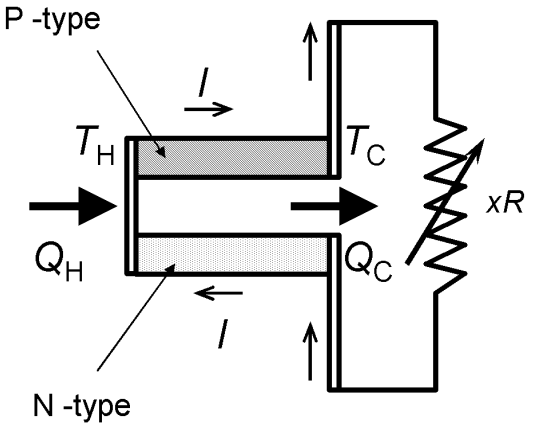

Fig. 2. Schematic figure of thermoelectric power generator. Parameters written in the figure are defined in the text.

where σ is the conductivity, and κ' is the thermal conductivity for $\mathbf{E}=0$. Then, for $\nabla T=0$, we can eliminate the electric field term from Eqs. (2) (4) (5), and obtain

$$\frac{\mathbf{q}}{T}=S\,\mathbf{j}. \tag{6}$$

Since the left hand side is the entropy current density, we can say that the thermopower S is equivalent to the ratio of the entropy current to the electric current, or is equivalent to entropy per carrier.

Figure 2 shows a schematic picture of a thermoelectric power generator [12]. For simplicity, we assume that the resistance R, the thermopower S, and the thermal conductance K of the generator are independent of temperature. The heat balance at the hot side (absorbed heat Q_{H} and temperature T_{H}) and at the cold side (emitted heat Q_{C} and temperature T_{C}) is given by

$$Q_{\mathrm{H}}=ST_{\mathrm{H}}I-\frac{1}{2}RI^2+K\Delta T, \tag{7}$$

$$Q_{\mathrm{C}}=ST_{\mathrm{C}}I+\frac{1}{2}RI^2+K\Delta T, \tag{8}$$

where $\Delta T=T_{\mathrm{H}}-T_{\mathrm{C}}$. By connecting an external load $R_{\mathrm{ext}}=xR$, we find the current $I=S\Delta T/(1+x)R$. The efficiency for the power generation η is given by

$$\eta\equiv\frac{I^2R_{\mathrm{ext}}}{Q_{\mathrm{H}}}=\frac{xI^2R}{ST_{\mathrm{H}}I-RI^2/2+K\Delta T}=\frac{x\Delta T}{(1+x)\overline{T}+(1+x)^2/Z+x\Delta T/2}, \tag{9}$$

where $\overline{T}=(T_{\mathrm{H}}+T_{\mathrm{C}})/2$. The parameter Z defined by

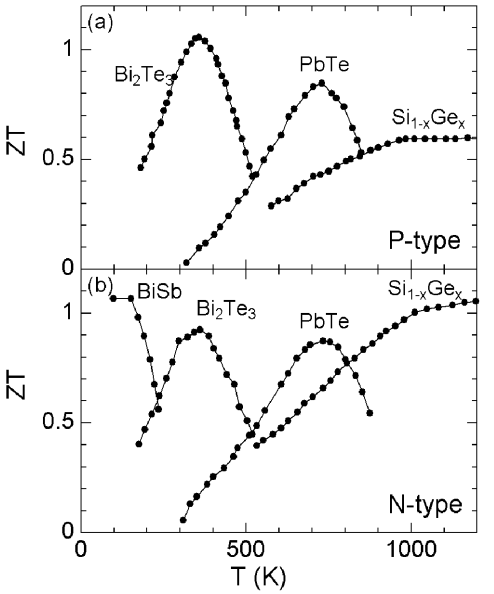

Fig. 3. Dimensionless thermoelectric figure of merit ZT for conventional thermoelectric materials.

$$Z = \frac{S^2}{RK} = \frac{S^2}{\rho\kappa}, \tag{10}$$

is called *the figure of merit*. By taking $d\eta / dx = 0$, we find that the maximum efficiency is

$$\eta_{\max} = \frac{\Delta T(\sqrt{Z\overline{T}+1}-1)}{T_{\mathrm{H}}\sqrt{Z\overline{T}+1}+T_C}. \tag{11}$$

According to Eq. (11), material properties are associated with the conversion efficiency through $Z\overline{T}$. In this sense, ZT is the most important parameters for thermoelectrics, and is called *the dimensionless figure of merit*. Note that $\eta_{\max}$ given by Eq. (11) reduces to the Carnot efficiency as $ZT \to \infty$. This is reasonable, because thermoelectric energy conversion is a conversion through the electron transport, which includes an irreversible process accompanying the Joule heat.

According to the above argument, a good thermoelectric material should have large ZT, that is, it should have large S, low ρ, and low κ simultaneously. Since these parameters are functions of carrier concentration, they cannot be controlled independently. Thus large ZT is very difficult to realize. ZT takes a maximum around unity in conventional thermoelectric materials, though $ZT > 3$ is needed to compete with a gas-compressor-based refrigerator [1].

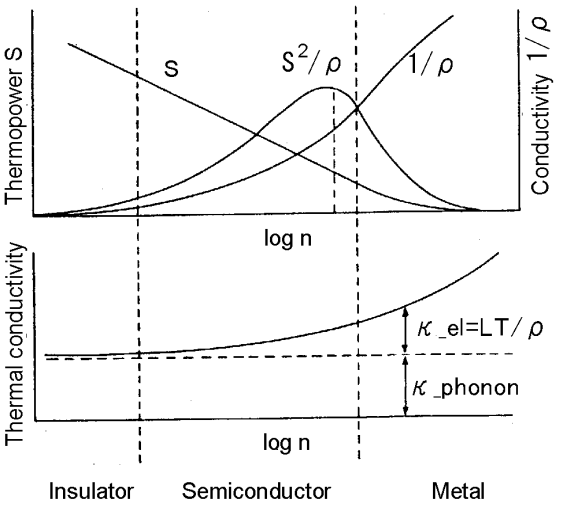

Fig. 4. Conductivity $\sigma = \rho^{-1}$, thermopower S and thermal conductivity κ plotted as a function of carrier concentration n. κ_{el} is the electron thermal conductivity estimated from the Wiedeman-Franz law (L is the Lorentz number).

Thermoelectric materials so far used for practical applications are Bi_2Te_3, PbTe, and $Si_{1-x}Ge_x$. N-type BiSb is superior at low temperatures, but has no p-type counterpart. Figure 3 shows ZT for various thermoelectric materials. Bi_2Te_3 shows the highest performance near room temperature, and is used for cooling applications such as Peltier coolers commercially available. PbTe shows the highest performance near 500-600 K, which is used for thermoelectric power generators. $Si_{1-x}Ge_x$ is superior above 1000 K, which has been used as a power source for a deep-space explorer.

In the framework of the nearly free electron model, let us consider a way to get large ZT. Figure 4 shows a schematic figure of $\sigma = \rho^{-1}$, S, κ and the power factor S^2/ρ as a function of carrier concentration n [1]. Here a simple parabolic band is assumed, and the electron-electron and electron-phonon interactions are neglected.

As is seen in this figure, the thermopower decreases with n, whereas the conductivity increases with n. Then S^2/ρ takes a maximum at an optimal carrier concentration n_0, below which the conductivity is too low, and above which the thermopower is too small. Assuming the Boltzmann distribution instead of the Fermi-Dirac distribution, one can evaluate that the optimum concentration is around 10^{19}-10^{20} cm^{-3}, which is close to n of degenerate semiconductors [1]. Since the conductivity is expressed as $\sigma = ne\mu$, the only way to maximize σ for $n = n_0$ is to maximize the mobility μ. As a matter of fact, the thermoelectric materials in Fig. 3 are high-mobility degenerate semiconductors.

For a carrier concentration of 10^{19} cm^{-3}, the electron thermal conductivity κ_{el}, which is evaluated to be LT/ρ through the Wiedeman-Franz law, is small enough to be neglected

(L is the Lorenz number). Thus the lattice thermal conductivity κ_{phonon} should be minimized. Heavy elements such as Bi, Te and Sb are effective to reduce the sound velocity, and solid solutions such as $Si_{1-x}Ge_x$ are effective to shorten the phonon mean free path.

3. LAYERED COBALT OXIDES

As mentioned above, one cannot expect that oxides are a good thermoelectric material, because their mobility is much poorer than that for the conventional thermoelectric materials. In spite of the pessimistic expectation, some oxides are found to be a good thermoelectric material. In 1997, the author and his co-workers discovered unusually large thermopower and low resistivity in Na_xCoO_2 ($NaCo_2O_4$) single crystals [2], and found the low thermal conductivity for polycrystalline samples [3]. After their discovery, several new layered cobalt oxides were synthesized and identified [13-37], all of which share a hexagonal CoO_2 block as a common unit. The thermoelectric layered cobalt oxides reported thus far are listed in Table 1.

In Fig. 5, crystal structures of the layered cobalt oxides are schematically shown. The left is the crystal structure of Na_xCoO_2, in which the CdI_2-type hexagonal CoO_2 block and the Na layer form a layered structure. The Na layer is highly vacant, and the crystal structure changes with the Na content [13, 15]. Large thermopower was observed for the x=0.5-0.6 sample [2], which is often called γ-phase, Na_xCoO_2 or $NaCo_2O_4$.

Table 1. Various layered cobalt oxides

Compound	Ref.	Comment
$NaCo_2O_4$ (γ-Na_xCoO_2)	2, 13, 14	Thermoelectric oxide discovered first
β-Na_xCoO_2	15, 16	Poorer thermoelectricity than $NaCo_2O_4$
$Na_xCoO_2{\cdot}yH_2O$	17	Superconductor of T_c=5 K
$NaCoO_2$ (α-phase)	15, 18	Insulator. SDW below 20 K.
$LiCo_2O_4$ (α-Li_xCoO_2)	19	Li- battery material
KCo_2O_4 (γ-K_xCoO_2)	20, 21, 22	Isomorphic to $NaCo_2O_4$. Unstable in air.
$RbCo_2O_4$ (γ-Rb_xCoO_2)	20, 23	Isomorphic to $NaCo_2O_4$. Unstable in air.
$Ca_{0.25}CoO_2$	24	Isomorphic to $NaCo_2O_4$.
$Sr_{0.35}CoO_2$	25	Isomorphic to $NaCo_2O_4$.
$NaLiCo_2O_4$	26	Na and Li are ordered along the c axis.
$Ca_3Co_4O_9$ ($[Ca_2CoO_3]_{0.6}CoO_2$)	27, 28	Misfit compound (see text)
$Sr_3Co_4O_9$ ($[Sr_2CoO_3]_{0.6}CoO_2$)	29	Misfit compound
$[Ca_2(Cu,Co)_2O_3]_{0.6}CoO_2$	30	Misfit with quadruple rock-salt block
$Bi_2Sr_2Co_2O_y$ ($[Bi_2Sr_2O_2]_xCoO_2$)	31, 32, 33	Analogous to Bi-2201 in high-T_c cuprates
$Bi_2Ba_2Co_2O_y$ ($[Bi_2Ba_2O_2]_xCoO_2$)	31, 34	Analogous to Bi-2201 in high-T_c cuprates
$Bi_2Ca_2Co_2O_y$ ($[Bi_2Ca_2O_2]_xCoO_2$)	31	Analogous to Bi-2201 in high-T_c cuprates
Pb-Sr-Co-O	35	Analogous to Pb-1201 in high-T_c cuprates
(Hg,Co)-Sr-Co-O	36	Analogous to Hg-1201 in high-T_c cuprates
Tl-Sr-Co-O	37	Analogous to Tl-1201 in high-T_c cuprates

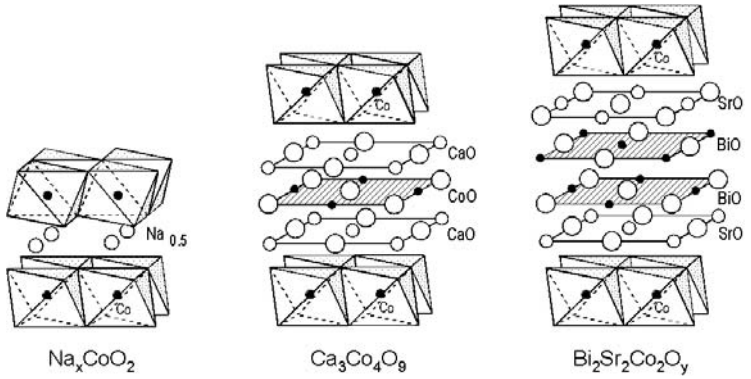

Fig. 5. Crystal structures of the layered Co oxides.

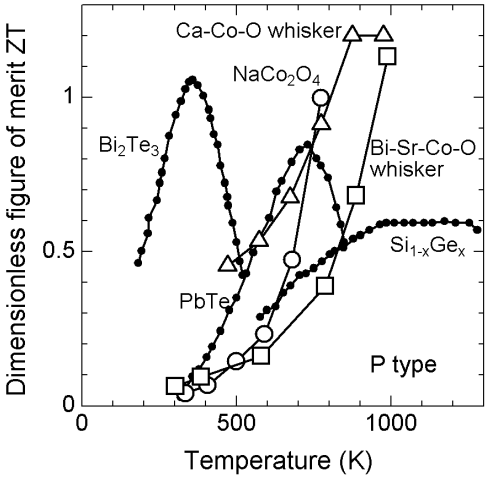

Fig. 6. Dimensionless figure of merit *ZT* of the layered Co oxides.

The center figure represents the Ca-based cobalt oxide. This has been long known as $Ca_3Co_4O_9$, but the exact crystal structure has been determined rather recently [27, 28]. This compound consists of the CdI_2-type hexagonal CoO_2 block and the NaCl-type square Ca_2CoO_{3-x} block. The lattice parameters of the subsystems are incommensurate in the *b* direction, and this material is a composite crystal with *b*-axis lattice misfit. Similar composite crystals are seen in sulfides [38], but the NaCl-type block and the CdI_2-type block are connected through the van der Waals bonding. In the Ca-based cobalt oxide, a strong ionic bonding tightly binds the NaCl block with the CdI_2 block, which causes significant interfacial stress.

The compound drawn in the right side is the Bi-based cobalt oxide $Bi_2Sr_2Co_2O_y$. This compound was originally known as an isomorphic compound to the high-temperature

superconductor $Bi_2Sr_2CaCu_2O_8$ [31]. Recently careful crystal analyses have revealed that this is another composite crystal with *b*-axis lattice misfit, where the CdI_2-type CoO_2 block and the NaCl-type $Bi_2Sr_2O_4$ block alternately stack along the *c* axis [32, 33].

It should be emphasized that all the three cobalt oxides have large ZT [39-42]. Figure 6 shows their ZT in comparison with ZT for the conventional p-type thermoelectric materials. As clearly shown, ZT exceeds unity above 700 K, and is larger than that for PbTe and $Si_{1-x}Ge_x$. This indicates that *the layered cobalt oxides are ready to use for practical applications*.

3.1 Na_xCoO_2

Figure 7 shows the thermoelectric parameters of Na_xCoO_2 single crystals [2, 43]. As shown in Fig. 7(a), the in-plane resistivity ρ_a is metallic from 300 K (from 1000 K [39]) down to 1.5 K, the magnitude of which is as low as 200 $\mu\Omega$cm at 300 K. Such a metallic conduction is comparable to that in the high-temperature superconductors, implying that Na_xCoO_2 is one of the best conductive materials among the transition-metal oxides. The out-of-plane resistivity ρ_c is about 100 times larger than the in-plane resistivity, indicating quasi-two-dimensional electronic states as expected from the layered structure. The broad peak near 200 K suggests that only the out-of-plane transport is incoherent above 200 K. This can happen when the mean free path is longer than the in-plane lattice parameter (0.3 nm), and shorter than the out-of-plane lattice parameter (1 nm), as was already discussed in the out-of-plane transport of the layered p-wave superconductor Sr_2RuO_4 [44, 45].

In Fig. 7(b), the in-plane thermopower is as large as 100 μV/K at 300 K, which is one order of magnitude larger than a typical thermopower of the high-temperature superconductors. The temperature dependence is roughly linear in T, suggesting that it can be understood as the diffusive part of the thermopower of a metal [46]. Accordingly the large thermopower can be attributed to a large electron specific heat, which was verified by the specific heat measurement for $(Na, Ca)_xCoO_2$ [5].

Figure 7(c) shows the in-plane thermal conductivity, which is highly dependent from sample to sample. Here we show three data for different crystals (#1-#3), which are largely different below 100 K. Nevertheless the room-temperature thermal conductivity lies near 40-50 mW/cmK. Assuming the Wiedemann-Franz law, we evaluate the lattice thermal conductivity to be 10-20 mW/cmK at room temperature, which is as low as that of the conventional thermoelectric materials. We attribute the low lattice thermal conductivity to the disordered Na layer in which Na ions and vacancies make a “solid solution” [7].

High temperature properties of Na_xCoO_2 were measured by Fujita et al. [39] Although they might overestimate the thermal conductivity, ZT reached to unity at 800 K. Unfortunately ceramic samples have higher resistivity, as is usually seen in the layered conducting oxides. Thus ZT for polycrystalline samples are lower than ZT for single crystals. The best value of ZT =0.7-0.8 was reported by Ohtaki et al. [47] and Ito et al. [48]. Very recently, Ito et al. have succeeded in making a good ceramic sample of Ag-added Na_xCoO_2, which exhibits a large ZT of 0.95 at 1000 K [49].

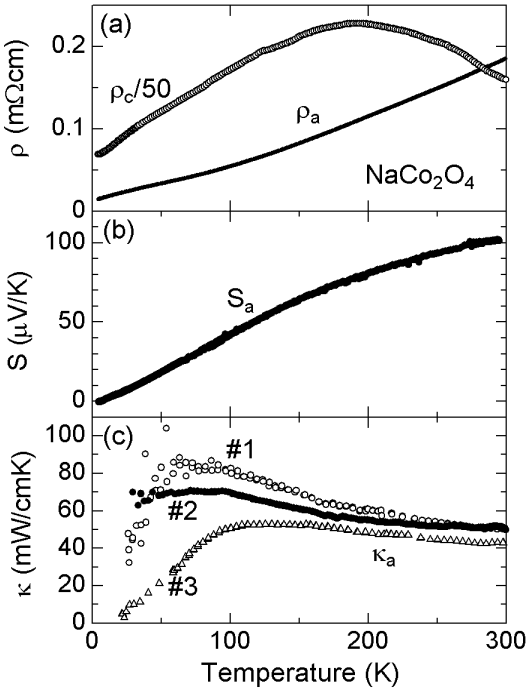

Fig. 7. Thermoelectric properties of Na_xCoO_2 single crystals. Since thermal conductivity scatters from sample to sample, typical data for three samples (#1-#3) are shown.

3.2 $Ca_3Co_4O_9$

Figure 8 shows the thermoelectric parameters of $Ca_3Co_4O_9$ single crystals [43]. Compared with Na_xCoO_2, the resistivity is more anisotropic, and the resistivity ratio is of the order of 10^3. Unlike Na_xCoO_2, the resistivity is nonmetallic at low temperature. The muon spin relaxation (μSR) measurement has revealed that the spin-density-wave (SDW) order develops below 100 K [50], which decreases in the density of states due to opening of the SDW gap. As a result, the resistivity shows the low-temperature upturn.

The *a*- and *b*-axis thermopowers shown in Fig. 8(b) are as large as 130 μV/K at room temperature. The temperature dependence is weak near room temperature, but increases above 500 K [51]. A slight but finite in-plane anisotropy is ascribed to the interfacial stress induced by the lattice misfit, which is discussed in the next subsection.

Thermal conductivity shown in Fig. 8(c) is 30 mW/cmK at room temperature, and slightly increases with decreasing temperature down to 100 K. These data imply that the lattice thermal conductivity and the phonon mean free path are fairly large, and that the lattice misfit is not so effective for the reduction of the thermal conductivity.

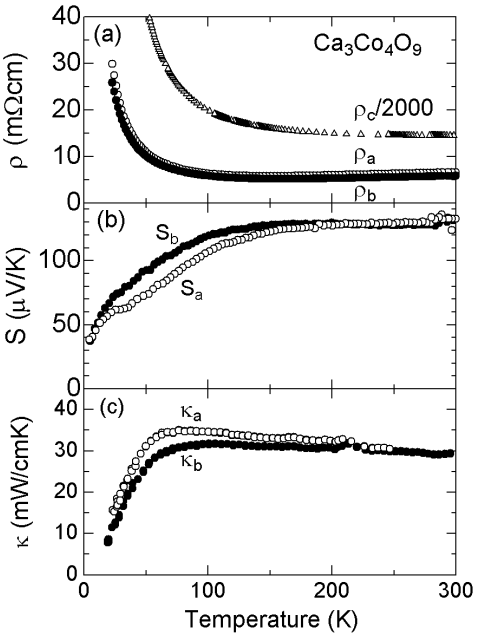

Fig. 8. Thermoelectric properties of $Ca_3Co_4O_9$ single crystals.

Funahashi et al. [40] found that a whisker crystal of Bi-doped $Ca_3Co_4O_9$ shows excellent thermoelectric properties above 1000 K, although polycrystalline samples [52] and flux-grown platelet crystals [42] show lower values. Since Ca is chemically more stable than Na, this compound has been most extensively investigated from the application point of view [53].

3.3 $Bi_{2-x}Pb_xSr_2Co_2O_y$

Figure 9 shows the thermoelectric parameters of $Bi_{2-x}Pb_xSr_2Co_2O_y$ single crystals [43, 54, 55]. Since this material is grown by the floating-zone technique, a large single crystal is easily available. Using large single crystals, we successfully measured the thermoelectric parameters for all the crystallographic directions. Note that the data are anisotropic among the *a*, *b* and *c* directions.

We attribute the in-plane anisotropy to the interfacial stress between the NaCl-type and CdI_2-type blocks [54]. In $Bi_{2-x}Pb_xSr_2Co_2O_y$, the NaCl structure is similar to that in $Bi_2Sr_2CaCu_2O_8$, and we expect that the interfacial stress distorts the hexagonal CoO_2 block to some extent. A similar, but smaller in-plane anisotropy is seen in the misfit oxide $Ca_3Co_4O_9$ (Fig. 8). According to the structure analyses by Miyazaki et al. [56], the Co-O layer in the Ca_2CoO_3 block is highly disordered, which would relax the interfacial stress due to the lattice misfit.

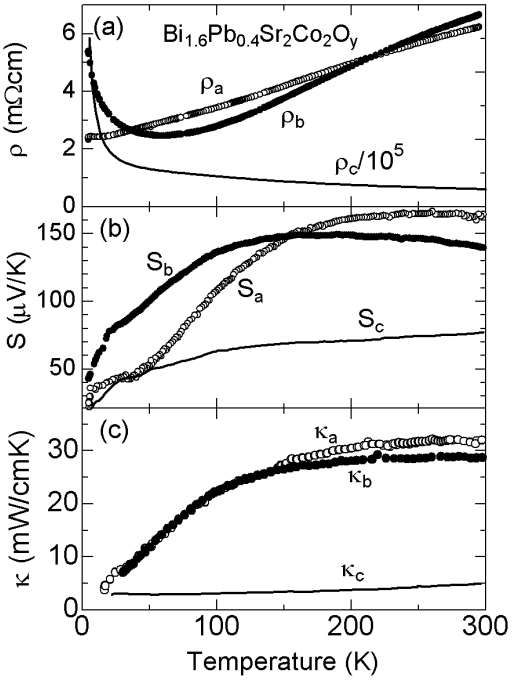

Fig. 9. Thermoelectric properties of $Bi_{2-x}Pb_xSr_2Co_2O_y$ single crystals.

The resistivity shows a dramatic anisotropy. The *a*-axis resistivity remains metallic down to 4 K, while the *b*-axis resistivity shows an upturn below about 100 K and the *c*-axis resistivity is nonmetallic from 300 down to 4 K. Thus we may say that the electric conduction shows a dimensional crossover from one-dimensional to two-dimensional near 100 K. We do not fully understand the origin, but speculate that an SDW opens a gap along the *b* direction.

The thermopower is also anisotropic. Note that the *b*-axis thermopower is two times larger than the *a*-axis thermopower near 50 K. This is anomalously large, because the distortion of the hexagonal CoO_2 layer due to lattice misfit is quite small. The *c*-axis thermopower is 80 μV/K at room temperature, and the anisotropy is much smaller than the resistivity. A larger resistivity tend to give a larger thermopower in conventional semiconductors (see Fig. 4), which cannot explain the difference between the *a*- (*b*-) and *c*-axis directions.

As shown in Fig. 9(c), the thermal conductivity is less anisotropic between *a* and *b* axes, possibly because the lattice properties are less sensitive to the interfacial stress [55]. The *c*-axis thermal conductivity is as small as 4 mW/cmK, which is very close to the minimum thermal conductivity [57]. The sound velocity is expected to small along the *c* axis because of the van der Waals bonding in the two Bi-O layers, and the lattice misfit can be a strong scattering center for the acoustic phonon.

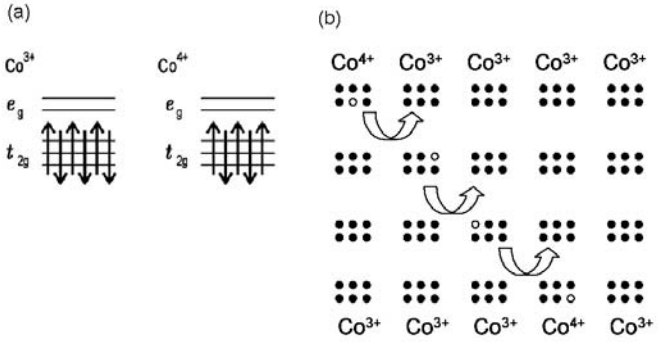

Fig. 10. (**a**) Electronic configuration of Co^{3+} and Co^{4+} ions. (**b**) Conduction mechanism of the layered Co oxides.

4. ORIGIN OF THE LARGE THERMOPOWER

As shown in Eq, (6), the thermopower S is the ratio of the entropy to the charge per carrier. This is directly seen in the Heikes formula, a simple (but rigorous) asymptotic form of the thermoelectric power in a high temperature limit where the thermal energy $k_B T$ is much larger than the transfer energy (bandwidth) [58].

Koshibae et al. [59] proposed an extended Heikes formula written by

$$S = \frac{k_B}{C} \log \frac{g_A}{g_B} \frac{p}{1-p} \tag{12}$$

where g_A and g_B are the degeneracy of the electron configuration of A and B ions, C is the charge difference between A and B ions, and p is the atomic content of the A ion. Note that

$$k_B \log \frac{g_A}{g_B} \frac{p}{1-p}$$

is equal to the entropy per carrier, and S for p=0.5 is simply reduced to $k_B \log(g_A / g_B) / C$.

Let us apply the above formula to Na_xCoO_2 (x=0.5). Magnetic measurements reveal that the Co^{4+} and Co^{3+} ions are in the low spin state in Na_xCoO_2. As shown in Fig. 10(a), the configuration of the low-spin-state Co^{3+} is $(t_{2g})^6$, whose entropy is zero. On the other hand, the low-spin-state Co^{4+} has a hole in the t_{2g} states, which is six-fold degenerate (two from spin and three from t_{2g} orbitals) to carry large entropy of $k_B$log6. Suppose electric conduction occurs by exchanging Co^{3+} and Co^{4+}, as is shown in Fig. 10(b). Then a hole on Co^{4+} can carry a charge of $+e$ with entropy of $k_B$log6, which causes a large thermopower of $k_B$log6/e (~150μV/K) This is very close to the saturated values of the thermopower of the layered cobalt oxide at high temperatures. Note that carriers in degenerate semiconductors have no internal degrees of freedom: they can only carry entropy due to their kinetic energy. In this sense, a hole in Na_xCoO_2 can carry much larger entropy than degenerate semiconductors, which leads us a new design for thermoelectric materials.

Although Koshibae's theory has successfully explained the high-temperature limit thermopower of Na_xCoO_2, the problem is not so simple. The thermopower of Na_xCoO_2 is 100 μV/K at 300 K, which is about 2/3 of $k_B$log6, which means that the large amount of entropy of $k_B$log6 in the high-temperature limit (~10^4 K) survives down to 10^2 K.

Usually various phase transitions occur in order to release an spin/orbital entropy per cites in the strongly correlated systems. In contrast, Na_xCoO_2 shows no structural, electric, and magnetic transitions from 2 to 1000 K. Then, if all the phase transition were blocked, the large entropy would inevitably point to the conducting carriers to form a "heavy-fermion"-like electron.

In fact, the electron specific heat coefficient and the spin susceptibility for Na_xCoO_2 are just close to those for the valence-fluctuation compound $CePd_3$, which has nearly the same values of S (80 μV/K at 300 K) and ρ (150 μΩcm at 300 K) [9, 10, 60]. Valla et al. [61] have performed a photoemission experiment for the layered cobalt oxides, and have successfully observed the coherent state at low temperatures, which reminds us of the Kondo resonance. Another similarity to the heavy fermion is seen in the pressure effects [60]. As shown before, the misfit compound $Bi_2Sr_2Co_2O_y$ exhibits large in-plane anisotropy, which is attributed to the interfacial stress arising from the misfit interface of the hexagonal CoO_2 block and the rock-salt square $Bi_2Sr_2O_4$ block.

5. UNCONVENTIONAL ELECTRONIC STATES

5.1 Impurity effects

Na_xCoO_2 is highly two-dimensional, and thus a small amount of substitution is expected to deteriorate the electric conduction. (Note that, according to the localization theory, a two-dimensional metal will be insulating at zero temperature in the presence of a finite amount of disorder). Contrary to this, the thermoelectric properties are improved against some kinds of impurities such as Cu and Pd [8, 9, 62].

Figure 11 shows Cu and Pd substitution effects on the thermopower in $NaCo_2O_4$. With increasing Cu content, the thermopower enhances for all the temperature range. In addition, it shows a peak at 10 K (more precisely, a dip at 22 K) for the x=0.2 and 0.3. This is a strong piece of evidence that the phase transition occurs at low temperatures [8, 9]. In contrast, the Pd substitution decreases the thermopower.

It is now accepted that the 22-K transition is an SDW transition like in metal Cr [63]. Motohashi et al. [64] reported a similar 22-K transition in rapid-annealed $Na_{0.75}CoO_2$, in which an SDW order was detected through μSR by Sugiyama et al. [65] The Cu substitution enhances the instability, and eventually causes the SDW transition at 22 K. This type of transition is called "order from disorder" [66]. In the case of rapidly-annealed $Na_{0.75}CoO_2$, it lies near the $\gamma - \alpha$ phase boundary, and perhaps is very close to the lattice instability. In other words, instabilities against various phases are competing or disordering in Na_xCoO_2, and any phase transitions are prohibited down to low temperatures. This does not mean that Na_xCoO_2 is far from the instability of phase transitions, but rather, is very susceptible to various transitions against various perturbations.

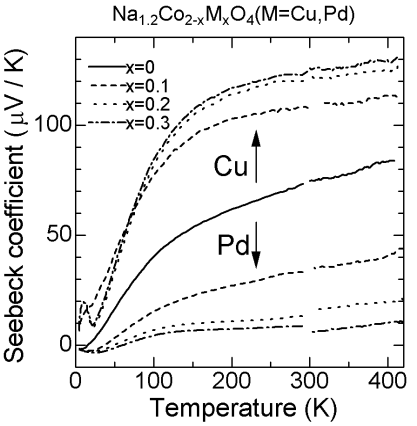

Fig. 11. Thermopower for polycrystalline samples of Cu- and Pd-substituted Na_xCoO_2.

Pd substitution gives different changes. The Pd substitution decreases resistivity and the thermopower, and *increases* the magnitude of the Hall coefficient R_H. Based on a simple Drude picture, these results indicate that the Pd substitution causes a decrease in n and m^*. Figure 12 shows the evaluated n, m^*, τ from the measured ρ, S, R_H as a function of the Pd content [62]. We should note that the effective mass decreases by one order of magnitude from x=0 to 0.2, which is a predominant origin of the decrease of thermopower shown in Fig. 11. This strongly suggests that the effective mass of Na_xCoO_2 is basically determined by the strong correlation, not the curvature of the band dispersion, because the calculated band has no singular curvature near Fermi level. Thus the Pd effects are another piece of evidence for the unusual electronic states of the layered cobalt oxides.

5.2 Magneto-transport

Magneto-transport is a powerful probe for the spin-charge coupling. A prime example is seen in the colossal magneto-resistive (CMR) materials [67], where magnetic field induces a metal-insulator transition. Very recently Wang et al. [68] have found that the thermopower of Na_xCoO_2 is highly dependent on magnetic field. A similar result is independently observed in Bi-Ca-Co-O single crystals by Maignan et al. [69] However, the magnetic field modifies not only the thermopower, but also the resistivity and the thermal conductivity. Thus the field dependence of the three parameters should be analyzed consistently.

Figure 13 shows the magnetic-field dependence of the thermoelectric parameters of $Bi_{2-x}Pb_xSr_2Co_2O_y$ [70]. The applied field decreases the resistivity, thermopower, and thermal conductivity. We should note that the magneto-thermal conductivity (not the magneto-thermal resistivity) is negative, whereas the magnetoresistance is negative. In other words, magnetic field increases the electric current, and decreases the thermal current. Since the thermal conductivity is mainly due to phonons, the magneto-thermal conductivity should also be attributed to phonons.

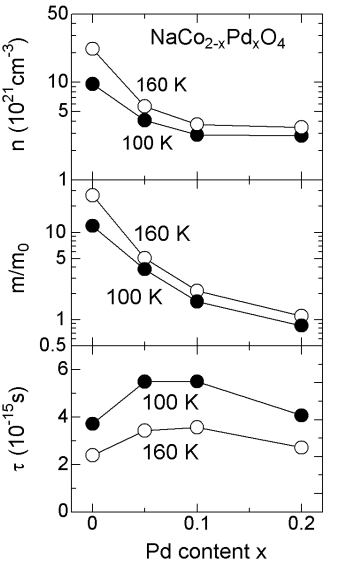

Fig. 12. Carrier concentration n, effective mass m^*, and scattering time τ of $Na_{1.2}Co_{2-x}Pd_xO_4$ evaluated from the measured resistivity, thermopower, and Hall coefficient.

In a two-dimensional metal, thermopower is inversely proportional to n [71], and accordingly the negative magneto-thermopower implies that the magnetic field increases n. $Bi_{2-x}Pb_xSr_2Co_2O_y$ opens the SDW-like pseudogap below about 50 K, and SDW is suppressed by the applied field. Thus, the observed magneto-transport in this system can be analyzed in terms of the pseudogap suppression by external field. In fact, the observed thermo-magnetic effects are remarkable below about 60 K, close to the pseudogap temperature. The suppressed pseudogap would increase conduction electrons that scatter phonons through the electron-phonon interaction. This would shorten the phonon mean free path to give negative magneto-thermal conductivity.

The interpretation of magnetoresistance is more complicated. The external field increases the carrier concentration, but also modifies the scattering time through the electron-electron (or magnetic) scattering. In fact, the magnetoresistance is either negative or positive in the Na_xCoO_2 family. The magnetoresistance of normally-prepared Na_xCoO_2 is negative at low temperatures as shown in Fig. 14(a) [9], which is ascribed to the field suppression of the SDW gap. On the other hand, rapidly-heated polycrystalline samples of $Na_{0.75}CoO_2$ shows a very low resistivity (less than 1 mΩcm at 300 K), and shows large positive magnetoresistance at low temperature [64]. The field dependence is approximately proportional to H^2, and roughly satisfies Kohler's rule [72]. This is clear evidence for classical magnetoresistance (the magnetoresistance due to the orbital change by the Lorentz force), implying that the high mobility at low temperatures.

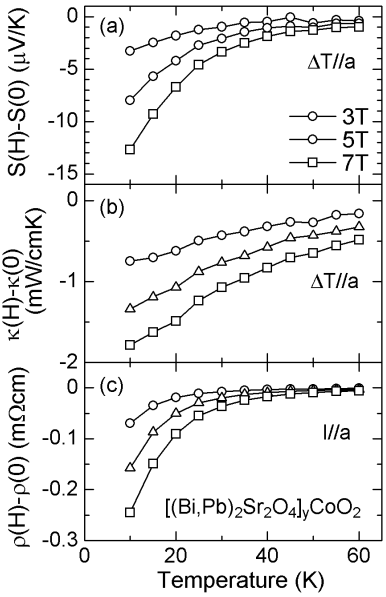

Fig. 13. Magnetic-field dependence of the thermopower, thermal conductivity, and resistivity of a $Bi_{2-x}Pb_xSr_2Co_2O_y$ single crystal.

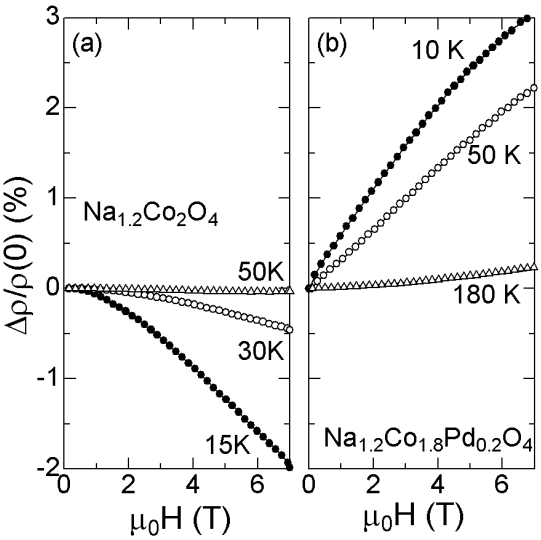

Fig. 14. Magnetoresistance of Na_xCoO_2 and Pd-substituted Na_xCoO_2.

An open question is a large positive magnetoresistance of the Pd-substituted samples, as shown in Fig. 14(b). At first glance, one may think that the positive magnetoresistance is the classical magnetoresistance, because the Pd-substituted sample shows the higher mobility estimated from the data in Fig. 12. A closer look at the field dependence reveals, however, that the observed magnetoresistance is anomalously linear in H. This cannot be explained in terms of the classical magnetoresistance, which should be proportional to H^2. Although there are several reports on the H-linear magnetoresistance in the literature [73-75], the origin is not well understood yet. A further study such as the precise measurement using single crystals is needed, but we failed the Pd-substituted single crystals.

6. SUMMARY AND FUTURE PROSPECTS

In this article, we have reviewed the thermoelectric properties of the various layered o oxides having the hexagonal CoO_2 block. The layered cobalt oxides do not only show high thermoelectric performance, but also exhibits interesting features from the viewpoint of basic science. In particular, their large thermopowers are considered to come from the large spin and orbital degrees of freedom on Co^{4+} in the low-spin state.

Carries in oxides are often coupled with the optical phonons, the spin degrees of freedom and the orbital degrees of freedom. These couplings form exotic electronic states such as polarons, heavy fermions, and spin liquids. Furthermore, the geometry and the dimensionality are easy to change in certain classes of oxides, where layered structures, ladder structures, chain structures can be controlled. Therefore I believe that many functional materials including thermoelectric materials will still sleep unknown. I hope that Na_xCoO_2 is just the beginning, and that a thermoelectric oxide of higher performance will appear in near future.

In this article we have proposed that Na_xCoO_2 is a material in which all the phase transition were blocked. Consequently, the large entropy of Co^{4+} would inevitably point to the conducting carriers to make the thermopower large. Physicists have focused their attention too much to materials exhibiting phase transitions. The layered cobalt oxides have told us an importance of blocked transitions. Beyond such studies, we believe that new directions of condensed-matter physics may spread out.

ACKNOWLEDGMENTS

The author would like to thank T. Fujii, R. Kitawaki, Y. Iguchi, A. Satake, H. Tanaka, S. Okada, and I. Tsukada for collaboration of the experiments cited in this article. He would also like to thank T. Caillat, R. Venkatasubramanian, H. R. Ott and A. V. Sologubenko for fruitful discussion on thermal conductivity. This work is partially supported by the CREST and PRESTO projects, Japan Science and Technology Agency.

REFERENCES

[1] G. D. Mahan, Solid State Phys. Vol. 51 (1998) 81.
[2] I. Terasaki, Y. Sasago and K. Uchinokura, Phys. Rev. B56 (1997) R12685.
[3] H. Yakabe, K. Kikuchi, I. Terasaki, Y. Sasago, and K. Uchinokura, Proceedings of the 16th International Conference on Thermoelectrics (ICT 97), IEEE, Piscataway (1998), pp. 523
[4] T. Kawata, Y. Iguchi, T. Itoh, K. Takahata, and I. Terasaki, Phys. Rev. B60 (1999) 10584.
[5] Y. Ando, N. Miyamoto, K. Segawa, T. Kawata, and I. Terasaki, Phys. Rev. B60 (1999) 10580.
[6] I. Terasaki, Proceedings of the 18th International Conference on Thermoelectrics (ICT 99), IEEE, Piscataway (2000), pp. 569.
[7] K. Takahata, Y. Iguchi, D. Tanaka, T. Itoh and I. Terasaki, Phys. Rev. B61 (2000) 12551.
[8] I. Terasaki, Y. Ishii, D. Tanaka, K. Takahata and Y. Iguchi, Jpn. J. Appl. Phys. 40 (2001) L65.
[9] I. Terasaki, I. Tsukada and Y. Iguchi, Phys. Rev. B 65 (2002) 195106
[10] I. Terasaki, Proceedings of the 21st International Conference on Thermoelectrics (ICT2002), IEEE, Piscataway (2002), pp. 185.
[11] K. Koumoto, I. Terasaki and N. Murayama (eds.), *Oxide Thermoelectrics*, Research Signpost, Trivandrum (2002).
[12] K. Uemura and I. Nishida, *Thermoelectric Semiconductors and their Applications*, Nikkan-Kogyo Shinbunsha, Tokyo (1988) (in Japanese).
[13] M. von Jansen, and R. Hoppe, Z. Anorg. Allg. Chem. 408 (1974) 104.
[14] T. Tanaka, S. Nakamura and S. Iida, Jpn. J. Appl. Phys. 33 (1994) L581.
[15] C. Fouassier, G. Matejka, J. Reau, and P. J. Hagenmuller, J. Solid State Chem. 6 (1973) 532.
[16] Y. Ono, R. Ishikawa, Y. Miyazaki, Y. Ishii, Y. Morii and T. Kajitani, J. Solid State Chem., in press.
[17] K. Takada, H. Sakurai, E. Takayama-Muromachi, F. Izumi, R. A. Dilanian, T. Sasaki: Nature 422 (2003) 53.
[18] M. Mikami, M. Yoshimura, Y. Mori, T. Sasaki, R. Funahashi and I. Matsubara, Jpn. J. Appl. Phys. 41 (2002) L777.
[19] S. Kikkawa, S. Miyazaki and M. Koizumi, J. Solid State Chem. 62 (1986) 35.
[20] M. von Jansen, and R. Hoppe, Z. Anorg. Allg. Chem. 408 (1974) 97.
[21] C. Delmas, C. Fouassier, P. Hagenmuller, J. Solid State Chem. 13 (1975) 165
[22] S. Nakamura, J. Ohtake, N. Yonezawa and S. Iida, J. Phys. Soc. Jpn. 65 (1996) 358.
[23] S. Nakamura and A. Ozawa, J. Phys. Soc. Jpn. 68 (1999) 3746.
[24] B. L. Cushing and J. B. Wiley, J. Solid State Chem. 141 (1998) 385.
[25] R. Ishikawa, Y. Ono, Y. Miyazaki and T. Kajitani, Jpn. J. Appl. Phys. 41 (2002) L337.
[26] Y. Okamoto, M. Nohara, H. Takagi and K. Kitaawa: JSAP 2002 Spring Meeting (in Japanese)
[27] A.C. Masset, C. Michel, A. Maignan, M. Hervieu, O. Toulemonde, F. Studer, B. Raveau and J. Hejtmanek, Phys. Rev. B 62 (2000) 166.

[28] Y. Miyazaki, K. Kudo, M. Akoshima, Y. Ono, Y. Koike, and T. Kajitani, Jpn. J. Appl. Phys. 39 (2000) L531.
[29] D. Pelloquin, S. Hebert, and A. Maignan, Solid State Sci. 6 (2004) 167.
[30] Y. Miyazaki, T. Miura, Y. Ono and T. Kajitani, Jpn. J. Appl. Phys. 41 (2002) L849.
[31] J. M. Tarascon, R. Ramesh, P. Barboux, M. S. Hedge, G. W. Hull, L. H. Greene, M. Giroud, Y. LePage, W. R. McKinnon, J. V. Waszczak and L. F. Schneemeyer, Solid State Commun. 71 (1989) 663.
[32] H. Leligny, D. Grebille, O. Pérez, A.-C. Masset, M. Hervieu, C. Michel and B. Raveau, C. R. Acad. Sci. Paris t.2, IIc, 409-414 (1999).
[33] T. Yamamoto, I. Tsukada, K. Uchinokura, M. Takagi, T. Tsubone, M. Ichihara and K. Kobayashi: Jpn. J. Appl. Phys. 39 (2000) L747.
[34] M. Hervieu, A. Maignan, C. Michel, V. Hardy, N. Créon, and B. Raveau: Phys. Rev B 67 (2003) 045112.
[35] D. Pelloquin, A. Maignan, S. Hébert, C. Martin, M. Hervieu, C. Michel, L. B. Wang, and B. Raveau, Chem. Mater. 14 (2002) 3100.
[36] A. Maignan, S. Hébert, D. Pelloquin, C. Michel and J. Hejtmanek, J. Appl. Phys. 92, (2002) 1964.
[37] S. Hébert, S. Lambert, D. Pelloquin, and A. Maignan, Phys. Rev. B 64 (2001) 172101.
[38] Y. Gotoh, M. Goto, K. Kawaguchi, Y. Oosawa and M. Onoda: Mat. Res. Bull. 25 (1990) 307 and references therein.
[39] K. Fujita, T. Mochida, and K. Nakamura, Jpn. J. Appl. Phys. 40 (2001) 4644.
[40] R. Funahashi, I. Matsubara, H. Ikuta, T. Takeuchi, U. Mizutani, and S. Sodeoka, Jpn. J. Appl. Phys. 39 (2000) L1127.
[41] R. Funahashi and I. Matsubara, Appl. Phys. Lett. 79, 362-364 (2001).
[42] M. Shikano and R. Funahashi: Appl. Phys. Lett. 82 (2003) 1851.
[43] A. Satake, H. Tanaka, T. Ohkawa, T. Fujii and I Terasaki, J. Appl. Phys. 96 (2004) 931.
[44] Y. Maeno, H. Hashimoto, K. Yoshida, S. Nishizaki, T. Fujita, J. G. Bednorz, and F. Lichtenberg, Nature 372 (1994) 532.
[45] K. Yoshida, Y. Maeno, S. Nishizaki, S. Ikeda anc T. Fujita, J. Low Temp. Phys. 105 (1996) 1593.
[46] J. M. Ziman, *Principles of the Theory of Solids*, Cambridge University Press, Cambridge (1972).
[47] M. Ohtaki, Y. Nojiri, and E. Maeda, *Proceedings of the 19th International Conference on Thermoelectrics (ICT2000)*, Babrow, Wales (2000) 190.
[48] M. Ito, T. Nagira, D. Furumoto, S. Katsuyama and H. Nagai, Scripta Mater. 48 (2003) 403.
[49] M. Ito, D. Furumoto, S. Katsuyama and S. Hara, *Proceedings of the 23rd International Conference on Thermoelectrics (ICT2004)*, IEEE, Piscataway (in press).
[50] J. Sugiyama, H. Itahara, T. Tani, J. H. Brewer and E. J. Ansaldo, Phys. Rev. B66 (2002) 134413.
[51] I. Terasaki, R. Funahashi and M. Mikami, Kinzoku 74 (2004) 773 (in Japanese).
[52] S. Li, R. Funahashi, I. Matsubara, K. Ueno, S. Sodeoka, and H. Yamada, Chem. Mater. 12 (2000) 2424.
[53] T. Tani, H. Itahara, C. Xia and J. Sugiyama: J. Mater. Chem. 13 (2003) 1865.
[54] T. Fujii, I. Terasaki, T. Watanabe and A. Matsuda, Jpn. J. Appl. Phys. 41 (2002) L783.

[55] I. Terasaki, H. Tanaka, A. Satake, T. Fujii and S. Okada, submitted to PRB
[56] Y. Miyazaki, M. Onoda, T. Oku, M. Kikuchi, Y. Ishii, Y. Ono, Y. Morii and T. Kajitani, J. Phys. Soc. Jpn. 71(2002) 491.
[57] D. G. Cahill, S. K. Watson, and R. O. Pohl, Phys. Rev. B46 (1992) 6131.
[58] P. M. Chaikin and G. Beni, Phys. Rev. B13 (1976) 647.
[59] W. Koshibae, K. Tsutsui, and S. Maekawa, Phys. Rev. B62 (2000) 6869.
[60] I. Terasaki, Materials Transaction, JIM **42** (2001) 951.
[61] T. Valla, P. D. Johnson, Z. Yusof, B. Wells, Q. Li, S. M. Loureiro, R. J. Cava, M. Mikami, Y. Mori, M. Yoshimura, and T. Sasaki, Nature 417 (2002) 627.
[62] R. Kitawaki and I. Terasaki, J. Phys. Condens. Matter 14 (2002) 12495.
[63] E. Fawcett, H. L. Alberts, V. Yu. Galkin, D. R. Noakes, and J. V. Yakhmi, Rev. Mod. Phys. 66 (1996) 25.
[64] T. Motohashi, R. Ueda, E. Naujalis, T. Tojo, I. Terasaki, T. Atake, M. Karppinen, and H. Yamauchi, Phys. Rev. B67 (2003) 064406.
[65] J. Sugiyama, H. Itahara, J. H. Brewer, E. J. Ansaldo, T. Motohashi, M. Karppinen, and H. Yamauchi, Phys. Rev. B 67 (2003) 214420.
[66] A. M. Tsuvelik, *Quantum Field Theory in Condensed Matter Physics*, Cambridge University Press, Cambridge (1995), p. 174.
[67] E. Dagotto, T. Hotta and A. Moreo, Physics Reports 344 (2001) 1.
[68] Yayu Wang, N. S. Rogado, R. J. Cava, and N. P. Ong, Nature 423 (2003) 425.
[69] A. Maignan, S. Hébert, M. Hervieu, C. Michel, D. Pelloquin and D. Khomskii, J. Phys.: Condens. Matter 15 (2003) 2711.
[70] I. Terasaki and T. Fujii, *Proceedings of the 22nd International Conference on Thermoelectrics (ICT2003)* IEEE, Piscataway, (2003), p.207
[71] J. B. Mandal, A. N. Das and B. Ghosh, J. Phys.: Condens. Matter 8 (1996) 3047.
[72] A. B. Pippard, *Magnetoresistance in Metals*, Cambridge University Press, Cambridge, (1989).
[73] S. Ogawa, Physica B91 (1977) 82.
[74] R. Jin, Y. Liu and F. Lichtenberg, Phys. Rev. B60 (1999) 10418.
[75] D. P. Young, J. F. DiTusa, R. G. Goodrich, D. Hall, J. Anderson, S. Guo, Julia Y. Chan, P. W. Adams, cond-mat/0202220.

COMMENSURATE AND INCOMMENSURATE MAGNETISM IN LAYERED ANTIFERROMAGNETS

J. Chovan and N. Papanicolaou

Department of Physics, University of Crete,
and Research Center of Crete, Heraklion, Greece

1. INTRODUCTION

Layered antiferromagnets have been the subject of intense experimental and theoretical study mainly in connection with high-T_c superconductivity [1]. While their basic magnetic properties can be accounted for by an isotropic two-dimensional (2D) Heisenberg model, anisotropy becomes important to understanding ordering phase transitions that typically occur below a certain critical temperature T_N. For example, La_2CuO_4 was shown to behave as a covert weak ferromagnet for $T < T_N = 325$ K [2-5] as a result of an antisymmetric exchange interaction usually referred to as Dzyaloshinskii-Moriya (DM) anisotropy [6,7]. The latter occurs in low-symmetry crystals and its typical manifestation is weak ferromagnetism whereby a net ferromagnetic moment develops in an antiferromagnet due to a slight misalignment of the sublattice magnetizations from their antiparallel (Néel) arrangement.

However, weak ferromagnetism is not the only possible implication of the DM anisotropy. Another possibility is helimagnetism where spins are arranged in a spiral structure whose period (pitch) may extend over several decades of unit cells. For example, the period of the spiral in the classic DM helimagnet MnSi [8,9] is equal to 39 unit cells (170 Å) and an even larger period of 149 unit cells (700 Å) is realized in FeGe [10]. Furthermore, under certain conditions, the period of the spiral may be significantly varied by applying an external magnetic field. In fact, Dzyaloshinskii [11] argued that an interesting incommensurate-to-commensurate (IC) phase transition may occur when the external field H exceeds a certain critical value H_c. For $H < H_c$ the ground state is an incommensurate spiral with period

$L = L(H)$ which grows to infinity in the limit $H \to H_c$. For $H > H_c$ the ground state becomes a commensurate spin-flop state.

A Dzyaloshinskii-type IC transition was first realized experimentally in chiral liquid crystals, where a field induced cholesteric-to-nematic transition was theoretically predicted and actually observed some time ago [12-14]. But a confirmation of the IC transition in its original context was achieved only recently [15-19] through the discovery of the layered compound $Ba_2CuGe_2O_7$ which exhibits spiral magnetic order at sufficiently low temperature $T < T_N = 3.2$ K. This compound proved to be especially well suited for experimental investigation thanks to a fortunate combination of physical properties. Unlike the extensively studied rare-earth magnetic metals [20,21], $Ba_2CuGe_2O_7$ is an insulator and its magnetic properties may be understood in terms of localized spins. Because of the low tetragonal symmetry (space group $P\bar{4}2_1m$) the corresponding Heisenberg Hamiltonian involves an interesting combination of antisymmetric (DM) and symmetric exchange anisotropies which lead to a rich phase diagram. The scale of energy set by an exchange constant of the order $J \sim 1$ meV is very convenient for neutron-scattering measurements. Similarly, the strength of anisotropy is such that magnetic phase transitions occur at critical fields that are well within experimental reach. Indeed, a series of experiments [15-19], including standard magnetometry, elastic and inelastic neutron scattering, has revealed the occurrence of a Dzyaloshinskii-type IC transition at a critical field of the order $H_c \sim 2$ T.

Our main aim in this Chapter (Secs. 2-8) is to provide a complete theoretical account of the IC transition observed in $Ba_2CuGe_2O_7$. Crystal symmetry provides the necessary input for the construction of a discrete Heisenberg Hamiltonian, but the main burden of the calculation is carried out within a continuum approximation which leads to a certain effective field theory that is a variant of the relativistic nonlinear σ model. The validity of the continuum approximation is justified because anisotropy is sufficiently weak and leads to a magnetic spiral with a reasonably long period of 37 unit cells (220 Å) at zero field. The nonlinear σ model may thus be safely employed for the study of ground state properties and the corresponding low-energy dynamics. While theoretical results are in general agreement with experiment, a more detailed study reveals the necessity for some important refinements. In particular, the IC phase transition is shown to be mediated by a certain "intermediate phase" [22,23] which was absent in the original description of Dzyaloshinskii [11]. Although some experimental evidence for the existence of an intermediate phase is available [18,19], a definite confirmation may require further experimental work guided by the current theoretical analysis.

We also discuss a variation of the main theme concerning the magnetic compound $K_2V_3O_8$. The space group of this compound is different (*P*4*bm*) but leads to an effective Heisenberg Hamiltonian that is very similar to the one encountered in $Ba_2CuGe_2O_7$. A recent experimental investigation of $K_2V_3O_8$ in its low-temperature phase ($T < T_N = 4$ K) revealed the occurrence of interesting spin-flop and spin-reorientation transitions [24] but provided no evidence for incommensurate magnetism. A theoretical discussion of this issue may be found in Ref. [25] and in Sec. 2 of this Chapter. Our main conclusions are summarized in Sec. 10.

2. SYMMETRY CONSTRAINTS IN $Ba_2CuGe_2O_7$

The unit cell of $Ba_2CuGe_2O_7$ is partially illustrated in Fig. 1 where we display only the magnetic Cu^{2+} ions with spin $s=1/2$. The lattice constants are $a = b = 8.466$ Å and $c = 5.445$ Å. Since the Cu atoms form a perfect square lattice within each layer, with lattice constant $d = a/\sqrt{2} = 5.986$ Å, it is also useful to consider the orthogonal axes x, y and z obtained from the conventional crystal axes a, b and c by a 45° azimuthal rotation. The complete magnetic lattice is formally divided into two sublattices labeled by A and B because the major spin interaction between in-plane neighbors is antiferromagnetic, while the interaction between out-of-plane neighbors is ferromagnetic [15].

The space group of this crystal is $P\bar{4}2_1m$ and imposes significant constraints on the possible types of spin interactions. We first note that an effective Hamiltonian restricted to terms that are at most quadratic in the spin operators is of the general form

$$W = \sum_{<kl>} \left[\frac{1}{2} \sum_{i,j} J_{kl}^{ij} \left(S_k^i S_l^j + S_k^j S_l^i \right) + \mathbf{D}_{kl} \cdot (\mathbf{S}_k \times \mathbf{S}_l) \right], \tag{2.1}$$

where the overall sum extends over bonds <*kl*> that connect any two magnetic sites labeled by k and l, and the indices i and j are summed over three values corresponding to the Cartesian components of the spin vectors along the axes x, y, and z. There are no single-ion terms in this spin $s = 1/2$ Hamiltonian.

The first term in Eq. (2.1) describes "symmetric" exchange interaction characterized by the 3×3 symmetric matrices $J_{kl} = (J_{kl}^{ij})$, one for each bond <*kl*>. For in-plane bonds connecting nearest-neighbor (nn) magnetic sites, symmetry requires that there exist only four distinct matrices of the form

$$J_I = \begin{pmatrix} J_1 & 0 & 0 \\ 0 & J_2 & J_4 \\ 0 & J_4 & J_3 \end{pmatrix}, \qquad J_{II} = \begin{pmatrix} J_2 & 0 & J_4 \\ 0 & J_1 & 0 \\ J_4 & 0 & J_3 \end{pmatrix},$$
$$J_{III} = \begin{pmatrix} J_1 & 0 & 0 \\ 0 & J_2 & -J_4 \\ 0 & -J_4 & J_3 \end{pmatrix}, \qquad J_{IV} = \begin{pmatrix} J_2 & 0 & -J_4 \\ 0 & J_1 & 0 \\ -J_4 & 0 & J_3 \end{pmatrix}, \tag{2.2}$$

where J_1, J_2, J_3, and J_4 are free scalar parameters. The matrices (2.2) are distributed over each layer as shown in Fig. 2 where in-plane nn bonds are accordingly labeled by I, II, III, and IV. For out-of-plane nn bonds, symmetry requires $J_{AA} = J_{BB} = \mathrm{diag}(J_5, J_5, J_6)$ where J_5 and J_6 are additional scalar parameters.

The second term in Eq. (2.1) describes "antisymmetric" exchange interaction which is usually referred to as the DM anisotropy. There exist only four distinct constant vectors $\mathbf{D}_{kl}$ that are distributed over the 2D lattice of Fig. 2 according to

$$\mathbf{D}_I = D_\perp \mathbf{e}_2 + D_z \mathbf{e}_3, \qquad \mathbf{D}_{II} = D_\perp \mathbf{e}_1 + D_z \mathbf{e}_3,$$
$$\mathbf{D}_{III} = D_\perp \mathbf{e}_2 - D_z \mathbf{e}_3, \qquad \mathbf{D}_{IV} = D_\perp \mathbf{e}_1 - D_z \mathbf{e}_3, \tag{2.3}$$

where $D_\perp$ and D_z are free scalar parameters, while $\mathbf{e}_1$, $\mathbf{e}_2$, and $\mathbf{e}_3$ are unit vectors along the axes *x*, *y*, and *z*. Symmetry also requires that DM interactions between out-of-plane neighbors vanish.

Since the ferromagnetic out-of-plane interaction is experimentally estimated to be rather weak [15], we shall neglect it in our theoretical development and thus restrict ourselves to the study of the 2D spin dynamics within a single layer. It is also safe to neglect next-nearest-neighbor (nnn) in-plane interactions for reasons briefly explained in Refs. [22,23]. We thus consider the 2D lattice of Fig. 2 where spin operators over the two sublattices are denoted by $\mathbf{A}_{\alpha\beta}$ and $\mathbf{B}_{\alpha\beta}$, respectively; α and β are integers that advance along the conventional crystal axes *a* and *b*. Taking into account the symmetry constraints summarized in Eqs. (2.2) and (2.3), the Heisenberg equations satisfied by the spin operators read

$$\frac{\partial \mathbf{A}_{\alpha\beta}}{\partial t} = \mathbf{A}_{\alpha\beta} \times \mathbf{F}_{\alpha\beta} \,, \qquad \frac{\partial \mathbf{B}_{\alpha\beta}}{\partial t} = \mathbf{B}_{\alpha\beta} \times \mathbf{G}_{\alpha\beta} \,, \tag{2.4}$$

where the effective fields **F** and **G** are given explicitly by

$$\begin{aligned}
\mathbf{F}_{\alpha\beta} = & -\left[J_1\left(B^x_{\alpha\beta} + B^x_{\alpha-1,\beta-1}\right) + J_2\left(B^x_{\alpha-1,\beta} + B^x_{\alpha,\beta-1}\right) + J_4\left(B^z_{\alpha-1,\beta} - B^z_{\alpha,\beta-1}\right)\right]\mathbf{e}_1 \\
& -\left[J_2\left(B^y_{\alpha\beta} + B^y_{\alpha-1,\beta-1}\right) + J_1\left(B^y_{\alpha-1,\beta} + B^y_{\alpha,\beta-1}\right) + J_4\left(B^z_{\alpha\beta} - B^z_{\alpha-1,\beta-1}\right)\right]\mathbf{e}_2 \\
& - J_3\left(B^z_{\alpha\beta} + B^z_{\alpha-1,\beta-1} + B^z_{\alpha,\beta-1} + B^z_{\alpha-1,\beta}\right)\mathbf{e}_3 \\
& - J_4\left(B^y_{\alpha\beta} - B^y_{\alpha-1,\beta-1} + B^x_{\alpha-1,\beta} - B^x_{\alpha,\beta-1}\right)\mathbf{e}_3 \\
& + \mathbf{D}_I \times \mathbf{B}_{\alpha\beta} + \mathbf{D}_{II} \times \mathbf{B}_{\alpha-1,\beta} - \mathbf{D}_{III} \times \mathbf{B}_{\alpha-1,\beta-1} - \mathbf{D}_{IV} \times \mathbf{B}_{\alpha,\beta-1} + g\mu_B \mathbf{H} \,, \\
\mathbf{G}_{\alpha\beta} = & -\left[J_1\left(A^x_{\alpha\beta} + A^x_{\alpha+1,\beta+1}\right) + J_2\left(A^x_{\alpha+1,\beta} + A^x_{\alpha,\beta+1}\right) + J_4\left(A^z_{\alpha+1,\beta} - A^z_{\alpha,\beta+1}\right)\right]\mathbf{e}_1 \\
& -\left[J_2\left(A^y_{\alpha\beta} + A^y_{\alpha+1,\beta+1}\right) + J_1\left(A^y_{\alpha+1,\beta} + A^y_{\alpha,\beta+1}\right) + J_4\left(A^z_{\alpha\beta} - A^z_{\alpha+1,\beta+1}\right)\right]\mathbf{e}_2 \\
& - J_3\left(A^z_{\alpha\beta} + A^z_{\alpha+1,\beta+1} + A^z_{\alpha,\beta+1} + A^z_{\alpha+1,\beta}\right)\mathbf{e}_3 \\
& - J_4\left(A^y_{\alpha\beta} - A^y_{\alpha+1,\beta+1} + A^x_{\alpha+1,\beta} - A^x_{\alpha,\beta+1}\right)\mathbf{e}_3 \\
& - \mathbf{D}_I \times \mathbf{A}_{\alpha\beta} - \mathbf{D}_{II} \times \mathbf{A}_{\alpha+1,\beta} + \mathbf{D}_{III} \times \mathbf{A}_{\alpha+1,\beta+1} + \mathbf{D}_{IV} \times \mathbf{A}_{\alpha,\beta+1} + g\mu_B \mathbf{H} \,.
\end{aligned} \tag{2.5}$$

Here, we also include the effect of an externally applied magnetic field **H**. Inspite of their complicated appearance, Eqs. (2.5) provide the basis for a relatively simple discussion of spin dynamics in $Ba_2CuGe_2O_7$ and related compounds.

Throughout this work the spin operators **A** and **B** in Eqs. (2.4) are approximated by classical vectors of magnitude $s = 1/2$. The resulting scheme is equivalent to the usual semiclassical approximation obtained by the $1/s$ expansion restricted to leading order. The omitted quantum (anharmonic) corrections are not negligible in this 2D problem [1] but are offset in part by the fact that the input parameters are consistently estimated within the classical approximation [15-19].

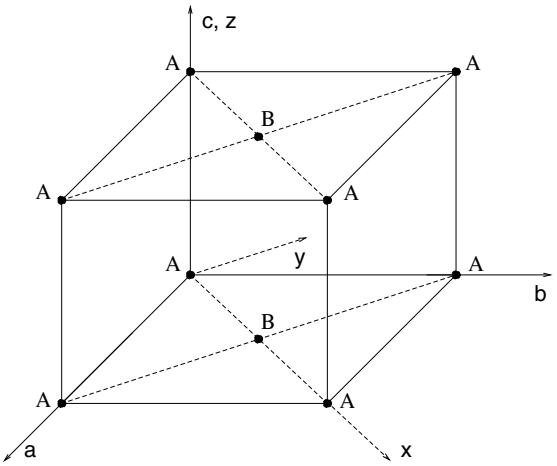

Fig. 1. Partial illustration of the unit cell of $Ba_2CuGe_2O_7$ or $K_2V_3O_8$ displaying only the magnetic Cu^{2+} or V^{4+} ions denoted by solid circles. Although the magnetic lattices are isomorphic in the two compounds, the space groups are different ($P\bar{4}2_1m$ and $P4bm$, respectively).

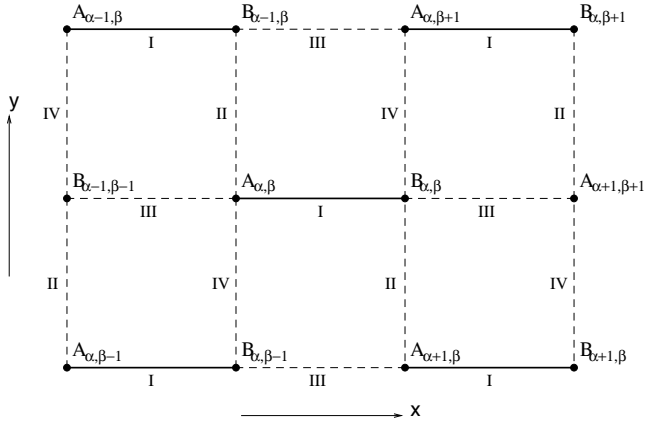

Fig. 2. Illustration of the dimerization process on a finite portion of the 2D lattice cut along the axes *x* and *y*. The indices α and β advance along the conventional crystal axes *a* and *b* not shown in this figure. The meaning of labels I, II, III, and IV on bonds connecting nn sites is explained in the text.

3. THE KSEA LIMIT

A special limit of the effective Hamiltonian constructed in the preceding section is motivated by the work of Shekhtman, Entin-Wohlman, and Aharony [26,27] in the context of high-T_c superconductors, some aspects of which had been anticipated by the earlier work of Kaplan [28]. To leading order the system is described by the isotropic Heisenberg Hamiltonian $J\sum(\boldsymbol{S}_k\cdot\boldsymbol{S}_l)$ where the exchange constant J is the same for all bonds. One then includes spin-orbit interactions by a perturbative treatment of the type originally described by Moriya [7] to derive the DM anisotropy, which is now carried to second order [27]. The resulting Hamiltonian is given by

$$W_{KSEA}=\sum_{<kl>}\left[\left(J-\frac{|\mathbf{D}_{kl}|^2}{4J}\right)(\mathbf{S}_k\cdot\mathbf{S}_l)+\mathbf{D}_{kl}\cdot(\mathbf{S}_k\times\mathbf{S}_l)+\frac{1}{2J}(\mathbf{S}_k\cdot\mathbf{D}_{kl})(\mathbf{D}_{kl}\cdot\mathbf{S}_l)\right], \quad (3.1)$$

where the constant vectors $\mathbf{D}_{kl}$ are restricted by symmetry as in Eq. (2.3). It is then not difficult to see that (3.1) is indeed a special case of the complete effective Hamiltonian constructed in Sec. 2 with

$$\begin{aligned} J_1&=J-\frac{D_\perp^2+D_z^2}{4J}, & J_2&=J+\frac{D_\perp^2-D_z^2}{4J},\\ J_3&=J-\frac{D_\perp^2-D_z^2}{4J}, & J_4&=\frac{D_\perp D_z}{2J}, \end{aligned} \quad (3.2)$$

and now contains three instead of six independent parameters.

The KSEA limit was actually invoked in Ref. [19] for the analysis of experimental data from $Ba_2CuGe_2O_7$. However, the original work in high-T_c superconductors had already made it clear that deviations from the KSEA limit should be expected [29] and are certainly not excluded by symmetry. Therefore, our general treatment in the following will be based on the complete effective Hamiltonian of Sec. 2, but detailed numerical calculations will also be restricted to the KSEA limit given by Eq. (3.2).

4. COMMENSURATE PHASE

On the assumption that the ground state is spatially uniform on each sublattice, the calculation of the homogeneous ($\mathbf{q}=0$) spin dynamics is significantly simplified. One may then suppress the indices α and β in Eqs. (2.4) and (2.5) or, equivalently, consider the two-spin cell Hamiltonian

$$W_C=4J_\perp(A^xB^x+A^yB^y)+4J_zA^zB^z+4D_z(A^xB^y-A^yB^x)-g\mu_B\mathbf{H}\cdot(\mathbf{A}+\mathbf{B}), \quad (4.1)$$

where we use the abbreviations

$$J_\perp = \frac{1}{2}\,(J_1 + J_2)\ , \qquad J_z = J_3\ . \tag{4.2}$$

A notable feature of Eq. (4.1) is that both the in-plane component of the DM anisotropy $D_\perp$ and the off-diagonal exchange constant J_4 have dropped out and thus do not affect the $\mathbf{q} = 0$ dynamics.

A semiclassical approximation of the ground state is furnished by the spin configuration that minimizes W_C treating **A** and **B** as classical vectors with magnitude s. To actually search for the minimum, we first introduce two new spin vectors $\mathbf{Q}_1$ and $\mathbf{Q}_2$ obtained by rotating **A** around the z-axis by an angle ψ, and **B** by an angle $-\psi$, i.e.,

$$\begin{aligned} A^x &= \cos\psi\ Q_1^x + \sin\psi\ Q_1^y\ , \quad A^y = -\sin\psi\ Q_1^x + \cos\psi\ Q_1^y\ , \quad A^z = Q_1^z\ , \\ B^x &= \cos\psi\ Q_2^x - \sin\psi\ Q_2^y\ , \quad B^y = \sin\psi\ Q_2^x + \cos\psi\ Q_2^y\ , \quad B^z = Q_2^z\ , \end{aligned} \tag{4.3}$$

with

$$\tan(2\psi) = \frac{D_z}{J_\perp}\ . \tag{4.4}$$

The cell Hamiltonian (4.1) is then written as

$$W_C = 4\sqrt{J_\perp^2 + D_z^2}\ (\ Q_1^x Q_2^x + Q_1^y Q_2^y\ ) + 4\,J_z\,Q_1^z Q_2^z - g\mu_B H\,(\ Q_1^z + Q_2^z\ )\ , \tag{4.5}$$

where we have also assumed that the external field H is applied along the z (or c) axis.

The obvious advantage of Hamiltonian (4.5) is that its classical minimum can be determined essentially by inspection. In this respect, an important quantity is the uniaxial anisotropy

$$\Delta = \sqrt{J_\perp^2 + D_z^2} - J_z\ , \tag{4.6}$$

whose algebraic sign determines in large measure the nature of the ground state. To get some insight, we invoke the KSEA anisotropy limit given by Eqs. (3.2) which are inserted in Eq. (4.6) to yield

$$\Delta = \frac{D_\perp^2}{4J} > 0\ . \tag{4.7}$$

Therefore, in this limit, Hamiltonian (4.5) describes an easy-plane antiferromagnet. Although our subsequent development is not restricted to the KSEA limit, we shall nevertheless assume that an easy-plane anisotropy ($\Delta > 0$) is appropriate for the description of $Ba_2CuGe_2O_7$. The case of an easy-axis anisotropy ($\Delta < 0$) will be discussed in Sec. 9 in connection with the magnetic compound $K_2V_3O_8$.

Now, for $\Delta > 0$, the absolute minimum is provided by the canted configuration

$$\mathbf{Q}_1 = s\,(\cos\chi, 0, \sin\chi)\ , \qquad \mathbf{Q}_2 = s\,(-\cos\chi, 0, \sin\chi)\ , \tag{4.8}$$

modulo an overall azimuthal rotation. The canting angle χ that corresponds to minimum energy is given by

$$\sin\chi = \frac{H}{H_F}\ , \qquad g\mu_B H_F = 4s\left[J_z + \sqrt{J_\perp^2 + D_z^2}\right]\ , \tag{4.9}$$

where H_F is a critical field above which the ground state is fully ordered (ferromagnetic) along the c axis ($\chi = \pi/2$).

The ground-state values of the original spin vectors **A** and **B** are calculated by inserting Eq. (4.8) in Eq. (4.3). In fact, a more transparent set of variables is provided by the magnetization **m** and the staggered magnetization **n** defined as

$$\mathbf{m} = \frac{1}{2s}\,(\mathbf{A} + \mathbf{B})\ , \qquad \mathbf{n} = \frac{1}{2s}\,(\mathbf{A} - \mathbf{B})\ , \tag{4.10}$$

and their ground state values are

$$\mathbf{m} = (\ 0\ , -\sin\psi\cos\chi,\ \sin\chi\ )\ , \qquad \mathbf{n} = (\ \cos\psi\cos\chi,\ 0\ ,\ 0\ )\ . \tag{4.11}$$

For future reference, we also approximate Eqs. (4.11) in the limit where anisotropy is small ($J_z \approx J_\perp \equiv J$, $D_z \ll J$) and the applied field is relatively weak ($H \ll H_F \approx 8sJ/g\mu_B$). One may then insert $\psi \approx D_z/2J$ and $\chi \approx g\mu_B H/8sJ$ in Eqs. (4.11) to obtain the leading-order approximation

$$\mathbf{m} \approx \left(0,\ -\frac{D_z}{2J},\ \frac{g\mu_B H}{8sJ}\right)\ , \qquad \mathbf{n} \approx (1,0,0)\ . \tag{4.12}$$

Therefore, the ground-state staggered magnetization is a constant unit vector that points along the x axis, up to an arbitrary azimuthal rotation, while a weak ferromagnetic moment develops along the y axis even at zero field ($H = 0$) provided that the out-of-plane component of the DM anisotropy is different from zero ($D_z \neq 0$). Incidentally, using parameters appropriate for $Ba_2CuGe_2O_7$ ($s = 1/2$, $g = 2.474$, $J = 0.96$ meV) the critical field required to establish ferromagnetic order is estimated to be $H_F \approx 27$ T. Hence the condition $H \ll H_F$ is well satisfied for fields of practical interest [15-19]. Furthermore, there is so far no experimental evidence for appreciable value of D_z in $Ba_2CuGe_2O_7$ and thus the condition $D_z \ll J$ is also expected to be satisfied.

Having determined the uniform or commensurate ground state, one could proceed to calculate the corresponding $\mathbf{q} = 0$ magnon frequencies by expanding the Hamiltonian (4.5) around the canted configuration (4.8) and diagonalizing the resulting small fluctuations through, say, an elementary Holstein-Primakoff transformation. However, the magnon spectrum may be computed more efficiently using the field theoretical framework developed in the following sections. The same framework will also allow us to examine the stability of the commensurate ground state to non-uniform ($\mathbf{q} \neq 0$) fluctuations and eventually establish the complete $T = 0$ phase diagram.

5. NONLINEAR σ MODEL

We now return to the complete Heisenberg equations (2.5) which can, in principle, be analyzed by standard spin-wave techniques. However, such a task is technically complicated by the large numbers of free parameters that remain in the theory even after the symmetry constraints have been incorporated. Nevertheless, the essential features of the ground state and the corresponding low-energy dynamics can actually be calculated from a simpler continuum field theory which is a suitable generalization of the relativistic nonlinear σ model. The relevance of the latter for the description of antiferromagnets is apparent in the early review article of Andreev and Marchenko [30] and in many related investigations [31-33].

It is understood that important features of the relevant nonlinear σ model depend on crystal symmetry. Here, we proceed directly from Eqs. (2.5) by a straightforward method that is somewhat tedious but safe [22,34]. We omit a number of technical details but stress the important facts. First, we define an average exchange constant

$$J = \frac{1}{3}\,(J_1 + J_2 + J_3)\,, \tag{5.1}$$

which sets the energy scale of the system. We further assume that all (anisotropy) constants that account for deviations of the present model from an isotropic Heisenberg model with exchange constant J are significantly smaller than J. Similarly, the applied magnetic field is assumed to be sufficiently weak; namely, $H \ll H_F \approx 8sJ/g\mu_B$, as discussed in Sec. 4. Under these conditions, which are reasonably satisfied in $Ba_2CuGe_2O_7$, the low-energy dynamics can be approximated by the continuum field theory described below.

We return to Fig. 2 and define space-time variables according to

$$\eta = \sqrt{2}\varepsilon\alpha\,, \qquad \xi = \sqrt{2}\varepsilon\beta\,, \qquad \tau = 2s\sqrt{2}\varepsilon Jt\,, \tag{5.2}$$

where ε is an arbitrary dimensionless scale whose formal significance will become apparent as the discussion progresses. Since α and β are integers that advance along the conventional crystal axes a and b, η and ξ are coordinates measured along the same axes. In fact, the final result will be stated in terms of

$$x = \frac{\xi + \eta}{\sqrt{2}}\,, \qquad y = \frac{\xi - \eta}{\sqrt{2}}\,, \tag{5.3}$$

which are coordinates along the axes x and y of Figs. 1 and 2. One should keep in mind that actual distances are given by xd/ε and yd/ε where $d = a/\sqrt{2}$ is the lattice constant of the square lattice formed by the Cu atoms.

Similarly, we introduce rescaled anisotropy constants and magnetic field as

$$d_\perp = \frac{D_\perp}{\varepsilon J}\,, \qquad d_z = \frac{\sqrt{2}D_z}{\varepsilon J}\,, \qquad \mathbf{h} = \frac{g\mu_B \mathbf{H}}{2s\sqrt{2}\varepsilon J}\,,$$
$$\kappa_0 = \frac{2}{\varepsilon^2 J}\left(J_1 + J_2 - 2J_3\right)\,, \tag{5.4}$$

where we display only those combinations of constants that survive in the effective low-energy dynamics. In particular, the off-diagonal exchange constant J_4 does not appear to leading order. The notational abbreviations

$$\kappa = \kappa_0 + d_z^2 - d_\perp^2\,, \qquad \mathbf{d}_z = d_z\,\mathbf{e}_3\,, \tag{5.5}$$

will also prove convenient for our subsequent calculations.

We now come to the crucial issue of selecting appropriate combinations of spin variables. In view of the antiferromagnetic nature of the main spin interaction, the simplest way to achieve continuity is to group the original spin variables **A** and **B** into dimers, as shown in Fig. 2. The dimerization process is clearly not unique, for one could also form dimers along the y instead of x axis. In either case, there exists exactly one dimer within each unit cell and may be equivalently represented by the magnetization **m** and the staggered magnetization **n** already defined in Eq. (4.10), which satisfy the classical constraints

$$\mathbf{m}\cdot\mathbf{n} = 0\,, \qquad \mathbf{m}^2 + \mathbf{n}^2 = 1\,, \tag{5.6}$$

that result from $\mathbf{A}^2 = s^2 = \mathbf{B}^2$. One may then reformulate Eqs. (2.5) in terms of **m** and **n** and derive the continuum approximation by a systematic formal expansion in powers of ε [34]. To leading approximation, **n** is of order unity and **m** of order ε. The classical constraints (5.6) then simplify to

$$\mathbf{m}\cdot\mathbf{n} = 0\,, \qquad \mathbf{n}^2 = 1\,, \tag{5.7}$$

and **m** is expressed entirely in terms of **n** by

$$\mathbf{m} = \frac{\varepsilon}{2\sqrt{2}}\left[\mathbf{n}\times\left(\dot{\mathbf{n}} + \mathbf{d}_z - \mathbf{n}\times\mathbf{h}\right)\right] - \frac{\varepsilon}{2}\partial_1\mathbf{n}\,. \tag{5.8}$$

The last term in Eq. (5.8) reflects the dimerization ambiguity mentioned earlier in the text and would be proportional to $\partial_2\mathbf{n}$ if dimers were oriented along the y axis [34]. Finally, the staggered magnetization **n** is a unit vector field whose ($T = 0$) dynamics is governed by the Lagrangian density $\mathcal{L} = \mathcal{L}_0 - V$ where

$$\begin{aligned} \mathcal{L}_0 &= \frac{1}{2}\dot{\mathbf{n}}^2 + \mathbf{h}\cdot(\mathbf{n}\times\dot{\mathbf{n}})\,, \\ V &= \frac{1}{2}(\partial_1\mathbf{n} - d_\perp \mathbf{e}_2\times\mathbf{n})^2 + \frac{1}{2}(\partial_2\mathbf{n} - d_\perp \mathbf{e}_1\times\mathbf{n})^2 \\ &\quad + \frac{1}{2}\kappa\, n_3^2 + \frac{1}{2}(\mathbf{n}\cdot\mathbf{h})^2 + (\mathbf{h}\times\mathbf{d}_z)\cdot\mathbf{n}\,. \end{aligned} \tag{5.9}$$

The overdot denotes differentiation with respect to the time variable τ, ∂_1 and ∂_2 are partial derivatives with respect to x and y, and (n_1, n_2, n_3) are the Cartesian components of **n** along the xyz axes of Fig. 1. Consistency requires that all physical predictions derived from Eqs. (5.8) and (5.9) must be independent of the specific choice of the scale parameter ε. This fact will be explicitly demonstrated or used to advantage in the continuation of this work.

The KSEA limit of the nonlinear σ model just derived is obtained by inserting Eqs. (3.2) into the definitions of parameters given in Eqs. (5.4) and (5.5) to yield the simple result $\kappa = 0$. Although our general analysis in the following sections will be carried out for $\kappa \neq 0$, explicit numerical predictions will be made for $\kappa = 0$ in order to directly compare them with some results of Ref. [19] obtained in the KSEA limit. For future reference, we collect here the values of the parameters that are thought to be appropriate for the description of $Ba_2CuGe_2O_7$. In addition to the parameters $s = 1/2$, g=2.474, J=0.96 meV already mentioned in Sec. 4, we choose the in-plane component of the DM anisotropy as $D_\perp$ = 0.17 meV and conveniently define the free parameter ε as $\varepsilon \equiv D_\perp / J$ = 0.18. Therefore, the dimensionless parameters that appear in the nonlinear σ model are

$$\kappa = 0\,, \qquad \varepsilon \equiv \frac{D_\perp}{J} = 0.18\,, \qquad d_\perp = 1\,, \tag{5.10}$$

and should be completed with the statement that frequency (energy) is measured in units of $2s\sqrt{2}\,\varepsilon J$ = 0.24 meV, distance in units of $d/\varepsilon = a/\varepsilon\sqrt{2}$ = 33.75 Å, magnetic field h in units of $2s\sqrt{2}\,\varepsilon J / g\mu_B$ = 1.68 T, and magnetic moment m per magnetic ion in units of $sg\mu_B$ = $1.237\mu_B$. An estimate of the out-of-plane component of the DM anisotropy D_z and the corresponding rationalized parameter d_z is left open for the moment due to present lack of direct experimental evidence. In this respect, one should note that the above parameter becomes important when the external field is applied in a direction perpendicular to the c axis, as discussed further in Sec. 8.

6. DYNAMICS OF THE COMMENSURATE PHASE

We now reproduce and extend the results of Sec. 4 using the field theoretical framework developed in Sec. 5. First, we restrict the Lagrangian (5.9) to the case of a field applied along the c axis, **h** = (0, 0, h), to obtain

$$\begin{aligned} \mathcal{L}_0 &= \frac{1}{2}\dot{\mathbf{n}}^2 + h\,(n_1\dot{n}_2 - \dot{n}_1 n_2)\,, \\ V &= \frac{1}{2}\left[(\partial_1\mathbf{n})^2 + (\partial_2\mathbf{n})^2 + \gamma^2 n_3^2 + d_\perp^2\right] \\ &\quad - d_\perp\left[(\partial_1 n_1 - \partial_2 n_2)\,n_3 - (n_1\partial_1 - n_2\partial_2)\,n_3\right]\,, \end{aligned} \tag{6.1}$$

where

$$\gamma^2 = \alpha^2 + h^2 , \qquad \alpha^2 \equiv \kappa + d_\perp^2 . \tag{6.2}$$

Implicit in the definition of the effective anisotropy parameter α^2 is the assumption $\kappa + d_\perp^2 > 0$ which corresponds to easy-plane anisotropy and is thought to be appropriate for $Ba_2CuGe_2O_7$. This is certainly the case in the KSEA limit where $\kappa = 0$ or $\alpha^2 = d_\perp^2$.

It should be noted that the term $(\mathbf{h} \times \mathbf{d}_z) \cdot \mathbf{n}$ in Eq. (5.9) has dropped out of Eq. (6.1) because $\mathbf{h} \times \mathbf{d}_z = 0$ when the field is applied along the c axis. A related fact is that the Lagrangian (6.1) is invariant under the simultaneous transformations

$$x + iy \rightarrow (x + iy)\, e^{i\psi_0} , \qquad n_1 + in_2 \rightarrow (n_1 + in_2)\, e^{-i\psi_0} . \tag{6.3}$$

This is a somewhat peculiar realization of U(1) symmetry in that the usual 2D rotation of spatial coordinates with angle ψ_0 is followed by an azimuthal rotation of the staggered magnetization with angle $-\psi_0$. This symmetry is broken when the external field is not parallel to the c axis. The case of a field perpendicular to the c axis is discussed in Sec. 8.

Now, to determine the semiclassical ground state, we search for a static unit field $\mathbf{n} = \mathbf{n}(x, y)$, $\mathbf{n}^2 = 1$, that minimizes the energy functional

$$W = \int V \, dx dy . \tag{6.4}$$

A more or less obvious stationary point of W is the constant unit field $\mathbf{n} = (1, 0, 0)$, modulo a U(1) transformation, with energy density $w = d_\perp^2 / 2$. We also calculate the corresponding magnetization from Eq. (5.8) applied with $\mathbf{n} = (1, 0, 0)$ and $\mathbf{h} = (0, 0, h)$ to obtain

$$\mathbf{m} = \frac{\varepsilon}{2\sqrt{2}} (0, -d_z, h) , \qquad \mathbf{n} = (1, 0, 0) . \tag{6.5}$$

If we now restore the original constants from Eq. (5.4), Eq. (6.5) is independent of ε, as expected, and reproduces Eq. (4.12) obtained by a more direct treatment in Sec.4.

The advantage of the present treatment is that we can easily calculate the magnon spectrum and, in particular, examine conditions for stability of the commensurate ground state. For this purpose, it is necessary to explicitly resolve the constraint $\mathbf{n}^2 = 1$ through, say, the spherical parametrization

$$n_1 + in_2 = \sin\Theta\, e^{i\Phi} , \qquad n_3 = \cos\Theta , \tag{6.6}$$

in terms of which the Lagrangian (6.1) reads

$$\begin{aligned} \mathcal{L}_0 &= \frac{1}{2} \left(\dot{\Theta}^2 + \sin^2\Theta \; \dot{\Phi}^2 \right) + h \, \sin^2\Theta \; \dot{\Phi} , \\ V &= \frac{1}{2} \left[(\nabla\Theta)^2 + \sin^2\Theta \, (\nabla\Phi)^2 + \gamma^2 \cos^2\Theta + d_\perp^2 \right] \\ &\quad + d_\perp \left[\cos\Theta \, \sin\Theta \; (\sin\Phi \; \partial_1\Phi + \cos\Phi \; \partial_2\Phi) - \cos\Phi \; \partial_1\Theta + \sin\Phi \; \partial_2\Theta \right] , \end{aligned} \tag{6.7}$$

where $\nabla = (\partial_1, \partial_2)$ is the usual 2D gradient operator, while the Laplacian will be denoted in the following by $\Delta = \partial_1^2 + \partial_2^2$.

The commensurate ground state then corresponds to $\Theta = \pi/2$, $\Phi = 0$ and small fluctuations around this state are calculated by introducing $\Theta = \pi/2 + f$, $\Phi = g$ in Eqs. (6.7) and keeping terms that are at most quadratic in the small amplitudes $f = f(x, y, \tau)$ and $g = g(x, y, \tau)$. The corresponding linearized equations are found to be

$$\ddot{f} - \Delta f + \gamma^2 f = 2d_\perp \partial_2 g\,, \qquad \ddot{g} - \Delta g = -2d_\perp \partial_2 f\,, \tag{6.8}$$

and are diagonalized by performing the usual Fourier transformation with frequency ω and wave vector $\mathbf{q} = (q_1, q_2)$ to obtain a homogeneous system whose solution requires that the corresponding determinant vanish. This condition leads to two branches of normal frequencies

$$\omega_\pm(\mathbf{q}) = \left[q_1^2 + q_2^2 + \frac{1}{2}\left(\gamma^2 \pm \sqrt{\gamma^4 + 16 d_\perp^2 q_2^2}\right)\right]^{1/2}, \tag{6.9}$$

which will be referred to as the optical and acoustic mode for the plus or minus sign, respectively. The calculated magnon dispersions are strongly anisotropic.

It is now interesting to examine some special features of the magnon spectrum (6.9). We first consider the magnon gap of the optical branch at $\mathbf{q} = 0$ where $\omega_+(\mathbf{q} = 0) = \gamma = (\alpha^2 + h^2)^{1/2} = (\kappa + d_\perp^2 + h^2)^{1/2}$. This result may be used to illustrate again our earlier claim concerning the role of the scale parameter ε. If we recall the definition of the rescaled parameters (5.4) and also include the factor $2s\sqrt{2}\,\varepsilon J$ to account for the physical unit of frequency, the calculated gap is independent of ε and is expressed entirely in terms of constants that appear in the original discrete Hamiltonian of Sec. 2. In particular, in the KSEA limit ($\kappa = 0$), we find that

$$\omega_+(\mathbf{q} = 0) = \left[\left(2s\sqrt{2}D_\perp\right)^2 + (g\mu_B H)^2\right]^{1/2}, \tag{6.10}$$

which may be applied with $s = 1/2$, $D_\perp = 0.17$ meV and $g = 2.474$ to yield the field dependence of the magnon gap, in reasonable agreement with experiment [19]. Incidentally, this special result is the only feature of the spectrum actually calculated in the above reference for nonzero field.

The acoustic branch $\omega_-(\mathbf{q})$ is the Goldstone mode associated with the U(1) symmetry (6.3) and is thus gapless at $\mathbf{q} = 0$. The low-$\mathbf{q}$ acoustic branch reads

$$\omega_-(\mathbf{q}) \approx \left[q_1^2 + \left(1 - 4d_\perp^2/\gamma^2\right) q_2^2\right]^{1/2} \tag{6.11}$$

and demonstrates that the spin-wave velocity depends on the direction of propagation. For example, the velocities along the x and y axes are $c_1 = 1$ and $c_2 = (1 - 4d_\perp^2/\gamma^2)^{1/2}$ measured in units of $2s\sqrt{2}\,dJ = 2s\,aJ$ with $s = 1/2$, $a = 8.466$ Å, and $J = 0.96$ meV.

Equation (6.11) also makes it clear that an instability arises when $\gamma^2 < 4\,d_\perp^2$. In fact, the complete acoustic frequency $\omega_-(\mathbf{q})$ of Eq. (6.9) becomes purely imaginary over a nontrivial region in $\mathbf{q}$ space when $\gamma^2 = \alpha^2 + h^2 < 4\,d_\perp^2$. Therefore, the commensurate ground state is locally stable only for sufficiently strong fields in the region $h > h_2$ where

$$h_2 = \sqrt{4d_\perp^2 - \alpha^2} \tag{6.12}$$

is a critical field depicted by the upper solid line in the ($T = 0$) phase diagram of Fig. 3. It should be noted that the commensurate ground state is locally stable for all fields ($h_2 = 0$) when the anisotropy constants satisfy the inequality $\alpha^2 > 4\,d_\perp^2$.

The KSEA limit $\kappa = 0$ or $\alpha^2 = d_\perp^2$ is indicated by the vertical dotted line in Fig. 3. The corresponding critical field is then given by $h_2 = \sqrt{3}\,d_\perp$. If we further employ the rationalized units given by Eq. (5.10), we find $h_2 = \sqrt{3}$ or, in physical units, $H_2 = 1.68\sqrt{3} = 2.9$ T. The predicted critical field is significantly smaller than the field $H_F = 27$ T required for complete ferromagnetic saturation, as discussed in Sec. 4, and hence there is no reason to doubt the validity of the continuum approximation. To summarize, in the KSEA limit, the commensurate ground state is predicted to be locally stable only for $H > H_2 = 2.9$ T. The nature of the ground state for $H < H_2$ will be discussed in Sec. 7.

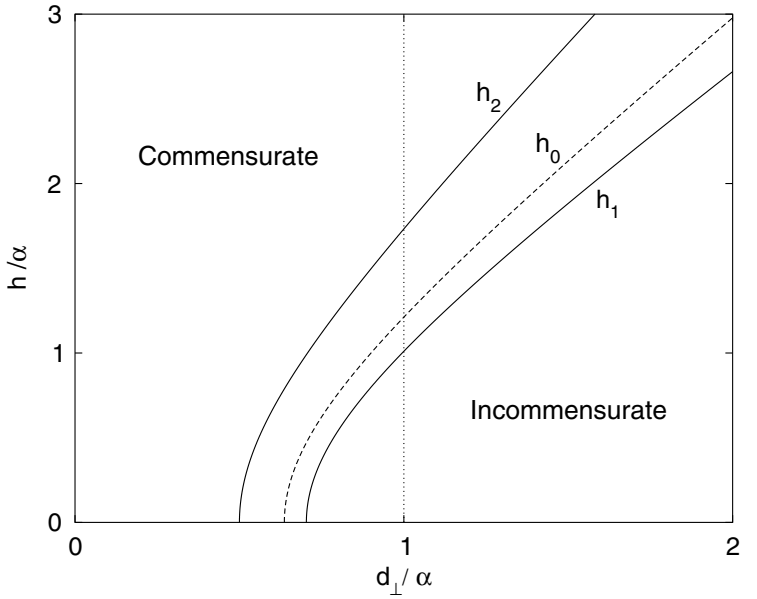

Fig. 3. $T = 0$ phase diagram for easy-plane anisotropy $\kappa + d_\perp{}^2 \equiv \alpha^2$ and a field of strength h applied along the c axis. The three characteristic fields h_1, h_0, and h_2 are given by Eqs. (7.20), (7.6), and (6.12). The intermediate phase extends between the curves h_1 and h_2. The vertical dotted line indicates the location of the KSEA limit.

This section is concluded with a brief discussion of the complete magnon dispersions (6.9) restricted to the KSEA limit. In view of Eq. (5.10), Eq. (6.9) should be applied with $d_\perp = 1$ and $\gamma^2 = 1 + h^2$ where the field h is greater than the critical field $h_2 = \sqrt{3}$. The translation to physical units already discussed in the concluding paragraph of Sec. 5 is extended with the stipulation that $\mathbf{Q} = \varepsilon\mathbf{q}$ is the wave vector defined on the complete square lattice formed by the Cu atoms within each layer. Relative units are then defined from $Q\,[\text{r.l.u.}] = Q/2\pi = (\varepsilon/2\pi)\,q$ and Eq. (6.9) should be applied with $q = (2\pi/\varepsilon)\,Q\,[\text{r.l.u.}] = 35.42\;Q\,[\text{r.l.u.}]$. Unfortunately, the largest field for which the magnon dispersions were measured by inelastic neutron scattering [19] is $H = 2.5$ T which is smaller than the currently predicted critical field $H_2 = 2.9$ T. Therefore, a direct comparison of Eq. (6.9) with experiment is not possible at this point [22].

7. INCOMMENSURATE PHASES

We now examine the nature of the ground state in the field region $h < h_2$ where the commensurate state is locally unstable. It is clear that the driving issue behind this instability is the "Lifshitz invariant" represented by the last term in Eq. (6.1) which contains first-order spatial derivatives. It is then possible that the energy of the uniform state $\mathbf{n} = (1, 0, 0)$ could be lowered by a nonuniform configuration $\mathbf{n}(x, y)$ that displays suitable spatial modulations. This section is devoted to the construction of the ground state for $h < h_2$. The argument proceeds in three main steps summarized in the following three subsections.

A. Spiral phase

The assumption of uniform ground state is relaxed in several steps. First, we consider a staggered magnetization $\mathbf{n}(x)$ that depends on a single coordinate, say, x. We further assume that the vector $\mathbf{n}$ is confined in the xz plane. In terms of the spherical parametrization (6.6) the above assumptions are summarized as

$$\Theta = \theta(x), \quad \Phi = 0; \qquad \mathbf{n} = (\sin\theta,\, 0,\, \cos\theta)\,, \tag{7.1}$$

modulo a U(1) transformation given by Eq. (6.3). Our task is then to determine the unknown amplitude $\theta = \theta(x)$ by minimizing the total energy W of Eq. (6.4) with

$$V = \frac{1}{2}\left[\,(\theta' - d_\perp)^2 + \gamma^2\cos^2\theta\,\right] \tag{7.2}$$

obtained by inserting the special Ansatz (7.1) in Eq. (6.1). Here, we use the notational abbreviation $\theta' = d\theta/dx$. Stationary points of the energy functional then satisfy the ordinary differential equation $\theta'' - \gamma^2\sin\theta\cos\theta = 0$ whose first integral is given by

$$\theta'^2 - \gamma^2\cos^2\theta = C\,, \tag{7.3}$$

where C is an arbitrary constant. The problem reduces to solving the first-order equation (7.3) for a suitable choice of the constant C that leads to minimum energy.

A natural choice appears to be $C = 0$, so that Eq. (7.3) contains as special solutions the commensurate ground-state configurations $\theta = \pm \pi / 2$ or $\mathbf{n} = (\pm 1, 0, 0)$ which are related to each other by the U(1) transformation (6.3) with $\psi_0 = \pi$ and both carry the same energy density $w = d_\perp^2 / 2$. Now, for $C = 0$, Eq. (7.3) also admits the domain wall solution

$$n_1 = \sin\theta = \tanh(\gamma x)\,, \qquad n_2 = 0\,, \qquad n_3 = \cos\theta = \frac{1}{\cosh(\gamma x)}\,, \tag{7.4}$$

which connects the two degenerate configurations $\mathbf{n} = (\pm 1, 0, 0)$ in the limits $x \to \pm\infty$. The excitation energy of the domain wall is then calculated from

$$W_{DW} = \frac{1}{2}\int_{-\infty}^{\infty} dx \left[(\theta' - d_\perp)^2 + \gamma^2 \cos^2\theta - d_\perp^2 \right] = 2\gamma - \pi d_\perp \tag{7.5}$$

and becomes negative for $2\gamma < \pi d_\perp$ or $h < h_0$ where

$$h_0 = \sqrt{\frac{\pi^2}{4} d_\perp^2 - \alpha^2} \tag{7.6}$$

is a critical field depicted by a dashed line in the phase diagram of Fig. 3.

Therefore, the commensurate ground state becomes unstable for $h < h_0$ through domain-wall nucleation, in accordance with the original argument of Dzyaloshinskii [11] and a similar argument invoked later to describe the field-induced cholesteric-nematic phase transition observed in chiral liquid crystals [12-14]. One may proceed further to suggest that the ground state for $h < h_0$ is a modulated structure that may be thought as a soliton lattice consisting of consecutive domain walls or, simply, as a spiral state. To actually construct the spiral we return to Eq. (7.3) which is now applied for nonzero C. It turns out that the minimum energy solution corresponds to positive $C \equiv \delta^2$ and is given by the implicit equation

$$x = \int_0^\theta \frac{d\vartheta}{\sqrt{\delta^2 + \gamma^2 \cos^2\vartheta}}\,, \tag{7.7}$$

which yields an amplitude $\theta(x)$ that is a monotonically increasing function of x. The corresponding staggered magnetization given by Eq. (7.1) repeats itself when θ is changed by an amount 2π; i. e., when x advances by a distance

$$L = 4\int_0^{\frac{\pi}{2}} \frac{d\theta}{\sqrt{\delta^2 + \gamma^2 \cos^2\theta}}\,, \tag{7.8}$$

which will be called the period (pitch) of the spiral. The free parameter δ is determined by the requirement that the average energy density $w = (1/L)\int_0^L V\,dx$ be a minimum, where V is the potential (7.2) calculated for the specific configuration (7.7). A direct computation based on $dw / d\delta = 0$ shows that δ must satisfy the algebraic equation

$$\frac{2}{\pi}\int_0^{\frac{\pi}{2}} d\theta\,\sqrt{\delta^2+\gamma^2\cos^2\theta}\;=\;d_\perp \tag{7.9}$$

and the corresponding energy density is

$$w=\frac{1}{2}\left(\,d_\perp^2-\delta^2\right)\,, \tag{7.10}$$

which is indeed smaller than the energy density $w = d_\perp^2/2$ of the commensurate ground state. It is clear that the root δ of Eq. (7.9) decreases with increasing γ. In fact, δ vanishes at a critical value of γ that is easily calculated by setting $\delta = 0$ in Eq. (7.9) to obtain $\gamma = \gamma_0 = \pi d_\perp/2$. Taking into account that $\gamma^2 = \alpha^2 + h^2$, the corresponding critical field h_0 coincides with that given earlier in Eq. (7.6). The spiral exists only for $h < h_0$ and its period $L = L(h)$ grows to infinity in the limit $h \to h_0$. In this limit the spiral degenerates into the domain wall configuration (7.4) with energy density $w = d_\perp^2/2$ which also coincides with the energy density of the commensurate state. We have thus described a Dzyaloshinskii-type incommensurate-to-commensurate (IC) phase transition where the ground state is thought to be an incommensurate spiral for $h < h_0$ and a commensurate spin-flop state for $h > h_0$.

Next we calculate the $T = 0$ magnetization $\mathbf{m} = (m_1, m_2, m_3)$ which can be obtained from Eq. (5.8) applied for $\mathbf{h} = (0, 0, h)$ and $\mathbf{n} = (\sin\theta, 0, \cos\theta)$, and averaged over the period L of the spiral. The only term that survives in the average is

$$m_3=\frac{\varepsilon h}{2\sqrt{2}}\frac{1}{L}\int_0^L(1-\cos^2\theta)\,dx \tag{7.11}$$

and can be expressed entirely in terms of quantities already considered, namely,

$$m_3=\frac{\varepsilon h}{2\sqrt{2}\,\gamma^2}\left(\gamma^2+\delta^2-\frac{2\pi d_\perp}{L}\right)\,,\qquad h<h_0\,, \tag{7.12}$$

to be completed with

$$m_3=\frac{\varepsilon h}{2\sqrt{2}}\,,\qquad h>h_0\,, \tag{7.13}$$

extracted from Eq. (6.5).

In order to make definite quantitative predictions, the preceding general results are restricted to the KSEA limit where $\alpha = d_\perp = 1$, $\varepsilon = 0.18$, and $\gamma^2 = 1 + h^2$, using the rationalized units defined from Eq. (5.10). The critical field (7.6) is then given by $h_0 = (\pi^2/4 - 1)^{1/2} = 1.21$ or $H_0 = 1.21\times1.68$ T = 2.04 T which is in reasonable agreement with the experimentally determined $H_c = 2.15$ T [19]. However, the currently predicted critical field $H_0 = 2.04$ T is significantly smaller than the critical field $H_2 = 2.9$ T obtained from the analysis of local stability of the commensurate state in Sec. 6. Therefore, the precise nature of the IC transition remains unclear at this point, an issue that will be addressed more carefully in Sec. 7C.

Nevertheless, we continue here the illustration of the physical picture based on the calculated spiral state. At zero field, we may set $d_\perp = 1 = \gamma$ in Eq. (7.9) to calculate the root $\delta^2 = 0.53$, while the corresponding period obtained from Eq. (7.8) is found to be $L = 6.50$. In

physical units $L = 6.50 \times 33.75$ Å $= 219$ Å which corresponds to about 37 lattice units along the x axis and thus provides an indication that the continuum approximation is reasonably justified. A related quantity is the incommensurability parameter $\zeta = \varepsilon / L = 0.18 / 6.50 = 0.027$. The angle of spin rotation over a distance $d = a/\sqrt{2}$ along the x axis is then given by $\Delta\theta = 2\pi\zeta = 9.7^{\circ}$, in agreement with experiment [15-19]. Actually, this cannot be taken as an independent confirmation of the theoretical prediction, because the observed $\Delta\theta$ was used as an input in order to determine the parameter $\varepsilon = D_{\perp}/J$.

Now, the field dependence of some quantities of key interest is calculated by first solving Eq. (7.9) with $d_{\perp} = 1$ and $\gamma^2 = 1 + h^2$ to obtain the root $\delta = \delta(h)$. The ground-state energy given by $w = (1 - \delta^2)/2$ for $h < h_0$ and $w = 1/2$ for $h > h_0$ is depicted by a solid line in Fig. 4(a) and exhibits an anomaly at the critical field $h_0 = 1.21$. The field dependence of the incommensurability parameter is calculated from

$$\frac{\zeta(h)}{\zeta(0)} = \frac{L(0)}{L(h)}, \qquad h < h_0, \tag{7.14}$$

where $\zeta(0) = 0.027$ and $L(0) = 6.50$ are the zero-field parameters already discussed, and is illustrated by a solid line in Fig. 4(b) where a comparison with experimental data is also made. The overall agreement is rough but may be viewed as satisfactory given that $T = 0$ theoretical predictions are compared to data taken at temperature $T = 2.4$ K that is relatively high compared to $T_N = 3.2$ K. Similarly, the field dependence of the $T = 0$ magnetization calculated from Eq. (7.12) and (7.13) is depicted by a solid line in Fig 5(a) and the corresponding susceptibility in Fig. 5(b) where we also include experimental data taken at $T = 2$ K [18]. Again, the significant depression and rounding of the observed susceptibility peak in the intermediate field region could possibly be attributed to a finite-temperature effect. The preceding analysis will be amended in Sec. 7C because of additional complications that arise in the intermediate region.

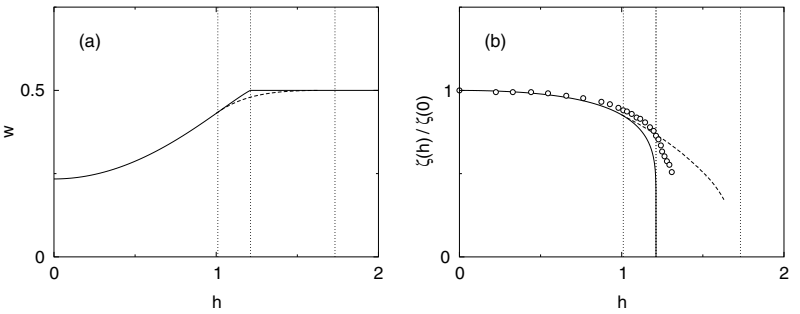

Fig. 4. $T = 0$ theoretical predictions for the field dependence of (**a**) the energy density w and (**b**) the incommensurability parameter ζ. Solid lines correspond to the flat spiral constructed in Sec. 7A and dashed lines to the nonflat spiral calculated in Sec. 7C. The three vertical dotted lines indicate the location of the three characteristic fields $h_1 = 1.01$, $h_0 = 1.21$, and $h_3 = 1.73$, in units of 1.68 T. Experimental data (open circles) measured at $T = 2.4$ K were extracted from Fig. 4 of Ref. [18].

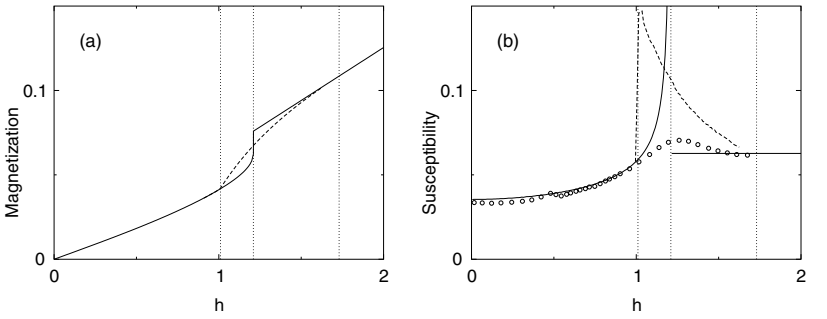

Fig. 5. $T = 0$ theoretical predictions for the field dependence of (**a**) the magnetization m_3 and (**b**) the susceptibility dm_3/dh, in rationalized units. Conventions are the same as in Fig. 4. Experimental data (open circles) measured at $T = 2$ K were extracted from Fig. 2 of Ref. [18].

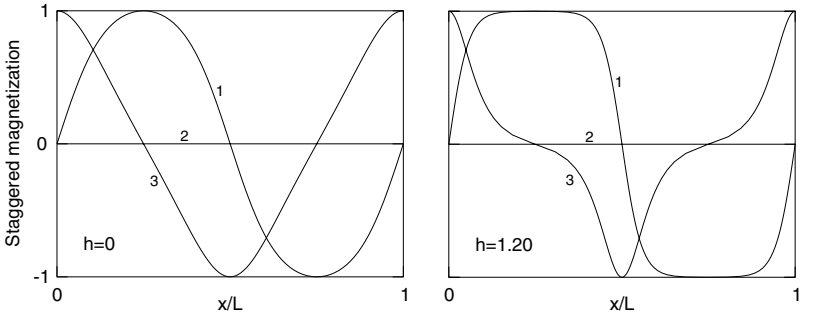

Fig. 6. Profile of the flat spiral discussed in Sec. 7A at zero field ($h=0$) and a field $h=1.20$ that is near the critical value $h_0=1.21$. The calculated period is $L=6.50$ and $L=11.34$, respectively. The three curves correspond to the three Cartesian components n_1, n_2, and n_3 of the staggered magnetization **n**.

To complete the description of the spiral state we illustrate in Fig. 6(a) the spatial dependence of the staggered magnetization at zero field. This configuration may be called a flat spiral because the order parameter **n** is confined in a single (xz) plane. In Fig. 6(b) we illustrate the flat spiral for a field $h = 1.20$ that is near the critical value $h_0 = 1.21$ and thus the staggered magnetization approaches the domain-wall configuration (7.4) within each half period. The resulting "soliton lattice" made of consecutive domain walls is indeed consistent with Dzyaloshinskii`s interpretation of the IC transition [11].

Finally, we return to the symmetry U(1) transformation of Eq. (6.3) which is applied to the special solution (7.1) to yield a family of degenerate ground-state configurations:

$$\Theta = \theta(x\,\cos\psi_0 + y\,\sin\psi_0)\,, \qquad \Phi = -\psi_0\,, \tag{7.15}$$

where ψ_0 is an arbitrary constant angle. In practice, the above degeneracy is broken by some small tetragonal anisotropy that is present in the real crystal [17] and pins the magnetic propagation vector along the x or the y axis. Such an anisotropy can be overcome by a relatively weak magnetic field applied in a direction perpendicular to the c axis and thus the symmetry transformation (7.15) acquires definite experimental significance to be discussed in Sec. 8.

B. Magnon spectrum

It is of obvious interest to describe theoretically the magnon excitations measured by inelastic neutron scattering [19]. Such a task is hindered by the great formal complexity of the calculation if one insists on employing the discrete Hamiltonian derived in Sec. 2. In contrast, the continuum field theory of Sec. 5 may be used for a relatively simple calculation of the low-energy magnon spectrum for any strength of the applied field and any direction of spin-wave propagation [22]. It is then possible to also study the local stability of the spiral phase and thus illuminate the precise nature of the IC phase transition.

The general strategy is identical to that followed in Sec. 6 for the discussion of the commensurate phase, but the calculation of the low-energy magnon spectrum in the spiral phase is significantly more complicated. We introduce new fields according to

$$\Theta = \theta + f\,, \qquad \Phi = \frac{g}{\sin\theta}\,, \tag{7.16}$$

where $\theta = \theta(x)$ is the profile of the spiral state given by Eq. (7.7) while $f=f(x, y, \tau)$ and $g=g(x, y, \tau)$ account for small fluctuations. The special rescaling chosen in the second equation is equivalent to working in a rotating frame [35] whose third axis is everywhere parallel to the direction of the background staggered magnetization $\mathbf{n} = (\sin\theta\,, 0, \cos\theta)$. The new fields (7.16) are introduced in the complete Lagrangian (6.7) which is then expanded to second order in f and g. The required algebra is lengthy but the final result for the corresponding linearized equations is sufficiently simple:

$$\begin{aligned} \ddot{f} - \Delta f + U_1 f &= 2h\cos\theta\ \dot{g} + 2d_\perp \sin\theta\ \partial_2 g\,, \\ \ddot{g} - \Delta g + U_2\ g &= -2h\cos\theta\ \dot{f} - 2d_\perp \sin\theta\ \partial_2 f\,, \end{aligned} \tag{7.17}$$

where

$$\begin{aligned} U_1 &= -\gamma^2\cos(2\theta)\,, \\ U_2 &= 2d_\perp\sqrt{\delta^2 + \gamma^2\cos^2\theta} - 2\gamma^2\cos^2\theta - \delta^2\,, \end{aligned} \tag{7.18}$$

are effective potentials that can be calculated for any desired set of parameters, on the basis of the calculation of the spiral state given is Sec. 7A.

We found it instructive to consider first the special case of spin-wave propagation along the x axis ($\partial_2 f = 0 = \partial_2 g$) at zero field ($h = 0$). This is actually the only case for which the low-energy spectrum was calculated starting from the discrete Hamiltonian in the KSEA limit

[19]. If we further perform the temporal Fourier transformation with frequency ω, Eqs. (7.17) reduce to

$$-f'' + U_1 f = \omega^2 f\,, \qquad -g'' + U_2 g = \omega^2 g\,, \tag{7.19}$$

where the prime denotes differentiation with respect to x. Therefore, in this special case, the eigenvalue problem is reduced to two decoupled one-dimensional (1D) Schrödinger-type equations with potentials U_1 and U_2 calculated from Eq. (7.18) at zero field. Also note that both potentials are periodic functions of 2θ and thus their period is actually $L/2$ where L is the period of the background spiral.

The eigenvalue problems (7.19) were numerically solved by standard Bloch analysis in Ref. [22]. The numerical procedure yields eigenfrequencies $\omega = \omega(q_1)$ as functions of Bloch momentum q_1. The latter can be restricted to the zone $[-2\pi/L, 2\pi/L]$, because the period of the potentials is $L/2$, or to the zone $[-\zeta, \zeta]$ where $\zeta = 0.027$ is the zero-field incommensurability parameter discussed in Sec. 7A and relative crystal momentum units are defined as in Sec. 6. Several low-lying eigenvalues ($E = \hbar\omega$) are illustrated in Fig. 7(a) using a reduced-zone scheme. Solid and dashed lines correspond to the first and second eigenvalue problems in Eq. (7.19) and are superimposed in the same paragraph for convenience. We also find it convenient to refer to the two types of modes as acoustic and optical. In either case, there is only one discernible gap that occurs between the first and second bands at the zone boundary. In the KSEA limit the calculated boundary gaps are 0.12 meV and 0.05 meV, respectively, while the absolute gap of the optical mode at the zone center is found to be 0.17 meV. All of the above theoretical predictions agree with those obtained in Ref. [19] by a different method. They also agree with experiment, except for the small (0.05 meV) gap that has not yet been resolved at zero field.

The same results are depicted in Fig. 7(b) using an extended-zone scheme. In fact, this figure displays two replicas of the acoustic mode centered at $\pm\,\zeta$. The need for two replicas follows from the structure of the dynamic correlation functions in the laboratory frame, rather than in the rotating frame actually used in the calculation of the magnon spectrum [19]. Our theoretical results in Fig. 7(b) are obviously consistent with experimental results obtained in the above reference via inelastic neutron scattering at zero field.

The main advantage of the present framework becomes apparent when one attempts to extend the preceding elementary calculation of the magnon spectrum to the general case of nonzero field and arbitrary direction of spin-wave propagation [22]. The external field h enters Eqs. (7.17) in two distinct ways. First, it affects the structure of the potentials U_1 and U_2 because the background spiral depends nontrivially on the applied field, as explained in Sec. 7A. Second, the field induces first-order time derivatives which couple the two linear equations (7.17). Additional coupling between the two equations appears in the case of arbitrary direction of propagation, because $\partial_2 f$ and $\partial_2 g$ no longer vanish. Altogether, we are faced with a nonstandard eigenvalue problem which was also solved in our recent work [22]. The theoretical predictions for the field dependence of the low-energy magnon spectrum first made in the above work were found to be in reasonable agreement with experimental data taken from Ref. [19]. However, some important new elements of the present theoretical analysis [22] had only vaguely been suggested by the original work [19] and thus need further experimental investigation.

The most important new element is yet another critical field

$$h_1 = \sqrt{2.02 d_\perp^2 - \alpha^2}\,, \tag{7.20}$$

which is also depicted by a solid line in the phase diagram of Fig. 3. The numerical factor 2.02 is a result of a detailed numerical investigation along the lines of Ref. [22]. The flat spiral constructed in Sec. 7A is locally stable only for $h < h_1$; i.e, below the critical field h_1 of Eq. (7.20) which is smaller than the field h_0 of Eq. (7.6) obtained through a Dzyaloshinskii-type interpretation of the IC transition. Also recall that the commensurate ground state is locally stable for $h > h_2$ where h_2 is the critical field of Eq. (6.12) which is greater than h_0. Therefore, our theoretical analysis directly suggests the existence of an intermediate field region $h_1 < h < h_2$ where neither the flat spiral nor the commensurate state is locally stable. It is thus necessary to reexamine the nature of the true ground state in this intermediate field region, as is done in Sec. 7C.

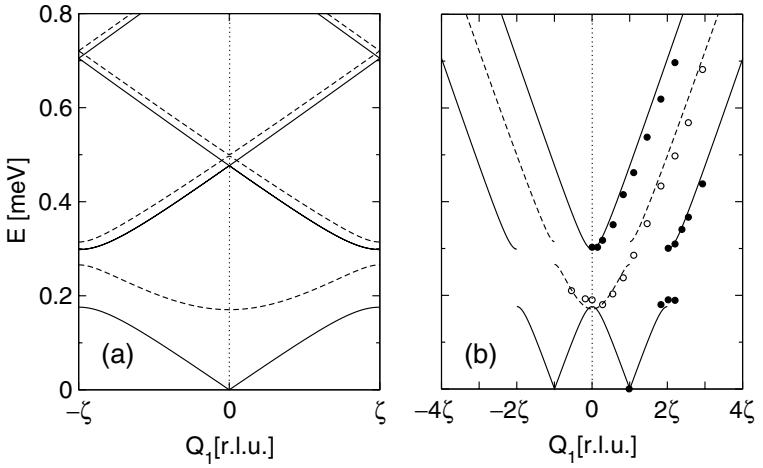

Fig. 7. Magnon spectrum for spin-wave propagation along the direction of the spiral (x axis) at zero field ($h = 0$). Solid and dashed lines distinguish between acoustic and optical modes. (**a**) The spectrum in a reduced-zone scheme and (**b**) the same spectrum in an extended zone scheme including two replicas of the acoustic mode centered at $\pm\zeta$ where $\zeta = 0.027$ is the zero-field incommensurability parameter. Experimental data (solid and open circles) were extracted from Fig. 5 of Ref. [19].

The present section is concluded with a summary of the three characteristic fields $h_1 < h_0 < h_2$ as predicted in the KSEA limit where $\alpha = d_\perp = 1$ and thus $h_1 = 1.01$, $h_0 = 1.21$, and $h_2 = 1.73$. In physical units $H_1 = 1.7$ T, $H_0 = 2$ T, and $H_2 = 2.9$ T. Hence an "intermediate phase" is predicted to occur in the field region 1.7 T < H < 2.9 T. Some experimental evidence for the existence of the lower critical field $H_1 = 1.7$ T is discussed in Refs. [18,19] and is in remarkable agreement with our theoretical prediction.

C. Intermediate phase

We now focus on the anticipated intermediate phase and examine its nature through a direct numerical minimization of the energy functional W of Eq. (6.4) where we insert the complete potential V taken from Eq. (6.1). The method of calculation is a relaxation algorithm formulated on the basis of a discretized form of the energy functional defined on a square grid. After long experimentation with 2D simulations, it progressively became apparent that the optimal configuration for $h > h_1$ is actually a 1D nonflat spiral characterized by a staggered magnetization whose three components n_1, n_2, and n_3 are all different than zero. Therefore, an accurate calculation of the nonflat spiral was eventually obtained by a relaxation algorithm applied directly to a 1D restriction of the energy functional assuming that the staggered magnetization **n** depends on the single coordinate x.

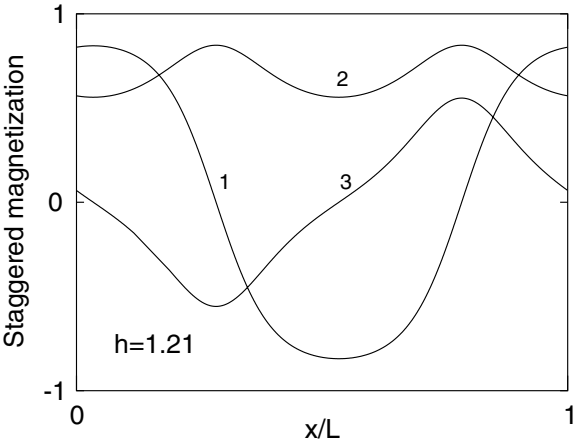

Fig. 8. Profile of the nonflat spiral discussed in Sec. 7C for a field $h = h_0 = 1.21$. The calculated period is $L = 8.84$. The three curves correspond to the three Cartesian components n_1, n_2 and n_3 of the staggered magnetization **n**.

Thus our numerical solution was carried out on a periodic 1D grid with specified length L, until a relaxed configuration was obtained with energy density $w = w(L)$. We then varied L to achieve the least possible energy for each field h and the corresponding optimal period $L = L(h)$. An important check of consistency is that the above algorithm reproduces the results for the flat spiral obtained analytically in Sec. 7A, but only when $h < h_1$. Instead, a nonflat spiral emerges as the optimal solution for $h > h_1$ and is illustrated in Fig. 8 for a field value deliberately chosen to be equal to the critical field h_0 of the Dzyaloshinskii-type IC transition. The nonflat spiral exists as a stationary point of the energy functional throughout the intermediate field region $h_1 < h < h_2$ and degenerates to the flat spiral $\mathbf{n} = (\sin\theta\,,\, 0,\, \cos\theta)$ near the lower critical field h_1, but to the commensurate state $\mathbf{n} = (\,0,\, 1,\, 0\,)$ polarized along the y axis near the upper critical field h_2. Actually, our calculation was not pushed all the way to

the critical field h_2 because of numerical difficulties that occur as the period grows to infinity. One should also stress that the nonflat spiral is here predicted to occur for a field applied strictly along the c axis and is not due to sample misalignment [18] or the presence of a transverse magnetic field [36].

The configuration of Fig. 8 may be viewed as a conical spiral that propagates along the x axis but nutates around the y axis. It is interesting that a simple conical spiral without nutation had been discussed theoretically in connection with the field-induced cholesteric-nematic phase transition in chiral liquid crystals [12] but has not yet been observed experimentally because its realization requires an anomalously small bend modulus [14]. In contrast, the parameters of $Ba_2CuGe_2O_7$ seem to favor the occurrence of the currently predicted intermediate phase.

In a sense, the intermediate phase smooths out the Dzyaloshinskii-type IC transition. This is apparent in the calculated energy of the nonflat spiral which is depicted by a dashed line in Fig. 3(a) and is smaller than the energy of both the flat spiral and the commensurate state throughout the intermediate region $h_1 < h < h_2$. Some smoothing is also apparent in the calculated field dependence of the period $L = L(h)$ which is inserted in Eq. (7.14) now applied for $h_1 < h < h_2$ to yield the results for the incommensurability parameter shown by a dashed line in Fig. 3(b). The same figure displays experimental data taken from Ref. [18] where they were analyzed in terms of the conventional IC transition based solely on a flat spiral. It should be noted that both the measured zero-field incommensurability parameter $\zeta(0) = 0.027$ and the experimental critical field $H_c = 2.15$ T were used as adjustable parameters in the theoretical analysis of Refs. [18,19] to obtain a reasonable overall fit. Yet the experimental data indicate some smoothing of the IC transition near the critical field. This fact is made apparent in our Fig. 3(b) where theoretical results for both the flat spiral (solid line) and the nonflat spiral (dashed line) are calculated using as input only the zero-field parameters given earlier in Eq. (5.10). The results of Fig. 3(b) cannot be interpreted as unambiguous evidence for the existence or absence of an intermediate phase, especially because the theoretically predicted critical fields could be tuned by considering anisotropy more general than KSEA ($\kappa \neq 0$).

Similarly, the $T = 0$ magnetization in the intermediate phase is calculated from

$$m_3 = \frac{\varepsilon h}{2\sqrt{2}} \frac{1}{L} \int_0^L (1 - n_3^2)\, dx\,, \qquad h_1 < h < h_2\,, \tag{7.21}$$

which is the analog of Eq. (7.11) except that n_3 is now the third component of the staggered magnetization in the nonflat spiral. The currently predicted partial smoothing of the IC transition is again apparent in the calculated magnetization shown by a dashed line in Fig. 4(a), but the corresponding result for the $T = 0$ susceptibility shown by a dashed line in Fig. 4(b) continues to overestimate the measured susceptibility in the intermediate field region. Perhaps the observed depression of the susceptibility peak is a finite-temperature effect because the experimental data were taken at the relatively high temperature $T = 2$ K compared to $T_N = 3.2$ K [18].

To summarize, the precise nature of the field induced IC transition in $Ba_2CuGe_2O_7$ is here predicted to be more complex than originally envisaged. The characteristic field h_0 of Eq. (7.6) obtained by Dzyaloshinskii`s argument based on domain-wall nucleation [11] is not

a true critical field. It is thus interesting to examine whether or not the upper critical field h_2 of Eq. (6.12) possesses a similar interpretation. In fact, it was shown in Ref. [22] that h_2 is the characteristic field below which the energy of the commensurate ground state can be lowered by vortex nucleation. It is then tempting to presume that the intermediate phase is characterized by the formation of a vortex lattice. However, we have not been able to calculate such a lattice with average energy density lower than that of the nonflat spiral.

8. IN-PLANE MAGNETIC FIELD

The physical picture was further probed experimentally [17] with an external field applied in some direction perpendicular to the c axis. For the moment, we assume that the field is applied along the y axis; $\mathbf{h} = (0, h, 0)$. The potential V of Eq. (5.8) reduces to

$$\begin{aligned} V = \frac{1}{2}\left[(\partial_1 \mathbf{n})^2 + (\partial_2 \mathbf{n})^2 + \alpha^2 n_3^2 + h^2 n_2^2 + d_\perp^2\right] \\ - d_\perp\left[(\partial_1 n_1 - \partial_2 n_2)\, n_3 - (n_1 \partial_1 - n_2 \partial_2)\, n_3\right] + h d_z n_1 \end{aligned} \tag{8.1}$$

and differs from the potential of Eq. (6.1) in several aspects. The strength $\alpha^2 = \kappa + d_\perp^2$ of the anisotropy along the third axis is now field independent, while the magnetic field induces a quadratic anisotropy of strength h^2 along the y axis and a peculiar linear anisotropy of strength hd_z along the x axis. The latter term is the only contribution that is directly proportional to the out-of-plane oscillating component ($\pm D_z$) of the DM vectors (2.3) and is absent in the theoretical analysis of Ref. [17].

On the assumption that the ground state is spatially uniform (commensurate) one finds two stationary points of V:

$$\mathbf{n} = (\pm 1, 0, 0)\ , \qquad w = \frac{1}{2}\left(d_\perp^2 \pm 2hd_z\right)\ , \tag{8.2}$$

where w is the corresponding energy density. Therefore, the least-energy commensurate state is now given by $\mathbf{n} = (-1, 0, 0)$ and is a candidate for the true ground state for sufficiently strong fields. To test the stability of this state, we relax the assumption of uniformity at least to the extent that the staggered magnetization is taken to depend on the single coordinate x, in order to take advantage of the Lifshitz invariant in Eq. (8.1), while it rotates in the xz plane, in order to eliminate the positive energy term $h^2 n_2^2$. In terms of the usual spherical parameters of Eq. (6.6) we again write $\Theta = \theta(x)$ and $\Phi = 0$. The potential (8.1) is then reduced to

$$V = \frac{1}{2}\left[\,(\theta' - d_\perp)^2 + \alpha^2 \cos^2\theta\,\right] + h d_z \sin\theta \tag{8.3}$$

and is significantly different from the potential (7.2) obtained earlier in the case of a field applied along the c axis.

Stationary point of the energy functional $W = \int V dx$ now satisfy the differential equation $\theta'' - \alpha^2 \sin\theta\cos\theta = h d_z \cos\theta$ whose first integral is given by

$$\theta'^2 - \alpha^2 \cos^2\theta - 2h d_z \sin\theta = C \equiv 2h d_z + \delta^2 . \tag{8.4}$$

Our choice of the integration constant C anticipates the fact that minimum energy is achieved for a positive value of the new constant δ^2. The actual configuration $\Theta = \theta(x)$ is then given by the implicit equation

$$x = \int_0^{\theta} \frac{d\vartheta}{\sqrt{\delta^2 + \alpha^2 \cos^2\vartheta + 2h d_z (1 + \sin\vartheta)}} \tag{8.5}$$

and the corresponding period is

$$L = \int_0^{2\pi} \frac{d\theta}{\sqrt{\delta^2 + \alpha^2 \cos^2\theta + 2h d_z (1 + \sin\theta)}} . \tag{8.6}$$

The average energy density $w = (1/L) \int_0^L V\, dx$ is minimized with respect to δ^2 when the latter satisfies the algebraic equation

$$\frac{1}{2\pi} \int_0^{2\pi} d\theta \sqrt{\delta^2 + \alpha^2 \cos^2\theta + 2h d_z (1 + \sin\theta)} = d_\perp \tag{8.7}$$

and the minimum energy density is then given by

$$w = \frac{1}{2} \left(d_\perp^2 - 2h d_z - \delta^2 \right) . \tag{8.8}$$

The spiral state just described exists and carries lower energy than that of the commensurate state **n** = (−1, 0, 0) of Eq. (8.2) for all fields for which Eq. (8.7) possesses a positive root δ^2. It is not difficult to see that this happens for sufficiently weak fields $h < h_c$ where the critical field h_c is obtained by setting $\delta^2 = 0$ in Eq. (8.8) to yield the algebraic equation

$$\frac{1}{2\pi} \int_0^{2\pi} d\theta \sqrt{\alpha^2 \cos^2\theta + 2h_c d_z (1 + \sin\theta)} = d_\perp . \tag{8.9}$$

At the critical field the energy of the spiral is given by Eq. (8.8) applied for $\delta^2 = 0$ and is thus equal to the energy of the state **n** = (−1, 0, 0) of Eq. (8.1). For $h > h_c$ the incommensurate spiral ceases to exist and the commensurate state **n** = (−1, 0, 0) may be thought to be the true ground state. Hence we again predict the occurrence of a Dzyaloshinskii-type IC transition provided that $d_z \neq 0$.

In the KSEA limit ($\alpha = d_\perp = 1$) a numerical solution of Eq. (8.9) yields

$$h_c = 0.316/d_z \tag{8.10}$$

which makes it clear that the IC transition is suppressed in the limit $d_z \to 0$, because $h_c \to \infty$, and the spiral reduces to a field independent state that coincides with the zero field flat spiral constructed in Sec. 7A. For $d_z = 0$ the zero field spiral is the ground state for any strength of a field applied in a direction perpendicular to the c axis. In fact, no appreciable field dependence of the spiral was detected in the actual experiment [17] for in-plane fields in the range $H < 2$ T or $h < 2/1.68 = 1.2$. One must thus conclude that $h_c = 0.316/d_z > 1.2$ or $d_z = \sqrt{2}\, D_z/\varepsilon J < 0.26$ and $D_z/J < 0.03$ which sets a rough upper bound for the magnitude of the out-of-plane component of the DM vectors (2.3).

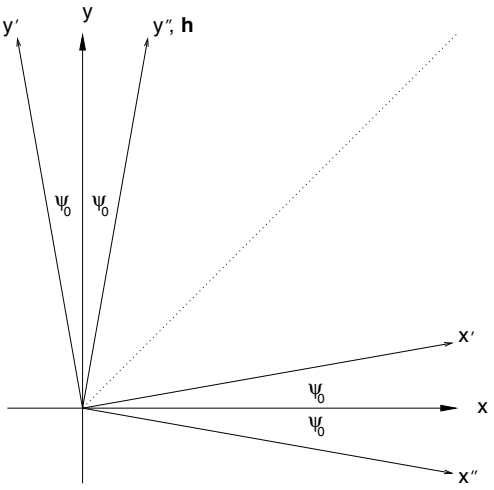

Fig. 9. Illustration of the bisection rule for an in-plane magnetic field **h** applied along the y'' axis. The spiral propagates along the x' axis and the staggered magnetization **n** rotates in the $x''z$ plane.

To complete the picture we discuss next the case of a magnetic field applied in an arbitrary direction in the basal (xy) plane. At this point, it is useful to recall the $U(1)$ transformation (6.3) which, in the absence of an in-plane field, yields a family of degenerate ground-state configurations given by Eq. (7.15). The effect of an in-plane field is to break the $U(1)$ symmetry and thus select a specific member of the above family in order to eliminate the positive energy term $(\mathbf{n}\cdot\mathbf{h})^2$ in Eq. (5.8). Hence for a field applied along the y axis the staggered magnetization **n** is confined in the xz plane and the spiral propagates along the x

axis, as discussed earlier in this section. Now, when the field is applied at an angle $-\psi_0$ with respect to the y axis, the in-plane component of **n** forms an angle $-\psi_0$ with the x axis, so that $\mathbf{n}\cdot\mathbf{h} = 0$. Accordingly, the direction of the spiral propagation forms an angle ψ_0 with the x axis as a result of the underlying $U(1)$ symmetry transformation given in Eq. (7.15). The emerging picture is schematically illustrated in Fig. 9 where the spiral propagation vector points along the x' axis, the magnetic field **h** is applied along the y'' axis, and the staggered magnetization **n** rotates in the $x''z$ plane. The special direction $\mathbf{e}_1 + \mathbf{e}_2$ indicated by a dotted line always bisects the angle formed by **h** and the spiral propagation vector. For the special choice $\psi_0 = 45°$ the directions of the magnetic field and the spiral propagation coincide and the resulting configuration is a screw-type spiral. Otherwise, the shape of **n** is the same with the one calculated earlier in this section for the special choice $\psi_0 = 0$.

The "bisection rule" described above was found to be in agreement with experiment [17] for in-plane fields with strength $H \geq 0.5$ T. For weaker fields, reorientation of the spin structure is apparently inhibited by a small tetragonal anisotropy that drops out of the leading-order continuum approximation but is present in the real crystal and breaks the $U(1)$ symmetry, albeit mildly. However, the effect of such an anisotropy is overcome by a sufficiently strong in-plane field ($H \geq 0.5$ T) because of the significant energy gain obtained by the reorientation of the spin structure to conform with the bisection rule. Incidentally, the bisection rule is valid for any strength of the out-of-plane component of the DM anisotropy d_z, including $d_z = 0$.

A complete theoretical analysis of the IC transition induced by an in-plane field at finite d_z can be carried out by methods similar to those discussed in Sec. 7 for the case of a field applied along the c axis. The details of such an analysis may be found in Ref. [23] where the analog of the phase diagram of Fig. 3 is constructed for an in-plane field and is shown to also entail an "intermediate phase". The phase diagram for an arbitrary field direction is thus predicted to be significantly more complicated than advocated in the existing literature [25,36]. Unfortunately, further progress is prevented at present by the lack of a direct experimental estimate of the out-of-plane component of the DM anisotropy in $Ba_2CuGe_2O_7$.

9. MAGNETIC PROPERTIES OF $K_2V_3O_8$

While the basic magnetic properties of $K_2V_3O_8$ may again be explained in terms of an isotropic 2D antiferromagnet [37], a clear ordering phase transition occurs at temperature $T_N = 4$ K below which anisotropy becomes essential to understanding the observed magnetic structure. In particular, there has been unambiguous experimental evidence [24] for field induced spin-flop and spin-reorientation transitions using modest field strengths in the region $H \leq 1$ T.

$K_2V_3O_8$ is composed of magnetic V^{4+}-O_5 pyramids, nonmagnetic V^{5+}-O_4 tetrahedra, and interstitial K^+ ions, which crystallize in a tetragonal unit cell with space group $P4bm$ and lattice constants $a = b = 8.870$ Å and $c = 5.215$ Å [38]. The magnetic lattice formed by the V^{4+} ions with spin $s = 1/2$ is isomorphic to the magnetic lattice of $Ba_2CuGe_2O_7$ shown in Fig. 1. Throughout this section, we shall again neglect interlayer spin interactions and thus describe the magnetic properties of $K_2V_3O_8$ in terms of a suitable 2D anisotropic Heisenberg model defined within each layer.

Although the space group of $K_2V_3O_8$ is different than that of $Ba_2CuGe_2O_7$, it leads to an effective spin Hamiltonian which is very similar to the one constructed in Sec. 2. Using notation established in Sec. 2, the symmetric exchange interaction is now described by matrices of the form

$$J_I = \begin{pmatrix} J_1 & 0 & 0 \\ 0 & J_2 & J_4 \\ 0 & J_4 & J_3 \end{pmatrix}, \qquad J_{II} = \begin{pmatrix} J_2 & 0 & -J_4 \\ 0 & J_1 & 0 \\ -J_4 & 0 & J_3 \end{pmatrix},$$
$$J_{III} = \begin{pmatrix} J_1 & 0 & 0 \\ 0 & J_2 & -J_4 \\ 0 & -J_4 & J_3 \end{pmatrix}, \qquad J_{IV} = \begin{pmatrix} J_2 & 0 & J_4 \\ 0 & J_1 & 0 \\ J_4 & 0 & J_3 \end{pmatrix}, \tag{9.1}$$

and the antisymmetric interaction by the DM vectors

$$\mathbf{D}_I = D_\perp \mathbf{e}_2 + D_z \mathbf{e}_3, \qquad \mathbf{D}_{II} = -D_\perp \mathbf{e}_1 + D_z \mathbf{e}_3,$$
$$\mathbf{D}_{III} = D_\perp \mathbf{e}_2 - D_z \mathbf{e}_3, \qquad \mathbf{D}_{IV} = -D_\perp \mathbf{e}_1 - D_z \mathbf{e}_3, \tag{9.2}$$

which differ from the corresponding results for $Ba_2CuGe_2O_7$ quoted in Eqs. (2.2) and (2.3) only by some minor sign changes. In particular, the KSEA limit obtained by inserting Eqs. (9.1) and (9.2) in Eq. (3.1) leads to relations that are identical to those quoted in Eq. (3.2).

The associated nonlinear σ model is obtained from the one derived in Sec. 5 by the simple substitution $y \to -y$. To be sure, rationalized parameters are again defined by Eqs. (5.4) and (5.5), the magnetization $\mathbf{m}$ is still given by Eq. (5.8), the free Lagrangian $\mathcal{L}_0$ is identical to that included in Eq. (5.9), but the potential V occurring in the latter equation should be now replaced by

$$V = \frac{1}{2}(\partial_1 \mathbf{n} - d_\perp \mathbf{e}_2 \times \mathbf{n})^2 + \frac{1}{2}(\partial_2 \mathbf{n} + d_\perp \mathbf{e}_1 \times \mathbf{n})^2$$
$$+ \frac{1}{2}\kappa n_3^2 + \frac{1}{2}(\mathbf{n} \cdot \mathbf{h})^2 + (\mathbf{h} \times \mathbf{d}_z) \cdot \mathbf{n}\,. \tag{9.3}$$

Furthermore, a substantial difference concerns the nature of anisotropy. For the description of $Ba_2CuGe_2O_7$ we assumed an easy-plane anisotropy $\kappa + d_\perp^2 \equiv \alpha^2 > 0$. Instead, the observed magnetic properties of $K_2V_3O_8$ require an easy-axis anisotropy:

$$\kappa + d_\perp^2 \equiv -\alpha^2 < 0\,, \tag{9.4}$$

which is impossible to occur in the KSEA limit $\kappa = 0$, as incorrectly stated in Ref. [24] and further discussed in Sec. 9A below. In other words, $K_2V_3O_8$ is an example where a significant deviation from the KSEA limit needs to be invoked albeit consistently with the underlying space group *P*4*bm*.

A. Commensurate magnetism

The available experimental evidence [24] is consistent with a ground state that is uniform (commensurate) on each sublattice and may thus be calculated from a two-spin cell Hamiltonian. The latter turns out to be identical to that of Eq. (4.1) inspite of the minor sign changes discussed in connection with Eqs. (9.1) and (9.2). An important issue is the nature of anisotropy as determined by the algebraic sign of the parameter Δ defined in Eq. (4.6). As mentioned already, the observed magnetic properties of $K_2V_3O_8$ suggest an easy-axis anisotropy ($\Delta < 0$). Hence the KSEA limit is now inappropriate because it would lead to an easy-plane anisotropy ($\Delta > 0$) in view of Eq. (4.7). This conclusion is at variance with a claim made by the authors of Ref. [24] in connection with the KSEA Hamiltonian quoted in their Eq. (3). Nevertheless, their overall conclusions are correct because they were actually derived from the more general cell Hamiltonian of Eq. (2) supplemented by the assumption of easy-axis anisotropy.

Our task is then to find the classical minimum of the two-spin Hamiltonian (4.1) for $\Delta < 0$ and various field strengths and orientations. A completely analytical treatment is possible in the limit of weak anisotropy where one may instead invoke the associated σ model. For static commensurate states of current interest one may further neglect all temporal and spatial derivatives in Eqs. (5.8) and (9.3) to write

$$\begin{aligned} \mathbf{m} &= \frac{\varepsilon}{2\sqrt{2}} \left[\mathbf{n} \times \mathbf{d}_z + \mathbf{h} - (\mathbf{n} \cdot \mathbf{h}) \mathbf{n} \right] , \\ V &= \frac{1}{2} \left[d_\perp^2 - \alpha^2 n_3^2 + (\mathbf{n} \cdot \mathbf{h})^2 \right] + (\mathbf{h} \times \mathbf{d}_z) \cdot \mathbf{n} . \end{aligned} \tag{9.5}$$

The magnetization **m** is thus calculated in terms of the staggered magnetization **n** which is in turn determined as the minimum of the effective potential V for any given applied magnetic field **h**.

For a field applied along the c axis the potential reduces to $V = 1/2 \left[d_\perp^2 + (h^2 - \alpha^2) n_3^2 \right]$ and its minimum is calculated by inspection. For a sufficiently weak field the minimum occurs at

$$\mathbf{n} = \pm \mathbf{e}_3 , \quad \mathbf{m} = 0 ; \qquad h < h_{sf} = \alpha , \tag{9.6}$$

which correspond to the usual Néel states polarized along the c axis. A spin-flop transition occurs at the critical field h_{sf} above which minimum energy is achieved by the configuration

$$\mathbf{n} = \mathbf{e}_1 , \quad \mathbf{m} = \frac{\varepsilon}{2\sqrt{2}} (-d_z \mathbf{e}_2 + h \mathbf{e}_3) ; \qquad h > h_{sf} , \tag{9.7}$$

which is defined up to an arbitrary azimuthal rotation and corresponds to the usual canted spin-flop configuration. Here we concentrate on the magnetic moment induced in a direction that is parallel to the applied field to write $m_c \equiv m_3$ or

$$m_c = \begin{cases} 0\,, & h < h_{sf} = \alpha\,, \\ \dfrac{\varepsilon h}{2\sqrt{2}}\,, & h > h_{sf}\,, \end{cases} \tag{9.8}$$

which summarizes the description of the spin-flop transition induced by a field applied along the (easy) *c* axis.

Next we consider the case of an in-plane magnetic field applied along, say, the *y* axis. The effective potential is then given by $V = 1/2\,(d_\perp^2 - \alpha^2 n_3^2 + h^2 n_2^2) + h d_z n_1$ and is minimized by a staggered magnetization that is confined in the *xz* plane in order to suppress the positive energy term $h^2 n_2^2$. One may thus write Eqs. (9.5) in the form

$$\mathbf{n} = \sin\theta\,\mathbf{e}_1 + \cos\theta\,\mathbf{e}_3\,, \qquad \mathbf{m} = \frac{\varepsilon}{2\sqrt{2}}\,(h - d_z \sin\theta)\,\mathbf{e}_2\,,$$
$$V = \frac{1}{2}\left(d_\perp^2 - \alpha^2 \cos^2\theta\right) + h d_z \sin\theta\,. \tag{9.9}$$

For a sufficiently weak field the potential V achieves its minimum when $\sin\theta = -h d_z/\alpha^2$. As the field increases from zero, the staggered magnetization **n** rotates continuously within the *xz* plane from a Néel state $\mathbf{n} = \mathbf{e}_3$ polarized along the *c* axis at zero field to a state $\mathbf{n} = -\mathbf{e}_1$ polarized along the *x* axis at and above the critical field $h_{sr} = \alpha^2/\,d_z$. The corresponding magnetization **m** remains parallel to the applied in-plane field and its magnitude is actually independent of the specific direction of the field within the basal plane. We may thus write $m_{ab} \equiv m_2$ or

$$m_{ab} = \begin{cases} \dfrac{\varepsilon h}{2\sqrt{2}}\left(1 + \dfrac{d_z^2}{\alpha^2}\right), & h < h_{sr} = \alpha^2/d_z\,, \\ \dfrac{\varepsilon}{2\sqrt{2}}\,(h + d_z)\,, & h > h_{sr}\,, \end{cases} \tag{9.10}$$

which summarizes the spin-reorientation transition that takes place in the presence of an applied in-plane field.

In practice, it is useful to reparametrize Eqs. (9.8) and (9.10) in a way that the two critical fields h_{sf} and h_{sr} are used as independent parameters instead of the anisotropy parameters α and d_z. We may also restore physical units to write the field induced magnetic moment per V^{4+} ion as

$$m_c = \begin{cases} 0\,, & H < H_{SF}\,, \\ \dfrac{g_c^2 \mu_B^2 H}{8J}\,, & H > H_{SF}\,, \end{cases} \tag{9.11}$$

for a field H applied along the c axis, and

$$m_{ab} = \begin{cases} \left[1 + \left(\dfrac{g_c H_{SF}}{g_{ab} H_{SR}}\right)^2\right] \dfrac{g_{ab}^2 \mu_B^2 H}{8J}, & H < H_{SR}, \\ \dfrac{g_c^2 \mu_B^2 H_{SF}^2}{8J H_{SR}} + \dfrac{g_{ab}^2 \mu_B^2 H}{8J}, & H > H_{SR}, \end{cases} \tag{9.12}$$

for a field applied in some direction within the basal *ab* plane. The independent parameters are now the two critical fields H_{SF} and H_{SR} for the spin-flop and spin-reorientation transitions, together with the gyromagnetic ratios g_c and g_{ab} for the corresponding field orientations, and the exchange constant J. In this parametrization, the spin value s does not enter explicitly and the exchange constant J merely sets the overall scale.

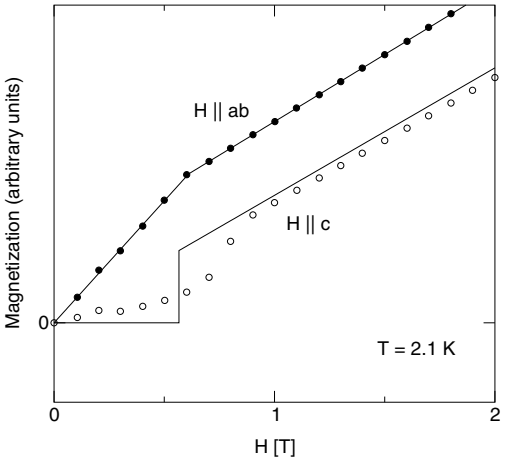

Fig. 10. Comparison of low-temperature (T = 2.1 K < T_N = 4 K) magnetization data taken from Fig. 2(b) of Ref. [24] with theoretical predictions based on Eqs. (9.11) and (9.12). Open circles correspond to a field applied along the *c* axis and solid circles to field applied in some direction within the basal (*ab*) plane. The critical fields for the corresponding spin-flop and spin-reorientation transitions are estimated to be H_{SF} = 0.57 T and H_{SR} = 0.61 T.

A comparison of the preceding theoretical results with experiment [24] is made in Fig. 10. We have employed the gyromagnetic ratios g_c = 1.922 and g_{ab} = 1.972 abstracted from EPR measurements [39], while the critical fields H_{SR} = 0.61 T and H_{SF} = 0.57 T were both determined from the requirement that Eq. (9.12) provide an optimal fit of the magnetization

measured in the presence of an in-plane field. The critical field H_{SF} thus determined was then employed in Eq. (9.11) to predict the magnetization for a field applied along the *c* axis. The resulting overall agreement with experiment is satisfactory, given that the observed partial smoothing of the spin-flop transition may be a finite-temperature effect.

The above description needs to be completed with two important remarks. First, the calculated critical fields are not terribly inconsistent with the values $H_{SR} = 0.65$ T and $H_{SF} = 0.85$ T abstracted from neutron diffraction [24]. Second, the magnetization data displayed in Fig. 10 are quoted in "arbitrary units" because we have been unable to ascertain the precise meaning of the magnetization unit employed in Fig. 2(b) of Ref. [24], whereas an attempt to contact some of the authors of the above reference received no attention. As a result, the exchange constant *J* that provides the overall scale in Eqs. (9.11) and (9.12) remains undetermined. It would be interesting to obtain an estimate of *J* from the $T = 2.1$ K magnetization data of Fig. 10, in order to compare it with the value $J = 12.6$ K extracted from high-temperature (T = 3-300 K) data fit to corresponding theoretical predictions within the 2D isotropic Heisenberg model [37].

B. Incommensurate magnetism

It is obviously interesting to theoretically examine conditions under which incommensurate magnetism could be observed in $K_2V_3O_8$. We shall only consider the case of a field applied along the *c* axis for which the effective potential (9.3) reduces to

$$V = \frac{1}{2}\left[(\partial_1 \mathbf{n})^2 + (\partial_2 \mathbf{n})^2 + \left(h^2 - \alpha^2\right) n_3^2 + d_\perp^2\right] - d_\perp\left[(\partial_1 n_1 + \partial_2 n_2)\, n_3 - (n_1 \partial_1 + n_2 \partial_2)\, n_3\right] \tag{9.13}$$

and differs from the potential encountered in the discussion of $Ba_2CuGe_2O_7$, Eq. (6.1) , in two respects. The anisotropy term $(h^2 - \alpha^2) n_3^2$ now favors an easy axis at low fields, and the symmetry transformation (6.3) becomes ordinary $U(1)$ whereby both the spatial coordinates and the staggered magnetization undergo an azimuthal rotation by a common angle ψ_0 instead of $\pm\psi_0$. Inspite of these differences, the appearance of a Lifshitz invariant in Eq. (9.13) suggests that incommensurate states are possible under suitable conditions.

The analysis is similar to that carried out in Sec. 7 and will not be presented here in any detail except to summarize the main conclusions in the form of the $T = 0$ phase diagram of Fig. 11. The three critical fields encountered in Sec. 7 are now modified by the simple replacement $\alpha^2 \to -\alpha^2$ to account for easy-axis anisotropy:

$$h_1 = \sqrt{2.02\, d_\perp^2 + \alpha^2}, \quad h_0 = \sqrt{\frac{\pi^2}{4} d_\perp^2 + \alpha^2}, \quad h_2 = \sqrt{4\, d_\perp^2 + \alpha^2}, \tag{9.14}$$

and a new critical field appears, namely

$$h_3 = \sqrt{\alpha^2 - \frac{\pi^2}{4} d_\perp^2}\,, \tag{9.15}$$

below which the ground state is Néel ordered along the c axis. In the special limit $d_\perp = 0$, h_3 reduces to the critical field $h_{\rm sf} = \alpha$ discussed in Sec. 9A in connection with the spin-flop transition. For $d_\perp \neq 0$, the spin-flop transition is preempted by an incommensurate flat spiral phase in the region between h_3 and h_1, and an intermediate nonflat spiral phase in the region between h_1 and h_2. In the region above h_2 the the ground state is a commensurate spin-flop state.

Therefore, the present lack of experimental evidence for incommensurate magnetism in $K_2V_3O_8$ may simply be due to an anomalously small in-plane component of the DM anisotropy $d_\perp \ll \alpha$. In such a limit, an incommensurate phase would appear only in a narrow field region near the critical field required for the observed spin-flop transition, in agreement with a conclusion reached by the authors of Ref. [25]. Incidentally, the same authors provided phase diagrams for easy-plane and easy-axis anisotropy which are simpler versions of our phase diagrams in Figs. 3 and 11, because the intermediate phase that had been predicted earlier in Ref. [22] was not incorporated in the analysis of Ref. [25].

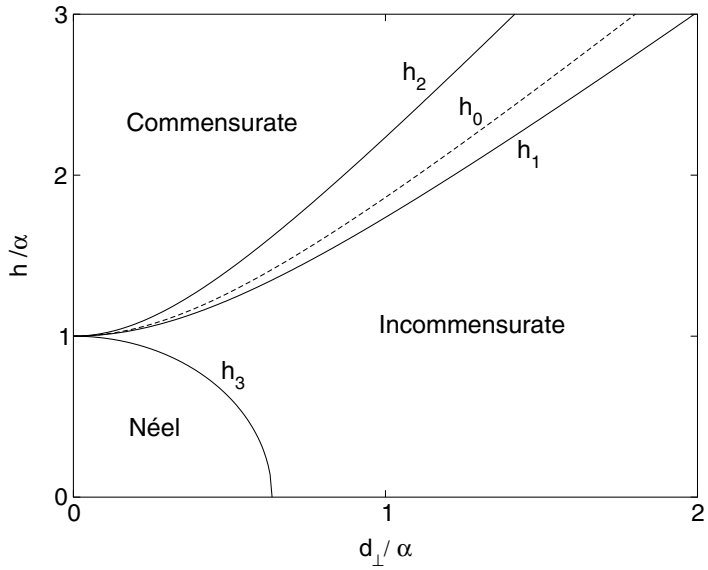

Fig. 11. $T = 0$ phase diagram for easy-axis anisotropy $\kappa + d_\perp^2 = -\alpha^2$ and a field of strength h applied along the c axis. The three characteristic fields h_1, h_0, and h_2 are given by Eq. (9.14) and the field h_3 by Eq. (9.15).

10. CONCLUSION

We have thus presented a field theoretical description of the commensurate and incommensurate magnetism observed in the layered antiferromagnets $Ba_2CuGe_2O_7$ and $K_2V_3O_8$. The physical picture derived is sufficiently complete to provide the basis for further refinements along the lines briefly outlined in this concluding section.

The field induced IC phase transition in $Ba_2CuGe_2O_7$ is theoretically predicted to be more complex than originally envisaged by Dzyaloshinskii [11] thanks to the appearance of an intermediate phase described by the nutating conical spiral calculated in Sec. 7C. Although some evidence for an intermediate phase is available [18], a clear identification requires additional experimental work guided by the present theoretical predictions. The situation is less clear in $K_2V_3O_8$ where interesting spin-flop and spin-reorientation transitions have been observed [24] but provided no evidence for incommensurate magnetism. The analysis of Sec. 9 may provide the necessary theoretical background in order to identify experimental conditions under which incommensurate magnetism may also be observed in $K_2V_3O_8$.

The original experimental work on $Ba_2CuGe_2O_7$ was recently extended to the study of the doped compound $Ba_2Cu_{1-x}Co_xGe_2O_7$ [40,41]. Incommensurate magnetism ceases to occur for $x > 0.05$, even at zero field, as a result of strong pinning due to the magnetic Co^{2+} ions. Assuming that the space group remains the same ($P\bar{4}2_1m$) in the extreme limit $x = 1$, the spin $s = 3/2$ magnetic compound $Ba_2CoGe_2O_7$ is again described by the Heisenberg Hamiltonian of Sec. 2 except that a single-ion anisotropy of the form $A(S^z)^2$ is now possible, while symmetry requires that the anisotropy constant A is the same for all magnetic sites. Magnon dispersions measured by inelastic neutron scattering [41] suggest a large positive value for A which destroys incommensurate magnetism, a conclusion that is consistent with the phase diagram of Fig. 3 applied for zero field ($h = 0$) and $\alpha \gg d_\perp$. It may thus be interesting to further study the IC transition as a function of anisotropy A at zero external magnetic field.

We must also comment on the two basic approximations adopted in the present work. The validity of the continuum approximation is justified by the fact that anisotropy is sufficiently weak and thus leads to magnetic domains (spirals) with relatively large periods. For example, in $Ba_2CuGe_2O_7$ the driving anisotropy constant is $\varepsilon = D_\perp / J = 0.18$ and leads to a spiral with a period approximately equal to 37 lattice spacings at zero field. The error induced by the continuum approximation is then estimated to be at the level of a few percent ($\varepsilon^2 \approx 0.03$) and is certainly acceptable. Nevertheless, discreteness effects are important to understanding the observed pinning of magnetic domains along the crystallographic (1,1,0) or $(1,\bar{1},0)$ directions; i.e., along the x or y axes of Fig. 1. This issue was phenomenologically addressed in Ref. [17] by invoking an additional tetragonal anisotropy. In principle, a more detailed investigation may reveal that the discrete Heisenberg Hamiltonian constructed in Sec. 2 already contains a mechanism that explains the observed lattice pinning of magnetic domains.

A more serious issue is the validity of the classical approximation. As mentioned already, the present approach is equivalent to the usual semiclassical $1/s$ expansion restricted to leading order. The omitted quantum corrections are estimated to be of the order of 20% in this 2D problem [1] and are offset in part by the fact that all parameters are consistently estimated within the classical approximation. Nevertheless, we have described a quantum ($T = 0$) phase transition by a semiclassical method whose validity is expected to be marginal

in two dimensions. Therefore, a proper treatment of the quantum IC transition is still an open problem. In this respect, one should mention that quantum phase transitions induced by deformations of the 2D isotropic Heisenberg model are of high current interest [42].

We are grateful to Stavros Komineas for an earlier collaboration on this subject [22] and related discussions. The present work was supported in part by an EU RTN program (HPRN-CT-2002-00315).

REFERENCES

[1] M. A. Kastner, R. J. Birgeneau, G. Shirane, and Y. Endoh, Rev. Mod. Phys. 70 (1998) 897.
[2] T. Thio, T. R. Thurston, N. W. Preyer, P. J. Picone, M. A. Kastner, H. P. Jenssen, D. R. Gabbe, C. Y. Chen, R. J. Birgeneau, and A. Aharony, Phys. Rev. B 38, (1988) 905.
[3] T. Thio, C. Y. Chen, B. S. Freer, D. R. Gabbe, H. P. Jenssen, M. A. Kastner, P. J. Picone, and R. J. Birgeneau, Phys. Rev. 41 (1990) 231.
[4] T. Thio and A. Aharony, Phys. Rev. Lett. 73 (1994) 894.
[5] J. Chovan and N. Papanicolaou, Eur. Phys. J. B 17 (2000) 581.
[6] I. E. Dzyaloshinskii, Sov. Phys. JETP 5 (1957) 1259.
[7] T. Moriya, Phys. Rev. 120 (1960) 91.
[8] Y. Ishikawa, K. Tajima, D. Bloch, and M. Roth, Solid State Comunn. 19 (1976) 525.
[9] Y. Ishikwa and M. Arai, J. Phys. Soc. Jpn. 53 (1984) 2726.
[10] B. Lebech, J. Bernhard, and T. Flertoft, J. Phys.: Condens. Matter 1 (1989) 6105.
[11] I. E. Dzyaloshinskii, Sov. Phys. JETP 19 (1964) 960; 20 (1965) 223; 20 (1965) 665.
[12] P. G. de Gennes, Solid State Commun. 6 (1968) 163.
[13] R. B. Meyer, Appl. Phys. Lett. 14 (1969) 208.
[14] P. G. de Gennes and J. Prost, *The Physics of Liquid Crystals*, Clarendon Press, Oxford (1995), p. 288.
[15] A. Zheludev, G. Shirane, Y. Sasago, N. Koide, and K. Uchinokura, Phys. Rev. B 54 (1996) 15163.
[16] A. Zheludev, S. Maslov, G. Shirane, Y. Sasago, N. Koide and K. Uchinokura, Phys. Rev. Lett. 78 (1997) 4857.
[17] A. Zheludev, S. Maslov, G. Shirane, Y. Sasago, N. Koide and K. Uchinokura, D. A. Tennant, and S. E. Nagler, Phys. Rev. B 56 (1997) 14006.
[18] A. Zheludev, S. Maslov, G. Shirane, Y. Sasago, N. Koide and K. Uchinokura, Phys. Rev. B 57 (1998) 2968.
[19] A. Zheludev, S. Maslov, G. Shirane, I. Tsukada, T. Masuda, K. Uchinokura, I. Zaliznyak, R. Erwin, and L. P. Regnault, Phys. Rev. B 59 (1999) 11432.
[20] J. Jensen and A. R. Mackintosh, *Rare-Earth Magnetism: Structure and Excitations*, Clarendon, Oxford (1975).
[21] Yu. A. Izyomov, Sov. Phys. Usp. 27 (1984) 845.
[22] J. Chovan, N. Papanicolaou, and S. Komineas, Phys. Rev. B 65 (2002) 064433.
[23] J. Chovan, PhD Thesis (2002).

[24] M. D. Lumsden, B. C. Sales, D. Mandrus, S. E. Nagler, and J. R. Thompson, Phys. Rev. Lett. 86 (2001) 159.
[25] A. N. Bogdanov, U. K. Roessler, M. Wolf, and K.-H. Müller, Phys. Rev. B 66 (2002) 214410.
[26] L. Shekhtman, O. Entin-Wohlman, and A. Aharony, Phys. Rev. Lett. 69 (1992) 836.
[27] L. Shekhtman, A. Aharony, and O. Entin-Wohlman, Phys. Rev. B 47 (1993) 174.
[28] T. A. Kaplan, Z. Phys. B 49 (1983) 313.
[29] T. Yildirim, A. B. Harris, A. Aharony, and O. Entin-Wohlman, Phys. Rev. B 52 (1995) 10239.
[30] A. F. Andreev and V. I. Marchenko, Sov. Phys. Usp. 23 (1980) 21.

[31] F. D. M. Haldane, Phys. Lett. A 93 (1983) 464; Phys. Rev. Lett. 50 (1983) 1153; 61 (1988) 1029.
[32] S. Chakravarty, B. I. Halperin, and D. R. Nelson, Phys. Rev. B 39 (1989) 2344.
[33] V. G. Bar`yakhtar, M. V. Chetkin, B. A. Ivanov, and S. N. Gadetskii, *Dynamics of Topological Magnetic Solitons - Experiment and Theory*, Springer Verlag, Berlin (1994).
[34] S. Komineas and N. Papanicolaou, Nonlinearity 11 (1998) 265.
[35] B. A. Ivanov, A. K. Kolezhuk, and G. M. Wysin, Phys. Rev. Lett. 76 (1996) 511.
[36] A. N. Bogdanov and A. Shestakov, Low Temp. Phys. 25 (1999) 76.
[37] Guo Liu and J. E. Greedan, J. Solid State Chem. 114 (1995) 499.
[38] J. Galy and A. Carpy, Acta Crystallogr. B 31 (1975) 1794.
[39] M. Pouchard *et al*., Bull. Soc. Chim. Belg. 97 (1988) 241.
[40] T. Sato, T. Masuda, and K. Uchinokura, Physica B 329-333 Part 2 (2003) 880.
[41] A. Zheludev, T. Sato, T. Masuda, K. Uchinokura, G. Shirane, and B. Roessli, Phys. Rev. B 68 (2003) 024428.
[42] T. Senthil, A. Vishwanath, L. Balents, S. Sachdev, and M. P. A. Fisher, Science 303 (2004) 1490.

MAGNETISM IN HIGHLY ANISOTROPIC BORATES: EXPERIMENT AND THEORY

M.A. Continentino, J.C. Fernandes, R.B. Guimarães, B. Boechat and A. Saguia

Instituto de Física, Universidade Federal Fluminense,
Av. Litorânea, s/n, Campus da Praia Vermelha
Niterói, 24.210-340, RJ, Brazil.

1.INTRODUCTION

Highly anisotropic organic and inorganic materials have been the object of intensive studies in the last decades. High T_c superconductivity, quantum Hall effect, charge and spin density waves, disordered magnetic chains, plateau magnetization, solitons and many other phenomena are examples of the physical richness presented by this large class of compounds. It is not surprising that anisotropic materials became so attractive for solid state physicists.

The $3d$ metal anhydrous borates, in which the boron ions have trigonal coordination forming the orthoborate $(BO_3)^{3-}$ or pyroborate $(B_2O_5)^{4-}$ anion groups, present high internal anisotropy revealed by the morphology of their crystals which appear as needles or plaquettes. The anhydrous borates possessing the orthoborate group are called orthoborates and frequently oxy-borates since, in these compounds, there are one or two oxygen ions per chemical formula not directly bound to the boron ions. The oxy-borates present more than ten different crystallographic structures among which the warwickites and ludwigites are the easiest to be synthesized. The borates possessing the pyroborate

groups are simply called pyroborates. They form a smaller class of compounds, also easy to be synthesized, but having all the oxygen ions within the borate groups. The borates for which the boron ions have tetrahedral coordination do not present any remarkable anisotropy. We may claim therefore that the high anisotropy in the anhydrous borates is a consequence of the boron trigonal coordination. It must be remarked that, since the borate anions in the anhydrous borates are isolated, they do not form polymerized subsystems as chains or planes. Chains or planes of anions groups appear in other borates as well as in many silicates in which the $(SiO_4)^{4-}$ or $(Si_2O_7)^{6-}$ tetrahedra form low-dimensional subsystems [1]. The number of oxy-borates with different crystallographic structure and chemical composition is very large so that the study of their physical properties is far from being exhausted. We may mention, as an example, the physical properties of bi-dimensional oxy-borates which have never been investigated. In this chapter we present an overview of the main magnetic properties of warwickites and ludwigites as well as those of two pyroborates. For the detailed properties of these compounds the reader will be referred to the original papers. Only the borates whose magnetic properties were investigated are addressed. The theoretical aspects of some specific phenomena presented by these borates will be discussed.

2.THE ANHYDROUS BORATES

There are three main groups of anhydrous borates: the warwickite group, the ludwigite or pinakiolite group and the pyroborate group. The respective general chemical formulae are: $M^{3+}M'^{2+}OBO_3$, $M^{3+}(M'^{2+})_2O_2BO_3$ and $M^{2+}M'^{2+}B_2O_5$ where M and M' represent different metals. If $M = M'$ the borate is said to be $homo - metallic$, otherwise it is $hetero - metallic$. There are also smaller groups of orthoborates and mixed ortho-pyroborates which will not be considered here. In any anhydrous borate the metals M and M' are found within an oxygen octahedra and every metal site of each structure may be randomly occupied by M or M' with different probabilities. For this reason hetero-metallic anhydrous borates are always disordered.

2.1 The Warwickites

Table 1 presents the symmetry space groups for the warwickites. All the hetero-metallic warwickites belong to the same space group [6]. The schematic structure of the warwickites projected on the plane ab is shown in Fig. 1. We can observe, in this figure, parallelograms which are orthogonal sections of substructures, similar to ribbons, indefinitely extended along the c axis. Such ribbons are formed by oxygen octahedra packed in the hexagonal form and sharing edges in such a way that three of their vertices lie on each one of the larger faces of the ribbons. These octahedra give rise to four columns, along the ribbons, and their centers define two types of equivalent crystallographic sites:

those on the border (sites 2) and those on the middle of the ribbons (sites 1). These sites form a triangular lattice and are randomly occupied by M or M' as shown in Fig. 2.

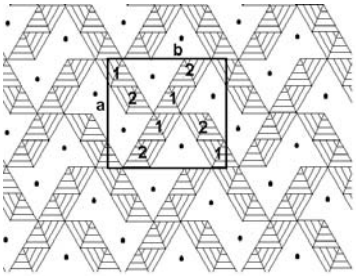

Figure 1: The structure of the warwickites projected in the plane ab. The sides a and b of the unitary cell and the crystallographic sites 1 and 2 are shown. The full circles represent the boron ions [6].

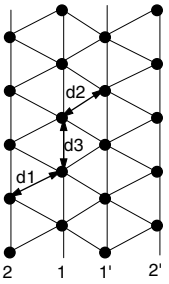

Figure 2: The internal structure of one ribbon. The full circles represent the metal ions. The numbers stand for the crystallographic site correspondent to each column and the d's are the intermetallic distances [7].

2.2 The Ludwigites

The ludwigite or pinakiolite group includes several crystalline structures under the general chemical formula given above. The more complex structures are stabilized by impurities. Table 2 gives the space group and one correspondent typical chemical composition for each structure belonging to this group. The schematic structure of the ludwigites *Pbam* projected on the plane ab is shown in Fig. 3. The zig-zag walls, called F walls by Norrestam and Bovin [15], have an hexagonal internal structure. However, the shortest distances between metals are found within the three column wall, also called C wall, formed by

Table 1: Space group of symmetry for the synthetic warwickites. The hetero-metallic warwickites have all the same space group.

Compound	*space group*	*ref.*
$MgScOBO_3$	$Pnam$	[2]
Mn_2OBO_3	$P2_1/n$	[3]
Fe_2OBO_3	$Pmcn$ *above* $317K$	[4, 5]
Fe_2OBO_3	$P2_1/c$ *below* $317K$	[4, 5]

columns of the crystallographic sites 4-2-4. Within these walls the metal sites form a three leg ladder rectangular lattice (see Fig. 4).

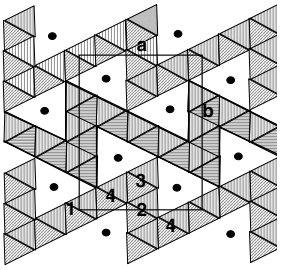

Figure 3: The structure of the ludwigites *Pbam* projected on the *ab* plane. The sides a and b of the unit cell and the numbers of the metal sites are shown. The full circles represent the boron ions [8].

2.3 The Pyroborates

The two pyroborates whose magnetic properties have been studied are the homo-metallic $Mn_2B_2O_5$ [17] and the hetero-metallic $MnMgB_2O_5$ [17, 18, 19]. Both are electrically insulating. In Fig. 5 it is shown the schematic structure of the pyroborates projected in the plane *bc*. In this figure, the ribbons and the anion groups $(B_2O_5)^{4-}$ appear clearly. It is to be remarked that the ribbons do not "touch" as in the warwickites.

3.MAGNETIC PROPERTIES

Wiedenmann et al. [20, 21] have probably been the first authors to point out the existence of quasi one-dimensional interactions in oxy-borates when studying the magnetic properties of $MgFeOBO_3$ and $Mg_2FeO_2BO_3$. However, the experimental and theoreti-

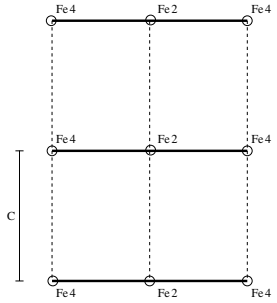

Figure 4: The internal structure of one C wall formed by three columns correspondent to sites 4-2-4. Such structure is called a three leg ladder [16].

Table 2: Space group of symmetry and chemical composition for synthetic (*) and mineral compounds with general chemical formula $M^{3+}(M'^{2+})_2O_2BO_3$.

name	*chemical formula*	*s.g.*	*ref.*
ludwigite$(*)$	$Co_3O_2BO_3$	$Pbam$	[8]
ludwigite$(*)$	$Cu_2FeO_2BO_3$	$P2_1/c$	[9]
hulsite	$Mg_{.64}(Fe^{2+})_{1.46}(Fe^{3+})_{.67}(Sn^{4+})_{.20}O_2BO_3$	$P2/m$	[10]
Pinakiolite	$Mg_{1.68}(Mn^{2+})_{.09}Mn^{3+}(Al,Fe,Mn)_{.11}BO_5$	$C2/m$	[11]
Orthopinakiolite	$Mg_{1.42}(Mn^{2+})_{.43}(Mn^{3+})_{.88}(Fe^{3+})_{.22}BO_5$	$Pnnm$	[12]
Takeuchiite	$Mg_{1.59}(Mn^{2+})_{.42}(Mn^{3+})_{.78}(Fe^{3+})_{.19}(Ti^{4+})_{.01}BO_5$	$Pnnm$	[13]
Blatterite	$Mg_{1.33}Mn_{1.44}Fe_{.05}Sb_{.17}O_2BO_3$	$Pnnm$	[14]

cally supported existence of random magnetic chains in oxy-borates was firstly shown by Fernandes et al. in the warwickite $MgTiOBO_3$ [22]. These authors verified that the temperature dependences of the susceptibility and magnetization in this oxy-borate are the same as those in the one-dimensional organic compounds based on the $TCNQ$ molecule, as reported by Boulaevskii et al. [23]. In this way the warwickite $MgTiOBO_3$ was the first inorganic compound found to present random quantum magnetic chain type of behavior. Its electronic structure has been theoretically investigated by Matos et al. [24] and by Marcucci et al. [25] and its low dimensionality has been confirmed. All the studied hetero-metallic borates, with boron in trigonal coordination, present similar magnetic behavior.

The homo-metallic borates have not an uniform behavior. The pyroborate $Mn_2B_2O_5$ exhibits the more interesting consequence of quasi one-dimensional magnetic interactions: its magnetization curve presents several inflection points indicating a hierarchy of such interactions [17]. In turn, the only known homo-metallic warwickites, Mn_2OBO_3 and Fe_2OBO_3, do not present any evidence of low dimensional magnetic interactions [26]. Charge ordering and magnetism seems to be dissociated in the homo-metallic borates ex-

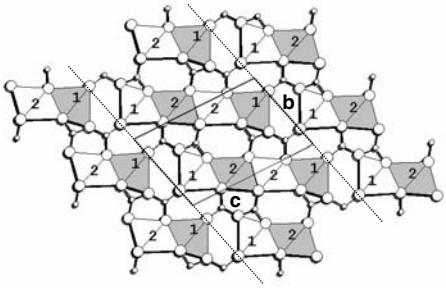

Figure 5: The structure of the pyroborate projected in the plane *bc*. We notice the ribbons, the borate groups and the sides *b* and *c* of the unit cell. The largest circles indicate oxygen ions while the smallest ones indicate the boron ions [18].

ception, perhaps, in the iron ludwigite $Fe_3O_2BO_3$ whose magnetic susceptibility presents an anomaly in the temperature region where a structural phase transition occurs [16]. As will be seen below, the low temperature phase associated to this transition presents charge density waves or, what is the same, structural anisotropy and long range charge ordering.

3.1 Hetero-metallic Borates

The hetero-metallic borates are naturally disordered materials since each metal crystalline site may be occupied by any one of the two metals which appear in the chemical formula. Both these metals may be magnetic (3*d* metals) but in the majority of the studied hetero-metallic borates only one metal is magnetic. This disorder generates a spectrum of intensities for the exchange and super-exchange interactions between the magnetic ions. In highly anisotropic borates such spectrum yields to disordered quantum magnetic chain type of behavior. The magnetic properties of the hetero-metallic borates show clearly the characteristic power law behavior associated with these random chains whatever is the respective crystalline structure: warwickite, ludwigite or pyroborate. The magnetic susceptibilities of the hetero-metallic warwickites and pyroborates depend very similarly on the temperature. For sufficiently high temperatures these materials are paramagnetic and obey the Curie-Weiss law with antiferromagnetic exchange interaction between nearest neighbors. As temperature is lowered, a short range interaction appears within the ribbon since k_BT approaches the intra-ribbon exchange energy between magnetic ions.

In this temperature range the susceptibility is larger than that given by the Curie-Weiss law and depends on the temperature as a power law. This is the temperature range for which the magnetic behavior of the system is that of a random magnetic chain. Further decreasing temperature there is eventually a spin glass transition at T_{sg} when the interaction between ions in adjacent chains becomes larger than k_BT. This transition is essentially a tri-dimensional (3D) phenomenon involving the whole system. This is the case in hetero-metallic warwickites and pyroborates. The spin glass nature of the transition is evident from the frequency dependence of the cusp in the a.c. susceptibility curve at T_{sg}. Fig. 6 and Fig. 7 show the magnetic susceptibility of $MgTiOBO_3$ [22] and $MgVOBO_3$ [27] respectively. The cusp at 6 K in the $MgVOBO_3$ curve indicates a spin-glass freezing. For $MgTiOBO_3$ no transition has been found down to 300 mK [28].

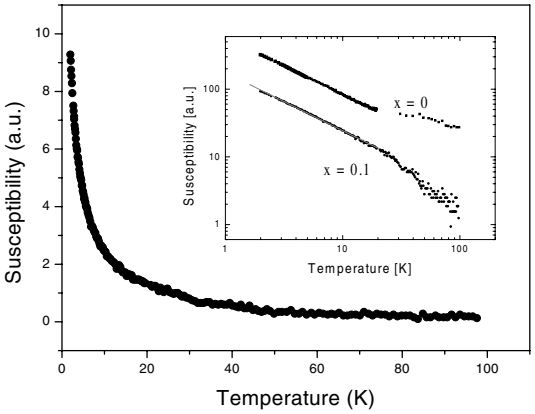

Figure 6: a.c. susceptibilities of the $Mg_{1-x}Ti_{1+x}OBO_3$ warwickites as a function of temperature for x=0 and x=0.1. The inset shows the power law behavior [22].

Bulaevskii et al. [23] developed a theory to account for the magnetic susceptibility χ and specific heat C temperature dependences of spin$-1/2$ random magnetic chains present in compounds based on the $TCNQ$ molecules. They also found an expression for the applied field dependence of the magnetization m in the field region where $k_BT << g\mu_BH << J$. In this inequality J is the highest exchange interaction in the chain. According to these authors:

$$\chi \propto T^{-\alpha} \tag{1}$$

$$C \propto T^{1-\alpha} \tag{2}$$

and

$$m \propto H^{1-\alpha} \tag{3}$$

where α is a weakly temperature dependent parameter. The above equations characterize the thermodynamic behavior of random spin$-1/2$ magnetic chains. Later on in this

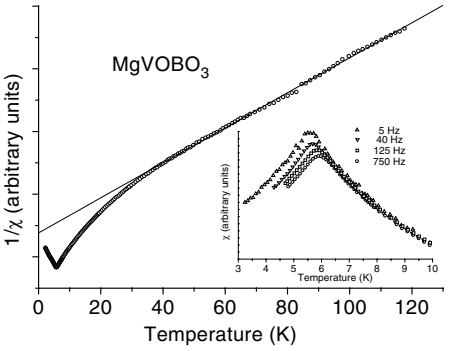

Figure 7: a.c. susceptibility of powdered $MgVOBO_3$ as a function of temperature for a frequency of 125 Hz and an alternating field of 10 Oe. The cusp at $T_{sg} = 6$ K is associated with a spin-glass transition. The inset on a logarithmic scale shows the power-law behavior of the susceptibility for $T > T_{sg}$ [27].

chapter we shall discuss in detail the physical nature of the power law dependence of these thermodynamic quantities and the case of random magnetic chains with spins larger than 1/2. In Table 3 are listed the studied hetero-metallic warwickites and pyroborates with respective relevant magnetic parameters.

In the iron ludwigites, if the divalent metal is magnetic, each metallic subsystem orders at different temperatures allowing the coexistence of magnetic order and paramagnetism. This is the case of $Ni_2FeO_2BO_3$ [29] and $Cu_2FeO_2BO_3$ [30]. The homo-metallic ludwigite $Fe_3O_2BO_3$ also present two different critical temperatures. This may be clearly seen in the Mössbauer spectra shown in Fig. 8 [31]. This compound will be discussed in detail below. In Table 4 are listed the iron ludwigites with the ordering temperatures of the iron and of the divalent metal subsystems. These are T_{iron} and T_{div}, respectively.

Table 3: Spin glass temperature, and the alpha parameter for hetero-metallic warwickites and pyroborates.

Compound	$T_{sg}(K)$	α	$ref.$
$MgTiOBO_3$	< 0.3	0.83	[22, 28]
$MgVOBO_3$	6	0.54	[27]
$MgCrOBO_3$	6.5	0.66	[7]
$MgFeOBO_3$	11	0.54	[7]
$ScNiOBO_3$	6	0.55	[7]
$ScMnOBO_3$	2.7	0.50	[7]
$MnMgB_2O_5$	0.6	0.56	[19]

Table 4: Ordering temperatures for the metallic subsystems in iron ludwigites. T_{iron} stands for the iron subsystem and T_{div}. for the divalent metal subsystem

Compound	$T_{iron}(K)$	$T_{div}(K)$	$ref.$
$Mg_2FeO_2BO_3$	10	$--$	[32]
$Fe_2FeO_2BO_3$	112	70	[31]
$Ni_2FeO_2BO_3$	106	46	[29]
$Cu_2FeO_2BO_3$	60	40	[30]

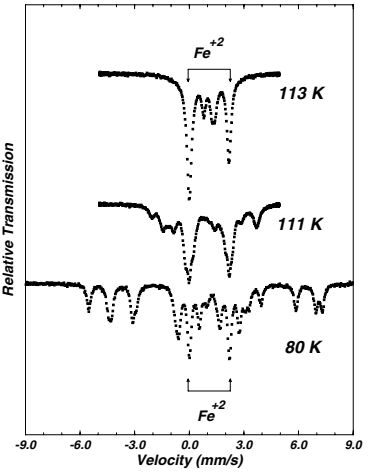

Figure 8: Mössbauer spectra of $Fe_3O_2BO_3$ at selected temperatures above and below T_iron [31].

The hetero-metallic pyroborate $MnMgB_2O_5$ behaves essentially as an hetero-metallic warwickite. Its T_{sg} is however much lower ($\approx$ 600 mK) [19] since, in this compound, the ribbons do not touch.

3.2 Homo-metallic Borates

The homo-metallic borates, with different ions of the same metal, present electrical conductivity and long-range charge ordering which is associated, in general, with a structural transition. In this case the metal is necessarily a $3d$ metal so that such borates are magnetic. In the case of identical ions, as in the pyroborate $Mn_2B_2O_5$, the material

Table 5: Structural transition and magnetic ordering temperatures for the homo-metallic borates.

Compound	$T_{struc}(K)$	$T_{mag}(K)$	T'_{mag}	$ref.$
$Mn_2B_2O_5$	$---$	23.3	$--$	[17]
Fe_2OBO_3	317	155	$--$	[5, 33]
Mn_2OBO_3	> 300	$104, 26$	$--$	[26, 34]
$Fe_3O_2BO_3$	283	112	70	[16, 31]

is electrically insulating and does not present any structural transition. The compound $Mn_2B_2O_5$ is an ordinary antiferromagnet with no net magnetization below its ordering temperature since there is no ESR signal in the ordered phase [17]. It presents a magnetization curve, measured in single crystals, showing some inflection points which indicate the intra-ribbons and inter-ribbons exchange values. Its magnetic ordering configuration is not yet known. The two known homo-metallic warwickites have magnetic critical temperatures much larger than the hetero-metallic spin glass critical temperatures. Their magnetic order configurations are not very simple: L-type ferrimagnetism in Fe_2OBO_3 [5, 33] and a complex ordering pattern in Mn_2OBO_3 presenting considerable frustration [34]. The last studied homo-metallic borate is the iron ludwigite $Fe_3O_2BO_3$. Its magnetic behavior is very intricate [31, 35] and its specific heat is rigorously linear between 70 K and 200 K [36]. Its internal anisotropy becomes evident through its needle shaped single crystals. There is a structural transition at 283 K and the low temperature phase presents charge density waves along the crystal c axis which is the needles axis. It must be remarked that the crystals of the pyroborate $Mn_2B_2O_5$ and of the ludwigite $Fe_3O_2BO_3$ are clearly needle shaped attaining easily more than 2 mm in length. For the homo-metallic warwickites their crystals are so small that it is impossible to determine clearly their morphology with the only aid of an optical microscope. This is compatible with the absence of low-dimensional features in their properties. Table 5 shows some magnetic parameters of the homo-metallic borates.

4.CHARGE ORDERING AND STRUCTURAL TRANSITION

As pointed out before, the homo-metallic oxy-borates have two different ions of the same metal. An ordered configuration of such ions, simultaneous to a structural phase transition, appears in these compounds as the temperature is lowered below a characteristic temperature T_c. The ordered charge configuration is different in each compound so that different mechanisms were considered responsible for the respective ordering processes.

The structure of the warwickite Mn_2OBO_3 can be considered to be a distorted modification of the orthorhombic warwickite structure. Following Norrestam et al. [3], the distortions, apparently caused by Jahn-Teller effects induced by the Mn^{3+} ions, remove the mirror symmetry of the parent undistorted warwickite. As a consequence, its space group is the monoclinic $P2_1/n$. The bond distances and calculated bond valence sums

indicate that, in the charge ordered state, the trivalent manganese ions are located in the two inner columns of the ribbons so that the divalent ones are in the two outer columns [3]. The probable T_c is not known for this compound since X-ray diffraction measurements have not been performed above room temperature.

Attfield et al. [4, 5] observed that the homo-metallic warwickite Fe_2OBO_3 presents a charge ordered phase below $T_c = 317$ K in which the divalent and trivalent iron ions are equally distributed over the structurally distinct iron sites 1 and 2 sown in Fig. 1. Above T_c the structure is orthorhombic with space group $Pmcn$ and below this temperature the space group is the monoclinic $P2_1/c$. These authors suggest that, in this case, the ordering mechanism is the electrostatic repulsion.

The homo-metallic ludwigite $Fe_3O_2BO_3$, as the warwickites, also presents a structural phase transition. In this case $T_c = 283$ K [16]. The high temperature space group is the orthorhombic $Pbam$ (n^o 55) and below T_c the space group is the orthorhombic $Pbnm$ (n^o 62). As the temperature goes below T_c, the only important change in the structure appears within the three leg ladders in the C walls (see section 2.2). The columns of sites 2 are zig-zag distorted, as seen in Fig. 9, so that the c edge of the unit cell is doubled relatively to the high temperature phase. Mössbauer Spectroscopy indicates that, below room temperature, the ions Fe^{2+} in sites 2 share electrons with ions Fe^{3+} in sites 4 so that $Fe^{2.5+}$ ions appear [37, 38]. Latgé and Continentino [39] proposed that this sharing is performed between site 2 and the nearest site 4a so that a transverse charge density wave arises along the c axis. These authors have shown that, if the ladder is viewed as a background of localized Fe^{3+} ions where the extra electrons of the Fe^{2+} ions are itinerant in a tight-binding band with infinite local repulsion, the distortion of the ladder lowers the total electronic energy. The magnetic character of the ions involved in the charge density wave has led Whangbo et al. [40] to suggest a magnetic mechanism as the cause of the structural instability of $Fe_3O_2BO_3$.

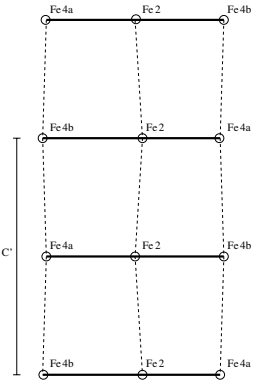

Figure 9: The three leg ladder which constitutes the C wall at $T < T_c$ [16].

5.RANDOM MAGNETIC CHAINS

The results on the magnetic properties of the oxy-borates presented in the previous sections provide a strong motivation to investigate theoretically these materials. The actual low dimensional structures which are relevant for the understanding of the magnetic behavior of the oxy-borates are ladders. In the case of the warwickites, four leg ladders in the ribbons (see Fig. 2) and for the ludwigites, three leg ladders (see Fig. 4). The Hamiltonian we will consider is the Heisenberg model describing local moments with spin$-S$ on the sites of a ladder interacting mostly through super-exchange interactions. This is appropriate since the $d-d$ overlap is not very significant in these materials although alternative approaches have been proposed [25, 40]. For the purpose of describing the magnetic properties of the oxy-borates, a localized Heisenberg model is adequate. Since in the hetero-metallic materials the occupation of these sites is random, this gives rise to a distribution of magnetic couplings. The properties of random Heisenberg ladders have been the subject of intense studies in the last years [41, 42, 43]. Mostly of these investigations have concentrated in the case of the spin$-1/2$, two leg ladder (2LL) and the spin$-1/2$ zig-zag ladder (ZZL) [42, 43]. The latter is topologically equivalent to single chains with nearest and next-nearest neighbors interactions. However, both ladders map into a random single chain problem, either with half-integer or integer spins. Additionally, the $2LL$ and zig-zag ladders lead to effective low energy models with only nearest neighbor interactions [42]. We may expect these results to hold for ladders with an arbitrarily finite number of legs for sufficiently low temperatures or energy scales. Consequently, the study of quantum random chains is essential for understanding the magnetic properties of low dimensional oxy-borates. Notice that for the pure case with no disorder, spin$-1/2$ ladders with an even number of legs map into the spin-1 chain problem while those with an odd number of legs map into the spin$-1/2$ case [41].

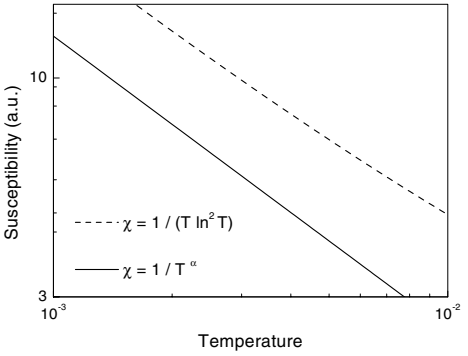

Figure 10: Susceptibility as a function of temperature comparing the power law behavior with a temperature independent exponent ($\alpha = 0.7$) and the random singlet phase result.

The nature of the low energy phases found in random Heisenberg chains and consequently in ladders are mainly of four types,

- A random singlet phase which is typical of random Heisenberg antiferromagnetic spin$-1/2$ chains. This phase is associated with an infinite randomness fixed point and low temperature thermodynamic properties characterized by power law behavior with exponents which depend weakly on temperature. The magnetic susceptibility $\chi(T) \propto T^{-\alpha}$, the specific heat $C/T \propto T^{1-\alpha}$ and the magnetization m as a function of the external magnetic field H varies as, $m(H) \propto H^{1-\alpha}$. These expressions with a temperature dependent exponent $\alpha(T)$ are useful representations of the actual temperature dependence of these quantities in the random singlet phase. For the magnetic susceptibility this is, $\chi \propto 1/(T \ln^2 T)$ and the free energy $F \propto T^2/(\ln^2 T)$.

- A Griffiths phase which is also characterized by power law behavior of the thermodynamic quantities, as in the previous case. It is distinguished from the random singlet phase by the fact that the relevant exponents depend on the distance δ to an infinite randomness quantum critical point, i.e., to the amount of disorder in the system. The susceptibility in the Griffiths phase is given by, $\chi(T) \propto T^{1/Z_\kappa(\delta)-1}$, where Z is the *dynamic exponent*. The specific heat in this phase is given by, $C(T)/T \propto T^{-1+1/Z_\kappa(\delta)}$ and for small magnetic fields H, the magnetization, $m \propto H^{1/Z_\kappa(\delta)}$. The dynamic exponent Z assumes the values $Z = \infty$ at the infinite randomness fixed point, i.e., at the random singlet phase ($\delta = 0$) and $Z = 1$ at the border of the Griffiths phase ($|\delta| = \delta_G$). The dynamic exponent is obtained from the *first gap distributions* [44] that saturate at low energies in the form, $P(-\log \Delta) \sim \Delta^{1/Z}$ for $\Delta \to 0$.

- A large spin (LS) phase characteristic of random magnetic chains with both ferromagnetic and antiferromagnetic interactions [45]. For weak disorder this phase shows universal behavior with a Curie like divergence of the magnetic susceptibility, $\chi(T) \propto 1/T$ and a specific heat that vanishes as, $C \propto T^{1/Z}|\ln T|$ with a constant dynamic exponent $Z \approx 0.44$. For strong randomness Z starts to vary with disorder but the magnetic susceptibility is still Curie-like. This phase is relevant for the antiferromagnetic zig-zag ladders which for strong and random next nearest neighbors interactions eventually map into a single chain problem with ferro and antiferromagnetic couplings. In the case of the oxy-borates the interactions are antiferromagnetic. There is in these materials, at high temperatures, a linear temperature dependent susceptibility but always with a finite negative paramagnetic Curie temperature, such that, this behavior can not be attributed to a LS phase.

- There is also for weak disorder a random dimer, Haldane-like gapped phase with vanishing susceptibility or still regions of the phase diagram where the dynamic exponent Z is constant [42].

It should also be noticed that experimentally it is not an easy matter to distinguish between the random singlet phase from the Griffiths phase. In Figure 10 we show a schematic plot of the magnetic susceptibility to illustrate this point. On the other hand the

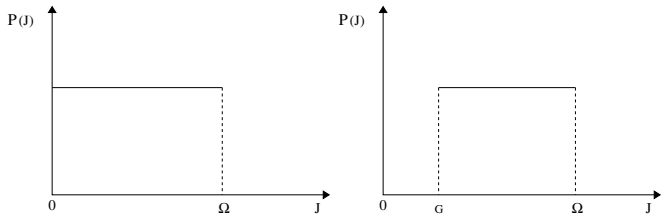

Figure 11: Initial distributions of interactions used in the renormalization group calculations. In the strong disorder case $G = 0$.

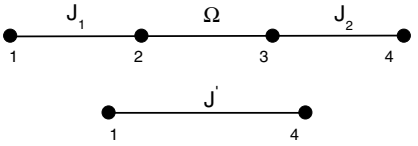

Figure 12: The MDH elimination procedures. Ω is the largest interaction in the chain. The strongest coupled pair of spins, 2 and 3 is eliminated giving rise to an effective interaction J' between spins 1 and 4.

LS phase is clearly characterized by the Curie-like behavior of the magnetic susceptibility. Having established that the low temperature phases of random magnetic ladders are similar in nature to those of random single chains we present below a study of the phase diagrams of the latter.

The random exchange Heisenberg antiferromagnetic chain (REHAC) plays a fundamental and paradigmatic role in the study of disordered quantum systems. Their study was initially motivated by experimental results in disordered organic chain materials which presented peculiar behavior [23]. Essentially, a magnetic susceptibility which diverges, at low temperatures, as a power law of temperature with an exponent $\alpha < 1$. The initial theoretical approaches to this problem associated this behavior with a distribution of exchange couplings with similar power law dependence, $P(J) \propto J^{-\alpha}$. A breakthrough from the theoretical side was the introduction by Ma, Dasgupta and Hu (MDH) [46] of a perturbative renormalization group method to treat the random Heisenberg chain. The REHAC system is defined by the following Hamiltonian for a chain of L spins:

$$H = \sum_{i=1}^{L-1} J_i \vec{S}_i . \vec{S}_{i+1}, \tag{4}$$

where $\vec{S}_i$ are spin$-1/2$ operators and J_i are positive random nearest neighbor interactions, taken from a distribution $P(J_i)$ with a cut-off Ω (see Fig. 11).

The MDH method consists in identifying the pair of spins with the strongest coupling in the random chain and eliminating it by considering the interaction with the neighboring spins of this pair as a perturbation. This procedure generates new couplings J' between

the two spins neighboring the eliminated pair, as shown in Fig. 12, and consequently the form of the distribution $P(J)$ is modified. One also gains a contribution to the free energy of the system from the eliminated pair. This process is then successively applied until a single pair of spins remains. The new effective coupling is given by,

$$J' = \frac{1}{2}\frac{J_1 J_2}{\Omega}. \tag{5}$$

Along the RG procedure, *independent of the initial distribution* $P(J)$, the system flows to an *infinite randomness fixed point* characterized by the fixed point form of the probability distribution of interactions given by

$$P(J) = \frac{\alpha}{\Omega}\left(\frac{\Omega}{J}\right)^{1-\alpha} \tag{6}$$

At zero temperature, the exponent α is a function of the cut-off Ω of the distribution and varies as,

$$\alpha = \frac{-1}{\ln \Omega} \tag{7}$$

This behavior characterizes the so-called random singlet phase [47]. The number of remaining active spins N_R as a function of the energy scale set by the cut-off Ω introduces a new exponent ψ which is defined by,

$$L = \frac{N}{N_R} = \frac{1}{n_\Gamma} = \frac{1}{|\ln \Omega|^{1/\psi}} \tag{8}$$

where N is the number of spins in the original chain. This establishes the connection between the characteristic length L and the energy scale Ω. This is an extension of the usual definition of a dynamic exponent ($\Omega \propto \tau^{-1} \propto L^z$) for the case of logarithmic scaling. For the random singlet phase the exponent ψ takes the value, $\psi = 1/2$. These results are well established for the spin$-1/2$ REHAC. The convergence of the MDH perturbative procedure for the exact result is guaranteed by the fact that in Eq. 5 the pre-factor $(1/2)$ assures that the new effective interaction J' is always smaller than those eliminated.

In order to generalize the MDH method to spin-1 chains, we consider the general bilinear, biquadratic, spin-1 chain [48] with L spins described by the Hamiltonian

$$H = \sum_{r=1}^{L-1} J_r \vec{S}_r . \vec{S}_{r+1} - \sum_{r=1}^{L-1} D_r \left(\vec{S}_r . \vec{S}_{r+1}\right)^2 \tag{9}$$

where J_r and D_r are random nearest-neighbor interactions with probability distributions $P_J(J_r)$ and $P_D(D_r)$ respectively and such that $0 \leq J_r \leq J$ and $0 \leq D_r \leq D$. The $\vec{S}_r$ are spin-1 operators and we are interested in the limit $L \to \infty$.

For the case of purely biquadratic interactions and no exchange we assume a distribution of random biquadratic couplings and take $J_r = 0$. Generalizing the procedure of Ma et al. [46] for this problem, we identify the pair of spins with the strongest biquadratic coupling. When we apply the elimination transformation to this strong coupled pair we

find an effective coupling between the spins neighboring the eliminated pair which is is given by [48] :

$$D' = \frac{2}{9}\frac{D_1 D_2}{D} \tag{10}$$

where D_1 and D_2 are the bonds connecting the strongest coupled pair of spins, with interaction strength D, to their neighbors. It is clear that in this case the successive application of the elimination transformation generates weaker and weaker couplings and the distribution of biquadratic interactions becomes peaked close to the origin as the cutoff D decreases. The physical properties of the system are then dominated by low energy excitations and this new phase is very similar to the *random singlet phase* of the disordered spin$-1/2$ random antiferromagnetic chain [47]. Disorder has a dramatic effect in this case since in the pure case the system has a dimerized phase with a gap for excitations and a short correlation length. The introduction of weak randomness on the biquadratic couplings gives rise to a new disordered phase with low energy excitations and long-range magnetic correlations. This behavior is universal in the sense that, independently of the initial distribution of couplings $P_D(D_r)$, the final distribution converges to a fixed point form which is approximately described by a power law with a singularity at the origin [46]. Notice that the equation above renormalizes to weak coupling faster than that for the spin$-1/2$ REHAC where the pre-factor of the recursion relation equivalent to Eq. 10 is $1/2$ [46]. We have found here a rather unusual situation where a phase with a gap and a short correlation length has become completely unstable and furthermore with long-range magnetic correlations due to the introduction of arbitrarily weak disorder [49].

We include now a weak random exchange interaction between nearest neighbor spins such that the cutoff $J << D$. A generalization of the elimination transformation gives, for the new exchange and biquadratic couplings between the spins neighboring the eliminated pair, the following coupled relations [48]

$$D' = \frac{2}{9}\frac{D_1 D_2}{D + J} \tag{11}$$

$$J' = \frac{4}{3}\frac{J_1 J_2}{(3D + J)}$$

where as before D_1, D_2, J_1 and J_2 are the bonds connecting the strongly coupled pair of spins, with interactions D and J between them, to their neighbors. Since $D >> J$ we expect, as before, that the renormalized distributions converge rapidly to a weak coupling situation, i.e., to develop more and more weight close to the origin as the cutoff decreases. Again the system attains a random singlet phase dominated by low energy excitations.

In the situation where $D_r = 0$, i.e., for the random exchange spin-1 chain, the elimination procedure yields the following relation for the new coupling between the spins neighboring the eliminated pair [48],

$$J' = \frac{4}{3}\frac{J_1 J_2}{J} \tag{12}$$

We find here a situation quite different from the previous case, since this recursion relation appears to iterate to strong coupling due to the factor $(4/3) > 1$. The generation of

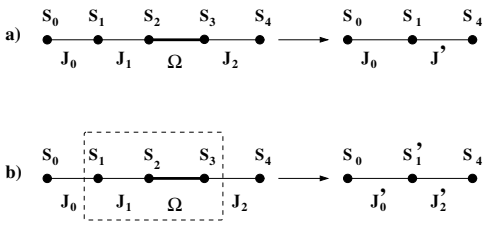

Figure 13: The two elimination procedures as described in the text ($J_1 > J_2$).

couplings which are larger than those eliminated would in fact invalidate the present approach based on perturbation theory. This problem is common to all spins larger than 1/2. The MDH elimination transformation has been extended for a quantum Heisenberg chain with arbitrary spin S and the following recursion relation has been obtained [48],

$$J' = \frac{2}{3} S(S+1) \frac{J_1 J_2}{J} \tag{13}$$

This result shows that perturbation theory in general fails for $S > 1/2$, so that, a universal random singlet phase in the Heisenberg chain with random exchange interactions is guaranteed only for spin$-1/2$ [50, 51, 52]. In this case the quantum fluctuations are sufficiently strong and the renormalization group equations yield a flow to a fixed point, universal distribution, singular at the origin. The above result led to an intense activity to overcome this type of difficulty and to obtain results for quantum random chains of arbitrary spin S. We discuss now the results for spin-1 chains [44, 53, 54].

Our generalization of the MDH method consists in either of the following procedures shown in Fig. 13 [44]. If the largest neighboring interaction to Ω is $J_1 < (3/4)\Omega$ we eliminate the strongest coupled pair, see Fig. 13a, obtaining an effective interaction between the neighbors to this pair which is given by Eq. 12. This effective interaction is always smaller than those eliminated.

Now suppose $J_1 > (3/4)\Omega$ ($J_1 > J_2$). In this case, we consider the *trio* of spins $S = 1$ coupled by the two strongest interactions of the trio, J_1 and Ω and solve it exactly (see Fig. 13b). The ground state of this trio of spins $S = 1$ is a degenerate triplet and it will be substituted by an effective spin-1 interacting with its neighbors through new renormalized interactions obtained by degenerate perturbation theory. This procedure which implies diagonalizing the $27X27$ matrix of the trio is carried out *analytically*. This is important for obtaining results on large chains and to deal with the large numbers of initial configurations that have been used. These procedures guarantee that we always comply with the criterion of validity of perturbation theory and *never* an interaction larger than those eliminated is generated, as shown in Fig. 14, differently from the MDH scheme.

We consider initial rectangular distributions of antiferromagnetic interactions, $P(J) = [1/(1-G)]\Theta(1-J)\Theta(J-G)$. The gap G is a measure of the amount of disorder being inversely related to it (see Fig. 11). The strong disorder case has $G = 0$ and corresponds to the quantum critical point of the phase diagram of Figure 15. At this point $G = 0$

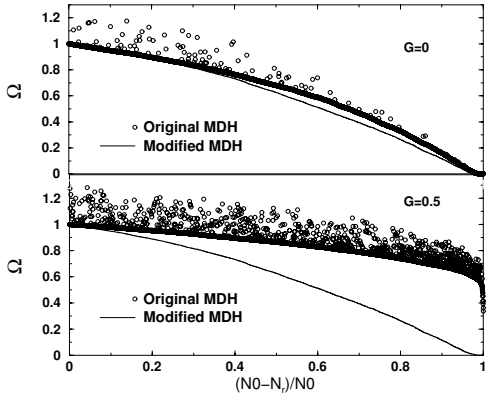

Figure 14: Evolution of the cut-off of the exchange distribution for a random chain as a function of the fraction of eliminated spins for the two renormalization procedures discussed in the text. Note that the naive MDH process generates interaction larger than those eliminated, even for strong disorder ($G = 0$). This never occurs in the new procedure used here [44].

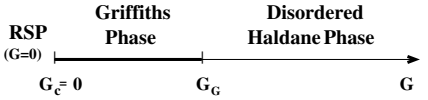

Figure 15: The phase diagram of the spin-1 random Heisenberg antiferromagnetic chain. Disorder is inversely related to the gap G of the initial rectangular distribution and $G_G \approx 0.45$ [44].

the system flows to an *infinite randomness fixed point* or random singlet phase [44]. This becomes clear when we obtain the fixed point form of the probability distribution of interactions for $G = 0$, which turns out to be given by Eq. 6. The exponent α as a function of the cut-off Ω is shown in Fig. 16 and varies as in Eq. 7. This behavior characterizes the strong disorder case, $G = 0$, as a random singlet phase [47].

Further evidence for a random singlet phase at $G = 0$ is obtained considering the fraction of remaining active spins ρ as a function of the energy scale set by the cut-off Ω [47]. In Fig. 17 the density $\rho = 1/L$ is shown as a function of the cut-off [44]. From this expression the exponent ψ appearing in Eq. 8 is extracted. As expected it takes the value $\psi = 1/2$ characteristic of the random singlet phase [47].

Finally, the distribution of first gaps [55, 56, 57, 58] at $G = 0$ is calculated. This is obtained starting from a given configuration of random interactions for a chain of size L and eliminating the spins, as described above, until a single pair remains. The interaction between these remaining spins yields the first gap Δ for excitation. Implementing this procedure for a large number of initial random configurations for chains of different sizes

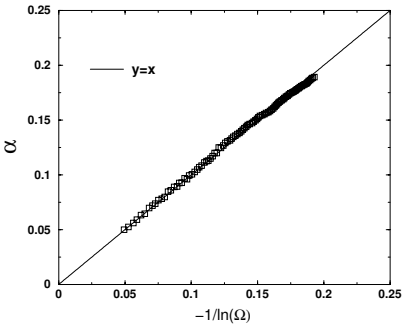

Figure 16: Exponent α of the fixed point, power law distribution, Eq. 7, as a function of the cut-off Ω in the low energy limit [44].

L yields the distributions $P_L(\log\Delta)$ shown in Fig. 18. We considered over 10^4 initial configurations to obtain the gap distributions. The widths of these distributions increase without limit as the sizes L of the chains increase, as expected for an infinite randomness fixed point.

According to the scaling form relating energy and length, Eq. 8, it is expected that the distribution $P(-\log\Delta/L^{\psi})$ will present a universal behavior, independent of the size L of the chains when plotted versus the variable $-\log\Delta/L^{\psi}$. This is indeed the case for $G = 0$ as shown in Fig. 18 for the random singlet phase exponent $\psi = 1/2$.

We now decrease disorder increasing the gap in the exchange distribution. Figure 19 shows the first gap distributions for different degrees of disorder as characterized by the gaps G in the initial distribution of interactions. In all cases investigated with $G \neq 0$, it is found that the first gap distributions saturate at low energies in a form described by the expression, $P(\log\Delta) \sim \Delta^{1/Z}$ for $\Delta \to 0$. The *dynamic exponent* Z becomes independent of L for L sufficiently large. Large chains have to be considered in order to observe this effect. We find $Z_\infty \sim 10.87$, $Z_\infty \sim 1.01$ and $Z_\infty \sim 0.68$ for $G = 0.1$, $G = 0.45$ and $G = 0.5$, respectively. From these values of the dynamic exponent it is possible to deduce the existence of a Griffiths phase extending up to $G_G \approx 0.45$ where the dynamic exponent reaches the value $Z = 1$ [44] (see Fig. 15). For values of the gap $G > G_G$, i.e., small disorder, the dynamic exponent $Z < 1$. The distribution of first gap for excitations, from which low temperature thermodynamic properties can be deduced, implies that $Z > 1$ is required to obtain a singular behavior for these quantities with decreasing temperature. Consequently at G_G there is a significant change in the nature of the thermodynamic behavior of the system. The phase for $G > G_G$ is a disordered Haldane phase with a pseudo-gap in the excitation spectrum (see Fig. 15).

We now consider spin$-3/2$ chains [59]. For these chains, after elimination of the strongest coupled pair, the MDH method yields for the new coupling between their neighbors,

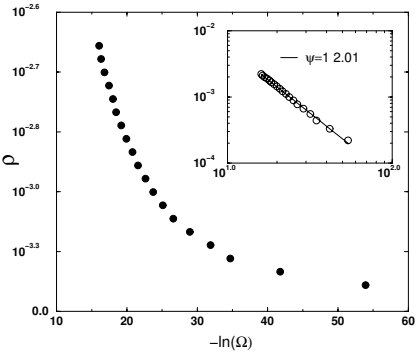

Figure 17: The density of active spins as a function of the cut-off in the low energy limit. The inset shows the expected behavior for a random singlet phase with the exponent $\psi \approx 1/2$ [44].

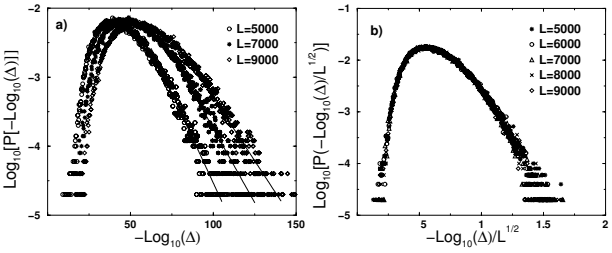

Figure 18: a) Probability distribution of the first gap at the transition point, $G = 0$. The distribution become broader and broader with L, which signals infinite randomness behavior. b) Scaling plot for the gap distributions. The collapse of the curves is obtained for $\psi = 1/2$ as expected for a random singlet phase [44].

$$J' = \frac{5}{2}\frac{J_1 J_2}{\Omega} \tag{14}$$

Consider the case $J_1 \geq J_2$. For $J_1 > (2/5)\Omega$ the new effective interaction J' is necessarily larger than one of those eliminated, in this case, than J_2. In order to deal with this problem, the MDH method has again to be generalized. If the largest neighboring interaction to Ω, $J_1 < (2/5)\Omega$, then we eliminate the strongest coupled pair obtaining an effective interaction between the neighbors to this pair which is given by Eq. 14 (see Fig. 13a). This new effective interaction is always smaller than those eliminated. Now suppose $J_1 > J_2$ and $J_1 > (2/5)\Omega$. In this case, we consider the *trio* of spins $S = 3/2$ coupled by the two strongest interactions of the trio, J_1 and Ω and solve it exactly (see Fig. 13b). The ground state of this trio of spins $S = 3/2$ is a degenerate quadruplet. It will be substituted by an effective spin$-3/2$ interacting with its neighbors through *new renormalized* interactions

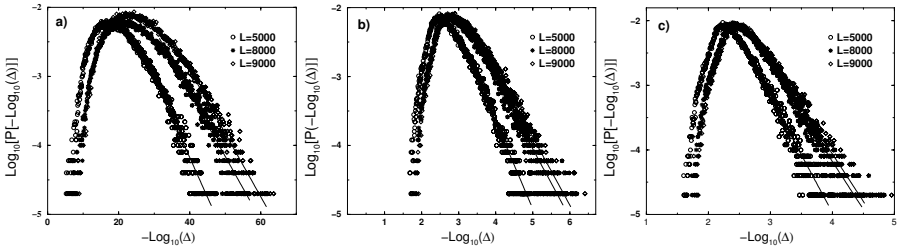

Figure 19: Probability distributions of the first gap obtained from initial rectangular distributions of couplings with a gap G and different systems sizes L [44]. For clarity not all values of L are shown. The solid lines represent best fits to the form $\log_{10}[P(-\log_{10}\Delta)] = A_L - \frac{1}{Z_L}\log_{10}\Delta$. a) $G = 0.1$, $Z_{5000} = 8.69$, $Z_{6000} = 8.70$, $Z_{7000} = 10.45$, $Z_{8000} = 10.85$ and $Z_{9000} = 10.87$. b) $G = 0.45$, $Z_{5000} = 0.79$, $Z_{6000} = 0.81$, $Z_{7000} = 0.96$, $Z_{8000} = 1.0$ and $Z_{9000} = 1.01$. c) $G = 0.5$, $Z_{5000} = 0.55$, $Z_{6000} = 0.58$, $Z_{7000} = 0.63$, $Z_{8000} = 0.67$ and $Z_{9000} = 0.68$.

obtained by degenerate perturbation theory acting on the ground state of the trio. The $64X64$ matrix associated with the trio is diagonalized *analytically*. This allows to obtain results on large chains and to deal with a large numbers of initial configurations. Fig. 20 shows that perturbation theory is now always satisfied. We have considered initial rectangular distributions of interactions with a gap G (see Fig. 11). Even for weak disorder, with a gap as large as $G = 0.5$ in the starting distribution, the method works very well and never an interaction larger than those eliminated is generated.

Figure 21 shows the first gap distributions for different degrees of disorder as characterized by different gaps G in the initial distribution of interactions. For all cases these distributions saturate at low energies in a form described by the expression, $P(-\log\Delta) \sim \Delta^{1/Z}$ for $\Delta \to 0$. The *dynamic exponent* Z becomes independent of L for L sufficiently large. Again, large chains have to be considered to observe this effect. The phase diagram is such that, for strong disorder which corresponds to $G = 0$, there is a Griffiths phase with a dynamic exponent $Z \sim 12.7$ (see Fig. 21). This phase is characterized by *first gap distributions* [44] that saturate at low energies in the form, $P(-\log\Delta) \sim \Delta^{1/Z}$ for $\Delta \to 0$. We find $Z_\infty \sim 0.43$ and $Z_\infty \sim 1.12$ for $G = 0.2$ and $G = 0.12$, respectively, from which the existence of a Griffiths phase extending up to $G_c \approx 0.11$ is deduced. At this point the dynamic exponent reaches the value $Z = 1$. Since, for example, the susceptibility $\chi \propto T^{1-Z}$, a singular low temperature behavior implies $Z > 1$. At G_c there is in fact a significant change in the nature of the thermodynamic behavior of the system [60]. The phase for $G > G_c$ is one with quasi-long range order, i.e., with spin correlations decaying algebraically with distance, similar to the zero temperature phase of the pure chain [60].

In order to check the possibility of a random singlet phase in the spin$-3/2$ chain we consider another class of distributions of exchange couplings associated with *extreme* disorder. These distributions are of the form, $P(J) \propto J^{-1+1/\gamma}$. For $\gamma = 1$ this reduces to the gapless case of rectangular distributions considered previously and for $\gamma > 1$, we

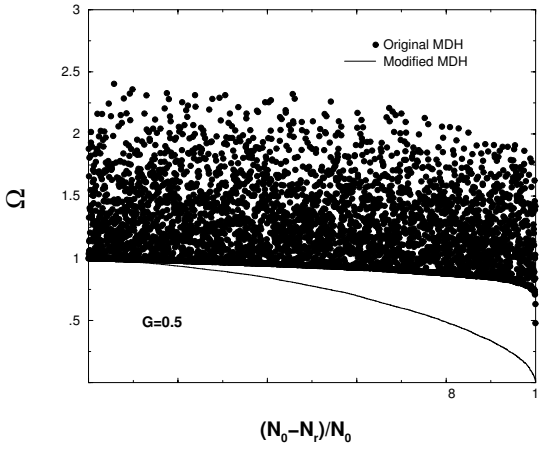

Figure 20: The evolution of the cut-off, for an initial rectangular distribution with $G = 0.5$, along the renormalization process of the spin-3/2 REHAC. The results for the original MDH and the present (modified) renormalization group procedures are shown [59].

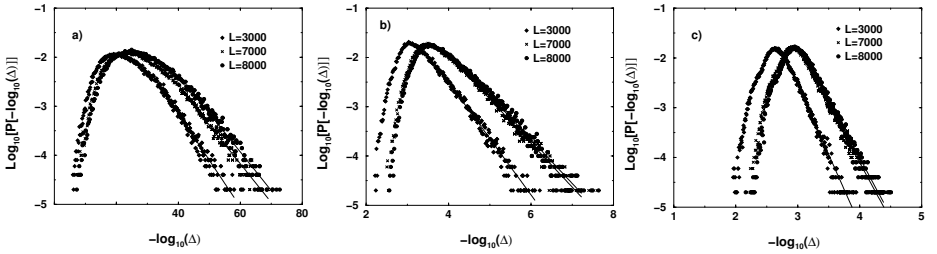

Figure 21: Probability distributions of *first gap* for initial rectangular distributions of couplings with gaps G and different systems sizes L [59]. For clarity not all values of L are shown. The solid lines represent best fits to the form $\log_{10}[P(-\log_{10}\Delta)] = A_L - \frac{1}{Z_L}\log_{10}\Delta$. a) $G = 0$, $Z_{3000} = 10.51$, $Z_{7000} = 12.68$, and $Z_{8000} = 12.70$. b) $G = 0.12$, $Z_{3000} = 0.87$, $Z_{7000} = 1.11$, and $Z_{8000} = 1.12$. c) $G = 0.2$, $Z_{3000} = 0.35$, $Z_{7000} = 0.43$, and $Z_{8000} = 0.43$.

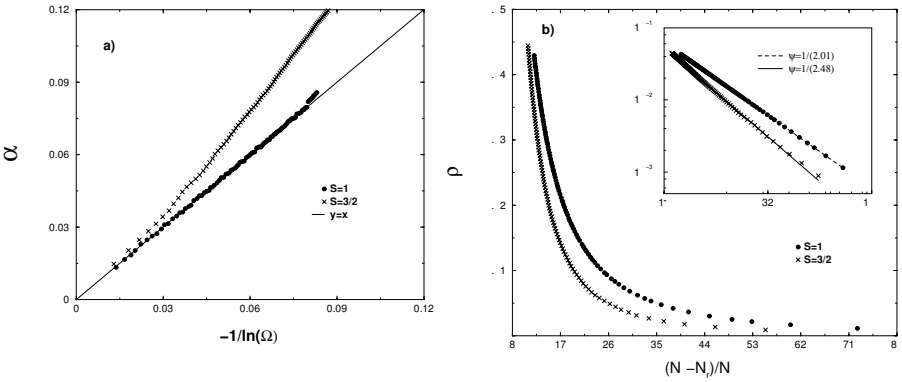

Figure 22: a) The exponent α describing the asymptotic low energy behavior of the renormalized exchange distribution as a function of the scale dependent cut-off. b) Fraction of active spins as a function of the cut-off [59]. For comparison the results for the spin-1 and spin-3/2 REHACs are shown. In both cases the starting distribution is extremely disordered with $\gamma = 20$ (see text).

have the extreme disordered cases. We now report our results for the random spin-3/2 chain obtained with the modified renormalization group procedure [44] for the case of an extremely disordered distribution with $\gamma = 20$ [59]. In the random singlet phase the fixed point distribution of interactions attained when the cut-off Ω is sufficiently reduced takes the form given by Eq. 6. Fig. 22a shows the exponents α of this equation obtained from the asymptotic form of the exchange distributions after the cut-off Ω has been sufficiently reduced. For comparison, the results for a spin-1 REHAC with the same original extreme disorder distribution are shown. In this case a random singlet phase is clearly established. Chains of size as large as $L = 4.5 \times 10^5$ have been considered in these calculations. Fig. 22b shows the density $\rho = 1/L$ of active spins as a function of the cut-off Ω (see Eq. 8). From this expression the exponent ψ (see Eq. 8) has been extracted. It takes the value $\psi = 1/(2.4)$ which is close to the value $\psi = 1/2$ expected for a random singlet phase [47]. As shown in this figure, for comparison, the spin-1 chain has clearly converged to this phase within the same scale of the cut-offs. These results suggest that in this case of extreme disorder, the spin$-3/2$ REHAC eventually reaches a random singlet phase, although the convergence is very slow.

The MDH elimination procedure can be generalized for finite temperatures and arbitrary spins S. It is given by [59]

$$J' = \frac{2}{3} S(S+1) \frac{J_1 J_2}{\Omega} W_S(\beta\Omega) \tag{15}$$

where

$$W_S(y) = \frac{(2S+1)^2 - \sum_{i=0}^{i=2S} (2i+1) e^{-\frac{1}{2} i(i+1) y} \left[1 + \frac{1}{2} i(i+1)\right]}{4S(S+1) \sum_{i=0}^{i=2S} (2i+1) e^{-\frac{1}{2} i(i+1) y}} \tag{16}$$

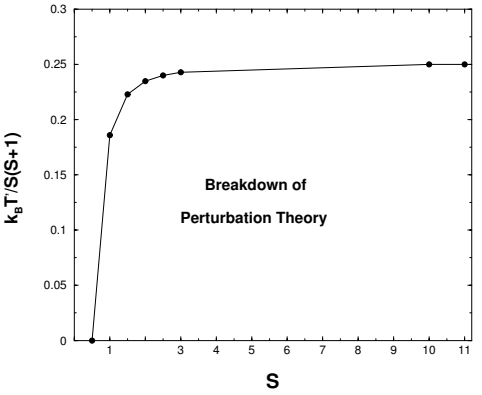

Figure 23: Temperature T^* below which the MDH perturbation theory breaks down for different values of the spin S. The energy $k_B T^*$ is in units of the cut-off Ω of the original exchange distribution [59].

Notice that for sufficiently high temperatures, the factor $\frac{2}{3}S(S+1)W_S(\beta\Omega) < 1$ and the MDH elimination procedure works in this case [49, 61, 62, 63, 64]. A random singlet phase is reached in the sense that the asymptotic distribution of exchange attains the form given by Eq. 6 at these temperatures. However, as T is reduced the problem becomes essentially non-perturbative for spins $S \geq 1$, as the equation above generates coupling larger than those eliminated. In particular at $T = 0$ the excited states which reduce the factor W_S from its value $W_S(T = 0) = 1$ are now frozen. In fact *none* of the excited states play a role in the problem at zero temperature. Notice that in the generalized renormalization scheme, degenerate perturbation theory is applied to the *ground state* of the spin trio. This is possibly the main reason for the discrepancy between the results above and those obtained by the authors of Refs. [61, 64]. These authors find that quantum chains of arbitrary spin$-S$ present random singlet phases even for weak disorder. The consideration of excited states in the problem favors the appearance of an infinite disorder random singlet phase, as occurs at finite temperatures.

In the limit $S \to \infty$ and $T \to 0$, replacing the sum by an integral and with a proper renormalization of the Hamiltonian, Eqs. 15 and 16 yield $J' = J_1 J_2/4k_B T$, in agreement with the result of Ref. [46] for classical spins. In Fig. 23 it is shown the temperature T^* below which the simple perturbative approach breaks down, for a given value of the spin of the random chain.

Notice that for rectangular distributions, the Griffiths phase of the spin-1 REHAC extends up to $G_c = 0.45$ and for spin-3/2 up to $G_c = 0.11$. For random classical spin chains, the susceptibility $\chi \propto P(0)|\ln T|$ where $P(0)$ is the finite weight at the origin of the original distribution $P(J)$ [46]. This weak logarithmic singularity is similar to that expected for quantum chains at the border of the Griffiths phase ($Z \approx 1$) as if in this case of classical spins and rectangular distribution, $G_c = 0$.

Then for rectangular distributions, the spin-3/2 REHAC presents a Griffiths phase up to a critical value of disorder. For extreme disorder, where the starting exchange distributions are singular for small values of the coupling our results only suggest that a random singlet phase will be asymptotically reached as the cut-off of the distribution $\Omega \to 0$. These results are consistent with those of Refs. [60] that find a random singlet phase in spin-3/2 chains for the case of extremely disordered distributions.

It is clear by now that the power law temperature dependent behavior observed in the magnetic susceptibility and other thermodynamic properties of the low dimensional oxy-borates can be traced to the mapping of their low dimensional magnetic structures to a random chain problem. The details of this mapping have yet to be explored. The oxy-borates were the first class of inorganic materials where this kind of low dimensional magnetic behavior has been found. They provide a strong motivation to make further theoretical progress in this problem and of other quantum systems with disorder [65].

We would like to thank Conselho Nacional de Desenvolvimento Científico e Tecnológico-CNPq-Brasil and Fundacão de Amparo a Pesquisa do Estado do Rio de Janeiro-FAPERJ (PRONEX/CNPq-FAPERJ-E-26/171.168/2003) for partial financial support.

References

[1] C. Klein in, *Manual of Mineral Science,* 22^{nd} *edition*: after James D. Dana; with continued contribution of Cornelius S. Hurlbut, Jr. Publisher: J.Wiley, New York, (2002).

[2] R. Norrestam, Z. fur Kristall. **189** (1989) 1.

[3] R. Norrestam, M. Kritikos, and A. Sjodin, J. Sol. State Chemistry. **114** (1995) 311.

[4] J.P. Attfield, A.M.T. Bell, L.M. Rodriguez-Martinez, J.M. Greneche, R.J. Cernik, J.F. Clarke, and D.A. Perkins, Nature **396** (1998) 655.

[5] J.P. Attfield, A.M.T. Bell, L.M. Rodriguez-Martinez, J.M. Greneche, R. Retoux, M. Leblanc, R.J. Cernik, J.F. Clarke, and D.A. Perkins, J. Mater. Chem. **9** (1999) 205; A. D. Balaev, O. A. Bayukov, A. D. Vasil'ev, D. A. Velikanov, N. B. Ivanova, N. V. Kazak, S. G. Ovchinnikov, M. Abd-Elmeguid, and V. V. Rudenko, JETP **97** (2003) 989.

[6] J.J. Capponi, J. Chenevas, and J.C. Joubert, J. Solid State Phys. **7** (1973) 49.

[7] R.B. Guimarães, J.C. Fernandes, M.A. Continentino, H.A. Borges, C.S. Moura, J.B.M. da Cunha, and C.A. dos Santos, Phys. Rev B **56** (1997) 292.

[8] R. Norrestam, K. Nielsen, I. Sotofte, and N. Thorup, Zeit. fur Kristall. **189** (1989) 33.

[9] M.A. Continentino, J.C. Fernandes, R.B. Guimarães, H.A. Borges, A. Sulpice, J-L. Tholence, J.L. Siqueira, J.B.M. Cunha, and C.A. dos Santos, Eur. Phys. J. **9** (1999) 613.

[10] D.A. Konnert, D.E. Applemen, J.R. Clark, W.L. Finger, T. Kato, and Y. Miura, Am. Mineral. **61** (1976) 116.

[11] P.B. Moore and T. Araki, Am. Mineral. **59** (1974) 985.

[12] Y. Takeuchi, N. Haga, T. Kato, and Y. Miura, Can. Mineral. **16** (1978) 475.

[13] J.-O. Bovin and M. O'Keeffe, Acta Cryst. **A37** (1981) 35.

[14] J.-O. Bovin, A. Carlsson, R. Sjovall, R. Thomasson, R. Norrestam, and I. Sotofte, Z. fur Kristall. **211** (1996) 440.

[15] R. Norrestam and J.-O. Bovin, Zeit. fur Kristall. **181** (1987) 135.

[16] M. Mir, R.B. Gumarães, J.C. Fernandes, M.A. Continentino, A.C. Doriguetto, Y.P. Mascarenhas, J. Ellena, E.E. Castellano, R.S. Freitas, and L. Ghivelder, Phys. Rev. Lett. **87** (2001) 147201.

[17] J.C. Fernandes, F.S. Sarrat, R.B. Guimarães, R.S. Freitas, M.A. Continentino, A.C. Doriguetto, Y.P. Mascarenhas, J. Ellena, E.E. Castellano, J-L. Tholence, J. Dumas, and L. Ghivelder, Phys. Rev. B **67** (2003) 104413.

[18] A. Utzolino and K. Bluhm, Zeit. Naturforsch. **51b** (1996) 912.

[19] J.C. Fernandes, R.B. Guimarães, M.A. Continentino, R. Rapp, J-L. Tholence, J. Dumas, Y. Blancquaert, S. Yates, and C. Paulsen, Phys. Rev B **69** (2004) 054418.

[20] A. Wiedenmann and P. Burlet, J. Physique **39** supplement au n^o8 (1978) C6-720.

[21] A. Wiedenmann, P. Burlet, and R. Chevalier, J. Mag. Mag. Matt. **15-18** (1980) 216.

[22] J.C. Fernandes, R.B. Guimarães, M.A. Continentino, H.A. Borges, J.V. Valarelli, and Alex Lacerda, Phys. Rev. B **50** (1994) 16754.

[23] L.N. Boulaevskii, A.V. Zvarykina, Yu. S. Karimov, R.B. Lyubovskii, and I.F. Shchegolev, Sov. Phys. JETP **35** (1972) 384.

[24] M. Matos, R. Hoffmann, A. Latgé, and E. V. Anda, Chem. Mater. **8** (1996) 2324.

[25] D. C. Marcucci, A. Latgé, E. V. Anda, M. Matos, and J.C. Fernandes, Phys. Rev. B **56** (1997) 3672.

[26] M.A. Continentino, A.M. Pedreira, R.B. Guimarães, M.Mir, J.C. Fernandes, R.S. Freitas, and L. Ghivelder, Phys. Rev B **64** (2001) 014406.

[27] M.A. Continentino, J.C. Fernandes, R.B. Guimarães, B. Boechat, H.A. Borges, J.V. Valarelli, E. Haanappel, A. Lacerda, and P.R.J. Silva, Philos. Mag. B **73** (1996) 601.

[28] M. Brunner, J.-L. Tholence, L. Puech, S. Haan, J.J. Capponi, R. Calemczuk, J.C. Fernandes, and M.A. Continentino, Physica B **233** (1997) 37.

[29] J.C. Fernandes, R.B. Guimarães, M.A. Continentino, H.A. Borges, A. Sulpice, J.-L. Tholence, J.L. Siqueira, L.I. Zawislak, J.B.M. da Cunha, and C.A. dos Santos, Phys. Rev. B **58** (1998) 287.

[30] M.A. Continentino, J.C. Fernandes, R.B. Guimarães, H.A. Borges, A. Sulpice, J.-L. Tholence, J.L. Siqueira, J.B.M. da Cunha, and C.A. dos Santos, Eur. Phys. J. **9** (1999) 613.

[31] R.B. Guimarães, M. Mir, J.C. Fernandes, M.A. Continentino, H.A. Borges, G. Cernicchiaro, M.B. Fontes, D.R.S. Candela, and E.M. Baggio-Saitovitch, Phys. Rev. B **60** (1999) 6617.

[32] H. Neuendorf and W. Gunsser, J. Mag. Mag. Matt. **173** (1997) 117.

[33] A. P. Douvalis, V. Papaefthymiou, A. Moukarika, and T. Bakas, Hyperf. Interactions **126** (2000) 319.

[34] R.J. Goff, A.J. Williams, and J.P. Attfield, Phys. Rev. B **70** (2004) 014426.

[35] J.P. Attfield, J.F. Clarke, and D.A. Perkins, Physica B **180 & 181** (1992) 581.

[36] J.C. Fernandes, R.B. Guimarães, M.A. Continentino, L. Ghivelder, and R.S. Freitas, Phys. Rev. B **61** (2000) R850.

[37] J.S. Swinea and H. Steinfink, Am. Mineral. **68** (1983) 827.

[38] J. Larrea, D.R. Sanchez, F.J. Litterst, and E.M. Baggio-Saitovitch, J. Phys.: Condens. Matter **13** (2001) L949.

[39] A. Latgé and M.A. Continentino, Phys. Rev. B **66** (2002) 094113.

[40] M. Whangbo, H.-J. Koo, J. Dumas, and M.A. Continentino, Inorg. Chem. **41** (2002) 2193.

[41] for a review see E. Dagotto and T. M. Rice, Science **271** (1996) 618.

[42] J. A. Hoyos and E. Miranda, Phys. Rev. **B 69** (2004) 214411.

[43] R. Mélin, Y.-C. Lin, P. Lajkó, H. Rieger, and F. Iglói, Phys. Rev. **B 65** (2002) 104415; E. Yusuf and K. Yang, Phys. Rev. **B 65** (2002) 224428; E. Yusuf and K. Yang, Phys. Rev. **B 68** (2003) 024425.

[44] A. Saguia, B. Boechat, and M. A. Continentino, Phys. Rev. Lett **89** (2002) 117202.

[45] E. Westerberger, A. Furusaki, M. Sigrist, and P. A. Lee, Phys. Rev. **B 55** (1997) 12578; T. Hikihara, A. Furusaki, and M. Sigrist, Phys. Rev. **B 60** (1999) 12116.

[46] S.K. Ma, C. Dasgupta, and C.K. Hu, Phys. Rev. Lett. **43** (1979) 1434; S.K. Ma and C. Dasgupta, Phys. Rev. **B 22** (1980) 1305.

[47] D.S. Fisher, Phys. Rev. **B 50** (1994) 3799; Phys. Rev. **B 51** (1995) 6411.

[48] B. Boechat, A. Saguia, and M.A. Continentino, Solid State. Commun. **98** (1996) 411.

[49] R.A. Hyman and K. Yang, Phys. Rev. Lett. **78** (1997) 1783.

[50] K. Hida, Phys. Rev. **B 45** (1992) 2207.

[51] K. Hida, Phys. Rev. Lett. **83** (1999) 3297.

[52] S. Bergkvist, P. Henelius, and A. Rosengren, Phys. Rev. **B 66** (2002) 134407; S. Todo, K. Kato, and H. Takayama, J. Phys. Soc. Jpn. **69** (2000) A355.

[53] A. Saguia, B. Boechat, and M.A. Continentino, Phys. Rev. **B 58** (1998) 58; Phys. Rev. **B 62** (2000) 5541.

[54] A. Saguia, B. Boechat, and M.A. Continentino, Phys. Rev. **B 63** (2001) 52414.

[55] R. Mélin, Y.-C. Lin, P. Lajkó, H. Rieger, and F. Iglói, Phys. Rev. **B 65** (2002) 104415.

[56] Y.-C. Lin, N. Kawashima, F. Iglói, and H. Rieger, Prog. Theor. Phys. Suppl. **138** (2000) 470.

[57] F. Iglói, Phys. Rev. **B 65** (2002) 064416.

[58] E. Carlon, P. Lajkó, and F. Iglói, Phys. Rev. Lett. **87** (2001) 277201.

[59] A. Saguia, B. Boechat, and M. A. Continentino Phys. Rev. **B 68** (2003) 020403(R).

[60] E. Carlon, P. Lajk, H. Rieger, and F. Igli, Phys. Rev. **B 69** (2004) 144416.

[61] G. Refael, S. Kehrein, and D.S. Fisher, Phys. Rev. **B 66** (2002) R060402.

[62] K. Damle, Phys. Rev. **B 66** (2002) 104425.

[63] C. Monthus, O. Golinelli, and Th. Jolicoeur, Phys. Rev. Lett. **79** (1997) 3254; Phys. Rev. **B 58** (1998) 805.

[64] K. Damle and D. A. Huse, Phys. Rev. Lett. **89** (2002) 277203.

[65] see *Quantum Scaling in Many-body Systems*, M. A. Continentino (World Scientific, Singapore) 2001.

METAL-INSULATOR TRANSITION AND MAGNETORESISTANCE IN MANGANITE THIN FILMS: LATTICE STRAIN AND DISORDER EFFECTS

V. Moshnyaga

Physikalisches Institut, Universität Göttingen, Friedrich-Hund-Platz 1,
D-37077 Göttingen, Germany

1. INTRODUCTION

Mixed-valence perovskite manganites have been known for more than half a century since the first paper by Jonker and van Santen [1] was published in 1950. These materials are ferromagnetic with Curie Temperatures, T_C=100-360 K, and exhibit an insulator to metal transition at T_{MI}~T_C. Great and continuous research interest in the manganites could be probably explained by the fact that they possess a number of crystallographic, electronic and magnetic phases, which can interact with each other, yielding very interesting and technologically useful effects. Furthermore, some new physical concepts, like "double exchange" interaction, the Jahn-Teller polaron and, quite recently, the so called "electronic phase separation" appeared as a result of theoretical and experimental study of the manganites.

In the last decade of 20th century the progress in High T_C superconductivity and related oxide thin film technologies has renewed a great interest in perovskite manganites. As a result the so called "colossal magnetoresistance" (CMR) effect was discovered in thin manganite films by R. von Helmolt et al. [2], K. Chahara et al. [3] and M. Mc Cormack et al. [4]. CMR is quantified as relative change of electrical resistivity in applied magnetic field, CMR=100%*[ρ(0)-ρ(B)]/ρ(B), and can be extremely large ~10^5 % [4] for magnetic fields of several Tesla. The discovery of the CMR effect stimulated a huge activity in fundamental and technological research. Thin manganite films and corresponding thin film technologies become important not only for applications but also for fundamental solid state physics – the reduced dimensionality (thickness and grain size) allows one to create specific boundary con-

ditions, which cannot be realized in bulk samples. Moreover, this brings new opportunities for "tuning" of the magnetotransport behavior.

The second renaissance of manganites occurred during the past few years and is naturally connected with great progress in nanoscience and nanotechnology. The intention to confine a condensed matter down to the nanometer scale, challenged both by computer technologies and by fundamental science, may have a concrete implication to manganites. It was observed experimentally and also argued theoretically that the electronic properties of manganites may be spatially inhomogeneous. Metallic and insulating electronic phases can coexist within the same sample of a definite chemical composition over different length scales: from micrometer down to few nanometers. The mesoscopic, nanometer-scale, electronic inhomogeneities seem to be very attractive for the future nanotechnology because they would allow one to fabricate spatially self-organized nanostructures with different functionality within a homogeneous medium. Closely connected to the above issue is the problem of preparation of the nanoscaled manganite films and manganite based composites. Reduced dimensions of manganites as well as novel architecture and phase counter partners in composites offer additional opportunity to control the magnetotransport.

In this work an overview of the magnetotransport in thin manganite films will be given with a special focus on the effects of lattice strain and disorder as well as inhomogeneous electronic properties of manganites. In §2 we discuss the background of manganites – crystalline structure, phase diagram as well as experimental evidences and theoretical ideas of the inhomogeneous electronic ground state in manganites. Preparation of thin films by means of metalorganic aerosol deposition (MAD) technique will be described in §3. The MAD technique is able to fabricate thin manganite films as well as other multinary oxide films of very high quality. Moreover, MAD is especially advantageous in the preparation of nanocomposite films. §4 concerns magnetotransport in manganite films with respect to the two mechanisms of film growth: "layer by layer" epitaxy (A-type) and 3D nucleation or island growth (B-type) both realized within MAD. It was observed that residual resistivity, metal-insulator transition temperature and CMR in the B-type films were governed by a mesoscopic scale, L~10-40 nm, which is much smaller than the grain size, D~200-400 nm. Moreover the relations between mesoscopic inhomogeneity and lattice strain and disorder, induced by hydrostatic pressure, were revealed. Another kind of disorder, namely, intrinsic magnetic disorder, associated with magnetic domains, was found to be promising for the low-field applications. Low field sensitivity as large as 20 %/Oe (H<20 Oe) was obtained for room temperature in properly microstructured epitaxial $La_{0.7}(Ca_{0.5}Sr_{0.5})_{0.3}MnO_3$ films. §5 describes the structure and magnetotransport of nanocomposite $\{La_{0.7}(Ca \text{ or } Sir)_{0.3}MnO_3\}_{1-x}$:$\{MgO\}_x$ films. We have prepared epitaxial nanocomposite films on MgO(100) substrates with a second phase of MgO, epitaxially co-grown with the LCMO primary phase. Magnetotransport in the LCMO was shown to be controlled by "negative" pressure, i.e. 3D tensile stress originated from MgO. Moreover a new structural phase transition in the LCMO phase was found. Nanocomposite LSMO:MgO films on Al_2O_3(0001) substrates contain a columnar nanostructure, where the second phase MgO makes effective tunnel barriers, yielding a fine network of vertical tunneling magnetoresistance (TMR) elements. In §6 we discuss the photoinduced effects in photoconductivity and second harmonic generation (SHG) in LCMO/MgO films. It was observed that laser irradiation (λ=760 nm) results in a large increase of the resistance in the ferromagnetic state ($T<T_C$) as well as to the broadening of the MI transition. Moreover, the magnetic SHG signal was suppressed under illumination indicating a photodemagnetization effect. We interpret the

above effects as photodoping by a large number of excess carriers (holes), which weaken the ferromagnetic double exchange interaction and enhance the electron-lattice interaction. The film in the photoexcited state behaves as an inhomogeneous magnetic medium, whereas "in dark" it is magnetically ordered. In the last section a summary and outlook on possible developments in the field of manganite thin films will be given. Special attention will be paid to the problem of controlling the electronic phase separation. Multiferroic nanocomposite films, which contain elastically coupled ferromagnetic and ferroelectric regions, will be also discussed.

2.BASIC PROPERTIES OF PEROVSKITE MANGANITES

2.1 Crystalline structure

Manganites with the general chemical formula $Re_{1-x}Ae_xMnO_3$ (Re=La, Nd, Pr are rare earth trivalent elements, Ae=Ca, Sr, Ba divalent alkali elements) crystallize in the ABO_3-type perovskite structure, shown in Fig. 1. Large Re- and Ae-ions occupy the A-site positions and small Mn-ions fill those of B-sites. The structure contains a cubic close packed array, formed by oxygen anions and large A-cations, and small Mn-cations in octahedral interstitial sites.

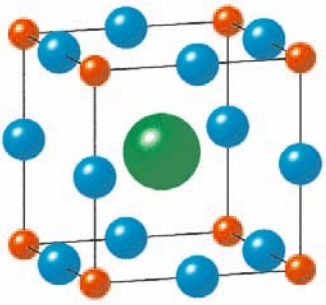

Fig. 1. Perovskite structure: large Re, Ae (La, Ca) cations (green), small Mn-cations (red) and oxygen anions (blue)

To characterize the perovskite structure there was introduced a geometrical parameter, tolerance factor, $t = (r_A + r_O)/\sqrt{2}(r_B + r_O)$ [4], which describes the ionic size mismatch when A-cation is too small to fit into the space between MnO_6 octahedra. Here r_A and r_B are ionic radii of A- and B-cations, respectively, and r_O is the ionic radius of oxygen. For an ideal cubic perovskite with $t=1$ one can get $r_A = r_O$=0.140 nm and $r_B = (\sqrt{2}-1)r_O$=0.058 nm [5]. In Table 1 the values of the ionic radii of some perovskite ions are presented [6]. Only very few manganites, for example, $La_{0.7}Ba_{0.3}MnO_3$ with large Ba-ion and t=0.998, possess a cubic structure. For smaller A- cations (Sr, Ca substitution leads to $t<1$) a free space between MnO_6 octahedra results in internal or "chemical" pressure, which is accommodated by means of enlarging the perovskite lattice cell and lowering the symmetry from cubic to rhombohedral($La_{0.7}Sr_{0.3}MnO_3$, t=0.98), orthorhombic ($La_{0.7}Ca_{0.3}MnO_3$, t=0.97) and further to tetrago-

Table 1. Ionic radii (nm) of perovskite ions.

Mn^{4+}	0.053	La^{3+}	0.1216	Sr^{2+}	0.131
Mn^{3+}	0.0645	Pr^{3+}	0.1179	Ca^{2+}	0.118
Mn^{2+}	0.083	Nd^{3+}	0.1163	Sn^{2+}	0.130
Fe^{3+}	0.0645	Sm^{3+}	0.1132	Ba^{2+}	0.147
Co^{3+}	0.061	Gd^{3+}	0.107	Pb^{2+}	0.135
Ni^{3+}	0.069				

nal and even monoclinic. Another source of distortion of the cubic perovskite structure and lowering its symmetry is the Jahn-Teller effect [7], which by means of elongation of MnO_6 octahedra along the (001) axis and compression in the (a,b)-plane results in a tetragonal distortion of the lattice.

Compared to the cubic perovskites the distorted ones have enlarged (Mn-O) bond lengths with (O-Mn-O) bond angles smaller than 180^o. These two structural characteristics are crucial for describing the electron transport in manganites and their change under the influence of chemical or hydrostatic pressure.

2.2 Phase diagram and disorder effects

Perovskite manganites show a rich variety of electronic phases, which can interact with each other leading to peculiar electronic transport and magnetic behavior. Parent stoichiometric compound $LaMnO_3$ (LMO) with tolerance factor t=0.954 possesses an orthorhombic P_{nma} structure and is known [8] as A-type antiferromagnet with a Neel temperature T_N=140 K. The spins of Mn-ions are ferromagnetically ordered within the (a,b)-plane along the a-axis with the sublattice moment 3.87 μ_B close to the spin-only contribution of the Mn-ions. However, adjacent planes are ordered antiferromagnetically, yielding zero or very weak total moment. LMO shows insulating behaviour because of localized electrons on atomic orbitals of the Mn^{3+} ions due to the Jahn-Teller effect.

Doping with divalent cations, for example Ca, changes magnetic and electron transport properties of LMO drastically. This is illustrated by the phase diagram in Fig. 2 from [9,10]. By moderate doping 0<x<0.15 the antiferromagnetic insulator transforms likely into a canted antiferromagnet and then to a ferromagnetic insulator. At x=0.175 a metal-insulator transition takes place and for 0.2<x<0.45 a ferromagnetic metallic phase is stable below Curie temperatures, T_C≈170-250 K. The optimal doping level x=0.33 yields maximal T_C≈250 K. With further increasing of Ca-doping 0.45<x<0.87 a charge ordered insulating phase appears for 100<T<250 K, which transforms into an antiferromagnetic insulator at low temperatures.

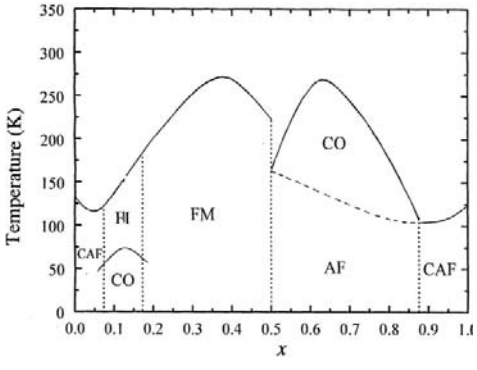

Fig. 2. Phase diagram for $La_{1-x}Ca_xMnO_3$.
FM - ferromagnetic metal; FI - ferromagnetic insulator; CAF – canted antiferromagnetic; AF – antiferromagnetic insulator; CO – charge ordered insulator

Ferromagnetic metallic behavior for 0.2<x<0.45 was explained within the double exchange interaction [11-13], which assumes that substitution of the RE^{3+} ions by divalent alkali ions creates a corresponding number of Mn^{4+} ions with ratio $Mn^{3+}/Mn^{4+} = (1-x)/x$. Mn^{4+} ions with configuration t_{2g} have "holes" on e_g orbitals, which can mediate ferromagnetic exchange between adjacent Mn^{3+} and Mn^{4+} ions. The essential ingredients of the double exchange model are strong on-site Hund's coupling (spin of e_g electron is parallel to the core spin of three t_{2g} electrons) and covalent mixture between e_g states of Mn^{4+} ions with 2p states of oxygen. The latter provides the itinerancy of the d-electrons, which occupy a one-

electron band with bandwidth *W*. Within the DE model [13] the bandwidth "*W*" is proportional to the spin-dependent resonance integral d_{ij}: $W \sim d_{ij} \approx \varepsilon_\sigma \lambda_\sigma^2 \cos\theta \cos(\varphi/2)$, where ε_σ is a one-electron energy, λ_σ a covalent mixing parameter, (180^o-θ) is the O-Mn-O bond angle and φ is the angle between spins of neighbouring Mn ions. One can control the bandwidth "*W*" and thus influence magnetotransport by: a) external hydrostatic pressure affecting the covalent mixing through λ_σ; b) tuning the structure by changing the tolerance "*t*" and thus influencing the angle θ; and c) applying a magnetic field to align Mn spins (angle φ).

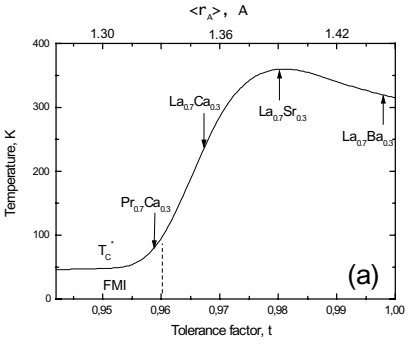

Fig. 3. Curie temperature vs tolerance factor (different average radii of A-ste cation) for isoelectronic manganites $Re_{0.7}Ae_{0.3}MnO_3$ [14].

In Fig. 3 we present a phase diagram from [14, 15], which demonstrates a dependence of the Curie temperature, T_C, on the internal lattice strain or chemical pressure for different manganites with optimal x=0.3 and thus maximal strength of DE. The change of the average radii of the A-site cations, $\langle r_A \rangle$, or in other words of the tolerance factor in the interval $0.95<t<1$ was achieved by different A-site substitutions in iso-electronic perovskites $Re_{0.7}Ae_{0.3}MnO_3$. Maximum T_C = 360 K and strongest DE is obtained for $La_{0.7}Sr_{0.3}MnO_3$ with t=0.98. It is interesting that LBMO with almost cubic structure (t=0.998) and thus optimal O-Mn-O angle θ=180° has a lower T_C=320 K, in disagreement with the DE model. A similar T_C-$\langle r_A \rangle$ phase diagram was obtained in [16] where the lattice strain was additionally increased by hydrostatic pressure for the same manganites shown in Fig. 3. The increase of T_C with pressure was obtained in accordance with DE predictions.

As one can see from Fig. 3 the strongest changes of T_C as a function of lattice strain occurs for $0.96<t<0.98$, i.e. for the La-Ca-Mn-O system, in which the DE contribution is weakened compared to that in LSMO. A competing electron-lattice interaction [17] due to the Jahn-Teller effect becomes dominant in manganites with a distorted perovskite structure, i.e. for $t<0.96$. For example, $Pr_{0.7}Ca_{0.3}MnO_3$ with t=0.95 is no more ferromagnetic; instead a charge ordered insulating state is stable for $T<T_{CO}$~240 K, which transforms into an antiferromagnetic insulating state at lower temperatures. Thus, the tolerance factor may be viewed as a structural parameter, which indicates a relative strength of DE and electron-lattice (EL) interactions [15]. With respect to the t-values the manganites are classified as those with: a) a large bandwidth i.e. DE>>EL - LSMO and LBMO with t~1; b) a middle bandwidth (LCMO, t=0.97) with DE~EL; and c) a small bandwidth (PCMO, t=0.95) with EL>>DE.

Another important structural characteristic, which influences the order parameter to a large extent [18], is A-site cationic disorder due to differences in ionic radii between Re^{3+}(La, Pr, Nd, Sm) and Ae^{2+}(Ca, Sr, Ba) ions. This kind of disorder is an intrinsic characteristic of manganites and arises due to random distribution of the A-site cation radii, composed of two

cations with different ionic radius. Cation disorder is characterized by the variance of the ionic radii $\sigma^2 = \sum y_i r_i^2 - \langle r_A \rangle^2$ about the mean $\langle r_a \rangle$, where y_i is the fractional occupancy and $\sum y_i = 1$. As was shown by L.M. Rodriguez-Martinez and P. Attfeld [18] the increase of the disorder parameter in the range σ^2=0.0016-0.0240 Å^2, while keeping constant $\langle r_a \rangle$=0.123 nm, leads to significant decrease of T_C and T_{MI} from 350 K down to 60 K. Moreover, the samples with large disorder σ^2>0.015 Å^2 show electronically inhomogeneous behavior indicated by two maxima on the R(T) curves, and by disparity between T_C and T_{MI} for σ^2=0.024 Å^2. A mixture of antiferromagnetic and ferromagnetic regions for $T>T_C$ was also suggested for "disordered" samples [18], basing on the observed deviation of the inverse magnetization from the classical Curie-Weiss behavior.

Taking into account the existence of A-site disorder one can understand the lowering of the Curie temperature for $La_{0.7}Ba_{0.3}MnO_3$ (T_C=320 K), which despite of the optimal large $\langle r_a \rangle$ reveals a very large disorder, σ^2=0.0131 Å^2, in comparison with $La_{0.7}Sr_{0.3}MnO_3$ with σ^2=0.0018 Å^2 and T_C=370 K. Furthermore, by analysing the dependence of the T_{MI} on the cationic disorder it was estimated [18] that so called ideal cubic manganite without disorder, σ^2=0, would show the highest T_{MI}≈530 K. The calculations based on DE model alone give T_{MI}=2500-5000 K [17], whereas those considering the Jahn-Teller distortions of MnO_6 octahedra result in more realistic value ~500 K [17, 19], similar to the estimated T_{MI} without disorder.

A-site cation disorder plays a crucial role in CMR. Small bandwidth manganites like $Pr_{1-x}Ca_xMnO_3$ possess also a negligible disorder, $\sigma^2<10^{-6}$ Å^2, because of exact matching of the ionic radii of Pr^{3+} and Ca^{2+}. An extremely large CMR ratio 10^6 at T=85 K was observed in Pr-based manganites, like $Pr_{0.75}Ca_{0.25}Sr_{0.05}MnO_3$ with small disorder [16, 20]. In contrast, other manganites with similar $\langle r_a \rangle$ and T_{MI}, for example $La_{0.6}Ca_{0.3}Y_{0.1}MnO_3$, show much smaller CMR=40 at T=120 K [21].

2.3 Electronic inhomogeneity of manganites

Even the complicated phase diagram shown in Fig. 2 does not reflect adequately the variety of electronic phases in manganites and their interrelationships. Namely, numerous studies pointed out that the phases in Fig. 2, wherever they are located, close to phase boundaries or far away from them, seem to be not pure electronic phases but, instead, are electronically inhomogeneous. For example, a small angle neutron scattering (SANS) [22] and magnetic resonance experiments [23] reported on the coexistence of ferromagnetic (FM) and antiferromagnetic (AF) regions in $La_{1-x}Ca_xMnO_3$ bulk samples for x=0.05, 0.08, i.e. far away from the MI-phase boundary, x=0.175. For LCMO with optimal doping, x=0.33, De Teresa et al. [24] have found short range FM correlations, i.e. small magnetic clusters (polarons) with diameter ~1.2 nm, which exist in the paramagnetic (PM) region for temperatures $T>T_C$. Moreover, another SANS measurement [25, 26] revealed an unconventional FM-PM transition for the compound with x=0.33, in which in contrast to conventional ferromagnet the spin wave excitations decrease as the temperature increases towards T_C while a quasi-elastic spin-diffusion component grows and dominates at the transition region. A model with two coexisting phases, FM-metallic with well defined spectrum of spin waves and PM-insulating (spin-diffusion), was proposed in [25], in which the fractions of two phases depend on the temperature.

A remarkable electronically inhomogeneous state of the manganites is manifest in LCMO with x≈0.5, i.e. at the border between the FM-metal/AF-charge ordered insulator [27, 28]. Such coexistence seems to be impossible within the double exchange model because charge localization (precursor state to charge ordering) assumes exclusively an AF insulating but not a FM metallic state. The latter one requires delocalization (hopping) of charge carriers, which can at least hop between the Mn ions. Nevertheless, as was viewed by electron microscopy, these phases do spatially coexist [27] as a mixture between incommensurate charge-ordered (CO) and FM charge-disordered clusters with a size of 20-30 nm. CO domains consist of paired and unpaired charge-ordered and Jahn-Teller distorted Mn^{3+} stripes. A phase separation on a very large scale was observed by M. Uehara et al. [28] for $La_{0.625-y}Pr_yCa_{0.325}MnO_3$ system with Pr-doping y=0.25-0.4, which induces a CO state with T_{CO}=210 K. The CO AF- and charge disordered FM-domains with characteristic sizes of about 0.3-0.5 μm were revealed by electron microscopy at T=17 K in the ferromagnetic state. With increasing temperature in the CO state, $T_C<T<T_{CO}$, the scale of the electronic phase separation decreases down to nm-size.

Spatially inhomogeneous electronic behaviour was detected in $La_{1-x}Ca_xMnO_3$ (x~0.3) single crystals and thin films by scanning tunnelling spectroscopy (STS) combined with scanning tunnelling microscopy (STM) [29]. Note that according to DE predictions and phase diagram (Fig. 2) a homogenous metallic state for $T<T_C$ should be expected for such doping concentrations. In contrast, the STS images reveal an inhomogeneous distribution of tunnelling conductance $\sigma = (dI/dV)$, measured at a bias 3V, on a sub-micrometer scale (500x500 nm^2) with "cloud-like" regions of about several tens of nanometers. The CMR value, calculated from the image-averaged conductance $\overline{\sigma}(0)$ and $\overline{\sigma}(9\ \mathrm{T})$ as CMR=($\overline{\sigma}(0)$ - $\overline{\sigma}(9\ \mathrm{T})$)/$\overline{\sigma}(0)$, is comparable with the global transport CMR. However, even for a maximal field of 9 T the STS image was still inhomogeneous. The phase separation in $La_{0.7}Ca_{0.3}MnO_3$ is different from that seen for $La_{0.5}Ca_{0.5}MnO_3$ [27, 28] since in the former the phases are not fully metallic or insulating. For $T<T_C$ they both show metallic-like behaviour with $(dI/dV) \neq 0$ at V=0, contrasting only by larger local σ-values for the "metallic" phase and lower conductivity for the "insulating" phase. To interpret the observed large scale separation the structural disorder (variation of oxygen content or twinning) was suggested [29], which acts to destroy the balance between DE and electron-lattice (Jahn-Teller) interactions, controlling the phase diagram in manganites.

A lot of experimental indications for inhomogeneous ground state of manganites have stimulated the appearance of new theoretic computational approaches which account for the competition between FM and AFM phases in the presence of electronic density fluctuations, chemical disorder, and very recently lattice strain. Within electronic phase separation scenario proposed by A. Moreo et al. [30] it was assumed that the observed inhomogeneities arise because of different hole densities in competing FM and AFM phases (Fig. 2). However, large (micrometer) scale coexistence [27, 28] of electrically charged domains is energetically unfavourable due to a drastic increase of the Coulomb energy[1]. To reduce the electrostatic energy these phase separated domains are expected to break into small regions of different shape like

[1] Note that micrometer scale phase separation might be naturally explained within a chemical phase separation while the reduction of the scale down to nanometer seems to be incompatible with a chemical scenario – the phases cannot be so small [31].

droplets or stripes. The formation of such nanophases with typical size in the nanometer scale was argued by E. Dagotto et al. [32] to be stable because they satisfy the electronic phase separation tendency and also prevent macroscopic charge accumulation.

Another model, disorder induced phase separation (PS), was also proposed by the Dagotto's group [32-34] for manganites to avoid the problems of large scale electronic phase separation related to Coulomb energy. The model focuses on the first order transition, e.g. FM-metal/AF-insulator at x~0.5, in the presence of A-site cation disorder discussed in § 2.2. Such a transition without disorder is characterized by a discontinuous jump of the order parameter and latent heat over the phase boundary. The stable ground state is then essentially metallic or insulating dependent on the location on the phase diagram. A. Moreo et al. [33] have shown by means of Monte-Carlo simulations within "one"- and "two"-orbital models that cation disorder (random distribution of hopping probabilities and exchange interactions) generates mixed phases with coexisting FM and AF domains in the vicinity of the phase transition, which becomes now continuous or percolative. Qualitatively a phase separated state can be stable due to two competing opposite tendencies: 1) The increase of the interface energy in coexisting FM and AF domains makes PS unfavourable, yielding the increase of the domain size; and 2) Disorder tends to minimize the size of domains down to the lattice spacing; at this scale the system favors either the FM or AF state according to disorder, fluctuating over the FM/AF phase boundary. As a result an equilibrium size of PS domains is stabilized. Note that the hole density, for instance x~0.5, is constant and no limitations from the Coulomb energy on the size of competing clusters arise. Thus even micrometer cluster sizes become possible. Another interesting feature is that the larger the disorder the smaller the domains. This seems to be important for understanding the CMR results on Pr-based compounds with small disorder, which assume that very large CMR is compatible with a large size of AF and FM domains.

The AF/FM-, FM/COI- and COI/PM- phase transitions shown in the phase diagram in Fig. 2 are of the first order [10, 14, 15]. However the FM/PM phase transition can be of the first order [24-26] or of the second order, depending on the constant of electron-lattice coupling [31]. For small (PCMO) and middle bandwidth (LCMO) manganites with significant electron-lattice interaction the FM/PM phase transition shows a hysteresis [15, 16, 24-26], indicating a first order transition. Taking into account also considerations about cation disorder (see § 2.2) it seems to be likely that $La_{1-x}Ca_xMnO_3$ system is good candidate to study the PS-effects.

A very recent model of K. Ahn et al. [35] assumes that strain instead of electron density or disorder is a driving force of the phase separation. Indeed lattice distortions [9] are of great importance for manganites – they govern to a large extent the phase diagram. The basic assumptions of the new model are: 1) without strain (undistorted state) the system is metallic and under strain (distorted state) it is insulating; and 2) there exist coupled short- and long-wavelength lattice distortions of the Jahn-Teller type, which modify elastic energy of the system yielding local (undistorted) and global (distorted) energy minima. Such "structural template" leads to the coexistence of mixed phases which are undistorted (metallic) and distorted (insulating).

A general conclusion can be made as following. Structural phase transformations and closely related to them electronic phase transitions are very sensitive to lattice strain and disorder effects whatever their origin, internal "chemical" pressure or external pressure. Based

on the above peculiar characteristic of manganites it looks very attractive to control magneto-transport in manganite thin films by means of tuning the lattice strain and disorder on the nanometer scale. To achieve this goal we have developed a metalorganic aerosol deposition (MAD) technique [36], which provides specific deposition conditions not possible within physical vacuum methods. The lattice strain was created by: a) substrate-film epitaxy mismatch; b) applying hydrostatic pressure, c) tuning the film microstructure (grain size and grain boundaries); and d) using nanocomposite film architecture with a second phase elastically coupled to the primary manganite phase.

3. METALORGANIC AEROSOL DEPOSITION (MAD) TECHNIQUE

Thin manganite films were grown by means of the MAD technique [36]. MAD is a chemical route, originally developed for the preparation of High-T_C superconducting $YBa_2Cu_3O_{7-x}$ films [37] and also successfully used to grow oxide films of different functionality [38-40]. Chemical deposition techniques like chemical vapour deposition (CVD), metalorganic chemical vapour deposition (MOCVD) as well as sol-gel and spray pyrolysis all involve chemical reactions as a preliminary stage to grow the film. In the case of oxide films this is a pyrolysis reaction, an example of which is written below:

$$Cu(C_3H_5O_2)_2 + 7O_2 \xrightarrow{T^oC} CuO + 6CO_2 \uparrow + 5H_2O \uparrow$$

Here, $Cu(C_3H_5O_2)$ is a Cu(acetylacetonate) precursor, which under heating up to ~250-300^o C decomposes with the formation of a cooper oxide in oxygen containing media. Two types of chemical reactions are important for applications: 1) homogeneous pyrolysis (the reaction takes place in the gas phase – gas condensation) is promising for the preparation of oxide nanoparticles (see for example [41]), and 2) heterogeneous pyrolysis (the reaction occurs on the interface between gas and a solid) is used to grow thin oxide films. The vapour phase deposition technique (CVD and MOCVD) requires volatile precursors, the large quantities of which can be congruently (without decomposition) vaporized at relatively low temperatures (20-100^o C) and low vacuum (1-100 Torr). Sol-gel and spray pyrolysis both use non-volatile precursors, which react being in solid state.

The MAD technique is based on using β-diketonate precursors with low decomposition temperature ~250-350 C. They usually have low volatility or even are thought to be non-volatile (precursors for rare earth elements). Very fine droplets (aerosols) of a few micrometer sizes allow one to perform so called “flash” or fast evaporation [42], which is advantageous for precursors with low volatility. Moreover the non-volatile precursors being in small portions can be decomposed quickly. The decomposition/vaporization of aerosols takes place in the close proximity to the heated substrate. This is a very important feature, which makes possible the preparation of a pure oxide phase with extremely smooth morphology; moreover, it prevents the reaction in a gas phase and, thus, a possible pollution of the growing film with nanoparticles.

The scheme of the MAD is shown in Fig. 4. The mixture of organometallic precursors, typically acetylacetonates of the corresponding metals (La, Ca and Mn, for instance), have been dissolved in an organic solvent (dimetylformamide). The precursor solution was atomized down to fine aerosols with diameter Ø=10-20 μ by means of a pneumatic nozzle and transferred onto heated substrate by a carrier gas (dried air or oxygen). Aerosol flow rate was

controlled in the range v=0.05-10 mL/min by measuring of the radiation of a GaAs diode laser, diffusively scattered by the droplets. The substrate temperature was controlled in the region T_S=300-1000 C by detecting the radiation, emitted from the backside of the substrate heater (SiC plate), using a Si-photodiode optically coupled to the heater by a fibre optic waveguide. The thickness of growing film, d=0-200 nm, was controlled by measuring the reflection of radiation of the He-Ne laser from the film surface. Deposition rate may be easily varied in the range r=1-300 nm/min by changing the concentration of the precursor solution, aerosol flow rate and substrate temperature.

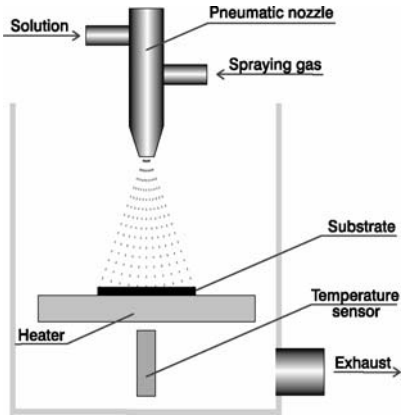

Fig. 4. The scheme of the MAD process.

Being simple in operation and allowing low-cost production of high quality films, MAD, compared with other chemical techniques possess several advantages: 1) precise control of the film composition; 2) no vacuum and gas transport lines; 3) high deposition rates and compatibility with large area substrates; 4) high oxygen partial pressure up to 10^5 Pa. Furthermore, the above deposition scheme (Fig. 4) is very flexible – a number of different nozzle-substrate geometries within several reactor assemblies were recently patented [43].

MAD seems to be very attractive for the preparation of manganite films, the properties of which are very sensitive to both the cation and oxygen stoichiometry. The latter is known to be a common problem for physical vacuum deposition techniques, like PLD and sputtering. Moreover, MAD offers a wide spectrum of deposition rates and supersaturation, if compared to those provided by PLD and MOCVD. Both features open a promising opportunity to control the growth mechanisms of manganite films with corresponding changes of the magneto-transport.

We have prepared thin films of manganites like $La_{0.7}Ca_{0.3}MnO_3$, $La_{0.7}Sr_{0.3}MnO_3$ and $La_{0.7}(Ca_{1-x}Sr_x)_{0.3}MnO_3$(LCMO) by means of the MAD technique. Precursors, commercial acetylacetonates (acac) of La^{3+}, Ca^{2+}, Sr^{2+} and Mn^{2+}, were dissolved in dimethylformamide or methanol to prepare the solution with the molar ratio close to stoichimetric: $[La(acac)_3]_{0.7}$:$[Ca,Sr(acac)_2]_{0.3}$:$[Mn(acac)_2]_1$. The concentration of the solution was usually n=0.025-0.1 M if calculated on $Mn(acac)_2$. The substrate was MgO(100), which is very suitable for the preparation of perovskite films. Typical deposition conditions for the preparation of epitaxial L(C,S)MO manganite films with thickness, d=10-200 nm, were: substrate temperatures, T_S=650-750 C, aerosol flux rate, v=0.1-0.5 mL/min, deposition rates, s=5-200 nm/min, spraying gas – compressed air. After deposition the films were cooled down in 10-15 min; they look smooth and shiny, and contain no defects as visualized by optical microscopy.

4. MAGNETOTRANSPORT IN SINGLE $La_{0.7}(Ca,Sr)_{0.3}MnO_3$ FILLMS.

4.1 Two mechanisms of film growth

X-ray diffraction analysis of MAD grown LC(S)MO/MgO(100) films reveals both out-of-plane (Fig. 5 a) and in-plane textures (Fig. 5b). (θ-2θ) patterns contain only the peaks of substrate (100) and (200) as well as those from the film, belonging to the {*00l*} system of crystallographic planes with *l=1,2,3,4*. Measured c-lattice parameters were c=0.3833-0.3892 nm for different films depending on the substrate and deposition conditions. Rocking curves of the (002) peak of LCMO show typical values FWHM=0.3-0.4^0. Typical ϕ-scans of the (111) or (220) peaks of LCMO (Fig. 5b) show a 4-fold symmetry [36, 44] in accordance with the pseudo-cubic structure of LCMO. Thus, we conclude that MAD prepared manganite films are "cube-on-cube" epitaxially grown on MgO(100) substrates.

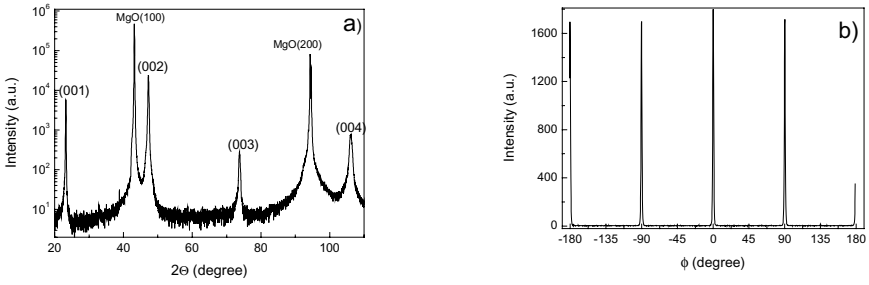

Fig. 5. (θ-2θ) diffraction pattern (a) and ϕ-scan of the (220) peak of LCMO/MgO(100) film**.**

Despite of a similar global crystalline structure the films may exhibit essentially different surface morphology in accordance with two observed growth modes [45]: A) layer-by-layer epitaxy, known also as Frank-van der Merwe [46] growth; and B) 3D nucleation or island growth (Volmer and Weber [47]) of crystallites. The A-type films show a very smooth and flat surface morphology as studied by means of AFM and STM. On the STM image of a LCMO film with thickness d=60 nm shown in Fig. 6 one can see terraces, having one unit cell of height, h≈0.4 nm. The calculated mean square roughness consists of RMS=0.2-0.3 nm. Moreover, a larger area images show the growth spirals over a length of about 500 nm.

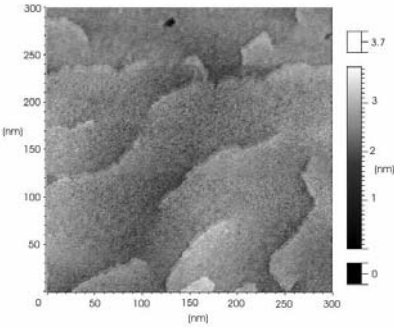

Fig. 6. STM image of layer-by-layer (A-type) grown LCMO film.

A completely different, "brick wall"-like morphology posses B-type films. In Fig. 7 an example of such microstructure is shown for a LCMO/MgO film with thickness d=250 nm. The film material consists of closely packed rectangular blocks aligned with their sides along the [100] and [010] crystallographic directions of MgO. The grain size is surprisingly homogenous in B-type films and, depending on the deposition conditions, varies in the range D=40-500 nm for different films [45]. Typical average roughness values are RMS=1-8 nm.

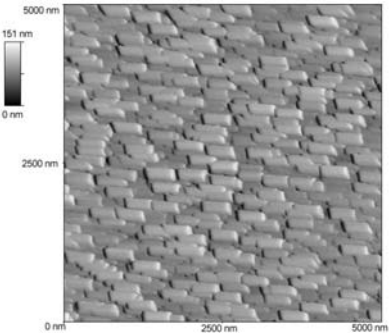

Fig. 7. AFM picture of a LCMO film with "brick wall" surface morphology [45].

As we have established experimentally, layer-by-layer mode of growth can be realized on MgO substrates for unstrained LCMO films with c=0.386(6-9) nm, which coincide with the bulk value [48], as well as for strained films on buffered $LaMnO_3$/MgO or $NdGaO_3$ (NGO) substrates with c=0.3833-0.3856 nm up to thicknesses d≈120-150 nm [45, 49]. Critical parameters seem to be the concentration, n, of the precursor solution and deposition rate, s.

Table 2. Characteristics of LCMO films and multiláyers grown by MAD [49].

Sample, buffer/substrate-Nr.	Thickness (nm)	c-axis (nm)	T_{MI} (K)	T_C (K)	E_A (meV)	ρ_{max} (Ω cm)	MR_{max} (%)	L_{XRD}^{-1} (nm^{-1})
NGO (A)	100	0.3833	240	-	-	0.22	190	-
LMO/MgO (A)	150	0.3841	245	-	71	0.12	160	-
MgO-10 (A)	100	0.3856	238	245	77	0.012	280	0.020
MgO-4 (B)	100	0.3876	173	240	100	0.13	800	0.055
MgO-13 (B)	240	0.3878	155	226	106	1.1	1400	0.067
MgO-14 (B)	250	0.3856	174	245	95	0.1	770	0.045
MgO-12 (B)	200	0.3868	215	-	80	0.04	300	0.031
MgO-15 (B)	230	0.3877	164	-	93	0.1	-	0.056
LCMO/LMO/ MgO-8	10×10	0.3892	0	265 130	122	10^8 Ω	10^5	0.10

The smaller the "n" the higher can be "s". The B-type films are obtained usually for low values of *v*<10 nm/min and higher thickness d>100 nm. They have usually enlarged c-axis parameters c=0.387-0.389 nm. In Table 1 we have summarized the structural as well as transport parameters of different LCMO films prepared by MAD.

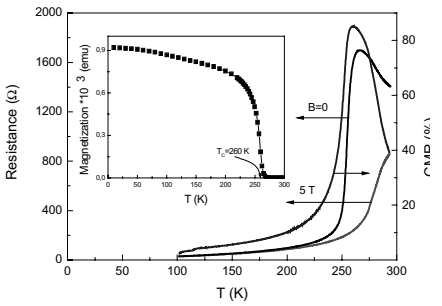

Fig. 8. Resistance vs Temperature for an A-type epitaxial LCMO/MgO film [50]. The inset shows temperature dependence of the magnetization.

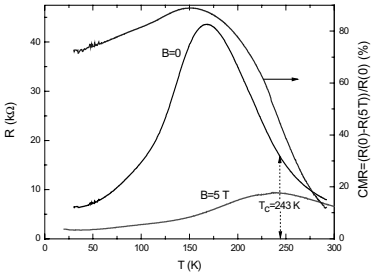

Fig. 9. Temperature dependence of the resistance and CMR in a B-type film [36].

4.2 Mesoscopic magnetotransport

The two types of films, i.e. of layer-by-layer and island growth, differ drastically in their magnetotransport properties. In Fig. 8 typical magnetotransport behavior of A-type films is shown. A sharp metal-insulator transition at T_{MI}=245-260 K, and a narrow CMR peak in the vicinity of the MI-transition with typical values $CMR_{max}(5T)$=200-800 % and vanishingly small CMR at low temperatures were observed. Moreover, the ferromagnetic-paramagnetic transition is coupled to the MI-transition, i.e. $T_C \sim T_{MI}$. In the insulating phase for $T>T_C$ the resistance shows an activation behavior with characteristic activation energies E_A~0.04-0.06 eV. A similar behavior, named bulk or intrinsic CMR, is usually observed in single crystals and epitaxial films of manganites [5, 51].

In contrast, B-type films (island growth) with "brick wall" like morphology possess essentially different magneto-transport, shown in Fig. 9. Here one can see the metal-insulator transition occurs at lowered T_{MI}=174 K accompanied by very large peak resistance. The magnetic transition (not shown here) is significantly broader with T_C-values comparable to those of A-type films. Thus T_C and T_{MI} are no longer coupled to each other and $T_{MI} \ll T_C$ (see also Table 1). The CMR(T) shows a broad temperature distribution with large CMR values also for low temperatures, $T \ll T_C$.

This is a typical extrinsic MR behavior seen in polycrystalline bulk and film samples [52-54]. It is attributed to a static or structural disorder, which usually is associated with grain boundaries. For a polycrystalline or granular manganite films [53] the resistivity, ρ, at low temperatures is inversely proportional to the grain size D, i.e. $\rho = \rho_G + (l/D)\rho_{GB}$. Here ρ_G and ρ_{GB} are the resistivity values for grains and grain boundaries (GB), respectively, and l, D are the thickness of GB and grain size, respectively. However, the residual resistivity, $\rho_{4.2K}$, for B-type films, which seem to contain grain boundaries (Fig. 9), does not scale with D^{-1} for

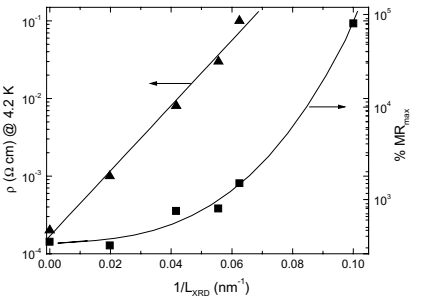

Fig. 10. Dependencies of the residual resistivity at T=4.2 K (▲) and maximal magnetoresitance (■) on the characteristic disorder length L_{XRD}^{-1} [45].

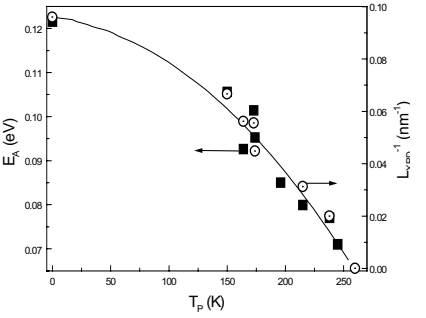

Fig. 11. Dependences of the activation energy (■) and disorder scale L_{XRD} (○) on the metal-insulator transition temperature [49].

grain size D=200-500 nm. This indicates that scattering at GB's is not a dominating mechanism for B-type films. The grains seem to contain internal inhomogeneities, which might be associated with a kind of disorder on the scale, L, much smaller then grain size, i.e. L<<200-500 nm.

We estimated the disorder scale for B-type films from ((θ-2θ) X-ray diffraction patterns according to the Scherer's formula [55]: $L_{XRD} = K\lambda / \beta(\theta)\cos\theta$, where $K \approx 1$, λ is X-ray wavelength, $\beta(\theta)$ the FWHM of the diffraction peak and θ is the diffraction angle. In Figs. 10 and 11 one can see that the main magnetotransport characteristics, like $\rho_{4.2K}$, CMR_{max}, T_{MI}, and activation energy of the resistance, E_A, scale well with the above L_{XRD}^{-1}, which, thus, seems to be a suitable disorder parameter. For different B-type films the determined magnitudes of L_{XRD}=10-40 nm are considerably smaller then the corresponding grain size. Note that the smallest disorder scale was observed in the $(LCMO)_{10}/(LMO)_{10}$/MgO multilayer structure (see Table 1 and [49]) with thickness of individual layers d=10 nm comparable with the disorder scale L_{XRD}. Such a structure shows the largest CMR=10^5 %.

Moreover we also found an interesting correlation (see Fig. 11) between the metal-insulator transition temperature, T_{MI}, and the activation energy, E_A, on one hand, and the disorder scale, L_{XRD}, on the other hand. Basically, the films can be classified according to the values of L_{XRD}. The A-type films with small disorder ($L_{XRD} \sim D$) exhibit high T_{MI}=240-260 K, which are typical for $La_{0.7}Ca_{0.3}MnO_3$, accompanied by small values of activation energies E_A~0,04-0,06 eV. B-type films with large disorder ($L_{XRD} << D$) posses low T_{MI}=150-180 K and show increased values of E_A~0.1 eV. Moreover the increase of disorder is accompanied by enlarging of the c-axis as seen from Table 1, indicating a possible coupling of the lattice strain and disorder effects (see more in § 4.2).

Note that the behavior, observed for B-type films seems to be a common behavior for disordered films. The same E_A=0.12 eV was obtained in highly ion irradiated insulating LCMO films (T_{MI}=0) [56]. The decoupling between T_C and T_{MI} and enlarged c-axis in sputtered films [57] and those obtained by PLD [58, 59] were attributed to structural/magnetic disorder, induced by oxygen deficiency. Al these effects tend to disrupt DE coupling and to localize charge carriers in accordance with polaronic models.

As we have discussed in §2.2 local cation disorder plays a major role for bulk LCMO manganites by controlling the order parameter and, possibly, inducing the phase separation. For thin LCMO films an additional type of disorder, originating from an island growth mechanism and intimately related to lattice strain seems to be relevant. It is known [60, 61] that grains in films prepared by island growth mode are inhomogenously strained along the grain surface because of non-complete strain relaxation. Deposition conditions, i.e. enhanced growth rate within MAD technique prevent the strain relaxation; the films remain in a strained state with an enlarged c-axis parameter compared to bulk LCMO (Table 2). Thus an inhomogeneous strain inside the grains can destroy a homogeneous electronic ground state. The grain breaks up in nanometer-sized FM metallic clusters (unstrained particles), which are separated by insulating strained regions.

Indeed T. Becker et al. [62, 63] by using scanning tunnelling spectroscopy/ /microscopy have observed an inhomogeneous distribution of the tunnelling conductance, which contains metallic (dI/dV≠0, at V=0) and insulating (dI/dV=0) regions in LCMO films with island growth mode. Fig. 12 a) is a topography image of a LCMO film with quadratic shaped grains with diameter D~30 nm. In Fig. 12 b) a map of the tunnelling conductance of the same region, measured in the ferromagnetic region for T=78 K (T_C=250 K) is shown. It consists of metallic regions with conductance σ=0.02 nA/V at V=0, shown by red colour, and insulating regions (blue), where σ=0 for a voltage range -0.15 V<V<0.15 V. The estimated size of insulating filaments was 5-10 nm, indicating an inhomogeneous state inside a single-crystalline grain. A. Biswas et al. [64] supports our observations, finding a phase separation behavior in island grown films LCMO on $LaAlO_3$. They have shown FM/AFI coexistence due to inhomogeneous strain distribution induced by the $LaAlO_3$ substrate.

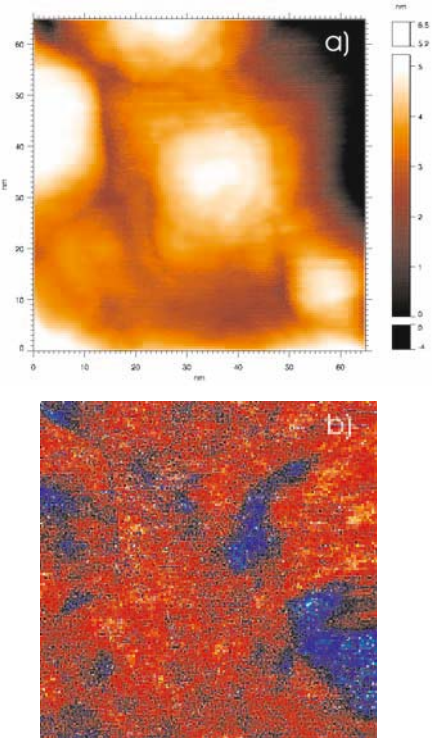

Fig. 12. STM topography image (a) and the distribution metallic (red) and insulating (blue) regions within the same area (b).

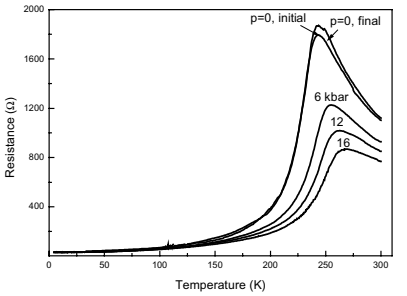

Fig. 13. Temperature dependece of the resistance for an A-type LCMO/MgO film [68] at different external pressures.

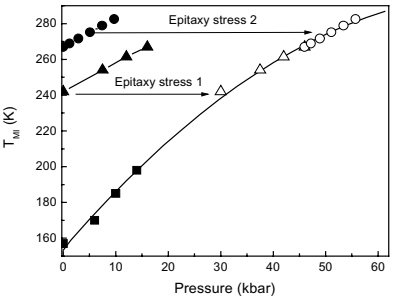

Fig. 14. Pressure dependence of T_{MI} for LCMO films with reversible pressure effect: (●) on $SrTiO_3$ from [69], (▲) on MgO (PLD), and (■) on MgO (MAD) [49].

4.3 Lattice strain effects

The influence of hydrostatic pressure on magnetic and electron transport properties of manganites was studied usually for bulk materials and single crystals [16, 65-67]. The effects of external hydrostatic pressure, usually in the range p=0-20 kbar, were found to be very similar to chemical or internal pressure due to A-site cation substitution [16]. Namely both T_C and T_{MI} increase with pressure. This was explained within compressing the Mn-O bond length and opening of the Mn-O-Mn bond angle, both leading to an increase of DE and stabilization of the metallic ferromagnetic phase. Thin films are expected to show a more complicated pressure effects simply because they can be already strained at ambient pressure due to: 1) to substrate induced epitaxy stress in layer-by-layer grown films (A-type), and 2) to a non-complete strain relaxation in 3D island grown B-type films.

We have observed two kinds of pressure effects in thin LCMO films [68]**.** "Intrinsic" or reversible pressure effect is characteristic for A-type epitaxial films and extrinsic (irreversible) effect was observed in B-type films for p>8 kbar. An example of a reversible pressure effect is shown in Fig. 13. The resistance decreases under pressure significantly, accompanied by a shift of the peak temperature, T_{MI}. After the pressure was released the resistance remains practically the same as that in the initial state for the whole temperature region, indicating no effects of strain relaxation or deterioration of the sample. This is qualitatively the same behavior as that observed for bulk manganites [14, 65-67]. However, quantitatively, the pressure dependence of T_{MI} in epitaxial LCMO films depends significantly on misfit epitaxy stress as is shown in Fig. 14. The films differ not only in T_{MI} at ambient pressure but also in the pressure coefficient of T_{MI}, $\alpha = dT_{MI}/dp\big|_{p=0}$, which varies as α=1.4-1.9 K/kbar. Remarkable is that the $T_{MI}(p)$ curves for different films join a common behavior [68], marked by open symbols, if one assumes different values of initial lattice strain caused by epitaxial growth. We estimated the relative strain $\Delta c/c$ (compared to the LCMO/MgO film prepared by MAD) from

the formula: $(\Delta c/c)\chi = P_{ES}$. Here $\chi = 5\times10^{11} N/m^2$ is the Young's modulus taken from [70] and P_{ES} is a fitting parameter used to shift T_{MI} values in Fig. 13, which is taken as 30 and 46 kbar for PLD films in Fig. 14. With c=0.3875 nm for a LCMO/MgO film [49] we calculate the c-axes for PLD grown films to be c=0.3836 nm (●) and c=0.3856 nm (▲). Estimated values fit very well the measured values c=0.383 nm for LCMO/$SrTiO_3$ from [69] and c=0.385 nm for PLD grown LCMO/MgO film [71]. This indicates that epitaxy lattice strain does governs T_{MI} in A-type films.

An irreversible pressure effect, observed in B-type (island growth) LCMO/MgO films, is shown in Fig. 15. For relatively low pressure, p≤8 kbar, the film shows usual pressure behaviour with decreasing the resistance and shift of T_{MI} towards high temperatures. However by further increase of pressure the resistance increases dramatically in the low temperature region, $T<T_{MI}$, and the second maximum appears at T~60 K for p=12 kbar. Moreover after releasing the pressure the resistance does not return to the initial value, but, in contrast, increases even more by about two orders of magnitude at low temperatures, thus showing a relaxation effect. For high temperatures $T>T_C$=240 K the pressure as well as temperature cycles do not lead to any significant changes in the R(T). To quantify the pressure effects in thin films we introduce a parameter $\beta = R_F(5K)/R_I(5K)$, which characterizes the increase of the residual resistance under pressure. Here R_F(5K) is the resistance at 5 K in the final state, after pressure release, and R_I(5K) is the resistance in the initial state (before application of pressure). The values β=100-600 were observed B-type LCMO/MgO films, showing irreversible pressure effect; for reversible pressure effect β=1, which is also demonstrated by Fig. 13. Interesting to note that irreversible pressure behaviour with β>>1 was observed for LCMO films with an extraordinarily large pressure coefficients dT_{MI}/dp=2.7-3.9 K/kbar. These values exceed significantly dT_{MI}/dp=0.5-2 K/kbar, obtained for bulk samples of manganites for the whole range of T_{MI}=370-90 K [66].

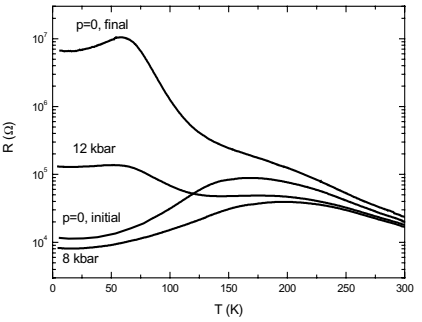

Fig. 15. Temperature dependence of the resistance for different pressure of a typical B-type LCMO/MgO film (MgO_497 see Table 2)

Thus we may conclude that application of hydrostatic pressure, p>10 kbar, enhances the disorder in B-type LCMO films, stabilizing the low temperature insulating phase and yielding an apparent phase separation with two maxima on R(T). One can see a clear difference between the pressure effects in homogenous and "inhomogeneous" (phase separated) manganites. Namely, in the former external pressure is equivalent to internal "chemical" pressure, which by increasing the tolerance factor, t, increases the electronic bandwidth, W, and stabilizes ferromagnetic metallic behavior. In contrast in the latter case initial stress may accumulate external pressure, enhancing the insulating antiferromagnetic behavior. Very recently C. Meneghini et al. [72] studied pressure effects in $La_{0.75}Ca_{0.25}MnO_3$. For p<60 kbar a usual pressure behavior discussed above was observed. However for p>60-70 kbar a JT-structural

transformation accompanied by charge localization effects instead of delocalization were found. It seems reasonable to suppose that for our initially strained B-type films the actual pressure, p^*, which yields the irreversible effect, can be written as a sum of "internal stress", p_0~30-50 kbar (see Fig. 14), and external pressure, p=12 kbar, thus giving $p^* = p_0 + p \approx 60\,\text{kbar}$. This estimation is consistent with critical pressure obtained in [72]. Moreover, the stabilization of the AF insulating phase by similar external pressure p=6-8 kbar was shown for charge-ordered phase separated manganites, like $(Nd, Sm)_{0.5}Sr_{0.5}MnO_3$ [73, 74], for $La_{0.9}Sr_{0.1}MnO_3$ [75] as well as pressure induced phase segregation was found in layered manganites $La_{2-2x}Sr_{1+2x}MnO_7$ [76] for p~10 kbar. Al this indicates the importance of lattice strain for phase separation phenomena.

4.4 Magnetic disorder and low-field magnetoresistance

As was shown in previous sections the CMR effect can be very large in disordered (phase separated) La-Ca-Mn-O as well as in small bandwidth Pr-Ca-Mn-O. In both cases the metal-insulator and ferromagnetic transitions are accompanied by a structural phase transition. However, CMR is limited to the transition temperature and large magnetic fields. Therefore for low-field magnetoresistance an intrinsic magnetic disorder, which naturally exists in a homogeneous ferromagnet due to the magnetic domain structure, rather then structural disorder seems to be important. Moreover, for potential device applications as magnetic sensors or MRAM elements, operating in the region of room temperature, large bandwidth manganites with high transition temperatures (LSMO with T_C=360 K) are interesting. The relevance of domain wall magnetoresistance in manganites [77, 78] as well as in ferromagnetic metal point contacts [79] was shown recently. Usually domain wall magnetoresistance was found to be very small, $\Delta R/R$~0.1-1 %. The only exception is shown in [78], where MR~16 % at room temperature for H=1 kOe was obtained for a LSMO film with a nanoconstricted area. However, the above field significantly exceeds the coercive field, H_C~10 Oe, thus making controversial the assignment of the observed effect to domain walls. Moreover, anisotropic magnetoresistance (AMR) was found to dominate the scattering of charge carriers by domain walls even in a multi-domain state, i.e $|H| < H_C$ [79].

The AMR effect, which is governed by the magnetization state of a structurally homogeneous ferromagnetic material, is more appropriate for low-field applications [80]; no special geometric limitations like nano-constrictions are required. Spontaneous AMR, originating from spin-orbit interaction [81-83], results in the anisotropy of the resistivity, $\Delta\rho = \rho_{\parallel} - \rho_{\perp}$, with respect to the magnetization direction. Here $\rho_{\parallel}$ and $\rho_{\perp}$ is the resistivity parallel and perpendicular to the magnetization direction, respectively, of a single-domain ferromagnet. Depending whether the voltage is probed parallel (V_X) or perpendicular (V_Y) to the current density, the electric field related to the AMR is given by [84]:

$$E_x = j\rho_{\perp} + j(\Delta\rho)\cos^2\alpha \quad \text{(longitudinal geometry)} \tag{1}$$

$$E_y = (j/2)(\Delta\rho)\sin(2\alpha) \,\text{(transverse geometry)} \tag{2}$$

Here, j is the transport current density in x-direction, and α is the angle between current and the magnetization. AMR is quantified by a ratio $\gamma = \Delta\rho/\rho_0$ (ρ_0 is bulk resistivity of the material at zero filed), which is only about 1 % for most ferromagnetic materials [81-83].

Therefore AMR, usually hardly seen in longitudinal geometry, can be detected in the transverse geometry (Eq. 2) using a properly microstructured epitaxial films. The information on AMR [85, 86] in manganites is scarce and controversial.

We have studied in details the AMR effect in epitaxial $La_{0.7}Ca_{0.3}MnO_3$ and $La_{0.7}(Ca_{0.5}Sr_{0.5})MnO_3$ (LSCMO) films [87], patterned photolithographically (see inset to Fig. 16). The length of the current line was L=6 mm, and widths were W=1 mm and W=0.3 mm for the LCMO and LSCMO films, respectively. The longitudinal voltage, V_X, was detected by probes placed at a distance L_X=2 mm along the sample, whereas the transverse voltage was detected with the V_Y contacts placed in the perpendicular direction. The Magnetic field was aligned parallel to the film surface.

The temperature dependences of the transversal, V_Y, and longitudinal, V_X, voltages for an epitaxial LCMO/MgO film and ambient magnetic field H=0 are shown in Fig. 16. For the paramagnetic region, $T>T_{MI}\sim T_C$=260 K, both V_X and V_Y show the same insulating behavior. A good correlation between the T_C- and T_{MI}-values indicates that the electron transport is characterized by intrinsic properties. The homogeneity of the LCMO film is also shown by the fact that $V_Y(T)$ and $V_X(T)$ curves measured for essentially different sample lengths exhibit the same temperature dependence. They differ by a temperature independent scaling factor, $V_Y(T)/V_X(T)=\delta/L_X=1.3*10^{-4}$, giving an estimated geometrical misalignment of the transverse contacts, $\delta\approx0.3$ μm, consistent with the accuracy of the optical photolithography. In the ferromagnetic regime another contribution to V_Y appears with a maximum at T=255 K (Fig. 16). Moreover, the $V_Y(T)$ curve for $T<T_C$ depends significantly on the "magnetic history", i.e. V_Y taken for zero field but after application of H=20 kOe at T=100 K (curve 1 in Fig. 16) was significantly larger than that measured after cooling the sample without any applied field for $T<T_C$ (curve 2).

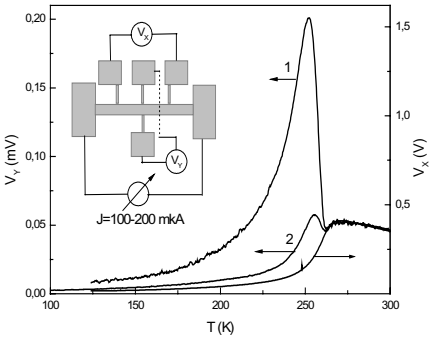

Fig. 16. Temperature dependencies of the transverse voltage V_Y (left scale), and the longitudinal voltage V_X (right scale) for the LCMO film at J=100 μA.

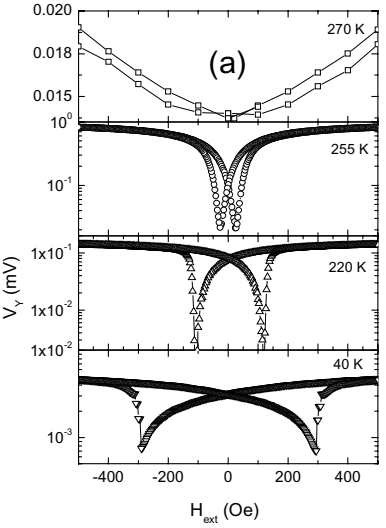

Fig. 17. Magnetic field dependences of the transverse voltage, V_Y, at different temperatures for LCMO/MgO film

The field dependence $V_Y(H)$ for the LCMO/MgO film is shown in Fig. 17. An extraordinarily large and sharp change of V_Y of about two orders of magnitude for low magnetic fields $|H|<500$ Oe was observed at $T\sim T_{MI}$; moreover the $V_Y(H)$ dependence is hysteretic. The peak-field, H_C, of the transverse voltage fit well with the coercive field [87], evidencing that $V_Y(H)$ is caused by magnetization reversal. With increasing temperature H_C decreases in accordance with the decrease of the magnetization, and finally for T=270 K the low-field sensitivity of V_Y vanishes. The data shown in Figs. 16 and 17 were measured with the transport current aligned at an angle $\alpha\approx45^o$ with respect to the magnetic field. In this case V_Y exhibits maximal change due to the applied field. Evidently, this agrees with Eq. 2 and indicates the AMR nature of the observed low-field behavior.

To prove this directly we measured the angle dependences $V_Y(\alpha)$ at room (ambient) temperature for the LSCMO film with T_{MI}=310-320 K. The $V_Y(\alpha)$ dependence, measured at H=0.5 kOe and shown in Fig. 18, was fitted by the equation:

$$V_Y(\alpha,H)=V_0(H)+V_{AMR}(H)\times\sin(2\alpha) \tag{3}$$

with parameters: V_0=0.27 mV and V_{AMR}=1 mV. The relatively small offset voltage, by which Eq. 3 differs from Eq. 2 for the AMR presumably appears due to a longitudinal misfit of the transverse contacts. Note that $V_{AMR}>0$, yielding $\rho_{\parallel}>\rho_{\perp}$ similar to the AMR in ferromagnetic metals [78]. The "pure" field dependence of the above two contributions, V_0 and V_{AMR}, was obtained at room temperature most accurately by:

$$V_0(H)=\left[V_Y(H,\alpha=0)+V_Y(H,\alpha=\pi/2)\right]/2 \tag{4}$$

and

$$V_{AMR}(H)=\left[V_Y(H,\alpha=\pi/4)+V_Y(H,\alpha=\pi/4)\right]/2 \tag{5}$$

To account for the low-field hysteresis we put into Eqs. 4 and 5 the measured $V_Y(H,\alpha)$ curves, considering whether the field is increasing or decreasing. The thus calculated $V_0(H)$ and $V_{AMR}(H)$ are shown in Fig. 19. A non-monotonous field behavior is clearly seen for the AMR contribution to the transverse voltage. The room temperature AMR in the LSCMO film is extremely sensitive at very low fields (see Fig. 19 b), showing two minima for $H_C=\pm10$ Oe, at which $V_{AMR}=0$ due to maximum degree of magnetic disorder, accompanied by the average magnetization $\langle M\rangle=0$. In contrast, V_0 shows a much weaker low-field dependence and becomes smaller than V_{AMR} already for H~40-50 Oe. Moreover, a change of the sign of V_0 was observed at H≈8 kOe (Fig. 19 a). For magnetic fields larger than the saturation field, H_S~500 Oe, V_{AMR} starts somewhat to decrease probably due to the CMR contribution.

Thus we conclude that the measured $V_Y(T,H)$ behavior is intimately related with the magnetization state of the film. For a thin film the magnetization vector, **M**, lies in the film plane due to the shape anisotropy. If we assume that there is no in plane magnetic anisotropy, which is typical for unstrained manganite films [70], then **M** follows the direction of the in-plane magnetic field, i.e. **M**||**H**. This is in agreement with the measured $V_Y(\alpha)$ dependence (see Fig. 18), where α is the angle between the current and the external magnetic field. In the paramagnetic regime, $\langle\mathbf{M}\rangle=0$, and there is no reason for AMR. For $T<T_C$ the film acquires spontaneous magnetization, i.e. $\langle\mathbf{M}\rangle\neq0$, yielding an additional non-zero AMR contribution, even at zero external magnetic field. Compared to the paramagnetic state, the resulting value, $V_Y(T<T_C)=V_0+V_{AMR}\sin(2\alpha)$, can be either increased or decreased or can even change its sign,

depending on the angle α and the magnitudes V_{AMR} and V_0. This probably explains the results of [86] without any assumptions about structural inhomogeneities and a distribution of T_C's and T_{MI}'s within the films.

To relate the transverse voltage with the microscopic properties of manganite films we apply Eqs. 2 and 3. The isotropic contribution V_0 is caused by longitudinal misalignment of the transverse contacts, δ, and can be written as $V_0=j\rho\delta$ (ρ is the resistivity of a film with the length, δ). For $\alpha=45^o$ and $V_{AMR}=E_YW$, where W is the width of the sample, Eq. 3 then yields:

$$V_Y(T,H) \approx j\rho(T,H)\delta + (j/2)\rho_0(t,H)\gamma(T,H) \qquad (6)$$

Here $\gamma=\Delta\rho/\rho_0$ is the AMR ratio. The AMR-term dominates the offset voltage if $\rho\delta<<\rho_0\gamma W/2$. This can be realized by reducing resistivity, ρ, down to $\rho\cong\rho_0$, i.e. to the limit of the intrinsic resistance of the film. This means that the films should not contain grain boundaries or other defects, which may increase the resistance significantly. We observed a correlation between the microstructure of the films, visualized by atomic force microscopy, and the offset resistance, $R_0=V_0/J$, for different LCMO films patterned in the same way. The smallest offset resistance, $R_0(T_{MI})=0.5$ Ω was detected in epitaxial "layer-by-layer" grown LCMO/MgO film; the estimated value $\rho(T_{MI})=0.05$ Ωcm on the transverse contacts is almost identical to the measured longitudinal resistivity, $\rho_0(T_{MI})=0.04$ Ωcm. In contrast for "island grown" films of LCMO/$SrTiO_3$ (T_{MI}=230 K) and LCMO/MgO (T_{MI}=190 K) the offset resistance was $R_0(230K)=30$ Ω and $R_0(190K)=50$ Ω, respectively. Consequently, very large values of $\rho(T_{MI})$~1-5 Ωcm make problematic the observation of the AMR effect even in transverse geometry.

As one can see in Fig. 19 the magnetic field dependence of the AMR voltage in the LSCMO films is extremely sharp for very low fields H=0-20 Oe, yielding a maximum room temperature field sensitivity of S≈20

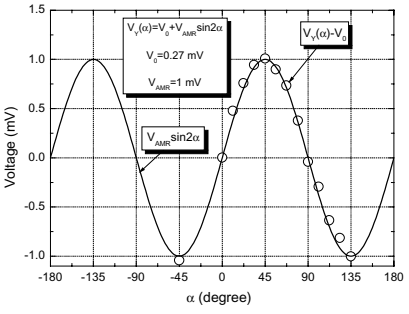

Fig. 18. The dependence of the transverse voltage V_Y on the angle α between the current and the external magnetic field for the LSMO film at room temperature for J=200 μA and H=0.5 kOe. Circles are the experimental points and the line is a fit function.

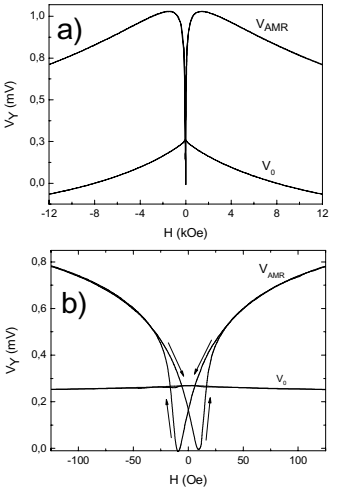

Fig. 19. Anisotropic, V_{AMR}, and isotropic, V_0, contributions to the transverse voltage (see Eq. 5) as a function of magnetic field for the LSCMO/MgO film at room temperature

%/Oe for H~±20 Oe. Another important quantity is the magnetovoltage ratio, MV=100%[$V_{AMR}(H)/V_0$], which describes the relative change of the transverse voltage in an applied magnetic field. For $\alpha=45^o$ and H=500 Oe with V_{AMR}=1 mV and V_0=0.25 mV (see Fig. 18) we get MV=400 %. Even for very low fields, H<40 Oe, it is MV(40 Oe)=220 %. The mentioned above parameters for manganite films considerably exceed S=6 %/Oe and MV=130 % at H=35 Oe, observed for the transverse AMR structures based on Co/Ni multilayers at room temperature [88]. Very recently, by improving the measurement conditions of LSCMO based prototype thin film sensor, we obtained the output sensitivity as large as S=380 μV/Oe for very low field H=1 Oe. With the actual noise level, V_N~0.1 μV, the DC magnetic field sensitivity was $H_N=V_N/S\approx 2*10^{-4}$ Oe at room temperature. All this makes manganite based MR sensors very attractive for a low-field sensing, which was already demonstrated by us at the international Hannover fair, 19-24 April 2004.

5. NANOCOMPOSITE MANGANITE BASED FILMS

5.1 "Negative" pressure and phase transition in epitaxial $(LCMO)_{1-x}$:$(MgO)_x$ films

The ordering temperatures (T_C and T_{MI}) and as a consequence the CMR effect in perovskite manganites are shown to be very sensitive, on the one hand, to different internal factors like doping level [10], average radius of A-site cation $\langle r_A \rangle$ [14], disorder σ^2 [18], and, on the other hand, to external stimuli (magnetic field [4], pressure [68] and even electromagnetic radiation, see §6). Extremely large effects, mediated by phase transitions, are caused by the strong coupling between of spin-charge-lattice degrees of freedom. Furthermore, the phases can coexist and counteract each other on a fine scale (sub-micrometer or even nanometer) resulting in a complicated mesoscopic texture [31]. All this opens promising avenues of research for new possibilities to influence locally the most important DE and electron lattice interactions on a nanometer scale, and, thus, to control the mesoscopic phase separation.

We proposed [44, 89] an approach based on epitaxial nanocomposite manganite thin films, containing a second insulating phase, which chemically and crystallograhically fits the primary manganite phase. Such composites could be interesting not only for low-field magnetoresistance associated with spin polarized tunneling of electrons through the ferromagnetic metal/Insulator/ferromagnetic metal interfaces [90, 91]. They can be viewed also as an artificially created "phase separated" system, consisting of three dimensional (3D) manganite nano-clusters, imbedded in an appropriate insulating oxide matrix. Thus, chemical phase separation will lead to an artificial electronic phase separation of the metal/insulator (MI) type, parameters and the scale of which can be controlled by processing conditions. Magnetotransport properties can then be compared with those recently observed in "naturally existing" electronic phase separated samples [28]. In addition the structure and magnetotransport of the manganite phase can be tuned by a surrounding second phase component, especially when both phases are co-grown epitaxially.

Epitaxial $(La_{0.7}Ca_{0.3}MnO_3)_{1-x}$:$(MgO)_x$ ($0<x<0.8$) composite films were grown on MgO(100) substrates by the MAD technique [44]. To obtain composite films an appropriate amount of $Mg(acac)_2$ was added to the basic precursor solution, used for the preparation of LCMO films. Thus a simultaneous growth of LCMO and MgO phases from a single precursor solution was realized. The nominal concentration, "x", of the insulating MgO phase in the

composite films corresponds to the molar concentration of the Mg-precursor in the precursor solution.

The microstructure of composite films was studied by TEM and HREM. Low magnification cross section TEM reveals that "pure" LCMO film with x=0 is characterized by a columnar structure, forming a pyramid shaped surface texture. The surface of composite films flattens with increasing "x". The microstructure of a composite film with x=0.5 is shown in Fig. 20. In the cross section image (Fig. 20a) one can see that both LCMO and MgO phases grow epitaxially on the MgO substrate. The mean diameter of the LCMO domains varies as D=40-50 nm. Sharp epitaxial interfaces are also seen in a HREM plane view image in Fig. 20b). Moreover, very small 4-5 nm inclusions of MgO within a LCMO domain are also clearly seen. The spatial distribution of Mg atoms, obtained by energy filtered TEM in a plane view, is shown in Fig. 20 c). It demonstrates no chemical intermixture between LCMO and Mg (bright regions in Fig. 20 c)) in very good agreement with the sharp contrast between these phases in the HREM image, shown in Fig. 20 d). Thus we conclude that composite films clearly contain chemically well separated nanocrystalline domains of LCMO and MgO phases, which are epitaxially oriented with respect to each other as well as to the substrate.

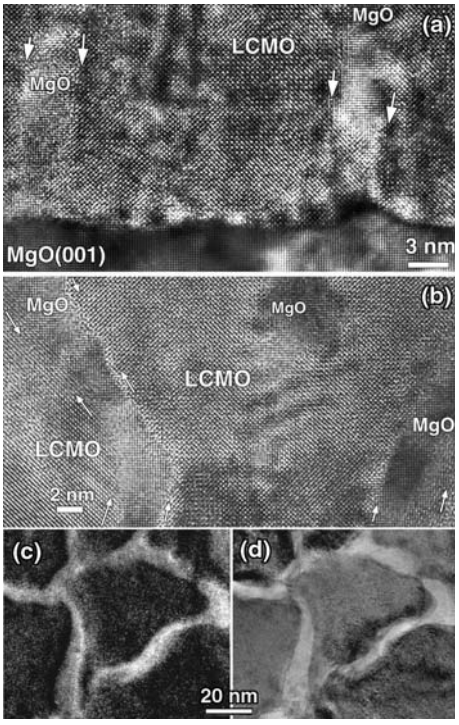

Fig. 20. Microstructure of a composite film with x=0.5: (a) and (b) are the HREM images in cross-section and plan view modes respectively. (c) In plane Mg-map, obtained by EFTEM; (d) - corresponding TEM plane view.

The global structure of LCMO and its evolution with increasing of the second phase component was studied by X-ray diffraction (XRD). (θ-2θ) patterns show perfect out-of-plane (*00l*) texture while the ψ-scans of (220) peak reveal the in-plane texture, both indicating a "cube-on-cube" epitaxy, similar to that observed for individual LCMO/MgO(100) films (see Fig. 5). The

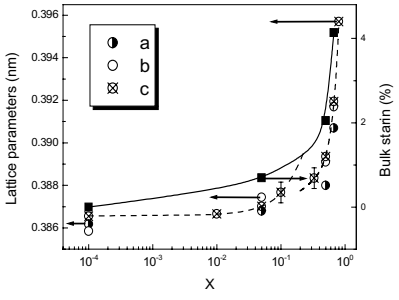

Fig. 21. Evolution of LCMO lattice parameters (left scale) and lattice strain (right scale) with concentration of MgO second phase.

values of the c-lattice parameter of the LCMO phase were estimated from the position of the (002) peak in (θ-2θ) patterns and the a- and b-lattice constants from the (220)-peak taking into account the corresponding ψ-values. The evolution of the a-, b-, and c-lattice parameters as a function of the MgO content "x" is shown in Fig. 21. Pure LCMO (x=0) is characterized by c=0.386(5) nm and a,b≈0.386 nm. They are close to bulk values [70] and indicate no residual strain or oxygen deficiency in a pure LCMO film. As long as the second phase, MgO, is added both out- and in-plane lattice constants increase significantly with increasing "x". Thus the manganite phase is under progressively increased tensile bulk lattice strain. The bulk strain, ε_b, quantified as the change of lattice volume normalized to the volume of a "pure" LCMO reaches $\varepsilon_b=\Delta V(x)/V(x=0)\sim 4\%$ for x=0.67. Note the dominating role of the bulk tensile strain as opposed to the Jahn-Teller strain. The latter described within the tetragonal lattice distortion, $\varepsilon^*=(1-a/c)$, varies in the range $\varepsilon^*=0.1\text{-}0.05$ % for x=0-0.67. Moreover, a discontinuous empirical c(x) behavior for $0.2<x<0.3$ can be also recognized in Fig. 21, indicating that a structural phase transition likely takes place for x≈0.3.

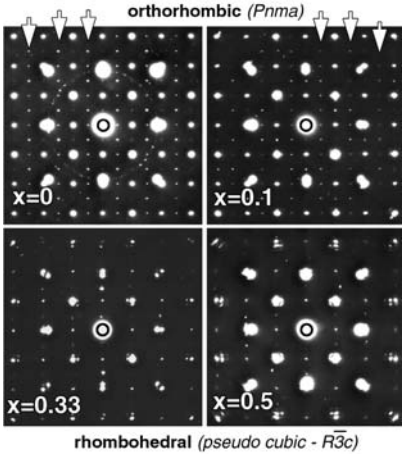

Fig. 22. Cross-section SAED patterns of $(LCMO)_{1-x}$:$(MgO)_x$ films.

Indeed, the cross section selected area electron diffraction (SAED), shown in Fig. 22 for films with different "x", reveals a structural phase transition. SAED patterns for films with x=0-0.1 were indexed within the usual orthorhombic Pnma structure. However, the rows of ED reflexes characteristic for the Pnma, structure, marked by arrows in Fig. 22, disappear in SAED patterns for samples with x≥0.33. This indicates a structural phase transition in LCMO into a pseudo-cubic, presumably rhombohedral $R\bar{3}c$ structure. Note that such rhombohedral $R\bar{3}c$ is not typical for the LCMO bulk samples or mono-phase thin films. Moreover this structural transformation cannot be realized due to external hydrostatic pressure or biaxial substrate-film misfit stress. In contrast it seems to be a result of accommodation of 3D tensile stress produced by the second phase MgO [89].

Magnetotransport characteristics in composite $(LCMO)_{1-x}$:$(MgO)_x$ films are summarized in Table 3. For $0<x<0.1$ the metal insulator transition temperature, T_{MI}, correlates well with the Curie temperature, T_C. Moreover, both quantities decrease systematically with increasing "x". Tight coupling between magnetic ordering and MI transition indicates that static disorder like grain boundaries in the LCMO phase plays no significant role in magnetotransport [57]. Remarkably, no low-field tunneling MR (LFMR) was seen in epitaxial $(LCMO)_{1-x}$:$(MgO)_x$ composite films. LFMR is associated with wide angle grain boundaries [92], which do not exist in epitaxial composite films due to the single crystalline aspect of the LCMO matrix. This leads to electron transport through the LCMO phase, which is apparently more "conducting" than the MgO. Electrical transport obeys a percolative behavior. The room temperature resistance increases with increasing "x" and no metal-insulator transition ($T_{MI}=0$) in ambient field

Table 3. Magnetotransport characteristics of the $(LCMO)_{1-x}$:$(MgO)_x$ composite films.

MgO content, x	0	0.01	0.05	0.1	0.33	0.5	0.67	0.8
T_{MI}(K)	257	260	205	149	-	-	-	-
T_C(K)	260	245	197	145	228	216	210	208
R_{300K} (kΩ)	2	3.5	6	10	18	57	9500	$>2*10^6$
M_S (emu/g) (T=4.2 K, B=0.5 T)	110	102	98	88	41	17	14	13
CMR_{max}(%)	500	700	$1.4*10^3$	$1.5*10^4$	10^5	-	-	-

(B=0) was observed for films with x≥0.33. A magnetic field of B=5T induces the insulator to metal transition at T_{MI}~110 K for film with x=0.33 (see Fig. 23), yielding CMR~10^5 %. In the inset the field dependence of the resistance for T=100 K is shown. Thus we conclude that percolation threshold in the conductivity is close to x_c=0.33. It can be overcome by a magnetic field, yielding a metallic-like conductivity, dR/dT>0, and very large CMR, which is a magnetic field induced metal-insulator transition. The value x_c≈0.33 agrees with the, x_c=0.25, observed for bulk composites of LCMO/$SrTiO_3$ [85].

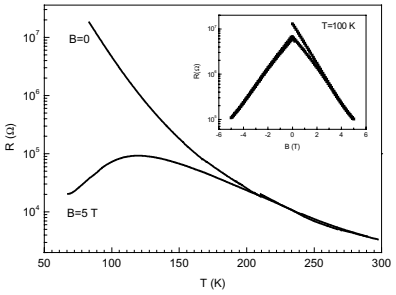

Fig. 23. Resistance vs Temperature behavior of $(LCMO)_{0.67}$:$(MgO)_{0.33}$ composite film.

The structure of composite films and their relation to magnetotransport was discussed in [44], basing on epitaxial character of the LCMO/MgO phase boundary. In pure LCMO/MgO(100) films epitaxy stress due to a large (8 %) lattice mismatch is completely released by the formation of misfit dislocations (see also [71]) and small angle grain boundaries [89], yielding a perfect columnar growth. Small-angle grain boundaries have no effect on the magnetotransport, which remains essentially intrinsic and determined by the LCMO matrix. As soon as MgO starts to grow simultaneously with LCMO there appears bulk tensile strain, induced by the second phase (MgO has larger lattice constant, a=0.421, nm than that of LCMO). The stress increases with "x" and cannot be released because MgO nano-islands (see Fig. 20b), tightly anchored on the substrate, prevent the formation of grain boundaries. The development of epitaxial 3D-strain is favored due to the small diameter, D~50 nm, of the LCMO domains (Fig. 20 c),d), which corresponds well to the thickness of strained LCMO films [93-96]. At the percolation threshold an infinite MgO cluster covers the LCMO grains completely and

makes 3D-strain extremely large and homogenous. As a result a structural phase transition (P_{nma}- $R\bar{3}c$) is coupled to the percolation threshold. In the phase diagram, shown in Fig. 24, we summarize the data on T_{MI} and T_C as well as the room temperature resistance as a function of the MgO content "x". The plots show a distinct correlation with structural transformation, induced by the MgO phase and coupled to the percolation threshold, x_c~0.3.

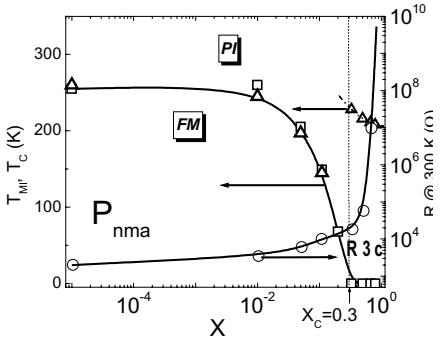

Fig. 24. T_C (△), T_{MI} (□) and R@300 K (○) of composite films as a function of the concentration of MgO second phase.

The change of T_C and T_{MI} observed in biaxially strained thin films [93-97] was quantified as an algebraic sum of the bulk, ε_b, and Jahn-Teller (JT), ε^*, components [98]: $T_C(\varepsilon)=T_C(0)(1-\alpha\varepsilon_b-1/2\Delta\varepsilon^{*2})$. Here $\alpha=1/T_C(dT_C/d\varepsilon_b)$ and $\Delta=1/T_C(d^2T_C/d\varepsilon^{*2})$. For LCMO in composite films the decrease of T_C (see Table 3) consists of $\Delta T_C(x)/T_C(0)=44$ % when MgO content increases from x=0 to x=0.1; the corresponding bulk strain is $\varepsilon_B\approx1$ % (Fig. 20) and ε^*~0.05 %. Hence the stress coefficient is $\alpha\approx44$, which is more than 4 times larger than that in biaxially strained films [96, 97]. Most likely this reflects again the fact that LCMO and MgO phases have a peculiar topology shown in Fig. 19, yielding a homogenous 3D tensile stress distribution.

An interesting observation is a non-monotonous $T_C(x)$ dependence seen in Fig. 24. Namely for x>0.3 T_C increases, which cannot be explained within the same orthorhombic P_{nma} structure. It seems necessary to suppose that the LCMO domain transforms into a more symmetric probably pseudocubic structure under strong 3D tensile stress. The line of transformation provides the surrounding epitaxial MgO matrix. Actually, the rhombohedral ($R\bar{3}c$) structure can be considered as a pseudo-cubic structure, which will perfectly fit the cubic MgO phase. We believe that the increase of T_C is intimately coupled with the relaxation of strain (at least partially) due to a structural phase transition into a more symmetric pseudo-cubic phase and correspondingly decreasing of the mismatch. One can see a clear analogy between the LCMO phase in our composite films and in the bulk $La_{0.7}(Ca_{1-y}Sr_y)_{0.3}MnO_3$ samples in which Ca cations are substituted by those of Sr with significantly larger ionic radius. As a result a negative "chemical" pressure develops and the P_{nma}-$R\bar{3}c$ structural phase transition takes place for y≈0.5, accompanied by an increase in T_C and T_{MI} [99, 100].

Some promising issues follow from the above results. Firstly, one can easily obtain very fine dispersed crystalline manganite phase in a special environment, providing conditions which cannot be achieved by external factors. Secondly, by choosing of different counterpartners (metallic, insulating, ferromagnetic, antiferromagnetic) in epitaxial manganite based composite films one can control the magnetotransport by fine tuning of the size, strain and disorder of the manganite phase.

5.2 Doping of interfaces in $(LSMO)_{1-x}:(MgO)_x$ nanocomposite films

Additional to the intrinsic CMR effect a new phenomenon was discovered by early studies of manganites, namely granular magnetoresistance [101]. This is an extrinsic effect, which occurs due to a structural interface between two manganite grains (or layers in a multilayer structure), decoupled magnetically by a very thin insulator or metal layer. Then the overall resistance is governed by spin polarized tunneling through electronic barriers, which can be significantly influenced by a magnetic field if the spin polarization is high enough [102]. Perovskite manganites with very large value of spin polarization P>0.8 for $T<<T_C$ [103] are advantageous for spintronic applications. Relatively large values of interfacial MR~20-60 % for low temperatures T=4.2-80 K and magnetic fields, H~1-10 kOe were observed in polycrystalline bulk samples and films with grain boundaries [101, 104-107] as well as in artificial multilayer structures and superlattices [108-110]. However grain boundaries in bulk samples were found to be difficult to control. Also in planar tunneling multilayer structures there are complications related to interfacial stress and roughness, which both decrease the magnitude of interfacial MR.

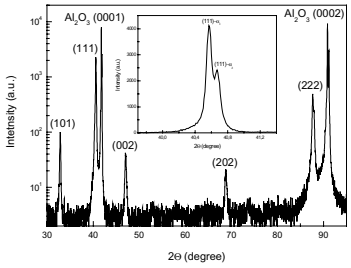

Fig. 25. (θ-2θ) patterns of a $(LSMO)_{0.95}:(MgO)_{0.05}$ film on Al_2O_3 substrate.

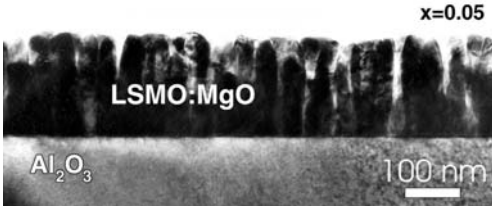

Fig. 26. Cross section TEM image of a LSMO:MgO film with a typical columnar microstructure

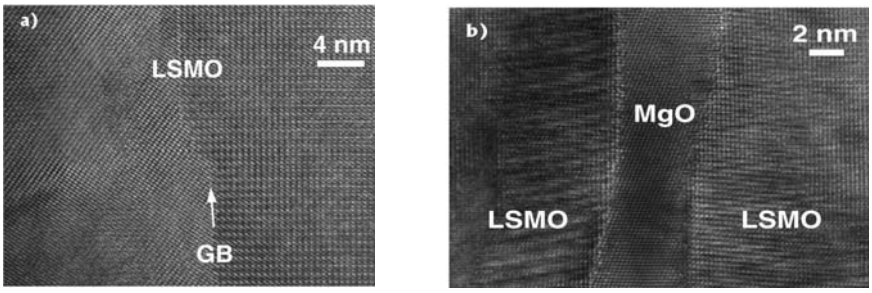

Fig. 27. High resolution TEM images of LSMO (x=0) (**a**) and composite $(LSMO)_{0.5}$: $(MgO)_{0.5}$ (**b**) films.

Recently G. Hammerl et al. [111] proposed a way to control the grain boundaries (GB) in High-T_C superconducting Y-Ba-Cu-O films. It was known that GB limit the critical current density, J_C, in superconducting films by means of depletion of carrier concentration at the GB due to band bending effect [112]. To compensate the band bending GB were doped by Ca [111], which resulted in increase of J_C for T=77 K by more than one order of magnitude. In contrast, to increase the low-field tunneling MR in manganites one should enhance electronic barriers on the interfaces i.e. to dope them with an insulating material. To realize this we used the approach based on nanocomposite manganite films discussed in §5.1.

$(La_{0.7}Sr_{0.3}MnO_3)$:$(MgO)_x$ (x=0-0.5) films were grown on Al_2O_3(0001) substrates by MAD technique [92]. In contrast to the MgO substrate the films on Al_2O_3 were not epitaxial but rather polycrystalline. In Fig. 25 the XRD pattern of a film composite with x=0.05 is shown. One can see dominant (111) as well as (101) out-of-plane orientations of LSMO crystallites. Remarkably composite films with x=0.05 and 0.1 show (α_1-α_2)-splitting of the (111) peak even at $2\theta=40.8^0$ (see the inset to Fig. 25). The FWHM of the (111) peak is 0.08^o and only two times larger than the FWHM of the substrate peak (0001). The estimated size of the LSMO domain in the vertical direction was D=120 nm, which is very close to the films thickness d=150 nm, measured by TEM. This indicates a single crystalline aspect of the films, containing perfect crystallites, growing from the substrate.

In Fig. 26 the microstructure of the composite film with x=0.05 visualized by TEM is shown. A distinct LSMO columnar structure is clearly seen. The columns are spread out through the whole film with their long axis perpendicular to the substrates. In the film plane triangular shaped crystallites with mean diameter, D~50 nm, were also observed by TEM and atomic force microscopy (not shown here).

Taking into account the observed two dominant textures, namely (111) and (101) planes in Fig. 25, one should suppose the existence of grain boundaries (GB) with the angle of 45^o, which is exactly the angle between the [111] and [101] crystallographic orientations. The structure of GB's was studied by cross section HREM (Fig. 27). Coherent 45^o-GB were observed by HREM shown in Fig. 26a) for a pure polycrystalline LSMO (x=0) film grown on Al_2O_3 substrate. For a doped films a heterophase GB was detected with an ultrathin (about

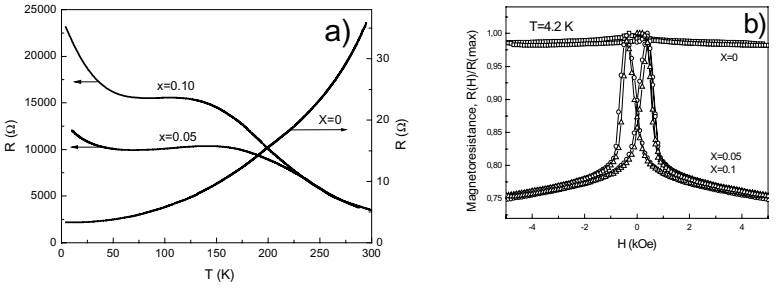

Fig. 28. Temperature (**a**) and magnetic field (**b**) dependences of the resistance in $(LSMO)_{1-x}$:$(MgO)_x$ films for x=0, 0.05 and 0.1.

3 nm) layer of MgO epitaxially grown in between two neighboring LSMO blocks (see Fig. 27b). Chemical mapping performed by EFTEM confirmed the microscopic observations and indeed detected Mg entirely in the region of original GB's.

The resistance as a function of temperature and magnetic field for $(LSMO)_{1-x}$:$(MgO)_x$ nanocomposite films is shown in Fig. 28. Pure LSMO films, which are polycrystalline and contain GB's, show metallic behavior (Fig. 28a) with dR/dT>0 in the whole temperature region, 4.2 K<T<300 K, and residual resistivity, ρ (4.2 K)~10^{-4} Ohmcm. Moreover, the low-field magnetoresistance for low temperatures (Fig. 28b) was less than 1 % and does not exceed 5 % for H=50 kOe. Thus pure polycrystalline films show intrinsic magnetotransport characteristics typical for epitaxial films and single crystals of LSMO [100, 104]. The magnetotransport changes drastically even when very small amounts of MgO (x~0.02) were added to the LSMO matrix. The R(T) shows an insulating like behavior (Fig. 28a) and a pronounced low-field MR~25 % appears at low temperatures (Fig. 28b). The high-field MR also increases significantly up to 50-60 % for T<200 K. Such a behavior is consistent with electron transport dominated by GB and spin polarized tunneling MR, reported earlier for polycrystalline bulk samples and films [103-109].

In Fig. 29 the empirical dependence of the room temperature resistance on the concentration of second phase, x, in $(LSMO)_{1-x}$:$(MgO)_x$ nanocomposite films with different thickness d=30-150 nm is shown. One can see that a fundamental change of the transport mechanism takes place already at very small concentrations of the second phase x<0.05, and then after the resistance does not change too much. The observed behavior differs drastically from the percolative transport observed in bulk composites [90, 91] as well as in epitaxial nanocomposite $(LCMO)_{1-x}$:$(MgO)_x$ films discussed in § 5.1 [44, 89]. The reason is a specific columnar microstructure (Fig. 26), containing the LSMO single crystalline domains (columns) with aspect ratio d/D~3, which spread

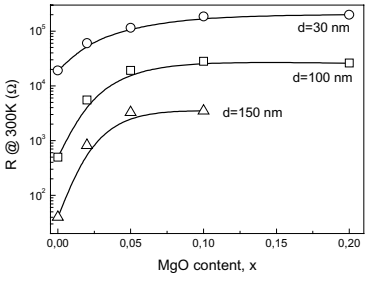

Fig. 29. The dependence of the room temperature resistance on the concentration of MgO.

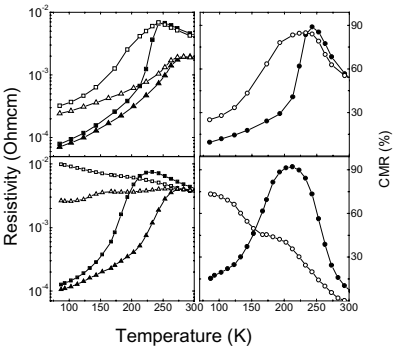

Fig. 30. Resistivty, ρ, and CMR=100%[ρ(0)-ρ(4T)]/ρ(0) vs Temperature for LCMO film with d=120 nm (a, b), respectively and for a trilayer structure LCMO(15 nm)/MgO(7nm)/LCMO(15 nm) (c,d). Closed and open symbols are ρ-values in dark and under illumination, respectively. Squares are ρ-values at H=0, and triangles denote ρ(H=40 kOe). Closed and open circles relate to the CMR data in dark and under irradiation respectively.

throughout the whole film thickness and are separated by wide-angle GB's. In this case the dimensionality of the sample can be reduced from 3D (pure LSMO films) down to a one dimensional like network (composite films) of columns separated by the second phase (MgO), which is known to diffuse exclusively in the GB region. Assuming that LSMO domains with diameter D=50 nm are homogeneously covered by tunneling transparent MgO layer with thickness a=1 nm one can calculate the concentration of the MgO as $x \sim 2(a/D)(\rho_{MgO}/(\rho_{LSMO})=2\text{-}4$ %. Taking into account the current flowing through the thinnest layers these values are in a good agreement with nominal MgO concentration, which yields an insulating like R(T) behavior and tunneling MR characteristics.

Thus the above nanocomposite films, opposite to multilayer planar tunneling MR systems [107-109], can be viewed as a network of lateral (vertical) magnetic tunnel junctions. In this case both LSMO and insulating MgO phases have been prepared as a self organized 3D epitaxy growth, yielding smooth and sharp vertical interfaces (Fig. 27). One can control the structural parameters and magnetotransport of these lateral LSMO/MgO/LSMO interface junctions by changing both the grain size, D, and the concentration of the second phase, x. Recently we have obtained that for a constant x=0.05 a metallic behavior in R(T) observed for relatively large grain sizes D>80-100 nm changes to an insulating one for D<50-60 nm. At that maximum MR values were seen for films with small grains, D=20-30 nm.

6. PHOTOINDUCED ELECTRONIC INHOMOGENEITY IN MANGANITE FILMS

6.1 Giant negative phtoconductivity in LCMO films

The complex phase diagram of perovskite manganites (Fig. 3) with competing FM metallic and AF insulating phases reflects a strong dependence of the ground state of the manganites on the hole doping, x. This opens a promising possibility to manipulate the order parameter by external control of the hole density in a single phase material by means of the injection of charge carriers as was shown previously for High-T_C superconductors [112]. In the case of manganites the extra carriers seem to be able to shift the AFM/FM phase balance, thus affecting the magnetotransport to a large extent. At the same time injected carriers do not affect the degree of existing chemical disorder in the material, thus opening an additional possibility to influence electronic phase separation [28, 29] by a pure electronic factor rather than by a lattice effect. Extra carriers can be injected by the field effect [113] as well as by optical pumping using laser radiation. The latter technique as a more simple one (no needs in gate dielectric with large breakdown field and high dielectric constant) was applied to study electron transport and optical properties of manganites under laser irradiation.

An insulator-to-metal (IM) transition was observed at low temperatures in a small bandwidth charge ordered $Pr_{0.7}Ca_{0.3}MnO_3$ (PCMO) crystals, exposed to X-ray [114] irradiation, as well as illuminated by a laser [115] with photon energy $\hbar\nu$ =1.2-1.6 eV. Photoinduced transition was found to be similar to the IM transition, which can be switched in PCMO by pressure, magnetic field or high voltage. All these factors create a current path in an insulating CO matrix thus resulting in a coexistence of FM metallic and CO insulating state. The corresponding increase of the sample magnetization, photomagnetization, was also revealed in a 0.01 % Cr-doped PCMO film [116] by pulse illumination with Nd:YAG laser (λ=532 nm,

Δt_{pulse}=2 ns). Moreover by using a SQUID microscope they observed a local increase of the spontaneous magnetization (creation of FM domains) after 11.5 min photoirradiation at T=3 K.

Ultrafast dynamics of laser induced changes in the electrical resistance was observed by Y.G. Zhao et al. [117] in a $La_{0.7}Ca_{0.3}MnO_3$ (LCMO) films. A decrease of the resistance under laser irradiation with very short relaxation times τ~150 ps for $T>T_C$ in LCMO film was interpreted as a photoionization of the Jahn-Teller small polarons. For $T<T_C$ the resistance increases under irradiation and the relaxation becomes slower, τ=1-10 ns, indicating the relevance of magnon excitation. Moreover, the increase of the relaxation time with increasing temperature towards T_C, may reflect a competition between the DE and JT contributions. Photoinduced increase of optical absorption (transmission) at 1.55 eV in LCMO film with relaxation times τ~100-400 ns was detected by pump-probe measurements in [118] and interpreted as the formation of charge ordered clusters, which yields demagnetization of the film. For "small bandwidth" manganites with low T_C=155 K like $(Nd_{0.5}Sm_{0.5})_{0.6}Sr_{0.4}MnO_3$ [119] photoinduced demagnetization is manifest after 200 ps after laser pulse and the spin correlation recovers in 300 ns. However, no distinct indications on the large photoinduced changes in magnetotransport as well as a detailed study of the temperature and magnetic field dynamics in LCMO films was obtained. The influence of film microstructure on the photoeffects also remains obscure.

We have performed a complex study [120, 50] of the transients of photoconductivity, optical absorption and second harmonic generation (SHG) on the slow time scale τ=0.1-100 s under Ti:Al_2O_3 laser irradiation (λ_ω=760 nm, Δt_{pulse}=100 fs, repetition rate 82 MHz, maxi-

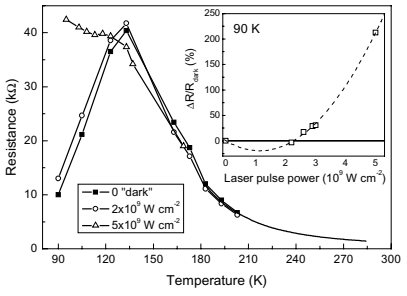

Fig. 32. Temperature dependence of the resistance in a LCMO film with T_{MI}≈140 K for different values of laser pulse power. The inset shows the photoconductivity, $\Delta R/R_{dark}$, as a function of laser pulse power for T=90 K.

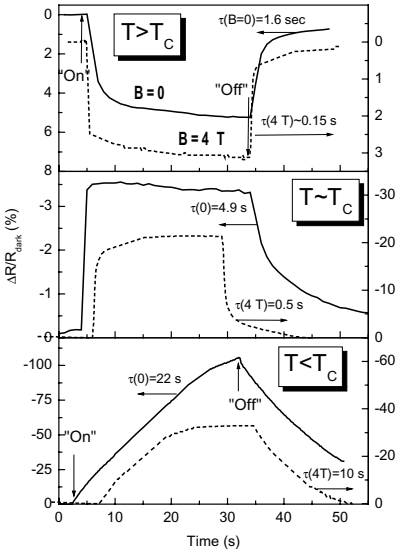

Fig. 31. Photoconductivity transients for a LCMO film obtained at B=0 and B=4 T for $T_C<T$=300 K (a), T_{MI}~T=250 K (b) and $T_C>T$=90 K (c).

mal average power 800 mW) for temperatures 90-300 K and magnetic field, B=0, 4T. Well characterized single epitaxial LCMO films with a thickness d=120 nm (sample "A") and a trilayer structure LCMO(15 nm)/MgO(5 nm)/LCMO(15 nm)/MgO(100) (sample "B") were studied. The films show T_C=260 K ("A") and 250 K ("B"), and sharp magnetic, (1/M)(dM/dT)=25 %/K, and resistive, (1/R)(dR/dT)=15 %/K transitions. In Fig. 30 the temperature dependences of the resisitivty, ρ(T), and CMR in dark and under illumination are shown. In dark the films exhibit a classical CMR behaviour with a sharp MI transition and narrow CMR temperature distribution with a peak at $T\sim T_{MI}$. Under the laser illumination the resistance increases drastically for $T<T_{MI}$, yielding maximal photoconductivity $\Delta R/R_{dark}=$ $=100\%*(\rho_{dark}-\rho_{light})/\rho_{dark}$, of -600 % ("A") and -10^4 % ("B"). In the paramagnetic state the resistance shows a small decrease under illumination. CMR decreases under irradiation and its temperature distribution shifts to lower temperatures. Note that the MI transition becomes broader and the thinner film "B" shows no metallic behavior under irradiation at zero field and behaves rather insulating with $d\rho/dT<0$ for T=90-300 K. Thus one can conclude that the films in dark behave as homogenous LCMO films with intrinsic magnetotransport (compare with Fig. 8 for layer-by-layer epitaxial films), whereas the illumination yields a magnetotransport similar to a disordered LCMO material (see Fig. 9 for island grown films). Moreover, the heating of the film by laser irradiation plays a minor role due to very short (Δt=100 fs) pulses and repetition rate (Δt=13 ns), which prevent the excitation of phonons. In addition maximum change of resistance is observed at the lowest T=90 K where the heating effect is negligible due to the smallest value of dR/dT.

Resistivity transients for LCMO film and different temperatures are shown in Fig. 31. Relaxation of the photoconductivity was fitted by an exponential form, $\Delta R(t)\sim\exp(-t/\tau)$. The slow relaxation was observed with characteristic times, τ~1-30 s, which depend on the temperature and magnetic field. For the paramagnetic region $T>T_C$ and B=0 the relaxation is relatively fast, τ=1.6 s, (Fig. 31a). In contrast in the ferromagnetic state the relaxation is slow, τ=22 s at T=90 K. A magnetic field, B=4 T, enhances the relaxation of the photoconductivity, yielding a decrease of τ down to 10 s at T=90 K and to about 0.15 s (T=300 K), which was the limit of our measurement setup.

The dependence of the photoconductivity on the laser pulse power, J, was found to be essentially nonlinear as is demonstrated in Fig. 32 for a LCMO film with T_{MI}=140 K. For relatively low J minor changes of the resistance were observed in the ferromagnetic region. Only for $J>2.5*10^9$ W/cm^2 the resistance increases drastically for $T<T_{MI}$. In the inset of Fig. 32 the dependence of the photoconductivity on the laser power for T=90 K is depicted. Experimental points were fitted by a quadratic function, $\Delta R\sim J^2$. Moreover, the sign of the photoconductivity depends on the laser power. For $J\approx 2.2*10^9$ W/cm^2 we detected reliably ~1% decrease of the resistance rather than increase observed for higher fluencies. Nonlinear or even a threshold power dependence of the photoconductivity indicates that photo induced effects play an important role. At that very large change of the resistance (Fig. 30) and metal to insulator transition are caused probably by pumping of a large number of extra carriers.

6.2 Second harmonic generation

Additional information on photoinduced effects in LCMO was obtained by second harmonic generation (SHG) [120, 50]. We have observed a strong optical SHG in LCMO thin films. Two types of films were studied, "layer-by-layer" films of A-type and 3D island grown (B-type) films. LCMO crystallizes in a perovskite center symmetric cubic structure (point group *m*3*m*), in which strong dipole-type SHG is forbidden in bulk, and only quadrupole-type bulk and dipole-type surface SHG are allowed. They are generally several orders of magnitude weaker. However, the SHG signal we observed for low laser power is comparable with the SHG signal from non-center symmetric media (ferroelectric thin film, for example). Recently it was shown that in magnetic center symmetric materials an unusual increase of SHG is caused by a magnetic contribution [121], an effect of which was not taken into account in previous works on manganites [122]. However, the grain boundary and interface SHG contributions can dominate the bulk magnetic contribution in granulated centrocymmetric ferromagnetic nanoparticles [123].

To distinguish between these two possible contributions we have measured the azimuth anisotropy $I_{2\omega}(\Psi)$ of the SHG at room temperature in reflection geometry, shown in Fig. 33, by rotating the sample around its normal. The X-, Y-, and Z-axes are aligned along the main crystallographic axes of the film and those of the substrate. Note that LCMO film was eptaxially "cube-on-cube" grown on the MgO(100) (See Fig. 5). Polarization indexes "s" and "p" denote the components of the electric field vector E of the fundamental wave at frequency ω (or SHG wave at frequency 2ω), which lie in the plane of incidence ("S") or perpendicular ("P") to it, respectively.

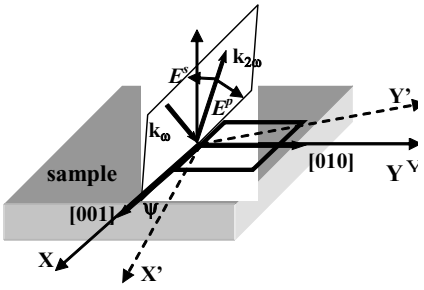

Fig. 33. Orientation of crystallographic axes of the film and electric field vectors of fundamental and SHG waves in reflection geometry

Fig. 34 (a-d) shows azimuth dependences of SHG intensity for different polarization combinations measured at room temperature. They all reveal 4-fold (for p-in, p-out; p-in, s-out; s-in, p-out polarization combinations) or 8-fold (for s-in, s-out polarization combination) symmetry,which can be fitted by a general truncated Fourier expansion:

$$I^{2\omega} = \left(f_0 + \sum_{i=1}^{4} (c_i \cos i\Psi + s_i \sin i\Psi) \right)^2 = \begin{cases} (f_0 + s_4 \sin 4\Psi)^2, \ for \ \ p-out \\ (c_4 \cos 4\Psi)^2, \ for \ \ s-out \end{cases} \quad (7)$$

It is important to note, that for s-out polarizations the SHG intensity in the minima of azimuth dependences equals zero within the error bar. The maximum intensity for all polarizations is higher for the A-type film: approximately 6 times for p-out and 3 times for s-out.

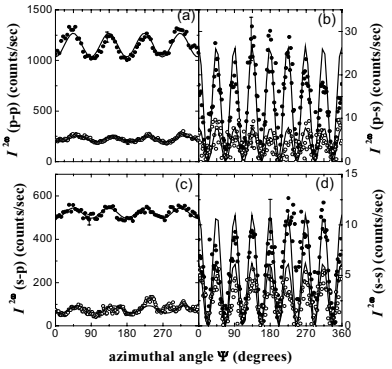

Fig. 34. Azimuth dependences of SHG intensity for different polarization combinations at room temperature: (**b**) – *p*-in, *p*-out; (**c**) – *p*-in, *s*-out; (**d**) – *s*-in, *p*-out; (**e**) – *s*-in, *s*-out for granulated (open circles) and continuous (solid circle) films. Solid lines: fits to data by Eq. 7

The crucial points to distinguish between contributions from bulk and interfaces are: 1) the shape of azimuthal dependence and 2) the contribution from inhomogeneity regions comparable with the wavelength in the form of either hyper-Raleigh scattering [123] or/and the appearance of forbidden isotropic contribution to s-polarized SHG signal [124]. The latter can be observed for m3m crystal as a change from a perfect 8-fold anisotropic dependences to a 4-fold one consisting in each of 4 periods of two maxima of non equal SHG intensity. On the contrary to [123, 124] in our experiments we never observed neither of these two possible confirmations of a significant contribution from inhomogeneity regions. The shape of the azimuthal dependence in our experiments perfectly falls under the theoretically predicted one for (001) face of m3m crystal, described by Eq. 7. For these reasons we consider that the bulk magnetization-induced polarization gives the dominant contribution to the SHG in LCMO films.

The time and temperature behavior of SHG was found to depend on the laser power for the ferromagnetic region ($T<T_C$), indicating the relevance of photoinduced effects. Two measurement regimes were used: steady and dynamic. For the steady regime the sample was illuminated constantly during a complete set of temperature (magnetic) measurements. For the dynamic regime for each value of temperature (magnetic field) the sample was first kept in dark for several minutes, then the shutter was opened and the signal was detected for about 1 min with a sampling time of 0.1 s. For low average power (50 mW) no difference in steady state and dynamic measurements on a time scale $t>0.1$s were observed. The increase of the average power up to 500 mW for the ferromagnetic state ($90\ K=T<T_C$) results in a non-steady behaviour (see Fig. 35), which means that SHG signal decreases under the laser illumination and saturates after about 20 s on a level significantly lower than immediately after opening the shutter. It is interesting, that characteristic decay times of the SHG, τ_{SHG}~2-6 s are comparable with the relaxation times of the photoconductivity.

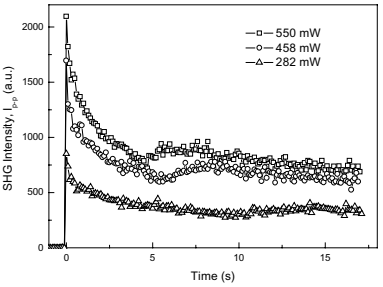

Fig. 35. SHG transients in *p*-in, *p*-out polarization combinations for A-type LCMO film for T=80 K.

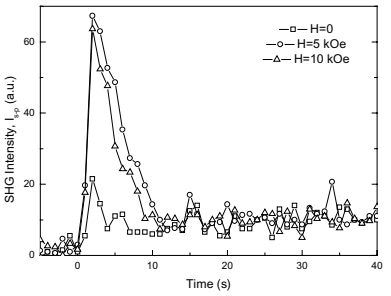

Fig. 36. SHG transients for different magnetic filed and T=80 K in s-in, p-out polarization combinations for A-type LCMO film.

A magnetic field increases the amplitude of SHG transient (about 3 times) under high laser intensity as is shown for A-type film in Fig. 36, for *p*-in, s-out, polarization combination. For p-in, p-out combination the corresponding increase consists of only about 10 %. For both polarization combination the magnetic field inhibits the decay of SHG, yielding an increase of the decay times by a factor of two.

In Fig. 37 we compare the temperature dependences of reisitivity, ρ, magnetization, M, and non linear optical properties of two types LCMO films. The temperature dependence of the SHG intensity depends on the laser power (Fig. 36 (c) and (d)). For high power, the temperature dependences of both initial value of the SHG intensity measured immediately after opening the shutter ($I_{t=0}$) and the steady state value ($I_{t=20s}$) look quite similar for A- and B-type films. The steady state value $I_{t=20s}$ does not change with temperature, whereas the initial value $I_{t=0}$ shows a T-dependence qualitatively similar to that of the magnetization, M(T), being constant at low temperatures (T<150 K) and then decreasing down to a steady state value at T_I=220 K. Note this value is about 30-50 K lower than T_C as it can be seen from the M(T) curves (thin lines in Fig. 37 a, b).

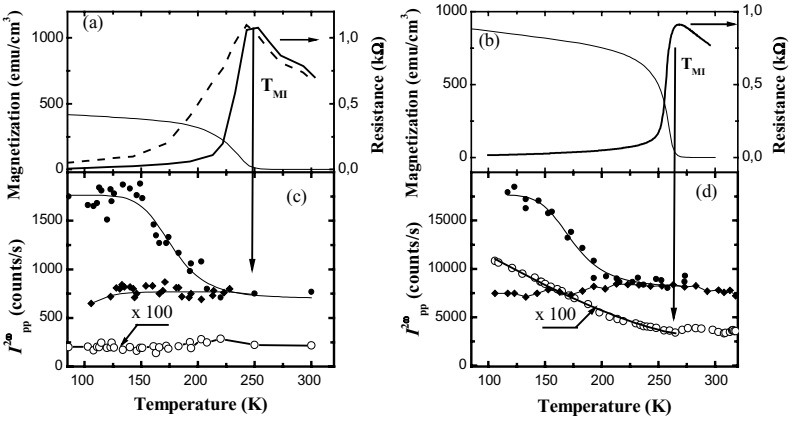

Fig. 37. Temperature dependence of magnetization (thin line, left scale) and resistance in dark (thick lines, right scale) for B-type (**a**) and A-type (**b**) LCMO films. For B-type film the reisiatnce under laser irradiation is also shown (dashed line). Temperature dependence of the SHG intensity for B-type (**c**) and A-type (**d**) films. (●) – initial SHG intensity after the shutter is open; (♦) - relaxed steady state (t=20 s) for P=500 mW. (○) – steady state SHG for average P=50 mW.

For low laser power, a drastic difference between A- and B-type of films was observed. Namely, for B-type film the steady state SHG intensity remains constant in the whole temperature range (Fig. 37 a, open circles), indicating suppression of the magnetic contribution of SHG. In contrast, for the A-type film the steady state SHG increases with decreasing temperature starting from T_{MI}=270 K (Fig. 37 d, open circles). For this laser power SHG remains constant after opening the shutter. This may mean either that the laser light of this power does not influence at all the optical properties of the film, or that the decay time is significantly shorter than 0.1 s.

Taking into account that SHG behaviour is governed by the bulk magnetization-induced non-linear polarization we can conclude that the observed time, temperature and power dependences of SHG reflect the film magnetization behavior. Thus the increase of the resistance (see Fig. 31) and the decrease of SHG intensity (Fig. 35) under laser irradiation for the ferromagnetic state $T<T_C$ are caused by photoinduced demagnetization of the film. By comparing the "true" M(T) behavior with T_C=265 K and 250 K for A- and B-type films, respectively (see Fig. 37 a, b), and SHG probed M(T) under the illumination (Fig. 37 c, d) we conclude that photoexcitation decreases the transition temperature down to $T_C(SHG)\approx 220$ K. Moreover, on can see that even for lower laser power, P=50 mW, the steady state non-linear optic magnetization (open circles in Fig. 37 d) drastically differs for the "true" M(T). Namely, the magnetic transition in optics looks extremely broadened compared to the M(T). It shows a power-law temperature behavior, $I_{2\omega}\sim(1-T/T_C)^{2n\beta}$ (β=0.34, n=2) similar to that observed for disordered or magnetically inhomogeneous LCMO films, which possess a distribution of T_C's [125]. This means that even for low laser power the illumination changes the film properties, probably on a time scale of pico- and nano-seconds as it was observed in [117] by resistivity transient measurements. Moreover our resistance measurements also show a broadening of the MI transition and CMR (Fig. 30) under illumination, indicating that LCMO film under the illumination behaves as electronically disordered medium whereas in dark it looks rather homogeneous.

The most probable mechanism of this influence is related to enhancement of electronic (optical) inhomogeneity of the film (phase separation) under photoexcitation of extra carriers (holes). The number of extra carriers, Δp, can be estimated as $\Delta p=\beta\alpha J\tau$ [126], where $\beta\sim 1$ is the quantum efficiency for band-to-band transitions, $\alpha(\lambda_\omega=760\text{ nm})\sim 10^5$ cm^{-1} [118] is absoprtion coefficient, τ=20 s (Fig. 31) the stationary lifetime of excess carriers, and $J\sim 10^{14}$ is the number of photons/cm$^2\times$s, generated by the laser system. This gives a very large number of excess carriers, $\Delta p\approx 10^{20}$ cm^{-3}. However it is still much smaller than equilibrium carrier concentration p=0.33/(unit cell)$^3\sim 5.6\times 10^{21}$ cm^{-3} due to Ca-doping. Therefore, it seems unlikely that the metal-insulator transition and demagnetization of LCMO under irradiation occurs on the same way as by increasing Ca-doping from x=0.33 to x=0.5. We believe that photoexcited carriers can trigger a cooperative Jahn-Teller transformation (orbital ordering) within small clusters in accordance with the phase separation scenario [28-35]. Note that according to estimations of K. Matsuda et al. [119] one photoinjected e_g electron reverses the direction of about $30t_{2g}$ spins, yielding thus a cumulative effect in photodemagnetization. Under irradiation the size and/or number of (COI AFM)-clusters increases at the expense of (metallic FM)-clusters, resulting in enhanced electronic (optical) inhomogeneity of the film. This process should be accompanied by a an increase of local mechanical strain because insulating domains suffer the JT stress. The observed very slow relaxation in the photoconductiv-

ity and SHG, which occur on the scale τ=1-30 s might be related to relaxation of the local stress in nm-size COI AFM domains after the irradiation was switched off. An analogy can be found in slow relaxation of the magnetization in charge ordered $La_{0.5}Ca_{0.5}MnO_3$ after changing a magnetic field - characteristic relaxation times were found to be in the range of τ~1000 s [127].

Very large photoinduced effects in electrical resistance were observed in very thin LCMO films, $d<<1/\alpha$=100 nm, shown in Fig. 30 (c, d), because a homogenous photogeneration of holes is possible. In thicker films d=120 nm (Fig. 29 a,b) photogeneration occurs mostly in a very thin layer, while the rest of the film remains metallic for $T<T_C$ and shunts the surface layer. Moreover, the films grown according to the island growth mechanism also are interesting. Here the inhomogeneous electronic state (see Fig. 12) exists already in dark due to inhomogeneous strain relaxation. However the film still shows globally metallic conductivity for $T<T_C$ because of the low concentration of the insulating phase. Percolation threshold in such inhomogeneous system can be achieved by a lower laser power compared to the case of homogeneous "layer-by-layer" grown films. This explains the higher sensitivity of B-type films to laser irradiation shown in Fig. 37.

7. SUMMARY AND OUTLOOK

The main results of this work can be formulated as the following:

1) A metalorganic aerosol deposition (MAD) technique was developed for the preparation of thin manganite films and manganite-based nanocomposite films. This is a solution based non-vacuum chemical method, which uses aerosols of metalorganic precursors (β-diketonates of metal chelates) to prepare oxide films by means of heterogeneous pyrolysis reaction.

2) Two types of growth mechanisms were realized within MAD technique: A) layer-by-layer growth, resulting in atomic smooth surface of the films with mean square roughness RMS=0.2-0-3 nm; and B) 3D island growth mode, which yields a rough surface morphology (RMS=1-8 nm), containing distinct crystalline grains with diameter, varying in the range D=30-400 nm depending on the processing conditions. LCMO and LSMO films were grown epitaxially on the MgO(100) substrates. The A-type films possess no mechanic strain, exhibiting pseudocubic lattice parameters typical for bulk samples. The B-type films are strained due to not complete strain relaxation, which seems to be kinetically regulated and thus dependent on the deposition rate.

3) Magnetotransport in two types of LCMO films was found to be essentially different. The A-type films show intrinsic electron transport with extremely sharp metal-insulator (TCR=25 %/K) and ferromagnetic (TCM=60 %/K) transitions, which are coupled together ($T_{MI} \cong T_C$). All this indicates electronically homogeneous behavior. In contrast, the B-type films look electronically/structurally disordered and show a mesoscopic magnetotransport, governed by a nm-scale inhomogeneities, with strong decoupling between T_C and T_{MI} ($T_{MI}<T_C$).

4) The metal-insulator (MI) transition in LCMO films depends crucially on lattice strain. Compared to bulk materials thin films can be additionally strained due to misfit epitaxy stress, which governs to a large extent the pressure dependence of the MI transition. At that a reversible pressure effect, stabilizing the ferromagnetic metallic state, is characteristic for A-type films with low disorder. An irreversible pressure effect, which enhances the insulating

phase and results in phase separated behavior with a second maximum in R(T) for T~50-70 K, was observed for external pressure p>8 kbar for B-type LCMO films with high disorder.

5) Intrinsic magnetic disorder associated with a magnetic domain structure in structurally homogeneous LCMO and LSCMO films was shown to be promising for low-field magnetoresistance (MR). By using anisotropic MR in transverse geometry a very high sensitivity, S=20 %/Oe for magnetic field H~0-20 Oe at room temperature was demonstrated in LSCMO films.

6) Epitaxial nanocomposite films of $(LCMO)_{1-x}$:$(MgO)_x$ were prepared. The structure and magnetotransport of the primary LCMO phase was shown to be controlled by 3D tensile stress (negative pressure) induced by elastically coupled second phase of MgO. Unusual structural phase transition ($P_{nma} \rightarrow R\bar{3}C$) and largest CMR~10^5 % are shown to be coupled to the percolation threshold in conductivity at x=0.33.

7) Doping of grain boundaries with insulating phase MgO was shown to be effective to control magnetotransport in columnar $(LSMO)_{1-x}$:$(MgO)_x$ nanocomposite films on Al_2O_3(0001) substrates. Pure LSMO (x=0) shows an intrinsic (bulk) metallic behaviour, whereas even slightly doped (x~0.02) films demonstrate an extrinsic grain boundary controlled magnetotransport with pronounced low-field MR~25 % at low temperatures.

8) Large photoinduced effects in resistance and second harmonic generation (SHG) were observed in LCMO/MgO(100) films prepared by MAD. The resistance of the films increases up to two orders of magnitude in the ferromagnetic state and even a metal to insulator transition takes place under irradiation by a femtosecond Al_2O_3:Ti laser with λ=760 nm. Strong SHG in centrosymmetric pseudocubic LCMO was shown to be due to intrinsic magnetization-induced nonlinear polarization, and thus probes the magnetization in the film. The suppression of SHG under illumination was observed and explained as photodemagnetization process. Moreover the illumination yields significant magnetic and electronic disorder, while in dark the LCMO film behaves as a homogeneous ferromagnet.

One of the most striking features of perovskite manganites is the spatial inhomogeneity of their electronic properties, which is realized as the coexistence of ferromagnetic metallic and antiferromagnetic insulating phases on a very fine, probably, nm-scale. Whatever the driving forces for the phase separation (local chemical disorder, strain etc.) as well as the boundary conditions to reveal it (chemical composition, temperature, the type of the phase transition etc.) this phenomenon seems to be extremely interesting not only for fundamental science but also for practical applications. Indeed, the presence of metallic and insulating regions in a chemically homogeneous material assumes the appearance of a non-linear electronic behaviour, which is exactly what one needs to fabricate electronic devices, like diodes and transistors. Therefore the controlling of the phase separation and, furthermore, its formation in a preliminary electronically homogeneous template become extremely interesting and challenging problems. One can also fantasy on a self organized “electronic phase lithography”[31], which does not involve the formation of any interfaces between different chemical phases to prepare a “p-n” junction, for example, with avoiding of corresponding diffusion problems.

It looks likely that such a control can already be initialzed *in situ* during the film growth by fine tuning deposition conditions within MAD technique (temperature, growth rate, supersaturation degree). To characterize in details the obtained disorder a.c. magnetotransport measurements in a broad frequency range will be useful. In addition local characterization

techniques (STM) should be improved to get quantitative rather than qualitative information. Another possibility, *ex situ* control of phase separation, provides the photoinduced effects, which as we have shown above destabilize ferromagnetic metallic phase and induce inhomogeneous electronic and magnetic behaviour. To specify further the influence of light the direct measurements of magnetization under laser irradiation as well as kinetics of the photoconductivity in a large time intervals (τ=10^{-9}-1 s) will be useful.

As was demonstrated above a crucial factor for inducing electronic inhomogeneity is the lattice strain. Thus it looks very likely that by manipulating the strain one can control phase separation. In this line the multiferroic epitaxial nanocomposite, containing manganite phase (LSMO) and ferroelectric phase, for example $Pb(Zr_{1-x}Ti_x)O_3$ look very promising. Very recently H. Zheng et al. [128], using our approach of epitaxial nanocomposite films [44], have prepared multiferroic $BaTiO_3$-$CoFe_2O_4$ film nanostructures, in which elastically coupled phases are also coupled magnetoelectrically, i.e. magnetization of $CoFe_2O_4$ changes at the ferroelectric Curie temperature. This opens a possibility to influence the manganite phase by controllable change of mechanical deformation of the ferroelectric phase, obtained by piezo- or pyroelectric effects.

The tuning of lattice strain by an external parameter can be interesting not only for phase separation but also for low-field AMR in manganites. Controlled changes in lattice strain of manganite films may be an appropriate method to "defreeze" the orbital momentum of Mn^{3+} and Mn^{4+} ions, for which $\langle L_z \rangle$=0 in a cubic crystal field of octahedral symmetry [129], and, thus, to increase the spin-orbit interaction. The observed variation of the AMR ratio in LSCMO films with different c-lattice parameter [87] supports the relevance of strain effect on AMR. This could be realized probably by using of ferroelectric substrate or buffer layer (PZT, $BaTiO_3$) which can be biaxially strained by applying voltage. A similar geometry was reported earlier [130] to affect the resistance by mechanic strain in LCMO films. Another possibility to affect low-field AMR is photoirradiation. Taking into account that low-field AMR is caused by magnetic domain structure it seems very interesting to study the influence of light on magnetic domains. Assuming the observed photoinduced magnetic inhomogeneity [50, 120] one can expect a decrease of the size of magnetic domains under irradiation as well as the change of hysteresis loop due to the creation of antiferromagnetic regions in the close proximity of FM domains.

ACKNOWLEGMENTS

I would like to thank Prof. K. Samwer for his "multidisciplinary" support of this work from the very beginning in Augsburg. Great and kindly thanks for R. Tidecks (University of Augsburg) for uncompromised discussions.

All the members of the I. Physical Institute at the University of Göttingen and, especially, U. Bete and C. Mahn are kindly acknowledged for their help. I would like to thank our collaborators at the Göttingen University - J. Faupel, H.-U. Krebs, P. Willbrandt.

Many thanks to our international collaborators, especially to A. Belecnhuk and O. Shapoval (Kishinev, Moldova), O.I. Lebedev (Antwerpen, Belgium), V. Tsurkan (Augsburg), V. Zakosarenko (Jena), and E. Mishina (Moscow, Russia). Without their creative contributions this work would lose a lot and even would be not possible.

REFERENCES

[1] G. Jonker and J. van Santen, Physica **16** (1950) 337.
[2] R. von Helmolt, J. Wecker, B. Holzapfel, L. Schultz, and K. Samwer, Phys. Rev. Lett. **71** (1993) 2331.
[3] K. Chahara, T. Ohno, M. Kasai, and Y. Kozono, Appl. Phys. Lett. **63** (1993)1990.
[4] M. Mc Cormack, S. Jin, T.H. Tiefel, R.M. Fleming, J.M. Phillips and R.Ramesh, Appl. Phys. Lett. **64** (1994) 3045.
[5] J.M.D. Coey, M. Viret and S. Molnar, Adv. Phys. **48** (1999) 167.
[6] R.D. Shannon and C.T. Prewitt, Acta Crystallogr. A**32** (1976) 785.
[7] Y. Tokura, *Fundamental features of colossal magnetoresistive manganite oxides*. In: Y. Tokura (Ed.), Contribution to Colossal Magnetoresistance Oxides, Monographs in Condensed Matter Science. Gordon & Bleach, London 1999.
[8] E.O. Wollan and W.C. Kohler, Phys. Rev. **100** (1955) 545.
[9] A. J. Millis, Nature **392** (1998) 147.
[10] P. Schiffer, A.P. Ramirez, W. Bao, and S.-W. Cheong, Phys. Rev. Lett. **75** (1995) 3336.
[11] C. Zener, Phys. Rev. **81** (1951) 440.
[12] P.W. Anderson and H. Hasegawa, Phys. Rev. **100 (**1955) 675.
[13] P.-G.de Gennes, Phys. Rev. **118** (1960) 141.
[14] H. Y. Hwang, S-W. Cheong, P.G. Radaelli, M. Marezio, and B. Battlog, Phys. Rev. Lett. **75** (1995) 914.
[15] W. Archibald, J.-S. Zhou, and J.B. Goodenough, Phys. Rev. B **53** (1996) 14445.
[16] H. Y. Hwang, T.T.M. Palstra, S.-W. Cheong and B. Battlog, Phys. Rev. B **52** (1995) 15046.
[17] A. J. Millis, P. B. Littlewood, and B. I .Shraiman, Phys. Rev. Lett. **74** (1995) 5144.
[18] L.M. Rodriguez-Martinez, and J.P. Attfeld, Phys. Rev. B **54** (1996) R15622.
[19] H. Roder, J. Zang and A.R. Bishop, Phys. Rev. Lett. **76** (1996) 1356.
[20] B. Raveau, A. Maignan and V. Caignaert, J. Solid. Chem. **117** (1995) 424.
[21] A. Maignan, Ch. Simon, V. Caignaert and B. Raveau, J. Appl. Phys. **79** (1996) 7891.
[22] M. Hennion, F. Moussa, G. Biotteau, J. Rodríguez-Carvajal, L. Pinsard and A. Revcolevschi, Phys. Rev. Lett. **81** (1998) 1957.
[23] G. Allodi, R. De Renzi and G. Guidi, Phys. Rev. B **57** (1998) 1024.
[24] J.M. Teresa, M.R. Ibarra, P.A. Algarbel, C. Ritter, C. Marquinna, J. Blasco, J. Garcia, A. del Moral and Z. Arnold, Nature **386** (1997) 256.
[25] J.W. Linn, R.W. Erwin, J.A. Borchers, Q. Huang, A. Santoro, J-L. Peng and Z.Y. Li, Phys. Rev. Lett. **76** (1996) 4046.
[26] J.A. Fernandez-Baca, P. Dai, H.Y. Hwang, C. Kloc and S-W. Cheong, Phys. Rev. Lett. **80** (1998) 4012.
[27] S. Mori, C.H. Chen and S-W. Cheong, Phys. Rev. Lett. **81** (1998) 3972.
[28] M. Uehara, S. Mori, C.H. Chen and S.-W: Cheong, Nature **399** (1999) 560.
[29] M. Fäth, S. Freisem, A. Menovsky, Y. Tomioka, J. Arts, J.A. Mydosh, Science **285** (1999) 1540.
[30] A. Moreo, S. Yunoki, E. Dagotto, Science **283** (1999) 2034.
[31] N. Mathur and P. Littlewood, Physics Today **56** (2003) 25.
[32] E. Dagotto, T. Hotta, A. Moreo, Physics Reports **344** (2001) 1.

[33] A. Moreo, M. Mayr, A. Feiguin, S. Yunoki, E. Dagotto, Phys. Rev. Lett. **84** (2000) 5568.
[34] J. Burgy, M. Mayr, V. Martin-Mayor, A. Moreo, and E. Dagotto, Phys. Rev. Lett. **87** (2001) 277202.
[35] K. Ahn, T. Lookman and A.R. Bishop, Nature **428** (2004) 401.
[36] V. Moshnyaga, I. Khoroshun, A. Sidorenko, P.A. Petrenko, A. Weidinger, M. Zeitler, B. Rauschenbach, R. Tidecks, and K. Samwer, Appl. Phys. Lett. **74** (1999) 2842.
[37] I.V. Khoroshun, E.V. Karyaev, V.T. Moshnyaga, G.A. Kiosse, M.A. Krachun, V.M. Zakosarenko, V. Yu. Davydov, Supercond. Sci. & Techn. **3** (1990) 493.
[38] A. I. Ivashchenco, E. V. Karyaev, I. V. Khoroshun, G. A. Kiosse, V. T. Moshnyaga and P. A. Petrenco, Thin Solid Films **263** (1995) 122.
[39] L. Kulyuk, I. Kravetsky, A. Micu, E. Karyaev, V. Moshnyaga, I. Khoroshun, I. Muscutariu, and V. Sokoliuc, *Non-linear Optics of Low-Dimensional Structures & New Materials*, Proc. of SPIE **2801** (1995) 135.
[40] V. Moshnyaga, I. Khoroshun, P. Petrenko, D. Shaban, L. Kulyuk, MRS Proc. **495,** (1997) 239.
[41] A. Konrad, T. Fries, A. Gahn, F. Kummer, U. Herr, R. Tidecks and K. Samwer, J. Appl. Phys. **86** (1999) 3129.
[42] G. Wahl, O. Stadel, O. Gorbenko, and A. Kaul, Pure Appl. Chem. **72** (2000) 2167.
[43] A. Belenchuk, O. Shapoval, K. Samwer, and V. Moshnyaga, German Patent 10347119.7 (2003).
[44] V. Moshnyaga, B. Damaschke, O. Shapoval, A. Belenchuk, J. Faupel, O. I. Lebedev, J. Verbeeck, G. van Tendeloo, M. Mücksch, V. Tsurkan, R. Tidecks, and K. Samwer, Nature Materials **2** (2003) 247-252.
[45] V. Moshnyaga, I. Khoroshun, A. Weidinger, S. Klimm, M. Zeitler, R Tidecks, S. Horn, and K. Samwer, J. Appl. Phys. **86** (1999) 5642.
[46] F.C. Frank and J.H. van der Merwe, Proc. Roy. Soc. London **A198** 216 (1949).
[47] M. Wolmer and J. Weber, Z. Physik. Chem. **119** (1926) 277.
[48] E.S. Vlakhov, R.A. Chakalov, R.I. Chakalova, K.A. Nenkov, K. Dörr, A. Handstein, and K.H. Müller, J. Appl. Phys. **83** (1998) 2152.
[49] V. Moshnyaga, S. Klimm, R. Tidecks, S. Horn, and K. Samwer, J. Mag. & Mag. Mater. **211/1-3** (2000) 166-171.
[50] E. Mishina, N. Sherstyuk, A. Sigov, T. Tamura, S. Nakabayashi, V. Moshnyaga, K. Samwer, L. Kuyuk, and Th. Rasing, Transactions of Magnetic Society of Japan, in press (2004).
[51] M.F. Hundley, M. Hawley, R.H. Heffner, Q.X. Jia, J.J. Nuemeier, and J. Tesmer, Appl. Phys. Lett. **67** 860 (1995).
[52] R. Mahesh, R. Mahendiran A.K. Raychaudhuri, and C.N.R. Rao, Appl. Phys. Lett. **68** (16), 2291 (1996).
[53] A. Gupta, G.Q. Gong; G. Xiao, P.R. Duncombe, P. Lecoeur, P. Trouilloud, Y.Y. Wang, V.P. Dravid, and J.Z. Sun, Phys. Rev. **B 54** (22), R15629 (1996).
[54] H.L. Ju and H. Sohn Sol. St. Comm. **102** (6) 463 (1997).
[55] S. Chattopadhyay, P. Ayyub, V.R. Palkar, and M. Multani, Phys. Rev. **B 52** (1995) 13177.
[56] R.M. Strud, J.M. Byers, V.M. Browning, W.W. Fuler-Mora, D. Koller, J. Kim, P.S. Broussard, J.O. Gross and D.L. Knies, MRS 1998 Fall Meeting (abstracts), Nov.30 – Dec.4 Boston, 323.

[57] J. Aarts, S. Freisem, and R. Hendrikx, H.W. Zandbergen, Appl. Phys. Lett. **72** (1998) 2975.
[58] M. Rajeswari, R. Shreekala, A. Goyal, S.E. Lofland, S.M. Bhagat, K. Ghosh, R.P. Sharma, R.L.Greene, R. Ramesh and T. Venkatesan, Appl. Phys. Lett. **73** (1998) 2672.
[59] J.Q.Guo, H.Takeda, and N.S.Kazama, K.Fukamichi, M.Tachiki, J.Appl.Phys. **81** (1997) 7445.
[60] Q. Xie, P. Chen and A. Madhukar, Appl. Phys. Lett. **65** (1994) 2051.
[61] Y. Chen and J. Washburn, Phys. Rev. Lett. **77** (1999) 4046.
[62] T. Becker, C. Streng, Y. Luo, V. Moshnyaga, B. Damaschke, N. Schannon, and K. Samwer, Phys. Rev. Lett. **89** (2002) 237203.
[63] T. Becker, Dissertation, Universität Göttingen, 2004.
[64] A. Biswas, M. Rajeswari, R.C. Srivastava, Y.H. Li, T. Venkatesan, R.L. Greene, and J. Millis, Phys. Rev. B **61** (2000) 9665.
[65] V. Laukhin, J. Fontcuberta, J.L. Garcia-Munoz, and X. Obrados, Phys. Rev. B **56** (1997) R10009.
[66] J. Fontcuberta, V. laukhin, and X. Obrados, Appl. Phys. Lett. **72** (1998) 2607.
[67] Y. Moritomo, H. Kuwahara, Y. Tokura, Physica B **237-238** (1997) 26.
[68] V. Moshnyaga, S. Klimm, E. Gommert, R. Tidecks, S. Horn, and K. Samwer, J. Appl. Phys. **88** (2000) 5305.
[69] T. Roch, S. Yaghoubzadeh, F.S. Razavi, B. Leibold, R. Praus, H.-U. Habermeier, Appl. Phys. A **67** (1998) 723.
[70] C. Kwon, M.C. Robson, K.-C. Kim, J.Y. Gu, S.E. Lofland, S. M. Bhagat, Z. Trajanovic, M. Rajeswari, T. Venkatesan, A. R. Kratz, R. D. Gomez, R. Ramesh, J. Magn. & Mag. Mater. **172** (1997) 229.
[71] E. Gommert, H. Cerva, J. Wecker, K. Samwer, J. Appl. Phys. **85** (1999) 5417.
[72] C. Meneghini, D. Levy, S. Mobilio, M. Ortolani, M. Nunez-Reguero, A. Kumar and D. Sarma, Phys. Rev. B **65** (2004) 012111.
[73] Y. Tokura, H. Kuwahara, Y. Moritomo, Y. Tomioka, and A. Asamitsu, Phys. Rev. Lett. **76** (1996) 3184.
[74] H. Kuwahara, Y. Moritomo, Y. Tomioka, A. Asamitsu, M. Kasai, R. Kunai, and Y. Tokura, Pyhs. Rev. B **56** (1997) 9386.
[75] R. Senis, V. Laukhin, B. Martinez, J. Fontcuberta, X. Obrados, A.A. Arsenov, and Y.M. Mukovskii, Phys. Rev. B **57** (1998) 14680.
[76] J.-S. Zhou, J.B. Goodenough, and J.F. Mitchell, Phys.Rev. B **61** (2000) R9217.
[77] N.D. Mathur, P.B. Littlewood, N.K. Todd, S.P. Isaac, S.-B. Teo, D.-J-. Kang, E.J. Tarte, Z.H. Barber, J.E. Evetts, and M.G. Blamire, J. Appl. Phys. **86** (1999) 6287.
[78] J. Wolfman, A.M. Haghiri-Gosnet, B. Raveau, C. Vieu, E. Cambril, A. Cornette, and H. Launois, J. Appl. Phys. **89** (2001) 6955.
[79] S.J.C.H. Theeuwn, J.Caro, K.I. Schreuers, R.P. van Gorkom, K.P. Wellock, N.N. Gribov, S. Radelaar, R.M. Jungblut, W. Oepts, R. Coehoorn, J. Appl. Phys. **89** (2001) 4442.
[80] P. Ciureanu and S. Middelhoek, *"Thin film resistive sensors"* (N. Y., Institute of Physics Publishing, 1992).
[81] T.R. McGuire and R.I. Potter, IEEE Trans. Magn. **11** (1975) 1018.
[82] J. Smit, Physica **16** (1951) 612.
[83] A.P. Malozemoff, Phys. Rev. B **32** (1985) 6080.
[84] G. Li, Z. Lu, C. Chai, H. Jiang, W. Lai, Appl. Phys. Lett. **74** (1999) 747.

[85] C. Mitze, C. Osthöver, F. Voges, U. Hasenkox, R. Waser, R.R. Arons, Sol. St. Commun. **109** (1999) 189.
[86] J. E. Nunez-Reguero, A.M. Kadin, J. Phys. D: Appl. Phys. **31** (1998) L1.
[87] V. Moshnyaga, B. Damaschke, R. Tidecks, and K. Samwer, J. Appl. Phys. **93** (2003) 6354.
[88] C. Prados, D. Garcia, F. Lesmes, J.J. Freijo, and A. Hernando, Appl. Phys. Lett. **67** (1995) 718.
[89] O. I. Lebedev, J. Verbeeck, G. van Tendeloo, O. Shapoval, A. Belenchuk, V. Moshnyaga, B. Damaschke, and K. Samwer, Phys. Rev. B **66** (2002) 104421.
[90] S. Gupta, R. Ranjit, C. Mitra, P. Raychaudhuri, and R. Pinto, Appl. Phys. Lett. **78** (2001) 362.
[91] D.K. Petrov, L. Krusin-Elbaum, J.Z. Sun, C. Feild, and P.R. Duncombe, Appl. Phys. Lett. **75** (1999) 995.
[92] S. A. Köster, V. Moshnyaga, K. Samwer, O. I. Lebedev, G. van Tendeloo, O. Sahpoval, and A. Belenchuk, Appl. Phys. Lett. **81** (2002) 1648.
[93] M. Bibes, Ll. Balcells, S. Valencia, S. Fontcuberta, M. Wojcik, E. Jedryka, and S. Nadolski, Phys. Rev. Lett. **87** (2001) 067210.
[94] B. Wiedenhorst, C. Höfener, Yafeng Lu, J. Klein, L. Alff, R. Gross, B. H. Freitag and W. Mader, Appl. Phys. Lett. **74** (1999) 3636.
[95] O.I. Lebedev, G. van Tendeloo, S. Amelinckx, B. Leibold, and H.-U. Habermeier, Phys. Rev. B **58** (1998) 8065.
[96] H. S. Wang, E. Wertz, Y. F. Hu, Qi Li, and D. G. Schlom, J. Appl. Phys. **87** (2000) 7409.
[97] R. Rao, D. Lavric, T. K. Nath, C. B. Eom, L. Wu, and F. Tsui App. Phys. Lett. **73** (1998) 3294.
[98] A.J. Millis, T. Darling, and A. Migliori, J. Appl. Phys. **83** (1998) 1588.
[99] P.G. Radaelli, M. Marezio, H.Y. Hwang, S-W. Cheong, and B. Batlogg, Phys. Rev. B **54** (1996) 8992
[100] Y. Tomioka, A. Asamitsu, and Y. Tokura, Phys. Rev. B **63** (2000) 024421.
[101] H.Y. Hwang, S.W. Cheong, N.P. Ong, and B. Battlog, Phys. Rev. Lett. **77**, 2041 (1996).
[102] M. Julliere, Phys. Lett. **54 A** (1975) 225.
[103] J.-H. Park, E. Vescovo, H.-J. Kim, C. Kwon, R. Ramesh, and T. Venkatesan, Nature **392** (1998) 794.
[104] A. Gupta and J.Z. Sun, J. Magn. & Mag. Mater. **200** (1999) 24.
[105] K. Steenbeck, T. Eick, K. Kirsch, K. H.-G. Schmidt and E. Steinbeiß, Appl. Phys. Lett. **73** (1998) 2506.
[106] A. Gupta, G.Q. Gong, G. Xiao, P.R. Duncombe, P. Lecoeur, P. Trouilloud, Y.Y. Wang, V.P. Dravid, J.Z. Sun, Phys. Rev. **B 54** (1996) R15629.
[107] J.B. Phillip, C. Höfener, S. Thienhaus, J. Klein, L. Alff, and R. Gross, Phys. Rev. B **62** 9248 (2000).
[108] C. Kwon, K.C. Kim, M.C. Robson, J.Y. Gu, M. Rajeswari, T. Venkatesan, and R. Ramesh, J. Appl. Phys. **81** (1997) 4950.
[109] Y. Lu, X.W. Li, G.Q. Gong, G. Xiao, A. Gupta, P. Lecoeur, J.Z. Sun, Y.Y. Wang, and V.P. Dravid, Phys. Rev. B **54** (1996) R8357.
[110] G.Q. Gong, A. Gupta, G. Xiao, P. Lecoeur, and T.R. McGuire, Phys. Rev. B **54** (1996) R3742.

[111] G. Hammerl, A. Schmehl, R.R. Schulz, B. Goetz, H. Bielefeldt, C.W. Scheider, H. Hilgenkamp, and J. Mannhart, Nature **407** (2000) 162.
[112] H. Hilgenkamp and J. Mannhart, Appl. Phys. Lett. **73** (1998) 265.
[113] C. H. Ahn, J.-M. Triscone and J. Mannardt, Nature **424** (2003) 1015.
[114] V. Kiryukhin, D. Casa, J.P. Hill, B. Keimer, A. Vigliante, Y. Tomioka, and Y. Tokura, Nature **386** (1997) 813.
[115] K. Miyano, T. Tanaka, Y. Tomioka, and Y. Tokura, Phys. Rev. Lett. **78** (1997) 4257.
[116] Y. Okimoto, Y. Ogimoto, M. Matsubara, Y. Tomioka, T. Kageyama, T. Hasegawa, H. Koinuma, M. Kawasaki, and Y. Tokura, APL **80** (2002) 1031.
[117] Y. G. Zhao, J. J. Li, R. Shreekala, H. D. Drew, C. L. Chen, W. L. Cao, C. H. Lee, M. Rajeswari, S. B. Ogale, R. Ramesh, G. Baskaran, and T. Venkatesan, Phys. Rev. Lett. **81** (1998) 1310.
[118] X. J. Liu, Y. Moritomo, A. Machida, A. Nakamura, H. Tanaka, and T. Kawai. Phys. Rev. B **63** (2001) 115105.
[119] K. Matsuda, A. Machida, Y. Moritomo, and A. Nakamura, Phys. Rev. B **58** (1998) R4203.
[120] V. Moshnyaga, A. Giske, K Samwer, E. Mishina, T. Tamura, S. Nakabayashi, A. Belenchuk, O. Shapoval, and L. Kulyuk, J. Appl. Phys. **95** (2004) 7360.
[121] M. Fiebig, D. Fröhlich, Th. Lottermoser, V. V. Pavlov, R.V. Pisarev, and H.-J Weber, Phys. Rev. Lett. **87** (2001) 137202.
[122] M. Fiebig, K. Miyano, Y. Tomioka, H. Kuwahara, Y. Tokura, and K. Reimann, Phys. Rev. Lett. **86** (2001) 6002.
[123] T.V. Murzina, T.V. Misuryaev, A.A. Nikulin, O.A. Aktsipetrov, J. Güdde, J. Magn. Magn. Mat. **258-259** (2003) 99.
[124] J. I. Dadap, B. Doris, Q. Deng, M. C. Downer, J. K. Lowell and A. C. Diebold, Appl. Phys. Lett. **64** (1994) 2139.
[125] A. Berger, G. Campillo, P. Vivas, J. E. Pearson, S. D. Bader, E. Baca, P. Prieto, J. Appl. Phys. **91** (2002) 8393.
[126] E. Arene and J. Baixeras, Phys. Rev. B **30** (1984) 2016.
[127] M. Roy, J.F. Mitchel and P. Schiffer, J. Appl. Phys. **87** (2000) 5831.
[128] H. Zheng, J. Wang, S.E. Lofland, Z. Ma, L. Mohaddes-Ardabili, T. Zhao, L. Salamanca-Riba, S.R. Shinde, S.B. Ogale, F. Bai, D. Viehland, Y. Jia, D.G. Shlom, M. Wutting, A. Roytburd, R. Ramesh, Science **203** (2004) 661.
[129] S. Krupicka ,*"Physik der Ferrite und der verwandten magnetischen Oxyde"* (Academia, Prague, 1973).
[130] T. Wu, S. B. Ogale, J. E. Garrison, B. Nagaraj, Amlan Biswas, Z. Chen, R. L. Greene, R. Ramesh, T. Venkatesan, and A. J. Millis, Phys. Rev. Lett. **86** (2001) 5998.

MAGNETISM OF INTERACTING TWO-DIMENSIONAL NANOSTRUCTURES

P. J. Jensen and K. H. Bennemann

Institut für Theoretische Physik, Freie Universität Berlin
Arnimallee 14, D-14195 Berlin, Germany

1. INTRODUCTION

Interacting two-dimensional (2D) magnetic nanostructures are currently the subject of intense research activity, driven both by their fundamental interest and technological perspectives [1]. To understand their magnetic properties, one has to know the effect of the most important interactions like the magnetic anisotropy, the exchange, and the magnetic dipole coupling. In this Review we concentrate on the investigation of the pronounced influence of the dipole coupling, which plays a major role in such systems due to its particular nature. This is especially true for densely packed nanostructures exhibiting a layered (2D) structure, or for ensembles where the particles are arranged in certain geometrical patterns. The particular importance of the dipole coupling is supported by many theoretical and experimental reports, which is enabled by the increasing ability of the controlled preparation of such structures with different degrees of structural and magnetic disorder [2]-[13]. In view of the tremendous technological interest for these magnetic structures, e.g., for the development of improved storage media and sensor applications, there is an increasing demand to identify and determine the key parameters which control the magnetic dynamics and relaxation, for instance. A number of important quantities for 2D ensembles of interacting magnetic particles will be addressed in the following Sections with the help of a Heisenberg Hamiltonian. These quantities are expected to determine important parameters which affect, for example, the temporal behavior of these systems.

Let us at first state what is meant by the phrases 'nanostructures' and 'nanophysics'. From a fundamental point of view, the investigation of systems ranging from a few 10 to a few 10000 atoms, having a size range of about 0.1 - 100 nm, bridges the gap between atoms and molecules on the one hand, and on mesoscopic and solid state physics on the other. Mesoscopic physics handles the corresponding systems like continuous media limited by surfaces, the atomic structure is usually neglected. The corresponding averaged physical quantities can be scaled in the sense that they are expressed solely by the geometrical surface-to-volume ratio of the system, i.e., by the relative weight of their bulk and surface values. Note that this scalable regime depends on the concerned quantity. In contrast, cluster- and nanophysics is considered with systems whose properties are not scalable because they can vary markedly by adding or removing a single atom or electron. The number of atoms is not large enough that such a cluster or particle can be treated as a continuous medium, since the consideration of the atomic structure is still important. Clusters can contain one or several kinds of chemical elements and are considered to be either free, deposited on a surface, or embedded into a bulk matrix. The physics of clusters mainly investigates internal, single-particle quantities and the influence of neighboring media. Interactions between clusters are usually neglected. In contrast, the field of nanophysics deals with extended interacting systems, where the building blocks or unit cells are objects of nanometre size range. Consequently, properties characterizing the whole ensemble of clusters or nanoparticles are the main concerns of investigation in this case.

The interest of 2D magnetic nanostructures origins from three different fields of research. The first results from the investigation of three-dimensional (3D) ferrofluids consisting of non-overlapping magnetic particles in a liquid or frozen solvent, for which numerous experiments have been performed previously [14]-[20]. These magnetic particles are subject to both single-particle couplings and long-range magnetic interactions between the particles. By varying the interparticle distance the ratio between these two contributions can be tuned appropriately. Of particular interest is the slow dynamics [21] or slow magnetic relaxation (magnetic ageing, magnetic viscosity) in these systems [22]-[25]. In the case of movable particles the pattern formation and the particle aggregation has been studied, and the fractal dimension was determined [26]-[30]. Recently, the investigation of 2D ferrofluid systems became feasible by reducing the thickness of 3D ferrofluids to within a few particle diameters [31]-[33].

The second approach to 2D magnetic nanosystems origins from the investigation of thin magnetic films, which have been studied thoroughly in the last decades [34]-[43]. These films are prepared by depositing single magnetic atoms on a nonmagnetic substrate by molecular beam epitaxy or by sputtering, for example. Evidently, before a continuous layer is formed, individual magnetic islands are present, interacting by long-range forces like the dipole coupling and, in case of a metallic substrate, by the Ruderman-Kittel-Kasuya-Yosida (RKKY) interaction [44]. Near the percolation threshold Θ_P of the growing thin film, which depends sensitively on, e.g., the growth mode, the island geometry, and the temperature, a long-range magnetic ordering due to the strong direct exchange interaction emerges. Quite remarkably, a remanent magnetization at comparable high temperatures has been observed also below Θ_P [40]. This property could be explained

either by nonequilibrium magnetic relaxation effects or by an equilibrium ordered state due to long-range interactions, see also the discussion in Appendix A.

Thirdly, the interest in magnetic nanostructures results from the study of disordered atomic spin glasses or random magnets, which have been intensively investigated experimentally as well as theoretically [45][46]. These systems consist of point-like single atoms or spins diluted in a nonmagnetic host and interact via nonuniform exchange couplings with given distributions and ranges of the interactions. In particular, the problem of a long-range magnetic order and the definition of the order parameter in a disordered system has been discussed and studied in detail. Often Ising-like spins are considered [47], which however are not appropriate for magnetic nanoparticles. Rather, these systems are better described by classical magnetic moments. For a 2D spin glass the question arises whether the Mermin-Wagner theorem is valid, which states that in a 2D isotropic magnet with short-range interactions an equilibrium long-range magnetic order is not present at finite temperatures [48]. Moreover, nonequilibrium effects such as the magnetic relaxational behavior and the corresponding relaxation laws have been studied. These methods are nowadays applied to magnetic nanostructures consisting of particles or clusters with a finite extension having a giant magnetic moment ('superspin glass') [11][24][25].

As mentioned, for magnetic nanostructures the interactions between the building blocks cannot be neglected. Let us first briefly review properties of noninteracting single magnetic clusters and nanoparticles. For experimental and theoretical reviews see, e.g., [49]-[51]. The interest in these systems is mainly twofold. First, surface-induced deviations of the magnetic state from the uniform bulk magnetic phase can occur. In particular, the spatial variation of the magnetic moment, of the exchange coupling, and of the magnetic anisotropy has been studied as function of the particle size for both free clusters [52]-[54] and after deposition of pre-formed particles [11][55]-[57]. Very important in this context are the determination of the hysteresis loops, the field-cooled and zero-field-cooled magnetization curves, and the linear and nonlinear susceptibilities [58]-[62]. A particular feature is the noncollinear magnetization in single particles, resulting in a surface spin canting [63][64]. Moreover, to avoid external stray fields the particle magnetization can assume a domain structure with, e.g., a circular shape [65]-[69]. This process requires a minimum size of the particle. The second main concern for single magnetic particles is the field-induced and thermal-assisted magnetic reversal [70]-[76] and the corresponding relaxation. For long times this nonequilibrium process can well be described by an Arrhenius-Néel-approach below the blocking temperature T_b, known as the superparamagnetic model [77]-[80]. For short times the gyroscopic term in the Landau-Lifshitz equation of motion [81] has to be considered explicitely [70][73]-[75][82]-[84]. For these purposes frequently micromagnetic models are applied [76][85]. Weak interactions between the particles can be considered perturbatively within a mean field approach [20][86]-[91].

In this Review we will be concerned with layered systems for which the interparticle interactions dominate the single-particle ones, hence a perturbative approach of the interactions is not appropriate. Rather, the magnetic properties like the resulting magnetic states and the magnetization dynamics are dominated by the collective magnetic behavior within a correlated region. New physical features will emerge which are absent

in single-particle systems, and which demand for improved theoretical approaches. With the help of such methods key quantities can be identified which unambiguously describe, for instance, the degree of collectivity, and the influences of the interactions.

As mentioned, we will focus here on the dipole interaction between the particles, in addition the exchange coupling will be considered for the case of overlapping particles. Magnetic nanostructures are often characterized by a considerable amount of structural disorder, resulting, for example, from the dispersion of the particle size and -shape, the positional disorder, or the random orientation of the anisotropy easy axes. For such irregular nanostructures the interparticle couplings are strongly nonuniform and may even compete with each other. In this case the properties of the system can be compared to the ones of a spin glass or random magnet, characterized by many metastable states and by strong magnetic noncollinearities [45][46]. Note that for 2D nanostructures an improved comparison with experiments is possible, since the sizes, shapes, and locations of the building blocks can be measured and controlled much better than for bulk systems.

Before introducing the particular problems addressed in greater detail in this Review, we will briefly mention other theoretical studies on interacting 2D magnetic nanostructures. In general, the low symmetry of the systems and the complicated nature of the interactions precludes simple analytical approaches. Hence, often numerical simulations have been performed in order to achieve a detailed microscopic description within the model. A number of studies were concerned with the calculation of the magnetic hysteresis loops, addressing the remanent and saturation magnetization as well as the coercive field as functions of, e.g., the spatial arrangement of the particles and the single-particle anisotropies [92]-[95]. An important problem is the determination of the magnetization as function of the temperature in presence or absence of a magnetic field, i.e., the field-cooled and zero-field-cooled magnetization [11][87][96]-[100]. Moreover, many studies focus on the determination of the (complex) linear and nonlinear susceptibilities $\chi^{1)}(T)$ and $\chi^{3)}(T)$, see, for instance, [97][101]-[103]. With the thelp of these quantities the onset of a collectively ordered, spin glass-like magnetic state at the spin glass ordering temperature $T_{\rm sg}$, and the (nonequilibrium) freezing temperature $T_{\rm f} \geq T_{\rm sg}$ is investigated, indicated by a maximum or singularity of $\chi^{3)}(T)$ [105]. Note that both polydispersity and interparticle interaction can suppress this maximum [97][104]. $T_{\rm f}$ has to be distinguished from the blocking temperature $T_{\rm b}$ which is used for noninteracting particles. These investigations allow for the determination of the magnetic relaxation, which has been simulated for instance as functions of the time, the packing density of the particles, the strength of the interactions, the degree of disorder, and the dispersion of the particle size [96]-[103]. Note that both single-particle anisotropies and interactions between particles can account for a slowing-down of the magnetization dynamics and for magnetic memory effects [106]. By an appropriate analysis these two contributions can be separated [24]. Different kinds of empirical relaxational behavior (power-law, exponential, logarithmic) has been reported for different systems [107][108]. From these studies it is evident that the low-temperature dynamics is dominated by collective particle properties. Usually the interactions lead to an increase of the magnetic relaxation time [19][24][89][101][102][104]. Note that under certain conditions also an acceleration of the relaxation seems to be possible [88][109]. With the so-called Henkel-plot the influence of the microstructure can

be studied [110][111]. Furthermore, movable particles, chain formation, and the particle agglomeration has been studied in [26]-[30][94][112]-[114]. Transport properties in interacting nanostructures like the magnetoresistance have been investigated in [115]-[117].

This Review discusses three major problems in greater detail. Using a Heisenberg model a number of properties for different kinds of interacting particle ensembles are calculated, which can be used to determine additional quantities of these magnetic nanostructures. For instance, with the knowledge of the average binding energy due to the dipole coupling the spin glass ordering temperature can be estimated. The contents of the remaining Sections are summarized in the following outline.

Section 2	Model Hamiltonian and magnetic interactions;
Section 3	Low-energy properties of dipole-coupled and non-overlapping magnetic particles located on an infinitely extended plane: distribution of states, average dipole energy, scaling behavior;
Section 4	Hysteresis loops for magnetic particles located on a large microsphere and for chains of those spheres;
Section 5	Magnetic properties of a growing ultrathin film: remanent magnetization, domain structure, relaxational behavior;
Section 6	Conclusion and outlook;
Appendix A	Binding energy of dipole-coupled spin pair, blocking temperature;
Appendix B	Cluster Monte Carlo method.

2. THE MODEL SYSTEM

In this Section we present the Hamiltonian and interactions common to all systems which are discussed. We consider ensembles of n magnetic particles. Due to the strong direct (ferromagnetic) exchange interaction J and the small size of the particles under consideration, each particle i is viewed as a single magnetic domain (Stoner-Wohlfarth particle) [118]. Internal degrees of freedom such as site-dependent exchange couplings and site-dependent anisotropies are not considered here. For the investigation of properties characteristic of single particles see, e.g., [49]-[51]. Here we assume that a particle containing N_i atoms carries a giant spin $M_i = N_i \mu_{at}$ and a magnetic anisotropy $K_i = N_i k_{\rm at}$ resulting from the spin-orbit interaction, where μ_{at} is the magnetic moment and $k_{\rm at}$ the anisotropy per atom. The large size of $\mathbf{M}_i$ justifies the description by a classical vector whose direction is characterized by the angles θ_i and ϕ_i.

To fulfil the single-domain condition the particle size should not be larger than the domain wall width $w \quad \sqrt{J/k_{\rm at}}$. The bulk domain wall width amounts to $\sim$ 10 nm for Co and $\sim$ 75 nm for Fe [119]. Particle larger than that width might break up into several smaller domains and form a Landau pattern [65]-[69][120]. Note that due to a considerably larger anisotropy for surface and edge atoms [12][34][121] the corresponding domain wall width of nanostructures can be markedly smaller [122][123].

The magnetic particles are located on sites $\mathbf{r}_i$, and are characterized by a certain size N_i and shape, which are specified in the corresponding Sections. For such a particle ensemble we consider the dipole-dipole interaction $E_{\rm dip}$ between the magnetic moments $\mathbf{M}_i$. Moreover, for the single-particle anisotropy energy $E_{\rm anis}$ we take into account a second order uniaxial contribution, for simplicity, with $\mathbf{n}_i$ the direction of the easy axis of particle i. The shape anisotropy resulting for the dipole interaction within a *single* particle can be absorbed into this term. Higher-order anisotropy terms with symmetries appropriate to the given lattice or system can be considered as well [124]. Furthermore, if two particles i and j touch each other they interact via the exchange interaction γ, the resulting energy $E_{\rm ex}$ is proportional to the number of interparticle bonds L_{ij}. Caused by the formation of domain walls γ is usually smaller than J. Finally, the Zeeman energy $E_{\rm Z}$ resulting from an external magnetic field $\mathbf{B}$ with arbitrary strength and direction is considered. The total magnetic energy $E_{\rm magn}$ is given by

$$\begin{aligned} E_{\rm magn} &= E_{\rm dip} + E_{\rm anis} + E_{\rm ex} + E_{\rm Z} \\ &= \frac{\mu_0}{2} \sum_{\substack{i,\\ i=}} \left[\mathbf{M}_i \, \mathbf{M}_j \, r_{ij}^{-3} - 3 \, (\mathbf{r}_{ij} \, \mathbf{M}_i) \, (\mathbf{r}_{ij} \, \mathbf{M}_j) \, r_{ij}^{-5} \right] - \sum_i \, K_{2,i} \, (\mathbf{n}_i \, \mathbf{M}_i / M_i)^2 \\ &\quad - \frac{\gamma}{2} \sum_{\substack{i,\\ i=}} L_{ij} \, (\mathbf{M}_i / M_i) \, (\mathbf{M}_j / M_j) - \mu_0 \, \mathbf{B} \, \sum_i \, \mathbf{M}_i \, , \end{aligned} \tag{1}$$

where $r_{ij} = |\mathbf{r}_{ij}| = |\mathbf{r}_i - \mathbf{r}_j|$ is the distance between the centers of particles i and j, and μ_0 the vacuum permeability. Which of these term is most effective depends on the particular problems discussed in the subsequent Sections. In Eq.(1) only the point dipole sum is given. For closely separated particles the leading correction due to the finite size of each particle (dipole-quadrupole interaction) is taken into account. which is outlined in detail in [125][126]. This correction is proportional to the squared ratio of the particle radius and the interparticle distance, and is comparable to the point-dipole sum for large particle coverages or small interparticle distances.

As mentioned in the Introduction, in case of a metallic substrate or matrix also the oscillating RKKY interaction between magnetic particles can be effective. Since little is known about this coupling for magnetic nanostructures, we do not consider this interaction explicitely. A number of results has been reported in [44][127]-[130], which indicate that the sign and strength of this coupling depends sensitively on the distance, shape, and relative orientation of the particles. Note that the RKKY interaction will cancel if the oscillation period is smaller than the particle size. This will happen for the case of diluted single spins in bulk, having a period of the order of the atomic lattice constant. For thin film systems a comparable long oscillation period was found, which however is confined to the layered structure [44][131]. In addition, for insulating substrates or matrices a superexchange between the particles could be present, which is usually weak and decreases strongly with distance.

In this Review we focus on situations where the single-particle couplings, i.e., the anisotropy, are weaker than interparticle ones. As a rule of thumb, a weakly interacting

particle ensemble is present if the energy minima due to single-particle anisotropies are still preserved for each particle. In a strongly interacting ensemble often a single minimum remains, similar to an effective magnetic field. This local field differs in strength and direction for each particle.

3. TWO-DIMENSIONAL DISORDERED PARTICLE ENSEMBLES

In this Section we investigate low-energy properties of dipole-coupled disordered 2D systems of magnetic particles. The treatment of the dipole interaction is complicated by its long range and anisotropic nature, however is expected to have a strong effect in particular for planar magnets. As mentioned in the Introduction, we concentrate on systems where the interparticle couplings are stronger than the single-particle ones, and an explicit treatment of the interactions is unavoidable [97][102][107][126]. We outline in Appendix A that the binding energy due to the dipole interaction between extended single-domain particles can be considerably large, in contrast to single spins. The relative importance of single-particle versus interparticle contributions can be tuned experimentally at least to some extent by changing sample characteristics such as the particle-size distribution or the average interparticle distance. Very important in this context is the consideration of structural disorder in the particle ensemble and a dispersion of the particle size.

As is well known, *periodic* arrangements of dipole-coupled spins or particles exhibit a magnetically ordered state [132]-[135]. An intriguing question in this context is whether this interaction results in a collectively ordered magnetic state also for *disordered* (planar) particle ensembles. Several experiments on interacting, high-density ferrofluids indicate the onset of such an ordered state below a characteristic, concentration-dependent temperature. For example, near this temperature a 'critical slowing down' of the magnetic relaxation is observed [14][15]. Note that the experimental determination of the ordering temperature is problematic, since the relaxation times are often very long, and the separation between equilibrium properties and nonequilibrium or 'blocking' effects becomes difficult. Therefore, the identification and understanding of the collectively ordered magnetic states present in such particle ensembles is important, in particular for the determination of their temporal behavior.

After a description of the considered particle arrangement and the determination of the energy minima, we present results for the distribution of the energy minima, the average dipole energy, and the scaling properties of the dipole energy as function of the particle coverage and -arrangement. Special attention is paid to the role of disorder and noncollinear states of the particle magnetic moments. All calculations are performed at zero temperature ($T = 0$).

3.1. Description of the structural particle arrangements

For the ensemble of magnetic particles a rectangular unit cell with periodic boundary conditions in the xy- plane is taken into account. Within this unit cell $n = n_x \times n_y$ mag-

netic particles with arbitrary positions, shapes and sizes are located, the only constraint is that they are not allowed to overlap each other. Introducing the average interparticle distance R_0 the size of the unit cell is given by $L_x \times L_y = (n_x\, R_0) \times (n_y\, R_0)$. We consider three different types of lateral particle arrangements: (i) a periodic array, i.e., the particle centers are located on the sites of a square or hexagonal particle lattice with lattice constant R_0; (ii) a disturbed (quasi-periodic) array for which the particle centers deviate randomly from the periodic array, using a Gaussian distribution with positional standard deviation σ_R; and (iii) a fully random distribution within the unit cell. A finite vertical extension of the unit cell (vertical positions of the particle centers) can also be taken into account. By considering a single unit cell a finite particle ensemble is realized as well. In this case the boundary effecs will strongly dominate the resulting magnetic arrangement.

A dispersion of the particle sizes N_i is introduced by, e.g., a Gaussian distribution around a mean particle size $\overline{N}$ and standard deviation σ_N. The particle radius r_i is given by $r_i/a_0 = \sqrt{N_i}$, where a_0 is the interatomic distance. For spherical particles the radius reads $r_i/a_0 = \sqrt[3]{N_i}$. In the present Section we consider a planar ensemble with disk-shaped particles. For such an array the overall surface coverage amounts to $C = \pi(r_0/R_0)^2$, with r_0 the average particle radius. Due to the demagnetizing effect of the dipole interaction we restrict the particle magnetizations to be confined to the film plane, for simplicity. The planar rotator $\mathbf{M}_i$ is then characterized by the in-plane (azimuthal) angle ϕ_i: $\mathbf{M}_i = (M_i^x, M_i^y, M_i^z) = M_i(\cos\phi_i, \sin\phi_i, 0)$. For general cases also the vertical (polar) angle θ_i has to be considered, e.g., in presence of anisotropies with vertical components of the easy axes, for particle ensembles not located on a single plane, or for the consideration of excited states.

3.2. Determination of the dipole energy

The infinite range of the dipole interaction is taken into account by applying an Ewald-type summation over periodically arranged unit cells of the extended layer [125][136]. In addition to the usual point-dipole sum we consider the dipole-quadrupole correction resulting from the finite particle size [125][126].

The energy unit of the dipole coupling is given by $E^0_{\rm dip} = \mu_{at}^2/a_0^3$, with μ_{at} in units of the Bohr magneton μ_B. In this Section we assume values appropriate to Fe ($\mu_{at} = 2.2\ \mu_B$, $a_0 = 2.5$ Å), yielding $E^0_{\rm dip} = 0.19$ K. No size dispersion is considered, i.e., $N_i = \overline{N}$ and $r_i = r_0$. Unless otherwise stated, the present results refer to a unit cell containing $n = 100$ particles with $\overline{N} = 1000$ atoms each.

As mentioned, a disordered particle ensemble exhibits a large number of (meta-)stable noncollinear magnetic states [45][46]. Hence, to gain information about the ensemble characteristics one has to average over a large number of states which in turn demands for an efficient search for these energy minima. This search procedure is described as follows. Starting from an arbitrary initial configuration of the magnetic directions, the total magnetic energy $E_{\rm dip}$ of the system is relaxed to the nearest local minimum (stationary

state, fix point) by varying all angles ϕ_i (and θ_i, if appropriate) of the particles using a conjugated gradient method [137]. Such a metastable state is characterized by its energy E_{dip} and by its set of angles $\{\theta_i, \phi_i\}$. A twofold symmetry is always present due to time inversion symmetry, i.e., the energy of a state does not change under the transformation $\theta_i \rightarrow \pi - \theta_i$, $\phi_i \rightarrow \phi_i + \pi$ performed simultaneously for all particles. These mirrored states are considered to be equivalent. Since the minimization procedure relaxes typically to the local minimum that is closest to the initial state, this frequency provides a measure of the size of the 'energy basin' belonging to that state in the high-dimensional configuration space [138]. We emphasize that the applied procedure is not intended to search preferently for the global energy minimum or ground state, which is the equilibrium state at $T = 0$.

The average energy and the distribution of states, which are derived from microscopic properties of the underlying magnetic nanostructure, represent important global quantites characterizing the system. From the knowledge of these quantities the relaxational behavior and the relaxation times can be derived. For instance, one can identify which features of the measured magnetic memory effects are due to single-particle properties, and which result from the interactions between the particles [24][25][106]. Vice versa, to obtain a particular temporal behavior of a magnetic particle ensemble its optimal spatial arrangement can be determined.

3.3. Results

3.3.1. Uniform particle lattices

Before presenting results for disordered particle arrangements, we recall shortly the resulting structures for uniform systems, i.e., the particles having all the same size and placed on a periodic array. The ground state for a square lattice is the so-called microvortex arrangement with a vanishing net magnetization [139]. It is important to mention that this phase exhibits a continuous degeneracy with respect to a proper in-plane rotation of all spins in a four-spin plaquette, which is depicted in Fig. 3.1. Particular solutions are the columnar states consisting of particle rows or columns with a parallel magnetization and with alternating magnetic orientations. The ferromagnetic solution, i.e., parallel directions of all particle magnetizations, is unstable for a square lattice. Also the honeycomb lattice has a ground state with a vanishing net magnetization [140]. In contrast, for a hexagonal particle lattice the ferromagnetic arrangement is the ground state, which is also continuously degenerate [125][141].

Note that a continuous degeneracy is one of the prerequisites for a vanishing long-range magnetic order of a 2D magnetic system at finite temperatures [48]. As has been shown [142][143], thermal, structural, or quantum disorder immediately lifts this continuous degeneracy and results in a long-range magnetic order at finite temperatures ('order-by-disorder-effect'). The thermally induced order-by-disorder-effect is caused by the fact that the entropy and the density of states differ for the axial and the diagonal directions of the square lattice. The corresponding free energy depends on the in-plane

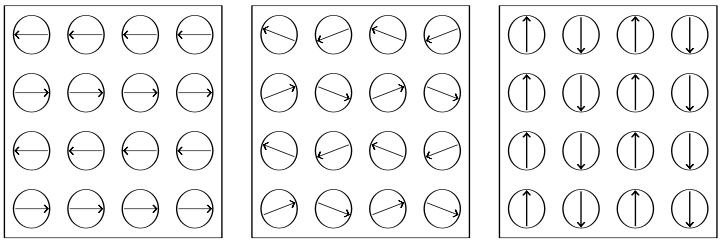

Fig. 3.1: Sketch of three microvortex arrangements of a dipole-coupled square lattice. The energy is continuously degenerate as function of the microvortex angle.

angle whereas the internal energy stays almost isotropic [144]. A similar behavior is expected also for other planar lattices [140]. Note furthermore that in the particular case of the dipole interaction already its long-range nature results in a net magnetic order for a 2D magnet at finite temperatures [145]. This is the reason why the dipole interaction is especially interesting for planar magnets.

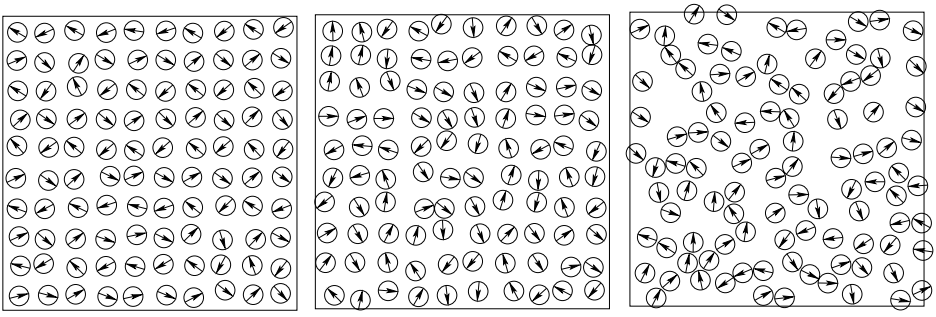

(a) (b) (c)

Fig. 3.2: Illustrations of stable magnetic arrangements in two-dimensional nanostructures. The particle positions are scattered around the lattice sites of a square array with positional standard deviations (a) $\sigma_R/R_0 = 0.05$, (b) $\sigma_R/R_0 = 0.10$, and (c) $\sigma_R/R_0 = 0.50$, where R_0 refers to the average interparticle distance. The surface coverage amounts to $C = 35$ %. The thin lines indicate the boundaries of the unit cells.

3.3.2. Visualization of disordered particle arrangements

Introducing now a size- or positional disorder into the particle array, the continuous angular degeneracy of the dipole interaction is immediately lifted. The system exhibits a (possibly very large) number of discrete states separated by energy barriers. Fig. 3.2 illustrates some representative low-energy metastable magnetic arrangements of disordered

particle arrays. For an increasingly disturbed square lattice, characterized by the positional standard deviation σ_R, the magnetic configurations of the relaxed solutions become increasingly noncollinear with a vanishing or small net magnetization. Results are given for the magnetic states of a slightly disturbed ($\sigma_R/R_0 = 0.05$), a moderately disturbed ($\sigma_R/R_0 = 0.10$), and a strongly disturbed ($\sigma_R/R_0 = 0.50$) particle setup having all the same coverage $C = 35$ %. For $\sigma_R/R_0 = 0.05$ the stable state resembles quite closely the microvortex arrangement. However, as can be seen in Fig. 3.2(b), already a moderate amount of positional disorder destroys this state. This is physically reasonable since the microvortex arrangement is tightly connected to the presence of a square-lattice symmetry of the particle ensemble. For large σ_R or for a random particle setup the resulting magnetic arrangement is dominated by the formation of chains and loops of magnetic moments with a correlated 'head-to-tail' alignment of the particle magnetizations, see Fig. 3.2(c) and also [29][112][114]. This reflects the tendency of the dipole interaction to favor a locally demagnetized state (flux closure). We emphasize that this noncollinear magnetization refers not simply to a disordered or paramagnetic phase, since the magnetic moments are strongly correlated by the dipole interaction.

3.3.3. Energy distribution of metastable states

At first we determine the dipole energy distribution of the local minima for different degrees of structural disorder. Applying the search procedure as described in Section 3.2, we monitor the numbers of trials yielding relaxed states with energies falling into given energy intervals $[E, E + \Delta E]$, with $\Delta E = 5 \cdot 10^{-3}$ K. Parameters appropriate to Fe are used. In Fig. 3.3 examples for the corresponding energy histograms (density of states) of slightly and moderately disturbed particle arrangements are presented. 20000 random initial configurations have been applied for each histogram, yielding distinctly different energy distributions for weak and strong disorder [126].

For weak disorder, $\sigma_R/R_0 = 0.05$, an *asymmetric* energy distribution is found, see Fig. 3.3(a). The lowest energy state is reached very often, resembling closely the microvortex state. In addition, a number of metastable states is obtained, with energies distributed over a relatively broad range, and which are reached far less frequently. In other words, for a weakly disturbed particle lattice the energy basin of the ground state is much larger than the ones of higher-energy states. Since those states often exhibit a finite net magnetization, one expects that an external magnetic field tends to stabilize higher-energy magnetic arrangements.

Already for moderate disorder, $\sigma_R/R_0 = 0.10$, the character of the energy distribution has changed significantly. An almost *symmetric,* Gaussian-like energy distribution is obtained around the average dipole energy $\overline{E}_{\mathrm{dip}}$, see Fig. 3.3(b). The number of metastable states has increased markedly, whereas each state is reached with a low frequency. This is in particular true for the ground state which is reached only few times, see the encircled region in Fig. 3.3(b). For an even stronger disorder this small peak in the frequency distribution disappears completely [126]. Hence, the identification of the ground state energy and its magnetic configuration seems to be quite difficult for strongly inhomogeneous particle arrangements, which is typical for spin glass systems or random magnets

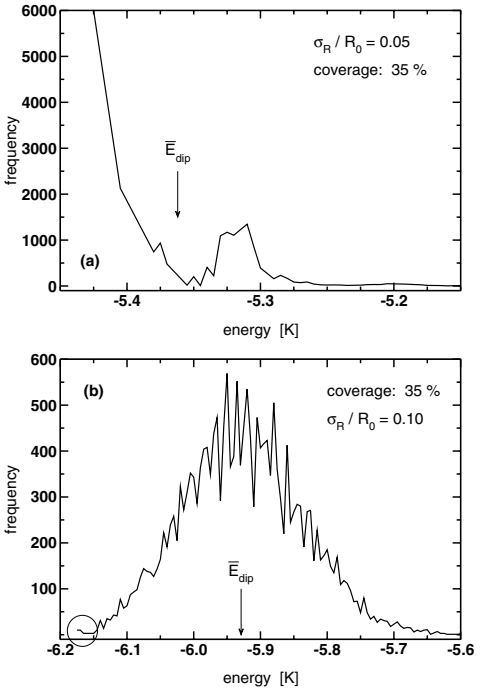

Fig. 3.3: Energy distribution of local energy minima for disturbed square particle arrays using two different positional standard deviations (a) $\sigma_R/R_0 = 0.05$, and (b) $\sigma_R/R_0 = 0.10$. The numbers of trials yielding relaxed states with energies falling into energy intervals of width $\Delta E = 5 \cdot 10^{-3}$ K are counted. Parameters appropriate to Fe are used. The particle coverage amounts to $C = 35$ %. The average dipole energy is indicated by $\overline{E}_{\rm dip}$.

[45][46]. Since the total number of metastable states increases strongly with increasing disorder, the corresponding energy basins shrink drastically.

3.3.4. Average magnetic dipole energy

From Fig. 3.3 one observes that the average dipole energy $\underline{E}_{\rm dip}$ per particle decreases with increasing positional standard deviation σ_R, thus we will determine $\underline{E}_{\rm dip}(\sigma_R, C)$ as function of σ_R and for different particle coverages C. In order to account for the large number of local energy minima occurring for particle arrangements with structural inhomogeneities, we determine the average energy resulting from many different trials for the same particle array. In addition, we average $\underline{E}_{\rm dip}$ over 20 different realizations of the unit cell, using the same global variables (C, σ_R, etc.) which characterize the particle ensemble. For comparison, $\underline{E}_{\rm dip}$ is also calculated for the same spatial setup by assuming a ferromagnetic state [126].

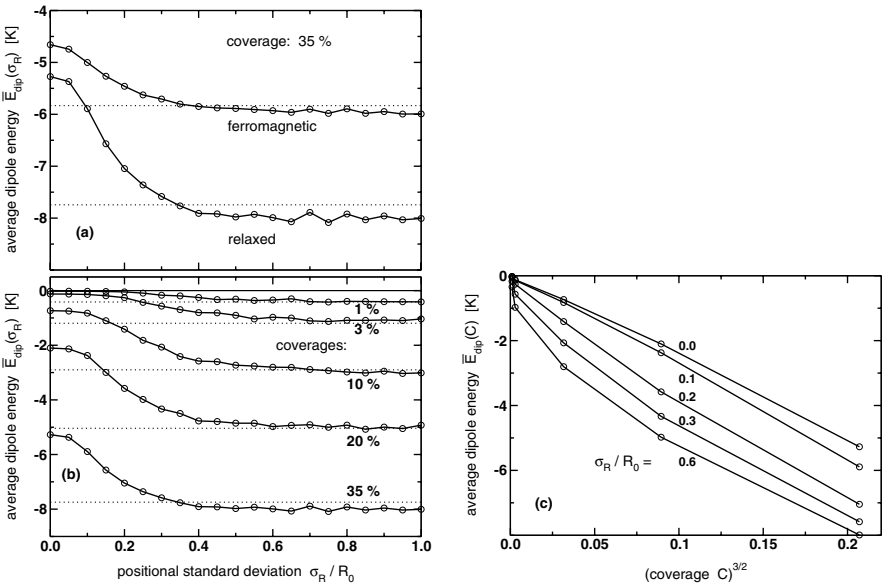

Fig. 3.4: (a) Average dipole energy $\overline{E}_{\rm dip}(\sigma_R)$ per particle of a two-dimensional array of magnetic particles as function of the positional standard deviation σ_R. R_0 is the average interparticle distance, the coverage amounts to $C = 35$ %. Displayed are $\overline{E}_{\rm dip}(\sigma_R)$ for states relaxed to local energy minima, and for ferromagnetic states. The dotted lines denote $\overline{E}_{\rm dip}$ for random particle setups with same particle sizes and coverages.
(b) $\overline{E}_{\rm dip}(\sigma_R, C)$ of relaxed magnetic arrangements as function of σ_R for different coverages C as indicated.
(c) $\overline{E}_{\rm dip}(\sigma_R, C)$ of relaxed magnetic arrangements as function of the particle coverage $C^{3/2}$ for different σ_R as indicated.

In Fig. 3.4(a), $\overline{E}_{\rm dip}(\sigma_R)$ is shown for a coverage $C = 35$ %. A square lattice corresponds to $\sigma_R = 0$. With increasing σ_R the average dipole energy *decreases* with *increasing disorder*. For $\sigma_R/R_0 \gtrsim 0.5$, $\overline{E}_{\rm dip}(\sigma_R)$ approaches a constant value which corresponds, within the numerical dispersion of the data, to the average dipole energy for a *random* particle array. The decrease of the average energy is caused by the nonlinear dependence of the dipole interaction with respect to the interparticle distance. Once disorder is introduced, the increase of $\overline{E}_{\rm dip}$ for enlarged distances r_{ij} between some particle pairs is more than counterbalanced by a corresponding decrease for reduced r_{ij} between other pairs of particles. A similar behavior is obtained for the ferromagnetic arrangement, albeit with a larger $\overline{E}_{\rm dip}(\sigma_R)$. On the other hand, since the dipole interaction is a bilinear function of the particle sizes N_i, the size dispersion effect averages out for particle sizes distributed around the mean $\overline{N}$, thus $\overline{E}_{\rm dip}(\sigma_N)$ stays approximately constant.

From Fig. 3.4(b) one observes that the overall dependence of $\overline{E}_{\rm dip}(\sigma_R)$ is not significantly affected by the particle coverage C [126]. An increase of the interparticle spacing R_0 decreases the magnitude of the average dipole energy, which should scale for a planar particle ensemble as $\overline{E}_{\rm dip} \quad R_0^{-3} \quad C^{3/2}$, see Section 3.1. The dependence of $\overline{E}_{\rm dip}$ on C is depicted in Fig. 3.4(c) for the relaxed solutions. Indeed, the expected behavior $\overline{E}_{\rm dip} \quad C^{3/2}$ is obtained for small positional disorder σ_R. However, for strong disorder and for small coverages a different dependence of $\overline{E}_{\rm dip}(\sigma_R)$ is observed. It seems that a strong noncollinearity of the magnetic configuration renders the simple scaling expectation no longer applicable. This interesting property is investigated in the next Subsection.

3.3.5. Scaling of the dipole energy

In Fig. 3.5 the absolute value of the average dipole energy per particle, $|\overline{E}_{\rm dip}(C)|$, as function of the particle coverage C for a fully random particle ensemble is shown for the relaxed and the ferromagnetic arrangements [146]. From the log-log-plot of $|\overline{E}_{\rm dip}(C)| \quad C^{\alpha}$ one observes that the exponent $\alpha = 3/2$, corresponding to the straightforward scaling of the dipole interaction, is approximately valid only for large coverages $C \gtrsim 20\,\%$. For smaller C one finds a smooth transition to a different dependence with clearly smaller effective exponents α^*. We obtain for the ferromagnetic arrangement $\alpha^*_{\rm fm} \simeq 1.0$ and, quite interestingly, for the relaxed solution an even smaller value $\alpha^*_{\rm r} \simeq 0.8 - 0.9$ in the considered coverage range.

This result can be qualitatively explained by the analysis presented in [146]. Consider two non-overlapping particles with radius r_0 in a D-dimensional space coupled by an interaction $E_n(r) \quad r^{-n}$. The mutual distance ranges between the lower bound $2\,r_0$ (hard core, excluded volume) and the upper bound $R_{\rm max}$, the latter is related to the particle concentration by $C \quad (r_0/R_{\rm max})^D$. For $n \geq D$ the *average* interaction energy $\overline{E}_n$ for $R_{\rm max} \to \infty$ is no longer proportional to $(R_{\rm max})^{-n}$. Instead, an effective exponent $n^* = D$ is obtained, thus one obtains $\overline{E}_n(C) \quad C^{\alpha^*}$ with $\alpha^* = 1$. The physical reason behind this behavior is that only the upper bound $R_{\rm max}$ scales with C, but not the lower bound $2\,r_0$. Hence, the average energy is given by the interaction $\quad (2\,r_0)^{-n}$ between neighboring particle pairs, times the probability to find such a particle pair which is proportional to C. In other words, as a consequence of the relatively strong distance dependence of the interaction for $n \geq D$, the average energy $\overline{E}_n(C)$ for a diluted particle ensemble is dominated by the short-distance contributions, and not by the energy corresponding to the average interparticle distance $R_{\rm max}$.

Thus, a $D = 2$ *random* ensemble of dipole-coupled magnetic particles ($n = 3$) exhibits a stronger than expected average dipole energy. In contrast, if one varies the interparticle distance in a *periodic* array the smallest distance between particles also scales with coverage, yielding therefore the straightforward scaling behavior with $\alpha = n/D$. The difference between α and α^* is significant for 1D and 2D systems, whereas for 3D systems one expects $\alpha \simeq \alpha^* \simeq 1$. Moreover, a difference is noted for the exponents $\alpha^*_{\rm r}$ and $\alpha^*_{\rm fm}$ obtained for the relaxed and ferromagnetic arrangements, see Fig. 3.5. This is an indication of the formation of particle chains with a correlated 'head-to-tail' alignment of the magne-

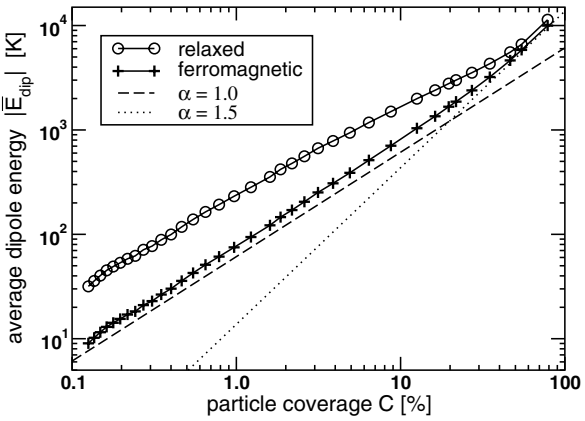

Fig. 3.5: Average dipole energy $|\overline{E}_{\rm dip}(C)|$ per particle of random 2D ensembles of magnetic particles as function of the particle coverage C. Results are given for the relaxed magnetic states (circles), and for the ferromagnetic ensemble magnetization (crosses). The straight lines correspond to $\overline{E}_{\rm dip}(C) \quad C^{\alpha}$, with $\alpha = 1$ (dashed) and $\alpha = 3/2$ (dotted).

tizations of closeby particles. Such a behavior is significant only for strongly interacting particle ensembles where the average interaction energy dominates the energy of single-particle anisotropies. In the opposite case of weak interactions a relaxation due to dipole coupling is negligible, thus resulting in $\alpha_{\rm r}^* \simeq \alpha_{\rm fm}^* \simeq 1.0$. In [146] we have shown that the unusual scaling behavior of $|\overline{E}_{\rm dip}(C)|$ is preserved also in presence of weak single-particle anisotropies. Hence, the determination of the scaling exponent α^* allows to distinguish between strongly and weakly interacting particle ensembles, since α^* is sensitive to the magnetic arrangement within the nanostructure. The scaling behavior should be analyzed also as function of temperature, since it is likely to be affected by thermally induced crossings of energy barriers between different magnetic arrangements. Experimentally, reduced values of $\alpha^* = 0.8 \pm 0.1$ have been observed in frozen high-density bulk (3D) ferrofluids [15]. Thus, it would be interesting to extend the present investigation also to 3D magnetic nanostructures.

4. DIPOLE COUPLED MAGNETIC PARTICLES LOCATED ON HOLLOW MICROSPHERES

In the preceding Section we have investigated magnetic properties of dipole-coupled non-overlapping particles arranged on an infinitely extended plane. As mentioned, for such an extended layered structure the dipole interaction plays a pronounced role due to its long-range character. In this Section we will study corresponding properties for a finite

layer exhibiting a pronounced curvature. Especially, the magnetic particles are assumed to be located on the surface of a large sphere. Such a body can be viewed as a 'hollow magnetic microsphere.' For example, the question arises whether such a body exhibits a finite magnetization, or resides in a demagnetized state. Furthermore, we will investigate also chains of these spheres. For comparison with measurements the calculation of the hysteresis loops of single spheres and of chains of spheres is of particular interest.

These investigations have been triggered by experimental investigations on corresponding systems [147][148]. Small magnetite (Fe_3O_4) particles consisting of a crystalline (ferrimagnetic) core (diameter ~ 5 nm) are placed onto the surface of a much larger polystyrene microsphere (diameter ~ 1 μm) solved in a liquid. To prevent agglomeration, to maintain a single-domain state, and to avoid oxidation of a metallic core, the magnetic particles are covered by an organic layer [4], which also suppresses the exchange interaction between neighboring particles. After preparation of these magnetic microspheres the liquid is cooled below its freezing point in presence or absence of a magnetic field. The spatial arrangement of the spheres is monitored with an optical microscope, and experiments like the measurement of the magnetic hysteresis loops are performed [147][148].

We note in general that, due to the interparticle dipole interaction, movable single-domain magnetic particles arrange themselves along long chains and even form spots of close-packed hexagonal 2D arrays [4][7]. As mentioned in Section 3.3.1, the ground state of an infinitely extended hexagonal layer is ferromagnetic [125][141]. An applied magnetic field enforces this magnetic state, in addition pre-formed chains and hexagonally ordered spots align parallel to the field direction.

If for the present experiments the liquid is frozen in a vanishing magnetic field, the microspheres are observed to be randomly spread in the specimen and do not exhibit ordered structures. Only in presence of an applied field the magnetic spheres start to form long chains parallel to the field [147][148]. Thus, there is a noticeable difference between movable single-domain magnetic particles and the hollow magnetic spheres suspended in a liquid. For the latter the dipole interaction between the microspheres appears not to be effective in a vanishing magnetic field, whereas becomes so in a finite one. Hence, the magnetic state of a microsphere can be controlled and switched by an external field. This behavior is explained by the fact that without applied field the spheres do not carry a finite magnetization. Rather, to avoid external stray fields the single-domain magnetic particles located on their surface arrange in such a way that the net magnetization vanishes. This demagnetization effect is well known for magnetized bodies (shape anisotropy) [149] where the resulting domain pattern is dominated by the strong exchange coupling. In the present case the exchange interaction is negligible, and the arrangement of the magnetic particles results from the dipole coupling between the particles and, if present, from the single-particle anisotropies. In this Section we will investigate such magnetic microspheres at vanishing temperature, taking into account the dipole interaction. In particular we determine the hysteresis loops of a single microsphere and for chains of spheres.

4.1. Structure of a microsphere

To investigate the magnetic properties of a microsphere with radius R_0 we place n magnetic particles on its surface. The organic cover layer is accounted for by distinguishing between the 'magnetic' radius r_m and the total radius r_0 of the particles, assuming a difference between r_m and r_0 of about 20 %. These particles are arranged either on 'latitude circles', or distributed all over the surface with approximately the same nearest neighbor distance. An accidental close neighborhood of some particles within a random distribution is avoided. The strength of the dipole interaction of a microsphere is varied by the 'packing density' $\xi = (n\, r_0/R_0)^2$ of the particles, i.e., the ratio between the area covered by all particles and the surface area of the sphere. In addition, a finite or an infinite number of such spheres can be arranged along a chain, maintaining a given distance $L \geq 2\, R_0$ between the centers of neighboring spheres.

The magnetic particles with given size and magnetic moment are subject to the interparticle dipole interaction and the external magnetic field, see Eq.(1). If not stated otherwise, spherical single-domain particles with magnetic radius $r_\mathrm{m} = 2.5$ Å carrying $N \simeq 4200$ Co atoms ($\mu_\mathrm{at} = 1.7\, \mu_\mathrm{B}$) are considered in this Section. Since the overall system is finite, the performance of the Ewald summation is not necessary in this case. For large surface densities or for small particle distances the dipole-quadrupole correction due to the finite particle size is applied [125][126]. As described in Section 3.2, starting from an initial magnetic arrangement the total magnetic energy is minimized by varying the set of both polar and azimutal angles $\{\theta_i, \phi_i\}$ of each particle i. The net magnetization $M(B)$ of a single microsphere and for chains of spheres will be monitored as function of the external magnetic field B. For the latter structure we consider an infinitely extended chain, i.e., a single sphere represents the unit cell of the chain. The external magnetic field will be directed either parallel to the chain axis or perpendicular to it.

4.2. Single microsphere

In Fig. 4.1 we show examples of the magnetic arrangements of particles located on the surface of a microsphere. The particles are either arranged along latitude circles, or scattered on the surface with equal packing density. For both types of arrangements a number of different (meta-)stable states is present. In accordance with randomly arranged magnetic particles on an extended plane, see Section 3, this number can in principle be very large if a large number of particles is considered. Common to all arrangements of magnetic particles on the microsphere surface is that for a vanishing applied field no single particle exhibits a notable radial component of its magnetization. The net magnetization of the sphere vanishes or is very small, since states with a finite magnetization usually have a larger magnetic energy. For the particles arranged along latitude circles their magnetizations are often arranged parallel to these circles, with an antiparallel orientation for neighboring rows of particles, reminiscent to a columnar state [139], compare Figs. 3.1 and 4.1(a). However, we have never observed such an ordered structure all over the sphere. Rather, vortex-like structural arrangements of magnetic particles are always present. Moreover,

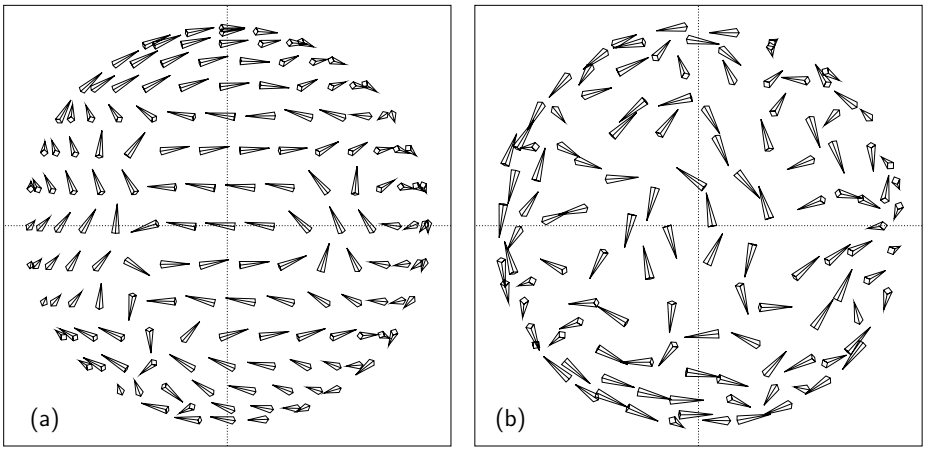

Fig. 4.1: Examples of magnetic arrangements of particles located on the surface of a hollow microsphere. The particles are (a) arranged along latitude circles and (b) scattered with equal density. The number of particles is (a) $n = 320$ and (b) $n = 250$. Only the particle magnetic directions of the upper hemisphere are shown.

simple scaling relations for the dipole energy per particle can be drawn as functions of the packing density ξ, the radius R_0 of the microsphere, and the number n of particles. Thus, calculated results for small systems can be compared with experiments which have been performed for much larger microspheres [147][148].

Corresponding hysteresis loops $M(B)$ of these structures are shown in Fig. 4.2. A smaller remanent magnetization $M(B = 0)$ is observed, which is caused by the fact that, starting from an aligned state, the magnetization of the microsphere stucks in a metastable state which is separated from other states by energy barriers. Since the calculations have been performed at $T = 0$, these energy barriers cannot be crossed. Because $M(B = 0)$ is obtained to be smaller for the particles arranged along latitude circles than for the scattered particle arrangement, obviously the former structure allows for a magnetic relaxation almost to the ground state, see Fig. 4.2(a). Moreover, frequent discontinuous jumps between different magnetic states are observed. At such a jump the energy barrier between two states vanishes. These jumps usually become smaller if a larger number n of particles is considered, since in effect a considerable change of the magnetic arrangement during the transition between two states is observed only for a comparable small part of the ensemble. Similar hysteresis loops have been obtained also for layered particle ensembles [92]-[95].

The effect of the packing density ξ is presented in Fig. 4.2(b) for a scattered particle arrangement. As expected, if ξ is reduced, or if the average particle distance increases, the magnitude of the dipole energy decreases and magnetic saturation of the microsphere by an applied field is facilitated.

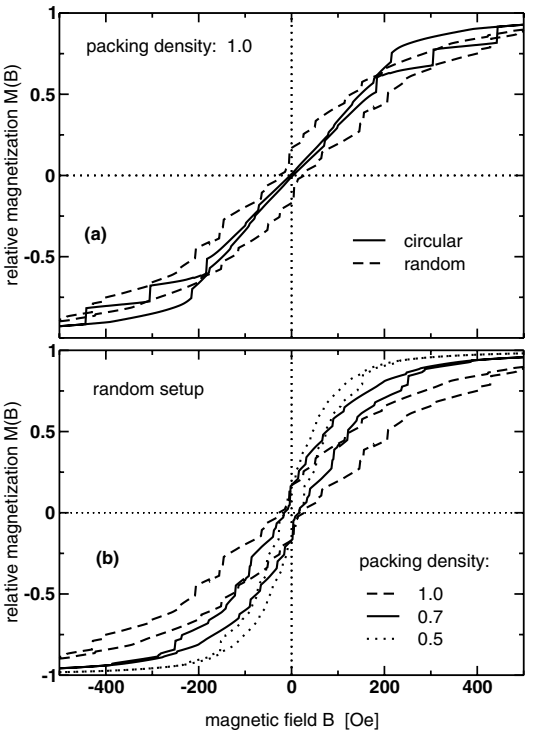

Fig. 4.2: Hysteresis loops $M(B)$ of a single microsphere as function of the applied magnetic field B. (a): The particles are arranged either along latitude circles ('circular') or scattered with equal density ('random') on the surface of the sphere. In (b) different packing densities are considered.

In contrast to a sphere, a net remanent magnetization is expected if the magnetic particles are located on the surface of a prolate ellipsoid. In this case the magnetization will be directed along its long axis, since a prolate ellipsoid approaches a long magnetized rod for which the dipole coupling favors a magnetization parallel to the rod axis [149]. On the other hand, for oblate ellipsoids a finite magnetization is not expected, since such a system resembles a magnetized disk. Here the magnetic direction of each particle will be directed in the plane of the disk, and will assume an in-plane demagnetized state to avoid stray fields protruding the edges of the disk [65]-[69][71]. Moreover, for comparison with measurements [147][148] the actual arrangement of the magnetic particles has to be considered. For instance, surface layers with a finite thickness should be considered, as well as microspheres with multilayered arrangements of the magnetic particles on their surfaces.

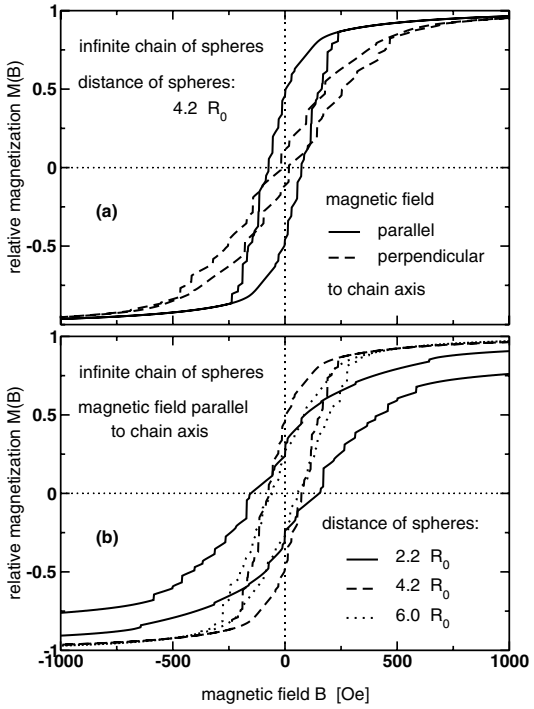

Fig. 4.3: Hysteresis loops $M(B)$ of an infinite chain of spheres as function of the applied magnetic field B. (a): $M(B)$ for B aligned parallel and perpendicular to the chain axis. (b): $M(B)$ for a parallel field and for different distances between centers of neighboring spheres, in units of their radius R_0.

4.3. Chains of spheres

Hysteresis loops of infinitely extended chains of microspheres are shown in Fig. 4.3. Saturation of the chain magnetization is easier if the field is directed parallel to the chain axis, and a much larger remanent magnetization $M(B = 0)$ is observed than for a perpendicular field, see Fig. 4.3(a). This behavior is in accordance with the shape anisotropy of a long magnetized rod [149], and also agrees with measurements on comparable systems [147][148]. As long as a net magnetization is induced in a sphere the dipole interaction between the spheres becomes effective, favoring a magnetization along the chain axis and supports thus a longitudinal field. The hysteresis loop of a single sphere is located in between the ones of a parallel and a perpendicularly directed field.

The enhancement of the magnetization is the stronger the closer the spheres are arranged, and the stronger the dipole interaction between the spheres. However, for almost

overlapping spheres this enhancement effect is no longer present, since the saturation of the chain magnetization is impeded and the opening of the hysteresis loop becomes more pronounced, see Fig. 4.3(b). Obviously, this behavior is caused by the finite extension of the spheres and the anisotropic nature of the dipole interaction. As outlined in Appendix A, two spins favor a parallel magnetic alignment if the angle between magnetization and the vector connecting the spin pair is smaller than the magic angle $\phi_{\mathrm{m}} = 54.7°$. An antiparallel alignment is favored for larger angles. A simple estimate for neighboring spheres shows that an antiparallel alignment between particles starts to become favorable for distances $L \leq \sqrt{2}\, R_0$, i.e., for already overlapping microspheres. For an exact analysis the actual arrangement of the particles on the surfaces of the spheres has to be taken into account.

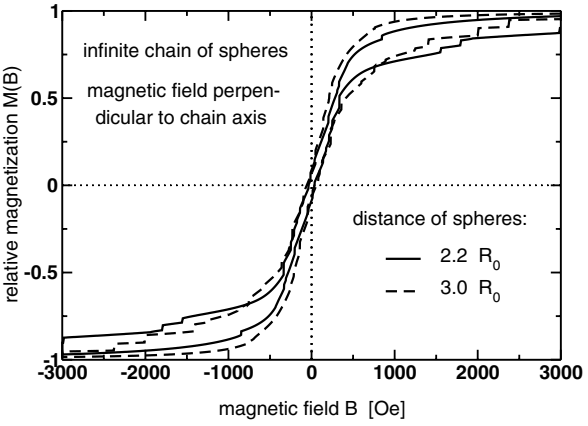

Fig. 4.4: Same as Fig.4.3(b) for a perpendicular magnetic field.

In the case of a perpendicular (transversal) field a particular behavior of the hysteresis loop is observed. For small field strengths the chain magnetization varies almost linearly. The opening of the hysteresis loop is small, whereas becomes markedly larger at intermediate field strengths. The field loop closes only for comparably strong magnetic fields, see Fig. 4.4. This behavior is more pronounced for smaller distances L between the spheres. The reason is that the dipole interaction in particular between different microspheres impedes the full magnetic saturation for an increasing field. Even for quite strong fields several particle pairs reside still in an almost antiparallel magnetic configuration. On the other hand, once saturated these antiparallel magnetized pairs are no longer present, and the chain magnetization follows the expected behavior by continuously approaching an almost demagnetized state with decreasing strength of the applied magnetic field.

The presented results have been obtained for an infinitely extended chain of spheres, where a single sphere represents the unit cell. The question arises whether also a finite chain with a small number of microspheres exhibits a finite self-polarization, dependent

on the particle density, the distance between spheres, etc. Such a self-polarization occurs if the state with a finite chain magnetization is the ground state also in absence of an applied field, in contrast to the ground state of a single sphere which exhibits a vanishing magnetization.

5. GROWTH OF THIN MAGNETIC FILMS

In this Section we turn to another nanostructured system, namely the investigation of the magnetic properties of growing ultrathin ferromagnetic films in the early states of growth [34]-[43]. Here the coverage ranges from individual magnetic particles or islands to a smooth film with filled layers. It is to be emphasized that during structural growth the magnetic system is far from equilibrium. Moreover, the equilibrium state to which the magnetic state is relaxing changes constantly. Experimentally, it is observed that many magnetic properties depend sensitively on the preparation conditions of such ultrathin films, indicating the nonequilibrium behavior of these systems. Above the structural percolation threshold Θ_P the Curie temperature T_C is dominated by the strong exchange interaction and amounts to several 100 K for, e.g., Fe and Co films [34]. In contrast, below Θ_P an exchange-induced long-range magnetic order is not expected. However, for a Co/Cu(001) thin film a remanent magnetization has been observed at comparable high temperatures also in this coverage range [40]. This temperature changes strongly near Θ_P ('T_C-jump'). In this Section we investigate whether the observed magnetization can be caused by the dipole coupling in this nanostructured system, or whether non-equilibrium behavior is decisive. A simple estimate is presented in Appendix A.

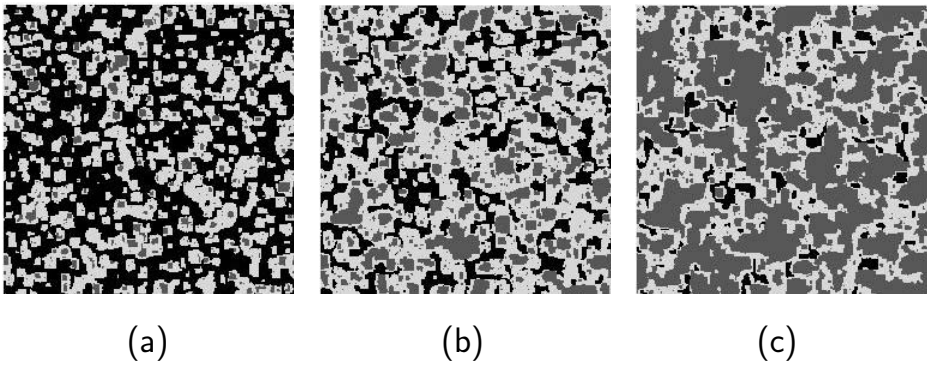

Fig. 5.1: Snapshots of the atomic structure of a growing thin film. The unit cell has 300×300 lattice constants and contains 450 islands. Three different coverages are depicted: (a) $\Theta = 0.5$ ML, (b) $\Theta = 1.0$ ML, and (c) $\Theta = 1.5$ ML. Black refers to the uncovered substrate, light gray to the first and dark gray to the second layer of magnetic atoms.

To our knowledge the only consistent theoretical analyses for the magnetic behavior of an ultrathin film during growth within a single model have been performed in [43][150][151]. Here the film thickness ranges from single atoms and islands to a smooth film, demanding thus for an appropriate consideration of the structural disorder. A newly developed cluster Monte Carlo method including coherent rotations of neighboring magnetic islands is presented, see Appendix B and [30][152]. This method allows for an efficient calculation of the relaxational behavior and the equilibrium magnetization, and enables an appropriate analysis of the influence of the anisotropy and dipole coupling besides the dominating exchange interaction. Note that conventional single-spin-flip algorithms [153] yield an extremely slow and unrealistic relaxation towards equilibrium in particular close to the percolation threshold with partly coagulated islands.

The remanent magnetization and the magnetic ordering temperature are determined as function of coverage, time, and temperature. A growth mode is applied which yields realistic atomic structures ranging from single atoms to extended islands within μm-range. The equilibrium and non-equilibrium properties at finite temperatures are considered by a kinetic Monte Carlo procedure [154][155].

5.1. Eden growth model and magnetic quantities

To avoid the time consuming determination of atomic diffusion, we apply a Monte Carlo method to simulate the molecular beam epitaxial (MBE) growth of a magnetic ultrathin film on a nonmagnetic substrate using a simple solid-on-solid growth model [150][151]. Within this so-called Eden model [156] each atom is randomly attached to already existing islands, and stays immobile afterwards. To take into account different growth modes we assume furthermore that the adatoms are placed on lattice sites i in layer z with varying probabilities

$$p(q_i, z) \quad \exp\left(-A(z)\sqrt{q_i}\right) . \tag{2}$$

The square-root dependence on the local coordination numbers q_i has been obtained to be approximately valid for metal surfaces [157]. By using layer dependent binding parameters $A(z)$ we are able to simulate with simple means different growth modes such as an island-type growth mode (3D islands) or a layer-by-layer growth mode, for example. Also various surface faces and island densities can be considered in accordance with experiments. This modified Eden growth model is valid for a fast surface diffusion, accompanied by a moderate step diffusion for which the mobility of the atoms is large enough to probe the different atomic positions of the island edges. A large number of nonequivalent sites ($\sim 10^6$ atoms) can be considered. During the growth all islands maintain their individuality. The assumption of individual magnetic islands with varying interactions is a good approximation as long as the system is laterally nanostructured. Snapshots of the resulting atomic structures are shown in Fig. 5.1.

For the obtained atomic structures a micromagnetic model for the total (free) energy of a system of interacting magnetic islands is applied, considering a single-island uniaxial anisotropy, the dipole interaction between the islands, and the interisland exchange for

overlapping islands, see Eq.(1) [43][150][151]. Due to the anisotropy we allow for only two directions for each island moment. Thus, our system refers to a *modified Ising model*, for which during magnetization reversal a possible anisotropy energy barrier is taken into account, hence allowing the consideration of magnetization dynamics. Moreover, an additional internal magnetic order of each island can be accounted for by a mean field estimate [43][100][150][151].

The remanent magnetization $M_{\rm rem}(\Theta, T, t)$ is determined as function of the Monte Carlo (MC) time t in units of MC steps (MCS). A cluster MC method is applied, which is described into greater detail in Appendix B and in [151]. The simulation starts from a completely aligned island spin state, i.e., the magnetic system is saturated by an external magnetic field, and $M_{\rm rem}(\Theta, T, t)$ is determined after removal of the field [40][158]. In addition, we calculate the equilibrium magnetization $M_{\rm eq}(\Theta, T)$ after the system has become equilibrated ($t \to \infty$). $M_{\rm rem}(\Theta, T, t)$ and $M_{\rm eq}(\Theta, T)$ are averaged over at least 20 different structural runs. Since the finite-sized unit cell undergoes eventually total magnetic reversals during MC probing, accidental cancellation of $M_{\rm rem}$ and $M_{\rm eq}$ during structural and temporal averaging may occur. To avoid the effect of total reversals we use in this study merely the *absolute values* $|M_{\rm rem}|$ and $|M_{\rm eq}|$.

In the present calculations we assume a 500×500 atomic and magnetic unit cell ($2.5 \cdot 10^5$ sites) on a (001) lattice with periodic boundary conditions. We choose as an example the bilayer growth mode of the first two atomic layers as observed for the Co/Cu(001) thin film system [36][43]. In accordance with experiment the island density is put equal to 0.005 per lattice site, corresponding to 1250 islands in the unit cell. A percolation coverage of about $\Theta_{\rm P} \approx 0.9$ ML is obtained. For the choice of the interaction parameters we refer to [151]. We point out that systems of dipole coupled single magnetic islands at low coverages as well as connected ferromagnetic films at high coverages are described within the same model.

5.2. Remanent magnetization

Snapshots of the resulting magnetic structure during thin film growth are shown in Fig. 5.2. At low coverages the average magnetic domain size resembles the average island size. With increasing film coverage the islands start to coagulate and form island clusters, allowing for the formation of large domains. A thorough discussion of the magnetic domain pattern and results for the average domain size and -roughness during thin film growth is presented in [150].

The effect of the cluster-spin-flip MC method on the simulation of the remanent magnetization is investigated into greater detail in [151]. We merely note that the main improvement of this method is obtained for coverages $\Theta \lesssim \Theta_{\rm P}$, characterized by a considerable amount of island cluster formation, and which is very difficult to be studied analytically. Hence, we are able to investigate appropriately the effect of the anisotropy and dipole interaction, which are usually much weaker than the exchange.

In Fig. 5.3(a) the combined effect of the dipole and the exchange interaction on the remanent magnetization $|M_{\rm rem}(\Theta, T, t)|$ is studied as function of MC time t for different

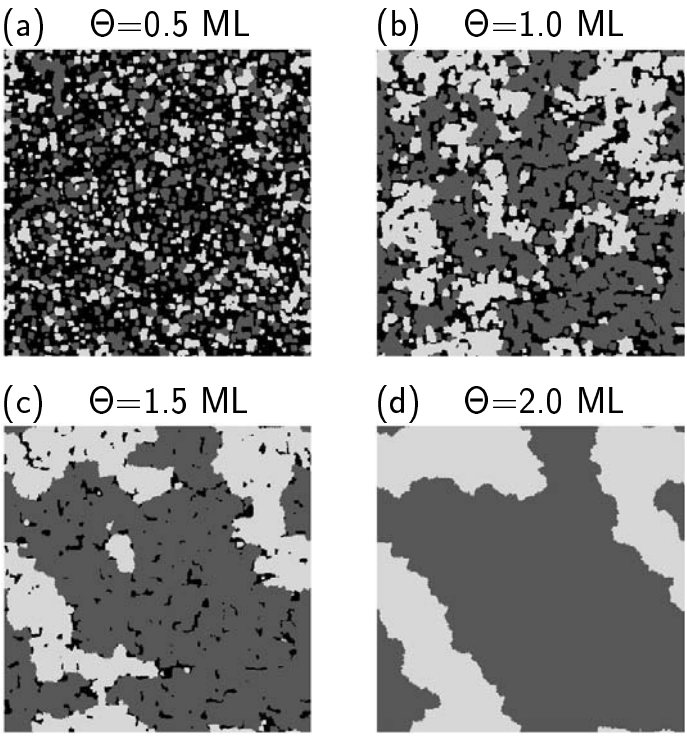

Fig. 5.2: Snapshots of magnetic domain structures for different coverages: (a) Θ = 0.5 ML, (b) Θ = 1.0 ML, (c) Θ = 1.5 ML, and (d) Θ = 2.0 ML. The unit cell has 500×500 lattice constants and contains 1250 islands. The two gray scales refer to the two magnetic directions, the uncovered substrate is black.

temperatures T, assuming a coverage $\Theta = 0.8\,\mathrm{ML} < \Theta_\mathrm{P}$. The dipole coupling leads to an additional magnetic order, since $|M_\mathrm{rem}| > |M^0_\mathrm{rem}|$, where for $|M^0_\mathrm{rem}|$ the dipole interaction is neglected. In Fig. 5.3(b) the equilibrium magnetization $|M_\mathrm{eq}(\Theta, T)|$ is shown as function of T and coverage Θ. Clearly, a long-range magnetic order resulting from the dipole interaction is observed. The ordering effect is the larger the larger the coverage, since with an increasing Θ the average island cluster size and thus the average dipole coupling energy increases. However, the corresponding ordering temperatures even for the largest investigated coverage are quite small, yielding $T_\mathrm{C} \approx 6$ K for $\Theta = 0.8$ ML. We note that for a stronger dipole interaction, as present for, e.g., 3D magnetic islands, the corresponding T_C will become markedly larger.

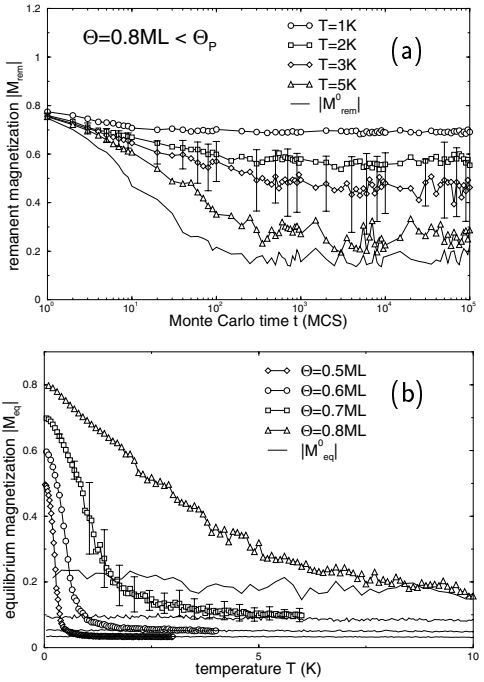

Fig. 5.3: Long-range magnetic ordering due to dipole interaction for coverages Θ below the percolation coverage $\Theta_{\rm P}$. Only dipole and exchange interactions are included. The quantities $|M^0_{\rm rem}|$ and $|M^0_{\rm eq}|$ are calculated without the dipole interaction. (a) Remanent magnetization $|M_{\rm rem}|$ as function of MC time t for $\Theta = 0.8$ ML $< \Theta_{\rm P}$ and different temperatures T. (b) Equilibrium magnetization $|M_{\rm eq}|$ as function of temperature T for different coverages $\Theta < \Theta_{\rm P}$.

The existence of a long-range magnetic ordering due to the dipole interaction has been calculated previously for *periodic* 2D lattices [132]-[135]. Similar as in Section 3, the magnetic state of such a nanostructured ultrathin film is expected to be strongly noncollinear and spin glass-like. We emphasize that also within an *irregular* island system below the percolation threshold the dipole interaction leads to a magnetic ordering. Corresponding magnetic ordering effects have also been obtained for disordered high-density 3D and 2D ferrofluids [26][159]-[162].

5.3. Magnetic relaxation

In Fig. 5.4 results for the nonequilibrium behavior of the remanent magnetization are presented. For simplicitely the dipole coupling is neglected here. The magnetic relax-

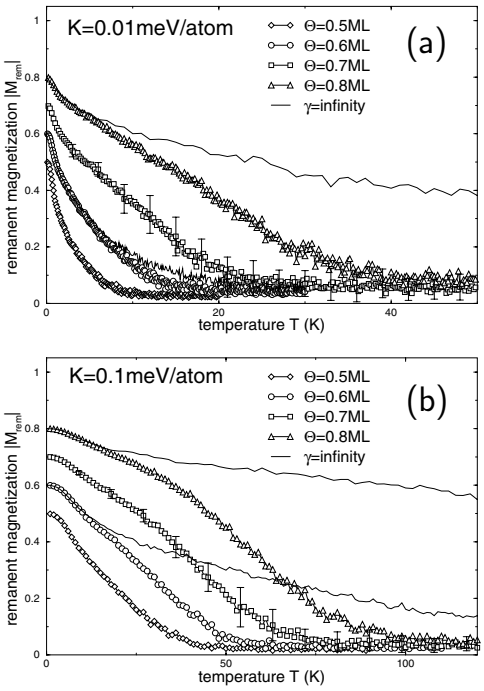

Fig. 5.4: Remanent magnetization $|M_{\rm rem}|$ after relaxing the magnetic structure for the time $t = 1000$ MCS as function of temperature for anisotropies (a) $K = 0.01$ meV/atom and (b) $K = 0.1$ meV/atom. Coverages Θ below the percolation coverage $\Theta_{\rm P}$ are considered. The full lines are calculated with an infinite exchange interaction γ between the islands [151].

ation is stopped after a finite MC time $t = 1000$ MCS. $|M_{\rm rem}(\Theta, T, t)|$ is monitored as function of temperature for different coverages $\Theta < \Theta_{\rm P}$, using the anisotropy parameters $k_{\rm at} \equiv K = 0.01$ meV/atom and 0.1 meV/atom. With increasing temperature the magnetization approaches the equilibrium value $|M^0_{\rm eq}|$, which is reached within the considered time range above the *blocking temperature* $T_{\rm b}(\Theta, K)$. Additional consideration of the dipole interaction leads to a slower magnetic relaxation and to a somewhat enhanced blocking temperature, in accordance with measurements [19][33]. This effect is visible in the whole temperature range up to $T_{\rm b}$, and is not limited to those small temperatures where the dipole coupling induces a magnetic ordering [151].

We emphasize that for such a magnetic nanostructure an increase of the anisotropy by a factor of 10 does not necessarily lead to an increase of $T_{\rm b}(\Theta, K)$ by the same factor as obtained from the Stoner-Wohlfarth model [118]. This is caused by *internal cluster excitations*, i.e., by creation and motion of domain walls inside the island clusters. As

is outlined in greater detail in [151], for low temperatures the magnetic relaxation happens mainly via coherent rotation, whereas for larger temperatures, as well as for larger coverages and anisotropies, both relaxation processes are present. Which process is most effective is determined by its energy barrier ΔE. We found that a particular relaxation process becomes effective above a temperature amounting to 5 – 10 % of ΔE [151]. The process of the internal cluster excitation depends in a complicated way on the actual nanostructure.

For coverages above the percolation threshold Θ_P the exchange coupling causes a fast magnetic relaxation and a strong long-range magnetic order. The corresponding blocking temperatures $T_b(\Theta)$ are still markedly larger than the ordering temperatures $T_C(\Theta)$ in the coverage range $\Theta \gtrsim \Theta_P$, where the structure of the percolated thin film is still very irregular, and nonequilibrium effects due to anisotropy barriers are pronounced. For even larger coverages T_b and T_C are virtually the same.

5.4. Ordering and blocking temperatures

In Fig. 5.5 the main results of this Section are summarized. The (nonequilibrium) blocking temperature $T_b(\Theta, K)$ and the (equilibrium) ordering temperature $T_C(\Theta)$ are presented as functions of coverage Θ in the whole investigated growth range. For a better visualization a logarithmic temperature scale is applied. T_b is determined for two different anisotropies $K = 0.01$ and 0.1 meV/atom, and $t = 1000$ MCS. Below the percolation coverage Θ_P the dipole interaction induces small ordering temperatures T_C of the order of 1 – 10 K for the assumed model parameters. Due to the coagulation of islands with increasing coverage the exchange interaction becomes increasingly important. This property results in a strong increase of T_C in particular close to Θ_P, in accordance with observations on Co/Cu(001) ultrathin films [40] and with a simplified mean-field calculation [43]. Also shown in Fig. 5.5 is the dipole-induced ordering temperature if the exchange coupling between islands is neglected. Evidently, a distinct variation of T_C near Θ_P is not obtained in this case.

The pronounced nonequilibrium behavior for coverages below Θ_P is caused by the slow magnetic relaxation of the corresponding irregular atomic structure. Consequently, blocking temperatures $T_b(\Theta)$ are obtained which are an order of magnitude larger than $T_C(\Theta)$ resulting from the dipole interaction. Additional simulations with a larger percolation threshold and correspondingly larger island sizes near Θ_P yield enhanced blocking and ordering temperatures, as expected. However, $T_b(\Theta)$ is obtained to be always markedly larger than $T_C(\Theta)$ for $\Theta < \Theta_P$. Thus, we conclude that the magnetization observed in this coverage range [40][43] is most probably caused by strong nonequilibrium effects. Our results show that both single-particle properties and interactions between the particles, as well as the equilibrium and the nonequilibrium behavior, have to be considered on equal footing for interacting ensembles of magnetic particles. This is in particular true if a considerable amount of disorder is present in the nanostructure, as is the case near the percolation threshold of a growing ultrathin film.

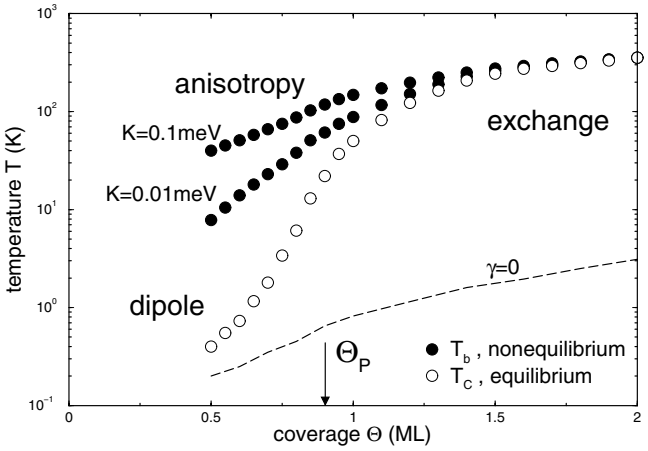

Fig. 5.5: Semi-logarithmic plot of the magnetic ordering temperature T_{C} and the blocking temperature T_{b} as functions of the film coverage Θ. The entire investigated coverage range below and above the percolation coverage Θ_{P} is shown. The different magnetic interactions dominate in different coverage and temperature ranges as indicated. The dashed curve refers to the dipole-coupling induced ordering temperature neglecting the exchange interaction γ between the islands.

Several possible improvements of our micromagnetic model are pointed out. In this study we have used Ising-like spins. By applying continuously varying vector spins $\mathbf{S}_i$ a noncollinear magnetic arrangement can be analysed [43], allowing also to determine the effects of an external magnetic field on these strongly inhomogeneous films. The movement of magnetic domain walls can be investigated, in particular for strongly connected island systems. Furthermore, various magnetic nanostructures like chains and stripes [38][121][163][164] can be studied easily by a proper variation of the parameters of the Eden-type growth model. Anisotropies with, e.g., a four-fold in-plane symmetry could be considered [124]. Finally, the relaxation laws and -times of the remanent magnetization for such thin film systems can be determined [158].

6. CONCLUSION AND OUTLOOK

In this Review we have studied several different interacting magnetic nanostructures. We have shown that these systems exhibit a very rich and promising field of research. An appropriate consideration of the interactions is extremely important, since many quantities like the magnetic states and the magnetization dynamics are dominated by collective magnetic properties. A number of important effects of the interparticle interactions are

still unsolved. This is in particular true for the temporal development and the memory effects of densely packed nanostructures. The results presented in detail in this Review will be very valuable for investigating these and many other problems of such systems. By further experimental and theoretical development a variety of new results is expected to be reported in near future. Especially 2D systems are of great interest, which have the enormous advantage that their structural properties can be controlled, monitored, and manipulated in a much larger degree than for 3D ferrofluids, thus facilitating comparison with simulations.

One of the fundamental problems is the detailed investigation of the spin glass behavior of these nanostructures. A large number of results have been obtained for simplified systems in the last decades [45]-[47]. Corresponding studies for real nanostructures are aggravated by the presence of Heisenberg (three-component) magnetic moments and by the long-range magnetic couplings like the indirect (RKKY) exchange interaction [127]-[130] and of course the dipole interaction. Furthermore, a certain degree of structural disorder including overlapping particles, and the effect of single-particle anisotropies have to be taken into account on equal footing. To identify and investigate properties reminiscent to a spin glass additional quantities such as the nonlinear susceptibility [58]-[62] and the time-dependent correlation functions [14][45] have to be considered. Since the complicated nature of the systems seem to preclude simple analytical approaches, numerical simulations are unavoidable in order to achieve a detailed microscopic description. Of course, it will be very desirable and challenging to derive simple trends for the magnetic properties of these interacting particle ensembles.

It is well known that the kind of magnetic relaxation and the relaxation times in such magnetic nanostructures depend sensitively on various quantities like the degree of disorder, the kind of interactions, the temperature, etc. Usually empirical laws are applied for the quantitative description of the magnetic relaxation behavior [107][108]. Since the flip time of a magnetic nanoparticle is much longer than that of an atomic spin, correspondingly much shorter time ranges can be measured for the former. By varying the temperature magnetic memory effects have been monitored [24][106]. Sufficiently large temperature jumps should erase this intrinsic memory, i.e., the system appears unaffected by previous ageing ('rejuvenation'), as present in atomic spin glasses [25]. A satisfactory theoretical approach for these phenomena is missing. Evidently, the presence or absence of memory effects depends on the temperature, the packing density, the degree of disorder, and other quantities of the nanostructure. Note that for the considered systems the structural and magnetic states are often far from equilibrium, thus the common linear response theories are not appropriate for those cases [91]. Our future goal, driven by both fundamental and technological interest, will be the study of the relaxation laws and -times and their dependence on the microstructure of the underlying system.

Possible approaches for this goals are sketched as follows. For the investigation of the magnetic relaxation the energy barriers or the saddle points in the high-dimensional parameter space have to be determined [138]. These transition states have to be obtained in addition to the energy minima as described in Section 3. As mentioned, due to their large number the identification of transition states and the calculation of the 'optimal

paths' between them is a considerable challenge for an inhomogeneous system of interacting magnetic particle ensembles. The transition from one to another energy minimum happens collectively, i.e., the magnetization directions of all particles vary simultaneously. For instance, the 'optimal path' and the saddle point separating two energy minima have been determined by a path integral method in the complex, high-dimensional parameter space [82][167]. Another promising approach employs the eigenvalues and -vectors of the Hessian matrix, together with an iterative, 'minimax' procedure [168][169].

The mapping of the saddle points and adjacent minima onto an effective network allows in principle the calculation of the temporal development and the magnetic relaxation for such complex systems in a comparably simple manner. For example, this problem has been tackled previously with an 'activation-relaxation technique' for the investigation of atomic cluster structures [170], as well as for glassy materials and polymers [169][171][172]. For disordered magnetic nanostructures this method has been applied in [168]. In this context the question arises whether all saddle points and all possible transition paths have to be determined a priori, which seems to be feasible only for comparably small systems. Alternatively, a certain subset of transition states could be considered, leaving still the important problem of the correct choice of that subset.

We like to mention several other problems of current interest for magnetic nanostructures. Whereas in the present Review either ensembles of non-overlapping particles or, in the case of growing thin films, a 2D network of magnetic islands were discussed, also chain-like structures have been investigated ('magnetic nanowires') [30][38][94][114]. Since a one-dimensional magnetic system should not exhibit a long-range magnetic order [48], nevertheless a remanent magnetization was observed in such structures [13][173]. As for nanostructures, very long relaxation time can be present for such nanowires. In addition, an important problem is the formation of these magnetic structures in a liquid [27]-[29],[112]-[113]. The transition from a ring-like to a chain-like structure as function of the applied magnetic field has been tackled in [174][175], for example. Furthermore, the occurrence of magnetic domains in nanowires [123], their orientation [176], and their influence on electric transport properties [177] have been investigated. A particular problem is the variation of the viscosity in a ferrofluid as function of the applied magnetic field [178][179]. The study of magnetic nanowires and patterned 2D systems is still in an early state of research.

Another very active field of current research is the investigation of the exchange-bias effect. For reviews see, e.g., [180][181]. This phenomenon occurs in coupled ferromagnetic (FM) – antiferromagnetic (AFM) systems. If such a system is cooled in an applied magnetic field from above to below the Néel temperature of the AFM, the hysteresis loop is no longer symmetric but appears shifted or 'biased'. In addition a temporal development ('training') is observed. The occurrence of the exchange bias effect requires a certain amount of disorder at the interface between the FM and the AFM, thus represents a truly nanostructured magnetic system. However, the microscopic origin of this effect is still unknown.

Finally, we remark that under certain conditions the quantum nature of magnetic nanostructures becomes visible. Usually such influences are observed for small systems.

These quantum effects are not simple limited to the replacement of the classical Langevin function by a Brillouin function. Rather a number of unique quantum effects are observed, like tunneling processes and transport properties in magnetic quantum dots and molecular magnets, which offer a rich field of future research. One of the main problems is the investigation of the spin-based electronics (spintronics) in these systems, which has a tremendous technological impact [182][183]. For instance, the spin-dependent Coulomb blockade and the Kondo effect in quantum dots has been studied in [184]-[187]. Moreover, macroscopic quantum tunneling [188]-[190] and the photo-induced switching [191] of the magnetization in single molecules was observed. The investigation of quantum effects in such structures will be a very promising field of future research.

The authors like to thank Dr. R. Brinzanik, Berlin, and Dr. G. M. Pastor, Toulouse, for numerous fruitful discussions. Support from the Deutsche Forschungsgemeinschaft, SFB 290 (TP A1) is gratefully acknowledged. P.J.J. acknowledges support from the EU GROWTH project AMMARE (contract number G5RD-CT-2001-00478).

APPENDIX A: DIPOLE ENERGY AND BLOCKING TEMPERATURE

A finite magnetization, not necessarily a collinear one, usually originates from a collectively ordered state in thermal equilibrium. For an ensemble of isolated particles such a magnetic state requires the presence of long-range magnetic interactions. We consider here the magnetic dipole coupling between particles. The corresponding ordering temperature T_{C} should be comparable to the average dipole energy per particle at least within a simple mean-field model. However, this average energy is difficult to determine for an irregular system. Furthermore, for disordered systems the relaxation times are known to be notoriously long, thus the measured magnetization can stuck in a nonequilibrium state for considerable amounts of waiting times. In this Appendix we present simple estimates for these two processes.

Before presenting these estimates we briefly repeat the preferred magnetic state of a spin pair and the corresponding 'magic angle'. For a parallel magnetization the dipole energy is given by $E_{\mathrm{dip}} \sim 1 - 3\cos^2\phi$, where ϕ is the angle between the magnetization and the vector connecting the spin pair. Hence, the dipole coupling favors a parallel magnetization of the two spins, if ϕ is smaller than the magic angle $\phi_{\mathrm{m}} = \arccos(1/\sqrt{3}) = 54.7^\circ$ or larger than $180^\circ - \phi_{\mathrm{m}}$. For angles in between these limits the preferred magnetic arrangement is antiparallel. Consequently, by consideration of nearest-neigbors only it is immediately clear that for a square dipole-coupled layer the preferred magnetic state is antiparallel or columnar, since $\phi = 90^\circ$, see Section 3.3.1 [139]. Performing the respective consideration for a hexagonal layer one would expect also a columnar state, since $\phi =$

$60^\circ > \phi_{\rm m}$. However, taking into account also more distant lattice sites the magnetic ground state for this symmetry turns out to be parallel (ferromagnetic) [125][141]. For dipole-coupled (3D) b.c.c. and f.c.c. lattices the ground state is found to be ferromagnetic, and antiferromagnetic for a s.c. lattice [132][165].

For the estimate of the magnetic dipole energy a pair of neighboring single-domain (Stoner-Wohlfarth) particles [118] with distance L is considered. Each particle contains N atoms, thus carries a giant magnetic moment $M = N\,\mu_{\rm at}$, with $\mu_{\rm at}$ the spin per atom. The radius of a flat (2D) particle is estimated to be $R/a_0 \sim \sqrt{N}$, and the one of a spherical (3D) particle is $R/a_0 \sim \sqrt[3]{N}$, where a_0 is the atomic lattice constant. If $\mu_{\rm at}$ is given in units of the Bohr magneton $\mu_{\rm B}$ and a_0 in Å, the dipole energy in units of K reads $E_{\rm dip} = 0.623\ M^2/L^3$. Assume now that for a densely packed particle ensemble one has $L \simeq R$, this energy is approximately given by $E_{\rm dip} \sim (\mu_{\rm at}^2/a_0^3)\,R \sim \sqrt{N}$ for flat particles, and $E_{\rm dip} \sim (\mu_{\rm at}^2/a_0^3)\,R^3 \sim N$ for spherical ones. If the values for bulk Fe are used, i.e., $\mu_{\rm at} = 2.2\ \mu_B$ and $a_0 = 2.5$ Å, and the particle size is put equal to a typical number of atoms $N = 1000$, the dipole energy of this particle pair amounts to $E_{\rm dip} \sim 6$ K for flat and to $E_{\rm dip} \sim 200$ K for spherical particles. For bulk Co these values are reduced by the factor $(1.7/2.2)^2 \sim 0.6$. Hence, depending on the size and distance of the particle pair, binding energies ranging from low to ambient temperatures seem to be possible. These values represent upper limits for the dipole-induced magnetic ordering temperature. The correct ones for extended nanostructures will be markedly smaller, since due to the anisotropic nature of the dipole interaction a partly cancellation of the pair binding energies is always present.

Furthermore, the magnetic relaxation to the equilibrium state is impeded by single-particle anisotropies, resulting in nonequilibrium blocking effects. This superparamagnetic behavior causes a finite time-dependent magnetization below the blocking temperature $T_{\rm b}$. Applying the common Arrhenius-Néel approach [77][78], one obtains $k_{\rm B}\,T_{\rm b} = N\,K/\ln(\tau_{\rm m}\,\Gamma_0)$, where K is the uniaxial magnetic anisotropy per atom, $\Gamma_0 = 10^9$ sec^{-1} the attempt frequency, $k_{\rm B}$ the Boltzmann constant, and $\tau_{\rm m}$ the time of measurement. Using $N = 1000$, $\tau_{\rm m} = 100$ sec, and $K = 0.01$ meV/atom $= 0.1$ K/atom, which is the measured value for the in-plane anisotropy of Co thin films [166], one obtains for the blocking temperature $T_{\rm b} \approx 4$ K.

These two rough estimates for the (equilibrium) ordering temperature and the (nonequilibrium) blocking temperature disagree with recent experiments on Co/Cu(001) ultrathin films [40][43]. Below the percolation coverage $\Theta_{\rm P}$ a comparably strong remanent magnetization has been observed up to temperatures as large as ~ 150 K. It is not immediately clear which of the two above mentioned mechanisms can cause such a strong remanence. Hence, improved calculations have to be performed which take better into account the inhomogeneous film structure characterized by varying particle or island sizes, -shapes, and -arrangements. In particular for coverages close to $\Theta_{\rm P}$ the island coagulation leads to a larger effective island size $N_{\rm eff}$ and thus to a larger average dipole energy. Correspondingly, also the blocking temperature will be larger than the single-island estimate. Thus, for a disordered film structure one may expect a remanent magnetization at much higher temperatures.

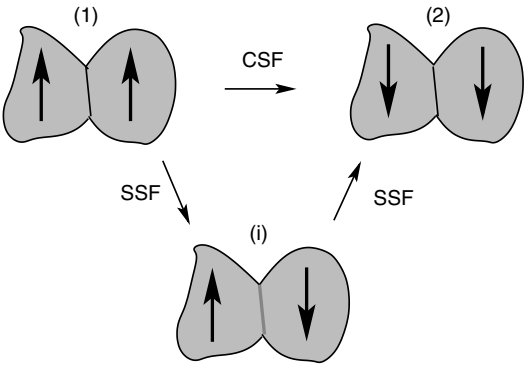

Fig. A1: Sketch of the magnetic reversal of two connected islands from state (1) to state (2). Subsequent rotations of the islands (single-spin-flips, SSF) inevitably cross the intermediate state (i) with a large exchange energy. State (i) is avoided by a simultaneous rotation of the island pair (cluster-spin-flip, CSF).

APPENDIX B: CLUSTER MONTE CARLO METHOD

The magnetic equilibrium and nonequilibrium properties as presented in Section 5 are calculated by performing kinetic Monte Carlo (MC) simulations [154][155]. It is emphasized that especially close to the percolation coverage Θ_P most of the magnetic islands are connected to neighboring islands and form large but still finite clusters. Application of the common single-spin-flip (SSF) MC algorithm [153] for such irregular atomic structures run into a severe problem, which is depicted in Fig. A1. Assign a 'super' spin to every island magnetic moment and consider the magnetic rotation $\uparrow\uparrow \rightharpoonup \downarrow\downarrow$ of an isolated island cluster consisting of two connected islands. Assuming Ising-like magnetic moments, inevitably the single-spin-flip method applies a *subsequent* rotation of the single island spins through the intermediate state $\uparrow\downarrow$. Such a process is very unlikely due to the large increase of exchange energy of this intermediate state. Hence, a conventional single-spin-flip algorithm considering subsequent flips only will yield an extremely slow and unrealistic relaxation towards thermodynamic equilibrium for such a structure [151]. Thus, a rotation of the island pair is very unlikely, and the dependence of the magnetic relaxation on dipole interaction and anisotropy is strongly underestimated. Obviously, a proper treatment of the magnetic relaxation requires the inclusion of a *coherent* or *simultaneous* rotation of the island pair. This is performed within a cluster-spin-flip (CSF) algorithm, which takes into account such simultaneous spin rotations of connected islands [30][152]. The CSF algorithm can be applied also to other inhomogeneous spin systems such as diluted magnets and spin glasses, and is described as follows.

In a first step a cluster $\mathcal{C}_\nu$ consisting of ν connected islands is constructed by the following scheme: (a) Choose randomly a single island i, representing the first (smallest) island cluster $\mathcal{C}_1 = \{i\}$. (b) Add a random second island j which is connected to island

i, forming the second island cluster $\mathcal{C}_2 = \{i, j\}$. (c) Construct subsequently larger island clusters $\mathcal{C}_\nu$ by adding a randomly chosen island to the preceeding cluster $\mathcal{C}_{\nu-1}$, provided that this island is connected to at least one of the $\nu - 1$ islands of $\mathcal{C}_{\nu-1}$. (d) Continue this construction procedure till either no additional adjacent islands are present or if a maximum allowed number $\lambda_{\max}$ of islands in the cluster is reached. From this procedure we obtain a set of $\lambda \leq \lambda_{\max}$ island clusters $\{\mathcal{C}_1, \ldots, \mathcal{C}_\lambda\}$. (e) Out of this set choose one cluster $\mathcal{C}_\nu$ with weight ω_ν for probing ($\sum_\nu \omega_\nu = 1$). A Monte Carlo step (MCS) is defined by the usual condition that the magnetic moments μ_i of all n islands in the system are probed. Employing a cluster $\mathcal{C}_\nu$ containing ν islands considers the portion ν/n of the system in a single update. To ensure that probing large clusters does not dominate the relaxation process, we assign the weight $\omega_\nu = 1/\nu$ for choosing $\mathcal{C}_\nu$ out of the set $\{\mathcal{C}_1, \ldots, \mathcal{C}_\lambda\}$. This definition implies that within a single MCS no additional relaxation channels are opened by the consideration of island cluster flips. We emphasize that not only the largest possible island cluster $\mathcal{C}_\lambda$ are probed for flipping, rather all island clusters out of the corresponding set are considered. The island moments within an island cluster need not to be parallel.

In the second step all ν island spins of the chosen cluster $\mathcal{C}_\nu$ are probed for a coherent flip. The corresponding flip rate Γ_ν will be calculated in the usual way as if these ν connected islands form a single large island [150]. The Ising-like states of $\mathcal{C}_\nu$ can refer to an energy maximum and minimum, which is treated with the usual Metropolis-type rate [153]. Alternatively, these states represent energy minima which are separated by an energy barrier ΔE_ν. In this case the flip rates for the forward and backward transitions are given by the common Arrhenius-Néel approach $\Gamma_\nu = \Gamma_0 \exp(\Delta E_\nu / k_B T)$ [77][78]. The use of a constant prefactor Γ_0, which determines the time unit of the magnetic relaxation in kinetic MC simulations, is widely applied in literature and is justified in [78]-[80].

The described CSF algorithm satisfies the condition of detailed balance. This is guaranteed by the fact that the probabilities for construction and choice of the cluster $\mathcal{C}_\nu$ are the same for both flip directions, and by the used flip rates which already obey detailed balance. Ergodicity is maintained since any spin state can be reached due to the allowance of single spin flips.

References

[1] J. L. Dorman, D. Fiorani, and E. Tronc, Adv. Chem. Phys. 98 (1997) 283

[2] M. Respaud, J. M. Broto, H. Rakoto, A. R. Fert, L. Thomas, B. Barbara, M. Verelst, E. Snoeck, P. Lecante, A. Mosset, J. Osuna, T. Ould Ely, C. Amiens, and B. Chaudret, Phys. Rev. B 57 (1998) 2925

[3] T. Aign, P. Meyer, S. Lemerle, J. P. Jamet, J. Ferré, V. Mathet, C. Chappert, J. Gierak, C. Vieu, F. Rousseaux, H. Launois, and H. Bernas, Phys. Rev. Lett. 81 (1998) 5656

[4] M. Giersig and M. Hilgendorff, J. Phys. D 32 (1999) L111

[5] V. Russier, C. Petit, J. Legrand, and M. P. Pileni, Phys. Rev. B 62 (2000) 3910

[6] S. Padovani, I. Chado, F. Scheurer, and J. P. Bucher, Phys. Rev. B 59 (1999) 11887

[7] S. Sun and C. B. Murray, J. Appl. Phys. 85 (1999) 4325

[8] S. Sun, C. B. Murray, D. Weller, L. Folks, and A. Moser, Science 287 (2000) 1989

[9] D. Babonneau, J. Briatico, F. Petroff, T. Cabioc'h, and A. Naudon, J. Appl. Phys. 87 (2000) 3432

[10] V. F. Puntes, K. M. Krishnan, and A. P. Alivisatos, Science 291 (2001) 2115

[11] C. Binns, M. J. Maher, Q. A. Pankhurst, D. Kechrakos, and K. N. Trohidou, Phys. Rev. B 66 (2002) 184413

[12] F. Luis, J. M. Torres, L. M. García, J. Bartolomé, J. Stankiewicz, F. Petroff, F. Fettar, J. L. Maurice, and A. Vaurès, Phys. Rev. B 65 (2002) 094409

[13] P. Gambardella, A. Dallmeyer, K. Maiti, M. C. Malagoli, W. Eberhardt, K. Kern, C. Carbone, Nature 416 (2002) 301

[14] Weili Luo, S. R. Nagel, T. F. Rosenbaum, and R. E. Rosensweig, Phys. Rev. Lett. 67 (1991) 2721

[15] Jinlong Zhang, C. Boyd, and Weili Luo, Phys. Rev. Lett. 77 (1996) 390

[16] B. Martinez, X. Obradors, L. Balcells, and C. Monty, Phys. Rev. Lett. 80 (1998) 181

[17] H. Mamiya, I. Nakatani, and T. Furubayashi, Phys. Rev. Lett. 82 (1999) 4332

[18] M. García del Muro, X. Batlle, and A. Labarta Phys. Rev. B 59 (1999) 13584

[19] P. E. Jönsson, M. F. Hansen, and P. Nordblad, Phys. Rev. B 61 (2000) 1261

[20] P. Allia, M. Coisson, P. Tiberto, F. Vinai, M. Knobel, M. A. Novak, and W. C. Nunes, Phys. Rev. B 64 (2001) 144420

[21] D. K. Lottis, R. M. White, and E. D. Dahlberg, Phys. Rev. Lett. 67 (1991) 362

[22] T. Jonsson, J. Mattsson, C. Djurberg, F. A. Khan, P. Nordblad, and P. Svedlindh, Phys. Rev. Lett. 75 (1995) 4138

[23] C. Djurberg, P. Svedlindh, P. Nordblad, M. F. Hansen, F. Bødker, and S. Mørup, Phys. Rev. Lett. 79 (1997) 5154

[24] M. Sasaki, P. E. Jönsson, H. Takayama, and H. Mamiya, cond-mat/0406546 (2004)

[25] P. E. Jönsson, H. Yoshino, H. Mamiya, and H. Takayama, cond-mat/0405276 (2004)

[26] J. J. Weis and D. Levesque, Phys. Rev. Lett. 71 (1993) 2729

[27] K. N. Trohidou and J. A. Blackman, Phys. Rev. B 51 (1995) 11521

[28] R. Pastor-Satorras and J. M. Rubí, Phys. Rev. E 51 (1995) 5994

[29] R. W. Chantrell, G. N. Coverdale, M. El Hilo, and K. O'Grady, J. Magn. Magn. Mater. 157/158 (1996) 250

[30] S. W. Davis, W. McCausland, H. C. McGahagan, and M. Widom, Phys. Rev. E 59 (1999) 2424

[31] W. Kleemann, O. Petracic, Ch. Binek, G. N. Kakazei, Yu. G. Pogorelov, J. B. Sousa, S. Cardoso, and P. P. Freitas, Phys. Rev. B 63 (2001) 134423

[32] F. Luis, F. Petroff, J. M. Torres, L. M. García, J. Bartolomé, J. Carrey, and A. Vaurés, Phys. Rev. Lett. 88 (2002) 217205

[33] P. Poddar, T. Telem-Shafir, T. Fried, and G. Markovich, Phys. Rev. B 66 (2002) 060403

[34] J. A. C. Bland and B. Heinrich, *Ultrathin Magnetic Structures I + II*, Springer Verlag, Berlin (1994)

[35] B. Voigtländer, G. Meyer, and N. M. Amer, Phys. Rev. B 44 (1991) 10354

[36] A. K. Schmid and J. Kirschner, Ultramicroscopy 42-44 (1992) 483

[37] F. O. Schumann, M. E. Buckley, and J. A. C. Bland, Phys. Rev. B 50 (1994) 16424

[38] J. Shen, M. Klaua, P. Ohresser, H. Jenniches, J. Barthel, C. V. Mohan, and J. Kirschner, Phys. Rev. B 56 (1997) 11134

[39] S. Hope, M. Tselepi, E. Gu, T. M. Parker, and J. A. C. Bland, Appl. Phys. 85 (1999) 6094

[40] U. Bovensiepen, P. Poulopoulos, W. Platow, M. Farle, and K. Baberschke, J. Magn. Magn. Mater. 192 (1999) 386

[41] F. Nouvertné, U. May, M. Bamming, A. Rampe, U. Korte, G. Güntherodt, R. Pentcheva, and M. Scheffler, Phys. Rev. B 60 (1999) 14382

[42] A. Kubetzka, O. Pietzsch, M. Bode, and R. Wiesendanger, Phys. Rev. B 63 (2001) 140407

[43] P. Poulopoulos, P. J. Jensen, A. Ney, J. Lindner, and K. Baberschke, Phys. Rev. B 65 (2002) 064431

[44] P. Bruno, Phys. Rev. B 52 (1995) 411

[45] K. Binder and A. P. Young, Rev. Mod. Phys. 58 (1986) 801

[46] A. P. Young, *Spin Glasses and Random Fields*, World Scientific, Singapore (1997)

[47] A. A. Pastor, V. Dobrosavljević, and M. L. Horbach, Phys. Rev. B 66 (2002) 014413

[48] N. M. Mermin and H. Wagner, Phys. Rev. Lett. 17 (1966) 1133

[49] R. H. Kodama, J. Magn. Magn. Mater. 200 (1999) 359

[50] A. Hernando, J. Phys.: Condens. Matter 11 (1999) 9455

[51] G. M. Pastor, *Atomic Clusters and Nanoparticles*, (Eds. C. Guet, P. Hobza, F. Spiegelman, and F. David) Springer Verlag, Berlin (2000), p. 335

[52] A. J. Cox, J. G. Louderback, L. A. Bloomfield, Phys. Rev. Lett. 71 (1993) 923

[53] I. M. L. Billas, A. Châtelain, and W. A. deHeer, Science 265 (1994) 1682

[54] M. B. Knickelbein, Phys. Rev. Lett. 86 (2001) 5255

[55] M. Jamet, W. Wernsdorfer, C. Thirion, D. Mailly, V. Dupuis, P. Mélinon, and A. Pérez, Phys. Rev. Lett. 86 (2001) 4767

[56] K. W. Edmonds, C. Binns, S. H. Baker, M. J. Maher, S. C. Thornton, O. Tjernberg, and N. B. Brookes, J. Magn. Magn. Mater. 231 (2001) 113

[57] Y. Qiang, R. F. Sabiryanov, S. S. Jaswal, Y. Liu, H. Haberland, and D. J. Sellmyer, Phys. Rev. B 66 (2002) 064404

[58] C. Papusoi, Jr., J. Magn. Magn. Mater. 195 (1999) 708

[59] J. Hesse, H. Bremers, O. Hupe, M. Veith, E. W. Fritscher, and K. Valtchev, J. Magn. Magn. Mater. 212 (2000) 153

[60] O. Iglesias and A. Labarta, Phys. Rev. B 63 (2001) 184416

[61] C. S. M. Bastos, M. Bahiana, W. C. Nunes, M. A. Novak, D. Altbir, P. Vargas, M. Knobel, Phys. Rev. B 66 (2002) 214407

[62] Y. L. Raikher and V. I. Stepanov, Phys. Rev. B 66 (2002) 214406

[63] Y. Labaye, O. Crisan, L. Berger, J. M. Grenèche, and J. M. D. Coey, J. Appl. Phys. 91 (2002) 8715

[64] D. A. Garanin and H. Kachkachi, Phys. Rev. Lett. 90 (2003) 065504

[65] R. P. Cowburn, D. K. Koltsov, A. O. Adeyeye, M. E. Welland, and D. M. Tricker, Phys. Rev. Lett. 83 (1999) 1042

[66] R. P. Cowburn, J. Phys. D: Appl. Phys. 33 (2000) 1

[67] M. Schneider, H. Hoffmann, and J. Zweck, Appl. Phys. Lett. 77 (2000) 2909

[68] S. P. Li, D. Peyrade, M. Natali, A. Lebib, Y. Chen, U. Ebels, L. D. Buda, and K. Ounadjela, Phys. Rev. Lett. 86 (2001) 1102

[69] V. Novosad, M. Grimsditch, K. Y. Guslienko, P. Vavassori, and S. D. Bader, Phys. Rev. B 66 (2002) 052407

[70] H. B. Braun, Phys. Rev. Lett. 71 (1993) 3557

[71] E. Y. Vedmedenko, H. P. Oepen, A. Ghazali, J. C. Lévy, and J. Kirschner, Phys. Rev. Lett. 84 (2000) 5884

[72] O. Fruchart, B. Kevorkian, and J. C. Toussaint, Phys. Rev. B 63 (2001) 174418

[73] W. Scholz, T. Schrefl, and J. Fidler, J. Magn. Magn. Mater. 233 (2001) 296

[74] V. Safonov and H. N. Bertram, Phys. Rev. B 63 (2001) 094419

[75] G. Brown, M. A. Novotny, and P. A. Rikvold Phys. Rev. B 64 (2001) 134422

[76] J. Kin Ha, R. Hertel, and J. Kirschner, Phys. Rev. B 67 (2003) 064418

[77] L. Néel, Ann. Geophys. 5 (1949) 99

[78] W. F. Brown, Jr., J. Appl. Phys. 30 (1959) 130; Phys. Rev. 130 (1963) 1677

[79] H. Pfeiffer, Phys. Stat. Sol. (a) 118 (1990) 295

[80] A. Würger, Phys. Rev. Lett. 81 (1998) 212

[81] L. D. Landau and E. Lifshitz, Phys. Z. Sowjetunion 8 (1935) 155

[82] D. V. Berkov, J. Magn. Magn. Mater. 186 (1998) 199

[83] O. A. Chubykalo, B. Lengsfield, B. Jones, J. Kaufman, J. M. Gonzales, R. W. Chantrell, and R. Smirnov-Rueda, J. Magn. Magn. Mater. 221 (2000) 132

[84] U. Nowak, Ann. Rev. Comp. Phys. 9 (2001) 105

[85] J. Fidler and T. Schrefl, J. Phys. D: Appl. Phys. 33 (2000) 135

[86] M. El-Hilo, K. O'Grady, and R. W. Chantrell, J. Magn. Magn. Mater. 114 (1992) 295, 307

[87] M. A. Załuska-Kotur, Phys. Rev. B 54 (1996) 1064

[88] M. F. Hansen and S. Mørup, J. Magn. Magn. Mater. 184 (1998) 262

[89] J. L. Dorman, D. Fiorani, and E. Tronc, J. Magn. Magn. Mater. 202 (1999) 251

[90] P. Jönsson and J. L. García-Palacios, Phys. Rev. B 64 (2001) 174416

[91] V. S. Zotev, G. G. Kenning, and R. Orbach, Phys. Rev. B 66 (2002) 014412

[92] D. Kechrakos and K. N. Trohidou, Phys. Rev. B 58 (1998) 12169

[93] V. Russier, J. Appl. Phys. 89 (2001) 1287

[94] V. Russier, C. Petit, and M. P. Pileni, J. Appl. Phys. 93 (2003) 10001

[95] A. A. Fraerman and M. V. Sapozhnikov, Phys. Rev. B 65 (2002) 184433

[96] R. Prozorov, Y. Yeshurun, T. Prozorov, and A. Gedanken, Phys. Rev. B 59 (1999) 6956

[97] R. W. Chantrell, N. Walmsley, J. Gore, and M. Maylin, Phys. Rev. B 63 (2000) 024410

[98] J. García-Otero, M. Porto, J. Rivas, and A. Bunde, Phys. Rev. Lett. 84 (2000) 167

[99] S. I. Denisov and K. N. Trohidou, Phys. Rev. B 64 (2001) 184433

[100] L. Wang, J. Ding, H. Z. Kong, Y. Li, and Y. P. Feng, Phys. Rev. B 64 (2001) 214410

[101] J. L. Dorman, L. Bessais, and D. Fiorani, J. Phys. C 21 (1988) 2015

[102] J. O. Andersson, C. Djurberg, T. Jonsson, P. Svedlindh, and P. Nordblad, Phys. Rev. B 56 (1997) 13983

[103] A. Ivanov and O. B. Kuznetsova, Phys. Rev. E 64 (2001) 041405

[104] P. Jönsson, T. Jonsson, J. L. García-Palacios, and P. Svedlindh, J. Magn. Magn. Mater. 222 (2000) 219

[105] T. Suzuki, Progr. Theor. Phys. 55 (1977) 1151

[106] Y. Sun, Y. Salamon, K. Garnier, R. S. Averback, Phys. Rev. Lett. 91 (2003) 167206

[107] M. Ulrich, J. García-Otero, J. Rivas, A. Bunde, Phys. Rev. B 67 (2003) 024416

[108] O. Iglesias and A. Labarta, (2003) cond-mat/0311139

[109] S. Mørup and E. Tronc, Phys. Rev. Lett. 72 (1995) 3278

[110] S. Thamm and J. Hesse, J. Magn. Magn. Mater. 154 (1996) 254; *ibid.* 184 (1998) 245

[111] N. S. Walmsley, A. Hart, D. A. Parker, C. Dean, and R. W. Chantrell, J. Magn. Magn. Mater. 170 (1997) 81

[112] R. Pastor-Satorras and J. M. Rubí, Phys. Rev. Lett. 80 (1998) 5373; J. Magn. Magn. Mater. 221 (2000) 124

[113] R. Botet, K. N. Trohidou, J. A. Blackman, and D. Kechrakos, Phys. Rev. E 64 (2001) 031401

[114] A. Ghazali and J. C. Lévy, Phys. Rev. B 67 (2003) 064408

[115] D. Kechrakos and K. N. Trohidou, Phys. Rev. B 62 (2000) 3941

[116] Z. Sefrioui, J. L. Menéndez, E. Navarro, A. Cebollada, F. Briones, P. Crespo, and A. Hernando, Phys. Rev. B 64 (2001) 224431

[117] J. Viana-Lopes, J. M. B. Lopes dos Santos, and Y. G. Pogorelov, Phys. Rev. B 66 (2002) 064416

[118] E. C. Stoner and E. P. Wohlfarth, Trans. Roy. Soc. A 240 (1948) 599

[119] A. Hubert and R. Schäfer, *Magnetic Domains,* Springer Verlag, Berlin (1998)

[120] J. Chapman, J. Phys. D: Appl. Phys. 17 (1984) 623

[121] P. Gambardella, S. Rusponi, M. Veronese, S. S. Dhesi, C. Grazioli, A. Dallmeyer, I. Cabria, R. Zeller, P. H. Dederichs, K. Kern, C. Carbone, and H. Brune, Science 300 (2003) 1130

[122] P. Bruno, Phys. Rev. Lett. 83 (1999) 2425

[123] M. Pratzer, H. J. Elmers, M. Bode, O. Pietzsch, A. Kubetzka, and R. Wiesendanger, Phys. Rev. Lett. 87 (2001) 127201

[124] P. Bruno, *Magnetismus von Festkörpern und Grenzflächen,* 24. IFF Ferienkurs, Forschungszentrum Jülich, Germany (1993), chap. 24

[125] P. Politi and M. G. Pini, Phys. Rev. B 66 (2002) 214414

[126] P. J. Jensen and G. M. Pastor, New J. Phys. 5 (2003) 68

[127] G. M. Genkin and M. V. Sapozhnikov, Appl. Phys. Lett. 64 (1993) 794

[128] P. Vargas and D. Altbir, J. Magn. Magn. Mater. 167 (1997) 161

[129] R. Skomski, Europhys. Lett. 48 (1999) 455; J. Appl. Phys. 87 (2000) 5890

[130] J. Viana-Lopes and Y. G. Pogorelov, J. Magn. Magn. Mater., in press (2004)

[131] S. S. P. Parkin, Phys. Rev. Lett. 67 (1991) 3598

[132] S. Romano, Phys. Rev. B 49 (1994) 12287

[133] K. De'Bell, A. B. MacIsaac, I. N. Booth, and J. P. Whitehead, Phys. Rev. B 55 (1997) 15108

[134] K. De'Bell, A. B. MacIsaac, and J. P. Whitehead Rev. Mod. Phys. 72 (2000) 225

[135] A. Carbognani, E. Rastelli, S. Regina, and A. Tassi, Phys. Rev. B 62 (2000) 1015

[136] P. J. Jensen, Ann. Physik (Leipzig) 6 (1997) 317

[137] W. H. Press, S. A. Teukolsky, W. T. Vetterling, and B. P. Flannery, *Numerical Recipes,* Cambridge University Press, Cambridge (1992)

[138] D. J. Wales, *Atomic Clusters and Nanoparticles*, (Eds. C. Guet, P. Hobza, F. Spiegelman, and F. David) Springer Verlag, Berlin (2000), p. 438

[139] P. Belobrov, R. S. Gekht, and V. A. Ignatchenko, Sov. Phys. JETP 57 (1983) 636

[140] S. Prakash and C. L. Henley, Phys. Rev. B 42 (1990) 6574

[141] V. M. Rozenbaum, V. M. Ogenko, and A. A. Chuĭko, Sov. Phys. Usp. 34 (1991) 883

[142] J. Villain, R. Bideaux, J. P. Carton, and R. Conte, J. Phys. (Paris) 41 (1980) 1263

[143] C. L. Henley, Phys. Rev. Lett. 62 (1989) 2056

[144] M. Dantziger, B. Glinsmann, S. Scheffler, B. Zimmermann, and P. J. Jensen, Phys. Rev. B 66 (2002) 094416

[145] Y. Yafet, J. Kwo, and E. M. Gyorgy, Phys. Rev. B 33 (1986) 6519

[146] P. J. Jensen and G. M. Pastor, Phys. Rev. B 68 (2003) 184420

[147] E. L. Bizdoaca, M. Spasova, M. Farle, M. Hilgendorff, and F. Caruso, J. Magn. Magn. Mater. 240 (2002) 44

[148] E. L. Bizdoaca, M. Spasova, M. Farle, M. Hilgendorff, L. M. Liz-Marzan, and F. Caruso, J. Vac. Sci. Technol. A 21 (2003) 1515

[149] E. Kneller, *Ferromagnetismus*, Springer Verlag, Berlin (1962)

[150] R. Brinzanik, P. J. Jensen, and K. H. Bennemann, J. Magn. Magn. Mater. 238 (2002) 258

[151] R. Brinzanik, P. J. Jensen, and K. H. Bennemann, Phys. Rev. B 68 (2003) 174414

[152] U. Wolff, Phys. Rev. Lett. 62 (1989) 361

[153] D. P. Landau and K. Binder, *A Guide to Monte Carlo Simulations in Statistical Physics*, Cambridge University Press, Cambridge (2000)

[154] A. F. Voter, Phys. Rev. B 34 (1986) 6819

[155] K. A. Fichthorn and W. H. Weinberg, J. Chem. Phys. 95 (1991) 1090

[156] M. Eden, *Symp. on Information Theory in Biology,* Pergamon Press, New York (1958), pp. 359

[157] M. Methfessel, D. Hennig, and M. Scheffler, Appl. Phys. A 55 (1992) 442

[158] J. Shen, R. Skomski, M. Klaua, H. Jenniches, S. S. Manoharan, and J. Kirschner, Phys. Rev. B 56 (1997) 8454

[159] D. Wei, G. N. Patey, and A. Perera, Phys. Rev. E 47 (1993) 506

[160] H. Zhang and M. Widom, Phys. Rev. B 51 (1995) 8951

[161] F. Lado, E. Lomba, and J.J. Weis, Phys. Rev. E 58 (1998) 3478

[162] E. Lomba, F. Lado, and J.J. Weis, Phys. Rev. E 61 (2000) 3838

[163] J. Hauschild, H. J. Elmers, and U. Gradmann, Phys. Rev. B 57 (1998) 677

[164] H. Zeng, R. Skomski, L. Menon, Y. Liu, S. Bandyopadhyay, and D. J. Sellmyer, Phys. Rev. B 65 (2002) 134426

[165] J. M. Luttinger and L. Tisza, Phys. Rev. 70 (1946) 954; *ibid.* 72 (1947) 257

[166] B. Heinrich, J. F. Cochran, M. Kowalewski, J. Kirschner, Z. Celinski, A. S. Arrott, and K. Myrtle, Phys. Rev. B 44 (1991) 9348

[167] R. Dittrich, T. Schrefl, D. Suess, W. Scholz, H. Forster, and J. Fidler, J. Magn. Magn. Mater. 250 (2002) 12

[168] P. J. Jensen, Proceedings of the 4th International Conference on Theory of Atomic and Molecular Clusters, Toulouse, France (2004)

[169] N. Mousseau and G. T. Barkema, Phys. Rev. E 57 (1998) 2419

[170] J. P. K. Doye and D. J. Wales, Z. Phys. B 40 (1997) 194

[171] G. T. Barkema and N. Mousseau, Phys. Rev. Lett. 77 (1996) 4358

[172] N. Mousseau and G. T. Barkema, cond-mat/0310422 (2003)

[173] H. J. Elmers, J. Hauschild, H. Höche, U. Gradmann, H. Bethge, D. Heuer, and U. Köhler Phys. Rev. Lett. 73 (1994) 898

[174] D. Tománek, S. G. Kim, P. Jund, P. Borrmann, H. Stamerjohanns, and E. R. Hilf, Z. Phys. D 40 (1997) 539

[175] F. Kun, W. Wen, K. F. Pál, and K. N. Tu, Phys. Rev. E 64 (2001) 061503

[176] E. Y. Vedmedenko, A. Kubetzka, K. von Bergmann, O. Pietzsch, M. Bode, J. Kirschner, H. P. Oepen, and R. Wiesendanger, Phys. Rev. Lett. 92 (2004) 077207

[177] U. Ebels, A. Radulescu, Y. Henry, L. Pireaux, and K. Ounadjela, Phys. Rev. Lett. 84 (2000) 983

[178] B. U. Felderhof, Phys. Rev. E 62 (2000) 3848; *ibid.* 64 (2001) 063502

[179] M. I. Shliomis, Phys. Rev. E 64 (2001) 063501

[180] J. Nogués and I. K. Schuller, J. Magn. Magn. Mater. 192 (1999) 203

[181] M. Kiwi, J. Magn. Magn. Mater. 234 (2001) 584

[182] C. Joachim, J. K. Gimzewski, and A. Aviram, Nature 408 (2000) 541

[183] S. A. Wolf, D. D. Awschalom, R. A. Buhrman, J. M. Daughton, S. von Molnár, M. L. Roukes, A. Y. Chtchelkanova, and D. M. Treger, Science 294 (2001) 1488

[184] K. Ono, D. G. Austing, Y. Tokura, and S. Tarucha, Science 297 (2002) 131

[185] J. Park, A. N. Pasupathy, J. I. Goldsmith, C. Chang, Y. Yaish, J. R. Petta, M. Rinkoski, J. P. Sethna, H. D. Abruña, P. L. Euen, and D. C. Ralph, Nature 417 (2002) 722

[186] W. Liang, M. P. Shores, M. Bockrath, J. R. Long, and H. Park, Nature 417 (2002) 725

[187] Y. Alhassid and T. Rupp, Phys. Rev. Lett. 91 (2003) 056801

[188] B. Barbara, L. Thomas, F. Lionti, I. Chiorescu, and A. Sulpice, J. Magn. Magn. Mater. 200 (1999) 167

[189] E. Keçecioğlu and A. Garg, Phys. Rev. B 67 (2003) 054406

[190] R. Tiron, W. Wernsdorfer, N. Aliaga-Alcalde, and G. Christou, Phys. Rev. B 68 (2003) 140407

[191] A. Goujon, B. Gillon, A. Gukasov, J. Jeftic, Q. Nau, E. Codjovi, and F. Varret, Phys. Rev. B 67 (2003) 220401

SURFACE AND INTERFACE MAGNETISM ON THE ATOMIC SCALE

H.H. Bertschat

Bereich Strukturforschung, Hahn-Meitner-Institut Berlin GmbH, D-14109 Berlin, Germany

1. INTRODUCTION

Functional materials may be realised in the future where extremely small clusters of atoms, molecules or even surface- and interface-attached single atoms are the basic building blocks in electronic and spintronic devices such as high-density storage, switches or sensors in data-processing. On the way to such systems, comprehensive basic research on the behaviour of isolated atoms in contact with surfaces or embedded in interfaces is necessary, *without* aiming at immediate applications.

This chapter presents our approach to study the behaviour of single atoms on surfaces and in interfaces, in particular in magnetic systems, by the use of radioactive impurity atoms as probes. Nuclear methods offer extreme high sensitivity compared to most other contemporary experimental methods, only 10^{-4} – 10^{-6} of an atomic layer is necessary for detection. A detailed motivation for this choice will be given in the following section. During the course of a broad experimental study, the coordination number of the impurity, i.e., the number of nearest neighbours (NN), emerged to play a central role.

Results obtained with radioactive atoms are also valid for stable atoms of the same element.

2. MOTIVATION

In the past 20 years we have witnessed an ever-increasing interest in the novel physical and chemical phenomena found in thin and ultra-thin films or multilayers of metals, semiconductors and insulators. Structural and electronic properties of interfaces (and surfaces)

in ultra-thin multilayers of metals, semiconductors, and insulators have been subject of increasing interest, both in basic research and in connection with technical applications. The field expanded greatly with the discovery of new phenomena, such as: metastable structural phases introduced during epitaxial growth, perpendicular magnetic moments of thin layers, and giant magneto resistance in multilayers. Many of these phenomena and discoveries offer possibilities for important applications in the field of present and future nano- and subnano-technologies. These developments are reflected in a variety of review articles and books, of which we restrict ourselves on selected publications on magnetism [1-3]. In addition, a series of comprehensive didactic publications on low-dimensional magnetic thin-layer systems is given in Ref. 4.

Miniaturisation of integrated circuits has been identified as one of the most challenging prospects in scientific as well as in technological developments. Particularly, when these nanostructures become extremely small, size effects are expected to become important for the physical properties. In such systems, the atomic structure and properties of interfaces play an increasing dominant role, e.g., in metallic multilayers or metal-semiconductor contacts. Furthermore, interdiffusion and reactions of atoms across the interfaces need to be studied in order to arrive at well-functioning electronic circuits in the nanostructural range.

Therefore a profound understanding of the underlying nano- and picoscopic properties are of special interest from the point of view of fundamental physics. Many *overall* properties (important for possible technical applications) of a thin-layer system depend sensitively on the *local properties on the atomic scale* at the interface or at the surface. These properties are not accessible to most conventional experimental methods, especially at buried interfaces. It is precisely here that the experimental techniques using radioactive atoms as local probes are expected to contribute substantially in gaining further knowledge. A variety of nuclear methods can be applied for investigations on the atomic scale, most suitable are methods which measure hyperfine interactions, e.g., Mößbauer spectroscopy [1, 5].

Electric and magnetic hyperfine interactions of radioactive atomic nuclei provide insight into local properties; the electric quadrupole moment of the probe nucleus interacts with electric field gradients (EFG) arising from a noncubic geometry of the adjacent atoms, the magnetic dipole moment interacts with magnetic hyperfine fields (B_{hf}) caused by polarised electrons. The short range of the hyperfine interaction allows for monolayer resolution of the measurement in layered systems or even for atomic resolution, e.g., on surfaces. The long penetration range of the nuclear radiation (in most cases gamma-radiation) enables measurements in any depth of the sample, in particular at buried interfaces.

With the application of isolated (radioactive) atoms in basic research of ultra-thin and ultra-small structures, i.e., with the determination of the properties of single atoms *in* their immediate atomic environment, the above-mentioned miniaturisation (going from larger to smaller and smaller units in size) can be regarded from a very different point of view: We *start* with the smallest possible units, isolated atoms embedded in picostructures. Out of the many fields indicated above where nuclear methods can be applied, the present chapter describes our selection: investigation of surface and interface magnetism.

The ultimate aim in magnetic storage (as an example for applications) is the use of single magnetic atoms (e.g., rare earth atoms) carrying information by the occupation of different magnetic and/or chemical and/or structural states. In order to prevent “cross-talk”, these atoms (or small clusters of these atoms) have to be separated from each other by

embedding them into two-dimensional structures of nonmagnetic atoms. Such magnetic/nonmagnetic structures are in the lower range of nanometers and could be the basis for tera-bit memories. Our basic research may serve for such goals.

3. HISTORICAL SURVEY

Numerous measurements of hyperfine interactions at probe nuclei in a large variety of bulk materials have been performed during the last five decades and several thousands of publications appeared in nearly all physical journals on basic research. Electric quadrupole interactions were studied in noncubic crystals, magnetic dipole interactions, e.g., in ferromagnetic materials. When ferromagnetic materials are noncubic in structure, combined hyperfine interactions occur. Around 1980, the first measurements were started with radioactive impurities on surfaces applying perturbed angular correlation spectroscopy (PAC, see section 5). Because of the noncubic symmetry at surfaces the probes are always exposed to electric field gradients. In the following paragraphs, we mention *selected* activities which are close in methods to our experiments described in this chapter.

The pioneering experiments were performed by G. Schatz et al. at the University of Konstanz/Germany and by H. Haas et al. (Hahn-Meitner-Institut Berlin/Germany) at the mass separator ISOLDE/CERN, Geneva, Switzerland. For the first ten years, these two groups concentrated on nonmagnetic surfaces, firstly, in order to test the feasibility of this type of experiment and secondly, to avoid the complexity of combined interactions.

In the Schatz group, the PAC probe ^{111}Cd decaying from ^{111}In was used. For laboratory experiments, this is an ideal probe because of the half-live of $T_{1/2}$ = 2.8 days and its other most suitable nuclear properties [6]. ^{111}In is commercially available in a Cl solution, however, it requires high experimental skill in order to transfer the probes onto surfaces in ultra-high vacuum (UHV) without a disturbing amount of Cl contamination. In the first experiments, the Schatz group studied the interaction of Cd impurities on metallic surfaces [7]. With the ability to grow well-defined ultra-thin metallic layers, studies at interfaces were possible [8].

The Haas group performed PAC experiments at the on-line mass separator ISOLDE at CERN. The mass separator provides a variety of different nuclear probes in unsurpassed purity. Taking advantage of its “on-line” arrangement, short-lived nuclear probes can be used such as ^{111m}Cd decaying with $T_{1/2}$ = 49 minutes into the PAC probe ^{111}Cd. Thus, PAC experiments can be performed comparing the same hyperfine interaction from different parents, because the sample preparation is always carried out with the nuclear parents [9]. Details of the experimental procedures at ISOLDE will be described in section 6 of this chapter.

The Groningen/Netherlands group (under the leadership of L. Niesen) developed a soft-landing procedure for probe ions by deceleration after they were mass separated in an isotope separator [10]. Applying this procedure to Ag surfaces with ^{111}Ag ions, they could perform PAC measurements with varying sample conditions. The probe nucleus ^{111}Cd can also be populated by the decay of ^{111}Ag with $T_{1/2}$ = 7.5 days (besides ^{111}In and ^{111m}Cd as parents, as mentioned above). In these experiments, the self-diffusion on the Ag surface was directly observed [11].

In the eighties/nineties of the last century, *magnetic* multilayer systems became subject of various methods performing hyperfine interaction investigations. We refrain from reporting on the many groups applying conversion electron Mößbauer spectroscopy (CEMS), but see Refs. 1 and 5. Mößbauer spectroscopy is usually restricted to Fe layers (^{57}Fe) and requires relatively long measuring times although CEMS has been developed to submonolayer sensitivity [12].

We also mention nuclear magnetic resonance (NMR) which can be applied on various nuclei, e.g., ^{59}Co in ultra-thin Co systems, frequently investigated by the J dryka group, Warsaw/Poland [13], or ^{55}Mn in interface systems containing Mn compounds [14].

The PAC method, working with highly diluted impurities, enables investigations of low-dimensional magnetic systems, although world-wide only a few groups take advantage of this method, e.g., the Lindgren group of the University of Uppsala/Sweden, investigating Co/Cu multilayers [15] and concentrating on theory (see later Refs. with Lindgren et al. [35, 45]), or the Lieb group, University of Göttingen/Germany, focussing on ion-irradiated thin ferromagnetic films in order to observe changes in the magnetic orientation by PAC and Mößbauer spectroscopy [16].

A broad spectrum of PAC measurements on magnetic multilayers was performed by the Rots group (University of Leuven/Belgium) which is also very active in theory (see section 8). The multilayers are activated by low-energetic ion beams (80 keV), i.e., the ions are uniformly implanted in different layers, emitting respectively different signals. Although this technique is not suitable for monolayer-resolved measurements, they can distinguish between hyperfine fields near the interface and further away as shown in Fe/Co multilayers [17]. One of the major projects of the Leuven group was the study of spin-density-wave magnetism in Cr applying PAC [18]. They could show the validity of PAC as a complementary approach to neutron diffraction experiments towards the study of the Cr magnetic ordering in thin films and Fe/Cr multilayers. This approach is being refined further, and valuable results were recently obtained on single Cr layers as thin as 8 nm [19].

Around 1990, the Berlin and Konstanz groups started working together on some experiments at the on-line mass separator ISOLDE at CERN setting up the UHV chamber ASPIC (see section 6). Common results at ISOLDE were obtained with ^{77}Se on the semiconductor Si(001) [20] and on ferromagnetic Ni and nonmagnetic Pd surfaces [21], after the Konstanz group in laboratory experiments had shown the feasibility of PAC experiments on Si [22] and on Ni [23] with the ^{111}Cd probe. The Konstanz group continued on Co systems and examined the very interesting Fe/Ag interface aiming to answer the question, whether and to what extent Ag will show induced and ordered moments when it is in contact with Fe [24]. (For Pd it was well known since several years, that it shows an induced ferromagnetic order when it is in contact with Fe or Ni, see section 10 of this chapter.) Their positive experimental result was questioned quantitatively by a theoretical study [25]. This experiment should be repeated using ^{111}Ag as the more appropriate radioactive precursor isotope. Meanwhile, low temperature nuclear orientation experiments revealed a strong Ag magnetic hyperfine field for the first atomic layer of Ag in contact with Fe [26].

While most groups applying PAC spectroscopy have investigated metallic systems, the Catchen group (University of Pennsylvania/USA) has studied the behaviour of ^{111}Cd preferentially on III-V semiconductor surfaces [27, 28]. It is desirable that this very powerful method, providing atomic resolution, should be applied more frequently for semiconductor surfaces. In particular, the study of semiconductor-metallic interfaces would be promising.

Finally, we note that scanning tunnelling microscopy (STM) on surfaces at present is probably the most powerful method with atomic resolution. Circular polarised synchrotron radiation meanwhile allows for investigations of magnetic systems (polarised *p-d-f*-electrons) far in the submonolayer region due to successful efforts to increase the sensitivity. The experiments described in the present chapter are performed using the PAC method which is complementary to both because it has access to the effects caused by polarised *s* electrons.

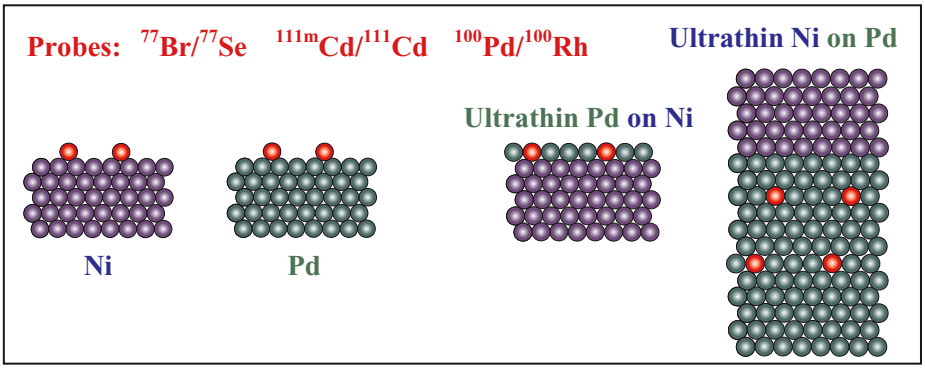

Fig. 1. Icons for three categories of experiments. From left: Surface studies; ultra-thin layers of Pd on Ni bulk; ultra-thin Ni layers on Pd bulk; probes in red colour.

4. THREE TYPES OF PRINCIPLE EXPERIMENTS

Fig. 1 shows three categories of experiments performed by our group in the first half of the last decennium of the last millennium [21, 29, 30]. The leftmost part depicts the icon representing radioactive probes (^{77}Se, ^{111}Cd) on a ferromagnetic Ni surface. Here, the nonmagnetic atomic probes experience induced magnetic hyperfine interactions because of the ferromagnetic substrate and simultaneously they experience electric quadrupole hyperfine interactions because of the noncubic environment. For a better distinction of these interactions, the same probes were also measured on isoelectronic palladium where only electric hyperfine interactions are present, second icon. The third icon shows probe atoms (^{100}Rh, ^{111}Cd) embedded in one atomic monolayer of Pd grown on a Ni single crystal. The probes in Pd show ferromagnetic-like behaviour of Pd. The induced magnetic interactions at the probe can be followed layer by layer either in Ni or in the different Pd layers grown on Ni. The third type of experiments is found in the rightmost icon of Fig. 1. On a single crystal of Pd, radioactive probes are positioned and some additional Pd layers are grown (4 or 7, as shown, each at a time) with the result, that the position of the probes is well defined in depth. Finally, a few atomic layers of Ni are grown on top allowing for the observation of magnetic interactions induced by the ferromagnetic coverage exactly at the probe position.

This chapter presents the studies continued on the above described three basic experiments. Induced magnetic properties of isolated nonmagnetic atoms positioned on all different sites of a ferromagnetic surface, see Fig. 1 left (and Figs. 9, 10), will be the central topic where meanwhile different theoretical treatments are available. In addition, experiments

on thin layers of Pd on Ni surfaces with incorporated probe atoms will be presented where calculations on magnetic hyperfine fields are in progress.

In the next two sections, a brief description of the applied PAC method and the sample preparation is given. After the four main sections 7-10, we finally present some ideas in the outlook section on possible future applications, e.g., how the structure for a two-dimensional magnetic memory with tera-bit capacity (one tera-bit per cm^2) could be approached.

5. COMBINED HYPERFINE INTERACTIONS AND PERTURBED ANGULAR CORRELATION SPECTROSCOPY (PAC)

The principles of PAC are described in Ref. 31. In this chapter, we focus on some aspects of the theory, which are necessary for the understanding of the presented results.

Nuclei of probe atoms located on a ferromagnetic surface or in a magnetic-layer system experience combined electric and magnetic hyperfine interactions during the life time of a suitable isomeric state. The electric quadrupole moment Q_N and the magnetic dipole moment μ as properties of the isomeric state with nuclear spin I are interacting with the electric field gradient (EFG) and the magnetic hyperfine field (B_{hf}), respectively, which are present at the probe nuclei due to the local electronic environment.

a) Electric Quadrupole Interaction

The EFG originates from a non-spherical distribution of electric charges around the nucleus. The EFG is a traceless tensor and can be diagonalised using an appropriate transformation [32]. In Cartesian coordinates, the EFG is well described by the set:

$$(V_{zz}, \eta, \alpha, \beta, \gamma) \text{ with the asymmetry parameter } \eta = \frac{V_{xx} - V_{yy}}{V_{zz}}, \quad (1)$$

where the largest diagonal element is taken as V_{zz}. The Eulerian angles α, β, γ define the orientation of the EFG within the laboratory coordination system with β as deviation from the normal of the sample surface and α, γ as orientation in the plane.

The interaction between the nuclear quadrupole moment Q_N and the EFG for η = 0, i.e., axial symmetry, is described by frequencies according to the splitting of the intermediate level. The electric quadrupole interaction frequency ω_Q is given as

$$\omega_Q = \frac{eQV_{zz}}{4I(2I-1)\hbar} = 2\pi \frac{\nu_Q}{4I(2I-1)}, \quad (2)$$

where $\nu_Q = \frac{eQV_{zz}}{h}$ is called the quadrupole coupling constant.

b) Magnetic Dipole Interaction

Most important for our purposes is the determination of the magnetic hyperfine field (B_{hf}), which results from polarised electrons at the probe nucleus. In general, B_{hf} consists of dipolar, orbital, core polarisation contributions and the valence electron Fermi-contact field [33], the latter being the main contribution for 4*sp* and 5*sp* elements as impurities in or on ferromagnets. The nuclear magnetic dipole moment is defined as $\vec{\mu} = \mu_N g_N \vec{I}$, where μ_N is

the Bohr nuclear magneton, g_N is the nuclear g-factor, and I the nuclear spin. All nuclear properties are found in Ref. 6. The interaction between the nuclear magnetic moment and the magnetic hyperfine field causes the nucleus to precess with the Larmor frequency ω_L [32]

$$\omega_L = -\frac{g_N \mu_N B_{hf}}{\hbar}. \tag{3}$$

c) Combined Interactions

Both interaction frequencies in the equations (2) and (3) are measured simultaneously in a PAC spectroscopy set-up and the combined interaction frequencies

$$\omega_c = \omega_c(\omega_L, \omega_Q, \eta, \beta) \tag{4}$$

are obtained from the PAC-time spectrum, see below.

d) PAC Spectroscopy

The gamma-gamma cascade in a PAC probe nucleus - populating and depopulating the isomeric state - produces an angular correlation function W(Θ), measurable with a two-detector set-up, where Θ is the angle between the two gamma-rays [34]. W(Θ) is described by Legendre polynominals and the nuclear coefficients A_k, depending on the nuclear spin, as $W(\Theta) = \Sigma\ A_k\ P_k(\cos\ \Theta)$. The electric and magnetic hyperfine interactions perturb this correlation during the life time of the intermediate isomeric state, therefore W becomes time dependent: W(Θ,t). In one of the simplest cases - the static magnetic field perpendicular to the detector plane - one obtains (with respect to Eq. (3)):
$W(\Theta,t) = \Sigma\ A_k\ P_k(\cos\ \Theta - \omega_L\ t)$.

The angular correlation becomes considerably more complex for general cases of combined interactions and can be treated only numerically [35].

The combined interaction frequencies ω_c of Eq. (4) (or the individual frequencies of Eqs. (2) and (3) in the special cases of pure electric quadrupole or magnetic dipole interaction, respectively) are measured in a PAC set-up, consisting of 4 gamma-ray detectors usually arranged at 90° and 180° to each other in a plane perpendicular to the sample surface. The detectors determine the time-dependent coincidence rates $C(\Theta, t)$ of the gamma-cascade, i.e., the populating and the depopulating gammas of the isomeric state in the probe nucleus. From these accumulated coincidences the time-dependent ratio function R(t) is deduced:

$$R(t) = \frac{2[C(180^\circ) - C(90^\circ)]}{C(180^\circ) + C(90^\circ)}. \tag{5}$$

R(t) is usually called the "PAC-time spectrum". Its amplitude is deduced from the nuclear anisotropy of the gamma-gamma cascade. The decay with time of the amplitude is called "damping". The damping can be caused by many reasons: mobility of the probes, contamination, nonregular sites, fluctuations, etc. The general expression describing the perturbed angular correlation for static electric and magnetic hyperfine interactions on single crystals is fitted to the data of the ratio function R(t). The fit provides the parameters of the amplitudes, frequencies, damping, etc., see caption of Fig. 2. There exist several computer codes providing numerical solutions for the fit. The experiments presented in this chapter are treated throughout with the Depack program of Lindgren [35]. In Fig. 2, the whole procedure is depicted and examples how the individual frequencies combine are demonstrated visually.

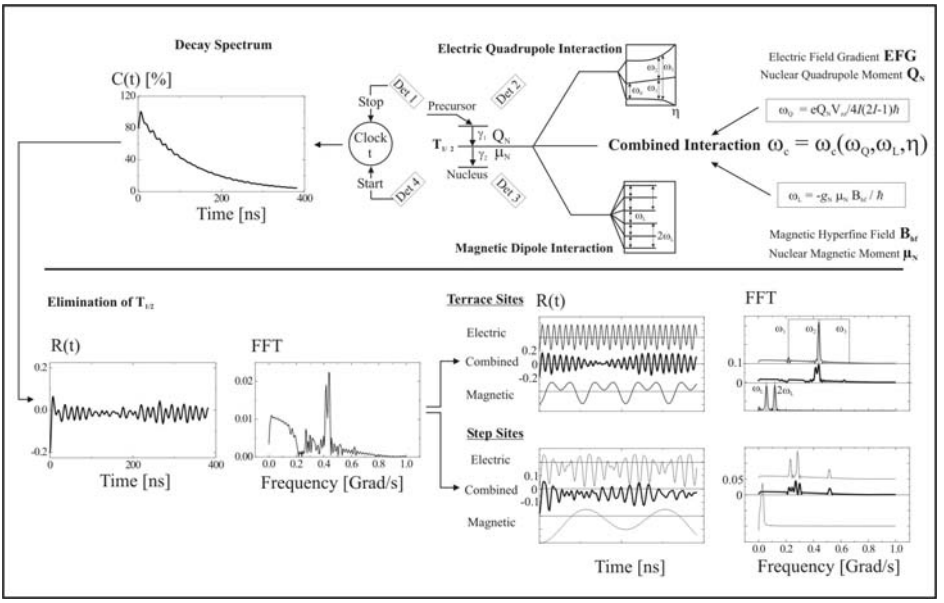

Fig. 2. Schematic presentation of perturbed angular correlation spectroscopy (PAC); example for an isomeric state with I = $^5/_2$, e.g., ^{111}Cd.
Top center*:* A nucleus with its isomeric state (half-life $T_{1/2}$) and gamma-gamma (γ_1, γ_2) cascade is shown: the PAC probe. The gamma-rays are recorded in four detectors and the "clock" measures the time between two gamma-rays in pairs of two detectors. Thus, the coincidences *C* are produced, creating the decay curve of the isomeric state, ***top left***. During the half-life of the isomeric state, the nuclear moments μ and Q_N are interacting with magnetic hyperfine fields B_{hf} and electric field gradients EFG, respectively, disturbing the nuclear anisotropy. The splitting into sublevels is shown and expressed in interaction frequencies for simple cases, ***top right***. Therefore, the decay curve of the isomeric state (intensity versus time) is modulated by the time-dependent variation of the anisotropy with the underlying frequencies of Eq. (4). ***Bottom left:*** Forming the ratio function R(t), Eq. (5), the half-life of the isomeric state is eliminated and the PAC-time spectrum obtained; an example of a spectrum with its Fourier transforms is shown. ***Bottom right:*** Two examples of simulated PAC-time spectra for probes at terrace and step sites are to be seen. The combined interactions are separated into the individual electric [Eq. (2)] and magnetic [Eq. (3)] time spectra. At steps, nonvanishing asymmetry parameters [Eq. (1)] are present. Usually more than one site is occupied, i.e., several fractions (each for a unique site) contribute to the time spectrum, each fraction having its own set of parameters like amplitude, frequency, etc. The partial amplitudes add up to the R(t) amplitude, thus the partial amplitudes are a direct measure of the fractions. For an unambiguous interpretation, one *dominant* site occupancy is desired and usually prepared.

6. SAMPLE PREPARATION AND MEASUREMENTS AT THE ON-LINE MASS SEPARATOR ISOLDE / CERN

The PAC measurements described in this chapter are performed in the ultra-high vacuum (UHV) chamber ASPIC (**A**pparatus for **S**urface **P**hysics and **I**nterfaces at **C**ERN). This chamber is connected to the on-line mass separator ISOLDE at the UHV beamline, Fig. 3. The target at ISOLDE is bombarded by 1.2 GeV protons from the BOOSTER facility of CERN [36]. By fission, spallation etc., a variety of radioactive nuclei is produced. The mass separator selects the experimentally desired species with very high purity for the UHV beamline. The procedure ensures that no additional contamination spoils the surface of the samples. The samples, metallic disks of single crystals of 1-2 mm thickness and about 12 mm diameter, are prepared by state-of-the-art techniques in the UHV chamber ASPIC [37, 38]. The samples are mounted on a temperature-controlled sample holder on a manipulator, with which they can be moved computer controlled to different positions, never breaking the vacuum. For growing ultra-thin metallic layers on top of the single crystals the samples are moved to various MBE (molecular beam epitaxy) instruments. For controlling of the structure and the chemical composition, they are positioned at LEED (low energy electron diffraction) or AUGER spectrometers, respectively. Finally they are moved to the detector position for PAC measurements, see Fig. 5. Some details are described as follows.

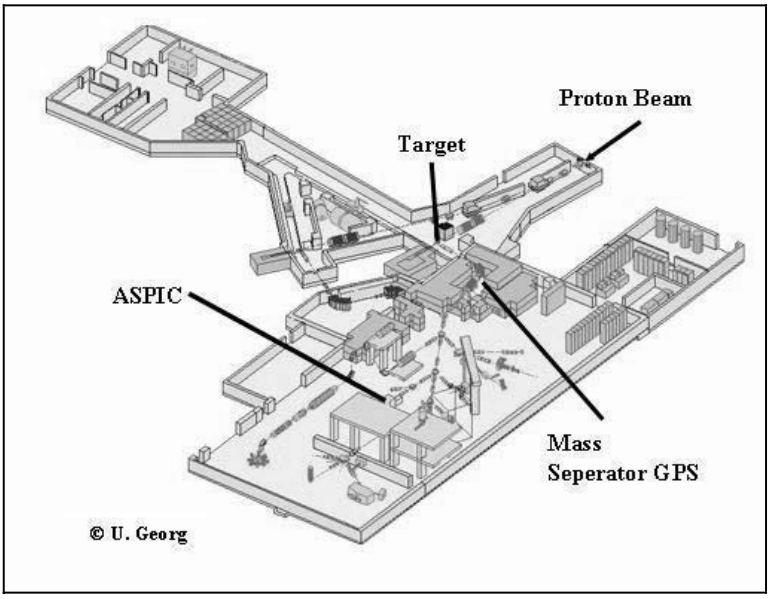

Fig. 3. The on-line mass separator ISOLDE at CERN. The ultra-high vacuum (UHV) chamber ASPIC (Apparatus for Surface Physics and Interfaces at CERN) is located in the center of the experimental hall. It is connected to the mass separator by a UHV beam line. (By courtesy of U. Georg, ISOLDE.)

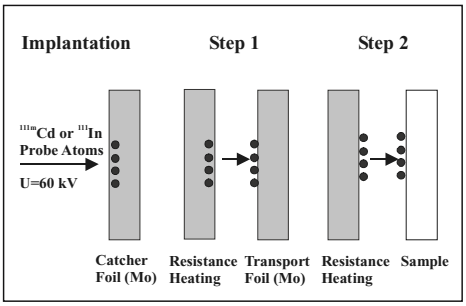

Fig. 4. Schematic description of the sample activation, see text below.

Selected accelerated radioactive ions with a charge state of 1^+ and the energy of 60 keV (in Fig. 4, ^{111m}Cd or ^{111}In are shown; the production of the isotope is dependent on the target and the ionisation technique [36]) are implanted into a precleaned catcher foil of Molybdenum (vertical mounted in the prechamber of ASPIC, see Fig. 5) until an activity of about 10 times the amount necessary for a PAC measurement is accumulated. Dependent on the probe species, this takes seconds (for ^{79}Kr) or a few hours (for ^{77}Br, ^{111}In). After the implantation, the catcher will be flashed at a temperature below the evaporation temperature of the probe atoms out of the Mo foil, in order to get rid of rest gas atoms on the surface. By resistance heating at high temperature, the probe atoms are evaporated from the catcher foil onto the carefully precleaned transport foil moved exactly below and very close to the catcher. The transport foil is then flashed at an appropriate temperature and moved into the main chamber of ASPIC. Again the positions of the transport foil and the sample (e.g., a single crystal of Ni) have to be adjusted to each other very carefully before the probe atoms are evaporated from the transport foil to the sample surface, now at a considerably lower temperature. By this "soft landing" procedure, the probe atoms can be brought even into adatom positions on the sample surface if the sample is at the appropriate temperature. At each evaporation step, only 30% of the probes are transferred. - Such a (nearly) contamination-free activation of the samples is only achieved with mass separators.

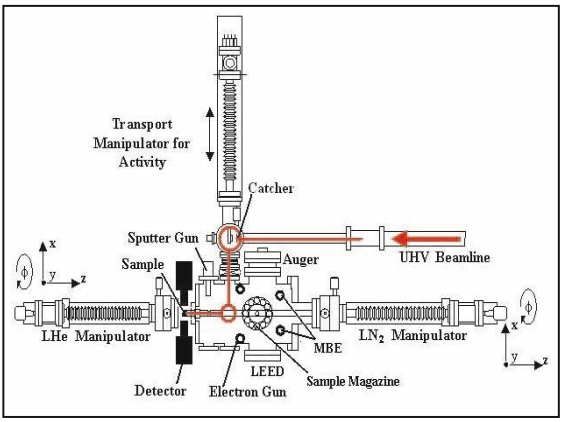

Fig. 5. The UHV chamber ASPIC is connected to the UHV beamline of the on-line mass separator ISOLDE, see Fig. 3. The path of the ions (probes) is shown in red colour. The two red circles mark the evaporation steps which are explained in Fig. 4.
This chamber was initially assembled by S. Seeger and H. Granzer, with the assistance of the Konstanz group. Its computer controlling was programmed by R. Kowallik.

7. ADATOMS ON FERROMAGNETIC SURFACES

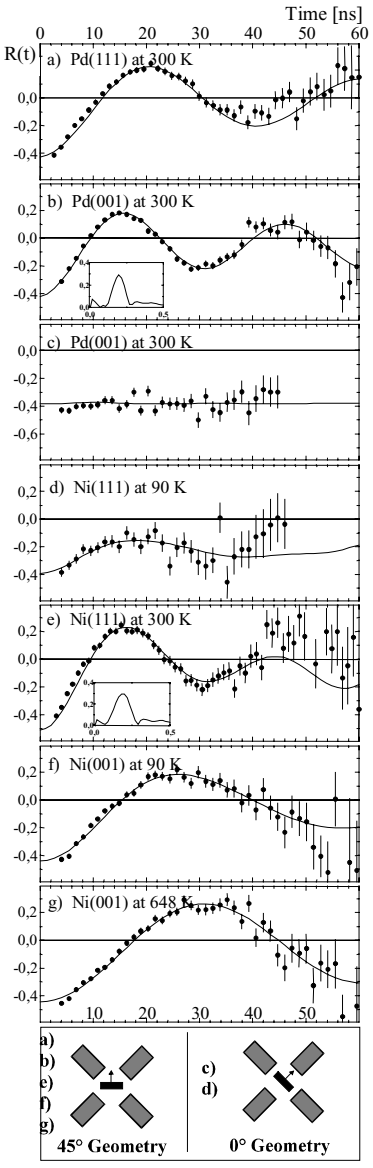

The magnetic hyperfine fields of many elements of the Periodic Table implanted into the ferromagnets Fe, Co, Ni, and Gd have been measured during several decades and most of them can be found in the compilation of Ref. 39. Meanwhile, for essential cases theoretical calculations were performed [40-42] and it was found that (besides the degree of the *s*-electron polarisation which rules the strength of the hyperfine fields) the bonding and antibonding *s*-states near the Fermi energy are responsible for the sign of the field, i.e., the antibonding states produce a positive sign.

The first measurement of the magnetic hyperfine field of an adatom on a ferromagnetic surface, i.e., outside of the lattice, was performed by the Konstanz group, although never published [43]. A field of $|B_{hf}| = 7.3(2)$ T was found for Cd (recently reproduced by the Berlin group at ISOLDE) on the Ni surface with (001) orientation and at a temperature of T = 80 K. The absolute value resembled the bulk value of Cd in Ni, $B_{hf} = -6.9(1)$ T [39, 44] and did hide the very interesting physics in this field emerging in the next few years. Meanwhile, calculations require a positive sign for the Cd-adatom hyperfine field [45]. We note here that adatoms are related to rather small coordination numbers, for Cd on Ni(001) the four-fold hollow site is occupied, the number of nearest neighbours is NN = 4, and on Ni(111) the three-fold hollow site with NN = 3, see also Figs. 9 and 10 in section 8.

Fig. 6. PAC-time spectra R(t) (see Eq. (5) in section 5) for ^{77}Se adatoms on Pd(111), Pd(001), Ni(111), Ni(001) surfaces at different temperatures. The detector geometry is shown below. The solid lines represent fits to the data [35]. In b) and e), Fourier transforms are inserted. (From Ref. 21)

In 1994, the Konstanz and the Berlin groups performed a series of adatom measurements on Ni(001) and Ni(111) surfaces using ^{77}Br which decays to the ^{77}Se-PAC probe. Within the 4*sp*-electron elements, Se - positioned in the middle of the series - experiences the largest magnetic hyperfine field in Ni bulk: $B_{hf} = +16$ T [46]. On the basis of no expectations, since no calculations for surfaces were known, the experimentally found values were $|B_{hf}| = 1$ T on Ni(001) and $|B_{hf}| = 3$ T on Ni(111) [21]. The half- live of the intermediate isomeric state of ^{77}Se (see Fig. 2) is rather short: $T_{1/2} = 9.3$ ns. Therefore, the PAC-time spectra are difficult to evaluate for combined interactions. In order to obtain unambiguous results for the magnetic fields, similar experiments were performed on isoelectronic Pd surfaces where only the electric field gradient is present; PAC spectra are shown in Fig. 6. Even the tendency of the temperature dependence could be measured, since the precursor isotope Br of the PAC probe remains an adatom over the whole temperature range of interest (in contrast to metallic impurities, next section). Fig. 7 presents all results.

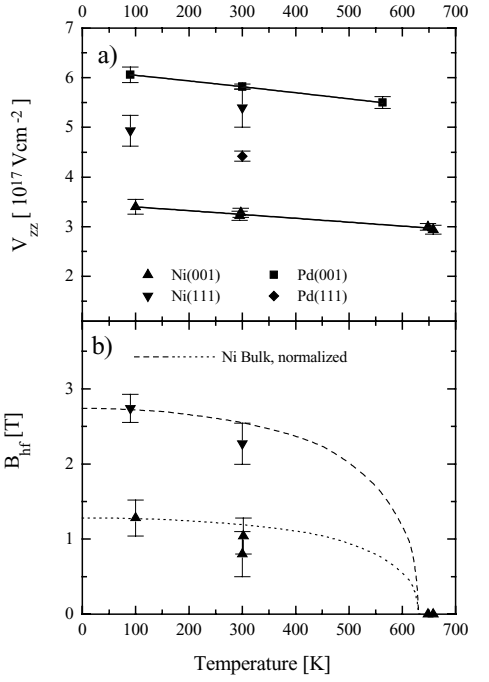

Fig. 7. Electric field gradients (V_{zz}) in a) for Se on Ni and Pd surfaces with (001) and (111) orientation and magnetic hyperfine fields (B_{hf}) in b) for Se on Ni(001) and Ni(111) surfaces. Solid lines in a) are fits to a linear temperature dependence. Dashed and dotted lines in b) refer to the bulk magnetisation of Ni according to Weiss and Forrer [47]. (From Ref. 21)

These findings for Se as adatoms on Ni showed a very different behaviour on surfaces as compared to the bulk, and immediately prompted a theoretical study [48]. The theoretical explanation is schematically depicted in Fig. 8.

Correlated with the reduced symmetry at the surface, in particular at the lower coordination number NN = 4 [impurity adatom on Ni(001)], the *s*- and *p*-impurity states form on-site sp_z - hybrids with z denoting the component perpendicular to the surface plane. Since two of such hybrids exist (outside/inside direction), a doubling of the number of bonding and antibonding states in the *s*-density of states is obtained for the adatom. Furthermore, the reduced coordination number causes a weaker hybridisation between the impurity states and the *d* orbitals of the Ni substrate atoms leading to a much smaller splitting of the bonding and antibonding *s* states. In summary, the calculations lead to a drastic change of the local density of states especially for the *s* electrons below and close to the Fermi level and consequently to a drastic change of the magnetic hyperfine fields.

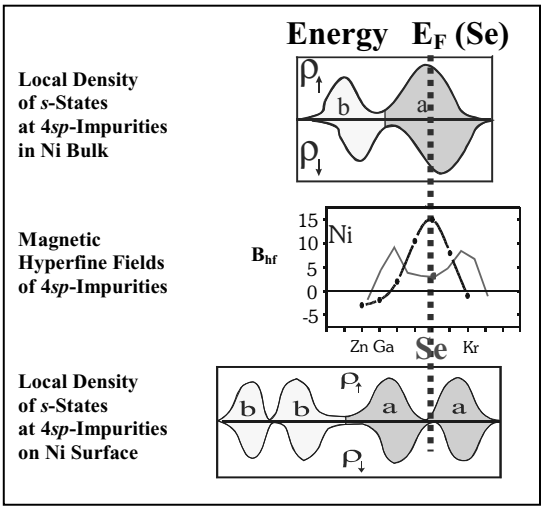

Fig. 8. Brief explanation for magnetic hyperfine fields (B_{hf}) of 4*sp* elements *in* and *on* Ni.
Top: Local density of *s*-states close to the Fermi energy E_F [40-42]. The dotted blue line, E_F, is at the maximum of the antibonding states (a). B_{hf} of Se is strong and positive.
Centre: Experimental values in Ni bulk [39, 46, 49], black line.
Red line: Theoretical predictions of Mavropoulos et al. [48] for adatoms on Ni(001); dot: experiment [21].
Bottom: On the surface, the bonding (b) and antibonding (a) states split due to the symmetry breaking [48], E_F is at a minimum, almost equalising spin up and spin down *s* electrons. B_{hf} is small but still positive.

Meanwhile the measurements on Ni have been extended to the other 3*d* elements Fe and Co (not yet published [50]). The result for Fe(001) ($|B_{hf}| = 6.1(3)$ T) is in accordance with the predictions [48] whereas for Co(0001) ($|B_{hf}| = 2.2(2)$ T) no calculations are performed. The fields in Fe and Co bulk are $B_{hf} = +69(5)$ T and $B_{hf} = +42(4)$ T, respectively [39].

So far, the drastic change was experimentally (and theoretically) treated from Ni bulk, where the site of the impurity is determined by the coordination number NN = 12, to the surfaces with the coordination number NN = 4. Now the question arose about the complete coordination-number dependence of the magnetic hyperfine fields and therewith the dependence of the *s*-electron polarisation at the impurity. This will be presented in the next section for the 5*sp* element Cd.

8. COORDINATION-NUMBER DEPENDENCE OF MAGNETIC HYPERFINE FIELDS AT Cd IMPURITIES ON Ni SURFACES

In order to study the coordination-number dependence of magnetic hyperfine fields at Cd impurities on surfaces, the different surface orientations may be regarded first. In Fig. 9, all regular sites for impurities on the Ni(001) surface are shown.

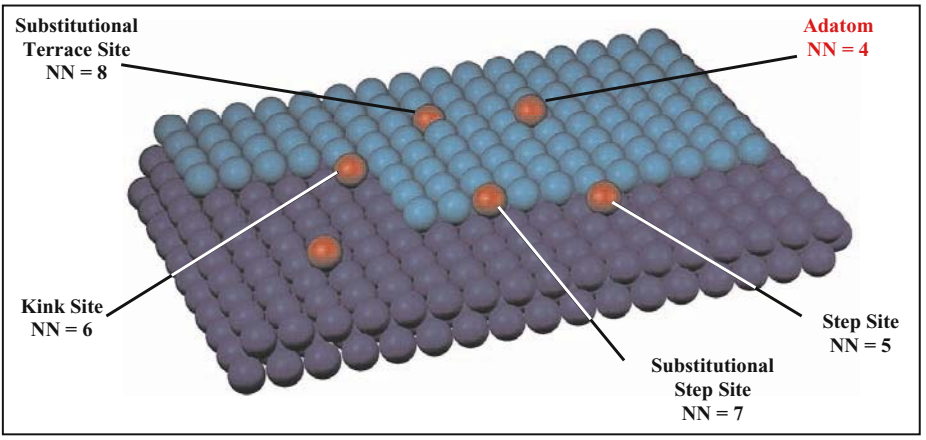

Fig. 9. 3D visualisation of an idealised surface of a Ni single crystal with (001) orientation and a step, indicated by the different blue colours. All possible regular lattice sites for impurity atoms as local probes are indicated in red. The probe atoms can be distinguished by the number of their immediate Ni neighbours, the coordination number NN, e.g., the adatom has the coordination number NN = 4 which is indicated in red colour and was treated for the 4*sp* element Se in the preceding section. In order to obtain NN = 3, the adatom has to be positioned on Ni(111), see Fig 10.

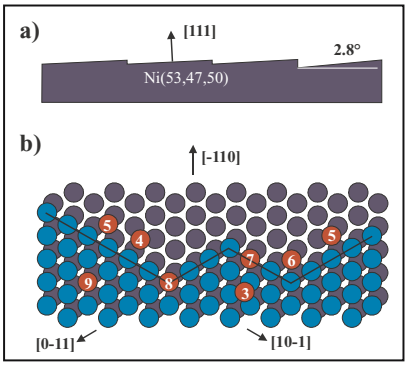

Fig. 10. Side view **a)** and top view **b)** of a vicinally cut (in the [-110] direction) single crystal of Ni(111). Zigzag-shaped steps are obtained as shown in the top view **b)**. All sites for impurities are given as full red circles including the respective coordination number.

By a carefully chosen sample preparation, mainly by the choice of temperature, each of these surface sites can predominantly be occupied by the probe atoms. Depositing the radioactive probes at lower temperatures, T < 90 K, essentially only adatom sites are occupied on Ni(001) because of the restricted surface motion for Cd. For Ni(111), we found stable adatom sites for T ≤ 36 K. Increasing the sample temperature after deposition, the probes move to steps, kinks, at further increased temperatures the probes are found to be incorporated in the first row of the steps. At room temperature, the probes usually are found to be incorporated in terraces. This can be optimised by annealing up to 400 K. The occupation of different surface sites does not only depend on the mobility of the impurity but also on the temperature-dependent mobility of the host atoms on the surface. A further successful manipulation is achieved, when the probes are deposited at a certain temperature and then a submonolyer of Ni is grown by MBE. Thus, by a rather complex sample preparation procedure, selected sites can be occupied in order to obtain PAC spectra for an unambiguous interpretation. Very helpful are the results of earlier experiments on similar but nonmagnetic metallic surfaces such as Pd(111) [9], Pd(001) [51], Cu(001) and Cu(111) [52]. The EFGs are not the same but they show comparable tendencies, in particular in the trend from large EFG values at substitutional terrace sites (with $\eta \approx 0 \approx \beta$) to small EFG values at free terrace sites (adatoms), also with $\eta \approx 0 \approx \beta$, see definition (1) in section 5. The EFGs at steps and kinks lie in between these values with respect to their strength; in addition, they have nonvanishing η and β values (see also appendix of this section).

The magnetic hyperfine fields are measured simultaneously and therefore the B_{hf} and EFG values have to be extracted from the same PAC-time spectra [53]. The magnetic hyperfine fields vary considerably from site to site. With the also varying EFGs, the PAC-time spectra show respectively different patterns. Fig. 11 presents three examples.

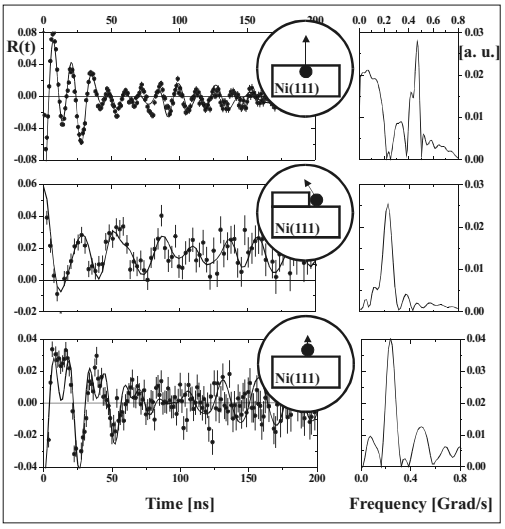

Fig. 11. PAC-time spectra of ^{111}Cd (with Fourier transforms on the right) at different sites on a Ni(111) surface. These selected sites are illustrated in the icons; the arrows indicate the size and the orientation of the EFG.
Top: Probe atoms are at substitutional terrace sites.
Centre: A non-repetitive pattern occurs at sites, where the axial symmetry is lost, $0 < \eta \leq 1$. The PAC measurement represents a fraction of 22(3) % probe atoms at kinks and 17(3)% at free step sites.
Bottom: Probe atoms at free terrace sites (adatoms) can only be observed at low temperatures.
(From Ref. 53)

Since each site of the Cd impurity is characterised by the coordination number of nearest Ni neighbours (NN), the measured $|B_{hf}|$ values can be ordered versus the (decreasing) coordination number, Fig. 12. The bulk value is included with B_{hf} = -6,9(1) T [44], the only measurement so far, where also the sign was determined experimentally. Calculations for the magnetic hyperfine fields at Cd as adatoms on Ni(001) and Ni(111) predict positive fields [45]; therefore, starting with a negative field for NN = 12 (bulk) and ending with positive fields for NN = 4 and NN = 3 on Ni(001) and Ni(111), respectively, the nonlinear curve (Fig. 12) for increasing magnetic hyperfine fields versus decreasing coordination numbers was found in the Ph.D. thesis of K. Potzger [54, 53]. However, several Ph.D. theses contributed single results: J. Voigt [43, 23] and H. Granzer [55, 30] at a time, when no ordering was possible, and (in cooperation with K. Potzger) A. Weber [50, 53].

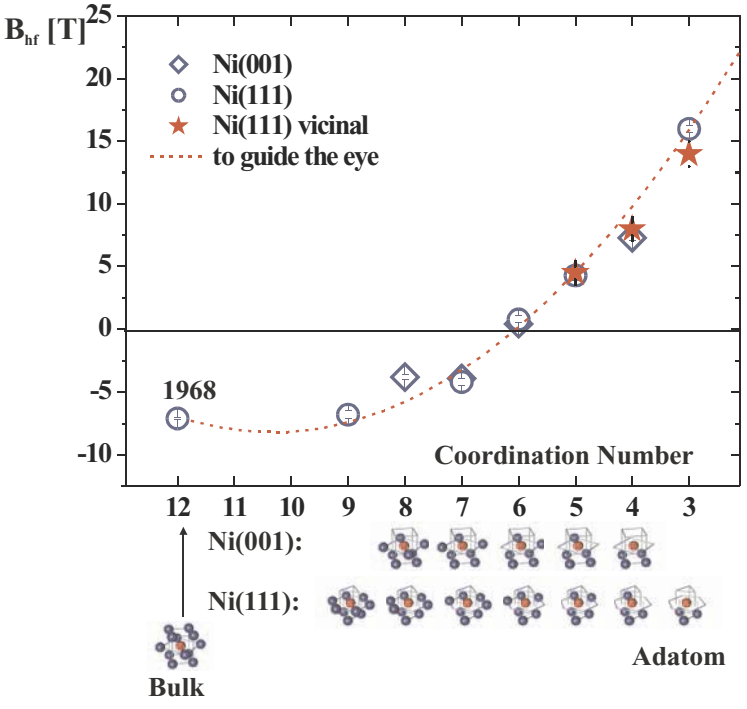

Fig. 12. Magnetic hyperfine fields B_{hf} at ^{111}Cd versus decreasing coordination number NN of neighbouring Ni atoms. The coordination numbers for the different surface orientations are depicted in the various icons on the x-axis. The values for NN = 4 and 6 of Ni(001) are taken from Ref. 43. The bulk measurement is included for which the only sign assignment exists, see Ref. 44. For NN = 3 and 4, positive signs were predicted [45]. The red stars refer to the measurement described in section 9.

The behaviour of magnetic hyperfine fields versus the coordination number is the subject of several recent calculations with different approaches. As mentioned in section 7, bulk values were calculated in the eighties [40-42] and the hyperfine fields for surface atoms in the nineties [45, 48]. The publication on the experimental coordination-number dependence [53] caused a theoretical study by Ph. Mavropoulos [56] extending the work of Ref. 48 where the 4*sp* elements were treated. The calculations were based on the local spin-density approximation of density-functional theory. The full-potential Korringa-Kohn-Rostoker Green's function method for defects at surfaces was employed [57]. This time [56], the calculations of the magnetic hyperfine fields were applied to the 5*sp* impurities for most of the coordination numbers. The result shows that also a strong coordination dependence is observed for calculated hyperfine fields, and, in addition, the coordination-number dependence is different and characteristic for each impurity. For Cd, the experimental trend was confirmed: increasing B_{hf} versus decreasing NN. An opposite behaviour is predicted for Te: small fields at the surface, a large value in the bulk (the latter was experimentally known [39]). Meanwhile, a second theoretical study was performed [58]. In this study, lattice relaxation around the impurity at the surface was taken into account. State of the art first-principles techniques, developed within the density-functional theory [59] were employed. Most of the calculations have been performed using the full-potential augmented plane wave + local orbitals method as implemented in the *WIEN2k* package [60]. Fig. 13 shows the results along with the experimental values taken from Fig. 12.

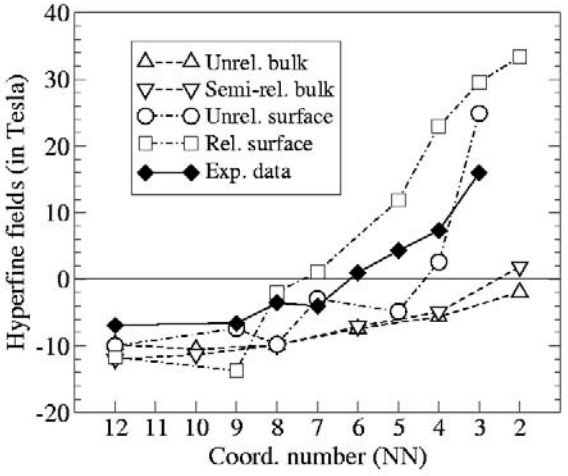

Fig. 13. Calculated coordination-number dependence of the Cd hyperfine field in and on Ni [58]. Circles show the results for an unrelaxed surface and are very close to the results of Mavropoulos [56]. Open squares represent the calculations taking into account surface relaxations around the impurity. The experimental data are from Fig. 12 [53]. (Triangles refer to simulations with bulk cells [58].) (By courtesy of S. Cottenier and V. Bellini.)

In parallel to our publication on the coordination-number dependence and shortly after, a series of studies in theory and experiment was published where the coordination number plays an important role on the magnetic properties. These studies treated small metallic clusters attached to surfaces. Adatoms and small clusters on Ag and Au surfaces where treated theoretically by Cabria et al. [61]; Lazarovits et al. [62] studied small Fe, Co and Ni clusters on a Ag surface. The magnetism of Co clusters in a Cu surface was considered by Klautau et al. [63]. Experiments on small Fe clusters on ultra-thin Ni were published by Lau et al. [64] and on small Co clusters on Pt surfaces by Gambardella et al. [65]. Already in earlier publications much attention was paid to magnetic systems where single transition-metal atoms were attached to metallic surfaces and their enhanced *d*-moments and spin-orbit coupling were calculated [66 - 68]. However, much less attention was paid to the change of the properties, in particular, the magnetic properties of the substrate atoms which are in contact with the clusters or adatoms. If we compare all these studies with our experimentally found coordination-number dependence for nonmagnetic impurities, we might conclude that the nonmagnetic impurities on a ferromagnetic substrate form cluster-like magnetic units together with their nearest neighbours: *impurity-induced magnetic units*. The nearest neighbours with their localised *d*-band are distinguished from all other atoms of the surface by the *sd* hybridisation with the impurity leading to the induced valence polarisation at the impurity [48].

In the above mentioned recent works on surface-attached clusters, in particular, in the experimental studies, the question of the symmetry dependence of the magnetic properties was addressed but not conclusively answered. For the impurity-induced magnetic units we found a symmetry *in*dependence for the coordination-number dependence in an experiment where we had to take advantage of the atomic resolution in PAC spectroscopy on surfaces in an *advanced* state-of-the-art experiment. This will be presented in the next section.

Appendix to section 8

The determination of surface sites for probe atoms is a nontrivial procedure and requires considerable knowledge on EFGs collected in many years on various "similar" surfaces as mentioned above with the citation of several other works [9, 51, 52]. In Fig. 14, the B_{hf} values are shown, this time with the respective V_{zz} values measured simultaneously. Thus, the identification of surface sites, i.e., the coordination number NN, is obtained with the mutual help of B_{hf} and V_{zz} values.

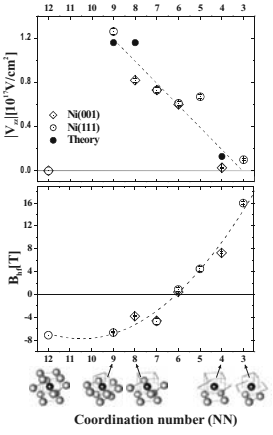

Fig. 14. Measured electric field gradients (V_{zz}) (***top***), theoretical values from Ref. 45; magnetic hyperfine fields B_{hf} (***bottom***) from Fig. 12. Although also the EFGs show a strong dependence on the coordination number, the underlying physical mechanisms for B_{hf}s and EFGs are quite different. The coordination-number dependence of the EFGs was treated very recently in a comprehensive study [69].

9. SYMMETRY INDEPENDENCE OF IMPURITY-INDUCED MAGNETIC UNITS

In Fig. 12, the coordination numbers on the x-axis are decorated by icons. The icons show how the different coordination numbers can be obtained on Ni(001) and on Ni(111). We noticed with interest that the corresponding hyperfine fields are the same, see NN = 6 and NN = 7. This observation raised the question whether the hyperfine fields are independent on the local structure and only dependent on the coordination number. However, the local structures at NN = 6 and NN = 7 are not too different in order to answer this question unambiguously. The local structures at lower coordination numbers are very different, as well as the magnetic hyperfine fields. In Fig. 15, the difference is seen in a 3D illustration including a model how the coordination number 4 might be realised on Ni(111).

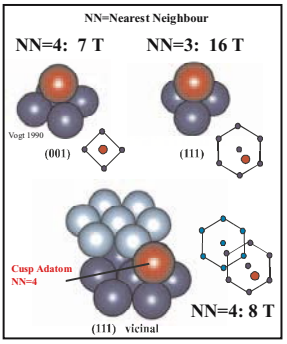

Fig. 15. 3D visualisation of NN = 3, NN = 4.
Top: Icons illustrating the fourfold hollow site on Ni(001) and the threefold hollow site on Ni(111).
Bottom*:* Positioning an impurity at NN = 4 on Ni(111) at a step: the surface of Ni(111) consists of hexagons. The impurity occupies a threefold hollow site on a lower terrace in contact with only *one* atom of a hexagon of the upper terrace. Fig. 16 demonstrates, how such a positioning is realised.
The respective measured B_{hf} values are inserted.

Recently, it has been possible to measure the magnetic hyperfine field for NN = 4 on Ni(111) [70]. This configuration is not easy to obtain and requires a very subtle sample preparation. The vicinally cut single crystal of Ni(111) was taken with zigzag-shaped steps, Fig. 10. Fig. 16 shows a cusp of such a step revealing two different types of ledges.

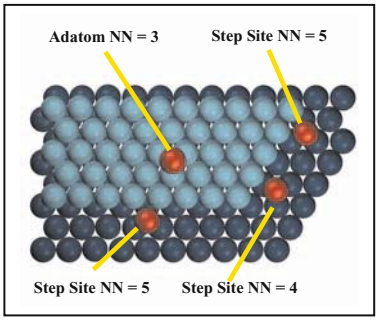

Fig. 16. Part of a zigzag-shaped step on Ni(111) from Fig. 10. The ledge in the [0-11] direction (horizontal) offers only sites with NN = 5, the ledge in the [10-1] direction offers additionally sites with NN = 4. (In Ref. 70, the designation is erroneously exchanged in the caption of Fig. 1). NN = 4 is required for the present investigation, see Fig. 15.

By soft landing of Cd probe atoms onto a Ni(111) surface at a temperature of 36 K, only the adatom position (NN = 3) is occupied [53]. Furthermore, it was found in Ref. 53, that at 45 K all adatoms had left their adatom position and were moved to steps. For the present experiment [70], the temperature of 39 K was chosen with the result, that most of the probe atoms moved to the two types of steps, see Fig. 16. A certain amount was still at the adatom position sufficient for identification in the PAC-time spectrum, Fig. 17.

The PAC spectrum, Fig. 17, revealed two known fractions [53], the adatoms with the largest B_{hf} value (NN = 3) and the step atoms for NN = 5 with $|B_{hf}| = 4.5(5)$ T. Besides these two fractions, a third so far unknown fraction was found, with an EFG similar to step atoms, but with $|B_{hf}| = 8.1(5)$ T. This new fraction was attributed to the only possible remaining regular site, to the step adatom with NN = 4, see Fig. 16. Although the local geometry is very different from NN = 4 for Ni(001), see Fig. 15, almost the same magnetic hyperfine field was obtained for both structures. The slight deviation from 7.3(2) T [43] to 8.1(5) T might be deduced from the following consideration: in the structure for NN = 4 on Ni(111) the fourth atom has a slightly larger distance. All three values are shown as red stars in Fig. 12.

The spin polarisation of the *s* electrons at the Cd impurity, transferred via the *sd*-electron hybridisation from the neighbouring Ni atoms, is independent of the local symmetry even at low coordination numbers. This observation unambiguously confirms the conclusion: predominantly the coordination number determines the magnetic behaviour at the 5*sp*-impurity on Ni. The nonmagnetic single atom obtains an *s*-moment induced by the nearest Ni neighbours. The impurity along with the Ni neighbours form a zero-dimensional cluster-like magnetic unit - mediated predominantly by the *sd*-hybridisation - on a two-dimensional ferromagnetic substrate. The size of the units can be manipulated by the choice of the surface site and the local symmetry can be changed without measurable effects.

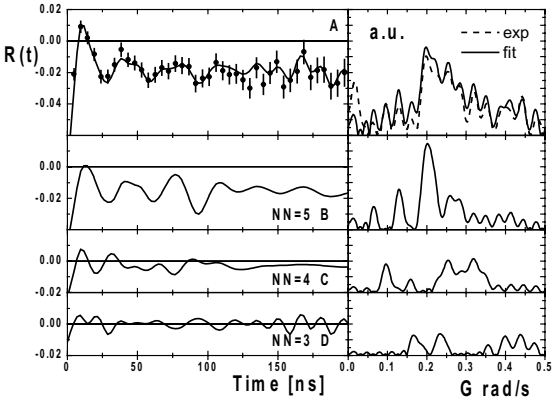

Fig. 17. PAC-time spectrum R(t) of ^{111}Cd on a terraced $Ni_v(111)$ surface at 39 K, (v = vicinal). Part **A** shows the data together with the fit of the three fractions. The fit function is partitioned into the three fractions of probe atoms: **B** free step atoms NN = 5, (20 %), **C** free step atoms NN = 4, (10 %), **D** adatoms NN = 3, (5 %). On the right, the respective Fourier transforms are shown.

10. MIXED COORDINATION NUMBERS

In an earlier experiment, Pd was grown on Ni(001) and the probes were incorporated in Pd on Ni [30]. In Pd, magnetic moments are induced by the ferromagnetic Ni substrate. These moments cannot be measured directly by hyperfine interactions; they were calculated to be 0.2 μ_B [71]. For ^{111}Cd in one (or two) monolayers of Pd on Ni(001) [30] as well as on Ni(111) [72], static magnetic hyperfine fields were measured confirming a ferromagnetic order in Pd induced by the ferromagnetic Ni substrate. A PAC-time spectrum for ^{111}Cd in Pd on Ni(001) is shown in Fig. 18.

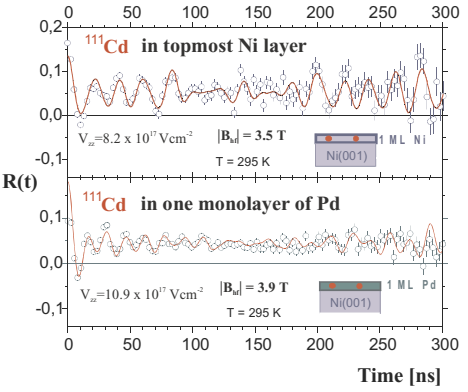

Fig. 18. PAC-time spectra of ^{111}Cd in the topmost layer of Ni(001) and in one monolayer Pd grown on Ni(001) at RT.

Proceeding systematically by growing 0.5, 1, 1.5, etc. monolayers of Pd on Ni, with (001) and (111) orientation, some of the neighbouring Ni atoms next to the Cd probe were replaced by Pd neighbours step by step and a variety of different mixed coordination numbers for the impurity Cd could be achieved. The respective hyperfine fields were measured. The results are collected in Fig. 19.

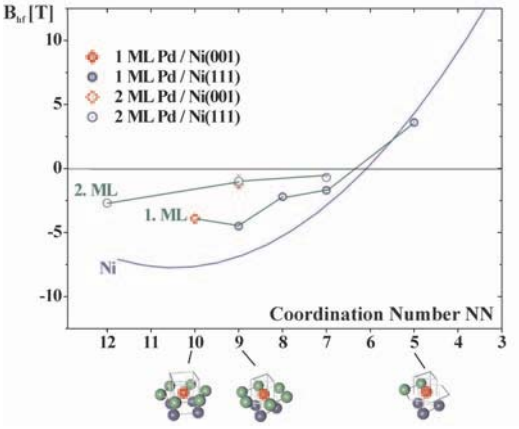

Fig. 19. Magnetic hyperfine fields versus mixed coordination numbers. The blue line represents the data from Fig. 12. The green lines correspond to measurements, were the probes are incorporated in the first or second monolayer of Pd on Ni. Some icons are shown on the x-axis, Ni atoms in blue, Pd atoms in green, probes in red colour. Note, that in this system even NN = 10 can be realised, since Pd grows on Ni(001) with an (111) orientation as on Ni(111).

In Fig. 19, it can be seen that with increasing number of Pd neighbours at Cd the B_{hf} values become smaller. This is expected because of the considerably smaller (induced) magnetic moment at Pd.

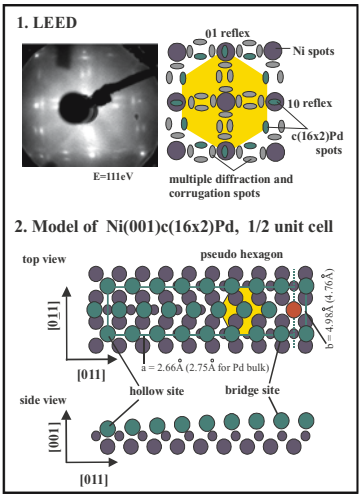

Fig. 20. LEED of Pd on Ni.
Upper part: LEED pattern of one monolayer Pd grown on Ni(001).
Lower part: Deduced model of a Ni(001)c(16x2)Pd unit cell (only left half of the cell is shown; Ni: blue circles, Pd: green circles). The top view depicts the varying Pd/Ni geometry, the side view shows the corrugation of Pd on Ni. One hollow site in the unit cell of Pd is replaced by a radioactive impurity probe (red colour).

A rather remarkable observation emerged during the course of this series of experiments. We start with its description by regarding Fig. 20 which shows a LEED (low energy electron diffraction) picture of one monolayer Pd on Ni(001). The different lattice parameters of Ni and Pd cause an incommensurable growth of Pd resulting in (16x2)Pd unit cells. Observing the Pd atoms with respect to the Ni atoms of the substrate, we note that the atomic Ni/Pd geometry varies from Pd atom to Pd atom. Consequently, the 3*d*-4*d*-electron hybridisation between Ni and Pd and the induced magnetic moments in Pd vary from neighbour to neighbour. Replacing stable Pd atoms by a (small number) of radioactive ^{100}Pd atoms decaying to the PAC probe ^{100}Rh (see Fig. 1) it is expected that a variety of magnetic hyperfine fields occur. This was proven in Ref. 29. However, if a Cd *impurity* is used in PAC measurements only *one* discrete frequency for the combined interaction could be observed, suggesting that only selected sites are occupied by the impurity within the unit cells. In Ref. 30, the bridge site occupation was assumed. After the finding of the strong coordination number dependence this assignment has to be revised, only the hollow site is in accordance with the coordination-number dependence.

A similar experiment with Pd on Ni(111) where Pd forms (13x13)Pd unit cells leads to a similar result. Only *one* magnetic hyperfine field is detectable for Cd incorporated in the monolayer Pd on Ni(111). The value of the magnetic hyperfine field is compatible with the (mixed) coordination number 9, Fig. 19.

Taking into consideration the results of section 8 and 9 in combination with the present section 10, the following conclusion is drawn: the nonmagnetic Cd atoms, embedded in an atomic Pd layer on a two-dimensional ferromagnetic Ni substrate, form cluster-like zero-dimensional magnetic units. - Replacing the nonmagnetic atoms by magnetic ones, this might be useful for possible applications as will be discussed in the following section.

11. CONCLUSIONS AND OUTLOOK

The studies on the atomic scale of the behaviour of single nonmagnetic atoms at ferromagnetic surfaces and interfaces result in two observations:

- The impurities induce cluster-like magnetic units by the inclusion of their nearest neighbours mediated by the *sd* hybridisation, illustrated in Fig. 21.
- Within the unit cell of an epitaxily grown Pd layer on Ni (with a considerable different lattice parameter) the impurities select only one type of sites (out of many) hinting at the opportunity for ordered structures, see an example in Fig. 22.

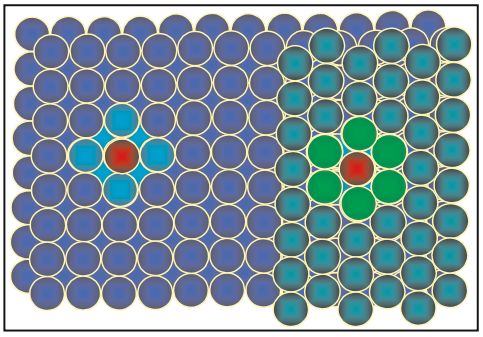

Fig. 21. Impurities (red colour) in a Ni(001) surface (blue colour) and in one monolayer Pd(111) (green colour) on Ni(001), both at terrace sites. The nearest neighbours (NN) of the impurities are displayed by lighter colours.
The impurity in Ni has 8 NN of Ni; the impurity in Pd has 4 NN of Ni and 6 NN of Pd.

In section 10, it was observed that in one monolayer of Pd on Ni(001) or on Ni(111), only *one* discrete combined interaction frequency can be found at room temperature in the PAC spectrum. Along with the strong coordination-number dependence, the conclusion could be drawn, that only hollow sites are selected by the impurity.

Although all experiments were performed with radioactive impurities, these results are also valid for stable atoms of the same element. Anticipating further experiments, we assume, that with the appropriate amount of impurity atoms approximately all hollow sites in the (13x13)Pd unit cell on Ni(111) - as shown in Fig. 22 - can be occupied, although in the experiments with radioactive probes, statistically only one hollow site out of 30 unit cells was occupied. Future experiments applying scanning tunnelling microscopy on a sample with stable atoms have to confirm these expectations.

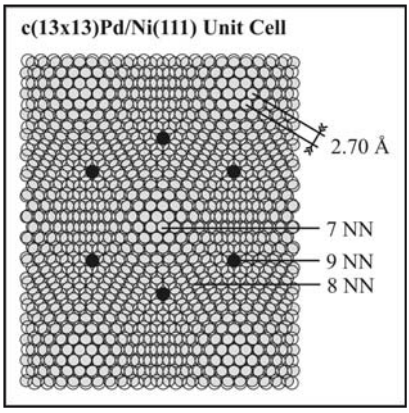

Fig. 22. Moiré pattern as modelled from a LEED investigation of Pd(111) on Ni(111) caused by the different lattice parameters. PAC spectroscopy with ^{111}Cd [72] revealed that sites with 7 or 8 NN, e.g., remain empty, only NN = 9 is occupied.
If all NN = 9 sites are occupied by stable impurities (black dots), the present figure is obtained.

We assume that the above mentioned two observations hinting at the opportunity for ordered structures of impurity-induced zero-dimensional cluster-like magnetic units in two-dimensional ferromagnetic surfaces are not only valid for Ni/Pd systems but also for a large variety of systems including Fe, Co or Gd. With such systems, we possibly obtain a basis for functional materials.

Let us discuss *one* possible example: from a simple consideration one can deduce that a two-dimensional magnetic peta-bit memory (10^{15} bits cm^{-2}) will never exist, because this is just about the number of atoms on 1 cm^2. The mutual influence ("cross talk"), in particular in collective phenomena, prohibits that each atom may carry a message, e.g., spin up or spin down. If single atoms (or small clusters) may carry information independently, they have to be separated from each other, e.g., by surrounding atoms of another species, by a number of about 100 or 1000. Consequently, at best we can expect a two-dimensional magnetic tera-bit memory (10^{12} bits cm^{-2}). The above described devices offer patterned structures, where 10^{13} unit cells/cm^2 are available, still allowing for 90% to be defect.

It is unlikely that nonmagnetic impurities are useful for basic magnetic building blocks in electronic or spintronic devices. More promising are magnetic atoms, such as rare earths. In Fig. 23, an artist's view is given for isolated or ultra-small clusters of rare earth impurities. Let us assume, that a 4*f*-5*d* impurity, e.g. Gd, is embedded in a 4*d* environment, e.g. Pd, on a ferromagnetic 3*d* substrate, e.g. Ni: the competition between 3*d*- 4*d*- 5*d*-electron couplings might even allow for two different states, stable at room temperature although at present, nothing is known about the magnetic behaviour of a rare earth atom in such an environment. - First experiments with Gd are in progress at ASPIC.

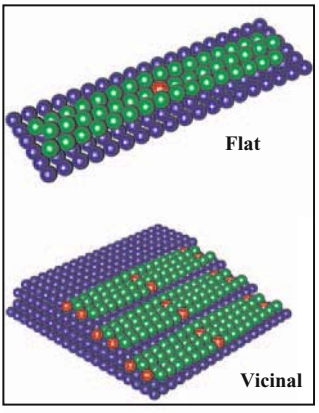

Fig. 23. Artist's views.
Top: An ordered structure of isolated impurities (e.g., rare earth atoms) embedded in a monolayer (e.g., Pd) on a ferromagnetic surface (e.g., Ni). Pd forms 10^{13} unit cells/cm^2 on Ni of which one is shown. The impurities occupy selected sites within the unit cell.
Bottom: Ordered structure of ultra-small clusters of impurities on a regular Pd-covered stepped surface.

ACKNOWLEDGMENTS

The author is grateful to all "members of ASPIC" who have engaged themselves in the construction and scientific use of the ASPIC equipment at CERN: S. Seeger, R. Kowallik, H. Haas, W.-D. Zeitz, Doris Forkel-Wirth, H. Granzer, K. Potzger, H.-H. Blaschek, A. Weber, Y. Manzhur, M. J. Prandolini, the Tel Aviv/Israel group, the Riken/Japan group, and in particular, the ISOLDE collaboration. J. Röhrich and P. Imielski supported the design of this chapter.

REFERENCES

[1] J.A.C. Bland and B. Heinrich (Eds.), *Ultrathin Magnetic Structures,* Springer-Verlag, Berlin (1994)

[2] Robert C. O'Handley, *Modern Magnetic Materials*, John Wiley & Sons, New York (2000) pp 432

[3] H.S. Nalwa (Ed.), *Magnetic Nanostructures,* American Scientific Publishers, California (2002)

[4] *Magnetismus von Festkörpern und Grenzflächen,* Vorlesungsmanuskripte Forschungszentrum Jülich (1993), ISBN 3-89336-110-3 *Magnetische Schichtsysteme in Forschung und Anwendung,* Vorlesungsmanuskripte Forschungszentrum Jülich (1998), ISBN 3-89336-235-5

[5] T. Shinjo, Surf. Sci. Rep. 12 (1991) 49 and Refs. therein
U. Gradmann in *Handbook of Magnetic Materials*, Vol.7 (Ed. K.H.J. Buschow), Elsevier S.P., Amsterdam, (1993), pp 1

[6] *Table of Isotopes,* 8th ed., (Eds. R.B. Firestone and V.S. Shirley), Wiley & Sons, New York (1996)

[7] W. Körner, W. Keppner, B. Lehndorff-Junges, and G. Schatz, Phys. Rev. Lett. 49 (1982) 1735

[8] W. Keppner, T. Klas, W. Körner, R. Wesche, and G. Schatz, Phys. Rev. Lett. 54 (1985) 2371

[9] E. Hunger and H. Haas, Surf. Sci. 234 (1990) 273

[10] C.R. Laurens, M.F. Ro u, F. Pleiter, and L. Niesen, Phys. Rev. Lett. 78 (1997) 4075

[11] M.F. Ro u, C.R. Laurens, A. Falepin, M.A. James, M.H. Langelaar, F. Pleiter, O.C. Rogojanu, and L. Niesen, Phys. Rev. Lett. 81 (1998) 4680

[12] M. Fanciulli, A. Zenkevich, and G. Weyer, Appl. Surf. Sci. 123/124 (1998) 207 B. Roldan Cuenya, M. Doi, and W. Keune, Surf. Sci. 506 (2002) 33 R. Röhlsberger, Hyperfine Interact. 144/145 (2002) 33

[13] E. J dryka, M. Wójcik, S. Nadolski, H. Pattyn, J. Verheyden, J. Dekoster, and A. Vantomme, J. Appl. Phys., 95 (2004) 2770

[14] M. Bibes, Ll. Balcells, S. Valencia, J. Fontcuberta, M. Wójcik, E. J dryka, and S. Nadolski, Phys. Rev. Lett. 87 (2001) 067210

[15] R. Fink, B. Lindgren, Pan Min, and M. Semple, Surf. Sci. 355 (1996) 47

[16] G.A. Müller, A. Kuli ska, Kun Zhang, R. Gupta, P. Schaaf, M. Uhrmacher, and K.P. Lieb, Hyperfine Interact. 151/152 (2003) 223

[17] B. Swinnen, J. Meersschaut, J. Dekoster, G. Langouche, S. Cottenier, S. Demuynck, and M. Rots, Phys. Rev. Lett. 78 (1997) 362

[18] J. Meersschaut, J. Dekoster, R. Schad, P. Beliën, and M. Rots, Phys. Rev. Lett. 75 (1995) 1638 S. Demuynck, J. Meersschaut, J. Dekoster, B. Swinnen, R. Moons, A. Vantomme, S. Cottenier, and M. Rots, Phys. Rev. Lett. 81 (1998) 2562

[19] J. Meersschaut, J. Dekoster, S. Demuynck, S. Cottenier, B. Swinnen, and M. Rots, J. Magn. Magn. Mater. 198-199 (1999) 641
J. Meersschaut, C. L'abbé, M. Rots, and S.D. Bader, Phys. Rev. Lett. 87 (2001) 107201
D. Aernout, S.M. Van Eek, B. Croonenborghs, C. L'abbé, M. Rots, J. Meersschaut, Appl. Phys. Lett. 83 (2003) 3957

[20] J. Lohmüller, H.H. Bertschat, H. Granzer, H. Haas, G. Schatz, and W.-D. Zeitz, Surf. Sci. 360 (1996) 213
[21] H. Granzer, H.H. Bertschat, H. Haas, W.-D. Zeitz, J. Lohmüller, and G. Schatz, Phys. Rev. Lett. **77** (1996) 4261
[22] G. Krausch, T. Detzel, R. Fink, B. Luckscheiter, R. Platzer, U. Wöhrman, G. Schatz, Phys. Rev. Lett. 68 (1992) 377
[23] J. Voigt, X.L. Ding, R. Fink, G. Krausch, B. Luckscheiter, R. Platzer, U. Wöhrmann, and G. Schatz, Phys. Rev. Lett. 66 (1991) 3199
[24] B.-U. Runge, M. Düppel, G. Fillebock, K. Jacobs, U. Kohl, and G. Schatz, Phys. Rev. Lett. 79 (1997) 3054
[25] C.O. Rodrigues, M.V. Ganduglia-Pirovano, E.L. Peltzer y Blancá, and M. Petersen, Phys. Rev. B 64 (2001) 144419
[26] T. Phalet, M.J. Prandolini, W.D. Brewer, P. De Moor, P. Schuurmans, N. Severijns, B.G. Turrell, A. Van Geert, B. Vereecke, and S. Versyck, Phys. Rev. Lett. 86 (2001) 902
[27] J.M. Adams, J. Fu, G.L. Catchen, and D.L. Miller, Appl. Phys. Lett. 61 (1992) 2668
[28] J.M. Adams, G.L. Catchen, D. Loubychev, J. Fu, and D.L. Miller, Nucl. Instr. Meth. in Physics Research B 143 (1998) 591
[29] H.H. Bertschat, H. Granzer, H. Haas, R. Kowallik, S. Seeger, and W.-D. Zeitz, Phys. Rev. Lett. 78 (1997) 342
[30] H.H. Bertschat, H.-H. Blaschek, H. Granzer, K. Potzger, S. Seeger, W.-D. Zeitz, H. Niehus, A. Burchard, and D. Forkel-Wirth, Phys. Rev. Lett. 80 (1998) 2721
[31] H. Frauenfelder and R.M. Steffen, in *Alpha-, Beta-, and Gamma-Ray Spectroscopy,* Vol.2 (Ed. K. Siegbahn), North-Holland, Amsterdam (1965), pp 997
[32] G. Schatz and A. Weidinger, *Nuclear Condensed Matter Physics,* John Wiley, New York (1992)
[33] W. Nolting, *Quantentheorie des Magnetismus,* Vol. 1, Teubner, Stuttgart (1986), p 90
[34] S.G. Cohen in *Hyperfine Interactions,* (Eds. A.J. Freeman, R.B. Frankel) Academic Press, New York (1967), pp 553
R.M. Steffen and K. Alder in *The Electromagnetic Interaction in Nuclear Spectroscopy*, (Ed. W. D. Hamilton) North-Holland, Amsterdam (1975), pp 505
[35] B. Lindgren, Hyperfine Interact. (C) 1 (1996) 613
[36] E. Kugler, D. Fiander, B. Jonson, H. Haas, A. Przewloka, H.L. Ravn, D.J. Simon, K. Zimmer, and ISOLDE Collab., Nucl. Instr. and Meth. in Phys. Res. B 70 (1992) 41
[37] K. Potzger, H.H. Bertschat, A. Burchard, D. Forkel-Wirth, H. Granzer, H. Niehus, S. Seeger, W.-D. Zeitz, and ISOLDE – Collaboration, Nucl. Instr. Meth. in Phys. Res. B 146 (1998) 618
[38] H.H. Bertschat, J. Magn. Magn. Mater. 198-199 (1999) 636
[39] G.N. Rao, Hyperfine Interact. 24-26 (1985) 1119
[40] J. Kanamori, H.K. Yoshida and K.Terakura, Hyperfine Interact. 9 (1981) 363
[41] P.H. Dederichs, R. Zeller, H. Akai, S. Blügel, and A. Oswald, Philos. Mag. B 51 (1985)137
[42] H. Akai, M. Akai, S. Blügel, B. Drittler, H. Ebert, K. Terakura, R. Zeller, and P.H. Dederichs, Prog. Theo. Phys. Suppl. 101 (1990) 11
[43] J. Voigt, Ph.D. thesis, Universität Konstanz (1990), unpublished
[44] D.A. Shirley, S.S. Rosenblum, and E. Matthias, Phys. Rev. 170 (1968) 363

[45] B. Lindgren and A. Ghandour, Hyperfine Interact. 78 (1993) 291 B. Lindgren, Z. Naturforsch. 57 a (2002) 544
[46] M. Mohsen and F. Pleiter, Hyperfine Interact. 39 (1988) 123
[47] P. Weiss and R. Forrer, Ann. Phys. (Leipzig) 15 (1926) 153
[48] Ph. Mavropoulos, N. Stefanou, B. Nonas, R. Zeller, and P.H. Dederichs, Phys. Rev. Lett. 81 (1998)1505 Ph. Mavropoulos, N. Stefanou, B. Nonas, R. Zeller, and P.H. Dederichs, Phil. Magazine B78 (1998) 435
[49] S. Seeger, H.H. Bertschat, R. Kowallik, H. Waldmann, W.-D. Zeitz, D. Forkel-Wirth, H. Haas, Physics Letters A 201 (1995) 349
[50] A. Weber, Ph.D. thesis, Freie Universität Berlin (2001), unpublished
[51] R. Fink, B.-U. Runge, K. Jacobs, G. Krausch, J. Lohmüller, B. Luckscheiter, U. Wöhrmann, and G. Schatz, J. Phys.: Condens. Matter 5 (1993) 3837
[52] T. Klas, R. Fink, G. Krausch, R. Platzer, J. Voigt, R. Wesche, and G. Schatz, Surf. Sci. 216 (1989) 270
[53] K. Potzger, A. Weber, H.H. Bertschat, W.-D. Zeitz, and M. Dietrich, Phys. Rev. Lett. 88 (2002) 247201
[54] K. Potzger, Ph.D. thesis, Freie Universität Berlin (2001), unpublished
[55] H. Granzer, Ph.D. thesis, Freie Universität Berlin (1996) Shaker Verlag, Aachen (1997) ISBN 3-8265-2176-5
[56] P. Mavropoulos, J. Phys.: Condens. Matter 15 (2003) 8115
[57] N. Papanikolaou, R. Zeller, and P.H. Dederichs, J. Phys.: Condens. Matter 14 (2002) 2799
[58] V. Bellini, S. Cottenier, M. Çakmak, F. Manghi, and M. Rots to appear in Phys. Rev. B70 (Sept. 2004)
[59] P. Hohenberg and W. Kohn, Phys.Rev. 136 (1964) B864 W. Kohn and L.J. Sham, Phys. Rev. 140 (1965) A1133
[60] P. Blaha, K. Schwarz, G. Madsen, D. Kvasnicka, and J. Luitz, *WIEN2k, An Augmented Plane Wave + Local Orbitals Program for Calculating Crystal Properties,* (Karlheinz Schwarz, Techn. Universität Wien, Austria) (1999), ISBN 3-9501031-1-2
[61] I. Cabria, B. Nonas, R. Zeller, and P.H. Dederichs, Phys. Rev. B 65 (2002) 0544414
[62] B. Lazarovits, L. Szunyogh, and P. Weinberger, Phys. Rev. B 65 (2002) 104441
[63] A.B. Klautau and S. Frota-Pessôa, Surf. Sci. 497 (2002) 385
[64] J.T. Lau, A. Föhlisch, R. Nietuby , M. Reif, and W. Wurth, Phys. Rev. Lett. 89 (2002) 057201
[65] P. Gambardella, S. Rusponi, M. Veronese, S.S. Dhesi, C. Grazioli, A. Dallmeyer, I. Cabria, R. Zeller, P.H. Dederichs, K. Kern, C. Carbone, and H. Brune, Science, 300 (2003) 1130
[66] P. Lang, V.S. Stepanyuk, K. Wildberger, R. Zeller, and P.H. Dederichs, Solid State Commun. 92 (1994) 755
[67] V.S. Stepanyuk, W. Hergert, K. Wildberger, R. Zeller, and P.H. Dederichs, Phys. Rev. B 53 (1996) 2121
[68] B. Nonas, I. Cabria, R. Zeller, P.H. Dederichs, T. Huhne, and H. Ebert, Phys. Rev. Lett. 86 (2001) 2146
[69] S. Cottenier, V. Bellini, M. Çakmak, F. Manghi, and M. Rots, to appear in Phys. Rev. B70 (Sept. 2004)

[70] M.J. Prandolini, Y. Manzhur, A. Weber, K. Potzger, H.H. Bertschat, H. Ueno, H. Miyoshi, and M. Dietrich, Appl. Phys. Lett. 85 (2004) 76
[71] S. Blügel, Europhys. Lett. 7 (1988) 743
[72] K. Potzger, A. Weber, H.H. Bertschat, W.-D. Zeitz, M. Dietrich, in preparation

MAGNETO–SUPERCONDUCTIVITY OF RUTHENO-CUPRATES

V.P.S. Awana*

National Physical Laboratory, K.S. Krishnan Marg, New Delhi-110012, India.
awana@mail.nplindia.ernet.in

1. INTRODUCTION

Co-existence of superconductivity and magnetism (in particular the ferromagnetism) has been a point of discussion over decades [1,2]. The two phenomenon being co-existing with each other were realised in various f-electron compounds viz. $ErRh_4B_4$ [3,4]. In more recent years, the phenomenon is observed in UGe_2 [5] and $ZrZn_2$ [6]. Various explanations were put forward to understand the phenomenon, viz. accommodation of superconductivity in spiral like magnetic structure [3], or the spin triplet paired superconductivity with spin fluctuating ferromagnetism [3-5]. In fact, according to a long-term common sense superconductivity and magnetic long-range order do not mutually exist within a single (thermodynamical) phase. This is the fundamental reason, which makes the magneto-superconducting compounds altogether more interesting. The topic has been widely discussed in condensed matter physics over decades.

As far as high T_c superconductivity is concerned, the coexistence of high-T_c superconductivity and magnetism was reported for a rutheno-cuprate of the Ru-1222 type, *i.e.* $RuSr_2(Gd_{0.7}Ce_{0.3})_2Cu_2O_{10-\delta}$ [7], and more recently for $RuSr_2GdCu_2O_{8-\delta}$ (Ru-1212) [8]. These reports further renewed the interest in the possible coexistence of superconductivity and magnetism. It is believed that in rutheno-cuprates the RuO_6 octahedra in the charge reservoir

---

* Work done in part during stay at:
Materials and Structures Laboratory, Tokyo Institute of Technology, Yokohama 226-8503, Japan; and Superconducting Materials Center, National Institute for Materials Science, 1-1 Namiki, Tsukuba, Ibaraki 305-0044, Japan.

are mainly responsible both for magnetism and for doping holes into the superconductive CuO_2 plane.

The structures of both $RuSr_2GdCu_2O_{8-\delta}$ and $RuSr_2(Gd,Ce)_2Cu_2O_{10-\delta}$ are derived from that of $RBa_2Cu_3O_{7-\delta}$ or $CuBa_2RCu_2O_{7-\delta}$, with Cu in the charge reservoir replaced by Ru such that the $CuO_{1-\delta}$ chain is replaced by a $RuO_{2-\delta}$ sheet [9]. In the $RuSr_2(Gd,Ce)_2Cu_2O_{10-\delta}$ structure furthermore, a three-layer fluorite-type block instead of a single oxygen-free *R* (= rare earth element) layer is inserted between the two CuO_2 planes of the Cu-1212 structure. Schematic unit cell of both Ru-1222 and Ru-1212 are shown below in Figure 1.

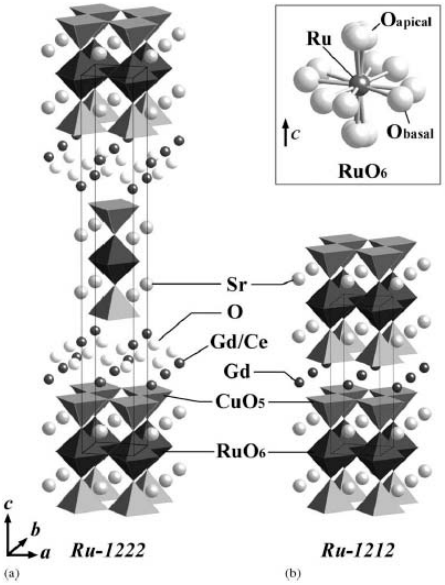

Fig. 1. Schematic diagrams of (**a**) Ru-1212 and (**b**) Ru-1222. The inset is schematic diagram for the average structure of RuO_6 octahedra.

Although bulk magnetism due to ordering of the Ru moments was confirmed for Ru-1212 from μSR (muon spin rotation/relaxation/resonance) and ESR (electron spin resonance) studies [8,10], the exact type of ordering is still debated [11]. In particular, the results revealed from neutron scattering experiments [11,12] and magnetization studies [8, 13-15] do not agree with each other. While the former concludes the ordering to be of antiferromagnetic nature, the latter indicates some ferromagnetic ordering. In fact even the most recent magnetization results have casted some doubts on earlier studies related to magnetism of Ru-1212 compounds [16,17]. Worth mentioning is the fact that the so-called ferromagnetic transition at around 140 K is not seen thermodynamically in heat capacity (C_P) measurements, only a broad hump extended until room temperature over a length of around 150 K is seen [15].

One of the puzzles in understanding the magnetization data of Ru-1212, is not only the antagonising nature of superconducting and magnetic order parameters, but also the presence

of magnetic Gd (8μB) along with the possibly magnetic Cu moment (Cu is paramagnetic in under-doped HTSC), which hinders in knowing the exact Ru spins magnetic contribution to the system. Ru-1212 can be formed with non-magnetic RE (rare earth) Y instead of Gd, but only with HPHT (high pressure high temperature) synthesis technique [12,18]

The bulk nature of superconductivity in these compounds was initially criticised due to lack of Meissner fraction in Gd/Ru-1212 and rather a crypto superconducting phase was proposed [19]. Appearance of bulk superconductivity in Ru-1212 is also confirmed from specific heat (C_P) measurements [20,21], though the existing reports do not agree with each other in terms of C_P measurements under magnetic field [C_p *(H, T)*]; in particular the T_c as viewed from the C_P peak increases with field in one report [20] but decreases with field in another [21]. While the former indicates towards the triplet pairing, the latter suggests a normal under-doped HTSC case. It is also suggested that small impurity of $GdSr_2RuO_6$ presumably present in the samples of Ref. 20 is responsible for the C_P *(H, T)* behaviour being different from that of Ref. 21 [22]. It seems that existing reports on the magneto-superconductivity in Gd/Ru-1212 do not agree completely with each other.

As far as Ru-1222 is concerned, the main features are the same as for both Ru-1212. The magnetic structure of Ru-1222 has been studied by neutron powder diffraction [23]. Despite the fact that various physical-property measurements have been carried out on Ru-1212 [8-22] and Ru-1222 [7,23-28], no final consensus has been reached, *i.e.* discussion on their basic characteristics in terms of the oxygen stoichiometry, valence state of Ru, carrier concentration and doping mechanism has not been completed yet. This becomes more important in the event when contradictory experimental results are obtained on different samples, as discussed above [20-22,29,30]. Also, it has been reported [30] that solid solutions of composition $(Ru_{1-x}Cu_x)Sr_2GdCu_2O_{8-\delta}$ can form within $0 < x < 0.75$ with T_c up to 74 K. Interestingly with the higher x values in the above composition the Ru spins do not order magnetically down to 5 K. Henceforth to conclude the coexistence of long-range magnetic ordering of Ru spins with superconductivity in the CuO_2 plane, one should strictly avoid the formation of $(Ru_{1-x}Cu_x)$-1212 solid solutions in pristine Ru-1212. Worth mentioning is the fact that Ru/Cu intermixing becomes more complicated as the two elements cannot be distinguished without ambiguity by neutron diffraction, a technique commonly used for fixing various cation occupancies in inorganic solids. Both Ru and Cu do have nearly the same scattering cross-sections for thermal neutrons. The concern of phase purity at the microscopic level in both Ru-1212 and Ru-1222 still remains unresolved. Also, we should look more carefully at the existing contradictions in the reported literature on rutheno-cuprates. Nevertheless, results of recent NMR (nuclear magnetic resonance) experiments on Ru-1212 were interpreted in terms of the coexistence of superconductivity and magnetism [31]. In current review, not only the existing literature is critically accessed, but also very recent data in terms of phase formation and structural, thermal, magnetic, electrical, spectroscopic and microscopic characterization for both Ru-1212 and Ru-1222 will be presented. Recent advancements regarding HPHT high pressure high temperature phase formation of both Ln/Ru-1212 and Ln/Ru-1222 (Ln = Lanthenides) is given along with their physical characterization. Also phase formation of higher derivatives of Ru-1212 and Ru-1222 families viz. Ru-1232 will be discussed. Instead of sticking to vastly studied Ln = Gd systems, the recent results for other lanthanide ruthenocuprates will be discussed. It is further stated that co-existence of superconductivity and ferromagnetism in these compounds is yet far from conclusive.

2. EXPERIMENTAL DETAILS

2.1 Normal Pressure High Temperature (NPHT) Synthesis

Samples of $RuSr_2GdCu_2O_{8-\delta}$ and $RuSr_2(Gd_{0.75}Ce_{0.25})_2Cu_2O_{10-\delta}$ were synthesized through a solid-state reaction route from stoichiometric amounts of RuO_2, SrO_2, Gd_2O_3, CeO_2 and CuO. Calcinations were carried out on mixed powders at 1000 ^oC, 1020 ^oC and 1040 ^oC for 24 hours at each temperature with intermediate grindings. The pressed bar-shaped pellets were annealed in a flow of oxygen at 1075 ^oC for 40 hours and subsequently cooled slowly over a span of another 20 hours down to room temperature. These samples are termed as "as-synthesized". Part of the as-synthesized samples were further annealed in high-pressure oxygen (100 atm) at 420 ^oC for 100 hours and subsequently cooled slowly to room temperature. These samples are termed as "100-atm O_2-annealed". Further some of the samples were treated in flow of N_2 gas at 420 ^0C for 24 hours and subsequently cool down to room temperature in same gas atmosphere. Though the heat treatments used for the samples in our study are in general similar to those as reported in literature [7-11, 13-15, 17, 19-30], minor differences do exist from one laboratory to another in terms of annealing hours and the temperatures used. Also, it has been reported that not always all samples of the same batch with similar heating schedule show superconductivity [19,22,29]. Our general experience is also the same particularly for Ru-1212, in which achieving superconductivity seems to be a tricky job.

2.2 High Pressure High Temperature (HPHT) Synthesis

Worth mentioning is the fact that for both Ru-1212 and Ru-1222, single-phase samples are achieved only for *R* = Gd, Sm and Eu, with the normal heating schedules mentioned above. For *R* = Y and Dy, *etc*., one needs to employ the HPHT (high-pressure high-temperature) procedure for attaining the Ru-1212 phase [12,16,18,31]. In case of Ln/Ru-1212 compounds starting materials for high-pressure synthesis were RuO_2 (99.9%), SrO_2, $SrCuO_2$, Ln_2O_3 (99.9) and CuO (99.9%). These materials were mixed in an agate mortar to obtain starting mixtures for high-pressure synthesis. About 300 mg of starting mixture was sealed in a gold capsule and allowed to react in a flat-belt-type high-pressure apparatus at 6 GPa, and at 1200–1300°C for 3 h, then quenched to room temperature. For Ln = Y system, high-purity sample was obtained with the `Ru-poor' starting composition, of $Ru_{0.9}Sr_2YCu_2O_{7.8}$. A similar procedure is followed in ref. [12,16,18,31]

For Ln/Ru-1222, the samples of composition $RuSr_2(Ln_{3/4}Ce_{1/4})_2Cu_2O_{10}$ with Ln = Ho, Y and Dy were synthesised through a HPHT solid-state reaction route. For the HPHT synthesis and to fix the oxygen at 10.0 level, the molar ratio used were: $(RuO_2) + (SrO_2) + (SrCuO_2) + 3/4(CuO) + 1/4(CuO_{0.011}) + 3/4(Ln_2O_3) + 1/2(CeO_2)$ resulting in $RuSr_2(Ln_{3/4}Ce_{1/4})_2Cu_2O_{10}$. $CuO_{0.011}$ is pure Cu-metal, for which precise oxygen content is determined before use. The materials were mixed in an agate mortar. Later around 300 mg of the mixture was sealed in a gold capsule and allowed to react in a flat-belt-type-high-pressure apparatus at 6GPa and 1200 ^0C for 2 hours [32]. Nearly no change was observed in the weight of synthesized samples, indicating towards their fixed nominal oxygen content.

We believe the oxygen content of all the samples is close to nominal i.e. 10. Determination of the oxygen content of synthesized samples is yet warranted to know the oxygen value for these samples. In case of Ru-1232 the samples of composition $RuSr_2(Ln_1Ce_2)Cu_2O_{12.25}$ with Ln = Y and Dy were synthesised through a HPHT solid-state reaction route. For the HPHT synthesis, the molar ratio used were: (RuO_2) + (SrO_2) + $(SrCuO_2)$ + 3/4(CuO) + 1/4($CuO_{0.011}$) + 1/2(Ln_2O_3) + 2(CeO_2) resulting in $RuSr_2(Ln_1Ce_2)Cu_2O_{12.25}$. $CuO_{0.011}$ is pure Cu-metal, for which precise oxygen content is determined before use. The materials were mixed in an agate mortar. Later around 300 mg of the mixture was sealed in a gold capsule and allowed to react in a flat-belt-type-high-pressure apparatus at 6GPa and 1200 ^{0}C for 2 hours. Nearly no change was observed in the weight of synthesized samples, indicating towards their fixed nominal oxygen content. We believe the oxygen content of both the samples is close to nominal i.e. 12.25.

2.3 Physical property experimentation for NPHT and HPHT samples

Thermogravimetric (TG) analyses (Perkin Elmer: System 7) were carried out in a 5 % H_2/95 % Ar atmosphere at the rate of 1 ^{o}C/min to investigate the oxygen non-stoichiometry. X-ray diffraction (XRD) patterns were collected at room temperature (MAC Science: MXP18VAHF[22]; CuK_α radiation). Magnetization measurements were carried out on a superconducting-quantum-interference-device (SQUID) magnetometer (Quantum Design: MPMS-5S). Resistivity measurements under an applied magnetic field of 0 - 7 T were performed in the temperature range of 5 - 300 K using a physical-property-measurement system (Quantum Design: PPMS). Electron diffraction (ED) patterns were taken at room temperature using an analytical transmission electron microscope (Hitachi: HF-3000S) with a cold field emission gun operated at an accelerating voltage of 300 kV. The SAED and CBED patterns were taken from specimen areas of about 100 and 8 nm, respectively. The HREM images were taken using a high-resolution, high-voltage transmission electron microscope (Hitachi: H-1500) operated at an accelerating voltage of 800 kV. The Ru L_{III}-edge XANES measurements were performed at room temperature for polycrystalline samples at the BL15B beamline of the Synchrotron Radiation Research Center (SRRC) in Hsinchu, Taiwan.

3. RESULTS AND DISCUSSION

3.1 Phase formation and lattice parameters: X-ray diffraction results for NPHT Gd/Ru-1212 and Gd/Ru-1222 samples

$RuSr_2GdCu_2O_{8-\delta}$ (Ru-1212) samples possess a tetragonal Ru-1212 structure with a space group *P*4/*mmm*. Lattice parameters were determined at $a = b = 3.8218(6)$ Å and $c = 11.476(1)$ Å. Corresponding X-ray diffraction pattern is shown in Fig. 2. Small amount of $SrRuO_3$ is also seen, which is marked on the pattern [33].

Essentially no difference is found in X-ray diffraction pattern or lattice parameters for the 100-atm O_2-annealed Ru-1212 sample, suggesting that the oxygen content remained unchanged upon the high-O_2-pressure annealing. Worth mentioning is the fact that earlier phase-pure (no trace of $SrRuO_3$ within the XRD detection limit) Ru-1212 sample was not

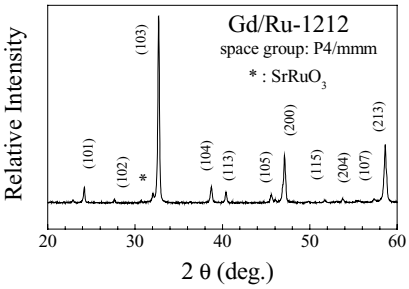

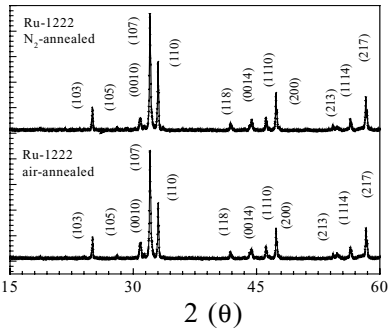

Figs. 2 & 3. X-ray diffraction pattern for an as-synthesized $RuSr_2GdCu_2O_{8-\delta}$ sample & for an as- synthesized and N_2 annealed $RuSr_2(Gd_{0.75}Ce_{0.25})_2Cu_2O_{10-\delta}$ sample.

superconducting, even with various types of post-annealing treatments [29]. Compared with Ru-1212, the Ru-1222 phase forms more easily in impurity-free form. Both the as-synthesized and the 100-atm O_2-annealed Ru-1222 samples were found to be of high quality in terms of phase purity. An X-ray diffraction pattern for an as-synthesized sample is shown in Fig. 3. The lattice parameters were determined from the diffraction data in the tetragonal space group *I*4/*mmm*: $a = b = 3.8337(6)$ Å and $c = 28.493(1)$ Å for the as-synthesized sample, and $a = b = 3.8327(7)$ Å and $c = 28.393(1)$ for the 100-atm O_2-annealed sample [34]. The shorter lattice parameters for the 100-atm O_2-annealed sample are believed to manifest the fact that it is more completely oxygenated than the as-synthesized sample. For N_2 – annealed sample the lattice parameters are $a = b = 3.8498(3)$ Å and $c = 28.4926(9)$ Å [35]. An increase in lattice parameters of N_2-annealed sample indicates an overall decrease in oxygen content of the sample. X-ray diffraction results, in terms of phase purity, space groups and the obtained lattice parameters are in general accordance with the reported literature for both Gd/Ru-1212 and Gd/Ru-1222 variusly annealed samples.

3.2 Phase formation and lattice parameters: X-ray diffraction results for HPHT Ln/Ru-1212, Ln/Ru-1222 and Ln/Ru-1232 samples

Phase formation of Ln/Ru-1212 compounds is reported in ref.[18]. Nearly single-phase materials were obtained for various Ln, but with slight off stoichiometry of Ru. For example in case Y/Ru-1212 the single phase formation is achieved with nominal composition of $Ru_{0.9}Sr_2YCu_2O_{7.8}$ [18]. In case of Ln/Ru-1222 samples with composition $RuSr_2(Ln_{3/4}Ce_{1/4})_2Cu_2O_{10}$ with Ln = Ho, Y and Dy were crystallised in a single-phase form in space group *I4/mmm* with lattice parameters $a = b = 3.819$ (1) Å, and $c = 28.439(1)$ Å for Ln = Y, $a = b = 3.813(2)$ Å, and $c = 28.419(1)$ Å for Ln = Ho, and $a = b = 3.824(4)$ Å, and $c = 28.445(1)$ Å for Ln = Dy. The volume of the cells is 413.2, 414.8 and 415.9 $Å^3$ for Ln = Ho, Y and Dy respectively. The trend of their cell volumes is in line with the rare earths ionic sizes. Figure 4 shows the X-ray diffraction patterns of finally synthesized Ln/Ru-1222 compounds. As seen from this figure these compounds are crystallised in a single-phase form with only small amount of $SrRuO_3$ present in Ln = Y sample [32].

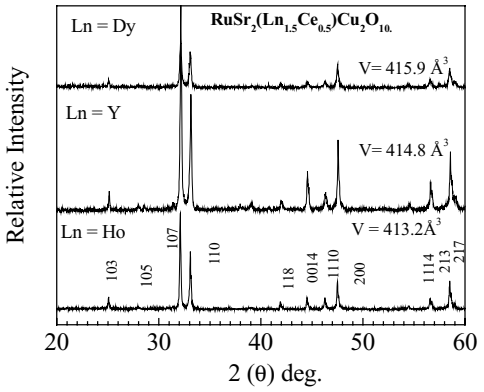

Fig. 4. X-ray diffraction pattern forLn/Ru-1222.

In Case of Ln/Ru-1232, the X-ray diffraction patterns of $RuSr_2(Y_1Ce_2)Cu_2O_{12+\delta}$ with δ = 0.0, 0.10 and 0.20 which could be readily indexed within tetragonal structure having space group *P4/mmm.* Also seen are small quantities of $SrRuO_3$ and $RuSr_2(RE_{1.5}Ce_{0.5})Cu_2O_{10}$ (Ru-1222). Though, all the three oxygen contents gave nearly similar X-ray patterns, we decided to work with δ = 0.25, with a pre-assumption that higher oxygen content could give rise to better superconductivity. Lattice parameters calculated are $a = b$ = 3.822(1) Å, and c = 16.3336(4) Å for Ln = Y and $a = b$ = 3.827(3) Å, and c = 16.3406(7) Å for Ln = Dy samples of the $RuSr_2(Ln_1Ce_2)Cu_2O_{12.25}$ series. The XRD patterns for $RuSr_2(Y_1Ce_2)Cu_2O_{12+\delta}$ with δ = 0.0, 0.10 and 0.20 are shown in Fig. 5.

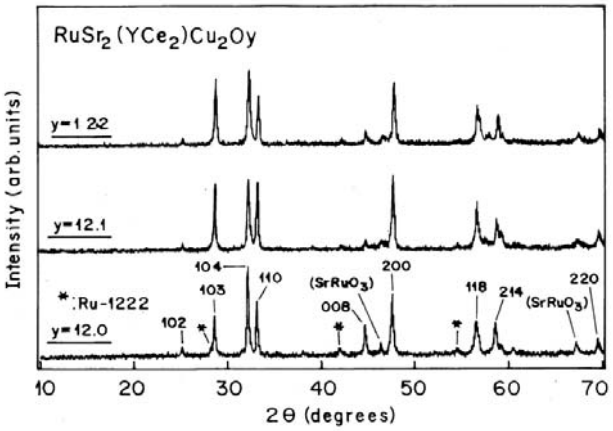

Fig. 5. X-ray diffraction pattern Ln/Ru-1232 with δ = 0.0, 0.10 and 0.20

3.3 Oxygen stoichiometry: TG results

Thermogravimetric reduction curves were recorded for both as-synthesized and 100-atm O_2-annealed samples of Gd/Ru-1212 and Gd/Ru-1222 [36]. Two examples of the obtained TG curves are shown in Fig. 6. For both the phases the decomposition of sample occurs in two distinct steps about 200–350 and 400–500 °C.

To clarify the process of the sample decomposition during the different steps of reduction, additional TG measurements were performed in the same atmosphere for the simple oxides of the constituent metals, i.e. RuO_2, CuO, Cu_2O and CeO_2. It was seen that RuO_2, CuO and Cu_2O decompose into corresponding metals at low temperatures of about 100, 150 and 330 °C, respectively, while CeO_2 remains stable at least up to 750 °C [36]. We therefore calculated the exact oxygen contents of the Ru-1212 and Ru-1222 samples from the weight losses seen in the H2/Ar reduction curves by 550 °C assuming the final decomposition product to be a mixture of oxides, SrO, Gd_2O_3 and CeO_2, and Ru and Cu metals.

The results are presented in Table 1, implying that the 100-atm O_2-annealed Ru-1212 sample is stoichiometric within the error bars of the analysis, while the 100-atm O2-annealed Ru-1222 sample is clearly oxygen deficient. Furthermore, as already assumed based on the lattice parameters and the Tc values, the difference between the 100-atm and 1-atm O2-annealed samples is larger for the Ru-1222 phase than for the Ru-1212 phase, see also the data for relevant samples in Refs. [25,33,34]. In Table 1, we also show the absolute oxygen content values for the samples annealed in Ar up to the highest temperatures before the break-down of the structure, i.e. 750 °C for Ru-1212 and 900 °C for Ru-1222. These values, i.e. 7.80(5) for Ru-1212 and 9.35(5) for Ru-1222, represent the minimum oxygen contents tolerated by these phases.

Table 1. The value of oxygen content as determined from TG analysis for variously treated Gd/Ru-1212 and Gd/Ru-1222 samples.

Synthesis/annealing conditions	$RuSr_2GdCu_2O_{8-d}$ (Ru-1212)	$RuSr_2Gd_{1.5}Ce_{0.5}Cu_2O_{10-d}$ (Ru-1222)
100-atm O_2, 420 ^{0}C	7.98(5) (T_c = 20 K)	9.63(5) (T_c = 43 K)
1-atm O_2, 1075 ^{0}C	7.93(5) (T_c = 20 K)	9.54 (5) (T_c = 23 K)
1-atm Ar, 750/900 ^{0}C (Ru-1212/Ru-1222)	7.80 (5) (No T_c)	9.35(5) (No T_c)

As far as the HTHT treated various Ln/Ru-1212, 1222 or 1232 compounds are concerned their oxygen stoichiometry is believed to be very close to nominal, because nearly no change was observed in the weight of synthesized samples, indicating towards their fixed nominal oxygen content. We believe the oxygen content of all the samples is close to nominal. Determination of the oxygen content of the HPHT synthesized samples is yet warranted.

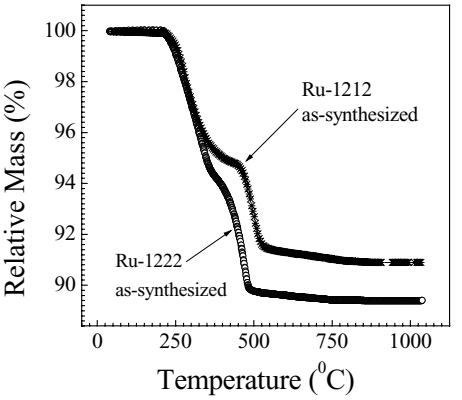

Fig. 6. TG curves for as-synthesized Gd/Ru-1212 and 1222 samples recorded in 5 % H_2/95 % Ar atmosphere.

3.4 Valence of Ru: XANES spectroscopy results

The Ru L_{III}-edge XANES spectra were obtained for an as-synthesized and a 100-atm O_2-annealed Ru-1222 samples [37]. The spectra were analyzed quantitatively by fitting them to certain linear combinations of those for reference materials Sr_2RuO_4 (Ru^{IV}) and Sr_2GdRuO_6 (Ru^{V}). All the spectra exhibited two peaks, the higher-energy one and the lower-energy one being due to $2p \rightarrow e_g$ and $2p \rightarrow t_{2g}$ transitions, respectively [38,39]: with increasing Ru valence from +IV to +V, the crystal-field splitting increases and thereby the separation between the two peaks enhances. Furthermore, the peaks were accordingly shifted by ~1.5 eV to the higher energy. It was concluded that both Ru-1222 samples are between the two reference materials in terms of the Ru valence. Fitting of the spectra revealed a valence value of +4.74 for the as-synthesized sample and +4.81 for the 100-atm O_2-annealed sample [37].

The obtained result suggests that the valence of Ru in Ru-1222 is affected by the change in oxygen content. It is therefore interesting to compare the presently obtained Ru valence values to that previously reported for a $RuSr_2(Gd_{0.7}Ce_{0.3})_2Cu_2O_{10-\delta}$ sample (+4.95) with $T_c \approx 60$ K [38]. For the three Ru-1222 samples the Ru valence/T_c values thus were: +4.74/30 K, +4.81/43 K and +4.95/60 K. (Note that the XANES measurements and analyses were carried out in parallel ways for all the three samples.) The latter two samples were both annealed under 100 atm oxygen pressure, but with different temperature programs. It is thus likely that the one previously reported [38] had somewhat higher oxygen content than the present 100-atm O_2-annealed sample. It seems that the valence of Ru in Ru-1222 depends on the oxygen content, thus indirectly suggesting that the changes in oxygen stoichiometry occur in the $RuO_{2-\delta}$ layer. Here it is interesting to note that a previous study had shown that Ru remains essentially unchanged (close to pentavalent) upon varying the Ce-substitution level within $0.3 \leq x \leq 0.5$ in fully oxygen-loaded $RuSr_2(Gd_{1-x}Ce_x)_2Cu_2O_{10-\delta}$ samples [38,39].

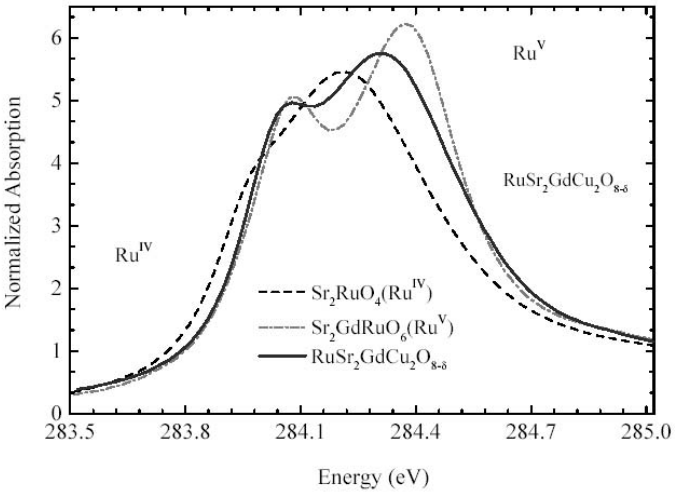

Fig. 7. Ru L_{III}-edge XANES spectra for reference materials, Sr_2RuO_4 (Ru^{IV}) and Sr_2GdRuO_6 (Ru^V), and for as-synthesized $RuSr_2GdCu_2O_{8-\delta}$ sample.

Ru L_{III}-edge XANES analysis for an as-synthesized (final annealing in O_2 at 1075 ^oC) $RuSr_2GdCu_2O_{8-\delta}$ sample revealed a valence value of +4.62 [36], see Fig.7. Same analysis procedure as discussed above was followed. This value is very close to that reported in Ref. [39] for a $RuSr_2GdCu_2O_{8-\delta}$ sample, *i.e.* +4.60, with the final annealing performed in O_2 at 1060 ^oC.

3.5 Superstructures: SAED/HRTEM results

3.5.1 SAED for NPHT synthesized Gd/Ru-1222 and Gd/Ru/1212 samples

Figs. 8(a)–(d) show SAED patterns of the Ru-1222 sample taken with [0 0 1], [1 0 0], [1 1 0] and [3 1 0] incidence, respectively. Main reflections of h k l can be indexed by the fundamental lattice, and the sharp reflections are seen in Figs. 2(b) and (c). On the other hand, superlattice reflections with diffuse streaks along the c* direction are seen in Fig. 2(d) as indicated by white arrowheads. It has been confirmed that the superlattice reflections are corresponding to those indicated by the white arrowheads in the [0 0 1] SAED pattern (Fig. 2(a)). The diffuse streaks along the c* direction suggest existence of domain structures or stacking disorders of the superlattice in the c direction [40].

Similar sets of SAED patterns of Ru-1212 are shown in Figs. 9(a)–(d) for [0 0 1], [1 0 0], [1 1 0] and [3 1 0] incidence, respectively, although main reflections of h k l can be indexed by the fundamental primitive tetragonal lattice which has already been reported as the 1212-type structure (P4/mmm: a = 0.38337(6) nm, c = 11.4926(9) nm) [259]. The superlattice reflections, which are corresponding to those caused by a supercell, are also observed in

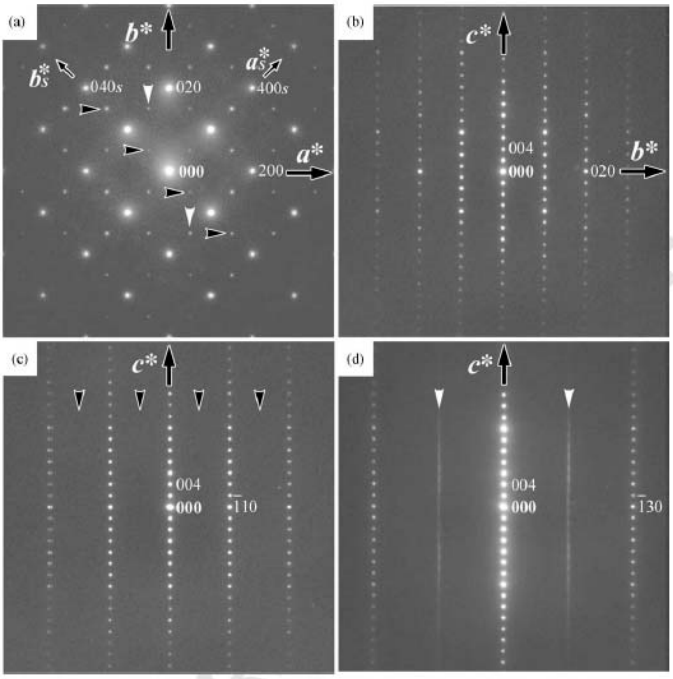

Fig. 8. SAED patterns of Ru-1222. h k l and h k lS are corresponding to the indexes of Reciprocal fundamental lattice (a*, b*, c*) and superlattice (a_S*,b_S*,c_S*), respectively: (**a**) [0 0 1] SAED pattern; (**b**) [1 0 0] SAED pattern; (**c**) [1 1 0]SAED pattern; and (**d**) [3 1 0] SAED pattern.

Fig.3(a) as indicated by the white and black arrowheads [41]. It should be noted that the superlattice reflections with diffuse streaks along c* direction are also observed in Fig. 3(d) as indicated by white arrowheads. Therefore, existence of domain structures or stacking disorders of the superlattice as seen in Ru-1222 are also expected in Ru-1212.

3.5.2 HRTEM for NPHT synthesized Gd/Ru-1222 and Gd/Ru/1212 samples

Fig. 10 shows a HREM (high resolution transmission electron microscopy) image of Gd/Ru-1222 taken with [1 0 0] incidence. The layers indicated by Ru, Sr and Cu are assumed to be corresponding to those of RuO_2, SrO and CuO_2, respectively. The two layers indicated by Gd and/or Ce are corresponding to parts of the fluorite-type block of $(Gd_{1.5}Ce_{0.5})_2O_2$. It is confirmed that the layers and the fluorite-type block are stacked along the c-axis following 1222-type structure without any intergrowths [42]. Fig. 11 shows a HREM image of Gd/Ru-1212 taken with [1 0 0] incidence. The layers indicated by Ru, Sr, Cu and Gd are assumed to be corresponding to those of RuO_2, SrO, CuO_2 and Gd, respectively. It is confirmed that the layers are stacked along the c-axis following 1212-type structure without any inter-growths [42].

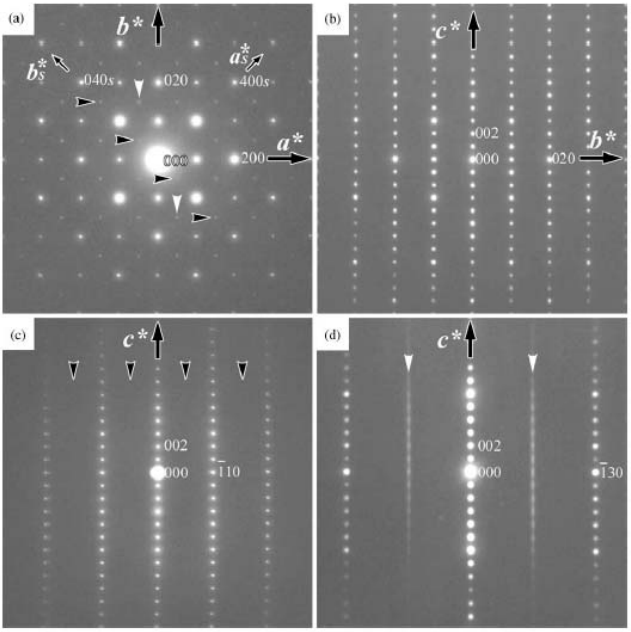

Fig. 9. AED patterns of Ru-1212: (**a**) [0 0 1] SAED pattern; (**b**) [1 0 0] SAED pattern; (**c**) [1 1 0] SAED pattern; and (**d**) [3 1 0] SAED pattern.

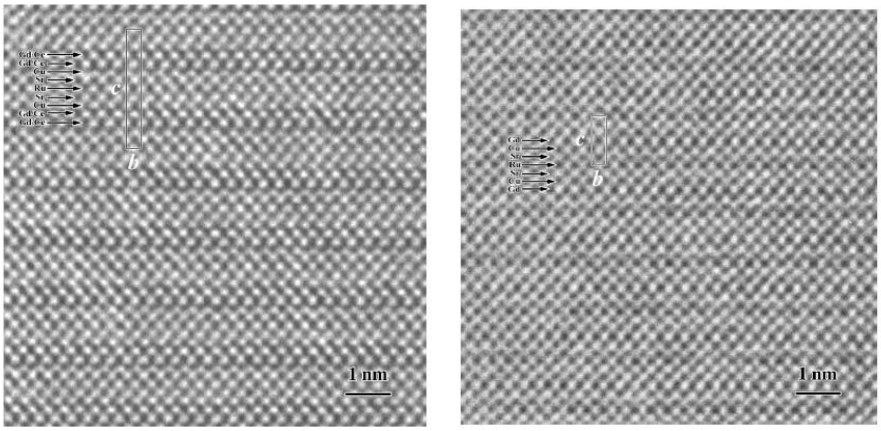

Figs. 10 & 11. HREM images of Gd/Ru-1222 and Gd/Ru-1212 being taken at [1 0 0] incidence. No stacking disorders due to intergrowths are observed.

3.5.3 Structural model based on SAED and HRTEM results for Gd/Ru-1222

Fig. 12(a) shows a schematic diagram of the fundamental structure of Ru-1222 in which only RuO_2 planes are shown as indicated by filled squares. The rectangular parallelepiped surrounded by solid lines represents the fundamental body-centered tetragonal lattice. The rectangular parallelepipeds surrounded by the dotted lines are corresponding to the superlattice. It is assumed on the basis of the result by Knee et al. [23] that the superlattice reflections observed in this electron diffraction study are due to an ordering of the RuO_6 octahedra rotated about the c-axis. Fig. 12(b) shows a schematic diagram of the ordering of rotations about the c-axis, that form the super-cell. The rectangular parallelepipeds surrounded by the solid lines and dotted lines are corresponding to the fundamental lattice and superlattice, respectively. Dark- and light-gray squares indicate right- and left-handed rotations of the RuO6 octahedra about the c-axis, respectively.

It is confirmed that there are two possible arrangements, A and B, of the rotated RuO_6 octahedra as indicated by arrowheads in Fig. 12(b) if we consider the rotative directions of the RuO_6 octahedra located at the body-center of the fundamental lattice of Fig. 12(a). The rotated RuO_6 octahedra in both cases of A and B are ordered along the c direction with an interval of c that is the same as that of the fundamental lattice of Fig. 12(a). It is confirmed that the lattice types of A and B can be considered as A- and B-centered orthorhombic superlattices (A and B superlattices), respectively, if the axes of a_S and b_S are fixed as shown in Fig. 12(b).

It should be noted that the A and B superlattices are crystallographically identical to each other, being mutually related by 90° rotation about the c-axis. However, we focus here on the A and B superlattices in order to interpret the experimental diffraction patterns. Fig. 12(c) shows a schematic diagram of an example of our proposed domain structure model for explaining the experimental results in this study. That is, Ru-1222 is composed of superlattice domains of about 10 nm in width distinguished by the A and B superlattices along the c direction as shown in Fig. 12(c).

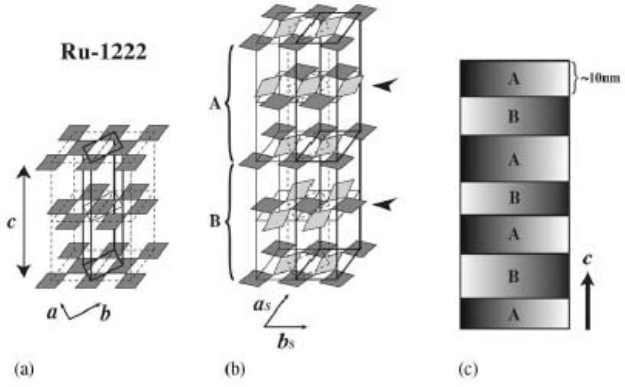

Fig. 12. Schematic diagrams of the fundamental lattices and superlattices of Ru-1222 the fundamental lattice of Ru-1222, only RuO_2 planes are shown (filled squares); (**b**) the two possible superlattices (A and B superlattices) of Ru-1222; (**c**) an example of a proposed domain-structure model for Ru-1222.

3.5.4. Structural model based on SAED and HRTEM results for Gd/Ru-1212

Fig. 13(a) shows a schematic diagram of the fundamental primitive tetragonal lattice of Ru-1212. It is assumed on the basis of the results by McLaughlin et al. [41] that the superlattices, which form the super-cell, are due to ordering of the RuO_6 octahedra rotated about the c-axis. We consider here two possible arrangements, P and I, of the rotated RuO_6 octahedra as indicated by arrowheads in Fig. 13(b) by analogy with the superlattice models of Ru-1222. The rotated RuO_6 octahedra of P and I are ordered along the c direction with intervals of c and 2c, respectively. The different periodicities between P and I are caused by the differences of rotative direction of the RuO_6 octahedra indicated by arrowheads in Fig. 13(c). It is confirmed that the lattice types of P and I are primitive and body-centered tetragonal superlattices (P and I superlattices), respectively. It should be noted that the P and I superlattices of Ru-1212 are crystallographically different to each other, while the A and B superlattices of Ru-1222 are crystallographically identical to each other. We propose a domain structure model of Ru-1212 as shown in Fig. 12(c), that is, Ru-1212 is composed of superlattice domains of about 10 nm in width distinguished by the P and I superlattices along the c direction.

From microstructures and superstructures studies of the Ru-1222 and Ru-1212 magneto-superconductors, it is revealed that both Ru-1222 and Ru-1212 are composed of nm-size domains stacked along the c direction. Origin of such domain is the ordering of rotated RuO_6 octahedral around the c-axis, which leads to the formations of characteristic superstructures. In Ru-1212, two types of superstructures with primitive (P) and body-centered (I) symmetries are derived, and they alternately repeated with nm-size periodicity along the c-axis. It is of great interest that Ru-1212 consists of domains of two crystallographically different superstructures, while Ru-1222 consists of domains of the single crystallographically identical superstructure, with base-centered orthorhombic symmetry, mutually related by 90° rotation around the c-axis.

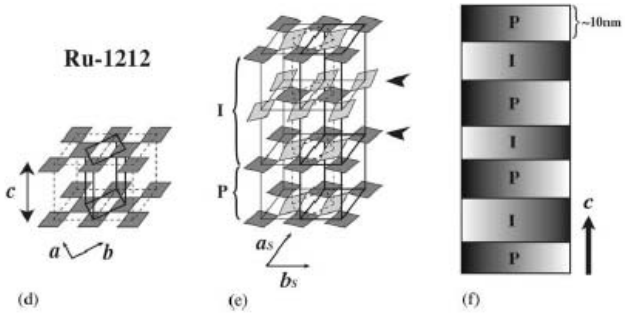

Fig. 13. An example of a proposed domain-structure model for Ru-1212; (**d**) the fundamental lattice of Ru-1212; (**e**) the two possible superlattices (P and I superlattices) of Ru-1212; and (**f**) an example of a proposed domain-structure model for Ru-1212.

3.6. Magneto-superconductivity and magnetic characteristics: SQUID results

3.6.1. Non-superconducting Ru-1212 samples

Figure 14 depicts both ZFC (zero-field-cooled) and FC (field-cooled) magnetic moment (*M*) *versus* temperature (*T*) plots for various $RuSr_2GdCu_2O_{8-\delta}$ samples with an applied field of 10 Oe [43]. As is seen from this figure the ZFC and FC magnetisation curves show a significant branching around 145 K for the as-synthesized sample with a further sharp drop in magnetisation around 2.6 K.

The branching of ZFC and FC curves at 145 K originates from the magnetic ordering of Ru moments and the sharp peak at 2.6 K is due to antiferromagnetic ordering of Gd moments. Interestingly in presently studied non-superconducting $RuSr_2GdCu_2O_{8-\delta}$ samples the ordering temperature of Ru moments appears to be 13 K higher than the value reported for similar but superconducting samples [8,15,33]. Both the ZFC and FC branching about 145 K and the sharp peak at 2.6 K are seen for all the samples including the high-O_2-pressure annealed and the argon annealed ones. None of the samples show any traces of superconductivity down to 2 K, even with very low field measurements at 1.5 Oe. Worth reminding is the fact that these samples of ours contain no traces of $SrRuO_3$, (see Fig. 15). These non-superconducting $RuSr_2GdCu_2O_{8-\delta}$ samples showed a similar ferromagnetic component at 5 K, as for reported superconducting samples.

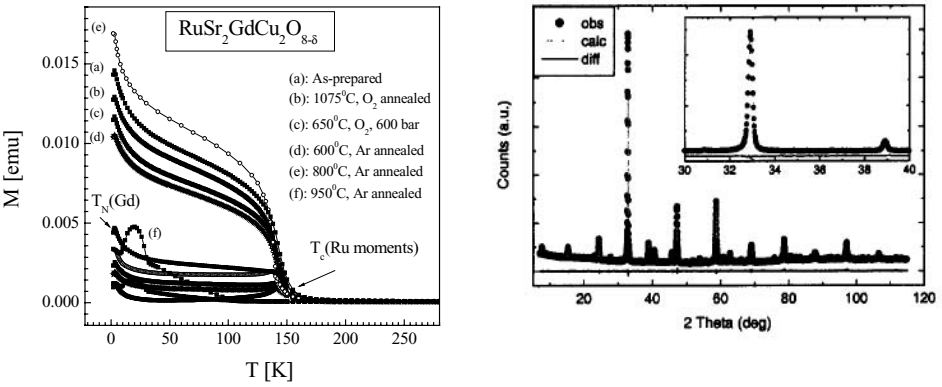

Figs. 14 & 15. *M-T* plots & XRD for various non-superconducting $RuSr_2GdCu_2O_{8-\delta}$ samples.

Except the fact that the present samples were non-superconducting and their phase purity was comparatively better than for reported samples, no other visible difference is observed, though it seems that non-superconducting samples have a bit higher magnetic ordering temperature. Worth emphasising is the fact that even after various post-annealing steps, the superconductivity could not be achieved. Also observed is the fact that the magnetic ordering temperatures of Ru or Gd moments were not affected by the post-annealing steps. This highlights the fact, discussed in section 3.2, that there is not much room left for tuning the oxygen stoichiometry of Ru-1212.

The magnetic susceptibility (χ) of the compound follows the paramagnetic behaviour above the magnetic ordering temperature of Ru moments. Considering Gd to be in trivalent state with a localised moment of 8 μ_B (same as in Gd-based Cu-1212), the calculated moment from Curie-Weiss relation for Ru in paramagnetic state is around 1.0 μ_B, suggesting Ru to be in pentavalent state in Ru-1212. However we should like to mention that moment extraction from Curie-Weiss relation can not be conclusive, without properly considering the exact state of Cu and the effect of possible crystal fields on the magnetic susceptibility of the compound. In fact effective paramagnetic moment for Ru in Ru-1212 has been reported as high as 3.17(4) μ_B based on high temperature (up to 900 K) fitting of the magnetic susceptibility [17]. The valence of Ru extracted from the magnetic susceptibility data vary from one report to another. We believe the fitting of high temperature magnetic susceptibility to simple Curie-Weiss relation is futile in determining the valence of Ru in rutheno-cuprates like Ru-1212 and Ru-1222, but spectroscopic methods such as XANES are more conclusive in determining the valence state of Ru.

3.6.2 Magneto-superconductivity of as-synthesized Gd/Ru-1212 samples

Figure 16 shows the χ-*T* behaviour in the temperature range of 5 K - 160 K for another as-synthesized $RuSr_2GdCu_2O_{8-\delta}$ sample with an applied field of 5 Oe, in both ZFC and FC situations. The ZFC and FC curves start branching around 140 K with a cusp at 135 K and a diamagnetic transition around 20 K in the ZFC part. The down-turn cusp at 135 K is indicative of antiferromagnetic nature of Ru-spin ordering. Interestingly for the same sample annealed in 100-atm O_2 atmosphere the diamagnetic transition was not observed down to 5 K (curve not shown) [43].

For the as-synthesized sample the FC part is seen increasing and later saturating probably due to contribution from paramagnetic Gd moments. Inset of Fig. 16 shows the isothermal *M versus* applied field (*H*) behaviour for this sample. The isothermal magnetization as a function of magnetic field may be viewed as:

$$M(H) = \chi H + \sigma_s(H) , \quad (1)$$

where χH is the linear contribution from antiferromagnetic Ru spins and paramagnetic Gd spins and $\sigma_s(H)$ represents the weak ferromagnetic component of the Ru sublattice. The contribution from the weak ferromagnetic component starts to appear only below 100 K and at higher fields above 3 T. Above this temperature the *M*-*H* plot remains purely linear.

Appearance of ferromagnetic component at low *T* within antiferromagnetically ordered Ru spins can happen due to slight canting of spins. Published neutron diffraction data clearly indicate such a possibility [11,12]. Non-linearity in *M*-*H* appears at high fields above 3 T. The *M*-*H* loop for the sample is shown in the lower inset of Fig. 16.

3.6.3 Magneto-superconductivity of as –synthesized Gd/Ru-1222 samples

Figure 17 shows the magnetic susceptibility χ-*T* behaviour in the temperature range of 5 to 160 K for an as-synthesized $RuSr_2(Gd_{0.75}Ce_{0.25})_2Cu_2O_{10-\delta}$ sample under applied fields of 5, 10 and 100 Oe, measured in both ZFC and FC modes. In an applied field of 5 Oe, the ZFC and

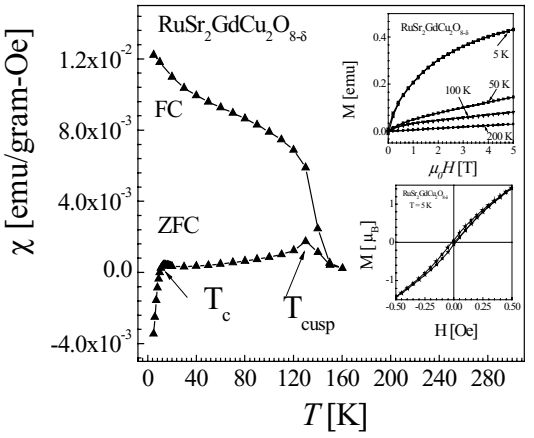

Fig. 16. χ-T plot for an as-synthesized, superconducting Gd/Ru-1212, the insets show the M-H loops for the same.

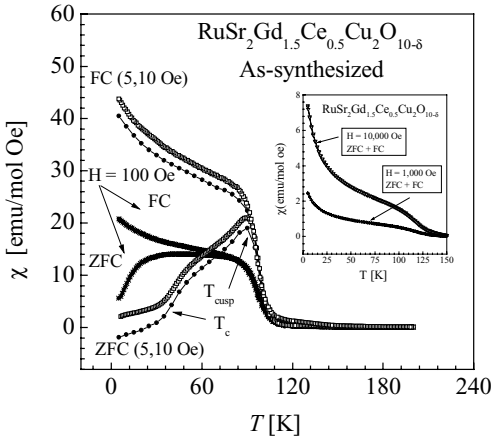

Fig. 17. χ-T plot for an as-synthesized, superconducting Gd/Ru-1222 samples.

FC curves start branching at around 140 K with a sharp upward turn at 100 K. The ZFC branch shows further a cusp at 85 K and a diamagnetic transition around 30 K. This is in general agreement with other reports [7,27,28]. The ZFC curve does not show any diamagnetic transition in applied fields of 10 and 100 Oe, but the transition is marked with a change in the slope of the ZFC curves. As the field strength exceeds a certain threshold value the positive contribution from both Gd and Ru moments overcomes the negative contribution

from superconductivity to the magnetic susceptibility. Interestingly the ZFC - FC branching temperature of 140 K in 5 Oe field decreases to around 60 K in an applied field of 100 Oe. This can be considered as a weak ferromagnetic behaviour. In fact no ZFC - FC branching is observed down to 5 K in 1,000 and 10,000 Oe fields where both the anomaly and the irreversibility in ZFC and FC branches look to be washed out, see inset in Fig. 17. The down-turn cusp at 85 K in low fields is indicative of antiferromagnetic or spin-glass nature of Ru spins. The FC curve is seen increasing or saturating due to the contribution from paramagnetic Gd spins.

3.6.4 Magneto-superconductivity of "100-atm O_2-annealed" Gd/Ru-1222 samples

Fig. 18 shows the magnetic susceptibility (χ) vs. T behaviour in the temperature range of 5 to 200 K for "100-atm O_2-annealed" Ru-1222 sample under applied fields of 5, 10 and 50 Oe, measured in both zero-field-cooled (ZFC) and field-cooled (FC) modes. In an applied field of 5 Oe, the χ vs. T show the branching of zero-field-cooled (ZFC) and field-cooled (FC) curves at around 90 K (T_{irr}), a step like structure in both at around 40 K (T_c) and further a diamagnetic transition around 40 K (T_d) in the ZFC magnetization.

Though the ZFC and FC magnetization branching is seen at around 90 K, the magnetic behaviour starts deviating from normal paramagnetic relation at much higher T say 160 K. The characteristic temperatures T_{irr}, T_c, and T_{mag} are weakly dependent on $H < 100$ Oe. For higher $H > 100$ Oe, both ZFC and FC are merged with each other, and only T_{mag} could be seen, see inset Fig. 16. This is in general agreement with earlier reports [7,27,28]. In fact no ZFC - FC branching is observed down to 5 K in both 1,000 and 10,000 Oe fields and both the anomaly and the irreversibility in both ZFC and FC branches look to be washed out. The ZFC

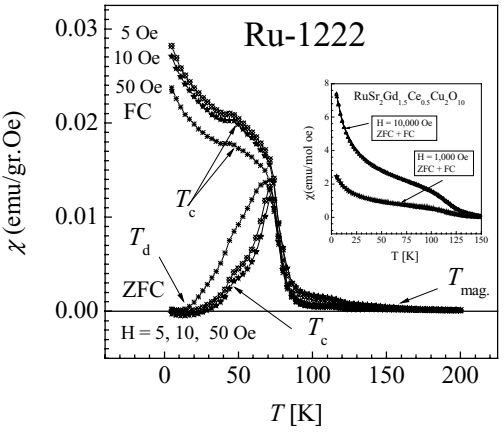

Fig. 18. χ-T plots for a 100-atm O_2-annealed Gd/Ru-1222 sample

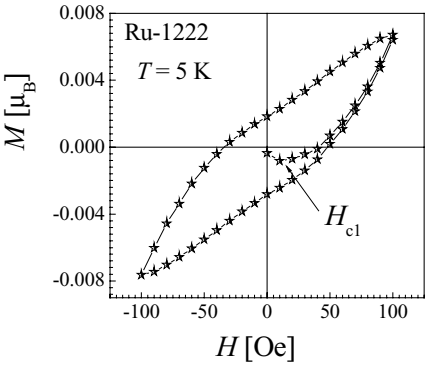

Fig. 19. (M) vs. applied field (H) plots for a 100-atm O_2-annealed Gd/Ru-1222 sample

curve did not show any diamagnetic transition (T_d) in $H > 50$ Oe. The magnetization data at $H = 10$ Oe, show nearly the same characteristics as for $H = 5$ Oe. A low field (-100 Oe H 100 Oe) M vs. H loop for currently studied Ru-1222 compound is shown in Fig.19. Interestingly the diamagnetic signal starts decreasing above applied fields of 25 Oe, and turns to zero at say 40 Oe. The compound seems to have a lower critical field (H_{c1}) of around 25 Oe. Interestingly the M vs. H plot shown in Fig. 19 does not appear to be a normal HTSC case. We will discus the low field (-100 Oe H 100 Oe) M vs. H loop of Fig.19 again after further magnetic characterization in next section.

To elucidate the magnetic property of Ru-1222 we show isothermal magnetization (M) vs. applied field (H) behaviour at various T (Fig. 20). Clear M vs. H loops are seen at 5, 10, 20, and 40 K. The applied fields are in the range of -2000 Oe H 2000. At 5 K, the returning moment (M_{rem}) i.e. the value of magnetization at zero returning field and the coercive filed (H_c) i.e. the value of applied returning field to get zero magnetization are respectively 0.35 μ_B and 250 Oe. Worth mentioning is the fact that Gd (magnetic rare earth) in the compound orders magnetically below 2 K and Ce is known to be in tetravalent non-magnetic state hence the M_{rem} and H_c arising from the ferromagnetic hysteresis loops do belong to Ru only. Hysteresis loops are not seen for M vs. H plots above 80 K. For various hysteresis loops being observed from M vs. H plots below 80 K, the values of both M_{rem} and H_c decrease with T. The plots for both are shown in upper and lower insets of Fig.20. Both M_{rem} and H_c of 0.35 μ_B and 250 Oe being observed for Ru-1222 are much higher than reported for other magneto-superconductor Ru-1212 [8,16]. For Ru-1212 the hysteresis loops are reported quite narrow with M_{rem} and H_c of 0.085 μ_B and 10 Oe respectively. This indicates that in Ru-1222 the ferromagnetic domains are less anisotropic and more rigid.

The isothermal magnetization as a function of magnetic field at 5 K with higher applied fields; 70000 Oe H 70000 Oe is shown in Fig.21. The saturation of the isothermal moment appears to occur above say 5 T applied fields. The contribution from the ferromagnetic component starts to appear below 100 K. The presence of the ferromagnetic component is confirmed by hysteresis loops being observed at 5, 10, 20 and 40 K in the M vs.

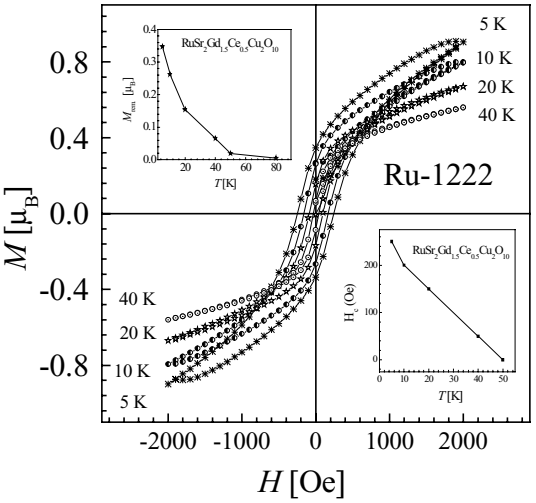

Fig. 20. *M* - *H* loops for a 100-atm O_2-annealed Gd/Ru-1222 at 5, 10, 20 and 40 K with -2000 *H* 2000 Oe. The upper and lower insets of the figure show $M_{rem.}$ vs. *T* and H_c vs. *T* plots for the same.

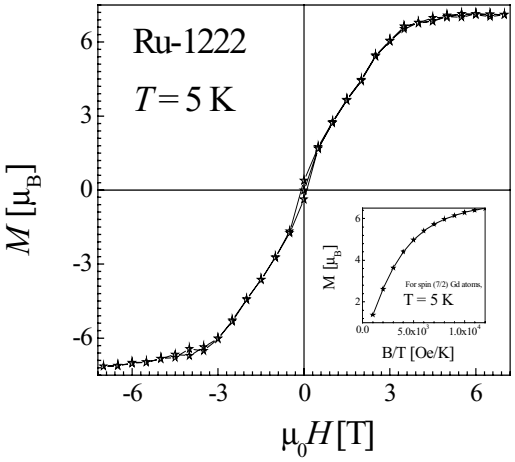

Fig. 21. *M* - *H* plot for 100-atm O_2-annealed Gd/Ru-1222 sample at *T* = 5 K, the applied field are in the range of –70000 Oe H 70000 Oe. The inset shows the theoretical plot for paramagnetic Gd contribution to the system.

H plots, (see Fig. 19). Ru spins order magnetically above say 100 K with a ferromagnetic component within (M_{rem}, H_c = 0.35 μ_B, 250 Oe) at 5 K. As far the value of higher field (> 5 T) saturation moment is concerned, one can not without ambiguity extract the value for Ru contribution. Basically besides paramagnetic Gd contribution at 5 K, the contribution from Cu can not be ignored, which in an under-doped HTSC compound contributes an unknown paramagnetic signal to the system. For paramagnetic Gd contribution the theoretical plot at 5 K is shown in the inset of Fig. 21. After taking out the Gd contribution from Ru-1222 effective moment in Fig.6, a value of ~ 0.75 μ_B is obtained for effective near saturation moment of Ru. This value is lees than for Ru^{5+} low spin state ordering. In Gd/Ru-1212 compound, based on various magnetization data the Ru^{5+} state is reported with an effective saturation moment of nearly 1μ_B [8,11], which ironically differs with more recent magnetic analysis [17].

Superconductivity is seen in terms of diamagnetic transition at below T_d, and T_c (R=0) at slightly higher temperature. It is known earlier that due to internal magnetic field, these compounds are in a spontaneous vortex phase (SVP) even in zero external field [44]. For $T_d < T < T_c$ the compound remains in mixed state. Hence though R= 0 is achieved at relatively higher temperatures the diamagnetic response is seen at much lower T and that also in quite small applied magnetic (H_{c1} < 25 Oe) fields. Now we can understand the M vs. H loop being shown in Fig.17. As discussed in previous section clear ferromagnetic component is seen in the compound at 5 K. Hence at 5K both ferromagnetic and the superconducting hysteresis loops are present in the M vs. H magnetization data, and at low applied fields viz. -100 Oe H 100 Oe, the compound simply exhibit the superimposition of the both, which is the case in Fig.19.

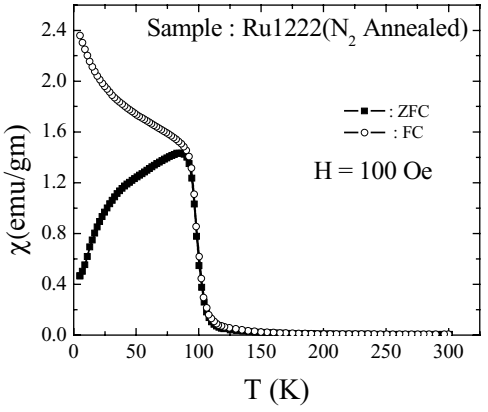

Fig. 22. Magnetic susceptibility (χ) vs. temperature (T) plot for N_2 – annealed Ru-1222 in both ZFC and FC modes with applied field of 100 Oe.

3.6.5 Magneto-superconductivity of "N_2-annealed" Gd/Ru-1222 samples

The χ-T behaviour in the temperature range of 2 to 300 K for N_2-annealed Ru-1222 sample in an applied fields of 100 Oe, measured in both zero-field-cooled (ZFC) and field-cooled (FC) modes, is shown in Fig.22. The general shape of FC and ZFC magnetization plots is similar to that for earlier discussed samples. The only interesting change is that $T_{mag.}$ (defined earlier) has increased to 106 K for N_2-annealed sample. Worth mentioning is the fact that N_2-annealed sample is not superconducting down to 2 K.

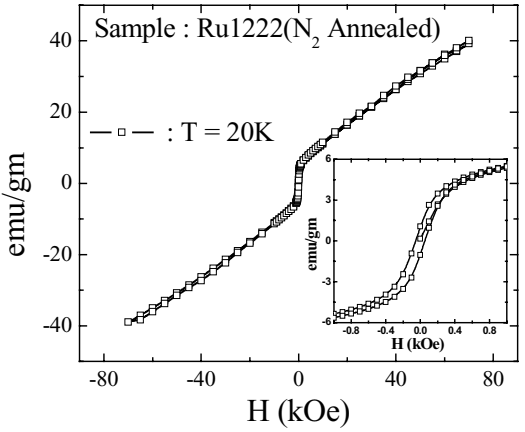

Fig. 23. Magnetization-Field (*M–H*) hysteresis loop for the N_2 – annealed Ru-1222 at 5 K, inset shows the same for –900Oe H +900Oe.

Figure 23 depicts the *M-H* plot at 5 K for N_2-annealed sample. This plot is similar to that observed for earlier discussed samples. The zoomed ferromagnetic component is shown in the inset. The interesting difference, when compared with as-synthesized and 100-atm-O_2 annealed samples, is that *M* does not saturate in applied fields of up to 7 Tesla. This is in contrast to the *M-H* plot for air/100-atm O_2 -annealed samples at 5 K for which M saturates in a field of 6 Tesla (see Fig. 19). The *M-H* plot for N_2-annealed sample is further zoomed in applied field of –900 Oe to 900 Oe, and shown in the inset of Fig.21. Ferromagnetic loop is seen clearly with M_{rem} (2emu/gram) and H_c(170Oe). Relatively lower characteresitc values of M_{rem} and H_c for N_2-annealed sample can be discussed on the basis of SAED and HRTEM studies. Our detailed micro-structural studies earlier for Ru-1222 showed that the observed super-lattice structures due to tilt of RuO_6 octahedra [40] might be coupled with the weak ferromagnetic domains constructed by ordering of the canted Ru moments below the magnetic transition temperature (T_{mag}). Hence ferromagnetic domains coupling depends on the long range ordering of tilted RuO_6 octaherdas in a given Ru-1222 system. In N_2-annealed sample, the long-range superstructures may break down relatively at smaller length scale than for other samples due to less oxygen in RuO_6 octahedra of the same giving rise to weak coupling of the ferromagnetic domains. This will give rise to lower values of M_{rem} and H_c.

This also explains the fifth point regarding the observed saturation of *M-H* curve for other samples and not for N_2-annealed sample. The saturation of *M-H* is dependent on the long range coupling of aligned ferromagnetic domains, which is observed for air-annealed sample only. Long range coupling of aligned moments is directly dependent on the stability of RuO_6 octahedra tilt angle superstructures, which is certainly less for N_2 - annealed sample due to break down in homogenous oxygen content close to 6.0 in the octahedra.

3.6.6 Magneto-superconductivity of HPHT synthesized Y/Ru-1212 sample

One of the puzzles in understanding the magnetization data of Gd/Ru-1212, is not only the antagonising nature of superconducting and magnetic order parameters, but also the presence of magnetic Gd (8μB) along with the possibly magnetic Cu moment (Cu is paramagnetic in under-doped HTSC), which hinders in knowing the exact Ru spins magnetic contribution to the system. Ru-1212 can be formed with non-magnetic RE (rare earth) Y instead of Gd, but only with HPHT (high pressure high temperature) synthesis technique. Magneto-superconductivity of Y/Ru-1212 is discussed below.

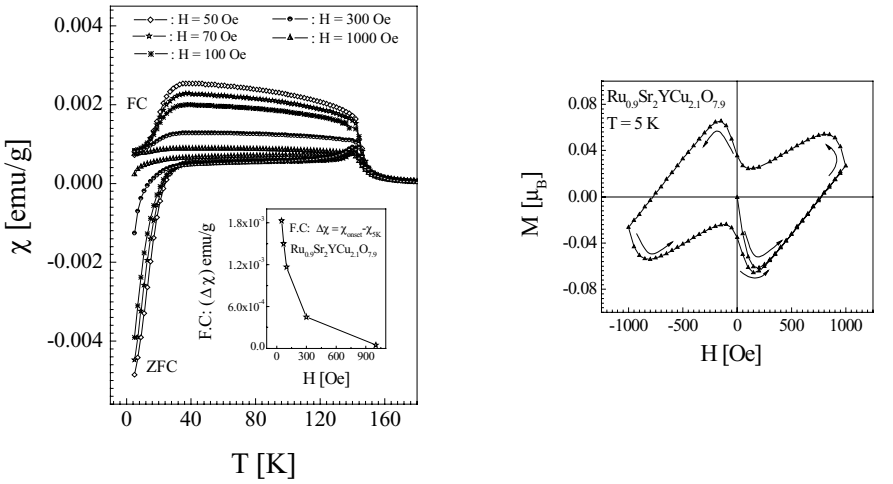

Figs. 24 & 25. Magnetic susceptibility versus temperature (χ vs. *T*) plots for $Ru_{0.9}Sr_2YCu_{2.1}O_{7.9}$ sample, in various applied fields of 50, 70, 100, 300, and 1000 Oe, inset shows the difference of magnetic susceptibility (Δχ) between T_c onset and 5 K for field-cooled (FC) transition for various fields, & the M vs H plot for the same at low fields at 5 K.

Figure 24 shows both ZFC (zero-field-cooled) and FC (field-cooled) magnetic susceptibility versus temperature (χ vs. *T*) plots for $Ru_{0.9}Sr_2YCu_{2.1}O_{7.9}$ sample, in various applied fields of 50, 70, 100, 300, and 1000 Oe. As seen from this figure the ZFC and FC magnetization curves show a significant branching at around 145 K. The branching of ZFC and FC at this temperature is indicative of the magnetic ordering of Ru moments. It is known

from neutron diffraction studies that Ru moments order antiferromagnetically at around 133 K for Gd/Ru-1212 compound [11,12]. As the real nature of the magnetic ordering of Ru moments is still debated, we denote this temperature as $T_{mag.}$ In an earlier report on HPHT synthesized Y/Ru-1212 compound T_{mag} of around 150 K was observed, which is in close agreement to the current value. With an increase in applied field (10 Oe > H > 1000 Oe) basically no change is observed in T_{mag}. The ZFC part of magnetic susceptibility at low T below 30 K, shows clear diamagnetic transitions till applied fields of 300 Oe. The extent of diamagnetic signal is field dependent, and is not observed at 1000 Oe. The diamagnetic signal onset temperature is described as superconducting transition temperature (T_c). Worth noting is the fact that the diamagnetic signal being observed in ZFC measurements does not saturate down to 5 K.

On the other hand, the FC part of the magnetic susceptibility remains positive down to 5 K. The rise in the FC part of magnetic susceptibility is nearly saturated below around 50 K, indicating towards a ferromagnetic transition, followed by a dip below 30 K with further saturation at temperatures lower than 10 K. The dip is FC susceptibility below 30 K, is dependent on applied field, higher is the field and less is the dip. For applied magnetic field of 1000 Oe, no dip is observed in magnetic susceptibility down to 5 K. Interestingly the dip in FC transitions occurs exactly at the temperature being defined as T_c, in ZFC transition. Though in FC transition the diamagnetic signal is not observed, the observation of clear dip at T_c guarantees the observation of bulk nature of superconductivity in the compound. This approves the bulk nature of superconductivity in the compound. The nature of bulk superconductivity was evidenced earlier in Gd/Ru-1212 compound by dip in FC transition at T_c at very low applied fields (< 2.5 Oe) [8]. In our Y/Ru-1212 compound bulk superconductivity is evidenced till applied fields of 300 Oe. The dip in FC magnetization at T_c decreases with the applied field. Numerically the dip in FC magnetization at T_c is defined as the difference of magnetic susceptibility ($\Delta\chi$) between T_c onset and 5 K, which is plotted in inset of Figure 24. It is clear from the inset in Figure 24, that $\Delta\chi$ decreases with an increase in H. However clear $\Delta\chi$ values are seen up to H = 300 Oe, confirming the presence of bulk superconductivity in the compound at least till these applied fields. Estimated Meissner superconducting volume fraction (calculated from $\Delta\chi$ value) is nearly 15 % at H = 50 Oe and above 4 % at H = 300 Oe. Worth discussing is the fact that the values obtained above are for superconductivity which is under internal magnetic field from Ru sub-lattice ferromagnetic field along with the external applied field. Ru-1212 and Ru-1222 compounds are supposed to be in spontaneous vortex phase (SVP) even in zero applied fields due to the application of internal magnetic field [8,44]. It is only with presently studied HPHT synthesized Y/Ru-1212 compound that sufficient dip in terms of $\Delta\chi$ is seen in FC transition up to H = 300 Oe, otherwise in earlier reports on Gd/Ru-1212 the FC transition is not observed even in quite low fields of H < 10 Oe.

Worth noting is the fact, that though the dip in FC magnetic susceptibility is saturated below say 10 K, the ZFC transition below T_c is not saturated down to 5 K. It seems that though the nature of superconductivity being observed at T_c is of bulk nature as indicated by dip and further saturation in FC magnetization, the same is not well connected and hence missing the most of surface screening currents. This is the reason that the diamagnetic transitions seen in ZFC part of magnetic susceptibility are not saturated down to 5 K. Possibly the superconducting domains of bulk nature are being disconnected with non-superconducting

clusters. This results in a two-phase (bulk- superconducting/non-superconducting clusters) system existing in the compound. This gets further credence from the fact, that no T_c (R = 0) state is observed in the compound. Only a partial drop in resistance is observed at around 30 K. There is a strong possibility of the formation of *SIS* (Superconducting-Insulating-Supercoducting) or *SNS* (Superconducting-normal-superconducting) junctions in the compound. Depending on the width (*d*) of *I* or *N* blocks between superconducting clusters and the coherence length (ξ) of the superconductor, one may or may not get the R = 0 state. In present situation it seems that $d >> \xi$.

Figure 25 depicts the *M* vs. *H* plot for the presently studied $Ru_{0.9}Sr_2YCu_{2.1}O_{7.9}$ compound. The applied field *H* is in the range of $0 < H < 1000$ Oe. It is seen from the figure that the magnetization is initially increasingly negative up to say 50 Oe, which later moves towards lower negative values and finally turns to positive above 700 Oe. The sequence of the *M-H* loop is though similar to a normal Type II superconductor, the shape of the curve is rather complicated. A closer look at the present *M-H* loop rather indicates towards the superimposition of a superconducting (negative diamagnetic) and the ferromagnetic (positive) magnetization. The ferromagnetic component of Ru-spins magnetic ordering being present in the compound at 5 K is riding over the superconducting signal. For example at returning fields from 1000 Oe, first a peak is observed in *M-H* loop and later at lower fields of < 300 Oe a clear dip is observed in the loop, before further increase at increasing negative fields. At returning lower fields the diamagnetic signal due to superconductivity again dominates the positive contributions from ferromagnetic component and hence the dip is observed in the loop. Calculating the critical current density (J_c) from magnetic loop is not feasible, because the exact contribution of the ferromagnetic Ru spins is not known. Also the nature of interactions between the two order parameters (superconducting and magnetic) is not understood.

The simple summation of the two signals might not be the exact situation. Further as we will show in the next section that the ferromagnetic contribution of Ru-spins magnetic ordering at 5 K is not yet clear. To our knowledge, ours is the first sample where an *M-H* loop is obtained which is being characteristic of the superconducting and ferromagnetic signals being riding over each other at least until few hundred Oe applied fields. Magnetization is a bulk measurement technique and hence it is no guarantee for the co-existence of superconductivity and ferromagnetism in the material at the microscopic level within the same phase.

In Figure 26 are shown various *M-H* loop for the compound at various *T* of 5, 20, 50, 100, 120 and 150 K, in applied fields of $-70000 < H < 70000$ Oe. Depicted *M-H* loops clearly show the ferromagnetic like behaviour at least below 120 K. In fact even at 150 K the *M-H* loop is not completely linear, indicating the fact that some ordered magnetic domains do exist even at this *T* also. The neutron diffraction studies on Gd/Ru-1212 compound earlier concluded that Ru-spins order antiferromagnetically at high temperatures and the ferromagnetic component is developed due to canting of moments only say below 20 K [11,12].

The *M-H* loops for our currently studied Y/Ru-1212 compound clearly demonstrate towards the ferromagnetic order with the magnetization getting nearly saturated below 20 K. As far as the saturation moment values etc are concerned one can observe that though the complete saturation of moments is not achieved at applied fields of as high as 7 T, the near saturation value observed at 7 T and 5 K is1.17μB, which is nearly the same at 20 K also.

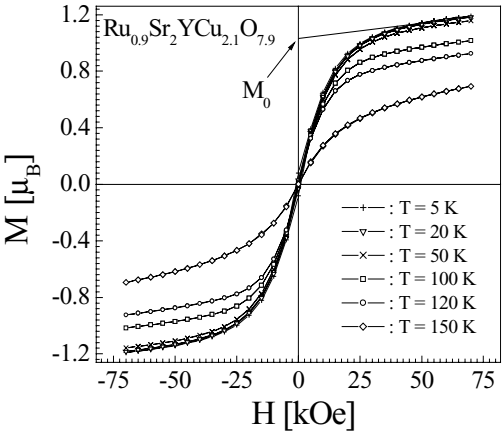

Fig. 26. M vs. H plot for the $Ru_{0.9}Sr_2YCu_{2.1}O_{7.9}$ compound at T = 5, 20, 50, 100, 120 and 150 K, the applied field H are in the range of -70 kOe < H < 70 kOe.

Interestingly this value is higher than as expected theoretically for magnetic ordering of low spin (1/2) states of Ru^{5+} and considerable less than for high spin (3/2) state. In such a situation we rather believe a mixed valence state of Ru (Ru^{5+}/Ru^{4+}) would be more appropriate.

3.6.7 Magnetism of HPHT synthesized Ln/Ru-1222 sample

Figure 27 show both zero-field-cooled (zfc) and fc magnetic susceptibility versus temperature (χ vs. T) plots for the Y/Ru-1222 sample, in external fields of 5 and 20 Oe. As seen from this figure the fc magnetization curve shows an increase near 150 K, followed by a significant jump at around 100 K. The zfc branch shows a rise in magnetization at around 110 K and a cusp like down turn in magnetization at 100 K. In general the magnetization behaviour of the compound can be assigned to a weak ferromagnetic transition at around 100 K. However what is not understood is the initial rise of fc magnetization at 150 K. The interesting difference is that in HPHT synthesized Ln/Ru-1222 compounds the 150 K transition in fc magnetization is more pronounced than for reported Gd/Ru-1222 [7,27,34].

Figure 28 shows both zero-field-cooled (zfc) and fc magnetic susceptibility versus temperature (χ vs. T) plots for the Ln/Ru-1222 samples, with Ln = Ho, Dy. The general behaviour of the all the samples is similar to that as for Y/Ru-1222. The fc transition is seen in both the samples at 150 K. The zfc cusp and the diamagnetic transition are though Ln dependent, but essentially in the same temperature ranges.

Though the studied samples are almost single phase in x-ray, the minute impurities like $SrRuO_3$ or Ln/Ru-1212 might be responsible for the fc transition at 150 K. To exclude such a possibility we would like to stress that in Ln/Ru-1212 compounds the 150 K fc

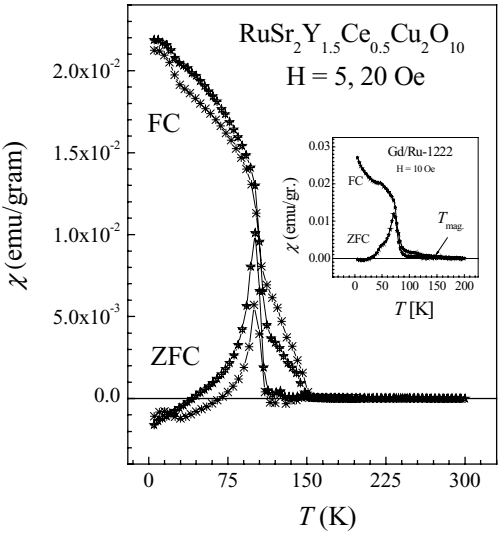

Fig. 27. Magnetic susceptibility versus temperature (χ vs. *T*) plots for Y/Ru-1222 sample, in various applied fields of 5, and 20 Oe, inset shows the same for reported Gd/Ru-1222 compound.

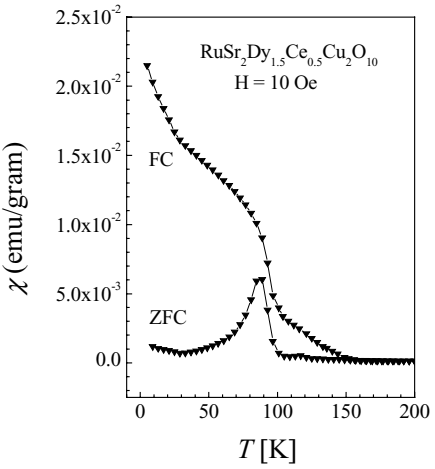

Fig. 28. (χ vs. *T*) plots for Dy/Ru-1222.

transition is followed by a cusp in zfc at same temperature and is also Ln dependent. For Ln = Ho and Dy in Ln/Ru-1212 the Ru spins magnetic ordering temperature is reported to be at 170 K [18]. In Ln/Ru-1222 compounds we do not observe a cusp in zfc and also the FC transition at 150 K is not Ln dependent. Hence the possible origin of fc transition at 150 K due to Ln/Ru-1212 is excluded. At this juncture we believe that the 150 K transition in fc magnetization of Ln/Ru-1222 compounds is intrinsic to this phase. This gets credence from the fact, that though Ln = Y sample unlike others contains small impurity of $SrRuO_3$, the 150 K transition in fc is same for all the studied compounds. In widely studied Gd/Ru-1222 compound also the rise in FC magnetization is reported at around 160-180 K, and was associated with an antiferromagnetic transition of Ru spins [7,27,34].

We did couple of *M* vs *H* experiments for Ln = Ho sample at various temperatures of 130, 120, 110, 100 and 5 K, the results are shown in Fig.29 (a, b, c, d and e). At temperature of 130 and 120 K the *M* vs. *H* hysteresis loops exhibit an antiferromagnetic like structure with canted moments, though at 110 K the same possess more like an S-type spin-glass shape. It seems that the re-orientation of Ru-spins or change in canting angle takes place at 110 K. Further at 5 K, it is more like a ferromagnetic loop. The 5 K, data for non-magnetic Ln = Y will be discussed in Fig. 28.

One wild speculation might be that before 100 K weak ferromagnetic transition, the Ru spins go through a spin-glass like transition at around 110 K and an antiferromagnetic transition at even higher temperature of say 150 K. Without detailed magnetic structure from neutron scattering experiments, it is difficult to comment on exact nature of the magnetism of various Ru-1222 compounds. Ironically, as we mentioned in the introduction, yet no detailed magnetic structure refinements from neutron scattering experiments are available for Ru-1222 compounds. Our current results are one step a head to widely reported Gd/Ru-1222 compound that the 150-160 K transition in magnetization before weak ferromagnetism at 110 K can not be left unnoticed as the same is quite sharp in our samples and is universal to all studied Ln/Ru-1222 compounds.

The zfc and fc significant branching temperature of 100 K for Y/Ru-1222 is relatively higher than previously reported ~ 80 K for Gd/Ru-1222. For reference, reported [34] χ vs. *T* plot for Gd/Ru-1222 is shown in inset of Fig.26. Interestingly for magnetic ordering temperature for Gd/Ru-1212 of ~133 K was also found to be relatively lower than for HPHT synthesized Y/Ru-1212 (~150 K) [12,16,18]. The zfc part of magnetic susceptibility at low temperature below 70 K shows a clear shoulder with further weak diamagnetic transition below ~50 K. The zfc curve did not show any diamagnetic transition (T_d) in H = 100 Oe. The shoulder at 70 K is known as T_c (superconducting transition temperature) from various experiments in Gd/Ru-1222. It is known earlier that due to internal magnetic field, these compounds are in a spontaneous vortex phase (SVP) even in zero external field [44]. For $T_d < T < T_c$ the compound remains in mixed state. Hence though possibly superconductivity is achieved at relatively higher temperatures the diamagnetic response is seen at much lower *T* and that also in quite small applied magnetic fields [7,27,34]. Worth mentioning is the fact that the electrical transport measurements being necessary for confirmation of superconductivity are yet not carried out on presently synthesised Ln/Ru-1222 compounds. Hence the superconductivity as such cannot be confirmed, detailed various measurements are underway and will be reported shortly.

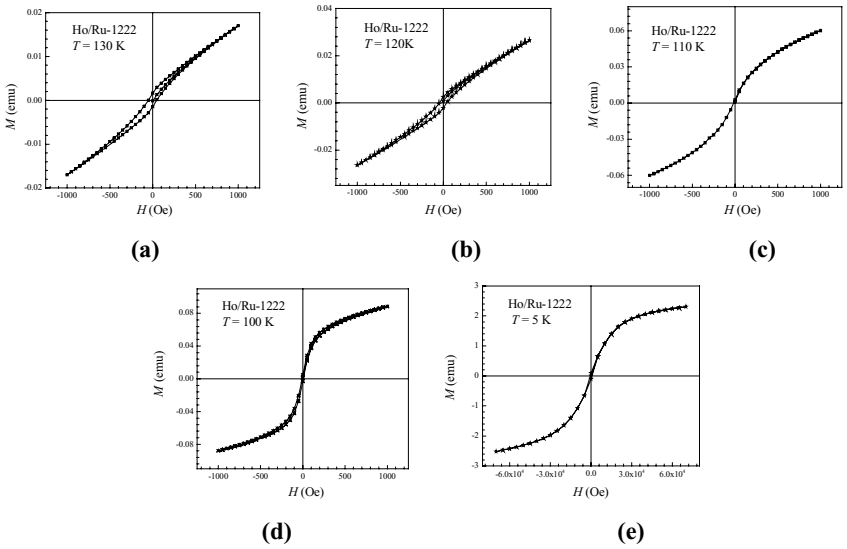

Fig. 29. *M* vs. *H* plot for the Ho/Ru-1222 compound at *T* = (a) 130 K, (b) 120 K, (c) 110 K, (d) 100 K and (e) 5 K.

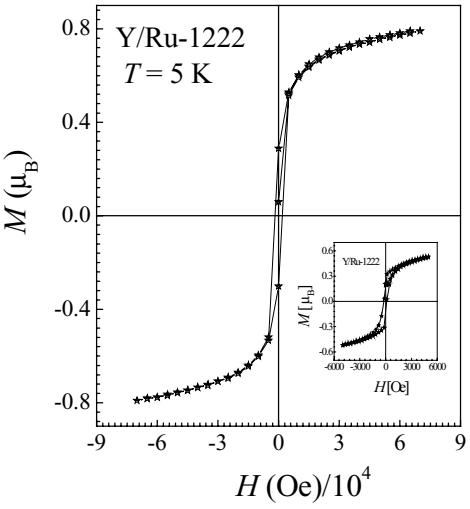

Fig. 30. *M* vs. *H* plot for the Y/Ru-1222 compound at *T* = 5 K, the applied field H are in the range Of -70 kOe < *H* < 70 kOe. The inset shows the *M* vs. *H* plot for the same at 5 K, with -50000 H 5000 Oe.

The isothermal magnetization as a function of magnetic field at 5 K with higher applied fields; 70000 Oe H 70000 Oe for Ln = Y sample is shown in Fig.30. The saturation of the isothermal moment appears to occur above say 4 T applied fields. The presence of the ferromagnetic component is confirmed by hysteresis loops being observed at 5 K in the M vs. H plots, (see inset Fig. 30). Ru spins order magnetically above say 100 K with a ferromagnetic component within (M_{rem}, H_c = 0.30 μ_B, 150 Oe) at 5 K. As far the value of higher field (> 4 T) saturation moment is concerned, one cannot without ambiguity extract the value for Ru contribution, because the contribution from Cu cannot be ignored. In an under-doped HTSC compound Cu contributes an unknown paramagnetic signal to the system. Without considering the Cu contribution an effective moment of ~ 0.80 μ_B is obtained for Ru. This value is lees than for Ru^{5+} low spin state ordering.

3.6.8 Magnetism of HPHT synthesized Ln/Ru-1232 sample

Figure 31 show both zero-field-cooled (zfc) and fc magnetic susceptibility versus temperature (χ vs. T) plots for the Y/Ru-1232 sample, in external fields of 10 Oe. As seen from this figure the fc magnetization curve shows an increase near 90 K ($T_{mag.}$). Furtrher, the zfc branch shows a cusp like down turn in magnetization at around 70 K. In general the magnetization behaviour of the compound can be assigned to a weak ferromagnetic transition at around 90 K. The zfc branch also shows a step like structure at around 45 K (T_c) and a diamagnetic transition around 35 K (T_d).

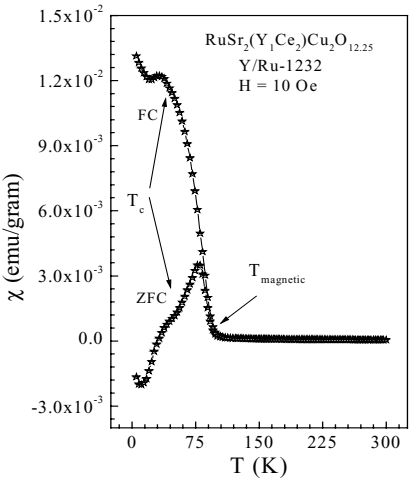

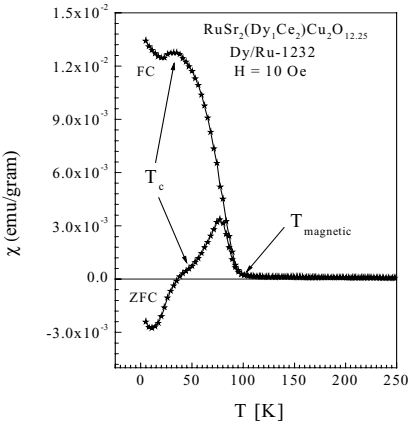

Figs. 31 & 32. Magnetic susceptibility versus temperature (χ vs. T) plots for Y/Ru-1232 & Dy/Ru-1232 samples, in various applied fields of 5 Oe.

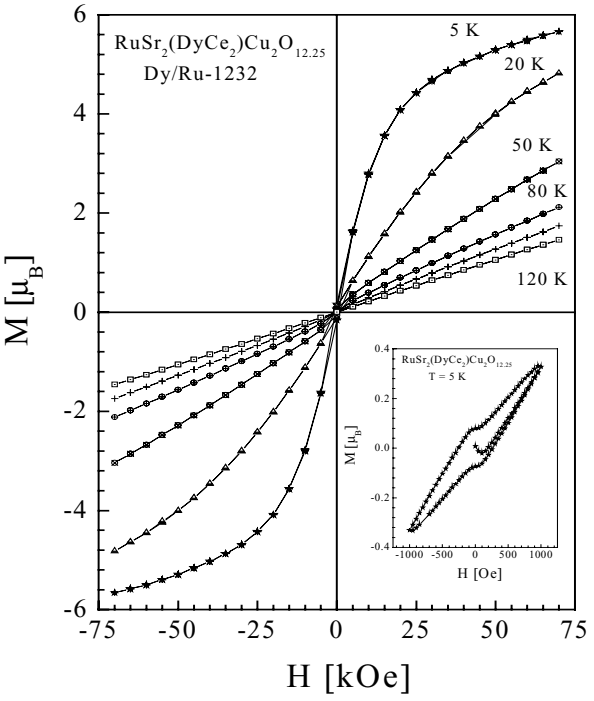

Fig. 33 (*M*) vs. applied field (*H*) plots for Dy/Ru1232 sample in higher applied fields.

Figure 32 shows both zero-field-cooled (zfc) and fc magnetic susceptibility versus temperature (χ vs. T) plots for the Dy/Ru-1232 sample. The general behaviour is similar to that as for Y/Ru-1232. The fc transition is seen at 90 K. The zfc cusp at around 70 K, the step like structure (T_c) at around 40 K and diamagnetic transition (T_d) is seen at around 35 K for Dy/Ru-1232 compound. Superconductivity is seen in terms of diamagnetic transition at below T_d. It is known earlier that due to internal magnetic field, these compounds are in a spontaneous vortex phase (SVP) even in zero external field. For $T_d < T < T_c$ the compound remains in mixed state. Hence though superconductivity might be achieved at relatively higher temperatures the diamagnetic response is seen at much lower T and that also in quite small applied magnetic fields.

To further elucidate on the magnetization of these compounds, the isothermal magnetization as a function of magnetic field at 5, 20, 50, 80 and 120 K with applied fields; -70000 Oe H 70000 Oe for Ln = Dy sample is shown in Fig.33. The saturation of the isothermal moment appears to occur above say 4 Tesla applied fields at 5 K. Further increase in magnetization above say 4 Tesla is due to the contribution from Dy moments. At higher temperatures of 20, 50, 80, 100 and 120 K the near saturation of M vs. H is not seen. The presence of the ferromagnetic component is confirmed by hysteresis loop being observed at

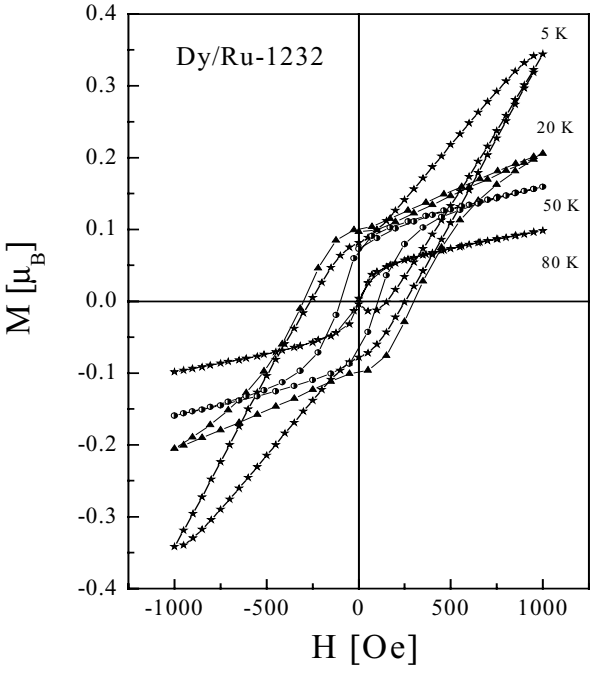

Fig. 34. (*M*) vs. applied field (*H*) plots for Dy/Ru1232 sample in low applied fields

5 K in the M vs. H plots (-1000 Oe H 1000), (see inset Fig. 33). Ru spins order magnetically above say 90 K with a ferromagnetic component within at 5 K. As far the value of higher field (> 4 T) saturation moment is concerned, one cannot without ambiguity extract the value for Ru contribution, because the contribution from Cu cannot be ignored. In an under-doped HTSC compound Cu contributes an unknown paramagnetic signal to the system.

Figure.34 shows the isothermal magnetization (*M*) vs. applied field (H) behaviour for Dy/Ru-1232 in low fields of 1000 Oe H 1000. Clear M vs. H loops are seen at 5, 20, and 50 K, but not at 80 K. The applied fields are in the range of -1000 Oe H 1000. The returning moment (M_{rem}) i.e. the value of magnetization at zero returning field and the coercive filed (H_c) i.e. the value of applied returning field to get zero magnetization are clearly seen up to 50 K. Worth mentioning is the fact that Dy (magnetic rare earth) in the compound must order magnetically below 0.5 K and Ce is known to be in tetravalent non-magnetic state hence the M_{rem} and H_c arising from the ferromagnetic hysteresis loops do belong to Ru only. Hysteresis loops are not seen for M vs. H plots at or above 80 K. For various hysteresis loops being observed from M vs. H plots below 80 K, the values of both M_{rem} and H_c decrease with increase in T. Both M_{rem} and H_c being observed for Ru-1232 are much higher than reported for other magneto-superconductor Ru-1212 and comparative to Ru-1222. For Ru-1212 the hysteresis loops are reported quite narrow. This indicates that in

Ru-1232 the ferromagnetic domains are less anisotropic and more rigid like Ru-1222 and unlike to that for Ru-1212. Worth mentioning is the fact that the Ln/Ru-1232 compounds are not yet synthesized in pure phase, see Figure 5. Hence their magneto-superconductivity can yet not be conclusive. In any case the preliminary unpublished results on Ln/Ru-1232 compounds are shown above in the present review of rutheno-cuprates.

3.7 The complex magnetic ordering of Ru in Ru-1212 and Ru-1222

It is discussed in the beginning of the review that the exact nature of the ordering of Ru moments in various rutheno-cuprate magneto-superconductors is not yet well understood. In fact recent magnetization results do conflict with each other viz. ref. [10,15,16]. Also the magnetization picture [15,16] is not the same as proposed via neutron scattering studies [11,12,31]. Most recent results on both Ru-1222 [27,45] and Ru-1212 [46] have provided even more complex picture of the magnetism of these compounds. Various magnetization measurements on Ru-1222 have provided the evidence for magnetic phase separation [27].

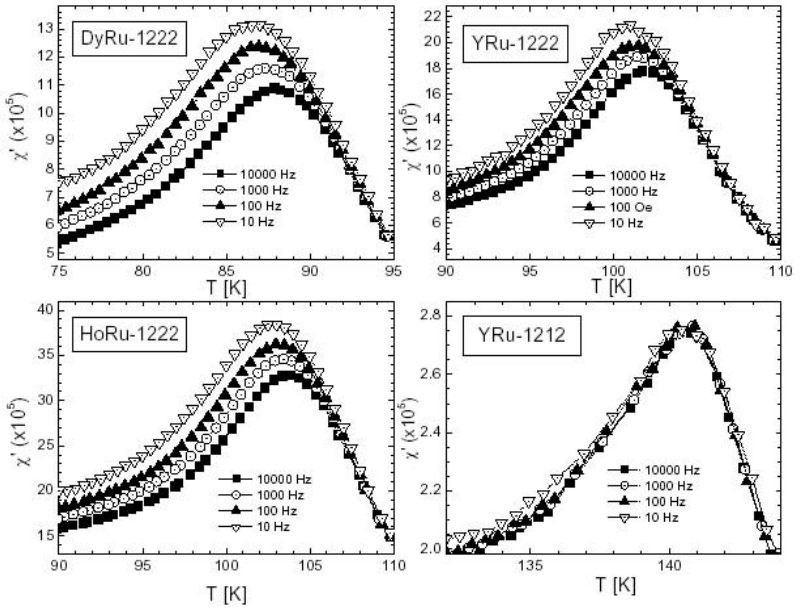

Fig. 35. Real part of the ac susceptibility as a function of temperature for H = 50 Oe and four different frequencies, for all four samples. The peak position defines the freezing temperature T_f (for the Ln/Ru – 1222 samples).

Also it was pointed out that magnetic structure of RuO_6 octahedra in Ru-1222 is different than that for Ru-1212 [27]. Here some of our very recent results [45,46] pertaining to the AC susceptibility measurements on both Ru-1222 and Ru-1212 are given. A very powerful technique to evidence spin-glass (SG) behavior is the ac susceptibility χ_{ac} measurements. It is expected to a spin-glass system that both components χ' and χ'' of χ_{ac} present a sharp, frequency dependent cusp. The position of the cusp χ' defines the freezing temperature T_f, which coincides with the inflection point in χ''. It is also well known that dc magnetic fields as low as a few hundreds of Oersted can round this cusp up. In Fig. 35 we present the ac susceptibility for our sample measured at H = 50 Oe. The main panel of Fig. 34 presents the temperature dependence of χ' for 4 different frequencies (10,100, 1000, and 10000 Hz). χ' presents a sharp, frequency dependent peak at $T_f \sim 72$ *K* for all Ln/Ru-1222 samples. The peak shifts to lower temperatures and its intensity increases as the frequency of the excitation field is decreased. Interestingly for Y/Ru-1212 sample the frequency dependence of χ' is not seen.

These results indicate that though the Ru-1222 compounds possess SG behaviour of Ru moments [45], the Ru-1212 system does not [46]. The presence/absence of SG component in these systems was shown by various other measurements viz. TRM (thermoremanent magnetization) and IRM (isothermal remanant magnetization) [45,46]. A moot question arises, why the two systems with similar RuO_6 octahedra do have different magnetic structure of Ru moments?. The answer perhaps lies with the fat that in Ru-1222 relatively larger variation of oxygen content is permitted than in Ru-1212. This implies necessary that RuO_6 becomes RuO_{6-d} with varying Ru^{4+}/Ru^{5+} valence states.

3.8 Electrical transport properties: PPMS results

3.8.1 Ru-1212 samples

Figure 36 shows the resistance (*R*) *versus T* for an as-synthesized (superconducting) $RuSr_2GdCu_2O_{8-\delta}$ sample in zero, 3 and 7 T applied fields. The *R-T* behaviour without any applied magnetic field is metallic down to 150 K and semiconducting between 150 K and 25 K, with a superconducting transition onset (T_c^{onset}) at 25 K and $R = 0$ at 20 K. This behaviour is typical of underdoped HTSC compounds. Also observed is an upward hump (T_{hump}) in *R-T* around 140 K, which indicates the possibility of antiferromagnetic ordering of spins. The *R-T* behaviour under an applied field of 7 T is nearly the same above T_c^{onset}, except that T_{hump} is completely smeared out due to possible change in the magnetic structure. Also in 7 T applied field the T_c^{onset} decreases to around 10 K and $R = 0$ is not observed down to 5 K.

In an intermediate field of 3 T, both T_c^{onset} and $T_c^{R=0}$ decreased, to 20 and 10 K respectively. For conventional HTSC, T_c^{onset} remains nearly the same under all possible applied fields, with decreasing $R = 0$ temperature and an increased transition width ($T_c^{onset} - T_c^{R=0}$). Therefore, a different type of broadening of the transition under a magnetic field is obtained for Ru-1212 from that reported for conventional HTSC. In earlier reports on Ru-1212, the T_c^{onset} under a magnetic field decreased like the present case. The present behaviour of transition broadening under a magnetic field is presumably due to formation of SNS/SIS junctions/clusters in the present and similar samples. Non-superconducting $RuSr_2GdCu_2O_{8-\delta}$ might be stacked between superconducting $Ru_{1-x}Cu_xSr_2GdCu_2O_{8-\delta}$, resulting in ideal SIS or SNS junctions within the material.

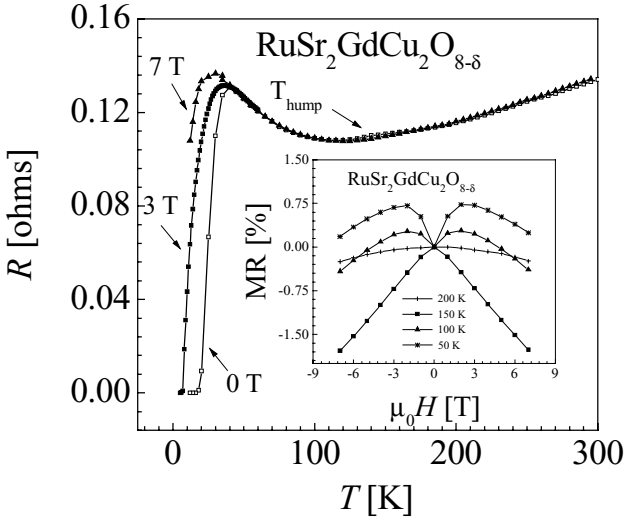

Fig. 36. R-T plot and magneto-transport behaviour for an as-synthesized (superconducting) $RuSr_2GdCu_2O_{8-\delta}$ sample.

Inset of Fig. 36 shows the magnetoresistance (MR) behaviour of the present Ru-1212 sample at various fields and temperatures. MR is negative in all applied fields upto 7 T above the magnetic ordering temperature, *i.e.* at 150 K and 200 K. Maximum negative MR of up to 2 % is observed at 150 K, which is close to the magnetic ordering temperature of around 140 K. At temperatures below the ordering temperature (100 K and 50 K), MR displays a positive peak at low fields and becomes negative at higher fields. This behaviour is in general agreement with previous reports.

The R-T plot and magneto-transport behaviour for a 100-atm O_2-annealed Ru-1212 sample revealed interestingly no $R = 0$ and only a T_c^{onset} was observed around 20 K. Other characteristics in terms of T_{hump} in R-T at around 140 K and the systematic changes in MR with applied field and T were the same as for the as-synthesized sample.

3.8.2 Ru-1222 samples

Figure 37 depicts the *R-T* plots in 0 and 7 T fields for an 100-atm O_2-annealed Ru-1212 sample. The *R-T* behaviour in zero field is similar to that observed for the as-synthesized sample with some improvement towards metallic conductivity. Superconductivity starts with T_c^{onset} at 51 K and the $T_c^{R=0}$ is seen at 43 K.

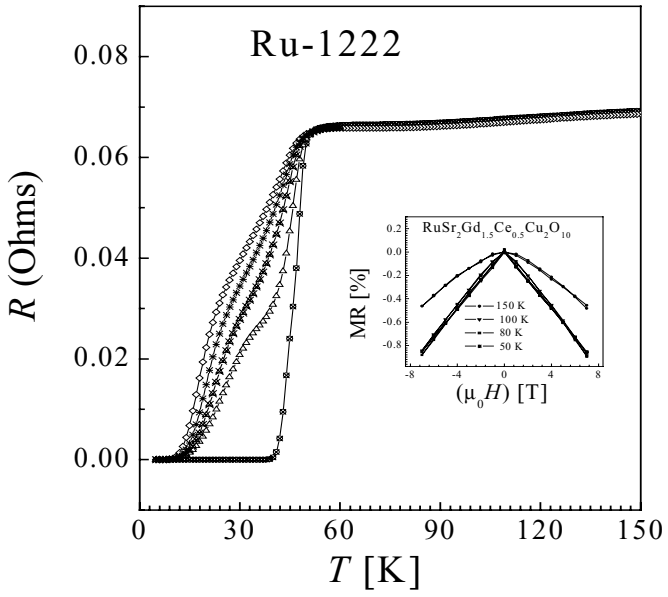

Fig. 37. *R-T* plot and magneto-transport behaviour for a 100-atm O_2-annealed $RuSr_2(Gd_{0.75}Ce_{0.25})_2Cu_2O_{10-\delta}$ sample. The inset shows the MR behaviour of the same.

The *R-T* behaviour under an applied field of 7 T is nearly the same as that of 0 T above T_c^{onset}. However in 7 T field $T_c^{R=0}$ is observed only around 12 K. In intermediate fields of 1 T, 3 T and 5 T, T_c^{onset} remains nearly invariant and $T_c^{R=0}$ are seen at 18 K 16 K, and 14 K, respectively. Also seen is a shoulder in the *R-T* curve in all applied fields, the origin of which is not known. When these results of magneto-resistivity are compared with results for the as-synthesized sample, one finds that $T_c^{R=0}$ is nearly doubled from 23 K to 43 K after the 100-atm O_2 annealing. Furthermore, $T_c^{R=0}$ is observed in 7 T field also, which is not the case for the as-synthesized sample. Magneto-resistivity results for the 100-atm O_2-annealed Ru-1212 sample substantiate the magnetization results, indicating that superconductivity is enhanced upon the 100-atm O_2 annealing.

In the inset of Fig. 37, the MR data of the same Ru-1222 sample is shown at various temperatures and fields, revealing a small negative MR effect in the whole temperature range. Below 100 K the degree of MR is nearly the same in all applied fields and the nature of the MR effect is of the tunnelling-magneto-resistance (TMR) type as judged from the curve shape. Also note that the MR behaviour of the present Ru-1222 sample is different from that of Ru-1212, section 3.6 (A). Ru-1212 exhibited systematic changes in sign of MR at various *T* and fields.

3.8.3 Magneto-transport of N_2-annealed non-superconducting Ru-1222 sample

Figure 38 depicts the resistance versus temperature (R-T) behavior for N_2-annealed Ru-1222 sample in magnetic fields of 0, 3 and 6 Tesla. The R-T behavior of this compound is semiconducting down to 2 K. No superconducting transition is observed in the whole temperature range studied (2-300 K). Further, in low temperature region, an appreciable MR is seen for the N_2-annealed sample. Magneto-resistance (MR), as a function of applied field, at temperatures of 5 and 10 K, for N_2-annealed sample, is plotted in inset of Fig.3. MR of >20 % is observed at 5 K in an applied field of up to 9 Tesla. At 2 K, around 20% MR is seen even in low applied field of 3 Tesla (plot not shown).

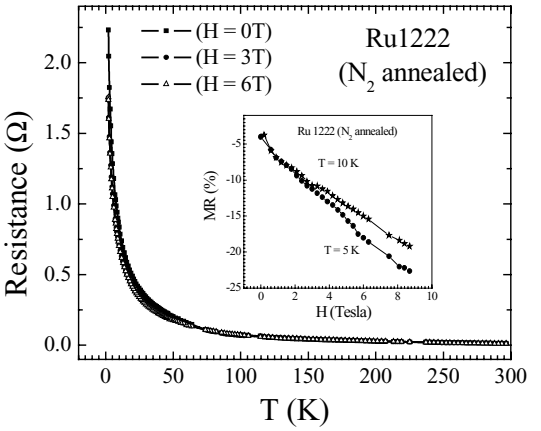

Fig. 38. Resistance (R) vs. temperature (T) plots in 0, 3, and 6 T applied magnetic fields for N_2-annealed Ru-1222. Inset shows the Magnetoresistance (MR%) at 5 K in applied fields up to 9 Tesla.

4. SUMMARY AND CONCLUDING REMARKS

We reviewed our various results on rutheno-cuprate magneto-superconductors $RuSr_2GdCu_2O_{8-\delta}$ (Ru-1212) and $RuSr_2(Gd_{0.75}Ce_{0.25})_2Cu_2O_{10-\delta}$ (Ru-1222) synthesized by NPHT process. Also reviewed are the results for HPHT synthesized various Ln/Ru-1212, 1222 and 1232. Various important results being reported by other international groups are incorporated and discussed critically. It is observed, that it is difficult to control the oxygen content of Ru-1212, though the same is possible up to some extent for Ru-1222. Samples of both phases exhibited superconductivity, presumably in the CuO_2 plane at low temperatures coexisting with magnetic ordering of Ru spins of predominantly antiferromagnetic type below 140 K having a ferromagnetic component appearing below 20 K. Electrical conductivity

measurements indicate that the $RuO_{2-\delta}$ layer takes part in conduction besides the CuO_2 plane. The magnetic ordering temperature of Ru spins is seen as a clear hump in the resistivity measurements, establishing the magnetic spins interaction with the conduction carriers.

The $Ru_{0.9}Sr_2YCu_{2.1}O_{7.9}$ being synthesized by HPHT (high pressure high temperature) solid-state reaction route exhibits superconductivity below 30 K. Also the Ru-spins are ordered magnetically above 143 K, with a ferromagnetic component at 5K. $Ru_{0.9}Sr_2YCu_{2.1}O_{7.9}$ shows clear diamagnetic transitions in zero-field-cooled (ZFC) magnetic susceptibility in applied fields of up to few hundred Oe (< 300 Oe) at superconducting transition temperature (T_c), followed by a dip in the field-cooled (FC) magnetization at same temperatures with near saturation of the FC signal below 10 K. Though the dip in FC magnetization at T_c followed by saturation below 10 K indicates towards good volume fraction of superconductivity, the ZFC transition is not saturated down to 5 K. This suggests that though superconductivity is of bulk nature, the same is not well connected to provide sufficient surface shielding currents for ZFC process. Interestingly the compound does not exhibit R = 0 state down to 5 K. Low field (<1000 Oe) *M* vs. *H* plots show clearly that both superconducting and the ferromagnetic components are present in the compound at 5 K. The sample shows ferromagnetic like hysteresis loops at 5, 20 K in *M* vs. *H* plots. Though the complete saturation of moments is not achieved at applied fields of as high as 7 T, the near saturation values observed at 7 T and 5 K is1.17μB. This value is higher than as expected theoretically for magnetic ordering of low spin (1/2) states of Ru^{5+} and considerable less than for high spin (3/2) state. The returning moment value as seen from hysteresis loop is 0.079 μB per Ru.

The Ln/Ru-1222 materials become magnetically ordered at T_M =152(2) K regardless of Ln [32,47]. The wide ferromagnetic-like hysteresis loops which open at 5 K, close themselves around T_{irr}= 90-100 K and the remanent magnetizations (M_{rem}) and the coercive fields (H_C) become zero. Surprisingly, at $T_{irr}<T< T_M$ a reappearance of the M_{rem} and H_C (with a peak at 120-130 K) is observed for all three samples studied. For the non-magnetic Ln=Y compound, the extracted saturation moment at 5 K and the effective paramagnetic moment are is 0.75 and 2.05 μ_B /Ru, values which are close to the expected 1 μ_B and 1.73 μ_B respectively, for the low-spin state of Ru^{5+}. We argue that the Ru-1222 system becomes (i) anti-ferromagnetically (AFM) ordered at T_M. In this range a metamagnetic transition is induced by the applied field (ii). At $T_{irr} < T_M$, weak-ferromagnetism (W-FM) is induced by the canting of the Ru moments.

Two most important issues related to rutheno-cuprates are about the phase purity of these compounds [48], and the discussion of ensuing basic physics [49] related to them. This is some thing, which need to be debated for any new material being invented. It is reported that $RuSr_2GdCu_2O_8$ decomposes under high-temperature treatment [48], giving rise to micro-islands of the melt depleted Ru and Cu-enriched phase. Interestingly enough Ru depleted phase viz. $Ru_{1-x}Sr_2GdCu_2O_8$ could invoke for superconducting but not magnetic material. For example composition like $Ru_{1-x}Sr_2GdCu_{2+x}O_8$ could show superconductivity with say x = 0.5 but not magnetic characteristics [50]. These doubts regarding phase separation in rutheno-cuprates were casted earlier also [25,29,33]. Recent reports [48,50] once again have asked for the phase purity of widely discussed Gd/Ru-1212 compounds. As discussed in introduction itself, the phase purity issue of rutheno-cuprates is still far from conclusive. It seems the magnet-superconductivity of rutheno-cuprates is yet in pre-mature stage and a lot more need to be done before concluding the physical properties of these materials.

ACKNOWLEDGEMENT

The vast amount of work being given in the current review would not have been possible beside the help of several collaborators during my visits to various international laboratories. The work on rutheno-cuprates was first started during my visit to Max-Planck Institute, Stuttgart Germany, for which the kind help and guidance from Prof. E. Gmelin and Dr. R.W. Henn is acknowledged. Later work was continued in Tokyo Institute of Technology (TITECH), Japan under the able guidance of Prof. H. Yamauchi and Prof. M. Karppinen. Several HPHT phases of rutheno-cuprates were synthesized and characterized in National Institute of Material Science (NIMS) Japan under guidance and encouragement by Dr. E. Takayama-Muromachi. Finally coming back to India now Prof. S.K. Malik from Tata Institute of Fundamental Research (TIFR) Mumbai is guiding and helping in further developing the field of rutheno-cuprate magneto-superconductors.

There are also some collaborators, being time to time involved for specific studies on rutheno-cuprates. They include Prof. R.S. Liu from Hsinchu, Taiwan, Prof. Oscar de Lima and Dr. Claudio A. Cardossso from Instituto de Fisica, UNICAMP, Brazil and Prof. I. Felner from Racah Institute of Physics Jerusalem, Israel. Infact Prof. I. Felner has been continuously a guiding spirit behind the work on rutheno-cuprates being presented in the current review.

REFERENCES

1. V.L. Ginzburg, Zh. Eksp. Teor. 31, 202 (1956), Sov. Phys. JETP **4**, 153 (1957).
2. B.T. Mathias, H. Suhl, E. and Corenzwit, Phys. Rev. Lett. **1**, 449 (1958).
3. S.K. Sinha, G.W. Crabtree, D.G. Hinks, and H.A. Mook, Phys. Rev. Lett. **48**, 950 (1982).
4. Review article by M.B. Maple, Physica B **215**, 110 (1995).
5. S.S. Saxena, P. Agarwal, K. Ahilan, F.M. Groshe, R.K.W. Haselwimmer, M.J. Steiner, E. Pugh, I.R. Walker, S.R. Julian, P. Monthoux, G.G. Lonzarich, A. Huxley, I. Sheikin, D. Braithwaite, J. Floquet, Nature **406**, 587 (2000).
6. C. Pfleiderer, M. Uhlarz, S.M. Hayden, R. Vollmer, H. Von Lohneysen, N.R. Bernhoeft, and G.G. Lonzarich, Nature 412, **58** (2001)
7. I. Felner, U. Asaf, Y. Levi, and O. Millo, *Phys. Rev. B* **55**, R3374 (1997).
8. C. Bernhard, J.L. Tallon, Ch. Niedermayer, Th. Blasius, A. Golnik, E. Brücher, R.K. Kremer, D.R. Noakes, C.E. Stronack, and E.J. Asnaldo, *Phys. Rev. B* **59**, 14099 (1999).
9. L. Bauernfeind, W. Widder, and H.F. Braun, *Physica C* **254**, 151 (1995).
10. A. Fainstein, E. Winkler, A. Butera, and J.L. Tallon, *Phys. Rev. B* **60**, 12597 (1999).
11. J.W. Lynn, B. Keimer, C. Ulrich, C. Bernhard, and J.L. Tallon, *Phys. Rev. B* **61**, R14964 (2000).
12. H. Takigawa, J. Akimitsu, H. Kawano-Furukawa, and H. Yoshizawa, *J. Phys. Soc. Jpn.* **70**, 333 (2001).
13. O. Chmaissem, J. D. Jorgensen, H. Shaked, P. Dollar and J. L. Tallon, *Phys. Rev. B* **61**, 6401 (2001).
14. J. D. Jorgensen, O. Chmaissem, H. Shaked, S. Short, P. W. Klamut, B. Dabrowski and J. L. Tallon, *Phys. Rev. B* **63**, 54440 (2001).
15. J.L. Tallon, C. Bernhard, M.E. Bowden, T.M. Soto, B. Walker, P.W. Gilberd, M.R. Preseland, J.P. Attfield, A.C. McLaughlin, and A.N. Fitch, *IEEE, J. Appl. Supercond*. **9**, 1696 (1999).
16. V.P.S. Awana, T. Kawashima and E. Takayama-Muromachi, Phys. Rev. B **67**, 172502 (2003).
17. A. Butera, A. Fainstein, E. Winkler, and J. Tallon, Phys. Rev. B 63, 054442 (2001).
18. E. Takayama-Muromachi , T. Kawashima, N. D. Zhigadlo, T. Drezen, M. Isobe, A. T. Matveev, K. Kimoto and Y. Matsui Physica C **357-360** (2001) 318.
19. C.W. Chu, Y.Y. Xue, S. Tsui, J. Cmaidalka, A.K. Heilman, B. Lorenz, and R.L. Meng, Physica C **335**, 231 (2000).
20. J.L. Tallon, J.W. Loram, G.V.M. Williams, and C. Bernhard, Phys. Rev. B **61**, R6471 (2000).
21. X.H. Chen, Z. Sun, K.Q. Wang, S.Y. Li, Y.M. Xiong, M. Yu, and L.Z. Cao, Phys. Rev. B **63**, 64506 (2001).
22. C.W. Chu, Y.Y. Xue, R.L. Meng, J. Cmaidalka, L.M Deznati, Y.S. Wang, B. Lorenz, and A.K. Heilman, cond-mat/9910056 (1999)
23. C.S. Knee, B.D. Rainford, and M.T. Weller, *J. Materials commun*. **10**, 2445 (2000).
24. I. Felner, U. Asaf, and E. Galstyn, *Phys. Rev. B* **66**, 24503 (2002).
25. V.P.S. Awana, S. Ichihara, J. Nakamura, M. Karppinen, and H. Yamauchi, *Physica C* **378-381**, 249-254 (2002) and V.P.S. Awana, M. Karppinen, and H. Yamauchi, *Pramana J. Phys.* **58**, 809 (2002).

26. Y.Y. Xue, D.H. Cao, B. Lorenz, and C.W. Chu, *Phys. Rev. B*, **65**, 20511 (2001).
27. I. Zivkovic, Y. Hirai, B.H. Frazer, M. Prester, D. Drobac, D. Ariosa, H. Berger, D. Pavuna, G. Margaritondo, I. Felner, and M. Onillion, *Phys. Rev. B*, **65**, 144420 (2001).
28. V. V. Petrykin, M. Kakihana, Y. Tanaka, H. Yasuoka, M. Abe and S. Eriksson, *Physica C*, **378-381**, 47 (2002).
29. R.W. Henn, H. Friedrich, V.P.S. Awana, and E. Gmelin, *Physica C* **341-348**, 457 (2000).
30. P.W. Klamut, B. Dabrowski, K. Kolesnik, M. Maxwell, and J. Mais, *Phys. Rev. B* **63**, 224512 (2001).
31. Y. Tokunaga, H. Kotegawa, K. Ishida, Y. Kitaoka, H. Takagiwa, and J. Akimitsu, *Phys. Rev. Lett*. **86**, 5767 (2001).
32. V.P.S. Awana and E. Takayama-Muromachi, Physica C **390**, 101 (2003).
33. V.P.S. Awana, S. Ichihara, J. Nakamura, M. Karppinen, H. Yamauchi, Jinbo Yang, W.B. Yelon, W.J. James and S.K. Malik, J. Appl. Phys. **91**, 8501 (2002).
34. V.P.S. Awana, E. Takayama-Muromachi, K. Karppinen and H. Yamauchi, Physica C **390**, 233 (2003).
35. V.P.S. Awana, M.A. Ansari, Anurag Gupta, R.B. Saxena, H. Kishan, Devendra Buddhikot, and S.K. Malik, submitted Phys. Rev. B (2004).
36. M. Matvejeff, V.P.S. Awana, H. Yamauchi and M. Karppinen, Physica C **392-396**, 87-92 (2003).
37. V.P.S. Awana, M. Karppinen, H. Yamauchi, M. Matvejeff, R.S. Liu, and L.-Y. Jang, *J. Low Temp. Phys*., **131**, 1211 (2003).
38. R.S. Liu, L.-Y. Jang, H.-H. Hung, and J.L. Tallon, *Phys. Rev. B* **63**, 212505 (2001).
39. G.V.M. Williams, L.-Y. Jang, and R.S. Liu, *Phys. Rev. B* **65**, 64508 (2002).
40. Tadahiro Yokosawa,, Veer Pal Singh Awana, Koji Kimoto, Eiji Takayama-Muromachi, Maarit Karppinen, Hisao Yamauchi and Yoshio Matsui, To appear in Ultramicroscopy (2004).
41. A.C. McLaughlin, W. Zhou, J.P. Attfield, A.N. Fitch, and J.L. Tallon, *Phys. Rev. B* **60**, 7512 (1999).
42. Y. Matsui, S. Horiuchi, H. Sawa, K. Obara and J. Akimitsu. Jpn. J. Appl. Phys. **28**, 1555 (1989).
43. V.P.S. Awana, M. Karppinen, H. Yamauchi, A Critical Review, in: International Book Series: Studies of High Temperature Superconductors, vol. **46**, A.V. Narlikar (Ed.), Nova Science Publishers, New York, 77-98 (2003).
44. E.B. Sonin, and I. Felner, Phys. Rev. B **57**, R14000 (1998).
45. C. A. Cardoso, F.M. Araujo-Moreira, V.P.S. Awana, E. Takayama-Muromachi, O.F. de Lima, H. Yamauchi, M. Karppinen, Phys. Rev. B **67**, 024407R (2003)
46. C. A. Cardoso, F.M. Araujo-Moreira, V.P.S. Awana, H. Kishan, O.F. de Lima, H. Yamauchi, M. Karppinen, to appear in Physica C (2004).
47. I. Felner, V.P.S. Awana and E. Takayama-Muromachi, Phys. Rev. B. **68**, 94508 (2003).
48. A.T. Matveev, A. Kulakov, A. Maljuk, C.T. Lin, and H.-U. Habermeier, Physica C **400**, 53 (2003).
49. W.E. Pickett, Phys. Rev. Lett. **83**, 3713 (1999).
50. P.W. Klamut, B. Dabrowski, S.M. Mini, M. Maxwell, J. Mais, I. Felner, U. Asaf, F. Ritter, A. Shengelaya, R. Khasanov, I.M. Savic, H. Keller, A. Wisniewski, R. Puzniak, I.M. Fita, C. Sulkowski, and M. Matusiak, Physica C, **387** (2003).

SUPERCONDUCTIVITY AND MAGNETISM IN LADDER AND CHAIN COMPOUNDS

– PHYSICS OF $(Sr,Ca)_{14}Cu_{24}O_{41}$ –

M. Uehara[1], N. Motoyama[2], M. Matsuda[3], H. Eisaki[4] and J. Akimitsu[2]

[1] Yokohama National University, Faculty of Engineering, Division of Intelligent Systems Engineering, 79-1 Tokiwadai, Hodogaya-ku, Yokohama, Kanagawa 240-8501, Japan

[2] Department of Physics and Mathematics, Aoyama-Gakuin University, 5-10-1 Fuchinobe, Sagamihara, Kanagawa 229-8558, Japan

[3] Advanced Science Research Center, Japan Atomic Energy Research Institute, Tokai, Ibaraki 319-1195, Japan

[4] Nanoelectronic Research Institute, AIST, Tsukuba, Ibaraki 305-8568, Japan

1. INTRODUCTION

The study of ladder materials has in recent years become one of the central issues in the field of condensed matter physics. Ladder materials, which contain a structural unit composed of coupled arrays of one-dimensional (1D) chains, are considered to be an interesting intermediate step between one- and two-dimensional (2D) systems [1-5]. In fact, it is now recognized that the crossover from 1D to 2D is far from straightforward and that ladder materials by themselves exhibit a variety of new physics.

Historically, studies on ladder material were motivated by the discovery of high-transition-temperature (high-T_c) superconductors occurring in 2D spin-1/2 (S=1/2) Heisenberg antiferromagnets [6]. Two theoretical predictions have particularly triggered extensive research [1,2].

First, ladders made from an even number of spin-1/2 Heisenberg chains (even-leg ladders) are expected to have a unique spin-liquid ground state with short range spin correlation, where there exists a finite energy gap ("spin gap") to the lowest excited state. The spin gap, more frequently called the pseudogap, is a key feature of high-T_c superconductors, particularly in the low carrier concentration region. Ladder materials are in this context considered to be good references to gain insights into the pseudogap physics of high-T_c superconductors.

Second, and a more intriguing hypothesis, is the possible occurrence of superconductivity in even-leg ladders when they are doped with holes, similar to the high-T_c materials in which holes are doped into 2D copper-oxygen (CuO_2) planes. The symmetry of pairing is predicted to be *d*-wave like [7], adding to the similarities between doped ladders and doped 2D planes.

Stimulated by these theoretical suggestions, intensive experimental studies have been carried out, with a variety of cuprate ladder materials having been newly discovered. For instance, (i) the existence of a spin gap was confirmed for $SrCu_2O_3$, a prototype of a two-ladder compound [8,9], (ii) hole-doping into two-legged ladders was first achieved on $LaCuO_{2.5}$ by replacing La with Sr [10], and (iii) superconductivity at 12.5 K was observed in $Sr_{14-x}Ca_xCu_{24}O_{41}$ under a pressure of 3 GPa [11].

Here, we review experimental results on cuprate spin ladder materials, emphasizing those for $Sr_{14-x}Ca_xCu_{24}O_{41}$. In Sec. 1.2, brief theoretical background is provided, while Sec. 1.3 introduces typical cuprate spin ladder materials. In Chap. 2, we review the magnetic properties of hole-doped edge-sharing S=1/2 chains, a constituent of $(Sr,Ca)_{14}Cu_{24}O_{41}$, after which the normal state properties of $(Sr,Ca)_{14}Cu_{24}O_{41}$ are considered in Chap. 3, with emphasis on the effect of Ca substitution on charge dynamics of hole-doped two-leg ladders. Superconducting properties are then discussed in Chap. 4, being followed by Chap. 5 which discusses the consistency between theory and experiments of ladder and summarizes novel physical insights obtained by a series of experiments on $(Sr,Ca)_{14}Cu_{24}O_{41}$. Readers should note that our review is in addition to other excellent reviews on spin ladder system [3-5].

1.2 Theoretical Background

1.2.1 Magnetic ground state of *S*=1/2 ladders

The S=1/2 Heisenberg antiferromagnetic (AF) ladders are defined by the Hamiltonian

$$H = J\sum_i S_i \cdot S_{i+\bar{x}} + J'\sum_i S_i \cdot S_{i+\bar{y}} .$$

Here i indicates lattice sites where spin-1/2 operators S_i are located, while J and J' are the AF exchange coupling constant (>0) along the leg and rung of the ladders, respectively (Fig. 1-1(a) and (b)). The width of the ladder depends on the number of legs, with the 1D chain and 2D plane respectively corresponding to one-leg and ∞-leg ladders having isotropic coupling J=J'. Note that 1D and 2D S=1/2 AF spin systems are both well understood. In 2D ones, the ground state is a long-range AF order, while in 1D ones the ground state is a "quasi" long-range AF order since a true long-range order is prevented due to a strong quantum fluctuation.

In the 1D chain and 2D plane there is no cost in energy to create an excited state with S=1, i.e., there is no spin gap.

In contrast to these two limiting cases, spin ladders with an even number of legs behave quite differently, in that the ground state is characterized by a short-range spin correlation. They are accordingly referred to as a "spin-liquid," having a finite spin gap in their spin excitation spectrum. An intuitive explanation is that J' is much stronger than J (strong coupling limit), i.e., two neighboring spins located on the same rung form a spin-singlet. The ground state corresponds to the direct product of these spin singlets (Fig. 1-1 (a)). Since each singlet has zero spin, the total spin of the system is zero. To create an excited state, a singlet is turned into a S=1 triplet, where one spin triplet has energy J' above the spin singlet. S=1 spin excitation propagating along the ladders is represented as the following dispersion

$$E(k) = J' + J\cos(k) \ .$$

This excitation spectrum apparently has a finite spin gap $\Delta_{SG}=E(\pi)=J'-J$. Although the above description assumes $J<<J'$, many theoretical studies have confirmed that the essential physics holds down to the other limit of $J'<<J$, providing J' is finite. In the isotropic ($J=J'$) case, numerical studies estimate Δ_{SG} to be $1/2 \cdot J$ [12,13]. Δ_{SG} decreases with the number of legs, n, which should be expected since the system approaches a gapless 2D plane with increasing n. However, Δ_{SG} is predicted to be finite as long as n takes an even and finite value [2].

Odd-leg ladders show different behavior, i.e., in the strong coupling limit the ground state of the spins located in the same rung has a total spin 1/2 (Fig. 1-1(b)). The system is therefore considered to be composed of S=1/2 1D AF chains with coupling constant J which is gapless.

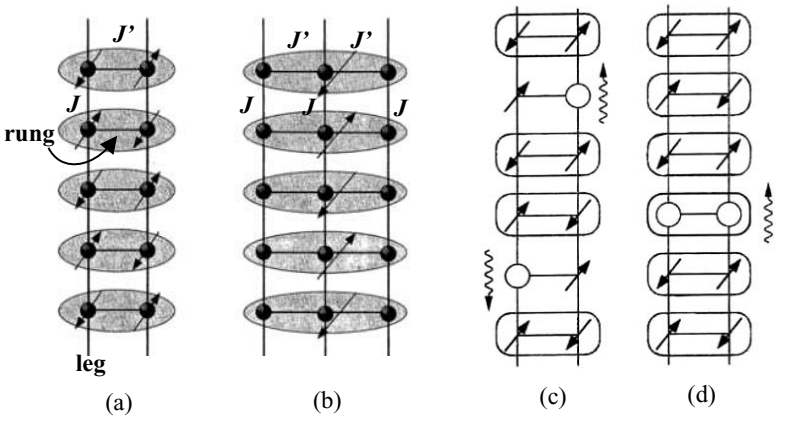

Fig. 1-1. Schematic representations of spin ladders. The ground state of a two- (**a**) and three- (**b**) leg ladder in the $J'>>J$ limit. Pairs of spins along the same rung form a S=0 (a) and S=1/2(b) state, respectively. (**c**) and (**d**) represent a two-leg ladders doped with two holes. When the holes are located in different rungs, each hole destroys one spin singlet. On the other hand, when two holes reside in the same rung, there is no broken singlet bond (figures from ref. [14]).

1.2.2 Hole-doping into spin ladders

When holes are doped into spin ladders they are expected to interact with the magnetic background. Again, let us consider the strong coupling limit case. When one hole is doped into a two-leg ladder it breaks up one spin singlet bond (Fig. 1-1 (c)) such that the system loses the energy gain caused by the singlet formation. If the second hole is located away from the first one, two singlet pairs are broken. On the other hand, if the two holes are located on the same rung, the number of the broken singlet bond is reduced from two to one. It is therefore energetically more favorable to create a hole pair in the same rung versus creating free spins in a different rung.

Superconductivity in doped ladders is expected to be *d*-wave like in a sense that the pairing amplitude along the legs has a sign opposite from that along the rungs. This is reminiscent of the *d*-wave nature of high-T_c superconductors, presumably suggesting a common origin of superconductivity in two-leg ladders and 2D planes.

Although hole pairing in two-leg ladders may persist as long as a spin gap exists, the spin gap ground state becomes unstable due to hole-doping. In fact, theoretical studies suggest that the magnitude of the spin gap decreases as hole-doping increases [1].

Finally, by making use of gapful spin modes which coexist with gapless ones, Kimura *et al*. [15] reported that superconductivity also appears in three-leg ladders.

1.3 Materials Overview

1.3.1 $SrCu_2O_3$ and $Sr_2Cu_3O_5$: prototypical two- and three-leg ladders

$SrCu_2O_3$ and $Sr_2Cu_3O_5$ were discovered by Hiroi *et al*. in 1991 [9], belonging to homologous series $Sr_{n-1}Cu_{n+1}O_{2n}$ (n = 3,5,···) composed of $Cu_{n+1}O_{2n}$ planes alternating with Sr_{n-1} planes. Figure 1-2 shows the structure of the Cu_2O_3 (Fig. 1-2(a)) and Cu_3O_5 (Fig. 1-2(b)) planes.

The indicated spin ladder structures are formed by introducing a parallel array of planar defects into 2D CuO_2 planes. A Cu^{2+} ion has a single hole in the $d_{x^2-y^2}$ orbital which points toward the oxygen atoms located at the corners of a CuO_4 square. Consequently, within the legs and also along the rungs, a strong superexchange interaction should occur through linear Cu-O-Cu bonds, while the interaction through 90° Cu-O-Cu bonds across the interface between ladders must be much weaker and could even be ferromagnetic. The inter-ladder interactions are also strongly frustrated due to geometrical considerations. Each ladder is nearly isolated as a result.

Magnetic susceptibility ($\chi(T)$), NMR, and μSR measurements of $SrCu_2O_3$ and $Sr_2Cu_3O_5$ have confirmed the predicted even-odd discrepancy between two- and three-leg ladders [8, 16, 17]. For $SrCu_2O_3$, the signature of a spin gap manifests itself as an exponential drop in $\chi(T)$. A fit using $\chi(T) \sim T^{1/2}\exp(-\Delta_{SG}/T)$ [18] yields Δ_{SG} = 420 K [8], while Δ_{SG} = 680 K is obtained from NMR results [16]. On the other hand, the magnetic ground state of $Sr_2Cu_3O_5$ is a long-ranged AF ordered state with Néel temperature T_N = 52 K [17].

Finally, these two systems can only be synthesized under high pressure which makes single crystal growth difficult, and carrier doping has not been successful on either system.

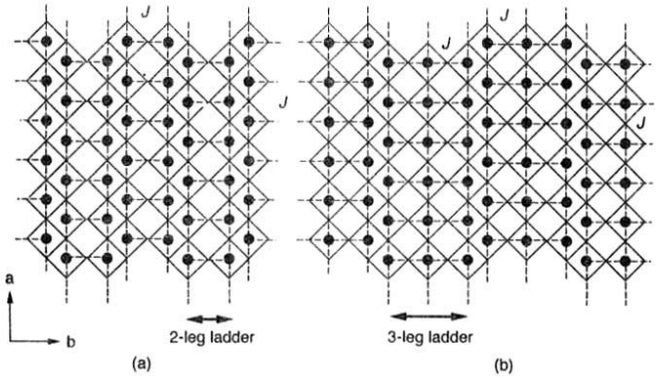

Fig. 1-2. Shematic drawings of the Cu_2O_3 plane of $SrCu_2O_3$ and Cu_3O_5 plane of $Sr_2Cu_3O_5$. The filled circles are Cu atoms and O atoms are located at the intersection of the solid lines [8].

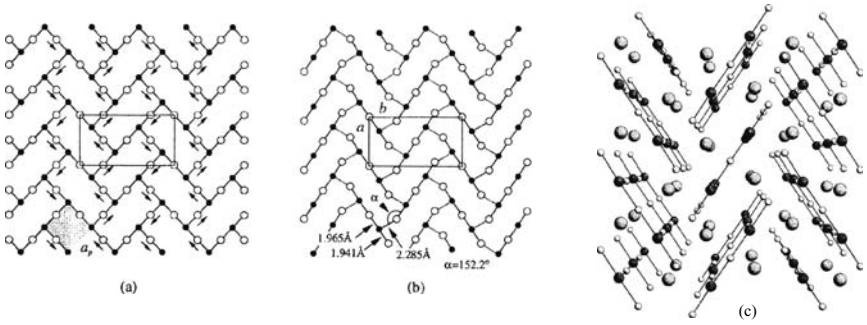

Fig 1-3. Schematic representation of CuO_2 planes in $LaCuO_{2.5}$. In $LaCuO_{2.5}$, one of the four oxygen atoms is missing (**a**). Jahn-Teller distortion forces the displacement of oxygen atoms as indicated by the arrows, resulting in the formation of two-leg ladder structures as shown in (**b**). In this figure, shorter (longer) Cu-O bonds are shown with solid (broken) lines. (**c**) Perspective view of $LaCuO_{2.5}$ along the *c*-axis. Components of each ladder unit are connected by solid lines. Large, medium, and small balls represent La, Cu, and O atoms, respectively [14].

1.3.2 $LaCuO_{2.5}$: a hole-doped ladder system

In 1995, Hiroi and Takano [10] succeeded in synthesizing $LaCuO_{2.5}$ using a high-pressure synthesis technique. This compound contains two-leg ladders within a 3D crystal structure. The framework of $LaCuO_{2.5}$ is deduced from the $LaCuO_3$ lattice by creating oxygen vacancies in the basal plane of the CuO_6 octahedra. Rows of oxygen atoms are eliminated along *c*-axis, thus forming 1D tunnels parallel to this direction. The 1D arrays of oxygen vacancies, together with the displacement of oxygen atoms due to a Jahn-Teller distortion, create two-leg ladder structures running along the *c*-axis.

Similar to 2D high-T_c cuprates such as $La_{2-x}Sr_xCuO_4$, one can dope holes into $LaCuO_{2.5}$ by substituting Sr for La ($La_{1-x}Sr_xCuO_{2.5}$). Resistivity measurements indicate that the insulator-to-metal transition takes place between x = 0.18 and x = 0.20 [10]. However, contradictory to theoretical conjectures, there is no signature of superconductivity in the metallic sample. Two explanations have been proposed to account for the absence of superconductivity: (1) superconductivity is suppressed due to the random potential caused by the replacement of Sr by La, and (2) finite interladder coupling may stabilize the 3D Néel ordered state instead of a spin-liquid state expected in an isolated spin ladder. Explanation (2) seems to be consistent with the NMR and μSR results which report the presence of an antiferromagnetic order below T_N~110 K in $LaCuO_{2.5}$ [19, 20].

1.3.3 $A_{14}Cu_{24}O_{41}$ (A=Sr, Ca, Ba, Y, La) : a superconducting ladder

$A_{14}Cu_{24}O_{41}$, a so called "telephone number" compound, was first reported by McCarron *et al.* and Siegrist *et al.* [21, 22]. It is classified as a composite crystal since it is composed of multiple interpenetrating layered substructures, namely, edge-sharing CuO_2 chain planes, A-planes, and Cu_2O_3-two-leg ladder planes (Fig. 1-4). The two Cu-O substructures are mutually incommensurate because the rate of their lattice constants along the *c*-axis (along the ladders/chains), c_{ladder}/c_{chain}, takes an irrational value. These two substructures become nearly commensurate at $10\times c_{chain} \sim 7\times c_{ladder} \sim 27$ Å. Due to mutual incommensurability, structural modulations between the substructures may occur. The *a*-axis (along the rung) and *b*-axis (perpendicular to the ladder planes) unit cell lengths are 11.48 and 13.41 Å, respectively. Single crystals can be grown by the traveling- solvent floating zone method, and a high O_2-gas pressure of 10 atm is needed for high-Ca doping samples.

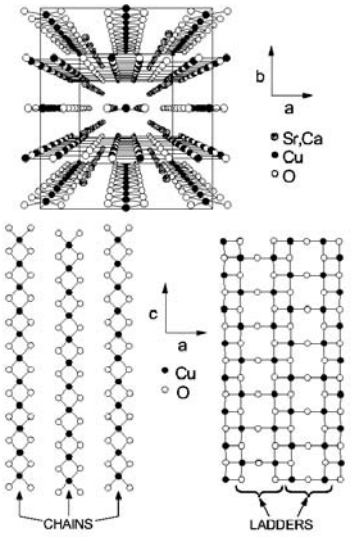

Fig. 1-4. Crystal structure of $(Sr,Ca)_{14}Cu_{24}O_{41}$

Physical properties dramatically change by the chemical substitution of Sr atoms. Although the nominal Cu valence of $Sr_{14}Cu_{24}O_{41}$ is +2.25 such that the holes are "self-doped" into the system even in a pristine form, $Sr_{14}Cu_{24}O_{41}$ nevertheless shows insulating behavior. The existence of a spin gap in the Cu_2O_3-two-leg ladder plane has been confirmed by many experiments [23-28], with metallic behavior being observed through the substitution by Ca in a form $Sr_{14-x}Ca_xCu_{24}O_{41}$ with x>10. Superconductivity appears when a high pressure, typically more than 3GPa, is applied to metallic samples.

As described in the following chapters, extensive experimental research on $Sr_{14-x}Ca_xCu_{24}O_{41}$ has revealed fundamental physical properties of hole-doped edge-sharing chains and two-leg ladders.

2. MAGNETISM IN THE EDGE-SHARING CuO_2 CHAINS

2.1 Magnetic Properties of the Edge-Sharing CuO_2 Chains for the $Sr_{14}Cu_{24}O_{41}$-type Compound

2.1.1 Basic properties of the $Sr_{14}Cu_{24}O_{41}$-type compound

$Sr_{14}Cu_{24}O_{41}$ consists of a Cu_2O_3-two-leg ladder plane and edge-sharing 1D CuO_2 chain plane. The low-energy magnetic properties exhibited by this compound are determined by those in the 1D chain, i.e., the spins in the Cu_2O_3 ladder form a singlet ground state with a large spin gap Δ_{SG} ~40 meV (described in Chap. 3). This section discusses magnetic properties of the 1D chain of the $Sr_{14}Cu_{24}O_{41}$-type compound.

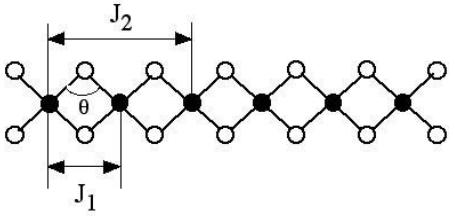

Fig. 2-1. A schematic structure of the edge-sharing 1D CuO_2 chain. Filled and open circles correspond to Cu and O ions, respectively. θ represents the bond angle between Cu and O.

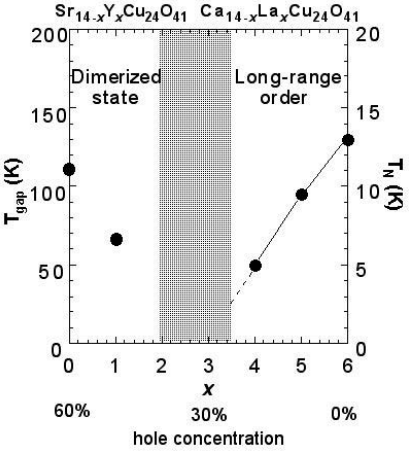

Fig. 2-2. The magnetic phase diagram in $Sr_{14-x}Y_xCu_{24}O_{41}$ and $Ca_{14-x}La_xCu_{24}O_{41}$ as a function of x or hole concentration.

Figure 2-1 shows a schematic structure of the edge-sharing 1D chain, where copper spins are coupled along the chains by the nearly 90° Cu-O-Cu interaction. The nearest-neighbor (NN) and the next-nearest-neighbor (NNN) exchange interactions are denoted by J_1 and J_2, respectively. The value of J_1 and J_2 strongly depend on the bond angle θ and bond distance $d_{Cu\text{-}O}$ [29]. In particular, J_1 changes its sign at $\theta = 95^{\circ}$.

Another interesting feature of the 1D chain in $Sr_{14}Cu_{24}O_{41}$ is that it can be hole-doped. The doped holes, which are located at O 2*p* orbitals, strongly couple with Cu^{2+} ions so as to form a S=0 singlet state (frequently referred to as Zhang-Rice (ZR) singlet) [30]. Hole-doping into the chains is therefore equivalent to introducing a S=0 state in the spin chain. For $Sr_{14}Cu_{24}O_{41}$, the number of holes can be controlled by the chemical substitution of trivalent ions such as La^{3+} or Y^{3+} ions at the Sr site in forms of $Sr_{14-x}Y_xCu_{24}O_{41}$ and $Ca_{14-x}La_xCu_{24}O_{41}$. Figure 2-2 shows a magnetic phase diagram of the substituted system, where the end material $Ca_8La_6Cu_{24}O_{41}$, in which all Cu atoms in the chains (also in the ladders) are divalent and carry S=1/2 spins, exhibits a magnetic order below T_N = 12.2 K [31, 32]. The Cu moments are aligned ferromagnetically along the chain (*c*-axis) such that these ferromagnetic chains form a spiral structure with a rotation angle of ~2π/5 along the *a*-axis [32]. Along the *b*-axis, however, the spins are aligned antiferromagnetically. Upon hole-doping, T_N gradually decreases as indicated. $Ca_9La_5Cu_{24}O_{41}$, in which holes are slightly introduced (~10%), has a long-range AF order below T_N = 10.5 K with a commensurate magnetic structure—a ferromagnetic arrangement within the chain and antiferromagnetic correlations between chains [33]. This long-range AF order disappears around x~3. For x < 3, a dimerized singlet state shows up as a magnetic ground state. The singlet ground state becomes most stable in the end material $Sr_{14}Cu_{24}O_{41}$ with a hole concentration of 60 %.

2.1.2 Singlet ground state in $Sr_{14}Cu_{24}O_{41}$

The singlet ground state in the 1D chain in $Sr_{14}Cu_{24}O_{41}$ was first reported using magnetization [31,34,35] and ESR measurements [35]. Figure 2-3 shows the temperature dependence of the magnetic susceptibility ($\chi(T)$) for $Sr_{14}Cu_{24}O_{41}$, together with those for the Y- and Ca-substituted samples [36]. Note that $\chi(T)$ is dominated by the contribution from the 1D chain since the spins in the Cu_2O_3 ladder form a singlet ground state with a large spin gap Δ_{SG} ~ 40 meV. As shown in Fig. 2-3 (a), $\chi(T)$ indicates a broad peak and a subsequent drop at low temperatures. This drop is isotropic and goes down to zero after subtracting the Curie term contribution; thereby suggesting the formation of a spin gap with magnitude of about 130 K. Many studies have been performed to elucidate the origin of the spin gap in the 1D chains, making it clear that the nonmagnetic Cu sites (ZR singlets) play an important role. For example, a neutron scattering study revealed that the spin singlet ground state consists of the dimmers formed by two S=1/2 Cu^{2+} spins and one ZR singlet located between the two Cu^{2+} spins [37]. The exchange interaction between the two Cu spins (~10 meV) is mediated via a nonmagnetic ZR singlet. A question arises as to how the dimers are arranged and interact with each other. Although it was first thought that each dimer is separated by one ZR singlet [37], ultimately each dimer was found to be separated by two ZR singlets as described next [24,38,39].

NMR studies have revealed local microscopic properties of the dimerized state [25-27,40,41]. Takigawa *et al*. [40] found NMR signals originating from both magnetic Cu^{2+} and

the nonmagnetic ZR singlet in the chain. A NMR peak originating from the ZR singlet gradually splits into two peaks below ~200 K with a subsequent splitting below ~100 K (Fig. 2-4). The temperature dependence of this shift suggests there are two inequivalent ZR singlet sites; i.e., one is the constituent of the dimmer located between two Cu^{2+} spins, while the other ZR singlet would be located between the dimers. NMR results, however, cannot determine spacial arrangement of the dimmers and ZR singlets.

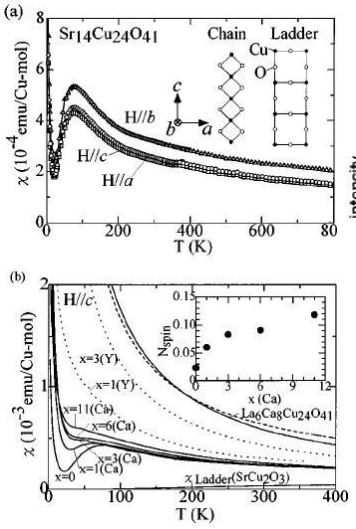

Fig. 2-3. Temperature dependence of the magnetic susceptibility in $Sr_{14}Cu_{24}O_{41}$, $Sr_{14-x}Ca_xCu_{24}O_{41}$, $Sr_{14-x}Y_xCu_{24}O_{41}$, and $La_6Ca_8Cu_{24}O_{41}$. [36]

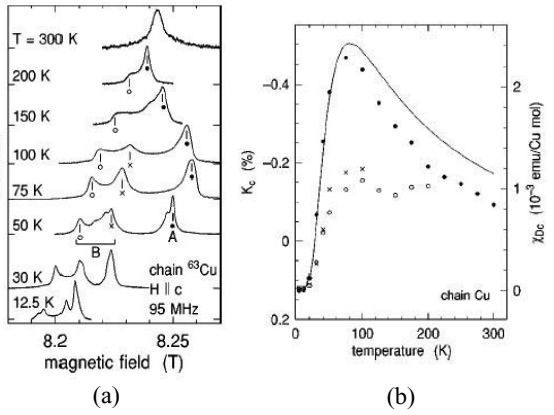

Fig. 2-4. (**a**) Temperature variation of the center line NMR spectrum at the chain ^{63}Cu sites obtained at 95 MHz for *H*//*c* in $Sr_{14}Cu_{24}O_{41}$. (**b**) Temperature dependence of the shift along the *c*-direction at the chain ^{63}Cu sites [40].

Based on neutron scattering results, Eccleston *et al*. [24] proposed a model in which each dimer is separated by two ZR singlets such that the magnetic unit cell is five times larger than the structural unit cell. Experimental results are quantitatively reproduced using the AF intradimer coupling constant 11.2 meV and ferromagnetic interdimer coupling –1.1 meV. It should be noted that due to insufficient resolution the two excitation branches expected from their model could not be separated. Finally, Regnault *et al*. [38] and Matsuda *et al*. [39] independently reported measuring two branches over a wide range of *Q* in the *ac* plane, originating from weak interchain couplings along both the *a* and *c* directions. The study by Matsuda *et al*. [39] is briefly summarized as follows.

Figure 2-5 shows the observed dispersion relation and energy-integrated intensities. In order to analyze the observed data, a model Hamiltonian is employed to describe the dispersion of the dimers which are weakly coupled along the *a*- and *c*-axis (Fig. 2-6). It is known that such dimers, namely weakly coupled dimers, can be well described by the Random Phase Approximation (RPA). The coupling constants indicated in Fig. 2-6 are

estimated to be J = 11 meV, J_a = 0.75 meV, and J_c=0.75 meV. In this dispersion relation the averaged excitation energy, band width of each excitation mode, and energy difference between the acoustic and optic modes are related to J, J_c, and J_a, respectively. Figure 2-5 indicates the calculated dispersion relation and energy-integrated intensities corresponding to the acoustic and optic modes, respectively. Experimental results are well described by RPA theory, guaranteeing the validity of the model shown in Fig. 2-6. However, the charge ordering obtained in this analysis has not been observed by either electron diffraction or synchrotron x-ray measurements, probably because charge ordering is not so long-ranged and static.

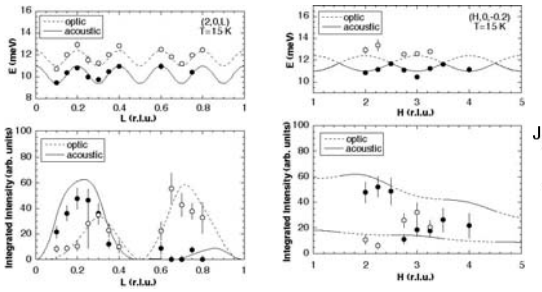

Fig. 2-5. Observed and calculated energies and intensities at (2,0,L) and (H,0,-0.2) measured at 15 K in $Sr_{14}Cu_{24}O_{41}$ [39]. Solid lines indicate the calculated curves.

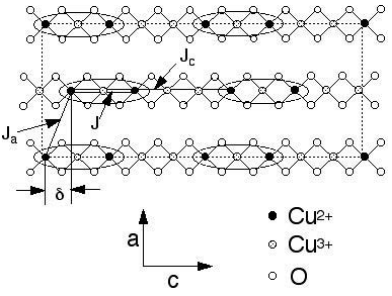

Fig. 2-6. A proposed model for the dimerized state and the ordering of Cu^{2+} and ZR singlet in the *ac* plane in $Sr_{14}Cu_{24}O_{41}$. [39]

Next we discuss other structural studies on the 1D chains plane for $Sr_{14}Cu_{24}O_{41}$. An electron diffraction study revealed a temperature-independent modulated structure along the chain which originates from the lattice mismatch between the 1D chain layer and Cu_2O_3 ladder layer and depends on oxygen stoichiometry [42]. It was found that more stoichiometric $Sr_{14}Cu_{24}O_{41}$ has a more homogeneous superstructure with a five times larger unit cell along the chain. From synchrotron x-ray studies, a specific structural coupling along the *c* direction was proposed based on temperature-dependent superlattice reflections, possibly originating from a structural distortion [43,44]. In particular, Fukuda *et al*. [44] reported a structural distortion with five times periodicity. The most comprehensive model was proposed by Gotoh *et al*. [45] based on a single crystal x-ray diffraction study together with a bond valence sum analysis. There is, however, another interpretation for the data, i.e., the additional reflections are due to interactions between the two structure blocks in this composite crystal such that their presence is not related to a possible charge order [46].

2.1.3 Substitution effect

The substitution effect on the singlet dimerized state was also investigated, with the introduction of Y^{3+} for Sr^{2+} resulting in turning the nonmagnetic ZR singlet into S=1/2 Cu^{2+}.

As shown in Fig. 2-3, Y substitution increases the Curie term contribution and reduces the magnitude of the spin gap [47]. Neutron scattering studies have shown that Y substitution broadens the magnetic excitation peaks and reduces the gap energy while preserving the periodicity of the dimer arrangement [37,48]. The isovalent Ca^{2+} substitution for Sr^{2+} is also known to gradually reduce the number of the holes in the chain because some amount of holes in the chains are transferred to the ladder layers by Ca substitution as explained in Chap. 3 [49]. Ca substitution subsequently affects the dimerized state in the chain similar to Y substitution, although its effect is weaker. NMR and magnetic susceptibility measurements showed that the gap energy does not change drastically with Ca substitution [26,31,34], while neutron scattering measurements in $Sr_{11}Ca_3Cu_{24}O_{41}$ showed that coupling constants J, J_c, and J_a and the periodicity of the dimer arrangement are nearly identical compared to the non-substituted $Sr_{14}Cu_{24}O_{41}$, although the dimerized state becomes unstable [39]. These results indicate that hole order sensitively depends on the hole concentration as well as disorder, and that long-range dimer formation is disturbed by Y or Ca substitution.

2.1.4 Magnetic interactions in the AF phase

The magnetic properties of the AF ordered phase were studied in $Ca_{14-x}La_xCu_{24}O_{41}$. Based on magnetization, heat capacity, [50] and ESR measurements [51], we know that $Ca_9La_5Cu_{24}O_{41}$ has an Ising-like anisotropy which is unusual for Cu oxides having spin-orbit coupling that is believed to be negligibly small.

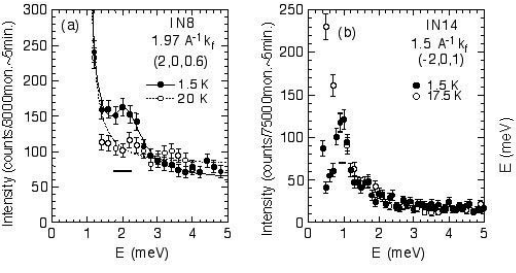

Fig. 2-7. Typical inelastic neutron spectra observed at (H,0,L) below and above T_N for the edge-sharing 1D chain in $Ca_9La_5Cu_{24}O_{41}$. The lines are guides to the eyes. The horizontal bars represent the instrumental energy resolution [54].

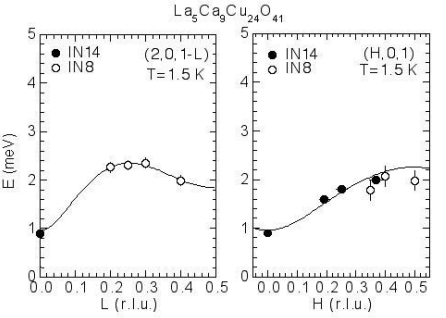

Fig. 2-8. ω-Q dispersion relation along and perpendicular to the c-axis for the edge-sharing 1D chain in $Ca_9La_5Cu_{24}O_{41}$ [54].

The origin of large spin-orbit coupling, giving rise to anisotropic exchange interactions, was theoretically studied by Yushankhai and Hayn [52] and Tornow *et al*. [53]. Inelastic neutron scattering measurements have also been performed on the AF phase of $Ca_9La_5Cu_{24}O_{41}$ [54]. Figure 2-7 shows typical inelastic neutron spectra observed at (H,0,L), where the peak width in energy is broader than the instrumental resolution even around the

zone center. It is remarkable that broadened excitations are observed even when the magnetic order is static and long-ranged. The excitation peak also becomes broader with increasing Q both parallel and perpendicular to the chain. To analyze the observed dispersion relation (Fig. 2-8), linear-spin-wave theory including uniaxial anisotropy was applied by introducing into the calculation exchange coupling constants between two spins (Fig. 2-9). The solid curve in

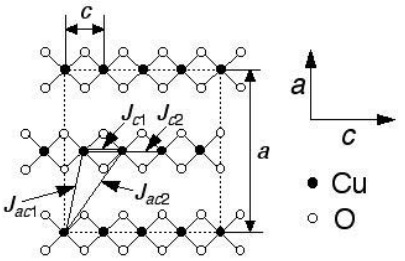

Fig. 2-9 Structure of the edge-sharing 1D chains in the *ac* plane in $Ca_9La_5Cu_{24}O_{41}$. Below T_N=10.5 K the Cu^{2+} spins align ferromagnetically along the chain (*c*-axis) with the propagation vector k = [110]. The spins point along the *b*-axis [54].

Fig. 2-8 represents the result of a fit with J_{c1} = 0.20(7) meV, J_{c2} = -0.18(5) meV, J_{ac1} = 2 J_{ac2} = 0.681(1) meV, and D = -0.211(1) meV, where D represents an effective uniaxial anisotropic interaction [54]. Calculated values reproduce experimental results reasonably well. The excitation gap at the zone center is due to uniaxial anisotropy along the *b*-axis originating from an anisotropic exchange interaction. The antiferromagnetic (J_{c1}>0) NN and ferromagnetic (J_{c2}<0) NNN interactions obtained from the neutron scattering data may prefer an antiferromagnetic order in the chain although the actual magnetic arrangement is ferromagnetic.

On the other hand, antiferromagnetic inter-chain couplings J_{ac1} and J_{ac2} are comparable to J_{c1} and have a number of bonds equal to twice that of J_{c1} (Fig. 2-9). Although there exist competing interactions between intra-chain couplings (J_{c1} and J_{c2}) and inter-chain couplings (J_{ac1} and J_{ac2}), the latter is dominant such that the magnetic arrangement in the chain becomes ferromagnetic. It should be noted that the end material $Ca_8La_6Cu_{24}O_{41}$ shows an incommensurate magnetic structure perpendicular to the chain (*a*-axis) with a ferromagnetic arrangement along the chain (*c*-axis) [32]. This observed incommensurate structure is possibly a consequence of a delicate balance of frustrating interactions between intra- and inter-chain interactions.

This neutron scattering study additionally showed that the uniaxial anisotropic interaction D is comparable with the small isotropic interactions both parallel and perpendicular to the chain, being unexpected based on the geometrical structure and giving rise to an enhancement of the Ising-like anisotropy. The small exchange interactions suggest that the bond angle between copper and oxygen ions is close to 95^o [29]. Since spin-wave excitations were also broadened considerably, the broadening is probably enhanced by frustrating interactions between intra- and inter-chain interactions, and by disorder due to a structural distortion and doped holes. Such behavior is also unexpected based on the simple geometrical structure.

A theoretical study showed that when the above simple model is based on semi-classical spin-wave theory, it is insufficient to describe the magnetic transition temperature and results

of magnetization measurements [55], which suggests that some formation of the charge order should be taken into account to fully understand the system's magnetic properties [56, 57].

Another interesting feature of this system is that magnetic moments can be induced at oxygen sites due to strong Cu *d*-O *p* hybridization. Weht and Pickett [58] theoretically predicted that large moments (~0.2 μ_B) lie on the oxygen ions in the CuO_2 chains in Li_2CuO_2. Finally, in the edge-sharing 1D chain of $Ca_9La_5Cu_{24}O_{41}$ it was observed that magnetic moments exist at oxygen sites (~0.02 μ_B) as well as at Cu sites (~0.2 μ_B) [33]. Oxygen moments were also observed in related compounds $Ca_2Y_2Cu_5O_{10}$ [59] and Li_2CuO_2 [60,61].

2.2 Magnetic Properties in a Related Compound $Ca_{2+x}Y_{2-x}Cu_5O_{10}$

The $Ca_{2+x}Y_{2-x}Cu_5O_{10}$ system [62-64] consists of edge-sharing CuO_2 chains which are nearly the same as those in $Ca_{14-x}La_xCu_{24}O_{41}$. Since the system does not have Cu_2O_3 ladder planes, it is a good candidate to study the hole-doping effect on the magnetic ground state and excitations purely in the chain. Figure 2-10 shows the structure of the edge-sharing CuO_2 chains in $Ca_{2+x}Y_{2-x}Cu_5O_{10}$. Hayashi *et al*. [64] reported that this system remains insulating even when holes are doped by 40%.

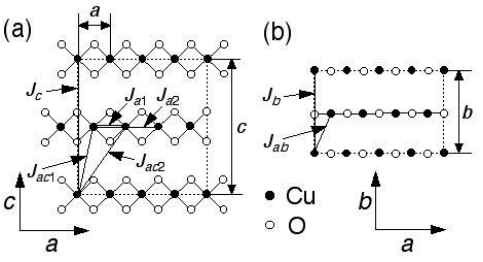

Fig. 2-10. Structure of edge-sharing CuO_2 chains in the *ac* plane in $Ca_2Y_2Cu_5O_{10}$. Oxygen ions are located at z~±0.125 in (**b**). Below T_N=29.5 K the Cu^{2+} spins align ferromagnetically along the chain (*a*-axis) with the propagation vector k = [001] [74].

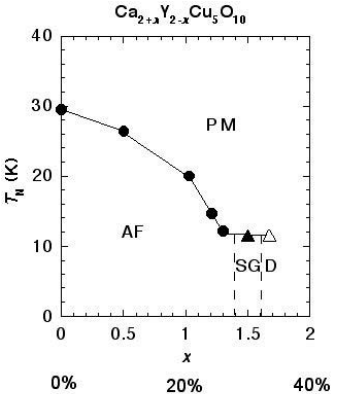

Fig. 2-11. The magnetic phase diagram in $Ca_{2+x}Y_{2-x}Cu_5O_{10}$ as a function of x and hole concentration. The open triangle shows that the magnetic state is minor. PM, AF, SG, and D indicate paramagnetic, antiferromagnetic, spin-glass, and nearly disordered phases, respectively [76].

Figure 2-11 shows the magnetic phase diagram of the $Ca_{2+x}Y_{2-x}Cu_5O_{10}$ system, where the end-material $Ca_2Y_2Cu_5O_{10}$, which has no holes, indicates AF order of the Cu^{2+} moment below T_N = 29.5 K with ferromagnetic coupling along the chain [65,66]. Note the magnetic structure in the CuO_2 plane (*ac* plane) is the same as that in $Ca_{14-x}La_xCu_{24}O_{41}$. The ordered moment of Cu^{2+} is ~0.9 μ_B at low temperatures, being comparable to the full magnetic moment of the free Cu^{2+} ion. The long-range AF order is suppressed by hole-doping and is replaced by a spin-glass behavior above x = 1. In the spin-glass region (x~1.5), magnetic susceptibility measurements show a difference between field-cooling and zero-field-cooling processes [67]. In the x = 1.5 crystal, a neutron scattering study showed a broad transition to short-range ordered magnetic phase below ~15 K. The magnetic correlation lengths are ξ_a~28 Å, ξ_b~12 Å, and ξ_c~2 Å at low temperature. In the x = 1.67 crystal, the ground state is considered to be a quantum disordered state with a trace of minor spin-glass phase, with magnetic properties being almost identical to those in the x = 1.5 crystal. With further hole-doping, dominant magnetic interaction becomes antiferromagnetic [67-69]. Some types of charge order have been reported for $Ca_{2+x}Y_{2-x}Cu_5O_{10}$ [68,69] and the related system $Ca_{1-x}CuO_2$ [70-72]. The possible existence of a spin gap associated with charge order has also been suggested [69].

In the end material $Ca_2Y_2Cu_5O_{10}$, which contains no holes, the magnetic arrangement in the chain is ferromagnetic. Although quantum fluctuations are considered to be less prominent in a ferromagnetic chain system, the magnetic excitation energy width is known to become broader with increasing Q along the chain as described below. Numerical calculations suggest that magnetic excitations from ferromagnetic chains are strongly affected when a finite antiferromagnetic inter-chain coupling exists or when frustration is introduced between the NN and NNN interactions in the chain [73].

Matsuda *et al*. [74] performed inelastic neutron scattering experiments to study the spin-wave excitations of $Ca_2Y_2Cu_5O_{10}$ in the AF state. By applying linear spin wave theory on a model Hamiltonian that includes uniaxial anisotropy, magnetic interactions can be determined as shown in Table 1, where the most interesting feature is that the magnetic excitation energy width becomes broader with increasing Q along the chain, although sharp excitations are observed around the zone center and perpendicular to the chain. Broadening of excitation energy width was also reported in a S=1/2 1D Heisenberg ferromagnet $CuCl_2$·DMSO [75], although such broadening is much more pronounced in $Ca_2Y_2Cu_5O_{10}$. Numerical calculations reveal that the anomalous magnetic excitation spectra in $Ca_2Y_2Cu_5O_{10}$ are mainly due to antiferromagnetic inter-chain interactions.

Table 1 Magnetic coupling constants in $Ca_{2+x}Y_{2-x}Cu_5O_{10}$ [76].

x	T(K)	J_{a1}(meV)	J_{ac1}(meV)	D(meV)		J_{ab}(meV)	J_a(meV)	J_b(meV)		
0	7	-6.9(1)		1.494(3)	-0.262(3)	0.030(1)		-0.061(6)	0(fixed)	
0	20	-6.9(fixed)	1.31(2)	-0.159(2)	0(fixed)		-		0(fixed)	
0	25	-6.9(fixed)	1.16(2)		-0.104(2)	0(fixed)		-		0(fixed)
1.5	3	-6.9(fixed)	0.5(fixed)	-0.09(fixed)	0(fixed)		-		0(fixed)	
1.67	3	-6.9(fixed)	0(fixed)		0(fixed)	0(fixed)		-		0(fixed)

Neutron scattering experiments were performed on hole-doped $Ca_{2+x}Y_{2-x}Cu_5O_{10}$ [76]. The systematic study of the hole concentration dependence of the magnetic excitations revealed that magnetic excitations are softened and broadened with increasing temperature or doping holes, irrespective of Q direction, with broadening being larger at higher Q. A

characteristic feature is that hole-doping is much more effective to broaden excitations along the chain. As shown in Table 1, although the intra-chain interaction (J_{a1}) does not change so much with increasing temperature or hole-doping, the anisotropic interaction (D) and the inter-chain interaction (J_{ac1}) are reduced. In the spin glass phase (x = 1.5) and nearly disordered phase (x = 1.67) the magnetic excitations are much broader in energy and Q.

The magnetic properties of $Ca_{2+x}Y_{2-x}Cu_5O_{10}$ qualitatively resemble those of $(Sr,Ca,La,Y)_{14}Cu_{24}O_{41}$. However, from a microscopic standpoint, the sign and absolute value of the intra-chain interaction are different in the two systems (0.20 meV for $Ca_9La_5Cu_{24}O_{41}$ and –6.9 meV for $Ca_2Y_2Cu_5O_{10}$), probably due to a slight difference in bond angle and distance between Cu and O [29]. The most characteristic feature is that spin glass behavior is observed in the former system. As the system has no frustrating interactions, yet becomes more one-dimensional with hole-doping, it is difficult to understand how the spin glass phase appears in the absence of frustrating interactions. The spin glass behavior probably appears because finite sized spin clusters, which give rise to cluster spin glass behavior, are formed due to the rather large intra-chain coupling even with ~30% hole-doping. The neutron scattering study indicates that the magnetic correlation length along the chain is larger than the averaged spin cluster size, which is expected when the holes are randomly distributed. This indicates that there is a possibility of a partial charge ordering, which is consistent with the cluster spin glass model.

3. PHYSICAL PROPERTIES OF TWO-LEG LADDERS IN $(Sr, Ca)_{14}Cu_{24}O_{41}$ UNDER AMBIENT PRESSURE

This chapter reviews the spin and charge dynamics of two-leg ladders in $(Sr, Ca)_{14}Cu_{24}O_{41}$. The physical properties of $(Sr, Ca)_{14}Cu_{24}O_{41}$ dramatically change with chemical substitution at the Sr site [31,34,77]. In spite of a high Cu valence of +2.25, $Sr_{14}Cu_{24}O_{41}$ shows an insulating behaviour. Metallic behavior is observed by substitution of Ca into $Sr_{14-x}Ca_xCu_{24}O_{41}$ with $x > 10$. As will be discussed in detail in Sec. 3-2, Ca substitution produces a rearrangement of holes, moving them from the CuO_2 chains into the Cu_2O_3 ladders. As a consequence of interplay between charge and spin degrees of freedom, a variety of ordered states appear, e.g., spin gap state, Néel state, and charge density wave (CDW).

3.1 Spin Gap and AF Ground States in Doped Ladders

$La_6Ca_8Cu_{24}O_{41}$: ladders without holes : By substituting Sr or Ca with La, the nominal Cu valence can be reduced from +2.25. The magnetic properties of undoped two-leg ladders can be experimentally studied using $La_6Ca_8Cu_{24}O_{41}$ in which all the Cu atoms are divalent. Neutron scattering [78] and NMR [41] experiments on this compound have confirmed the spin gap ground state. From the T-dependence of ^{17}O Knight shift, Imai *et al.* [41] estimated the magnitude of the spin gap as Δ_{SG}=510 ± 40 K using

$$\chi(T) \propto \frac{1}{\sqrt{T}} \exp\left(\frac{-\Delta}{k_B T}\right)$$

From the ^{17}O Knight shift, Imai *et al*. also estimated the exchange coupling constant J' = 850 ± 300 K and J' / J ~ 0.5 (J (J') to be the AF exchange coupling constant along the leg (rung)), whereas an inelastic neutron scattering experiment by Matsuda *et al*. [78] reported J = J'= 110 meV = 1300 K, and a four-spin exchange interaction J_{ring} = 16.5 meV = 190 K.

$Sr_{14}Cu_{24}O_{41}$: slightly doped ladders : Several groups have reported results of NMR experiments on $Sr_{14}Cu_{24}O_{41}$. Tsuji *et al*. [25] estimated the magnitude of a spin gap Δ_{SG} = 470 K from the nuclear spin-lattice relaxation ratio (T_1) of Cu-NQR, while Magishi *et al*. [27] also measured the ^{63}Cu Knight shift and estimated Δ_{SG} = 550 ± 30 K. From NQR results, Takigawa *et al.* [40] estimated Δ_{SG} = 430 K from the Knight shift and Δ_{SG} = 650 K from $1/T_1$, respectively (Fig. 3-1). A neutron scattering experiment by Eccleston *et al*. [24] estimated Δ_{SG} = 32.5 ± 0.1 meV (~380 K), J = 130 meV, and J' = 72 meV. Raman scattering experiments have been performed by Sugai *et al*. [79] and Gozar *et al*. [80], with their results indicating agreement and yielding J = 110 ± 20 meV and J' / J ~ 0.8.

Distinct from $La_6Ca_8Cu_{24}O_{41}$, the number of holes residing in the ladders of $Sr_{14}Cu_{24}O_{41}$ is finite. Takigawa *et al*. [40] found that $1/T_1$ measured by zero-field NQR is dominated by fluctuations of the electronic field gradient at low temperature, which might be associated with the freezing of the doped holes. Imai *et al*. [41] found that the crossover temperature of the magnetic state from the spin gap regime to the paramagnetic regime occurs at 325 ± 25 K, and suggested that above this temperature the holes frustrate the singlet ground state which eventually transforms the system into a paramagnetic state.

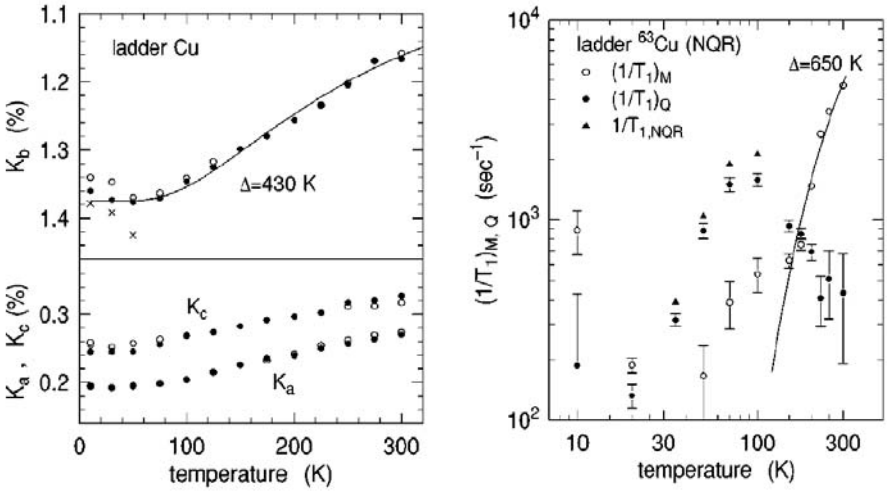

Fig. 3-1. NQR Knight shift and $1/T_1$ for $Sr_{14-x}A_xCu_{24}O_{41}$ [40]

$Sr_{14-x}Ca_xCu_{24}O_{41}$: heavily doped ladders: The magnitude of Δ_{SG} as a function of Ca content x has been measured by NMR and neutron scattering experiments. NMR T_1-relaxation rate experiments have been carried out by many groups, all of which indicate that Δ_{SG} apparently decreases with increasing x as shown in Fig. 3-2.

On the other hand, a neutron scattering measurement for x(Ca) = 11.5 estimated Δ_{SG} = 32.5 ± 0.3 meV (~370 K), almost the same magnitude as x = 0 [81]. Recently, Fujiyama *et al*. [82] pointed out that the activation energy of $1/T_1$ at the Cu sites is determined by the damping of excitations near $k = (\pi, \pi)$ and may not directly reflect the spin gap.

At a high Ca concentration $x \geqq 11.5$, a long-range magnetic order is observed at low temperatures [83-86], with clear antiferromagnetic transitions having been observed using specific heat measurements (Fig. 3-3). The proposed magnetic structure based on the neutron scattering for a sample with x = 11.5 is shown in Fig. 3-4 [87]. The AF ordering temperature increases with increasing Ca content from 2.1 K for x = 11.5 to 3.6 K for x = 13.6 [85,87]. Remarkably, the singlet ground state and AF ground state coexist in high-Ca substituted samples.

Using a neutron structural analysis and bond valence sum calculation, Isobe *et al*. [88] estimated the hole distribution in the chain and proposed a spin structure which explains observed magnetic Bragg reflections [87].

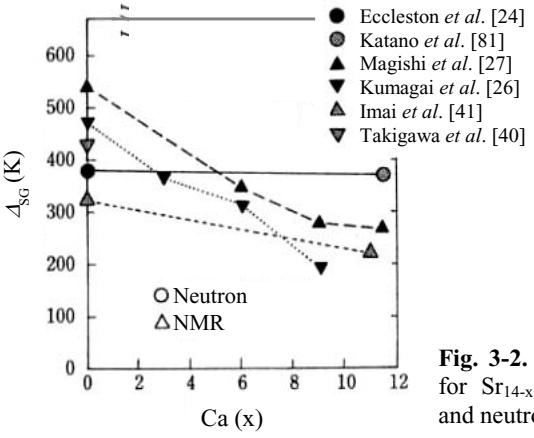

Fig. 3-2. Ca (x) dependence of spin gap Δ_{SG} for $Sr_{14-x}Ca_xCu_{24}O_{41}$ measured by NMR T_1 and neutron scattering.

3.2 Effect of Ca Substitution

Although Ca^{2+} substitution at the Sr^{2+} site in $(Sr,Ca)_{14}Cu_{24}O_{41}$ does not change the average valence of Cu ions, it dramatically changes the electronic properties. Figure 3-5 shows the resistivity of $(Sr,Ca)_{14}Cu_{24}O_{41}$ single crystals along c- and a-axis.

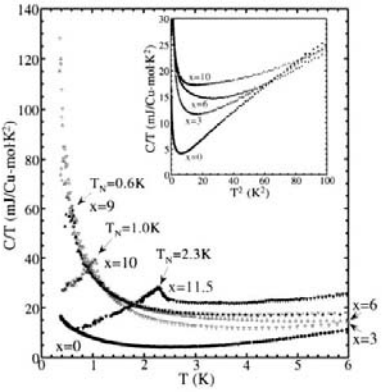

Fig. 3-3. Specific heat data for $Sr_{2.5}Ca_{11.5}Cu_{24}O_{41}$ [87].

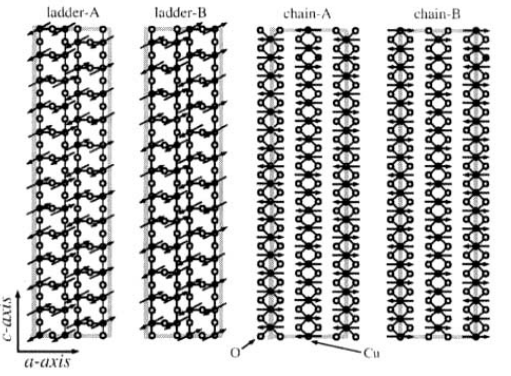

Fig. 3-4. The proposed magnetic structure based on the neutron scattering of $Sr_{2.5}Ca_{11.5}Cu_{24}O_{41}$ [87]. Each layer is stacked alternatively along *b*-axis.

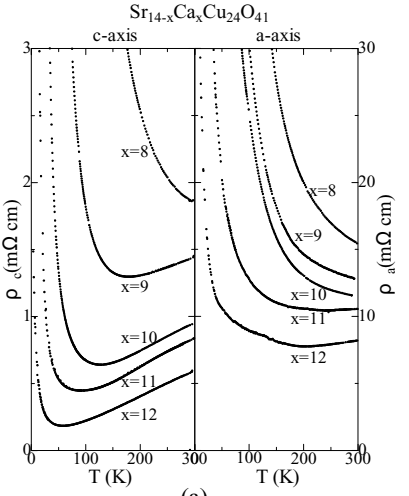

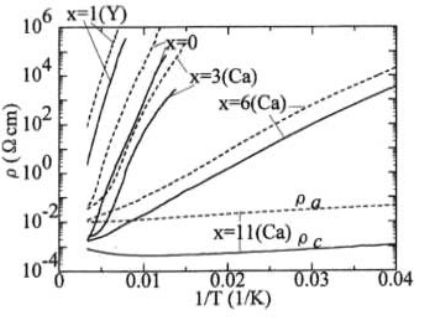

Fig. 3-5. (**a**) *T*-dependence of resistivity for $Sr_{14-x}Ca_xCu_{24}O_{41}$ along *a*- and *c*-directions [89]. (**b**) The Arrenius plot of resistitvity for $Sr_{14-x}Ca_xCu_{24}O_{41}$ and $Sr_{13}YCu_{24}O_{41}$ along *a*- and *c*-directions [36].

At x(Ca) < 8, the resistivity shows insulating behavior ($d\rho / dT<0$) along both directions, whereas at higher x(Ca) ~ 9, resistivity along the c-axis (ρ_c) shows a metallic behavior which is characterized by nearly T-linear dependence above certain T, similar to the in-plane resistivity of high-T_c cuprates at optimal hole doping. Such similar T-dependence and the similar magnitude of resistivity (≦1 mΩ cm) strongly suggest that the conductivity along the c-axis is most likely governed by the 180° Cu-O-Cu networks with strong Cu3d-O2p σ bonding, rather than the CuO_2 chains with 90° Cu-O-Cu bonds.

The transition from an insulating to metallic behavior with increasing x(Ca) suggests that Ca substitution results in transferring holes from chains to ladders, with optical conductivity measurements on $(Sr,Ca)_{14}Cu_{24}O_{41}$ supporting this picture [49]. Figure 3-6 shows optical conductivity spectra of $(Sr, Ca)_{14}Cu_{24}O_{41}$ along the c-axis ($\sigma_c(\omega)$), where the spectrum of the most insulating sample $Sr_{11}Y_3Cu_{24}O_{41}$ is typical of a charge transfer (CT) insulator, characterized by a peak at 2.0 eV arising from excitation between Cu3d and O2p states which is commonly observed in a parent insulators of high-T_c cuprates. Moving to $Sr_{14}Cu_{24}O_{41}$ and further to $(Sr,Ca)_{14}Cu_{24}O_{41}$, the conductivity in the low energy region below 1.2 eV increases, while the CT spectral weight decreases, suggesting a spectral weight transfer from a high- to low-energy region similar to that occurring in high-T_c cuprates when a parent insulator is doped with holes. The 3 eV peak does not exist in high-T_c cuprates and decreases with x, which can be attributed to the excitation of doped holes in the CuO_2 chains.

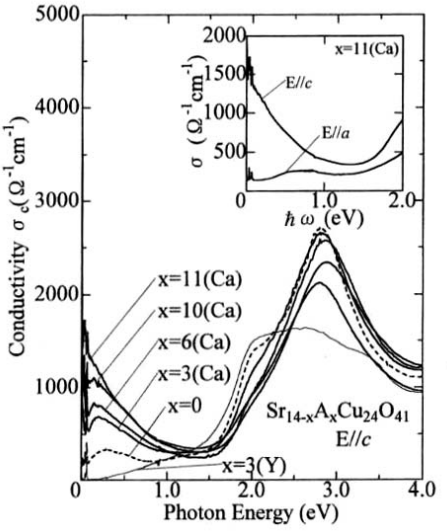

Fig. 3-6. Optical conductivity spectra of $Sr_{14-x}Ca_xCu_{24}O_{41}$ along the c-axis ($\sigma_c(\omega)$). The inset shows the anisotropic spectra along a- and c-directions for x=11 sample [49].

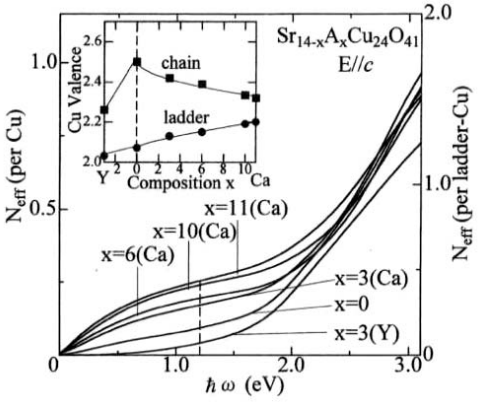

Fig. 3-7. Estimated electron number N_{eff} per Cu (left-hand scale) as a function of energy. N_{eff} per ladder Cu is indicated on the right hand scale. Inset shows the estimated Cu valence of the ladder and the chain [49].

From the optical conductivity spectra, one can estimate the effective electron number participating in the low-energy charge dynamics using

$$N_{eff}(\omega) = \frac{2m_0 V}{\pi e^2} \int_0^{\omega} \sigma_c(\omega')d\omega',$$

where m_0 is the free electron mass, V the volume containing one Cu atom, and $N_{eff}(\omega)$ being proportional to the number of electrons involved in optical excitations up to an energy $\hbar\omega$. The results are shown in Fig. 3-7.

$N_{eff}(\omega)$ takes the same value at 2.5 eV for all $(Sr,Ca)_{14}Cu_{24}O_{41}$ samples, indicating that spectral weight transfer takes place in the energy range below 2.5 eV. Assuming that (1) the chain Cu valence is +2.5 for $Sr_{14}Cu_{24}O_{41}$ and (2) the number of holes in Cu_2O_3 ladders is proportional to N_{eff} (1.2 eV), the Cu valence of the ladder and the chain is estimated as shown in the inset of Fig. 3-7. Note that the carrier number of x = 11 is as large as 0.2, which corresponds to the hole number of optimally doped high-T_c cuprates.

Takahashi *et al.* [90] performed angle-resolved photoemission spectroscopy experiments on $(Sr,Ca)_{14}Cu_{24}O_{41}$ with x = 0 and x = 9, finding two dispersive features which are attributed to the band dispersion of CuO_2 chains and Cu_2O_3 ladders. Upon Ca substitution, the feature ascribed to the two-leg ladders approaches the Fermi energy, indicating that the holes are doped into the ladders with Ca substitution.

Using polarization dependent O 1*s* x-ray absorption spectroscopy on $(Sr,Ca)_{14}Cu_{24}O_{41}$, Nücker *et al.* [91] investigated the character of doped holes into the Cu_2O_3 ladders and CuO_2 chains, finding that the holes are doped into O 2*p* orbitals along the rung upon Ca substitution. They claim that the total hole count in the ladders increases only marginally, being in contrast to results using optical conductivity.

3.3 Anisotropic Charge Dynamics in Metallic Ladders

Figure 3-8 shows the T-dependence of resistivity for $Sr_3Ca_{11}Cu_{24}O_{41}$ in all three directions, where the inter-ladder resistivity, ρ_a, is 15 to 40 times larger than ρ_c,, and the resistivity perpendicular to the ladder plane, ρ_b, is larger than ρ_a by two orders.

The T-dependence of ρ_a (and also ρ_b) is anomalous in that ρ_a is insulating ($d\rho_a / dT < 0$) in the temperature range where ρ_c shows metallic behavior ($d\rho_c / dT > 0$). Such contrasting T-dependence between intra- and inter-ladder conduction is analogous to that observed between in-plane (ρ_a) and out-of-plane (ρ_c) resistivity in underdoped high-T_c cuprates.

The anisotropic charge dynamics has been further investigated by optical measurements. Figure 3-9 shows optical conductivity along the a-axis ($\sigma_a(\omega)$) for x = 8 and x = 11 at various temperatures, where for both x values the low-energy spectral weight is transferred to high energies when the sample is cooled down. This behavior is similar to the "pseudogap" observed in interplane optical conductivity ($\sigma_c(\omega)$) of high-T_c cuprates such as YBCO and LSCO in the under doped region [92]. Obviously then, the insulating resistivity along the a-axis originates from the suppression of low-energy conductivity due to opening the pseudogap in $\sigma_a(\omega)$.

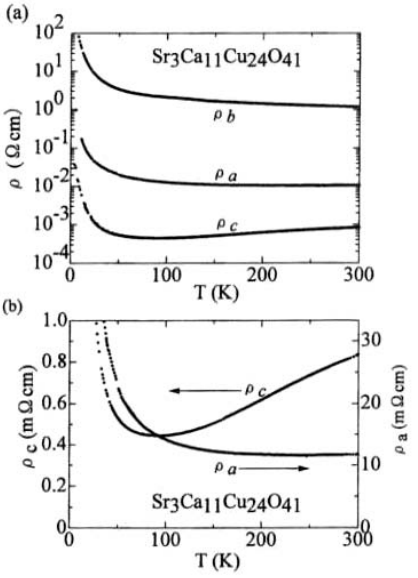

Fig. 3-8. *T*-dependence of resistivity for $Sr_3Ca_{11}Cu_{24}O_{41}$ along all three directions. (**a**) log-scale. (**b**) The *c*- and *a*-axis resistivity with linear scale [36].

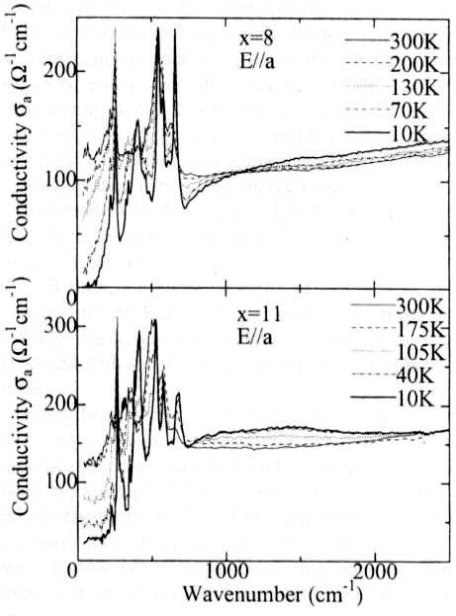

Fig.3-9. *a*-axis optical conductivity for $Sr_{14-x}Ca_xCu_{24}O_{41}$ (x = 8 and 11) [93].

The energy scale of the pseudogap is ~ 1100 cm^{-1} (140 meV) for x = 8 and ~600 cm^{-1} (74 meV) for x = 11. The magnitude of the pseudogap is comparable with that in high-T_c materials, e.g., 600 cm^{-1} for $YBa_2Cu_3O_{6.70}$, presumably reflecting the same microscopic origin [92]. NMR experiment shows that the temperature below which a spin gap opens in doped ladders (x = 11.5) coincides with the temperature where ρ_a starts to show negative T-dependence, indicating that the spin gap has a close connection with the optical pseudogap [27].

Figure 3-10 shows that in contrast to the pseudogap in $\sigma_a(\omega)$, the c-axis optical conductivity $\sigma_c(\omega)$ is characterized by a low energy peak which rapidly grows with decreasing T, where the peak in $\sigma_c(\omega)$ is located at ~100 cm^{-1} for x= 8, and ~50 cm^{-1} for x = 11. The peak is distinct from a Drude peak of free carriers since it is located at finite energies and develops when ρ_c shows insulating behavior.

The observed peak in $\sigma_c(\omega)$ can be interpreted to be a signature of a collective mode of a pinned charge-density wave (CDW). First of all, peak width in $\sigma_c(\omega)$ is quite narrow, suggestive of a well-defined collective mode, and secondly the T-dependence of the peak intensity follows a BCS gap equation which is an expected formula for CDW systems. In this framework the pseudogap in $\sigma_a(\omega)$ signals a formation of hole pairs that would be confined within a ladder and unable to hop between ladders. The T-dependence of $\sigma_c(\omega)$ and $\sigma_a(\omega)$ indicate that the holes are progressively paired with decreasing T and the pairs readily form a short-range charge order which is locally pinned by impurities and/or lattice imperfections.

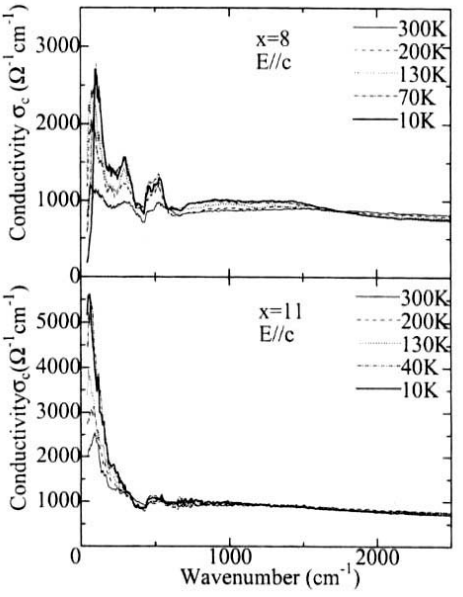

Fig.3-10. c-axis optical conductivity for $Sr_{14-x}Ca_xCu_{24}O_{41}$ (x = 8 and 11) [93]

For x = 8, the collective mode is strongly pinned at finite energy ~100 cm^{-1} and does not contribute to the DC conductivity, resulting in an insulating behavior. For x = 11, CDW may be de-pinned by thermal fluctuations and therefore contribute to metallic conduction along the c-axis. On the other hand, across the ladders, a hole pair must be dissociated into two single holes by thermal excitation across the gap, thus resulting in an insulating a-axis transport.

Independent of the above studies, there has been systematic optical studies by Ruzicka *et al.* [94] on $Sr_{14-x}Ca_xCu_{24}O_{41}$ (x=0, 5 and 12). Although some quantitative differences exist, conclusions are consistent with each other.

3.4 Charge Order in $Sr_{14}Cu_{24}O_{41}$

The charge dynamics of $Sr_{14}Cu_{24}O_{41}$ (and small Ca substituted samples) is quite different from its higher-x counterpart. As shown in Fig. 3-5, the resistivity of $Sr_{14}Cu_{24}O_{41}$ indicates an insulating behavior both along the c- and a-axis. Kitano *et al.* [95] found a dramatic increase of microwave conductivity below 170 K. Detailed study of the frequency dependence of the conductivity revealed the existence of a sharp resonance-like peak around 55 GHz (~0.2 meV). Since the peak frequency is much smaller than the thermal energy per carrier, this peak is attributed as a resonance mode of some collective charge excitation, similar to the pinned phase mode of charge- and spin- density wave (C/SDW) systems [96]. Similar nonlinear conduction was also observed by Gorshunov *et al.* [97,98], while subsequent Raman scattering and AC conductivity measurements by Blumberg *et al.* [99] have strengthened this picture. It should be noted that C/SDW correlation in $Sr_{14}Cu_{24}O_{41}$ persists up to 630 K, indicating that charge-spin correlations do not arise from phonons as in usual C/SDW systems, but rather from interactions stronger in energy such as in AF exchange or Coulomb interaction. Optical conductivity measurements on $Sr_{14}Cu_{24}O_{41}$ revealed that the transfer of spectral weight is extended to a high energy up to the CT gap, which suggests that C/SDW in $Sr_{14}Cu_{24}O_{41}$ involves a very large energy scale comparable to Coulomb energy.

Hess *et al.* [100] and Kudo *et al.* [101] showed that thermal conductivity ($\kappa(T)$) is useful to investigate interactions between the magnetic excitations and charge dynamics of doped holes, finding that the T-dependence of the magnon mean free path, l_{mag} in ladders correlates with the mobility of holes. In particular, they found a drastic enhancement of l_{mag} associated with the charge order in ladders.

4. PHYSICAL PROPERTIES OF TWO-LEG LADDERS IN $(Sr, Ca)_{14}Cu_{24}O_{41}$ UNDER HIGH PRESSURE

4.1 The Discovery of Pressure-Induced Superconductivity in Two-Leg Ladder Compound $Sr_{0.4}Ca_{13.6}Cu_{24}O_{41.84}$

Superconductivity in ladder material was first discovered by Uehara *et al.* [11] in two-leg ladder compound $Sr_{0.4}Ca_{13.6}Cu_{24}O_{41.84}$. They found that the solubility limit of Ca ions, or the hole-doping limit into Cu_2O_3 ladders, can be extended up to x=13.6 by synthesizing samples under high-O_2 pressure. The recipe for synthesizing polycrystal samples adopted by Uehara *et al.* follows.

A sample with nominal composition $Sr_{0.4}Ca_{13.6}Cu_{24}O_{41}$ was synthesized from $SrCO_3$, $CaCO_3$, and CuO powders with purities higher than 99.9%. The powder mixture was calcined at 1000 ^oC for 50 h under flowing O_2 using four intermediate grindings. The resultant powders were then formed into pellets and sintered using a HIP furnace at 1200 ^oC for 8 h under 20% O_2 + 80% Ar at a total pressure of 2000 atm. Oxygen content was determined by the inert gas fusion-infrared absorption method.

Figure 4-1 shows the x-ray powder diffraction pattern of $Sr_{0.4}Ca_{13.6}Cu_{24}O_{41.8}$, where all peaks are indexed indicating the sample is single phase. At ambient pressure the lattice parameters *a*, *b*, and *c* are 11.14, 12.44, and 27.02 Å, respectively. Because the 1D-chain and ladder are linked incommensurately, the *c*-axis length could only be calculated using (0 0 7*n*) (*n* = integer) reflections which indicate the *c*-axis length of the ladder.

Figure 4-2 shows the *T*-dependent electrical resistivity of a polycrystal sample under a pressure (*P*) of 0, 1.5, 2, and 3 GPa, where the magnitude of electrical resistivity at room temperature decreases monotonically with increasing pressure. The electrical resistivity at 0 and 1.5 GPa is almost flat above 200 K and shows a broad maximum at ~110 K. A similar broad peak has also been observed in the nearly metallic ladder compound $(Sr_{0.4}Ca_{0.6})_{14}Cu_{19.2}Co_{4.8}O_{41}$ [102] and was thought to be a characteristic feature of this system when it is close to the metallic state. Such behavior is now considered to be extrinsic, possibly arising from the "parallel circuit" effect of polycrystal samples. As discussed in Chap. 3, in high-Ca samples the resistivity is anisotropic, being metallic along the *c*-axis and insulating along the *a*- and *b*- axis. In polycrystal samples the resistance of the sample is the combined parallel circuit resistance of ρ_a and ρ_c, such that a broad peak appears at the temperature where the difference between ρ_a and ρ_c becomes very large. The electrical resistivity increases again below ~60 and ~30 K at 0 and 1.5 GPa, respectively. The *T*-dependence of the electrical resistivity at 2 GPa is metallic above 150 K and shows similar behavior to that at 1.5 GPa below 150 K. The superconducting transition occurs at 12.5 K at 3 GPa with metallic behavior above T_c, and the zero resistivity temperature is 8 K. Figure 4-3 shows the *T*-dependence of the electrical resistivity at 3, 4, and 6 GPa below 50 K. It is clear that the value of T_c (onset) decreases from 12.5 to 9 K with increasing *P* from 3 to 4.5 GPa. Finally, the superconducting transition disappears under an applied pressure of 6 GPa. Note that the effect

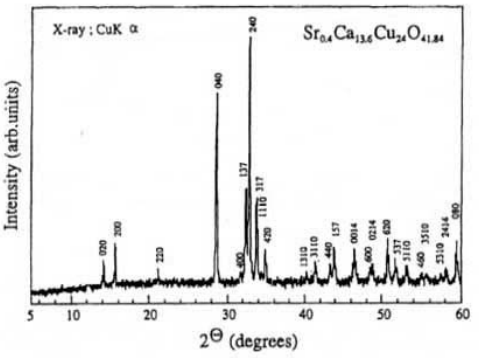

Fig. 4-1. x-ray powder diffraction pattern of $Sr_{0.4}Ca_{13.6}Cu_{24}O_{41.84}$ [7]

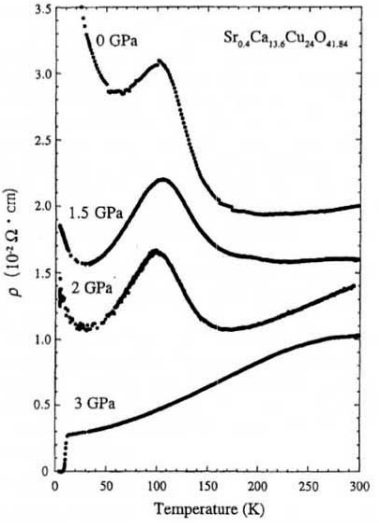

Fig. 4-2. *T*-dependence of the electrical resistivity of $Sr_{0.4}Ca_{13.6}Cu_{24}O_{41.84}$ under pressure of 0, 1.5, 2 and 3 GPa [11].

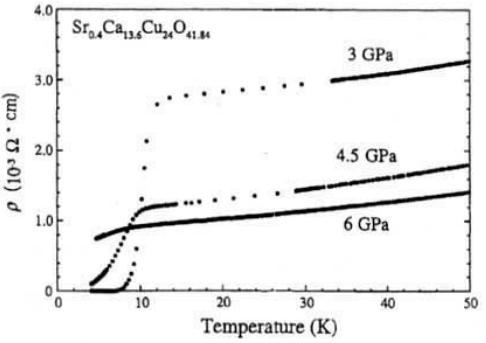

Fig. 4-3. *T*-dependence of the electrical resistivity of $Sr_{0.4}Ca_{13.6}Cu_{24}O_{41.84}$ under pressure of 3, 4.5 and 6 GPa below 50 K [11].

of pressure observed in this compound is much larger than in any other high-T_c cuprates in which application of pressure by itself does not cause insulator-superconductor-metal transition without changing the doping concentration.

As discussed in Chap. 3, Ca substitution leads to redistribution of hole carriers from the 1D chain to ladder plane [49]. As the Ca^{2+} ion is smaller than that of Sr^{2+}, the substitution of a Ca ion results in (chemical) pressure applied to the system. It is therefore reasonable that the role of pressure is essentially the same as Ca substitution and causes further hole-doping into the ladder plane. Under this hypothesis, the critical hole concentration for superconductivity is achieved only when physical and chemical pressures are applied. However, this postulation may turn out to be insufficient for understanding the role of pressure in the emergence of superconductivity, as will be discussed in Sec. 4.4 based on experimental results using a single crystal.

4.2 Crystal Structure under High Pressure

In order to confirm bulk superconductivity in $Sr_{0.4}Ca_{13.6}Cu_{24}O_y$, Isobe *et al*. [103] examined the crystal structure of $Sr_{0.4}Ca_{13.6}Cu_{24}O_{41.84}$ at high *P* and low *T*. They concluded using x-ray diffraction results that the $Sr_{0.4}Ca_{13.6}Cu_{24}O_y$ phase persists at least up to 9 GPa and down to 7 K without serious decomposition or phase transition.

Figure 4-4 shows x-ray diffraction patterns at various P and T, where a comparison of the diffraction pattern at ambient pressure and room temperature indicates there is no significant difference in the x-ray pattern at P = 5 GPa and T = 7 K when the sample is in the superconducting state. In addition to primary reflections, an extra peak, which increases its intensity at high P is observed as indicated by arrows. Isobe *et al*. considered the extra peak to be a higher-order satellite caused by a slight structural modulation. It has therefore been concluded that superconductivity actually comes from $Sr_{0.4}Ca_{13.6}Cu_{24}O_{41.84}$ and not from any impurity phase stabilized under high pressure.

Figure 4-5 shows P-dependent lattice constants measured at room temperature, where lattice constants smoothly decrease with increasing P. Of particular interest, it is clear that the compression rate of the b-axis is the largest among three axes (0.73%/GPa). This trend is similar to Ca-substitution dependence of lattice parameters; a similarity that suggests external pressure plays the same role as Ca substitution, i.e., transferring hole carriers from the CuO_2 chains to the Cu_2O_3 ladders through the hybrid orbitals of $Cu_{1Dchain}$-$O_{1Dchain}$-Cu_{ladder}. Precise crystal structure analysis using a super-symmetric group has indeed shown that the oxygen atoms of 1D chains displace towards the ladder and act as apical oxygen in Cu_{ladder} [45,104]. Such an apical oxygen probably works as the pathway for hole-redistribution from the 1D chain to the ladder.

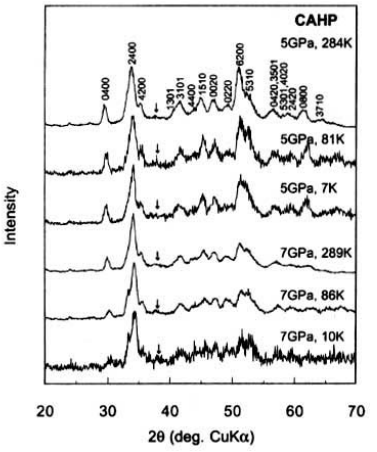

Fig. 4-4. The x-ray diffraction patterns of $Sr_{0.4}Ca_{13.6}Cu_{24}O_y$ at various pressure and temperature. The weak extra peak is shown by arrows [103].

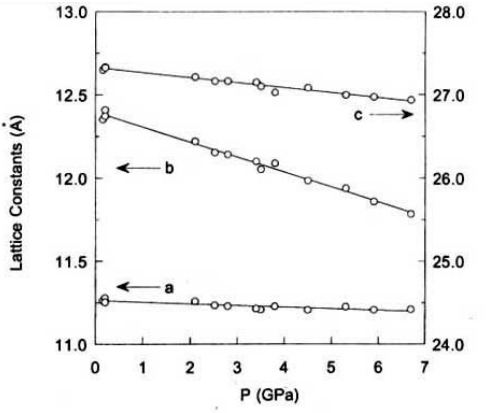

Fig. 4-5. The pressure dependence of lattice constants of $Sr_{0.4}Ca_{13.6}Cu_{24}O_y$ at room T [103].

The above discussion based on high-P x-ray studies is summarized as follows: (1) there is no significant P-induced structural change and/or phase decomposition which confirms bulk superconductivity in $Sr_{0.4}Ca_{13.6}Cu_{24}O_y$, and (2) external pressure results in shrinking the lattice parameters especially along the b-axis. Accordingly, the effect of Ca substitution and external pressure are quite similar to each other.

4.3 Evolution of Spin Gap of $(Sr,Ca)_{14}Cu_{24}O_{41}$ with Pressure

As described in the Chap. 3, the magnitude of the spin gap, Δ_{SG}, decreases with Ca substitution, i.e., hole-doping into the ladder. According to Magishi *et al.*'s [27] data of a ^{63}Cu Knight shift, for example, the spin gap decreases with Ca-doping from $\Delta_{SG} = 550 \pm 30$ K for $Sr_{14}Cu_{24}O_{41}$ to 350 ± 30 K, 280 ± 30 K, and 270 ± 30 K for $x = 6$, 9 and 11.5, respectively. A more interesting issue is how the spin gap evolves under pressure at which the sample is in a superconducting state.

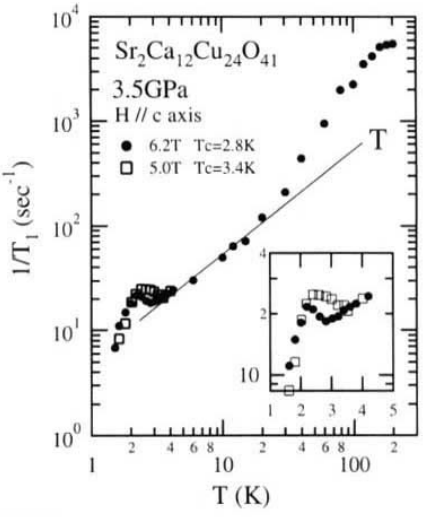

Fig. 4-6 Nuclear magnetic relaxation rate $1/T_1$ for ^{63}Cu nuclei. The solid line shows Korringa relation. $1/T_1$ at low temperature around T_c is expanding as indicated in the inset [108].

High-P NMR measurements were first performed by Mayaffre *et al*. [105] on $Sr_2Ca_{12}Cu_{24}O_{41}$, showing a superconducting transition at 5 K and 3 GPa. Based on experimental data, they concluded that the spin gap collapses at $P > 3$ GPa and a superconducting phase sets in. Results, however, were based on extracted data in the normal state above T_c. Piskunov *et al*. [106,107] performed similar experiments and obtained similar results. Recently, Fujiwara *et a*l. [108] performed precise NMR measurement with an improved high-P technique using a large, high-quality crystal of $Sr_2Ca_{12}Cu_{24}O_{41}$. Figure 4-6 shows the T-dependence of T_1^{-1}, where the spin gap appears even under high P as an activated T-dependence of T_1^{-1} at $T > 30$ K. Δ_{SG} is estimated to be 173 K. Near T_c (2.8 K under 6.2 T and 3.4 K under 5.0 T), a peak occurs which the authors interpret to be a superconducting coherence peak, i.e., there is a finite gap in the quasiparticle excitation indicating that the superconductivity possesses an s-wave-like character. At a pressure of 3.5 GPa and below 30 K, a T-linear component in T_1^{-1} was observed versus an activation-type one. The authors attributed this gapless mode to the free motion of holon-spinon bound states [109]; a behavior that occurs due to hole doping and whose pairing likely causes superconductivity. If true, the spin-gap formation observed from T_1^{-1} at high temperature would not contribute to the pairing formation of superconductivity. It is also pointed out that (i) the spin fluctuation of a $Sr_{14-x}Ca_xCu_{24}O_{41}$ system measured by NMR is much smaller than that in 2D high-T_c cuprates [108], and (ii) the T_c of these materials might be scaled by the magnitude of the spin fluctuation, rather than by the energy scale of the spin gap.

High-P inelastic neutron scattering experiments for $Sr_{2.5}Ca_{11.5}Cu_{24}O_{41}$ were performed by Katano *et a*l.[81], where in contrast to NMR results, they found Δ_{SG} does not change with Ca substitution. Moreover, even under pressure, Δ_{SG} remains unchanged and takes the same value of ~33 meV similar to undoped material $Sr_{14}Cu_{24}O_{41}$.

4.4 Evolution of Electrical Properties of $Sr_{2.5}Ca_{11.5}Cu_{24}O_{41}$ Single Crystal with Pressure

As described in Chap. 3, the charge dynamics of $Sr_{14-x}Ca_xCu_{24}O_{41}$ is quite anisotropic under ambient pressure. To understand the charge dynanmics in the superconducting phase, it is helpful to evaluate how inter-ladder coupling evolves with *P*. Anisotropic electrical reisitivity measurements under high *P* were carried out by Nagata *et al.* [110] using a single crystal of $Sr_{2.5}Ca_{11.5}Cu_{24}O_{41}$. Figure 4-7 shows *T*-dependence of resistivity, ρ_c and ρ_a, of $Sr_{2.5}Ca_{11.5}Cu_{24}O_{41}$ at various *P* up to 4.5 GPa. At ambient pressure, ρ_c shows metallic *T*-dependence above ~100 K, and applying *P* causes both ρ_c and ρ_a to decrease. The insulating behavior observed at low *T* is weakened with increasing *P,* nearly vanishing at 4.5 GPa, while simultaneously a superconducting transition sets in at 9 K. Note that the superconducting ground state emerges from the insulating ground state without going through the non-superconducting metallic region; a behavior that is quite similar to that of high-*T*c superconductors in which superconductor- to insulator (SI) transition takes place when some impurities such as Zn ions are doped in the CuO_2 planes [111]. At *P* higher than 5 GPa [inset of Fig.4-7(a)], T_c starts to decrease, being qualitatively consistent with previous results using polycrystal samples.

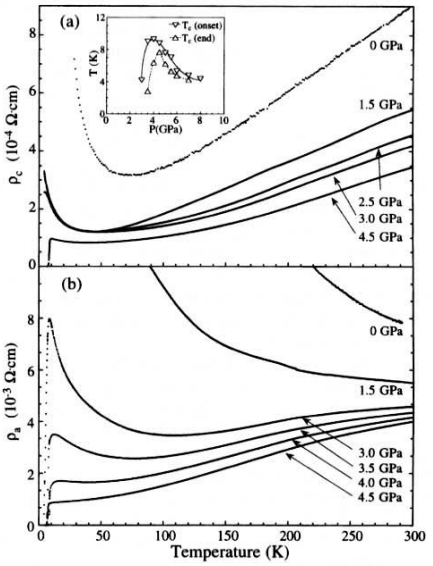

Fig. 4-7. Effect of pressure on temperature dependence of the resistivity (**a**) along the ladder direction (ρ_c) and (**b**) across (perpendicular to) the ladder in the ladder plane (ρ_a) of single crystal $Sr_{2.5}Ca_{11.5}Cu_{24}O_{41}$ at indicated pressure. Inset shows the pressure dependence of T_c [110].

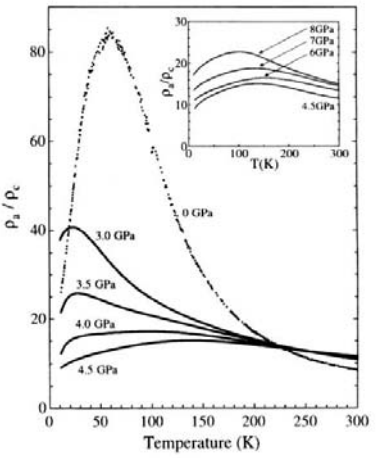

Fig. 4-8. Effect of pressure on temperature dependence of the anisotropic ratio ρ_a/ρ_c of single crystal $Sr_{2.5}Ca_{11.5}Cu_{24}O_{41}$ at indicated pressure. Inset shows the anisotropic ratio ρ_a/ρ_c above 4.5 GPa [110].

At ambient P, ρ_a shows an insulating behavior with negative T coefficient, indicating incoherent charge dynamics across the ladders. By applying pressure, the T coefficient crosses over from negative to positive such that the temperature region of the positive T coefficient widens. At $P > 4.5$ GPa, ρ_a shows metallic behavior all the way down to T_c, which indicates that high P induces concomitant occurrence of superconductivity and coherent charge dynamics perpendicular to the ladders. One may consider that the decrease in ρ_a and ρ_c results from hole-doping into the ladders, i.e., by transfer from the 1D chain to ladder plane, similar to Ca substitution. However, a clear difference exists between the application of external pressure and Ca substitution in that with Ca substitution the anisotropy ρ_a/ρ_c is *enhanced* (see Fig. 3-5(a)), whereas external pressure *reduces* the anisotropy so as to realize 2D metallic charge transport under high P.

Figure 4-8 shows the temperature dependence of anisotropy ratio ρ_a/ρ_c at various pressures, where the ρ_a/ρ_c at room temperature is about 10 and almost independent of P. With decreasing T at ambient pressure, ρ_a/ρ_c increases, reaching a maximum value of 85 at 50 K due to metallic ρ_c and insulating ρ_a. Application of external pressure suppresses the enhancement of ρ_a/ρ_c at low T. Finally, ρ_a/ρ_c becomes nearly T independent above ~ 4.0 GPa where superconductivity sets in.

To summarize the single crystal transport experiment by Nagata *et al*. [110], the application of pressure causes not only effective carrier doping into the ladder but also dimensional crossover in the charge dynamics from one to two, and superconductivity of the ladder appears on the 2D electrical background rather than 1D.

4.5 Pressure Effect in the Low Ca Region

Systematic high-P resistivity measurements at various x have been carried out by Motoyama *et al*. [112]. Even under high P, compounds with $x \leqq 8$ continue to be insulating except for x=0 which undergoes an insulator-to-metal transition, presumably due to the distraction of the charge-ordered state. On the other hand, for $x \geqq 10$, a superconducting transition occurs at $P \geqq$ 3–5 GPa. Based on these experimental results and extrapolated behavior to $T = 0$ K, the x-P phase diagram of $Sr_{14-x}Ca_xCu_{24}O_{41}$ can be drawn as shown in Fig. 4-9.

For $x \geqq 10$, there is a temperature region where $d\rho_c/dT > 0$ and $d\rho_a/dT < 0$, whereas for $0 < x \leqq 8$, both ρ_c and ρ_a always show a negative T coefficient at any P below 300 K. These results suggest the existence of two distinct insulating phases in $Sr_{14-x}Ca_xCu_{24}O_{41}$ with a boundary at $x \sim 8$. Apparently, the different nature of the two insulating phases might be related to the occurrence and non-occurence of superconductivity at high P.

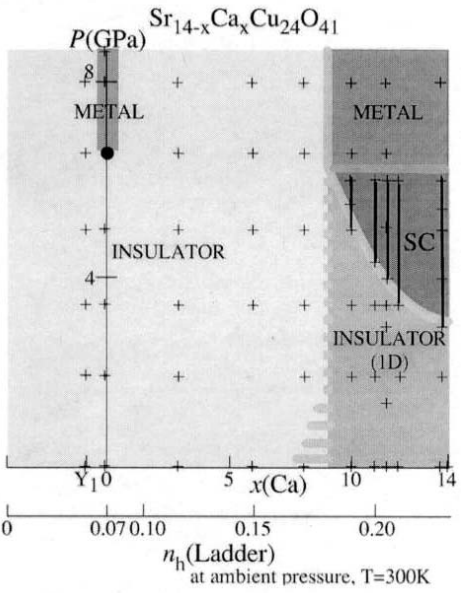

Fig. 4-9. The *x*-*P* phase diagram of $Sr_{14-x}Ca_xCu_{24}O_{41}$. Crosses represent points where measurements have been carried out. The crossover in the nature of the insulating state is indicated by a thick-dashed vertical line. The superconducting phase is restricted at high *P* and for $x \geqq 10$ [89].

4.6 Upper Critical Field under Pressure

Nakanishi *et al*. described the superconducting upper critical magnetic field, $H_{c2}(T)$, in a $Sr_{14-x}Ca_xCu_{24}O_{41}$ ($x = 12$) single crystal with $T_c \sim 5$ K at $P = 3.0$ GPa [113]. They measured the *T*-dependence of AC susceptivility at 4.0 GPa in magnetic fields applied along the *a*-, *b*-, and *c*-axis, determining $H_{c2}(T)$ for these three directions down to about 1.6 K.

Figure 4-10 shows the *T*-dependence of $H_{c2}(T)$ for directions Ha_{c2} (*H* parallel to *a*), Hb_{c2} (*H* parallel to *b*), and Hc_{c2} (*H* parallel to *c*), where *T*-dependence of H_{c2} is different in that $Ha_{c2} > Hc_{c2} > Hb_{c2}$ within the measured temperature range. This result indicates that the superconducting state is anisotropic and that the coherence length, ξ, has the following relation, $\xi_a > \xi_c > \xi_b$, i.e., the shortest coherence length among three directions is the *b*-axis, which is consistent with that expected from a layered crystal structure.

However, the relation $\xi_a > \xi_c$ is not considered appropriate in that superconducting coherence along the *a*-axis is stronger than that along the *c*-axis, or that the electronic band-width in the normal state is larger along the *a*- than *c*-axis. This conflicts with conductivity measurements showing ρ_a/ρ_c is about 15 from 300 ~ 4.2 K at 4 GPa, i.e., conductivity along the *c*-axis is clearly higher than the *a*-axis [110]. Further experimental and theoretical efforts are need to clarify the point.

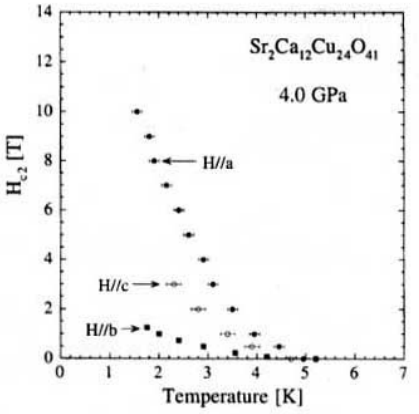

Fig. 4-10. *T*-dependence of the upper critical field, $H_{c2}(T)$ of $Sr_2Ca_{12}Cu_{24}O_{41}$ at 4.0 GPa for *H* parallel *a*- (closed circles), *b*- (closed squares) and *H* parallel *c*-axis (open circles) [113].

5. SUMMARY ON SPIN GAP AND SUPERCONDUCTIVITY OF TWO-LEG LADDER

In the spin ladder compound $Sr_{14-x}Ca_xCu_{24}O_{41}$, experiments indicate that (1) Ca substitution corresponds to hole carrier doping into the two-leg ladder through hole-charge redistribution from the CuO_2 chain to the ladder, (2) spin gap as predicted by theory exists, and (3) superconducting transition occurs with $x \geqq 11.5$ and at applied pressure higher than ~3 GPa. Accordingly, the basic phase diagram of $Sr_{14-x}Ca_xCu_{24}O_{41}$ can be described as shown in Fig. 5-1 (Magishi *et al* [27], see Fig. 4-9 also).

In addition to the basic properties of $Sr_{14-x}Ca_xCu_{24}O_{41}$ represented in Fig. 5-1, novel single crystal transport and NMR measurements under high-*P* have newly revealed relevant information such that it is now possible to expand discussions on the physics of $Sr_{14-x}Ca_xCu_{24}O_{41}$. These recent experimental results allow us further discussions on the origin of superconductivity in the ladder compounds.

(1) spin gap

It has been theoretically predicted that spin gap remains finite against carrier doping and that superconductivity appears by taking advantage of spin gap. The magnitude of the spin gap has been predicted to decrease by carrier doping [1], while NMR experiments provide evidence that Δ_{SG} decreases by carrier doping at ambient pressure, being consistent with theoretical predictions. Neutron experiments, however, reveal that Δ_{SG} is almost unchanged.

The reason for the discrepancy between NMR and neutron experiments remains unclear. It should be noted that these two methods observe spin excitations with different wave vector *k,* which could be one explanation for such differences.

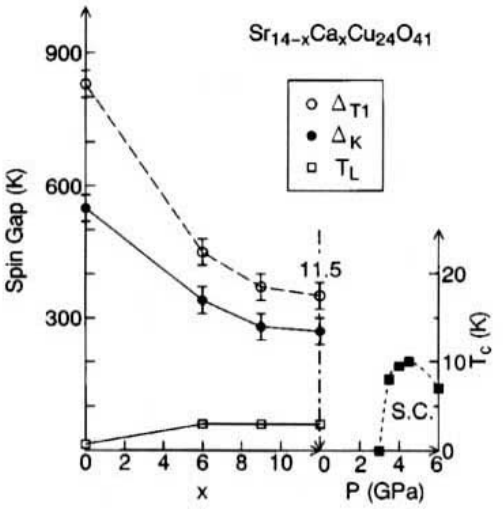

Fig. 5-1. Phase diagram of $Sr_{14-x}Ca_xCu_{24}O_{41}$ as functions of x and pressure. The spin gaps Δ_K (•) and Δ_{T1} (○) are obtain from the Knight shift and the T_1 measurements, respectively. T_c of x=11.5 sample is also plotted by solid squares (scale on right axis). See ref. [27] for more detail.

High-P NMR measurements demonstrate that spin gap behavior crosses over to a gap-less Korringa-like behavior above T_c (3–30 K). Such results can be interpreted to indicate that the free motion of holon-spinon bound states could be the origin of gap-less state., i.e., the spin gap survives in the superconducting state although it does not provide the crucial contribution to superconductivity [108]. Inelastic neutron scattering experiments at P = 2.1 GPa for x = 11.5 sample confirmed the existence of spin gap [81], where this pressure is close to the critical pressure for the emergence of superconductivity, suggesting that the spin gap might survive even under high P where the superconducting ground state exists at low T.

(2) Superconductivity

It has been theoretically predicted that superconductivity in ladder systems emerges due to the formation of electron (hole) pairs created by minimizing the energy-loss from breaking spin singlet pairs. The magnitude of the spin gap is on the order of hundreds of degrees Kelvin. Such a high energy scale leads us to expect high-T_c superconductivity in the ladder materials which has indeed triggered extensive experimental material research. However, the highest T_c of the existing ladder material is thus far limited to 12.5 K, being an order of magnitude smaller than 2D high-T_c cuprates, which suggests that the origin of superconductivity in real materials is not exactly the same as that expected from the simple spin gap-mediated superconductivity mechanism.

From single crystal resistivity experiments we know that external pressure possibly induces charge redistribution from the CuO_2 chain to Cu_2O_3 ladder. Such pressure also transfers the system from a 1D metal to an anisotropic 2D metal, with superconductivity of the ladder occurring in the anisotropic 2D electronic state.

Optical, transport, and NMR measurements suggest a formation of hole pairs associated with pseudogap formation for a high Ca-concentration ($x > 10$) sample at ambient pressure. These hole pairs would be confined within a ladder and unable to hop between ladders. In contrast, charge dynamics along a leg can possibly be characterized by a collective mode of a pinned CDW. Theoretically, both superconductivity and CDW are expected to be ground states in the hole doped two-leg ladder system and may be competing with each other.

In spin gap-mediated superconductivity, while theories predict the *d*-wave symmetry of the superconducting gap [7], the presence of a coherence peak observed in high-P NMR results seems to rule out simple *d*-wave superconductivity in $Sr_{14-x}Ca_xCu_{24}O_{41}$ [108].

Considering all the research, it is surmised that the superconductivity of $Sr_{14-x}Ca_xCu_{24}O_{41}$ probably takes place under the presence of a spin gap, yet the spin gap formation itself does not seem to play a crucial role in superconductivity. At present, the pairing mechanism of $Sr_{14-x}Ca_xCu_{24}O_{41}$ remains unclear. Further experimental and theoretical efforts directed at clarifying for example how much the spin gap state contributes and what effect CDW instability applies regarding the pairing mechanism should be useful to elucidate the origin of superconductivity.

Finally, we must emphasize that at this moment $Sr_{14-x}Ca_xCu_{24}O_{41}$ is the only spin ladder compound exhibiting superconductivity. It seems a little too naive, however, to conclude that the experimental results obtained on $Sr_{14-x}Ca_xCu_{24}O_{41}$ indeed reflect the general physics of two-leg ladder materials. In fact, $Sr_{14-x}Ca_xCu_{24}O_{41}$ cannot be regarded as a simple model case for a two-leg ladder system since the ladder may strongly be influenced by the random potential originating from the large buckling of oxygen atoms in 1D CuO_2 chains. This makes it reasonable to surmise that in order to overcome the excess random potential the superconductivity of $Sr_{14-x}Ca_xCu_{24}O_{41}$ shows up not in an "optimal-doped" region but rather in an "over-doped" one. The actual T_c is therefore lower than what should be expected and the relationship between spin gap and superconductivity is not so straightforward. Actually, superconductivity appears at nearly optimal value and clearly decreases with pressure higher than ~ 4.5 GPa. The so-called "under-doped" region observed in high-T_c cuprates where T_c increases toward an optimal value by carrier doping seems to be missing. It is strongly expected that researchers will discover new superconducting ladder materials that are "cleaner" than $Sr_{14-x}Ca_xCu_{24}O_{41}$.

ACKNOWLEDGEMENTS

This work was partly supported by a Grant-in-Aid for Scientific Research from the Ministry of Education, Culture, Sports, Science and Technology, Japan.

Two of authors (N. M. and J. A.) are thankful for a Grant-in-Aid for Science Research from the Ministry of Education, Culture, Sports, Science and Technology, Japan and 21st COE program.

REFERENCES

[1] E. Dagotto, J. Riera and D. Scalapino, Phys. Rev. B 45 (1992) 5744.
[2] T. M. Rice, S. Gopalan and M. Sigrist, Europhys. Lett. 23 (1993) 445.
[3] E. Dagotto and T. M. Rice, Science 271 (1996) 618.
[4] B. Levy, Phys. Today (1996) October 17.
[5] E. Dagotto, Rep. Prog. Phys., 62 (1999) 1525.
[6] J. G. Bednorz, and K. A. Müller, Z. Phys. B64 (1986) 189.
[7] M. Sigrist, T. M. Rice and F. C. Zhang, Phys. Rev. B 49 (1994) 12058
[8] M. Azuma, Z. Hiroi, M. Takano, K. Ishida and Y. Kitaoka, Phys. Rev. Lett., 73 (1994) 3463.
[9] Z. Hiroi, M. Azuma, M. Takano and Y. Bando, J. Solid State. Chem. 95 (1991) 230
[10] Z. Hiroi and M. Takano, Nature 377 (1995) 41.
[11] M. Uehara, T. Nagata, J. Akimitsu, H. Takahashi, N. Môri and K. Kinoshita, J. Phys. Soc. Jpn. 65 (1996) 2764.
[12] T. Barnes, E. Dagotto, J. Riera, and E. S. Swanson, Phys. Rev. B47 (1993) 3196.
[13] S. R. White, R. M. Noack, and D. J. Scalapino, Phys. Rev. Lett. 73 (1994) 886.
[14] Z. Hiroi, J. Solid State. Chem. 123 (1996) 223.
[15] T. Kimura, K. Kuroki and H. Aoki, Phys. Rev. B 54 (1996) R9608.
[16] K. Ishida, Y. Kitaoka, K. Asayama, M. Azuma, Z. Hiroi and M. Takano, J. Phys. Soc. Jpn. 63 (1994) 3222.
[17] K. Kojima, A. Keren, G. M. Luke, B. Nachumi, W. D. Wu, Y. J. Uemura, M. Azuma and M. Takano, Phys. Rev. Lett. 74 (1995) 2812.
[18] M. Troyer, H. Tsunetsugu, and D. Würtz, Phys. Rev. B 50 (1994) 13515.
[19] S. Matsumoto, Y. Kitaoka, K. Ishida, K. Asayama, Z. Hiroi, N. Kobayashi and M. Takano, Phys. Rev. B 53 (1996) 11942.
[20] R. Kadono, H. Okajima, A. Yamashita, K. Ishii, T. Yokoo, J. Akimitsu, N. Kobayashi, Z. Hiroi, M. Takano and K. Nagamine, Phys. Rev. B 54 (1996) 9628.
[21] E. M. McCarron, M. A. Subramanian, J. C. Calabrese and R. L. Harlow, Mater. Res. Bull 23 (1988) 1355.
[22] T. Sigrist, L. F. Schneemeyer, S. A. Sunshine, J. V. Waszczak and R. S. Roth, Mater. Res. Bull 23 (1988) 1429.
[23] R. Eccleston, M. Azuma and M. Takano, Phys. Rev. B 53 (1996) 14721.
[24] R. Eccleston, M. Uehara, J. Akimitsu, H. Eisaki, N. Motoyama and S. Uchida, Phys. Rev. Lett. 81 (1998) 1702.
[25] S. Tsuji, K. Kumagai, M. Kato and Y. Koike, J. Phys. Soc. Jpn. 65 (1996) 3474.
[26] K. Kumagai, S. Tsuji, M. Kato, and Y. Koike, Phys. Rev. Lett. 78, (1997) 1992.
[27] K. Magishi, S. Matsumoto, Y. Kitaoka, K. Ishida and K. Asayama, M. Uehara, T. Nagata and J. Akimitsu, Phys. Rev. B 57 (1998) 11533.
[28] L. P. Regnault, A. H. Moudden, J. P. Boucher, E. Lorenzo, A. Hiess, A. Vietkin, A. Revcolevschi, Physica B 259-261 (1999) 1038.
[29] Y. Mizuno, T. Tohyama, S. Maekawa, T. Osafune, H. Eisaki, and S. Uchida, Phys. Rev. B57 (1998) 5326.
[30] F. C. Zhang and T. M. Rice, Phys. Rev. B37 (1988) 3759.
[31] S. A. Carter, B. Batlogg, R. J. Cava, J. J. Krajewski, W. F. Peck Jr. and T. M. Rice, Phys. Rev. Lett. 77 (1996) 1378.

[32] M. Matsuda, K. Katsumata, T. Yokoo, S. M. Shapiro, and G. Shirane, Phys. Rev. B54 (1996) R15626.
[33] M. Matsuda, K. M. Kojima, Y. J. Uemura, J. L. Zarestky, K. Nakajima, K. Kakurai, T. Yokoo, S. M. Shapiro, and G. Shirane, Phys. Rev. B57 (1998) 11467.
[34] M. Kato, K. Shiota and Y. Koike, Physica C 258 (1996) 284.
[35] M. Matsuda and K. Katsumata, Phys. Rev. B 53 (1996) 12201.
[36] N. Motoyama, T. Osafune, T. Kakeshita, H. Eisaki, and S. Uchida, Phys. Rev. B55 (1997) R3386.
[37] M. Matsuda, K. Katsumata, H. Eisaki, N. Motoyama, S. Uchida, S. M. Shapiro, and G. Shirane, Phys. Rev. B54 (1996) 12199.
[38] L. P. Regnault, J. P. Boucher, H. Moudden, J. E. Lorenzo, A. Hiess, U. Ammerahl, G. Dhalenne, and A. Revcolevschi, Phys. Rev. B59 (1999) 1055.
[39] M. Matsuda, T. Yosihama, K. Kakurai, and G. Shirane, Phys. Rev. B59 (1999) 1060.
[40] M. Takigawa, N. Motoyama, H. Eisaki and S. Uchida, Phys. Rev. B57 (1998) 1124.
[41] T. Imai, K. R. Thurber, K. M. Shen, A. W. Hunt and F. C. Chou, Phys. Rev. Lett., 81 (1999) 220.
[42] Z. Hiroi, S. Amelinckx, G. Van Tendeloo, and N. Kobayashi, Phys. Rev. B 54 (1996) 15849.
[43] D. E. Cox, T. Iglesias, K. Hirota, G. Shirane, M. Matsuda, N. Motoyama, H. Eisaki, and S. Uchida, Phys. Rev. B57 (1998) 10750.
[44] T. Fukuda, J. Mizuki, and M. Matsuda, Phys. Rev. B66 (2002) 12104.
[45] Y. Gotoh, I. Yamaguchi, Y. Takahashi, J. Akimoto, M. Goto, M. Onoda, H. Fujino, T. Nagata and J. Akimitsu, Phys. Rev. B 68 (2003) 224108.
[46] S. van Smaalen, Phys. Rev. B67 (2003) 26101.
[47] M. Kato, T. Adachi, and Y. Koike, Physica C265 (1996) 107.
[48] M. Matsuda, K. Katsumata, H. Eisaki, N. Motoyama, S. Uchida, T. Yokoo, S. M. Shapiro, G. Shirane, and J. L. Zarestky, Phys. Rev. B56 (1997) 14499.
[49] T. Osafune, N. Motoyama, H. Eisaki and S. Uchida, Phys. Rev. Lett., 78 (1997) 1980.
[50] U. Ammerahl, B. Büchner, C. Kerpen, R. Gross, and A. Revcolevschi, Phys. Rev. B62 (2001) 2882.
[51] V. Kataev, K.Y. Choi, M. Grüninger, U. Ammerahl, B. Büchner, A. Freimuth, and A. Revcolevschi, Phys. Rev. Lett. 86 (2001) 2882.
[52] V. Y. Yushankhai and R. Hayn, Europhys. Lett. 47 (1999) 116.
[53] S. Tornow, O. Entin-Wohlman, and A. Aharony, Phys. Rev. B60 (1999) 10206.
[54] M. Matsuda, K. Kakurai, J.E. Lorenzo, L.P. Regnault, A. Hiess, and G. Shirane, Phys. Rev. B68 (2003) R060406.
[55] R. Leidl and W. Selke, Phys. Rev. B69 (2004) 56401.
[56] W. Selke, V. L. Pokrovsky, B. Büchner, and T. Kroll, Eur. Phys. J. B30 (2002) 83.
[57] M. Holtschneider and W. Selke, Phys. Rev. E68 (2003) 26120.
[58] R. Weht, W. E. Pickett, Phys. Rev. Lett. 81 (1998) 2502.
[59] M. Matsuda, K. Kakurai, H. Yamaguchi, T. Ito, C. H. Lee, and K. Oka, Applied Physics A74 (2002) S637.
[60] U. Staub, B. Roessli, A. Amato, Physica B289-290 (2000) 299.
[61] E. M. L. Chung, G. J. McIntyre, D. McK. Paul, G. Balakrishnan, and M. R. Lees, Phys. Rev. B68 (2003) 144410.
[62] P. K. Davis, J. Solid State Chem. 95 (1991) 365.

[63] P. K. Davis, E. Caignol, and T. King, J. Am. Ceram. Soc. 74 (1991) 569.
[64] A. Hayashi, B. Batlogg, and R. J. Cava, Phys. Rev. B58 (1998) 2678.
[65] M. Matsuda, K. Ohyama, and M. Ohashi, J. Phys. Soc. Jpn. 68 (1999) 269.
[66] H. F. Fong, B. Keimer, J. W. Lynn, A. Hayashi, and R. J. Cava, Phys. Rev. B59 (1999) 6873.
[67] K. Kudo, S. Kurogi, Y. Koike, T. Nishizaki, and N. Kobayashi, cond-mat/0408628.
[68] M. D. Chabot and J. T. Markert, Phys. Rev. Lett. 86 (2001) 163.
[69] S. Kurogi, K. Kudo, T. Noji, Y. Koike, T. Nishizaki, and N. Kobayashi, J. Low Temp. Phys. 131 (2003) 353.
[70] J. Dolinsek, D. Arcon, P. Cevc, O. Milat, M. Miljak, and I. Aviani, Phys. Rev. B57 (1998) 7798.
[71] Z. Hiroi, M. Okumura, T. Yamada, and M. Takano, J. Phys. Soc. Jpn. 69 (2000) 1824.
[72] M. Isobe, K. Kimoto, and E. Takayama-Muromachi, J. Phys. Soc. Jpn. 71 (2002) 782.
[73] Y. Mizuno, T. Tohyama, and S. Maekawa, Phys. Rev. B60 (1999) 6230.
[74] M. Matsuda, H. Yamaguchi, T. Ito, C. H. Lee, K. Oka, Y. Mizuno, T. Tohyama, S. Maekawa, and K. Kakurai, Phys. Rev. B63 (2001) 180403(R).
[75] S. K. Satija, J. D. Axe, R. Gaura, R. Willett, and C. P. Landee, Phys. Rev. B25 (1982) 6855.
[76] M. Matsuda, K. Kakurai, S. Kurogi, K. Kudo, Y. Koike, H. Yamaguchi, T. Ito, and K. Oka, in preparation.
[77] H. Yamane, Y. Miyazaki and H. Hirai, J. Ceramic Soc. Jpn., 98 (1990) 105.
[78] M. Matsuda, K. Katsumata, R. S. Eccleston, S. Brehmer, and H. J. Mikeska, Phys. Rev. B 62 (2000) 8903.
[79] S. Sugai and M. Suzuki, Phys. Stat. Sol. (b), 215 (1999) 653.
[80] A. Gozar, G. Blumberg, B. S. Dennis, B. S. Shastry, N. Motoyama, H. Eisaki, and S. Uchida, Phys. Rev. Lett. 87 (2001) 197202.
[81] S. Katano, T. Nagata, J. Akimitsu, M. Nishi and K. Kakurai, Phys. Rev. Lett., 82 (1999) 636.
[82] S. Fujiyama, M. Takigawa, N. Motoyama, H. Eisaki and S. Uchida, J. Phys. Soc. Jpn. 69 (2000) 1610.
[83] T. Nagata, H. Fujino, J. Akimitsu, M. Nishi, K. Kakurai, S. Katano, M. Hiroi, M. Sera, and N. Kobayashi, J. Phys. Soc. Jpn., 68 (1999) 2206.
[84] S. Ohsugi, M. Magishi, S. Matsumoto, Y. Kitaoka, T. Nagata and J. Akimitsu, Phys. Rev. Lett., 82 (1999) 4715.
[85] M. Isobe, Y. Uchida and E. Takayama-Muromachi, Phys. Rev. B 59 (1999) 8703.
[86] K. Ohishi, T. Yokoo, K. Kakuta, H. Fujino, T. Nagata, J. Akimitsu and R. Kadono, J. Phys. Soc. Jpn., 69 (2000) 2427.
[87] T. Nagata, H. Fujino, K. Satoh, N. Yamamori, J. Akimitsu, S. Katano, M. Nishi, K. Kakurai, M. Hiroi, M. Sera, and N. Kobayashi, K. Tenya, H. Amitsuka, T. Takigawa, H. Inago and T. Sakakibara, J. Phys. Soc. Jpn., 68 (1999) 2206.
[88] M. Isobe, M. Onoda, T. Ohta, F. Izumi, K. Kimoto, E. Takayama-Muromachi, A. W. Hewat, and K. Ohoyama, Phys. Rev. B 62 (2000) 11667.
[89] K. M. Kojima, N. Motoyama, H. Eisaki and S. Uchida, J. Electron Spectroscopy and Related Phenomena 117-118 (2001) 237.
[90] T. Takahashi, T. Yokoya, A. Ashihara, H. Fujisawa, A. Chainani, M. Uehara, T. Nagata, J. Akimitsu and H. Tsunetsugu, Phys. Rev. B 56 (1997) 7870.

[91] N. Nücker, M. Merz, C. A. Kuntscher, S. Gerhold, S. Schuppler, R. Neudert, M. S. Golden, J. Fink, D. Schild, S. Stadler, V. Chakarian, J. Freeland, Y. U. Idzerda, K. Conder, M. Uehara, T. Nagata, J. Goto, J. Akimitsu, N. Motoyama, H. Eisaki, S. Uchida, U. Ammerahl, and A. Revcolevschi, Phys. Rev. B 62 (2000) 14384.
[92] T. Timusk and B. Statt, Rep. Prog. Phys., 62 (1999) 61.
[93] T. Osafune, N. Motoyama, H. Eisaki, S. Uchida, and S. Tajima, Phys. Rev. Lett., 82 (1999)1313.
[94] B. Ruzicka, L. Degiorgi, U. Ammerahl, G. Dhalenne and A. Revcolevschi, Eur, Phys. J. B 6 (1998) 301
[95] H. Kitano, R. Inoue, T. Hanaguri, A. Maeda, N. Motoyama, M. Takaba, K. Kojima, H. Eisaki and S. Uchida, Europhys. Lett. 56 (2001) 434. ; Physica C 341-348, (2000) 463.
[96] A. Maeda, R. Inoue, H. Kitano, N. Motoyama, H. Eisaki, and S. Uchida, Phys. Rev. B 67 (2003) 115115.
[97] B. Gorshunov, P. Haas, T. Rõõm, M. Dressel, T. Vuleti , B. Korin-Hamzi , S. Tomi , J. Akimitsu and T. Nagata, Phys. Rev. Lett., 66 (2002) 060508.
[98] T. Vuleti , B. Korin-Hamzi , S. Tomi , B. Gorshunov, P. Haas, T. Rõõm, M. Dressel, J. Akimitsu, T. Sasaki and T. Nagata, Phys. Rev. Lett., 90 (2003) 2570021.
[99] G. Blumberg, P. Littlewood, A. Gozar, B. S. Dennis, N. Motoyama, H. Eisaki, and S. Uchida, Science 297 (2002) 584.
[100] C. Hess, H. ElHaes, B. Büchner, U. Ammerahl, M. Hücker, and A. Revcolevschi, Phys. Rev. Lett. 93 (2004) 027005.
[101] K. Kudo, S. Ishikawa, T. Noji, T. Adachi, Y. Koike, K. Maki, S. Tsuji and K. Kumagai, J. Phys. Soc. Jpn., 70 (2001) 437.
[102] M. Uehara, M. Ogawa and J. Akimitsu, Physica C 255 (1995) 193.
[103] M. Isobe, T. Ohta, M. Onoda, F. Izumi, S. Nakano, J. Q. Li, Y. Matsui, E. Takayama-Muromachi, T. Matsumoto and H. Hayakawa, Phys. Rev. B 57 (1998) 613.
[104] T. Ohta, F. Izumi, M. Onoda, M. Isobe, E. Takayama-Muromachi and A. W. Hewat, J. Phys. Soc. Jpn, 66 (1997) 3107.
[105] H. Mayaffre, P. Auban-Senzier, M. Nardone, D. Jérome, D. Poilblanc, C. Bourbonnais, U. Ammerahl, G. Dhalenne and A. Revcolevschi, Science 279 (1998) 345.
[106] Y. Piskunov, D. Jerome, P. Auban-Senzier, P. Wzietek, Y. Ammerhal, G. Dhalenne and A. Revcolevschi, Eur. Phys. J. B 13 (2000) 417.
[107] Y. Piskunov, D. Jerome, P. Auban-Senzier, P. Wzietek, C. Bourbonnais, U. Ammerhal, G. Dhalenne and A. Revcolevschi, Eur. Phys. J. B 24 (2001) 443.
[108] N. Fujiwara, N. Môri, Y. Uwatoko, T. Matsumoto, N. Motoyama and S. Uchida, Phys. Rev.Lett., 90 (2003) 1370011.
[109] H. Tsunetsugu, M. Troyer and T. M. Rice, Phys. Rev. B 49 (1994) 16078.
[110] T. Nagata, M. Uehara, J. Goto, J. Akimitsu, N. Motoyama, H. Eisaki, S. Uchida, H. Takahashi, T. Nakanishi, and N. Môri, Phys, Rev. Lett., 81 (1998) 1090.
[111] Y. Fukuzumi, K. Mizuhashi, K. Takenaka and S. Uchida, Phys. Rev. Lett., 76 (1996) 684.
[112] N. Motoyama H. Eisaki, S. Uchida, N. Takeshita, N. Môri, T. Nakanishi and H. Takahashi, Europhysics Letters 58 (2002) 758.
[113] T. Nakanishi, H. Takahashi, N. Takeshita, N. Môri, N. Motoyama, H. Eisaki, S. Uchida, H. Fujino, T. Nagata and J. Akimitsu, Physica B 281&282 (2000) 957.

AN EXPERIMENTAL REALIZATION OF THE SHASTRY-SUTHERLAND MODEL

Hiroshi Kageyama*

Department of Chemistry, Graduate School of Science, Kyoto University, Kyoto 606-8502, Japan

1. INTRODUCTION

The known classes of quantum spin antiferromagnets show long-range magnetic ordering, or Néel ordering cooled down from the paramagnetic, high temperature state. The ordering temperature is basically of the order of the exchange coupling constants. However, quantum fluctuations due to the small spins that are involved and a low dimensionality of the interconnecting exchange paths significantly suppress the ordering temperature. Instead, novel and more interesting phases with short range correlations may exist that compete with long range ordering [1]. These phases are described within the concepts of spin glasses or spin liquids, instead of the classical Néel ordered state. In the last two decades, much experimental effort has been put into understanding the quantum antiferromagnetic fluctuations in quasi-one-dimensional (1D) magnetic systems. This interest has been revived by the discovery of quasi-2D $S = 1/2$ spin correlations in the superconducting cuprates [2], and these correlations are proposed to be relevant for the yet incompletely understood mechanism of high temperature superconductivity.

In the course of these studies, many new 1D magnetic systems with a spin-singlet ground state have been discovered, e.g., the $S = 1/2$ spin-Peierls chain $CuGeO_3$ [3], the $S = 1$ Haldane chains Y_2BaNiO_5 [4] and $Ni(C_2H_8N_2)_2NO_2(ClO_4)$ [5], the $S = 1/2$ ladders $SrCu_2O_3$ [6] and $Cu_2(C_5N_2H_{12})_2Cl_4$ [7], the $S = 1/2$ alternating chain $Cu(NO_3)_2 2.5H_2O$ [8], to name only a few. The spin dynamics of these systems show a spin excitation gap from the nonmagnetic singlet

* e-mail: kage@kuchem.kyoto-u.ac.jp (Hiroshi Kageyama)

ground state to the first excited triplet state, which may be regarded as a direct consequence of the quantum spin fluctuations. The conditions for an effective 1D magnetic network are satisfied in many real compounds and the effects of quantum fluctuations are present in the observed magnetic properties. However, in spite of the fact that the high temperature superconductivity has been achieved on a charge carrier doped $S = 1/2$ square lattice, there are unfortunately only few examples establishing a quasi 2D spin-singlet ground state, and thus the effect of quantum fluctuations in 2D remains poorly understood. To the author's knowledge, such a system was first realized experimentally in CaV_4O_9 [9], for which a model based on the plaquette singlets is considered to explain the origin of the spin gap [10].

The concept of competing (ground) states and competing interactions is of very high relevance for such systems with strong fluctuations. Competing interactions originate from the interplay of the local crystallographic geometry or topology of the magnetic ions on the underlying lattice with their electronic configurations. This aspect highlights in an unprecedented way the interdisciplinary approach combining chemistry and crystallography with solid state physics, which is characteristic for this field of quantum magnetism [1]. Competing interactions provide new sorts of phases, successive phase transitions and novel critical phenomena. A number of studies have been devoted, both theoretically and experimentally, to various triangle-based lattices like the triangular lattice, the kagomé lattice, and the pyrochlore lattice [11, 12]. For example, the compromise spin arrangement, the so-called 120° state is realized for the triangular lattice with antiferromagnetically interacting Heisenberg spins on triangles, in order to reduce the total magnetic energy. It is once again quite unfortunate that little is known about the effect of frustration in various spin gap systems. The idea of Anderson's resonating valence bond (RVB) state, in which the "RVB" singlet pairs flow on the triangular lattice [13], has not yet been observed in an experimental system. The role of the frustrating next-nearest interaction with respect to spin-phonon interaction is still controversial in the spin-Peierls compound $CuGeO_3$ to establish the observed spin-singlet ground state.

Within this background, real compounds having a 2D spin-singlet ground state with frustrating spin configuration have been long desired since early 1990's. In 1996 when I was looking for low-dimensional inorganic compounds in the office of Prof. Kosuge at Kyoto University, I came across a paper in which the synthesis and the crystal structure of $SrCu_2(BO_3)_2$ were described [14]. A unique 2D magnetic network of Cu^{2+} ions (carrying well-localized $S = 1/2$ spins), in which strong frustration effects are expected, inclined me to prepare a $SrCu_2(BO_3)_2$ sample and investigate its magnetic properties. Several magnetic measurements on the powder sample revealed that this material could be regarded as a second example of a 2D spin-gap system. In addition, high-field magnetization measurement at low temperatures, from which I just intended to estimate exchange coupling constants, unexpectedly detected the existence of several quantized plateaus [15].

However, in the early stage of this research, there was no theoretical verification on the spin gap and magnetization plateaus observed in $SrCu_2(BO_3)_2$. After joining Yutaka Ueda's group at the Institute for Solid State Physics, the University of Tokyo in 1998, I showed the experimental data to Kazuo Ueda and Shin Miyahara at a welcome party. It did not take one month till they proposed a new theoretical ansatz on the basis of a simple 2D Heisenberg antiferromagnetic model [16]. They noticed that this model has an exactly solvable ground state. Furthermore, they gave a reasonable explanation of why quantized plateaus appear in the magnetization curve. Soon after that, it was found that the magnetic network in

$SrCu_2(BO_3)_2$ is topologically equivalent to the lattice which B. S. Shastry and B. Sutherland considered in 1981 [17]. Following these unforgettable events, intensive and extensive studies have been performed worldwide both from experimental and theoretical sides, to elaborate on the physics of $SrCu_2(BO_3)_2$. In particular, the success of bulk single crystals, thanks to a long-term and fervid motivation from the Raman specialist Peter Lemmens, has opened the doors to physicists to use all available sophisticated techniques of solid state physics. In solid-state physics, a close collaboration between experimentalists and theorists is the most important aspect for understanding the nature of systems studied, sometimes giving us full of delight and satisfaction. Such a collaboration is, I believe, most effectively and idealistically performed through the research on $SrCu_2(BO_3)_2$ and corresponding Shastry-Sutherland model. This article will review the rich and novel magnetic properties of this exotic quantum spin system, mainly from experimental point of view. Theoretical issues have been recently reviewed by S. Miyahara and K. Ueda [18].

2. GEOMETRICALLY FRUSTRATED SPIN MODELS

Before describing structural aspects of $SrCu_2(BO_3)_2$, I wish to address how geometrically frustrated lattices can be tailored, classifying them into two groups. This is to facilitate readers to realize an intimate relation between the $SrCu_2(BO_3)_2$ lattice and other lattices of the same category, putting special emphasis to their relevance for the understanding of high temperature cuprate superconductors.

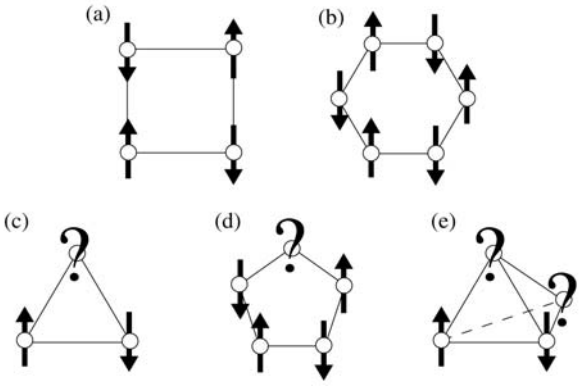

Fig. 1. Non-frustrated and frustrated units: (**a**) square, (**b**) hexagon, (**c**) triangle, (**d**) pentagon, and (**e**) tetrahedron.

A conventional way of constructing geometrical spin frustration models with macroscopic degeneracy is to use a rigid triangle with three spins sitting on each corner as a basal unit, as shown in Fig. 1 (c). In the Ising spin limit and considering only interactions between nearest

neighbors, its ground state is six-fold degenerated in the absence of magnetic field, i.e., ⇑⇑⇓, ⇑⇓⇑, ⇓⇑⇑, ⇑⇓⇓, ⇓⇑⇓, ⇓⇓⇑. More generally, polygons with odd number of corners such as a pentagon (Fig. 1 (d)) yield spin frustration, while it is straightforward to find energetically stable spin arrangement for those with even number of corners, which include a square (Fig. 1 (a)) and a hexagon (Fig. 1 (b)). A tetrahedron with four triangles shown in Fig. 1 (e) or in general polyhedra that contain polygons with odd number of corners are also regarded as a basis of frustrated lattices.

Arranging such units of polygons or polyhedra in a periodic fashion by sharing corners, edges or even faces, one obtains geometrically frustrated spin models, which are realized in real compounds. An arrangement of triangles in a row by corner sharing yields a Δ-chain, while both corner- and edge-sharing configurations give rise to a zigzag-chain model, as illustrated in Figs. 2 (a) and (b), respectively. Shown in Fig. 2 (c) is a triangular lattice, in which triangles are fully packed on a plane. Periodic extraction of 1/4 lattice points from the triangular lattice leads to the corner shared triangles, or the kagomé lattice named after weave pattern of Japanese basket (Fig. 2 (d)). A pyrochlore lattice, or B-site spinel lattice (Fig. 2 (e)) can be constructed by an alternative stack of triangular and kagomé lattices. This lattice can also be constructed out of corner-sharing tetrahedra. There has been a lot of experimental and theoretical work on these triangle-based frustrated systems; a discussion of their properties is beyond the scope of this article. Here, I just want to stress that there exist already a large number of real compounds having a wide range of interaction types, anisotropies and magnitude of spins.

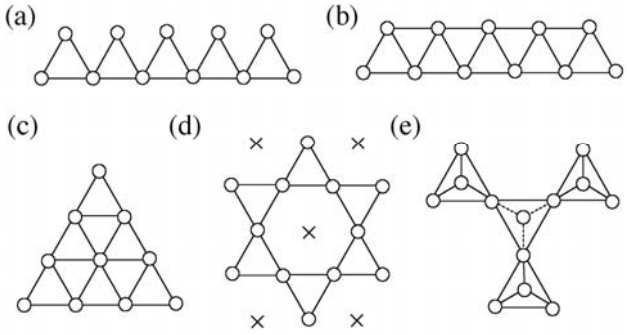

Fig. 2. Geometrically frustrated lattices with units of rigid triangles: (**a**) Δ-chain, (**b**) zigzag chain, (**c**) triangular, (**d**) kagomé, and (**e**) pyrochlore models.

It appears that there is no chance to built a frustrated lattice from squares as a basis considering nearest neighbor interactions. In fact, a square-lattice antiferromagnet is known to have an ordered ground state approximated by the Néel state, as shown in Fig. 3 (a). This model, however, can be modified to a frustrated by removing 1/5 of the sites periodically, as exemplified by CaV_4O_9 (Fig. 3 (b)) [9]. Creation of vacancies reduces the coordination number and makes otherwise equivalent bonds inequivalent, as visualized by the solid and dotted bonds in the figure. Theory suggests that, depending on the ratio of interactions, various states such as plaquette spin-singlet state appear [10].

An alternative of modeling frustrated geometry based on the square lattice is to add diagonal interactions. Changing the filling ratio of diagonal bonds on the square lattice, various models exist as shown in Figs. 3 (c)-(f). According to the quantum Heisenberg model for the 2D J_1-J_2 lattice (Fig. 3 (c)) with full filling, where J_1 and J_2 are the nearest- and the next-nearest-neighbor interactions, different situations occur depending on the ratio of J_2/J_1, which range from the antiferromagnetic state, to the dimer singlet state and the collinear ordered state [19]. Several new compounds, such as $VOMoO_4$, $Pb_2VO(PO_4)_2$, Li_2VOGeO_4, and Li_2VOSiO_4 have been investigated to check the theory [20]. In Fig. 3 (d), a distorted (or anisotropic) triangular lattice is shown, corresponding to a 50 % filling of diagonal bonds. One of the model materials Cs_2CuCl_4 shows interesting properties in the presence of small magnetic fields, which is interpreted in terms of a 2D fractionalized RVB state [21], while isostructural Cs_2CuBr_4 displays a 1/3 plateau in the magnetization ascribed to quantum fluctuations [22]. Projection of the 3D pyrochlore onto a layer yields the 2D checkerboard lattice, or the so-called 2D pyrochlore lattice (Fig. 3 (e)). This model corresponds to 50 % filling of diagonal bonds similar to the case of the distorted triangular lattice but different with respect to the arrangement of the bonds. Although no real compound has been reported so far, the checkerboard lattice shows a rich phase diagram and critical properties that are accessible by theory, as this is a simpler model than the 3D pyrochlore case. The lattice displayed in Fig. 3 (f) is the Shastry-Sutherland lattice [17] corresponding to a 25 % filling, which is topologically equivalent to the magnetic network in $SrCu_2(BO_3)_2$, as shown later. An intriguing difference between triangle-based and square-based models is that the former have basically a unique interaction, while the latter possess two inequivalent interactions. Strictly speaking, the diagonal and horizontal bonds in Figs. 2 (a)-(b) are not equivalent.

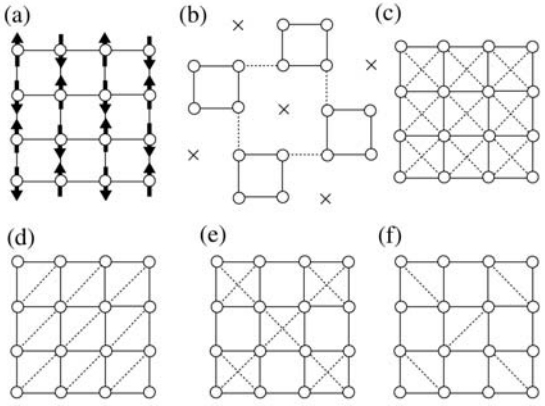

Fig. 3. (**a**) Antiferromagnetic ordering on the square lattice. (**b**)-(**f**) Geometrically frustrated models with square units: (**b**) 1/5-depleted square lattice, (**c**) 2D J_1-J_2, (d) distorted triangular, (**e**) checkerboard, and (**f**) Shastry-Sutherland models.

3. CRYSTAL STRUCTURE

$SrCu_2(BO_3)_2$ was prepared originally by R.W. Smith and D. A. Keszler in 1991 using conventional solid state reaction with stoichiometric amount of $Sr(NO_3)_2$, $Cu(NO_3)_2 2.5H_2O$ and B_2O_3, and its structural determination was made at room temperature [14]. The crystal structure is of tetragonal symmetry with a space group of $I\bar{4}2m$ (No. 121) and a = 8.995 Å, c = 6.649 Å. Figure 4 shows the structure of $SrCu_2(BO_3)_2$ projected along the c-axis. Layers of $(BO_3)^{3-}$ groups and Cu^{2+} ions stack along the c-axis rotated by 90 °, with nonmagnetic Sr^{2+} ions separating these layers. All cupper ions with a localized spin S = 1/2 are crystallographycally equivalent, sitting on the 8*i* site. For a given $CuBO_3$ layer, the copper ions along with the oxygen ions of the BO_3 group form dimers of planer, edge-sharing CuO_4 groups. The spin dimers are connected orthogonally by triangular BO_3 groups. The copper dimer is coordinated from both sides by two symmetry equivalent oxygens (O2) belonging to the same BO_3 group in the form of a "chelate", the bridging oxygens between the two coppers are formed by the remaining third oxygen atom (O1) of the BO_3 group. The coordination of copper by the rigid BO_3 groups with three-fold symmetry leads to a pronounced angular distortion of the CuO_4 square, which is rather unusual for a Cu^{2+}-containing oxo-cuprate.

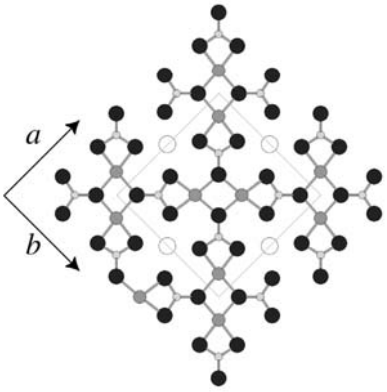

Fig. 4. The [001] view of the crystal structure of $SrCu_2(BO_3)_2$, where open circles denote Sr^{2+}, closed circles O^{2-}, large gray circles Cu^{2+}, and small gray circles B^{3+} ions. Solid lines represent a chemical unit cell.

It is possible to deduce magnetic interactions to some extent only from structural features. The distances between nearest and next-nearest Cu neighbors in the same layer are 2.905 Å and 5.132 Å and the interlayer distance (i.e., $c/2$) is 3.325 Å. It appears that the intradimer interaction J and the interdimer interaction between layers J'' are dominant over the interdimer interaction in the layer J'. However, the plausible paths for the superexchange are through O^{2-} for J and molecular orbital of $(BO_3)^{3-}$ for J', while such a pathway is not observable for J'' as the Sr^{2+} ion intercalated between layers has a closed shell. Therefore, the magnitude of J'' should be much smaller than those of J and J'. If this is the case, the

magnetism of $SrCu_2(BO_3)_2$ would be in principle interpreted by a 2D Heisenberg model with $S = 1/2$, represented as

$$H = J\sum_{nn} s_i \cdot s_j + J'\sum_{nnn} s_i \cdot s_j \ . \qquad (1)$$

It should be pointed out that, if J is positive (antiferromagnetic), the spins connected through J' always feel a spin frustration irrespective to the sign of J'.

As mentioned above, the lattice shown in Fig. 3 (f) and Fig. 5 (c) is called the Shastry-Sutherland model, which has been known to have an exact dimer ground state when J'/J is small [16, 17]. But the physical condition for finding the ground state involves apparently an "impossible-to-satisfy" inequality, where interactions for "longer bonds" must exceed those in magnitude that are on "shorter bonds". Nature solves the problem with amazing dexterity and cleverness by producing a topologically equivalent structure (Fig. 5 (a)), and yet manages to squeeze the "long bonds" below the length of the "short bonds". Furthermore, the interaction parameters, as inferred from magnetic susceptibility measurement, locate this system in the proximity to one of the most interesting points of the phase diagram, close to a quantum critical point.

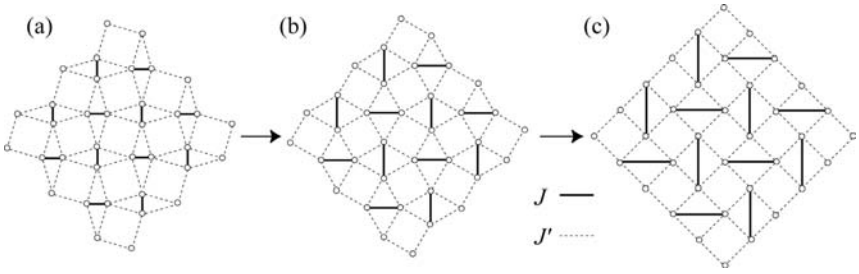

Fig. 5. Transformation from the (**a**) the $S = 1/2$ network in $SrCu_2(BO_3)_2$, through (**b**) the Nd^{3+}-network in Nd_2BaZnO_5 to (**c**) the Shastry-Sutherland lattice. The bonds J and J' symbolize, respectively, intra- and interdimer interactions.

4. SINGLE CRYSTAL GROWTH

For the synthesis of powder samples of $SrCu_2(BO_3)_2$, the preparation procedure given in [14] has been followed, but using CuO, $SrCO_3$, B_2O_3 instead as starting reagents. This avoids the emission of NO_x during heating. Additionally, 5 % molar excess of B_2O_3 was added in order to compensate its loss due to the high volatility. These components were mixed intimately, pressed into pellets, and then heated at 600 °C overnight. After regrinding, the sample was heated at 900 °C for 48 hours with intermediate grindings. Powder x-ray diffraction experiments performed using an MPMS18 Mac Science diffractometer with Cu$K\alpha$ radiation confirmed the single phase product without any traces of impurities.

Although physical properties can be derived to a certain extent from experiments using powder samples, the use of single crystals is in general crucial to advance our understanding. Since $SrCu_2(BO_3)_2$ melts incongruently in air at a peritectic melting point of 970 °C, it is essential to use an appropriate solvent for its single crystal growth. A flux method using the solvent $LiBO_2$ and a Pt crucible was reported [14]. However, bunches of tiny crystals are obtained typically with a dimension of 0.20mm×0.08mm×0.03mm, which is sufficient for structural determination but not for most of the magnetic measurements. Modifying the flux, the composition and size of the crucible, and cooling rate did not improve the crystallite size or even worse, resulted in a decomposition of $SrCu_2(BO_3)_2$.

A traveling solvent floating zone (TSFZ) method was finally employed using the same solvent $LiBO_2$. Consequently, a dramatic improvement was achieved [23]. As a precursor, the light blue powder of $SrCu_2(BO_3)_2$ was isostatically water-pressed under 400 kg/cm^2 in the form of rods (6-10 mm in diameter and ~100 mm in length), yielding densities of about 70 %. The rods were subsequently sintered at 850 °C for 1 day under oxygen flow. We also prepared a solvent disk (2-3 mm in thickness) composed of a mixture of $LiBO_2$ and $SrCu_2(BO_3)_2$, in the weight ratio of 1:3. The crystal growth was carried out using FZ-T10000N 10 KW high-pressure type (Crystal System. Inc.) with four halogen lamps as heat sources. The solvent disk was placed between the upper and the lower rods. By gradually increasing the lamp power, the solvent disk was molten. Growth rates were 0.3-0.5 mm/h and both rods were rotated at about 20-30 rpm in opposite directions to secure the homogeneity of the liquid as well as a homogeneous temperature distribution within the liquid zone.

The crystals obtained were dark blue and cleave easily along the *ab* plane as confirmed by Laue x-ray diffraction. Figure 6 (a) shows a photo of a typical crystal rod (6 mm in diameter) containing a single domain of 65 mm length. It is stressed that slow growth rates are important to grow bulk crystals with excellent quality. To date, grown single crystals have been provided to many physicists around the world for various experiments such as electron spin resonance (ESR), Raman scattering, and neutron scattering experiments.

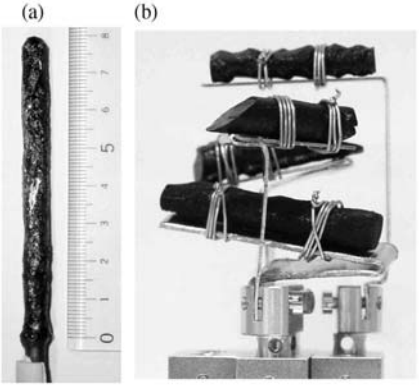

Fig. 6. Single crystals of $SrCu_2(BO_3)_2$ grown by TSFZ method. (**a**) After a growth of about 15 mm, the crystal rod becomes a single domain. (**b**) Aligned crystals of ^{11}B-enriched $SrCu_2(^{11}BO_3)_2$, used for inelastic neutron scattering experiments.

5. SPIN-GAP FORMATION

In Fig. 7, the temperature T dependence of the magnetic susceptibility χ_{raw} for the powder sample of $SrCu_2(BO_3)_2$ is shown [15]. A prominent characteristic is that, with reducing temperature, χ_{raw} reaches a maximum at around 20 K and rapidly drops toward zero suggesting the nonmagnetic ground state and the existence of an energy gap in the spin excitation spectrum. At high temperatures above 160 K, χ_{raw} was fitted well to the Curie-Weiss law for $S = 1/2$, giving Weiss temperature $\theta = -92.5$ K and the effective g factor $g = 2.14$, accompanied with a constant susceptibility $\chi_0 = -2.01\times10^{-5}$ (emu/mol Cu). As seen in the inset of Fig. 7, a small upturn corresponding to 0.72 % of nearly free $S = 1/2$ impurities was observable below 4 K. This is assigned to magnetic impurities and/or defects of Cu^{2+} spins in $SrCu_2(BO_3)_2$. The spin part of the susceptibility χ_{spin} was finally evaluated after subtracting the Curie-tail and χ_0. By fitting χ_{spin} in a low-T region to the activated type of temperature dependency, i.e., $\chi_{spin} \propto \exp(-\Delta/T)$, the gap was roughly determined to be $\Delta = 19$ K.

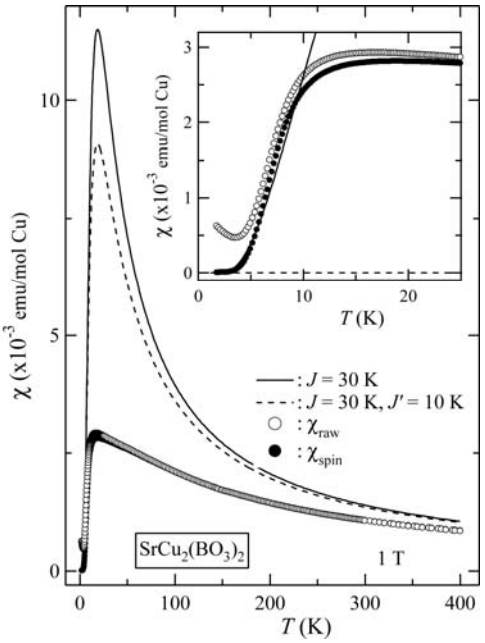

Fig. 7. Temperature dependence of the magnetic susceptibility of $SrCu_2(BO_3)_2$ powder obtained at 1 T. The open and closed circles represent the measured susceptibility χ_{raw}, and spin susceptibility χ_{spin}, respectively. The solid (broken) line shows the theoretical curves based on an isolated (modified) dimer model. The enlarged plot is shown in the inset, where the solid curve indicates a fit given in the text. (reproduced from [15])

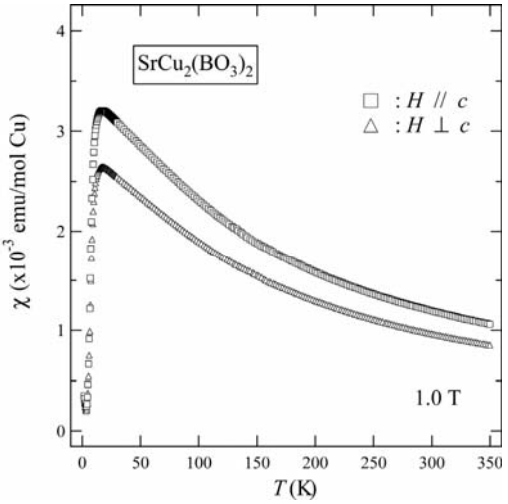

Fig. 8. Temperature dependence of the magnetic susceptibilities of the single crystal of $SrCu_2(BO_3)_2$. (reproduced from [24])

Figure 8 demonstrates the T dependence of the magnetic susceptibilities for a single crystal, $\chi_{//}$ and $\chi_{\perp}$, where the magnetic field H of 1.0 T was applied parallel and perpendicular to the c-axis, respectively [24]. Both curves are almost identical except for a weak anisotropy. The difference is attributable merely to the anisotropic g-factor. The two susceptibility data can be completely normalized by $g_{//} = 2.28$ and $g_{\perp} = 2.07$ that are obtained from ESR experiments [25]. The small anisotropy supports the point that the magnetism of this compound is described by the Heisenberg model. Similar values, $\theta = -102.5$ K and $\chi_0 = -2.603\times10^{-5}$ (emu/mol Cu) were obtained from a fit to the high-temperature Curie-Weiss behavior. A tiny Curie-tail corresponding to 0.14 % of $S = 1/2$ impurities was observed below 4 K, which ensures the high quality of the crystal. This made it possible to estimate the Δ value more reliably; Irrespective to the direction of applied magnetic field, the fit to $\chi_{spin} \propto \exp(-\Delta/T)$ gave a slightly higher value $\Delta = 34\pm1$ K [24].

A microscopic investigation by means of Cu nuclear quadrupole resonance (NQR) performed on the powder sample has confirmed the existence of the spin-singlet ground state with the finite energy gap in $SrCu_2(BO_3)_2$ [15]. Typical spin-echo spectra of $^{63}Cu/^{65}Cu$ NQR lines measured at constant τ (τ being the time separation between the exciting and refocusing rf pulses) of 80 μs are shown in the inset of Fig. 9. On cooling, the NQR line signal splits into two components, which is ascribed to the nuclear spin-spin coupling in the dimer. The $1/T_1$ vs. T curve (Fig. 9) was well fitted to $1/T_1 \propto \exp(-\Delta/T)$ with $\Delta = 30$ K, which is similar to that obtained from the susceptibility analysis on the single crystal [24].

Following the susceptibility and Cu-NQR experiments, various kinds of experiments mainly using single crystals were performed. All experiments performed so far are in accordance with a spin-singlet ground state with $\Delta = 34$ K. Table 1 summarizes estimated values of Δ.

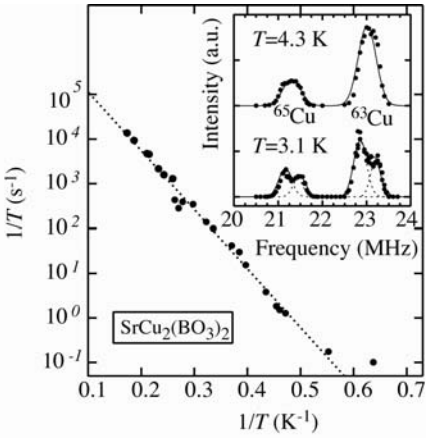

Fig. 9. Temperature dependence of $1/T_1$ measured by saturation and inversion recovery methods. The dotted line shows the activated T dependence with Δ = 30 K. In the inset is shown the Cu NQR spectra measured at 4.3 K and 3.1 K. (reproduced from [15])

Table 1. Spin gap Δ estimated from various experiments on $SrCu_2(BO_3)_2$. P and S denote, respectively, powder and single crystal used for each experiment.

experiment	sample	Δ (K)
magnetic susceptibility [15, 28]	P	19
magnetic susceptibility [24]	S	34
Cu-NQR ($1/T_1$) [15]	P	30
magnetization curve [15, 28]	P	31.3
magnetization curve [24, 29, 30]	S	34.1
specific heat [26, 27]	S	35.0
B-NMR ($1/T_1$) [31, 32]	S	36
Cu-NMR (Knight shift) [31, 32]	S	35
neutron scattering [33]	S	35
ESR [25, 34]	S	34.7
Raman scattering [35, 36]	S	35.2
far infrared spectroscopy [37]	S	34.8
sound velocity [38, 39]	S	30

Since space is limited, let me present the result of specific heat, which also includes the magnetic field dependence. The experiment was performed on a single crystal by a heat-relaxation method under magnetic fields for H = 0-12 T [26, 27]. The total specific heat divided by T, C/T, measured in the absence of a magnetic field is plotted as a function of T by closed circles in the main panel of Fig. 10. The C/T curve reaches a rounded maximum at

7.5 K. This behavior is typical of spin-singlet system with a finite spin gap to the lowest excited state. Similar Schottky anomalies appear when magnetic fields are applied, indicating that the system still has a spin-gapped ground state. However, the peak in C/T shifts to lower temperature with rising H, which implies the reduction in the actual size of the spin gap $\Delta(H)$. This is due to Zeeman splitting of the low-lying excited triplet (S = 1) states. Namely, the three-fold degeneracy of the triplet state at H = 0 is lifted by the application of a magnetic field. In the inset of Fig. 10, CT^2 is plotted against $1/T$ in a logarithmic scale. In a low-T region, the experimental data points obey

$$C(H) \propto T^{-2} \exp\left(-\Delta(H)/T\right) . \tag{2}$$

Applying equation (2) to each data set leads to Δ(0 T) = 35.9 K, Δ(6 T)= 27.5 K, Δ(9 T) = 22.5 K and Δ(12 T) = 16.8 K. To get a better estimate, these values were subsequently used for a least-square fit to the Zeeman equation $\Delta(H) = \Delta(0) - g\mu_B H$, which gave a more reasonable value Δ(0) = 35.0 K.

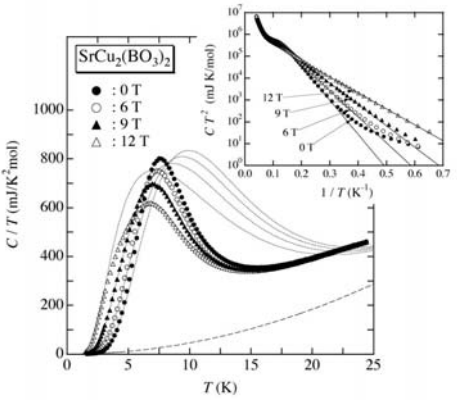

Fig. 10. C/T versus T measured at H = 0 T, 6 T, 9 T and 12 T. The magnetic field is applied perpendicular to the *ab* plane. Dotted curves are the calculations based on the isolated dimer model assuming Δ(0) = 34.4 K. The dashed curve represents the phonon term, βT^3 (β = 0.460 mJ/K^2). Inset: Logarithmic plot of CT^2 as a function of $1/T$. Solid lines denote a fit to equation (2). (reproduced from [27])

6. EXACT DIMER SINGLET GROUND STATE

Now that we are sure that $SrCu_2(BO_3)_2$ has the energy gap of Δ = 34 K between the singlet ground and exited triplet states, the next step is to probe the origin and evolution of spin gap formation in the ground state. From first glance on the arrangement of magnetic Cu^{2+} ions, one may intuitively expect that the magnetic properties of this compound would be just those

of dimers. An $S = 1/2$ dimer model is simplest among known spin-gap systems and is widely applicable to many existing materials, CsV_2O_5 [40] and various Cu complexes [41]. It is reasonable to suppose that the intradimer exchange interaction J is antiferromagnetic ($J > 0$), because the dimer bridging angle ($\angle$Cu-O-Cu) of 102.42 ° exceeds the critical angle of 97.6 °, below which one has $J < 0$ according to the Goodenough-Kanamori rules [42]. So, the χ_{spin} data was first analyzed using an $S = 1/2$ isolated antiferromagnetic dimer model [43], where the spin susceptibility is expressed as

$$\chi = \frac{Ng^2\mu_B{}^2}{3k_BT}\left[1+\frac{1}{3}\exp\left(\Delta/T\right)\right]^{-1}, \tag{3}$$

where N, μ_B, and k_B are Avogadro number, the Bohr magneton, and Bolzmann constant. However, the calculated susceptibility (solid line in Fig. 7) deviates markedly from the experimental result. Even a modified dimer theory which incorporates the interdimer interaction J' as a mean-field [44] hardly improves the fitting (broken line). This fact strongly suggests that J' is of similar strength as J and thus must be considered more seriously. In other words, the system is the prototype of a strongly frustrated quantum spin systems. The effect of spin frustration is indeed seen in the fairly small spin gap in contrast to the large Weiss temperature.

The specific heat data also shows a large discrepancy from the isolated dimer model [26, 27]. In the absence of magnetic field, for example, the specific heat is given by

$$C(0) = \frac{3R\left(\Delta(0)/T\right)^2\exp\left(\Delta(0)/T\right)}{\left[1+3\exp\left(\Delta(0)/T\right)\right]^2}, \tag{4}$$

where R is 8.30 (J/K/mol). Note that, in the low-T limit, the magnetic specific heat for the isolated dimer model can be reduced to equation (2). The total specific heat is given by the sum of the magnetic and phonon term, $C(H)$ and βT^3. Dotted curves in Fig. 10 represent the results of the global least-square fits in the temperature range well below the spin-gap size. We obtained a reasonable value of $\Delta(0) = 34.4$ K along with $\beta = 0.460$ (mJ/K mol) and $g = 2.03$. It seems that the isolated dimer model nicely reproduces the experimental data, providing a consistent value of $\Delta(0)$. In the higher-T regime, however, the deviation between experiment and theory are appreciable, which indicates that spin system of $SrCu_2(BO_3)_2$ is effectively correlated at higher temperatures. In fact, the experimental magnetic entropy at 25 K is still 62 % of the total magnetic entropy. It is noteworthy that, in the isolated dimer model, the magnitude of J is identical with $\Delta(0)$.

Miyahara and Ueda that were not aware of [17] considered the Heisenberg Hamiltonian (1) and noticed its most remarkable property that the direct product of the singlet states on J bonds,

$$|\psi\rangle = \prod_a |s\rangle_a = \prod_a \frac{1}{\sqrt{2}}\left(|\uparrow\downarrow\rangle_a - |\downarrow\uparrow\rangle_a\right), \tag{5}$$

is always an exact ground state as long as $J'/J < 0.70$ [16], where *a* denotes the *J* bonds. They soon realized that the model for $SrCu_2(BO_3)_2$ is topologically equivalent to the Shastry-Sutherland model found almost twenty years ago. The exact wave function originates from the orthogonality of neighboring dimers. In order to estimate the exchange constants, the *T* dependence of the magnetic susceptibility was calculated by using the transfer matrix method for finite clusters. The best fit was obtained for $J'/J = 0.635$ and $J = 85$ K, where *J* was determined so that the spin gap obtained from the exact diagonalization becomes 35 K [45]. It was also shown that $SrCu_2(BO_3)_2$ is in the dimer singlet phase and is located in the proximity to the quantum phase boundaries. This fact has some important implications, which will be discussed later.

The exact dimer ground state (5) is also found in the well known Majumdar-Ghosh model [46] (and its analogues [47-49]) but the exactness holds only at the fully frustrated point, i.e., $J_2/J_1 = 1/2$ [46] and thus it would be impossible to find an experimental correspondence. From theoretical point of view, tremendous effort has been made to discover exactly soluble systems by mathematicians and theoretical physicists. Probably the oldest and most famous in the field of magnetism is Onsager's exact solution on the Ising square lattice [50]. However, exactly soluble models in quantum spin systems are found mainly for 1D systems including the supersymmetric *t-J* type chain model with long-range exchange and transfer [51]. In this respect, the Shastry-Sutherland model makes a marked contrast to other solvable models as it is based on a "two-dimensional" and an "$S = 1/2$" system and that nature indeed provides an ingenious realization of such a theoretical model.

7. THREE-DIMENSIONAL SHASTRY-SUTHERLAND LATTICE

In sections 5 and 6, the magnetic properties of $SrCu_2(BO_3)_2$ were described in terms of in-plane couplings *J* and *J'*, neglecting interlayer coupling *J''*. Hamiltonian (1) is certainly an appropriate starting point for $SrCu_2(BO_3)_2$. In the courser of study, however, it was suggested that *J''* is not completely negligible in order to fully explain experimental results. The interlayer dimer network is depicted in Fig. 11 (b), where the dimers along the *c*-axis are also connected orthogonally, but in a different fashion. Because of this geometry, the dimer chain model, considered by M. Gelfand [52], also has an exact dimer ground state for small J''/J. The 3D structure of $SrCu_2(BO_3)_2$ is constructed by a combination of the Shastry-Sutherland and the Gelfand models, as shown in Fig. 11 (c). It is clear that the dimer singlet state (5) is still an exact ground state [53]. Strictly speaking, the room-temperature structure shows an additional buckling of the $CuBO_3$ plane, and the dimers in each plane in $SrCu_2(BO_3)_2$ are not on the same plane [14]: the plane of horizontal dimers in Fig. 11 (a) is slightly shifted from the plane of vertical dimers. Because of this shift, the distance between Cu^{2+} ions of adjacent dimers along the *c*-axis is 3.593 Å or 4.233 Å. Nevertheless, even if the alternation along the *c*-axis is included as J''_1 and J''_2, the exactness of equation (5) still holds since the condition of the orthogonality of the dimers remains unchanged.

Powder and single crystal x-ray diffraction experiments show a displacive, second order-like structural phase transition at $T_s = 395$ K from the space group $I\bar{4}2m$ below T_s to $I4/mcm$ above T_s [54]. Plotted in Fig. 12 is the intensity of reflection (013) of type 0*kl* (*k* and *l* being odd), indicating continuous evolution of the structural distortion over a broad *T* range below T_s and extinction at and above T_s. This structural transition is characterized by a temperature

dependent tilt of the two neighboring CuO_4-squares sharing a common edge below T_s. Due to the mirror plane perpendicular to the *c*-axis in space group *I*4/*mcm*, both the BO_3-group and the pair of edge sharing CuO_4-groups are required by symmetry to be flat and coplanar (see Fig. 13). As the corrugation of the $CuBO_3$ layer reduces upon heating the shortest interlayer Cu-Cu distances approach each other and become degenerate in the high-temperature phase. Differential scanning calorimetry (DSC) experiments support a second order-like transition at 395 K, with only small peaks associated with it (Fig. 12). With decreasing temperature through the structural transition, a strong anharmonic soft mode at 62 cm^{-1} was observed [55]. The symmetry group analysis and doping dependence identify this mode as an in-phase motion of almost all ions along the interlayer direction, indicating that the main aspect of the structural phase transition is buckling distortions due to this strong anharmonicity.

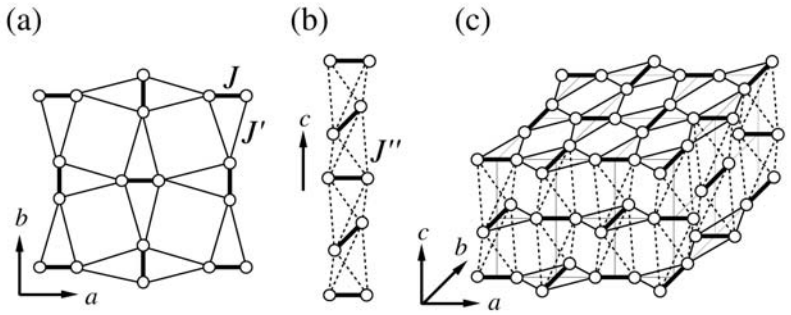

Fig. 11. (**a**) The dimer arrangement in the layer corresponding to the original Shastry-Sutherland model. (**b**) The dimer arrangement along the *c*-axis, which is topologically equivalent to the Gelfand model [52]. (**c**) The 3D magnetic network in $SrCu_2(BO_3)_2$.

Interestingly, SQUID magnetometry shows, besides the low-temperature features already discussed, a small but significant drop of the magnetic susceptibility just below T_s [54]. The step is the response of the magnetic system to a structural phase transition and reflects the modification of the interlayer exchange interaction for temperatures below T_s. The magnitude of the step normalized to the maximum of the susceptibility is $\Delta\chi(T)/\chi_{max} = 4\times10^{-3}$. Interlayer coupling is now discussed as a relevant parameter of this unusual quantum spin system and estimated J''/J ranges from 0.09 to 0.21 [45, 56]. To a first approximation, the interlayer coupling simply reduces the magnetic susceptibility. The structural change associated with the jump in the magnetic susceptibility allows testing this effect.

Isovalent substitution for the Sr site corresponds to the application of chemical pressure, and may be a useful tool to tune the exchange couplings systematically. The lattice parameters of $Sr_{1-x}A_xCu_2(BO_3)_2$ sample (*A* = Ca, Ba) prepared up to $x = 0.3$ vary according to the ionic-size difference (Fig. 14) [57]. Reflecting the layered structure, the interlayer distance exhibits more pronounced change, suggesting the effective tuning of J''. However, the magnetic behavior does not show a systematic change, possibly due to a difference in sample quality and randomness arising from the substitution. On the contrary, the chemical pressure dramatically affects the T_s value [58]. In contrast to the low-*T* structure, the $CuBO_3$ plane in

the high-T structure is a mirror plane. Accordingly there is an inversion centre at the midpoint of the J-bond so that the intradimer Dzyaloshinsky-Moriya (DM) interaction vanishes. If further Ca-substitution is possible and the high-T phase is stabilized down to 0 K, the effect of the intradimer DM interaction on the physical properties of Shastry-Sutherland model could be investigated in comparison with non-substituted $SrCu_2(BO_3)_2$. This would be interesting especially because recently this interaction together with the staggered g-tensor for $SrCu_2(BO_3)_2$ is suggested to induce a field-induced staggered magnetization at low magnetic field and the persistence of the spin-gapped phase near the critical field [59].

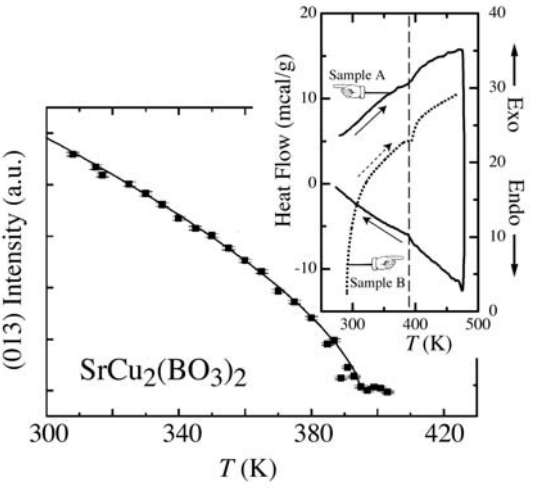

Fig. 12. Temperature dependence of the (013) reflection for $SrCu_2(BO_3)_2$. The continuous line is a fit to the data points using $I(T) \propto (T - T)^{2\beta}$ with $\beta = 0.34(1)$. Inset: DSC measurements upon heating and cooling for sample A and upon heating for sample B. (reproduced from [54])

The crystal structure and lattice dynamics of $SrCu_2(BO_3)_2$ have recently been investigated by angle-dispersive synchrotron x-ray powder diffraction and Raman spectroscopy under extremely high pressures at room temperature [60]. The experiment shows that $SrCu_2(BO_3)_2$ undergoes a subtle tetragonal-to-monoclinic structural distortion near 5 GPa and a first-order structural transition at 15 GPa. The effect of these transitions on the magnetic properties at low temperatures is worth further investigations.

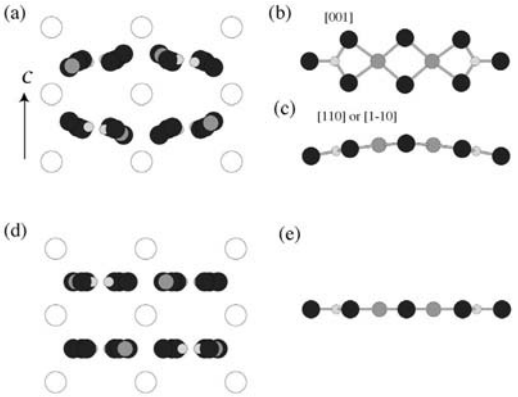

Fig. 13. Comparison of the crystal structures of $SrCu_2(BO_3)_2$ between (**a-c**) low-T and (**d**, **e**) high-T phases. Open circles denote Sr^{2+}, closed circles O^{2-}, large gray circles Cu^{2+}, and small gray circles B^{3+} ions. Projection of the layers along [100] (**a**, **d**). Projection of the $2CuBO_3$ plaquette along [001] (b) and along [110] (**c**, **e**).

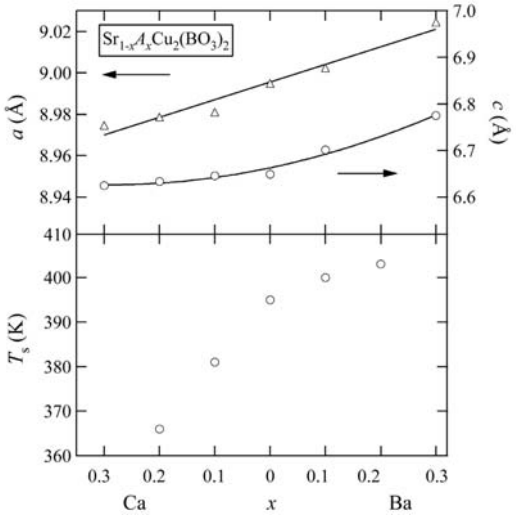

Fig. 14. Upper: Compositional dependence of the lattice parameters of $Sr_{1-x}A_xCu_2(BO_3)_2$ (A = Ca, Ba) for $0 \le x \le 0.3$. Solid lines are guides to the eye, not fits. Lower: Structural transition temperature T_s plotted against x. (reproduced from [57, 58])

8. QUANTUM PHASE TRANSITION AT ZERO FIELD

There have been intensive theoretical studies on the phase diagram of the (generalized) Shastry-Sutherland models. Regarding the original 2D Shastry-Sutherland model, the exact dimer singlet ground state is realized for small J'/J. It has a spin gap and does not have long-range magnetic ordering. On the other hand, given $J = 0$ and $J' > 0$, the model is reduced to the square lattice Heisenberg model, where there is a consensus that the ground state consists of gapless antiferromagnetic long-range ordering as shown in Fig. 3 (a). Therefore, a quantum phase transition between these two states is expected to occur as a function of J'/J. Miyahara and Ueda considered this problem using exact diagonalization up to 20 sites and claimed that the phase transition occurs at the critical value $(J'/J)_c = 0.70$ [16]. After that, Zheng, Hamer and Oitmaa applied a variety of series expansion methods to the model and obtained a similar value $(J'/J)_c = 0.691$ [61]. Initially, the in-plane exchange constants $J = 100$ K and $J' = 68$ K ($J'/J = 0.68$) were estimated from the experimental susceptibility of powder [16]. This means that $SrCu_2(BO_3)_2$ is located in proximity to the most important point of the phase diagram, in the vicinity of the phase boundary dividing long range from short range order. Quantum criticality is also proposed to be of relevance for the physics of high temperature superconductors dividing pseudo gap from superconducting and long range antiferromagnetic phases [62].

An alternative scenario consists of an intermediate phase somewhere in between these two phases [63, 64]. A considerable stability of this helical ordered state is proposed by Albrecht and Mila based on Schwinger boson mean-field theory [63]. This theory, however, might underestimate the effect of quantum fluctuations in spin-1/2 systems, which favor a commensurate order or spin-liquid phase rather than a helical phase with incommensurate propagation vector. Accordingly, a RVB plaquette singlet phase, proposed by Koga and Kawakami who divided the second term of Hamiltonian (1) into two parts [64], would be a more plausible candidate for the intermediate phase, if it exists at all. This additional singlet phase is stable in a range between $(J'/J)_{c1} = 0.677$ and $(J'/J)_{c2} = 0.86$. Here one may suspect that the RVB plaquette singlet state might be realized as the ground state of $SrCu_2(BO_3)_2$. But an oscillating behavior in the spin-echo intensity of Cu-NMR provides firm evidence for the "dimer" singlet ground state [31, 32]. It is interesting to point out that the Koga-Kawakami model is topologically equivalent to the 1/5-depleted square lattice with diagonal bonds being added, which was used for the study on CaV_4O_9 [65]. It turned out later that in-plane exchange constants alone cannot satisfactorily reproduce the experimental results. In particular, the magnetic susceptibility at high temperatures well above the spin gap deviates from the experiment, which motivated to take an interlayer coupling into account [45]. Theoretically, Koga proposed the phase diagram for the generalized 3D Shastry-Sutherland model using the series expansion methods, as seen in Fig. 15 [66]. Using the magnetic susceptibility and specific heat data on single crystals, Miyahara and Ueda obtained $J = 85$ K, $J' = 54$ K and $J'' = 8$ K ($J'/J = 0.635$, $J''/J = 0.09$) [45]. A different set of exchange parameters $J = 71$ K, $J' = 43$ K and $J'' = 15$ K ($J'/J = 0.603$, $J''/J = 0.21$) was proposed by Knetter *et al*. [56]. In each case, as you can see from Fig. 15, $SrCu_2(BO_3)_2$ is still near the border either to the antiferromagnetic state or the RVB plaquette singlet phase.

Experimentally, several efforts to induce such phase transitions at finite temperature have been made. First, chemical pressure effect using the solid solution $Sr_{1-x}A_xCu_2(BO_3)_2$ (A = Ca, Ba) does not show a systematic change with x and A due to marked difference of sample

quality, which makes it difficult to estimate the exchange constants in this solid solution [57]. Second, physical pressure P is regarded as a cleaner tool for tuning the physical parameters. The first high-pressure experiment was conducted in 1998, when magnetic susceptibility was measured using a pressure cell made by CuBe alloys [67]. However, because of Co impurities in the commercially available alloys, the pressure cell itself has a finite magnetization, which is comparable with the magnetizations of the sample and is temperature- and field dependent. Thus it was difficult to extract the intrinsic part of magnetization and evaluate the pressure dependence. Recent technological innovation, i.e., a new high-pressure clamp cell consisting of CuTi alloys with 3 wt% Ti [68], has resolved these difficulties. The advantage of this cell over the previous one is that its magnetization is extremely small, of the order of 10^{-7} emu, and is almost independent of both temperature and pressure. These properties allow one to precisely measure weak magnetization of low-dimensional quantum spin systems. Figure 16 demonstrates the result of the temperature dependence of the magnetic susceptibility for $3 < T < 30$ K at P = 0, 2.0, 4.0, 6.0 and 7.0 kbar [69]. At high temperatures, the obtained susceptibilities are almost independent of P, while prominent P-dependence appears at low temperatures. The temperature at maximum susceptibility T_{max} systematically decreases with the application of P, suggesting a reduction of Δ, although the dimer singlet state persists at least till 7.0 kbar. Hence the system is approaching the quantum phase boundaries.

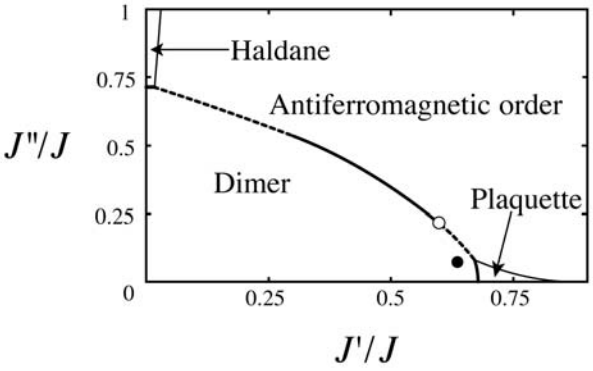

Fig. 15. Phase diagram for the 3D Shastry-Sutherland system. The thick and thin lines represent the phase boundaries, where first- and the second-order quantum phase transitions occur, respectively. The solid and open circles indicate the locations of $SrCu_2(BO_3)_2$ obtained by Miyahara and Ueda [45] and Knetter *et al*. [56]. (reproduced from [66])

The origin of the pressure effect was stated in [69]. Considering the layered crystal structure, it may be natural to assume that pressure would affect only interlayer distance, thus changing J'' but keeping J and J' unchanged. In this case, the compound should go up straight on the phase diagram in Fig. 15. This is not the case since, according to theoretical considerations, the gap is independent of J'' for given values of J and J'. In fact, Fig. 16 resembles the theoretical susceptibilities as a function of J'/J [16]. From these facts, most likely is that pressure varies both J'/J and J''/J in $SrCu_2(BO_3)_2$ and shifts it toward the phase

boundaries. Recent NMR measurements under pressure up to 15 kbar (unpublished results) indicate that the decrease of Δ is nearly proportional to pressure and also some anomalies are observed implying a kind of phase separation. Further pressure study and reconsideration of the phase diagram are necessary toward a better understanding.

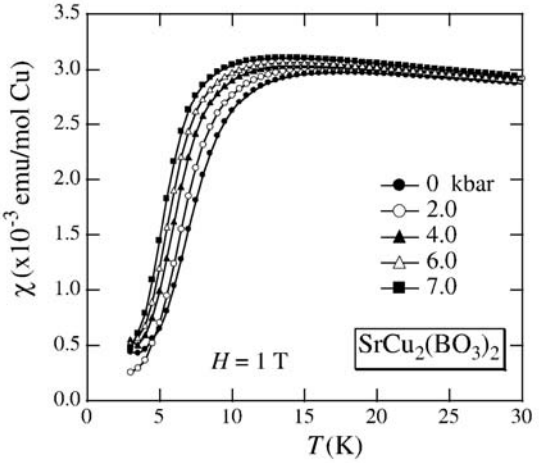

Fig. 16. Temperature dependence of the magnetic susceptibility of $SrCu_2(BO_3)_2$ at high pressures up to 7.0 kbar. (reproduced from [69])

9. EXTREMELY LOCALIZED TRIPLET EXCITATIONS

In order to probe directly the wave vector dependence of the spin excitations of $SrCu_2(BO_3)_2$ with J'/J close to the critical point, neutron scattering experiments on bulk single crystals were performed using the thermal neutron source at JAERI, Tokai, Japan [33]. The ^{11}B-enriched (99.6 %) single crystals of $SrCu_2(BO_3)_2$ were used. Typical energy scans obtained at 1.7 K and 24 K for a scattering vector of Q = (2, 0, 0) are shown in Fig. 17 (a). The 1.7 K spectrum consists of three peaks centered at 3.0, 5.0 and 9.7 meV (transitions I, II, and III, respectively), while that for 24 K no longer has any appreciable peak, indicating that all excitations are of magnetic origin. The transition I at Δ = 3.0 meV (~34 K) is the excitation of one triplet from the singlet ground state, consistent with other results (Table 1). Transitions I-III start to lose intensity with increasing T and disappear at around 13 K (see Fig. 17 (b)). The excitation mode II at around 5 meV can be interpreted as a coupled two-triplet excitation. The continuum like excitations at even higher energy up to 12 meV can be understood as multi-triplet excitations.

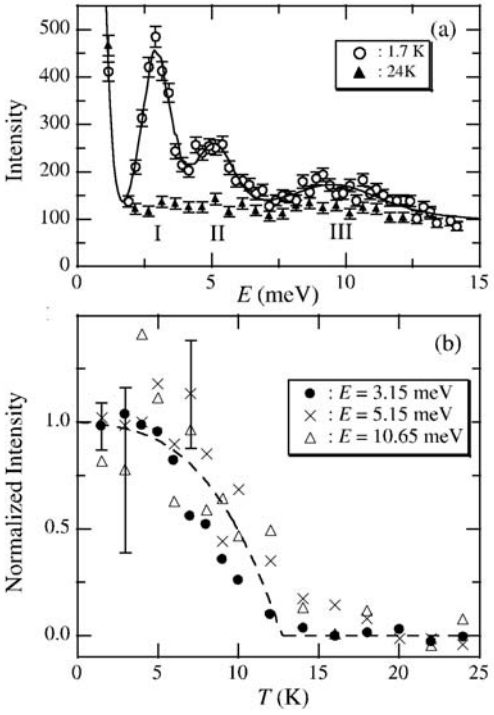

Fig. 17. (**a**) Energy scans at Q = (2, 0, 0) obtained at T = 1.7 K (circles) and 24 K (triangles). (**b**) The temperature variation of the normalized intensities at E = 3.15 meV and Q = (1.5, 1.5, 0) (circles), E = 5.15 meV and Q = (2, 0, 0) (crosses), and E = 10.65 meV and Q = (2, 0, 0) (triangles). The broken line is a guide to the eye. (reproduced from [33])

The Q dependence of a one-triplet excitation is shown in Fig. 18. Most importantly, the excitation energies are almost Q independent. In other words, the magnitude of the dispersion, the difference between the maximum and minimum of the excitation energy, is ΔE = 0.2 meV (~2 K) at most. Well-isolated cluster of exchange-coupled paramagnetic ions, where intercluster interactions are rarely important, exhibit such flat dispersions in the spin excitation spectrum. Examples are $Cs_3Cr_2Br_9$ (ΔE = 1.8 meV) [70] and $BaCuSi_2O_6$ (ΔE = 0.7 meV) [71]. In $SrCu_2(BO_3)_2$, the physical situation is completely different because, as already shown, the dimers within the Shastry-Sutherland (*ab*) plane are not isolated but strongly interacting. In fact, the system is located at the vicinity of the Néel ordered state, yet the dispersion is extremely small compared with the estimated exchange interactions.

It is not spatial isolation but topological features that explain why a one-triplet excitation of a spin system with interactions is so dispersionless. In $SrCu_2(BO_3)_2$, the dimers are certainly strongly coupled but the two interdimer exchange paths (J') form a triangular lattice

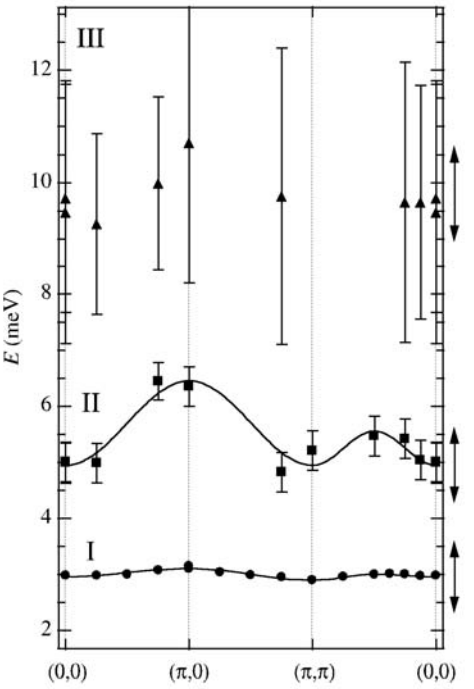

Fig. 18. Q dependence of the excitation energies of the bands I, II, and III obtained at $T = 1.7$ K. The arrows represent the energy resolutions of the instrument (FWHM). The solid curves are guides to the eye. The bars represent the intrinsic linewidth (FWHM) of band II and III. (reproduced from [33])

together with the intradimer exchange (J) due to the orthogonal arrangement of the dimers, thus causing strong frustration. This frustration then leads to a localized nature of the first triplet excitation. It is theoretically shown that, because of this unique geometry, one triplet states can propagate only starting with sixth order in the perturbation of J'/J, imposing the significant constraint on the hopping process [16]. Further series expansion studies indeed revealed a nearly flat dispersion, which increases to some extent as $J'/J \rightarrow (J'/J)_c$ [61]. A similar conclusion is expected for the Gelfand model (Fig. 11 (b)) since adjacent dimers are also orthogonally connected. But due to the difference in the orthogonal geometry, one triplet cannot propagate along the chain at all at any order in J''/J, which should be reflected by a "completely" flat dispersion. The neutron experiment, however, showed that the dispersion for the one-triplet excitation along the c-axis is within our experimental accuracy as wide as that in the ab plane [72].

In contrast, the excitation mode II at around 5 meV apparently has a bandwidth of 1.5 meV, reflecting the dispersive nature of the coupled two-triplets. It was interpreted

theoretically that, owing to the correlations between two triplets, motions of the two-triplet states become possible from second-order perturbation, meaning that coupled two-triplets are still localized but are much easier to move compared with the one-triplet case, giving wider dispersion curve [56, 73]. However, later neutron scattering experiments using cold neutron source with well-defined energy resolution revealed that the excitation II consists of several discrete modes with prominent Q-dependence of spectrum weight (unpublished data). The bandwidth of the two-triplets mode is much narrower than the previous estimation of 1.5 meV. This result has already induced considerable attention of theoretical groups (see, e.g. [74]).

10. MULTI-TRIPLET EXCITATIONS

Pulsed-high-field ESR studied by Nojiri *et al*. revealed a rich and complicated structure in the magnetic excitation spectrum which has been identified as not only one-triplet excitations but also variety of multi-triplet bound states; singlet, triplet, and quintet states (Fig. 19) [75]. The one-triplet mode around 722 GHz shows a splitting into two branches and the energy separation clearly depends on the magnetic field orientation. As discussed in section 12, interdimer DM interaction plays a crucial role in this splitting. Miyashita and Ogasahara calculated the ESR spectrum in the Shastry-Sutherland model including the interdimer DM interaction, which is in excellent agreement with the observed data [76].

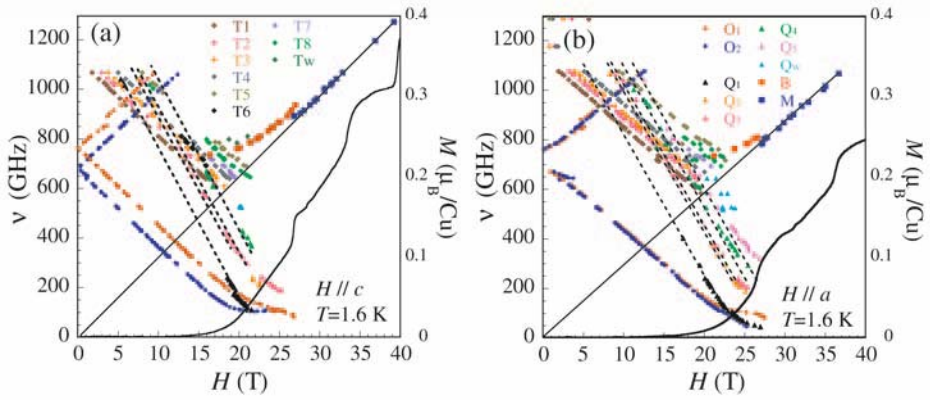

Fig. 19. Frequency-field diagram at 1.6 K (**a**) for H // c and (**b**) for H // a. O, T, Q, B, M are one-triplet, triplet bound states, and quintet bound states, new signal, and a paramagnetic-like signal. Solid lines show the paramagnetic resonance ($\nu = g\mu_B H$, ν: frequency). Dashed lines are guides to the eyes. In addition, the magnetization curves are plotted. Anti-level crossing between one-triplet mode and bound singlet mode is observed at 646 and 860 GHz. (reproduced from [75])

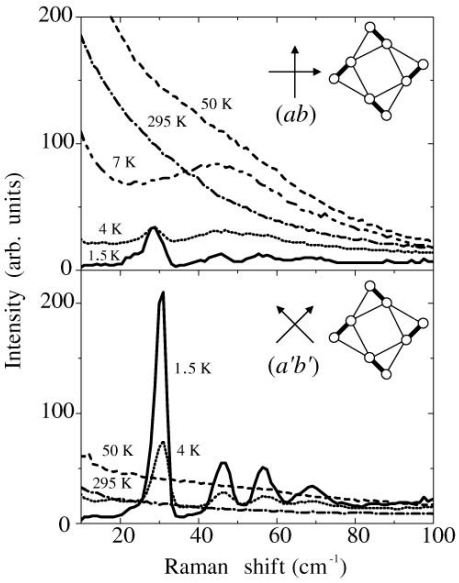

Fig. 20. Raman spectra of $SrCu_2(BO_3)_2$ in two scattering geometries. The arrows represent the polarization of incident and scattered light with respect to the crystallographic axes. (reproduced from [36])

The intensity of the bound states is extremely strong because the one-triplet process is strongly suppressed in the orthogonal dimer system. The triplet bound state splits into six branches at least, possibly due to distant neighbor spins, which is not fully but partially consistent with recent neutron scattering result (unpublished data) and theoretical calculations [74]. In addition, at least five modes are indexed as the quintet bound states with $S = 2$. Among them, four modes exist above the two-triplet continuum threshold starting at $2\Delta = 1444$ GHz. Hence it is natural to assign them to three-triplet bound state and such a state is indeed found in theoretical calculations. The proximity to a quantum critical point is inferred from the observation of a bound singlet state that is slightly below the energy gap of the one-triplet state (see Fig. 19).

Raman light scattering experiments also shows a rich structure in the magnetic excitation spectrum, including several well-defined bound state modes at low temperatures [36]. This technique essentially probes two-particle excitations and is therefore very sensitive to collective and multi particle states. In the energy regime comparable to the one-triplet gap $\Delta = 24$ cm^{-1}, drastic changes and a large shift of spectral weight occur with decreasing temperature. In Fig. 20, Raman spectra of $SrCu_2(BO_3)_2$ are shown to illustrate these effects at different temperatures and in two scattering configurations with light polarizations within the *ab* plane of the crystal. At low temperatures ($T << \Delta$) four well-defined modes with energies 30, 46, 56 and 70 cm^{-1} appear. Furthermore, a strongly broadened maximum exists at around

100 cm^{-1}. These modes do not split nor shift in an applied magnetic field and therefore are assigned to spin singlet states. They are interpreted as collective two-particle (30, 46 cm^{-1}) and novel three-particle (56, 70 cm^{-1}) singlet bound states of strongly localized triplets. The triplet-triplet interactions can lead to large binding energies and scattering intensities, and consequently make the collective modes observable, since quantum fluctuations are absent in the ground state. At intermediate ($T \sim \Delta$) and high ($T >> \Delta$) temperatures, where the quantum (interaction) effects are not important, light scattering is dominated by more coherent two-magnon excitations and finally by diffusive spin excitations that lead to a quasielastic contribution, respectively.

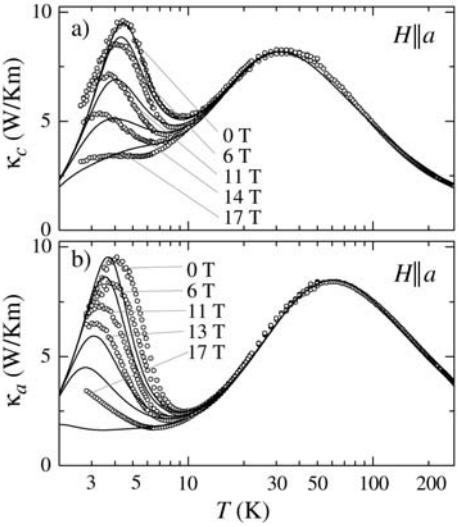

Fig. 21. Thermal conductivity κ_c (**a**) and κ_a (**b**) of $SrCu_2(BO_3)_2$ on a logarithmic temperature scale for various magnetic fields. The lines are theoretical curves. (reproduced from [79])

A remarkable magnon contribution to the heat current in low-dimensional quantum spin gap systems, e.g., $Sr_{14}Cu_{24}O_{41}$ [77] and $CuGeO_3$ [78], has be highlighted. Three groups independently performed thermal conductivity experiment on single crystals of $SrCu_2(BO_3)_2$ [79-81]. In zero magnetic field the thermal conductivity both along and perpendicular to the *ab* plane shows a pronounced double-peak structure as a function of *T*, as shown in Fig. 21 [79]. The low-*T* maximum occurs at ~4.5 K, while the high-*T* maximum lies at ~60 K for κ_a and ~30 K for κ_c. The low-*T* maximum is drastically suppressed with increasing magnetic field. The behavior of κ is reminiscent of that found in other low dimensional spin systems. In $CuGeO_3$, for example, this has been interpreted in terms of a magnetic κ^{mag} and phononic κ^{ph} contribution to the heat current. A similar interpretation is not possible for $SrCu_2(BO_3)_2$, which is due to (1) the nearly flat dispersion of triplet excitation as discussed in the previous section, (2) the lack of a strong anisotropy expected for κ^{mag} in low-dimensional magnetic

systems, and (3) the inconsistency with the magnetic specific heat that exhibits a maximum at higher temperature of 7 K (see Fig. 10). As a cause of the double-peak structure and strong damping of the heat current by a magnetic field, Hoffmann *et al*. proposed a novel resonant scattering of phonons by magnetic excitations that involves bound triplet states [79].

11. QUANTIZED MAGNETIZATION PLATEAUS

As already stressed, the one-, two- and multi-triplets excitations on the background of the sea of singlets have an extremely localized nature due to the unique spin topology. What happens if more triplets are induced in the sea of singlets? The application of a magnetic field at low temperatures provides an opportunity to tune the density of triplets after closing the spin gap. High-field magnetization measurements were conducted using an induction method with a wire-wound pulse magnet at ISSP, University of Tokyo and at KYOKUGEN in Osaka University. Figure 22 shows the obtained magnetization curves of $SrCu_2(BO_3)_2$ for $H \perp c$ and $H \,//\, c$, where within the experimental accuracy, no hysteresis was observed upon increasing or decreasing the magnetic fields.

The most intriguing phenomena in the presence of magnetic fields is the appearance of three quantized magnetization plateaus corresponding to 1/3, 1/4 and 1/8 of the Cu^{2+} saturation moment [15, 29]. For the field direction $H \,//\, c$, the 1/8 plateau is observable for

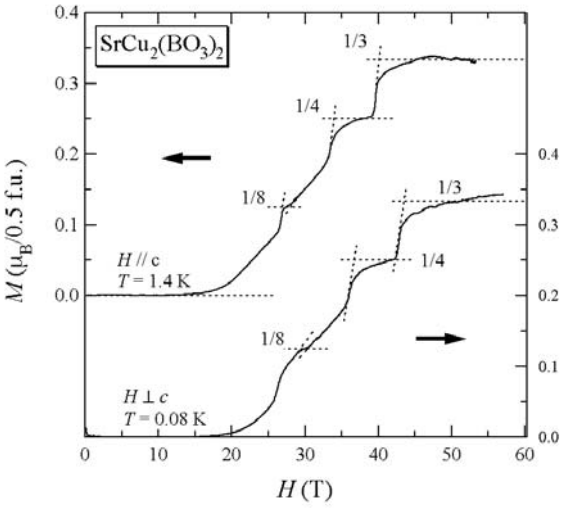

Fig. 22. Magnetizations curves measured at 0.08 K for $H \perp c$ and at 1.4 K for $H \,//\, c$, showing the magnetization plateau at 1/3, 1/4 and 1/8 of the total magnetization. (reproduced from [29])

29.6 T < H < 29.6 T, the 1/4 plateau for 36.7 T < H < 43.6 T, and the 1/3 plateau for H < 39.1 T. For $H \perp c$, these plateaus are also observed at somewhat higher critical fields. We found that the magnetization curves for $H \perp c$ and $H \,//\, c$ (or the critical fields) coincide with respect to each other when normalized by the g-factors as $(g/2)H$, where $g_{//} = 2.28$ and $g_{\perp} = 2.05$ determined by ESR [25] are used. There exist one exception of this scaling as a sizable difference just below 1/8 plateau phase, as seen in Fig. 23 [29]. These results indicate that the plateaus appear in every field direction and not originate from magnetic anisotropy. This is in striking contrast to highly anisotropic (classical) magnetic systems, where magnetization plateaus appear only when magnetic fields are applied along the easy-axis, as exemplified by the 1/3 plateau in the triangular lattice Ising ferrimagnet $Ca_3Co_2O_6$ [82] .

One central issue from theoretical point of view is the quantization condition of the magnetization for the appearance of such a plateau state, which is expressed as

$$n(S-m) = \text{integer}, \tag{6}$$

where n is the period of the ground state in the field, S is the magnitude of the spin and m is the magnetization per site in units of $g\mu_B$ [83]. Note here that n does not necessarily equal the periodicity of the Hamiltonian. Intensively investigated are 1D system, e.g., an S = 1/2 ferromagnetic-ferromagnetic-antiferromagnetic Heisenberg chain [84] and an S = 1 antiferromagnetic Heisenberg chain with bond alternation [85], all of which satisfy the condition (6). Oshikawa has extended the argument in [83] to arbitrary dimensions, proving that the necessary condition (6) is still valid [86]. Experimentally, a 1/2-plateau and 1/4- and 3/4-plateaus have been indeed found in the S = 1 antiferromagnetic Heisenberg chain with bond alternation $[Ni_2(medpt)_3(\mu\text{-ox})(\mu\text{-}N_3)]ClO_4 0.5H_2O$ [87] and in the S = 1/2 double chain NH_4CuCl_3 [88], respectively. However, a plateau accompanied by symmetry breaking, where n differs from the period of the lattice, does not seem to be found in real materials.

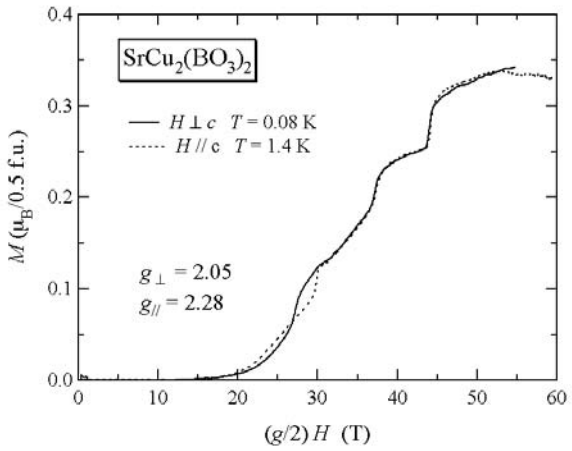

Fig. 23. Normalized parallel and perpendicular magnetizations, where $g_{//} = 2.28$ and $g_{\perp} = 2.05$ are used. (reproduced from [29])

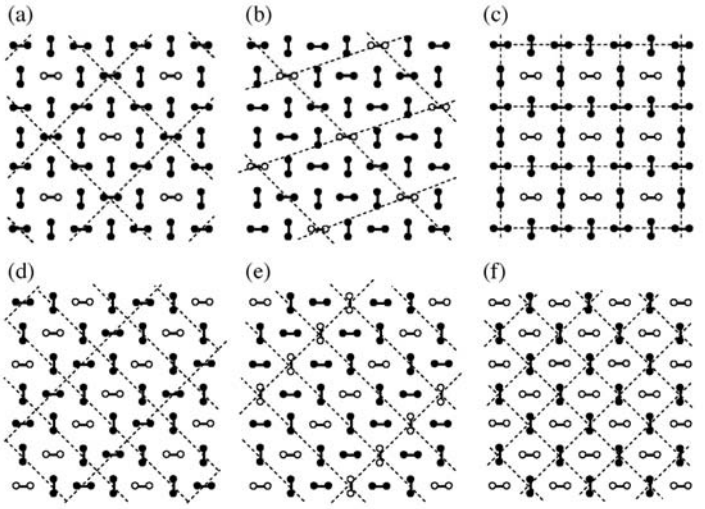

Fig. 24. Proposed spin structures derived from the hard-core boson model for (**a**, **b**) the 1/8 plateau, (**c**, **d**) the 1/4 plateau, (**e**) the 1/3 plateau, and (**f**) the 1/2 plateau.

Miyahara and Ueda claimed that the occurrence of the magnetization plateaus in $SrCu_2(BO_3)_2$ is attributable to the highly frustrated geometry of the orthogonal dimer lattice, leading to the localized nature of excited triplets [16]. In general, there is a competition between the kinetic energy of excited triplets and the repulsive interaction between the triplets. At certain densities of triplets, where the commensurability energy is significant, it is expected that the crystallization of the triplet excitations, leading to a finite energy gap and a magnetization plateau, is particularly favorable. This is analogous to a Wigner crystallization or charge ordering of electron systems. In terms of the localization-to-delocalization transitions, various theories have been provided to explain the nature of magnetization plateaus [89-93].

At the initial stage, when only 1/4 and 1/8 plateaus were observed [15], these plateaus had been considered to appear only when corresponding superstructures are tetragonal, in the light of the tetragonal symmetry of the crystal structure [16]. Namely the commensurability energy associated with the superstructures is more favorable when a magnetic unit cell is a simple square. This leads to plateaus in the magnetization curve at 1/2, 1/4, 1/8, 1/10, 1/16, 1/32… of the saturation moment. Proposed superstructures for 1/2, 1/4 and 1/8 plateaus are shown in Figs. 24 (a), (c) and (f), respectively. Subsequently, Momoi and Totsuka [89] and Miyahara and Ueda [90] independently employed a hard-core boson model for triplet excitations and reached at the same conclusion that the superstructure for the 1/4 plateau is of the stripe type with a rectangular unit cell, as shown in Fig. 24 (d). According to their theory, the triplet-triplet interaction between n-th nearest-neighbor pair of dimers V_n does not exhibit a monotonous decrease with n. For instance, V_2 is considerably smaller than V_3 for any J'/J. Hence the stripe superstructure in Fig. 24 (d), where there is no loss in energy from V_3, is

more stable than the superstructure in Fig. 24 (c). By the same reason, they predicted the existence of a 1/3 plateau characterized by a similar stripe superstructure with a rectangular unit cell, as shown in Fig. 24 (e). Motivated by this prediction, Onizuka *et al*. performed magnetization measurement at higher magnetic fields and succeeded in observing the 1/3 plateau [29]. It is noted that a tetragonal unit cell is not compatible with the 1/3 plateau.

Recent magnetization experiment performed up to 69 T for H // c shows that the 1/3 plateau persists at least up to 69 T, indicating the amazing stability of this phase [67]. The width of the 1/3 plateau is at least 6 times as wide as that of 1/4 plateau. To date, there are various theoretical calculations that try to fit the experimental magnetization. Among them, the Chern-Simons theory assuming J = 74 K and J' = 29.5 K [93] appears to reproduce our data most nicely, in particular with respect to the critical fields and the rounding feature of the lower-field edge of the 1/3 and 1/4 plateaus. This theory, however, claims that the 1/3 plateau ends at about 53 T, in disagreement with experiment [67]. On the contrary, theories [89, 90] predict that the 1/3 plateau survives up to 80 T and 110 T, respectively, though the agreement with the experiment in the low-field region looks poor. One of the important issues to be solved in the future is the question of whether or not the 1/2 plateau exists. Theory [90] that weighs long-range interactions of triplets bets on the existence of the plateau, while theory [89] that weights correlated hopping terms bets against it. Higher field experiments to cover the whole magnetization along with more elaborated theoretical treatment are needed to advance our understanding of triplet excitations and dynamics at high fields.

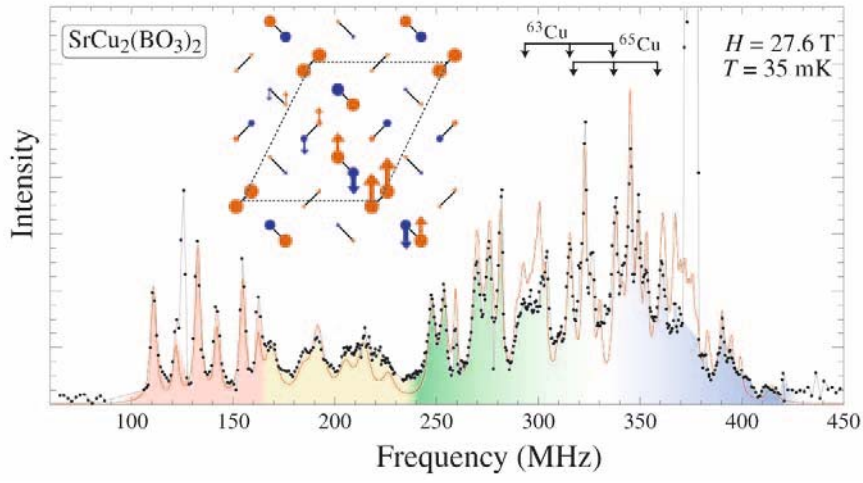

Fig. 25. Cu NMR spectrum of $SrCu_2(BO_3)_2$ at 35 mK and 27.6 T. The arrows indicate the resonance frequency without hyperfine field. The strong signal in the range 371 to 379 MHz comes from ^{11}B nuclei. The peak at 125.6 MHz is due to ^{10}B nuclei. Inset represents the magnetization profile. Red circles indicate positive $\langle S_z \rangle$, blue circles indicate negative $\langle S_z \rangle$, and the circle size represents the magnitude of $\langle S_z \rangle$. (reproduced from [94])

Although possible superstructures have been proposed for the observed plateaus based on the simple hard-core boson model, where triplets are completely confined on a single dimer, no experimental evidence for superstructures had yet been reported, until Kodama *et al*. performed Cu-NMR measurement at 35 mK using a 20-MW resistive magnet at the Grenoble High Magnetic Field Laboratory equipped with a dilution refrigerator [94]. The NMR spectrum at 26 T which is just below the lower critical field of the 1/8 plateau can be represented as superposition of six lines due to three line split by electric quadrupolar interaction for each of two isotopes ^{65}Cu and ^{63}Cu, indicating that the magnetization is largely uniform and thus triplets are itinerant. Once the system enters the 1/8 plateau region, a drastic change of the spectrum was observed with the appearance of many sharp peaks distributed over a wide frequency range, providing clear evidence for a commensurate magnetic order breaking the translational symmetry, as shown in Fig. 25. A satisfactory fitting of the spectrum at 27.6 T (red line in Fig. 25) requires at least 11 Cu sites with different hyperfine fields. In particular, the six sharp lines in the red zone (105-165 MHz) are ascribed to the sites with the largest local magnetization $\langle S_z \rangle = 0.30$. Likewise the spectrum in the yellow zone (165-235 MHz) represent another sites with $\langle S_z \rangle = 0.20$. Interestingly, the spectrum in the blue zone has positive hyperfine fields, implying that spins are polarized opposite to the magnetic field direction. Although a simple symmetry consideration supports a rhomboid cell with eight dimers, the superstructure in Fig. 24 (b) contradicts the NMR result because the hard-core boson model gives $\langle S_z \rangle = 0.50$ for 1/8 of the Cu sites and $\langle S_z \rangle = 0$ for the rest.

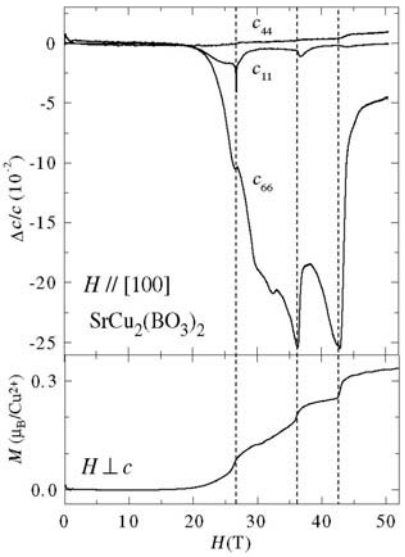

Fig. 26. The elastic constants c_{11}, c_{44}, and c_{66} as a function of magnetic field in $SrCu_2(BO_3)_2$ at $T = 1.5$ K, in comparison with the magnetization for $H \perp c$. The ultrasonic frequency was 10 MHz (c_{44} and c_{66} modes) and 86 MHz (c_{11} mode). (reproduced from [39])

In order to reproduce the rich texture of the spin distribution experimentally observed, the original Hamiltonian, equation (1), must be solved. Because a pronounced softening of the sound velocity observed at the edges of the magnetization plateaus it is suggested that a lattice distortion occurs in $SrCu_2(BO_3)_2$ (see Fig. 26) [39]. Therefore, an adiabatic spin-phonon coupling was included in equation (1) and was solved by exact diagonalization. The read line in Fig. 25 shows a successful fit. The obtained magnetization profile, shown in the inset of Fig. 25, has a rhomboid cell with an eight-dimer cluster that extends over the entire unit cell, with one strongly polarized triplet-like dimer surrounded by decaying oscillation of the magnetization. A similar structure has also been observed around impurities in quantum spin chains [95] and in cuprate superconductors [96]. It is analogous to the Friedel oscillation near impurities in metals.

Quantum melting of various ordered structures, for example, vortex lattices in superconductors and charge or orbital order in perovskite transition metal oxides, has attracted increasing attention. In many cases, the phase transition is controlled by chemical doping, which also introduces disorder and increases complexity. In the present system we have a clean system with an exotic ordered structure, in which the phase transition can be tuned by a magnetic field. For the 1/8 plateau, a discontinuous phase transition has been observed as a function of H and T [94]. Spin superlattices for other plateaus as well as the nature of phase transitions remain to be solved. In particular, a "supersolid" phase or the coexistence of Mott-insulating and superfluid components, proposed by Momoi and Totsuka [91], is worth investigating further experimentally.

12. DZYALOSHINSKY-MORIYA INTERACTION

Until now it has been demonstrated that the magnetic properties of this exotic spin compound are basically represented by the pure Shastry-Sutherland model. Some experiments, e.g., magnetization curve, however indicate the existence of small spin anisotropy terms in the Hamiltonian (1) of $SrCu_2(BO_3)_2$. Although anisotropies are expected to be small in this system, they may be essential to understand important features of the system.

The field-frequency diagram (Fig. 19) shows that the one-triplet mode splits into two branches and the energy separation clearly depends on the magnetic field orientation. A zero-field splitting between $S_z = +1$ and $S_z = -1$ is largest when magnetic field is applied parallel to the c-axis. Furthermore, while two branches are almost parallel for H // c, they become very closer for H // a accompanied by the bending around zero field. Thus the principle axis of the interaction causing the splitting should point nearly to the c-axis. This fine structure in ESR can be understood when anisotropic DM terms in the interdimer interactions

$$H_{\mathrm{DM}} = \sum_{\mathrm{nnn}} D\left(s_i^x s_j^y - s_i^y s_j^x\right), \tag{7}$$

are introduced. DM vectors were initially assumed to be perpendicular to the ab plane, with an alternation of the DM vector direction from bond to bond. The DM interaction is, in contrast to the exchange interactions, not frustrated because of the alternation of its vector. Hence the degeneracy of the localized triplets is lifted to first order in D, suppressing the spin gap.

Inelastic neutron scattering experiments using the cold neutron triple axis instrument at JAERI gave a complex structure in the dispersion of one-triplet excitations (Fig. 27) [97], which was not detected by the thermal neutron experiment (Fig. 18) [33]. It can be recognized that the one-triplet excitation around 3 meV energy transfer indeed consists out of at maximum three excitation branches. At Q = (1, 0, 0), one observes clearly a three-peak structure, while only one resolution limited peak at Q = (1.5, 0.5, 0) is observable. Magnetic fields further split these peaks [97, 98]. These phenomena in the dispersion with and without magnetic fields can also be understood in terms of the out-of-plane component of DM terms. Namely, the first order in D lifts the degeneracy of the localized triplets and introduce small but appreciable dispersion.

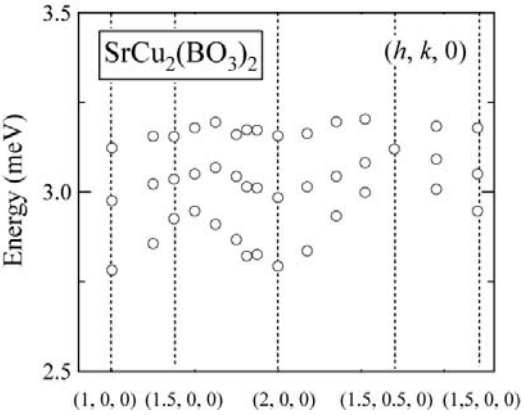

Fig. 27. Dispersion of the one-triplet excitations (reproduced from [97])

The above theory predict a specific Q-dependence along (1, 1, 0) direction including the degeneracy restored at π, in accordance with the single peak structure at Q = (1.5, 0.5, 0). However, it would predict the same behavior in (1, 0, 0) direction, i.e., a single peak structure at Q = (1.5, 0, 0). The experiment, in contrast, shows a splitting (see Fig. 27). Here the corrugated $CuBO_3$ plane at low-T structure may justify additional interdimer DM component, i.e., an in-plane component of DM vector. Introducing in-plane component partially lifting the frustration in the triangular interdimer configuration, the dispersion in (1, 0, 0) direction is modified in accordance with the experiment, while that in (1,5, 0, 0) remains unchanged. The values of out-of- and in-plane components of DM interaction are determined as 0.18 meV and 0.07 meV, respectively. Using these parameters, theory successfully reproduces the rich texture in the ESR spectrum [76]. It is to be noted that ESR and infrared transitions between the singlet ground state and the excited triplet state are usually forbidden, and the observation of absorption requires some anisotropies [37, 75]. For $SrCu_2(BO_3)_2$, the lattice symmetry leads to zero amplitude even in the presence of the static DM couplings considered above. As a possible source, a dynamical DM interaction has been proposed [98, 99].

Several aspects of magnetic properties at low-T and high-H remain mysterious: i) A finite magnetization appears well below the expected critical field for the gap closing $H_c = \Delta/g\mu_B$ [29]. This is not due to a thermal effect since, as can been seen in Fig. 28, magnetization curves at 1.5 K and 0.08 K are essentially the same [30]. ii) A gap seems to persist above H_c [59, 75, 100]. iii) A large staggered magnetization is induced by the magnetic field [59]. iv) There appears no phase transition down to 0 K at fields below the 1/8 plateau, which means that no Bose condensation occurs, while a transition has been observed above it [100]. v) The magnetization shows a discontinuous jump at the lower boundary of the 1/8 plateau [30]. The properties i)-iii) suggest that triplet states are mixed into the ground state by some anisotropic interactions. The interdimer DM interaction considered above, however, does not have matrix elements between singlet and one-triplet states. Kodama *et al*. showed that the intradimer DM interaction and the staggered g-tensor, which give the single-triplet mixing and level repulsion, qualitatively accounts for i)-iii) [59]. Raman scattering and X-band ESR experiments also suggest a significant contribution of the intradimer DM interaction to the magnetic behavior [55, 101]. Note that a finite intradimer DM interaction is allowed for the low-T structure due to the buckling of $CuBO_3$ layer.

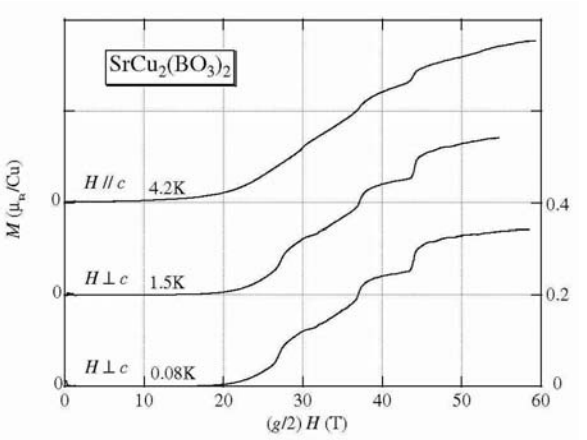

Fig. 28. Temperature dependence of normalized magnetization curves. (reproduced from [30])

In general, dimerized spin system spin-phonon coupling plays an important role in determining the magnitude of spin gap and the strength of dimerization [102]. Optic- and/or acoustic-phonon anomalies can accompany the onset of a dimerized state as reported in $CuGeO_3$ [103] and $SrCu_2(BO_3)_2$ [38]. In $SrCu_2(BO_3)_2$, the soft mode corresponding to in-plane motions of almost all ions along the interlayer direction was observed upon approaching T_s, as already mentioned. An additional softening of this anisotropic phonon mode by 3 % for temperatures below the spin gap is a consequence of strong spin-phonon coupling [55]. It was also found from ultrasound experiments that the in-plane elastic constant c_{66} shows a pronounced softening of 4.5 % for temperatures below 25 K [38, 39], which is attributed to an exchange striction coupling. Furthermore, under a magnetic field applied along the (1, 0, 0)

direction an enormous softening of the in-plane c_{11} and c_{66} elastic constants takes place in the vicinity of the magnetization plateaus where excited triplets are expected to become highly mobile (see Fig. 26).

These results show that in a realistic model for $SrCu_2(BO_3)_2$ spin-phonon interactions, DM interactions and lattice dynamics should be taken into account to understand a variety of physical properties such as the spin gap, the proximity to a quantum critical point, and anomalous behavior of the spectroscopic data. As a result, it can be said that $SrCu_2(BO_3)_2$ is closer to a quantum critical point than previously predicted based on pure 2D or 3D spin models.

13. SEARCH FOR NEW SHASTRY-SUTHERLAND COMPOUNDS

Without doubt, the discovery of $SrCu_2(BO_3)_2$ and following cooperative developments by theories and experiments has unveiled many exotic properties of the Shastry-Sutherland model and its derivatives. To check the obtained features and further deepen and expand our understanding of the theoretical model system, it is desirable to explore other real compounds that are topologically equivalent to this model.

In particular, if one could obtain such a compound and make it metallic (or superconducting) by doping carriers, the comparison with cuprate superconducting would be interesting as pointed out by Shastry and Kumar [104]. Such an attempt was recently made by Iiu *et al*., who prepared a series of compounds $M_{0.1}Sr_{0.9}Cu_2(BO_3)_2$ with Sr substituted by M = Al, La, Na and Y, but no superconductivity was observed [105].

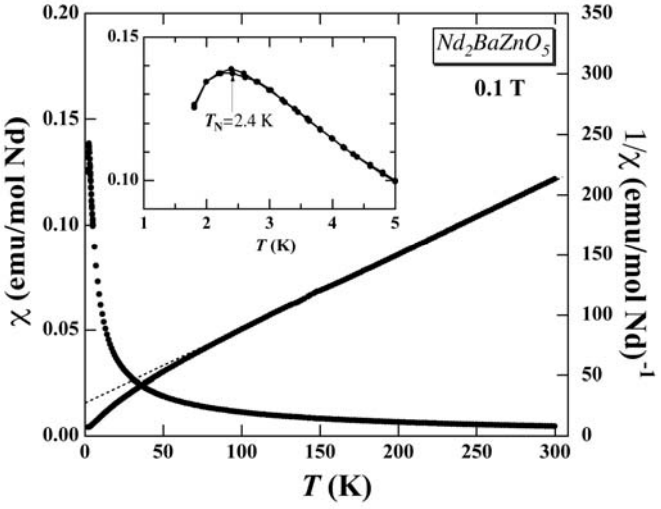

Fig. 29. Magnetic susceptibility and reciprocal susceptibility for Nd_2BaZnO_5. The inset represents the enlarged plot for the low-T region (reproduced from [65])

The insulating neodymium oxide Nd_2BaZnO_5 has a layered structure with the space group *I*4/*mcm* and cell parameters a = 6.760 Å and c = 11.546 Å [106]. The Nd-O and Ba-Zn-O layer layers alternatively stack along the c direction. The magnetic ions, i.e., the Nd^{3+} occupying a crystallographycally equivalent site (8*h*), form the 2D network shown in Fig. 5 (b), where the nearest-neighbor and the next-nearest-neighbor Nd^{3+}-Nd^{3+} distances are very close: d_{nn} = 3.324 Å and d_{nnn} = 3.525 Å. Since Nd^{3+} ions carry a large magnetic moment, this system is regarded as a classical Shastry-Sutherland model, where Néel order or helical order is stable over a wide range of J'/J [17]. The T dependence of magnetic susceptibility of Nd_2BaZnO_5 (Fig. 29) shows the Curie-Weiss behavior with the Weiss constant $\theta = -44.5$ K, indicative of antiferromagnetic interaction [67]. On cooling, deviations from Curie-Weiss behavior are observed from about 70 K possibly due to development of short-range ordering, and further cooling results in the antiferromagnetic transition at T_N = 2.4 K. Competing interactions are derived from the large frustration factor $-\theta/T_N = 19$.

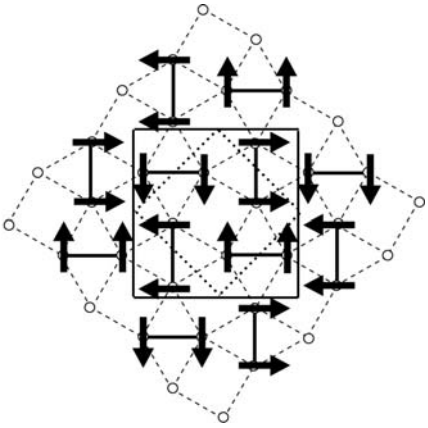

Fig. 30. Magnetic structure for Nd_2BaZnO_5. The squares drown by dotted and solid lines denote, respectively, chemical and magnetic unit cells.

The powder neutron diffraction pattern shows the presence of magnetic peaks below T_N = 2.4 K, accompanied by translational symmetry breaking (unpublished data). The magnetic structure as shown in Fig. 30 is commensurate but is different from that expected for the square lattice antiferromagnet. Single-ion anisotropies and/or third-nearest neighbor interactions in the layer would play a crucial role for this magnetic structure. It is interesting to note that R atoms in the intermetallic compounds RB_2C (R = Dy, Ho) also form a lattice that is topologically equivalent to the Shastry-Sutherland model. The observed magnetic structures for RB_2C are commensurate but are neither that for Nd_2BaZnO_5 nor the square lattice antiferromagnet [107]. In this case, RKKY type interactions may be taken into consideration.

14. CONCLUSIONS

In this article, an attempt has been made overview the recent cooperative developments in theory and experiment studying $SrCu_2(BO_3)_2$. The main conclusions are the following:

i) Geometrically frustrated models can be categorized into two groups: triangle-based models and square-based models. The former include the well-known triangular lattice and the kagomé lattice, while the latter includes the 1/5-depleted square lattice and the Shastry-Sutherland lattice. Such a classification scheme facilitates to extract the key factors from various observed phenomena recently at issue in solid-state physics.

ii) Bulk single crystals of $SrCu_2(BO_3)_2$ can be grown by TSFZ method using $LiBO_2$ as a solvent. The success of the single crystal growth allowed us to perform various measurements, from which a number of unusual properties have been revealed.

iii) The Cu^{2+} (S = 1/2) in $SrCu_2(BO_3)_2$ forms a 2D magnetic network, where Cu^{2+}-Cu^{2+} dimers are connected in an orthogonal manner within a plane. This lattice is topologically equivalent to the Shastry-Sutherland model, in which the direct product of the dimer singlets is the exact ground state when J'/J is small because of the orthogonality of adjacent dimers. A visualization of this deformation between two lattices is available at:

http://kuchem.kyoto-u.ac.jp/kinso/kage/SrCuBO.html

The most remarkable fact is that such an exact ground state has been for the first time found in $SrCu_2(BO_3)_2$. Various experiments provide evidence for a dimer ground state with the gap Δ = 34 K.

iv) Because of the orthogonal dimer network along the c-axis, which is topologically equivalent to the Gelfand model, even the 3D structure of $SrCu_2(BO_3)_2$ is characterized by the exact dimer ground state for small J''/J. The second order-like structural phase transition occurs at T_s = 395 K. The flat $CuBO_3$ plane becomes buckled below T_s, losing a mirror plane. This buckling leads to the alternation of interlayer coupling constants and also affects the inter- and intra-dimer DM interactions.

v) The isolated dimer model fails to reproduce the experimental data (magnetic susceptibility and specific heat etc.), implying sizable interdimer interaction, or strong geometrical frustration. Actually, the exchange constants are estimated as J = 85 K, J' = 54 K, J'' = 8 K [45] or J = 71 K, J' = 43 K, J'' = 15 K [56]. $SrCu_2(BO_3)_2$ is thus located very close to the quantum phase boundaries either to a Néel ordered state or to the RVB plaquette singlet state. It turned out that pressure is a very effective tool to modify the exchange constants and to put the compound closer to the boundaries reducing the spin gap. Unusual temperature dependence of the magnetic susceptibility is a consequence of the closeness to the transition point. Further (pressure) experiments are needed to detect evidence for phase transitions and complete the phase diagram of this system.

vi) The dispersion of the one-triplet excitations in the ab plane is 0.2 meV (~2 K) at most, showing the extremely localized nature of triplet excitations, despite much stronger in-plane interactions. Again, the orthogonality of neighboring dimers plays a crucial role:

it makes the propagation of the one-triplet excitation possible starting with sixth order in the perturbation J'/J.

vii) ESR, far infrared spectroscopy, Raman scattering show rich structures of triplet bound states with discrete energies, reflecting the localized nature of triplets. It is theoretically suggested that the propagation of multi-triplets is easier compared to the one of single triplets due to pronounced correlation effects of coupled triplets. Dynamical aspects of multi-triplet states call for further experiments.

viii) Reflecting the localized nature of excited triplets, magnetization curves at temperatures well below the gap exhibit quantized plateaus at 1/3, 1/4 and 1/8 of the Cu saturation moment. This is the localization-to-delocalization transition of excited triplets. It is considered that when the density of triplets becomes a certain value, which is commensurate with respect to underlying lattice, the long-range ordering of triplets occurs. The superstructure for the 1/8 plateau, determined by the high-field NMR experiment, has a large rhomboid unit cell with spin polarization oscillating and spreading on the lattice, breaking translational symmetry. The stripe type of superstructures is predicted for the 1/3 and 1/4 plateaus.

ix) The interdimer and intradimer DM interactions are responsible for some observed anomalies in this compound. The former lifts the degeneracy of the one-triplet excitations as observed in ESR and neutron scattering. The latter together with the staggered g-tensor plays a crucial role in mixing the singlet state with the triplet excited state, causing the finite magnetization below the 1/8 plateau and a field-induced staggered magnetization and so on.

ACKNOWLEDGMENT

I have benefited from long-term collaborations, discussions and exchange of ideas and results with a large number of people, both from experimental side and from theoretical side. First of all, I would like to express sincere thanks to Y. Ueda for continuous support and interest. I am also grateful to experimental physicists M. Takigawa, K. Kodama, M. Horvatic, C. Berthier, N. Aso, M. Nishi, K. Kakurai, N.V. Mushnikov, T. Goto, K. Yoshimura, Y. Narumi, K. Kindo, P. Lemmens, H. Nojiri, A.N. Vasil'ev, T. Rõõm, Y.J. Uemura, Y. Takano, A. Lappas and B. Lüthi. Special thanks would be given to theoretical physicists S. Miyahara, K. Ueda, B.S. Shastry, K. Totsuka, T. Momoi, A. Koga, S. Miyashita, G.S. Uhrig, G. Misguich, T. Ziman and F. Mila. Finally, I wish to thank Ritsuko and Yoto Kageyama for their continuous encouragement.

REFERENCES

[1] P. Lemmens and P. Millet, Lect. Notes. **645** (2004) 433.

[2] B. Keimer, N. Belk, R.J. Bigeneau, A. Cassanho, C.Y. Chen, M. Greven, M.A. Kastner, A. Aharony, Y. Endoh, R.W. Erwin, and G. Shirane, Phys. Rev. **B 46** (1992) 14034.

[3] M. Hase, I. Terasaki, and K. Uchinokura, Phys. Rev. Lett. **70** (1993) 3651.

[4] J. Darriet and J.P. Regnault, Solid State Commun. **86** (1993) 409.

[5] J.P. Renard, M. Verdaguer, L.P. Pegnault, W.A.C. Erkelens, J. Rossat-Mignod, and W.G. Stirling, Europhys. Lett. **3** (1987) 945.

[6] M. Azuma, Z. Hiroi, M. Takano, K. Ishida, and Y. Kitaoka, Phys. Rev. Lett. **73** (1994) 2626.

[7] B. Chiari. O. Piovesana, T. Tarantelli, and P.F. Zanazzi, Inrog. Chem. **29** (1990) 1117.

[8] J.C. Bonner, S.A. Friedberg, H. Kobayashi, and D.L. Meier, Phys. Rev. **B 27** (1983) 248.

[9] S. Taniguchi, T. Nishikawa, Y. Yasui, Y. Kobayashi, M. Sato, T. Nishioka, M. Kontani, and K. Sano, J. Phys. Soc. Jpn. **64** (1995) 2758.

[10] N. Kato and M. Imada, J. Phys. Soc. Jpn. **64** (1995) 4105.

[11] A.P. Ramirez, Annu. Rev. Mater. Sci. **24** (1994) 453.

[12] J.E. Greedan, J. Mater. Chem. **11** (2001) 37.

[13] P.W. Anderson, Mater. Res. Bull. **8** (1973) 153.

[14] R.W. Smith and D.A. Keszler, J. Solid State Chem. **93** (1991) 430.

[15] H. Kageyama, K. Yoshimura, R. Stern, N.V. Mushnikov, K. Onizuka, M. Kato, K. Kosuge, C.P. Slichter, T. Goto, and Y. Ueda, Phys. Rev. Lett. **82** (1999) 3168.

[16] S. Miyahara and K. Ueda, Phys. Rev. Lett. **82** (1999) 3701.

[17] B. S. Shastry and B. Sutherland, Physica **B 108** (1981) 1069.

[18] S. Miyahara and K. Ueda, J. Phys. Condens. Matter **15** (2003) R327.

[19] S. Sachdev and R.N. Bhatt, Phys. Rev. **B 41** (1990) 9323.

[20] A. Bombardi, J. Rodriguez-Carvajal, S.Di Matteo, F.de Bergevin, L. Paolasini, P. Carretta, P. Millet, and R. Caciuffo, Phys. Rev. Lett. **93** (2004) 027202, and the references therein.

[21] R. Coldea, D.A. Tennant, K. Habicht, P. Smeibidl, C. Wolters, and Z. Trlczynski, Phys. Rev. Lett. **88** (2002) 137203.

[22] T. Ono, H. Tanaka, H. Aruga Katori, F. Ishikawa, H. Mitamura, and T. Goto, Phys. Rev. **B 67** (2003) 104431.

[23] H. Kageyama, K. Onizuka, T. Yamauchi, and Y. Ueda, J. Crystal Growth **206** (1999) 65.

[24] H. Kageyama, K. Onizuka, T. Yamauchi, Y. Ueda, S. Hane, H. Mitamura, T. Goto, K. Yoshimura, and K. Kosuge, J. Phys. Soc. Jpn. **68** (1999) 1821.

[25] H. Nojiri, H. Kageyama, K. Onizuka, Y. Ueda, and M. Motokawa, J. Phys. Soc. Jpn. **68** (1999) 2906.

[26] H. Kageyama, H. Suzuki, M. Nohara, K. Onizuka, H. Takagi, and Y. Ueda, Physica **B 281&282** (2000) 667.

[27] H. Kageyama, K. Onizuka, Y. Ueda, M. Nohara, H. Suzuki, and H. Takagi, J. Exp. and Theor. Phys. **90** (2000) 129.

[28] H. Kageyama, K. Onizuka, Y. Ueda, N.V. Mushnikov, T. Goto, K. Yoshimura, and K. Kosuge, J. Phys. Soc. Jpn. **67** (1998) 4304.
[29] K. Onizuka, H. Kageyama, Y. Ueda, T. Goto, Y. Narumi, and K. Kindo, J. Phys. Soc. Jpn. **69** (2000) 1016.
[30] H. Kageyama, Y. Narumi, K. Kindo, K. Onizuka, Y. Ueda, and T. Goto, J. Alloys and Compounds **317-318** (2001) 177.
[31] K. Kodama, J. Yamazaki, M. Takigawa, H. Kageyama, K. Onizuka, and Y. Ueda, J. Phys. Condensed. Matter. **14** (2002) L319.
[32] K. Kodama, J. Yamazaki, M. Takigawa, H. Kageyama, K. Onizuka, and Y. Ueda, *Quantum Properties of Low-Dimensional Antiferromagnets* (Ed. Y. Ajiro & J-P. Boucher), Kyushu University Press, pp. 102-108 (2002).
[33] H. Kageyama, M. Nishi, N. Aso, K. Onizuka, T. Yosihama, K. Nukui, K. Kakurai, K. Kodama, and Y. Ueda, Phys. Rev. Lett. **84** (2000) 5876.
[34] H. Nojiri, H. Kageyama, K. Onizuka, Y. Ueda, and M. Motokawa, Physica **B 284-288** (2000) 1450.
[35] P. Lemmens, M. Grove, M. Fisher, G. Güntherodt, V.N. Kotov, H. Kageyama, K. Onizuka, and Y. Ueda, Physica **B 281&282** (2000) 656.
[36] P. Lemmens, M. Grove, M. Fisher, G. Güntherodt, V.N. Kotov, H. Kageyama, K. Onizuka, and Y. Ueda, Phys. Rev. Lett. **85** (2000) 2605.
[37] T. Rõõm, U. Nagel, E. Lippmaa, H. Kageyama, K. Onizuka, and Y. Ueda, Phys. **B 61** (2000) 14342.
[38] S. Zherlitsyn, S. Schmidt, B. Wolf, H. Schwenk, B. Lüchi, H. Kageyama, K. Onizuka, and Y. Ueda, Phys. Rev. **B 62** (2000) 6097.
[39] B. Wolf, S. Zherlitsyn, S. Schmidt, B. Lüthi, H. Kageyama, and Y. Ueda, Phys. Rev. Lett. **86** (2001) 4847.
[40] M. Isobe and Y. Ueda, J. Phys. Soc. Jpn. **65** (1996) 3142.
[41] D.J. Hodgson, Prog. Inorg. Chem. **19** (1975) 173.
[42] V.H. Crawford, H.W. Richardson, J.R. Wasson, D.J. Hodgson, and W.E. Hatfield, Inorg. Chem. **15** (1976) 2107.
[43] R.L. Carlin, *Magnetochemistry* (Springer-Verlag, Berlin, 1986), Chap 5, p. 75.
[44] Y. Sasago, M. Hase, K. Uchinokura, M. Tokunaga, and N. Miura, Phys. Rev. **B 52** (1995) 2533.
[45] S. Miyahara and K. Ueda, J. Phys. Soc. Jpn. (Suppl.) **B 69** (2000) 72.
[46] C. Majumdar and D. Ghosh, J. Math. Phys. **10** (1969) 1388.
[47] K. Takano, J. Phys. A: Math. Gen. **27** (1994) L269.
[48] S. Xiong, Phys. Lett. **A 168** (1992) 225.
[49] T. Oguch and H. Kitatani, J. Phys. Soc. Jpn. **64** (1995) 612.
[50] L. Onsager, Phys. Rev. **65** (1944) 117.
[51] Y. Kuramoto and H. Yokoyama, Phys. Rev. Lett. **67** (1991) 1338.
[52] M. Gelfand, Phys. Rev. **B 43** (1991) 8644.
[53] K. Ueda and S. Miyahara, J. Phys.: Condens. Matter **11** (1999) L175.
[54] K. Sparta, G.J. Redhammer, P. Roussel, G. Heger, G. Roth, P. Lemmens, A. Ionescu, M. Grove, G. Güntherodt, F. Hüning, H. Kageyama, K. Onizuka, and Y. Ueda, Eur. Phys. J. **B 19** (2001) 507.
[55] K.-Y. Choi, Yu.G. Pashkevich, K.V. Lamonova, H. Kageyama, Y. Ueda, and P. Lemmens, Phys. Rev. **B 68** (2003) 104418.

[56] C. Knetter, A. Bühler, E. Müller-Hartmann, and G.S. Uhrig, Phys. Rev. Lett. **85** (2000) 3958.
[57] H. Kageyama, K. Onizuka, Y. Ueda, S. Hane, H. Mitamura, T. Goto, K. Yoshimura, and K. Kosuge, *Quantum Phenomena in Advanced Materials at High Magnetic Fields* (Ed. G. Kido), National Research Institute for Metals, Tsukuba (1999), pp. 235-237.
[58] H. Kageyama, T. Nakajima, M. Ichihara, F. Sakai, and Y. Ueda, *Quantum Properties of Low-Dimensional Antiferromagnets* (Ed. Y. Ajiro & J-P. Boucher), Kyushu University Press, pp. 135-142 (2002).
[59] K. Kodama, S. Miyahara, M. Takigawa, M. Horvatic, C. Berthier, F. Mila, H. Kageyama, and Y. Ueda, cond-mat/04704482.
[60] I. Loa, F. Zhang, K. Syassen, P. Lemmens, W. Crichton, H. Kageyama, and Y. Ueda, Proceedings of SCES'04 (July 26-30, Karlsruhe).
[61] W. Zheng, J. Oitmaa, and C.J. Hamer, Phys. Rev. **B 60** (1999) 6608.
[62] H. Yasuoka, J. Phys. Soc. Jpn. (Suppl.) **B 69** (2000) 161.
[63] M. Albrecht and F. Mila, Europhys. Lett. **34** (1996) 145.
[64] A. Koga and N. Kawakami, Phys. Rev. Lett. **84** (2000) 4461.
[65] K. Ueda and H. Kontani, M Sigrist, and P.A. Lee, Phys. Rev. Lett. **76** (1996) 1932.
[66] A. Koga, J. Phys. Soc. Jpn. **69** (2000) 3509.
[67] H. Kageyama, Y. Ueda, Y. Narumi, K. Kindo, M. Kosaka, and Y. Uwatoko, Prog. Theo. Phys. Suppl. **145** (2002) 17.
[68] K. Koyama, S. Hane, K. Kamishima, and T. Goto, Rev. Sci. Instrum. **69** (1998) 3009.
[69] H. Kageyama, N.V. Mushnikov, M. Yamada, T. Goto, and Y. Ueda, Physica **B 329-333** (2003) 1020.
[70] B. Leuenberger, A. Stebler, H.U. Güdel, A. Furrer, R. Feile, and J.K. Kjems, Phys. Rev. **B 30** (1984) 6300.
[71] Y. Sasago, K. Uchinokura, A. Zheludev, and G. Shirane, Phys. Rev. **B 55** (1997) 8357.
[72] N. Aso, K. Nukui, M. Nishi, H. Kageyama, K. Onizuka, T. Yosihama, K. Kakurai, and Y. Ueda, J. Phys. Soc. Jpn. (Suppl.) **A 71** (2001) 177.
[73] K. Totsuka, S. Miyahara, and K. Ueda, Phys. Rev. Lett. **86** (2001) 520.
[74] C. Knetter and G.S. Uhrig, Phys. Rev. Lett. **92** (2004) 027204.
[75] H. Nojiri, H. Kageyama, Y. Ueda, and M. Motokawa, J. Phys. Soc. Jpn. **72** (2003) 3243.
[76] S. Miyashita and A. Ogasahara, J. Phys. Soc. Jpn. **72** (2003) 2350.
[77] K. Kudo, S. Ishikawa, T. Noji, T. Adachi, Y. Koike, K. Maki, S. Tsuji, and K. Kumagai, J. Low Temp. Phys. **117** (1999) 1689.
[78] Y. Ando J. Takeya, D.L. Sisson, S.G. Doettinger, I. Tanaka, R.S. Feigelson, and A. Kapitulnik, Phys. Rev. **B 58** (1998) R2913.
[79] M. Hofmann, H. Kierspel, T. Lorentz, G.S. Uhrig, O. Zabara, A. Freimuth, H. Kageyama, and Y. Ueda, Phys. Rev. Lett. **87** (2001) 047202.
[80] K. Kudo, T. Noji, Y. Koike, T. Nishizaki, and N. Kobayashi, J. Phys. Soc. Jpn. **70** (2001) 1448.
[81] A.N. Vasil'ev, M.M. Markina, A.V. Inyushkin, and H. Kageyama, JETP Letters **73** (2001) 633.
[82] H. Kageyama, K. Yoshimura, K. Kosuge, H. Mitamura, and T. Goto, J. Phys. Soc. Jpn. **66** (1997) 1611.
[83] M. Oshikawa, M. Yamanaka, and I. Affleck, Phys. Rev. Lett. **78** (1997) 1984.

[84] K. Hida, J. Phys. Soc. Jpn. **63** (1994) 2359.
[85] T. Tonegawa, T. Nakao, and M. Kaburagi, J. Phys. Soc. Jpn. **65** (1996) 3317.
[86] M. Oshikawa, Phys. Rev. Lett. **84** (2000) 1535.
[87] Y. Narumi, M. Hagiwara, R. Sato, K. Kindo, H. Nakano, and M. Takahashi, Physica **B 246-247** (1998) 509.
[88] W. Shiramura, K. Takatsu, B. Kurniawan, H. Tanaka, H. Uekusa, Y. Ohashi, K. Takizawa, H. Mitamura, and T. Goto, J. Phys. Soc. Jpn. **67** (1998) 1548.
[89] T. Momoi and K. Totsuka, Phys. Rev. **B 61** (2000) 3231.
[90] S. Miyahara and K. Ueda, Phys. Rev. **B 61** (2000) 3417.
[91] T. Momoi and K. Totsuka, Phys. Rev. **B 62** (2000) 15067.
[92] Y. Fukumoto and A. Oguchi, J. Phys. Soc. Jpn. **69** (2000) 1286.
[93] G. Misguich, T. Jolicoeur, and S.M. Girvin, Phys. Rev. Lett. **87** (2001) 097203.
[94] K. Kodama, M. Takigawa, M. Horvatic, C. Berthier, H. Kageyama, Y. Ueda, S. Miyahara, F. Becca, and F. Mila, Science **298** (2002) 395.
[95] M. Takigawa, N. Motoyama, H. Eisaki, and S. Uchida, Phys. Rev. **B 55** (1997) 14129.
[96] M.-H Julien, T. Fehér, M. Horvatic, C. Berthier, O.N. Bakharev, S. Ségransan, G. Collin, and J.-F. Marucco, Phys. Rev. Lett. **84** (2000) 3422.
[97] K. Kakurai, N. Aso, K. Nukui, M. Nishi, H. Kageyama, Y. Ueda, H. Kadowaki, and O. Cépas, *Quantum Properties of Low-Dimensional Antiferromagnets*, (Ed. Y. Ajiro & J-P. Boucher) Kyushu University Press, pp. 102-108 (2002).
[98] O. Cépas, K. Kakurai, L.P. Regnault, T. Ziman, J-P. Boucher, N. Aso, M. Nishi, H. Kageyama, and Y. Ueda, Phys. Rev. Lett. **87** (2001) 167205.
[99] O. Cépas and T. Ziman, *Quantum Properties of Low-Dimensional Antiferromagnets*, (Ed. Y. Ajiro & J-P. Boucher) Kyushu University Press, pp. 175-182 (2002).
[100] H. Tsujii, R.C. Rotundu, B. Andraka, Y. Takano, H. Kageyama, and Y. Ueda, cond-mat/0301509.
[101] A. Zorko, D. Arcon, H.van Tok, L.C. Brunell, and H. Kageyama, Phys. Rev. **B 69** (2004) 174420.
[102] P. Lemmens, G. Güntherodt, and C. Gros, Phys. Rep. **B 65** (2003) 1.
[103] M. Braden, B. Hennion, W. Reichardt, G. Dhalenne, and A. Revcolevschi, Phys. Rev. Lett. **80** (1998) 3634.
[104] B.S. Shastry and B. Kumar, Prog. Theor. Phys. Suppl. **145** (2002) 1.
[105] G.T. Iiu, J.L. Luo, T. Xiang, N.L. Wang, Z.H. Wu, X.N. Jung, and D. Jin, cond-mat/0406306.
[106] M. Taibi, J. Aride, J. Darriet, A. Moqine, and A. Boukhari, J. Solid State Chem. **86** (1990) 233.
[107] J. van Duijin, J.P. Attfield, R. Watanuki, K. Suzuki, and R.K. Heenan, Phys. Rev. Lett. **90** (2003) 087201.

COLLECTIVE SPIN AND CHARGE EXCITATIONS IN $(Sr,La)_{14-x}Ca_xCu_{24}O_{41}$ QUANTUM SPIN LADDERS

A. Go ar[1,2] and G. Blumberg[1]

[1] Bell Laboratories, Lucent Technologies, Murray Hill, NJ 07974, USA
[2] University of Illinois at Urbana-Champaign, Urbana, IL 61801, USA

1 $(Sr,La)_{14-x}Ca_xCu_{24}O_{41}$: The Structure and General Properties

In 1988, material research focussed around the study of high temperature superconducting copper-oxides brought about new phases of Cu-O based systems, the two-leg spin-ladders (2LL's), that have the general formula $(A_{1-}\ A'\ )_{14}Cu_{24}O_{41}$, with A an alkaline earth metal and A' a trivalent (transition or lanthanoid) metal [1, 2]. There were well-founded hopes that these materials could provide useful insight for the unresolved problems posed by the 2D cuprates [3, 4] and from this perspective two main reasons triggered the interest of the scientific community. One of them was based on a number of physical properties that are common for both ladders and high T_c's. These include the presence of similar Cu-O-Cu antiferromagnetic (AF) correlations which give rise to a finite spin gap and were predicted to generate *d*-wave like pairing of doped carriers [5], the evidence for 'pseudo-gap' phenomena in optical absorption spectra [6] and, most importantly, the discovery of superconductivity under pressure evolving with hole doping in the AF environment [7, 8]. The second reason resides in the crystal similarities and more precisely the fact that one can imagine building the 2D square Cu-O lattice by gradually increasing the coupling between individual 2LL's [9], the simplicity of the latter making them more tractable for theoretical analysis.

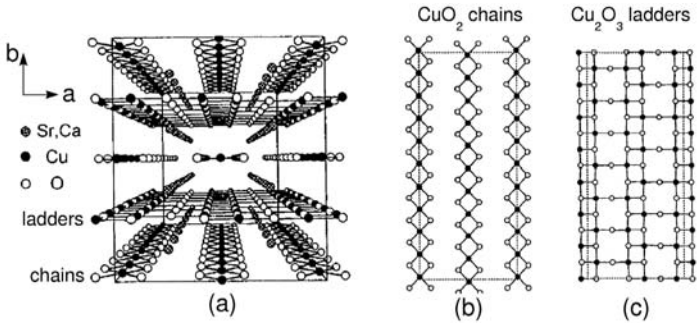

Fig. 1. (**a**) The 3D structure of $Sr_{14}Cu_{24}O_{41}$ viewed in the (*ab*) plane; (**b**) the CuO_2 chains. (**c**) the Cu_2O_3 two-leg ladders. In (**b**) and (**c**) the black dots are Cu atoms and the empty circles represent O atoms.

The unit cell of $Sr_{14}Cu_{24}O_{41}$ contains four formula units, 316 atoms in all, this large number of atoms being due to the presence of two nearly commensurate substructures: the CuO_2 chains and the Cu_2O_3 2LL's. A better understanding of the two interacting blocks can be achieved by decomposing the chemical formula into $(Sr_2Cu_2O_3)_7(CuO_2)_{10}$: planes of CuO_2 chains are stacked alternately with planes of Cu_2O_3 ladders and these are separated by Sr buffer layers, see Fig. 1. The lattice constants of the individual subsystems satisfy the approximate relation $7\ c_{ladder} \approx 10\ c_{chain}$. The *b*-axis is perpendicular to the Cu-O layers which define the (*ac*) plane, the *c*-axis being along the ladder/chain direction. A valence counting shows that $Sr_{14}^{2+}Cu_{24}O_{41}^{2-}$ is intrinsically doped, the average valence per Cu atoms being +2.25. Optical conductivity [10], X-ray absorption [11], *dc* resistivity and magnetic susceptibility [12] measurements, as well as evaluations of the Madelung potential [13] and valence-bond-sums [12] support the idea that in this compound the holes reside mainly in the chain structures and the isovalent Ca substitution for Sr in Sr_{14-} Ca $Cu_{24}O_{41}$ induces a transfer of holes into the more conductive ladders. A relatively large ladder carrier density change from 0.07 hole per Cu for $x = 0$ to about 0.2 for $x = 11$ due to Sr substitution was inferred from low energy optical spectral weight transfer[10], but X-ray absorption [11], while still supporting the hole migration scenario, is in favor of a less pronounced hole transfer. On the other hand, La^{3+} and Y^{3+} substitutions for Sr decrease the total hole concentration, the $La_6Ca_8Cu_{24}O_{41}$ compound containing no holes per formula unit. As a result, the ladder systems provide the opportunity to study not only magnetism in low dimensional quantum systems like undoped ladders but also competing ground states and carrier dynamics in an antiferromagnetic environment. Data interpretation, encumbered by the presence of two interacting subsystems in $(Sr,La)_{14-}$ Ca $Cu_{24}O_{41}$ crystals, is being helped by experimental reali ations of other related compounds like $SrCu_2O_3$, which contains only 2LL planes (Fig. 1c), or Sr_2CuO_3 and $SrCuO_2$, which incorporates only quasi-1D Cu-O chain units with a similar coordination as in Fig. 1b. Unfortunately, doping in these latter systems has not been achieved so far.

Ca substitution in Sr_{14-} Ca $Cu_{24}O_{41}$ has an important impact on the transport properties because of the chain-ladder hole transfer. Indeed, while $Sr_{14}Cu_{24}O_{41}$ is an insulator

showing an activation gap $\Delta \approx 2100$ K (180 meV), a crossover from insulating to metallic conduction at high temperatures takes place around $x = 11$ and for $x = 12$ the c-axis dc resistivity has a minimum around 70 K separating quasi-linear metallic (above T = 70 K) and highly insulating behavior at low temperatures [6]. At higher Ca concentrations superconductivity under pressure has been observed, for example, a T_c of 12 K under a pressure P = 3 GPa was found in x = 13.6 Sr_{14-} Ca $Cu_{24}O_{41}$ [7].

These properties, many of them common also to the 2D superconducting cuprates, underscore the potential value of the ladder systems for the understanding of superconductivity and also for the problem of identifying possibly competing order parameters in doped Mott-Hubbard systems. The plan for this chapter is to present the magnetic properties of $S = 1/2$ 2LL's along with our Raman scattering data on the two-magnon (2M) excitation in $Sr_{14}Cu_{24}O_{41}$, showing its polari ation, resonance and relaxation properties. This is followed by the the analysis of Ca substitution effects on the low and high energy charge/spin degrees of freedom, our data supporting a scenario involving density-wave fluctuations as one of the competing orders for superconductivity.

2 Magnetic Properties of $Sr_{14}Cu_{24}O_{41}$

2.1 Energy Scales

Responsible for the magnetic properties are the Cu atoms which carry a spin $S = 1/2$ due to a missing electron on their $3d$ shells. The AF super-exchange between them is mediated by the O ligand $2p$ orbitals. The optical absorption due to transitions across the charge-transfer gap (determined by the energy difference between the Cu$3d$ and O$2p$ orbitals) is seen to occur at around 2 eV [10]. The sign of the super-exchange as a function of the Cu-O-Cu bond angle can be qualitatively estimated semi-empirically as the balance of two terms: the first term is a relatively small, weakly bond angle dependent, ferromagnetic interaction while the second is antiferromagnetic, large for a 180° Cu-O-Cu bond but strongly varying with the bond angle, tending to ero around 90° [14].

Cu-O chains – As a result of nuclear magnetic/quadrupole resonance (NMR/NQR) [15], X-ray [16] and inelastic neutron scattering (INS) [17, 18] measurements, the following picture provide clarification over some controversial aspects regarding charge/spin ordering in these structures. NMR/NQR data identified two Cu_{chain} sites, one carrying spin 1/2 and one non-magnetic because of Zhang-Rice (ZR) singlet formation, that is a spin $S = 0$ state made out of a O$2p$ hole and a Cu$3d$ hole due to orbital hybridi ation. The data suggested the existence of a superstructure from the multipeak structure of the NMR spectra below about 150 K [15]. X-ray studies [16] established a five-fold charge modulation in the chains' ground state along the c direction which exists at all temperatures below 300 K and a correlation length longer than 200 Å, confirming an ordered pattern involving AF spin dimers separated by two ZR singlets, see Fig. 2. Neutron scattering further supports such a superstructure by analy ing magnetic excitations out of the chain structures and evaluates the dominant intra-dimer exchange to be $J_1 \approx 10$ meV [17, 18] which is also sets the value of spin gap in the dimeri ed chain. Surprisingly, the inter-dimer and inter-chain exchanges were found to be of the same order of magnitude but of

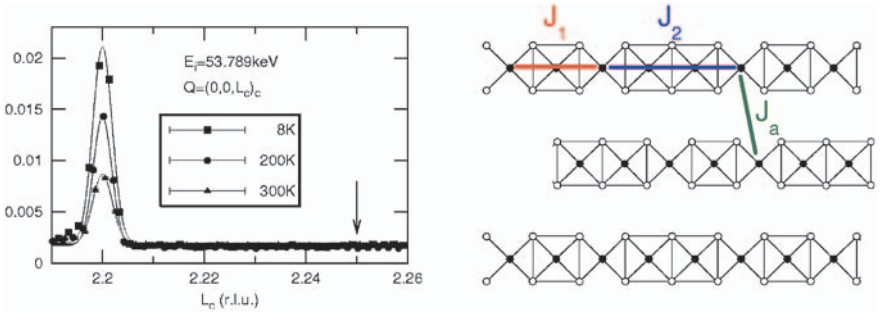

Fig. 2. (**a**) X-ray intensity of the super structure peak seen at (0,0,2.2) in a $\theta - 2\theta$ scan for several temperatures indicating a 5-fold charge modulation, from Ref. [16]. Q is the momentum transfer measured in chain reciprocal units. (**b**) Charge pattern in the chains and the associated AF interactions as determined from Ref. [18]. The squares denote Zhang-Rice singlets.

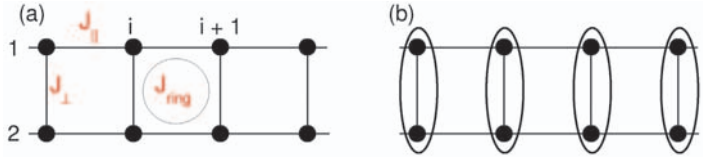

Fig. 3. (**a**) Schematic of a two-leg ladder. $J_{\parallel}$ and $J_{\perp}$ represent the nearest neighbor AF exchanges along the ladder legs and rungs respectively. The circle is an example of a higher order spin interaction, in this case the ring exchange J_{ring}, which is thought to play an important role in the magnetic dynamics of the ladders, see text. (**b**) The ground state of the two-leg ladder in (a) in the limit $= J_{\parallel}/J_{\perp} \to 0$. The ovals represent spin singlet states: $1/\sqrt{2}(|\uparrow\downarrow> - |\downarrow\uparrow>)$

different signs: $J_2 \approx$ -1.1 meV and $J_a \approx = 1.7$ meV [18] and, consistent with NMR/NQR data [15], 2D spin correlations due to J_a were shown to develop below a characteristic temperature of about 150 K. Notable is the fact that if the ZR complexes are effectively made of truly Cu^{3+} ions, the modulation shown in Fig. 1.2 would correspond to a Cu_{chain} valence of 2.6+ meaning that all the holes are located in the chains. Residual carriers are however present in the ladders and microwave [19] and NMR/NQR [15] data suggested the possibility of charge ordering in these systems too.

Cu-O ladders – At low temperatures $Sr_{14}Cu_{24}O_{41}$ can be regarded as an example of a 2LL structure close to half-filling (undoped with carriers). Moreover, an individual 2LL, shown in Fig. 3 is expected to incorporate the essence of the spin dynamics in this subsystem. This is because the Cu-O-Cu bonds which are close to 180° generate a strong super-exchange $J_{\parallel}$ and $J_{\perp}$ (see Fig. 3) of the order of 130 meV ($\approx 1000\text{cm}^{-1}$). This value is about two orders of magnitude stronger than the (frustrated) ferromagnetic inter-ladder interaction, see Fig. 1. From the 2D cuprates experience, an expected Raman signature

at energies of several J's is a two magnon (2M) like excitation consisting of a pair of spin-flips. Low temperature behavior seen in magnetic susceptibility and NMR data show that, unlike in the cuprates, the low frequency spin behavior is not determined by gapless spin-wave modes, expected when one ignores small anisotropies which can create long wavelength gaps. Here there is a substantial spin-gap from the singlet ground state to the lowest triplet ($S = 1$) excitation. The gap value for $Sr_{14}Cu_{24}O_{41}$ extracted from the temperature dependent Knight shift in Cu-NMR data was $\Delta_S \approx 32$ meV (260 cm^{-1}) [15, 20], in good agreement with the gap extracted from neutron scattering data [17] in the same material as well as with the quasi-activated magneti ation data [$\chi(T) \propto (1/\sqrt{T})e^{-\Delta/k_BT}$ see Ref. [3]] in the 2LL $SrCu_2O_3$ [21]. Spin-gap determination from magneti ation measurements in $Sr_{14}Cu_{24}O_{41}$ is more ambiguous due to the prominent contribution from the chains. The magnetic properties of the $Sr_{14}Cu_{24}O_{41}$ ladders, is the concern of the following sections.

2.2 Undoped Two-Leg Ladders: Theoretical Aspects

The starting point for the determination of the ladder excitation spectrum has been the AF nearest-neighbor isotropic Heisenberg Hamiltonian, allowing for the leg and rung couplings $J_\parallel$ and $J_\perp$, see Fig. 3a. This Hamiltonian reads:

$$H = H_\parallel + H_\perp = J_\parallel \sum_{i,\alpha=1,2} \mathbf{S}_{i,\alpha} \cdot \mathbf{S}_{i+1,\alpha} + J_\perp \sum_i \mathbf{S}_{i,1} \cdot \mathbf{S}_{i,2} \qquad (1)$$

From the crystal structure one can anticipate that the relevant parameter range for the leg to rung super-exchange ratio is $= J_\parallel/J_\perp \approx 1$. The excitation spectrum could be easily understood starting from the strong coupling limit, $J_\parallel/J_\perp \to 0$: the ground state is a simple product of singlets sitting on each rung, see Fig 3b. Excited N-particle states (where N is the number of triplets) are highly degenerate and are obtained by exciting elementary triplets on N different rungs [3, 4, 5, 22]. The nature of the ground and first excited states evolves smoothly when a small $J_\parallel$ is present. This allows the rung triplets to propagate along the ladder giving rise to dispersion in the reciprocal space. The bandwidth is proportional to $J_\parallel$ and the band minimum of the one-triplet branch is at the Brillouin one boundary, $k = \pi$ [22]. In the limit of uncoupled AF $S = 1/2$ chains, $J_\parallel/J_\perp \to \infty$, the result is also known and the ground state is characteri ed by an algebraic decay of magnetic correlations, the excitation spectrum is gapless with soliton-like $S = 1/2$ excitations (spinons) [23].

The picture described above is supported by theoretical calculations, and it turns out that in the general case the 'physics' of undoped 2LL's is dominated by the strong coupling limit.

- *The ground state* is disordered and has exponential falloff of the spin-spin correlations. A good description of the magnetic correlations is achieved within the resonance valence bond (RVB) model [24]. For a pictorial representation see Fig. 6b. Although a high $J_\parallel/J_\perp$ increases singlet correlations beyond nearest-neighbors, a ground state built up as a superposition of short-ranged resonating valence bonds remains a good approximation. For odd-leg ladders long-ranged singlets must be included in the ground state description [24].

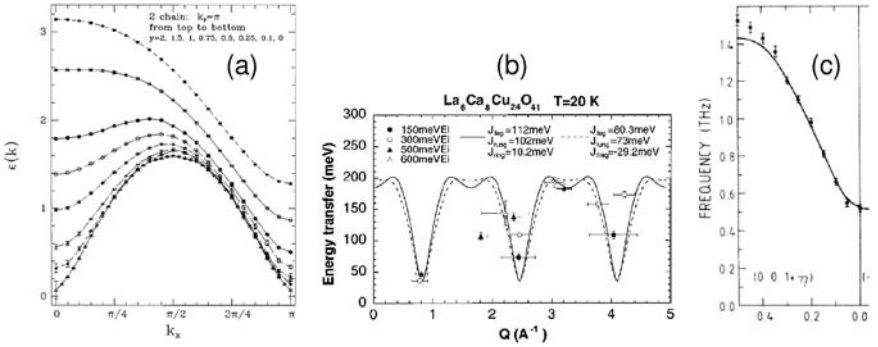

Fig. 4. (**a**) Results of series expansions calculations (Ref. [25]) around the Ising limit for a two-leg ladder Hamiltonian, Eq.(1.1). From top to bottom the elementary one-magnon excitation was computed for a decreasing ratio $J_\perp/J_\parallel$ from 2 to 0. The limit $J_\perp/J_\parallel \to 0$ corresponds to spinons, the limit $J_\perp/J_\parallel \to \infty$ corresponds to uncoupled dimers on the ladder rungs. (**b**) Neutron scattering results for the elementary triplet dispersion in $La_6Ca_8Cu_{24}O_{41}$ (from Ref. [26]) (**c**) Dispersion inferred from neutron scattering data (Ref. [27]) along the chain direction in the Haldane system $CsNiCl_3$. The similarity with Fig. 4a becomes obvious in the strong coupling limit, $J_\perp > J_\parallel$.

- *The one particle excitations* of the ladder have a gap Δ_S because any finite $J_\perp$ confines the $S = 1/2$ spinons binding them to an integer $S = 1$ 'magnon'. Results of series expansions around the Ising limit for 2LL's at various couplings $= J_\parallel/J_\perp$ from Ref. [25] are shown in Fig. 1.4a. These results are further confirmed by exact diagonali ations [5], numerical [22] and perturbative [28] analysis. It has been also found that the spin gap remains finite for even leg ladders (although the gap decreases with increasing the number of legs) while odd-legged ladders are gapless and have a power law fall-off of spin-spin correlations [24]. This resembles the gapless and gapped alternance of the spectrum for isotropic AF half-integer and integer spin chains [29]. The similarity is not accidental since a spin S chain can be described as $2S$ coupled spin $S = 1/2$ chains with appropriately chosen interchain coupling. This analogy is beautifully confirmed by the dispersion found above the Néel temperature in an experimental reali ation of a Haldane system, $CsNiCl_3$, a quasi-1D nearly isotropic $S = 1$ AF chain [27]. In Fig. 4 we show for comparison the experimental elementary magnon dispersion in $CsNiCl_3$ along with experimental data and theoretical predictions for 2LL.

- *The two-particle states*: The elementary magnon branch will generate a two-magnon continuum starting from $2\Delta_S$ at $k = 0$. In addition, this spectrum contains additional magnetic bound/antibound states. These are states with discrete energies which are found below/above the two particle continuum [30]. Bound states have been found in the singlet ($S = 0$), triplet ($S = 1$) and quintuplet ($S = 2$) sec-

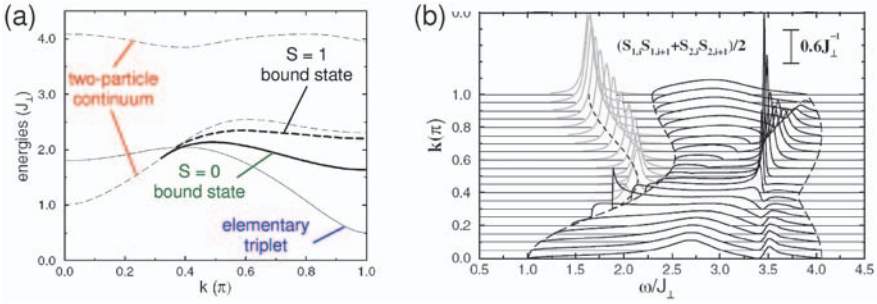

Fig. 5. (**a**) Excitation spectrum in the one and two-particle channels at isotropic coupling $J_{\parallel}/J_{\perp} = 1$ from Ref. [28]. The elementary triplet, the two-particle continuum as well as the two-magnon singlet and triplet bound states are indicated in the figure. (**b**) The k-resolved spectral density $I(k,\omega)$ of the $\mathbf{S}_{i,1} \cdot \mathbf{S}_{i+1,1} + \mathbf{S}_{i,2} \cdot \mathbf{S}_{i+1,2}$ operator. This is proportional to the magnetic Raman response in parallel polari ation with the electric field along the leg direction. The divergences observed around $k \approx 0.6$ are due to the hump-dip structure of the $S = 0$ bound state in (**a**). Data from Ref. [28].

tors. A typical excitation spectrum calculated perturbatively for isotropic coupling, $J_{\parallel}/J_{\perp} = 1$, and containing several types of two-particle excitations discussed above is shown in Fig. 5. A particularity of 2LL's is the fact that the bound states 'peel off' the continuum at finite values of k. The importance of higher order spin terms will be stressed in the following sections in connection with data analysis. This analysis will show that one has to go beyond the nearest neighbor Heisenberg Hamiltonian of Eq. (1) in order to explain the experimental data. Regarding the question whether the best description at all energies is in terms of fractional or integer spin excitations, it is worth noticing that, at least in the limit $J_{\parallel}/J_{\perp} \leq 1$, there is no necessity to resort to fractional spin states. A description in terms of truly bosonic excitations works well in the sense that spectral densities of spin-ladders can be described well by using integer spin excitations [28].

2.3 Low Temperature Two-Magnon Light Scattering in $Sr_{14}Cu_{24}O_{41}$

In this section we will discuss symmetry, spectral and resonance properties of the 2M excitation in $Sr_{14}Cu_{24}O_{41}$ at T = 10 K. Figure 6 shows Raman spectra in (cc), (aa) and (ac) polari ation taken with an excitation energy $\omega_{in} = 1.84$ eV. The spectra consist of a lower energy part where phonons are observed (see caption of Fig. 6) and a sharp asymmetric peak at 3000 cm^{-1} present in parallel polari ations. In both (aa) and (cc) polari ations the 3000 cm^{-1} peak is situated at exactly the same energy. In (ac) polari ation this feature is not present. The energy of the 3000 cm^{-1} mode, much larger than the relevant magnetic interactions in the chain structures, allows an unambiguous assignment of this excitation to the ladder systems. A comparison with the 2D tetragonal cuprates [31, 32]

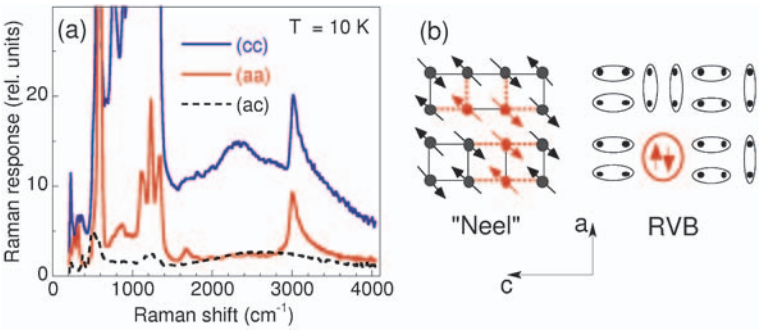

Fig. 6. (**a**) Low temperature Raman spectra in several polari ations. The sharp, asymmetric peak at 3000 cm^{-1} is the two-magnon feature. The strong features below about 1200 cm^{-1} as well as the bump around 2350 cm^{-1} (which has about four times the energy of the 580 cm^{-1} Oxygen mode) in (*cc*) polari ation represent single and multi phonon excitations. (**b**) Cartoon showing the two-magnon excitation. Left: assuming a local AF Néel order the spin exchange can take place along the rungs/legs of the ladder. Broken bonds and exchanged spins are shown in red. Right: a snapshot of the short-range RVB ground state which is a superposition of states like the top figure. The bottom picture represents a locally excited singlet state of two triplets.

in terms of energy scales argues for the interpretation of the 3000 cm^{-1} peak in terms of ladder 2M excitations. Moreover, in 2D cuprates the 2M feature has B_{1g} symmetry, this representation becoming the identical representation in the orthorhombic group to which the ladder structure belongs. Indeed, as can be seen from Fig. 6, in $Sr_{14}Cu_{24}O_{41}$ this excitation is fully symmetric.

Although for the 2D cuprates a semi-classical counting of broken magnetic bonds within a local Néel environment (see Fig. 6b) gives a good estimate ($3J$) for the 2M energy (which is found by more elaborate calculations to be situated around 2.7 J), in 2LL's this approach is not suitable. On one hand any small anisotropy in the exchange parameters $J_{\parallel}$ and $J_{\perp}$ should lead to different peak energies in (*aa*) and (*cc*) polari ations, see Fig. 6b, which is not observed, and on the other hand, even in the improbable case of less than 0.03% anisotropy given by our energy resolution, this 'Ising counting' estimates $J \approx 200$ meV which is almost 50% higher than the super-exchange in related 2D cuprates. The failure of this approach may be related to the fact that the ground state of the 2LL's cannot be described classically. A RVB description of the ladder ground state has been proposed [24]. This can be understood as a coherent superposition of 'valence bonds', which are spin singlets, shown in Fig. 6c. For even leg ladders the RVB states are short ranged (the singlets extend only over nearest neighbor Cu spins) and in this context, starting from an 'instantaneous configuration' of the ground state, the 2M excitation can be visuali ed as a state in which two neighboring singlets get excited into a higher energy singlet state made out of two triplet excitations.

Symmetry – The polarization selection rules for the 2M scattering can be explained using the effective spin Hamiltonian corresponding to the photon induced spin exchange process [33, 34] which reads

$$H_{FL} \propto \sum_{<i,j>} (\mathbf{e}_{in} \cdot \mathbf{r}_{ij})(\mathbf{e}_{out} \cdot \mathbf{r}_{ij})\mathbf{S}_i \cdot \mathbf{S}_j \tag{2}$$

where $\mathbf{S}_i$, $\mathbf{S}_j$ are Cu spins on the lattice sites i and j, $\mathbf{r}_{ij}$ in the vector connecting these sites and $\mathbf{e}_{in}/\mathbf{e}_{out}$ are the unit vectors corresponding to the incoming/outgoing polarizations. The polarization prefactor shows that the 2M scattering should occur only in parallel polarizations, consistent with the experimental observations.

Determination of J's – The problem of quantitatively estimating the magnitude of the super-exchange integrals is non-trivial in spite of the fact that there are several experimental techniques which probed magnetic excitations like neutron scattering [17, 26], Raman [35, 36] and IR spectroscopy [37, 38]. For the latter technique, the authors claim that the strong mid-IR absorption features between 2500 and 4500 cm^{-1} are due to phonon assisted 2M excitations. The main problem was to reconcile by using only the Hamiltonian from Eq. (1) the smallness of the one boundary spin gap $\Delta_S = 32$ meV [17] with respect to the magnitude of the one triplet energies close to the Brillouin one center (see Ref. [26] and Fig. 4), which is thought to determine the position of the 2M Raman peak [39] as well as the structure and the large energy range in which the mid-IR magnon absorption is seen [37, 38]. The proposed solution to this problem was to consider, besides $J_\parallel$ and $J_\perp$ the presence of a ring exchange J_{ring} [40], which is a higher order spin correction whose effect can be understood as a cyclic exchange of the spins on a square plaquette determined by two adjacent ladder rungs, see Fig. 4. The net effect of including such an interaction, which has the form $H_{ring} = 2J_{ring}[(\mathbf{S}_{1,i} \cdot \mathbf{S}_{1,i+1})(\mathbf{S}_{2,i} \cdot \mathbf{S}_{2,i+1}) + (\mathbf{S}_{1,i} \cdot \mathbf{S}_{2,i})(\mathbf{S}_{1,i+1} \cdot \mathbf{S}_{2,i+1}) - (\mathbf{S}_{1,i} \cdot \mathbf{S}_{2,i+1})(\mathbf{S}_{1,i+1} \cdot \mathbf{S}_{2,i})]$, is to renormalize down the spin gap so that the ratio of the magnon energy at the one boundary with respect to the one at the one center is decreased. The introduction of $J_{ring} \approx 0.1 J_\perp$ helped fitting the INS data (see Ref. [26] and Fig. 4) and an even higher ratio is able to better reproduce the experimental Raman and IR data (see Fig. 7). The parameter sets used for the quantitative analysis of the spectroscopic data have $J_\parallel/J_\perp$ between 1.25 and 1.3 and a sizeable cyclic exchange, $J_{ring}/J_\perp$ of about 0.25 - 0.3. The absolute value chosen for $J_\perp$ is 1000 - 1100 cm^{-1}. Both the value of J and J_{ring} are quantitatively consistent with those inferred for the 2D AF cuprates [41]. In the latter case, the cyclic exchange was used in order to reproduce the neutron scattering findings regarding the k dependence of the energy of the one-magnon excitations in the proximity of the Brillouin one boundary [41]. However, as opposed to the cuprates, the 2M seen in Fig. 6 at 3000 cm^{-1} cannot provide a direct determination of the super-exchange, even if no terms other than $J_\parallel$ and $J_\perp$ had to be included in the spin Hamiltonian. This problem is related to the fact that, in spite of the theoretical results shown in Fig. 7b which suggest good agreement with the experiment, the spectral shape of the sharp 2M feature and its origin is still an open question; this issue will be discussed in the following.

Two-magnon relaxation – While in the case of 2D cuprates theory has problems with explaining the large scattering width of the 2M excitation, in 2LL's the situation

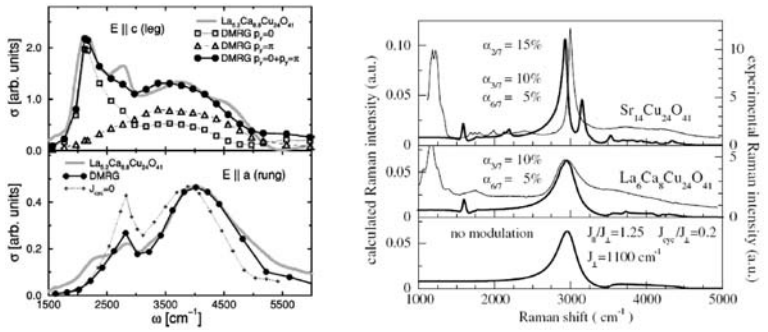

Fig. 7. Left: IR absorption data (thick grey line) for two polari ations of the electric field along with theoretical calculations for the phonon assisted two-magnon absorption (from Ref. [38]). The parameters used are: $= J_{\|}/J_{\perp} = 1.3$, $J_{\perp} = 1000$ cm^{-1} and a ring/cyclic exchange (see text and Fig. 4) $J_{ring}/J_{\perp} = 0.2$ Right: Calculated (thick lines) Raman response for the two-magnon scattering using a perturbative approach from Ref. [39]. The parameters used are: $= J_{\|}/J_{\perp} = 1.25$, $J_{\perp} = 1100$ cm^{-1} and $J_{ring}/J_{\perp} = 0.2$. The experimental data (thin lines) in $La_6Ca_8Cu_{24}O_{41}$ and $Sr_{14}Cu_{24}O_{41}$ are taken from Ref. [35]. The upper two panels are calculated using an additional super-modulation on the magnon dispersion due to the interaction induced by the charge ordering in the chain structures (see the text for discussion). The parameter α specifies the kind of the superimposed supermodulation.

is reversed; this is one of the most interesting points made in Ref. [36]. To emphasi e the 2M sharpness, we compare it in Fig. 8 to the corresponding excitation in $Sr_2CuO_2Cl_2$ which has one of the sharpest 2M feature among 2D AF copper oxides [31] as well as to the multi-spinon scattering from a 2LL at quarter filling (which can be mapped on a quasi 1D $S = 1/2$ AF chain), as seen in the high temperature phase of NaV_2O_5. For $Sr_2CuO_2Cl_2$ the FWHM is about 800 cm^{-1} [31] and this is comparable, in relative units, with the large scattering width observed for the spinon continuum. In $Sr_{14}Cu_{24}O_{41}$ the width is only about 90 cm^{-1}. The 2M approximation for the magnetic light scattering in 2D cuprates, while giving a good estimate for the 2M peak energy, cannot reproduce its spectral profile. This approximation makes the following three basic assumptions:

- the ground state is a fully ordered Néel state;
- the spin pair excitations consist of states which have exactly two spins flipped with respect to the Néel configuration;
- since the light wavelength is much larger than the unit cell, only combinations of $(k, -k)$ magnons are allowed.

This approach neglects quantum fluctuations which means that the true ground state will also contain configurations of flipped spins and also that the spin-pair states will be

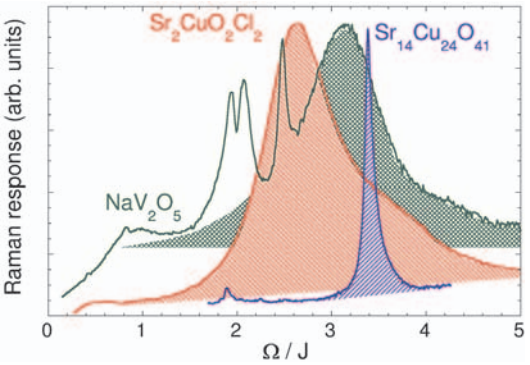

Fig. 8. Magnetic Raman continua in several AF spin $S = 1/2$ systems. Red: $Sr_2CuO_2Cl_2$ (a 2D square lattice with long range order). Green: NaV_2O_5 (a two-leg ladder at quarter filling factor which can be mapped on a quasi 1D AF chain). Blue: $Sr_{14}Cu_{24}O_{41}$, the excitation seen in Fig. 7 but in this case taken with $\omega_{in} = 2.65$ eV incoming laser energy.

admixtures of 2, 4, 6 ... spin flips in the ground state. The narrow calculated width of the 2M was found, however, to be stable with respect to the inclusion of higher order spin interactions. Neither exact diagonali ation nor Monte Carlo simulations were able to fully reproduce the 2M scattering width [42] although these calculations improved the results obtained within the 2M approximation. It has been proposed by Singh *et al.* in Ref. [43] that it is the quantum fluctuations effects inherent to the Heisenberg model with $S = 1/2$ which lead to the observed broadening. The importance of intrinsic inhomogeneities and the role of phonons have also been invoked in the literature.

We were surprised that even in lower dimensionality (the structure determined by the 2LL's is quasi-1D), where the quantum fluctuations are expected to be stronger, the 2M Raman spectra display a narrow profile, a phenomenon which questions the importance attributed to these effects in low spin systems [43]. This prominent question triggered theoretical work, part of which is shown in Fig. 7. The authors of Ref. [39] challenged our point and claimed a resolution in terms of both the existing quasi-commensuration between the unit cell constants of the chain and ladder structures ($7\, c_{ladder} \approx 10\, c_{chain}$) and the supermodulation induced by the charge order in the chain structures, which is shown in Fig. 2. The calculation of the 2M Raman response without the modulation (lower panel in Fig. 7b) reveals indeed a broader 2M peak [44], while inclusion of chain-ladder interaction renders a sharp 2M excitation because of the backfolding of the dispersion of the elementary triplet (Figs. 1 and 2 in Ref. [39]). This opens gaps at the points of intersection with the supermodulation wavevectors and will have a drastic effects in the spectral shape because of the induced divergences in the density of states.

The agreement with the experimental data in Fig. 7 is pretty good; however, these claims have recently been put to rest by a Raman experiment, Ref. [45], in the undoped 2LL compound $SrCu_2O_3$ (which contains no chains but only undoped 2LL's), experiment which revealed a 2M peak as sharp as in $Sr_{14}Cu_{24}O_{41}$. This clearly shows that the sharpn-

ess is related neither to the interaction between the two substructures in $Sr_{14}Cu_{24}O_{41}$ nor to the residual carriers in the 2LL structure of $Sr_{14}Cu_{24}O_{41}$ but instead it is due to intrinsic 2LL's effects. Two major differences between the 2LL's and 2D cuprates or 1D AF spin chains are the facts that in the former the low energy relaxation channels are suppressed due to the presence of a spin gap and also that the excitation spectrum of 2LL's supports the existence of magnetic bound states outside the continuum of excitations. Although this may be a plausible explanation, the 2M singlet bound state peels off the continuum only at finite values of k, see Fig. 5, and besides that, the energy at $k = 0$ is too small ($2\Delta_S = 64$ meV $= 512$ cm^{-1}) to account for the observed peak energy at 3000 cm^{-1}. If the sharpness is from the hump-dip feature in the dispersion of the elementary triplet close to the Brillouin one center, Fig. 5b and the corresponding Van Hove singularities, it seems that such divergences are found only at finite values of k while at $k = 0$ the spectral density is quite broad [28]. This is why we suggest here an explanation in relation to a possible spin density wave (SDW) modulation which is intrinsic to 2LL's and will lead to a backfolding of the magnon dispersion. This effect is similar in spirit with the one proposed in Ref. [39] but this time due to intrinsic effects. Regarding the asymmetry of the 2M feature it would also be worth considering multi-magnon interaction effects which may lead to the asymmetric Fano-like shape of the sharp 3000 cm^{-1} feature due to the interaction with the underlying magnetic continuum.

Noteworthy is the resemblance of the elementary triplet dispersion in 2LL's and the k dependence of the one-magnon excitation in La_2CuO_4 away from the Brillouin one center. There are several articles, some of them very recent [46], which stress the failure of the spin wave models in 2D cuprates arguing that the 'physics' of magnetic excitations is fundamentally different at low and high energies: while semi-classical magnon theory holds at low energies, it has been argued that at short wavelengths the effect of fluctuations is more pronounced and the spin dynamics suggest an underlying structure similar to the one provided by 2LL's, which is due to a SDW-like modulation in the 2D planes. Interestingly, the data in $Sr_2CuO_2Cl_2$ and NaV_2O_5 from Fig. 8 suggest instead a more pronounced similarity to the magnetic scattering in 1D $S = 1/2$ AF chains. It seems at this point that not only the 2M profile in 2LL's but also the one in 2D cuprates constitute open questions which have recently received renewed attention. It would be very interesting if the physics in these two systems is found to be related to each other.

Two-magnon excitation profile – A summary of our experimental study of the 2M dependence on the incoming photon energy is shown in Fig. 9. Like the 2D cuprates, the Cu-O based ladders are known to be charge-transfer (CT)-type Mott insulators, the CT gap being determined by the energy difference between the Cu $3d$ and O $2p$ orbitals. A Raman resonant study is interesting since, along with optical absorption, it gives information about the nature of the ground as well as of high energy electronic states across the CT gap. This is because the photon induced spin exchange takes place in two steps: a photoexcited state consisting of an electron-hole pair is created by the interaction of the system in its ground state with an incoming photon and then this intermediate state collapses into an excited magnetic state characteri ed by broken AF bonds. One expects therefore that such a process, in which the interaction with light occurs in the 2^{nd} order perturbation theory, will show a strong dependence on the incoming photon energy [31].

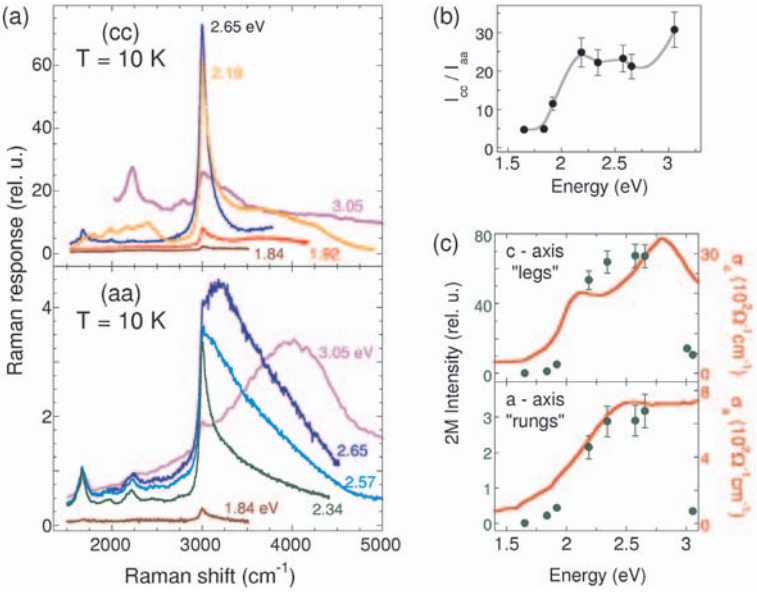

Fig. 9. Two-magnon resonance profile in $Sr_{14}Cu_{24}O_{41}$ at T = 10K. (**a**) Data in (*cc*) (upper panel) and (*aa*) (lower panel) polari ations for different excitation energies ω_{in}. (**b**) The relative intensity of the 2M excitation in (*cc*) compared to (*aa*) polari ation as a function of the incoming photon energy. (**c**) The resonance profile of the 2M peak (filled circles, left scale) and the optical conductivity (solid line, right scale). As in (**a**), the upper/lower panels refer to the data in which the electric field is parallel to the ladder legs/rungs.

This is what we observe in $Sr_{14}Cu_{24}O_{41}$: the Raman data at T = 10 K are shown in Fig.9a. In Fig. 9b we show the ratio of the 2M intensity in (*cc*) polari ation with respect to (*aa*) configuration as a function of ω_{in} and in Fig. 9c the resonant Raman excitation profile (RREP) is plotted along with the optical conductivity data provided by the authors of Ref. [10]. For both (*cc*) and (*aa*) polari ation the resonant enhancement has a maximum around 2.7 eV, about 0.7 eV higher than the CT edge. The intensity is small for $\omega_{in} < 2$ eV and increases monotonically as the photon energy approaches the CT gap, this increase being followed by a drop for excitations about 3 eV. The intensity displays an order of magnitude variation as the incident photon energy changes in the visible spectrum. Besides the correction for the optical response of the spectrometer and detector, by using the complex refractive index derived from ellipsometry and reflectivity measurements, the 'raw' Raman data were also corrected for the optical properties of the material at different wavelengths.

We observe changes in the spectral shape of the 2M as the incident frequency is changed, in the 2LL's case the 2M acquiring sidebands on the high energy side. These changes are more pronounced in (*aa*) polari ation where for instance the 2.65 eV spectrum (which is close to the edge seen in the *a*-axis conductivity) shows a 2M as a gap-like onset

of a continuum. While the fact that the 2M profile changes substantially with ω_{in} is also true for 2D cuprates, one can notice several differences too. One of them is that the RREP in 2LL's follows more closely the edges of the optical conductivity data. Moreover, if in the case of cuprates *two* peaks were predicted (and confirmed experimentally) to occur for the 2M peak at $2.8J$ in the RREP [47] (when the incoming energy is in resonance with the bottom and top of the electron-hole continuum) from the data we show in Fig. 9c up to $\omega_{in} = 3.05$ eV we observe only one, rather broad, peak. It has been argued from numerical diagonali ations of finite clusters [48] that this dissimilarity between the 2D cuprates and 2LL's is due to the difference in the spin correlations characteri ing the initial and final excited magnetic states, i.e. the weight of the long ranged Néel type spin-spin correlations in calculating the matrix elements of the current operator plays an important role.

It also turns out that, due to the special topology of 2LL's, a study of the 2M RREP in conjunction with an angular dependence of the 2M intensity in parallel polari ation in 2LL's can be helpful for determining a relation between the ratio of the super-exchange integrals $J_{\parallel}$ and $J_{\perp}$ and microscopic parameters like hopping integrals and on site Coulomb interactions [49]. Using the effective expression for the photon induced spin exchange coupling mechanism, Eq. (2), taking into account the anisotropy of the coupling constants denoted by A and B along the rung and leg directions and using the relationship between H_{FL} and the 2D Heisenberg ladder Hamiltonian from Eq. (1), one can derive the following angular dependence of the 2M intensity for $\mathbf{e}_{in} \parallel \mathbf{e}_{out}$: $I_{\parallel}(\omega,\theta) = I(\omega,\theta)[\cos^2(\theta) - \frac{A}{B}\frac{J_{\perp}}{J_{\parallel}}\sin^2(\theta)]$ [49]. From this formula, $J_{\perp}/J_{\parallel}$ can be calculated if the A to B ratio is known. At angles $\theta \neq 0°, 90°$ from an experimental point of view one has to be careful that the different optical properties of the ladder materials along the a and c axes will induce a non-negligible rotation of the polari ation of the incident electric field inside the crystal [50]. As we see from Fig. 9b the value of A/B is excitation energy dependent and our data suggest that this ratio approaches a constant value in the preresonant regime. From Fig. 9 and using an anisotropy ratio $= J_{\parallel}/J_{\perp} = 1.25$ (see Fig. 7) we obtain $A/B \approx 2.5$ in the preresonant regime, which would be compatible with an anisotropic local Cud-Op excitation and slightly different hopping parameters along and across the ladder [49].

3 Effects of Temperature and Ca(La) Substitution on the Phononic and Magnetic Excitations in $Sr_{14}Cu_{24}O_{41}$

3.1 Temperature Dependent Electronic and Magnetic Scattering in $Sr_{14}Cu_{24}O_{41}$

The effects of temperature and Ca(La) substitution for Sr discussed in this section set the stage for the following section in which low energy Raman, transport and soft X-ray data argue for the existence of density wave correlations in $(Sr,La)_{14-}$ Ca $Cu_{24}O_{41}$ compounds. In Fig. 10a we show the temperature dependence of the c-axis conductivity $\sigma_c(\omega)$ and in panel (b) the Raman response in $Sr_{14}Cu_{24}O_{41}$ for T =300 and 10 K. In both IR and Raman

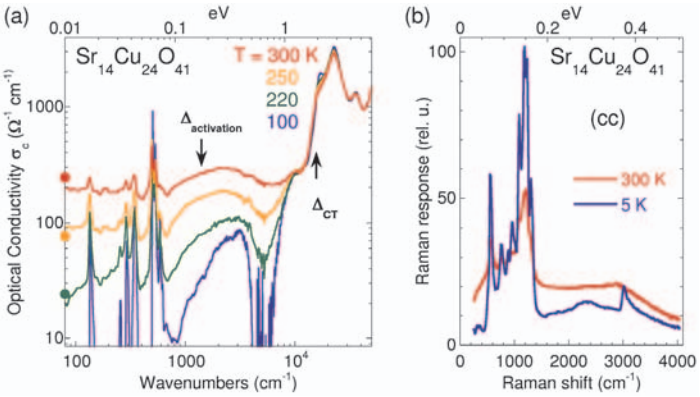

Fig. 10. (**a**) Temperature dependence of the *c*-axis optical conductivity (data provided by the authors of Ref. [51]) in log-log scale. The arrows point towards the activation energy determined by *dc* resistivity above about 150 K and the characteristic energy corresponding to the charge transfer gap. The circles on the vertical axis represent the *dc* conductivity values. (**b**) Raman response in $Sr_{14}Cu_{24}O_{41}$ taken with $\omega_{in} = 1.84$ eV in (*cc*) polari ation at 300 and 5 K.

data large changes are observed as the $Sr_{14}Cu_{24}O_{41}$ crystal is cooled from room temperature. In Fig. 10a there is a strong suppression of spectral weight below an energy scale of about 1 eV. The same figure shows two relevant energy scales of this system: one is the CT gap around 2 eV which was discussed in connection to the resonance properties of the 2M , and the other one is the activation energy inferred from the Arhenius behavior of the *dc* resistivity above about 150 K [52]. As for the optical sum rule, all the weight is recovered above the CT gap, within an energy scale of $\omega_c \approx 3$ eV. The rapid decrease of the conductivity in the region below 1 eV is correlated to the high activation energy of about 180 meV ($= 1450$ cm$^{-1} = 2090$ K). Concomitant to this suppression, which is surprisingly 'uniform' in the 0 to 1 eV range, one observes the development of a broad mid-IR feature and also a sharpening of the phononic features below 1000 cm^{-1}. Interestingly, the position of the mid-IR band seems to be close to the semiconducting-like activation energy revealed by the *dc* resistivity. Fig.10b shows that a similarly large reduction in the overall intensity of Raman response takes place in an energy range of at least 0.5 eV (4000 cm^{-1}). The features which become sharp with cooling are the single and multi-phonon excitations seen around 500, 1200 and 2400 cm^{-1} as well as the 2M feature at 3000 cm^{-1}.

In Fig. 11 we show temperature dependent Raman data in two frequency regions: one below 1000 cm^{-1} (panel a) and one around 3000 cm^{-1} where the 2M feature lies (panel b). A different spectral shape than in Figs. 6 and 10 is seen due to resonantly enhanced side band structures (see Fig. 9). The 2M peak is weak and heavily damped at room temperature. Upon cooling we notice two main features: firstly, the spectral weight increases by almost an order of magnitude, and secondly, the 2M peak sharpens from a width of about

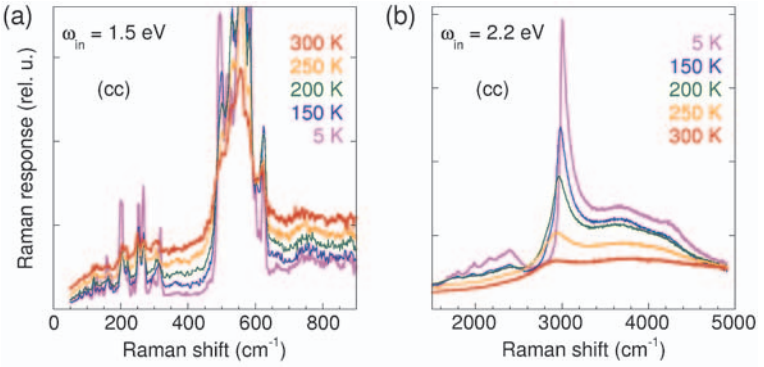

Fig. 11. Temperature dependent Raman spectra in (*cc*) polari ation for $Sr_{14}Cu_{24}O_{41}$. (**a**) Phononic spectra taken with $\omega_{in} = 1.5$ eV (some phonons are truncated). (**b**) The 2M peak at 3000 cm^{-1} for different temperatures. The spectra in this panel are taken using $\omega_{in} = 2.2$ eV

400 cm^{-1} at 300 K to 90 cm^{-1} FWHM at T = 10 K. Because J/k_BT remains a large parameter even at room temperature, the magnitude of the observed effects are surprising. For example, in 2D cuprates the 2M peak remains well defined even above 600 K [53]. The side bands around 3660 and 4250 cm^{-1} observed for the $\omega_{in} = 2.2$ eV also gain spectral weight, proportionally with the sharp 2M feature. Fig. 11b shows that these sidebands are situated about 650 and 2 $\times$650 cm^{-1} from the 3000 cm^{-1} resonance. Taking into account that strong phonon scattering characteristic of O modes is found at this frequency, one may argue that these side bands are due to coupled magnon-phonon scattering and bring evidence for spin-lattice interaction in $Sr_{14}Cu_{24}O_{41}$. These energy considerations favor this scenario compared to one involving multi-magnon scattering because the magnetic continuum starts lower, at $2\Delta_S = 510$ cm^{-1}. The latter interpretation remains however a reasonable possibility because in these higher order processes the spectral weight can integrate from a larger part of the Brillouin one and the boundary of the 2M continuum is dispersive.

The continuum shown in Fig. 11a also gets suppressed with cooling. Our data confirms the presence of low lying states at high temperatures, observed also in NMR and *c* axis conductivity, Refs. [6, 51] and Fig. 10. We observe that there is a sharp onset of scattering around 480 cm^{-1}, close to twice the spin-gap energy. The 495 cm^{-1} mode has been interpreted as evidence for Raman two-magnon scattering [35]. However, the temperature dependence of this mode which follows that of the other phonons, the similar suppression with cooling seen not only below this energy but also at higher energies in the 650 to 900 cm^{-1} region and the absence of magnetic field effects contradict this proposal.

The connection between the low and high degrees of freedom in Fig. 11a-b is presented in Fig. 12. The increase of the electronic Raman background intensity with heating is correlated with the damping of the 2M peak at 3000 cm^{-1}. The introduced low energy states reduce the lifetime of the magnetic excitation due to additional relaxational channels provided by the small amount of ladder self-doped carriers. We note that the drastic

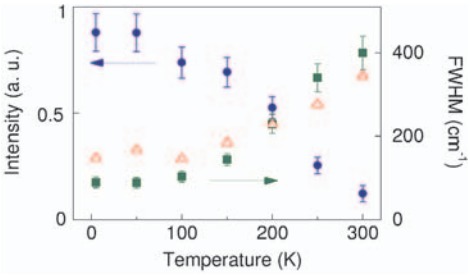

Fig. 12. The integrated intensity (blue circles, left scale), and the FWHM (green squares, right scale) of the two-magnon peak in $Sr_{14}Cu_{24}O_{41}$ from Fig. 11b as a function of temperature. The triangles represent the continuum intensity (in arbitrary units) around 700 cm^{-1} from the data in Fig. 11a.

changes with temperature take place roughly above 150 K while below this temperature the variation with temperature is much weaker. This is the temperature at which the *dc* resistivity changes its activation energy from 2090 K to about half its value, 1345 K [56]. $T^* = 150$ K is also the temperature at which the charge ordering in the chain structures is fully established [16, 18] suggesting an interaction between chains and ladders, possibly due to a charge transfer between these systems. It is possible that this charge transfer takes place also as function of temperature and that it gets suppressed below T^*.

3.2 The Chain-Ladder Interaction in $Sr_{14}Cu_{24}O_{41}$: Superstructure Effects in the Phononic Spectra

Raman data in $Sr_{14}Cu_{24}O_{41}$ reveals the presence of a very low energy excitation in parallel polari ations. At low temperatures this mode is found around 12 cm^{-1} and we observe a softening of about 20% with warming up to 300 K. The temperature dependence of the Raman spectra is shown in Fig. 13 for both (*cc*) and (*aa*) polari ations. An excitation at similar energy is seen also in IR absorption data [54] consistent with the lack of inversion symmetry in the $Sr_{14}Cu_{24}O_{41}$ crystal. Applied magnetic fields up to 8 T do not influence the energy of this excitation which suggests that its origin is not magnetic. This peak is absent in x = 8 and 12 Sr_{14-} Ca $Cu_{24}O_{41}$ crystals but it is present around 15 cm^{-1} in the $La_6Ca_8Cu_{24}O_{41}$ compound [55]. These properties along with the unusually low energy make us interpret this excitation as a phononic mode associated with the superstructure determined by the chain and the ladder systems. The chain-ladder commensurability given by the approximate relation 7 c_{ladder} = 10 c_{chain} will result in a back-folding of the phononic dispersions, which in the case of the acoustic branches will lead to a low energy mode. The high effective mass oscillator is understood in this context as a collective motion involving the large number of atoms in the big unit cell of the $Sr_{14}Cu_{24}O_{41}$ crystal.

In Fig. 13b-c we plot the temperature dependent energy and width of this low energy phonon. The crossover below a characteristic temperature of about 120 - 150 K mentioned in the previous subsection is emphasi ed again by the these data. The energy of the

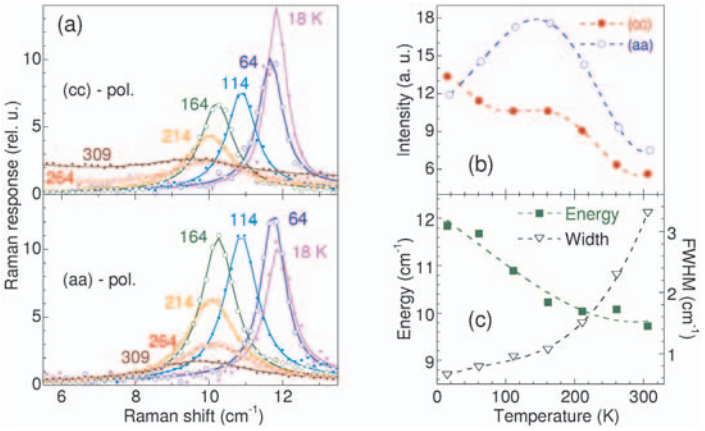

Fig. 13. (**a**) Temperature dependence of a low energy $Sr_{14}Cu_{24}O_{41}$ phonon taken with $\omega_{in} = 1.65$ eV in (*cc*) (upper panel) and (*aa*) (lower panel). Points represent Raman data and the solid lines are Lorent ian fits. (**b**) The dependence on temperature of the phonon intensity in (*cc*) (filled red circles) and (*aa*) (empty blue circles) polari ations. (**c**) The phonon energy (left scale) and the width (right scale) of the phononic excitation from (**a**). Dashed lines in panels (**b**) and (**c**) are guides for the eye.

peak increases rather uniformly with decreasing temperature from 300 to about 15 K but its FWHM shows a variation with temperature which is diminished below 150 K. The behavior of the integrated intensity of this mode is different in (*cc*) and (*aa*) polari ations. Fig. 13b shows that in (*cc*) configuration a kink appears about 150 K in the temperature dependent spectral weight while a maximum is seen in the (*aa*) polari ed spectra around this temperature.

In the scenario presented above the presence of the low energy mode Fig. 13 is evidence of ladder-chain interaction. Such an excitation should be sensitive to disorder and even slight modifications in the crystal structure as happens if Sr is substituted by Ca/La. Symmetry arguments discussed in the next subsection confirm the requirement to consider the full crystal structure for the phononic analysis in $Sr_{14}Cu_{24}O_{41}$ and the fact that the disorder introduced by Ca substitution smears out the rich phononic spectra due to the superstructure. The absence of this mode in Ca substituted crystals thus supports our interpretation.

3.3 Disorder Induced by Ca(La) Substitution

This part deals with the effects of inter Cu-O layers cation substitution. If Sr is replaced by Ca then the nominal hole concentration in Sr_{14-} Ca $Cu_{24}O_{41}$ does not change, but what may happen is that the amount of holes in the chain and ladder structures gets redistributed [10, 11]. Sr^{2+} substitution by La^{3+} reduces the amount of holes and in $La_6Ca_8Cu_{24}O_{41}$ the chains and the ladders are at half filling. So in analy ing the

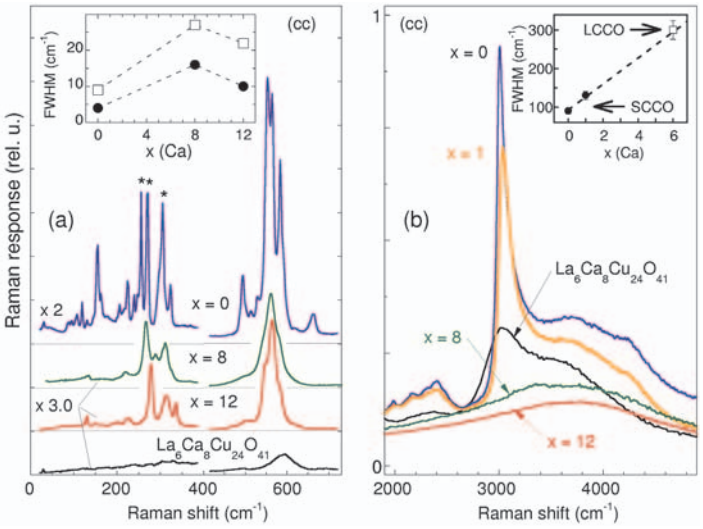

Fig. 14. (**a**) T = 10 K Raman data for ω_{in} = 2.57 eV in $La_6Ca_8Cu_{24}O_{41}$ and Sr_{14-} Ca $Cu_{24}O_{41}$ with x = 0, 8, 12 in (*cc*) polari ation. The inset shows the full width at half maximum of the 255 and 565 cm^{-1} phonons which corresponds to Sr(Ca) (filled circles) and O (empty squares). Dashed lines are guides for the eye. (**b**) Two-magnon spectra taken with ω_{in} = 2.2 eV in (*cc*) polari ation at T = 10 K in $La_6Ca_8Cu_{24}O_{41}$ and Sr_{14-} Ca $Cu_{24}O_{41}$ with x = 0, 1, 8, 12. The inset shows the FWHM of the 3000 cm-1 peak as a function of the numbers of Ca atoms in the formula unit.

spin/charge response of the 2LL's one has to consider both the doping and the disorder effects induced by inter-layer cation replacement.

An investigation of these effects is certainly worth pursuing in the context of the constraints imposed by the low dimensionality on the charge dynamics and the occurrence of superconductivity. Most of the studies in the literature have been focussed on the spin and charge dynamics in pure crystals, although cation substitution is also a source of a random potential. It is known that in 1D an arbitrary random field locali es all electronic states [57] and, in view of the existence of collective excitations of the charge density wave type, pinning effects due to disorder change qualitatively the *dc* and the finite frequency transport properties. X-ray structural analysis show that the ladder interatomic bonds are modulated upon Sr replacement by Ca [58] and it was pointed out in a Raman study [59] that the phononic width increases with Ca concentration in Sr_{14-} Ca $Cu_{24}O_{41}$. Theoretical work shows that the gapped phases of 1D spin systems like 2LL's or dimeri ed chains are stable against weak disorder and magnetic bond randomness [60]. However, in the doped case, superconductivity in the *d*-channel was found to be destroyed by an arbitrarily small amount of disorder.

Ca substitution and phononic scattering – If inhomogeneous broadening plays an important role it has to be seen in all the sharp spectroscopic features. What we

try to argue in the following is that the width of both cation and the Cu-O plane modes are renormali ed with Ca content. Fig. 14a shows low temperature phononic Raman spectra in the 0 - 700 cm^{-1} energy region. The data is taken in (*cc*) polari ation with the excitation energy $\omega_{in} = 2.57$ eV; the higher the incoming photon energy the more pronounced is the phononic resonant enhancement. For $Sr_{14}Cu_{24}O_{41}$ we observe a total of 22 clearly resolved phononic modes extending from 25 to 650 cm^{-1}. For $La_6Ca_8Cu_{24}O_{41}$ and Sr_{14-} Ca $Cu_{24}O_{41}$ crystals the features characteristic of O vibrations in the $400 < \omega < 700$ cm^{-1} region broaden into an unresolved band and the rich fine structure below $\omega < 400$ cm^{-1} is smeared out. Clear evidence for the interaction between the chain and the ladder structures in $Sr_{14}Cu_{24}O_{41}$ can be inferred from symmetry considerations alone. If these two units were considered separately a total number of six fully symmetric phonons should be observed in (*cc*) polari ation [61], three from the chain structure, *Amma* (D_{2h}^{17}) space group, and three from the ladder structure, *Fmmm* (D_{2h}^{23}) space group [1]. If one considers the full crystal structure, two 'options' are available. The first one is to take into account a small displacement of the adjacent Cu-O chains with respect to each other (see Fig. 3 in Ref. [1]) and analy e the phonons within the *Pcc*2 (C_{2v}^{3}) space group which will give a total of 237 A_1 modes. The second one is to neglect this small displacement, as it is the case of $Sr_8Ca_6Cu_{24}O_{41}$ which belongs to the *Cccm* (D_{2h}^{20}) centered space group [1] and this approach renders a number of 52 A_{1g} modes. The 22 observed modes in $Sr_{14}Cu_{24}O_{41}$ show that one has to include the chain-ladder interaction and the consideration of the higher *Cccm* symmetry is sufficient.

Marked with asterisks in Fig. 14 are three modes in the region between 250 and 320 cm^{-1} which show a blue shift consistent with the lower mass of Ca atoms and the reduction in the lattice constants upon Ca substitution [12]. Based on the energy shift and on previous phonon analysis done for the $(SrCa)_2CuO_3$ [62] compound we assign the modes to Sr/Ca vibrations. The FWHM of the 255 cm^{-1} phonon in $Sr_{14}Cu_{24}O_{41}$ is 4 cm^{-1} as compared to 16 and 10 cm^{-1} in the x = 8 and 12 Sr_{14-} Ca $Cu_{24}O_{41}$ samples respectively. We observe a similar behavior in the phononic modes originating from Cu-O planes. Three prominent features are seen in the 550 – 600 cm^{-1} region for the $Sr_{14}Cu_{24}O_{41}$ crystal. We assign the mode with intermediate energy around 565 cm^{-1} to O_{ladder} vibration. The lower and upper modes around 545 and 585 cm^{-1} have frequencies close to vibrations of the O atoms in the chains as observed in $(SrCa)_2CuO_3$ and CuO [61, 62] compounds. Fits for the 550 cm^{-1} band in SCCO crystals reveal that the FWHM of the 565 cm^{-1} mode increases from 9 cm^{-1} for $Sr_{14}Cu_{24}O_{41}$ to 27 and 22 cm^{-1} for x = 8 and 12 Sr_{14-} Ca $Cu_{24}O_{41}$ crystals, see the inset of Fig. 14a. This is similar to what happens to the 255 Ca/Sr mode suggesting that the Sr_{14-} Ca $Cu_{24}O_{41}$ crystals become again more homogeneous at higher Ca substitution level. The data for the LCCO crystal shows that in this material phonons are affected the strongest by disorder which is most likely due to the high La mass and atomic si e compared to Ca or Sr atoms.

Ca substitution and magnetic scattering – Regarding the sharp 2M Raman resonance, Fig. 14b, one can see dramatic changes taking place with Ca substitution at T = 10 K and that these changes also affect the 2M sidebands. In $Sr_{14}Cu_{24}O_{41}$ the FWHM is 90 cm^{-1}. Ca substitution leads to hardening and to substantial broadening of the magnetic peak accompanied by a drastic decrease in its scattering intensity. One

Ca atom in the formula unit of Sr_{14-} Ca $Cu_{24}O_{41}$ increases the spectral width by 30%, see inset of Fig. 14b. This effect can be ascribed to the intrinsic inhomogeneity rather than a marginal effect on the lattice constants and hole transfer from the chains to the ladders [10]. The FWHM in x = 8 Sr_{14-} Ca $Cu_{24}O_{41}$ and $La_6Ca_8Cu_{24}O_{41}$ are about the same within the error bars which is remarkable because the latter is an undoped material so the width of the peak seems not to be related to the presence of carriers in the ladders. Comparison of our data in $La_6Ca_8Cu_{24}O_{41}$ and $SrCu_2O_3$ [45], both containing 2LL's at half filling, shows clearly that out-of-plane inhomogeneities have major impact on the magnetic properties of the ladders.

By comparing Fig. 11b and 14b One can also note a resemblance between the effect of temperature in $Sr_{14}Cu_{24}O_{41}$ and Ca substitution in Sr_{14-} Ca $Cu_{24}O_{41}$. Fig. 15 shows that temperature effects in $La_6Ca_8Cu_{24}O_{41}$ and $Sr_6Ca_8Cu_{24}O_{41}$ are suppressed compared to $Sr_{14}Cu_{24}O_{41}$. In this sense one could introduce an 'effective' temperature associated with the cation substitution level. A comparison to 2D cuprates is again interesting: in the latter case the 2M is broad to start with even in pure materials, but a different number of cation types between the Cu-O layers (higher in insulating $Bi_2Sr_2Ca_{0.5}Y_{0.5}Cu_2O_8$ than for instance La_2CuO_4) does not lead to qualitative changes in the 2M width [32].

The data in Fig. 14b suggest that an appropriate phenomenological model to describe the ladder Hamiltonian in Ca doped crystals is $H = \sum_{leg} J_{||}^{ij} \mathbf{S}_i \cdot \mathbf{S}_j + \sum_{rung} J_{\perp}^{ij} \mathbf{S}_i \cdot \mathbf{S}_j$ where the super-exchange integrals J^{ij} in the lowest order have a contribution proportional to the relative local atomic displacements $\mathbf{u}_{ij}$ according to $J^{ij}(\mathbf{u}) = J_0 + (\nabla J)\mathbf{u}_{ij}$. The effects of thermal fluctuations on the super-exchange integrals J_{ij} can be included in a similar phenomenological approach [63] which could explain the strong resemblance between the Ca substitution and temperature seen in Figs. 14b and 15. We expect the ratio $< J_{\perp} > / < J_{||} >$ to change with Ca content as structural studies show that the Cu-O bonds along the rungs are less affected by Ca substitution than the Cu-O bonds parallel to the ladder legs [58]. Also the hardening of the magnetic peak from 3000 cm^{-1} in $Sr_{14}Cu_{24}O_{41}$ to about 3375 cm^{-1} in x = 8 Sr_{14-} Ca $Cu_{24}O_{41}$ is consistent with the reduction in the lattice constants at higher Ca substitutional level which will lead to a higher super-exchange J, a parameter very sensitive to the interatomic distances [64].

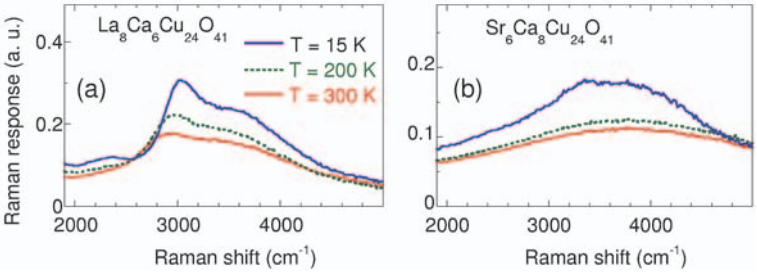

Fig. 15. Two-magnon scattering in $La_6Ca_8Cu_{24}O_{41}$ and x = 8 Sr_{14-} Ca $Cu_{24}O_{41}$ in (*cc*) polari ation for three temperatures.

4 Density-Wave Correlations in Doped Two-Leg Ladders

4.1 Density Waves: Competing Ground State to Superconductivity

So far we have been investigating mainly the magnetic properties of 2LL's around half filling factor and analy ed the effects of temperature and Sr substitution especially in terms of their influence on the high energy 2M scattering around 3000 cm^{-1}. We observed that both the temperature and the isovalent cation substitution produce drastic changes in the optical and Raman spectra from far IR up to energies of several eV. These properties, along with the established metal-insulator transition found around 60% Ca doping, the occurrence of superconductivity and the similarities with 2D cuprates, nurture the hope that a study of low energy physics in Sr_{14-} Ca $Cu_{24}O_{41}$ may reveal universal aspects related to the nature of the ground states in low dimensional correlated spin $S = 1/2$ systems. It is the purpose of this section to bring evidence for the existence of density wave correlations in doped 2LL's at all Ca substitution levels [55]. Ground states with broken translational symmetry have been discussed in the context of low dimensional systems [9]. Examples are states which display a long ranged oscillation of the charge and/or spin densities as well as ones which acquire a topological bond order due to the modulations of the inter-atomic coupling constants, for example of the super-exchange integrals. It has been indeed found that the charge density waves (CDW) and superconductivity are the predominant competing ground states and the balance between them is ultimately determined by the microscopic parameters of the theoretical models [3, 4].

So, what are the low energy excitations one expects from a doped 2LL? Most of the theoretical studies of 2LL's consist of numerical evaluations, especially exact diagonali ation (ED) and density matrix renormali ation group techniques (DMRG), performed within the $t_{\|} - J_{\|}, t_{\perp} - J_{\perp}$ model, see Fig. 16, but not taking in to account the long range Coulomb interactions. It is interesting to discuss first the cases corresponding to only one or two holes in the ladder structure. If one hole is present on a ladder rung (Fig. 16a) it can sit on a bonding or antibonding orbital. Hopping will lead to bands separated roughly by $2t_{\perp}$ and a bandwidth proportional to $t_{\|}$ [65]. How tight is the charge bound to the remaining free spin? This question is connected to the problem of possible spin-charge separation. Evaluations of hole-spin correlations on a 2×10 cluster suggest that the unpaired spin remains tightly bound to the injected hole [65], so that this composite state carries both charge and spin, in this sense being similar to a quasi-particle. This is in contrast with the spin-charge separation in the 1D AF chain.

If two holes are present (Fig. 16b) there appears a property which seems to be very robust for 2LL's: pairing. The following discussion can be intuitively understood starting from the strong coupling limit but studies of finite clusters within the $t_{\|} - J_{\|}, t_{\perp} - J_{\perp}$ model show that this qualitative discussion holds to the relevant isotropic limit $J = J_{\|} = J_{\perp}$ and $t = t_{\|} = t_{\perp}$. If one additional hole is injected in the ladder, it will tend to align on the same ladder rung, see Fig. 16b, in order to minimi e the magnetic energy [3, 4]. The lowest band will be generated by the coherent propagation of hole pairs and it is found in the spin singlet channel. At finite energies there will be continua of electronic states

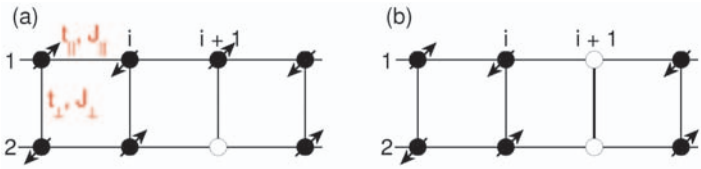

Fig. 16. Intuitive understanding of the origin of hole pairing in 2LL's in the strong coupling limit ($J_\perp \gg J_\parallel$). If an initial hole sits on rung 'i+1' (panel **a**) the second added hole (panel **b**) sits on the same rung in order to minimi e the number of broken AF bonds.

generated by breaking the pairs, the singlet and the triplet states being almost degenerate when the holes are far apart [65]. One can note that in the case of 2LL's it is the purely spin-spin correlations which effectively lead to hole pairing and not an explicit hole-hole attractive interaction and also that the main energy gain due to pairing is given by the magnitude of the spin gap. The 'easy' pairing and the kinetic energy gain of the paired holes when pairs are far apart from each other is a non-trivial difference with respect to the 2D cuprates in the sense that in the latter case evaluations prompted by the above arguments lead to macroscopic phase separation.

Since the spin gap Δ_S is to some degree a measure of the hole binding energy it is interesting to discuss what is its evolution with doping. In the undoped case the lowest triplet excitation is the branch with a minimum at π shown in Fig. 5 and its magnitude is governed by $J_\perp$. The spin gap remains substantial at isotropic coupling, relevant for experiments, and in this case it is known exactly to be $J/2$ in the model of Eq. (1). This excitation evolves continuously with doping. For instance, calculations on a 2×24 cluster at 1/8 doping and isotropic coupling shows that the spin gap is about $0.275J$, about half of the value in the undoped case [66]. Interestingly, pairing generates a different type of singlet-triplet transition [65, 66]. This excitation, present only in the doped case, will consist of breaking of a singlet hole pair into two separate quasi-particles in the triplet channel. The different kinetic energy gain of the separate holes versus the magnon in the undoped case will lead to different energies of these two types of magnons. It was argued [65] that the spin gap evolves discontinuously in 2LL's because it is the 2^{nd} type of magnon which costs less energy. Later ED and DMRG work [67] confirmed this point and showed that in a relevant parameter range the energy of this new type of spin-gap is smaller than the pair breaking continua because a triplet can hybridi e with a state formed by two holes (one in bonding and one in antibonding orbitals) forming bound $S = 1$ magnon-hole states.

Once the stability of the hole pair is confirmed to exist in the relevant ranges of the microscopic parameters, it is up to the estimation of residual interactions between the hole pairs and spins to determine what kind of ground state is chosen. Superconductivity fluctuations were probed within the $t - J$ model by evaluating numerically the pair-pair correlation function, a measure of the stability of the motion of the hole pair in the spin-gapped phase. This function, which is to be evaluated in the limit of $l \to \infty$, is defined as $P(l) = \frac{1}{N} \sum_i < \Delta_i^\dagger \Delta_{i+l} >$ where Δ_i is the pair destruction operator at site 'i' given by

$\Delta_i = \frac{1}{\sqrt{2}}(c_{i1,\uparrow}c_{i2,\downarrow} - c_{i1,\downarrow}c_{i2,\uparrow})$ (here the 'c' operators are defined within the subspace of no double occupancy). Early work showed an increase in the pairing tendency as the ratio $J_\perp/J_\parallel$ was increased [5] It has been found for a 2×30 cluster at $n = 1/8$ doping that SC correlations are dominant and they decay algebraically with l [68]. The exponent was found to be smaller than one while density-density correlations were observed to decrease as l^{-2} implying that SC is the dominant phase. In the same system, by using Green's function techniques, the frequency and wavevector dependence of the superconducting gap [66] showed a structure with nodes, much like the d-wave pairing symmetry in 2D cuprates.

Pairing does not necessarily mean superconductivity. Another possibility is that the bound (or single) holes form a spatially ordered pattern, i.e. a CDW ground state. It has been argued from DMRG calculations that a phase diagram of the isotropic $t - J$ 2LL's, in a relevant range given for instance by $J/t < 0.4$, will have as generic phase one with gapped spin modes and gapless charge mode [69]. This 'C1S0' phase [70] is characteri ed by d-wave like pairing and $4k_F$ CDW correlations, with superconductivity being the dominant phase [69]. Note that this $4k_F$ CDW renders a wavelength which is half of the one in conventional Peierls transition. Phase separation will occur roughly at values $J/t > 2.5$ [65, 69]. These numerics also argue that besides these two phases, there are small fully gapped regions (for both spin and charge sectors), to be found generally at commensurate dopings, where a CDW occurs [69]. The characteristic wavevector of this state is given by $2(k_{Fb} + k_{Fa})$ where k_{Fb}/k_{Fa} stand for the Fermi wavevectors of the bonding/antibonding electronic orbitals, discussed in the paragraph related to the charge dynamics in a ladder with one hole. Interestingly, a finite spin gap is not found to be crucial for the existence of such a CDW so, if the spin gap determines the pairing, the hole crystal can be made either out of single hole or out of hole pairs [69].

On the experimental side, in $(Sr,La)_{14-}$ Ca $Cu_{24}O_{41}$ the study of low energy physics is encumbered, compared to 2D cuprates, by the following 'non-intrinsic' facts:

- The structure is quite complicated due to the presence of the chains and ladders. We found that these subsystems interact, so one expects that supermodulation will affect carrier dynamics.

- $Sr_{14}Cu_{24}O_{41}$ has a finite hole concentration in the ladder structure to start with. Ca substitution (and maybe temperature) redistributes the charges between chains and ladders but up to now there is no accurate quantitative determination of this effect. On the contrary, there are conflicting views in the literature [10, 11].

- The effect of O stoichiometry at the crystal surface may be important in accurately determine the carrier concentration; besides, fresh surfaces are not easy to obtain because these materials do not cleave in the (ac) plane.

The problem of what happens with the spin gap in the doped ladder is an open issue from an experimental point of view. On one hand neutron scattering finds $\Delta_S = 32$ meV in both $Sr_{14}Cu_{24}O_{41}$ [17] and x = 11.5 Sr_{14-} Ca $Cu_{24}O_{41}$ [71] which says that the spin gap does not change its value. On the other hand, from the Knight shift (proportional to the uniform susceptibility) and the spin-lattice relaxation data, NMR measurements find a

decrease by about 50% of the ladder spin gap [20]. Mayaffre *et al.*, by using the same technique, tried to relate directly the disappearance of the spin gap to the occurrence of superconductivity under pressure [72]. Although a finite spin gap is a central issue which underlies the up to date theories predicting that doped ladders are superconducting, it is still not quite clear what the origin of the discrepancy between the INS and NMR data is.

4.2 Electromagnetic Response of Charge Density Wave Systems

The purpose of this section is to discuss the main properties of CDW systems and their characteristic excitations. In the CDW state a gap opens at the Fermi energy and this is observed in *dc* transport as a metal insulator transition taking place at T_c. Due to the change in the lattice constant there also are new phononic modes allowed in the CDW state. In real systems, which are not strictly 1D, it is possible that not all the Fermi surface gets gapped, so the metallic behavior can continue below T_c, as is the case of $NbSe_3$. Since the CDW transition involves ionic motions, it can be directly probed by X-rays or neutron scattering [73].

Excitations out of the CDW state – One feature which can be seen in the optical absorption spectra is due to the excitations of electrons across the CDW gap 2Δ. This belongs to the single particle channel. Since the Debye energy is much smaller than the Fermi energy the superconducting gaps from BCS theory are typically smaller than the gap excitations in the CDW state. For instance, in blue bron e ($K_{0.3}MoO_3$) which is one of the most studied quasi-1D CDW materials, this energy is found at about $2\Delta = 125$ meV [75]. There are also collective excitations out of the condensate and they are related to the space and time variations of the complex order parameter. Excitations occur due to both phase (phasons) and amplitude (amplitudons) fluctuations. The interest is to understand the long wavelength limit of these excitations. As for the amplitude mode, its energy ω_A in the limit $q \to 0$ is finite. An oscillation of the gap amplitude $\delta(\Delta)$ will also lead to an oscillation of the ionic positions $\delta(u)$. The decrease in the condensation energy, $\delta(E_{cond}) = D(\epsilon_F)\delta(\Delta^2)/2$ will be equal to the extra kinetic energy associated with ionic displacements, $MN\omega_A^2(q=0)\delta(u^2)/2$ where M, N are the ionic mass and number respectively. As a result one obtains a finite value for $\omega_A(q \to 0)$.

The situation is different for the long wavelength phase mode. Such motion is a superposition of electronic charge along with ionic oscillations which leads to a high 'effective mass', m^*. In the $q \to 0$ limit involves a translational motion of the undistorted condensate so it will cost no energy. Its dispersion in the $q \to 0$ limit is given by $\omega_\Phi^2(q) = (m/m^*)v_F^2q^2$ [76]. Since phase fluctuations involve dipole fluctuations due to the displacements of the electronic density with respect to the ions the phason is a feature which will be seen in the real part of the optical conductivity data. The amplitude mode at $q \to 0$ does not involve such displacements so it is expected to be a Raman active mode.

Most interesting is that in the ideal case considered here the phase mode is current carrying and it can slide without friction [74]. As a result this excitation will be seen as a δ function at ero frequency. The spectral weight of this peak is given by m/m^* and this is stolen from the single particle conductivity which becomes an edge, instead of a singularity reflecting the divergence in the density of states [76], see also Figs. 8 and 9

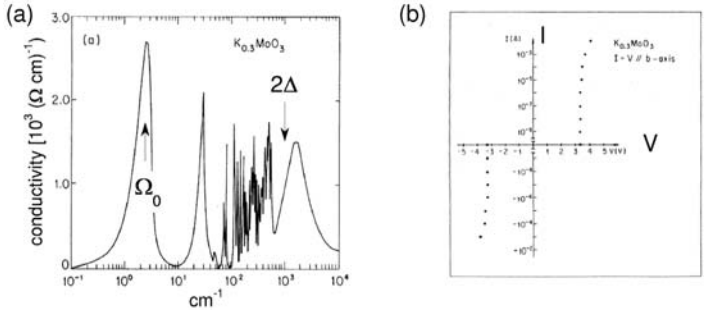

Fig. 17. Collective excitations and transport in $K_{0.3}MoO_3$. (**a**) Optical conductivity in the CDW phase from Ref. [75] showing the pinned mode at Ω_0 and the single particle edge starting at 2Δ. Many new electron-phonon coupled modes appear in the mid-IR region below the transition. (**b**) The observation of the second threshold, Fröhlich superconductivity, in $K_{0.3}MoO_3$ (from Ref. [77]).

in Ref. [75]. The interaction with impurities or lattice commensurabilities destroys the infinite conductivity, and the phase mode will be pinned. As a result, this excitation will be shifted to finite frequencies which characteri e the particular impurity potential. In Fig. 17 is shown the example of the blue bron e, the pinning mode as well as the gap feature being seen around 2 and 1000 cm^{-1} respectively.

Zero frequency and microwave transport in the CDW state – The existence of a gap and low energy collective excitations leads to several other properties which were seen in *dc* and finite frequency (typically in the microwave region) conductivity. In a $I-V$ characteristic one can talk roughly speaking about three regimes. At low electric fields there is an Ohmic behavior and the conductivity at finite temperatures will be due to thermally excited electrons (normal carriers) out of the condensate. Above a threshold field, $E_T^{(1)}$, related to the magnitude of the pinning potentials, the contribution of the condensate sets in. The CDW starts moving as a whole and this motion is accomplished through distortions of the phase and/or amplitude of the condensate. At high fields, above some other threshold field $E_T^{(2)}$, the external forces cause a fast sliding motion of the CDW which 'ignores' the underlying pinning potentials and the current increases very steeply (almost infinite differential conductance) for small variations of the applied voltage, see Fig. 17b. This regime is reminiscent of the ideal case where 'Fröhlich superconductivity' should occur. The $I-V$ curve in 2^{nd} and 3^{rd} regimes is non-linear and temperature dependent. Notable is that for an applied *dc* voltage, the motion of the CDW will also lead in a clean sample to a finite frequency component of the current. The fundamental frequency of this oscillatory component is directly related to the wavelength of the density wave.

Low frequency CDW relaxation – Another low energy feature observed in many well established CDW compounds is a relaxational peak which has a strong temperature dependent energy and damping related to the *dc* conductivity of the material. This loss peak is seen typically in the microwave region at energies much lower than the pinning

frequency. For example in $K_{0.3}MoO_3$ the frequency range is 10^4 - 10^6 H for temperatures between 50 to 100 K while the pinned mode is roughly at $\Omega_0 \approx 60$ GH see Figs. 18d and Figs. 17a respectively. In Ref. [79] the author proposes a scenario to reconcile the observations at low and high frequencies, a summary of the results being shown in Fig. 18a-c. The interpretation of the damped excitation is that it is a longitudinal density wave relaxational mode due to the interaction with normal carriers. It is argued that this mode, which should not be seen in the transverse channel, is seen however in the dielectric response because of the non-uniform pinning which introduces disorder. By making the wavevector k, according to which the modes can be classified as transverse or longitudinal, a 'not so good quantum number', disorder mixes the pure longitudinal and transverse character of the excitations. In other words, breaking of the selection rules make the longitudinal modes appear as poles, rather than eros, of the dielectric response function.

The main results of the theory in Ref. [79] are shown in Fig. 18 where the CDW dielectric function is plotted as a function of frequency. The distribution of pinning centers (a measure of disorder) is modeled by a function $g_n(x) = (n^{n+1}/n!)x^n \exp(-nx)$ which is peaked at $x = 1$ and satisfies $g_{n\to\infty}(x) = \delta(x-1)$. In Fig. 18a one can see that the disorder leads to the appearance of a mode at lower frequencies which steals spectral weight from the pinning mode situated at the average frequency Ω_0. The stronger the disorder, the higher is the spectral weight redistribution between the two modes. Panels (b) and (c) in Fig. 18 show the real and the imaginary part of the CDW dielectric function for a given n. They are related by Kramers-Krönig relations, so the drop in $Re(\varepsilon)$ leads to a peak in $Im(\varepsilon)$. These data are plotted for several values of the relaxational time τ_1 which mimics (through the dependence on conductivity, see the caption of Fig. 18) a linear variation in temperature. Decreasing temperature leads to a decrease in conductivity and a higher τ_1 and to the softening of the relaxational peak which moves away from Ω_0.

CDW coupling to the uncondensed carriers – Here is a simplified version for the derivation of the longitudinal screening mode shown in Fig. 18. In this approach the CDW is modeled by an oscillator with a characteristic pinning frequency Ω_0 and we neglect internal distortions. The only other ingredients of the model are the presence of a finite electron density corresponding to thermally activated quasi-particles and the assumption that the interaction between these two fluids is only *via* an electromagnetic field. The calculation of the longitudinal CDW modes as well as the coupling to the normal, uncondensed, electrons follows almost identically the treatment of longitudinal phonons and their coupling to plasma oscillations in metals. In the following, $\vec{u}$ is a uniform displacement of the CDW (in a real crystal this will be within a volume determined by the longitudinal and transverse correlation lengths), ρ_c and m^* are the CDW charge and mass densities and γ_0 is an intrinsic damping coefficient. The time derivatives for oscillations at a given frequency ω are replaced by $\partial/\partial t \to -i\omega$. The derivation can be made using the general relations of the Born and Huang model [80]:

$$-\omega^2\vec{u} = -\Omega_0^2\vec{u} + i\omega\gamma_0\vec{u} + \frac{\rho_c}{m^*}\vec{E} \tag{3}$$

$$\vec{P} = \rho_c\vec{u} + \frac{\varepsilon_\infty - 1}{4\pi}\vec{E} \tag{4}$$

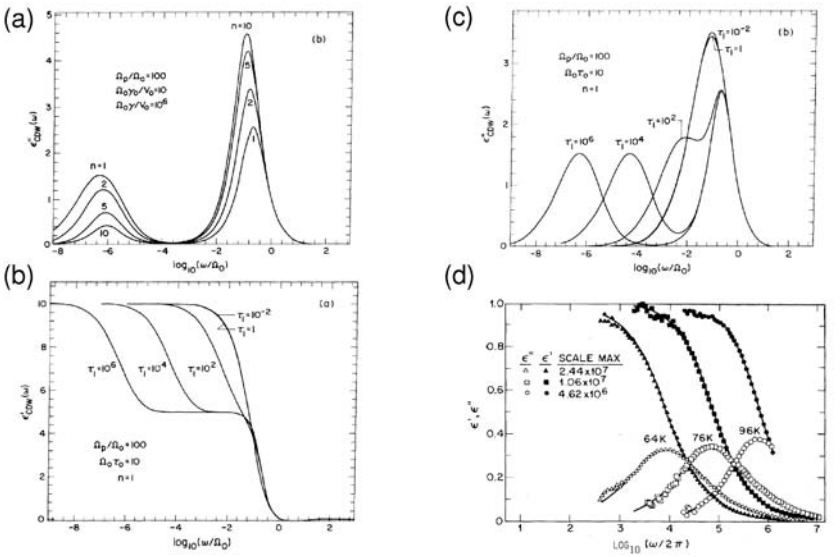

Fig. 18. The dependence of the real and imaginary part of the CDW dielectric function on frequency on the log scale. Panels (**a**), (**b**) and (**c**) show theoretical results from Ref. [79]. Ω_0 and Ω_p are the pinning and the CDW plasma frequencies, γ_0 is an intrinsic damping parameter and V_0 in panel (**a**) is the pinning potential. τ_0 and τ_1, defined by $\tau_0 = \gamma_0/V_0$ and $\tau_1 = \gamma/V_0 = \rho_c^2/\sigma V_0$ (with σ and ρ being the *dc* conductivity and the CDW density), are characteristic relaxational times. The parameter n represents a measure of the distribution in pinning frequencies: $n \to \infty$ means that there is only one mode in the distribution, the smaller n is, the broader the distribution. Panel (**d**) shows experimental determination of the real and imaginary parts of the dielectric function for three representative temperatures (data from Ref. [78]).

Here ε_∞ takes care of the background carrier contributions arising from interband transitions. In the absence of carriers, neglecting the damping and using the electrostatic approximation ($\nabla \times \vec{E} = 0$ which means that the field is purely longitudinal and as a result $\vec{E} = \vec{E}_L$), these equations allow us to determine the characteristic transverse and longitudinal frequencies. The equation $-\omega^2 \vec{u}_T = -\Omega_0^2 \vec{u}_T$ (because $\vec{E}_T = 0$) allows the identification $\Omega_0 = \Omega_T$, i.e. the frequency of the transverse mode. The longitudinal modes will generate a finite electrostatic field. Eq. (4) and Gauss' law $\nabla(\vec{E} + 4\pi\vec{P}) = 0$ lead to $\nabla(4\pi\rho_c \vec{u}_L + \varepsilon_\infty \vec{E}) = 0$ so $\vec{E} = -4\pi\rho_c \vec{u}_L/\varepsilon_\infty$. Plugging this relation in Eq. (4) one obtains $-\omega^2 \vec{u}_L = -\Omega_0^2 \vec{u}_L - 4\pi\rho_c^2/\varepsilon_\infty m^* \vec{u}_L$ which gives the frequency of the longitudinal mode $\Omega_{in} = \sqrt{\Omega_0^2 + \Omega_p^2/\varepsilon_\infty}$ where the plasma frequency is given by $\Omega_p^2 = 4\pi\rho_c^2/m^*$.

What is the dynamics of the CDW in an external field E_0 of frequency ω? In the transverse channel the force in the right hand side of Eq. (3) will be $\rho_c E_0/m^*$ leading to

$\vec{u}_T = [(\rho_c/m^*)/(-\omega^2 + \Omega_0^2 - i\omega\gamma_0)]\vec{E}_0$. Using Eq. (4), the relation $\varepsilon = 1 + 4\pi\chi$, where $\chi = P/E$, as well as the fact that the conductivity is given by $\varepsilon(\omega) = 1 + 4\pi i\sigma/\omega$, one obtains for the collective contribution to the dielectric function and the real part of the conductivity:

$$\varepsilon_{CDW}(\omega) = \frac{\Omega_p^2}{\Omega_0^2 - i\omega\gamma_0 - \omega^2} \qquad \sigma_{CDW}(\omega) = \frac{1}{4\pi}\frac{-i\omega\Omega_p^2}{\Omega_0^2 - i\omega\gamma_0 - \omega^2} \tag{5}$$

These equations will render a peak at the pinning frequency Ω_0 in both $\varepsilon(\omega)$ and $\sigma(\omega)$.

We deal now with the dynamics of the longitudinal modes in the presence of carriers. One has to worry in this case about the associated internal fields and screening effects. One can derive a relation between the CDW displacement $\vec{u}_L$ and the local field which should become $\vec{E} = -4\pi\rho_c\vec{u}_L/\varepsilon_\infty$ in the limit of ero *dc* conductivity. The only difference now is that the first Maxwell equation changes to $\nabla(\vec{E}+4\pi\vec{P}) = \rho_{qp}$, where ρ_{qp} is the quasiparticle density. The continuity equation $-i\omega\rho_{qp}+\nabla\vec{j} = 0$ and Ohm's law $\vec{j} = \sigma_{qp}\vec{E}$ lead to the relation $i\omega\rho = \sigma_{qp}\nabla\vec{E}$ so, using Gauss' law, one obtains $\nabla(4\pi\sigma_{qp}\vec{E}-i\omega\vec{E}-4\pi i\omega\vec{P}) = 0$. Inserting the expression for polari ation from Eq. (4) and taking into account that we deal with longitudinal fields one obtains:

$$\vec{E} = \frac{4\pi i\omega\rho_c}{4\pi\sigma_{qp} - i\omega\varepsilon_\infty}\vec{u}_L \tag{6}$$

Obviously, for $\sigma_{qp} = 0$, Eq. (6) gives the result of obtained in the previous paragraph in the absence of carriers. For calculating the longitudinal response, one has thus to replace $\vec{E}$ in (3) with the sum of the external field $\vec{E}_0$ and the polari ation field given by (6) obtaining a linear relation between $\vec{u}_L$ and $\vec{E}_0$. Using (4) one obtains the CDW contribution to the longitudinal dielectric function ε_L, which is relevant for Raman scattering, as:

$$\varepsilon_L(\omega) = \frac{\Omega_p^2}{\Omega_0^2 - \omega^2 - i\gamma_0\omega - \frac{i\omega\Omega_p^2}{4\pi\sigma_{qp} - i\omega\varepsilon_\infty}} \tag{7}$$

In the limit of high frequencies this function has a pole at $\sqrt{\Omega_0^2 + \Omega_p^2/\varepsilon_\infty}$ corresponding to the CDW plasmon and which is the energy of the longitudinal collective mode. In the limit of low frequencies and neglecting the intrinsic damping γ_0, Eq. (7) reduces to the following relaxational mode:

$$\varepsilon_L(\omega) = \frac{A}{1 - i\omega\tau} \quad \text{with} \quad A = \frac{\Omega_p^2}{\Omega_0^2} \quad \text{and} \quad \Gamma = \frac{1}{\tau} = 4\pi\sigma_{qp}\frac{\Omega_0^2}{\Omega_p^2} = 4\pi\sigma_{qp}\frac{1}{\varepsilon_0 - \varepsilon_\infty} \tag{8}$$

Equations (5) and (8) describe the features seen in Fig. 18. The proportionality in (8) between Γ and the *dc* conductivity is the result of normal carrier backflow which screens the collective polari ation and dissipates energy, suffering lattice momentum relaxation.

4.3 Density Waves in $Sr_{14}Cu_{24}O_{41}$

4.3.1 Low Energy Transport and Raman

In Fig. 19a we show the components of the dielectric response $\varepsilon = \varepsilon_1 + i\varepsilon_2$ as a function of frequency (in log scale) for several temperatures [56]. The imaginary part shows strongly

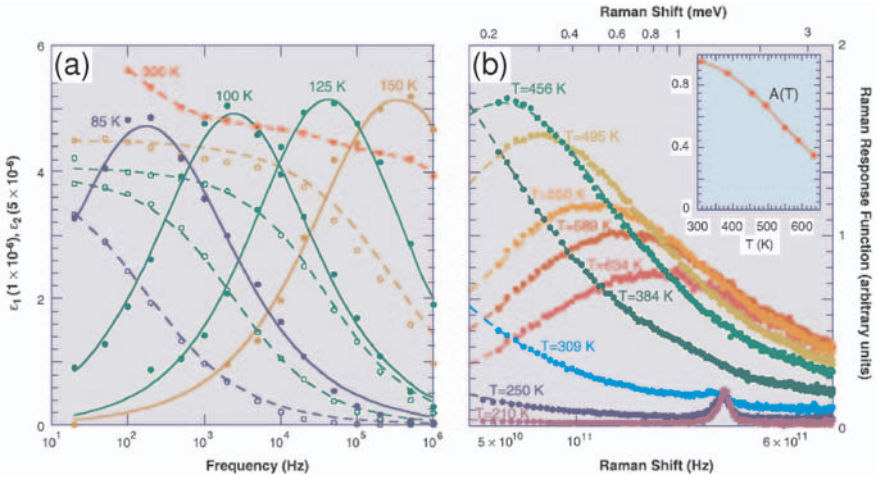

Fig. 19. (**a**) The temperature dependence of the real (open circles) and imaginary (solid circles) of the complex dielectric function between 85 and 300 K. The solid and dashed lines are guides for the eye. (**b**) Raman response function in (*cc*) polari ation at several temperatures. The dots are the data and solid lines are fits to a relaxational behavior as described by Eq. (9). The excitation energy used is $\omega_{in} = 1.55$ eV. The excitation around 350 GH seen for $T < 300$ K is the phonon shown in Fig. 13. The inset shows the temperature dependence of the quasielastic intensity $A(T)$ (data from Ref. [56]).

damped, inhomogeneously broadened peaks whose energies are temperature dependent. These relaxational modes lead to variations in the real part of the dielectric function ε_1 up to 300 K and even above. This data resembles with the dielectric response measured in the CDW compound $K_{0.3}MoO_3$ which is shown in Fig. 18. Fig. 19b shows Raman data in a higher temperature range. Similarly to Fig. 19a we observe an overdamped feature which moves to lower frequencies with cooling. This excitation disappears below our lower energy cut-off of about 1.5 cm^{-1} (equivalent to 50 GH or 0.185 meV) below about T = 200 K. The Raman response function can be well fitted with the expression:

$$\chi''(\omega, T) = A(T)\frac{\omega\Gamma}{\omega^2 + \Gamma^2} \tag{9}$$

The temperature dependence of the peak intensity is shown in the inset of Fig. 19. $A(T)$ decreases by about 60% from 300 to 640 K. The temperatures shown in this figure include laser heating effects and they were determined from the ratio of Stokes anti-Stokes spectra for each temperature.

The data in Fig. 19a also allow the extraction of a characteristic transport relaxational time $\tau(T)$ at every temperature by a fit to a relaxational type behavior. Using this result, in the entire temperature range the dielectric response between 20 H and 10^6 H from Fig. 19 can be scaled on a universal generali ed Debye relaxational curve given by:

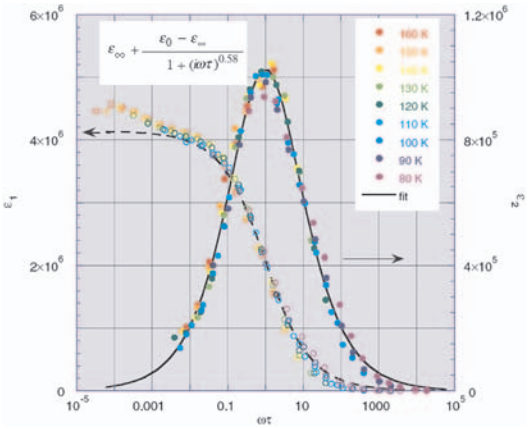

Fig. 20. Scaling of the complex dielectric function $\varepsilon = \varepsilon_1 + i\varepsilon_2$. Empty (solid) circles correspond to the real (imaginary) part of ε. (Data from Ref. [56].)

$$\varepsilon(\omega) = \varepsilon_\infty + \frac{\varepsilon_0 - \varepsilon_\infty}{1 + [i\omega\tau(T)]^{1-\alpha}} \tag{10}$$

The parameter α characteri es the width of the distribution of relaxation times. The equation for the conventional Debye relaxation has $\alpha = 0$. The fit to Eq. (10) is shown in Fig. 20 where the real and imaginary part of ε is plotted as a function of the dimensionless parameter $\omega\tau$. The parameter α determined from the fit is $\alpha = 0.42$

The temperature dependencies of the relaxational frequencies extracted from the Raman data, $\Gamma(T)$, and from the microwave conductivity data, $\tau^{-1}(T)$, are plotted as a function of inverse temperature in Fig. 21. On the same plot we show the Arhenius behavior of the *dc* conductivity. The *dc* conductivity in this figure shows activated behavior and the break around $T^* = 150$ K points to the existence of two regimes. At high temperatures the activation energy we obtained is $\Delta_{dc}^{T>T^*} = 2078$ K, consistent with previous results [52]. A value $\Delta_{dc}^{T<T^*} = 1345$ K is obtained at low temperatures. In this figure we observe that the relaxational frequencies have an activated behavior and that the corresponding activation energies match those of the conductivity both above T* (the Raman data) and below T* (the microwave transport data). This characteristic temperature at which the *dc* activation changes was discussed also in the end of section 1.3.1 where we noted that it was related to the increase of the electronic Raman continuum, to the variation of the 2M scattering width and also to the temperature dependent intensity of the chain superstructure peaks seen by X-ray scattering.

The inset in Fig. 21 shows the *dc* conductivity as a function of the applied field. The arrows mark two threshold fields. Below $E_T^{(1)} \approx 0.2$ V/cm the conductivity obeys Ohm's law and it has the Arhenius temperature dependence shown in the main panel. For electric fields above $E_T^{(1)}$ the $I - V$ characteristics change from linear to approximately quadratic. At much higher fields, above 50 V/cm, there is a second threshold which marks

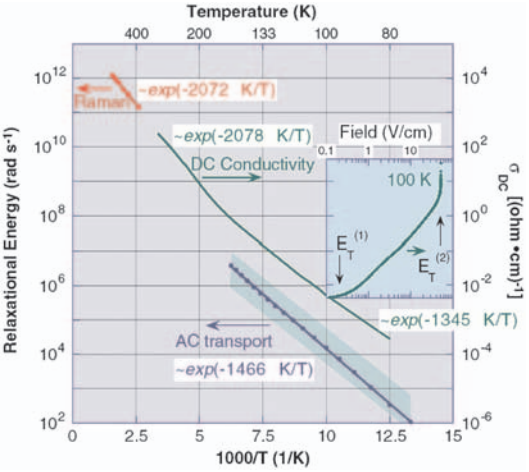

Fig. 21. Measured *dc* conductivity (right scale) and the scattering rates (left scales) obtained from fits to the Raman data (using Eq. (9)) and the imaginary parts of the complex dielectric function (using Eq. (10)) shown in Fig. 19. Green line: *dc* conductivity. Red: the dots are the scattering rates $\Gamma(T)$ from the Raman data in Fig. 19b and the line is an Arhenius fit showing an activated behavior with $\Delta_{Raman} = 2072$ K. Blue: the dots are the scattering rates $\tau^{-1}(T)$ from the dielectric response in Fig. 19b and the line is a similar exponential fit rendering $\Delta_{\varepsilon} = 1466$ K. In both regimes the scattering rates show the activated behavior of the *dc* conductivity. The shaded area shows the range of scattering rates calculated as described in the text. The inset shows the nonlinearity in the *dc* conductivity as a function of applied electric field measured at $T = 100$ K. Note that the vertical scale for the inset coincides with the vertical scale of the main panel. (Data from Ref. [56].)

a very sharp rise of the current. The differential conductivity in this regime is very high, more than $10^5\ \Omega^{-1}cm^{-1}$, an estimate limited by contact effects and most likely carried by inhomogeneous filamentary conduction.

We turn now to the interpretation of the data shown in Figs. 19, 20 and 21. We remark that the energy range of the relaxational peaks seen in Fig. 19 is much lower than the thermal energy or the magnetic and *dc* activation gaps. Therefore, this is incompatible with single-particle type excitation and suggest that the low energy charge dynamics is driven by correlated collective behavior. We identify this strongly temperature dependent feature to be a CDW relaxational mode in the longitudinal channel, screened due to the interaction with thermally excited quasiparticles, as described in the previous section. We note that electronic Raman scattering can probe directly the longitudinal channel [81] because the Raman response function, $\chi''(\omega)$, is proportional to $\mathrm{Im}[1/\varepsilon(\omega)]$, a quantity proportional to ε_L from Eq. (7). We can support in what follows this assignment by quantitative comparison with this simple two-fluid model and by the results of the non-

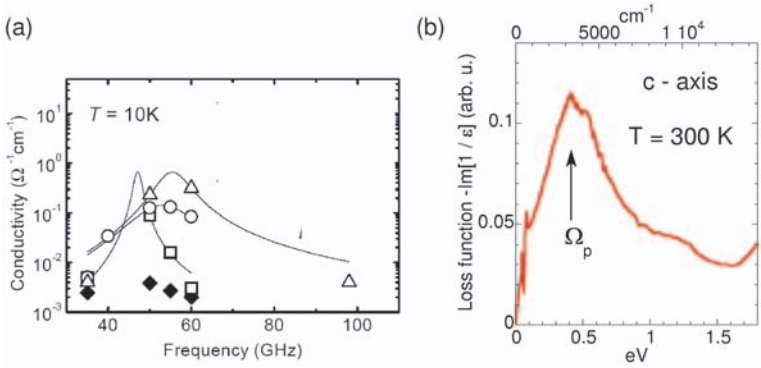

Fig. 22. (**a**) Low temperature microwave c (a) axis conductivity at T = 10 K for $Sr_{14}Cu_{24}O_{41}$ crystals from three different batches is shown by open (solid) symbols (data from Ref. [19]). The solid lines are Lorent ian fits. (**b**) The c-axis loss function in $Sr_{14}Cu_{24}O_{41}$ at 300 K. Ω_p indicates a plasma edge around 3300 cm^{-1}.

linear conductivity measurements as a function of electric field. Microwave and millimeter wave spectroscopy [19] supports our assignment. In the end of this chapter, we discuss recent (and direct) evidence for the existence of CDW correlations in $Sr_{14}Cu_{24}O_{41}$ provided by X-ray measurements [82].

The immediate question prompted by our claim, which essentially ascribes to a common origin our observations in Fig. 19 and the properties of $K_{0.3}MoO_3$ (an established CDW material) shown in Figs. 17 and 18, is: If we observe a property related to the pinning of an existent CDW, where is the pinned phase mode? A microwave experiment performed by Kitano *et al.* reported a relatively small and narrow peak between 30 and 70 GH in the c-axis conductivity which was observed up to moderately high temperatures [19]. The authors attributed this resonance to a collective excitation and speculated about a possible CDW origin. It turns out that our data along with the results of Kitano *et al.* as well as results of reflectivity measurements form a basis on which these results can be analy ed quantitatively. In Fig. 22 are shown the main result in [19] and the plot of -Im$[1/\varepsilon(\omega)]$ obtained by our Kramers-Krönig analysis of 'raw' reflectivity data, see Ref. [10].

We believe that the microwave resonance in the 30 to 70 GH range in Fig. 22a corresponds to the average pinning frequency of the CDW in $Sr_{14}Cu_{24}O_{41}$. Along with a plasma edge $\Omega_p \approx 3300$ cm^{-1} extracted from the loss function (see Fig. 22b) and using Eq. (5) which gives $\varepsilon_0 - \varepsilon_\infty = \Omega_p^2/\Omega_0^2$, one obtains for the low frequency dielectric function values of the order of 10^6, consistent with the experimental observations in Fig. 19. The two-fluid model described in the previous section, see Eq. (8), predicts that the relaxational energy is proportional to the activated *dc* conductivity. Indeed, the Arhenius behavior of the relaxational energies, extracted both from Raman and transport measurements in Fig. 19, shows from fits with $e^{-\Delta/k_BT}$ activation energies similar to those of *dc* conductivity. Moreover, we remark that the similarity is not only up to a proportionality factor,

but the calculated theoretical values for $\tau^{-1}(T)$ according to Eq. (8) using the measured values of ε_0 and σ_{qp} are in agreement with the experiment. This can be seen in Fig. 21 where the calculated values (the shaded area whose thickness takes into account the error bars in the determination of the *dc* value of the dielectric function ε_1) match the measured τ^{-1} (blue dots).

The non-linear transport data shown in the inset of Fig. 22 for T = 100 K further confirm the existence of density wave correlations in $Sr_{14}Cu_{24}O_{41}$. The three regimes observed are typical for systems in which the CDW is pinned by impurities [73, 77]. Below $E_T^{(1)}$ the pinned CDW does not contribute to transport and σ_{dc} is governed by the quasiparticle response. Around this value of the field there is an onset of the CDW conductivity due to the relatively slow sliding of the condensate. In this 2^{nd} regime the predominant damping mechanism is the screening of internal electric fields produced by local CDW deformations by backflow quasi-particle currents. The 3^{rd} regime defined by fields $E > E_T^{(2)}$, indicates a regime of free sliding CDW, the Fröhlich superconductivity, also observed in $K_{0.3}MoO_3$, see Fig. 9. In this case the velocity of the condensate is so high that it does not feel the background quasi-particle damping.

The overall consistency among the measured temperature dependencies of the dielectric function, *dc* conductivity and relaxational energies demonstrates the applicability of the hydrodynamic model description for the low energy carrier dynamics in a CDW ground state. However, there are several issues which have to be mentioned. One difference with respect to what happens in well established CDW systems is that the observed relaxational peak in Raman response is at higher energies than the pinned mode at Ω_0. This may be because there is a broad distribution of pinning frequencies and the origin of the Raman relaxational peak is in the high energy side of this distribution. Up to date there are no measurements of the pinned phase mode at or above 300 K. Another issue is that although the absolute values of $\tau^{-1}(T)$ calculated according to Eq. (8) are in agreement with the experiment, the same is not true for the Raman relaxation frequencies $\Gamma(T)$. The calculated values are about 50 times smaller than the measured ones. A reduction in the density wave amplitude, as suggested by the decrease in the peak intensity, inset of Fig. 19b, would produce a concomitant increase in Γ. Further enhancement in the scattering rate may come from additional relaxational channels due to low lying states which are seen at temperatures higher than about 150 K by magnetic resonance [15], c-axis conductivity (Fig. 10) or Raman scattering (Fig. 11).

The existence of density wave correlations in $Sr_{14}Cu_{24}O_{41}$ at temperatures of the order of 650 K gives this compound a distinctive property compared to classical CDW systems. These high temperatures suggest that in this case it is not the phonons which support the CDW but rather the strong magnetic exchange $J \approx 1300$ K may play an important role in the charge and spin dynamics. One aspect mentioned in the previous section was that hole pairing in 2LL's is a robust feature due to the AF exchange correlations. In this respect, an interesting question is: What is the fundamental current carrying object? Is it due to single or paired electrons? Helpful in this regard would be to try to measure current oscillations and interference effects (For a description see Chapter 11 in Ref. [73]). In fact this is probably the only prominent 'classical' transport signature of a CDW state which has not been checked yet in $Sr_{14}Cu_{24}O_{41}$ and it would be an interesting project.

4.3.2 Soft X-ray Scattering from $Sr_{14}Cu_{24}O_{41}$

The most direct way to measure CDW ordering is by neutron or X-ray scattering because they can measure directly super-lattice peaks associated with the distortions of the lattice or electronic clouds. In conventional CDW materials this is the case and the electron-phonon interaction causes atomic displacements and local electronic density modulations of the order of the atomic numbers. However, up to date, conventional hard X-ray experiments (using photons with typical energies of the order of tens of keV) failed to detect carrier ordering in the ladder structure of Sr_{14-} Ca $Cu_{24}O_{41}$ compounds.

Is there any way to observe weak charge modulations which do not involve detectable distortions in the structural lattice? One way to enhance the scattering amplitude from the doped holes is by exploiting those changes in the optical properties of the materials which occur as a result of doping. This often involves, as is the case for cuprates, using incident photons with energies about two orders of magnitude smaller than in conventional X-ray experiments. A real space charge modulation will lead to a proportional change in the Fourier transformed density which in turn is proportional to the dielectric susceptibility of the material, $\chi(k, \omega)$. The X-ray scattering amplitude is determined by the electronic density and as a result will scale proportionally to $\chi(k, \omega)$.

It turns out that in 2D cuprates [83] and Sr_{14-} Ca $Cu_{24}O_{41}$ ladders [11] there are features seen in the X-ray absorption spectra (XAS) which arise directly as a result of hole doping. The situation is simpler in 2D cuprates and it can be illustrated for $La_2CuO_{4+\delta}$: For the insulating compounds the oxygen K-edge around 540 eV (which marks the beginning of a continuum of excitations consisting of electron removals from O1s orbitals), has also a prepeak at 538 eV which, due to hybridi ation, corresponds to intersite O1$s \rightarrow$ Cu3d transitions. If holes enter O2p orbitals, there will be another prepeak appearing at 535 eV due to the fact that additional O valence states are available to be filled by the excited O1s electron. The spectral weight of this carrier induced feature is stolen from the 538 eV prepeak. It is clear that the opening of a new absorption channel at 535 eV will change the optical properties at this energy, in particular of the susceptibility $\chi(k, \omega)$. This also means that X-ray scattering amplitude for 535 eV incident photons will be enhanced with respect to the non-resonant case by factor proportional to the 'susceptibility contrast' which can be defined as the percentage change of the susceptibility in the doped versus undoped case [83]. Note that this enhancement applies only to the signal from the doped carriers.

In $(Sr,La)_{14-}$ Ca $Cu_{24}O_{41}$ the XAS spectra have the same general characteristics but the situation is more complicated because the mobile carrier absorption feature is split into chain and ladder features [11]. However these excitations can be resolved and they are shown in Fig. 23b. This figure shows the characteristic energies of the oxygen K-edge. The carrier prepeaks are resolved by using different polari ations of the incoming photon fields and one can see that the ladder absorption at 528.6 eV occurs at about 0.5 eV higher energy than the corresponding feature in the chains, consistent with the XAS study in Ref. [11]. A 2D scan in reciprocal space for incident photon energies of 528.6 eV is shown in Fig. 23a. In this figure the momentum transfer $Q = (2\pi/a\ H, 2\pi/b\ K, 2\pi/c_L\ L_L)$ is in ladder reciprocal units along the c-axis. The vertical line is due to specular reflection

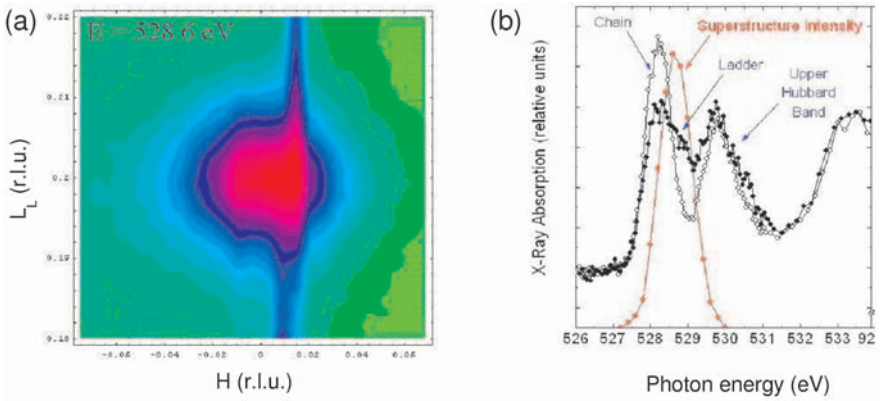

Fig. 23. (a) The superlattice peak seen at 528.6 eV OK ladder carrier prepeak in the reciprocal space in $Sr_{14}Cu_{24}O_{41}$. L_L on the vertical axis refers is in ladder units. The rod at $H = 0.01$ is due to the specular reflection from the sample surface. (b) Black symbols represent X-ray absorption spectra taken with photon polari ations $E \parallel c$ (filled circles) and $E \parallel a$ (empty circles). The carrier prepeaks corresponding to the chains/ladders are indicated by arrows. Red symbols are for the integrated intensity of the superlattice reflection seen in panel (a) as a function incident photon frequency. Data from Ref. [82].

from the surface and the displacement from $H = 0$ is due to crystal miscut, the normal to the surface making a finite angle with respect to the c-axis. A superlattice reflection at $(0, 0, 0.2)$ indicates a a charge modulation of 5 ladder units. In terms of the large crystal structure this momentum transfer corresponds to $L = (c/c_L)\ L_L = 1.4$, where c and c_L are the lattice constants corresponding to the big unit cell and ladder unit cell satisfying $c = 7c_L = 27.3$ Å [1]. This Bragg reflection is a true superlattice peak since it does not have the periodicity of the 27.3 Å unit cell and it should not be confused with the five-fold modulation in the chain structures [16].

The $(0, 0, 0.2)$ reflection has an unusual excitation profile. The resonance is shown in Fig. 23b where the energy dependence is plotted along with the absorption spectra. One can notice that this reflection is seen only in resonance with the ladder absorption at 528.6 eV, being absent for all other energies, including the oxygen K-edge. This proves two main aspects: The Bragg peak arises solely from the doped *ladder* holes, and it cannot be due to any structural modulation which would track *all* the features in the OK absorption. The superlattice peak width in k space gives the correlation lengths $\xi_c = 255$ Å and $\xi_a = 274$ Å indicating that the order is two dimensional. This observation is very interesting given the fact that magnetic properties due to the different exchange parameters (Cu-O-Cu bonds making 90° or 180° degrees along the a and c axes respectively, see Fig. 1) as well as the dc transport remain anisotropic, highlighting the importance of inter-ladder Coulomb interactions.

This X-ray scattering study confirms the transport data shown in the previous section in establishing the existence of charge density modulations in doped 2LL's. The findings

are consistent with the predictions of a crystalline order of ladder holes as a competing state to superconductivity [5, 69]. The absence of structural distortions argues that it is not the conventional electron-phonon interactions, but many-body electronic effects which drive the transition. One question to address is whether the CDW correlations exist in Ca substituted $Sr_{14}Cu_{24}O_{41}$ crystals. This is the topic of the next section where, based on the similarities with the Raman data in $Sr_{14}Cu_{24}O_{41}$ we argue that fluctuations of the density wave order persist at high Ca concentrations and high temperatures.

4.4 Signatures of Collective Density Wave Excitations in Doped Sr_{14-} Ca $Cu_{24}O_{41}$. Low Energy Raman Data.

In Fig. 24a we show low frequency Raman response in x = 12 Sr_{14-} Ca $Cu_{24}O_{41}$ at several temperatures. The (*cc*) polari ed spectra above 300 K are dominated by a quasi-elastic peak, very similar to the one in $Sr_{14}Cu_{24}O_{41}$, see Fig. 19. The solid lines are fits using the same Eq. (9) as in Fig. 19. A small contribution of the background, as shown in the inset, was subtracted. The polari ation and doping dependence of this relaxational feature are shown in Fig. 24b-e. We note that the quasi-elastic feature is present only

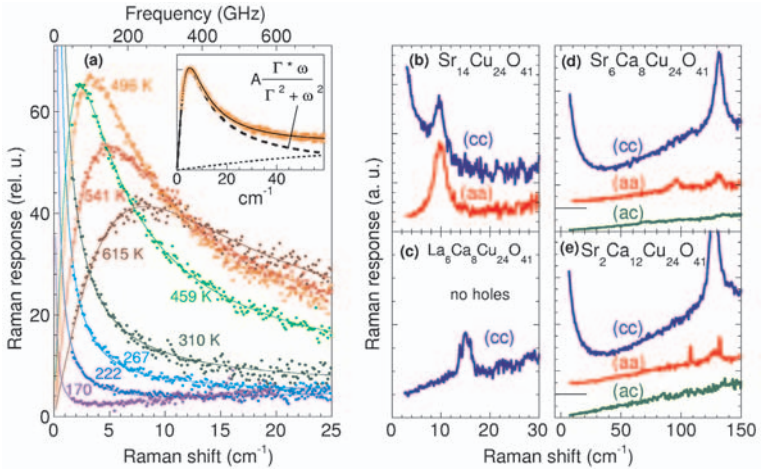

Fig. 24. A summary of the quasi-elastic Raman scattering in Sr_{14-} Ca $Cu_{24}O_{41}$ and $La_6Ca_8Cu_{24}O_{41}$ compounds. (**a**) Temperature dependence of the Raman response in x = 12 Sr_{14-} Ca $Cu_{24}O_{41}$ in (*cc*) polari ation taken with $\omega_{in} = 1.55$ eV. This plot is the analogue of Fig. 19b. The inset shows a typical fit of the Raman data with a relaxational form, Eq. (9), and a small contribution from an underlying background. Panels (**b**), (**c**), (**d**) and (**e**) show polari ed low energy Raman response for $Sr_{14}Cu_{24}O_{41}$, $La_6Ca_8Cu_{24}O_{41}$ and x = 8 and 12 Sr_{14-} Ca $Cu_{24}O_{41}$ respectively. Note that the quasi-elastic Raman peak is absent in the undoped $La_6Ca_8Cu_{24}O_{41}$ crystal and it is present, only for the polari ation parallel to the ladder legs, in all studied Sr_{14-} Ca $Cu_{24}O_{41}$ samples.

in (*cc*) polari ation and we find it in Sr_{14-} Ca $Cu_{24}O_{41}$ for all Ca concentrations studied (x = 0, 8 and 12). This low energy excitation is absent however in $La_6Ca_8Cu_{24}O_{41}$ which contains no holes per formula unit, confirming the fact that it is due to the presence of doped carriers. We confirmed also that there is no influence of magnetic fields either on this feature or on the modes seen in panels (a) and (c) at 12 and 15 cm^{-1} respectively. This supports the assignment of these modes, shown also in Fig. 13 for $Sr_{14}Cu_{24}O_{41}$, to a phonon.

Interestingly, it turns out that the extracted temperature dependent relaxational energy $\Gamma(T)$ for x = 12 Sr_{14-} Ca $Cu_{24}O_{41}$ reveals, similarly to $Sr_{14}Cu_{24}O_{41}$ in Fig. 21, an activated behavior of the form $\Gamma(T) \propto \exp(-\Delta/k_BT)$. Moreover, the activation energies are found to be about the same: $\Delta \approx 2100$ and 2070 K in $Sr_{14}Cu_{24}O_{41}$ and x = 12 Sr_{14-} Ca $Cu_{24}O_{41}$, respectively, see Fig. 25c. While this energy is close to the activation energy of the *dc* conductivity in $Sr_{14}Cu_{24}O_{41}$, in x = 12 Sr_{14-} Ca $Cu_{24}O_{41}$ the temperature dependence of the conductivity is far from exponential, and this can be seen comparing panels (a) and (b) of Fig. 25. In fact, the behavior shown in panel (b) is very similar to the one in underdoped 2D cuprates: there is a low temperature insulating and a high temperature metallic behavior, in this latter regime the resistivity growing linearly with temperature [6, 84].

In the previous paragraphs we argued that the quasi-elastic Raman scattering in $Sr_{14}Cu_{24}O_{41}$ is a signature of collective CDW dynamics. The main argument in this respect was the Arhenius behavior of the scattering rate with the activation given by the *dc* transport. The low energy scale and the strong similarity between the Raman results in $x = 0$ compared to $x = 8$ and 12 Sr_{14-} Ca $Cu_{24}O_{41}$ allow us to claim that collective density wave excitations are also present at all Ca substitutional levels. Confirmation of this scenario comes also from more recent transport and optical conductivity data of Vuletić *et al.* [85] who observe the persistence of the microwave relaxational mode in x = 3 and 9 Sr_{14-} Ca $Cu_{24}O_{41}$. The authors of this work argue however that Ca substitution suppresses the CDW phase and long range order does not exist above x = 10. In this respect we argue that the feature observed in the Raman data in Fig. 24 at quite high temperatures in x = 12 Sr_{14-} Ca $Cu_{24}O_{41}$ is due to local fluctuations of the CDW order.

How can one reconcile the observation of the same activation energy for $\Gamma(T)$ with the fact that in the insulating regime σ_{dc} in x = 12 Sr_{14-} Ca $Cu_{24}O_{41}$ is not activated and, moreover, it turns metallic at high temperatures, a behavior clearly not consistent with the prediction of Eq. (8)? One possible explanation suggested by the *c*-axis optical conductivity data is the following: in $Sr_{14}Cu_{24}O_{41}$ one can observe a relatively broad mid-IR peak with an onset around 140 meV, see Fig. 10 and Refs. [10, 51]. In Sr_{14-} Ca $Cu_{24}O_{41}$ this peak continues to be present [10] and remains a distinct feature although there is a large spectral weight transfer to low energies. We propose that the common mid-IR feature is responsible for the similarly activated behavior of the relaxation parameter $\Gamma(T)$ and observe that the energy scale of this peak (which is also seen in high T_c cuprates) is set by the ladder AF exchange energy of about 135 meV. In this perspective, a speculative explanation for non-Fermi-liquid like metallic *dc* conductivity at high Ca substitution levels could be based on a collective density wave contribution. Ca substitution introduces disorder that could lead to a much broader distribution of pinning frequencies which may

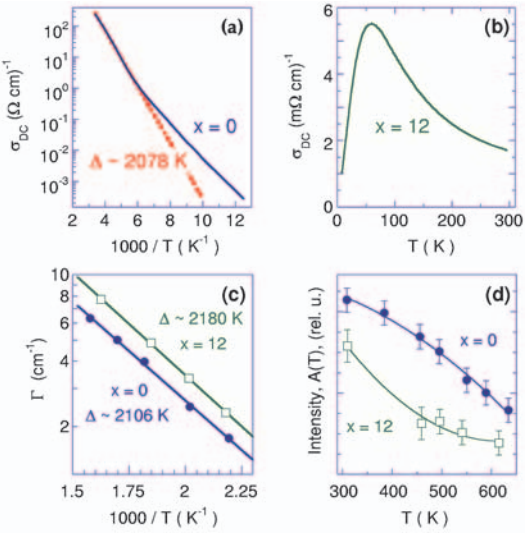

Fig. 25. Panels (a) and (b) show the temperature dependent *dc* conductivity for x = 0 and 12 Sr_{14-} Ca $Cu_{24}O_{41}$. Panel (c) shows Arhenius temperature dependence of the relaxational rate $\Gamma(T)$ for x = 0 (filled circles) and x = 12 (empty squares). The variation of the quasi-elastic peak intensity, $A(T)$, with temperature (solid lines are guides for the eye) is shown in panel (d).

extend to very low energies, towards the *dc* limit, rendering a Fröhlich type component contributing to σ_{dc}. Intuitively one can imagine that the current carrying objects are not quasi-particles but (because of a small CDW correlation length) 'patches' of holes organi ed in a density wave order.

Another more conventional scenario for the metallic behavior in x = 12 Sr_{14-} Ca $Cu_{24}O_{41}$ could be based on an anisotropic and partially gapped Fermi surface in the context of higher dimensionality of the electronic system. The soft X-ray study described before, see Fig. 23, shows that the CDW correlations are two dimensional in $Sr_{14}Cu_{24}O_{41}$ and recent low frequency dielectric response measurements [86] were able to track down the relaxational peak in a configuration with the electric field parallel not only to the ladder legs but also to the rung direction. One should keep in mind however that the transport along the rung and leg directions is different, as is proven by the ratio of the a to c-axis conductivities, $\rho_a/\rho_c \approx 10$, for a large range of Ca dopings. This can also be related to the fact that we do not observe in Fig. 25a the screened longitudinal CDW relaxational mode in (aa) polari ation although the hole ordering is two dimensional. Additional support for this conjecture comes from an angle resolved photoemission study [87] which shows that while for $Sr_{14}Cu_{24}O_{41}$ the gap is finite, for $Sr_5Ca_9Cu_{24}O_{41}$ the density of states rises almost to the chemical potential and also from the fact that it is known that the low energy optical spectral weight transfer is enhanced with furt-

her increase in Ca substitution [10]. In this picture, the insulating behavior in x = 12 Sr_{14-} Ca $Cu_{24}O_{41}$ below 70 K can be understood in terms of carrier condensation in the density wave state which leads to a completely gapped Fermi surface. In order to explain the similar relaxation rates $\Gamma(T)$ for $Sr_{14}Cu_{24}O_{41}$ and x = 12 Sr_{14-} Ca $Cu_{24}O_{41}$ one has to invoke however a strongly momentum dependent scattering rate and coupling of the condensate to normal carriers.

Irrespective of the exact microscopic model, the low energy properties of Sr_{14-} Ca $Cu_{24}O_{41}$ crystals bring challenging and unresolved aspects. Moreover, the proof for existence of CDW correlations along with strong similarities between local structural units and transport properties in Cu-O based ladders and underdoped high-T_c materials suggest that carrier dynamics in 2D Cu-O sheets at low hole concentration could be also governed by a collective density wave response.

5 Summary

In this chapter we focussed on magnetic and electronic properties of two-leg ladder materials. We observed at high frequencies (3000 cm^{-1}) in the $Sr_{14}Cu_{24}O_{41}$ compound a two-magnon (2M) resonance characteristic of an undoped ladder which we analy e in terms of symmetry, relaxation and resonance properties. Our findings regarding the spectral properties of this excitation were contrasted to 2M Raman measurements in other magnetic crystals and existing theoretical calculations, emphasi ing the sharpness of the 2M peak in the context of increased quantum fluctuations in one-dimension. This comparison made us suggest that the spin-spin correlations in an undoped two leg ladder may have a modulated component besides the exponential decay characteristic of a spin liquid ground state. We found that the 2M peak resonates with the Mott gap determined by $O2p \rightarrow Cu3d$ transitions, following the behavior of the optical conductivity in the 2-3 eV region. Interplane Sr substitution for Ca in $Sr_{14}Cu_{24}O_{41}$ introduces strong disorder leading to inhomogeneous broadening of the 2M resonance in the undoped system. The doped holes in the spin liquid ground state further dilute the magnetic correlations, suppressing considerably the spectral weight of this excitation.

Sr_{14-} Ca $Cu_{24}O_{41}$ crystals at high Ca concentrations are superconducting under pressure and hole pairing was proposed to be a robust feature of doped ladders. The measured dielectric response in the microwave region, the low energy Raman data, the non-linear transport properties along with soft X-ray scattering allowed us to conclude that the ground state in Sr_{14-} Ca $Cu_{24}O_{41}$ for a wide range of Ca concentrations ($x \leq 12$) is characteri ed by charge density wave correlations. This state seems to be driven not by phonons but by Coulomb forces and many-body effects. We highlighted the similarity in the finite frequency Raman response as opposed to the very different behavior of the *dc* resistivity between undoped and doped ladders. We found that at high Ca concentrations, although the resistivity shows a crossover between insulating and linear in temperature metallic regime, the carrier relaxation is characteri ed by the same large activation energy ($\approx$ 2000 K) which determines the Arhenius behavior of the CDW compound $Sr_{14}Cu_{24}O_{41}$. This observation prompted us to suggest an unconventional metallic transport driven by collective electronic response.

Acknowledgments

We acknowledge collaboration with P. Abbamonte, B. S. Dennis, M. V. Klein, P. Littlewood, A. Rusydi, and T. Siegrist. The ladder crystals were provided by H. Eisaki, N. Motoyama, and S. Uchida.

References

[1] E. M. McCarron *et al.*, Mater. Res. Bull. **23** (1988) 1355.
[2] T. Siegrist *et al.*, Mater. Res. Bull. **23** (1988) 1429.
[3] E. Dagotto and T. M. Rice, Science **271** (1996) 618.
[4] E. Dagotto, Rep. Prog. Phys. **62** (1999) 1525.
[5] E. Dagotto , J. Riera, and D. Scalapino, Phys. Rev. B **45** (1992) 5744; T. M. Rice, S. Gopalan, and M. Sigrist, Europhys. Lett. **23** (1993) 445.
[6] T. Osafune *et al.*, Phys. Rev. Lett. **82** (1999) 1313.
[7] M. Uehara *et al.*, J. Phys. Soc. Jpn. **65** (1996) 2764.
[8] S. Maekawa, Nature **273** (1996) 1515.
[9] S. Sachdev, Science **288** (2000) 475.
[10] T. Osafune *et al.*, Phys. Rev. Lett. **78** (1997) 1980.
[11] N. Nücker *et al.*, Phys. Rev. B **62** (2000) 14384.
[12] M. Kato *et al.*, Physica C **258** (1996) 284.
[13] Y. Mi uno *et al.*, Physica C **282** (1997) 991.
[14] P. W. Anderson, Exchange in insulators, Ch. 2 in Magnetism, Vol. 1, ed. Rado and Suhl, Academic Press (1963).
[15] M. Takigawa *et al.*, Phys. Rev. B **57** (1998) 1124.
[16] T. Fukuda *et al.*, Phys. Rev. B **66** (2002) 012104.
[17] R. S. Eccleston *et al.*, Phys. Rev. Lett. **81** (1998) 1702.
[18] L. P. Regnault *et al.*, Phys. Rev. B **59** (1999) 1055.
[19] H. Kitano *et al.*, Europhys. Lett. **56** (2001) 434.
[20] K. Magishi *et al.*, Phys. Rev. B **57** (1998) 11533.
[21] M. A uma *et al.*, Phys. Rev. Lett. **73** (1994) 3463.
[22] T. Barnes *et al.*, Phys. Rev. B **47** (1993) 3196.
[23] L. D. Fadeev and L. A. Takhtajan, Phys. Lett. **85A** (1981) 375.
[24] S. R. White *et al.*, Phys. Rev. Lett. **73** (1994) 886.
[25] J. Oitmaa *et al.*, Phys. Rev. B **54** (1996) 1009.
[26] M. Matsuda *et al.*, J. of Applied Phys. **87** (2000) 6271.
[27] W. J. Buyers *et al.*, Phys. Rev. Lett. **56** (1986) 371.
[28] C. Knetter *et al.*, Phys. Rev. Lett. **87** (2001) 167204.
[29] F. D. M. Haldane, Physics Letters **93A** (1983) 464; Phys. Rev. Lett. **50** (1983) 1153.
[30] S. Trebst *et al.*, Phys. Rev. Lett. **85** (2000) 4373; S. Trebst, PhD Thesis, Bonn University (2002).
[31] G. Blumberg *et al.*, Phys. Rev. B **53** (1996) R11930.
[32] S. Sugai *et al.*, Phys. Rev. B **42** (1990) 1045.

[33] P. A. Fleury and R. Loudon, Phys. Rev. **166** (1968) 514.
[34] B. S. Shastry and B. I. Shraiman, Phys. Rev. Lett. **65** (1990) 1068; B. S. Shastry and B. I. Shraiman, Int. J. of Mod. Phys. B, **5** (1991) 365.
[35] S. Sugai and M. Su uki, Phys. Status Solidi (b) **215** (1999) 653.
[36] A. Go ar *et al.*, Phys. Rev. Lett. **87** (2001) 197202.
[37] M. Windt *et al.*, Phys. Rev. Lett. **87** (2001) 127002.
[38] T. Nunner *et al.*, Phys. Rev. B **66** (2002) 180404.
[39] K. P. Schmidt *et al.*, Phys. Rev. Lett. **90** (2003) 167201.
[40] S. Brehmer *et al.*, Phys. Rev. B **60** (1999) 329.
[41] A. A. Katanin and A. P. Kampf, Phys. Rev. B **60** (2002) R100403 and references therein.
[42] C. M. Canali and S. M. Girvin, Phys. Rev. B **45** (1992) 7127; A. W. Sandvik *et al.*, Phys. Rev. B **57** (1998) 8478.
[43] R. R. P. Singh *et al.*, Phys. Rev. Lett. **62** (1989) 2736.
[44] K. P. Schmidt, C. Knetter and G. S. Uhrig, Europhys. Lett. **56** (2001) 877.
[45] A. Gößling *et al.*, Phys. Rev. B **67** (2003) 052403.
[46] J. M. Tranquada *et al.*, Nature **429** (2004) 534.
[47] A. V. Chubukov and D. M. Frenkel, Phys. Rev. Lett. **74** (1995) 3057; A. V. Chubukov and D. M. Frenkel, Phys. Rev. B **52** (1995) 9760.
[48] T. Tohyama *et al.*, Phys. Rev. Lett. **89** (2002) 257405; H. Onodera, T. Tohyama and S. Maekawa, Physica C **392-396** (2003) 203.
[49] P. J. Freitas and R. R. P. Singh, Phys. Rev. B **62** (2000) 14113.
[50] A. Go ar, Phys. Rev. B **65** (2002) 176403.
[51] H. Eisaki *et al.*, Physica C **341-348** (2000) 363.
[52] M. W. McElfresh *et al.*, Phys. Rev. B **40** (1989) 825.
[53] P. Knoll *et al.*, Phys. Rev. B **42** (1990) 4842.
[54] C. Homes, private communications.
[55] A. Go ar *et al.*, Phys. Rev. Lett. **91** (2003) 087401.
[56] G. Blumberg *et al.*, Science **297** (2002) 584.
[57] A. A. Abrikosov and I. A. Ry hkin, Adv. Phys. **27** (1978) 147.
[58] T. Ohta *et al.*, J. Phys. Soc. Jpn. **66** (1997) 3107; C. Bougerol-Chaillout *et al.*, Physica C **341-348** (2000) 479.
[59] N. Ogita *et al.*, Physica B **281&282** (2000) 955.
[60] E. Orignac *et al.*, Phys. Rev. B **57** (1998) 5812; R. A. Hyman *et al.*, Phys. Rev. Lett. **76** (1996) 839.
[61] Z. V. Popović *et al.*, Phys. Rev. B **62** (2000) 4963.
[62] M. Yoshida *et al.*, Phys. Rev. B **44** (1991) 11997.
[63] F. Nori *et al.*, Phys. Rev. Lett. **75** (1995) 553.
[64] S. L. Cooper *et al.*, Phys. Rev. B **42** (1990) R10785.
[65] M. Troyer, H. Tsunetsugu and T. M. Rice, Phys. Rev. B **53** (1996) 251.
[66] D. Poilblanc, D. J. Scalapino and S. Capponi, Phys. Rev. Lett. **91** (2003) 137203 and references therein.
[67] D. Poilblanc *et al.*, Phys. Rev. B **62** (2000) R14633.

[68] D. Poilblanc *et al.*, Phys. Rev. Lett. **75** (1995) 926.
[69] S. R. White, I. Affleck and D. J. Scalapino, Phys. Rev. B **65** (2002) 165122.
[70] L. Balents and M. P. A. Fisher, Phys. Rev. B **53** (1996)12133.
[71] S. Katano *et al.*, Phys. Rev. Lett. **82** (1999) 636.
[72] H. Mayaffre *et al.*, Science **279** (1998) 345.
[73] G. Grüner, Density waves in solids. Perseus, Cambridge, MA (1994).
[74] H. Fröhlich, Proc. Roy. Soc. London **A223** (1954) 296.
[75] L. Degiorgi *et al.*, Phys. Rev. B **44** (1991) 7808.
[76] P. A. Lee, T. M. Rice and P. W. Anderson, Solid State Commun. **14** (1974) 703.
[77] G. Grüner, Rev. Mod. Phys. **60** (1988) 1129.
[78] R. J. Cava *et al.*, Phys. Rev. B **30** (1984) 3228.
[79] P. B. Littlewood, Phys. Rev. B **36** (1987) 3108.
[80] M. Born and K. Huang, Dynamical theory of crystal lattices. Oxford (1954).
[81] M. V. Klein, Chap. 4 in Light Scattering in Solids I, (Ed. M. Cardona) Springer-Verlag (1983).
[82] Abbamonte P *et al.* (2004) Nature, in print.
[83] P. Abbamonte *et al.*, Science **297** (2002) 581 and references therein.
[84] Balakirev F F *et al.* (1998) http://xxx.lanl.gov/abs/cond-mat/9808284 preprint.
[85] T. Vuletić *et al.*, Phys. Rev. Lett. **90** (2003) 257002.
[86] Vuletić T *et al.* (2004) http://xxx.lanl.gov/abs/cond-mat/0403611 preprint.
[87] T. Takahashi, Phys. Rev. B **56** (1997) 7870.

ELECTRONIC PROPERTIES OF α -NaV_2O_5

A. Gozar[1,2] and G. Blumberg[1]

[1] Bell Laboratories, Lucent Technologies, Murray Hill, NJ 07974, USA
[2] University of Illinois at Urbana-Champaign, Urbana, IL 61801, USA

1 General Properties of $\alpha - NaV_2O_5$ and Motivation for a Spectroscopic Study

Introduction – $\alpha'-NaV_2O_5$ is one of the several phases in the class of $Na_xV_2O_5$ systems [1] and until now it is by far the most studied of them. Since 1996 this compound (denoted in the following simply by NaV_2O_5) has received considerable attention because it was thought to be the second realization, after $CuGeO_3$, of a quasi-one dimensional (1D) *inorganic* material displaying a spin-Peierls (SP) transition. The interest was justified given the scarcity of inorganic materials having this property, which is quite interesting especially for the scientific community working in the field of low dimensional quantum spin systems. However, it turned out that the physics of NaV_2O_5 is more complicated and intriguing than that and the degrees of freedom involved are not only the ones describing the spins and the lattice.

What is a SP transition? We discussed in Chapter [2] the general properties of a Peierls distortion which is a transition to charge density wave state. This means that below some temperature T_P the crystal gets distorted and the electronic density acquires a periodic spatial modulation, a process during which the loss in elastic energy is compensated by the gain in the kinetic energy of the electrons. A crucial role is played by the nesting properties of the Fermi surface (i.e. the property that enables one to connect points of the Fermi surface by wavevector characteristic of other excitations, in this case phonons) which makes low dimensional systems especially susceptible to such an instability. A pure SP

transition is one in which the lattice distortion is caused by the magneto-elastic coupling, the gain in energy in this case being related to the spin degrees of freedom [3]. In other words, it is a lattice instability driven by the magnetic interactions. This phenomenon leads to the formation of a spin-singlet ($S = 0$) ground state and the opening of a spin-gap in the magnetic excitation spectrum, i.e. a finite energy is required to excite the system from its ground state to lowest triplet ($S = 1$) state. A signature of a SP state is thus an isotropic activated temperature dependence in the uniform magnetic susceptibility below the transition at T_{SP}. In addition, as opposed to an usual Peierls transition, the direct participation of the spins leads to specific predictions for the dependence of T_{SP} on external magnetic field H [4]. This has to do with the fact that in the spin case the filling factor of the electronic band and accordingly the magnitude of the nesting wavevectors can be varied continuously by a magnetic field. This statement should not be taken *ad litteram*, but in the sense that the magnetic problem can be mapped onto a fermion like system by using a transformation of the spin operators, the magnetic field playing the role of the chemical potential, see Refs. [3, 4] for more details.

So what is the difference between $CuGeO_3$ and NaV_2O_5 ? In the former, the SP nature of the transition observed around 14 K was inferred from the exponential drop in the magnetic susceptibility below this temperature and especially from the dependence of T_{SP} on an applied external field [5], see Fig. 1a. As predicted by theory, it was found that the field dependence was quadratic, $1-T_{SP}(H)/T_{SP}(H=0) = \alpha \cdot [(\mu_B H)/(k_B T_{SP}(H=0))]^2$. Moreover, the experimental proportionality factor $\alpha = 0.46$ was also in very good agreement with the theoretical mean field value [4]. Finally, neutron scattering experiments and detailed investigations of the field-temperature phase diagram confirmed the previous SP interpretation [6].

As for NaV_2O_5 , many common properties with $CuGeO_3$ were observed. In 1996 an isotropic activated behavior below $T_c = 34$ K was observed by Isobe and Ueda [1], see Fig. 1b. Soon after that there appeared the first report of X-ray and inelastic neutron scattering (INS) data in NaV_2O_5 [7]. The authors reported the existence below $T_c \approx 35$ K of superlattice peaks due to a modulation given by $k = (2\pi/2a, 2\pi/2b, 2\pi/4c)$. This wavevector characterizes distortions corresponding to unit cell doubling along the a and b axes and quadrupling along the c direction. In the same paper, INS results showed that the transition is accompanied by the opening of a spin gap whose value was estimated to be $\Delta_S \approx 9.8$ meV. So far these results are qualitatively similar to the ones in $CuGeO_3$ but it is worth noting that a value $2\Delta_S/k_B T_c$ of approximately 6.5 already suggests a departure from the mean field value 3.52. The interpretation in terms of a simple SP transition became more questionable when experiments in magnetic fields were performed. Note the inset of Fig. 1 where the susceptibility derivative is shown for two values of the external field. Specific heat measurements in chemically well characterized crystalline samples of $Na_xV_2O_5$ with $0.95 \leq x \leq 1$ in fields up to 16 T revealed a single λ-shaped anomaly at $T_c = 33.5$ K and an isotropic decrease of the anomaly with $\Delta T_c \propto H^2$ [8]. However, the proportionality factor, the parameter α introduced in the previous paragraph, was found to be only 20% of the mean field value [4]. Similar measurements aided by magnetic susceptibility data showed a $T_{SP}(H = 0) - T_{SP}(H = 14T) \approx 0.15$ K, about a factor of 7 smaller than the expected value [9]. Heat capacity measurements also pointed out

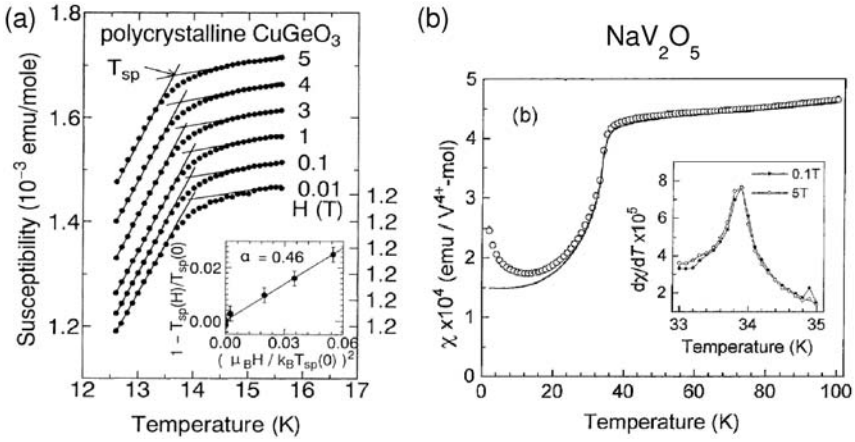

Fig. 1. (**a**) Magnetic susceptibility of polycrystalline $CuGeO_3$ as a function of temperature for several values of external magnetic fields. Inset: the reduced temperature $1 - T_{SP}(H)/T_{SP}(H = 0)$ as a function of the dimensionless parameter $\mu_B H/k_B T_{SP}(H = 0)$; the proportionality coefficient is 0.46. Data from Ref. [5]. (**b**) Temperature dependent susceptibility in powder samples of NaV_2O_5 . The inset shows the derivative $d\chi(T)/dT$ as function of temperature for 0.1 and 5 T. Data from Ref. [1].

incompatibilities with a simple SP transition [10]. The authors of this paper could not reconcile the mean field predictions of the magnetic contribution to the heat capacity with the experimental data: the specific heat jump $\delta C/k_B T_c$ was found to be a factor of 20 higher than 1.43, which is the mean-field value, if the linear contribution $C = \gamma T$ at high temperatures was fixed to the theoretical expectations for a 1D $S = 1/2$ antiferromagnetic (AF) chain.

The discussion above gives us a feeling about some of the important parameters and energy scales one has in mind when discussing the properties of NaV_2O_5 . The connection made with the 1D AF $S = 1/2$ chain will get support from the description of the crystal structure which is done in the following and will become more clear also in the next section where other properties of NaV_2O_5 in the high temperature phase are discussed. However, we conclude from what has been said that in order to explain quantitatively the experimental findings one has to take into account other degrees of freedom, contrary to the initial belief that at T_c one deals solely with a magnetically driven phase transition. It has become clear that the coupling of the lattice to the charge degrees of freedom is crucial for understanding the details of what happens at T_c. The slow advance in this field was also due to the difficulty in the interpretation of X-ray diffraction data and because of a wrong identification of the crystal structure in an early study [11] which generated a plethora of subsequent papers which were at odds with each other. Diffraction anomalous fine structure spectroscopy (also called resonant X-ray diffraction, an example of which was discussed in Chapter [2] in connection to the existence of a density wave order in

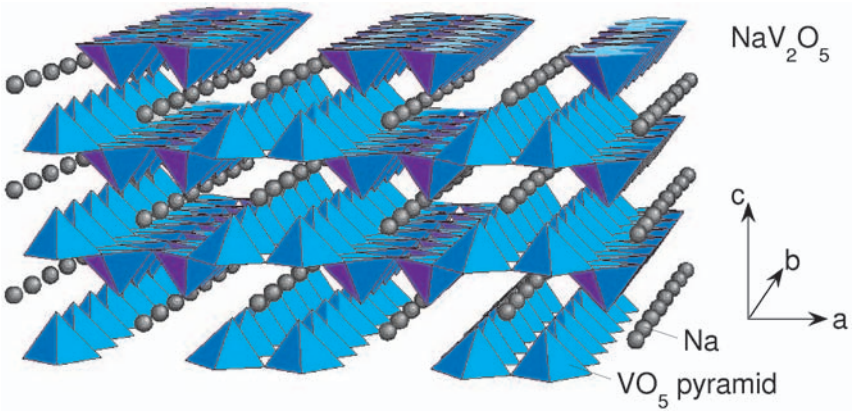

Fig. 2. The 3D crystal structure of NaV_2O_5 (adapted from Ref. [9]). Na atoms form 1D chains along the *b*-axis and pairs of corner sharing VO_5 pyramids pointing in the same direction form V_2O_5 ladder rungs. The legs of these ladders run along the *b*-axis, see also Fig. 3.

doped two-leg ladder structures) finally brought more understanding of the nature of the charge ordering in NaV_2O_5 , see Ref. [12] and citations therein. However, in spite of years of intensive investigation of both the high and low temperature phases of NaV_2O_5 , no microscopic model has successfully explained all the features of the transition and, as we will discuss in more detail, the nature of prominent excitations seen in spectroscopic experiments as well as the light coupling mechanisms to the collective spin and/or charge excitations is still far from being clear.

Structure and electronic properties – The crystal structure of NaV_2O_5 is shown in Fig. 2. It contains Vanadium-Oxygen planes stacked along the *c*-axis and separated by Na chains. Each V-O plane is formed from pairs of edge sharing VO_5 pyramids running along the *b*-axis (the vertices of the pyramids in every such pair of chains are pointing in opposite direction along the *c*-axis), each pair being connected in turn to a neighboring one by corner sharing pyramids. In the (*ab*) plane, see also Fig. 3, one can identify two-leg ladder (2LL) units, very similar to the ones found in $Sr_{14-x}Ca_xCu_{24}O_{41}$ compounds. One can look for instance at a pair of adjacent rows of VO_5 pyramids pointing in the same direction along the *c*-axis. The rungs of the ladder, oriented along the *a*-axis are formed by a pair two V ions bridged by an O atom which is at the common corner of two pyramids.

Can this structure be mapped onto an array of quasi-1D electronic units? A valence counting for $Na^+V_2^{4.5+}O_5^{2-}$ shows that the formal V valence is 4.5+. The electronic configuration of a neutral V atom is $3d^34s^2$, so a V^{5+} ion has a closed shell configuration while the V^{4+} has one $3d$ electron on the upper shell. On the average there is one electron shared by two V ions and this makes the 2LL's to be at quarter filling factor. The initially proposed non-centrosymmetric $P2_1mn$ crystal symmetry group at 300 K [11] allowed for two inequivalent V positions, interpreted as magnetic V^{4+} and non-magnetic V^{5+} sites.

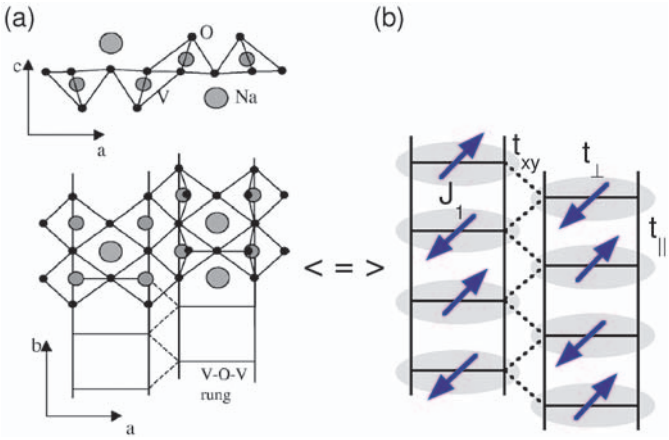

Fig. 3. (**a**) Schematic representation of the NaV_2O_5 in the (010) (upper figure) and (001) (lower figure) planes (from Ref. [13]). (**b**) Cartoon with the spin structure in the high temperature phase. The structure can be mapped on a weakly interacting array of quasi 1D $S = 1/2$ spin chains. J_1 is the superexchange between neighboring spins along the b-axis and $t_\perp$, $t_\parallel$ and t_{xy} are the rung, leg and inter-ladder hopping parameters.

The magnetic properties were thought to be determined by rows of $S = 1/2$ V^{4+} ions along a leg of a ladder (with the other one remaining magnetically inert), each row of V^{4+} ions being only weakly coupled to to the adjacent one due to large separation between them. It is now accepted based on X-ray diffraction studies that above T_c the correct space group is the centrosymmetric *Pmmn* group [14, 15, 16]. This is important in what regards the number of distinct of V atoms existent in the high temperature phase: the inversion center and the the two vertical mirror planes (i. e. perpendicular to the (ab) plane) imply that there is only one type of V atoms with an effective valence of 4.5+. The fact that NaV_2O_5 is in a mixed-valence state is further supported by nuclear magnetic resonance (NMR) studies which confirmed the average oxidation state of all vanadium atoms to be $V^{4.5+}$ [17].

Accordingly, one can think about the ladder structure of NaV_2O_5 as having on each rung an electron equally shared by pairs of V atoms forming the rungs. Susceptibility data also indicate that the coupling between the spins of these electrons is antiferromagnetic (AF) [1]. The local symmetry splits the five-fold degeneracy of the d shell and makes the d_{xy} band (the zero's of the wave function are along the a and b axes) the lowest in energy compared to the bands generated by the other orbitals [14]. Consequently, the d_{xy} orbital is the relevant atomic state for the analysis of the low energy charge excitations. How about the quasi one dimensionality? A density functional calculation [14] of the energy bands and their mapping on tight-binding models yields for the hopping terms the following values: a rung hopping $t_\perp \approx 0.38$ eV, a leg hopping $t_\parallel \approx 0.17$ eV and a inter-ladder hopping $t_{xy} \approx 0.012$ eV. A difference of more than an order of magnitude

between the intra-ladder and inter-ladder wavefunction overlap is theoretical proof for the quasi-1D nature of the system. As we will show later in relation to the low temperature phase, the dispersions of the low energy collective excitations along the a-axis, which were found to be much smaller than the ones along the leg direction, confirm experimentally this hypothesis. This is also true at 300 K, as can be inferred from the band dispersions derived from an angle resolved photoemission (ARPES) study [18].

In a regular Fermi liquid system, the V valence would make this compound metallic. However, an insulating character inferred from resistivity measurements was confirmed to exist both above and below T_c [10]. This behavior is due to correlation effects [19] and it is explained below within a simple model. Consider a rung having one electron in a bonding orbital. The next excitation would be a transition to the antibonding state situated somewhere about $2t_\perp$ above. Assuming that the on-site Coulomb energy U is infinite, i.e. no two electrons can be found on the same V d shell, an electron can hop only on an empty site of a neighboring rung. However, this will cost an energy of the order of $2t_\perp$. The quarter filled ladder becomes thus equivalent to a half filled Hubbard chain with an "effective" on-rung repulsion $U_{eff} = 2t_\perp$ [19], explaining in principle why the vanadium ladders are insulating.

Experimental – In the following we will discuss properties of the high and low temperature phases of NaV_2O_5, concentrating on the results of our Raman scattering experiments. The single crystal we measured had the $a \times b \times c$ dimensions around $2 \times 4 \times 0.5$ mm and was grown as described in [20]. Data were taken in a backscattering geometry using linearly and circularly (the latter only at the lowest temperatures in magnetic fields) light from a Kr^+ laser. All the data were corrected for the spectral response of the spectrometer. In addition, the resonance profile at 300 K took into account the change in the optical properties of the material as the excitation energy ω_{in} was swept from infra-red (IR) to violet. The incident photons propagated along the c-axis and by (xy) we denote a polarization configuration with the incoming photon polarization $\mathbf{e}_{in} \parallel \hat{x}$ and outgoing polarization $\mathbf{e}_{out} \parallel \hat{y}$.

2 Magnetic Raman Continuum in the High Temperature Phase ($T \geq 34$ K)

2.1 Experimental Properties: Polarization, Resonance, and Temperature Dependence

Before illustrating the experimental properties of the observed broad Raman continua, we show the main features of the absorption spectrum in an energy range up to about 4 eV [21]. The absorption properties will be discussed in some detail because we will use these results in the analysis of our resonance Raman study. Optical conductivity data from Ref. [21] are shown in Fig. 4. The spectra show the relevant energy scales involving electron dynamics along and across the legs. The left panel the electric field is was polarized along the rung direction while in the right panel the polarization was parallel to the legs direction. The a-axis polarized spectra show a strong peak at 0.9 eV (peak A) with a shoulder at 1.4 eV and another peak at 3.3 eV (peak B). A similar, but

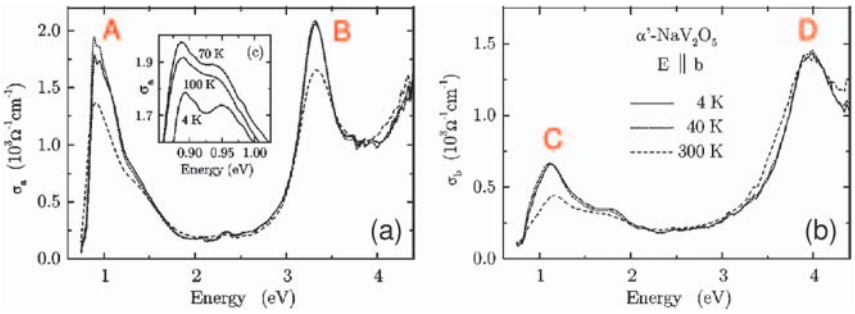

Fig. 4. Optical conductivity at 4, 40 and 300 K for electric fields $E \parallel a$ (left) and $E \parallel b$ (right) from Ref. [21]. The letters A, B, C and D mark the main absorption features in the 0 - 4 eV energy range.

blueshifted sequence, is observed for light polarization along the b direction, the energies of the observed excitations being around 1.2 (peak C), 1.9 and 3.9 eV (peak D). It should be noted that the relevant electronic orbitals to be taken into account when discussing excitations in this energy range are the Vanadium $3d$ and Oxygen $2p$ states.

In Ref. [21] the authors assign peak A to an optical transition from a bonding to an anti-bonding orbital made out of symmetric (and antisymmetric) combinations of d_{xy} orbitals of the two V atoms forming a rung. This is the fundamental gap of the optical spectrum. This interpretation was supported on one hand by an ARPES study [18] which shows that the top of the bands generated by the O $2p$ orbitals are about 3 eV below the V $3d$ manifold as well as by a band structure calculation [14] and on the other hand, by a study of the evolution of this excitation with Ca doping in $Na_{1-x}Ca_xV_2O_5$ [21]. It has been observed that the spectral weight of this peak decreases linearly with Ca concentration which is consistent with a diminishing intensity due to the fact that with two electrons per rung (Ca has a 2+ valence) the many-body 2-particle state no longer allows a low energy bonding-antibonding transition [22]. The above mentioned Ca dependence was also used to rule out the scenario that the 0.9 eV peak is a result of V $3d \leftrightarrow 3d$ transition, the argument being that such an excitation would be proportional to the number of V^{4+} ions which increases with Ca doping. If peak A is essentially an on-rung excitation, peak C at 1.1 eV was assigned to an optical excitation involving neighboring rungs [21]. The final wave function is different than the one corresponding to peak A because it involves combination of states having one rung with zero electrons and another one being doubly occupied, the red-shift of about 0.3-0.5 eV seen in a-axis polarization reflecting thus excitonic effects for the on-rung electron hole pair.

As for peaks B and D, they are thought to arise likely from transitions between O $2p$ and V $3d_{xy}$ manifolds. Remarkable is also the substantial absorption all the way up to 4 eV and even beyond which explains the black color of the NaV_2O_5 crystals. We will discuss in the following polarization, resonance of the Raman continuum we observe in the 0 - 200 meV energy range as well as its temperature dependence. A discussion of our proposed scenario for its origin will be contrasted to other present interpretations.

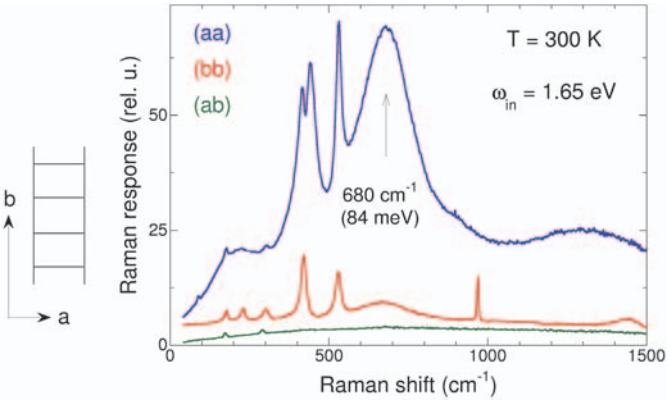

Fig. 5. T =300 K Raman spectra of NaV_2O_5 in (aa), (bb) and (ab) polarizations taken using $\omega_{in} = 1.65$ eV laser excitation energy.

Polarization properties – Fig. 5 shows three room temperature Raman spectra taken in (aa), (bb) and (ab) polarizations and using the $\omega_{in} = 1.65$ eV excitation energy. The (ab) polarized spectrum has the lowest intensity and it is rather featureless. Next in terms of the overall background intensity comes the spectrum in (bb) polarization. Several relatively sharp features are seen at 420, 530 and 968 cm^{-1} and also some weaker ones at lower energies, 177, 230 and 300 cm^{-1}. Besides these modes, there is a broad excitation peaked at 680 cm^{-1}, but not particularly strong. The sharp modes are phonons, excitations which were studied intensively both by Raman and IR spectroscopy [23]. The strong continuum which extends all the way from the origin and having a main a peak around 680 cm^{-1} becomes the most prominent feature of the Raman spectrum in (aa) polarization. There are differences in phonons, for instance in this geometry we see two modes close to 420 cm^{-1} as opposed to only one in (bb) configuration and also the 968 cm^{-1} peak is not present. We also note the observation of a smaller shoulder at about 200 cm^{-1} and, interestingly, of another excitation around 1320 cm^{-1}, which is approximately twice the energy of the main peak at 680 cm^{-1}.

Raman resonant profile at $T = 300$ K – In Fig. 6 we show the dependence of the intensity of this continuum as a function of the energy of the incoming photons ω_{in}. The resonance behavior is shown for the three polarizations shown in Fig. 5. Line colors for each of the spectra shown are chosen so that they roughy correspond to the actual color of the laser excitation beam in the visible spectrum. Besides the usual spectrometer/detector correction, the spectra shown in this figure were corrected for the optical properties of the crystal. The absorption coefficients the refraction indexes as well as the transmission at the sample interface were calculated using the real and the imaginary parts of the complex dielectric function provided to us by the authors of Ref. [21]. The spectral weight of the Raman continuum in the (aa) polarized spectra seems to be peaked at the extremities of the excitation range of the Kr^+ laser, 1.55 and 3.05 eV respectively. As

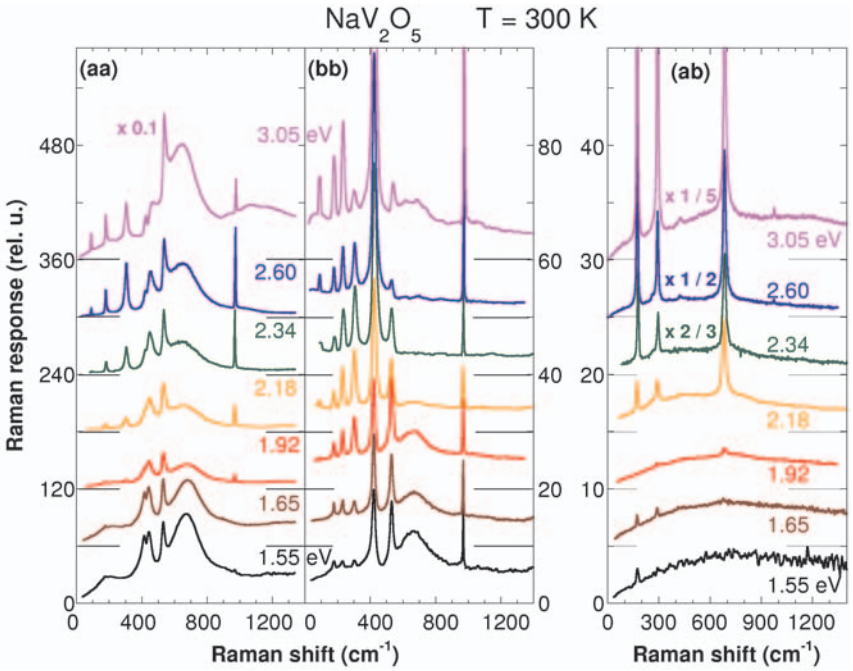

Fig. 6. Raman response at $T = 300$ K in (aa) (left panel), (bb) (middle panel) and (ab) (right panel) polarizations for different incoming photon energies. Note the relative intensity scales for the three polarizations as well as the multiplication factors used for the 3.05 eV spectrum in (aa) polarization and 3.05, 2.60 and 2.34 eV spectra in (ab) configuration.

for the $\omega_{in} = 1.65$ eV spectrum shown in Fig. 5, the broad Raman band is present also in (bb) polarization and the resonant enhancement in this configuration follows roughly the behavior in (aa) geometry. Obvious signatures of the (bb) polarized continuum can be seen for instance in the $\omega_{in} = 1.55$, 1.65, 1.92 or 3.05 eV spectra, while for excitation energies corresponding to the yellow, green and blue in the visible spectrum this Raman band is absent. It is important to note that although in cross polarization we do not observe a similar structure of the continuum as in (aa) and (bb) geometries, i.e. a broad Raman band peaked around 680 cm^{-1}, the overall intensity of the Raman background is excitation dependent, and a simple inspection of the right panel in Fig. 6 suggests that in (ab) configuration we see a slight decrease of the background as ω_{in} is decrease from 1.55 to 1.92 eV followed by an uprise at the other end of the spectrum, see the multiplication factors used for the 2.34, 2.60 and 3.05 eV.

The large width of the observed continuum makes it a distinct feature compared with the other sharp phononic lines seen in the spectra of Fig. 6 and points strongly to its

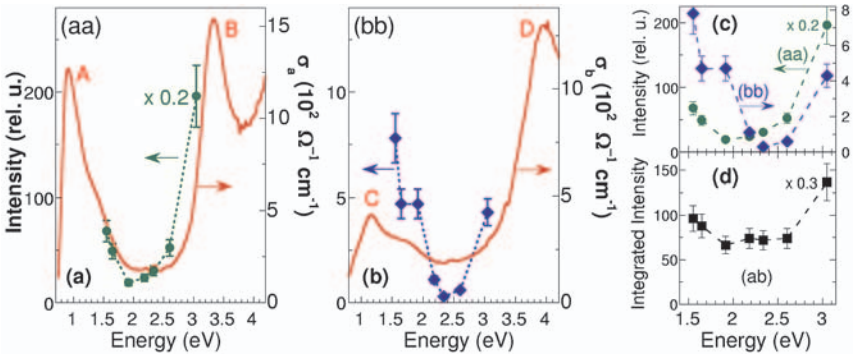

Fig. 7. (**a**) Intensity of the electronic Raman band (extracted from the 680 cm^{-1} peak hight) in (*aa*) polarization as function of the excitation energy ω_{in} (green solid circles). Dashed lines are guides for the eye. The a-axis optical conductivity σ_a is plotted on the right scale (solid red line). (**b**) The b-axis optical conductivity σ_b is shown by a solid red line, and the resonant profile in (*bb*) polarization is shown by blue diamonds. (**c**) Resonance profiles in (*aa*) (left scale) and (*bb*) (right scale) polarizations from panels (**a**) and (**b**) but this time plotted together. The same symbols as in (**a**) and (**b**) are used. Note the blue shift of the profile in (*bb*) configuration. (**d**) The intensity of the continuum in (*ab*) polarization obtained by integrating the Raman response, $\int \chi''(\omega)\ d\omega$, between 100 and 1200 cm^{-1} with the phonons masked. The optical conductivity data is courtesy of the authors of Ref. [21].

electronic origin. Since the phonons are not the focus of the present study, we make only a few remarks about these features at room temperature. The interested reader can consult Raman and IR studies in Refs. [23, 24, 25] for a detailed analysis of their behavior as a function of polarization, excitation energy and temperature along with some lattice dynamical calculations. In all three polarizations we observe an enhancement in the Raman intensity of the low energy phonons in the 100 - 400 cm^{-1} energy range. Some of the phonons situated in the region where the electronic Raman band is more intense have a pronounced asymmetric (Fano) shape due to the interaction with the underlying continuum. The 531 cm^{-1} mode (assigned to V-O$_{leg}$ stretching mode [23]) is proof for the interaction between the the lattice and the electronic degrees of freedom [24], see for instance the spectra corresponding to excitation energies $\omega_{in} \geq 2.34$ eV in (*aa*) polarization.

Fig. 7a-b shows the Raman resonant excitation profile for the 680 cm^{-1} band plotted against the optical conductivity data, see Fig. 4 and Ref. [21]. The red line is the the optical conductivity $\sigma(\omega)$ and the same notations as in Fig. 4 are used for the main four absorption features seen in *a* and *b* axes polarized spectra. The dots represent the intensity of the Raman band extracted from the 680 cm^{-1} peak height. This way of analyzing the data was chosen in the absence of a suitable fitting function for the background and also because of the presence of strong phononic features interacting with

the continuum. The resonant enhancement towards both ends of the visible spectrum remarked in the discussion of Fig. 6, can be clearly observed here. The efficiency of the inelastic cross section follows very closely the absorption bands, showing that this excitation is always seen 'in resonance'. Importantly, if the resonance profiles for (aa) and (bb) polarizations are plotted together, see the inset of Fig. 7c, one can observe that the blue shift of the b-axis polarized optical peaks with respect to the peaks in the a-axis spectra is also reflected in the dependence of the Raman band intensity as a function of excitation frequency. Although the clean phononic selection rules we see in the data which can be easily checked for instance by comparison of cross and parallel polarized spectra, see Figs. 15 and 16, are strong reasons to believe that the (bb) continuum is not a result of sample misalignment in conjunction with polarization "leakage" from the (aa) spectra, the agreement between the blue shift seen in both the optical spectra and the resonance profile for the two polarizations leaves no doubt that the feature seen in (bb) data is a true Raman signal.

The 680 cm^{-1} peak is absent in (ab) polarization, but we still see in this case a signal which is excitation energy dependent. This signal is not coming from spurious effects related to crystal quality and the complete absence of scattering in the 0-2Δ energy region in the low temperature phase, where $\Delta = 66$ cm^{-1} is the T = 10 K low temperature spin gap which opens below $T_c = 34$ K, supports this statement. In Fig. 7d we show the integrated (ab) polarized Raman response $\chi''(\omega)$ between 100 and 1200 cm^{-1} with the sharp phononic features masked. As was the case for the data in parallel polarizations, we observe again an enhancement in the background for the lowest and highest excitation energies ω_{in}.

According to the interpretation of the optical features seen in Fig. 4, the intermediate electronic states responsible for the resonant behavior involve on-rung bonding-antibonding transitions, inter-rung excitations as well as transitions from the lower O $2p$ states to the V $3d$ bands. Irrespective of the interpretation, we established so far that the continuum peaked at 680 cm^{-1} appears in both (aa) and (bb) polarizations, the peak is not present in cross polarization and is a strongly excitation energy dependent feature, which allows us to clearly see its next overtone for incoming photon frequencies $\omega_{in} \geq 2.6$ eV or $\omega_{in} \leq 1.65$ eV.

Temperature dependence for $34 < T < 300$ K and the role of fluctuations above the critical temperature – We show in Fig. 8a the dependence on temperature of the Raman continuum as we cool down from 300 K to just about the transition. The data are taken in (aa) polarization and the excitation energy used was $\omega_{in} = 1.83$ eV. We remark two effects regarding this spectra. The first is the downshift with cooling of the strong Raman band in the 680 cm^{-1} region accompanied by an increase in its spectral weight from the low energy side. Although the interaction with the 530 cm^{-1} phonon may lead to an additional shift compared to its "bare" energy, one can observe by simple inspection of the spectra a substantial softening of about 80 cm^{-1} with cooling from 300 to 45 K. No qualitative changes in the band are seen with further decreasing temperature below the transition.

The second effect is the appearance of another band below 200 cm^{-1}. The 0-200 cm^{-1} energy region is important because this is where many new collective excitations are seen

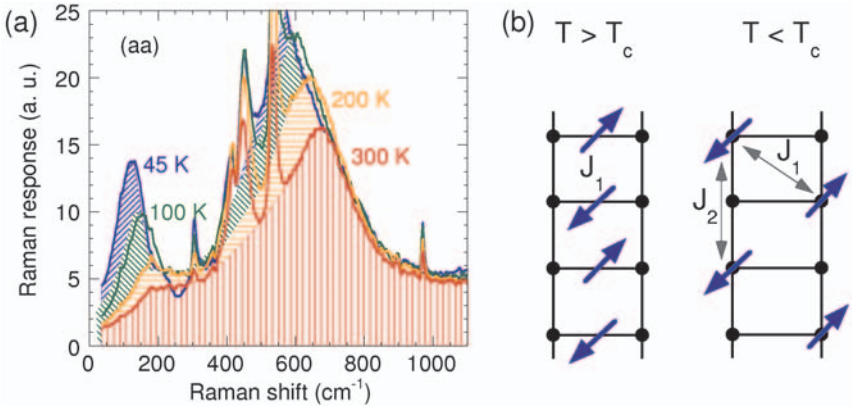

Fig. 8. (**a**) Raman scattering continuum in NaV_2O_5 taken in (*aa*) polarization at 300, 200, 100 and 45 K using the $\omega_{in} = 1.83$ eV excitation energy. Note the softening of the band peaked at 680 cm^{-1} at room temperature as well as the development of another continuum at frequencies below 200 cm^{-1}. The sharp modes are phonons. (**b**) Cartoon showing the average distribution of the valence electrons provided by V atoms (represented by solid black dots) within a given ladder above (left) and below the transition (right). The picture on the right does not show the additional lattice dimerization and the alternation of the nearest neighbor superexchange J_1, see the following section for a more detailed discussion of the low temperature phase.

below $T_c = 34$ K as a result of lattice distortions and the opening of the spin gap. By now it is established that below T_c the in-plane ordering of the spin/charges on the outer Vanadium *d* shell involves, in each ladder, a zig-zag pattern like the one shown in Fig 8b [12]. The band at low energies can thus be understood as a precursor of the strong and sharp collective modes in the ordered phase, see Section 3. It is important that this continuum exist in an incipient form at 300 K and can be clearly seen already at 200 K. Similarly with the band peaked at 680 cm^{-1}, this low energy counterpart gains substantial spectral weight from the low energy side with cooling. We consider the data in Fig. 8a as proof that the transition at 34 K is preceded almost up to 300 K by strong fluctuations of the low temperature order and suggest that the reason the critical temperature is so low is not because of intra-ladder dynamics, but it is rather due to the phasing of the zig-zag charge order between coplanar and inter-layer ladders. This statement is supported by frequency and temperature dependent electron spin resonance (ESR) linewidth, see Ref. [26]. At 36 K the authors of this work estimate a characteristic frequency of about 700 GHz (≈ 25 cm^{-1}), for the precursor fluctuations.

We also note that the topology of the ladder at quarter filling and the charge pattern below T_c suggest that other magnetic terms are important beside the nearest neighbor exchange J_1 shown in Figs. 3b and 8b. For instance, if one compares in Fig. 8b the low temperature exchange path between two V atoms sitting on two adjacent rungs (which

is related to J_1) to the exchange path between next nearest neighbors (which is related J_2), one can argue that the difference may not necessarily be large. On the contrary, the superexchange J_2, taking place on a straight line across one vanadium and two O_{leg} atoms, could be comparable to J_1. A quantitative estimation of possible competing interactions would be very welcome and important for the interpretation of the magnetic excitation spectrum. The statements about the importance of other magnetic terms is supported by measurements of the temperature dependent magnetic susceptibility and its comparison with the theoretical expectations within the model of 1D AF Heisenberg chains characterized only by nearest neighbor exchange, see Ref. [20]. The authors of this work show that the measured susceptibility $\chi(T)$ above 34 K is not in good quantitative agreement with the predictions of $S = 1/2$ uniform Heisenberg chain with only nearest neighbor interaction. The data can be reconciled with theory only if additional magnetic exchanges are included and/or the superexchange itself is temperature dependent. In view of the discussion above, we believe that a significant temperature dependence of the effective magnetic interactions as well as of the relative importance of competing exchange terms could be understood if one invokes the increasing charge imbalance on each V-O-V rung with cooling.

2.2 Interpretation of the Raman Continuum in Terms of Multi-spinon Raman Scattering

In discussing the nature of the Raman band we have to acknowledge the existence of a substantial body of prior spectroscopic (Raman and IR) work, see for instance Refs. [22, 23, 24, 25, 27], as well as concomitant or subsequent to our study [28, 29]. Interesting properties were observed in addition to what has been discussed in the previous section. One of them is its dependence on the Na concentration in $Na_xV_2O_5$ crystals [28]. With a decrease of the Na concentration a pronounced weakening in the continuum intensity as well as a downshift in energy from 680 to about 480 cm^{-1} has been observed as x was varied from from 1.0 to 0.85 (and implicitly decreasing the number of rung electrons). Another property is related to the presence of a broad continuum of excitations in the far IR part of the optical conductivity data, extending from very low frequencies (below about 100 cm^{-1}) almost up to the electronic excitations seen around 1 eV, when the electric field was parallel to the a-axis [22]. This continuum, whose energy scale resembles much the one seen in Raman spectra, was interpreted by the authors of Ref. [22] in terms of "charged two-magnon" excitations. In order to insure an electric dipole coupling to these double spin flip excitation the authors had to introduce a rather artificial charge asymmetry between the legs of each ladder, represented by an energy difference for the single particle on-site energy depending if it sits on the left or right of the V-O-V rung. Moreover, the model, which includes the hopping parameters $t_\perp$ and $t_\parallel$ together with Coulomb repulsion U for double site occupancy, neglects the Coulomb interaction between nearest neighbor sites which seems to be an important ingredient for the analysis of charge dynamics of the quarter filled ladder [19]. While the energy scales certainly suggest a common origin for the Raman and IR continua, the interpretation of both of these features is a matter of debate.

The common interpretation of the Raman continuum is that it is related to Raman active transitions between crystal split d levels of the V atoms [25, 28], while the inter-

action with the phonons resulting in the so called Fano shape is due to electron-phonon coupling. This assignment is not however based on specific calculations. On the contrary, its energy scale seems to be too low as band structure calculations [14] show that the splitting between vanadium d bands involves energies at least of the order of 2500 cm^{-1}. The temperature dependence showed in Fig. 8 remains also unexplained in this scenario. In fact, it was pointed out in Ref. [27] that with cooling the broad band should recover the discrete nature of an excitation between well defined atomic electronic levels. The band remains however broad to the lowest temperatures (around 5 - 10 K) measured.

Although the possibility that the Raman continuum has a magnetic origin was mentioned in literature, this idea has been ruled out, see Refs. [25, 27, 28] and the main argument was that this excitation appears only in (aa) polarization and it is not present in (bb) polarization. The latter geometry was considered the expected scattering configuration where a two-magnon type excitation should be observed if one takes into account the spin structure shown in Fig. 3b and also the fact that, according to the Fleury-Loudon Hamiltonian [30, 31], the b-axis is parallel to the dominant exchange path. A second reason was that a two-magnon continuum peaked at 680 cm^{-1} would yield a value of the nearest neighbor superexchange J_1 too large in comparison to estimations from magnetic susceptibility [20] and inelastic neutron scattering [32]. We will return to this issue later in this section. For the moment we mention that it was demonstrated in Figs. 6 and 7 that the continuum, although weaker, is present also in the configuration when the incoming and outgoing photons are parallel to the ladder legs. Moreover, a strong argument in our view against d to d transitions is the presence of the second overtone of this excitation around 1320 cm-1, see Fig. 5, whose weaker intensity suggests that it results from second order scattering. There is no intrinsic reason that the crystal field split bands are distributed in such a way that another set of Raman allowed transitions is to be found at exactly double the frequency of the main peak. Finally, there is a counterpart of this Raman continuum in the spin-Peierls compound $CuGeO_3$ whose origin is generally agreed on to be in double spin-flip processes [33]. The different energy scales of the continua in $CuGeO_3$ and NaV_2O_5 can be understood in a simple way if one takes into account the ratio of the dominant magnetic exchange interactions in these two compounds.

The above arguments allow us to propose that the origin of the Raman band peaked at 680 cm^{-1} is magnetic and that it represents a two-magnon like continuum of excitations. Moreover, we will show in the following that this assignment is compatible with its temperature dependence, resonance and polarization properties, which further strengthen the identification of the origin of this band as magnetic. We will also discuss the possibility of reconciling the obtained value for the magnetic superexchange with the ones existent in the literature. Given the fact that in the high temperature phase NaV_2O_5 can be mapped onto an array of weakly interacting $S = 1/2$ AF chains (see Fig. 3), we will discuss first their characteristic excitations within the Heisenberg model.

Excitations out of a quasi 1D $S = 1/2$ AF chain and the two spin-flip Raman continuum – The purpose in this part is to show that a broad band as observed experimentally is consistent with the theoretical predictions for spin-flip excitations in a 1D AF $S = 1/2$ chain. Consider a system like in Fig. 8b and the Hamiltonian:

$$H = J_1 \sum_{(i,j)=NN} \mathbf{S}_i \cdot \mathbf{S}_j \; + \; J_2 \sum_{(i,j)=NNN} \mathbf{S}_i \cdot \mathbf{S}_j \qquad (1)$$

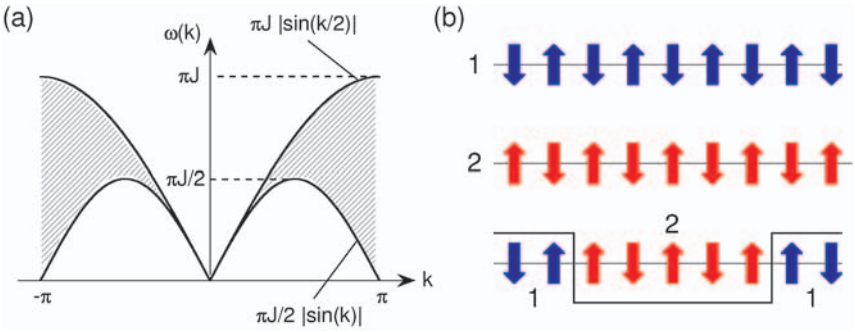

Fig. 9. (**a**) Excitation spectrum of a 1D $S = 1/2$ AF linear chain with nearest neighbor Heisenberg exchange J. The lower line, $(\pi J/2)|\sin(k)|$ is the dispersion for one spinon. The $\pi J|\sin(k/2)|$ curve marks the higher energy edge of the two-spinon continuum. (**b**) Cartoon with a two spinon excitation. 1 and 2 are two degenerate configurations in the AF ground state. The two spinon excitation in the lower part can be thought of as a pair of domain walls between regions of type 1 and 2. The total spin of this state compared to the states 1 and 2 amounts to one spin flip.

where $\mathbf{S}_i$ and $\mathbf{S}_j$ represent spins on chain sites i and j respectively while NN and NNN stand for nearest neighbor ($j = i \pm 1$) and next nearest neighbors in the same ladder ($j = i \pm 2$). J_1 and $J_2 = \alpha J_1$ are the corresponding superexchange integrals and we consider the case where both of them are positive. The NNN term leads to spin frustration, but due to the larger spatial separation in the high temperature phase it is generally expected that J_2 is only a fraction of J_1. Let us look at the $J_2 = 0$ case first. The excitations out of a $S = 1/2$ 1D AF chain in this limit are gapless domain wall solitons called spinons which have a dispersion given by $\omega(k) = \frac{\pi J}{2}|\sin(k)|$ [34]. Spinons carry a spin of 1/2 and they can be created only in pairs, each pair corresponding to one spin flip and thus having integer spin. In some sense one can think about a magnon like excitation as being composed out of two spinons. Similarly, a state with two spin flips (two-magnon Raman scattering) would correspond to the creation of four spinons. Figure 9a shows the excitation spectrum of the spinons and the continuum of two-particle excitations. Panel b is an intuitive visualization of a two-spinon excitation carrying a total spin $S = 1$.

Here we come back again to a remark made in Chapter [2]: which way provides a better description of the spin dynamics, one that starts from true elementary excitations (in our case the spinons which are fractional spin excitations) or a description in terms of elementary triplet ($S = 1$) excitations, which are bosonic modes (corresponding to the known textbook magnons in the case where there is long range magnetic order and a semi classical approach applies)? This question is probably most relevant for the $S = 1/2$ 1D AF chain with only NN interactions because this is the archetype of a gapless critical model whose true elementary excitations are known to be the spinons, and not triplons (elementary triplets) [34]. This question was addressed by the authors of Ref. [35], who perturbatively calculated spectral densities for various operators R connecting the

ground state to states with different number of excited triplets according to: $I(\omega) = \sum_f | < f|R|0 > |^2 \delta(\omega_f - \omega_0 - \omega) = -\pi^{-1} Im[< 0|R(\omega + \omega_0 - H)^{-1} R|0 >]$ where H is given by Eq. 1 with $J_2 = 0$, $|f >$ and $|0 >$ denote excited and the ground state while ω_f and ω_0 represent their energies. Using a continuous unitary transformation which conserves the number of elementary triplets and appropriate interactions R, they could evaluate separate relative contributions to $I_{tot} = \int_0^\infty d\omega \; I(\omega) = \sum_{n=1}^\infty \; I_n$ from sectors with only one, two and three triplets (the total intensity being calculated using the sum rule $I_{tot} =< 0|R^2|0 > - < 0|R|0 >^2$). The main result was that the sum rule is very well fulfilled by taking into account only the contributions up to (and including) three triplets [35], implying that there is no necessity to resort to fractional excitations. It would be interesting to check if this statement remains true at all energies, an issue which could be addressed probably by evaluating relative contributions to energy and wavevector dependent spectral densities, $I(k, \omega)$.

How does the excitation spectrum evolve with increasing the NNN frustrating parameter $\alpha = J_2/J_1$? It turns out that for $0 \leq \alpha \leq \alpha_c$ the excitation spectrum remains gapless and qualitatively the same as in Fig. 9 [36] and the true excitations are again spinons. However, there is a critical value $\alpha_c \approx 0.24$ above which the low energy spectrum develops a finite spin gap. The spin-spin correlations become short ranged from the power law fall-off characteristic of the uniform unfrustrated chain. For an intuitive picture, the value $\alpha = 0.5$ is very interesting because in this case the ground state is doubly degenerate and it is known exactly to be made of products of NN singlets. In the notation of Eq. 1, this means that for this value of α the two degenerate ground states are $|0 >_1 = 2^{N/2} \prod_{i=1}^N (| \uparrow_{2i-1} > | \downarrow_{2i} > - | \downarrow_{2i-1} > | \uparrow_{2i} >)$ and $|0 >_2 = 2^{N/2} \prod_{i=1}^{N-1} (| \uparrow_{2i} > | \downarrow_{2i+1} > - | \downarrow_{2i} > | \uparrow_{2i+1} >)$. The value of $\alpha = 1/2$ for 1D chains is known as the Majumdar-Ghosh point [37]. This is also the moment to advertise the compound discussed in Chapter [38], $SrCu_2(BO_3)_2$, which is the only experimental realization of a two-dimensional structure, well described by a NN and NNN Heisenberg terms, having an exactly known ground state. Similarly to the 1D case, this ground state can be also written in terms of independent nearest neighbor singlet states.

As it is also discussed in the Chapter [38], in the absence of spin-orbit coupling and because of the spin selection rules, Raman scattering usually couples to double spin flip states *via* the photon induced spin exchange process [30, 31]. The effective spin Hamiltonian corresponding to this interaction in the off-resonance regime is given by:

$$H_{int} \propto \sum_{<i,j>} (\mathbf{e}_{in} \cdot \mathbf{r}_{ij})(\mathbf{e}_{out} \cdot \mathbf{r}_{ij}) \mathbf{S}_i \cdot \mathbf{S}_j \tag{2}$$

where $\mathbf{r}_{ij}$ is the vector connecting these sites and $\mathbf{e}_{in}/\mathbf{e}_{out}$ are the unit vectors corresponding to the incoming/outgoing polarizations. Because the light wavevector is very small, the total momentum of the excitations probed has to be zero. From Fig. 9 one can infer that the energy range spanned by four spinon excitations with zero total momentum is quite large: from $\omega = 0$ up to $\omega = 2\pi J$. One also expects that the Raman form factor is peaked in the middle of this region, at $\omega = \pi J$, reflecting the divergence in the spinon density of states at this energy. The large energy range corresponding to the multi-spinon continuum along with the well established inelastic light coupling to double spin flip ex-

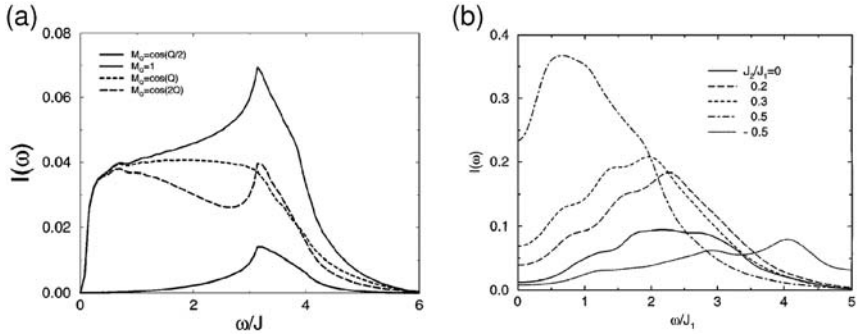

Fig. 10. (**a**) Raman intensity for four spinons evaluated with different matrix elements, $M = \cos(Q/2), 1, \cos(Q), \cos(2Q)$, from Ref. [39]. A nearest neighbor (NN) Fleury-Loudon interaction (Eq. 2) corresponds to $M = \cos(Q)$ and a next nearest neighbor (NNN) interaction to $M = \cos(2Q)$. (**b**) Raman intensity for the Heisenberg model (Eq. 1) for various ratios of the NNN exchange J_2 with respect to the NN term J_1. Note that an increase of J_2/J_1 results in a downshift of the four spinon continuum spectral weight. The results in this panel are also from Ref. [39].

citations is thus compatible with the existence of the broad Raman continuum observed in Figs. 5, 6 and 8.

In fact numerical calculations using the Hamiltonian Eq. 1 and an interaction of the form $H_{int} \propto \sum_i \mathbf{S}_i \cdot \mathbf{S}_{i+2}$ revealed that the Raman intensity corresponding to the four spinon excitations corresponds indeed to broad continuum like feature, see Fig. 10a and Ref. [39]. Note that this interaction is nothing else but a particular form of Eq. 2 for (*bb*) polarization (polarization along the chain direction) where a NNN term was chosen. It is also important to observe that because of the commutation relations with the system Hamiltonian, the interaction H_{int} could have been as well chosen to be $H_{int} = \sum_i \mathbf{S}_i \cdot \mathbf{S}_{i+1}$, i.e. to describe spin exchange between NN spins, but in this case it would have been necessary to include NNN terms in Eq. 1 so that $[H, H_{int}] \neq 0$. While the exact shape of the four-spinon continuum from Fig. 10a does not exactly correspond to the experimental findings in NaV_2O_5 (Figs. 5 and 6) or $CuGeO_3$ (Ref. [33]), it nevertheless proves that the four spinon Raman continuum is an excitation relevant on an energy scale ranging from zero up to energies of about $6J$ (which corresponds to the $0 - 2\pi J$ range inferred from Fig. 9). The overestimation of the low energy spectral weight has to do with the choice for the Raman matrix elements. One can compare Fig. 10a with results obtained by exact diagonalization and/or mean field approximation for the frustrated spin chain [40, 41]. These calculations reproduce better the experimental findings because the divergence at πJ is replaced by a broader peak and also because they eliminate the preponderant low frequency part.

Discussion of the temperature dependence – Here we intend to show that the temperature dependence from Fig. 8a is also consistent with an interpretation of the continuum in terms of multi-spinon excitations. The experimental observation there was

related to the softening of the Raman band with cooling from room temperature to about 40 K. An interesting connection can be made between Fig. 10b and the discussion about the role of fluctuations and higher order magnetic exchange terms regarding the results in Fig. 8a-b. In this respect, note also that, according to Eqs. 1 and 2, the inclusion of terms beyond the nearest neighbor (either in the system Hamiltonian or in the interaction Hamiltonians) are crucial for observing any inelastic magnetic signal.

Fig. 10b shows that there is a substantial overall downshift in the four-spinon spectral weight with increasing the NNN frustrating interaction J_2. When we analyzed the data in Fig. 8a-b we brought evidence that the fluctuations of the low temperature order start at high temperatures and also that magnetic susceptibility results cannot be understood if only the NN exchange J_1 is taken into account. In particular, we discussed that the tendency of the charges to arrange themselves in a zig-zag pattern can make the NNN exchange J_2 an important parameter. So the reasoning goes as follows: (1) decreasing the temperature leads to a more and more pronounced charge disproportionation along the left and right legs of the ladder; (2) this may lead on one hand to a decrease of J_1 because the exchange path gets modified (the two electrons on a rectangular plaquette formed by two rungs will like to stay along the diagonal) and on the other hand to a relative increase of J_2 because the NNN Vanadium atoms become connected by a straight, shorter superexchange path; (3) according to Fig. 10, both effects in (2) will lead to a softening of the four spinon Raman continuum. While still speculative (in the absence of a quantitative estimation of the charge imbalance as a function of temperature or of quantitative microscopic calculations of the relative strengths of the magnetic interactions) our point was to provide a possible basis for the understanding of the data in Fig. 8.

Discussion of polarization properties – In a strictly 1D system, because any two spin sites can be connected only by vectors $\mathbf{r}_{ij} \parallel \hat{b}$-axis, the Fleury-Loudon polarization selection rules (Eq. 2) would not allow coupling in a polarization perpendicular to the chain direction, the (aa) configuration. However, we do observe scattering in this geometry.

Here is the place to reiterate some issues about the symmetry of the high temperature phase. The importance of symmetry resides in the fact that it is the most direct way to establish the spin/charge pattern above T_c. We discussed in the introduction that more recent X-ray scattering as well as NMR data support a centrosymmetric group in the high temperature phase and the existence of only one type of V atoms with an average valence of +4.5. This means that, because the rung hopping $t_\perp$ is the dominant term compared to the inter-ladder hopping t_{xy} or the overlap along the chain direction $t_\parallel$ [14], on each rung there is only one electron which is rapidly hopping from the left to the right side making (averaged over the timescale characteristic of each experimental probe) the two rung vanadium atoms look equivalent. At a quantum mechanical level, one can think about the electronic wavefunction as a superposition of 'instantaneous' states having electrons arranged in different configurations so that when the charge density is averaged over the left and right legs of the ladder one gets (almost) equal fractional charges $q = e/2$.

In spite of the preference of the centrosymmetric group $Pmmn$ [9, 14, 15, 16] over the $P2_1mn$ group [11], this assignment is not entirely unambiguous and the analysis of the X-ray data becomes quite involved because both the crystallographic symmetries render almost identical diffraction patterns [9]. In fact a small, finite charge imbalance between

V-O-V ladder legs existent even at room temperature could not be completely excluded. This is fully consistent with the Raman data in Fig. 8 which shows that the effects of the fluctuations of the low temperature zig-zag order can be tracked down at all measured temperatures above $T_c = 34$ K and that this temperature has to do mostly with the inter-ladder phase coherence. This in turn means that locally and on relatively short time scales the charge pattern on each ladder is different from the average distribution seen by X-ray diffraction and that a cartoon for the high temperature phase like the one shown in Fig. 3 is only an idealized approximation.

If one agrees with the notion that inside each ladder the charge/spin distribution is not strictly 1D, then the selection rules derived from Eq. 2 allow scattering in (aa) polarization. So four spinon continuum should be seen in both (aa) and (bb) geometries, consistent with our experimental observations. This also implies that the temperature dependence of the magnetic Raman band should track the evolution of the zig-zag order in the V-O planes, in particular we should observe an increase of its spectral weight with cooling, a process driven by closer proximity to the low temperature phase. This is one aspect we already noted when discussing the Raman results, i.e. that the softening of the 680 cm^{-1} peak is also accompanied by an increase in the spectral weight on the lower energy side. Once the selection rules allow it, the peak in (aa) can be imagined as being the result of the well known phonon induced spin exchange process: an electron-hole pair is created by an electron dipole interaction involving bonding-antiboding V $3d$ orbitals and O $2p$ bands, see Fig. 4; in the intermediate state two pairs of spinons are emitted before the collapse into an excited spin state. Why is the signal in (aa) stronger than in the expected geometry (bb)? This has to do with the fact that the coupling when the electric field is perpendicular to the ladder is different from that along the b-axis and this is especially the case with the Raman vertex in resonance conditions. We showed in Fig. 6 that the intensity of the Raman band follows very closely the features seen in absorption, so one cannot talk about off-resonant conditions. In this respect we note that quite different couplings in (aa) with respect to (bb) polarization of fully symmetric excitations are also observed for phonons, see Fig. 5. It is known from the case of 2D cuprates that very strong enhancements of the magnetic signal can occur [42] and they have been observed in resonant Raman spectra [43]. A quantitative understanding of the anisotropy in the (aa) and (bb) intensities would require specific evaluations of the Raman matrix elements, but in principle it is compatible with our observations

A zig-zag pattern also implies finite magnetic scattering in (ab) polarization. In Fig. 7d we show that the integrated intensity in this geometry is excitation energy dependent, but the 680 cm^{-1} peak is not observed. In fact this is not surprising, because the spin flip scattering in cross polarization should have a different form factor and it belongs to a different irreducible representation in an orthorhombic group. As a result, it is a priori expected to have a different spectral shape than in parallel polarization. Due to the distinct form factor in different scattering configurations, the Raman intensity integrates from different parts off the Brillouin zone and symmetry properties may lead to the cancellation of the zone boundary divergence in the density of states at πJ. Examples in this regard are again the 2D cuprates where the inclusion of terms beyond the nearest neighbors in the effective light coupling Hamiltonian led automatically to the appearance

of magnetic scattering not only in B_{1g}, but also in A_{1g} and B_{2g} symmetry channels [44]. However, the spin pair scattering in each channel comes in with its own resonance and spectral properties.

Evaluation of the magnetic superexchange – The peak position of the four spinon continuum at 680 cm^{-1} (84 meV) (see Fig. 5) and the expected maximum in the Raman response at πJ_1 reflecting the divergence in the density of states (see Fig. 10a) lead to an estimation for the NN superexchange $J_1 \approx 27$ meV (218 cm-1 or 310 K). Given the spectral weight downshift induced by the presence of the NNN term J_2 (Fig. 10b) we can say that this value is a lower bound for the NN superexchange. Our value is in good agreement with the initial determination of J_1 from a fit to the magnetic susceptibility data [1] by the Bonner-Fisher prediction (Ref. [45]) as well as with the estimation from charged bi-magnon continuum observed in the optical conductivity data [22]. The interpretation of the IR absorption data relies on a global charge asymmetry between the ladder rungs. Seemingly artificially introduced, this assumption may be regarded retrospectively in a more favorable light in the context of strong fluctuations of the low temperature order. It is also possible that the difficulties in a precise distinction of the symmetry in the high temperature phase can be related to the same phenomenon. As for the magnetic susceptibility data from Ref. [1], it was pointed out in a more recent paper, Ref. [20], that it could not be reproduced quantitatively in subsequent studies. Moreover, the authors of this latter work obtained from an approximate fit (because they argued that the data cannot be quantitatively fit by a simple Bonner-Fisher expression involving only NN Heisenberg interactions) a value for J_1 which is almost twice as high as ours.

A fit to the experimental dispersion of the elementary triplet excitation in the low temperature phase obtained in a INS study, see Ref. [32], allowed the extraction of a value $J_1 \approx 60$ meV, also about a factor of two higher than 27 meV. Regarding this data we note that the maximum neutron energy transfer was 40 meV while the inferred maximum for the triplet dispersion was 93 meV. Accordingly, the value of the energy at the zone boundary, which is of crucial interest to us (see Fig. 9), was not determined directly but only by using an approximate fitting function [32]. Neither the authors of the INS work, nor those of Ref. [20] consider the possible influence of NNN exchange terms which we believe play an important role in determining the structure of the magnetic excitation spectrum.

We conclude by saying that our estimation for the lower bound of the superexchange, while not contradicting other analyses, is still too far apart to be explained by error bars. In our view, a quantitative determination of the relevant $J's$ is still an open issue and the underlying reason is in the strongly fluctuating low temperature order and the induced frustration effects. We also believe that the overall consistency between the interpretation of the strong Raman band in the high temperature phase in terms of multi-spinon excitations and our experimental findings strongly argues for its magnetic origin.

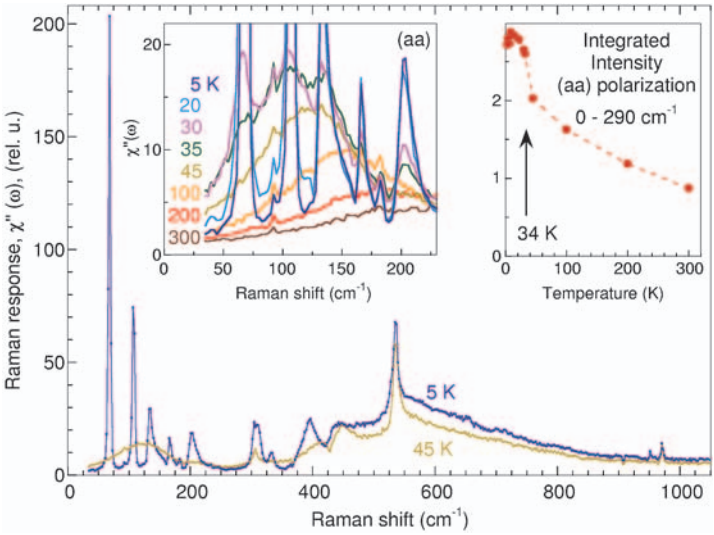

Fig. 11. The main panel shows the Raman response $\chi''(\omega)$ in (aa) polarization for T = 45 and 5 K. The data is taken using the $\omega_{in} = 1.92$ eV excitation energy. Left inset: Temperature dependence of the (aa) polarized spectra in the 0-250 cm^{-1} region. The data for 45 and 5 K are zoomed in spectra from the main panel. Right inset: Integrated intensity, $\int \chi''(\omega)\, d\omega$, between 0 and 290 cm^{-1} as a function of temperature.

3 Collective Excitations in the Low Temperature Phase of NaV_2O_5 ($T \leq 34$ K)

3.1 General Features of the Transition

In the main panel of Fig. 11 we show two Raman spectra taken at 45 and 5 K in (aa) polarization. One can notice that drastic changes occur across the transition at 34 K especially at low frequencies where many new modes appear. The most prominent three features below 150 cm^{-1} are a very strong mode at 66 cm^{-1}, another one around 105 cm^{-1} and the sharp edge at 134 cm^{-1} ($\approx 2 \cdot 66$ cm^{-1}) marking the onset of a continuum. Other new excitations which are clearly seen in the T =5 K spectrum are found around 166, 202, 308, 332, 393 and 949 cm^{-1}. Besides these modes, other weaker excitations are seen around 122 and 182 cm^{-1}. In Fig. 8 we argued that the strong temperature dependence in the low frequency part of the spectra and the development of the low frequency continuum between 0 and 250 cm^{-1} is a precursor feature signaling fluctuations of the low temperature order at temperatures above T_c. That this is true can be seen in the left inset of Fig. 11 which shows that below about 34 K, this broad excitation 'splits' into very sharp resonances. While above T_c the individual ladders do not know about each other at large distances, below 34 K a global phase coherence of the charge and lattice

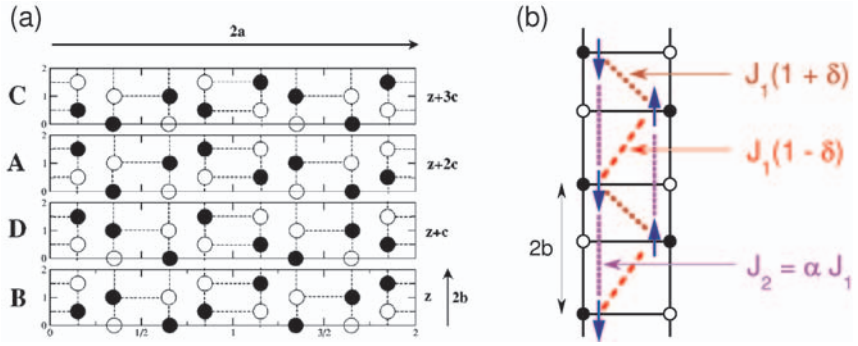

Fig. 12. (**a**) Schematic representation of the 3D charge/spin order (from Ref. [12]). Black (open) circles are V^{4+} (V^{5+}) atoms. Each of the four rectangles shown represents a unit cell in the low temperature phase. The sequence *B D A C* represents one of the stacking sequences along the *c*-axis which are consistent with X-ray diffraction data, i.e. it has to the inter-layer phasing of the zig-zag order in each layer. Note the doubling (along *a* and *b* directions) and the quadrupling of the unit cell along the *c*-axis. (**b**) Cartoon with the zig-zag order and relevant intra-ladder magnetic interactions. The parameter δ characterizes the dimerization of the superexchange due to the unit cell doubling along the ladder legs. Inter-ladder interactions are not shown.

dynamics is established. Also, the drop in the 0-200 cm^{-1} continuum marks the opening of a gap in this energy region. The integrated Raman response in the 0-290 cm^{-1} region, $\int \chi''(\omega)\, d\omega$ shown in the right inset of Fig. 11, increases with decreasing T almost all the way down to the lowest measured temperature, their weight relating most probably to the variation of the charge/spin order and lattice distortion in the low temperature phase.

How are these changes to be understood and what are the energy scales below T_c? As for the crystal structure it is known that in the V-O layers there is a doubling of the unit cell along both the *a* and *b* directions [7, 12, 46]. Moreover, in every ladder there is a zig-zag type ordering of the Vanadium valence electrons rendering, crudely speaking, V^{4+} and V^{5+} atoms on each rung of the ladder, see one rectangle in Fig. 12a. Given the $2a \times 2b$ supercell, there are exactly four realizations of this superstructure in each plane, and they are denoted by A, B, C and D. The existence of four such possibilities to accommodate the zig-zag order provided a clue for the understanding of the quadrupling of the lattice constant along the *c*-direction. Initially an average face centered orthorhombic structure was proposed to explain the X-ray data at low temperatures [46]. The authors proposed a stacking disorder pattern along the *c*-axis rendering an effective global orthorhombic structure characterized by the face centered space group $Fmm2$. However, this group has two mirror planes parallel to the *c*-axis which is at odds with the zig-zag order in each plane. The resolution of this problem suggested in Ref. [46] was that because X-rays are sensitive only to the average structure, a model lacking mirror symmetry in each plane but having the appropriate stacking disorder along the *c* axis can be in accordance with the measured diffraction pattern. A later resonant X-ray study argued for a lower

(monoclinic) symmetry of the low temperature structure and proposed only two almost degenerate stacking patterns perpendicular to the ladder planes [12]. One of them, the B D A C model is shown in Fig 12a. It was proposed that the true crystal structure below T_c involves the existence of stacking faults of different possible patterns. The data was suggested to reflect the presence of competing arrangements along the c direction of nearly degenerate units. This may lead to a rich phase diagram as a function of a parameter which could directly affect the inter-layer interactions. Indeed, X-ray diffraction data under pressure, see Ref. [47], show the development of a series of modulation wavevectors corresponding to an array of commensurate phases in the $P-T$ diagram. The complicated observed sequences were qualitatively understood within the devil's-staircase-type phase transitions driven by two (presently unknown) competing interactions along c.

The above details and the discussion in the previous section give an idea about the difficulty in understanding quantitatively what exactly happens with the structure both above and below the transition. However, what can be surely said about the changes in the in-plane magnetic interactions as a result of the transition? A qualitative picture of what happens inside a given ladder can be obtained from Fig. 12b. The unit cell doubling along the b direction leads to an alternation in the NN superexchange J_1 which is quantified by the parameter δ. Due to the particular arrangement of charges in the zig-zag pattern, it seems that the NNN term may also play an important role in the spin dynamics. The single ladder hamiltonian can be thus written as:

$$H = J_1 \sum_i [(1 + (-1)^i \delta)\mathbf{S}_i \cdot \mathbf{S}_{i+1} \ + \ \alpha \mathbf{S}_i \cdot \mathbf{S}_{i+2}] \tag{3}$$

The charge/spin order coupled to the lattice dimerization in the direction perpendicular to the ladders may lead to a complicated 2D pattern of magnetic exchanges (see for instance the discussion in the caption of Fig. 14). However, assuming a relatively weak inter-ladder coupling, which is confirmed experimentally by the small dispersion of the magnetic modes along a-axis, one can assume that the backbone Hamiltonian for the magnetic interactions is given by Eq. 3, i.e. a dimerized and frustrated 1D AF $S = 1/2$ chain.

We will discuss later the excitations from dimerized and frustrated chains in more detail. This topic has been the focus of many theoretical studies [48, 49, 50]. Here we are preoccupied only with the main result of the dimerization of the NN exchange, which is shown in Fig. 13a-b. If in the uniform case, panel a, the excitation spectrum is gapless (see also Fig. 9), any finite dimerization δ will open up a spin gap at the Brillouin zone center. This gap, denoted by Δ, scales as $\Delta \propto \delta^{3/2}$ apart from logarithmic corrections [48, 49]. Given the fact that in the absence of any dimerization a gap can be opened only due to frustration for $\alpha \geq \alpha_c \approx 0.24$, one can see that in the (δ, α) parameter space the spin gap and the magnetic excitation spectrum in general can be quite complicated. Results of calculations for concrete sets of parameters are shown for instance in Fig. 17. This figure will be discussed later in connection with the possible observation of Raman active magnetic collective modes in the low temperature phase. As for the short wavelength excitations, we mention that in general, for quite a wide range of parameters δ and α, the energies of the elementary triplet excitations at the zone boundary are not strongly renormalized from $\pi J_1/2$, which is the value corresponding to the uniform NN AF spin chain.

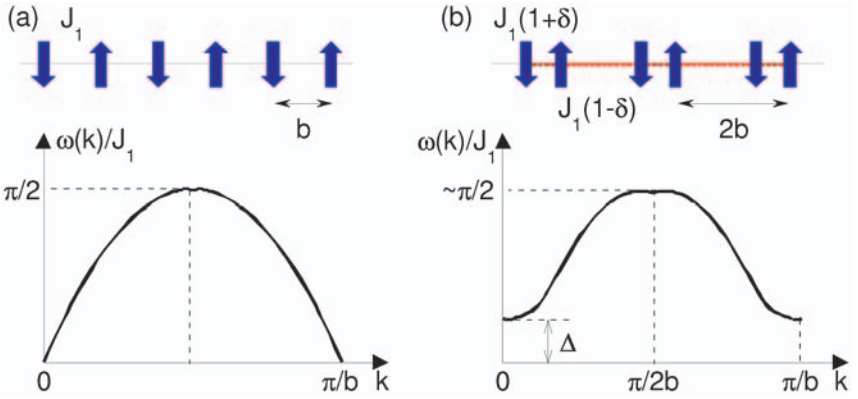

Fig. 13. (**a**) Cartoon showing the dispersion of the elementary excitations (spinons) in a uniform $S = 1/2$ AF chain (the same as in Fig. 9a). (**b**) Qualitative changes in the (slightly) dimerized Heisenberg chain. The unit cell along the chain becomes $2b$ and the alternation of superexchange is given the parameter δ (the same as in Fig. 12). The elementary excitations are $S = 1$ triplets and a spin gap Δ opens up at the Brillouin zone center. Apart from logarithmic corrections, Δ scales as $\delta^{2/3}$ [48].

The low temperature phase has been quantitatively explored by various techniques. INS data show that below T_c there are two close-by gapped magnon excitations which have a large dispersion along the b-axis (inferred to be of about 80 meV - 645 cm^{-1}) and the corresponding $k = 0$ values between 8 and 11 meV (see the caption of Fig. 14 for a discussion) [32]. The magnitude of the a-axis modulation is much smaller, of the order of only 1 meV, confirming weak inter-ladder interaction. We note that one of the spin gaps found by INS is situated at 8.3 meV (66.9 cm^{-1}), an energy which, within error bars, is equal to the one corresponding to the very strong Raman active mode seen at 65.9 cm^{-1} in Fig. 11 below T_c. Note that the double folding of the branch corresponding to the 8.3 meV spin gap (shown in Fig. 14b) leads to the appearance of another Brillouin zone center feature with an energy of 10.9 meV (87.9 cm^{-1}). The presence of spin-orbit coupling allows the observation of some of these elementary triplet excitations also in far IR [51] and ESR spectra [52]. A low temperature gap of 8.13 meV (65.5 cm^{-1}) is determined with high resolution by these two techniques.

We observed so far that the transition at 34 K involves several aspects: (1) crystallographic distortions leading to doubling of the in-plane lattice constants along and across the ladder legs as well as a quadrupling of the unit cell in a direction parallel to the c-axis; (2) in-plane zig-zag charge ordering which has a very complicated pattern in a direction perpendicular to the plane; (3) development of gapped magnetic branches (with spin gaps in the 9 meV energy range) which are much more dispersive along the ladder legs than in the transverse direction. The question is what is the driving force of this transition? Is it a spin-Peierls transition as it was initially thought, is it driven only by Coulomb forces

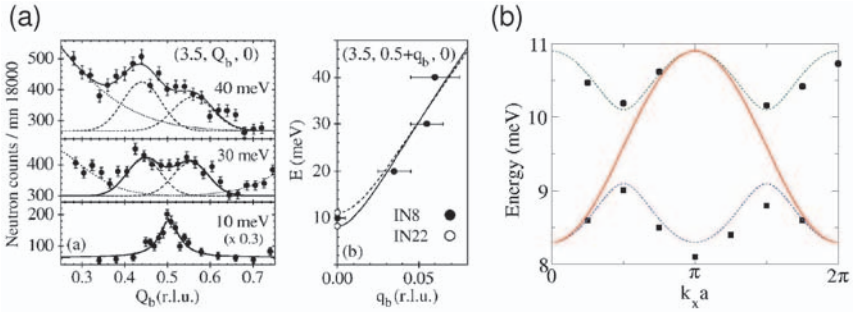

Fig. 14. Inelastic neutron scattering data from Ref. [32] (**a**) Left panel: Constant energy scans along the chain direction. The wavevector Q_b is defined in units of $1/b$. Right panel: Energy dispersion of the elementary triplet excitation along the chain direction (b-axis); $q_b = Q_b - 0.5$. The empty and filled circles at $q_b = 0$ in this figure correspond to data taken on two thermal neutron spectrometers, IN8 and IN22. (**b**) Dispersion along the a-axis for $Q_b = 1$ of the elementary triplet branch showing the folding of this excitation due to the unit cell doubling in the direction perpendicular to the ladders. Consequently, its periodicity is π/a. The red line corresponds to the unfolded branch; note that its periodicity is $2\pi/a$. According to the interpretation in Ref. [32], in the Brillouin zone of the high temperature phase there is a second branch analogous to the one shown by the red line and very close in energy, whose dispersion is phase shifted by $\pi/2$. The reason this branch appears is because the superexchange J_1 are slightly different in adjacent ladders as a result of charge/spin ordering. In the low temperature phase this second branch gets folded too (see Fig. 4 in Ref. [32]), and the data in (**a**) refers to this particular excitation. In the end, there are four Brillouin zone center modes corresponding to 8.3 (66.9) and 10.9 (87.9) meV (cm^{-1}), from the first branch shown in panel (**b**) and to 9.1 (73.4) and 10.1 (81.5) eV (cm^{-1}) from the second branch.

which stabilize the zig-zag ordering, leading also to lattice distortions *via* electron-phonon coupling or does it occur mainly as a result of a structural instability? Note that in the latter two scenarios the opening of a spin gap in the magnetic excitation spectrum is a by-product of the lattice/charge ordering rather than the main cause of the transition.

The arguments against an ordinary spin-Peierls scenario were mentioned in the introduction and they rely mainly on the absence of magnetic field effects on T_c, the absence of other incommensurate states at high fields and the observation of a large entropy release at the transition which could not be accounted by the spin degrees of freedom alone. Seo and Fukuyama proposed in Ref. [53] a model Hamiltonian containing single d_{xy} V orbitals and taking into account on-rung, ladder leg and inter-ladder hopping parameters $t_\perp$, $t_\parallel$ and t_{xy} (see Fig. 3), as well as on site (U) and nearest neighbor Coulomb interactions $V_\perp$, $V_\parallel$ and V_{xy} (these latter notations are in correspondence with the notations used for the hopping parameters). Three stable AF solutions were found within the Hartree approximation and they correspond to: (1) the uniform phase (all V atoms are equivalent, i.e.

what is thought to be realized in the high temperature phase); (2) the chain type having V^{4+} atoms on a given ladder leg and V^{5+} ions on the other (which would correspond to the initial room temperature crystal structure determination [11]); (3) the zig-zag type, which is the one shown in Fig. 12. It was found that for a large (and relevant) range of parameters, including the ones proposed in Ref. [14], the lowest energy state (above a small critical value of the intersite Coulomb interaction defined as $V = V_\perp = V_\parallel = V_{xy}/\sqrt{2}$) is one having zig-zag order with alternate charge disproportionation on each rung. Depending on the relative magnitude of the hopping parameters it was proposed that the drop in susceptibility below T_c is related to a singlet state formation of essentially localized pairs of spins. The zig-zag order was also found consistent with the observed in-plane unit cell doubling. As a result, the authors suggested that the charge ordering due to Coulomb interaction is the driving force of the transition at 34 K in NaV_2O_5 [53].

Using a similar Hamiltonian except for excluding double occupancy of V d_{xy} orbitals, equivalent to making $U \to \infty$, a subsequent study confirmed the stabilization of the zig-zag pattern [19]. The authors of Ref. [19] also pointed out that this kind of charge ordering along with inter-ladder correlations will automatically lead to an alternation of the exchange integrals along the ladder direction, $J_{i,i+1} = J_1(1+(-1)^i\delta)$, where i is a rung index. This alternation will open up a spin gap and lead to an exponential drop of the susceptibility below T_c. Another important point was related to the interaction between charges *via* lattice distortions: the zig-zag structure is also favored by the displacements of the rung O atoms which are pushed by the large V^{4+} ions.

More recent exact diagonalization results, see Ref. [54], also support the prominent role of the Coulomb interactions for the 34 K transition in NaV_2O_5 . The authors highlight the importance of phonons in the stabilization of the zig-zag structure, especially of the alternate c-axis displacements of the V atoms in the low temperature phase, which were seen in X-ray data [16]. It was found that the coupling of the electrons to the lattice can substantially reduce the critical value of the intersite Coulomb repulsion (see the previous paragraph) at which the formation of the charge ordered state occurs.

Interestingly, besides the low energy spin excitations arising as a result of dimerization, the characteristic low energy charge excitations are proposed to be soliton-like modes, similar to some degree to the spinons which are domain walls between degenerate ground state configurations, see Fig. 9. In this case, for an individual ladder there are two equivalent zig-zag patterns forming the ground state, the difference between them being a lattice translation with a high temperature lattice constant b. A low energy kink-like excitation will involve local on-rung electron hopping and will smoothly interpolate between the two degenerate configurations, see for instance Fig. 6 in Ref. [54]. One can conclude this section dedicated to the nature of the low temperature phase by saying that both experimental and theoretical works are strongly in favor of a transition driven by Coulomb interactions, with the spin gap formation playing only a secondary role.

3.2 Observation of a Folded Triplet Excitation. Selection Rules and Interpretation

Polarization properties and selection rules in magnetic fields – We discussed in the previous section that INS data reported the existence of Brillouin zone center spin flip excitations around 11 meV. At low temperatures and in (ab) polarization we observe a relatively weak feature around 86 cm^{-1}, see Fig. 15. What relatively weak means compared to other features seen in cross and parallel polarizations can be inferred from in Fig. 18 where this feature is denoted by T in the lower left panel. In finite external fields this feature has the following properties: it shows no shift for $\mathbf{B}$ parallel to the a-axis but we observe a splitting for the other two orthogonal directions of the external magnetic field. Both the upward and downward dispersing branches change their energies in an approximately linear fashion, with a proportionality factor given by one Bohr magneton μ_B. This shows that we are looking at a $S = 1$ excitation and we identify it with the elementary zone center triplet seen by neutron scattering. Note that in finite fields there is an extra mode around 90 cm^{-1}. This is a fully symmetric phononic feature which appears because in finite magnetic fields, the orthorhombic (or even smaller) crystal symmetry leads to a Farady rotation of the polarization inside the sample preventing the observation of clean selection rules. In fact the finite field spectra were taken after the polarization optics were rotated in order to minimize the intensity of strong features seen in parallel polarization (for instance the 66 cm^{-1} mode from Figs. 11 and 18).

Fig. 15 reveals an interesting behavior of the 86 cm^{-1} mode. Because of the spin selection rules, Raman scattering usually couples to singlet ($S = 0$) excitations. The observed magnetic field dependencies clearly indicate the triplet nature of this mode. This is possible in the presence of spin-orbit coupling which mixes the spin and orbital degrees of freedom, see the Introduction for a more detailed discussion. In what follows we try to identify the coupling mechanism responsible for the experimental observations from Fig. 15 as well as the corresponding selection rules.

The role of the antisymmetric Dzyaloshinskii-Moriya interaction – It is often possible to capture the effects of certain spin-orbit interactions by writing effective spin Hamiltonians. Such a Hamiltonian was inferred from macroscopic considerations in 1958 by Dzyaloshinskii [55] and two years later by Moriya [56], who derived a similar expression from a microscopic approach which needed superexchange (wavefunction overlap) and spin-orbit coupling as the only ingredients. If one writes down the most general bilinear interaction between two spins at lattice sites i and j in the form $\sum_{\alpha,\beta} S_i^{\alpha} J_{ij}^{\alpha\beta} S_i^{\beta}$ and considers only the antisymmetric part of the $J_{ij}^{\alpha\beta}$ tensor, one obtains the general form of the Dzyaloshinskii-Moriya (DM) interaction:

$$H_{DM} = \sum_{(ij)} \mathbf{D}_{ij} \cdot (\mathbf{S}_i \times \mathbf{S}_j) \tag{4}$$

This type of interaction appears usually in crystals with lower symmetry and it is often responsible for the phenomenon of weak ferromagnetism. An example in this sense is the $La_{2-x}Sr_xCuO_4$ system discussed in more detail in [57].

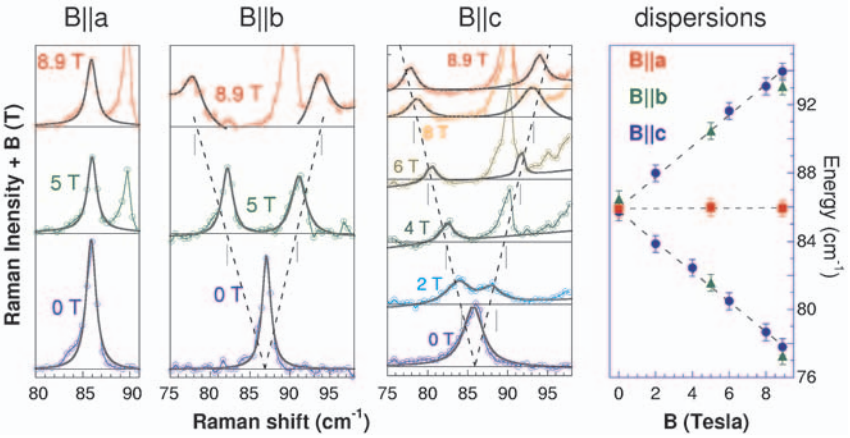

Fig. 15. From left to right, the first three panels show Raman response at 5 K as a function of magnetic field. Each spectrum is off-set by an amount equal to the value of the field at which is was taken. The colored symbols are data and the thick dark grey lines through the data points are results of Lorentzian fits to the triplet component(s). The feature appearing around 90 cm^{-1} in finite fields is a phonon which exists also in the high temperature phase. Note that the 86 cm^{-1} mode splits for magnetic fields $\mathbf{B} \parallel \hat{b}$ and $\mathbf{B} \parallel \hat{c}$ but it does not shift for $\mathbf{B} \parallel \hat{a}$-axis. Panel (**d**) shows the dispersion with field of the 86 cm^{-1} mode for the three field configurations (squares for $\mathbf{B} \parallel \hat{a}$; triangles for $\mathbf{B} \parallel \hat{b}$ and circles for $\mathbf{B} \parallel \hat{c}$).

The importance of the DM interaction was already suggested by ESR experiments which detected a considerable anisotropy of the absorption lines with respect to the magnetic field orientation [52, 26]. The direct observation of singlet-triplet transitions at low temperatures in ESR [52] and low frequency IR absorption spectra [51] also proposed that the DM interaction is the mechanism which allows the coupling of the photon field to single magnon excitations. We note that below $T_c = 34$ K, the local crystal symmetry is low enough to allow the presence of DM type terms between neighboring spins. In a theoretical study, Valenti *et al.* studied Raman scattering in quasi-1D AF spin chains. The main conclusion of this paper is that a single magnon excitation probed by Raman scattering has a very clear experimental signature: it should show no splitting in an external magnetic field parallel to **D** and it should split in two branches for a field perpendicular to the DM vector.

The authors of Ref. [58] also noted that there is no experimental confirmation of their prediction and so it is up to now to the best of our knowledge. Inspection of Fig. 15 shows that what we observe experimentally resembles closely the theoretical predictions if $\mathbf{D} \parallel \hat{a}$. Although the Raman selection rules for accessing the elementary triplet states may look complicated and were derived in Ref. [58] based on a non-trivial cluster-model approach, we believe that some understanding can be gained if we look at the problem from the weakly coupled dimer limit. That is, let us assume that the ladders are magnetically

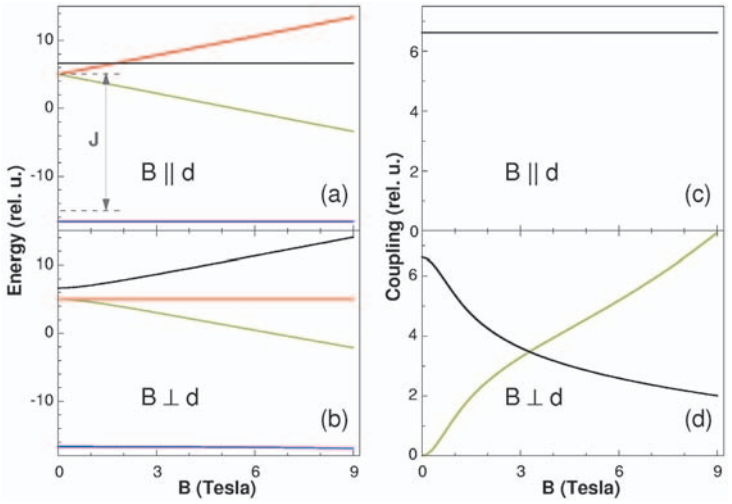

Fig. 16. Energy levels and light couplings as a function of magnetic field for a system of two spins with Dzyaloshinskii-Moriya interaction. The Hamiltonian reads $J\mathbf{S}_1 \cdot \mathbf{S}_2 + \mathbf{D} \cdot (\mathbf{S}_1 \times \mathbf{S}_2) + g\mu_B \mathbf{B} \cdot (\mathbf{S}_1 + \mathbf{S}_2)$ with $\mathbf{D}$ chosen parallel to the $\hat{z}$ axis. The way the energy levels split for $\mathbf{B} \parallel \mathbf{D}$, panel (**a**), and for $\mathbf{B} \perp \mathbf{D}$, panel (**b**), are illustrated for $J = 20$ and $D = 12$. Panels (**c**) and (**d**) show the moduli square of the nonvanishing matrix elements of the $\mathbf{S}_1 \cdot \mathbf{S}_2$ operator between the ground state and the three excited states (the same color coding is used as on the left side of the figure).

decoupled and in each individual ladder the alternation parameter δ from Eq. 3 is very close to unity. In this limit one deals in the zero order approximation with independent antiferromagnetically coupled spin dimers. Let us include an intra-dimer DM interaction of the form given by Eq. 4 and diagonalize this two spin problem in the presence of an external magnetic field. The results, exemplified for $J = 20$ and $D = 0.6J$ (which are values not extracted from any experimental data), are shown in Fig. 16. This simple exercise is also useful for the understanding of some of the results in the $SrCu_2(BO_3)_2$ chapter [38], where a slightly more complicated system (four spins instead of two) is used in order to understand the low energy magnetism in the quantum spin system the $SrCu_2(BO_3)_2$ orthoborate. However, in spite of the additional complication, many of the features discussed here are more visible and apply to the orthoborate case.

Panels (a) and (b) show the energy levels as a function of magnetic field for two directions: perpendicular and parallel to the DM vector. In the absence of field and for $\mathbf{D} \equiv 0$ we have a singlet at energy $-3J/4$ and a triple degenerate $S = 1$ excitation at $J/4$. A DM interaction (chosen parallel to the z-axis) in zero field will mix the singlet and the triplet states, in particular the vectors corresponding to zero component of the z projection of the total spin operator $S^z = S_1^z + S_2^z$. As a result the states with $S^z = \pm 1$ will remain at J and the $1/\sqrt{2}(|\uparrow>_1 |\downarrow>_2 \mp |\downarrow>_1 |\uparrow>_2)$ states (corresponding to the singlet ground state and excited $|S = 1, S^z = 0> \equiv |1, 0>$ state respectively) will repel each

other. The $|0,0>$ ground state will have an energy $\frac{-3J}{4} + \frac{J}{2}\left(1 - \sqrt{1+\frac{D^2}{J^2}}\right) \approx \frac{-3J}{4} - \frac{D^2}{4J}$ for $D \ll J$ while the $|1,0>$ state will be at $\frac{J}{4} + \frac{J}{2}\left(1 + \sqrt{1+\frac{D^2}{J^2}}\right) \approx \frac{J}{4} + \frac{D^2}{4J}$ for $D \ll J$. If the field is parallel to the DM vector, the $S^z = \pm 1$ states will split with one Bohr magneton per Tesla while the other two states will not change their energies. If the field is perpendicular to the DM vector the mixing of the states will be different and this will lead to a different splitting of the triplet multiplet, see Fig. 16b. Although at high fields the dispersion with field is again linear, the derivative of the energy with respect to the field as $B \to 0$ is vanishing in this second case. The curvature of the dispersion at small fields is a measure of the strength of D.

Having in mind that the Fleury-Loudon coupling contains sums of scalar products of spins, see Eq. 2, in Fig. 16c-d we evaluated the moduli square of the matrix elements of the $\mathbf{S}_1 \cdot \mathbf{S}_2$ operator and in these two panels we show all the non-vanishing terms for both field configurations. In zero field the coupling is finite only for the $|1,0>$ state. If $\mathbf{B} \parallel \hat{z}$ no additional coupling appears and the intensity of the $|0,0> \leftrightarrow |1,0>$ transition is field independent. If $\mathbf{B} \perp \hat{z}$ there will be a finite coupling to the up and down dispersing branches. The crossing points of intensities in panel (d) is also a measure of D. Overall, what these two panels say is that if the magnetic field is parallel to the DM vector one should see only one mode which does not change its energy with field, while if it is perpendicular to it two modes should be seen in finite fields, and both of them should shift with increasing field. The conclusions of this simple model are essentially the same as those of Ref. [58] which says that a local picture in terms of independent dimers is qualitatively appropriate.

According to the experimental results from Fig. 15a-d and the theoretical predictions from Ref. [58] our data can be understood as a result of the Raman coupling to one magnon excitations through the DM interaction with $\mathbf{D} \parallel \hat{a}$-axis in the low temperature phase. A quantitative analysis of the intensity dependence is not possible because of the induced changes in the polarization directions inside the sample when magnetic fields are applied (changes that could not be controlled rigorously) as well as because of the appearance of the 90 cm^{-1} feature which obscured the upward dispersing branch. From the observed linear (within our resolution) magnetic field dependence of the modes energies as well as from the similar spectral weights of the split triplet components at all measured fields in the $\mathbf{B} \parallel \hat{b}$ and/or $\mathbf{B} \parallel \hat{c}$ configurations ($2 \leq B \leq 8.9$) we infer that possible non-linearities in the energy dispersions or strong variations in intensities take place below the value $B = 2$ T. Clearly, the intensity variations predicted in Fig. 16d are not seen in the experimental data which shows that the two peaks in panels (b) and (c) have similar intensities. We think that this discrepancy occurs because the actual spin structure is much more complicated than a simple ensemble of uncoupled spin dimers and higher order spin interactions and possibly inter-ladder interactions have to be taken into account.

We clarified the existence of a single magnon excitation at 86 cm^{-1} in Raman scattering spectra. The feature is weak compared to other observed excitations in the Raman data. The question we want to address in the following is whether we observe other magnetic modes, in the singlet channel, besides phononic excitations. This is the topic of the following section.

3.3 Do We Observe Magnetic Bound States Below the Two-Particle Continuum?

Excitations out of 1D $S = 1/2$ AF chains with dimerization and frustration – We argued above that the relevant spin Hamiltonian for an individual ladder is given by Eq. 3 so a closer look at the magnetic excitation spectrum of a dimerized and frustrated spin chain is useful. We discussed there that any finite dimerization parameter δ and/or values of the frustration parameter α above a critical value will open up a spin gap $\Delta = \Delta(\delta, \alpha)$. Qualitatively, the dispersion of the elementary triplet (one magnon) excitation given by $\epsilon(k)$ looks like in Fig. 13b. The two triplet continuum (defined as the range of energies $\omega(k) = \epsilon(k_1) + \epsilon(k_1)$ with the wavevectors satisfying $k = k_1 + k_2$) will have a minimum at $k = 0$ and starts from an energy $\epsilon = 2\Delta$. It turns out that the Hamiltonian of Eq. 3 also allows for the existence of two triplet bound states, which means that at certain wavevectors there are two triplet excitations with energies below the continuum [48, 49, 50].

An example of a perturbational calculation [50] of single and two triplet dispersions for certain points in the (δ, α) parameter space is shown in Fig. 17. Note that in these figures the wavevectors are on the vertical scales and the energies are on the horizontal axes. Panel (a) shows elementary triplet excitations for several points in the (δ, α) parameter space. The dispersion is similar to Fig. 13b, there is a rapid variation of the zone center values but not much happens at the Brillouin zone center where the energies are not far from $\pi J_1/2$ (note that the unit of energy in this figure is not J_1 but $J_1(1+\delta)$). Results for the two-particle sectors are shown in panels (b) and (c) and one can see the continuum marked by the light blue color. One important thing to note in these two figures is the occurrence of two-triplet bound states whose dispersions are shown by black (solid, dashed or dash-dotted lines) lines. Panel (b) shows the results for states in which two triplets are bound into a $S = 1$ state while panel (c) shows the same thing but for triplets bound in a state having a total spin $S = 0$. For each case there are more than one bound states, the difference for the numerical parameters shown being that the binding energies of the triplet bound states are finite only at finite values of k while for the singlet channel there is a branch split from the continuum in the whole Brillouin zone.

Fig. 17d shows the ratio of the energy of lowest singlet bound state at the Brillouin zone center $m_{S=0}$, with respect to the value of the elementary triplet gap Δ. The vertical line corresponds to the critical value of α at which a frustration induced gap opens up in the absence of any dimerization δ. At α_c, the above ratio is $m_{S=0}/\Delta = \sqrt{3}$ (the horizontal line refers to this value) and its value decreases with increasing frustration. Note that at $\alpha = 0$, $m_{S=0}/\Delta \approx 2$, and this is true irrespective of the chosen values for δ which means that it is the frustration which leads to finite binding energies of the singlet bound states. One interesting point which is not shown in panel (d): there exists a singular point, the Majumdar-Ghosh point given by $(\delta, \alpha) \equiv (0, 0.5)$ (see the discussion of Fig. 9), where $m_{S=0}/\Delta$ equals unity. At this point the single magnon and the two-magnon bound state are degenerate, which is a remarkable property of the Hamiltonian of Eq. 3 [48].

Experimental observations and discussion – How is this discussion related to our experimental findings in NaV_2O_5? In Fig. 18 we show several Raman spectra with

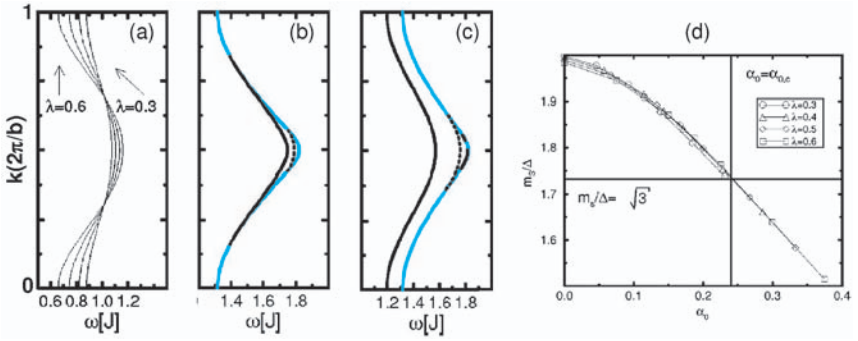

Fig. 17. Results of perturbative calculations using continuous unitary transformations for the excitations of a 1D AF chain with dimerization and frustration (from Ref. [50]). The results shown here are for the NNN exchange $J_2 = \alpha J_1$ with $\alpha = 0.25(1-\delta)$ and the energies are given in units of $J_1(1+\delta)$. The parameter λ is defined in terms of the dimerization δ as $\lambda = (1-\delta)/(1+\delta)$. (**a**) Elementary triplet dispersion $\omega(k)$ for $\lambda = \{0.3, 0.4, 0.5, 0.6\}$ which translates into $(\delta, \alpha) = \{(0.54, 0.115); (0.43, 0.143); (0.33, 0.167); (0.25, 0.187)\}$. Panels (**b**) and (**c**) show two-triplet bound states (black lines) with total spin $S = 1$ and $S = 0$ respectively calculated for $\lambda = 0.6$ ($\delta = 0.25$). The lower bound of the two particle continuum is shown by the light blue line. (**d**) The ratio of the singlet ($S = 0$) bound states (at $k = 0$) to the value of the spin gap as a function of α (denoted by the authors of Ref. [50] by α_0) for several dimerization parameters. The vertical line corresponds to the critical frustration where a gap opens in the spin excitation spectrum in the absence of any dimerization (see the discussion related to Fig. 9) and the horizontal line denotes $\sqrt{3}$.

the purpose of emphasizing the new excitations which appear below the phase transition. We discuss first an aspect related to the crystal symmetry in the low temperature phase and illustrated in panels (c) and (d) of this figure. We show there four Raman spectra, two in (aa) polarization at 300 and 4 K, Fig. 18c, and two in (ab) polarization at the same two temperatures, Fig. 18d. In the high temperature phase the V-O_{rung} stretching mode [23, 25] is present at 969 cm^{-1} in parallel polarizations, but not in (ab) geometry and, therefore it is a fully symmetric excitation of the $Pmmn$ space group. Below T_c this mode acquires a second component, seen at 948 cm^{-1}, due to the in-plane unit cell doubling, i.e. we assign it to a folded phononic branch. More importantly, both the 968 and 949 cm^{-1} excitations are seen not only in (aa) but also in (ab) polarization. The simultaneous presence of these modes in both the diagonal and off-diagonal components of the Raman tensor indicates that in the low temperature phase the double reflection symmetry of the $Fmm2$ group is broken. Our data confirm the resonant X-ray data [12] which argues for a lower (monoclinic) symmetry below T_c.

We comment now on the spectra shown in Fig. 18a-b. In panel (a) we show the emergence of new (aa) polarized collective modes in the low temperature phase and several of them are indexed by letters: A (56.9cm^{-1}), B (105.0 cm^{-1}), C (131.2 cm^{-1}),

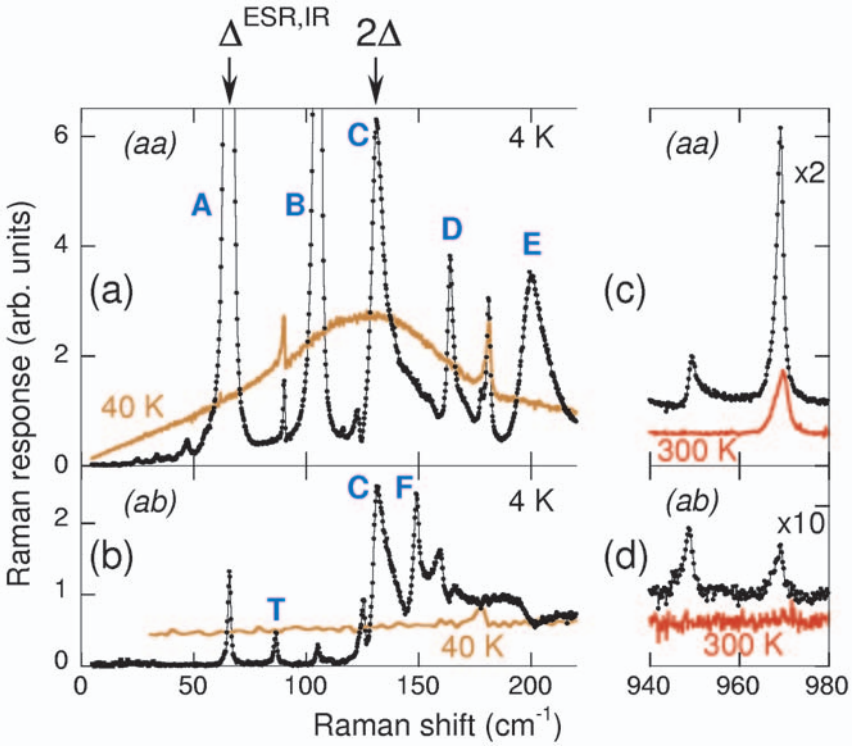

Fig. 18. Low energy Raman scattering spectra in (*aa*) (upper panels) and (*ab*) (lower panels) polarizations at 4, 40 and 300 K measured using the $\omega_{in} = 1.92$ eV excitation. Below about 34 K many new resonances appear in the 0-200 cm^{-1} region. The arrows at the top correspond to the energies of the elementary triplet excitation determined by high resolution IR [51] and ESR [52] studies and twice that value. The 968 cm^{-1} phonon in parallel and cross polarization is shown on the right. Panel (**d**) shows that below T_c a folded counterpart appears which is seen in both (*aa*) and (*ab*) polarizations indicating a lower crystal symmetry.

D (164.0 cm^{-1}) and E (200.4 cm^{-1}). In panel (b) we similarly marked the modes T (86.5cm^{-1}) and F (149.0cm^{-1}) seen in the (*ab*) polarized spectra. This list of modes does not exhaust all of the new excitations appearing in the low temperature phase but highlights a few of them which are of importance for the following discussion. What is the origin of these new modes? Are they phonons, are they magnetic or are they some collective topological charge excitations of the type described in Ref. [54]. While not excluding the latter option, it seems that the observation of purely charge modes is less probable because it involves higher energies of the order intersite Coulomb interactions which are

of the order of eV's [19, 54]. Moreover, the characteristic energy scales of these excitations (0-25 meV) can be better related either to magnetic excitations seen in ESR, far IR or INS experiments (see Fig. 14) or (in the context of existing lattice instabilities which drive the 34 K transition) to the folding of low energy zone boundary phonons in the high temperature phase. Accordingly, we will focus here on the possibility of observing phonons or single/multi-triplet magnetic excitations [48, 59].

We discuss here the spin excitations scenario. This picture draws its appeal primarily from the fact that the Hamiltonian of Eq. 3, which seems to be a good description for the staggered spin configuration in the low temperature phase, allows for a multitude of magnetic bound states, both in the singlet and triplet channels, see Fig. 17. First, we note that some of the new resonances observed below the transition are definitely magnetic. In Fig. 15 we showed that the 86.5 cm^{-1} excitation, denoted by T in Fig. 18, is a $S = 1$ magnon. The singularity seen at 131.2 cm^{-1} (16.27 meV) in Fig. 18a-b situated at twice the energy of the spin gap value of 65.5 cm^{-1} (8.13 meV) and the continuum present from above this frequency as opposed to the clean gap seen for $\omega \leq 130$ cm^{-1} (except for a few resonances) leaves little doubt that the mode C marks the onset of the two-triplet continuum of excitations. How about the most prominent excitations denoted by A and B in Fig. 18a? The similar resonance profile of these two excitations shown in Fig. 19 indicates that they have a common origin. It is interesting to remark that the energy of mode A coincides with the energy of the spin gap determined with high resolution in ESR and IR absorption data [51, 52]. Can this excitation be the $k = 0$ elementary triplet? Panels (a) and (b) in Fig. 19 show that neither mode A nor mode B splits or shifts by more than 1 cm^{-1} in applied magnetic fields up to 8.9 T (and we checked that this is true for any direction of the applied magnetic field). Moreover, if these excitations were $S = 1$ triplets and the same spin-orbit interaction would insure the coupling to them as for mode T, one could not explain that the spectral weight of mode A is more than two orders of magnitude higher than that of mode T.

The arguments above seem to exclude the possibility that modes A and B are triplet excitations but the possibility that they are bound states in the singlet sector still needs to be explored. The ratio $\omega_B/\Delta = 1.59$ appears to qualify mode B for a singlet bound state according to Fig. 17d. How about mode A, can it be also a singlet bound state? As discussed previously, a singlet bound state degenerate with the spin gap is only realized for a singular combination of parameters, $(\delta, \alpha) \equiv (0, 0.5)$. It deserves further argumentation why this set of values is realized in the low temperature phase of NaV_2O_5. However, assuming that this is the case, one could assign mode B to the folded counterpart of mode A. In this scenario one could also argue that the magnetic frustration may be the driving force of the transition at 34 K in the following way [59]. The tendency for zig-zag ordering increases the value of the NNN frustrating interaction J_2. At 34 K, $\alpha = J_2/J_1$ reaches the critical value α_c (see the caption of Fig. 17) and a gap opens in the magnetic excitation spectrum. Further cooling will push α close to 0.5 and the singlet bound state gets very close (practically degenerate) to the spin gap. Going into more details of this pictures some of the other excitations can be understood as combination modes or continuum edges. For instance, based on energy considerations, one can say that F = A + B, H = B + B or that mode F in Fig. 18b is the A + T continuum edge.

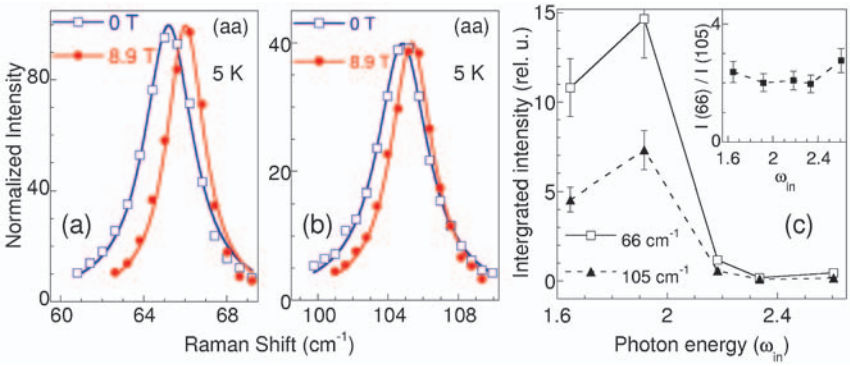

Fig. 19. Panels (**a**) and (**b**) display the T = 5 K Raman spectra showing the magnetic field (in)dependence of the 66 and 105 cm^{-1} resonances which appear below the transition. In both cases a shift of about 0.9-1 cm^{-1} was observed as the magnetic field was varied from 0 to 8.9 T. (**c**) Integrated intensity of the 66 (empty squares) and 105 cm^{-1} (filled triangles) modes at 5 K as a function of the incoming photon energies ω_{in}. The inset of this panel shows that the ratio of the integrated intensities of these two modes depend only slightly on ω_{in} (as opposed to the data shown in Fig. 6, the data in the main panel were not corrected for the optical properties of the material; however these effects cancel out in the ratio because these modes are very close in energy).

However, the fact that the physics of the Majumdar-Ghosh point is realized for a singular combination of parameters makes this appealing scenario less probable. The variety of selections rules which have been experimentally observed in Raman, ESR and IR data still needs to be explained. The second possibility is to assign the main new features appearing below T_c in the 0-200 cm^{-1} energy range to folded phonons. In fact, this scenario is supported by the small but finite shift observed in Fig. 19a-b. This is what one expects in a simple two level system: one phonon, one close by magnon along with some off-diagonal matrix elements because of a non-vanishing spin-phonon interaction. As expected, the shift of the 65.9 cm^{-1} mode (of about 0.8 cm^{-1}) is slightly higher than the shift of the 105 cm^{-1} mode (of abut 0.5 cm^{-1}) which is further apart in energy from the spin gap value. Based on lattice dynamical calculations and the relative temperature dependence of the spin gap seen in ESR data [52] and that of the energies of measured IR active modes, a more recent study also argues for the phononic nature of modes A and B [29].

We conclude this section by saying that many features of the transition at 34 K in NaV_2O_5 are still under debate and more than just a clarification is needed regarding the nature of the observed excitations or the effects of the electron-phonon interactions.

4 Summary

In this chapter we studied electronic excitations in NaV_2O_5 by Raman scattering and the transition taking place at $T_c = 34$ K. From the description of the crystal structure and the discussion of the electronic properties as seen by various techniques we showed that NaV_2O_5 can be thought of as an array of quasi one-dimensional (1D) two-leg ladders at quarter filling factor. Two models were proposed to capture the essential physics of the magnetic degrees of freedom: one for the high temperature phase (Heisenberg chains with nearest and next nearest antiferromagnetic interactions, see Eq. 1), and another model for the low temperature phase (Heisenberg chains with dimerization and frustration, see Eq. 3).

Three main topics were discussed. The first was related to a broad continuum of excitations found in the 200-1500 cm^{-1} range and peaked around 680 cm^{-1} in parallel polarizations. In literature a magnetic origin of this feature was ruled out and a scenario involving crystal field excitations was proposed instead. The resonant Raman profile of this excitation, the polarization selection rules and the presence of its overtone in resonance conditions allowed us to conclude that the origin of this feature is magnetic. More precisely, we proposed that it arises as a result of light coupling to multi-spinon Raman excitations. Within this scenario we also argued for a scenario explaining the puzzling temperature dependence of the magnetic continuum in terms of an increasing role of next nearest neighbor frustration and in the context of a strongly fluctuating low temperature phase.

The second topic was related to the observation of a folded $S = 1$ magnetic mode which displayed very clear selection rules as a function of the magnetic field orientation, see Fig. 15. We proposed that the coupling of the photon field to this excitation takes place *via* the antisymmetric, Dzyaloshinskii-Moriya (DM), interaction which, in a simple dimer model, can also explain the observed selection rules: no splitting or shifts for magnetic fields parallel to the DM vector and the observation of two (upward and downward) dispersing branches for fields perpendicular to the DM vector.

Finally, we discussed the nature of several new resonances seen below T_c and focussed on the possibilities that they are either folded phonons or singlet bound states of two triplet excitations. In particular we emphasized the existence of two modes at 66 and 105 cm^{-1}, the first one being degenerate with one of the spin gap modes. In the spin excitations scenario we proposed a model in which frustration has a determinant role. However, in order to accommodate theoretical results with the observed energies, a very particular set of parameters characterizing the dimerized and frustrated spin chains (the Majumdar-Ghosh point) had to be invoked. The above argument and the small energy shifts in magnetic fields up to 9 T suggested that the strong mode degenerate with the elementary triplet as well as the 105 cm^{-1} mode are phonons. The conclusion of our study is that many features of the spin/charge and lattice dynamics in NaV_2O_5 are still to be understood.

Acknowledgments

We acknowledge discussions and collaborations with B. S. Dennis, M. V. Klein, U. Nagel, T. Rõõm, A.M. Sengupta and S. Trebst. The crystals were provided by P. Canfield.

References

[1] M. Isobe and Y. Ueda, J. Phys. Soc. Jpn. **65**, 1178 (1996).

[2] A. Gozar and G. Blumberg, "Collective Spin and Charge Excitations in $(Sr,La)_{14-x}Ca_xCu_{24}O_{41}$ Quantum Spin Ladders", also in the present volume.

[3] E. Pytte, Phys. Rev. B **10**, 4637 (1974); M. C. Cross and D. S. Fisher, Phys. Rev. B **19**, 402 (1979).

[4] L. N. Bulaevskii, A. I. Buzdin and D. I. Khomskii, Solid State Commun. **27**, 5 (1978); M. C. Cross, Phys. Rev. B **20**, 4606 (1979).

[5] M. Hase, I. Terasaki and K. Uchinokura, Phys. Rev. Lett. **70**, 3651 (1993).

[6] For a review of $CuGeO_3$ properties see J. P. Boucher and L. P. Regnault, J. de Physique I **6**, 1939 (1996).

[7] Y. Fujii *et al.*, J. Phys. Soc. Jpn. **66**, 326 (1997).

[8] W. Schnelle, Yu. grin and R. K. Kremer, Phys. Rev. B **59**, 73 (1999).

[9] A. Damascelli, Ph. D. Thesis, 1999.

[10] J. Hemberger *et al.*, Europhys. Lett. **42**, 661 (1998).

[11] P. A. Carpy and J. Galy, Acta Cryst. B **31**, 1481 (1975).

[12] S. Grenier *et al.*, Phys. Rev. B **65**, R180101 (2002); Y. Joly, S. Grenier and J. E. Lorenzo, Phys. Rev. B **68**, 104412 (2003).

[13] M. J. Konstantinović *et al.*, Phys. Rev. B **65**, 012404 (2002).

[14] H. Smolinski *et al.*, Phys. Rev. Lett. **80**, 5164 (1998).

[15] A. Meetsma *et al.*, Acta Cryst. C **54**, 1558 (1998).

[16] J. Lüdecke *et al.*, Phys. Rev. Lett. **82**, 3633 (1999).

[17] T. Ohama *et al.*, Phys. Rev. B **59**, 3299 (1999); T. Ohama *et al.*, J. Phys. Soc. Jpn. **69**, 2751 (2000).

[18] K. Kobayashi *et al.*, Phys. Rev. Lett. **80**, 3121 (1998).

[19] M. V. Mostovoy and D. I. Khomskii, Solid State Commun. **113**, 159 (2000); M. V. Mostovoy, D. I. Khomskii and J. Knoester, Phys. Rev. B **65**, 064412 (2002).

[20] D. C. Johnston *et al.*, Phys. Rev. B **61**, 9558 (2000).

[21] C. Presura *et al.*, Phys. Rev. B **61**, 15762 (2000); C. Presura *et al.*, Phys. Rev. B **62**, 16522 (2000).

[22] A. Damascelli *et al.*, Phys. Rev. Lett. **81**, 918 (1998); A. Damascelli *et al.*, Phys. Rev. B **61**, 2535 (2000).

[23] S. A. Golubchik *et al.*, J. Phys. Soc. Jpn. **66**, 4042 (1997); Z. V. Popović *et al.*, Solid State Commun. **110**, 381 (1999); M. N. Popova *et al.*, J. Exp. Theor. Phys. **88**, 1186 (1999).

[24] M. J. Konstantinović *et al.*, Phys. Stat. Sol. **215**, 661 (1999).

[25] M. J. Konstantinović *et al.*, J. Phys.: Condens. Matter **11**, 2103 (1999); M. J. Konstantinović *et al.*, Solid State Commun. **112**, 397 (1999).

[26] H. Nojiri *et al.*, J. Phys. Soc. Jpn. **69**, 2291 (2000).

[27] M. Fischer *et al.*, Phys. Rev. B **60**, 7284 (1999).

[28] M. J. Konstantinović *et al.*, Phys. Rev. B **65**, 012404 (2001); M. J. Konstantinović *et al.*, Phys. Rev. B **65**, 245103 (2001).

[29] M. N. Popova *et al.*, Phys. Rev. B **65**, 144303 (2002).

[30] P. A. Fleury and R. Loudon, Phys. Rev. **166**, 514 (1968).
[31] B. S. Shastry and B. I. Shraiman, Phys. Rev. Lett. **65**, 1068 (1990); B. S. Shastry and B. I. Shraiman, Int. J. of Mod. Phys. B, **5**, 365 (1991).
[32] B. Grenier *et al.*, Phys. Rev. Lett. **86**, 5966 (2001).
[33] P. H. M. van Loosdrecht *et al.*, Phys. Rev. Lett. **76**, 311 (1996).
[34] L.D. Faddeev and L.A. Takhtajan, Phys. Lett. A **85**, 375 (1981); J. des Cloizeaux and J. J. Pearson, Phys. Rev. **128**, 2131 (1962).
[35] K. P. Schmidt and G. S. Uhrig, Phys. Rev. Lett. **90**, 227204 (2003); C. Knetter *et al.*, Phys. Rev. Lett. **87**, 167204 (2001).
[36] G. Castilla, S. Chakravarty and V. J. Emery, Phys. Rev. Lett. **75**, 1823 (1995).
[37] C. K. Majumdar and D. K. Ghosh, J. Phys. C **3**, 911 (1970); J. Math. Phys. (N.Y.) **10**, 1388, (1969).
[38] A. Gozar and G. Blumberg, "Collective Magnetic Excitations in $SrCu_2(BO_3)_2$", also in the present volume.
[39] R. R. P. Singh, P. Prelovšek and B. S. Shastry, Phys. Rev. Lett. **77**, 4086 (1996).
[40] V. N. Muthukumar *et al.*, Phys. Rev. B **54**, R9635 (1996).
[41] W. Brenig, Phys. Rev. B **56**, 2551 (1997).
[42] A. V. Chubukov and D. M. Frenkel, Phys. Rev. Lett. **74**, 3057 (1995); Phys. Rev. B **52**, 9760 (1995).
[43] G. Blumberg *et al.*, Phys. Rev. B **53**, R11930 (1996).
[44] R. R. P. Singh *et al.*, Phys. Rev. Lett. **62**, 2736 (1989).
[45] J. C. Bonner and M. E. Fisher, Phys. Rev. **135**, A640 (1964).
[46] S. van Smaalen *et al.*, Phys. Rev. B **65**, R060101 (2002).
[47] K. Ohwada *et al.*, Phys. Rev. Lett. **87**, 086402 (2001).
[48] S. Trebst, Ph. D. Thesis, Bonn University, 2002.
[49] G. S. Uhrig and H. J. Schulz, Phys. Rev. B **54**, R9624 (1996); G. Bouzerar, A. P. Kampf and G. I. Japaridze, Phys. Rev. B **58**, 3117 (1998); S. Trebst *et al.*, Phys. Rev. Lett. **85**, 4373 (2000); C. J. Hammer, W. Zheng and r. R. P. Singh, Phys. Rev. B **68**, 214408 (2003).
[50] K. P. Schmidt, C. Knetter and G. S. Uhrig, Phys. Rev. B **69**, 104417 (2004).
[51] T. Rõõm *et al.*, Phys. Rev. B **69**, 144410 (2004).
[52] S. Luther *et al.*, J. Phys. Soc. Jpn. **67**, 3715 (1998).
[53] H. Seo and H. Fukuyama, J. Phys. Soc. Jpn. **67**, 2602 (1998).
[54] M. Aichhorn *et al.*, Phys. Rev. B **69**, 245108 (2004); E. Ya. Sherman *et al.*, Phys. Rev. B **48**, 648 (1999).
[55] I. Dzyaloshinskii, J. Phys. Chem. Solids **4**, 241 (1958).
[56] T. Moriya, Phys. Rev. **120**, 91 (1960).
[57] A. Gozar, B.S Dennis, G. Blumberg, S. Komiya, and Y. Ando, Phys. Rev. Lett. **93**, 027001 (2004).
[58] R. Valenti, C. Gros and W. Brenig, Phys. Rev. B **62**, 14164 (2000).
[59] G. Blumberg *et al.*, unpublished.

COLLECTIVE MAGNETIC EXCITATIONS IN SrCu (BO)

A. Gozar[1,2] and G. Blumberg[1]

[1] Bell Laboratories, Lucent Technologies, Murray Hill, NJ 07974, USA
[2] University of Illinois at Urbana-Champaign, Urbana, IL 61801, USA

1 Introduction: Why SrCu (BO) ?

Several properties make $SrCu_2(BO_3)_2$ a unique and one of the most interesting quantum magnets [1]. This compound is a 2D spin system with a disordered ground state even at very low temperatures and a spin gap of about 24 cm^{-1} (3 meV) in the magnetic excitation spectrum [1, 2]. It has been established that the elementary excitations in this system, which consist of a transition from the singlet (S = 0) ground state to the lowest energy triplet (S = 1) state, are local, weakly dispersive in the reciprocal space while many-'particle' magnetic states are more mobile, i.e. show more dispersion. The strengths of the relevant magnetic interactions place this compound close to a quantum critical point (QCP) separating the gapped phase from a gapless state having long range magnetic AF order. Moreover data in high magnetic fields show plateaus at commensurate (1/8, 1/4 and 1/3) values of the saturation magnetization [2, 3, 4]. The plateau states can be thought of as crystalline arrangements of magnetic moments separating regions of continuous rise in magnetization, these latter regions allowing for an interpretation in terms of Bose-Einstein condensation of triplet excitations [5]. It has also been suggested [6] that doping in this system (regarded as a Mott-Hubbard insulator) may lead to a superconducting phase mediated by antiferromagnetic (AF) fluctuations, a mechanism similar in spirit to one of the scenarios proposed for the high T_c cuprates [7].

The first synthesis of $SrCu_2(BO_3)_2$ was achieved in 1991 by Smith and collaborators [8] but the authors did not elaborate on the magnetic properties. This compound was redi-

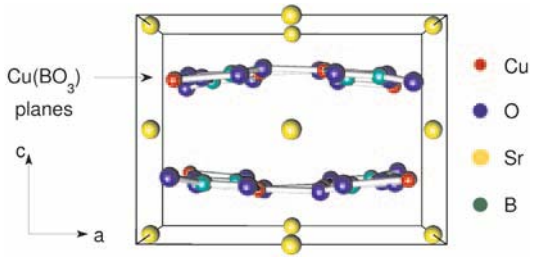

Fig. 1. 3D view of the $SrCu_2(BO_3)_2$ crystal showing the layered structure along the c-axis. Above 395 K the $Cu(BO_3)$ planes are flat, mirror symmetry elements.

scovered in 1999 by Kageyama *et al.* [2], who also pointed out the outstanding magnetic properties and the importance of $SrCu_2(BO_3)_2$ in the physics of low dimensional quantum magnets. The crystal belongs to the tetragonal symmetry and it has a layered structure in which $Cu(BO_3)$ units are separated by closed shell Sr^{2+} atoms, see Fig. 1. At T = 395 K the system undergoes a 2^{nd} order phase transition from the space group $I4/mcm$ to $I\bar{4}2m$ on cooling from high temperature. In the $I4/mcm$ phase the planes containing the Cu atoms are flat and they form mirror symmetry elements. Below 395 K the transition can be intuitively understood as the buckling of the Cu planes which lose their mirror symmetry.

The magnetic properties of $SrCu_2(BO_3)_2$ are determined by the $S = 1/2$ spins sitting on the Cu^{2+} sites. The crystal structure imposes a distribution of the magnetic moments in weakly coupled 2D layers which define the (ab) planes. In each of these sheets the spins form orthogonal dimer lattices and the c-axis is perpendicular to them. The in-plane magnetic interactions can be described in an effective spin model by taking into account the magnetic exchange between nearest neighbor Cu spins bridged O atoms forming a 147° Cu-O-Cu bond which points toward an AF coupling denoted by J_1, see Fig 2. Besides this interaction one can consider the next nearest neighbor super-exchange taking place *via* the BO_3 complexes. Curie-Weiss type fits of the high temperature magnetization data suggest that this coupling, denoted by J_2, is also AF. Indeed, as we will discuss later, these two terms seem to capture many aspects regarding the magnetic properties of $SrCu_2(BO_3)_2$. The addition of a weak inter layer exchange J' to the above two terms constitute the starting point for treating the 3D spin dynamics in this compound.

The schematic of the magnetic lattice is shown in Fig. 2 where the nearest neighbor AF bonds are represented by a solid line while the next nearest neighbor interaction is shown by dashed lines. Note an important property of this lattice: ignoring the solid bonds (the J_1 interactions), the topology of the spin structure, determined by the J_2 bonds, is equivalent to that of a 2D square lattice. The corresponding Hamiltomian for one $Cu(BO_3)$ plane reads:

$$\hat{H} = J_1 \sum_{(i,j)\ NN} \mathbf{S}_i \cdot \mathbf{S}_j + J_2 \sum_{[i,j]\ NNN} \mathbf{S}_i \cdot \mathbf{S}_j \qquad (1)$$

Here i and j are nearest neighbor (NN) or next nearest neighbor (NNN) Cu sites.

Why is a Raman study of this compound interesting? Several magnetic properties, features of the excitation spectrum or the occurrences of the magnetization plateaus, can be explained by taking into account the J_1 and J_2 interactions. As will be discussed in the review of the main theoretical results, this compound is believed to be characterized by a ratio $x = J_2/J_1$ close to 0.7, which is the value around which the system ground state changes. One reason to study this compound is that an accurate determination of this ratio is still missing and this is important due to the proximity to the QCP. In this regard the recent observation of a mode below the spin gap brings into question the quantitative determination of the AF exchange parameters of the system since the existence of such excitation has not been predicted by theory. Another reason is brought about by a different set of questions related to the way the external radiation field couples to magnetic excitations. Magnetic modes in the triplet sector have been probed spectroscopically, besides inelastic neutron scattering (INS) [2, 16], also by electron spin resonance (ESR) [17, 18] and infra-red (IR) [19, 21] absorption experiments. The nature of the mixing interactions originating in spin-orbit coupling which usually allows transitions from the singlet ($S = 0$) to excited ($S = 1$) states is still to be understood. Our approach, which is a study of collective magnetic excitations in terms of symmetry, resonance and coupling mechanisms in external magnetic fields, is illuminating in this respect.

This chapter will be focussed on the low temperature properties of $SrCu_2(BO_3)_2$. The discussion of the low temperature phononic excitations as seen in Raman spectra in the next part will be followed by a review of experimentally found magnetic properties with an emphasis on spectroscopic techniques. Then we will present a description of the basic properties emerging from the Hamiltonian (1) which describes a Shastry-Sutherland lattice and the structure of the magnetic excitation spectrum. The effects of other interactions, in particular of the antisymmetric Dzyaloshinskii-Moriya (DM) terms, will be described. Then we will present our low temperature Raman data and discuss our results in reference to the open questions mentioned above.

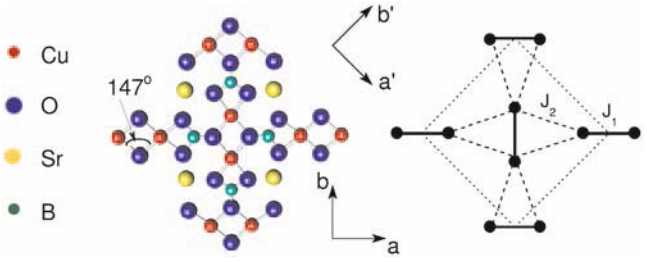

Fig. 2. Left: The (ab) planes and crystal axes notation. Right: The effective magnetic lattice with the unit cell of the dimer structure being shown by the short dashed square. The circles are the $S = 1/2$ Cu spins, the solid and long dashed lines represent the intra-dimer (J_1) and inter-dimer (J_2) AF superexchange interactions. Below 395 K [9] the vertical and horizontal dimers become slightly non-coplanar

2 Low Temperature Phononic Spectra in SrCu (BO)

The analysis of the low temperature lattice dynamics is important for several reasons. In general this is because there are many examples of low dimensional crystalline compounds which undergo transitions to phases in which the appearance of a spin gap in the magnetic excitation spectrum is accompanied by real space lattice symmetry breaking due to spin-phonon coupling. The lowering of the crystal symmetry may involve newly allowed phononic modes which could be checked directly in the Raman spectra. In the particular case of $SrCu_2(BO_3)_2$ spin-lattice interaction has been suggested to be relevant to the magnetic dynamics at low temperatures and/or high magnetic fields. In order to explain the selection rules of the transitions seen in IR absorption, spin-phonon induced antisymmetric DM spin interactions have been invoked [21]. It has been argued that this coupling will induce virtual phonon transitions which will instantaneously lower the crystal symmetry, allowing for non fully-symmetric effective singlet triplet mixing terms. On the other hand the spin-lattice coupling was taken into account in order to be able to describe the spin density profile at high fields in the magnetization plateaus states. NMR data brought evidence for the broken translational symmetry at the 1/8 plateau by the existence of at least 11 nonequivalent Cu sites [4]. The role of the phonons coupled adiabatically to the spin degrees of freedom in this case is to lift the degeneracy of the ground state, picking a state with a certain magnetization texture and allowing the ground state magnetization to be a defined quantity.

So far the study of phononic excitations has been especially focussed in relation to the structural phase transition at T = 395 K [9, 10]. The lattice soft mode of the 2^{nd} order transition from the $I4/mcm$ to the $I\bar{4}2m$ group can be seen in Fig 3. The phonon which condenses belongs to the B_{1u} representation of the higher symmetry group and, in terms of Cu atoms, it involves mainly an alternate displacement along the c-axis of the nearest neighbor dimers, see Fig 1.

A symmetry analysis of the phononic excitations in $SrCu_2(BO_3)_2$ is done in the following. The unit cell contains 4 formula units and a total of 44 atoms. The number of $k = 0$ modes is given by $3 \times 44/2 = 66$, the factor of 2 coming from the fact that the unit cell is body centered. In this case, the symmetry lowering at 395 K does not

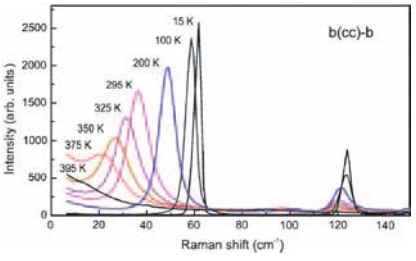

Fig. 3. The fully symmetric soft mode below the $I4/mcm$ - $I\bar{4}2m$ transition from Ref. [10] seen in cc polarization. Note the strong two-phonon excitation around 120 cm^{-1}.

Table 1. Symmetry of the phononic excitations of $SrCu_2(BO_3)_2$ in the high ($I4/mcm$, point group D_{4h}) and low ($I\bar{4}2m$, point group D_{2d}) temperature phases. The first column contains the atom types and the rest of the columns correspond to irreducible representations of the point groups.

	$I\ \ m\ m$										$I\bar{4}2m$				
Atom	A_{1g}	A_{2g}	B_{1g}	B_{2g}	E_g	A_{1u}	A_{2u}	B_{1u}	B_{2u}	E_u	A_1	A_2	B_1	B_2	E
Cu	1	1	1	1	1	-	1	1	-	2	2	1	1	2	3
O1	1	1	1	1	1	-	1	1	-	2	2	1	1	2	3
O2	2	2	2	2	2	1	1	1	1	4	3	3	2	2	6
B	1	1	1	1	1	-	1	1	-	2	2	1	1	2	3
Sr	-	1	-	-	1	-	1	-	-	1	-	1	-	2	2

change the number of atoms in the unit cell. The associated point group of the $I4/mcm$ space group is D_{4h} while D_{2d} corresponds to $I\bar{4}2m$. The analysis is based on the tables in Ref. [23] and uses the site symmetry approach. Oxygen atoms mediating the intra-dimer superexchange (O1) and the Oxygens allowing for the inter-dimer superexchange (O2) occupy a different symmetry positions. In the high temperature phase the Cu, O1 and B atoms have C'_{2v}, O2 atoms have C_s and Sr atoms occupy D_4 site symmetries respectively. Table 1 summarizes the number of modes corresponding to each atom both above and below the transition. The part of the table related to the $I\bar{4}2m$ group can be easily inferred from the analysis of the high temperature phase. One has to drop the 'u' and 'g' indices (corresponding to odd and even modes) because the inversion symmetry is lost and by using compatibility tables which show that the representations $A_{1u}, A_{2u}, B_{1u}, B_{2u}$ of the D_{4h} point group become B_1, B_2, A_1, A_2 representations (in this order) in D_{2d}. Both the E_u and E_g representations remain double degenerate.

Inversion symmetry breaking results in the fact that certain phonons, which were dipole active, become Raman allowed. The appearance of several new modes below 395 K is shown in Fig. 4 where data from Refs. [9, 10] is reproduced. Notable are the shoulders appearing around 160 and 220 cm^{-1} below 395 K in *ca* polarization (which probes double degenerate modes with E symmetries) suggesting either an almost degeneracy of E_u and E_g modes in the high temperature phase or, even more interestingly, the possibility that the symmetry of the low temperature phase is lower than what has been inferred so far and accordingly, the modes corresponding to higher dimensional representations become non-degenerate. [9, 10] is reproduced.

We show in Fig. 5 our low temperature Raman data taken with in plane polarizations and using $\omega_L = 1.92$ eV laser excitation energy. In the D_{2d} group the (RR), (RL), (aa), (ab), $(a'a')$ and $(a'b')$ probe $A_1 + A_2$, $B_1 + B_2$, $A_1 + B_1$, $A_2 + B_2$, $A_1 + B_2$ and $A_2 + B_1$ symmetries respectively. The modes below 60 cm^{-1} are not indexed since they are magnetic and will be discussed in the next section. The modes are sharp and they are sitting at this low temperature on a flat background with almost vanishing intensity. The 60 cm^{-1} mode corresponds to the soft mode of the structural transition. At 121.8 cm^{-1} we observe in the A_1 channel the two phonon excitation seen also in (cc) polarization, Fig. 3, and very close to it another sharp mode with B_1 symmetry. We observe, similarly

to the spectra shown in Fig. 4b, several pairs of modes having very similar energies. For example doublet structures are observed around 284 cm^{-1} where we see a pair of A_1 and B_1 excitations and also two modes having B_1 and B_2 symmetries are found around 320 cm^{-1}.

One way to explain this behavior is to follow up the suggestion in Ref. [10] and assume that in the high temperature phase there are phonons which are odd and even with respect to inversion but very close in energy and to try to identify them by looking at similar atomic vibrations corresponding to 'u' and 'g' representations respectively. The (A_1,B_1) group around 284 cm^{-1} in Fig. 5 would correspond in this scenario either to a group of (A_{1g},A_{1u}) or (B_{1g},B_{1u}) in the high temperature phase since A_{1u} representation becomes B_1 and B_{1u} representation becomes A_1 at low temperatures. Similar reasoning would suggest for the (B_1,B_2) group around 320 cm^{-1} that it originates either from a pair of (B_{1g},A_{2u}) or (B_{2g},A_{1u}) modes above 395 K. We performed a symmetry analysis of the $k = 0$ atomic vibrations. The conclusion is that this approach does not provide an a priori reason for the quasi-degeneracy and one has to perform a quantitative normal mode energy calculation by using appropriate inter-atomic elastic constants. There is a simple way to see why this is true. Looking at the character table of the D_{4h} group it can be noticed that the even modes are symmetric with respect to the mirror symmetry in the $Cu(BO_3)$ planes while the odd modes are antisymmetric with respect to this symmetry operation. This means that the 'u' phonons in the high temperature phase correspond to vibrations of the atoms along the c-axis while the 'g' modes consist of in-plane movements. Due to the different oscillation pattern it is hard to explain the closeness of phononic energies at this qualitative level. We note that one can easily find vibrations corresponding to different group representations which involve similar oscillations at the 'molecular' level (for instance groups of atoms forming the Cu-O spin dimer structure or pairs O2 atoms between nearest neighbor dimers) and having a certain inter-molecular phase pattern, but they do not correspond to the experimentally observed symmetries. We suggest that, remaining within the conclusions of X-ray studies which have not found evidence for additional crystallographic changes at low temperatures, good candidates for understanding this intriguing behavior are provided by the inter-dimer BO_3 molecular

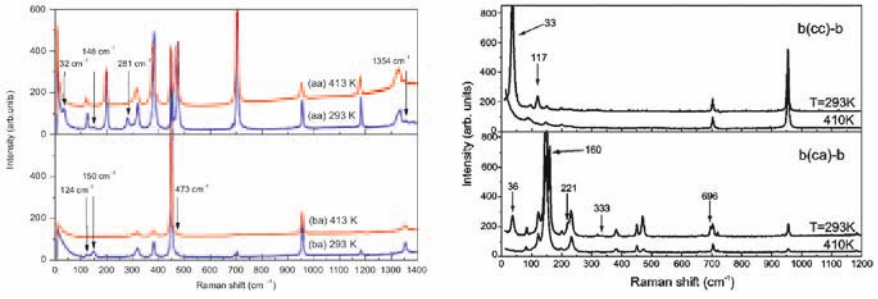

Fig. 4. Phononic data from Ref. [9] (left) and Ref. [10] (right) showing in plane and out of plane polarized spectra above and below the structural transition. Newly allowed Raman phonons are marked by arrows.

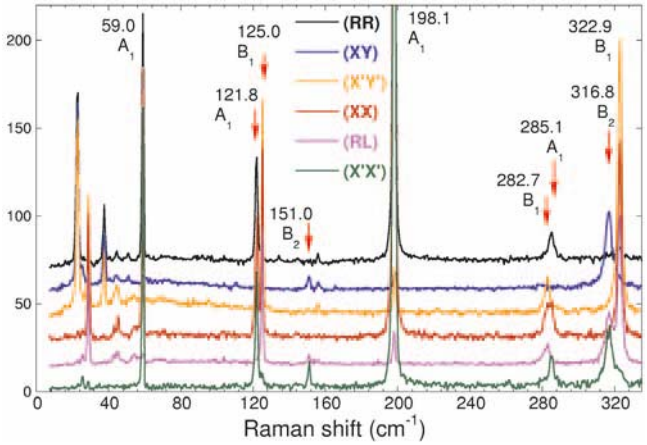

Fig. 5. Raman data at T ′ 3 K in six polarizations taken with the 1.92 eV laser excitation energy. The energy and symmetry of the modes above 60 cm^{-1} are shown in the figure.

complexes whose rotations as a whole around the a' and c-axes or whose in and out of the plane translations may turn out to be similar in energies.

3 Magnetic Properties of $SrCu_2(BO_3)_2$

3.1 Experimental and Theoretical Reviews

Experimental review – In this part we discuss data which relate to the most interesting properties and set the relevant energy scales of $SrCu_2(BO_3)_2$. Magnetization and INS data provided for the first time evidence for the existence of a gapped phase in this compound [2]. Fig. 6a shows that there is a drop in χ below about 15 K suggesting a gapped phase. Another important thing pointed in the inset of this figure is the strong suppression of the magnetization peak around 20 K compared to the prediction of a simple dimer model which points towards the importance of other magnetic interactions. Neutron scattering, Fig. 6, probed the excitations out of this phase and confirmed the existence of a gap of about 3 meV (24 cm^{-1}) and found additional excitations around 5 and 9 meV. Notable is the flat dispersion (less than 6%) of the gap branch seen at 3 meV as a function of in-plane wavevectors meaning that the lowest excitations are very local. The dispersion of the higher energy branches is more pronounced suggesting more mobile excitations in the multi-triplet channels. The inability of the dimer model to describe the experimental data suggests that inter-dimer interactions are important and points towards a very interesting physics of frustration in this system.

Besides INS and magnetization, ESR and IR data in magnetic fields confirmed the magnetic nature of these excitations. These experiments, along with high resolution INS data display a rich internal structure of the magnetic excitations and various selection

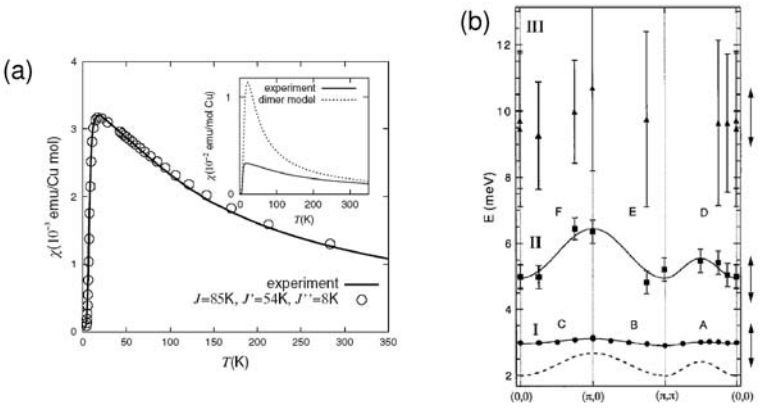

Fig. 6. Temperature dependence of the magnetization (**a**) and inelastic neutron scattering results as a function of in plane wavevectors at low temperatures in $SrCu_2(BO_3)_2$ (**b**) from Ref. [2]. The solid line in (**a**) shows the result of a fit from numerical calculation using $x = J_2/J_1 = 0.635$, $J_1 = 59\ \mathrm{cm}^{-1}$ (7.32 meV) and also an interlayer coupling $J_3 = 5.5\ \mathrm{cm}^{-1}$. The interactions J_1 and J_2 alone provide a good description of the low temperature data, including specific heat, but a finite J_3 was necessary to explain the high temperature behavior of the magnetization where a Weiss temperature θ = -92.5 K was obtained from the fit between 160 and 400 K [2].

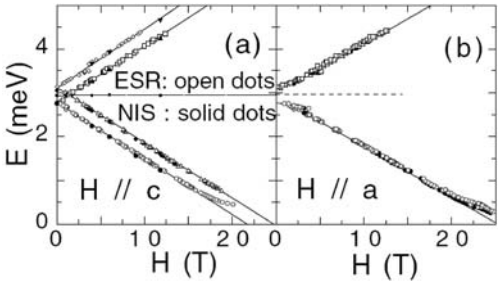

Fig. 7. Neutron (Ref. [16]) and ESR (Ref. [17]) data at low temperatures as a function of magnetic fields parallel (**a**) and perpendicular (**b**) to the c-axis.

rules for in and out of the plane applied magnetic fields, see Fig. 7. In particular, the gap multiplet is shown to be made of 6 branches, which is expected since the unit cell contains 4 spins and therefore exciting a triplet on each of them while the other one is in a singlet state will give a total of 6 excitations. Out of these 6 modes, 4 are seen to be symmetrically disposed around the gap value $\Delta = 24.2\ \mathrm{cm}^{-1}$. The observed splitting suggests that besides the superexchange interactions there are other low energy scale interactions which have to be taken in to account.

Theoretical review – This section discuses the salient properties of the magnetic structure of $SrCu_2(BO_3)_2$ and the excitations of the Hamiltonian (1). Among them, the ground state properties, the localization of the elementary triplets leading to the dispersionless magnon branches from Fig. 6b, the existence of strongly bound two-triplet states as well as the presence of additional spin orbit couplings generating the fine structure seen in Fig. 7.

In the approximation given by Eq. (1) the wavefunction given by the direct product of singlet dimers is always an eigenstate of the system and it can also be shown that it is the ground state for a continuous set of parameters $x = J_2/J_1$. For the proof of the eigenstate one has to take into account only the second term in (1) since the dimer product is obviously an eigenstate of the AF coupled independent dimers. The application of the $J_2(\mathbf{S}_1 \cdot \mathbf{S}_3 + \mathbf{S}_2 \cdot \mathbf{S}_3)$ on the $|s_{12} > \otimes |s_{34} >$ vanishes because the operator $(\mathbf{S}_1 + \mathbf{S}_2)$ applied to the singlet state $|s_{12} >$ vanishes. This is essentially due to the different parity of the singlet and triplet states with respect to the $1 \leftrightarrow 2$ exchange and the fact that on the orthogonal dimer lattice the Hamiltonian conserves the parity. This remains true even if the interlayer coupling is considered [1].

For $x \leq 0.5$ one can show that the singlet dimer product, $|\psi >$, is indeed the ground state. The Hamiltonian (1) can be written as $\hat{H} = \sum_i^{N_t} \hat{h}_i$ where N_t is the number of triangles of the type formed by the spins 1, 2 and 3 in Fig. 9 and $\hat{h}_i = (J_1/2)(\mathbf{S}_1 \cdot \mathbf{S}_2) + J_2(\mathbf{S}_1 \cdot \mathbf{S}_3 + \mathbf{S}_2 \cdot \mathbf{S}_3)$. The ground state of each $\hat{h}_i$ is $e_g^i = -3/8 J_1$ if $x \leq 0.5$. Accordingly, denoting the true ground state of $\hat{H}$ by $|\phi >$, one has $E_g = < \phi|\hat{H}|\phi > = \sum_i^{N_t} < \phi|\hat{h}_i|\phi > \geq -3/8 J_1 N_t$ because $|\phi >$ is a variational function for $\hat{h}_i$. Considered as a variational wavefunction for $\hat{H}$ and taking into account that the action of the second term in Eq. (1) on $|\psi >$ is identically zero, one obtains immediately that $< \psi|\hat{H}|\psi >= -3/4\ J_1 N_d = -3/8\ J_1 N_t$ because the number of dimers, N_d, is half of that of the triangles. On account of the variational principle, the true ground state energy satisfies $E_g \leq -3/8 J_1 N_t$. From the two inequalities one obtains that $E_g = -3/8 J_1 N_t$ and so the product of singlet dimers is indeed the ground state. The underlying reason for these beautiful properties is the fact that the magnetic lattice of $SrCu_2(BO_3)_2$ is a realization of a 2D Shastry-Sutherland model which up to now has been discussed only at a theoretical level.

Turning to the question of the flat dispersion of the excitations in the one-triplet sector one can consider in Fig. 9 the case of two nearest neighbor orthogonal dimers having an excited triplet state on the vertical bond and a singlet on the horizontal one. The propagation of the triplet on the horizontal bond by the NNN term in Eq. (1) is only possible if a triplet is left behind on the vertical dimer. This is due to the reflection symmetry of singlet and triplet excitations with respect to a mirror plane parallel to the horizontal bond, Fig. 9a and the fact that the Hamiltonian of the system must be a fully symmetric operator. If a triplet is left behind, then the hopping of one triplet to a neighboring dimer is very restricted and is possible only by virtually forming closed paths of triplets, the smallest of these paths involving three adjacent dimers. As a result, one triplet hopping appears only in the 6^{th} order of perturbation theory showing that these excitations are very localized in real space and explaining the flat k dispersion seen in Fig. 6. The motion of two triplets is different however. It has been shown [11] that in this case correlated hopping processes can occur and it was found that two-particle hopping

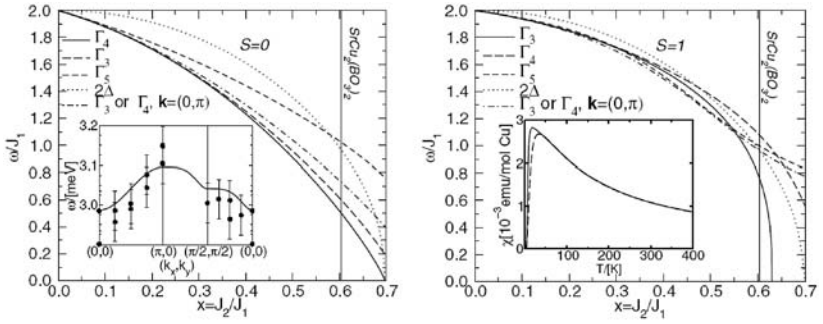

Fig. 8. Predictions for the two-triplet bound states in the singlet (left) and triplet (right) of a perturbative analysis of the Shastry-Sutherland Hamiltonian of Eq. (1) from Ref. [11]. Γ_1, Γ_2, Γ_3, Γ_4 and Γ_5 correspond to A_1, B_1, B_2, A_2 and E in the notation of Table 1.

appears in 2^{nd} order perturbation theory. This explains the larger dispersion seen by INS for the excitations around 5 meV.

We saw that the products of dimer singlets is the ground state of $\hat{H}$ at least for $x \leq 0.5$. What is the value of x above which this is no longer true? That there should be a finite value is obvious from the fact that in the limit $x \to \infty$ the lattice is topologically equivalent to a 2D square lattice which has long range order at T = 0 K and a spin-wave approximation is more appropriate. Theoretical work [1, 11, 12, 14] shows that below a ratio $x = J_2/J_1 \prime\ 0.7$ the ground state remains the same and the system has a finite spin gap, Δ to the lowest excited $S = 1$ state. The spin gap is equal to J_1 for $x = 0$ but with increasing this ratio Δ gets renormalized down due to many body effects, see Fig. 8. At high values of x the system has long range order, other possible intervening states separated by QCP's have been proposed to exist around $x = 0.7$. The gap renormalization as a function of x is shown in Fig. 8. As shown here and also in the parameters used to fit magnetization data in Fig. 6, $SrCu_2(BO_3)_2$ is closed to a QCP having a gap renormalized significantly, to a bit more than 50% of the 'bare' value given by $J_1 \prime\ 85$ K (59 cm^{-1} or 7.3 meV), see Ref. [1].

Another characteristic of this magnetic lattice seen in Fig. 8 is the existence of bound states in the two-triple sectors, see Fig. 8. These are states which have an energy below the inset of the two-magnon continuum starting at 2Δ. Many of these have been predicted along with their symmetries. The vertical line in Fig. 8 showing the position of $SrCu_2(BO_3)_2$ in the phase diagram was inferred from the experimentally found values of the spin gap $\Delta = 24$ cm^{-1} (3 meV) and the observation by Raman scattering of a strong and sharp resonance (attributed to collective $S = 0$ two-triplet bound state) around 30 cm^{-1} [20]. We will discuss such excitations in the next section devoted to the analysis of low temperature Raman data in $SrCu_2(BO_3)_2$.

Before that, another observation in connection to the experimental results shown in Fig. 7: there it is seen that the 6 branches of the gap multiplet around 24 cm^{-1} are split in three pairs of doublets. Cépas and collaborators proposed that this is due to the existence

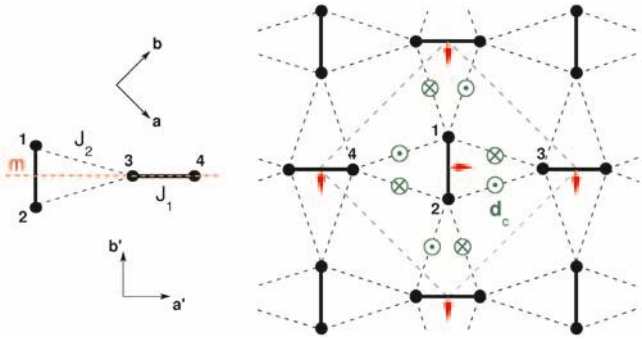

Fig. 9. Left: Cartoon with two nearest neighbor dimers discussed in the text related to the exact ground state and hopping of triplet excitations. m denotes a mirror plane; the singlet and triplet states on the $1-2$ dimer will have different symmetries with respect to this reflection operator. Right: The unit cell of the magnetic lattice from Fig. 2 with the inter-dimer Dzyaloshinskii-Moriya term suggested in Ref [16] which is parallel to the c-axis. The arrows perpendicular to each dimer correspond to our proposed antisymmetric intra-dimer interaction leading to singlet-triplet mixing.

of inter-dimer DM interactions which have a direction parallel to the c-axis, see Fig. 9. The proposed Hamiltonian (for the spins in the unit cell) reads:

$$\hat{h}_c = \vec{d}_c^{\,13}(\mathbf{S}_1 \times \mathbf{S}_3) + \vec{d}_c^{\,14}(\mathbf{S}_1 \times \mathbf{S}_4) + \vec{d}_c^{\,23}(\mathbf{S}_2 \times \mathbf{S}_3) + \vec{d}_c^{\,24}(\mathbf{S}_2 \times \mathbf{S}_4) \tag{2}$$

The DM vectors satisfy $\vec{d}_c^{\,13} = \vec{d}_c^{\,24} = -\vec{d}_c^{\,14} = -\vec{d}_c^{\,23}$ due to the crystal symmetry, in particular due to the existence of mirror planes orthogonal to the dimers as shown in Fig. 9 and the existence of C_2 rotation axes parallel to the c-axis and passing through the middle of the dimers. It was found that this interaction reproduces the behavior in magnetic fields perpendicular and parallel to the (ab) plane, which is shown by solid lines in Fig. 7. The energy of the upper and lower pairs is given by $\Delta \pm d_c$ and they remain degenerate, see also Fig 11c where we show symmetry analysis results. Importantly, the inter-dimer DM interactions parallel to the c-axis are allowed both above and below the structural phase transition at 395 K. Other DM terms, for instance the red arrows in Fig. 9, the are not allowed above T_c because the $Cu(BO_3)$ plane is a mirror symmetry element.

3.2 Magnetic Raman Scattering Results in $SrCu_2(BO_3)_2$

Here are some experimental details related to our data discussed in the following. The spectra were taken from the (ab) single crystal surface in a backscattering geometry. We used an incident power of about 0.6 mW focussed on a 100 μ diameter spot. The crystallographic axes orientation was determined by X-ray diffraction. The data in magnetic fields, taken at a sample temperature of about 3 K, were acquired having the continuous flow cryostat inserted in the horizontal bore of a superconducting magnet. We used the $\omega_L = 1.92$ and 2.6 eV excitation energies of a Kr^+ laser and a triple-grating spectrometer

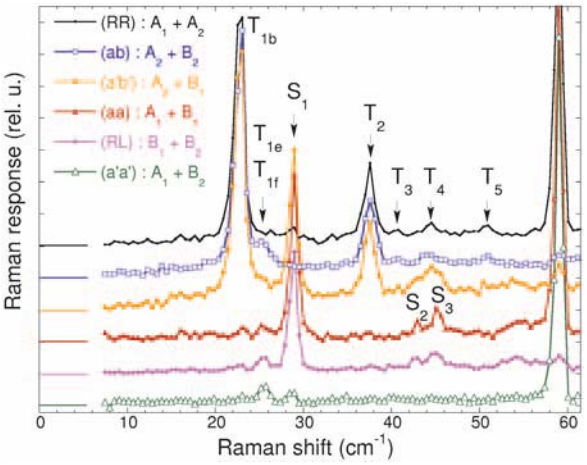

Fig. 10. Zero field Raman data in $SrCu_2(BO_3)_2$ taken with $\omega_L = 1.92$ eV excitation energy at T = 3 K in six polarizations. The legend shows the tetragonal symmetries probed in each scattering geometry.

for the analysis of the scattered light. The data were corrected for the spectral response of the spectrometer and detector. Polarization configurations are denoted by $(\mathbf{e}_{in}\mathbf{e}_{out})$ where these two vectors are along the polarization direction of the incoming and outgoing photons. Circular polarizations are denoted by (RR) and (RL) where $\mathbf{e}_{in,out} = (\hat{a} \pm i\hat{b})/\sqrt{2}$.

In Fig. 10 we show six low temperature Raman spectra in zero applied field and using a laser frequency $\omega_L = 1.92$ eV. The symmetries probed by each polarization in the tetragonal group are shown in the legend. The mode seen at 60 cm^{-1} is the soft mode of the structural transition, also seen in Fig. 3, which belongs as expected to the fully symmetric representation. Three strong features are seen in the spectra at 23, 29 and 38 cm^{-1} and they are denoted by T_{1b}, S_1 and T_2. These excitations belong to the A_2, B_1 and A_2 representations respectively. Besides these three modes, we observe several other weaker excitations. Among them we see a set of three A_2 symmetric modes denoted by T_3, T_4 and T_5. One can also observe the presence of other very weak feature at 25.5 cm^{-1} in all polarization configurations except (RR). This suggest that at this frequency there are two quasi-degenerate excitations and that they belong to the B_1 and B_2 representations which would justify their observations in five out of six scattering geometries. The symmetry analysis discussed later confirms indeed the above assumption. The modes are denoted by T_{1e} and T_{1f}. A summary of the zero field energies and their experimentally observed symmetries can be found in Table 2. The energy at which we observe these modes, the comparison with the INS, ESR and IR data, part of which are shown in Figs. 6 and 7 as well as our data in magnetic fields confirm the magnetic origin of these modes and the predominant $S = 1$ character of the 'T' modes. The T_{1b}, T_{1e} and T_{1f} excitations modes seem thus to belong to the spin gap multiplet while T_2, T_3, T_4 and T_5 would correspond to multi-particle $S = 1$ channels.

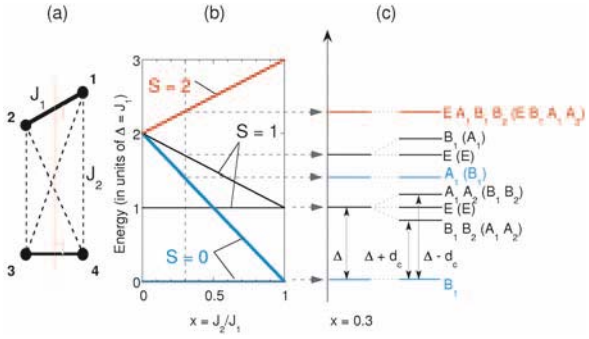

Fig. 11. (**a**) The cluster used for the symmetry analysis of the $k = 0$ modes generated by the four spins in the unit cell of Fig. 9. (**b**) The eigenvalues of the Hamiltonian corresponding to the 4-spin cluster in (**a**) taking into account the J_1 and J_2 terms as a function of the ratio $x = J_2/J_1$. (**c**) Results of the symmetry analysis for this cluster in the D_{2d} group. The energy levels correspond to a value $x = 0.3$. On the right we show the energy splittings and the absolute and relative to the ground state (in parenthesis) symmetries of the 16 magnetic modes when a finite inter-dimer DM interaction d_c is present. A finite intra-dimer DM term d_{ab} will further split the modes which belong to the one-dimensional representations, see Fig. 9.

The zone center elementary excitations are generated by the spins within the magnetic unit cell. If the picture of real space localized elementary triplets is true, then one expects that the analysis of the 4-spin cluster forming the unit cell is able to predict correctly the experimentally observed symmetries of these excitations. Accordingly we calculated the energies and symmetries of the excitations generated by the magnetic cluster shown in Fig. 11a and the Hamiltonian of Eq. (1). The total number of states, 16, consist of two singlet, $S = 0$, states, three triplet, $S = 1$, states and one quintuplet, $S = 2$ state. The energies are shown in Fig. 11a as a function of $x = J_2/J_1$ and one can observe their linear variation with the this ratio. The points at $x = 0$ and $x = 1$ can be easily understood. The first one corresponds to two independent AF coupled by J_1 on the bonds $1 \leftrightarrow 2$ and $3 \leftrightarrow 4$ so the energies will be just the sum of those corresponding to singlet and/or triplet states sitting on each dimer separately. For the second point one can see that $[\hat{H}, \mathbf{S}_{tot}] = 0$ so the energies will be, up to a constant factor, equal to the total spin eigenvalues $S(S+1)$ (in units of $\hbar^2$). Starting with four $S = 1/2$ spins one can have for the total spin the values $S = 0, 1$ and 2.

The cluster in Fig. 11a belongs to the D_{2d} group which is, as it should be, the point group associated with the space symmetry of the crystal. We performed the group symmetry analysis of the eigenstates by decomposing the representation obtained starting with the canonical spin basis (the direct product of $|\uparrow>$ and $|\downarrow>$ spinors representing each Cu atom) into the irreducible representations of the D_{2d} point group. Each symmetry element of the D_{2d} group involved the action on spinor state in the origin of the coordinate system as well as the corresponding permutation of spin indices. Using projec-

Table 2. Collective spin excitations in zero field: notation, the predominant spin character, S_{tot} and z projection S_z, energy and transition symmetries as observed experimentally and predicted from the 4-spin cluster in Fig. 1 corresponding to $k = 0$ excitations.

Mode	S_{tot} (S_z)	Energy	Symmetry	
			Experiment	Group Theory
T_{1a}	1 ($\pm$1)	22.8	-	A_{1g}
T_{1b}	1 ($\pm$1)	22.8	A_{2g}	A_{2g}
T_{1c}	1 (0)	24.2	-	E
T_{1d}	1 (0)	24.2	-	E
T_{1e}	1 ($\pm$1)	25.6	B_{1g}	B_{1g}
T_{1f}	1 ($\pm$1)	25.6	B_{2g}	B_{2g}
S_1	0 (0)	28.9	B_{1g}	-
T_2	1	37.5	A_{2g}	-
T_3	1	40.8	A_{2g}	-
S_2	0	43.0	B_{1g}	-
T_4	1	44.5	A_{2g}	-
S_3	0	45.2	B_{1g}	-
T_5	1	50.9	A_{2g}	-

tion operators we block diagonalized the Hamiltonian and numerical analysis (including the DM terms shown in Fig. 9 and discussed in more detail later) allowed us to identify the energy and the predominant spin character of each eigenstate.

Indeed, as it is shown in the right-most column of the Table 2 and Fig. 11c, the symmetries of the observed one-triplet excitations correspond to the results of group theory analysis. The latter predicts for the six elementary triplets the A_1, A_2, B_1, B_2 and E symmetries, see Fig. 11. The E modes, T_{1c} and T_{1d}, cannot be observed in zero field when the light propagates parallel to the c-axis because they are accessible only in (ca) or (cb) polarizations. The fully symmetric T_{1a} mode which, within the spin model including J_1, J_2 and the out-of-plane inter-dimer DM interaction proposed in Ref. [16], should be degenerate with the strong T_{1b} (A_2 symmetric) excitation at 22.8 cm^{-1} is also not observed. This is most probably due to a much weaker coupling to light in this symmetry channel. The analysis shown in Fig. 11 shows that the pair of T_{1e} and T_{1f} modes at 25.6 cm^{-1} are to be seen in the B_1 and B_2 symmetry channels which explains the weak feature seen in Fig. 10 in all polarizations except the (RR) scattering geometry. The observation of the T_{1e} (T_{1f}) modes with B_1 (B_2) symmetries 2.8 cm^{-1} above the A_2 symmetric mode T_{1e} allows the determination of the magnitude of the inter-dimer interaction d_c (see Fig. 11) and also of its absolute sign because a sign change will interchange the position of these modes around the gap Δ. Finite intra-dimer Dzyaloshinskii-Moriya interactions (red arrows in Fig. 9) will split slightly the energies of the states in Fig. 11 which belong to the one dimensional representations. These effects will be discussed in more detail later where we analyze quantitatively the behavior of the spin excitations in magnetic fields applied parallel and perpendicular to the c-axis.

We turn now to the discussion of two-triplet states. Besides the singlet ground state and six one-triplet states, the symmetry analysis of the 4-spin cluster shown in Fig. 11

predicts the following: one $S = 0$ two-triplet bound state to be observed in the B_{1g} channel, three branches with A_1 and double degenerate E symmetries which belong to another bound $S = 1$ excitation and five branches of a quintuplet ($S = 2$) state to be accessed in the A_1, A_2, B_1 and E channels. Their symmetries, along with the energies for the particular value $x = 0.3$ chosen as an example, are shown in Fig. 11c. We observe that due to symmetry reasons none of the A_2 symmetric modes from T_2 to T_5 having energies higher than 30 cm^{-1} qualify for an interpretation as triplet bound states generated within the 4-spin cluster. This is consistent with the fact that larger cluster sizes are necessary in order to capture the more delocalized nature of these excitations which implies that they have contributions from the different parts of the Brillouin zone. The fact that the existence of the strong A_2 symmetric bound triplet state at an energy $1.55 \cdot \Delta = 37.5$ cm^{-1} has not been predicted by high order perturbative analysis [11] suggest that other spin interactions have to be taken into account in order to explain the excitation spectrum. Apparently, symmetry considerations would allow the 28.9 cm^{-1} feature denoted by S_1 in Fig. 10 to be interpreted as the singlet bound state of two triplets within a unit cell. As we show in the following section, this 28.9 cm^{-1} mode does not shift in external fields, which is compatible with a collective singlet excitation as discussed in [20], but suggests that its internal structure is not the one derived from the 4-spin cluster.

In Fig. 12, using the same mode notations, we show the influence of an external magnetic field applied parallel and perpendicular to the c-axis on the low temperature Raman spectra from Fig. 10. The relevant aspects are the following. In panel (a) we observe the splitting of the T_{1a} and T_{1b} modes in magnetic fields B $\parallel c$, the B = 1 T showing that the A_2 mode (T_{1b}) present in zero field disperses upwards with increasing the magnitude of the field. Dashed lines in this figure mark the dispersion of the much weaker modes T_3, T_4 and T_5. In Fig. 12b one of the E modes becomes Raman active due to symmetry lowering for $\vec{B} \perp \hat{c}$ configuration and we observe three dispersing branches of the gap multiplet. Fig. 12c shows that the B_1 symmetric excitation at 28.9 cm^{-1} does not change its energy with field, only a very small negative shift of the order of 0.5 cm^{-1} from 0 to 6 T is seen because of the crossing with the upward dispersing gap branches seen in (RR) polarization. Panel (d), which is a zoomed in region of Fig. 12b, shows that several modes become Raman active in finite fields $\vec{B} \perp \hat{c}$ around 38 cm^{-1} where the T_2 excitation lies. The internal structure of this higher energy multiplet is composed of modes dispersing up, down or independent of magnetic field. Remarkable is their similar selection rules and dynamics in magnetic fields of the collective modes around 38 cm^{-1} and 24 cm^{-1}. The emergence in finite fields of several strong modes in the spin gap region precludes the observation of the weak T_{1e} and T_{1f} modes from Fig. 10.

Fig. 13 summarizes the magnetic field dependencies of the energies and spectral weights of the most intense Raman excitations. The symbols in Fig. 13a-d correspond to experimental data, dashed lines are guides for the eye while the solid lines are results of a numerical diagonalization of a 4-spin cluster using the same set of parameters. Taking into account that the 4-spin cluster neglects many-body gap renormalization effects (see Fig. 8) leading to a singlet-triplet energy independent of $x = J_2/J_1$ as well as the fact that when using periodic boundary conditions there is an effective doubling of the J_2 and inter-dimer DM interactions from Eq. (2), we chose the following values: $J_1 = \Delta = 24.2$ cm^{-1} which

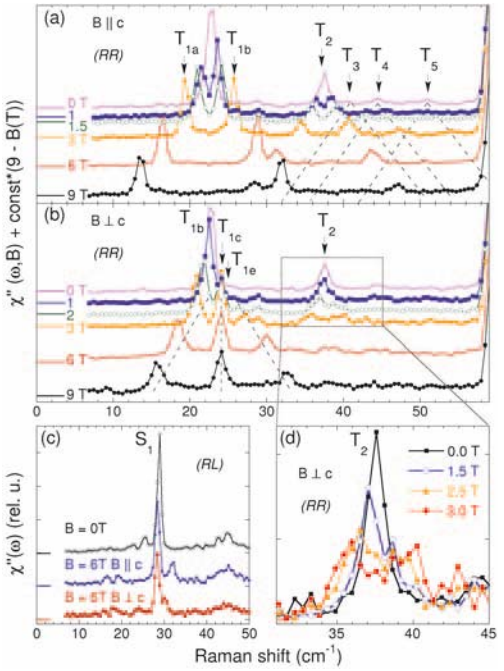

Fig. 12. Magnetic field dependences of the magnetic excitations at T = 3 K using the $\omega_L = 1.92$ eV excitation energy in the following geometries: (**a**) (RR) $\vec{B} \parallel \hat{c}$. (**b**) (RR) $\vec{B} \perp \hat{c}$. In (**c**) the (RL) polarized data is shown for 0 and 6 T magnetic fields for both $\vec{B} \parallel \hat{c}$ and $\vec{B} \perp \hat{c}$. In (**a**) and (**b**) the vertical shift is proportional to the magnetic field difference with respect to the 9 T spectrum and the dashed lines are guides for the eye.

is the value of the spin gap, see the Table 2; $x = 0.556$ from the ratio of the energies of the sub-gap mode at 21.5 cm^{-1} [18, 21] with respect to the gap Δ (see Fig. 11); an inter-dimer DM term parallel to the c-axis, $d_c = 1.4$ cm^{-1}, which produces the splitting of the $T_{1a,b}$ and $T_{1e,f}$ branches from 24.2 cm^{-1} (our value is consistent to the one proposed in the literature [16]); finally, from the magnetic field value around which the intensities crossing in Fig. 13 takes place, the value chosen for the intra-dimer interaction was $d_{ab} = 2.66$ cm^{-1}.

The term containing the intra-dimer DM interaction is proposed by us in order to explain the coupling and selection rules with magnetic fields. Symmetry considerations impose in the $I\bar{4}2m$ group for the directions of the in plane DM vectors the ones depicted in Fig. 9 with the Hamiltonian reading:

$$\hat{h}_{ab} = \vec{d}_{ab}^{12}(\vec{S}_1 \times \vec{S}_2) + \vec{d}_{ab}^{34}(\vec{S}_3 \times \vec{S}_4) \tag{3}$$

The interaction terms responsible for the coupling to the external photon field and which were used for the calculation of intensities in Fig. 13c-d are discussed in the next part. We

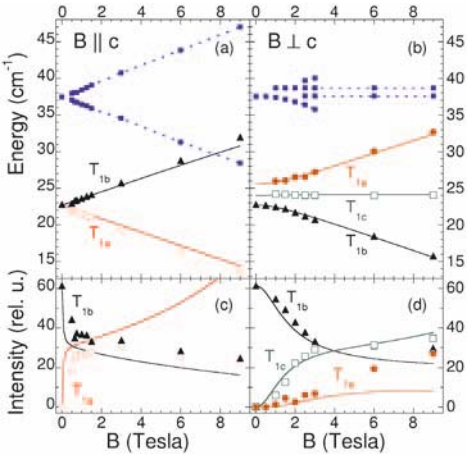

Fig. 13. Energies (panels **a** and **b**) and intensities (panels **c** and **d**) of the spin excitations for $\vec{B} \parallel \hat{c}$ (right) and $\vec{B} \perp \hat{c}$ (left) from Fig. 3a-b. Symbols represent experimental points, solid lines are the results of 4-spin cluster diagonalization as described in the text, dashed lines are guides for the eye.

also plotted (filled squares and dashed lines) the field dependence of other higher energy modes observed in Fig. 12.

We remark an overall qualitative agreement for this choice of parameters which suggests that the intra-dimer interaction has to be taken into account in the spin Hamiltonian. The agreement is quantitative as regards the energies and the intensity variations for the $\vec{B} \perp \hat{c}$ case. The term described in Eq. (3) plays a crucial role in obtaining a finite coupling to the excited $S = 1$ triplets which is not realized by the d_c terms in Eq. (2). Regarding the apparent degeneracy of the T_{1a} and T_{1b} as well as that of the T_{1e} and T_{1f} modes although they belong to different representations, we note that these two groups of excitations are split by $\hat{h}_{ab}$ but the splitting is very small, of the order of $d_{ab}^2/\Delta \prime\ 0.25$ cm^{-1}. The largest discrepancy between the experimental data and the calculation is seen in Fig. 13. One aspect in this regard is that the value d_{ab} had to be chosen greater than that of d_c. This is intriguing because the d_c term is allowed by symmetry both above and below the structural phase transition at 395 K [9] whereas the existence of a finite intra-dimer DM interaction is allowed only below 395 K when the mirror symmetry of the (ab) plane is just slightly broken. Additional terms may be responsible for this disagreement, possible candidates being in-plane components of the inter-dimer DM interaction, which should also be allowed below the structural phase transition.

We discuss now the issue related to the existence of a magnetic mode *below* the spin gap value [18, 21]. In order to reproduce the upward dispersion with fields $\vec{B} \parallel \hat{c}$ of the T_{1b} mode we had to choose a value of x which is greater than 0.5, otherwise this excitation would have displayed a downward dispersion. From Fig. 11 we observe that a ratio of $x = J_2/J_1 \geq 0.5$ implies that the position of the bound singlet state is below Δ.

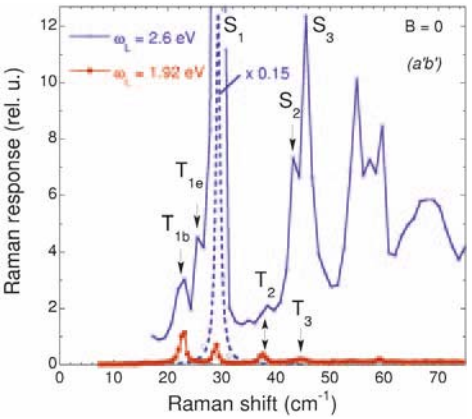

Fig. 14. T = 3 K Raman data in $(a'b')$ polarization for $\omega_L = 1.92$ (filled squares) and 2.6 eV (empty circles) excitation energies. The data points corresponding to the resonantly enhanced singlet bound state at 29 cm^{-1} are multiplied by 0.15 and the corresponding line represents a Lorentzian fit.

We suggest that this state is responsible for the observations of the 21.5 cm^{-1} mode in Refs. [18, 21]. The presence of this excitation will also influence the specific heat measurements and, in conjunction with the finite intra-dimer interaction d_{ab}, also the low temperature magnetization data whose quantitative understanding has not been achieved yet [1]. The existence of this magnetic mode is at odds with theoretical predictions [11, 12, 14]. However, the experimental finding of the set of A_2 symmetric modes (T_2 to T_5 in Fig. 2, all of them below the two-magnon continuum starting at $2\Delta \prime$ 48 cm^{-1} and also not predicted by theory) already shows that the understanding of the spin dynamics in higher particle sectors is not complete.

Fig. 14 shows two low temperature Raman spectra taken in $(a'b')$ polarization with two incoming laser frequencies, $\omega_L = 1.92$ and 2.6 eV. The point we make is that we observe two types of behaviors. Firstly we notice that the intensities of the group of A_2 symmetric modes, T_{1b} and T_2 is about the same for the two photon energies used. On the other hand, the modes corresponding to the group formed by the T_e, S_1, S_2 and S_3 resonances are more than two orders of magnitude stronger for $\omega_L = 2.6$ eV than for $\omega_L = 1.92$ eV. Other modes in the 50 to 70 cm^{-1} energy range also become visible in the $\omega_L = 2.6$ eV spectrum.

Our data prove that the coupling to these two groups of excitations takes place by two distinct light scattering mechanisms. The resonance of the B_1 symmetric T_e magnetic mode, enhanced for $\omega_L = 2.6$ eV, is similar to the one corresponding to S_1, S_2 and S_3 excitations as well as to the behavior of the new modes seen around 55, 59 and 68 cm^{-1}. On the account of this similarity alone, one cannot identify the latter as magnetic bound states as well. However, the lack of energy shift in magnetic fields and the results of perturbational analysis regarding energy scales and symmetries [11] are not contradicting their interpretation as Raman active collective $S = 0$ magnetic bound states [20].

We discuss below the nature of the two light coupling mechanisms to magnetic excitations. As for the set of A_2 symmetric modes we propose that the coupling takes place *via* the spin-orbit coupling which can be written in an effective form as $(\mathbf{e}_{in} \times \mathbf{e}_{out})\vec{S}^z_{tot}$ [22]. This interaction Hamiltonian probes excitations with A_2 symmetry and the calculated magnetic field dependence in Fig. 13 is also in agreement with the experimental results. The coupling to the T_{1e} and T_{1f} modes from Fig. 10 can be understood if we invoke the usual effective spin interaction corresponding to the photon induced spin exchange process $\sum_{<i,j>}(\mathbf{e}_{in} \cdot \mathbf{r}_{ij})(\mathbf{e}_{out} \cdot \mathbf{r}_{ij})\vec{S}_i \cdot \vec{S}_j$. Here the sum runs over pairs of lattice sites, $\vec{S}_i$ and $\vec{S}_j$ are the exchanged spins on sites i and j respectively, while $\mathbf{r}_{ij}$ is the vector connecting these sites [22]. Writing down the explicit expression of this interaction for several polarizations in the 4-spin cluster approximation (Figs. 9 and 11) one indeed gets finite coupling in B_1 and B_2 channels for the triplet T_{1e} and T_{1f} states. This explains the presence of the 25.6 cm^{-1} modes in all polarizations except (RR).

The difference in the coupling strengths seen in Fig. 14 is thus understandable because these two coupling mechanisms need not be simultaneously in resonance with the same high energy excited electronic states. The photon induced spin exchange Hamiltonian has been usually invoked in order to explain Raman active $S = 0$ two-magnon type excitations in various magnetic systems [22]. $SrCu_2(BO_3)_2$ is an example where this Hamiltonian, in the presence of singlet-triplet mixing DM interactions, can be used to account for coupling to $S = 1$ states. A remaining question is why do we not see the bound singlet mode with an energy below Δ for any of the two excitations used? In principle the photon induced spin exchange, resonant in this case at higher photon energies, could provide coupling to this excitation also, as to the 28.9 cm^{-1} mode denoted by S_1. One possible explanation to be explored in more detail from a theoretical point of view is that the Raman form factors for exciting a pair of magnons both at $k = 0$ is vanishing as opposed to the case of a pair of zone boundary modes. For instance this is the case when the Raman vertex is calculated for the 2D square lattice within the spin-wave approximation and using the Fleury-Loudon interaction Hamiltonian. Consequently, the 21.5 and the 28.9 cm^{-1} excitations could be both attributed to $S = 0$ bound states originating from different parts of the reciprocal space and having substantially different binding energies.

3.3 Summary

We showed in this chapter low temperature Raman data on phononic and magnetic excitations in $SrCu_2(BO_3)_2$. Regarding the former, in the 0 to 350 cm^{-1} range we find several pairs of quasi-degenerate modes which have different symmetries. Group theoretical analysis suggests that the existence of these modes is related to quite different atomic vibrational pattern, i.e. in-plane and c-axis motions and as a result a quantitative investigation would be very interesting. Collective magnetic excitations were studied in terms of symmetry, resonance and coupling mechanisms in zero and applied magnetic fields. The analysis of the 4-spin cluster shown in Figs. 9 and 11 allows us to understand the group symmetries of the zero field Brillouin zone center spin gap branches around 24 cm^{-1} confirming the picture of local elementary one-triplet modes. By considering an additional intra-dimer DM interaction we are also able to understand the observed selection rules and intensity variations of the spin gap branches in external magnetic fields applied par-

allel or perpendicular to the dimer planes. These selection rules also require that the energy of the $S = 0$ two-triplet bound state made out of magnons confined within a unit cell is *below* Δ (in the 4-spin cluster this is equivalent to $x \geq 0.5$ in Fig. 10) suggesting a very high binding energy for this two particle excitation. The 4-spin cluster analysis fails to account for the two-triplet excitations which shows that they have contributions from the different parts of the reciprocal space. The existence of a set of four modes below the onset of two-triplet continuum, at 37.5, 40.8, 44.5 and 50.9 cm^{-1}, in the A_2 symmetry channel, shows that further theoretical analysis is required in order to understand the nature of these composite excitations. Finally, we identified two effective magnetic light scattering Hamiltonians responsible for the coupling to the magnetic modes which allowed us to explain their resonance behavior.

Acknowledgments

We acknowledge discussions and collaborations with B. S. Dennis, M. V. Klein and T. Rõõm. The crystals were provided by H. Kageyama.

References

[1] For a recent theoretical review see S. Miyahara and K. Ueda, J. Phys.: Condens Matter **15** (2003) R327.
[2] H. Kageyama *et al.*, Phys. Rev. Lett. **82** (1999) 3168.
[3] K. Onizuka *et al.*, J. Phys. Soc. Japan, **69** (2000) 1016.
[4] K. Kodama *et al.*, Science **298** (2002) 395.
[5] T. M. Rice *et al.*, Science **298** (2002) 760.
[6] B. S. Shastry and B. Kumar, Prog. Theor. Phys. Supp. **145** (2002) 1.
[7] P. W. Anderson, Science **235** (1987) 1196.
[8] R. W. Smith and D. A. Keszler, J. Solid State Chem. **93** (1991) 430.
[9] K. Sparta *et al.*, Europhys. J. B **19** (2001) 507.
[10] K.-Y. Choi *et al.*, Phys. Rev. B **68** (2003) 104418.
[11] C. Knetter *et al.*, Phys. Rev. Lett. **85** (2000) 3958.
[12] S. Miyahara and K. Ueda, J. Phys. Soc. Japan (Suppl.) **69** (2000) 72.
[13] C. Knetter and G. S. Uhrig, Phys. Rev. Lett. **92** (2004) 027204.
[14] S. Miyahara and K. Ueda, Phys. Rev. Lett. **82** (1999) 3701.
[15] H. Kageyama *et al.*, Phys. Rev. Lett. **84** (2000) 5876.
[16] O. Cépas *et al.*, Phys. Rev. Lett. **87** (2001) 157205.
[17] H. Nojiri *et al.*, J. Phys. Soc. Japan **68** (1999) 2906.
[18] H. Nojiri *et al.*, J. Phys. Soc. Japan **72** (2003) 3243.
[19] T. Rõõm *et al.*, Phys. Rev. B **61** (2000) 143342.
[20] P. Lemmens *et al.*, Phys. Rev. Lett. **85** (2000) 2605.
[21] T. Rõõm *et al.*, http://xxx.lanl.gov/abs/cond-mat/0405434 (2004) preprint.
[22] P. A. Fleury and R. Loudon, Phys. Rev. **166** (1968) 514.
[23] D. L. Rousseau, R. P. Bauman and S. P. S. Porto, J. Raman Spectroscopy **10** (1981) 253.

MAGNETIC AND CHARGE CORRELATIONS IN $La_{2-x-y}Nd_ySr_xCuO_4$: RAMAN SCATTERING STUDY

A. Go ar[1,2], Seiki Komiya[3], Yoichi Ando[3], and G. Blumberg[1]

[1] Bell Laboratories, Lucent Technologies, Murray Hill, NJ 07974, USA
[2] University of Illinois at Urbana-Champaign, Urbana, IL 61801, USA
[3] Central Research Institute of Electric Power Industry, Komae, Tokyo 201-8511, Japan

1 The Phase Diagram and Structural Properties of the High Temperature Superconductor $La_{2-x}Sr_xCuO_4$

La_{2-} Sr CuO_4 is one of the most studied Cu-O based layered perovskites [1]. It exhibits some of the most important aspects related to the physics of strongly correlated electrons and, more important, is one of the compounds which belong to the family of high temperature superconducting cuprates. In fact the high T_c superconductivity (SC) rush which began in 1986 started with a variant of La_{2-} Sr CuO_4, a Ba-La-Cu-O based compound [2], where the authors observed a highest onset SC temperature T_c in the 30 K range.

The phase diagram of La_{2-} Sr CuO_4 is shown in Fig. 1, see also Ref. [3]. Several electronic ground states as well as structural phases evolve with Sr concentration. For (Sr) $\leq$ 0.02 the crystals have long range antiferromagnetic (AF) order and one can observe a very rapid suppression of the Néel ordering temperature T_N with the amount of Sr. While for $x = 0$ the AF transition is slightly above room temperature, T_N decreases in the 150 - 200 K range for $x = 0.01$ and it is completely suppressed above $x = 0.02$. The phase diagram shows also a SC dome starting at $x = 0.05$ and ending around $x = 0.32$. The maximum T_c of about 40 K is reached at the optimal doping $x = 0.2$. The highest

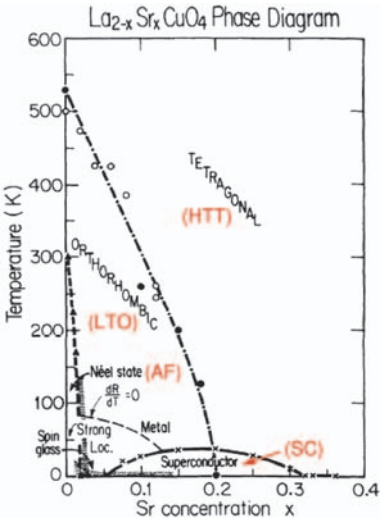

Fig. 1. Phase diagram of La_{2-} Sr CuO_4 from Ref. [3]. HTT and LTO stand for the high temperature tetragonal and low temperature orthorhombic phases respectively. AF denotes the long ranged antiferromagnetic region (Néel state) at low dopings and SC denotes the superconductivity dome with a maximum around $x = 0.2$ Sr concentration.

SC temperature (T_c = 51.5 K) in the La_{2-} Sr CuO_4 family was achieved in thin films under epitaxial strain [4]. There are also two structural phases of the this compound. One is tetragonal and the other one is orthorhombic, see Fig. 2. Sr substitution for La decreases the orthorhombicity and the crystal remains tetragonal at all temperatures at values of x(Sr) which correspond roughly to the region of maximum T_c. Other intervening phases shown in Fig. 1, spin glass at low temperatures and low Sr concentration, Fermi or non-Fermi liquid behavior depending on if one is in the far right side of the phase diagram or not, are discussed in literature [1].

The crystal structure of La_{2-} Sr CuO_4 is shown in Fig. 2. The occurrence of several structural phases is typical for perovskites and they generally happen as a result of the lattice strain between the rare-earth and the CuO_2 layers. The strain is often released by various bucklings of the transition metal - oxygen planes and this is also the case here. The HTT phase has flat CuO_2 planes and the transition to the LTO phase can be understood within a good approximation as a rigid rotation of the CuO_6 octahedra around an axis making 45° with respect to the orthorhombic axes. As a result, half of the O atoms will be situated above and the other half below the plane determined by the Cu atoms, see Fig. 2. The lattice constants of the LTO phase at low temperatures are $a = 5.354$ Å, $b = 5.401$ Å and $c = 13.153$ Å. So the orthorhombicity, defined by $2(a-b)/(a+b)$, is small, only of about 0.8%.

In the parent compound, La_2CuO_4 , one has La^{3+} and O^{2-} non-magnetic ions so copper will be in a Cu^{2+} oxidation state to insure neutrality. As a result, the last Cu $3d^9$ shell will

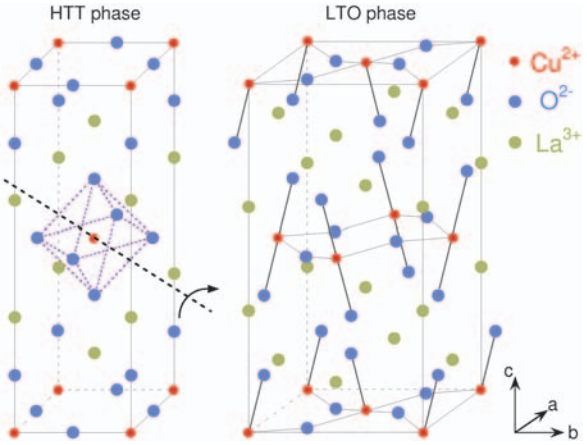

Fig. 2. The layered perovskite structure of La_{2-} Sr CuO_4. Left: the high temperature tetragonal (HTT) phase where the CuO_2 planes are flat. Right: the low temperature orthorhombic (LTO) phase, (*Bmab*) space group which is obtained from the HTT structure by rigid CuO_6 octahedra rotations as shown. In the *Bmab* setting the *b*-axis is parallel to the corrugation in the CuO_2 planes.

contain a hole carrying a spin $S = 1/2$ which is responsible for the magnetic properties. Sr^{2+} substitution for La leads to hole doping of the CuO_2 planes. It is believed that hole pairing and the acquirement of 3D coherence lead to the occurrence of superconductivity.

In this chapter we will also talk about certain properties of Nd doped La_{2-} Sr CuO_4 and we mention here some well established effects associated with Nd substitution for La. One is that Nd in $La_{2-\ -y}Nd_ySr$ CuO_4 suppresses superconducting correlations. For instance magnetic susceptibility data in $La_{2-\ -y}Nd_ySr$ CuO_4 with $x = 0.2$ show that SC vanishes for values of y greater than about 0.6 [5]. Another effect is that this suppression of SC is accompanied by the enhancement of other types of correlations, the appearance of the so called 'stripes' [6], which are proposed to be quasi-1D in plane charge and/or spin super-modulations. While the discussion above suggests that these two states act against each other, it is not clear at this moment if the stripes are helping or competing with SC. Another effect is related to changes in the crystal structure as a result of interlayer chemical modifications. Nd doping brings in another phase, the low temperature tetragonal (LTT) structure, which can be imagined as a rigid CuO_6 octahedra tilt around the axis whose vector is defined by $1/\sqrt{2}(\hat{a} + \hat{b})$ where a and b are the orthorhombic axes of the LTO phase.

In the following we will discuss low energy magnetic properties of La_{2-} Sr CuO_4 at light x(Sr) doping level. Although much is known about the physics of 2D $S = 1/2$ antiferromagnets, there are recent experiments which show surprising properties in macroscopically orthorhombic crystals in the presence of external magnetic fields. It is worth mentioning in this respect that recent neutron scattering in such crystals studies show

that even the crystal structure has not rigorously been determined yet [7] although the deviations from the *Bmab* symmetry may be very small. We will show later in this chapter, especially in connection to the phononic and electronic properties, that the effects of orthorhombicity are surprisingly large. In the following we discuss long wavelength spin-wave excitations as a function of temperature, doping and magnetic field. We show that the low energy spin dynamics allows us to observe a spin ordered state induced by magnetic fields, a state which persist up to quite high temperatures in crystals with long range AF order [8]. It will be shown that although the orthorhombicity is small, there are dramatic anisotropy effects in the in plane electronic and phononic excitations. Our data indicate that at commensurate hole doping $x = 1/8$ $La_{2-}{}_{-y}Nd_ySr$ CuO_4 and independent of Nd concentration there are local deviations in the crystal structure due to a spread in the CuO_6 tilt angle. We will discuss this behavior in connection with possible spin and charge modulations in the CuO_2 planes [9].

2 Magnetic and Electronic Properties of Macroscopically Orthorhombic $La_{2-x}Sr_xCuO_4$ at Light Doping ($0 \leq x \leq 0.03$)

2.1 Why Is a Study of Low Energy Magnetism Interesting?

SC as well as the normal properties of 2D Mott-Hubbard systems have already triggered a lot of effort to understanding the evolution of the ground state and of the AF correlations as a function of doping. However, in spite of the small orthorhombicity, the impact of the low energy magnetism on the carrier and lattice dynamics in *de winned* La_{2-} Sr CuO_4 crystals has recently been shown to be significant and surprising new effects were found.

What does detwinned mean in the first place? On cooling from the HTT to the LTO phase the crystal develops orthorhombic domains, called twins, on the nanometer to micron scale. The sign of the orthorhombic distortions changes across the twin boundaries, as shown in Fig. 3a. Accordingly, for a macroscopic probe (and a Raman setup which uses a focussed laser spot larger than about several μ diameter is an example) the sample looks effectively tetragonal. If uniaxial pressure of about 15-30 MPa is applied while slowly cooling the crystal through the HTT-LTO phase transition, a detwinned, i.e. macroscopically orthorhombic, crystal can be grown [11].

This leads to non-trivial effects if one looks in Fig. 3b-c. The magneti ation data shows two peaks at the Néel transition of around 300 K in La_2CuO_4 and the magnetic anisotropy is preserved in a wide range of temperatures above T_N. The susceptibility along the *a*-axis, $\chi_a(T)$, is featureless showing that this axis is magnetically inert, at least at small fields. The structure with two peaks is due to the various spin anisotropy terms present in La_{2-} Sr CuO_4 crystals, they will be discussed in more detail later in the section [11]. La_2CuO_4 is an insulator, but small carrier concentrations in the CuO_2 planes give rise to metallic behavior of the resistivity at high temperatures[12]. Moreover, the *dc* resistivity shows also si eable anisotropy if measured along the *a* and *b* orthorhombic axes. The relative anisotropy is almost 30% for x = 0.01 around the metal-insulator transition

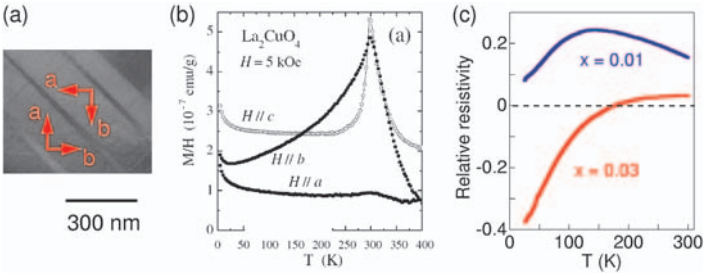

Fig. 3. (**a**) Typical orthorhombic domains in a twinned La_{2-} Sr CuO_4 sample (from Ref. [10]). (**b**) Magnetic susceptibility in a detwinned single crystal of La_2CuO_4 (data from Ref. [11]). (**c**) Relative resistivity defined by $2(\rho_a - \rho_b)/(\rho_a + \rho_b)$ in x = 0.01 and 0.03 detwinned La_{2-} Sr CuO_4 crystals (see also Ref. [13]).

and goes beyond this value in x = 0.03 at low temperatures. One can also notice at high temperatures a decrease of the resistivity anisotropy with doping from x = 0.01 to x = 0.03 and that there is a sign change in this anisotropy around 170 K for x = 0.03 [13]. The magnetoresistance can be very large (up to 80%) at low temperatures [14].

One can conclude form Fig. 3 that detwinned samples show non-negligible effects in transport and magneti ation data. The Zeeman energy in finite external magnetic fields becomes comparable with the spin-anisotropy induced gaps and this will influence the low temperature thermodynamics. As for the intrinsic ground state properties at small dopings, inelastic neutron scattering (INS) argues that there are changes in the low frequency magnetic scattering (45° rotation in the k space of low energy incommensurate magnetic peaks) when superconductivity occurs around $x = 0.05$ in La_{2-} Sr CuO_4 [15] and also that macroscopic phase separation takes place below $x = 0.02$ [16].

All the above constitute general arguments for a detailed high energy resolution study of long wavelength spin excitations as a function of doping and temperature. Even more interesting is a recent magnetic field experiment done at room temperature in $x = 0.01$ La_{2-} Sr CuO_4. The main result of the experiment is shown in Fig. 4 and it says that the b orthorhombic axis follows the direction of the applied field [17]. So magnetic fields of about 10-14 T are able to produce structural changes and detwin the La_{2-} Sr CuO_4 crystal. The switch of the crystallographic axes is reversible and can be monitored by using a regular optical microscope. It is worth noting that 300 K is roughly about 100 K above the 3D long range AF ordering temperature in 1% doped crystals. Two interesting points can be mentioned in this regard. One is that there is strong spin-lattice interaction in this material. The other one is related to the coupling of the spins to the external field. While magnetic field induced structural changes are easier to be understood in ferromagnetic crystals because the net magnetic moment can provide a substantial coupling to the external field, the fact that these effects take place in a AF system makes La_{2-} Sr CuO_4 a unique compound. The rotation of the orthorhombic axes can be also observed in *dc* resistivity or magnetic susceptibility measurements by monitoring the changes in the anisotropic properties shown in Fig. 3 as a function of the direction of the applied external magnetic field $\vec{H}$.

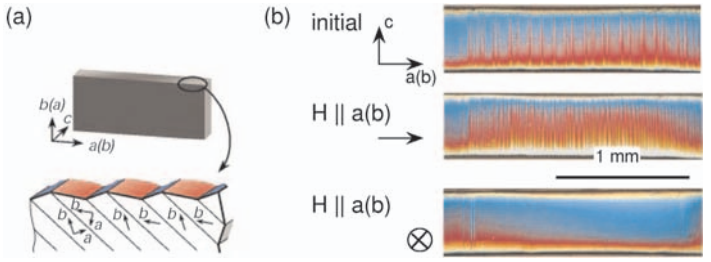

Fig. 4. (**a**) A 3D picture with a twinned x = 0.01 La_{2-} Sr CuO_4 crystal whose top surface is parallel to the *c*-axis. The blue and red areas correspond to different twins, (*ac*) or (*bc*) domains. (**b**) The upper figure is an image of the top crystal surface in ero external magnetic field taken with an optical microscope. Vertical stripes represent the (*ac*) and (*bc*) LTO domains as in panel (**a**). The middle and bottom images show the structural changes occurring with an application of an external field of about H = 14 T. One can see that the *b* orthorhombic axis follows the direction of $\vec{H}$.

These results highlight the importance of a magnetic field study of the low energy magnetism in low doped La_{2-} Sr CuO_4 . We believe that the field induced spin ordering we observe at temperatures up to 300 K in samples displaying long range AF order is related to the effects shown in Fig. 4.

2.2 Low Energy Magnetism in Detwinned La_{2-} Sr CuO_4 with ($0 \leq x \leq 0.03$)

(A) The 2D Heisenberg antiferromagnets and effects of inter-layer coupling. CuO_2 planes form 2D square lattices and the $S = 1/2$ Cu spins interact antiferromagnetically *via* the intermediate O atoms. The nearest neighbor super-exchange J takes place along the 180° Cu-O-Cu bonds and it has a value of approximately 140 meV [18]. The inter-layer correlations are weak for two reasons: on one hand the spacing between the layers is large and on the other hand the magnetic interaction along this direction is frustrated. So in the first approximation the spin dynamics (especially in the paramagnetic phase) will be dominated by the properties of a 2D isotropic Heisenberg antiferromagnet. The starting Hamiltonian to characteri e these systems is then:

$$\hat{H}_{2D} = \sum_{<i,j>} J_{ij} \vec{S}_i \cdot \vec{S}_j \qquad (1)$$

where $\vec{S}_i$, $\vec{S}_j$ are spins on the sites i and j and $J_{ij} = J \approx 140$ meV when $< i, j >$ corresponds to a pair of nearest neighbor (NN) spins.

The spin-spin correlation function $\xi(T)$ is one of the fundamental parameters characteri ing the paramagnetic state. This quantity is extracted from an equation relating the average staggered magneti ation to the inter-site distance, of the type: $< \vec{S}_i \cdot \vec{S}_j > \propto \exp(-r_{ij}/\xi)$. Here r_{ij} is the distance between the sites i and j. Continuum field theory predicts in the paramagnetic phase a spin-spin correlation length given

by: $\xi(T) \propto \frac{c}{2\pi\rho} \exp[\frac{2\pi\rho}{k_B T}]$ [19]. The parameters c and ρ_s are for the spin-wave velocity and spin stiffness respectively. This correlation length diverges as $T \to 0$ leading to true long range magnetic order only at ero temperature. This microscopic result is consistent with a theorem showing rigorously that at any finite temperature a 1D or 2D isotropic Heisenberg model with finite-range interactions can be neither ferromagnetic nor antiferromagnetic [20]. However, in agreement with theoretical predictions, neutron scattering measurements show that the number of correlated spins within the 2D CuO_2 planes is substantial even at high temperatures. For example, at 500 K which is about 200 K above the 3D ordering temperature in La_2CuO_4 , ξ is of the order of 50 Å [3], approaching values of 200 - 300 lattice constants around T_N.

A small interlayer coupling $J_\perp$ pushes the Néel ordering temperature to finite values but does not affect significantly the 2D magnetic correlations. It is believed that the magnitude of the inter-layer exchange is very small, $J_\perp \approx 10^{-5} J < 0.02$ K [1, 19, 21]. In spite of such a small perpendicular exchange, the AF ordering temperatures are quite high and this is due to the large in-plane correlation lengths. Agreement in terms of the order of magnitude for T_N using the above value for $J_\perp$ can be obtained simply by comparing the thermal and magnetic energies in:

$$k_B T_N \approx J_\perp (m_s S)^2 \left[\frac{\xi(T_N)}{a}\right]^2 \tag{2}$$

where m_s is the sublattice magneti ation in units of $g\mu_B$ and $[\xi(T)/a]^2$ is proportional to the number of 'ordered' spins in each CuO_2 plane. It should be noted that in the HTT phase of La_{2-} Sr CuO_4 every Cu atom has eight nearest neighbors in the adjacent planes (four above and four below its own CuO_2 plane). Due to symmetry, the super-exchange is almost exactly cancelled and the effective $J_\perp$ is even smaller than $10^{-5}J$. It is the distortion associated with the LTO phase, see Fig. 2 which partially lifts this degeneracy giving rise to a reasonably si ed, although very small, inter-layer exchange.

Eq. (2) leaves an open question: how to reconcile similar 3D ordering temperatures (T_N's typically in the range between 200 and 300 K) for various layered Cu-O based materials (examples are La_{2-} Sr CuO_4 , $Sr_2CuO_2Cl_2$, $YBa_2Cu_3O_{6+\delta}$, Nd_2CuO_4 or Pr_2CuO_4, see Refs. [1, 22]) with rather different exchange paths and accordingly values of $J_\perp$ that can be quite far apart. For instance in $Sr_2CuO_2Cl_2$ the CuO_2 planes are exactly flat so it is expected that the cancellation of terms because of the inter-layer frustration would decrease $J_\perp$ by another few orders of magnitude, requiring anomalously high $\xi(T_N)$ in order to satisfy Eq. (2). It has been suggested that the 3D ordering temperature T_N follows immediately after a 2D Kosterlit -Thouless (KT) phase transition at T_{KT} due to the in-plane spin anisotropy of the XY type which characteri es all the above mentioned AF materials. It was found that T_{KT} is appreciable, $\approx 0.25 J/k_B$, and quite insensitive to the magnitude of the in-plane anisotropy [22]. This would explain the magnitude as well as the similarity between the measured T_N's in various Cu-O based 2D AF's.

What does the excitation spectrum of a 2D AF ordered square lattice look like? Within the spin-wave approximation the excitations are coherent transverse oscillations of the ordered moments. Taking into account only the nearest neighbor exchange J the wavevector dependent spin-wave energies are given by

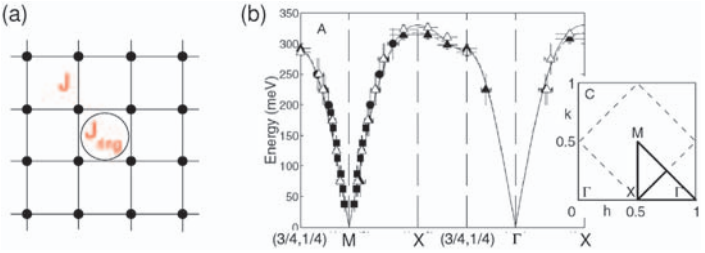

Fig. 5. (**a**) The 2D square lattice. The nearest neighbor superexchange is denoted by J and the circle represents a higher order term considered important for the cuprates, the ring exchange J_{ring}. (**b**) The main panel shows the dispersion of the magnetic excitations in La_2CuO_4 at T = 10 K along different directions in the 2D Brillouin one (shown in the lower left panel). The inelastic neutron scattering data is from Ref. [18]. Squares, circles and triangles correspond to incoming neutron energies of 250, 600 and 650 meV respectively. The solid line is a fit to the data as described in the text.

$$\omega(k) = zSJ\sqrt{1-\gamma_k^2} \quad \text{with} \quad \gamma_k = \frac{\cos(k\ ) + \cos(k_y)}{2} \tag{3}$$

where $S = 1/2$ is the total spin and $z = 4$ is the number of nearest neighbors for the simple square lattice [23]. Note that in the 2D isotropic Heisenberg AF lattice there will be two degenerate acoustic spin-wave branches. In Fig. 5 we show relatively recent INS results for the spin-wave dispersion up to high energies.

While the dispersion predicted by the nearest neighbor isotropic Hamiltonian reproduces qualitatively the experimental results, there are discrepancies at high energies. One can note that along the AF one boundary we have $k\ + k_y = \pi$ and this implies that the spin-wave energy along this line is a constant given by $2J$. The experimental data in Fig. 5 shows that there is substantial dispersion for instance along the $(\pi, 0)$ to $(3\pi/2, \pi/2)$ line. The authors resolve this discrepancy by including higher order spin interactions. In particular, the most prominent term is due to J_{ring} which corresponds to a spin exchange around a square plaquette as shown in Fig. 5a. Quantitatively, from the fit to the experimental data which includes quantum corrections [24] (the solid line in Fig. 5b), this term turns out to be as high as 41% of the nearest neighbor J at low temperatures, $J_{ring} \approx 61$ meV, and it is about twenty times larger than the second and third nearest neighbor exchanges [18]! In support for such a claim we note that a large value of J_{ring} was needed to explain the dispersion of the elementary triplet excitations in two-leg ladder materials. The same J_{ring} seems also to improve the results concerning the large absorption frequency range in which the phonon induced two-magnon excitation is thought to be observed in 2D insulating cuprates [25].

(B) In-plane magnetic anisotropies. There are two dominant in-plane magnetic anisotropies characteri ing each CuO_2 plane. In general these terms, arising as a result of spin-orbit coupling, connect the spin space to the real space and can be sometimes described in terms of effective magnetic interactions. One of these interactions is the

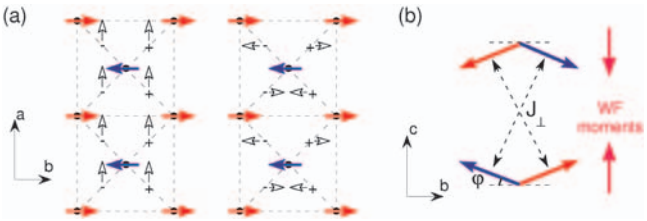

Fig. 6. (**a**) Top views of the CuO_2 planes corresponding to the two possible configurations of the DM interactions (black arrows). Cu atoms are represented by black dots; their spins (lying mainly in the (ab) plane because of the XY spin anisotropy and forming a two-sublattice AF structure) are shown by red and blue arrows. By '+' and '–' signs we denote the intermediate O atoms which are below and above the plane of the paper, see Fig. 2. (**b**) Cartoon with the 3D four-sublattice configuration of spins seen in the (bc) plane and the weak ferromagnetic moments (proportional to the canting angle ϕ) of each CuO_2 plane due to the D yaloshinskii-Moriya interaction $\vec{d} \parallel \hat{a}$ shown in the left of panel (**a**).

XY exchange anisotropy term mentioned above in connection to the 3D Néel ordering and its origin is in the layered structure of the cuprates, i.e. it has nothing to do with the buckling of the CuO_2 plane in the LTO phase. Due to to the XY term the NN spin-exchange interaction in Eq. (1) changes to $(J+\alpha)(S_i\,S_j + S_i^y S_j^y) + JS_i^z S_j^z$. Because $\alpha > 0$ the classical configuration giving the minimum energy is one with all the spins lying in the (ab) plane. The other important anisotropy term is due to the antisymmetric D yaloshinskii-Moriya (DM) interaction and it has the form: $\vec{d}_{ij} \cdot (\vec{S}_i \times \vec{S}_j)$ where $\vec{d}_{ij}$ is the DM vector [26, 27]. The two-spin classical ground state configuration for this interaction considered alone is one with $\vec{S}_i \perp \vec{S}_j \perp \vec{d}_{ij}$.

The balance of these terms determines the equilibrium position of the spins. These anisotropy terms are expected to be much smaller than J and can be quantitatively determined from the energy of the spin-waves in the long wavelength limit as will be discussed in the next section. A few words are in order about the DM term. Due to the existence in the LTO phase of a C_2 (rotation by 180°) symmetry axis which passes through in-plane O atoms and is perpendicular to the (ab) surface, the DM vector between two adjacent Cu atoms has to satisfy $\vec{d} \perp \hat{c}$ [28]. The symmetry elements of the $Bmab$ space group associated to the LTO phase allow the DM vectors $\vec{d}_{ij}$ to form the configurations shown in Fig. 6a. Once a convention is made that the order of spins in the vector product of the $\vec{d}_{ij} \cdot (\vec{S}_i \times \vec{S}_j)$ term is always from a given sublattice to the other, it can be noted that there are two possible arrangements for the DM vectors: one involving $\vec{d} \parallel \hat{a}$ and the other one in which the DM vectors are parallel to the b-axis but have alternating signs.

The effective two-dimensional spin Hamiltonian and the associated free energy density at T = 0 K which takes the XY, DM terms as well as an external field into account can be written as:

$$\hat{H} = \sum_{<i,j>} [(J+\alpha)(S_i\,S_j + S_i^y S_j^y) + JS_i^z S_j^z + \vec{d}_{ij} \cdot (\mathbf{S}_i \times \mathbf{S}_j)] - \vec{H} \sum_i \vec{S}_i \qquad (4)$$

$$f = z(J+\alpha)(M_1 M_2 + M_1^y M_2^y) + zJM_1^z M_2^z + z\vec{d}\cdot(\vec{M}_1 \times \vec{M}_2) - \vec{H}(\vec{M}_1 + \vec{M}_2) \qquad (5)$$

In Eq. (4) the sum runs over the nearest neighbors. In Eq. (5) z is the number of nearest neighbors and $M_{1,2}$ are the sublattice magneti ations. The 'thermodynamic' D yaloshinskii vector $\vec{d}$ in Eq. (5) is given in terms of the 'microscopic' Moriya terms $\vec{d}_{ij}$ in Eq. (4) by $\vec{d} = (1/z)\sum_{NN}\vec{d}_{ij}$ and from Fig. 6 one can infer that $\vec{d} \parallel \hat{a}$ [29]. The relative strength of the DM terms corresponding to the two configurations in Fig. 6a is determined by microscopic parameters. It is interesting to note here a point made by the authors of Ref. [29], i.e. that the identification of $\vec{d}$ to the microscopic $\vec{d}_{ij}$ is a non-trivial problem in the sense that a difference between them is a necessary condition for the existence of an observable weak ferromagnetism (WF) with a specific value of the net WF moment. In other words, although $\vec{d}$ is parallel to the a-axis, it is required that the DM vectors in both configurations shown in Fig. 6a are finite. If on one hand only vectors $\vec{d}_{ij} \parallel \hat{b}$ are considered (frustrating interaction), then $\vec{d} \equiv 0$ and the spins order antiferromagnetically without any WF moment. On the other hand if one takes into account only vectors $\vec{d}_{ij} \parallel \hat{a}$ (non-frustrating interaction) the classical ground state cannot be characteri ed as ferromagnetic because it consists of a manifold of degenerate configurations having a net WF moment ranging continuously from ero to some finite value [29].

The equilibrium position of the spins in ero external field is shown in Fig. 6b. For a 2D plane this can be obtained from the minimi ation of the free energy in Eq. (5) with respect to the angles between the magneti ations and crystallographic axes with the constraint $m = |\vec{M}_1| = |\vec{M}_2|$. The canting angle is given by $\tan(2\varphi) = 2d/(2J+\alpha)$ and since $d \ll J$ (in reality $\varphi < 0.5^\circ$) the net WF moment of each plane is approximately $M_F \approx 2m\varphi = 2dm/(2J+\alpha)$. Here m is the sublattice magneti ation. The interaction $J_\perp$ does not significantly change this angle.

Long wavelength spin-wave excitations. On general grounds, from Eq. (5) one can say the following about the behavior the spin-wave modes in the long wavelength limit: (1) if $\alpha = d = 0$ there will be two acoustic modes; (2) if $\alpha \neq 0$ and $d = 0$ or $\alpha = 0$ and $d \neq 0$ there will be one acoustic and one gapped spin-wave branch; (3) if $\alpha \neq 0$ and $d \neq 0$ both spin-wave branches will be gapped. This is because unless we are in case (3), there is a global continuous symmetry which is broken at the AF transition due to the ordering of the magnetic moments (the gapless branches are typical Goldstone modes).

The situation described above is shown schematically in Fig. 7. One can intuitively understand how the spin gaps look like at a classical level by solving the equations of motion:

$$\beta\frac{\partial\vec{M}_j}{\partial t} = \vec{M}_j \times \nabla_{\vec{M}_j} f \quad j = 1,2 \qquad (6)$$

where β is a constant related to the Bohr magneton and f is the free energy from Eq. (5). The equilibrium condition $\nabla_{\vec{M}_j} f = 0$ gives the ground state shown in Fig. 6b. Lineari ing the equations of motion from (6) around equilibrium and choosing oscillatory solutions for the obtained set of homogeneous equations one can get (to first order in anisotropy terms) the following energies corresponding to the XY and DM gap respectively:

$$\omega_{XY} = z\ m\ \sqrt{2\alpha J} \quad \text{and} \quad \omega_{DM} = z\ m\ d \qquad (7)$$

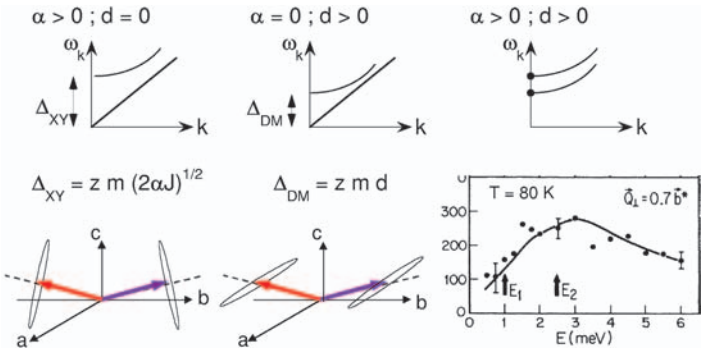

Fig. 7. The upper row shows schematically the dispersions of the spin-wave branches in the limit $k \to 0$ if: only the XY (left), only the DM (middle) and both of these anisotropy terms are present (right). The lower row shows the pattern of oscillating magneti ations corresponding to the XY (left) and DM (middle) spin gaps at $k = 0$ as well as the INS experimental data from Ref. [30] showing these two gaps in La_2CuO_4 (E_1 and E_2 correspond to the DM and XY gaps respectively).

With $z = 4$, $m = 1/2$ and taking $J = 145$ meV [18] one can calculate from Eq. (7) the anisotropy parameters α and d if ω_{XY} and ω_{DM} are known. If the quantum corrections for the spin-wave velocity are taken into account [24] the expressions for the gap energies become $\omega_{XY} = 2.34\sqrt{2\alpha J}$ and $\omega_{DM} = 2.34dJ$ [1]. The ellipses shown in Fig. 7 are very elongated, the ratio of their small and big axes being essentially given by ratios of the anisotropy parameters with respect to the large super-exchange J. This is why in the literature the XY mode (which corresponds to the precession of the net WF moment around the c-axis) is also called the out-of-plane gap while the DM mode (which corresponds to the c-axis oscillations of the WF moment) is called the in-plane gap.

In Fig. 7 we also show the low energy INS measurements in La_2CuO_4 of Peters *et al.* [30]. The dots are the experimental data and the solid line is a fit using the spin-wave approximation convoluted with the experimental resolution. The energies of these two gaps are shown by arrows. The most direct way to check the magnetic nature of these modes is to apply an external magnetic field which has not been done so far. It is also desirable that such a study be performed with a higher energy resolution probe.

2.3 Magnetic Field, Temperature, and Doping Dependence of the Dzyaloshinskii-Moriya Gap in La_{2-} Sr CuO_4 ($0 \leq x \leq 0.03$)

(A) Field dependent Dzyaloshinskii-Moriya gap in La_2CuO_4. Fig. 8 shows 10 K Raman spectra taken from 93% detwinned La_2CuO_4 crystal using circular (RL) polari ation. A sharp resonance is seen in ero field at 17 cm^{-1}. This excitation disperses continuously upwards (downwards) for $\vec{H} \parallel \hat{a}$ ($\vec{H} \parallel \hat{b}$) axes. For $\vec{H} \parallel \hat{c}$, Fig. 8c, the mode disperses downwards until the magnetic field reaches the value $H_{WF} \approx 6$ T. At this point

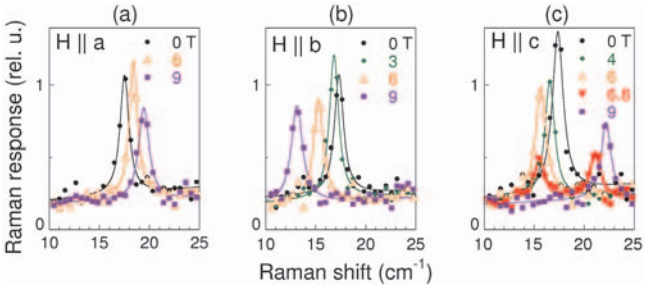

Fig. 8. T = 10 K magnetic field dependence of the D yaloshinskii-Moriya gap in La_2CuO_4. The Raman spectra are taken in (RL) polari ation. The dots are experimental data and the solid lines are Lorent ian fits.

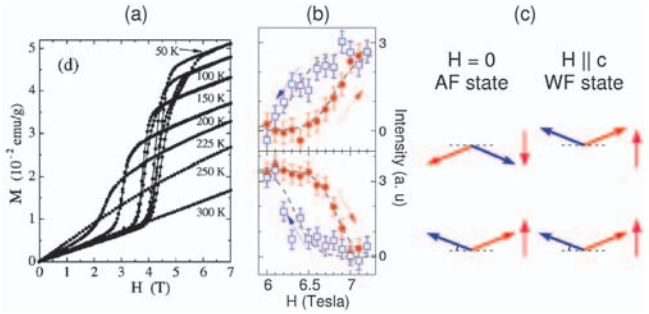

Fig. 9. (**a**) Magneti ation as function of magnetic field parallel to the c-axis for several temperatures. Data are from Ref. [14] and they are taken from a x = 0.01 La_{2-} Sr CuO_4 crystal. (**b**) Hysteretic loops of the 21 cm^{-1} (upper panel) and 15 cm^{-1} (lower panel) modes from Fig. 8c at the WF transition. (**c**) The spin arrangements in the 3D AF and WF states.

a transition to the WF state takes place. Initially observed in magnetic field dependent magneti ation data [21] this first order transition could be also studied by neutron scattering measurements [31] because due to the change in magnetic symmetry the scattering form factors allowed new Bragg peaks. In the 6 - 7 T range the resonance remains around 15 cm^{-1} but decreases in intensity and we observe a concomitant appearance of another feature around 21 cm^{-1}. The 6.8 T spectrum in Fig. 8c shows clearly the coexistence of AF and WF states. Recent magneti ation data [14] and with a cartoon comparing the spin configuration in ero field and in the WF state are shown in Fig. 9. The hysteretic loops in the magnetic field dependent magneti ation correspond to the hysteretic loops of the 15 and 21 cm^{-1} modes shown in Fig. 8b. This is in turn very similar to the behavior of the (100) and (201) magnetic Bragg peaks [31], reflecting the dynamics of magnetic domains in the presence of small crystalline imperfections.

The energies of the 17 cm^{-1} resonance as a function of magnetic field are plotted in Fig. 10a. The expressions for the fitting functions and the values for the fitting parameters used for the data in this figure are summari ed in the following. If $\vec{H} \parallel \hat{a}$ and $\vec{H} \parallel \hat{b} \quad \Rightarrow \quad \Delta_H = \sqrt{\Delta_{DM}^2 + \gamma H^2}$ with $\Delta_{DM} = 17.35 \pm 0.25$ cm^{-1} and $\gamma_{H\|a} = 0.96$ and $\gamma_{H\|b} = -1.65$ (cm T)$^{-2}$. If $\vec{H} \parallel \hat{c}$ and $H \geq H_{WF} \quad \Rightarrow \quad \Delta_H = \sqrt{\Delta_{DM}^2 + \beta H}$ with $\beta = 22.6$ $cm^{-2}T^{-1}$. The quadratic dependence in the first two cases can be understood because the spin re-arrangement in finite magnetic fields is independent of the directions parallel to the a or b axes along which the field is applied. This is not the case if $\vec{H} \parallel \hat{c}$ and the system is in the WF state, see Fig. 9c. Note that if $\vec{H} \parallel \hat{c}$ but $H \leq H_{WF}$ one observes again a quadratic dispersion with field. Moreover, the similar field dispersion for $\vec{H} \parallel \hat{b}$ versus $\vec{H} \parallel \hat{c}$ ($H < H_{WF}$) seen in Fig. 10a is intriguing because this degeneracy does not follow from the model of Eq. (5) but it rather suggests rotational symmetry with respect to the a-axis.

Confirmation that the 17 cm^{-1} (in ero field) resonance observed in Fig. 8 is the DM spin-wave gap comes from a 2D semiclassical spin-wave calculation. Assuming a fully ordered moment on Cu sites ($m = 1/2$), a ero field DM gap $\Delta_{DM} = 17$ cm^{-1} and minimi ing Eq. (5), one can obtain the dispersions of the $k = 0$ DM gap for the three directions of the applied field. The results are shown in Fig. 10b and the reasonable agreement with the experimental data allows one to assign this excitation to the DM interaction induced spin gap. Two comments on Fig. 10b. The first is that the 2D calculation can account only for the situation where the two sublattices in adjacent CuO_2 planes 'respond similarly' to the external field. This is the case for $\vec{H} \parallel \hat{a}$, $\vec{H} \parallel \hat{b}$ and $\vec{H} \parallel \hat{c}$ with $H \geq H_{WF}$ and one can see that in all these cases the theoretical predictions agree with the experiment. If $\vec{H} \parallel \hat{c}$ and $H \leq H_{WF}$ the 2D approximation clearly breaks down and Eq. (5) cannot be used in this region. The second comment is just a remark that it is surprising that a semi-classical spin-wave calculation as shown in Fig. 10 is able to reproduce with relatively good accuracy the experimental data in a low spin system. This is in view of the expectation that such an approximation is valid to order $1/S$ [32] which is not a 'small' number for $S = 1/2$. One may conclude from here that in order to explain the low energy spin dynamics in undoped 2D cuprates one does not need to go beyond a semiclassical approximation.

We believe that the magnetic field dependent data shown in Figs. 8 and 10 may also be relevant for a quantitative estimation of higher order spin interactions which are thought to be important in cuprates. One example is the ring exchange, see Fig.5, and it would be interesting to check the influence of J_{ring} on the DM gap energy and possible renormali ation effects on its magnetic field dependence. An example of a system where substantial effects of J_{ring} on the spin-gap were pointed out is that of two-leg spin ladders. Using the expression $\Delta_{DM} = 2.34d$ we can extract for La_2CuO_4 the value $d = 0.92 \pm 0.013$ meV.

(B) Doping and temperature effects on the Dzyaloshinskii-Moriya gap. The results of doping and temperature on the DM gap are summari ed in Fig. 11. The Néel temperatures for the x = 0 and 0.01 crystals studied here are 310 and 215 K respectively. The 1 and 3% Sr doped crystals were detwinned in proportion of 98 and 97%. In Fig. 11a

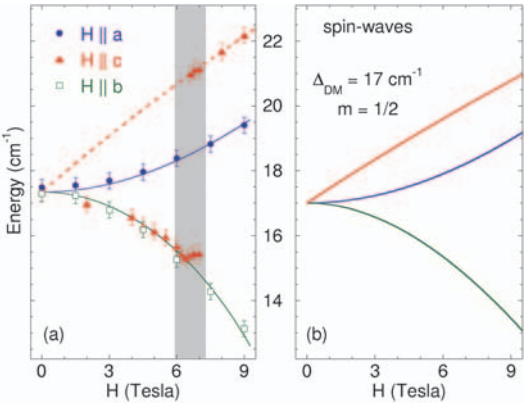

Fig. 10. (**a**) Magnetic field dependence of the DM gap in La_2CuO_4 for $\vec{H} \parallel \hat{a}$ (filled blue circles), $\vec{H} \parallel \hat{b}$ (empty green squares) and $\vec{H} \parallel \hat{c}$ (filled red triangles). The $\vec{H} \parallel \hat{c}$ data show the transition to the WF state depicted in Fig. 9c. The shaded area corresponds to the region of coexistence of the AF and WF states. The continuos lines are fits as described in the text. (**b**) Results of a 2D spin-wave calculation for the DM gap dispersion using Eqs. (5) and (6) and assuming a fully ordered moment on Cu sites.

we show the gap as a function of doping at 10 K. The 17 cm^{-1} resonance in the undoped crystal seen in the B_{1g} orthorhombic channel becomes weaker in intensity, remains as sharp as in La_2CuO_4 and softens to 12.5 cm^{-1} for x = 0.01, an energy 30% smaller compared to what we see for x = 0. We note also the absence of the DM mode in x = 0.02 and 0.03 La_{2-} Sr CuO_4 crystals.

The doping dependence shows that the the DM mode is present at low temperatures only in the long range AF ordered region of the phase diagram (Fig. 1). This behavior is somehow surprising because one would expect to see for 2 or 3% doping at least a broadened feature in view of the large 2D magnetic correlations just outside the AF ordered phase. Such fluctuations are not observed in our data and this suggests that the presence of the long wavelength DM excitation is related to the existence of a true 3D order. A point discussed in the preceding section was related to the fact that it is the orthorhombicity which generates the DM interaction. The decrease of almost 30% in its energy from x = 0 to 0.01 is much more pronounced compared with the decrease in orthorhombicity and this relates this renormali ation effects to a strong sensitivity on hole doping and points to a considerable renormali ation of the ordered Cu moment at only 1% hole doping. Our data suggest that the antisymmetric interaction is strongly competing with other sources of disorder in the magnetic system and we suggest that this is most likely due to the frustration effects and the associated spin distortions induced by hole doping [33]. A last point we make regarding Fig. 11a is in regard to the macroscopic phase separation scenario proposed by the authors of Ref. [16] to take place for $x \leq 0.02$. If this were true than one would observe in the $x = 0.01$ crystal two features: one

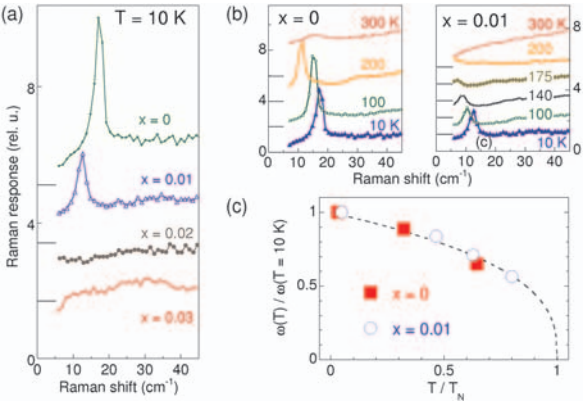

Fig. 11. Doping and temperature dependence of the DM gap in La_{2-} Sr CuO_4 in (ab) polari ation for ero applied field. (**a**) T = 10 K data for x = 0, 0.01, 0.02 and 0.03. (**b**) Temperature dependent spectra for x = 0 and 0.01. (**c**) The energy of the DM gap with respect to the value at 10 K, $\omega(T)/\omega(10K)$, as a function of T/T_N. The dashed line is a guide for the eye.

corresponding to the undoped region which would be found at 17 cm^{-1} and another one corresponding to the region with carrier concentration $c_h \approx 0.02$. The 30% decrease in energy observed in the $x = 0.01$ crystal with respect to the undoped case seems to rule out the scenario proposed in Ref. [16].

As a function of temperature what we see in Fig. 11b-c is that the DM gap softens with raising the temperature and disappears below 5 cm^{-1} as we approach the Néel temperature from below in both $x = 0$ and 0.01 La_{2-} Sr CuO_4 samples. The temperature dependence of the peak energies in the two crystals is shown in Fig. 11c to be similar and points towards a conventional soft mode behavior of this excitation, i.e. both its energy and its intensity approach ero in the limit $T \to T_N$, $T < T_N$. These spectra support the statement made in the previous paragraph that the DM induced gap exists in the narrow (T,x) region of the phase diagram from Fig. 1 where the AF order is long ranged. It is possible that the reason it disappears at higher dopings is because the low energy magnetic fluctuations move away from the Brillouin one center [34]. Interestingly, a broad peak at 300 K is seen around 15 cm^{-1} for $x = 0$. This peak becomes a kink at 200 K and, as opposed to the conventional behavior of the DM gap, it disappears with further cooling. It is the purpose of the following section to investigate this excitation.

2.4 Magnetic Field Induced Spin Ordering in $x = 0$ and 0.01 La_{2-} Sr CuO_4

Magnetic field dependent (RR) polari ed Raman spectra in La_2CuO_4 at several temperatures in $\vec{H} \parallel \hat{b}$ configuration are shown in Fig. 12a. At 10 K and in ero external field the Raman spectrum is featureless. For $H = 6$ T we see a sharp field induced mode (FIM) situated at 37.5 cm^{-1} which moves to slightly higher frequency (38.3 cm^{-1}) for

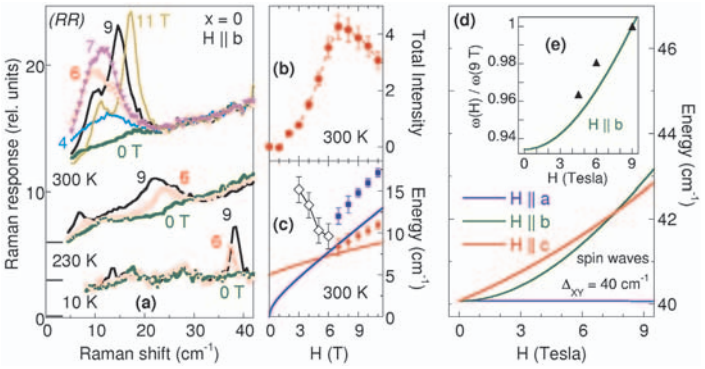

Fig. 12. (**a**) Magnetic field dependence of (RR) polari ed spectra in La_2CuO_4 at T = 10, 230 and 300 K. Data are vertically offset. (**b**) Integrated intensities obtained by subtracting the room temperature 0 T spectrum from the finite field data at the same temperature. (**c**) The energies of the observed magnetic modes at T = 300 K. Empty diamonds show the energy of the broad peak seen for magnetic fields $H \leq 6$ T. The solid lines in this panel are calculated using eqs. (5) and (6) assuming $\alpha = 0$, see the text for a discussion. (**d**) This panel shows the results of a T = 0 K spin-wave calculation similar as the one shown in Fig. 10 but in this case for an XY gap assumed to be at $\Delta_{XY} = 40$ cm^{-1}. (**e**) Using the calculation from (**d**), the solid line in the inset shows the magnetic field dependence of the ratio $\omega(H)/\omega(9T)$ for fields $\vec{H} \parallel \hat{b}$ axis. The dots represent the same quantity extracted from the T = 10 K experimental data in panel (**a**).

$H = 9$ T. The triangles in Fig. 12e show the relative energy of this excitation with respect to the value at 9 T. The extra data point corresponding to the 4.5 T Raman spectrum (not shown for clarity in panel (a)) marks the magnetic field at which the FIM starts to be seen. We remark only a small hardening (of about 4%) with magnetic field from 4.5 to 9 T. At 230 K the FIMs in 6 and 9 T fields are broader than at 10 K. However, with increasing field the FIM softens gaining spectral weight from the lower energy side. At 300 K, as long as the field is less than about 6 T, we observe qualitatively similar behavior as at 230 K. For magnetic fields beyond that value we see the emergence of two independent peaks and both of them harden with further increasing the field. Fig. 12b we plot the total integrated intensity of the magnetic modes (for T = 300 K) at a given field, the data showing a maximum around $H = 7$ T, and in panel (c) the symbols denote the position of the FIMs as the magnetic field is swept from 0 to 11 T.

If $\vec{H} \parallel \hat{a}$ or $\vec{H} \parallel \hat{c}$ we do not observe any changes in the (RR) polari ed Raman spectra. Note that the spectra showing the DM gap in Fig. 8 were taken in (RL) polari ation. Circular polari ations probe 'good' symmetries if the crystal has a symmetry higher than tetragonal. Because the orthorhombicity in our samples is small it allows to separate the excitations appearing in these two geometries, but because it is finite we observe small 'leakage' effects. Their magnitude can be estimated for instance by looking at the small

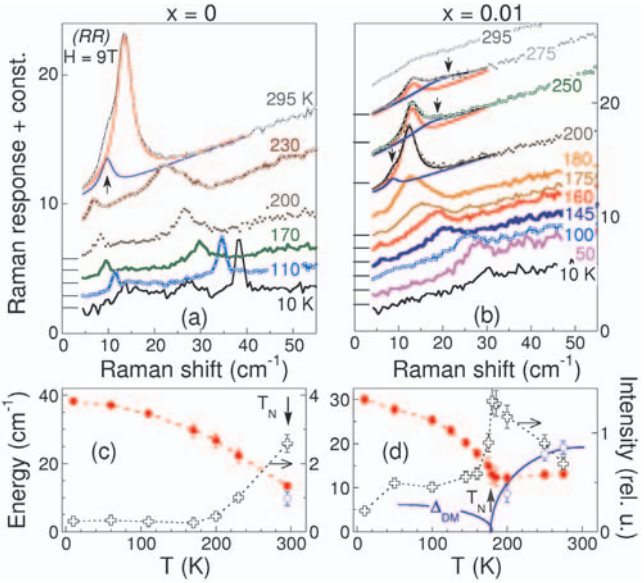

Fig. 13. Temperature dependence of the field induced mode (FIM) in La_{2-} Sr CuO_4 for $x = 0$ (left) and 0.01 (right). (**a-b**) Data (vertically offset) in (RR) polari ation for $\vec{H} \parallel \hat{b}$ at 9 T. The continuous lines for T = 295 K in (**a**), T = 200, 250 and 275 K in (**b**) are two-Lorent ian fits to the data. (**c-d**) Variation with temperature of the FIM energies (filled red circles, left scales) and intensities (crosses, right scales). The empty blue circles correspond to the arrows in (**a-b**). The blue lines in (**d**) are guides for the eye. We also show by arrows the Néel temperatures for $\vec{H} \parallel \hat{b}$ at 9 T in the two samples.

feature corresponding to the DM gap which is found around 6-7 cm^{-1} in the H = 9 T and T = 230 K spectrum from Fig. 12a.

In La_2CuO_4 the FIMs dynamics marks two events. The first seems to be a phase transition at 300 K and fields around 6 T. This is indeed the case because we know that the Néel temperature in La_2CuO_4 is around 310 K and that the magnetic susceptibility χ_b shows T_N decreasing at a rate of about 1 K/T if the magnetic field is applied parallel to the b-axis, as is the case in Fig. 12. Moreover, the narrow widths of the magnetic excitations above 6 T (2 cm^{-1} $\approx$ 0.25 meV) at temperatures more than two orders of magnitude higher (300 K $\approx$ 25 meV) argue strongly for the collective nature of these excitations which correspond to another magnetically ordered state with a well defined gap in the excitation spectrum. Such a transition is expected from the low temperature data shown in Figs. 8 and 10, more precisely from the behavior of the DM gap for $\vec{H} \parallel \hat{b}$. In this configuration we can fit the behavior of the DM gap by $\sqrt{\Delta_{DM}^2 + \gamma_b H^2}$ with $\gamma_b < 0$. Extrapolating to higher fields would lead to a collapse of this gap marking a field induced transition. The second event, a crossover taking place between 230 and 10 K, is reflected

in the opposite dispersion with field and different peak widths at these two temperatures.

As for the doping dependence, except for a much weaker intensity (see Fig. 13), we observed the same qualitative behavior in x = 0.01 La_{2-} Sr CuO_4. The FIM is not seen (in fields up to 9 T) at any temperature for $x \geq 0.02$. Accordingly, it seems that, like the DM gap, this feature is a characteristic of the phase diagram where long range AF order exists. As for the DM gap, the reason for its absence at higher dopings could be because the low energy magnetic excitations move away from $k = 0$ concomitant to the development of incommensurate magnetic excitations. In the following we try to identify the nature of the FIM and field induced transition by looking at the effects of the temperature on the Raman data in magnetic fields.

Fig. 13 shows temperature dependent (RR) polari ed spectra in a 9 T field $\vec{H} \parallel \hat{b}$ for $x = 0$ and 0.01. The data in panel (a) show that the crossover mentioned above (regarding the change in the FIM width and energy dispersion with field) takes place around 150 K. This is the temperature below which the FIM width narrows. Fig. 13c shows that the intensity of this excitation increases as we approach T_N from below and that around 300 K we observe the splitting due to the occurrence of the field induced ordering. At this temperature the data for $x = 0$ can be clearly fit with two peaks, see panel (a), and these two peaks correspond to those observed in Fig. 12a for T = 300 K and $H \geq 7$ T.

The temperature dependence of the FIM across the Néel boundary can be studied in the x = 0.01 crystal which has a lower T_N, see the panels (b) and (d) from Fig. 13. We mention here that for the $x = 0.01$ La_{2-} Sr CuO_4 crystal T_N was measured (for fields lower than 7 T) to decrease on the average by almost 4 K/T for fields $\vec{H} \parallel \hat{b}$ axis. Given a $T_N(0T) \approx 215$ K, in a 9 T field one expects that $T_N(9\ T) \approx 180$ K. Indeed, at 9 T and below 180 K the behavior for x = 0.01 is very similar to that in the undoped crystal showing a softening of the FIM as we warm to T_N but the situation changes with further warming. The 200 K data show that the FIM has, similarly to the 295 K data for x = 0, a low energy shoulder which is marked by an arrow. The data at 250 and 275 K can also be fitted by two Lorent ians. Along with the 200 K spectrum, these data seem to suggest the following picture: above 180 K we observe two features, one whose energy does not show significant magnetic field dependence and another one which softens from 20 to

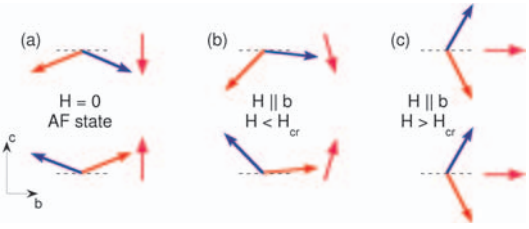

Fig. 14. Cartoon showing the proposed changes in the spin structure in x = 0 and 0.01 with the application of magnetic fields $\vec{H} \parallel \hat{b}$ axis, starting from the AF state, panel (**a**). For small fields there is a slight rotation of the WF moments, panel (**b**), which will lie in the (ab) planes at high fields, panel (**c**).

about 8 cm^{-1} with decreasing the temperature from 275 to 200 K. This latter excitation is marked by arrows in Fig. 13c and its energy is plotted in panel (d) by empty circles. The filled red circles in the same panel show the energy of the other mode (whose frequency is almost magnetic field independent above 180 K). The solid lines offer an explanation for the softening of the peak marked with arrows in panel (b): this is a magnetic soft mode corresponding to the field induce spin order taking place at $T \approx 180$ K in x = 0.01 La_{2-} Sr CuO_4 for $\vec{H} \parallel \hat{b}$ and $H = 9$ T. Its energy approaches ero on cooling towards T_N and we propose that it becomes the DM gap in the Néel phase. Fig. 13d also shows that the plot of the integrated intensities of the FIMs as a function of temperature is peaked at T_N. This points toward an unusual behavior in the sense that in a conventional picture the intensities of long wavelength gap modes scale with the AF order parameter, i.e. both of them vanish as T_N is approached from below [35].

What is the nature of the FIM within the AF phase? A possible explanation is its identification to the XY gap. Support for this assignment is the presence of this mode only in x = 0 and 0.01 La_{2-} Sr CuO_4 as well as the comparison to INS data [3, 35] which estimates $\Delta_{XY} \approx 40$ cm^{-1} at 10 K in La_2CuO_4. The very small experimentally found hardening of the FIM with increasing field from 4.5 to 9 T at T = 10 K shown in Fig. 12e is consistent within 20% with the predictions of the spin-wave theory, which was found to describe fairly well the DM gap. This difference may be also accounted for if one invokes possible gap renormali ation effects induced by higher order spin interactions [18].

Regarding the nature of the magnetic field induced order we propose a state like the one depicted in Fig. 14c. This is suggested by the magnetic susceptibility data which shows that the moments on Cu sites remain confined in the (bc) plane above T_N [11] and also by recent magnetoresistance measurements [14] which are consistent with a gradual rotation of the WF moments. In fact a departure from a two step transition [36], involving a spin-flop process occurring between the states shown in Fig. 14b-c and which is characteri ed by a large component of the staggered magneti ation along the a orthorhombic axis, is expected. In a regular spin-flop transition a magnetic field applied parallel to the easy axis (which in our case is the b orthorhombic axis, see Fig. 6b) will end up rotating the staggered magneti ation along a direction perpendicular to this axis. The reason is that above some critical value of the field the magnetic anisotropy energy becomes smaller than the gain in magnetic energy due to the larger transverse susceptibility in the AF state [37]. In the La_{2-} Sr CuO_4 case, the situation seems not to be the same: because the transverse susceptibility, χ_a, is the smallest below 300 K for x = 0 and 0.01 (see Fig. 3), the spins cannot partake of the field energy $-(\chi_a - \chi_b)H^2/2$. Accordingly, a flop along the a-axis is not favorable from this point of view [38].

The identification of the FIM with the XY gap can also explain other observed features. The crossover around 150 K shown in Figs. 12 and 13 may be understood as a departure of the direction of the WF moments from perpendicular to the (ab) plane to a direction almost parallel to the b-axis (see Fig. 14) where the XY anisotropy, weaker due to temperature fluctuations, ceases to play a decisive role. Physically, this corresponds to the fact that the conventional out-of-plane XY mode changes its nature as the WF moment rotates away from the c-axis. Prompted by this idea we calculated (solid lines in Fig. 12c) the spin-wave dispersions using Eq. (5) and (6) in the extreme case of $\alpha = 0$

and a small DM gap which still confines the moments in the (bc) plane. Although finite temperature effects have to be taken into account, we note that this simple estimation reproduces, at least qualitatively, the experimental dispersions. We also comment on the possible relevance of our findings to the switch of orthorhombic axes in magnetic fields [17]. If a state like Fig. 14c is reali ed (which is shown in Fig. 13b to persist to temperatures close to 300 K even for x = 0.01) then the magnetic force in an external field is significantly enhanced due to the net in-plane ferromagnetic moment. Still, the origin of the coupling between the spins and the tilt of the CuO_6 octahedra remains as a very interesting question.

The qualitative scenario we propose regarding the nature of the FIMs and the nature of the magnetic field induced order leaves several open questions. One of them is the following: if the FIM in the AF state is the XY gap, why is its spectral weight peaked at T_N, as shown in Fig. 14b for x = 0.01 La_{2-} Sr CuO_4 ? A second question is related to the finite intensity of the FIMs only for magnetic fields $\vec{H} \parallel \hat{b}$-axis. On the other hand if we assume that the FIM mode is an excitation other than the XY gap, arising for instance as a result of the 4-sublattice structure, then the common interpretation of the excitation around 40 cm^{-1} found in several 2D layered AF's has to be reconsidered.

One may wonder if up to now there are any other transport signatures of this magnetic field induced transition which could back up our spectroscopic conclusions. As for the undoped La_2CuO_4 crystal, where the transition should be most prominent and which has strongly insulating behavior, to our knowledge there are no magnetoresistance measurements so far and in terms of magneti ation it would be highly desirable to see measurements especially as a function of magnetic field at several temperatures down to 10 K. Higher fields than 7 T are needed though as the temperature is decreased below 300 K. However, relative magnetoresistance data in twinned samples of x = 0.01 La_{2-} Sr CuO_4 (Fig. 2 in Ref. [14]) show a 'peel off' from a temperature independent curve. For a given magnetic field value, this phenomenon is seen to occur at temperatures where magneti ation data indicate the transition outside the AF order. This shows that the dc transport responds to field induced changes in the AF environment in the anticipated (H,T) parameter space. Supplementary magneti ation, magnetoresistance and especially neutron scattering measurements in magnetic field would be necessary to verify our claims.

2.5 Phononic and Electronic Anisotropy in Detwinned La_{2-} Sr CuO_4

We observed in the previous section that detwinned La_{2-} Sr CuO_4 crystals revealed strong anisotropy effects in terms of the dynamics of long wavelength spin excitations. Here we show that the small lattice orthorhombicity has drastic effects also on the phononic and electronic Raman continuum. A summary of our results in this perspective is shown in Fig. 15. The left panel shows T = 10 K Raman data in La_2CuO_4 taken in (aa) and (bb) polari ations. The axes notation is shown in the inset. Both these symmetries probe fully symmetric excitations and, in terms of phonons, there are 5 allowed in the LTO phase. Four of them, denoted by A, B, C and D are in the energy region below 300 cm^{-1}. All the five A_g modes and their atomic displacements will be discussed in more detail in the section devoted to Nd doped La_{2-} Sr CuO_4 . For now we remark that while in the insulating

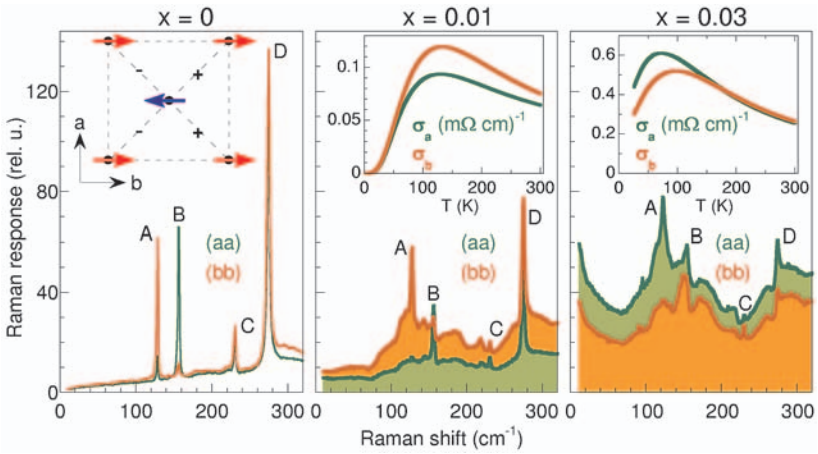

Fig. 15. Main panels show (from left to right) T = 10 K Raman data in (*aa*) and (*bb*) polari ations in x = 0, 0.01 and 0.03 La_{2-} Sr CuO_4. *A*, *B*, *C* and *D* denote 4 of the 5 fully symmetric Raman modes in the LTO phase. The inset in the left panel shows a unit cell of the LTO structure, the directions of spins on Cu sites and the axes notations (see also Figs. 2 and 6). The insets for the x = 0.01 and 0.03 panels show *dc* conductivities along the *a* and *b* axes. The same vertical scale was used for the Raman spectra in panels (**a**), (**b**) and (**c**).

La_2CuO_4 the Raman continuum is, as expected, very weak at low temperatures, there is a tremendous intensity anisotropy in the *A* and *B* phonons. Mode *A* is seen clearly in (*bb*) polari ation and has almost vanishing intensity in (*aa*) polari ation and the situation is reversed for mode B.

In the middle panel we observe that the anisotropy in these two modes is preserved. However one can note that we observe intense Raman backgrounds (shaded areas), quite different in intensity in (*aa*) versus (*bb*) polari ations. The relative intensities of the continua match the anisotropy in the *dc* conductivity along the *a* and *b* axes [13] shown in the inset. Looking at the $x = 0.03$ data (right panel) one can notice that the sign of the low temperature resistivity anisotropy changes with respect to the $x = 0.01$ case. Similarly, the Raman background in (*aa*) polari ation becomes stronger than in (*bb*) polari ation and this change is also accompanied by the reversal of the intensity anisotropy of the *A* and *B* phonons.

This switch is a remarkable effect. Could it be that it is induced by structural changes, in particular a 90° rotation of the CuO_6 octahedra between 1 and 3% Sr doping? X-ray data showed that this is not the case, suggesting that the reversal is due to the development of a new kind of anisotropy in the spin-charge dynamics at low doping, possibly occurring as the the system crosses at low temperatures the boundary of the long range AF order. Beyond this observed switch between 1 and 3% doping, the strong

phononic anisotropy seen most clearly in La_2CuO_4 data is an interesting problem by itself. Since it is determined by the CuO_6 octahedra tilt around the a-axis, one may suspect that the p_z orbitals of the apical oxygens may be involved in the coupling process and its hybridi ation with in plane orbitals is not negligible. We remark one other point in regard to the phononic features shown in Fig. 15: While in La_2CuO_4 the observed number of modes does not exceed the number predicted by group theory (we observe also the 5^{th} mode in (cc) polari ation at 430 cm^{-1}, see Fig 20), a much larger number of additional features sitting on top of the Raman continuum is seen for $x = 0.01$ and 0.03. It is possible that this is connected to charge and/or spin supermodulation within the 2D CuO_2 planes. While not explained, the experimental observations in Fig. 15 pose intriguing questions, some of them, like the possibility of 2D spin and/or charge order, being tied to problems actively scrutini ed in relation to the occurrence of superconductivity in cuprates.

3 Spin and Lattice Dynamics at Commensurate $x = 1/8$ Sr Doping in $La_{2-x-y}Nd_ySr_xCuO_4$

3.1 Motivation: Intrinsic Spin/Charge Modulations in the CuO_2 Planes?

The origin of the interest in studying lattice and electronic dynamics in 2D cuprates at carrier concentrations commensurate with the lattice is essentially due to the increased tendency of the doped system to form real space patterns characteri ed by certain periodic modulations of the charge and spin density. Among correlated systems, this situation is not peculiar to high T_c's but it has been discussed for instance in different type of materials like manganites or nickelates. Ground states in which charges self organi e in quasi-1D 'rivers' (called stripes) acting as AF domain walls were predicted at the mean field level as early as 1989 [39] and later it has been proposed that the charge and/or spin ordering is not necessarily static, but the carriers could form electronic liquid-crystal like phases [40].

From the experimental point of view, one of the observed '$x = 1/8$' effects, discovered initially in La_{2-} Ba CuO_4 [41] but also observed in Nd doped La_{2-} Sr CuO_4 [42], was a suppression of superconductivity manifested through a decrease of the transition temperature T_c. In fact a similar observation (but in terms of the *onset* of superconductivity as seen by magneti ation measurements [43]) was made in Nd free La_{2-} Sr CuO_4 at 1/8 Sr doping. The 'stripology' in cuprates got a lot of momentum after the discovery of a constellation of neutron Bragg peaks in $La_{1.475}Nd_{0.4}Sr_{0.12}CuO_4$. The data showed superlattice peaks associated with static spin and hole ordering, the magnetic moment modulation being characteri ed by a wavelength twice as big as the one observed for the charge [44]. Some of the effects discussed above are illustrated in Fig. 16.

The almost complete suppression of T_c in $La_{1.475}Nd_{0.4}Sr_{0.12}CuO_4$ as well as the fact that in this compound neutron scattering sees long ranged charge and spin supermodulations suggested that the stripes may be the 'looked for' competing state to superconductivity. The presence of the incommensurate magnetic peaks also in Nd free La_{2-} Sr CuO_4 and their observation in *elastic* neutron scans at $x = 1/8$ doping show that $La_{2-\ -y}Nd_ySr$ CuO_4 with $x = 1/8$ are some of the most suitable 2D cuprate compounds to look for the effects of such modulations. It is important to note that while in

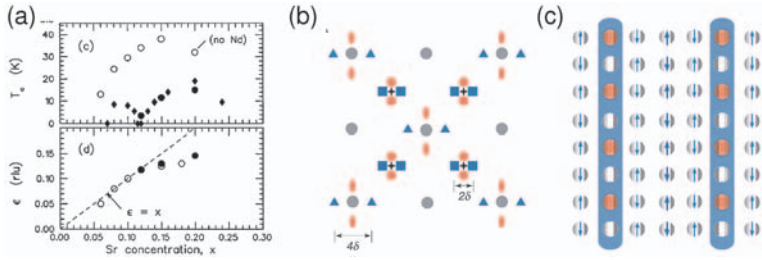

Fig. 16. (**a**) The superconducting temperatures (upper panel) and the evolution of the incommensurate splitting (lower panel) in La_{2-} Sr CuO_4 (empty symbols) and $y = 0.4$ $La_{2-\ -y}Nd_ySr$ CuO_4 (filled symbols) as a function of Sr concentration x. Data from Ref. [42]. The symbol ϵ in (**a**) is denoted by δ in (**b**) and (**c**). Neutron scattering: reciprocal and real space are shown in panels (**b**) and (**c**). In (**b**) the grey circles at $(2\pi/a)(m, n)$ with (m, n) being a pair of integers correspond to fundamental structural Bragg peaks in the HTT phase. The black stars at $(2\pi/a)(m, n) + (\pi/a, \pi/a)$ are for the commensurate AF Bragg peaks. The points separated by 2δ are incommensurate dynamic or static peaks which replace the AF Bragg peaks upon Sr doping. Their associated wavelength is $\lambda_{spin} = 1/\delta$. The points separated by 4δ correspond to the charge order with $\lambda_{charge} = 1/2\delta$ in $y = 0.4$ $La_{1.475}Nd_{0.4}Sr_{0.12}CuO_4$. In (**c**) the real space charge-spin structure inferred from the results in (**b**). Charges are confined in the blue channels and the blue arrows on the external grey circles indicate the magnitude and direction of the magnetic moments on Cu sites.

Nd doped La_{2-} Sr CuO_4 the charge ordering was also confirmed by X-rays [45], this is not the case (yet) in Nd free samples. Raman spectroscopy can be a powerful technique in this respect because optical phonons can be used as local probes of fast changes in the charge distribution and magnetic Raman scattering provides information about local AF correlations. However, it can also provide information regarding the side effects of Sr substitution and what we argue in the study presented in the following is that some of those effects, structural distortions as well as the disorder introduced by Sr substitution, are important at 1/8 doping in La_{2-} Sr CuO_4 irrespective of Nd concentration [9].

It was mentioned in the introduction that in $La_{2-\ -y}Nd_ySr$ CuO_4 the various changes in the crystal structure are due to the lattice mismatch between the cation and CuO_2 layers. Like La_{2-} Sr CuO_4, the $La_{1.475}Nd_{0.4}Sr_{0.12}CuO_4$ compound undergoes a transition from the HTT to the LTO phase above room temperature. This transition is followed around $T_{LTT} = 70$ K by another structural change, from the LTO to the low temperature tetragonal (LTT) phase where the CuO_6 octahedra tilt around an axis parallel to the Cu-O-Cu bonds. The structural order parameter of these transitions is the libration of the CuO_6 octahedra shown in Fig. 17. It was noticed in $La_{1.475}Nd_{0.4}Sr_{0.12}CuO_4$ that the LTO-LTT transition takes place over a range of temperatures and that disorder in the striped phase leads to a glassy nature of the ground state. Intermediate states characteri ed by a tilt angles in between those of the LTO and LTT phase have also been proposed [5]. The

coexistence in $La_{2-\ -y}Nd_ySr\ CuO_4$ of several phases in a complex mixture was suggested by transmission electron microscopy [10].

So there are interesting topics associated to the presence of Nd, but after all why are these structural effects, especially the ones related to the tilt of CuO_6 octahedra, relevant to the spin and charge dynamics? The importance of the local structural distortions for the superconducting properties characteri ed in cuprates by a short coherence length should not be ignored. The stabili ation of the LTT phase was observed to trace the suppression of superconductivity in Nd doped La_{2-} Sr CuO_4 [46] and also in the related La_{2-} Ba CuO_4 compound [47]. A critical value of the CuO_6 tilt was associated with the stabili ation of magnetic against superconducting order, see Fig. 17b and Ref. [5]. Rapid suppression of superconductivity, similar to that due to Cu replacement by non-magnetic impurities, was observed with increasing the cation radius variance [48].

In this context our study provides direct spectroscopic information about the LTO-LTT transition in $La_{1.475}Nd_{0.4}Sr_{0.12}CuO_4$ and local deviations from the average structure existent in Nd doped and Nd free La_{2-} Sr CuO_4 structures. The persistent fluctuations of the structural order parameter down to T = 10 K reveal substantial disorder in the cation-oxygen layers. The distinct Raman signatures accompanying a transition to a state with deep spin/charge modulations are not observed in the temperature dependence of the two-magnon (2M) scattering around 2200 cm^{-1} and the c-axis polari ed phonons below 500 cm^{-1} [9].

3.2 Inhomogeneous CuO_6 Octahedra Distribution in $x = 1/8$ $La_{2-\ -y}Nd_ySr\ CuO_4$

In the following we will show Raman data from $La_{2-\ -y}Nd_ySr\ CuO_4$ with the following doping concentrations: $x \approx 1/8$, $y = 0$; $x \approx 1/8$, $y = 0.4$; and $x = 0.01$, $y = 0$. The spectra were taken from the $(a'c)$ and (ab) faces of the $x = 1/8$ $La_{2-\ -y}Nd_ySr\ CuO_4$ samples and from the (ac) surface of a $x = 0.01$ La_{2-} Sr CuO_4 crystal as determined by X-ray diffraction. See Fig. 17 for axes notations. Note that they are consistent with the ones in Fig. 2, the primed letters corresponding to directions parallel to the Cu-O-Cu bonds The laser excitation energy used was $\omega_{in} = 1.92$ eV.

Raman spectra taken in the (ca') geometry may provide direct information about tetragonal to orthorhombic distortions. In this polari ation we probe phononic modes with B_{2g} and B_{3g} symmetries in the LTO phase which become degenerate with E_g symmetry in the LTT phase. In Fig. 18 we show the temperature dependence of the modes around 250 cm^{-1} corresponding to the apical O vibrations parallel to the CuO_2 plane in $La_{1.475}Nd_{0.4}Sr_{0.12}CuO_4$ [49]. One can think about the spectral changes in analogy to the evolution with temperature of the orthorhombically split X-ray diffraction Bragg peaks [46]. We observe a broad peak around 245 cm^{-1} at room temperature which, with cooling, becomes resolved into two components, one hardening and one softening. A new central peak can be seen at 50 K around 248 cm^{-1} which gains spectral weight as the temperature is decreased to 10 K. While the total integrated intensity of the modes remains constant, Fig.18c, we observe a redistribution of spectral weight among the three modes as a function of temperature. The split components become weaker but can still be seen

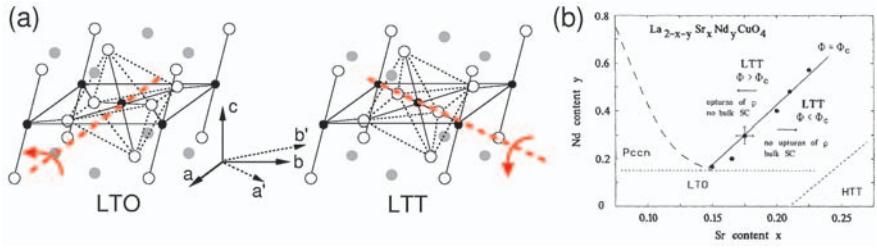

Fig. 17. (**a**) Buckling of the CuO_2 planes and the tilt pattern of the CuO_6 octahedra in the LTO and LTT phases. (**b**) A schematic of the T = 10 K structural phase diagram of $La_{2-\ -y}Nd_ySr\ CuO_4$ as a function of x(Sr) and y(Nd) (from Ref. [5]). The main point of this plot is that the LTT region characteri ed by a CuO_6 tilt angle $\Phi > \Phi_c \approx 3.6°$ has no bulk superconductivity (SC) and low temperature insulating behavior while SC is found in the LTT region with $\Phi < \Phi_c$. In other words it is proposed that there is a critical buckling angle compatible with long range SC and that the stabili ation of the LTT phase suppresses SC correlations.

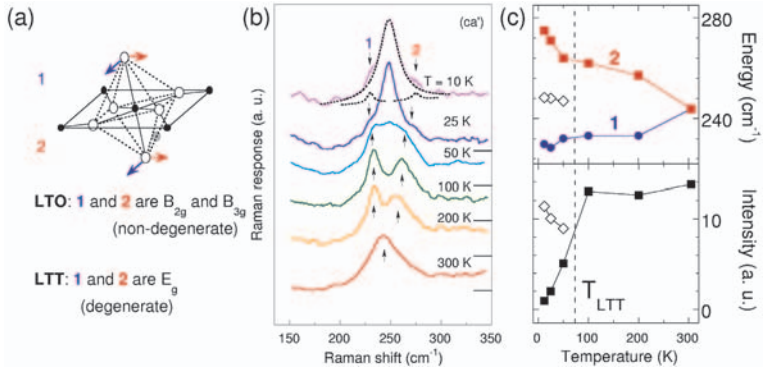

Fig. 18. (**a**) Cartoon with the apical Oxygen vibrations having B_{2g} and B_{3g} symmetry in the LTO phase and degenerate with E_g symmetry in the LTT phase. (**b**) Temperature dependence of the O modes described in (a) in $La_{1.475}Nd_{0.4}Sr_{0.12}CuO_4$. The finite intensity of modes 1 and 2 even at T = 10 K shows that there exists a residual orthorhombicity at this temperature. (**c**) The temperature dependence of the energies (upper panel) and intensities (lower panel) of the phonons in (**b**) obtained by Lorent ian fits.

as 'orthorhombic satellites' of the central peak down to 10 K. The coalescence of the features into the 248 cm^{-1} mode signals the recurrence of a phase with tetragonal symmetry which should be the expected LTT phase of $La_{1.475}Nd_{0.4}Sr_{0.12}CuO_4$. However, the finite residual intensity of the satellites appearing on the tails of the broad central peak shows an incompletely developed LTT phase and that even at 10 K there exists about 7% LTO

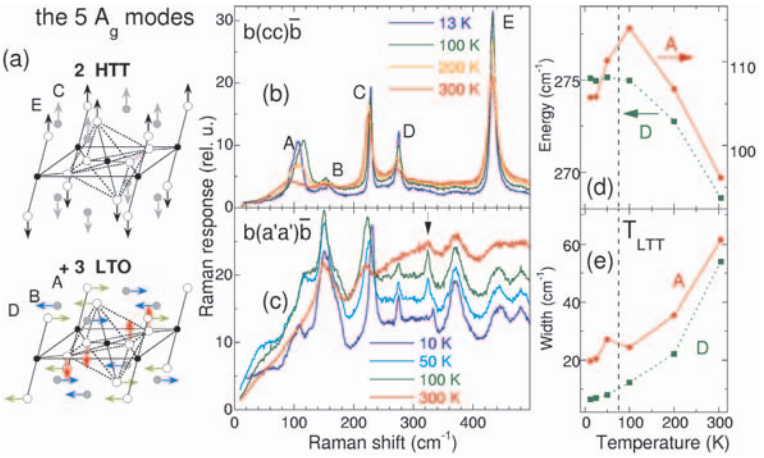

Fig. 19. (**a**) Group theory predicts two A_{1g} modes in the HTT phase (denoted by C and E) and the appearance of 3 additional A_g phonons in the LTO phase (denoted by A, B and D). They are linear combinations of the atomic displacements shown in this panel. Temperature dependence of the $b(cc)\bar{b}$ (panel **b**) and $b(a'a')\bar{b}$ (panel **c**) polari ed Raman spectra. In (**d**) and (**e**) we show the temperature dependent energies and intensities of modes A and D from panel (**b**).

phase (determined from the relative ratio of phonon intensities). Note that the width of the main peak at T = 10 K is comparable to the widths of the components of the doublet seen at temperatures as high as 200 K.

Raman data in (*cc*) polari ation is well suited for the study of lattice dynamics due to weaker coupling to underlying electronic excitations. Temperature dependent Raman spectra in this scattering geometry are shown in Fig. 19b. Group theory predicts five fully symmetric modes at $k = 0$ in each of the LTO and LTT phases and only two for the HTT phase. The two fully symmetric modes of the HTT along with the additional three modes in the LTO phase are shown in Fig. 19a. In Fig. 19b we observe all the five phonons corresponding to the LTO and LTT phases and they are denoted by A, B, C, D and E. Four out these five modes can also be seen in Fig. 15 where the same notation was used. Although every one of these excitations should be considered as linear combinations of all the A_g movements depicted in Fig. 19a, one could roughly say that they are mainly composed of the following vibrations. The modes C and E (which at T = 10 K are found at 228 and 433 cm^{-1}) are inherited from the HTT phase and they correspond to the *c*-axis vibrations of La/Sr/Nd and O atoms respectively, see the upper part of Fig. 19a. Mode A is the soft mode of the HTT-LTO transition (the CuO_6 octahedra tilt), mode B is mainly due to the vibration of La/Sr/Nd atoms in the direction imposed by the CuO_6 tilt and mode D consists of *c*-axis vibrations of the in-plane O atoms [49, 50, 51]. The energies of the last three phonons at the lowest temperature are: 106 cm^{-1} (mode A), 156 cm^{-1} (mode B) and 275 cm^{-1} (mode D).

The above qualitative description indicates that we could expect a strong coupling between the lowest energy modes (A and B). These two excitations can be distinguished in Fig. 19b from the other ones because they remain much broader and look like composite features even at the lowest temperature in comparison with the the modes C, D and E which harden and sharpen smoothly through the LTO-LTT transition taking place around 70 K. As seen in Fig. 19b, the temperature variation of the intensities of the modes C and E inherited from the HTT phase is not as pronounced which is not surprising. A comparison of the temperature dependent energy and full width at half maximum (FWHM) of modes A and D is shown in Fig. 19d-e. The large variation in energy and width of mode A above the transition (see also the inset of Fig. 20), the softening below 70 K, as well as its energy around 110 cm^{-1} in agreement with neutron scattering studies [52] show that this mode corresponding to the octahedra tilt is the soft mode of the structural changes [50]. The smooth decrease in the energy in the LTT phase is only apparent because this space group is not a subgroup of the LTO group and as a result a true LTO-LTT transition is expected to be of first order. Although unresolved due to broadening effects, the large width of mode A around 70 K shows the coexistence of the LTO and LTT tilts, the latter appearing as a result of folding of the LTO Z-point to the Γ-point of the LTT phase which was observed also in La_2NiO_4 [53].

We infer from our data that the large FWHM of mode A reflects the spatial distribution of the octahedra tilt. The simultaneous broadening of the mode B shows coupling between the OP and La/Nd/Sr vibrations and as a result the influence of the dynamics in the cation-O layers on the properties of CuO_2 planes. Both modes B and C involve cation displacements as discussed above, the former perpendicular and the latter parallel to the c axis. However, at 10 K the FWHM of mode C is 8 cm^{-1}, smaller compared to the FWHM of mode B which is around 20 cm^{-1}. We conclude that the large observed widths of the modes A and B are mainly caused by the locally fluctuating OP and not due to the inhomogeneous broadening introduced by the simultaneous presence of La, Nd and Sr in the inter-layer composition which should have been reflected also in a large width of mode C.

It is interesting to compare the (cc) polari ed phononic spectra with those in which the polari ation of the incoming photon field is parallel to the CuO_2 planes. Fig. 19c shows the temperature dependent Raman spectra in the $b(aa)\bar{b}$ geometry. Different coupling to the electronic degrees of freedom when the polari ation of the incident field is parallel to the CuO_2 planes leads to a stronger intensity in the underlying Raman continuum relative to the phononic features and also a different intensity/shape of the fully symmetric features observed in (cc) polari ation. A continuous suppression with cooling of the electronic background is due to the opening of a pseudogap in $La_{1.475}Nd_{0.4}Sr_{0.12}CuO_4$ [54]. The electron-phonon coupling allows the observation of additional peaks around 370 and 480 cm^{-1} evolving smoothly from 300 to 10 K, both of which allowing an interpretation in terms of two-phonon scattering if some anharmonic interaction is taken into account. Marked by an arrow in this panel is a B_{1g} symmetric excitation in the LTO phase which shows a jump from 325 to 335 cm^{-1} as the crystal enters in the LTT phase.

In order to understand the surprising behavior of the tilt pattern as reflected in the phononic data from Fig. 19 a comparison with different materials from the same

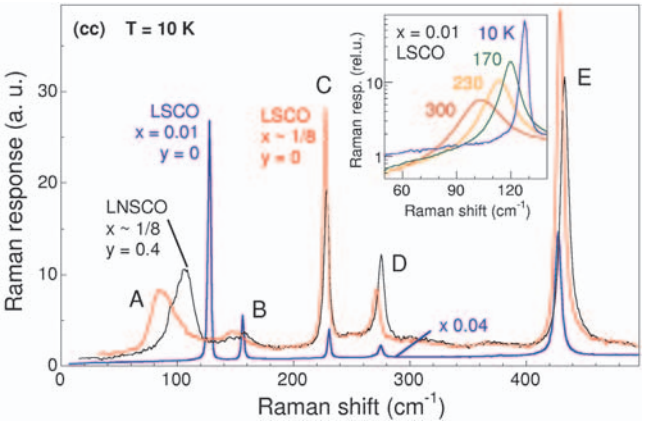

Fig. 20. T = 10 K Raman spectra in $b(cc)\bar{b}$ configuration for $x = 1/8; y = 0$ (red), $x = 1/8; y = 0.4$ (black) and $x = 0.01; y = 0$ (blue) $La_{2-\ -y}Nd_ySr\ CuO_4$. The inset shows the temperature dependence in $b(cc)\bar{b}$ polari ation of the the intensity of mode A (CuO_6 octahedra tilt) in x = 0.01 $La_{2-}\ Sr\ CuO_4$.

class is useful. In Fig. 20 we show the 10 K (cc) polari ed Raman spectra of three crystals: $La_{1.475}Nd_{0.4}Sr_{0.12}CuO_4$, x = 0.01 and 0.12 $La_{2-}\ Sr\ CuO_4$. For $x = 0.01$ $La_{2-}\ Sr\ CuO_4$ mode A has a FWHM of 2.5 cm^{-1} (Note in the inset the strongly temperature dependent intensity and width which is a characteristic of a soft mode). For $x \approx 1/8$ LSCO the same phonon is around 85 cm^{-1} and its FWHM of about 23.5 cm^{-1} is larger than the width of mode A in the Nd doped crystal where it is slightly below 20 cm^{-1}. Comparison of these relative phononic widths confirms the conclusion discussed before that Nd doping of LSCO crystals and the closer proximity to the T′ phase induced by Nd doping in the La_2CuO_4 structure [55] cannot be responsible for the large observed broadening effects. Intrinsic phonon anharmonicity would lead to a broad mode A in $x = 0.01$ LSCO which is not the case. Neither can the tilt disorder across twin domains be the cause of such dramatic effects because the volume fraction occupied by these boundaries is expected to be very small [10]. The 7% relative ratio of the orthorhombic satellites to the central peak in Fig. 18b would rather be consistent with such a small contribution. If the satellites are indeed due to twinning effects the data show that at 10 K the larger LTT domains are separated by regions of pure LTO tilt. The absence of the broadening effects on the vibrations along the c-axis points towards an 'anisotropic' disorder relating primarily to bond randomness along directions parallel to the CuO_2 planes.

Could the spin-lattice coupling or the interaction with the stripe-ordered carriers in CuO_2 planes be the main cause of broadening? Stripe correlations are enhanced in $La_{1.475}Nd_{0.4}Sr_{0.12}CuO_4$ which displays however a smaller width of mode A. Also, it is not clear why only the modes A and B would be affected by this interaction. In this sense one expects the movements of the in-plane atoms to be more sensitive to stripe ordering but

we see no similar effects on mode D. Although less probable, spin-lattice induced broadening cannot be completely ruled out and the answer to this question lies in a Sr doping dependence of the (cc) polari ed spectra. Our data can be reconciled however with recent studies of local structure in Nd free and Nd doped La_{2-} Sr CuO_4 systems [56]. Model analysis of the pair distribution function from X-ray absorption fine structure suggests that in this material class the average structure determined by diffraction is different from the local pattern which is characteri ed by disorder in the CuO_6 tilt direction and magnitude [56]. The Raman data shown in Figs. 19 and 20 are spectroscopic evidences that the $La_{2-\ -y}Nd_ySr$ CuO_4 system is characteri ed by disorder in the cation layers and that the locally fluctuating octahedra tilt is responsible for the observed effects.

Information about the relative magnitude of charge disproportionation in $La_{2-\ -y}Nd_ySr$ CuO_4 can be gained by comparison with Raman spectra in compounds like the nickelates [57, 58] or manganites [59, 60] where charge and spin modulations are well established [61]. New Raman active modes have been observed below the charge ordering within the Mn-O layers in $La_{0.5}Ca_{0.5}MnO_3$ [59] and also in Bi_{1-} Ca MnO_3 [60]. Conspicuous changes in the lattice dynamics have also been observed in x = 0.33 and 0.225 La_{2-} Sr NiO_4 by Raman scattering [57, 58]. Lowering of the crystal symmetry at the stripe ordering transition gives rise to folding of the Brillouin one and the appearance of new $k = 0$ phononic modes. Charge locali ation creates non-equivalent Ni sites generating phonon 'splitting'. The c axis stretching modes corresponding to La and apical oxygens split by 14 and 30 cm^{-1} respectively [57]. Within about 3 cm^{-1} resolution imposed by the phononic widths we do not observe such splittings in our spectra. The ratio of the integrated intensities of the split oxygen modes in Ref. [57] is about the same as the ratio of doped versus undoped Ni sites. If we assume the same relation to hold for the case of cuprates, a factor of 12% in split phononic intensity should have been seen in our spectra. However, the latter argument has to take into account that different electron-phonon coupling might change this proportionality relation. Last but not least is the observation that we see, at least in (cc) polari ed spectra only the phononic excitations predicted by group theory for the LTO/LTT phases. We conclude that any charge ordering taking place in our case is much weaker than in the related compounds referred to above. This is not contradicting X-ray diffraction data [45] which estimated a factor of 10^2 between the relative magnitude of charge modulations in cuprates and nickelates.

3.3 Two-Magnon Raman Scattering in $x = 1/8$ $\mathbf{La_{2-\ -y}Nd_ySr\ CuO_4}$ and $x = 0 - 0.03$ $\mathbf{La_{2-}\ Sr\ CuO_4}$

Two-magnon (2M) Raman scattering provides an additional way to look at the effects of stripe correlations on magnetic excitations. For 2D square lattices the 2M peak is predicted to be seen in the B_{1g} channel, probed by (ab) polari ation [62]. Fig. 21 shows 2M scattering around 2200 cm^{-1} at 300 and 5 K taken with the resonant $\omega_{in} = 3.05$ eV incident frequency. As in other tetragonal 2D AF's [63] we observe the spin pair excitations in the expected scattering geometry. The $c(a'b')\bar{c}$ polari ation shows a featureless background which probably has a contribution from luminescence.

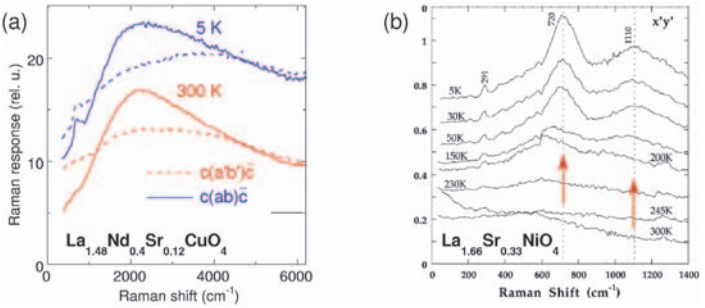

Fig. 21. (a) Two-magnon Raman scattering in $La_{1.475}Nd_{0.4}Sr_{0.12}CuO_4$ for T = 300 (red) and 5 K (blue). The T = 5 K spectra is vertically off-set. Dashed (solid) lines are for spectra in $c(a'b')\bar{c}$ and $c(ab)\bar{c}$ polari ations respectively. (b) Two-magnon scattering in the striped phase of $La_{\frac{5}{}}Sr_{\frac{1}{}}NiO_4$ from Ref. [57]. The two red arrows stand for two magnetic bands corresponding to two spin exchange channels, see text.

In La_{2-} Sr NiO_4 there is a clear signature of the effect of stripe ordering on the high energy spin pair excitations: in the undoped case (x = 0) the 2M Raman band is seen around 1650 cm^{-1} [63]. At 33% Sr doping this excitation is not present at that frequency but instead two peaks at lower energies, 720 and 1110 cm^{-1} [57], are observed below the magnetic ordering temperature, see Fig. 21b. In Ref. [57], assuming an unrenormali ed value for the superexchange $J \approx 240$ cm^{-1} with respect to the undoped case, it is proposed that these peaks originate from the two spin exchange channels opened due to the stripe order, one of them within and the other one across the antiphase AF domains depicted in Fig. 16. A more recent neutron scattering study, whose authors are however in favor of a renormali ation of the magnetic super-exchange in the stripe phase, is in support of this assignment regarding the higher frequency peak at 1110 cm^{-1} ($\approx 2 \cdot 70$ meV) by finding that the upper edge of the spin-wave dispersion branch is around 70 meV [64]. Irrespective of the microscopic origin, the 2M scattering is definitely a good probe for the study of local effects induced by the stripe order. Comparison with our high energy Raman spectra shown in Fig. 21a shows, as in the case of phonons, that in $La_{2-\ -y}Nd_ySr$ CuO_4 we observe only slight changes from 300 to 10 K emphasi ing weak local spin modulations in this compound.

The differences we observe between cuprates and nickelates can be related to the much stronger carrier self-confinement in the latter [65]. It has also been shown [66] that anomalies in phonon dispersions occur in La_{2-} Sr CuO_4 at points in the Brillouin one commensurate with charge ordering wavevectors inferred from neutron scattering studies. But as discussed, the charge modulation in Nd doped La_{2-} Sr CuO_4, where the stripe correlations were shown to be stabili ed, is too weak to produce observable changes in the lattice unit cell. The number of phononic modes we observe can be explained solely in terms of LTO/LTT distortions. Our data, however, do not contradict the possible existence of charge modulations in the CuO_2 plane. In fact, the dynamics in the cation-O

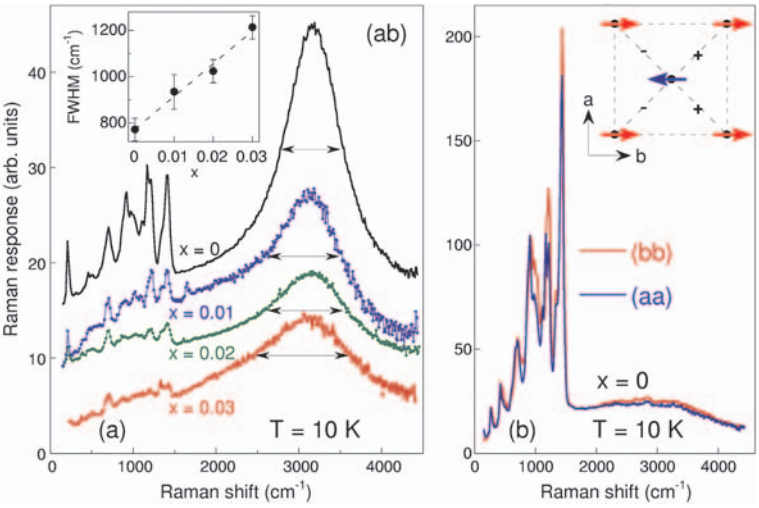

Fig. 22. T = 10 K data in La_{2-} Sr CuO_4. (a) The Raman two-magnon excitation around 3000 cm^{-1} in (ab) polari ation for $x = 0 - 0.03$. Spectra are vertically offset. The sharp features below about 1500 cm^{-1} are higher order phonons. The inset shows the full width at half maximum for the four dopings. (b) Raman data in a detwinned La_2CuO_4 crystal (see section 1.2 in this chapter) in (aa) and (bb) polari ations. Note that the strong two-magnon feature is absent in this polari ation and the anisotropy of the spectra at high frequencies.

layers and the magnitude of octahedra tilt disorder affects the carrier distribution and our Raman results impose constraints on the magnitude of the charge modulations.

In the context of sensitive short wavelength magnetic excitations to possible spin/charge modulations in the transition metal oxygen planes, see Fig. 21, and also the strong anisotropy effects found in detwinned La_{2-} Sr CuO_4 crystals in terms of both phononic and low lying electronic excitations, see Fig. 22, it is interesting to take a look at the evolution with hole concentration of the 2M excitation in lightly doped La_{2-} Sr CuO_4 crystals as well as to check whether one can find at high frequencies (2000 - 4000 cm^{-1}) anisotropy effects similar to those observed in Fig. 15. Our Raman results regarding these problems are shown in Fig. 22. In panel (a) we show the 2M feature at low temperatures in the B_{1g} channel (probed in (ab) polari ation, see the axes notations in Figs. 2 and 17) for four dopings.

The length of the arrows roughly indicate the evolution of the scattering width with increasing x from 0 to 0.03. We found quite a si eable effect in terms of the 2M FWHM. In the undoped sample the FWHM is around 770 cm^{-1} and although the in plane correlation lengths remain large in the lightly doped regime [3], we observe an approximately linear increase of about 60% with doping from $x = 0$ to 0.03 (inset of Fig. 22b). One may try to correlate this to the increase in the low energy electronic Raman background seen in Fig. 15 in parallel polari ation. We remark that although this enhancement is obvious for (aa)

and (bb) scattering geometries, we checked that in (ab) configuration the intensity of the Raman background at T = 10 K is doping independent. It is easier to understand that the magnetic spin-wave gap excitations in the long wavelength limit disappear together with the disappearance of long range magnetic order, however, the drastic change in the two-magnon scattering, which in principle requires 'good' AF correlations on a much smaller scale (about 4 lattice constants), is not so straightforward to grasp. For an explanation one may resort again to the argument that in the CuO_2 plane, a hole entering the O2p bands is more delocali ed and one hole breaks effectively more magnetic bonds than just one between a pair of nearest neighbor spins.

Regarding possible anisotropy effects, Fig. 22b shows that the (aa) and (bb) polari- ed spectra look very much alike at high frequencies and although there are differences, the second and third order phononic scattering is much less sensitive to the macroscopic orthorhombicity than the one phonon excitations in the 0 to 500 cm^{-1} region. Unfortunately, as predicted by the Fleury and Loudon (see Ref. [62]) and seen in Fig. 22, the strongest 2M scattering is supposed to be seen in B_{1g} tetragonal channel which in not probed in (aa) and (bb) polari ations ((aa) and (bb) configurations probe A_{1g} + B_{2g} tetragonal symmetries) so we cannot directly probe the effects of the macroscopic lattice spin anisotropy on the strong 2M feature from Fig. 22a. What we can however say is that if the finite Raman background between 2000 and 4000 cm^{-1} has some fully symmetric (A_{1g}) magnetic contribution from higher order light scattering Hamiltonian, see Ref. [67], the influence of the lattice orthorhombicity on that contribution is negligible.

4 Summary

Two aspects in connection with the magnetic properties of $La_{2-\ -y}Nd_ySr\ CuO_4$ single crystals were discussed in some detail. One of them was related to long wavelength magnetic excitations in $x = 0$, 0.01, and 0.03 La_{2-} Sr CuO_4 detwinned crystals as a function of doping, temperature and magnetic field. Two magnetic modes were observed within the AF region of the phase diagram. The one at lower energies was identified with the spin-wave gap induced by the antisymmetric DM interaction and its anisotropic properties in magnetic field could be well explained using a canonical form of the spin Hamiltonian. A new finding was a magnetic field induced mode whose dynamics allowed us to discover a spin ordered state outside the AF order which was shown to persist in a 9 T field as high as 100 K above the Néel temperature T_N for x = 0.01. We proposed for the field induced magnetic order a state with a net WF moment in the CuO_2 plane and analy ed the field induced modes in the context of in-plane magnetic anisotropy. For these single magnon excitations we mapped out the Raman selection rules in magnetic fields and we also found that their temperature dependent spectral weight (in the presence of a constant external magnetic field) was peaked at the Néel temperature.

The second aspect was related to phononic and magnetic Raman scattering in $La_{2-\ -y}Nd_ySr\ CuO_4$ with three doping concentrations: $x \approx 1/8$, $y = 0$; $x \approx 1/8$, $y = 0.4$; and $x = 0.01$, $y = 0$. We observed that around 1/8 Sr doping and independent of Nd concentration there exists substantial disorder in the tilt pattern of the CuO_6 octahedra in both the orthorhombic and tetragonal phases which persist down to 10 K and are coupled

to bond disorder in the cation layers. The weak magnitude of existing charge/spin modulations in the Nd doped structure did not allow us to detect specific Raman signatures on lattice dynamics or two-magnon scattering around 2200 cm^{-1}.

It is possible that the discovery of weak charge modulations in the hole doped 2D CuO_2 planes characteristic of high T_c materials is just a matter of time. The problem of doped Mott-Hubbard insulators seems however to be one in which numerous possible ground states are allowed and the supremacy of any one of them could require really fine tuning of microscopic parameters. In this respect, even if such a charge density modulation were observed, the question whether it helps understanding the mechanism of superconductivity or not would still need to be answered.

Acknowledgments

We acknowledge discussions and collaborations with B. S. Dennis, M. V. Klein and A. N. Lavrov.

References

[1] M. A. Kastner *et al.*, Rev. Mod. Phys. **70** (1998) 897 and references therein.
[2] J. G. Bednor and K. A. Müller, Z. Phys. B - Condensed Matter **64** (1986) 189.
[3] B. Keimer *et al.*, Phys. Rev. B **46** (1992) 14304.
[4] I. Bo ovic *et al.*, Phys. Rev. Lett. **89** (2002) 107001.
[5] B. Büchner *et al.*, Phys. Rev. Lett. **73** (1994) 1841.
[6] J. M. Tranquada *et al.*, Nature **375** (1996) 561.
[7] B. Keimer and M. Reehuis, private communications.
[8] A. Go ar *et al.*, Phys. Rev. Lett. **93** (2004) 027001.
[9] A. Go ar *et al.*, Phys. Rev. B **68** (2003) 052511.
[10] Y. Horibe, Y. Inoue and Y. Koyama, Phys. Rev. B **61** (2000) 11922; Y. Inoue, Y. Horibe, and Y. Koyama, Phys. Rev. B **56** (1997) 14176.
[11] A. N. Lavrov *et al.*, Phys. Rev. Lett. **87** (2001) 017007.
[12] Y. Ando *et al.*, Phys. Rev. Lett. **87** (2001) 017001.
[13] Y. Ando *et al.*, Phys. Rev. Lett. **88** (2002) 137005.
[14] Y. Ando, A.N. Lavrov, and S. Komiya, Phys. Rev. Lett. **90** (2003) 247003.
[15] S. Wakimoto *et al.*, Phys. Rev. B **60** (1999) R769.
[16] M. Matsuda *et al.*, Phys. Rev. B **65** (2002) 134515.
[17] A.N. Lavrov, S. Komiya, and Y. Ando, Nature **418** (2003) 385.
[18] R. Coldea *et al.*, Phys. Rev. Lett. **86** (2001) 5377.
[19] S. Chakravarty, B. I. Halperin and D. R. Nelson, Phys. Rev. B **39** (1989) 2344.
[20] N. D. Mermin and H. Wagner, Phys. Rev. Lett. **17** (1966) 1133.
[21] T. Thio *et al.*, Phys. Rev. B **38** (1988) 905.
[22] M. Matsuda *et al.*, Phys. Rev. B **42** (1990) 10098; H.-Q. Ding, Phys. Rev. Lett. **68** (1992) 1927.
[23] A. W. Sandvik *et al.*, Phys. Rev. B **57** (1998) 8478.

[24] Rajiv R. P. Singh, Phys. Rev. B **39** (1989) R9760.
[25] J. Loren ana, J. Eroles and S. Sorella, Phys. Rev. Lett. **83** (1999) 5122.
[26] I. D yaloshinskii, J. Phys. Chem. Solids **4** (1958) 241.
[27] T. Moriya, Phys. Rev. **120** (1960) 91.
[28] T. Moriya, Weak Ferromagnetism, Ch. 3 in Magnetism, Vol. 1, ed Rado and Suhl, Academic Press (1963).
[29] L. Shekhtman, A. Aharony and O. Entin-Wohlman, Phys. Rev. Lett. **69** (1992) 836; L. Shekhtman, O. Entin-Wohlman and A. Aharony Phys. Rev. Lett. **47** (1993) 174.
[30] C. J. Peters *et al.*, Phys. Rev. B **37** (1988) 9761.
[31] M A. Kastner *et al.*, Phys. Rev. B **38** (1988) 6636.
[32] P. W. Anderson, Phys. Rev. **86** (1952) 694.
[33] A. Aharony *et al.*, Phys. Rev. Lett. **60** (1990) 1330; R.J. Gooding *et al.*, Phys. Rev. B **55** (1997) 6360.
[34] J. M. Tranquada *et al.*, Nature **429** (2004) 534 and references therein.
[35] B. Keimer *et al.*, Z. Phys. **91** (1993) 373.
[36] T. Thio *et al.*, Phys. Rev. B **41** (1990) 231.
[37] F. Keffer, Handbuch der Physik, ed. S Flügge, Springer-Verlag, Berlin (1966).
[38] S. Ono *et al.*, http://xxx.lanl.gov/abs/cond-mat/0408604 (2004) preprint.
[39] J. Zaanen and O. Gunnarsson, Phys. Rev. B **40** (1989) R7391; M. Kato and K. Machida, J. Phys. Soc. Jpn. **59** (1990) 1047.
[40] S. A. Kivelson, E. Fradkin and V. J. Emery, Nature **393** (1998) 550.
[41] A. R. Moodenbaugh *et al.*, Phys. Rev. B **38** (1988) 4596.
[42] J. M. Tranquada *et al.*, Phys. Rev. Lett. **78** (1997) 338.
[43] K. Yamada *et al.*, Phys. Rev. B **57** (1998) 6165.
[44] J. M. Tranquada *et al.*, Nature **375** (1995) 561; J. M. Tranquada *et al.*, Phys. Rev. B **54** (1996) 7489.
[45] M.V. Zimmermann *et al.*, Europhys. Lett. **41** (1998) 629.
[46] M.K. Crawford *et al.*, Phys. Rev. B. **44** (1991) R7749.
[47] J.D. Axe *et al.*, Phys. Rev. Lett. **62** (1989) 2751.
[48] Judith A. McAllister, and J. Paul Attfield, Phys. Rev. Lett. **83** (1999) 3289.
[49] I. Ohana *et al.*, Phys. Rev. B **39** (1989) 2293.
[50] S. Sugai *et al.*, Phys. Rev. B **39** (1989) 4306.
[51] W.H. Weber *et al.*, Phys. Rev. B **38** (1988) 917.
[52] T.R. Thusrton *et al.*, Phys. Rev. B **39** (1989) 4327.
[53] G. Burns *et al.*, Phys. Rev. B **42** (1990) R10777.
[54] M. Dumm *et al.*, Phys. Rev. Lett. **88** (2002) 147003.
[55] A. Manthiram, and J.B. Goodenough, J. Solid State Chem. **92** (1991) 231.
[56] D. Haskel *et al.*, Phys. Rev. Lett. **76** (1996) 439; S.-W. Han *et al.*, Phys. Rev. B **66** (2002) 094101.
[57] G. Blumberg, M.V. Klein, and S-W. Cheong, Phys. Rev. Lett. **80** (1998) 564; K. Yamamoto *et al.*, Phys. Rev. Lett. **80** (1998) 1493.
[58] Yu.G. Pashkevich *et al.*, Phys. Rev. Lett. **84** (2000) 3919.
[59] M.V. Abrashev *et al.*, Phys. Rev. B **64** (2001) 144429.

[60] S. Yoon *et al.*, Phys. Rev. Lett. **85** (2000 3297).
[61] C.H. Chen, S-W. Cheong, and A.S. Cooper, Phys. Rev. Lett. **71** (1993) 2461; C.H. Chen, and S-W. Cheong, Phys. Rev. Lett. **76** (1996) 4042.
[62] P. A. Fleury and R. Loudon, Phys. Rev. **166** (1968) 514; B. S. Shastry and B. I. Shraiman, Phys. Rev. Lett. **65** (1990) 1068.
[63] S. Sugai *et al.*, Phys. Rev. B **42** (1990) 1045.
[64] A. T. Boothroyd *et al.*, Phys. Rev. B **67** (2003) 100407.
[65] V. I. Anisimov *et al.*, Phys. Rev. Lett. **68** (1992) 345.
[66] R. J. McQueeney *et al.*, Phys. Rev. Lett. **87** (2001) 077001.
[67] P. E. Sulewsky *et al.*, Phys. Rev. Lett. **67** (1991) 3864.

SUBJECT INDEX

Printing: Strauss GmbH, Mörlenbach
Binding: Schäffer, Grünstadt